

See discussions, stats, and author profiles for this publication at: <https://www.researchgate.net/publication/377565518>

INTERMITTENT DRYING OF GUAVA FRUIT USING SOLAR PHOTOVOLTAIC ASSISTED DRYER *_{1a}

Article in *European Chemical Bulletin* · January 2024

CITATIONS

0

READS

26

4 authors, including:



Shekar .K

Ballari Institute of Technology and Management

9 PUBLICATIONS 6 CITATIONS

SEE PROFILE



Rakesh P. Tapaskar

K L E Technological University, Formerly known as B.V. Bhoomaraddi College of E...

45 PUBLICATIONS 199 CITATIONS

SEE PROFILE



Prashant Revankar

KLE Technological University

64 PUBLICATIONS 58 CITATIONS

SEE PROFILE



INTERMITTENT DRYING OF GUAVA FRUIT USING SOLAR PHOTOVOLTAIC ASSISTED DRYER

^{*1a}K. Shekar, ^{*2} Prasad B Rampure, ^{*3} Rakesh P Tapaskar, ^{*4} P.P. Revankar

^{*1}Ballari Institute of Technology and Management, Ballari, India

Visvesvaraya Technological University, Belagavi 590018, India

²KLE College of Engineering & Technology, Chikodi, India

^{3,4}KLE Technological University, Hubballi, India

a) Corresponding author: sekermail10@gmail.com

Article History: Received: 12.05.2023

Revised: 25.05.2023

Accepted: 05.06.2023

Abstract

The intermittent drying behaviors of guava were experimentally studied using a Solar Photovoltaic assisted dryer. This research aimed to investigate the performance of dryer for drying applications utilizing a Taguchi design of experiment (DoE), ANOVA analysis. The drying experiments were carried for drying guava fruit of varying thickness from 2 to 7 mm and with different intermittent ratios ($\alpha = T_r / (T_r + T_t)$), where T_r and T_t are the rest time and total (heating and tempering) time for each 60 minutes' duty cycle $\alpha = 0, 0.25, 0.5$ and 0.75 , respectively. The drying regime was observed all through a major falling rate. The study articulates that intermittent ratio and fruit thickness considerably effects dehydration process. The intermittency ratio of 0.25 resulted in optimum drying rate, reducing the effective drying time. Solar radiation is measured was ranged from 251 to 956 W/m². The maximum collector & dryer efficiency was 70% & 18% respectively. The biological test resulted showed the suitability of safe consumption. The statistical analysis shows, that the Henderson & Pabis and logarithmic model is a preferred to explain intermittent drying nature of Guava fruit.

Keywords: Intermittent Drying, intermittent ratio, Guava fruit drying. Antioxidant activity.

1. INTRODUCTION

Guava is a "super-fruit" of a Myrtaceae fruit family owing to its antioxidant and phenols virtue [1,4]. India leads guava production, followed by China [2, 3]. The purpose of dehydration is to remove water content to an optimal value such that no degrading microbial reactions are encouraged. In conventional drying continual heat is delivered throughout the dehydrating resulting in surface hardening of the product owing to less moisture at surface. Thus, it causes quality degradation by

reducing drying rate and wastage of high-grade heat energy. The strategy of intermittent drying permits enough time for the moisture to mitigate at the surface from the center through the tempering period. The antioxidant properties and quality of dried guava slices strongly depend on pre-treatment and drying methods adopted along with drying conditions like air quality, temperature, and velocity [6]. Several constraints like medium temperature, inlet air velocity, and relative humidity, and fruit thickness influence drying kinetics. Modern-day techniques for

devising drying procedures consist of developing a numerical model of moisture transport in drying known as 'drying kinetics' [7]. Dehydration of agricultural produce is well-defined by thin layer drying mathematical models. Drying kinetics are normally evaluated experimentally by observation of drying sample mass over a period [8,9]. Dehydration process Mathematical models are employed in enhancing existing drying systems, devising new systems, and optimization of dehydration process [10]. Fick's law of diffusion is generally employed to explain the dehydration process. Moisture ratio models are used to study the drying curves to understand dehydration of agricultural produce. The dry basis Moisture content at varying temperatures and velocities is transformed into a Moisture Ratio to normalize the curves.

This research aimed to experimentally explore the effects of intermittent-ratio and thickness for guava fruit on the drying curves of guava (*Sodium guajava* L) fruit grown in the Ballari (15.1394 °N, 76.9214°E) area of Karnataka state, India, utilizing developed Micro-controller-based solar photovoltaic assisted fruit dryer. The purposes of the study were to experimentally explore the Guava fruit drying kinetics for varying drying parameters via, the effect of intermittent ratio and fruit thickness upon drying characteristics and study the fitness of semi empirical models developed by Henderson - Pabis [11], Page [12], and Wang- Singh [13] for explaining the dehydration process.

2. MATERIALS AND METHODOLOGY

2.1 EXPERIMENTAL SETUP

The schematic of the solar photovoltaic assisted fruit dryer setup is shown in Figure1. The dryer was used for experimental work, which assured required drying environments over a range of operational conditions. The drier comprises of 2mx1msolar flat plate collector with integral fins on selectively black coated 1mm absorber plate on 25mm glass wool insulated base and a two-drying cabinet insulated wall, two stainless steel mesh trays arranged in a vertical row (length 0.45m x width 0.45m x height 0.009m), dc fans for air circulation, and auxiliary heaters of 100w power were housed in a common air handling unit duct with two times of drying chamber. A flow control valve is utilized to regulate the hot air to the drying chamber. The hot air supply switching approach was used with four intermittent ratio α for drying fruit in a hot air cabinet. Flow control vale was used to achieve the required intermittent ratios=0, 0.25, 0.5 and 0.75, respectively ($\alpha = T_r / T_t$) where T_r and T_t are the rest time and total time of each 60 minutes' duty cycle. Thus $\alpha = 0$ indicates conventional continuous heating and 0.75 intermittency (α) refers larger rest period. Digital temperature indicator, air filter, Relay indicator (Automatic), auxiliary heater, a control panel was used to regulate the required temperature of air. Fruit mass and air flow were measured with Digital electronic balance ($\pm 0.1\text{mg}$).

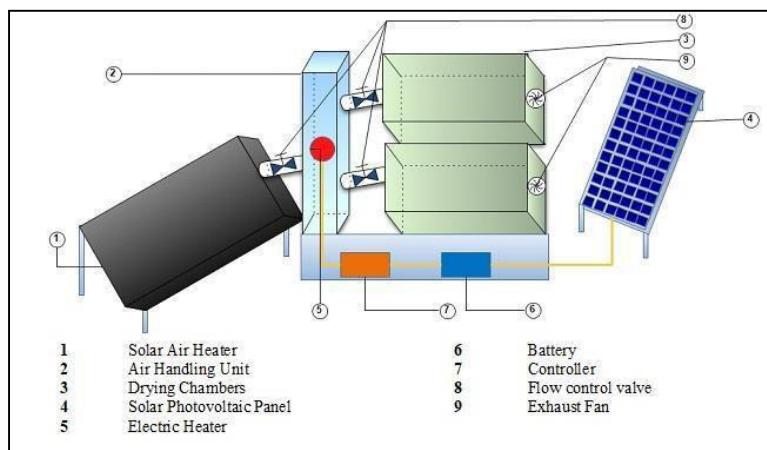


FIGURE1. Solar Photovoltaic assisted dryer Experimental setup

The trial runs were performed on 30mm fruit slice diameter guava fruit slices with thickness of 2 mm, 3 mm 5 mm, and 7mm mass of 120gms respectively. Drying experiments were performed for sunny days of May month. Solar Drier was run for 60 minutes to reach a steady-state condition Before drying experiments for the selected temperature of 64 °C hot air from 8 am to 5 pm each day. Drying chamber temperature is adjusted automatically with the help of auxiliary heater and relay. Air flows parallel through the stainless-steel wire mesh trays, on which the samples were arranged in a thin layer. The fruit samples during drying were weighed at every regular interval and later the readings were used for evaluation of drying curves. The process of drying was carried till the fruit reached equilibrium moisture content (EMC). The dry sample was cooled down till room temperature and packed in heat-sealed vacuum-packed LDPE (low-density polyethylene) bags. The final fruit mass was evaluated corresponding to a known initial mass, ahead of the experiment and the initial fruit moisture content, using

equation (1) [14]

$$M_R = \frac{M_i - M_e}{M_o - M_e} \text{----- (1)}$$

Where M_R is Moisture Ratio, M_i is Instantaneous Moisture content of the sample, M_e is Moisture content at equilibrium, M_o is Initial Moisture content.

2.2 TAGUCHI STATISTICALDESIGN

The guava dehydration process was carried out under different combinations of thicknesses and intermittent heating-tempering ratio, employing triplicate readings for each experiment, and averaged reading is used to calculate the effect. The Drying time and Equilibrium moisture content (EMC) were tabulated through weight lost by comparing initial and final fruit mass. The experimental combination of process parameter followed the Taguchi design using Minitab 17 software.

Table;1 Design matrix

Intermittent Ratio	Air Velocity	Air Temperature	Rh	Fruit Thickness	Intermittent Ratio	Air Velocity	Air Temperature	Rh	Fruit Thickness
	in m/s	in °C		in mm		in m/s	in °C		in mm
0	0.5	60	46	2	0.5	0.5	68	52	3
0	1	64	48	3	0.5	1	70	50	2
0	1.5	68	50	5	0.5	1.5	60	48	7
0	2	70	52	7	0.5	2	64	46	5
0.25	0.5	64	50	7	0.75	0.5	70	48	5
0.25	1	60	52	5	0.75	1	68	46	7
0.25	1.5	70	46	3	0.75	1.5	64	52	2
0.25	2	68	48	2	0.75	2	60	50	3

The design matrix provides the best probable combination of operational conditions of the model by decreasing total trial experiments. In this experimental work the dehydration process was carried out varying intermittent ratio, velocity, and fruit thickness, as they make a significant impact on the drying behavior of guava fruit. The 5 factors were coded at 4 levels of variation resulting 16 runs of experiments as indicated in fig 2. The curve-fitting is used to determine drying constants and coefficients for chosen

empirical models. The results of the models were validated through commonly used statistical indicators for fruit drying models such as adjusted coefficient of determinant R^2 .

In this experiment, the variables explored were intermittent ratio, temperature, air velocity, relative humidity, and fruit thickness, the possible combinations of exploratory variables with their ranges, and the experimental design is depicted in Tables 1 and 2.

TABLE:2 The Exploratory Variable

Exploratory Variable	Variable Ranges			
Intermittent Ratio	0	0.25	5	0.75
Air Velocity (m/s)	0.5	1	1.5	2
Temperature (°C)	60	64	68	70
Relative Humidity	46	48	50	52
Fruit Thickness in mm	2	3	5	7

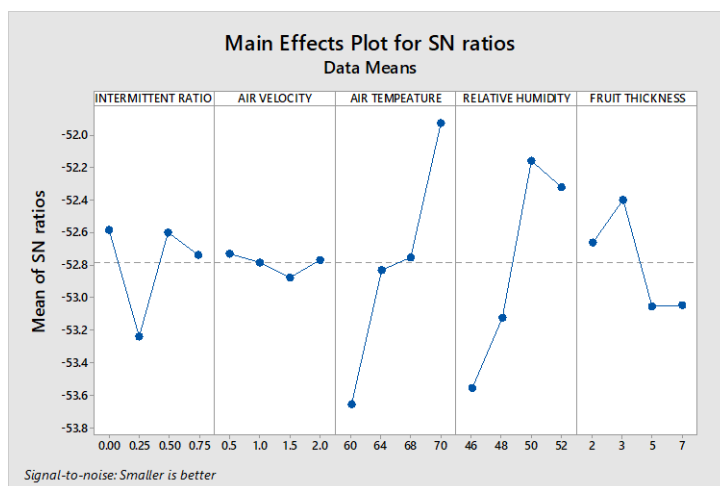


Figure 2: Signal to Noise Ratio plot

The figure 3 indicates the SN curve related to the selected parameter such as Intermittent Ratio and fruit thickness, the $\alpha=0.25$ and thickness 5mm shows the optimum combination for the present study by considering least drying time as a response variable.

The thermal performance of collector and dryer was assessed utilizing the equations [15,16,] given below.

$$Q_u = A[S - U_L(T_{pm} - T_a)] \quad 2$$

$$U_L = U_g + U_b + U_s \quad 3$$

$$U_b = \frac{t_{bottom}}{K_i} \quad 4$$

$$U_s = \frac{(L_1 + L_2) * L_3 * K_i}{L_1 * L_2 * t_s} \quad 5$$

$$U_g = \left\{ \frac{N}{\frac{C}{T_{pm}} \left[\frac{T_{pm} - T_a}{N + f} \right]} e \right\} + \frac{A_1}{B_1 + C_1 - N} \quad 6$$

$$A_1 = \sigma (T_{pm}^2 + T_a^2) (T_{pm}^2 + T_a^2) \quad 7$$

$$B_1 = (\epsilon_p + 0.0591 N h_w)^{-1} \quad 8$$

$$h_w = 2.8 + 3.0 V_w \quad 9$$

$$C_1 = \frac{2N + f - 1 + 0.0133 \epsilon_p - N}{\epsilon_g} \quad 10$$

$$f = (1 + 0.089 * h_w - 0.1166 * h_w * \epsilon_p) * (1 + 0.07866 * N) \quad 11$$

$$e = 0.430 \left(1 - \frac{100}{T_{pm}} \right) \quad 13$$

$$T_{pm} = T_{fi} + \frac{Q_u/A}{F_R U_L} (1 - F_R) \quad 14$$

$$T_{fm} = T_{fi} + \frac{Q_u/A}{F_R U_1} (1 - F''') \quad 15$$

$$F_R = \frac{m \times C_p}{A \times U_L} \left[1 - e^{-\frac{U_L A F''}{m \times C_p}} \right] \quad 16$$

$$F' = \left[1 + \frac{U'_L}{h_e} \right]^{-1} \quad 17$$

$$h_e = h_{fp} \left(1 + \frac{2 \times l_f \times \phi_f \times h_{ff}}{W \times h_{fb}} \right) + \frac{h_r h_{fb}}{h_r + h_{fb}} = \quad 18$$

$$\phi_f = \frac{\tanh^* mlf}{mlf} \quad 19$$

$$mlf = \left[\frac{2 \times h}{K \times t_{fin}} \right]^{0.5} * H \quad 20$$

$$h_{fb} = h_{fp} = \frac{N_u K}{d_e} \quad 21$$

$$d_e = \frac{4 \times (l1 \times l2)}{2 \times (l1 + l2)} \quad 22$$

$$U'_L = U_t + \frac{h_r U_b}{h_r + h_{fb} + U_b} \quad 23$$

$$h_r = F * 4 * \varepsilon_g * \sigma * \left[\frac{T_g + T_{sky}}{2} \right]^3 \quad 24$$

$$\eta_i = \frac{Q_u}{A \times S_p} \times 100 \quad 26$$

$$\eta_d = \frac{M_w * h_{fg}}{A_p * S * t_d} \times 100 \quad 27$$

Table 3 Selected thin layer drying models.

Sl. No.	Model name	Model
1	Page model (A)	$MR = \exp(-kt^n)$
2	Henderson & Pabis (B)	$MR = a * \exp(-kt)$
3	Wang & Singh (C)	$MR = 1 + at + bt^2$

Where a, b, k, and n, are drying coefficients k is the drying constant in min^{-1} and t is the drying time in min. The values of parameters for different models for thin layer drying at optimum temperatures, intermittent ratio, velocity, and fruit thickness utilizing the Analysis of variance method and presented in table 3

3.2 Biological analysis of sample

The dried guava slices were subjected to microbiological analysis to determine the product quality in terms of Antibacterial Activity, Antioxidant activity and Nutritional value. [17,18,19]

Determination of Antibacterial Activity

The bacterial colonies and fungal growth in dried samples were analyzed via pour plate method in two-stage that involving sample preparation and examination respectively. In first stage saline (Na Cl) solution was prepared in two separate beakers and mixed with dried fruit samples. The sterilized samples material was distributed on two Petri dish plates and then nutrient agar medium was added with to enable bacterial growth. The procedure for fungal growth analysis used 1 ml of sterilized sample poured on Petri-dish plates and added dextrose agar medium for enabling fungal

growth during 3 to 4 days of solidification on Petri-dish placed in room temperature. After sample preparation the samples were examined for bacterial colony growth the microbial count in Quebec colony counter.

Determination of Antioxidant Content

Free radical scavenging ability of the methanol extract dried samples was tested by 1,1-diphenyl-2-picryl hydroxyl (DPPH) radical scavenging assay. The hydrogen atom donating ability of the dried sample extracts was determined by the de-colorization of methanol solution of (DPPH). 1 mL of different concentrations dried extract was added to 3 mL of 0.1mm methanolic solution of DPPH. The changes in absorbance of samples were measured at 517nm. A control reading was obtained using methanol.

Determination of Nutritional Composition

Nutritional value of the dried fruit was assessed by total fat, protein, carbohydrate energy and crude fiber was determined using respective standard protocol according to the standard procedure as mentioned in table 4.

Table:4 Nutrients analyzed

Sl No	Selected Parameter	Protocol
1	Total Fat	IS:12711: 1989
2	Total Protein	IS: 7219 : 1973
3	Carbohydrate	IS:1656: 2013
4	Energy	TAL/SOP/CM/122/00
5	Crude Fiber	IS: 10226 (Part 1) :1982

RESULTS AND DISCUSSION

The variation of Moisture content (MC) reduction with a drying time is illustrated by figure 3. It is observed the drying time

for intermittent drying is longer than the continuous drying. The moisture removal rate was faster at higher temperatures and the drying time shortened considerably as air temperature increased.

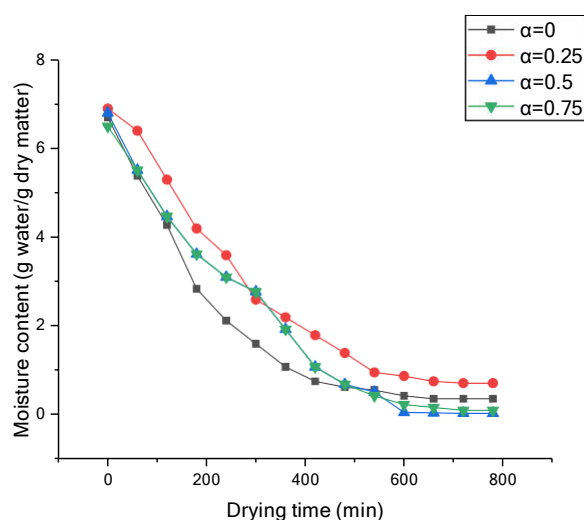


FIGURE 3 Variations of Moisture Content Vs Drying Time

It is observed that for a slice thickness of 5 mm, 1.5 m/s velocities, an intermittent ratio of 0.25 required 610 minutes, whereas 700 minutes was required for attaining EMC at 0.75 intermittent ratios. The soothing period substantially influenced the rate of drying as moisture mitigation from the center to the exterior controls the drying process. This agrees with the former research [20].

It is noted that intermittent ratio and temperature have a key influence on the drying rate. The increase of air temperature during the heating, increased the moisture removal rate. In Contrast increase in the tempering period in the heating cycle reduces the moisture removal as temperature difference at the surface of the fruit reduces.

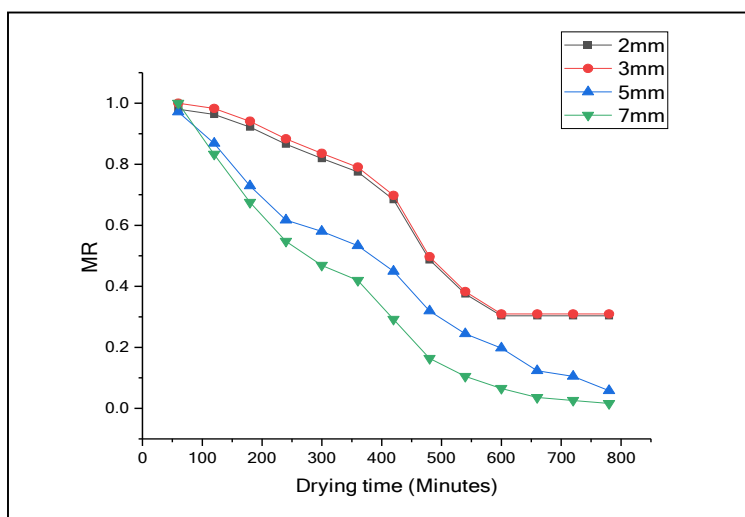


FIGURE 4 Variations of Moisture Ratio Vs Drying Time

Figure 4 Illustrates the change in Moisture Ratio with drying time for different thickness at 64°C air temperature. It is seen that a rise in slice thickness extends the total drying time. The total effective drying time reduces by 25% when compared with thickness from 7 mm to 2 mm, further

thickness reduction from 3mm to 2 mm reduced the total drying time. It is observed that the moisture removal is faster during the start of the dehydration and reduces as the drying continues, indicating an exponential reduction of the moisture ratio along the drying time.

TABLE:5 Estimated Drying model parameters

Fruit	Fruit Thickness	Model	Constant	Drying coefficient			Statistical Indicator
	in mm		k (min ⁻¹)	a	b	n	
Guava	3	1	0.00162	-----	-----	1.49	0.95
	5		0.00139	-----	-----	1.56	0.97
	7		0.00178	-----	-----	1.46	0.94
	3	2	0.00488	1.21	-----	0.948	0.96
	5		0.00469	1.32	-----	0.958	0.98
	7		0.0039	1.37	-----	0.967	0.95
	3	3	-----	0.0015	0.08	0.948	0.94
	5		-----	0.0028	0.05	0.958	0.95
	7		-----	0.0018	0.06	0.967	0.93

The selected model was fitted to the experimental data using the nonlinear regression. The higher the value of the coefficient of determination (R^2) were chosen as the criteria for goodness of fit. The estimated parameters and results of the statistical analysis for the models are summarized in Table 5. It is observed from

the tabulated results that high coefficients of determination were obtained for Henderson - Pabis gave higher values of R^2 (0.98). The predicted and experimental values showed the suitability of the Henderson - Pabis equation in describing the intermittent drying behavior Guava Fruit.

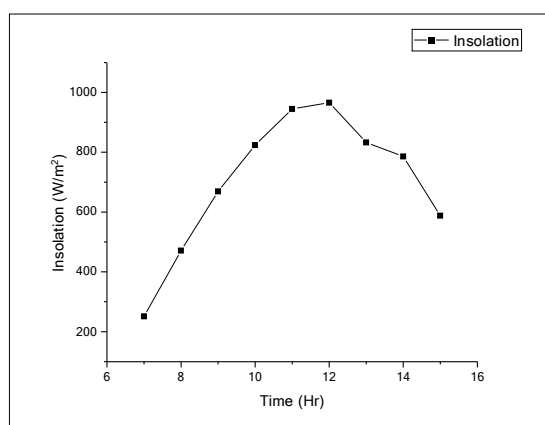


FIGURE 5: Variation of Insolation Vs Time

Figure 5 illustrates the variation of insolation along with time, it is observed that the solar insolation gradually increased in value till solar noon and remains constant with a value of 987 W/m^2 till 13:00 hrs. and reduces gradually to lower value by 17:00 hrs.

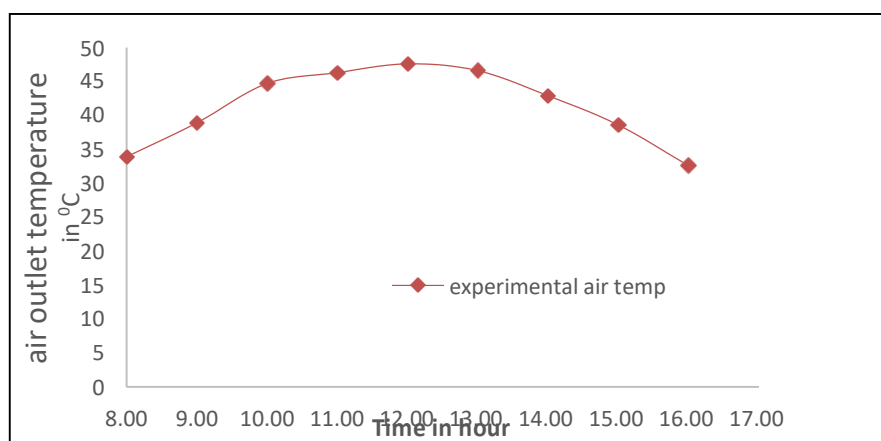
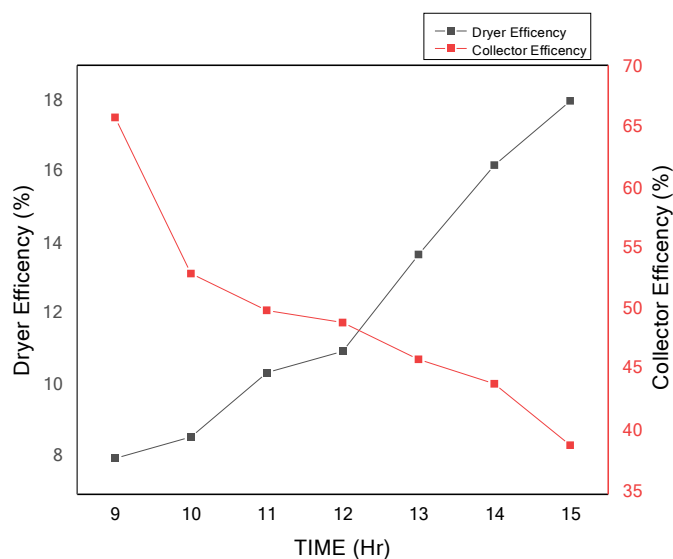


FIGURE 6. The Air outlet temperature Vs Time

Figure 6 depicts variations in exit air temperature of air heater with time for the month of June. The highest recorded air temperature was 48°C for a mass flow of 0.03 kg/s during the period close to solar noon.



Figure; 7 Variation of Experimental thermal efficiency

Figure 7 depicts Variation of Experimental thermal efficiency of SPV assisted collector and Dryer efficiency along time. lower values during period close to solar noon owing to higher inlet air temperatures that contributed to enhanced heat losses. The earlier and later part of the day exhibited a better instantaneous efficiency due to lower thermal losses. The dryer efficiency exhibited a reducing trend from 17 % to 8% as the available moisture to evaporate was reduced . The dependance of losses indicated that the efficiency of 68 percent

for mass flow rate of 0.03 kg/s .

Biological analysis

The bacterial activity studies revealed that the microbial count on intermittently dried guava slice were within safe limit 2 log10cfu/g ((less than 8.0log10cfu/g)) for fruits [20], however fungal growth was visually not observed in 0.1ml samples through microscope.

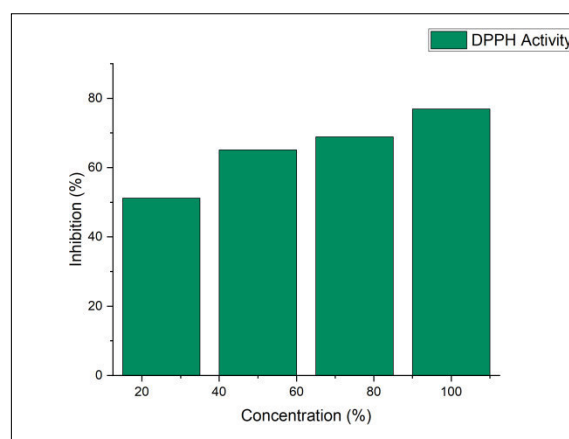


FIGURE 8: DPPH Percentage inhibition v/s sample solution concentration

The figure 8 Illustrates DPPH radical scavenging assay to determine antioxidant activity. The changes in absorbance of samples were measured. The tests were performed in triplicate and the graph was plotted with the mean values of inhibition percentage against the concentration of the

sample solutions. The mean activity was found to begin at 48 % and showed maximum activity of 75%. The dried product had Antioxidant activity value of 51.2 mg/ml that amounted to less than 1% of fresh fruit value of chosen variety of guava fruit.

Table 6: Dried guava sample Nutrient contents

Sl No	Parameters	Units	Dried Sample	Fresh Fruit	Difference
1	Total Fat	G/100g	0.1	0.42	0.32
2	Total Protein	G/100g	3.1	2	-1.1
3	Carbohydrate	G/100g	78	81	3
4	Energy	K. Cal/100g	324.8	334.6	9.8
5	Crude Fiber	G/100g	1.1	2.9	1.8

The intermittently dried product nutritional value of the essential nutrients per 100 gram indicate an 0.32, 3, 1.8 grams' reduction of total fat, carbohydrate and crude fiber and 9.8 K Cal drop in Energy content in comparison with fresh guava fruit (allabhad safada variety). The microbiological analysis highlighted the suitability of Solar Photovoltaic assisted dryer for intermittent drying application.

4 CONCLUSIONS

The intermittent drying behavior of guava fruit was studied in the present experimental study as a function of varying drying conditions. Fruit slice thickness, as well as the intermittent ratio, was found to be a significant parameter affecting intermittent drying behavior of guava slices. A higher resting period resulted in a lower drying rate because of reduced air heat supply to the product besides the slower movement of moisture within the structure. The complete drying regime happened in the falling period. Fruit

thickness, drying medium temperature, and intermittent ratio affect the total drying time predominantly.

In a heating cycle of 60 minutes, 45 minutes of heating and 15 minutes of resting period allows the moisture present in the fruit layer to mitigate to a surface which can be removed in the next heating cycle. The slice thickness of 5mm and intermittent ratio of 0.25 resulted in an increased drying rate consequently resulting in better moisture mitigation ratio during drying.

It was observed that the maximum collector thermal efficiency and Dryer efficiency were 65.7% and 18%, respectively. The dryer efficiencies improved with time as the moisture content of the produce reduced and it was found between 8 and 18.6% during day. The microbial count on intermittently dried guava slice is found to be within safe limit for fruits. The dried product had Antioxidant activity value of 51.2 mg/ml that amounted to less than 1% of fresh fruit value. The dried product nutritional value of the essential nutrients

per 100 grams for Total fat, Total protein, Carbohydrate, Energy and Crude fiber were 0.1 g, 3.1, 78 g, 324.8 kcal and 1.1 g respectively. The microbiological study highlighted the suitability of Solar Photovoltaic assisted dryer for intermittent drying application.

The statistical analysis indicates Henderson - Pabis model ($R^2=0.982$) as the most appropriate model to describe the defining guava fruit intermittent drying indicating the suitability of Solar Photovoltaic assisted dryer for intermittent drying application.

REFERENCES

1. Somogyi, L. P., Barrett, D. M., Hui, Y. H., Processing Fruits: Science and Technology - Major processed product, (Technomic Publishing, Inc., Lancaster, Pennsylvania, 1996).
2. Jagtiani, J, Chan, H. T, Sakai, W. S., Guava in Tropical fruit processing (New York Academic Press, 1998).
3. Lim Y. Y and Murtijaya J, Antioxidant properties of Phyllanthus amarus extracts as affected by different drying methods, *Food Science and Technology*, 40(9), 2007, 1664-1669.
4. Dattatreya M, Kadam, Pratibha Kaushik and Ramesh Kumar, Evaluation of Guava Products Quality, *International Journal of Food Science and Nutrition Engineering*, 2(1), 2012, 7-11.
5. Panchariya, P. C., Popovic, D., Sharma, A. L., Thin Layer Drying modeling of black tea process, *Journal of Food Engineering*, 52, 2002, 349 - 357.
6. Henderson, S. M., Progress in developing the thin layer equation, *Transactions of ASAE*, 17, 1974, 1167-1172.
7. Hernandez, J. A., Pavon, G., Garcia, M. A., Analytical solution of mass transfer equation considering shrinkage for modeling food drying kinetics, *Journal of Food Engineering*, 45, 2000, 1 - 10.
8. Mujumdar, A. S., Handbook of industrial drying, (Marcel Dekker, New York, 1987.) 1-40.
9. Menges, H. O., Ertekin, C., Modeling of air drying of Hacihaliloglu-type apricots, *J Sci Food Agric.*, 86, 2006, 279-291
10. S. K. Modi, M. Basavaraj and others, "Effect of moisture content and temperature on thermal conductivity of Psidium guajava L. by line heat source method (transient analysis)," *International Journal of Heat and Mass Transfer*, vol. 78, pp. 354-359, 2014.
11. Henderson, S. M., Pabis, S, Grain drying theory. II. Temperature effects on drying coefficients, *J Agric Engg.*, 6, 1961, 168 - 174.
12. Page, G. E., Factors influencing the maximum rates of air drying shelled corn in thin layers. Unpublished M.S. thesis, Department of Mechanical Engineering, Purdue University, Purdue, USA, 1949.
13. Wang, C. Y., Singh R. P., A single layer drying equation for rough rice, ASAE Paper No. 78-3001, ASAE, St Joseph, MI, 1978.
14. Moghimi, P., H. Rahimzadeh, and A. Ahmadpour. "Experimental and numerical optimal design of a household solar fruit and vegetable dryer." *Solar Energy* 214 (2021): 575-587.
15. Kumar, Rajesh, and Prabha Chand. "Performance enhancement of solar air heater using herringbone corrugated fins." *Energy* 127 (2017): 271-279.
16. Bisht, Vijay Singh, Ankit Singh Bisht, and Pooja Joshi. "Theoretical Study of Solar Air Heater Using MATLAB." *Advances in*

- Interdisciplinary Engineering*. Springer, Singapore, 2019. 715-724.
17. Venkatachalam, Ravi Narayan, Kanchanlata Singh, and Thankamani Marar. "Phytochemical screening in vitro antioxidant activity of Psidium guajava." *Free Radicals and Antioxidants* 2.1 (2012): 31-36.
 18. Tan, Si, et al. "The effects of drying methods on chemical profiles and antioxidant activities of two cultivars of Psidium guajava fruits." *LWT* 118 (2020): 108723.
 19. Kumar, Manoj, et al. "Guava (Psidium guajava L.) leaves: nutritional composition, phytochemical profile, and health-promoting bioactivities." *Foods* 10.4 (2021): 752.
 20. Lima, Leiliane Silva Lopes, et al. "Study of Continuous and Intermittent Drying of Pear Through Mathematical and Diffusion Models." *Journal of Agricultural Studies* 10.1 (2022): 29-47.
 21. Van Engeland, Charlotte, et al. "Comprehensive analysis of intermittent drying. A theoretical approach." *Food and Bioprocess Processing* 131 (2022): 86-101.

NOMENCLATURE

M_R	Moisture Ratio	h_w	Convective heat transfer coefficient between glass cover and ambient, W/m ² K
M_i	M_i is Instantaneous Moisture content in kg H ₂ O/kg dry material	ε_p	emissivity for absorber plate
M_e	M_e is Moisture content at equilibrium in in kg H ₂ O/kg dry material	ε_g	emissivity of cover
M_O	M_O is Initial Moisture in kg H ₂ O/kg dry material	m	Mass flow rate, m/s
Q_u	Useful heat gain	F_R	collector heat removal factor
A	Area of the collector in m ²	F'	Efficiency factor of the solar air heater
S	Hourly insolation upon collector W/m ²	FR	Heat removal factor for the solar air heater
T_{pm}	Mean Plate Temperature in °C	h_w	Convective heat transfer coefficient between glass cover and ambient, W/m ² K
T_a	Ambient temperature °C	h_{fp}	Convective heat transfer coefficient between the absorber plate and the air stream, W/m ²
U_L	overall loss coefficient	h_{fb}	Convective heat transfer coefficient between the bottom plate and the air

			stream, W/m ²
U_g	top loss coefficient	h	Convective heat transfer coefficient between the bottom plate and the air stream, W/m ²
U_b	bottom loss coefficient	K_{fin}	Thermal Conductivity of fin in W/mK
U_s	Side loss coefficient	t	thickness of the fin
d_e	Equivalent diameter of the air tunnel, m	H	distance between the absorber plate and the glass cover
K_i	Thermal Conductivity of Insulation in	W	Distance between fins, m
N	number of transparent covers	N_u	Nusselt number
C	Specific heat of air at constant pressure, J/kgK	η_i	Efficiency of solar air collector
T_{pm}	mean absorber surface temperature	η_d	Efficiency of solar dryer
T_a	ambient temperature	M_w	Mass of water evaporated, kg
f	friction factor	h_{fg}	Latent heat of evaporation, J/kg
T_{fi}	Mean fluid temperature, K	t_d	Drying time, hour
T_g	Cover plate Temperature in °C	α	Intermittent ratio
τ	Transmittance of glass cover	T_r	Rest time, min
T_0	Fluid outlet temperature, K	T_t	Total time (in duty cycle), min
V_w	velocity of air, m/s		

ISSN 2063-5346



A STUDY OF ORIENTATED CANTILEVER BEAM MOUNTED WITH TIP MASS AND BOUNDED WITH PZT-5A AND PZT-5H FOR VIBRATION ENERGY HARVESTING.

Laxmi.B.Wali ^{1, a *}, T.K.Chandrashekar ^{2, b}, Manjunath N ^{3, c},
Manjunatha T H ^{4, d}

Article History: Received: 10.05.2023

Revised: 29.05.2023

Accepted: 09.06.2023

Abstract

Energy harvesting is extracting energy from ambient sources. Vibration is one the energy source available freely in surrounding environment. Research on vibration energy harvesting have received the attention of many researchers to power wireless sensors and low-power electronic devices from smart materials. In this paper, the effect of PZT-5A and PZT- 5H piezoelectric material on the cantilever beam mounted with tip mass and oriented at 10^0 , at the resistance of 1500 ohms is studied. MatLab program is developed considering the Euler Bernoulli beam assumptions, constitutive equations of piezoelectric material and Hamilton's principle. The MatLab program is validated with the previous work on orthonormalisation electromechanical finite element unimorph beam and good agreement is obtained.

Keywords: Orientation, Piezoelectric Material, Vibration, Energy harvesting, FEM.

¹Assistant Professor, Department of Mechanical Engineering, RNSIT, VTU, Bengaluru, Karnataka, INDIA

²Associate Professor, Department of Mechanical Engineering, RNSIT, VTU, Bengaluru, Karnataka, INDIA

³Assistant Professor, Department of Mechanical Engineering, RNSIT, VTU, Bengaluru, Karnataka, INDIA

⁴Associate Professor, Department of Mechanical Engineering, BITM, Ballari, Karnataka, INDIA

^a laxmibwali@gmail.com, ^b tkcmite@gmail.com, ^c manju.badri@gmail.com, ^d manjunatha.th@bitm.edu.in

DOI:10.48047/ecb/2023.12.9.160

Introduction

In the recent years, many researchers are attracted towards the area of energy harvesting from various sources available in the surrounding environment [1]. Energy from vibration is one of source which is available freely from machines, human motion having low frequency vibration excitation which can be used to meet the demand without depending on conventional sources. Research in the area of energy harvesting is increasing with the development of smart electronic devices. Limitation in batteries capacity to power the devices and life span for supplying continuous energy for wireless technologies necessitate for energy harvesting. Smart structures based on piezoelectricity are currently generating a demand and piezoelectric material forms the alternate source for the creation of lifelong energy harvesters with compact configuration which will be utilized in engineering and medical applications. Research of piezoelectric elements in energy conversion applications necessitates a thorough understanding of solid mechanics and geometrical shapes [2]. Researchers have focused on analytical and numerical studies of unimorph and bimorph beam which forms the basis for the study of energy harvesting [3-5] due to its compatibility and ease of applications. Authors have studied experimentally, the effect of orientation of beam by attaching harvester to human leg and concluded that optimum results are obtained for 70° orientation of harvester with reference to coordinate system [6]. Researchers have focused on orientation of harvester for rotational motion by changing the distance between the rotating center and fixed end of beam [7]. A study on configurations of energy harvester for IoT sensor applications in smart cities [8] and optimal location of piezoelectric patch on the length of slat in aircraft applications is carried [9,10]. A less information is available in the literature on The shape functions are given in equation (2-5)

the study of orientation of the beam with tip mass on free end and base excitation at fixed end bounded with different piezoelectric materials [11, 12]. The aim of this work is to develop the MatLab program for the study of effect of PZT-5A and PZT 5H material on orientation of the beam with tip mass, to study voltage, current and power frequency response function (FRF) and describe its dynamic behavior. The MatLab program is validated with the previous work on orthonormalisation electromechanical finite element of unimorph beam and good agreement is obtained.

2. Methodology

The Finite element method plays the major role in the complex problem analysis. In vibration based energy harvesting, piezoelectric unimorph beam forms the basic structure. The formulation of beam with piezoelectric (PZT) layer is considered as shown in Fig.1

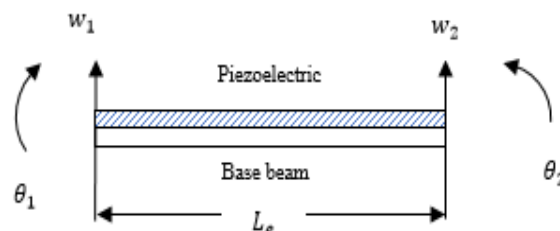


Figure 1 .Element with base beam bounded with PZT

The beam with piezoelectric has two degree of freedom at each node, transverse (w) and rotational (θ)

The displacement function of the beam element is given as

$$w(x) = c_0 + c_1x + c_2x^2 + c_3x^3 \quad (1)$$

Eqn. 1 is the displacement equation with four unknown coefficients. Applying boundary conditions at node 1 and 2 of element, the four coefficients in polynomial equation are solved.

$$[N] = [N_1 \quad N_2 \quad N_3 \quad N_4]$$

where

$$[N_1] = \left(1 - 3 \left(\frac{x}{L_e} \right)^2 + 2 \left(\frac{x}{L_e} \right)^3 \right) \quad (2)$$

$$[N_2] = \left(L_e \left(x - 2 \left(\frac{x}{L_e} \right)^2 + \left(\frac{x}{L_e} \right)^3 \right) \right) \quad (3)$$

$$[N_3] = \left(3 \left(\frac{x}{L_e} \right)^2 - 2 \left(\frac{x}{L_e} \right)^3 \right) \quad (4)$$

$$[N_4] = \left(L_e \left(- \left(\frac{x}{L_e} \right)^2 + \left(\frac{x}{L_e} \right)^3 \right) \right) \quad (5)$$

Strain $S(x)$ is represented by

$$S(x) = -z \frac{d^2 w(x)}{dx^2} = -zB \quad (6)$$

Where $B = [B_1, B_2, B_3, B_4]$

Differentiating Eq. (2-5)

$$\frac{d^2 N_1}{dx^2} = \frac{-6}{L_e^2} + \frac{12x}{L_e^3} = B_1 \quad (7)$$

$$\frac{d^2 N_2}{dx^2} = \frac{-4}{L_e} + \frac{6x}{L_e^2} = B_2 \quad (8)$$

$$\frac{d^2 N_3}{dx^2} = \frac{6}{L_e^2} - \frac{12x}{L_e^3} = B_3 \quad (9)$$

$$\frac{d^2 N_4}{dx^2} = \frac{-2}{L_e} + \frac{6x}{L_e^2} = B_4 \quad (10)$$

The electromechanical coupling of a piezoelectric can be demonstrated in two ways. In direct piezoelectric effect, an applied mechanical pressure produces a proportional voltage response and in converse effect, an applied voltage produces a deformation of the material.

The direct effect Eq.11 and the converse effect Eq.12 may be modelled as

$$\{D\} = [e]^T \{S\} + [\varepsilon^S] \{E\} \quad (11)$$

$$\{T\} = [c^E] \{S\} - [e] \{E\} \quad (12)$$

The constitutive equation for 1-dimensional form with constant electric field and strain

$$\begin{Bmatrix} T_1 \\ D_3 \end{Bmatrix} = \begin{bmatrix} c_{11}^E & -e_{31} \\ e_{31} & \varepsilon_{33}^S \end{bmatrix} \begin{Bmatrix} S_1 \\ E_3 \end{Bmatrix} \quad (13)$$

The base beam and piezoelectric plane stress field equation is given by Eq.14 and 15

$$T_1^{(1)} = c_{11}^{(1)} S_1^{(1)} \quad (14)$$

$$T_1^{(2)} = c_{11}^{(2)} S_1^{(2)} - e_{31} E_3 \quad (15)$$

$\vartheta(z) = \frac{z-z_n+h_p}{h_p}$ is the shape function over the interval $z_n - h_p \leq z \leq z_n$

$z_n = \frac{c_{11}^{(1)} h_s^2 + c_{11}^{(2)} h_p^2 + 2c_{11}^{(1)} h_s h_p}{2(c_{11}^{(1)} h_s + c_{11}^{(2)} h_p)}$ = distance from the neutral axis to the top layer of the beam with piezoelectric

$\varphi(z) = \vartheta(z)v_p$ is electrical potential

$\Omega(z)$ = first derivative of shape function $= \frac{d\vartheta(z)}{dz} = 1/h_p$,

The electric field equation

$$E_3 = -\Omega(z)v_p \quad (16)$$

where v_p = voltage

Substituting Equation (6) into Equation (14)

$$T_1^{(1)} = -zc_{11}^{(1)}B \quad (17)$$

Substituting Equation (6) and (16) into Equation (15)

$$T_1^{(2)} = -zc_{11}^{(2)}B + e_{31}\Omega(z)v_p(t) \quad (18)$$

$$D_3 = -ze_{31}B - \varepsilon_{33}^S \Omega(z)v_p \quad (19)$$

The electromechanical piezoelectric cantilever energy harvesting is formulated by the Hamiltonian principle,

$$\int_{t_1}^{t_2} [\delta(k - \dot{p} + \omega) + \delta\varpi] dt = 0 \quad (20)$$

Representation of equations in matrix form utilizing extended Hamilton's principle [3]

$$\begin{bmatrix} M & 0 \\ 0 & 0 \end{bmatrix} \begin{Bmatrix} \ddot{w} \\ \ddot{v}_p \end{Bmatrix} + \begin{bmatrix} C & 0 \\ P_{sr} & P_d \end{bmatrix} \begin{Bmatrix} \dot{w} \\ \dot{v}_p \end{Bmatrix} + \begin{bmatrix} K & P_{rs} \\ 0 & 0 \end{bmatrix} \begin{Bmatrix} w \\ v_p \end{Bmatrix} = \begin{Bmatrix} F \\ i_p \end{Bmatrix} \quad (21)$$

Element Stiffness Eq.22, mass matrix Eq.23 is given by

$$[K] = \int z^2 c_{11}^{(1)} [B^T] [B] dv^{(1)} + \int z^2 c_{11}^{(2)} [B^T] [B] dv^{(2)} \quad (22)$$

$$[M] = \int \rho^{(1)} [N^T] [N] dv^{(1)} + \int \rho^{(2)} [N^T] [N] dv^{(2)} \quad (23)$$

Adding tip mass terms to Eq. (23)

$$2I_0^{tip} x_c [N^T] \frac{d[N]}{dx} + I_0^{tip} [N^T] [N] + I_2^{tip} \frac{d[N^T]}{dx} \frac{d[N]}{dx} \quad (24)$$

Offset distance from proof mass centroid [5] is

$$x_c = \frac{\rho^{tip} b l_{tip}^2 h_{tip} + \rho^{(1)} b l_{tip}^2 h_s}{2(\rho^{tip} b l_{tip} h_{tip} + \rho^{(1)} b l_{tip} h_s)} \quad (25)$$

Zeroth and second mass moment of inertia [5] is given by

$$I_0^{tip} = \rho^{tip} b l_{tip} h_{tip} + \rho^{(1)} b l_{tip} h_s \quad (26)$$

$$I_2^{tip} = \left(\rho^{tip} b l_{tip} h_{tip} \left(\frac{l_{tip}^2 + h_{tip}^2}{12} \right) + \rho^{tip} b l_{tip} h_{tip} \left(z_n - h_p + \frac{h_{tip}}{2} \right)^2 + \left(\frac{l_{tip}}{2} \right)^2 \right) + \left(\rho^{(1)} b l_{tip} h_s \left(\frac{l_{tip}^2 + h_s^2}{12} \right) + \rho^{(1)} b l_{tip} h_s \left(-z_n - h_p + \frac{h_s}{2} \right)^2 \left(\frac{l_{tip}}{2} \right)^2 \right) \quad (27)$$

Damping matrix C is given as

$$C = \alpha M + \beta K \quad (28)$$

Mechanical Force F is given by

$$F = -Q \ddot{w}_{base} \quad (29)$$

Where

$$Q = \int \rho^{(1)} N^T dV^{(1)} + \int \rho^{(2)} N^T dV^{(2)} \quad (30)$$

Adding tip mass terms to Eq. (29)

$$-I_0^{tip} x_c \frac{d[N^T]}{dx} - I_0^{tip} [N^T] \quad (31)$$

Electromechanical coupling is given by

$$P_{sr} = - \int z \Omega(z)^T e_{31} B dV^{(2)} \quad (32)$$

Capacitance matrix is given by

$$P_D = - \int \Omega(z)^T \epsilon_{33} \Omega(z) dV^{(2)} \quad (33)$$

Transformation matrix is given by

$$T = [\cos(\theta) \ 0 \ 0 \ 0; \ 0 \ 1 \ 0 \ 0; \ 0 \ 0 \ \cos(\theta) \ 0; \ 0 \ 0 \ 0 \ 1]$$

Formulating the Eq. (21).into global matrix based on electromechanical vector transformation. Voltage, current and power frequency response function obtained by direct non-orthonormalised electromechanical dynamic equation is given by [5]

$$\frac{V_p}{-\omega w_b e^{j\omega t}} = \left[j\omega C_p - \frac{1}{R_{load}} j\omega \Theta^T * [\underline{K} - \omega^2 \underline{M} + j\omega \underline{C}]^{-1} \Theta \right]^{-1} * j\omega \Theta^T [\underline{K} - \omega^2 \underline{M} + j\omega \underline{C}]^{-1} Q \quad (34)$$

$$\frac{i}{-\omega^2 w_{base} e^{j\omega t}} = \frac{1}{R_{load}} \left\{ [C_p i\omega + R_l - \Theta^T i\omega [-\underline{M}\omega^2 + \underline{C}i\omega + \underline{K}]^{-1} \Theta]^{-1} * \Theta^T i\omega [-\underline{M}\omega^2 + \underline{C}i\omega + \underline{K}]^{-1} Q \right\} \quad (35)$$

$$\frac{P}{(-\omega^2 w_{\text{base}} e^{i\omega t})^2} = \frac{1}{R_{\text{load}}} \left\{ \left[C_p i\omega + R_l - \Theta^T i\omega [-M\omega^2 + \zeta i\omega + K]^{-1} \Theta \right]^{-1} \right. \\ \left. * \Theta^T i\omega [-M\omega^2 + \zeta i\omega + K]^{-1} Q \right\}^2 \quad (36)$$

The dynamic equations are solved assuming system response is linear under harmonic base excitation and beam is excited in transverse direction. The electromechanical piezoelectric cantilever energy harvesting beam equations are formulated by the Hamiltonian principle. The numerical work of the author [5] is extended to outline the key equations and include orientation for the electromechanical dynamic equation.

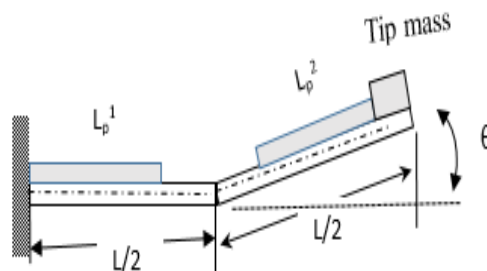


Figure 2 Orientation of Cantilever beam bounded with piezoelectric patches and tip mass at free end.

2.1 Model of orientated beam bounded with piezoelectric patches and tip mass

The study on energy harvesting is carried on cantilever beam of length 'L'. The beam is divided into two parts L/2 each, L_p^1 and L_p^2 is the length of PZT patches, h_b and h_p is the thickness of base beam and PZT patch, θ is the orientation of second half part of beam bounded with PZT patch and mounted with tip mass.

The geometrical and material property of the beam are presented in table 1. Tip mass is mounted on extended length of base beam. The length of the piezoelectric patches L_p^1 and L_p^2 is 20 mm each. The angle of orientations of the beam is 10° . The analysis of the beam is carried out using MATLAB program in the frequency range of 0 to 1000 Hz. The Cantilever beam is divided into 50 elements.

Table 1 Geometry and material properties[5,13,14]			
Length, l	50e-3 (m)	Modulus of Elasticity of the PZT -5A and PZT -5H, E_p	66 (Gpa) 62 (Gpa)
Width, b	6e-3 (m)	Density, $\rho^{(1)}$	9000 (kg/m3)
Thickness, h_b	0.5e-3 (m)	Density of the PZT -5A and PZT -5H layer, $\rho^{(2)}$	7800 (kg/m3)
Thickness of PZT, h_p	0.127e-3 (m)	Piezoelectric constant of PZT -5A and PZT -5H, e_{31}	-12.54 (C/m ²) -19.84 (C/m ²)
Modulus of Elasticity of the base beam, E_b	105 (Gpa)	Permittivity of constant strain of PZT -5A and PZT -5H ϵ_{33}	1.593×10^{-8} 3.363×10^{-8}
Length of tip mass	15 (mm)	height of tip mass	10(mm)
Density of tip mass	9000 (kg/m3)	Damping constant	$\alpha=4.886$; $\beta=1.2433e-05$

3. RESULTS

The vibration energy in the environment occur with various frequencies. To exploit the vibration energy, the frequency of the

model considered have to operate close to the vibration source. The importance to find the natural frequency is to obtain maximum output. The validation of the model is given in Table 2 and 3

Table 2 Comparison of Natural frequencies for unimorph beam without tip mass

Natural frequency	Literature paper [3]	MatLab results
1 st	47.8	47.81
2 nd	299.6	299.62
3 rd	838.2	838.93

Table 3 Comparison of First natural frequency with tip mass

Literature paper [5]	MatLab results
18.5	18.48

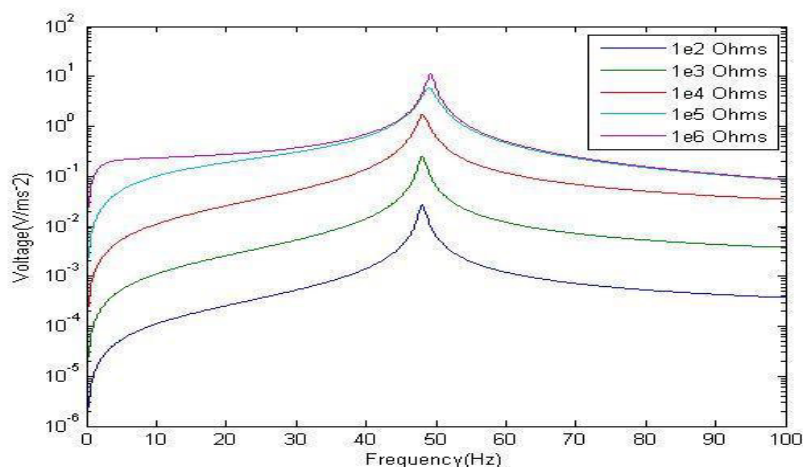


Figure 3. Plot of Voltage FRF

The MatLab program is validated with material and geometrical properties of literature paper [3] and [5] and comparison of natural frequencies of unimorph piezoelectric energy harvester beam

without tip mass and with tip mass at 0° orientation of beam is carried. The comparison of MatLab Voltage FRF with the literature paper [4] is shown in Fig. 3

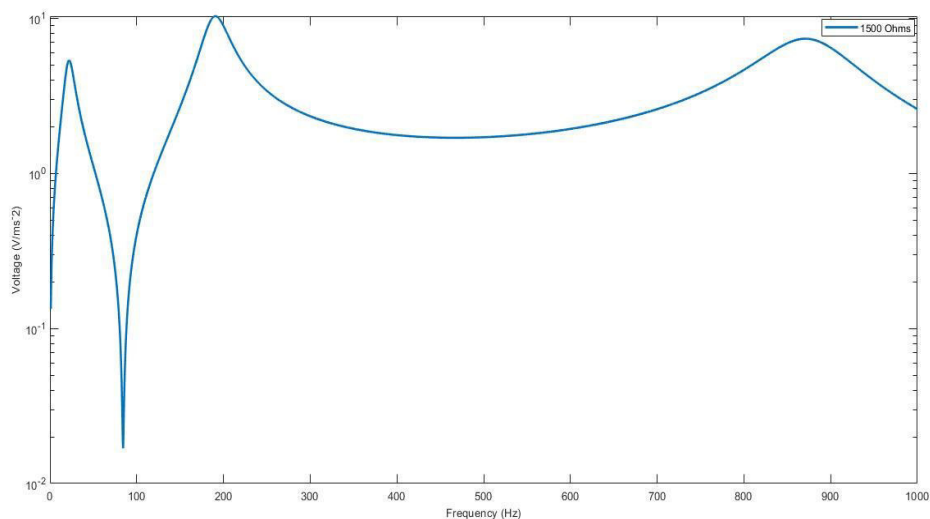


Figure 4. Voltage FRF of PZT-5A

Figure 4. Shows the voltage FRF of cantilever beam oriented at 10^0 mounted with tip mass and bounded with PZT -5A.

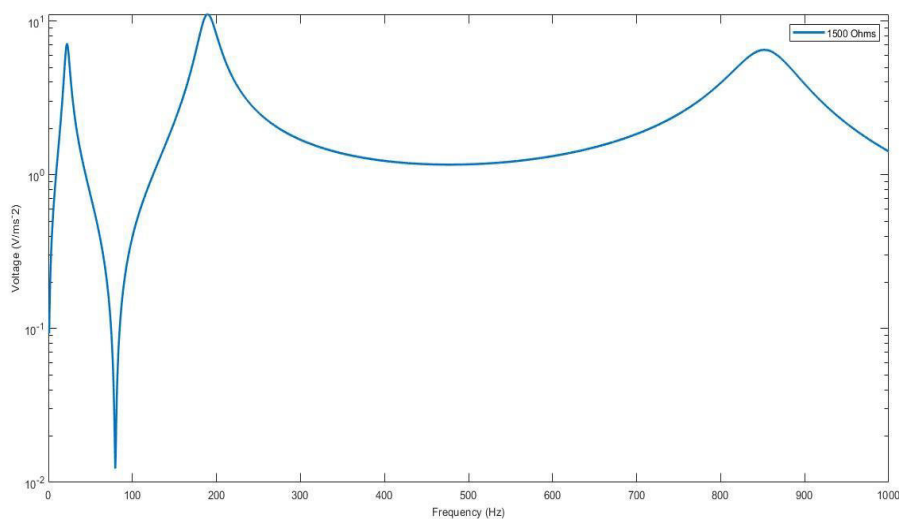


Figure 5. Voltage FRF of PZT-5H

Figure 5. Shows the voltage FRF of cantilever beam oriented at 10^0 mounted with tip mass and bounded with PZT -5H.

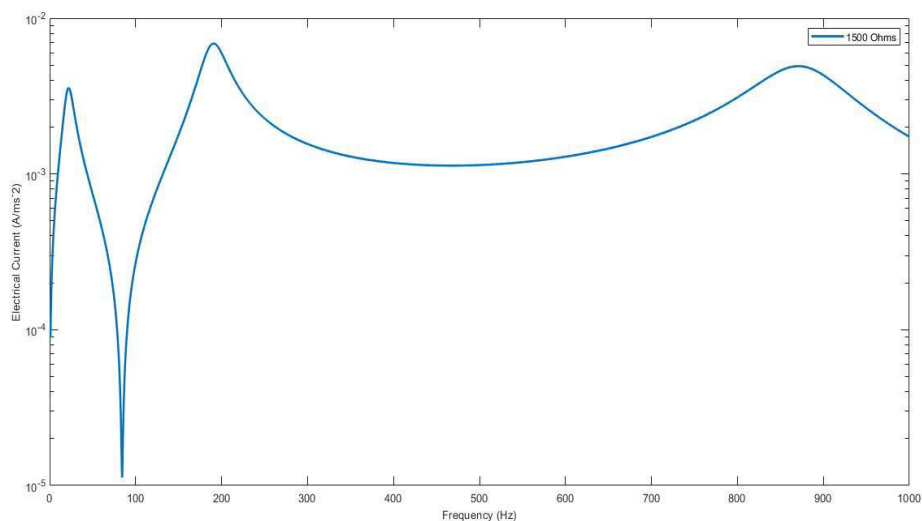


Figure 6.Current FRF of PZT-5A

Figure 6.Shows the current FRF of cantilever beam oriented at 10^0 mounted with tip mass and bounded with PZT -5A.

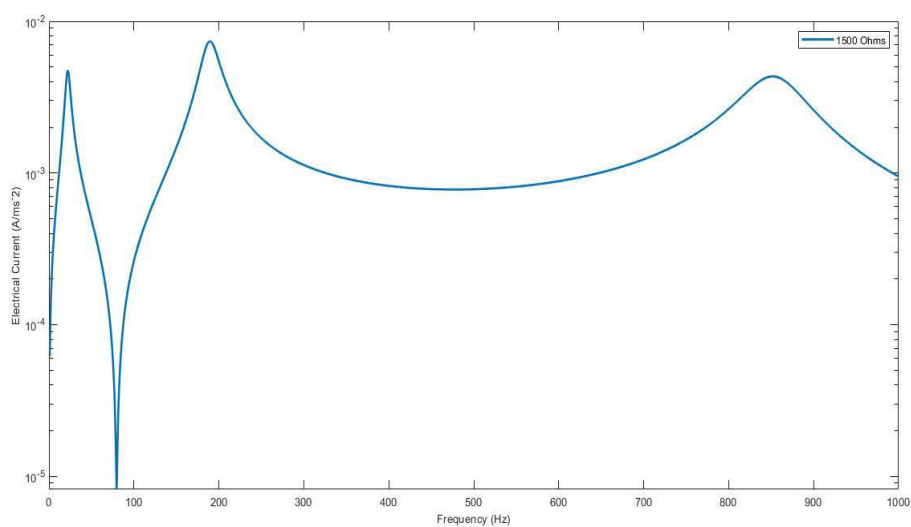


Figure 7.Current FRF of PZT-5H

Figure 7.Shows the current FRF of cantilever beam oriented at 10^0 mounted with tip mass and bounded with PZT -5H.

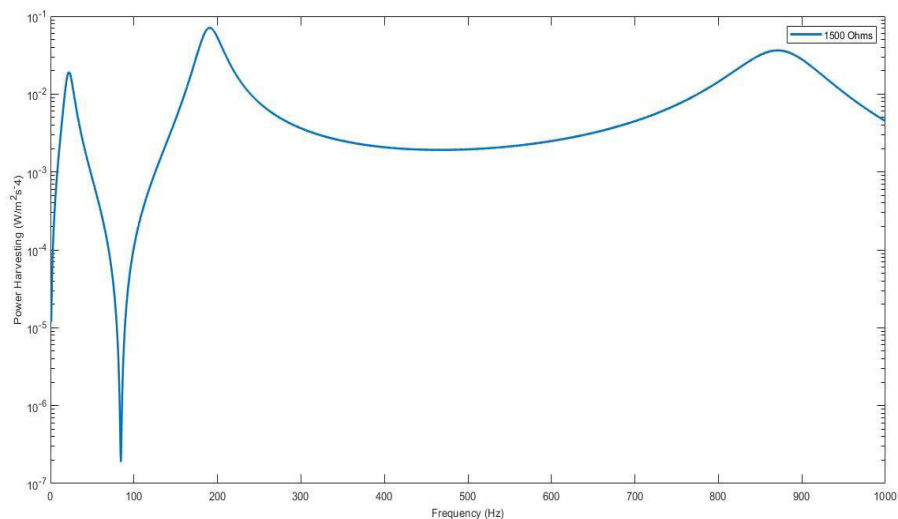


Figure 8.Power FRF of PZT-5A

Figure 8.Shows the power FRF of cantilever beam oriented at 10^0 mounted with tip mass and bounded with PZT -5A.

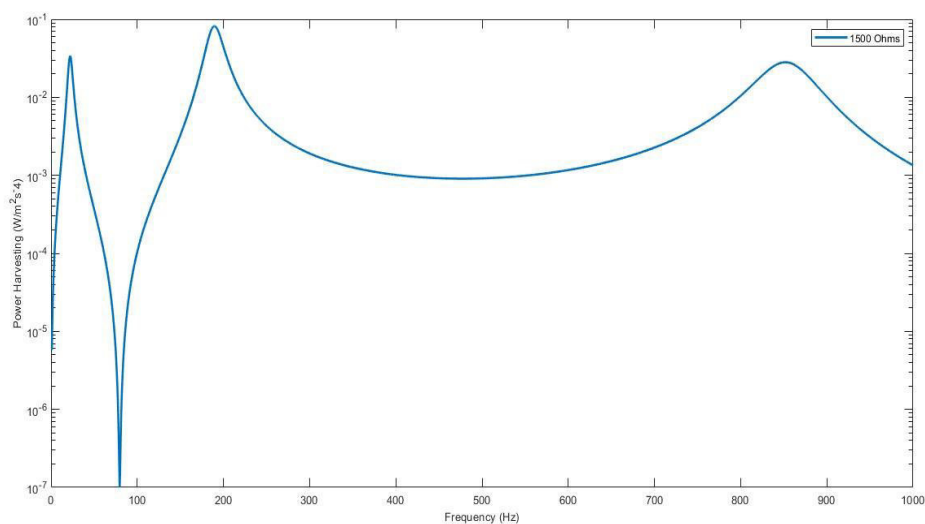


Figure 9.Power FRF of PZT-5H

Figure 9.Shows the power FRF of cantilever beam oriented at 10^0 mounted with tip mass and bounded with PZT -5H.

Figure 4-9 shows the voltage, current and power FRF of cantilever beam orientated at 10^0 , bounded with PZT -5A and PZT -5H piezoelectric patches and beam mounted with tip mass at the free end. At resistance of 1500 ohms and frequency range of 0 to 1000Hz. The following observations are made.

The voltage, current is higher for PZT-5A in first and second peak and lower for third peak compared to PZT-5H.

The higher power is achieved for PZT-5H in first and third peak and lower for second peak compared to PZT-5A.

5. CONCLUSIONS

MatLab program is developed using finite element method considering the Euler Bernoulli beam assumptions, constitutive equations of piezoelectric material and Hamilton's principle. The paper focuses on the study of effect of PZT-5A and PZT-5H piezoelectric patches on orientated cantilever beam mounted with tip mass using the direct method with non-orthonormalisation to derive the voltage, current and power frequency response function (FRF). It is observed that for the 10^0 orientation, 0.127mm thickness of piezoelectric material and 1500 ohms resistance. The higher voltage and current is achieved for PZT-5A in first and second peak and lower for third peak compared to PZT-5H. The higher power is achieved for PZT-5H in first and third peak and lower for second peak compared to PZT-5A.

REFERENCES

- [1] **Shad Roundy, Paul K. Wright, Jan Rabaey** A study of low level vibrations as a power source for wireless sensor nodes, Computer Communications 2003.
- [2] **Henry A. Sodano and Daniel J. Inman** A Review of Power Harvesting from

Vibration using Piezoelectric Materials, The Shock and Vibration Digest. 2004; 36(3), 197-205.

- [3] **A.Erturk , D. J. Inman** A Distributed Parameter Electromechanical Model for Cantilevered Piezoelectric Energy Harvesters, Journal of Vibration and Acoustics 2008
- [4] **Eziwarman, Mikail F. Lumentut.** Comparative Numerical Studies of Electromechanical Finite Element Vibration Power Harvester Approaches of a Piezoelectric Unimorph. IEEE/ASME International Conference on Advanced Intelligent Mechatronics (AIM) Besançon, France 2014
- [5] **Mikail F.Lumentut, Ian M.Howard** Parametric design-based modal damped vibrational piezoelectric energy harvesters with arbitrary proof mass offset: Numerical and analytical validations, Mechanical Systems and Signal Processing 2016, 68-69 562–586
- [6] **Iman Izadgoshasb et.al** Optimizing orientation of piezoelectric cantilever beam for harvesting energy from human walking, Energy Conversion and Management 2018
- [7] **Wei-Jiun Su et.al** Analysis of a Cantilevered Piezoelectric Energy Harvester in Different Orientations for Rotational Motion, Sensors 2020 MDPI
- [8] **Iman Izadgoshasb** Piezoelectric Energy Harvesting towards Self-Powered Internet of Things (IoT) Sensors in Smart Cities, Sensors 2021 MDPI
- [9] **Jiang Ding et.al** A piezoelectric energy harvester using an arc-shaped piezoelectric cantilever beam array, Microsystem Technologies 2022
- [10] **Domenico Tommasino et.al** Vibration Energy Harvesting by Means

- of Piezoelectric Patches: Application to Aircrafts, Sensors 2022 MDPI
- [11] **Laxmi.B.Wali et.al** A review of vibration energy harvesting using piezoelectric materials, IJRECE Vol 6, Issue 3, 439-445.
- [12] **Laxmi.B.Wali et.al** Finite element modelling of cantilever beam bounded with piezoelectric patch subjected to vibration for energy harvesting, IRJET, Vol 8, Issue 10, 392-400
- [13] **Wali, L.B et.al** Modelling and Optimization of Orientated beam with tip mass for vibration energy harvesting using piezoelectric patches. Journal of Mines, Metals and fuels, 70(10A), 374-379.
- [14] **Laxmi.B.Wali et.al** A study of effect of tip mass density, orientation and resistance on vibration energy harvester. CIMS, 29(2), 96-108

Nomenclature

$\{D\}$	electric displacement vector
$\{T\}$	stress vector
$[e]$	dielectric permittivity matrix
$[c^E]$	matrix of elastic coefficients at constant electric field strength
$\{S\}$	strain vector
$[\varepsilon^S]$	dielectric matrix at constant mechanical strain
$\{E\}$	electric field vector
I	Moment of inertia
Q	charge
\ddot{w}_{base}	Base excitation acceleration
Y	Young's Modulus
\dot{k}	Kinetic energy
\dot{p}	Potential energy
ω	Electrical energy
ϖ	External work
C_p	trace of the global capacitance matrix
θ^T	transformed electromechanical coupling
R_{load}	Resistance
$\underline{K}, \underline{M}, \underline{\zeta}$	Global stiffness, mass and damping matrix
ω	frequency

WASTE TO ENERGY USING LOW CAPACITY INCINERATOR

Raju Jadar, K. Raghavendra , Ganesh B, Raghavendra Karnool

Department of Mechanical Engineering, Ballari, Institute of Technology and Management
Ballari-Karnataka-583104

Abstract

Waste disposal is a major problem everywhere in the world. The government believes that it is challenging to properly arrange wastes, both industrial and residential, as cities become more and more urbanised. While it is possible to dispose of domestic garbage at landfills in rural areas, this is not an option for the urban network. In developing countries like India, where the majority of households rely on urban/metropolitan labour, every one of these wastes is placed in landfills, which is the most common method of rubbish collection. However, these dumps pollute the air and water. Incineration and combustion are other methods for getting rid of trash. Here, wastes are burned under regulated circumstances. This method has its drawbacks, but it is still a better option than the long-term problems associated with landfills. However, incinerators are expensive, and the great majority of people are not informed of the benefits of using domestic incinerators. This goal of current work is to create a family-sized incinerator that can be transported about easily. Additionally, the garbage that is burned will be converted into thermal and electrical energy. It must also be mild.

Selection

Keywords: Incinerator, Electricity, Thermo Electric Generator (TEG), Population, Solid Waste, Heat

1. Introduction

Solid waste is undesirable or pointless stuff that is produced by human activity in residential, commercial, or industrial sectors. Metropolitan India, home to roughly 377 million people, generates 63 million tonnes of municipal stable waste (MSW) annually, of which about 31 million tonnes (or 50%) are disposed of in landfills, 11.9 million tonnes (or 20%) are processed, and 43 million tonnes (or 70%) are collected. The estimation of urban municipal stable waste (MSW) generation may rise to 165 million tonnes in 2030 and 430 million tonnes by 2050 due to changes in economic growth and consumption habits [4-6]. The frequent mention of solid waste as a major factor contributing to environmental degradation. 20 to 30 percent of the waste produced overall does not get collected on average, posing environmental problems in urban areas. Asian nations were the principal recipients of unmanageable solid waste as a result of unplanned development and rapid industrial expansion. In addition to helping with energy recovery, the waste incineration process transforms combustible and natural garbage to non-combustible materials like ash and causes weight loss that may be properly disposed of on land or in underground pits [1-4] In India, Municipal Solid Waste (MSW) is becoming a significant problem. The primary goal of this study was to reduce solid waste production through the

introduction of incineration, and the secondary goal was to recover and transmit the waste energy produced during combustion. The outputs are clean surroundings, power from a thermoelectric generator, and waste thermal energy. The inputs are fuel and readily available MSW. The project's ultimate goal is to recover the most energy possible from burning waste, produce thermal and electrical energy, minimise the volume of waste collected, and make use of waste leftovers. For the purpose of reducing environmental contamination, waste treatment is essential. All nations have strict regulations and laws in place to handle this garbage. Waste remediation systems must be rigorously evaluated with continuous in-cycle management to guarantee that minimal performance criteria are reproducibly satisfied. The production of waste is a never-ending process that is accelerating with urbanisation. For the garbage created to be handled effectively, waste management is absolutely necessary. The old-fashioned method of gathering waste and discarding it in an open area gradually contaminates the soil, water, and air around us [4-6].

2. Experimental and Methods

There are several factors influencing the input and output of the worth and capacity of the municipal solid waste incineration. Some of them are [7-8]:

- Production of waste from industrial, households and commercial sites.
- By preventing the production of waste both in industry and households, we will able to lower our waste generation.
- In addition to the waste collected by the municipal solid waste incineration process, it also incorporates residue from the waste treatment technologies.
- Separate collection of waste influences the quantities of the municipal solid waste incineration can be reduced by separate collection of small electrical appliances. Significant reduction in quantity of waste for treatment is observed through source separation of biogenic waste and recyclables and qualities of waste for incineration. For example, up to 80% of Cu content in the bottom ash

2.1. Municipal Solid Waste Incineration.

During the incineration process, a variety of solid and liquid residual materials, as well as gaseous effluents are produced. As a general rule, approximately one-fourth of the waste mass remains as solids in a wet state. It sestimatedhat the residue volume corresponds to one tenth

of the volume of the original waste. Typical MSWI by-products from grate combustion include [9-10]:

- Bottom ash is gathered in a quenching/cooling tank near the combustion chamber's exit and is mostly composed of coarse non-combustible materials and unburned organic waste.
- The process of "grate sifting entails gathering the comparatively fine particulates that flow through the grate at the combustion chamber's base. Because it is typically not practicable to separate these two waste streams, bottom ash and grate sifting together make about 20-30% by mass of the original waste on a wet basis.
- Boiler and economizer ash, which will be representing the coarse fraction of the particles carried over by the flue gases from the combustion chamber, makeup 10% of the initial waste by mass on a wet basis. At the heat recovery stage, it will be collected. Before the gaseous effluents are subjected to any additional treatment, the fine particulate matter or fly ash is removed. An MSW incinerator produces the 1-3% of waste input mass on a wet basis amount of fly ash.

3. Design Methodology

Design becomes a crucial component in the building of the incinerator to reduce the effectiveness of the burning process. This will aid in the reduction of emissions, the avoidance of clinker formation and ash slagging (inside the main chamber), and the preservation of refractory materials. Small-scale incinerators are seldom used to achieve the desired temperature, residence duration, and other parameters. To effectively burn trash and properly handle the waste, however, small incinerators must be built. Also, they will handle garbage appropriately.

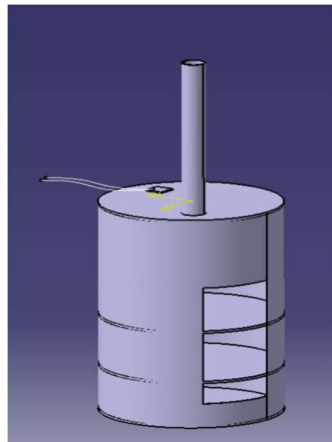
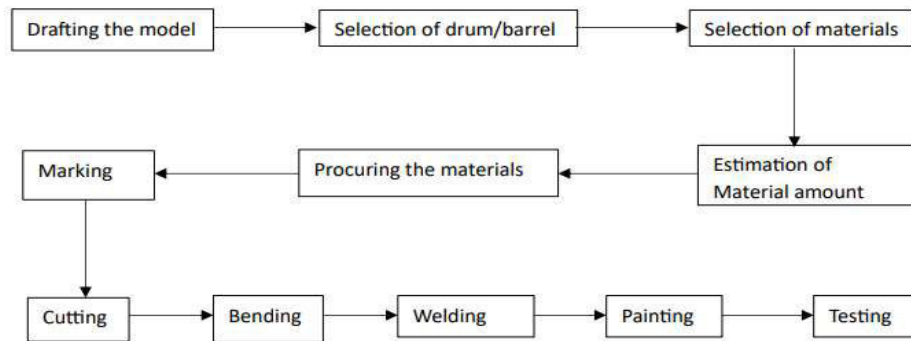


Fig 1: 3D CAD Design of Model

3.1 Fabrication of Incinerator



4. Incinerator Components And Materials

The main components of small-scale incinerator consists of [1-4]:

- a) Barrel Drum
- b) Chimney
- c) Thermo Electric Generators(TEG)
- d) Ash and Residue collector

Barrel drum: One of the key parts that serves as an easily constructed and accessible incinerator for burning the waste is a barrel drum. Steel, laminated paper board, and plastic are used to make these drums. The steel drum can be used for incineration since it is simply adaptable to the needs. The 55 gallon steel barrel is chosen because it is ideal for the miniature incinerator.

Chimney: The chimney's primary function is to release the burned gases into the atmosphere. The small-scale incinerator's chimney is made of a hollow iron pipe.

Thermo Electric Generator: The heat energy must be transformed into electrical energy via TEGs. They can be utilised in large quantities in small incinerators. Power can be produced by connecting devices in series.

Residue and Ash collector: The Ash/Residue collector is located at the bottom of the incinerator. It is divided into two parts by mesh-style iron rods that were welded in place. The space will be kept open for debris.

5. Fabrication Process

Going through many past journals and theories, it is observed that fabrication method of this small-scale incinerator inflicts collective efforts. To come up with a satisfactory viable outcome, various available papers had been taken as reference and going through at of each theoretical and sensible design is executed. The selection of materials is the first step in the fabrication process. The choice of a barrel drum as an incinerator nearly completes the fabrication process of the incinerator. The chosen drum is a steel 55-gallon open head (open on one end) drum with a 220-liter oil capacity. Square bars that have undergone thermo mechanical treatment (TMT) are taken into consideration when creating the mesh that will

support the weight of the garbage inside the drum and serve as a layer between wastes that has already been burned and waste that is still to be burned. As a chimney, a hollow iron pipe of the requisite height is chosen. To increase the flow of oxygen naturally for burning and to drain the water during times of rain, the air holes for the oxygen supply have been closed. The gate for the incinerator is secured with hinges to allow for free operation and rubbish disposal. The connections for the modules of the thermoelectric generator are provided as needed. The incinerator has finished being constructed and is now ready for testing as shown in fig.



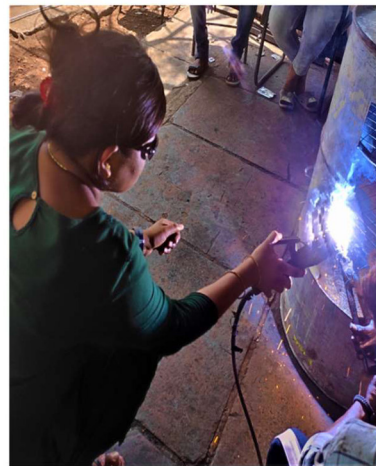
(i) Cutting Door



(ii) Welding Grate



(iii) Removing Extra Material



(iv) Welding Grate to Drum



(v) Welding the Hinges and Door



(vi) Painting the Model



(vii) Finished Model of Incinerator

Table 1: Incinerator specifications

Item	Dimensions	symbol
Outer diameter	580 mm	D1
Inner diameter	572 mm	D2
Inner diameter of Chimney	70 mm	D3
Outer diameter of Chimney	75 mm	D4
Height of Drum	851 mm	H1
Height of Gate	485 mm	H2
Total capacity	220 lit	V1
Chimney height	630 mm	H3
1 st Grate height (from base)	185 mm	L1
2 nd Grate height (from base)	210 mm	L2
Gate from base	100 mm	L3

6. Experimental Setup

The constructed small-scale incinerator, the garbage placed inside of it, and the connections of the thermoelectric generator (TEG) modules are assembled to form the test setup. The waste is first burned by utilising some fuel for initial burning, and that burned waste creates thermal energy, which is computed in accordance with the temperature variations that occur as a function of time. At various locations throughout the incinerator, Thermo electric generator (TEG) modules are connected in parallel and series. The thermal energy (from heat from burning waste) of the garbage is converted into electricity by the TEG modules, who then produce voltage. With a multimeter, the electrical energy produced may be estimated.



Fig 2 . Experimental Setup

7. Results and Discussions

WASTE VOLUME REDUCTION: The waste products burned in the small-scale incinerator include dried twigs wood, paper, cardboards, and leaves, among other things. The amount of rubbish that was gathered and burned during the specified period is shown in the table below. To minimise the volume and weight of the garbage, it is burned in the incinerator's burning chamber.

Table 2: Voltage produced for 1 kg of MSW incinerated.

Sl. No.	Temperature in °C	Voltage produced				
		1 MODULE	2 MODULE	3 MODULE	4 MODULE	5 MODULE
1	40	290 mV	360 mV	550 mV	900 mV	1.1 V
2	60	0.5 V	0.9 V	1.5 V	2.1 V	2.5 V
3	80	0.875 V	1.3 V	1.9 V	2.4 V	2.9 V
4	100	0.95 V	1.5 V	2.2 V	2.8 V	3.3 V
5	120	1.2 V	1.9 V	2.6 V	3.2 V	4 V

Table 3: Current produced for 1 kg of MSW incinerated.

Sl. No.	Temperature in °C	Current produced				
		1 MODULE	2 MODULE	3 MODULE	4 MODULE	5 MODULE
1	40	66.97 mA	83.10 mA	127 mA	207.8 mA	0.25 A
2	60	0.15 A	0.2 A	0.35 A	0.5 A	0.6 A
3	80	0.2 A	0.3 A	0.43 A	0.55 A	0.7 A
4	100	0.21 A	0.34 A	0.50 A	0.64 A	0.8 A
5	120	0.3 A	0.43 A	0.6 A	0.73 A	1 A

Generation Of Thermal/Heat Energy

In the small-scale incinerator, the generation of heat energy depends upon various factors like waste burnt, the calorific value, the moisture content present in waste and type of the waste burnt. The overall capacity of the small-scale incinerator can be of 200 kg but the construction made that it can burn only up to 80 kg, of which varying in between 40 to 70 kg of waste is burnt for effective burning. By burning each kg of waste, the temperature achieved is about 80 to 160 ° C. The supply of waste will be through the gate of the incinerator and is placed over the mesh and is burnt. The heat energy i.e. temperature can be calculated by measuring instruments of heat. The heat energy produced by burning waste can be used for cooking, heating water, drying, etc. as shown in the figure.

Generation Of Electrical Energy

The amount of TEGs used and the temperature difference between the hot and cold sides of the TEG modules determine how much electricity is produced by this incinerator. The TEG Module, which can produce up to 4 volts, generates electricity based on the temperature difference and the maximum voltage. Different voltages can be generated by different temperature variations.

The parallel current (in Amps) generated by thermoelectric generator modules.

CONCLUSION

Like we observe in other nations, waste of every kind is produced in Indian cities as well. Yet, there is a lack of waste management due to improperly planned and scientific techniques of waste control. The leftover waste at the dump yards is typically made up of a greater number

of inert and putrescible natural resources thanks to any of the strong regulations on waste burning and recycling. A straightforward solid waste incinerator was created, constructed, and successfully tested in order to generate thermal and electrical energy through the burning process.

In addition to the releases of flue gases and other byproducts like fly ash and bottom ash, the solid waste incineration process takes into account the reduction in weight, size, and smell of garbage. The public's health is being negatively impacted by the prevalent waste management procedures due to the developing problems with waste control in urban areas. Incineration is a noteworthy option because there is a constant need to enhance the waste management system and apply modern, scientific waste disposal techniques.

According to test results, the system can be used for energy recovery and garbage disposal. Despite the fact that the concentrations of several dangerous gases in the flue gases were over the required criteria, it is necessary to show that the device and combustion chamber require similar work before it can be certified for use in large-scale applications.

References

- 1) Nigam, Shyam Swaroop, Adil Usman, and BP Divakar BP. "Effective utilization of low cost incineration and its by-products in India." In IEEE Global Humanitarian Technology Conference (GHTC 2014), pp. 682-686. IEEE, 2014.
- 2) Sabbas, Thomas, Alessandra Poletti, Raffaella Pomi, Thomas Astrup, Ole Hjelm, Peter Mostbauer, Giovanna Cappai et al. "Management of municipal solid waste incineration residues." *Waste management* 23, no. 1 (2003): 61-88.
- 3) Nidoni, Pooja G. "Incineration process for solid waste management and effective utilization of by products." *International Research Journal of Engineering and Technology* 4, no. 12 (2017): 378-382.
- 4) Tang, Jiao. "A Cost-Benefit Analysis of Waste Incineration with Advanced Bottom Ash Separation Technology for a Chinese Municipality—Guanghan." Unpublished master dissertation, Vienna University of Technology (2012).
- 5) Lee, Se-Jin, Sung-Deuk Choi, Guang-Zhu Jin, Jeong-Eun Oh, Yoon-Seok Chang, and Sun Kyoung Shin. "Assessment of PCDD/F risk after implementation of emission reduction at a MSWI." *Chemosphere* 68, no. 5 (2007): 856-863.
- 6) Hjelm, Ole. "Disposal strategies for municipal solid waste incineration residues." *Journal of hazardous materials* 47, no. 1-3 (1996): 345-368.
- 7) Li, Xiaodong, Jianhua Yan, and Y. Chi. "Development of municipal solid waste incineration technologies." *Better air quality in Asian and Pacific rim cities (BAQ 2002)* 16 (2002).
- 8) Ghezzi, U., S. Pasini, and L. DA Ferri. *Incineration versus gasification: a comparison in waste to energy plants*. No. CONF-950729-. American Society of Mechanical Engineers, New York, NY (United States), 1995.
- 9) Olisa, Y. P. "The Design and Construction of a Step Grate Incinerator." *Global Journals of Research in Engineering* 16, no. A3 (2016): 63-67.

- 10) Oyelola, O. T., A. I. Babatunde, and A. A. Abiodun. "Appraisal of municipal solid waste management in Lagos Metropolis." *Continental journal of water, air and soil pollution* 2, no. 1 (2011): 23-30.
- 11) Liu, Xiaozhou, Guangyu Zhu, Taimoor Asim, and Rakesh Mishra. "Application of momentum flux method for the design of an α -shaped flame incinerator fueled with two-component solid waste." *Energy* 248 (2022): 123647.
- 12) Bull. Environ. Contam. Toxicol. (2003) 71:819-825 © 2003 Springer-Verlag New York Inc. DOI: 10.1007/s00128-003-0208-9.
- 13) *Environmental Management* Vol. 24, No. 4, pp. 517–528 r 1999 Springer-Verlag New York Inc.
- 14) *Jr. of Industrial Pollution Control* 27(2)(2011) pp 1-7 © EM International Printed in India. All rights reserved. <https://www.researchgate.net/publication/294555682>.
- 15) Ramanna Havinal. *International Journal of Engineering Research and Applications* www.ijera.com ISSN: 2248-9622, Vol. 11, Issue 2, (Series-II) February 2021, pp. 55-62.
- 16) *Korean J. Chem Eng.*, 16(6), 795-797 (1999). 225 Bamburgh Circle, Suite 901, Scarborough, Ontario, M1W3X9, Canada.
- 17) 0263-7863/02/\$22.00 # 2002 Elsevier Science Ltd and IPMA. All rights reserved. PII: S0263-7863(01)00054-0. *International Journal of Project Management* 20 (2002) 535–543.

See discussions, stats, and author profiles for this publication at: <https://www.researchgate.net/publication/377565265>

Computational Models for Assessment of Renewable Energy Potential and Load Analysis Section A-Research paper Eur

Article in European Chemical Bulletin · January 2024

DOI: 10.48047/ecb/2023.12.si5.309

CITATIONS

0

READS

67

5 authors, including:



Shekar .K

Ballari Institute of Technology and Management

9 PUBLICATIONS 6 CITATIONS

SEE PROFILE



Rakesh P. Tapaskar

K L E Technological University, Formerly known as B.V. Bhoomaraddi College of E...

45 PUBLICATIONS 199 CITATIONS

SEE PROFILE



Prashant Revankar

KLE Technological University

64 PUBLICATIONS 58 CITATIONS

SEE PROFILE



Mahesh Gorwar

B.V. Bhoomaraddi College of Engineering and Technology (BVBCET)

38 PUBLICATIONS 49 CITATIONS

SEE PROFILE



COMPUTATIONAL MODELS FOR ASSESSMENT OF RENEWABLE ENERGY POTENTIAL AND LOAD ANALYSIS

^{*1} K. Shekar ^{*2} P.B. Rampure, ^{*3} Naveen R, ^{*4} Rakesh P Tapaskar, ^{*5} P.P. Revankar, ^{*6} M.B. Gorawar

^{*1} Ballari Institute of Technology and Management,
Visvesvaraya Technological University, Belagavi 590018,

^{*2} KLE college of Engineering. Chikodi

^{*3} Proudhadaveraya Institute of Technology, Hosapete

^{*4,5,6} KLE Technological university, Hubballi.

Article History: Received: 02.05.2023

Revised: 14.06.2023

Accepted: 25.07.2023

Abstract

The primary concern of the Nations worldwide has been the growing energy demand. In view of changing energy scenario, renewable energy emerges as a feasible solution to address circumstances that do not permit centralized energy grid extensions owing to socio-economic problems. The present study has identified a remote cluster of villages located in Sringeri Taluk, Chikkamagalur district of Karnataka state in India. HOMER based Simulation approach was adopted to choose different combinations of PV-WIND-MH-HK systems based on strategies as Development side and Demand Side. The various resource combinations were investigated on the grounds of Net Present Cost (NPC) and Cost of Energy (COE). The results showed that Development side load strategy was optimal for PV-MH-HK combination with \$217,191.5 and \$0.166/kWh for NPC and COE values. On the contrary, Demand-side Load strategy yielded values of NPC and COE as \$120,825 and \$ 0.158/KWh respectively. The data indicated a poor wind potential at the area investigated, evident through omission of WIND system in optimal combination. The long term or multiyear simulations carried out for the optimal solution indicated 4.45% rise in COE owing to 4.54% drop in energy production through PV.

Key words- simulation, Load strategies, Optimization studies, cost of Energy, Net present cost, Multiyear simulation

DOI:10.48047/ecb/2023.12.si5.309

Abbreviations-MNRE: Ministry of Renewable Energy sources,MH:Micro-Hydro Generator,BGG:BioGas Generator,BMG:Biomass Generator,PV-Photovoltaic,DG-Diesel Generator,HOMER-Hybrid optimization of Multiple Electrical Renewables,COE:Cost

of Energy,NPC:Net Present cost,IRES:Integrated Renewable Energy Systems,HK:Hydro Kinetic Generator,HH:House Hold,IMD:Indian Meteorological Department.CRF:Capital Recovery Factor:LRHP-Low rate watt High Performance.

Nomenclature

Q_D : Direct surface run off depth(mm),	η_{Hydro} : efficiency of the Micro Hydro turbine,
I : monthly rainfall(mm)	ρ_{water} : density of water 1000Kg/m ³
S Maximum potential retention in a watershed(mm)	Q_{tur} : discharge from the turbine.
CN : curve number	A_{tur} is the surface area of the turbine from the manufacturer is the Average velocity of the stream flow
Q : the rate of run off or discharge in m ³ /s	C_p is the coefficient of performance
T_p : is the time to peak run off(hour)	V : Velocity of the water stream flow
T_c : is the time of concentration(hour),	η_r : rotor efficiency
L_w : is the length of the water shed	η_b : Blade efficiency of Hydrokinetic
A : is the area of the Water shed	η_g : Generator efficiency
H_{net} : Net Head available	D : Diameter of the turbine
v_{ct} : is the cut in speed	i : Interest factor%
v_R : is the rated speed of the turbine	N : Number of years
v_{CO} : is the cut out speed	
P_R : is maximum rating of power from the turbine	
V_{hub} : Velocity at the hub height	
$\alpha=0.43$ (coefficient value for mountain, terrain)	
Z_1, Z_2 =Reference heights wind turbine	
R_{pv} : rated power output from the turbine,	
DF : Derating factor in %,	
I_T : instantaneous solar radiation	

1.Introduction

Availability of Energy is the primary criteria for the development of any site/location/area/city, utilizing its primary and secondary resources, commercial and Non-commercial energy resources, and Renewable and Non-renewable energy sources[1].The Government of India has established MNRE(Ministry of Renewable energy Sources) to utilize the full potential alternative energy resources. India's renewable energy potential is about 900GW, from the contribution of Wind-12%,solar-83%,Bioenergy-3% and Small Hydro-2.2%[2]. The energy demand will always show an increasing trend for all the developing and developed countries. In India, rural electrification progress has made a revolutionary development, but

some of the electricity access to villages has remained as a barrier. There are a large number of socio-economic challenges that have to be overcome in providing the grid extension[3]. When rural electrification is concerned, the major challenge is to provide the grid to the rural and remote areas[4].It is found to be uneconomical to pass the grid extension to the remote hilly areas and another reason is that flora and fauna at the place for grid extension are mostly get affected[5]. The remote areas are usually found with two or more potential resources, utilizing these resources is far better than passing the extension. The alternative solution is to integrate the potential renewable energy systems to meet the demands of the rural people, especially remote area living people. The optimization process for better

integration selection of the systems is to be carried out to assess the feasibility and suitability of the system[6]. An Economic and Environmental pollution study[7] is carried out for the cluster of 9 villages using HOMER tool taking the components MHG/BGG/PV/DG with Battery and obtaining the optimal COE and NPC values for all the configurations. Suitable strategy adopting DSM for standalone IRES[8] in the remote area is made taking PV/WIND/MHG/BGG/BMG

configuration to assess the cost of COE and NPC using the Genetic algorithm approach. Optimal modeling of IRES for the remote area electrification[9][10] in Chamaraja Nagar District, Karnataka is studied for obtaining the optimal sizes of components of the system. The research on simulation and optimization studies[11] of Hybrid energy systems using software tools on various platform are suggested. Different optimal sizing methodologies[12] are referred and suggested which include probabilistic methods, analytical methods, Iterative methods, and Hybrid Methods. WIND-PV-DG[13] system integration is carried out for sizing the systems to provide electrification in rural Algeria using the MATLAB/Simulink environment. A feasibility study of a standalone PV-WIND with Battery[14] is made to assess the NPC and COE with different possible system types in remote island using HOMER tool. A combination of PV/BMG with battery bank[15] for the non-connected zones are studied using the HOMER software and systems are designed and installed at Distributed energy resources Laboratory. A new approach[16] is studied for PV-WIND and energy storage systems in diesel-free isolated communities which proposes the various models handled for optimizing the cost functions. Off-grid generation options are studied[17] to deliver a load of 110KWh/day in rural villages of Cameroon using the PV(18kW)-MH(14kW) and LPG generator(15KW) using HOMER. The remote area study[18–20] for the Uttarkhand District villages is performed

using the PV/WIND/BMG/BGG/MH. This study gives the feasibility of integrating all the systems in remote areas by conducting the load survey in the villages. The integration of the systems require proper assessment of the resource load and demand load. The demand load is carried out by enquiring with the local people and Grama panchayat available at the location. The study on the Operation of optimal energy systems[21] by considering the Demand-side strategies are simulated as load response from the renewable systems. In this study, optimization strategy is proposed and demonstrated for the single-family residential home. Optimization of PV-WIND -DG[22] is studied for their integration in isolated communities in Brazil for results of NPC and COE. The optimal studies on remote isolated island-sandwip, Bangladesh [23] is studied for the combination OF PV- Diesel taking the various loading parameters and adopted the Genetic Algorithm(GA) approach for the simulation of NPC and COE. The experimental studies related to off-grid areas[24] are conducted using the PV-Diesel Generator without the battery storage and found that the operation of diesel generator is to be designed for the Peak load demand of the area. The operation of the diesel contributing 60%-80% is observed from the nominal power demand. A review study on IRES[25] are the integration of renewable systems, sizing methodologies, storage technology options for storage durations, and the uncertainties of integration are mentioned by referring the various works of literature. Techno-economic study for MH-PV-WIND-BG-BM-DG is conducted[26] for five un-electrified villages using HOMER software and found best optimal configuration with the least cost of COE as \$0.197/kWh. The study[27] was made on using HOMER software for seven un-electrified clusters of villages in Limkheda taluk and Dahood District in Gujarat State using HOMER tool for obtaining the value of NPC and COE. The study[28] is made on a cluster of

un-electrified villages in Odisha state, obtained the results for NPC and COE using the salp swarm algorithm utilizing the MATLAB environment for its robustness and convergence efficiency for optimal solutions. The research study, [29] and [30] suggested a Demand response program (DRP) for the performance of PV/FC/Battery – WT/Battery to reduce cost and emissions and latter suggested for smart distribution system (SDS). Studies on Demand side management [31] also gives information for distributed network supply for electric vehicle operations.

From all the above literature studies, it is inferred that the integration of Renewable energy systems is feasible and sustainable for remote areas. The studies are made taking the potential resources available at the locations. The studies related to the configuration of PV-WIND-BM-BG with Diesel generator is more of concern and found less literature on the part of Integrating the Micro-Hydro and Hydro Kinetic turbine. These two renewables sources are site-sensitive and largely depend on the rainfall at the selected areas. Few literature are found integrating the Hydro Kinetic turbine as a resource. The Multi-year simulation results using HOMER are not carried out in various literature. A simulation for Development side strategy is not made in the literature. Here, an integration of MH-HK with the PV- WIND is made for optimal simulation on the un-electrified remote cluster of villages near sringeri Taluk, Karnataka state which is found to be experience with high rainfall status in the Karnataka state region. A different combination for simulation to integration of renewable energy system is carried out to obtain the best optimal solution taking two strategies. The reported

research gives an insight into the study in the sections of Load demand and Resource demand assessment, Modeling of Renewable energy systems, optimization studies, Results and discussions and Multi-year simulation results.

2. Motivation for present study and Methodology

This study is carried out to obtain the best optimal integrated combination and solution for NPC and COE simulation using HOMER pro soft for a different combination of potential resources at the site. To size different renewable energy systems to accommodate the load demand by considering the two strategies, 1. Development side Load strategy and 2. Demand side Load strategy. This research also assess the NPC and COE using the Multiyear simulation module in HOMER Pro soft. This study involves getting the local coordinates for the site under study for watershed area assessment using the Google save location Mobile app and then elevation contours are developed using the Google earth and ArcGis software. The meteorological data are obtained from using the Meteoronorm 7.3 software for solar data and wind data is recorded using the Typical Meteorological year data. The simulations are carried in the recent version of the HOMER Pro soft. [Figure 1](#) shows the Main tool menu in HOMER Pro available for simulation.

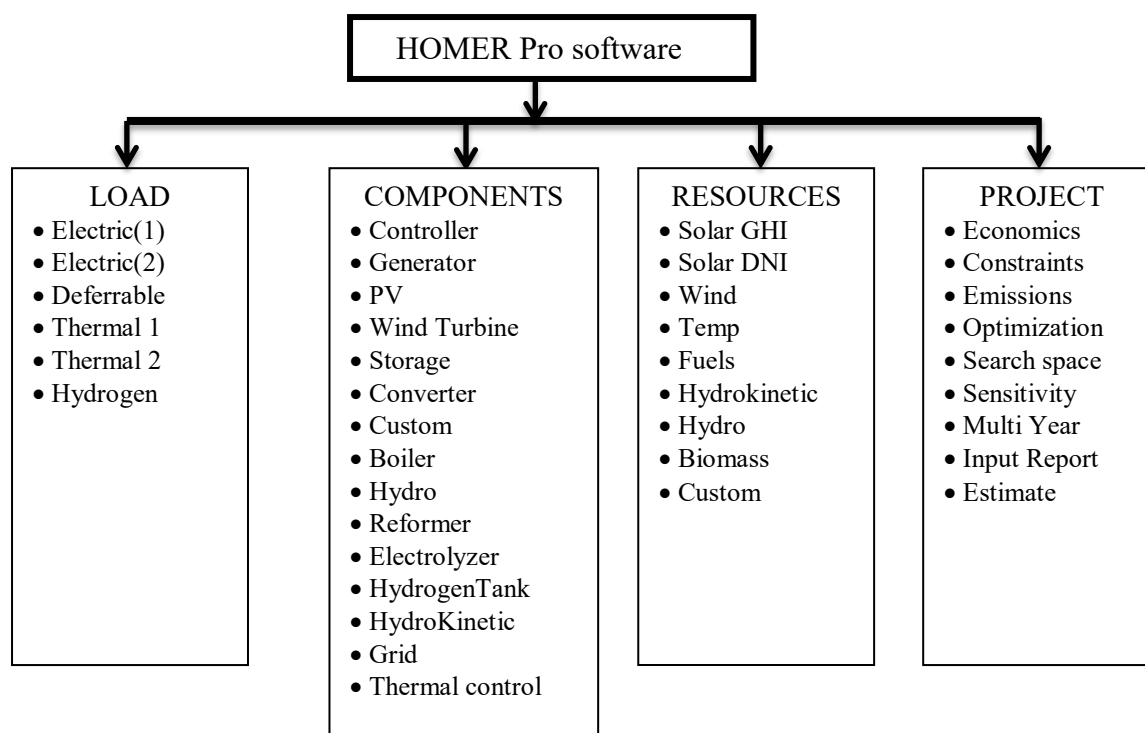


Figure 1.HOMER Pro software main menu tools for simulation.

3. Load Assessment of Study Area

The study area is selected from the cluster of Remote villages nearby Sringeri Taluk(Latitude 13.417 N Longitude 75.252 E),chikkamagalur District,Karnataka.The villages were first identified by grouping the villages into urban villages(which are near urban area/city),Rural villages(which are near to Rural taluks) and Remote rural villages(which are remotely residing near to Rural taluks).The electrification to urban and rural villages are already benefitted by the NJY(Nirantara Jyoti scheme) implemented by the Government of Karnataka, for the rural village Electrification. The electrification to remote villages is difficult for the Government to pass the grid lines and these grid lines are posing endanger to the flora and fauna at the remote sites. The cluster of villages are identified at the radial distance of 1-2km, having the study location at Longitude 75.152837 E, Latitude 13.470276 N.

3.1 Load Demand at the study area

The load demand for the study is made by considering the two strategies of Development side Load strategy and Demand side Load strategy. The former strategy is evolved on basis of development required at the remote areas by collecting data from the Local/Grama panchayat-which is a village governance body in Indian villages and the tribal people, about the various developments required like schools, outpatient Hospital, community halls, small industrial loads(flour mills, water pumps),stationary shops(food items/groceries and others) by preparing the questionnaire and communicating with local people and Grama panchayat members who are elected by the village people for governing the village issues. on the contrary the latter uses actual demand required in the present situation, which is estimated by collecting load data from the Residential Houses.Here only Domestic Loads are considered. The Table 2 shows the Load point estimation of Domestic, community loads and commercial Loads.

Table 1 Demography of the cluster of Remote villages

Name of the Village	No. of House holds	population
Tarulli Kodige	27	132
Anukulli bylu	15	45
Bylubaru	6	25
shunti hakkalu	6	18
kote	25	112
Total	79	332

Table 1 gives the demography of villages for load assessment. Hourly load demand for the year is obtained by categorizing the year into four quarters (Jan- March, April-June, July-Sept and Oct-Dec). In obtaining the hourly load demand for Development Load strategy, loads are categorized into

Domestic loads, community loads and Commercial Load. But for the Demand side Load strategy, only Domestic loads are considered because It is observed the local people living are not availed of community and commercial services in the study area.

Table 2 Load points estimation for obtaining the Hourly demand at the study site

Domestic loads	
Appliances	Quantity
CFL LIGHT(40W)	4 Points in each House Hold
LCD TV(70W)	1 Point in each House Hold
Radio(25W)	1 Point in each House Hold
Fan(75W)	2 Points in each HH
Community loads	
Appliances	Quantity
CFL LIGHT(40W)	3 points for Hospital, 4 points for School Building
Refrigerator (1000W)	1 Point for Hospital Usage
Fan(75W)	3 points for Hospital, 4 points for School Building.
Commercial Loads	
Appliances	Quantity
CFL LIGHT(40W)	2 shops having 1 point for 79HH
Street light(60W)	1 pole for every 3 HH
Fan(75W)	2 shops having 1 point for 79HH.
Pumping water(3.76 KW)	3 water pumps for 79HH
Flour mill (5KW)	1 Point having 5KW for 79HH

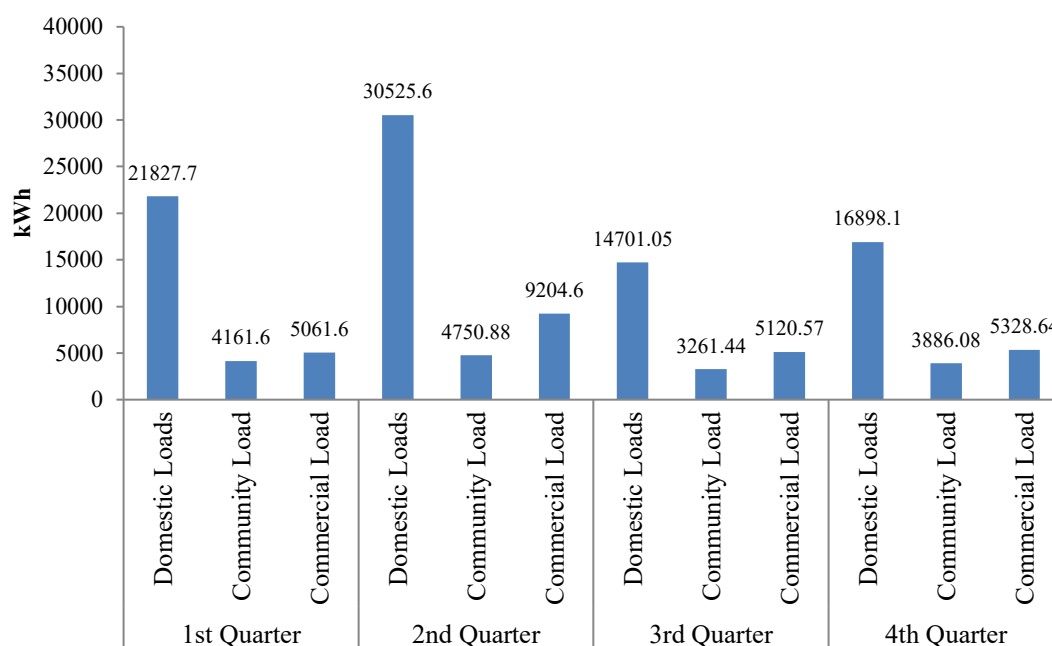


Figure 2. Annual Energy Demand estimation in each quarter for Development side strategy Load.

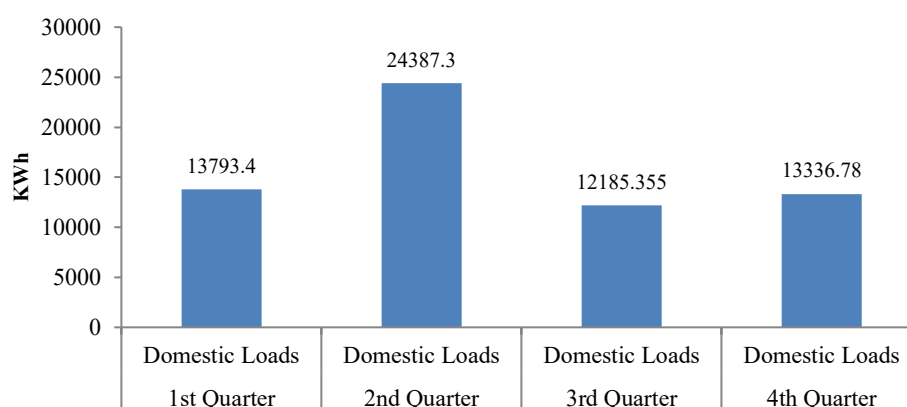


Figure 3. Annual Energy Demand Estimation in each quarter for Demand-side Management strategy.

Table 2 gives the details about the appliances and the number of points estimated in each Household (HH). The Load points are assessed by enquiring with the Local people and Grama panchayat members. Hourly Energy demand (KWh) is then calculated in each quarter of the year. The Energy demand in each hour, in each quarter, is assumed to be constant. Figure 2 and Figure 3 show the energy demand in each quarter for Development side strategy and Demand-side management strategy. The load assessment is carried out based

upon their life style during the various seasons and usage of their energy. The tribal people have their own kind of habitat of work. Their usage is found to be more during the second quarter (April-June). Total Annual Energy demand required for Development side strategy is 124727.86 KWh/Year with annual average of 341.72 KWh/year and Peak load of 65.08 KW/day. For the Actual Total energy Demand for the cluster of villages is found to be 63702.83 KWh/year with annual average of 175.5 KWh/year and the Peak load demand of

45.04 KW/day. While calculating the load on Demand side Low rate Watt with High performance(LRHP) appliances(like LED bulbs) are considered. The Demand-side load is found to be 51% of the Development side load strategy.

4. Resource Load Assessment at the study area

Potential Renewable sources available at the study area are identified as Wind, solar, Micro-Hydro and Hydrokinetic resource.

4.1 Wind Load assessment

The wind speed available at the location is retrieved from the typical Meteorological Year chosen for 10 years from 2008 to 2018[32]. The wind data is also collected from the local IMD(Indian Meteorological Department) center at Karwar,Karnataka.The wind velocity is observed high during June-september from the data.

Figure 4 shows the Typical meteorological data for wind speed generated and mean wind speed was found to be 4.2m/s.

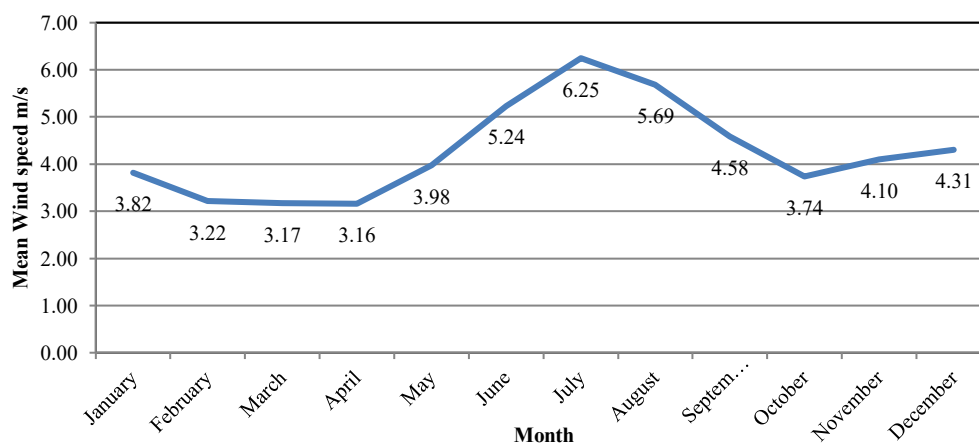


Figure.4.Mean wind speed velocity calculated from the Typical meteorological year Data

4.2 Solar energy load Assessment

Solar radiation data of sringeri taluk are obtained from the Meteonorm 7.3 software application for the period of 10years by giving the geographical coordinates as input. Solar intensity kWh/m²/day for each month available at the site is then calculated

as shown on Figure 5. The average solar intensity in kWh/m²/day for the year was found to be 5.44 kWh/ m²/ day/year.The solar insolation is found be high during the summer season from February-June from the Data.

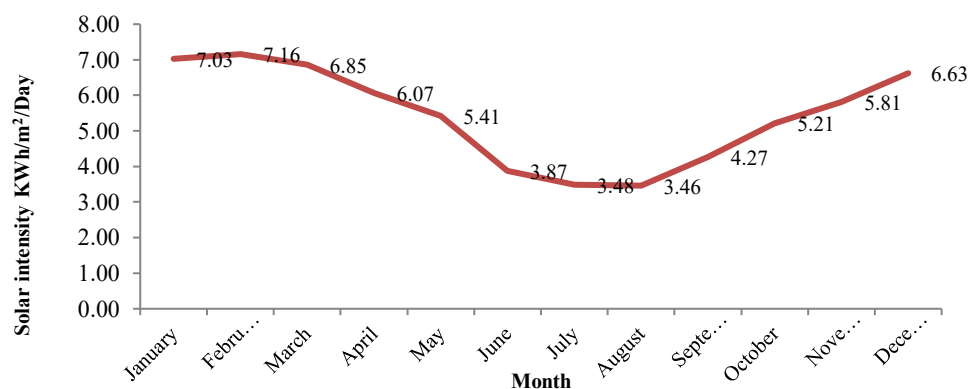


Figure 5. solar intensity KWh/m²/day available at the site for all the months

4.3 Micro-Hydro Load Assessment

To assess the Hydro potential at the study site for Micro-Hydro turbine, the discharge to the turbine is calculated by using the Soil conservation services Curve Number Method(CN), developed by the USA in 1969 for estimating the actual run off depth based on the Rainfall data.

Actual run off depth is calculated by the Equation 1 as[33]

$$Q_D = \frac{(I-0.2S)^2}{(I+0.8S)} \text{ when } I > 0.2S \quad (1)$$

$$S = \frac{25400}{CN} - 254 \quad (2)$$

Where Q_D is the direct surface run off depth(mm), I is the monthly rainfall(mm) and S is the Maximum potential retention in watershed(mm) and CN is curve number ranging from 48-58 for dense forest. The peak rate of run off or discharge are calculated by the equations as follows

$$T_P = 0.6T_C + \sqrt{T_C} \quad (3)$$

$$T_C = 0.0195 \left[\sqrt{\frac{L_w^3}{H_{net}}} \right]^{0.77} \quad (4)$$

$$Q = \frac{0.0208 \times A \times Q_D}{T_P} \quad \text{---} \quad (5)$$

Where Q is the rate of runoff or discharge in m^3/s , T_P is the time to peak run off(hour), T_C is the time of concentration(hour), L_w is the length of the water shed and A is the area of the Water shed. These are calculated from developing the watershed contours using the Google Earth and ArcGiS 10.8 software. The exact geographical coordinates of the location are obtained for the implementation of Hydro turbine site. Table 1 gives the calculated values of average Discharge values of Q taking the rainfall data of 10 years using the meteorological information from the Meteorological department at IMD, karwar District, Karnataka and from the online resource website[34]. It is estimated that Average of 3379.7 litres/s for the year is available as a discharge to the Micro-Hydro turbine output. Figure 6(a) shows Elevation contours developed from the ArcGIS soft at the site and elevation is calculated as 625m and length of the watershed is 1125m. Figure 6(b) and Figure 6(c) are the watershed area contour and Topography of the study location respectively.

Table 3 Calculation of Discharge from the Curve Number Method

Months	Average Rainfall Data (mm)			CN	Avg Q (m^3/s)
	2009-12	2013-16	2017-20		
January	6.11	2.84	6.76	52	0
February	3.42	9.175	4.96	52	0
March	10.89	15.83	16.75	52	0
April	65.5	41.9	62.42	52	0.130
May	92.61	67.69	200.32	52	3.898
June	99.94	69.54	190.63	52	3.706
July	123.31	85.74	214.75	52	5.265
August	122.25	76.7	220.76	52	5.342
September	125.37	76.6	237.24	52	6.0451
October	129.41	71.47	442.15	52	15.175
November	103.07	32.77	87.19	52	0.93592
December	19.19	8.92	62.89	52	0.0570

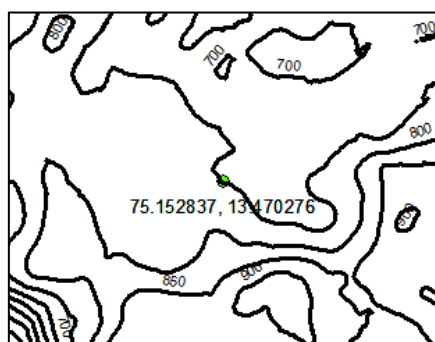


Figure.6(a) Elevation contours at the site (ArcGIS)
area contour

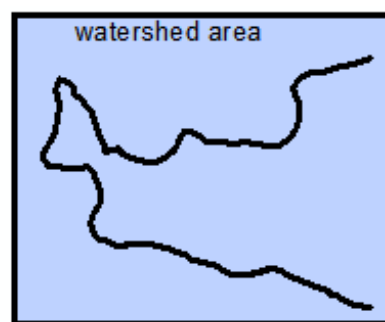


Figure6(b) watershed

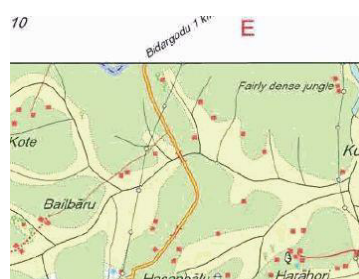


Figure 6(c) Topography of study area

4.4 Hydro-kinetic resource Load assessment

The study site is identified with water stream flow suitable for generating the power using the Hydro-kinetic turbine. This requires the data for the average velocity of water streams. Average velocity of water

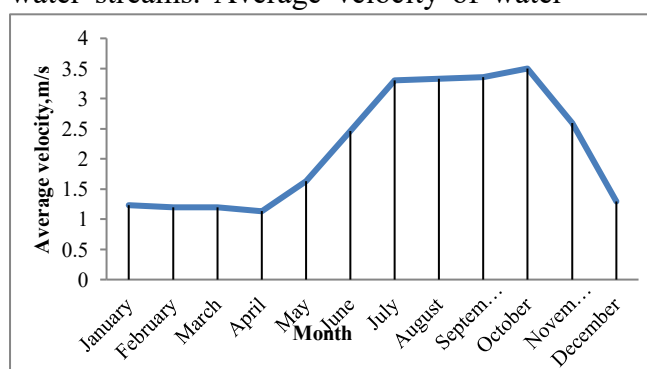


Figure7. Average water stream flow velocity in each month

flowing is obtained for each month using the Electro-Mechanical current meter device. To obtain the monthly data, current meter is used to get the velocity readings for mid-day of the month for 12 hours, keeping the device at 0.5m, 1m and 2m depth from the surface level of water.

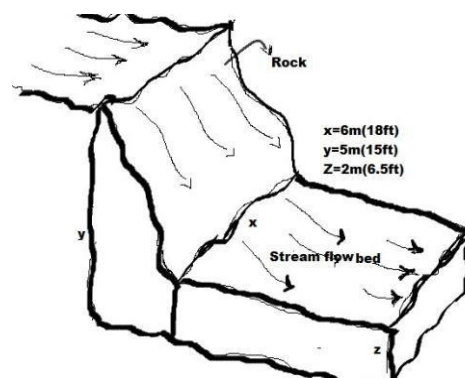


Figure 8. HK resource model

The average velocity of stream flow obtained is shown in Figure 7. This velocity is assumed to be constant throughout each month for obtaining the Hourly analysis. Figure 8 shows the details of the Hydro-kinetic resource model at the location. The

average water stream velocity is high during the rainy season from June-october.

5. Modeling of the Energy Resources

This study is made identifying the energy resources of Wind energy, solar energy,

5.1 Modeling of Wind power output

The power output from the wind turbine is calculated by the Equation 1 [35][36] as

$$\left. \begin{aligned} P_W &= 0 && (\text{for } v < v_{CI}) \\ P_W &= P_R (v - v_{CI}) / (v_R - v_{CI}) && (\text{for } v_{CI} \leq v \leq v_R) \\ P_W &= P_R && (\text{for } v_R \leq v \leq v_{CO}) \\ P_W &= 0 && (\text{for } v > v_{CO}) \end{aligned} \right\} \quad (1)$$

Where v_{CI} is the cut in speed, v_R is the rated speed of the turbine and v_{CO} is the cut out speed, P_R is maximum rating of power from the turbine. The power curve from the manufacturer details are correlated for calculation of power output in HOMER optimization by taking the effect of air density ratio and multiplied by the Power output from the wind turbine at STP (standard Temperature Pressure) conditions. For the calculation of power from the turbine is taken at hub height of 30 m, which is given by the Equation 2 as

$$V_{hub} = V * (Z_2 / Z_1)^\alpha \quad (2)$$

Where $Z_2 = 30\text{m}$, $Z_1 = 10\text{m}$ and $\alpha = 0.43$ (coefficient value for mountain, terrain) Power calculations are obtained for each hour data for 8760 hours

5.2 Modeling of Photovoltaic systems

Power calculations for the PV output are carried out using the Equation 3 [37]

$$P_{PV} = R_{PV} DF(\%) \left[\frac{I_T}{I_{STC}} \right] \quad (3)$$

Where R_{PV} is the rated power output from the turbine, DF is the Derating factor in %, I_T is the instantaneous solar radiation and I_{STC} is the solar radiation at the standard Test conditions.

MicroHydro and Hydro kinetic resources available at the locality.

5.3 Modeling of Micro Hydro system

Power output from the Hydro turbine is obtained from the Equation 4 [38] as

$$P_{MH} = \frac{\eta_{Hydro} * \rho_{water} * H_{net} * Q_{tur}}{1000} \text{ KW} \quad (4)$$

Where η_{Hydro} is the efficiency of the Micro Hydro turbine, ρ_{water} is the density of water 1000kg/m^3 , H_{net} is the net head available to the turbine and Q_{tur} is the discharge from the turbine. The discharge to turbine is calculated from the soil conservation curve method as explained in the resource load assessment section.

5.4 Modeling of Hydro-Kinetic turbine

Hydrokinetic turbines are placed under water which may be fixed or floating type against the stream water flow, normally these are placed at a minimum depth of 1m from the surface level of water. The power output from the Hydro-kinetic turbine is calculated by the Equation 5 [39] as

$$P_{HK} = 0.5 * \rho_{water} * A_{tur} * V^3 * C_p \quad (5)$$

Where A_{tur} is the surface area of the turbine from the manufacturer is the Average velocity of the stream flow and C_p is the coefficient of performance of the turbine taken value of 0.59 (Betz Limit).

Equation 5 is modified by taking the rotor efficiency(η_r), Blade efficiency (η_b) and Generator efficiency(η_g), taking the values of 0.6 for rotor efficiency, blade efficiency and generator efficiency values equal to 0.9, We get

$$P_{HK} = 0.5 * \rho_{water} * A_{tur} * V^3 * C_P * \eta_r * \eta_b * \eta_g \quad (6)$$

Substituting $A_{tur} = \pi D^2/4$, the equation gives

$$P_{HK} = 0.112 * D^2 * V^3 \quad (7)$$

In HOMER, Power curve from the manufacturer is taken as reference, the values are interpolated to the manufacturer details.

6. Optimization Simulation studies

In this study, optimization for the Economic analysis for different combinations of renewable energy sources is carried out using HOMER pro Optimizer tool. HOMER performs the sizing operations for the feasibility analysis. The NPC(Net Present cost) and COE(Cost of Energy) are the two parameters considered for analyzing the feasibility and suitability of the systems. Each simulation is provided with Load data by taking some suitable sensitive parameters as sensitivity analysis. Net present cost is the Present cost involving all the cost components deducting all the revenues it earns all throughout its Project Lifetime.

In economic analysis, NPC is calculated by Equation 7[35] as

$$NPC = \frac{C_{Totalyear}}{CRF}$$

$$C_{Totalyear} = C_{FCyear} + C_{RCyear} + C_{OMyear} \quad (8)$$

$$CRF = \frac{i(1+i)^N}{(1+i)^N - 1}$$

Cost of Energy(COE) is the annualized Total cost of producing the Energy generation to the Total energy served by the Renewable energy systems given by Equation 9 as

$$COE = \frac{C_{Totalyear}}{E_{served}} \quad (9)$$

HOMER does not Rank the Renewable Integration system based on the COE .In determining the cost components of the Renewable systems, HOMER analyzes the cost considering the Fixed cost, Replacement cost, and Operation and Maintenance cost. Therefore, the capital cost of the system per KW is assessed by taking various costs involved, the distribution of various costs are obtained by manufacturing details and with the Engineers associated with the installation of Renewable energy systems. Figure 9 shows the percentage of distribution of various costs involved for installation of Renewable energy system per KW or MW.

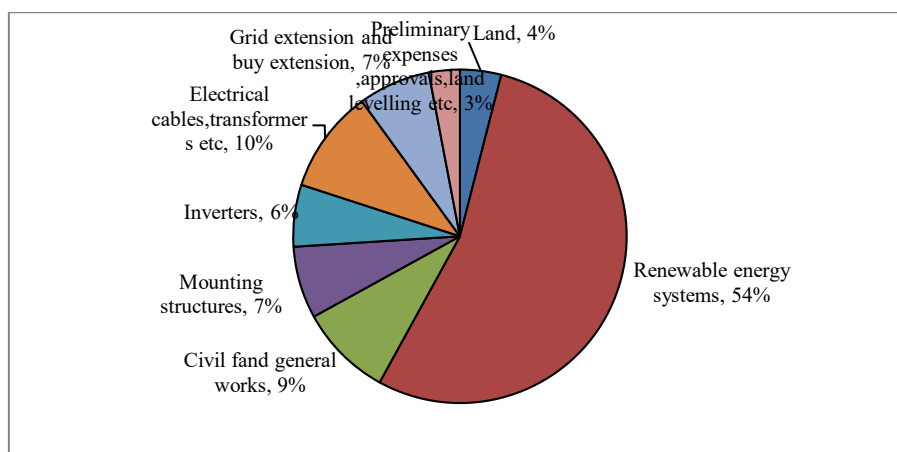


Figure 9. Percentage distribution of various costs installing RE system.

It shows from the Figure 9 that, 54% of the capital cost is involved for Renewable Energy systems and other 46% is accounted for costs of supporting activities required at the installation of the system. The optimal Simulation method followed is shown in the Figure 10. With the available Resources at the Location, integrating the different combinations of systems are performed considering as only the Potential resources available at the study area. Each combination simulation is being performed with different sensitive parameters concerning scaling factor, Renewable

energy fraction, and other variables for the systems. HOMER gives the feasibility of the combination with the values of Net present cost and cost of Energy. The load input for the Development side strategy and Demand side strategy for each run of the combining the Integrated renewable system. In all the simulations Battery and Inverter capacity and cost are considered same. Thus, all the individual run combinations give the values for NPC and COE. Then the best possible combination for sustainability is selected on the optimization results.

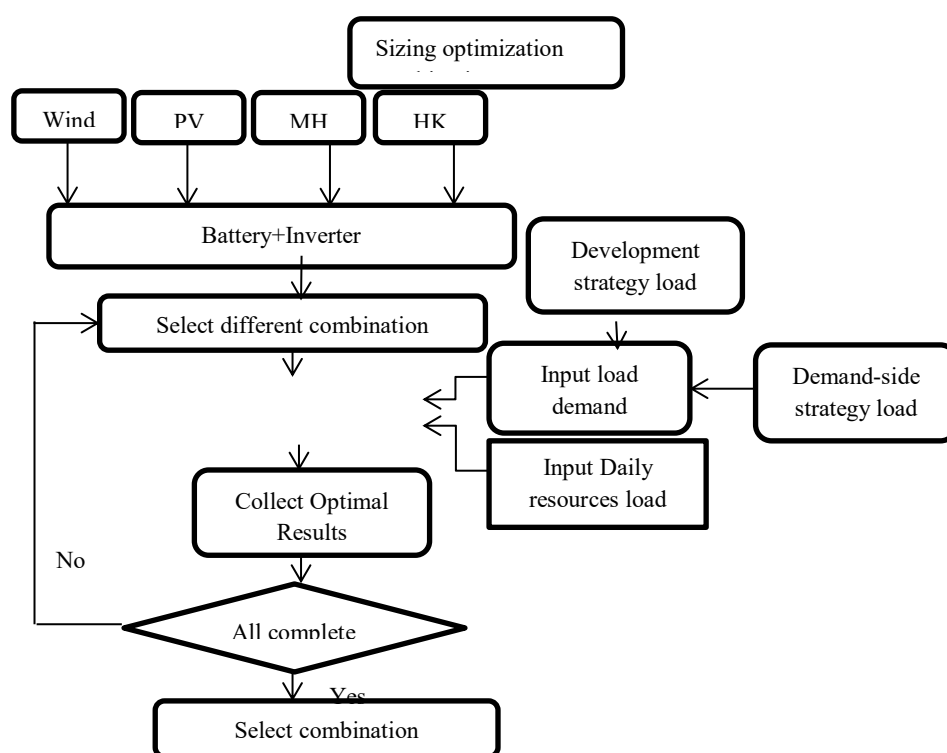


Figure10. Flow chart for the Optimization studies

7. Results and Discussion

Simulations for the different possible combinations are performed by considering the size of Battery(1KWh) Lead Acid and converter size varying between 10KW to 50KW. The Load demand for Development side strategy is explained in the load demand assessment section, which is found to be of Annual Average 341.68KWh/day

with a peak Demand of 65.08 KW. The Demand side load strategy is having annual average of 175.5KWh/day with a Peak demand of 45.04 KW. Hourly Assessment of load demand is carried out by taking the four quarters of a year. Hourly demand of load is assumed to be constant for the particular quarter and time. For the two strategies, seven possible combinations are considered as an optimal integration

renewable system. This involves integration of PV-BATT/PV-WIND-BATT/WIND-BATT/MH-HK-BATT/WIND-MH-HK-BATT/PV-MH-

HK-BATT and PV-WIND-MH-HK-BATT. Table 4 gives details of the costs of systems considered for simulation.

Table 4 various costs of systems considered for simulation in HOMER

Systems	Capital cost(\$)	Replacement cost(\$)	O&M cost(\$)
PV-1KW	\$2,500.00	\$2,500.00	\$10.00
BATTERY-1KWh(LA)	\$300.00	\$300.00	\$10.00
CONVERTER	\$300.00	\$300.00	\$0.00
WIND-95KW	\$4,75,000.00	\$4,00,000.00	\$4,000.00
MH-49KW	\$52,266.00	\$50,000.00	\$1,045.00
HK-40KW	\$14,000	\$14,000.00	\$280.00

In HOMER simulation, the costs of renewable energy systems are divided under three categories, which consist of capital cost, Replacement cost and Operating and Maintenance cost. The other costs involved with renewable system are not included. Various other costs associated are mentioned in the [Figure 9](#) are taken as reference and made include in the capital cost of the systems. The costs calculated do not involve in other direct and indirect taxes and are according to the price value in

Indian country. It is also observed that the costs tend to change with the demand for the respective renewable energy system, like in the cases of PV panels and wind turbines. Micro-Hydro and Hydro Kinetic are site specific and demand for there is less when compared with other systems. The cost of converter and Battery are depends on the type used. Lithium-Ions batteries cost are more compared with lead acid battery and thus it increases the Net present cost and COE.

Table 5 Simulation results based on Two strategies

Simulations Results based on Development Strategy- Annual Average -341.68KWh/day--65.08 KW-Peak Demand								
S.N	Renewable systems	PV (KW)	WIND (Nos)	MH (KW)	HK (Nos)	CONVERTER (KW)	BATTERY, 1KWh(Nos)	COE (\$/KWh)
1	PV-BATTERY	116				48.7	729	\$0.685
2	PV-WIND(95KW)-BATTERY	115	1			44.0	643	\$0.693
3	WIND (95KW)-BATTERY		14			46.3	318	\$1.76
4	MH-HK(40KW)-BATTERY			57.7	2	10.7	46	\$0.153
5	WIND(95KW)-MH-HK(40KW)		1	57.7	2	10.9	32	\$0.692
6	PV-MH-HK(40 KW)-BATTERY	1.8		49.4	2	26.6	129	\$0.166
7	PV-WIND(95KW)-MH-HK(40 KW)-BATTERY	1.78	1	49.4	2	33.2	151	\$0.589
Simulation Results Based on Demand Side Strategy- Annual average -175.5 KWh/Day ;45.04 KW --Peak demand								
S.N	Renewable systems	PV (KW)	WIND (Nos)	MH (KW)	HK (Nos)	CONVERTER (KW)	BATTERY, 1KWh(Nos)	COE (\$/KWh)
1	PV-BATTERY	76				43.3	476	\$0.8203
2	PV-WIND(95KW)-BATTERY	11.7	1			35.3	245	\$1.07
3	WIND (95KW)-BATTERY		2			25.2	168	\$1.9
4	MH-HK(40KW)-BATTERY			57.7	2	1.72	8	\$0.154
5	WIND(95KW)-MH-HK(40KW)		1	57.7	2	0.807	2	\$0.875
6	PV-MH-HK(40 KW)-BATTERY	1		57.7	2	1.74	5	\$0.158
7	PV-WIND(95KW)-MH-HK(40 KW)-BATTERY	0.4	1	57.7	2	0.173	1	\$0.876

Table 6 Energy consumptions(Kwh)/year of PV-MH-HK in Demand side strategy Load

Component	Production (KWh/yr)	Percent
Generic flat plate PV	8114.3	1.2
GenericHydro Kinetic(40KW)	407068.2	60.2
Hydro	261010.5	38.6
Total	676,193	100

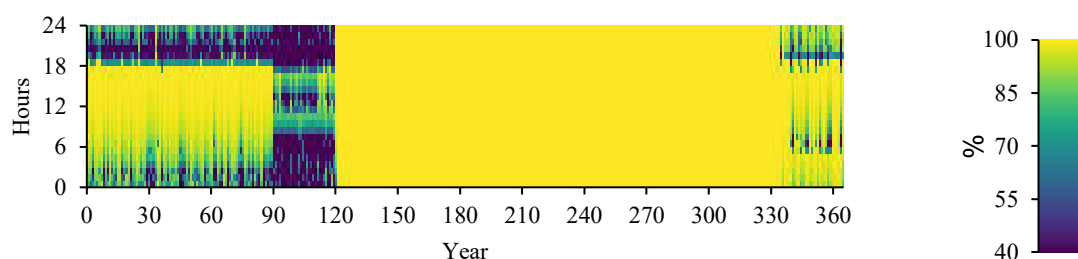
**Figure 11.**State of charge% Generic Lead acid Battery(1KWh) for PV-MH-HK Demand side load

Table 6 shows the energy consumptions of PV,MH,HK systems when simulated for Demand side Load strategy similarly the same trend has been observed in the case of Development side strategy. The contributions of MH and HK is more with respect to PV system. This shows that the location has a more potential in Hydro energy resource that can be utilized to full extent. [Figure 11](#) shows the simulation result to the number of hours of Battery operation during the year. It shows that batteries are operated for maximum hours during the Second quarter of the year.

Table 5 shows the simulation details of possible integrated systems for the study area considering the two load strategies. In the case of Development side Load strategy, MH-HK –Battery integrated system can give Least cost NPC of \$166,816 and COE of \$/KWh 0.153 with 46 Battery Numbers. The next best possible integrated system is PV-MH-HK-Battery with NPC of \$217,191.5 and COE of \$0.166. The cost of NPC and COE is found to be high if it is proposed for only Wind – Battery system. In case of Demand side strategy, the value of Least NPC is \$120,841 and the COE is \$0.154, it is found

to be almost same for MH-HK-Battery and PV-MH-HK-Battery integrated system. The number of Batteries required is 8 and 5 for these integrated systems. The NPC is increased by 27.5% and 44.3% for MH-HK and PV-MH-HK-Battery systems respectively when compared to the Development side strategy load Management. But, the COE remains almost the same for these two cases of the integrated system. The size of the converter in KW required is observed to be less with these two combinations. The inclusion of the wind turbine in any of the combinations gives more value of NPC and COE. This shows that the wind is not able to deliver the expected energy demand at the site. For the wind data available, it is found to be not suitable for a sustainable resource. Micro-Hydro and Hydrokinetic alone can contribute to the delivery of the energy demand. The carbon emissions are zero for the Global emissions demand. It is also observed from the results that the contribution of MH and HK together is more than 80% in generating the Energy in KWh/year. This shows that the Hydro potential is more sustainable in these areas. This study area is near to Augumbe forest

reserve where more rainfall occurs through the year as the data is collected from the nearest rain gauge station. Thus it is

suggested that keeping the above results into consideration, the PV-MH-HK with battery is more suitable for the location.

Table 7 Present study comparison with other relevant studies on Remote areas in India

Configuration	NPC(\$)	COE(\$/KWh)	Peak Load(KW)	Reference	Remarks
PV-MHP-Battery	4,67,644	0.106	108.6	[35]	HOMER tool used to study the Effect of different batteries is analyzed with and without Dieselgenerator. Hydrokinetic resource is not considered.
MH-BM-BG-WT-BT	6,05,376	0.087	170	[40]	Cluster of villages in remote area are analyzed. Hydrokinetic resource is not considered
PV-WT-BM-BG	141142	0.069	-	[27]	HOMER tool used HK resource is not considered
PV-BM-Battery	----	0.21779	64	[28]	MATLAB metaheuristic algorithms study .HK resource is not considered.

8. Multiyear simulation results

Multi-year simulation module in the HOMER software provides futuristic values of various parameters integrated into the system. This module takes the values of PV degradation of production, annual increase in the fixed maintenance cost and annual increase of electrical load

requirement. The simulation results on various parameters like PV production kWh/year, AC primary load, Battery losses (kWh/year), converter losses (kWh/year), unmet electrical load (%) and capacity shortage (%) are noted 10 year simulation output. Table 8 shows the Multi-year simulation for the optimal result obtained.

Table 8 Multi-year simulation of optimal result for Development side strategy

PV-MH-HK-BATT SYSTEM PV-10KW BATT-300, CONV-40.0KW, WIND-1(275 KWh/day)							
Year	PV production KWh/year	LCOE(PV) \$/KWh	AC Primary Load KWh/year	Battery Losses KWh/year	Rectifier / Converter Losses KWh/year	Unmet Electrical Load in %	Capacity shortage in %
1	794	0.146	92,426	1883	476/374	7.93	10.5
2	791	0.144	93,865	1912	484/385	8.35	10.8
3	784	0.145	95,312	1934	491/391	8.74	11.4
4	781	0.146	96,775	1955	497/392	9.14	11.6
5	772	0.152	98,256	1978	502/395	9.54	12.7
6	773	0.152	99,717	1994	506/404	10.1	12.5
7	772	0.152	101,195	2004	509/401	10.2	13.5
8	765	0.152	102,684	2012	511/402	10.2	13.6
9	766	0.152	104,175	2015	513/405	11.3	14.5
10	754	0.154	105,712	2025	515/405	11.7	14.6

Table 9 Multi-year simulation of optimal result for Demand side Load strategy

PV-MH-HK-BATT SYSTEM -PV-0.5 KW, BATT-5, CONV-1 KW							
Year	PV production KWh/year	LCOE(PV) \$/KWh	AC Primary Load KWh/year	Battery Losses KWh/year	Rectifier / Converter Losses KWh/year	Unmet Electrical Load in %	Capacity shortage in %
1	795	0.146	58,717	31.3	6.06/7.81	8.06	10.8
2	795	0.146	59,657	32.2	6.06/7.81	8.44	11.2
3	782	0.147	60,605	32.2	6.14/8.02	8.81	11.4
4	784	0.148	61,560	32.6	6.12/8.06	9.14	12.3
5	776	0.151	62,527	33.1	6.10/8.13	9.55	12.7
6	7754	0.152	63,506	33.2	6.07/8.15	9.96	13.2
7	777	0.153	64,497	33.6	6.09/8.26	10.34	13.4
8	761	0.153	65,499	33.7	6.11/8.41	10.71	13.8
9	760	0.155	66,510	33.8	6.01/8.42	11.21	14.5
10	758	0.155	67,533	34.1	5.94/8.45	11.41	14.5

From **Error! Reference source not found.**8 , % change of PV production (decrease) – 4.3%, COE (%) -4.74%, AC primary Load-14.35%, Battery Losses-7.498%, converter/Rectifier Losses-8.17%/7.37%, unmet electrical load-3.88%, capacity shortage-4.5%. From Table 9, % change of PV production (decrease) – 4.4%, COE (%) -5.44%, AC primary Load-15.01%, Battery Losses-8.28%, converter/Rectifier Losses-0.825%/8.38%, unmet electrical load-3.43%, capacity shortage-4.0 %. The Multi-year simulations gives the degradation of PV systems is around 4.4% to 8% in all the cases studied, AC primary load is increased from 12.33% to 18% for the cases, the battery losses is around 3.9% to 19% and the unmet load is increased in the range of 1.3% to 6% in all the cases studied.

Conclusions

This paper presents the simulation studies for a different combination of the integrated

renewable energy system for obtaining the least NPC and COE. The potential resources available in the study area are first identified as PV-WIND-MH-HK. The seven different combinations are simulated for obtaining the optimal value of NPC and COE considering the Developing side Load strategy and Demand-side Load strategy which gives 14 combinations of simulation studies. It is found that Demand side Load strategy is 51% of Development side Load strategy for the annual Energy Demand Estimation. In all the simulations, Battery system should be included as it provides a continuous uninterrupted power supply. In the Development side Load strategy, the best optimal solution is found to be of MH-HK(40KW) with a NPC of \$166,816 and COE is \$0.153. The second optimal solution is with the combination of PV-MH-HK with NPC of \$217,191.5 and COE is \$0.166. From the feasible and sustainable point of view, the PV-MH-HK is found to be better for the location considering

rainfall situations. For the Demand side load strategy, it is found that same two combinations hold good as the best possible solution. Here, NPC and COE values obtained are almost same having values \$120,481(MH-HK)-\$120,824(PV-MH-HK) and \$ 0.154(MH-HK)-\$0.158(PV-MH-HK). The optimal values were obtained by considering sensitivity parameters in HOMER pro soft. Integration with WIND turbine system gives more value of NPC and COE. It can be identified the generation from the WIND turbine is not a feasible solution at the location. Further, the Multiyear simulation results carried out for the best optimal solution for 10 years gives the parameters effect is well within the lower range. From all the observations, it is clear that the site is having a good potential for Hydro resources and is more feasible and sustainable with zero emissions.

Acknowledgments

The author wishes to thank the Local people and the Grama Panchayat for providing useful information about the local resources.

Author contributions

Naveen R: Conceptualization, organizing, Methodology, Software, Naveen R.: Data curation, Investigation, Writing- Original draft preparation. Prashanth P Revankar: Visualization, Supervision: Prashanth P Revankar: Software, Validation, Writing- Reviewing and Editing.

Competing Interests

There are no competing interests reported by the Authors

References

- [1] E. C. B. Code, "Bureau of Energy Efficiency," 2017.
- [2] E. Cuce and P. M. Cuce, "A comprehensive review on solar cookers," *Applied Energy*, vol. 102, pp. 1399–1421, 2013.
- [3] E. Dugoua, R. Liu, and J. Urpelainen, "Geographic and socio-economic barriers to rural electrification: New evidence from Indian villages," *Energy Policy*, vol. 106, pp. 278–287, 2017.
- [4] R. Naveen, P. Revankar, and S. Rajanna, "Integration of Renewable Energy Systems for Optimal Energy Needs-a review," *International Journal of Renewable Energy Research (IJRER)*, vol. 10, no. 2, pp. 727–742, 2020.
- [5] A. M. Patel and S. K. Singal, "Economic analysis of integrated renewable energy system for electrification of remote rural area having scattered population," *International Journal of Renewable Energy Research*, vol. 8, no. 1, pp. 258–265, 2018.
- [6] O. Ellabban, H. Abu-Rub, and F. Blaabjerg, "Renewable energy resources: Current status, future prospects and their enabling technology," *Renewable and Sustainable Energy Reviews*, vol. 39, pp. 748–764, 2014.
- [7] N. Varshney, M. Sharma, and D. Khatod, "Sizing of hybrid energy system using HOMER," *International Journal of Emerging Technology and Advanced Engineering*, vol. 3, no. 6, pp. 436–44, 2013.
- [8] S. Rajanna and R. Saini, "Selection of suitable strategy with peak load shifting based DSM strategy of standalone integrated renewable energy system for a remote rural area," in *2016 IEEE 1st International Conference on Power Electronics, Intelligent Control and Energy Systems (ICPEICES)*, 2016, pp. 1–6.
- [9] S. Rajanna and R. Saini, "Optimal modeling of Solar/Biogas/Biomass based IRE system for a remote area electrification," in *2014 6th IEEE Power India International Conference (PIICON)*, 2014, pp. 1–5.
- [10] S. Rajanna and R. Saini, "Optimal modeling of an integrated renewable energy system with battery storage for off grid electrification of remote rural area," in *2016 IEEE 1st International Conference on Power Electronics, Intelligent Control and Energy Systems (ICPEICES)*, 2016, pp. 1–6.

- [11] K. Mitchell, M. Nagrial, and J. Rizk, "Simulation and optimisation of renewable energy systems," *International Journal of Electrical Power & Energy Systems*, vol. 27, no. 3, pp. 177–188, 2005.
- [12] R. Luna-Rubio, M. Trejo-Perea, D. Vargas-Vázquez, and G. Ríos-Moreno, "Optimal sizing of renewable hybrids energy systems: A review of methodologies," *Solar energy*, vol. 86, no. 4, pp. 1077–1088, 2012.
- [13] D. Saheb-Koussa, M. Haddadi, and M. Belhamel, "Economic and technical study of a hybrid system (wind–photovoltaic–diesel) for rural electrification in Algeria," *Applied Energy*, vol. 86, no. 7–8, pp. 1024–1030, 2009.
- [14] T. Ma, H. Yang, and L. Lu, "A feasibility study of a stand-alone hybrid solar–wind–battery system for a remote island," *Applied Energy*, vol. 121, pp. 149–158, 2014.
- [15] E. Hurtado, E. Peñalvo-López, Á. Pérez-Navarro, C. Vargas, and D. Alfonso, "Optimization of a hybrid renewable system for high feasibility application in non-connected zones," *Applied Energy*, vol. 155, pp. 308–314, 2015.
- [16] A. Ahadi, S.-K. Kang, and J.-H. Lee, "A novel approach for optimal combinations of wind, PV, and energy storage system in diesel-free isolated communities," *Applied Energy*, vol. 170, pp. 101–115, 2016.
- [17] E. Nfah, J. Ngundam, M. Vandenberg, and J. Schmid, "Simulation of off-grid generation options for remote villages in Cameroon," *Renewable Energy*, vol. 33, no. 5, pp. 1064–1072, 2008.
- [18] A. Chauhan and R. Saini, "Renewable energy based power generation for stand-alone applications: A review," in *2013 International Conference on Energy Efficient Technologies for Sustainability*, 2013, pp. 424–428.
- [19] A. Gupta, R. Saini, and M. Sharma, "Modelling of hybrid energy system—Part I: Problem formulation and model development," *Renewable Energy*, vol. 36, no. 2, pp. 459–465, 2011.
- [20] A. Gupta, R. Saini, and M. Sharma, "Modelling of hybrid energy system—Part I: Problem formulation and model development," *Renewable Energy*, vol. 36, no. 2, pp. 459–465, 2011.
- [21] X. Wang, A. Palazoglu, and N. H. El-Farra, "Operational optimization and demand response of hybrid renewable energy systems," *Applied Energy*, vol. 143, pp. 324–335, 2015.
- [22] T. T. Sepulveda and L. Martinez, "Optimization of a hybrid energy system for an isolated community in Brazil," *International Journal of Renewable Energy Research*, vol. 6, no. 4, pp. 1476–1481, 2016.
- [23] B. Bala and S. A. Siddique, "Optimal design of a PV-diesel hybrid system for electrification of an isolated island—Sandwip in Bangladesh using genetic algorithm," *Energy for sustainable Development*, vol. 13, no. 3, pp. 137–142, 2009.
- [24] D. Yamegueu, Y. Azoumah, X. Py, and N. Zongo, "Experimental study of electricity generation by Solar PV/diesel hybrid systems without battery storage for off-grid areas," *Renewable energy*, vol. 36, no. 6, pp. 1780–1787, 2011.
- [25] A. Chauhan and R. Saini, "A review on Integrated Renewable Energy System based power generation for stand-alone applications: Configurations, storage options, sizing methodologies and control," *Renewable and Sustainable Energy Reviews*, vol. 38, pp. 99–120, 2014.
- [26] A. Bhatt, M. Sharma, and R. Saini, "Feasibility and sensitivity analysis of an off-grid micro hydro–photovoltaic–biomass and biogas–diesel–battery hybrid energy system for a remote area in Uttarakhand state, India," *Renewable and Sustainable Energy Reviews*, vol. 61, pp. 53–69, 2016.
- [27] D. P. Pathak and D. Khatod, "Economic Aspects of Integrated Renewable Energy System for Remote Area Electrification," in *2017 14th IEEE India Council International Conference (INDICON)*, 2017, pp. 1–5.
- [28] P. P. Kumar and R. P. Saini, "Optimization of an off-grid integrated hybrid renewable energy system with different battery technologies for rural electrification in India," *Journal of Energy Storage*, vol. 32, p. 101912, 2020.

- [29] M. Ghahramani, M. Nazari-Heris, K. Zare, and B. Mohammadi-Ivatloo, "Energy and reserve management of a smart distribution system by incorporating responsive-loads/battery/wind turbines considering uncertain parameters," *Energy*, vol. 183, pp. 205–219, 2019.
- [30] S. Nojavan, M. Majidi, A. Najafi-Ghalelou, M. Ghahramani, and K. Zare, "A cost-emission model for fuel cell/PV/battery hybrid energy system in the presence of demand response program: -constraint method and fuzzy satisfying approach," *Energy Conversion and Management*, vol. 138, pp. 383–392, 2017.
- [31] M. Ghahramani, M. Nazari-Heris, K. Zare, and B. Mohammadi-ivatloo, "Optimal energy and reserve management of the electric vehicles aggregator in electrical energy networks considering distributed energy sources and demand side management," in *Electric vehicles in energy systems*, Springer, 2020, pp. 211–231.
- [32] E. S. Hub, "The European Commission's Science and Knowledge Service.,<https://ec.europa.eu/jrc/en/pvgis>," 2018.
- [33] S. Rajanna, "Integrated renewable energy system for a remote rural area," Ph. D. thesis, Alternate Hydro Energy Center, IIT Roorkee, 2016.
- [34] 2020 world weather online(WWO), .
- [35] M. Ramesh and R. P. Saini, "Effect of different batteries and diesel generator on the performance of a stand-alone hybrid renewable energy system," *Energy Sources, Part A: Recovery, Utilization, and Environmental Effects*, pp. 1–23, 2020.
- [36] H. Yang, L. Lu, and W. Zhou, "A novel optimization sizing model for hybrid solar-wind power generation system," *Solar energy*, vol. 81, no. 1, pp. 76–84, 2007.
- [37] N. R. E. L. (NREL). 2019. T. hybrid optimization of multiple energy resources (HOMER). [https:// www.homerenergy.com](https://www.homerenergy.com), .
- [38] S. Rajanna and R. Saini, "Modeling of integrated renewable energy system for electrification of a remote area in India," *Renewable energy*, vol. 90, pp. 175–187, 2016.
- [39] C. M. Niebuhr, M. Van Dijk, V. S. Neary, and J. N. Bhagwan, "A review of hydrokinetic turbines and enhancement techniques for canal installations: Technology, applicability and potential," *Renewable and Sustainable Energy Reviews*, vol. 113, p. 109240, 2019.
- [40] S. Rajanna and R. Saini, "Development of optimal integrated renewable energy model with battery storage for a remote Indian area," *Energy*, vol. 111, pp. 803–817, 2016.

Development of Brake Friction Material for Automotive Application

Vijay Kumar B. P.¹, Dr. Raghavendra Joshi², Dr. V. Venkata Ramana³
Dr. Manjunatha T. H.⁴

¹Assistant Professor, Department of Mechanical Engineering, Ballari Institute of Technology and Management, Ballari, Karnataka, India

²Professor and COE, Ballari Institute of Technology and Management
Ballari, Karnataka, India

³Professor and Head, Department of Mechanical Engineering, Ballari Institute of Technology and Management, Ballari, Karnataka, India

⁴Associate Professor, Department of Mechanical Engineering, Ballari Institute of Technology and Management, Ballari, Karnataka, India

Abstract

Brakes in any automobile are intended to regulate and stop the moving vehicles safely. The overall braking efficacy depends on various components, their ability to convert kinetic energy to heat energy through friction (b/w pad and drum). Therefore, the pad material properties are of significance, to name a few, clothing forfeiture, coefficient of friction (COF), wear and mechanical behaviour. Normally, Phenol formaldehyde (PF) / Epoxy resin (ER) and some fibre materials along with glass, asbestos and carbon fibres in proper proportions are preferred. Whereas, asbestos is readily available in the market and regularly used. But, this asbestos is toxic in nature and there is every need to explore alternatives. An endeavour made to substitute this asbestos with materials like glass fibre (GF), carbon fibre (CF) coconut casing powder (CSP) etc. which are eco-friendly. Also, inorganic materials like BaSO₄ - barium sulphate and CaCO₃ – calcium carbonate are explored as well in terms of filler followed by aluminium

¹Corresponding Author, email: bpviji6@gmail.com

© Common Ground Research Networks, Vijay Kumar B. P., All Rights Reserved.

Acceptance: 24July2023, Publication: 28July2023

²Second Author

³Third Author

⁴Fourth Author

oxide, graphite and antimony sulphide tested for frictional additives. This paper depicts certain trials made on, Asbestos Free Brake Friction Material (AFBFM) combinations – PF with GF, PF doped CF, ER & GF mixture, and ER with CF for wide proportions of fibres and matrix. The results suggested the combination of ER and 15% CF is suitable for brake shoe material.

Keywords

Brakes, Pulverized cow hooves, Non-Asbestos, Tribological properties

1. Introduction

Automobile braking system consists of components like drum, pad, cylinder etc., which control the vehicle speed by converting mobile energy to heat due to friction. During this process the brake shoes are in action and should maintain sufficient frictional factor with the disc to avoid failures. These shoes are made of asbestos mixed with several other ingredients which is toxic and harmful in nature need to be substituted. Quite a few research works done in this direction suggested new asbestos free materials from agricultural wastes. The emerging materials for brake pads are commercially viable and eco-friendly.

Researchers like Idris, Namessan, Koya, Fono, Aigbodion, Ibadode and Dagwa, Ruzaidi worked with banana peels, kenaf (*Hibiscus cannabinus*) fibres and palm kernel shell respectively, and concluded these materials can be used effectively as an alternate to asbestos. All the researchers used the standard procedure to assess the suitability of these materials. In the same line this paper presents the work documented on fabrication of brake pad material without asbestos (AFBFM) with different combinations of PF and ER mixed with glass fibre (GF), carbon fibre (CF) (PF+GF, PF with CF, ER added to GF and ER+CF). Compression moulding was preferred for preparing samples and relative analysis with the commercial available pads is made.

2. Materials

The materials selected for the study are E-glass, carbon fibres (reinforcement), epoxy resin and Phenol Formaldehyde (base material). The E-glass fibres possess excellent electric resistance apart from resistance to heat, temperature, resistance to chemical action, resistance to moisture etc. Further, these fibres maintain their strength over a varied temperature conditions. The chemical composition of the E-glass comprises of oxides of silicon (55%), aluminium (14%), boron (7%), calcium (22%), magnesium, and the physical properties are tensile strength of

3.44GPa, density 2.58g/cm³ elongation of 4.8%, Thermal Expansion Co-efficient of 54x10⁻⁷⁰C etc. The carbon fibre is composed of carbon atoms which are extremely stiff, strong, and light, properties close to that of steel and as light as plastic. Thus the strength to weight ratio (as well as stiffness to weight ratio) of a carbon fibre part is much higher than steel or plastic. Carbon fibre is extremely strong; typical engineered for structural, aerospace, civil, military, and motorsports applications addressing lifecycle costs and performance. A few properties of this carbon fibre are, tensile strength-5880MPa, density- 1.8g/cm³, thermal conductivity of 70W/mK etc., but they are costly.

The Table 1 Material list in percentage compositions

Table 1. Material – Composition in volume fractions

Sl. No	Materials		Density (g/cm ³)	Volume fraction		
				SAMPLE (A1,B1,C1&D1)	SAMPLE (A2, B2,C2 &D2)	SAMPLE (A3,B3,C3&D3)
1	Fibres	E-glass	2.55	5	10	15
		Carbon	2.0			
2	Matrix	Phenol formaldehyde	1.21	60	55	50
		Epoxy resin	1.56			
3	Fillers	BaSO ₄	4.5	8	8	8
		CaCO ₃	2.71	4	4	4
		Coconut casing powder	1.6	10	10	10
4	Additives	Aluminium Oxide	3.95	9	9	9
		Graphite	2.26	2	2	2
		Sulphide of Antimony	4.64	2	2	2

Table 1.1 indicates combinations of base material and additives with constant values, used to prepare the samples of AFBFM. Minimum of 50% matrix and maximum 15% fibre (in volume fraction) including fillers and additives are taken for fabrication purpose.

Table1.1 AFBFM: Matrix - Fibre Combinations in %age vol. fractions

Sl. No	Fibre	Matrix	Sample-a		Sample-b		Sample-c	
			Volume Fraction Fibre	Volume Fraction Matrix	Volume Fraction Fibre	Volume Fraction Matrix	Volume Fraction Fibre	Volume Fraction Matrix
1	Glass	Phenol Formaldehyde	5.0	60.0	10.0	55.0	15.0	50.0
2	Glass	Epoxy Resin	5.0	60.0	10.0	55.0	15.0	50.0
3	Carbon	Phenol Formaldehyde	5.0	60.0	10.0	55.0	15.0	50.0
4	Carbon	Epoxy Resin	5.0	60.0	10.0	55.0	15.0	50.0

3. Methodology

Among the available methods to fabricate any composite compression moulding technique is most preferred (high pressure application). The mould is preheated to 150⁰C, 120 bar pressure is applied, charged with ER or PF, and all selected additives. Later, subjected to curing for a predetermined period of ½ to ¾th hour. The samples are pulled out of mould cavity and subjected to treatment for a day at 80⁰C. The sample size is 200 X 160 X 5 mm and finally, the fabricated PF and ER samples are sized. The standard (ASTM) specimens for various tests like impact, and compression are prepared.

4. Mechanical Testing and Structural Characterization

The prepared samples are subjected to the various tests to evaluate mechanical, wear etc. properties. This paper is concentrating specifically on impact ,compression ,hardness properties looking into their rolein terms of brake shoe is concerned for the system. The ASTM D-695 standard trial was selected to explore compressive strength.

4.1 Compressive Strength



Figure 4.1 ASTM D-695 work pieces for compression test

In order to conduct experiments, UTM, a job of $12.7 * 12.7 * 25.4$ mm (figure 4.1), ASTM D-695 procedure with 2 mm/min speed is set. The job is subjected to compression till fracture. The compression strength is noted for fracture against the load applied for the given sample.

4.2 Impact Strength

The impact analysis (izod), test ASTM D-256 (Figure 4.2) is selected and different pendulum hammers are used till failure occurs and readings are tabulated. All types of samples are subjected to same treatment.

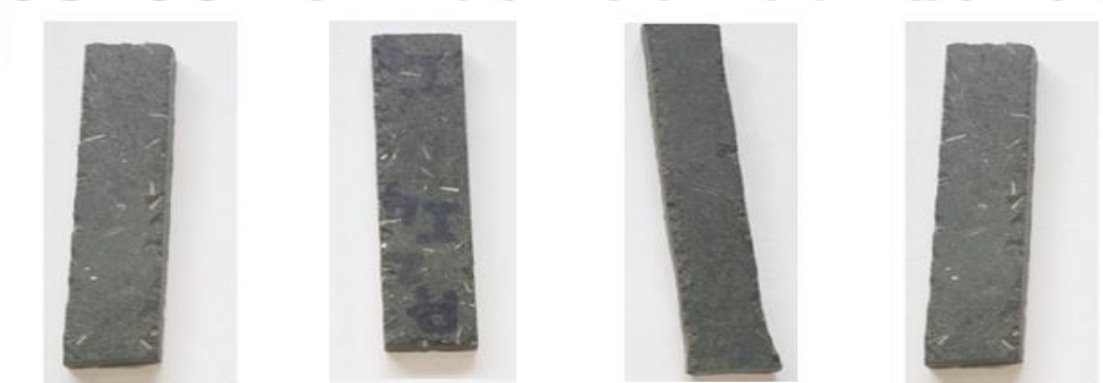


Figure 4.2 ASTM D-256 Work Pieces for Impact test

4.3 Hardness Number

In the present work, Shore-Durometer (Shore-D) test was used. The Shore A scale is used for 'softer' polymers while the Shore D scale is used for 'harder' composites, ASTM D-2240 standard is used to measure the hardness. Different volume fractions of PF and ER reinforced with glass and carbon fiber brake friction materials shown in were used to conduct hardness test.

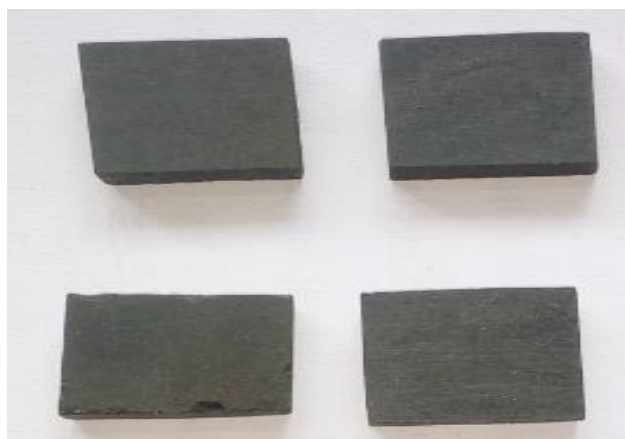


Figure 4.3 ASTM D-2240 Work Pieces for Hardness test

For each sample, hardness number was measured at different locations on the specimen and average hardness numbers for each sample were tabulated. All types of samples are subjected to same treatment.

5. Deliberations on Outcomes

Compressive Strength

Table 5.1 Compressive strength: GF & CF plus PF& ER commercial Brake Pads

S L N o	% age of Reinf orcem ent	Compressive strength of asbestos free brake friction composite material, MPa				Compressive strength of Commercial asbestos based brake pads, MPa		Compressiv e strength of Commercial brake pads (Literature), MPa CABBPM
		PF+GF	PF+CF	ER+GF	ER+CF	ABBPM-2	ABBPM-2	
1	5	79.24	85.63	87.66	93.93	104.33	112	110
2	10	83.32	92.13	90.33	98.67			
3	15	87.33	101.83	105.26	121.33			

From the above table, the compressive strength tabulated for (15% vol.) GF plus PF amalgam is 87.33 MPa. The values are 03 tests average of each vol. fraction used for further analysis. Equally, for 5% and 10% the values are 79.24 and 83.32 MPa respectively. Similarly, the strength obtained for 05, 10 and 15 percent carbon fibre inclusion with phenol-formaldehyde are 85.63, 92.13, and 101.83 MPa respectively.

For the combination of epoxy with glass fibres (5%, 10% and 15%) the compressive strength resulted as 87.66, 90.33, 105.26 MPa respectively and with carbon fibre for same volume

fraction addition the strength was 93.93, 98.67 and 121.33 MPa respectively. Now if we check the values of asbestos pads (ABBPM-1 & ABBPM-2) the values are 104.33 and 112 MPa for 1, 2 types correspondingly. This is depicted in table.

Further, keen observations reveal that the compressive strength of the prepared material (without asbestos) improved with percentage hike in reinforcement apart from even dispersion alloying elements. In addition, Epoxy resin combinations fared well relative to PF based blends with proper mixing and bonding. The tested combinations when compared to asbestos, the ER & CF -15% carbon fibre compressive strength is 121.33 MPa higher by 14.01% and 7.68% respectively (ABBPM-1 and ABBPM-2).

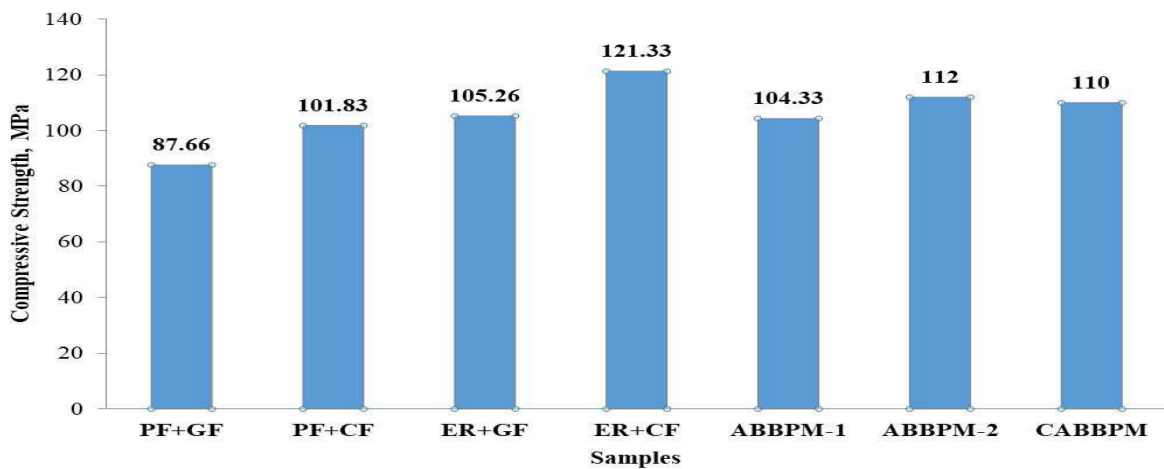


Figure 5.1 bar chart showing Compressive Strength – with and without Asbestos

Impact strength

Some trials were carried out with glass and carbon reinforcements plus PF and ER as base in with ASTM D256 in different vol. fractions. For each combination, 05 samples were measured and average values are tabulated (Table 5.2).

Table 5.2 Impact strength: GF & CF plus PF & ER vs Commercial Brake Pads

Sl No	% age Reinf orcem ent	Impact strength without asbestos, J/mm ²				Impact strength of asbestos based, J/mm ²		Impact strength of Commercial brake pad (Literature) CABBPMJ/mm ²
		PF +GF	PF+ CF	ER+ GF	ER+CF	ABBPM- 1	ABBPM-2	
1	5	0.063	0.072	0.066	0.079	0.0833	0.091	0.111
2	10	0.067	0.076	0.068	0.083			
3	15	0.07	0.081	0.071	0.0852			

The tabulated values of impact strength of the combinations without asbestos show significant increase with percentage addition of reinforcement, better bonding. A related trend is seen with carbon addition as these fibres possess superior intrinsic mechanical properties comparatively. Further, CF+ER (15%) combination 2.58% higher impact strength in relation to regular asbestos based materials.

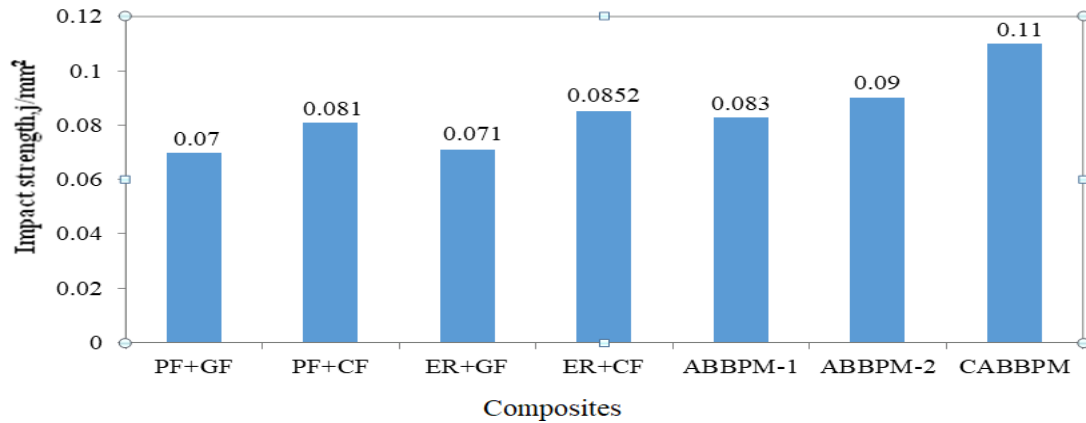


Figure 5.2 Bar chart showing Impact Strength with and Without Asbestos

Hardness

The hardness of composite materials was measured using Shore- Durometer (**Shore-D**) test. It is a measure of resistance offered by materials for indentation which is depicted as hardness number. Experiments were conducted for different volume fractions of glass and carbon fiber reinforced PF and ER based friction materials on the surface and average hardness numbers for each combination are tabulated in Table 5.3 These values were compared with the asbestos based brake pad materials and found that asbestos free brake friction composite material is harder compared to that of commercial brake pad materials

Table 5.3 hardness number: GF & CF plus PF& ER vs Commercial Brake Pads

Percent Reinforcement (%)	PF+GF	PF+CF	ER+GF	ER+CF	ABBPM-1	ABBPM-2	CABBPM (Literature)
5	79	82	85	88	82	83	82
10	80	84	87	90			
15	82	85	90	92			

Figure 5.3 shows the hardness number for 15% volume fraction of GF and CF reinforced composites and asbestos based commercial brake pads. It is observed that, Epoxy Resin based composites have higher hardness compared to PF based and commercial brake pad materials. This is due to better interfacial bonding of fiber, filler and frictional additives with ER.

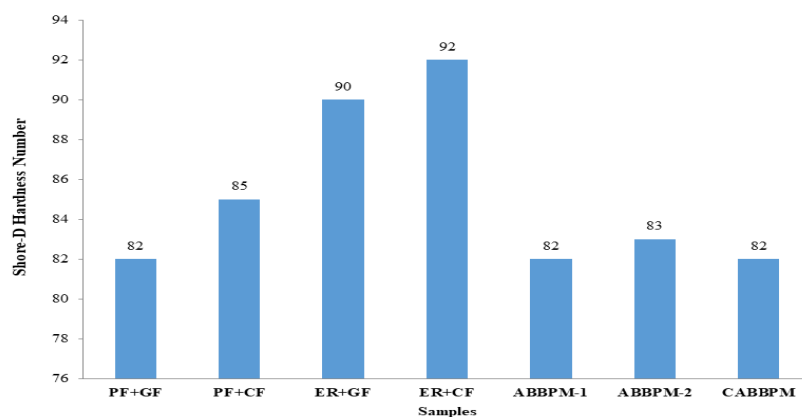


Figure 5.3 Bar chart showing hardness value with and Without Asbestos

The Shore D hardness of GF and CF reinforced composites enhanced with increase in fiber content. This is due to more resistance offered by the fibres as its content increases in the composites. Addition of CF in matrix has resulted in the highest hardness value among the considered composites due to the better mechanical properties of CF

6. Conclusions

The experimental compressive strength of epoxy doped with carbon fibre (5 – 15%) has shown gradual increase from 93.333 to 121.333 MPa, higher than both asbestos and glass fibre pads. Similarly the glass and carbon fibres with phenol formaldehyde the carbon reinforced samples have better strength (14.01% high for 15% addition) comparatively. The reasons are due to less rigidity and strength of glass fibres relatively. The samples when tested under impact, the 15% of CF & GF in PF matrix, recorded values are 0.08 J/mm² and 0.07 J/mm² respectively. As urge in impact strength when CF added with 15% GF is 13.58%. For the same percentages of CF & GF supplemented to ER the values are 0.085 J/mm² and 0.071 J/mm² respectively. Also, when 15% CF put into ER noticed 16.66% higher impact strength. The same in relation to regular asbestos there is marginal hike of 2.58%. The samples when tested under hardness test, Hardness of ER+15% V_f CF is 92. It is 2% higher than the hardness of ER+15% V_f of GF which is 90%. ER+15% V_f CF composites hardness is 10% and 9 % higher than ABBPM-1 and ABBPM-2 respectively. Therefore, it can be concluded that ER+15% of carbon fibre is of dominant combination for brake pad material.

References

1. D Chan and G.W Stachowiak, “Review of Automotive Brake Friction Materials”, PROC. Instn Mech. Engrs, Vol.218, part D: J. Automobile Engineering, 2004, pp 953 – 966.

2. Rao, R. Umamaheswara, and G. Babji. "A Review paper on alternate materials for Asbestos brake pads and its characterization." *International Research Journal of Engineering and Technology* 2, no. 2 (2015): 556-562.
3. Jiusheng Bao, Yan Yin, Zhencai Zhu, Minming Tong, Yuhao Lu, Yuxing Peng "Wear modalities and mechanisms of the mining non-asbestos composite brake material." *Applied Composite Materials* 20.4 (2013): 331-339.
4. V. Thiyagarajan, R. Vijay, K. Sivakumar, R.I. Harigovindhan "Tribo-Thermal Based Evaluation of Non Asbestos Disc Brake Pad Formulation." *Applied Mechanics and Materials*. Vol. 766. Trans Tech Publications, 2015.
5. Aranganathan, N., and JayashreeBijwe. "Development of copper-free eco-friendly brake-friction material using novel ingredients." *Wear* 352 (2016):79-91.
6. Zhang, Hui, Zhong Zhang, and Klaus Friedrich. "Effect of Fibre length on the wear resistance of short carbon Fibre reinforced epoxy composites. " *Composites science and technology* 67.2 (2007): 222-230.
7. Pihtili, Hasim. "An experimental investigation of wear of glass Fibre–Epoxy Resin and glass Fibre–polyester resin composite materials." *European polymer journal* 45.1 (2009): 149-154.
8. Shivamurthy, B., K. UdayaBhat, and S. Anandhan. "Mechanical and sliding wear properties of multi-layered laminates from glass fabric/graphite/epoxy composites." *Materials & Design* 44 (2013): 136-143.
9. Jayashree Bijwe, MukeshKumar, P.V.Gurunath, Yannick Desplanques, G'erard Degallaix "Optimization of brass contents for best combination of tribo-performance and thermal conductivity of non-asbestos organic (NAO) friction composites." *Wear* 265.5 (2008): 699-712.
10. Ganguly, Arnab, and Raji George. "Asbestos free friction composition for brake linings." *Bulletin of Materials Science* 31.1 (2008): 19-22.
11. U.D.Idris, V.S.Aigbodion, I.J.Abubakar, C.I.Nwoye "Eco-friendly asbestos free brake-pad: using banana peels." *Journal of King Saud University-Engineering Sciences* 27.2 (2015): 185-192.
12. Elakhame, Z. U., O. A. Alhassan, and A. E. Samuel. "Development and Production of Brake Pads from Palm Kernel Shell Composites." *IJSER* 5 (2014).

13. Ilanko, Ashok Kumar, and Srinivasan Vijayaraghavan. "Wear behavior of asbestos-free eco-friendly composites for automobile brake materials." *Friction* 4, no. 2 (2016): 144-152.
14. Ashafi'e, Mustafa, Mohd Fadzli bin Abdollah, Nurhidayah Ismail, Hilmi Amiruddin, and Noritsugu Umehara. "Pre-materials selection for eco-aware lightweight friction material." (2014): 1-17.
15. Adeyemi, I. Olabisi. "Development of Asbestos-Free Automotive Brake Pad Using Ternary Agro-Waste Fillers." *Development* 3, no. 7 (2016).



A Comparative Study on Abrasive Wear Behavior of TiB₂/Graphite Reinforced Cast and Hot Rolled Al7075-Based Hybrid MMCs

R M Shabbir Ahmed¹ · Banakara Nagaraj² ·
N Kiran Kumar³ · S G Sujith Kumar⁴ ·
Amithkumar Gajakosh⁴ 

Received: 1 June 2023 / Accepted: 8 August 2023 / Published online: 27 August 2023
© The Institution of Engineers (India) 2023

Abstract Among well-known substances for reinforcing, graphite, a softer and well-known material, is a preferred choice due to its thermal properties, lubrication characteristics, lightweight, and chemical stability. Titanium diboride is another common ceramic reinforcing substance with excellent thermal conductance, a higher melting temperature, outstanding rigidity, and exceptional micro-hardness at varying temperatures. The current study investigates the effect of titanium diboride and graphite additives on the wear characteristics of AA7075 aluminum. Stir casting and hot rolling were used to make the composite materials. Using the in situ reaction method, eight percent titanium diboride particles were formed, and four and eight percent graphite particles were added later. The casting composite materials were hot rolled with an 80 percent reduction ratio at 400 °C. Microstructural studies, grain size analyses, and abrasive wear tests were performed on hot rolling and casting matrix alloys and their composite materials. According to microstructural investigations, titanium diboride and graphite reinforcement particles are distributed uniformly, with excellent bonds between the matrices and the reinforcing agents in both the casting and hot rolling conditions. Under the same test conditions, both hot rolling and casting composite materials

outperform un-reinforced alloys in terms of abrasive wear resistance. When compared to cast 7075 alloy 5wt% TiB₂ and 8wt% Graphite reinforced composite, weight loss was reduced by 35% and 47%, respectively, for cast and hybrid conditions. Scanning electron micrograph was used to investigate into possible wearing mechanisms on worn-out areas.

Keywords Al7075 · Titanium diboride · Graphite · Microstructure · Abrasive wear · Metal matrix composites

Introduction

Due to their appealing qualities, metal matrix composites (MMCs) have attracted a great deal of interest over the last thirty years. Aluminum alloys are widely used in engineering constructions, automobiles, and aerospace, especially heat-treatable alloys like AA7075. The combination of lightness, elasticity, durability, suitable resistance to abrasion, and higher stiffness due to the insertion of strong reinforcement particles are the main drivers behind composite manufacturing. The research findings also mentioned that the thin sheets made from aluminum metal matrix composites (AMCs) with hard phase-reinforcing agents are fascinating for engineering structures because of their featherweight in addition to their durability and resistance to wear. Other reasons for composite making, such as adjusting the desired thermal expansion, were also highlighted. Higher specific strength, better specific stiffness, and improved wear resistance are advantages of aluminum metal matrix composites (AMCs), which are crucial as lightweight materials advance. AMCs are widely used in the automotive, aerospace, and transportation industries. The most often used particles for AMCs reinforcement right now are ceramic and metallic. The advantage of using metallic particles as MMC

✉ Amithkumar Gajakosh
amithkumargajakosh@gmail.com

¹ EDICT Department Engineering, Bahrain Polytechnic, PO Box 33349, Isa Town, Kingdom of Bahrain
² Department of Mechanical Engineering, Ballari Institute of Technology and Management, Ballari, Karnataka 583104, India
³ Department of Mechanical Engineering, Vemana Institute of Technology, Bengaluru, Karnataka 560034, India
⁴ Department of Mechanical Engineering, T. John Institute of Technology, Bengaluru, Karnataka 560083, India

reinforcement is that the aluminum matrix and reinforcement particles' interface wettability is strengthened, leading to better interface bonding strength. Graphite and titanium boride (TiB_2) belong to a significant group of metallic materials that have been employed as reinforcement in AMCs. In terms of friction, wear, and strength, AMCs excel. The majority of investigations on aluminum composites indicated that the tribological properties of composites increased when reinforced with a number of well-known reinforcements, including Al_2O_3 , ZrO_2 , B_4C , and TiC . In addition, Si_3N_4 and graphite have superior mechanical and physical properties, such as higher melting temperatures, larger elastic moduli, and higher thermal conductivities. Graphite and TiB_2 both have the potential to replace ceramics as materials that resist wear. In addition to having flaws, including blowholes, shrinkage cavities, and uneven dispersion that are challenging to remove during the casting process, aluminum hybrid composites have been discovered to have poor interface bonding between the ceramic reinforcement and the aluminum matrix. Extrusion, forging, and rolling are examples of secondary forming techniques that are essential for preventing casting flaws and enhancing material properties. These processes have a significant impact on the interfacial bonding between the matrix and reinforcing phases, the dispersion of ceramic particles, the production of grain refinement, and the removal of porosity [1–3].

For metal matrix composites based on aluminum, rolling is the secondary forming technique that is most frequently employed since it can produce a wide range of products using various casting techniques. Finally, by rapidly undergoing large amounts of plastic deformation, rolling increases the component's strength. Thickness is decreased during hot rolling, which has a significant impact on mechanical properties and grain refinement. The three key rolling factors that determine the microstructure and mechanical properties of a rolled component are the direction of rolling, rolling temperature, and depth of reduction. In industrial aerospace applications, it is necessary to take into account how hot rolling affects the microstructure and mechanical behavior of metal matrix composites based on aluminum [4].

To create Al7075–titanium carbide/graphite hybrid composites, Patil et al. [5] employed friction stir processing (FSP), one of the most significant severe plastic deformations (SPD) procedures. The Al7075 alloy has been shown to change the wear processes from adhesion or fatigue to abrasion by mechanically mixing graphitized- TiB_2 layers to reduce wear rate during dry sliding motion. In this study, it was discovered that graphite reinforcement affected the wear characteristics of composite materials. Due to higher graphite exfoliation during dry sliding, there were fewer severe delaminations and abrasions discovered. The most crucial factor in determining the wear rate of the finished composites has been identified as the aluminum metal matrix

composite, which served as the foundation for the interface adhesion of graphite/titanium carbide composite material. The hot-extruded composite material has a lower COF and greater wear resistance than heated composites, according to An et al. [6], who was the first to manufacture and investigate the friction and wear properties of Al alloys. In their study of the tribological properties of silicon carbide-reinforced aluminum composites made by casting and hot extrusion, Dasgupta et al. [7] discovered that hot-extruded composites always experience less material loss than cast components. Al-Beryl composites were made by hot rolling and examined for wear characteristics by Reddappa et al. [8]. They claimed that dynamic recrystallization (DRX), which takes place during hot rolling, lowers the specific wear resistance of the rolled aluminum composites when compared to cast composites. Al_2O_3 and graphite reinforcement particles were added to Al7075 by Baradeswaran et al. [9], who claimed that this improved the material's hardness, tensile strength, and flexural strength when compared to the base metal. The presence of graphite in hybrid composite material revealed a tendency to maintain wear on the tribo-surface to a minimum because thin layers of graphite formed on wear surfaces.

In a study to determine the impact of graphite amount and milling on microstructure, mechanical, and wear behavior, Lara et al. [10] constructed Al7075–graphite composites using hot extrusion and mechanical alloying. They claimed that successful grain refining, homogenous graphite dispersion, and alloying element incorporation are all outcomes of hot extrusion and mechanical alloying. More graphite content and longer milling times provide the composites with better mechanical characteristics. Microstructural analyses of debris and worn surfaces show that the strength and hardness of the composite have risen as a result of the inclusion of graphite particles and the prolonged milling time, which may enhance the composite material's dry wear qualities.

Despite the fact that the strength of aluminum decreases by 9% when compared to the previous experiments, Ashwini et al. [11]'s research shows that the addition of fly ash improves the mechanical properties of the aluminum with graphite by 3 and 6%, respectively. The micro-hardness of the composite decreases by nine percent when compared to the earlier samples, but the addition of 3 and 6 wt% fly ash to aluminum and graphite. Increases the materials' hardness. The volume of wear rate of hybrid composites drops to a lesser extent and then declines along with the increase in fly ash content. The friction coefficient experiences the opposite trend. As the amount of fly ash varies (3, 6, and 9%), the density of aluminum with graphite decreases. Fly ash and SiC are added to composites to increase their mechanical strength and hardness, according to Lokesh et al. [12]. The wear resistance increases along with the fly ash and SiC content. The fly ash and SiC were firmly linked with the matrix,

Table 1 Composition of alloy

Elements	Cu	Cr	Mn	Mg	Si	Ti	Zn	Fe	Al
Wt%	1.74	0.26	0.41	1.9	0.44	0.17	3.2	0.44	Balance

with no cracks at the particle–matrix contact, according to the microstructures.

Uvaraja et al. [13] used liquid metallurgy to prepare the homogeneous composite structure and introduced SiC and B₄C reinforcement particles in both Al7075 and Al6061 alloys. Particle dispersion in both matrix systems is homogeneous, as seen by optical micrographs. The results of the hardness tests show that the filler increased the composite's micro-hardness. On the other side, the composite material's wear rate was enhanced. Furthermore, silicon carbide was added to the Al7075-based composite to slow down the rate of wear. According to the standards, Basavaraj et al. [14] examined the tribological behavior of Al-fly ash-SiC and Al-graphite-SiC. The materials experience some hardening when they are combined with fly ash and graphite, and SiC. Prior to a specific loading capability, metal matrix composites have good tribological characteristics. Fly ash, Graphite, and SiC were added to the composite to increase its strength and hardness. The stir-casting method was employed by Danappa et al. [15] to create Al7075–graphite–TiO₂ metal matrix composites. It has been determined that the load applied, as well as the titanium oxide particle content, has an impact on wear resistance. Hard titanium particles were added, and this decreased wear by 94%.

According to the literature reviews, hot rolling and stir casting are very effective methods for examining and characterizing the tribological characteristics and morphology of a hybrid composite material made of Al7075 alloy with graphite and titanium boride. The abrasive wear performance of hybrid composites has been studied under various loads and grit sizes.

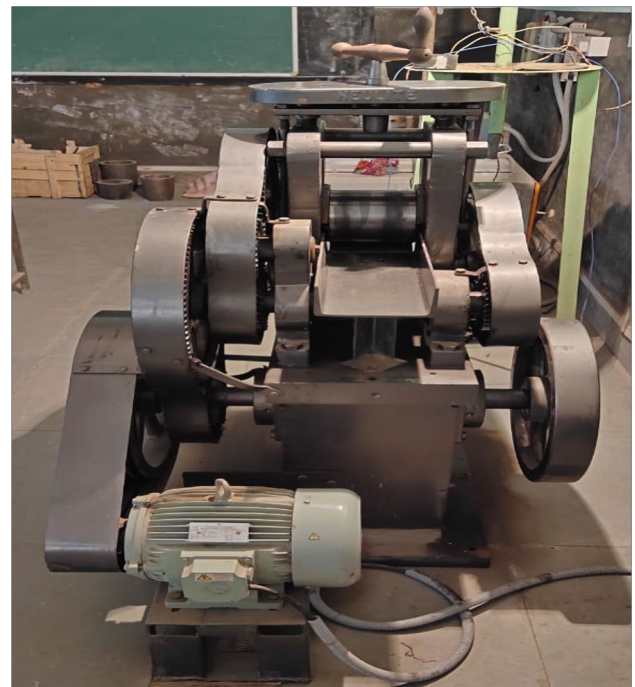
Experimentation

Processing

Hot rolling and stir casting techniques were used to create Al7075 hybrid composites, and Table 1 details the material's composition. As shown in Table 2, five distinct composites of various titanium diboride (TiB₂), graphite (Gr), and two un-reinforced alloy compositions were made under casting and rolling circumstances. Figure 1 depicts the morphologies of composites. A stainless-steel stirrer, graphite crucible, and permanent cast-iron mold were utilized. Al7075 alloy bars are cleaned, positioned in a graphite crucible, and heated in an electric furnace to 800 °C. The trapped gases from the melt were released

Table 2 Variation of TiB₂ and graphite content in composites

Sl. No.	Composition of composites
1	Al7075
2	Al7075–2%graphite–5%TiB ₂
3	Al7075–4%graphite–5%TiB ₂
4	Al7075–6%graphite–5%TiB ₂
5	Al7075–8%graphite–5%TiB ₂

**Fig. 1** Photograph of hot rolling machine

using the hexachloroethane (C₂Cl₆) tablet. A 400-rpm stirrer rotation produces a vortex. The melt's vortex receives one or more reinforcement particles. Stirring helps ensure uniform reinforcement particle dispersion in the matrix by keeping the reinforcement particles suspended in the melt. After that, a mold is filled with the composite melt to allow it to set. The base Al7075 alloy and as-cast Al7075 alloy were hot rolled in a 2-high roll mill at 450 °C with a reduction ratio of 80% and a 10% reduction in each pass. Table 1 provides specifics on the processing methodology and reinforcement characteristics. The photograph of hot rolling machine is shown in Fig. 1.

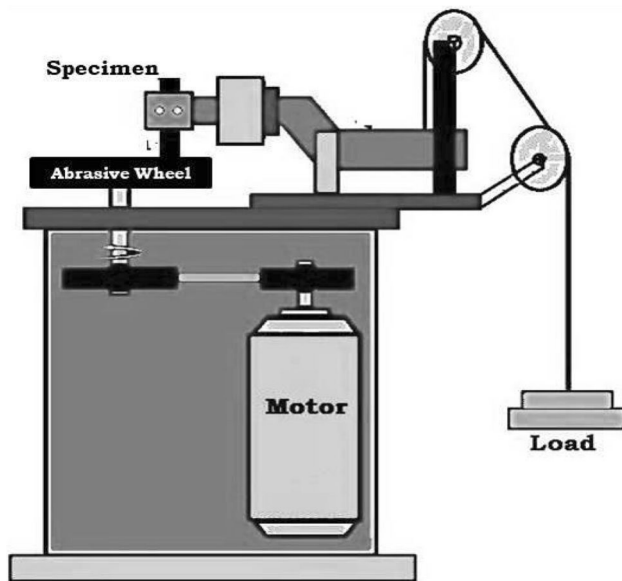


Fig. 2 Photograph of abrasive wear test setup

Microstructure

The specimens were partitioned into appropriate segments and subjected to abrasion using various grades of silicon carbide sheets, followed by disc polishing in order to attain a highly reflective surface. The samples underwent polishing using alumina suspensions on a polishing cloth for optical and scanning electron microscopy (SEM) analyses. To attain a highly reflective surface, it is recommended to initiate the polishing process with more coarse abrasives and gradually transition to finer ones. The samples were meticulously cleaned using acetone and were fully dried prior to microscopy analysis.

Wear Test

The investigation of abrasive wear was conducted utilizing the pin-on-disc apparatus as illustrated in Fig. 2. The abrasive media utilized in this study comprised of silicon abrasive wheels characterized by grit sizes of 60, 80, and 120. The pin-on-disc wear testing machine is equipped with abrasive wheels that have been affixed to its disc. In stage 5, the load has been modified within the range of 5–25 N, while maintaining a constant sliding speed of 2.5 m/s. The mass loss of the samples during the abrasive wear experiment was measured using an electronic computer balance with a precision of 0.1 mg. The dimensions of the specimen used for measuring abrasive wear are depicted in Fig. 3. During the abrasive wear test, a total of three specimens were subjected to testing under each condition. Table 3 illustrates the correlation between grit and particle size. The scanning electron microscope (SEM) was employed to analyze the samples

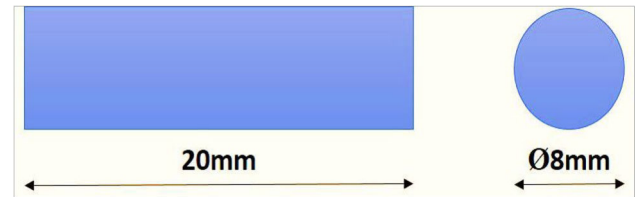


Fig. 3 Dimension of abrasive wear specimen

Table 3 Grit size conversion

Grit size of SiC abrasive paper	120	80	60
Average size of abrasive particle (μm)	102	165	254

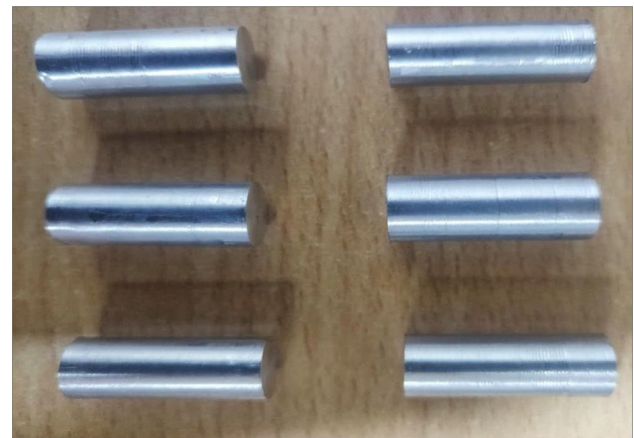


Fig. 4 Photograph of abrasive wear specimen

subsequent to the wear test. Figure 4 displays a photograph depicting specimens exhibiting abrasive wear. The depth of grooves in the wear tracks of the examined samples was determined using a form talysurf surface roughness tester equipped with a diamond tip measuring 4 m in diameter.

Results and Discussion

Microstructure

Figure 5 shows scanning electron microscopic maps of casting and hot rolling Al7075–graphite–titanium diboride in situ composite materials. The interaction between Al7075, titanium boride, and graphite results in the appearance of graphite and titanium diboride particles along the grain borders and inside alpha-aluminum grains. The development of alpha-aluminum grains during crystallization is responsible for most of the graphite and titanium diboride particles near grain borders. Particles of graphite and titanium

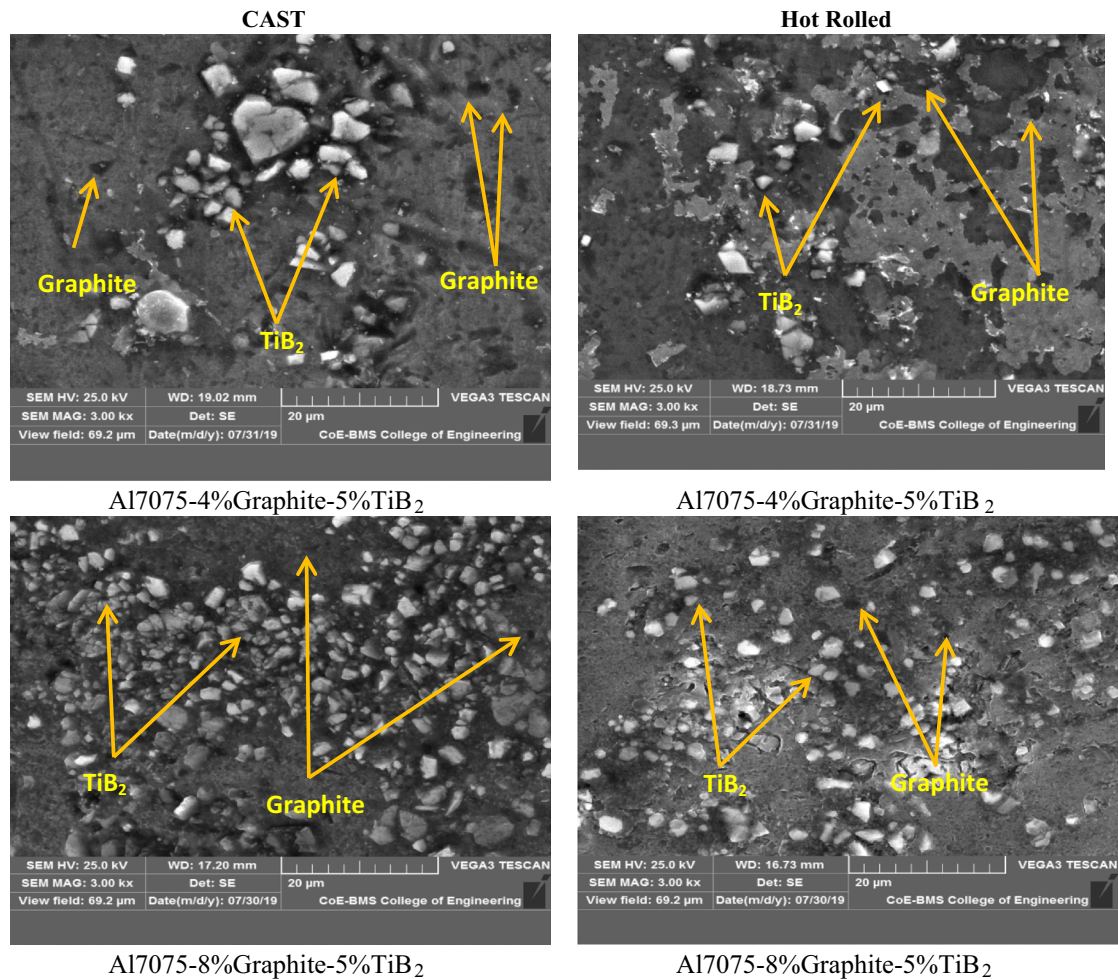
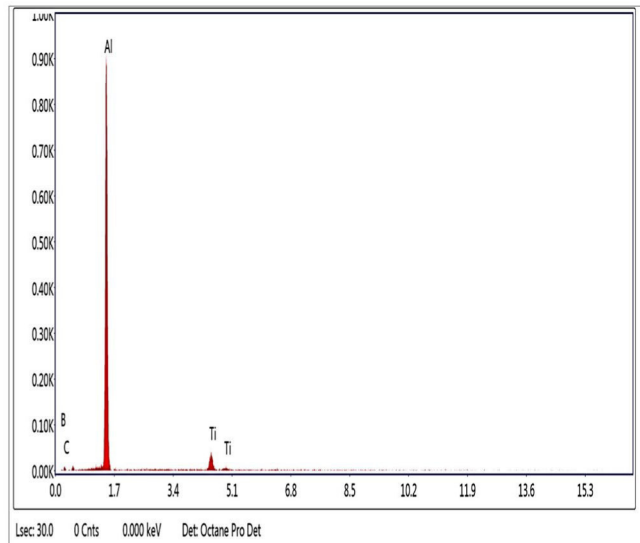
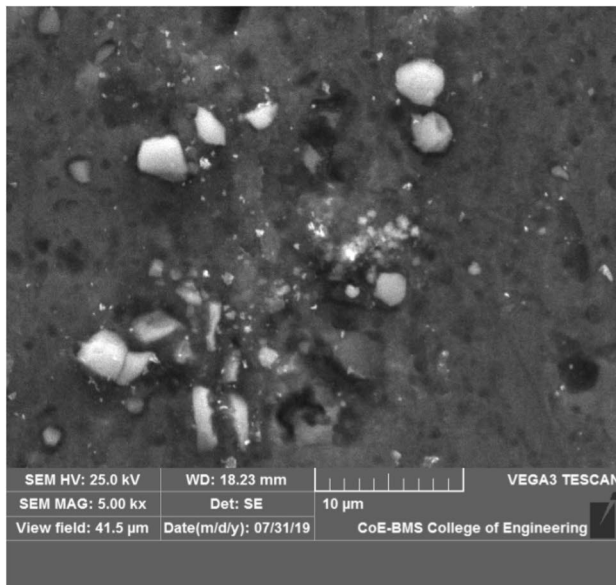
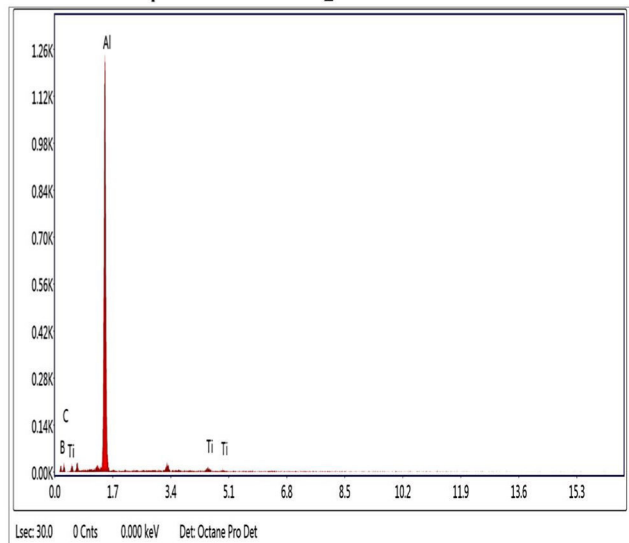
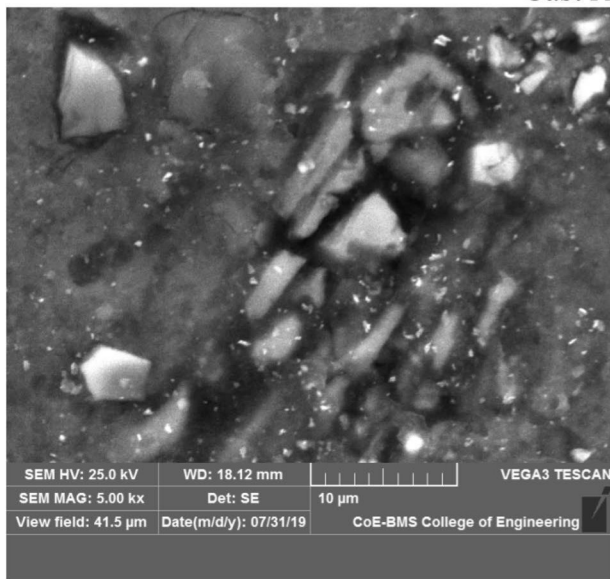


Fig. 5 SEM of Al7075/TiB₂/graphite hybrid composites in Cast and Hot Rolled Conditions

diboride are forced toward the front of crystallization and are wedged among the dendritic branches. The resulting areas of ultimately solidified liquids are the alpha-aluminum grain boundaries, where graphite and titanium diboride particles eventually settle. The distribution of graphite and titanium diboride particles has been discovered to be homogeneous all across the matrix after hot rolling. Particle distribution in the matrix material constitutes one of the key factors for enhancing mechanical and wear performance. It is evident that the intermediate connection had been strong and that the distribution remained homogeneous. After hot rolling and a 90% decrease in thickness, a compact microstructure forms, which is particularly advantageous in terms of mechanical and wear qualities. The examination of casting and rolling specimens performed using energy dispersive spectroscopy is shown in Fig. 6. According to Fig. 6, titanium diboride and graphite particles were present in the sample based on the energy dispersive spectroscopy results that indicated peaks for aluminum, carbon, titanium, and boride elements.

Moreover, a scanning electron microscope of hybrid composite material made of Al7075, graphite, and titanium diboride in casting and hot rolling processes reveals a strong connection between the matrix and reinforcement at high resolutions. The distribution of the particles was enhanced by the 4–8% increase in graphite content.

Suheel et al. [16] also worked on similar reinforcements but with the varied composition of reinforcing particles. The results are representative of both the hot rolling and as-cast specimen composite materials. The scanning electron microscopy of hybrid composite materials made of Al7075–titanium diboride–graphite was also studied. Although few titanium diboride particles have been found within the alpha-aluminum grains, most of them were found at the alpha-aluminum grain borders. Graphite and titanium diboride particulate aggregation may be visible in a few locations in this casting composite. Both reinforcing agents were supposed to be dispersed uniformly, with a smooth surface as well as strong interface adhesion. The

Cast Al7075-8%Graphite-5%TiB₂Cast Al7075-8%Graphite-5%TiB₂**Fig. 6** SEM image and corresponding EDAX spectra: Al7075/TiB₂/graphite hybrid composites in cast and hot rolled samples

microstructure did not contain any areas where reinforcing agents were grouped. If any non-homogeneous distribution created during casting is broken into distinct pieces and forms a strong bond thanks to the use of compression pressures, which is the primary aspect of hot rolling. In comparison with casting hybrid composite materials, there is no appreciable variation in the morphologies of composite materials. In the casting hybrid composite material that was discovered, particles from cluster centers of a few were dissolved after becoming treated to hot rolling. In scanning electron microscopy images, the homogeneous distribution

of titanium diboride particles during hot rolling is very obvious. Since there was no effect on the behavior at the contact, the binding between the titanium diboride and aluminum grains particulate was very strong. The examination of EDS of a hot rolling specimen is depicted in the results and clearly demonstrates that both the components of graphite, as well as titanium diboride particles, are present. The typical grain size of the Al7075 aluminum, as well as the hybrid Al7075–titanium diboride–graphite composite materials, is shown in each hot rolling and casting condition. According to the results, the hot rolling Al7075 aluminum lowers

grain size by 10% when contrasted to the metal under casting conditions, as seen in the. Hot rolling, as well as casting hybrid composite materials, show substantial drops of 72% and 45%, correspondingly, when contrasted to un-reinforced matrix materials when cast. As compared to un-reinforced casting materials, the composite material demonstrated a significant drop in the mean grain size. The presence of titanium diboride and graphite granules in the composite helps to improve the mechanical characteristics and decrease the grain size. The cause of this is believed to be particulate obstruction of developing grains during composite chilling. The aluminum grains in composite materials are smaller as contrasted to Al7075 aluminum without graphite as well as titanium diboride particles. Whenever un-reinforced aluminum alloy, as well as its composite material, are hot-rolled, dynamic reprocessing takes place during thermo-mechanical treatment, which causes a further reduction in the mean grain size. The alloy's combination of graphite and titanium diboride particles plays a crucial role in reducing grain growth as well as promoting recrystallization. Scanning electron microscope analyses can be used to show that titanium diboride contains particulate matter, which enables new types of grains that really are finer compared to the un-reinforced alloy. Titanium diboride and graphite particles round out the grain structure of these recently created grains. The matrix grain constraints in hot rolling techniques are determined by certain graphite and titanium diboride particulates. Whenever recrystallized crystals are created simultaneously with an increased concentration of distortions, the existence of graphite and titanium diboride particulates

reduces the driving power required in the aluminum matrix more to create a better grain structure [17–22].

Effect of Reinforcing Agents

Figure 7 illustrates the weight reduction of the casting and rolling specimens under consistent loading conditions and sliding velocities. The inclusion of titanium boride and graphite resulted in a decrease in the weight loss observed in the specimens. The Al7075 base material exhibited the highest degree of weight reduction in both casting and rolling scenarios. Nevertheless, the incorporation of reinforcing particles resulted in a notable decrease in weight loss. The sample with a graphite concentration of 2% exhibited the highest rate of weight loss in both experimental conditions, while samples with graphite concentrations of 4 and 6% experienced significantly slower weight loss. Furthermore, it can be observed that there is a significant decrease in weight loss as the particle concentration increases. Specifically, the sample that contains 8% graphite exhibits the lowest weight loss. As previously stated, enhanced wear resistance is linked to increased hardness and the utilization of a counterface with a reduced contact area that minimizes or eliminates contact with the surface of the sample. Consequently, the majority of the load is borne by these resilient particles, leading to a reduction in the rate of wear observed in specimens comprising 4% and 8% graphite. The hardness of the composites is enhanced due to the presence of highly rigid graphite and graphite reinforcing particles, which selectively impart their properties to the more pliable

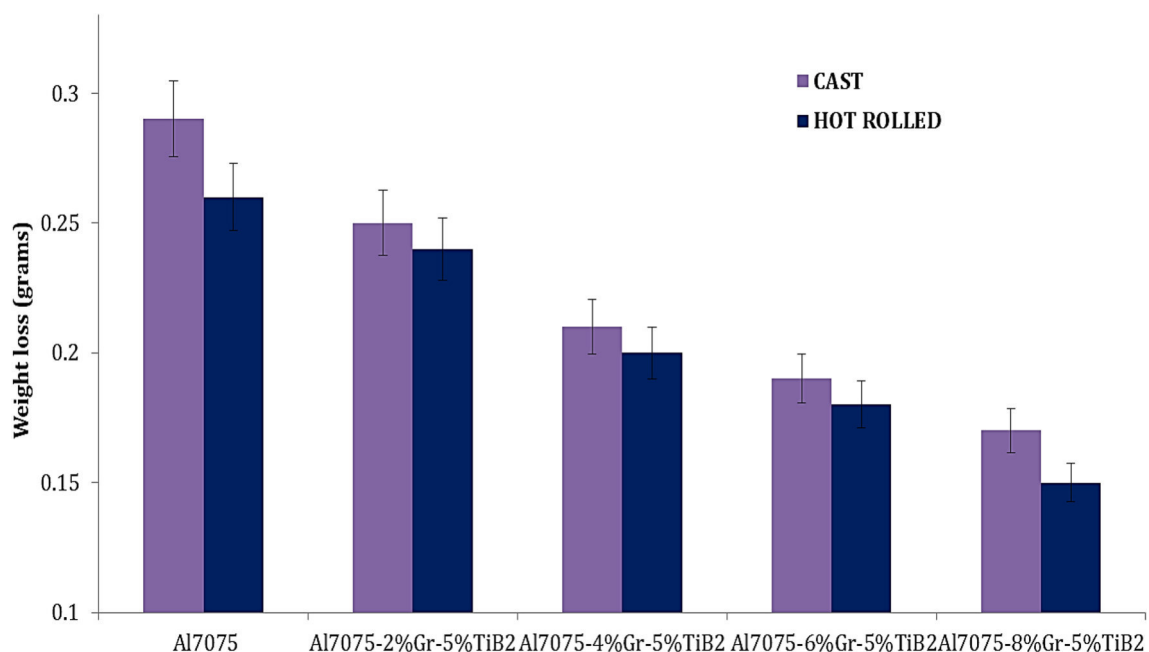


Fig. 7 Weight loss of the casting and hot-rolled samples

and ductile Al7075 matrices. The restriction of dislocation mobility by the reinforcements results in the strain-induced resilience of the surrounding material against deformation caused by an indenter. The primary factor responsible for the augmentation of hardness and tensile strength is the refinement of grain structure facilitated by the presence of reinforcing particles. The incorporation of reinforcement particles in the Al7075 matrix enhances its microstructure by providing a nucleation region for the growth of new crystals and effectively pinning the grain boundaries to regulate further expansion. The interfacial adhesion between different materials exhibits notable strength in the context of hot rolling processes involving composite materials. The hardness of rolling composites is significantly enhanced as a result of the improved bonding and the restriction of dislocation movement by the reinforcing particles. In addition, the reinforcing particles within the aluminum matrix serve as impediments to the motion of dislocations, thereby augmenting the tensile strength necessary for dislocation movement. The incorporation of reinforcements during the hot rolling process resulted in enhanced mechanical properties of composites, thereby leading to improved wear characteristics. Historically, researchers have conducted investigations on the impact of forging on the tribological characteristics of Al–Mg composites reinforced with titanium boride. The coefficient of friction of hot-forged composite is significantly lower compared to that of as-cast composite across various weight levels and sliding velocities, leading to reduced weight loss.

The worn surface morphologies of different reinforced samples are depicted in Fig. 8a–f. Figures 8a–c depict scanning electron micrographs illustrating the worn surface morphologies of casting composite materials. These materials were examined under controlled conditions of fixed sliding velocity and wear load. The use of reinforcing cast composite materials results in a decrease in adhesive impressions and debonding compared to the un-reinforced cast alloy, which demonstrates a greater degree of adhesive impression and deformation.

Scanning electron microscopic images of worn surface morphologies of casting composite materials are depicted in Fig. 8d–f. These materials were examined under conditions of fixed sliding velocity and wear load, but did not contain any reinforcement agents. The adhesions and delaminations of the rolling composite materials, both with and without reinforcement, experienced a slight increase due to their heightened vulnerability to fractures. The study focused on the hot rolling composite materials with and without reinforcement, while maintaining a constant sliding velocity and wear load. Based on the analysis of the microstructures, it was observed that the composite reinforcement materials demonstrate similar wear fracturing properties when graphite particle concentrations are lower, as evidenced by the

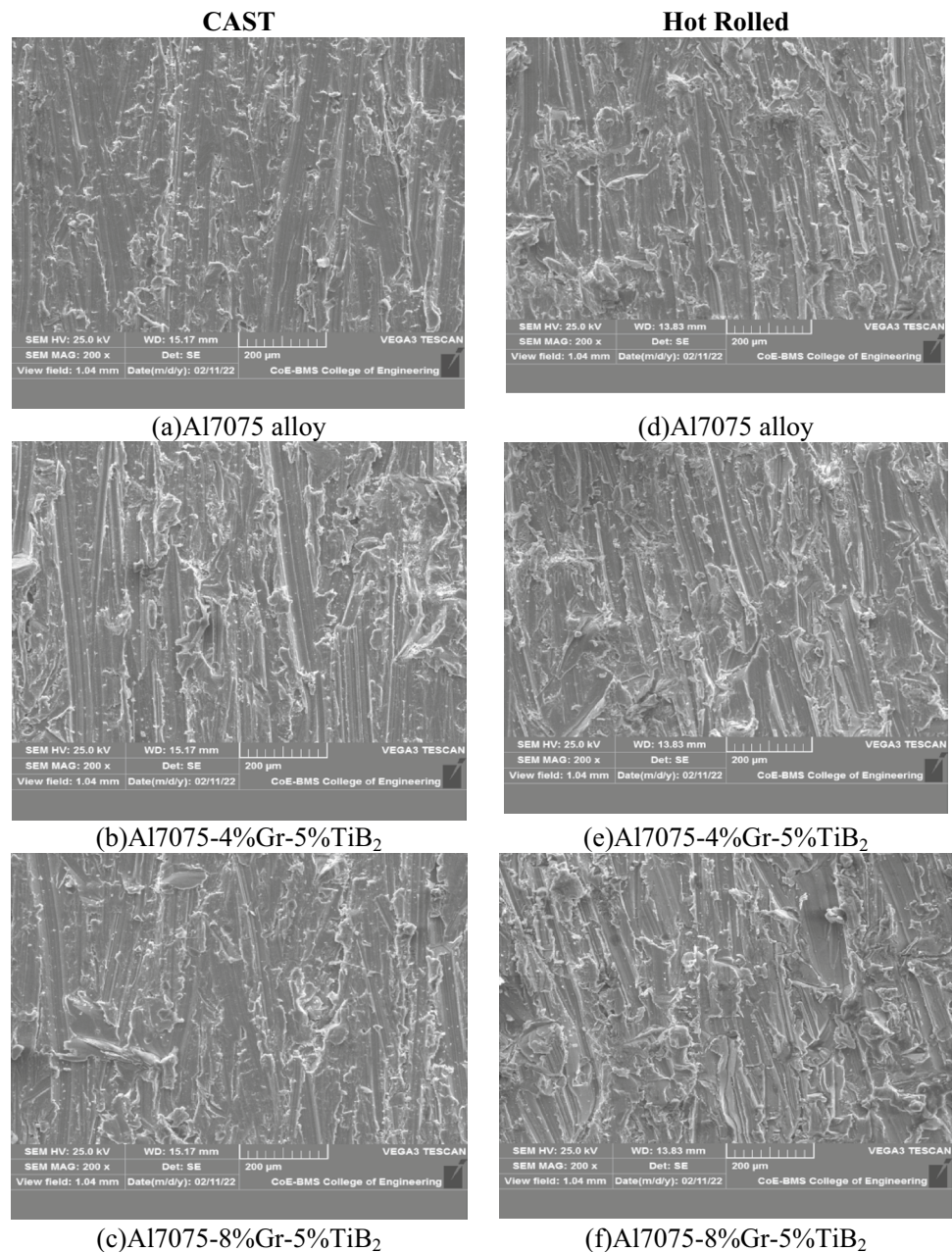
presence of delamination marks and adhesive impressions. The un-reinforced rolled alloys exhibit comparable characteristics to alloys with reduced reinforcing content. Composite materials with high graphite concentrations, when cast and rolled, demonstrate worn-out characteristics similar to those of ionic compounds. Furthermore, the adhesions and delamination marks observed in these materials are indistinguishable from those found in specimens with lower concentrations of graphite reinforcement particles [16–18].

Effect of Wear Load

Figure 9 illustrates the tribological properties of the cast and rolled materials at different load conditions (ranging from 5 to 25 N) as determined through tests conducted at a consistent sliding velocity of 2.5 m/s. The wear rates were found to be highest in both casting and rolling for samples containing 2% graphite, while samples containing 8 percent graphite exhibited the lowest wear rates. The wear rate of both casting and rolling specimens exhibited a significant decrease when the wear loading was increased to 20 N. In specimens exhibiting a graphite content ranging from 4 to 8%, the distribution of reinforcements is uniform, thereby enhancing interfacial bonding and resulting in an augmentation of micro-hardness. The observed increase in micro-hardness exhibits a notable influence on the mass reduction of both the casting and rolling specimens. The application of the Archard formula demonstrates an inverse relationship between the wear rate and the micro-hardness of a material. The findings of the study also indicated that the wear rate is comparatively higher in as-cast samples in comparison with hot-rolled samples. This can be attributed to the fact that hot-rolled samples exhibit superior hardness and a more uniform dispersion of reinforcement.

The scanning electron micrographs presented in Fig. 10a–h depict the surface morphologies of cast materials without reinforcement (20, 100 N) and with 8% graphite (Fig. 10a–d), subjected to two distinct load conditions. The velocity of sliding was maintained at a constant value of 2.5 m/s. Figure 6a and c illustrate that, when subjected to a force of 5 N, the wear behavior of the casting samples without reinforcement and those with reinforcement exhibits a similar or nearly identical pattern. The inclusion of reinforcements on the composite surface hinders the action of the disc plate, resulting in a modest improvement in wear resistance for the reinforced sample compared to the casted sample without reinforcements. Both samples exhibit surface patterns resulting from the combined effects of abrasion and adhesion. Both cast samples exhibited cracking under increased wear load of 25 N, as depicted in Fig. 10b–d. The morphological analysis provides clear evidence of increased wear in the samples. This is indicated by a higher quantity of abrasion and adhesive wear impressions, which are caused

Fig. 8 a–f SEM images of worn surface of cast and hot-rolled samples



by an increase in friction between the pin and counter surface due to the elevated load. Additionally, post-wear examination revealed the presence of grooves and delaminations on the surface of the samples. Based on the aforementioned findings, it was concluded that adhesion and abrasion were the wear processes observed under lower load conditions (specifically, at 5 N). Conversely, micro-cutting abrasion and surface delamination were identified as the wear mechanisms occurring under higher loads (specifically, at 25 N), in both casting specimens. Figure 10e–h depict scanning electron microscopic images of casting samples without reinforcement (Fig. 10e, f) and with 8% graphite (Fig. 10g, h), respectively. These images were obtained under two distinct load

conditions (5 and 25 N) while maintaining a constant sliding velocity of 2.5 m/s. The worn morphologies of both the unreinforced and reinforced samples exhibited similar wear behavior in both loading scenarios. All specimens exhibit abrasion and adhesion marks, similar to those observed in casting specimens. However, the hot-rolled specimens displayed a reduced intensity of these wear marks. The wear rate exhibited a slight increase for the samples subjected to higher wear load in comparison with the wear morphology observed for samples tested at a lower load (specifically, at 5 N and 25 N, respectively). The delamination of metallic sheets occurs when cracks propagate toward the subsurface under conditions of elevated stress. As the applied load

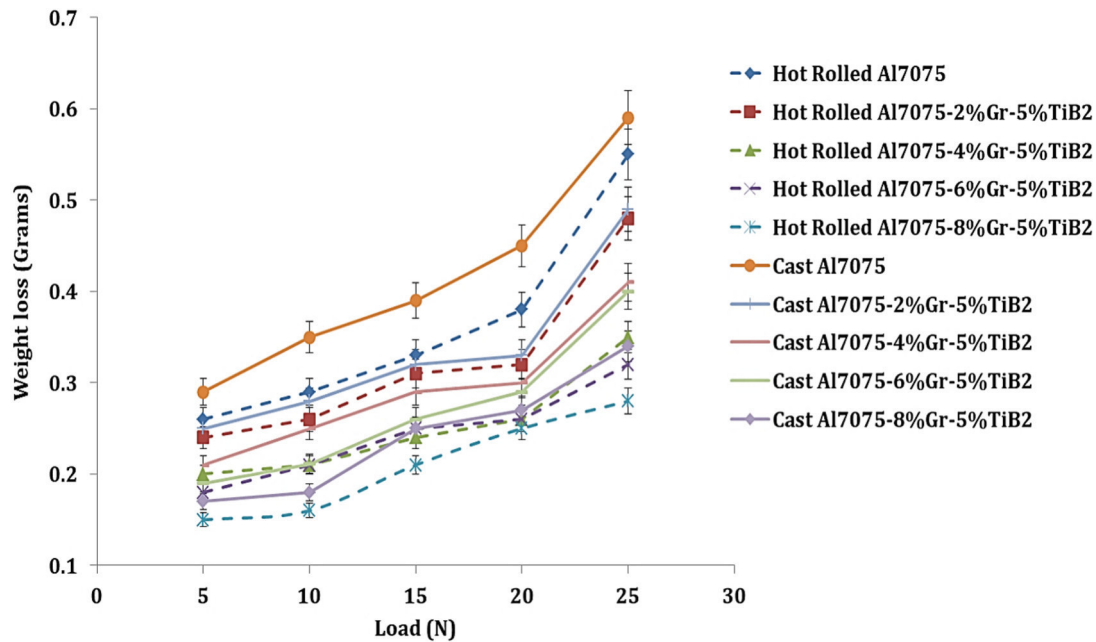


Fig. 9 Variations in weight loss of the cast and hot-rolled samples with different loads

intensifies, there is a significant rise in the temperature of the worn surface, leading to a notable softening of the matrix material. Consequently, there is a significant escalation in the likelihood of material removal through the process of delamination. Consequently, there is a significantly higher probability of material loss due to delamination. The predominant wear mechanism observed was found to be delamination wear. The rolling samples exhibited a more uniform surface texture and displayed a reduced occurrence of abrasion and adhesion wear marks compared to the casting samples. Samples with a high hardness result in reduced material loss due to the fracturing of the asperities on the counter face during the rolling process. In a manner analogous to the prevention of direct contact between the pin surface and the counter surface, the reinforcement particles serve to mitigate matrix softening, enhance hardness, and diminish matrix softening [18–22].

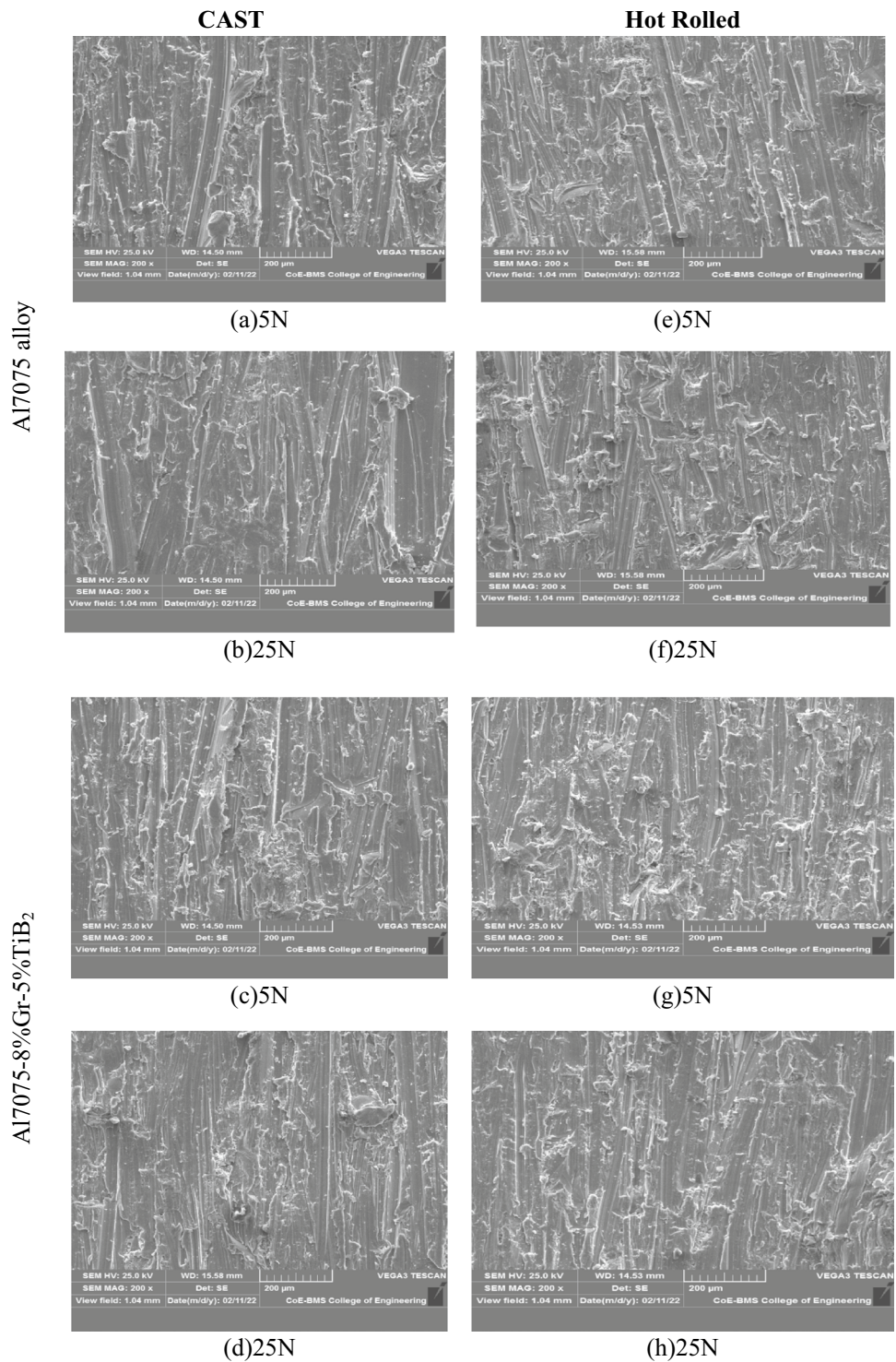
Effect of Abrasive Grit Size

Figure 11 illustrates the weight reduction observed in the casting and rolling samples as a function of different grit sizes. The inclusion of titanium boride and graphite resulted in a decrease in the weight loss observed in the specimens. The Al7075 base material exhibited the highest degree of weight reduction in both casting and rolling scenarios. Nevertheless, the incorporation of reinforcing particles notably mitigated the weight loss. The weight loss exhibited a negative correlation with the increase in grit size. As the grit

size number increases, there is a corresponding decrease in the size of the abrasive particles. This reduction in particle size ultimately results in a decrease in the rubbing action between the work piece and grit paper, consequently leading to a reduction in weight loss.

The increase in micro-hardness of composites resulting from the incorporation of rigid ceramic particulates can be attributed to a decrease in weight loss observed with an increase in the fraction of titanium diboride particles present in the matrix alloy. Hard reinforcing agents can resist the coefficient of friction, resulting in a reduction in the amount of substance that is removed. Moreover, the microscopy observations reveal a robust interfacial adhesion between the matrices and the reinforcing agents in both the casting and rolling procedures. The wear and friction behavior of composite materials is primarily influenced by two key parameters: reaction-less interfaces and a strong interfacial bond between the matrices and the reinforcing agents. The presence of a weak interfacial bond between the matrices and the reinforcing agents facilitates the facile removal of the reinforcing particles from the matrices, resulting in elevated wear rates when compared to the alloy. It has been suggested that the interfacial region serves as a site for the initiation of fractures and exhibits a propensity to attract the particulate matter away from the worn surface in situations where the adhesion at the interface is weak. The scanning electron microscopy (SEM) image depicted in Fig. 5 illustrates a robust interfacial bonding between the matrices and the reinforcing agents of the cast Al7075–8%graphite–5%titanium

Fig. 10 a–h SEM images of worn surface of cast and hot-rolled samples



diboride composite subsequent to the abrasion experiment. By conducting an analysis of the surface properties, it is possible to assess the extent of degradation to the eroded surface morphologies. The greater the quantity of debris that is eliminated through the excavation and ploughing out procedure, the more pronounced the wear becomes in the affected areas. However, the amount of material removed

volumetrically decreases as the worn surface becomes finer. In comparison with the process of casting composite material and the matrix material, the worn areas of the composite materials under rolled conditions exhibited superior surface quality, as depicted in Fig. 12. The surface roughness measurements, expressed as Ra values, for the hot rolling alloy Al7075–8%graphite–5%titanium diboride composite and the

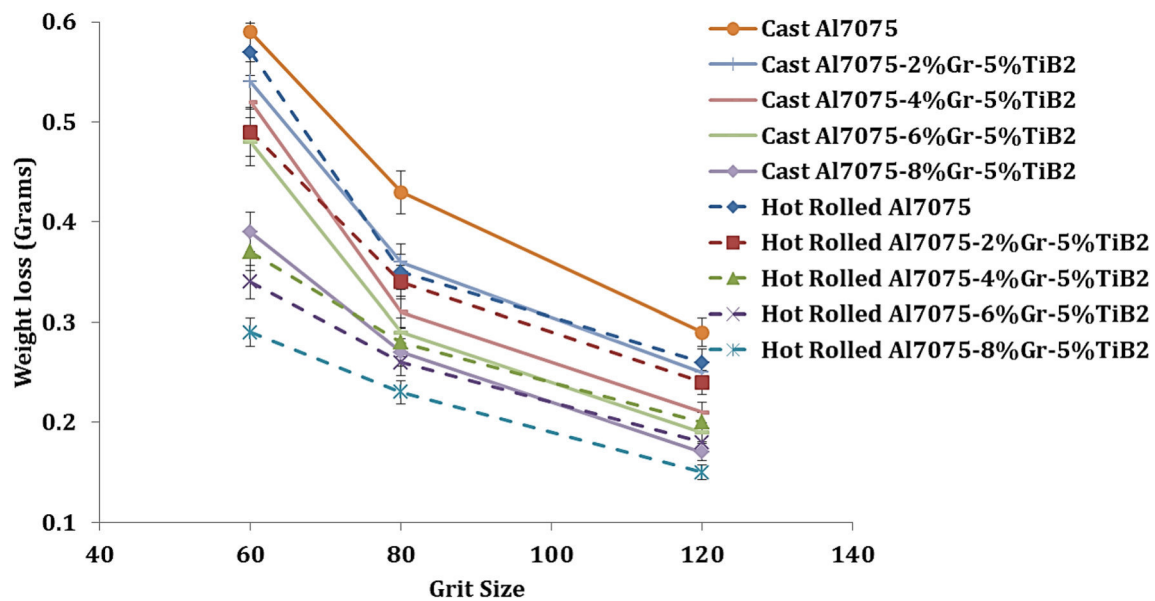


Fig. 11 Variations in weight loss of the cast and hot-rolled samples with different grit size

hot rolling alloy are as follows: 5.8 microns, 2.4 microns, 3.6 microns, and 1.9 microns, respectively. The results of this study unequivocally demonstrate that forged composite materials exhibit the lowest wear rate reduction due to their worn surfaces displaying the least roughness measurements. The excessive loss of weight when using larger abrasive particles is attributed to the increased penetration of these particles. Larger abrasive particles possess the capability to penetrate deeply and dislodge delamination as a result of the significant contact pressure they exert. When considering the presence of minuscule particles, a denser system exhibits heightened friction rather than a ploughing effect, leading to a reduction in delamination.

Figure 13a–h displays the scanning electron microscopy images of worn-out regions under different grit sizes and fixed loads. Each of the microstructures exhibits multiple parallel abrasion tracks oriented in the direction of wear.

It is apparent that in all cases, the tracks produced by larger-sized abrasives demonstrate greater width and depth in comparison with those produced by smaller-sized abrasives. In contrast to their respective alloys, composite materials fabricated via casting and hot rolling demonstrate diminished occurrences of slotting and penetration. When comparing the analysis of wearing areas on large-sized abrasives to that of small-sized abrasives, it is observed that the examination of wearing areas on small-sized abrasives exhibits a distinctively smooth texture characterized by minute grooves.

Microscopic analysis reveals that hot-rolled composite materials exhibit a notable reduction in surface defects compared to casting composite materials. As previously

mentioned, the significant surface deformation observed in un-reinforced alloys may be attributed to the diminished micro-hardness of their surfaces. Furthermore, it has been observed that the microstructure of worn composite regions in all examined cases exhibits variations compared to that of the un-reinforced alloy. Figure 13a–d exhibits the presence of more profound trenches on the surfaces of the matrices; whereas, Fig. 13e–h illustrate the occurrence of more delicate grooves on the surfaces of composite materials. This discovery substantiates the notion that composite materials exhibit a diminished level of wear in comparison with alloys that lack reinforcement. The material underwent complete elimination through intense elastic deformation, as evidenced by micrographs (Fig. 13c and f).

Numerous scholars conducted research on comparable investigations. In their study, Kumar et al. [23] employed the stir casting technique to fabricate metal matrix composite materials consisting of AA6061–zirconium boride. The composite materials were synthesized through in-situ reactivity, involving the incorporation of 3% boron and 10% zirconium into major aluminum alloys. Subsequently, the in situ composite materials were subjected to a rolling process at a temperature of 400 °C. The investigation focused on examining the morphology, frictional properties, and tribology characteristics of both hot rolling and casting samples, along with the corresponding in situ composite materials. The present study investigates the tribological and frictional characteristics of in situ metal matrix composite materials, specifically examining the effects of roll direction, orthogonal direction, and orientations at a 45° angle to the roll direction. The addition of zirconium boride particulates resulted

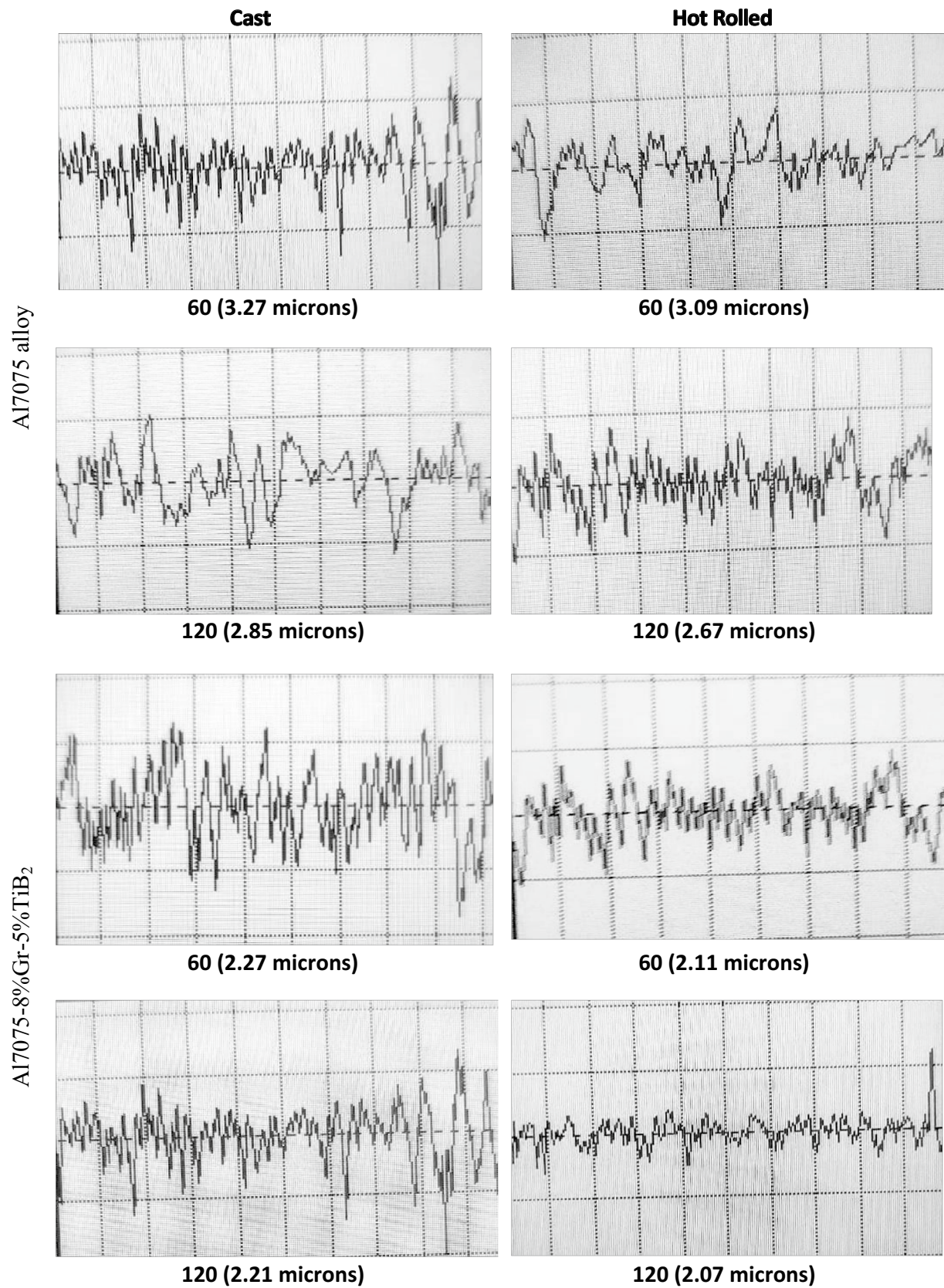
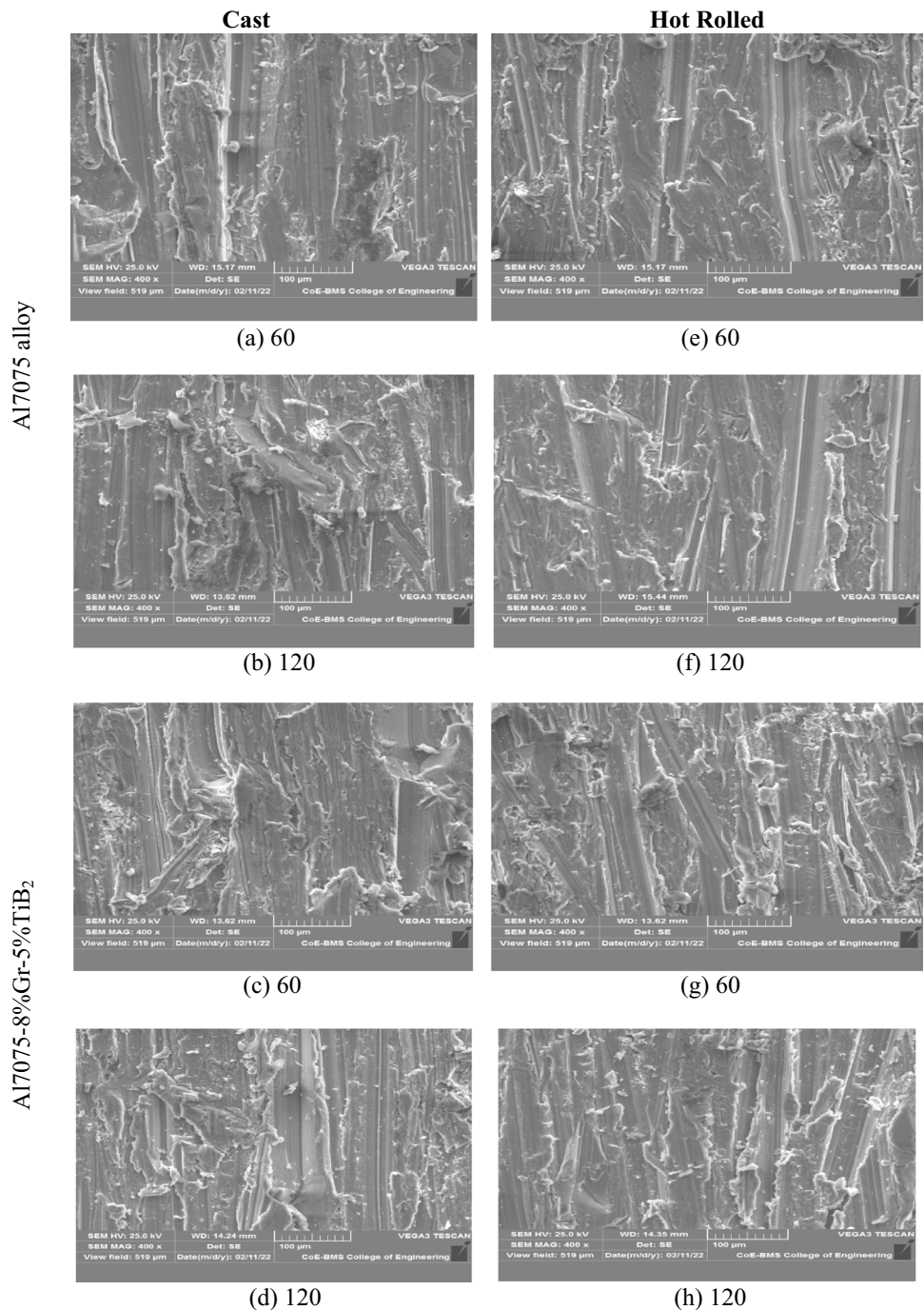


Fig. 12 Surface roughness graphs of the casting and hot-rolled samples

Fig. 13 a–h SEM images of worn surface of cast and hot-rolled samples



in an improvement in the wear resistance of the composites and a reduction in their coefficient of friction (COF).

The test specimens that were oriented in the rolling direction and at a 45° angle demonstrated lower coefficients of friction and mass losses in comparison with the specimens tested in the transverse direction.

In the study conducted by Gajakosh et al. [4] an examination is carried out on the impact of hybrid reinforcing agents, specifically titanium dioxide and graphite, on both the morphology and mechanical properties of the AA7075

alloy. Stir casting and hot forging techniques were employed to fabricate AA7075 and its hybrid composite specimens. A reduction ratio of 90% has been employed in the process of hot forging, conducted at a temperature of 450 °C. The examination of the morphology indicated that the particles of titanium dioxide and graphite reinforcement exhibited a high degree of dispersion and exhibited excellent bonding with the AA7075 matrix alloy.

The positioning of these reinforcement particles in the forging direction during hot rolling has been discovered.

When compared to cast composite materials, the process of hot forging has been observed to significantly enhance the micro-hardness and strength characteristics of said materials. A separate investigation conducted by Gajakosh et al. [24] focuses on the morphology and mechanical properties of composite materials based on Al7075, incorporating titanium diboride through an in situ treatment approach. Casting alloys and composites have undergone hot forging at an operating temperature of 45 °C. The overall decrease was 80% as a result of four runs. The investigation encompassed an examination of the morphology, micro-hardness, and tensile behavior of both the aluminum matrix and composite materials in both cast and rolling configurations. A thorough examination of the morphology indicates that the particles of titanium boride exhibit a high degree of dispersion and establish a strong interconnection with the matrix material. Materials that have been strengthened have undergone the process of hot rolling, whereby their orientation is aligned with the direction of rolling. The hot-forged alloy, as well as the composites, exhibited significant enhancements in micro-hardness, tensile strength, and toughness.

The investigation conducted by Harish et al. [25] examines the influence of titanium carbide reinforcing agents on the wear characteristics of copper metal matrix composite materials. The composite materials were fabricated using the stir-casting technique, followed by the subsequent application of hot forging. Hot rolling with a 90% reduction ratio was conducted at a temperature of 510 °C. Optical microscopy, scanning electron microscopy with elemental dispersion spectroscope, and Brinell hardness testers were employed to carry out investigations pertaining to the morphology, dispersion of reinforcing particles, and macro-hardness. The findings from the morphology analyses indicate a strong interfacial bonding between the copper matrix and the titanium carbide reinforcement. The incorporation of titanium carbide in the cast and roll sample has resulted in a notable enhancement in micro-hardness. A pin-on-disk apparatus was employed to conduct experiments on dry sliding wear and friction. The experiments involved varying loading rates within the range of 30–120 N, as well as sliding velocities ranging from 6.29×10^{-1} to 25.13×10^{-1} m/s. In both cast and roll circumstances, it has been observed that composite materials exhibit a lower coefficient of friction (COF) and experience less mass loss compared to the matrix material. The increase in loading and sliding speed resulted in an increase in wear loss for both un-reinforced and reinforced casting and hot rolling materials. The utilization of titanium carbide has resulted in a decrease in wear loss and coefficient of friction (COF). Copper metal matrix composite materials exhibit significantly reduced coefficients of friction (COF) and wear rates in comparison with un-reinforced casting and rolling alloys. The utilization of a scanning electron microscope was employed in order

to validate the adhesion bonding and detect any surface delaminations. Ultimately, it was determined that the current investigation produced superior outcomes in comparison with previous studies.

The positioning of these reinforcement particles in the forging direction during hot rolling has been discovered. When compared to cast composite materials, the process of hot forging has been found to substantially enhance the micro-hardness and strength characteristics of these materials. A separate investigation conducted by Gajakosh et al. [24] focuses on the morphology and mechanical properties of composite materials based on Al7075, incorporating titanium diboride through an in-situ treatment approach. Casting alloys and composites have been subjected to hot forging at an elevated temperature of 45 °C. The overall decrease was 80% as a result of four runs. The investigation encompassed an examination of the morphology, micro-hardness, and tensile properties of both the aluminum matrix and composite materials in both cast and rolling configurations. The analysis of morphology indicates that the particles of titanium boride exhibit a high degree of dispersion and demonstrate a strong interconnection with the matrix material. The orientation of reinforced materials has been aligned with the direction of rolling during the hot rolling process. The hot-forged alloy, as well as the composites, exhibited significant enhancements in micro-hardness, tensile strength, and toughness [26, 27].

Conclusions

The following findings were made following the successful fabrication of the Al7075–titanium diboride–graphite composite materials in the current work using the stir casting technique and hot rolling.

- The microstructure results show that there is strong matrix bonding and that the titanium graphite-graphite reinforcement particles are distributed uniformly.
- It was discovered that the casted sample wore out faster than the hot-rolled sample. The presence of uniformly dispersed titanium graphite-graphite reinforcing agents with improved interfacial binding is the main cause of the low mass losses in the hybrid composite material when compared to the un-reinforced material. When compared to cast 7075 alloy 5 wt% TiB₂ and 8 wt% Graphite reinforced composite, weight loss was reduced by 35% and 47%, respectively, for cast and hybrid conditions.
- When compared to un-reinforced alloys, cast and hot rolled hybrid composites reduced weight loss by 42% and 54%, respectively, for a load value of 25 N.
- It was found that when subjected to a grit size of 120, cast and hot rolled hybrid composites showed a reduc-

tion in weight loss of 39% and 46%, respectively, when compared to un-reinforced alloys.

- Low wear loads result in adhesion and abrasion in the wear mechanism, while high wear loads result in delamination and oxidation. Furthermore, in terms of abrasion resistance, hot rolling and casting composite materials outperform un-reinforced alloys under the same test conditions.
- Scanning electron micrographs have been used in worn-out sections to look for any plausible wearing mechanisms. The size and load of larger abrasives caused more grooving, which increased the risk of abrasive wear damage for both reinforced and un-reinforced materials.

Funding This research work has not received any funding.

Declarations

Conflict of interest Authors here by declared that there is no conflict of interest.

References

1. B. Venkataraman, G. Sundararajan, Correlation between the characteristics of the mechanically mixed layer and wear behaviour of aluminium, Al-7075 alloy and Al-MMCs. *Wear* **245**, 22–38 (2000)
2. F. Karpasand, A. Abbasi, M. Ardestani, Effect of amount of TiB₂ and B₄C particles on tribological behavior of Al7075/B₄C/TiB₂ mono and hybrid surface composites produced by friction stir processing. *Surf. Coat. Technol.* **390**, 125680 (2020)
3. A. Mandal, M. Chakraborty, B.S. Murty, Effect of TiB₂ particles on sliding wear behaviour of Al–4Cu alloy. *Wear* **262**, 160–166 (2007)
4. A.K. Gajakosh, R. Keshavamurthy, T. Jagadeeshac, R. Suresh Kumar, Investigations on mechanical behavior of hot rolled Al7075/TiO₂/Gr hybrid composites. *Ceram Int* **47**(10), 14775–14789 (2021)
5. N.A. Patil, S.R. Pedapati, O. Mamat, A.M.H.S. Lubis, Morphological characterization, statistical modeling and wear behavior of AA7075–titanium carbide–graphite surface composites via friction stir processing. *J. Mater. Res. Technol.* **11**, 2160–2180 (2021)
6. J. An, Y.B. Liu, Y. Lu, J. Wang, B. Ma, Friction and wear characteristics of hot-extruded leaded aluminum bearing alloys. *J Mater Eng Perform* **11**(4), 433–443 (2002)
7. R. Dasgupta, S. Das, S. Chaturvedi, A.K. Jha, Effect of extrusion on properties of Al based composite. *Trans Nonferr Met Soc Chin* **20**(12), 2229–2233 (2010)
8. H.N. Reddappa, K.R. Suresh, H.B. Niranjana, K.G. Satyanarayana, Effect of rolling on microstructure and wear behavior of hot rolled Al6061–beryl composites. *Adv Mat Res* **463–464**, 444–448 (2012)
9. A. Baradeswaran, A. ElayaPerumal, Study on mechanical and wear properties of Al 7075/Al₂O₃/graphite hybrid composites. *Compos Part B Eng* **56**, 464–471 (2014)
10. R. Deaquino-Lara, N. Soltani, A. Bahrami, E. Gutiérrez-Castañeda, E. García-Sánchez, M.A.L. Hernandez-Rodríguez, Tribological characterization of Al7075–graphite composites fabricated by mechanical alloying and hot extrusion. *Mater Des* **67**, 224–231 (2015)
11. M.V. Ashwini, S. Patil, P. Robionson, Evaluation of mechanical and tribological properties of AL7075 hybrid metal matrix composite reinforced with fly ash and graphite. *Mater Today Proc* **45**, 311–317 (2021)
12. G.N. Lokesh, M. Ramachandra, K.V. Mahendra, T. Sreenith, Effect of hardness, tensile and wear behavior of Al-4.5wt%Cu alloy/flyash/SiC metal matrix composites. *Int J Mod Eng Res* **3**(1), 381–385 (2013)
13. V.C. Uvaraja, N. Natarajan, Comparison on Al6061 and Al7075 alloy with SiC and B₄C reinforcement hybrid metal matrix composites. *IJART* **2**(2), 1–12 (2012)
14. S. Basavaraj, K. Arasukumar, C. Bendigeri, C.K. Umesh, Studies on mechanical properties and tribological characteristics of LM25–graphite–silicon carbide and LM25–flyash–silicon carbide-hybrid MMC's. *Int J Innov Res Sci Eng Technol* **1**(1), 1 (2012)
15. G.T. Danappa, C.R. Raghavendra, R.P. Swamy, K. Naik, Dry sliding wear behaviour of Al7075/Gr/nano TiO₂ MMC using RSM. *Mater Today Proc* **38**, 2797–2802 (2021)
16. S. Suhael Ahmed, H.N. Girisha, R. Keshavamurthy, Impact of hot rolling on mechanical characteristics of AA7075/TiB₂/graphite hybrid composites. *J Inst Eng India Ser D* (2022). <https://doi.org/10.1007/s40033-021-00311-z>
17. R.K. Sabat, P.K. Samal, S.M. Ahamed, Effect of strain path on the evolution of microstructure, texture and tensile properties of WE43 alloy. *Mater Sci Eng A* **715**(7), 348–358 (2018)
18. R.K. Sabat, M.V.S.S.D.S. Surya Pavan, D.S. Aakash, M. Kumar, S.K. Sahoo, Mechanism of texture and microstructure evolution during warm rolling of Ti–6Al–4V alloy. *Philos Mag* **98**(28), 2562–2581 (2018)
19. S. Sankaranarayanan, R.K. Sabat, S. Jayalakshmi, S. Walker, S. Suwas, M. Gupta, Using heat treatment effects and EBSD analysis to tailor microstructure of hybrid Mg nanocomposite for enhanced overall mechanical response. *Mater Sci Technol* **30**(11), 1309–1320 (2014)
20. K.T. Kashyap, T. Chandrashekar, Effects and mechanisms of grain refinement in aluminium alloys. *Bull. Mater. Sci.* **24**, 345–353 (2001)
21. P. Sahoo, M.J. Koczak, Microstructure-property relationships of in-situ reacted TiC/Al–Cu metal matrix composites. *Mater Sci Eng A* **131**, 69–76 (1991)
22. C.S. Ramesh, R. Keshavamurthy, S. Pramod, P.G. Koppad, Abrasive wear behavior of Ni–P coated Si₃N₄ reinforced Al6061 composites. *J Mater Process Technol* **211**, 1423–1431 (2011)
23. R. Vasanth Kumar, R. Keshavamurthy, C.S. Perugu, M. Alipour, C. Siddaraju, Influence of hot rolling on friction and wear behaviour of Al6061–ZrB₂ in-situ metal matrix composites. *J Manuf Process* **69**, 473–490 (2021)
24. A. Kumar Gajakosh, R. Keshavamurthy, G. Ugrasen, H. Adarsh, Investigation on mechanical behavior of hot rolled Al7075–TiB₂ in-situ metal matrix composite. *Mater Today Proc* **5**, 25605–25614 (2018)
25. S. Harish, R. Keshavamurthy, D.P. Basheer, A.K. Gajakosh, Effect of hot rolling on friction and wear characteristics of TiC reinforced copper-based metal matrix composites. *Adv Mater Sci Eng* **2023**, 15 (2023). <https://doi.org/10.1155/2023/8956234>
26. G.S. Pradeepkumar, R. Keshavamurthy, P. Kupahalli, P. Kumara, Influence of hot forging on tribological behavior of Al6061–TiB₂ in-situ composites. *IOP Conf Ser Mater Sci Eng* **149**(1), 012087 (2016)
27. R. Keshavamurthy, J.M. Sudhan, N. Gowda, R.A. Krishna, Effect of thermo-mechanical processing and heat treatment on

the tribological characteristics of Al based MMC's. IOP Con Ser Mater Sci Eng **149**(1), 012118 (2016)

Publisher's Note Springer Nature remains neutral with regard to jurisdictional claims in published maps and institutional affiliations.

Springer Nature or its licensor (e.g. a society or other partner) holds exclusive rights to this article under a publishing agreement with the author(s) or other rightsholder(s); author self-archiving of the accepted manuscript version of this article is solely governed by the terms of such publishing agreement and applicable law.



Pest detection via hybrid classification model with fuzzy C-means segmentation and proposed texture feature

Madhuri Devi Chodey^{a,*}, C. Noorullah Shariff^b

^a Electronics and Communication Engineering, Navodaya Institute of Technology, Raichur, Karnataka, India

^b Department of AIML, Ballari Institute of Technology and Management, Ballari, Karnataka, India

ARTICLE INFO

Keywords:

Pest Detection
Segmentation
Feature Extraction
Classification
Optimization

ABSTRACT

Due to the frequent outbreaks of agricultural pests, agricultural production is limited and crop yield is minimized. Several types of agricultural pests, on the other hand, provide greater obstacles to workers when it comes to recognizing them. Currently, present agricultural pest detection techniques are frequently unable to meet the demands of agricultural production due to model inefficiency. The goal of this paper is to present a pest identification model that detects the *Heliothis armigera* (Cotton bollworm) and *Leptocorisa acuta* (rice bug) using four primary phases: i) Pre-processing (ii) Object tracking and Segmentation (iv) Feature extraction and (v) Classification. The input video frame (pictures) is first subjected to a pre-processing phase, during which the video frames are pre-processed. Object tracking and segmentation are then applied to the pre-processed pictures. The Fuzzy C-means (FCM) technique is used to segment the foreground and background in this case. The suggested GLCM based texture feature, color, edge, and form based characteristics are derived from the segmented pictures. Furthermore, the collected features are fed into the detection process, which employs hybrid classifiers such as LSTM and RNN. The RNN training is done utilizing the Self Improved Tunicate swarm Algorithm (SITSA) by finding the ideal weights for exact detection outcomes. Finally, the suggested scheme's performance is compared to those of other current schemes using metrics such as FDR, specificity, accuracy, precision, FNR, sensitivity, FPR, Thread score, FMS, FOR, NPV, and MCC.

1. Introduction

Agriculture is critical for feeding both human and livestock populations around the world. Agriculture's role in clean energy generation has expanded with the advent of green energy technologies such as biodiesel fuels. Furthermore, agriculture provides a source of raw materials for textile production, chemicals, and pharmaceuticals. One of the basic sources of developing countries is agriculture which provides a significant role in economic and social development. However, the presence of crop pests mainly affects the agriculture development in countries [9 10]. The vital technique used for controlling the pest is the application of chemical pesticides. Furthermore, it is more complex to correctly match the related pesticide types due to the low professional information of the huge range of pests in the agricultural field [11 12]. In addition, the IPM has implemented the idea, in which the real-time and early monitoring such as recognition and localization of pests are assessed to trend their upcoming progress on enhancing the application of pesticide regards environmental, ecological, and economic losses

[13]. However, this monitoring technique relies for a long time on the artificial investigation; thus it faces several obvious defects (i.e.,) wasting material resources, time-consuming and manpower. The information acquisition may not gain the real-time outcomes and thus attains the unstable identification accuracy. Consequently, it is a large implication to discover real-time and an accurate intelligent pest detection approach for replacing the existing artificial models [14 15].

Specifically, pest prevention and control are larger-priority-based agricultural problems in this world. More pest monitoring systems are widely used in practical crop monitoring systems due to their efficient automation and cost-effectiveness [16 17 18]. Moreover, its applications require the usage of the mobile camera or stationary camera for observing the in-field pest images and then determining the advanced image processing systems to analyze and recognize the pest-related data for prediction and decision-making [19]. Though the application of advanced systems enables large achievement in effective classification and recognition of certain insect types, the major problem appears in enhancing the recognition accuracy of insect types through novel machine learning [49 42] algorithms. Implementing novel features;

* Corresponding author.

E-mail addresses: madhuridevichodey@gmail.com (M.D. Chodey), dr.cns@bitm.edu.in (C. Noorullah Shariff).

Nomenclature			
Abbreviation	Description		
AP	Average Precision	IPFC	In-Field Pest in Food Crop
ANN	Artificial Neural Networks	IPM	Integrated Pest Management
AF-RCNN	Anchor-Free Region Convolutional Neural Network	LMPW	Large-Scale Multi-Class Pest Dataset In The Wild
CSA	Channel Spatial Attention	LSTM	Long Short-Term Memory
CDF	Cumulative Density Function	LIRA	Limited Receptive Area
CNN	Convolutional Neural Network	MDM	Multi-Projection Pest Detection Model
CPB	Colorado Potato Beetle	mAP	Mean Average Precision
DBN	Deep Belief Network	MCC	Matthews Correlation Coefficient
DL	Deep Learning	MBB	Mexican Bean Beetle
D-NU	Distributed intensity based LBP Features	NPV	Net Predictive Value
EHO	Elephant Herding Optimization	NN	Neural Network
FOR	False Omission Rate	PDF	Probability Density Function
FC	Fully Connected	PSSM	Position-Sensitive Score Map
FCM	Fuzzy C-means	RoIs	Regions of Interest
FPR	False Positive Rate	RPN	Region Proposal Network
FMS	F-Measure	RSC	Random Subspace Classifier
FDR	False Discovery Rate	RNN	Recurrent neural Network
FNR	False Negative Rate	RF	Random Forest
GLCM	Gray Level Co-Occurrence Matrix	SITSA	Self Improved Tunicate Swarm Algorithm
		SVM	Support Vector Machine
		WOA	Whale Optimization Algorithm
		TSA	Tunicate Swarm Algorithm

however, given more attention to develop the required automatic pest monitoring systems as LMPW. The existing pest detection approaches worked well with few types in ‘lab-based small-scale pest dataset’; still, it attains poor robustness and low accuracy on processing the practical large-scale multi-class pest dataset [20 21]. Similarly, their performance is limited through several concerns including overlapping or dense distribution of tiny objects, lighting illuminates, etc.

In recent times, the advancement in deep learning models [46 45 44] leads to drastically promising progress in the object detection field, in which the majority of learning focused on implementing complex object detection networks to increase the accuracy in extended network variants, unsupervised multi-stage feature learning, and Super-FAN [22 23]. Moreover, the CNN [43 47 48] based model also plays a major role in detecting the presence of pests. Several researchers focused on implementing different feature extraction schemes for the feature space expansion to enhance the pest identification accuracy [24 25]. The major contributions of the adopted model are given below:

- Proposes a novel GLCM version for obtaining texture features.
- Introduces the Self Improved Tunicate Swarm Optimization Algorithm (SITSA) for determining the ideal weights for training the RNN.
- The Self Improved Tunicate Swarm Optimization Algorithm is the improved version of the conventional Tunicate Swarm Optimization Algorithm.

In this paper, the review on pest detection is described in section II. The overview of the proposed pest detection model is portrayed in section III. Preprocessing via histogram equalization process, object tracking, and segmentation process are portrayed in section IV. Section V describes feature extraction: edge/shape, color, and proposed texture features. Section VI depicts pest detection by optimized hybrid long short-term memory and recurrent neural network. RNN weight optimization by self-improved tunicate swarm optimization algorithm is determined in section VII. Section VIII specifies the result and discussion. In the end, the conclusion of this paper is depicted in section IX.

2. Literature review

2.1. Related works

In 2020, Lin et al. [1] has developed an AF-RCNN model for precision recognition and classification of 24-classes pests. Initially, a feature fusion model was proposed for extracting the efficient feature regarding agricultural pests, particularly small pests. Subsequently, an AFRPN model was proposed and it was used for obtaining the proposals with the large-quality object under fusion feature maps as a probable pest position. Moreover, the AF-RCNN model was determined for detecting the 24- classes’ pest through an end-to-end manner via integrating the Fast R-CNN with AFRPN into a particular network. Finally, the simulation results of the adopted model shown its betterment on the pest dataset consisting of 24 classes and 20 k images, and it obtained 85.1 % mrecall and 56.4 % mAP on 24-classes pest dataset, 56.5 % and 39.4 % superior to YOLO detector, and 15.3 % and 7.5 % superior to Faster R-CNN.

In 2020, Fangyuan et al. [2] has proposed a new 2 phases of mobile vision based on a cascaded pest detection model named “Deepest” with the extensive multiple pest data species. Further, the adopted model would extract the information regarding the multi-scale contextual images as the preceding information to construct a context-aware attention network during the pest image’s primary classification into crop category. Next, an MDM was implemented and trained via the crop-related pest images. Then, the data augmentation and attention system were utilized to enhance the efficiency during in-field pest detection. Finally, the experimental outcomes of the adopted model were evaluated on the large-scale dataset IPFC and it has shown better results than other conventional detection models in in-field pest detection.

In 2018, Karen et al. [3] have implemented an automatic pest detection system through the ANN. Moreover, the adopted model would detect the 2 defoliating pests on bean crops and potatoes automatically: CPB and MBB in the final stage. For beetle detection, the neural classifiers have used LIRA and RSC. The MBB images were given as the classifiers inputs that were attained on Mexican plantations. The CPB images were gathered from different internet sources. Finally, the experimental outcomes of the adopted model were compared on image databases using both classifiers. Finally, the RSC classifier has revealed superior recognition results; whereas, the LIRA also attained a superior recognition rate.

In 2018, Yu et al. [4] have presented a DL detection model in the pheromone trap to directly count the adult RTBs. Furthermore, the bark beetles' images were taken through a digital camera implanted in the pheromone trap of the collected cup. The downsized detector was improved through residual classification subnet and k-means anchor optimization. The proposed scheme was trained on a GPU workstation with data augmentation and then determined on embedded strategy with the smallest preprocessing. Finally, the experimental outcome of the adopted model has evaluated that the average runtime on the Raspberry Pi 3b and Jetson TX2 were 23.44 s and 0.448 s, and the object level AP was 0.746 correspondingly. The adopted method has proven capable outcomes both quantitatively and qualitatively within incomplete computational budgets.

In 2019, Liu et al. [5] have introduced a region-based end-to-end model known as PestNet for the large-scale multi-class pest detection and classification on the basics of DL. Moreover, the PestNet has included 3 major parts. Initially, a new module CSA was implemented to be fused into the CNN framework for feature extraction and enhancement. Next, the RPN was implemented to provide the proposals region based on extracted feature maps as the positions of potential pest from images. Further, the PSSM was used to restore the FC layers for bounding box regression and pest classification. At the end, the simulation outcomes of the adopted PestNet have shown 75.46 % mAP than other existing scheme.

In 2020, Chen et al. [6] has combined image recognition technologies and artificial intelligence with IoT and environmental sensors for pest identification. Moreover, the pest identification systems and real-time agricultural meteorology on mobile applications were determined based on the environmental IoT data and intelligent pest identification. Deep learning and current mature AIoT technology were combined and then applied in smart agriculture. The DL YOLOv3 was used for obtaining the Tesseractoma papillosa location for image recognition and analyzed the environmental information from weather stations via LSTM for predicting the pest's occurrence. At last, the experimental outcomes have revealed 90 % pest identification accuracy than other existing models.

In 2019, Selvaraj et al. [7] has developed a pest detection system and an AI-based banana disease via a DCNN for supporting banana farmers. Large datasets of pest symptom/damage images and expert pre-screened banana disease were gathered from different hotspots in Southern India and Africa. The three different CNN architectures were retrained to build a detection model by a transfer learning model. Moreover, the total of 6 dissimilar methods was determined from 18 various classes through the collected images from the banana plant. The proposed model has revealed that the InceptionV2 based models and ResNet50 were superior when compared to MobileNetV1.

In 2018, Shen et al. [8] have implemented a $4.5 \times$ local zoom model for insect pest images with local high-magnification and no decrement in the complete FOV of wide FOV. The proposed system has provided the imaging channel with local zoom for the peripheral imaging channel and pest recognition to search the pests in a wide FOV. Moreover, 2 imaging channels were present in a similar image plane. Furthermore, the simulation setup was used for the imaging of aphids on plant leaves. The MSRCR and MSR systems were proposed for enhancing the contrast and brightness of the local zoomed images. Finally, the experimental outcomes have verified the enhanced pest recognition accuracy in simplifying imaging processing algorithm and outdoor environments.

2.2. Motivation of the work

Table 1 shows the review on pest detection. Initially, AF-RCNN model was deployed in [1], which presents more effective, better precision, and increased recall; however, the data augmentation technologies were not used in the adopted model to increase the number of data in those classes. DeepPest approach and MDM model have exploited in [2] that offer improves detection performance, lowest top-1 error, and

Table 1

Review On Existing Pest Detection Methods: Features And Challenges.

Author [citation]	Adopted scheme	Features	Challenges
Lin et al. [1]	AF-RCNN model	<ul style="list-style-type: none"> • More effective. • Better precision. • Increased recall. • Fast recognition and localization of pests. 	<ul style="list-style-type: none"> • The data augmentation technologies were not used in the adopted model to increase the number of data in those classes. • The consumption time is high. • Costly technique. • The context-aware attention network cannot use the in-field pest image. • It cannot be able to accurately classify the image.
Fangyuan et al. [2]	DeepPest approach and MDM model	<ul style="list-style-type: none"> • Improves the detection performance. • Lowest top-1 error. • Improved accuracy. • Extracts the multi text contextual image. • Appropriate attention mechanism and data augmentation strategy. 	<ul style="list-style-type: none"> • The connections were not trainable in LIRA classifier. • High computation complexity.
Karen et al. [3]	LIRA and RSC neural classifiers	<ul style="list-style-type: none"> • Better efficiency is achieved. • Lower number of errors. • Demonstrate good results in pest image recognition. • It can be used in a real time application. 	<ul style="list-style-type: none"> • The connections were not trainable in LIRA classifier. • High computation complexity.
Yu et al. [4]	Deep learning detection method	<ul style="list-style-type: none"> • Average runtime • Maximum precision • Higher recall • Better accuracy • Robust performance both qualitatively and quantitatively within limited computational budgets 	<ul style="list-style-type: none"> • Need to focus on the RTB monitoring development of IoTs. • Processing time is high.
Liu et al. [5]	CSA module	<ul style="list-style-type: none"> • Higher Map • Improved detection performance • Better recall • Computational cost is reduced 	<ul style="list-style-type: none"> • PestNet would not get enhancement in class #12 of shallow convolutional network. • Continuous monitoring is required.
Chen et al. [6]	YOLO series neural network algorithm	<ul style="list-style-type: none"> • Increased number of pest training samples • Improved recognition accuracy • Better efficiency • Appropriate pest control methods that decrease crop losses and reduce the environmental damage. 	<ul style="list-style-type: none"> • Needs to maximize the different angles in the images for solving the problems of insufficient training samples. • To overcome the issue of insufficient training samples, the number of different views in the images must be continually increased.
Selvaraj et al. [7]	DCNN model	<ul style="list-style-type: none"> • Maximum mAP • Best training time • Higher accuracy • The cost is reduced. 	<ul style="list-style-type: none"> • The proposed model needs to develop a fully automated mobile app for helping the banana farmers. • Sustainable development is required. • It only uses the few data samples.
		<ul style="list-style-type: none"> • Better contrast 	

(continued on next page)

Table 1 (continued)

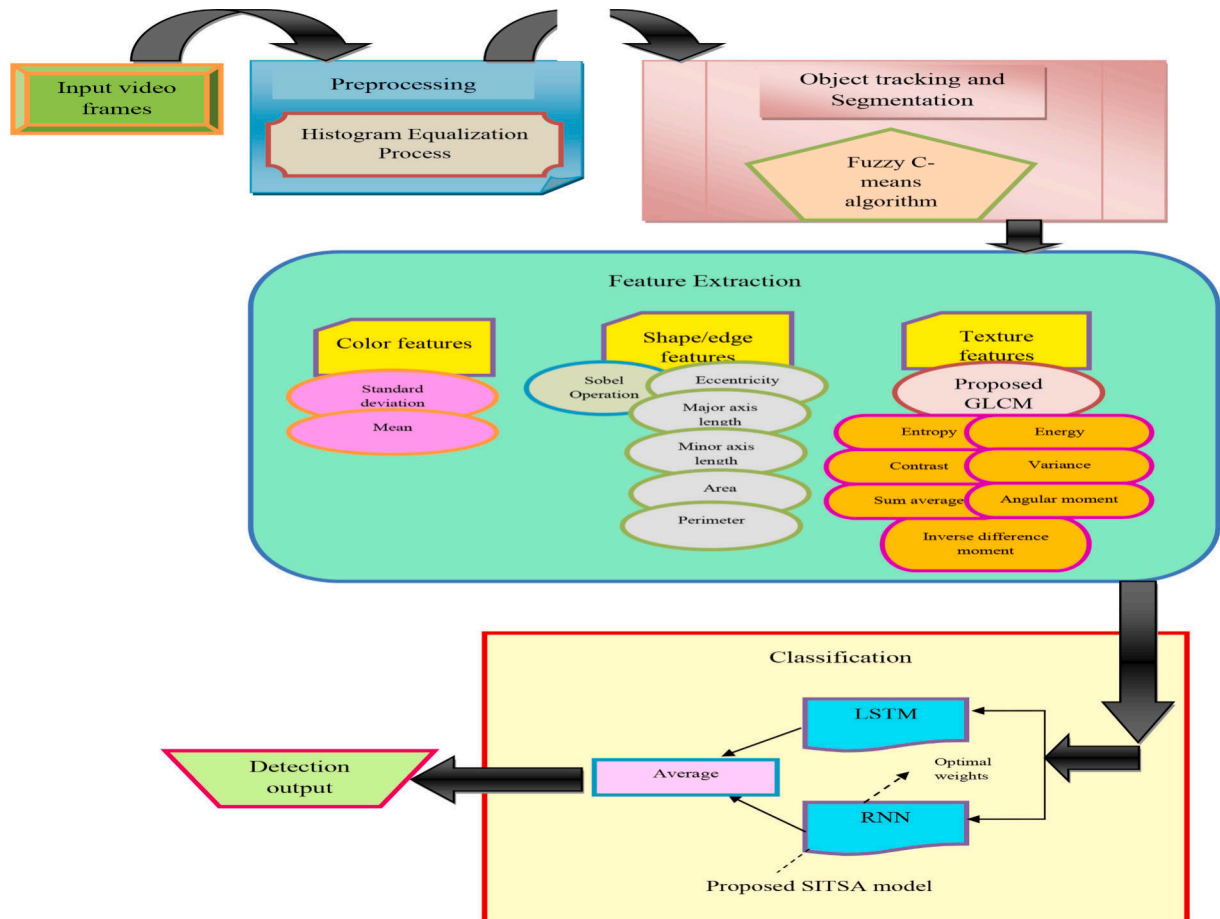
Author [citation]	Adopted scheme	Features	Challenges
Shen et al. [8]	MSRCR and MSR algorithms	<ul style="list-style-type: none"> Improving pest recognition accuracy Well used for the imaging of pests at different local magnifications. 	<ul style="list-style-type: none"> Real-time image processing algorithms were not implemented into the local zoom system. Costlier method. High complexity computation.

improved accuracy, but the context-aware attention network cannot use the in-field pest image. Moreover, RSC and LIRA neural classifiers were deployed in [3] that offer maximum recognition rate, and a lower number of errors. Nevertheless, the connections were not trainable in LIRA classifier. Likewise, the deep learning detection method was exploited in [4], which offers average runtime, maximum precision, higher recall, and better accuracy. However, need to focus on the RTB monitoring development of IoTs. CSA module was exploited in [5] that has mapped, improved detection performance, and better recall; however, PestNet would not get enhancement in class #12 of shallow convolutional network. In addition, the YOLO series neural network algorithm was introduced in [6], which offers increased count of pest training samples, improved recognition accuracy, and better efficiency. However, needs to maximize the different angles in the images for solving the problems of insufficient training samples. DCNN model was suggested in [7] that offer maximum mAP, best training time, and higher accuracy. However, the proposed model need to develop a fully

automated mobile app for helping the banana farmers. Finally, MSR and MSRCR algorithms was implemented in [8], which offers increase in the local magnification, better contrast, and improving pest recognition accuracy; however, real-time image processing algorithms were not implemented into the local zoom system. Such limitations have to be taken into account for pest detection in the present work effectively. To overcome the drawback present in the existing model the improved adopted model is used.

3. Overview of the proposed pest detection model

This paper intends to introduce a novel pest detection model (detecting *Heliiothis armigera* (Cotton bollworm) and *Leptocorisca acuta* (rice bug)) that includes five major phases: “(i) Pre-processing (ii) Object tracking (iii) Segmentation (iv) Feature extraction and (v) Classification”. Initially, the input video frames is subjected to the pre-processing phase in which the video frames gets pre-processed by using the histogram equalization process. The pre-processed images are then subjected to object tracking and segmentation process, which is carried out using FCM algorithm. From the segmented images, the proposed GLCM based texture features, color, edge and shapes are extracted. The sobel operation is used to extract the shape and edge features of an image. The colour features are extracted from R-Channel of RGB, H-channel and V-channel of HSV, and L-channel of LUV image frames. Further, the texture based features of proposed GLCM includes 7 attributes such as energy, entropy, sum average, variance, contrast, angular moment, contrast, and inverse difference moment. These extracted features are then subjected to Hybrid classifier LSTM-RNN for detecting the pest. For precise detection results, the RNN training is carried out using SITSA model via selecting the optimal weights. Fig. 1 illustrates the overall framework of

**Fig. 1.** Overall framework of the proposed model.

the proposed model.

4. Preprocessing via histogram equalization Process, object tracking and segmentation process

4.1. Preprocessing

The input video is enhanced using the histogram equalization process. Each frame Im_{frame} had undergone the histogram equalization process.

Histogram equalization is an approach used to adjust the image intensities for enhancing the contrast. Moreover, it is the well-known enhancement system. The dynamic range and contrast of an image in histogram equalization is modified through varying the image, where the histogram intensity has a required shape. Further, it is attained through the CDF as the mapping function. The intensity levels are changed in which the histogram peaks are compressed and stretched the troughs. If the image has pix pixels dispersed indiscrete intensity levels IL and the number of pixels num_i with i_i intensity level, then the image PDF is specified as per the following equations (1) and (2).

$$f_i(i_i) = \frac{num_i}{pix} \quad (1)$$

$$F_i(i_i) = \sum_{j=0}^i f_j(i_j) \quad (2)$$

The pre-processed image frames are indicated as Im_{pre} , which is subjected for the next process.

4.2. Object tracking and segmentation

The object in the frame can be identified and tracked using segmentation and morphological operation. FCM is used to separate the background and foreground objects. The morphological operations such as opening and closing are performed.

(i) FCM: The most widely used systems in fuzzy clustering is the FCM algorithm [33]. Consider $Y = \{y_1, y_2, \dots, y_m\}$ as a group of given data in which each data point $y_k (k = 1, 2, \dots, m)$ is a vector in \mathbb{N}^s , c be an integer $2 \leq c < m$, and V_{cm} is a set of real $c \times m$ matrices. Subsequently, the fuzzy c-partition space for Y is given in Eq. (3). Where, v_{hk} denotes the membership value of y_k in cluster $h (h = 1, \dots, c)$.

$$P_{fcm} = \left\{ \begin{array}{l} V \in V_{cm} : v_{hk} \in [0, 1] \\ \sum_{h=1}^c v_{hk} = 1, \quad 0 < \sum_{k=1}^m v_{hk} < m \end{array} \right\} \quad (3)$$

The main objective of the FCM model is to find an optimal fuzzy c-partition and related prototypes reducing the objective function.

$$I_p(V, U; Y) = \sum_{k=1}^m \sum_{h=1}^c (v_{hk})^p \|y_k - u_h\|^2 \quad (4)$$

In Eq. (4), $U = (u_1, u_2, \dots, u_c)$ indicates the matrix of unknown cluster centers $u_h \in \mathbb{N}^s$, the weighting exponent p in $[1, \infty)$ as constant which influenced the membership values, and $\|\cdot\|$ denotes the Euclidean norm.

The fuzzy constraints is defined in Eq. (3) for minimizing the I_p . Let us consider the c value, p and ε (i.e., a low positive constant; subsequently, a fuzzy c-partition V^0 is generated randomly and set iteration numbers $= 0$. Moreover, the membership values $v_{hk}^{(ts)}$, the cluster centers $u_h^{(ts)} (h = 1, \dots, c)$ are determined in Eq. (5).

$$u_h^{(ts)} = \frac{\sum_{k=1}^m (v_{hk}^{(ts)})^p y_k}{\sum_{k=1}^m (v_{hk}^{(ts)})^p} \quad (5)$$

Further, the new cluster centers $u_h^{(ts)}$ and update the membership

values $v_{hk}^{(ts)}$ as given in Eq. (6).

$$v_{hk}^{(ts+1)} = \left[\sum_{j=1}^c \left(\frac{\|y_k - u_h^{(ts)}\|^2}{\|y_k - u_{jl}^{(ts)}\|^2} \right)^{\frac{2}{p-1}} \right]^{-1} \quad (6)$$

When $|V^{(ts+1)} - V^{(ts)}| \leq \varepsilon$ or a predefined number of iterations is achieved once the process stops.

(ii) Morphological operations: To these formulated clusters, the morphological operations like Closing and opening are determined. The clustered image is denoted as Im_{clus} .

Opening: "In mathematical morphology, opening is the dilation of the erosion of a set Im_{clus} through a structuring element A ". The general formula for opening is given in Eq. (7).

$$Im_{clus} \circ A = (Im_{clus} \ominus A) \oplus A \quad (7)$$

Closing: "In mathematical morphology, the closing of a set (clustered image) Im_{clus} by a structuring element B is the erosion of the dilation of that set". The mathematical formula for closing is given in Eq. (6).

$$Im_{clus} \cdot A = (Im_{clus} \oplus A) \ominus A \quad (8)$$

The obtained segmented image is denoted as (Im_{seg}) .

5. Feature extraction: Edge/shape, color, and proposed texture features

The feature extraction process includes three features that includes.

- Edge/shape features
- Color features
- Proposed Texture features

5.1. Edge/shape features

The sobel operation is used to extract the shape and edge features of an image. Further, the sobel edge related to edge features is extracted. The sobel edge features are used to extract the pixel intensities. There are two sobel derivatives such as horizontal and vertical. The horizontal sobel derivate is obtained through the convolution of the binarized image Im_{bin} with a matrix known as kernel that has only 7 sizes. The vertical sobel derivate is acquired via the convolution of the binarized image Im_{bin} with a matrix known as kernel with odd size. The sobel edge detection is determined for the binarized image Im_{bin} by the function given in Eq. (9).

$$fl_{ed} = cv2.sobel(Im_{bin}, depth, column, row, kernelsize) \quad (9)$$

The final edge feature is the sobel edge feature (fl_{ed}). The shape features like minor axis length, eccentricity, major axis length, perimeter and area are extracted from the shape image. The shape features extracted is denoted as fl_{sh} . Table 2 describes the feature length of shape and edge feature.

5.2. Colour feature extraction

The colour features are extracted from V-channel and H-channel of

Table 2
Feature length of Edge and Shape Feature.

S. No.	Features	Length
1.	Sobel edge (Edge features)	1×256
2.	Minor axis length, Eccentricity, major axis length, perimeter and area (Shape features)	1×5

HSV, R-Channel of RGB, and L-channel of LUV image frames. Moreover, the standard deviation and mean of these channels are considered as the statistical features. The mean μ can be mathematically expressed as in Eq. (10).

$$\mu = \frac{\sum z}{S} = \frac{\text{Sum of data entries}}{\text{Number of entries}} \quad (10)$$

The standard deviation σ is given in Eq. (11). The overall colour features extracted is denoted as fl_{co} . The feature length of colour features is described in Table 3.

$$\sigma = \sqrt{\frac{\sum (z - \mu)^2}{S}} \quad (11)$$

5.3. Proposed GLCM

This section briefly discusses grey-level co-occurrence matrix features, which are one of the diverse texture features. The GLCM [32] determined the 2nd order statistical texture features by the intensity values of statistical distributions, which combines the image at various positions close to each other. The statistics of an image are divided into 1st, 2nd, and higher order based on the number of intensity points. The higher orders statistics are better but not executed due to the computation complexities. The texture features consists of the information concerning the surfaces' structural arrangement and its surrounding. The proposed GLCM is defined as in Eq. (12).

$$C_{qr} = \sum_{e=0}^{E-1} \sum_{d=0}^{F-1} \delta(e, d) \quad (12)$$

$$\delta(e, d) = \begin{cases} 1, & \text{if } f(e, d) = q, g(e, d) = r \\ 0, & \text{otherwise} \end{cases} \quad (13)$$

$$g(e, d) = \frac{10}{1 / \left[\frac{f(e, d-1) + f(e+1, d+1) + f(e+1, d) + f(e+1, d-1) + f(e, d-1) + f(e-1, d-1) + f(e-1, d) + f(e-1, d+1) + 2f(e, d)}{10} \right]} \quad (14)$$

Here, $g(e, d)$ is the harmonic mean of neighbouring pixels. The harmonic mean can be calculated as per Eq. (15).

$$\text{Harmonic mean} = \frac{nl}{\sum \left[\frac{1}{e_i} \right]} \quad (15)$$

Further, the texture based features of GLCM includes 7 attributes such as energy, entropy, sum average, variance, contrast, angular moment, contrast, and inverse difference moment. Moreover, the features were calculated in 4 directions like $0^\circ, 45^\circ, 90^\circ, 180^\circ$.

1 Energy is given in Eq. (16), where $Q(a, b)$ is the $(a, b)^{th}$ entries in GLCM.

$$\text{Energy} = \sum_{x=1}^{K-1} \sum_{a=1}^{K-1} Q(a, b)^3 \quad (16)$$

2 Entropy is given in Eq. (17).

$$\text{Entropy} = \sum_{x=1}^{K-1} \sum_{a=1}^{K-1} Q(a, b) * \log(Q(a, b)) \quad (17)$$

3 Contrast is offered in Eq. (18).

$$\text{contrast} = \sum_{NR=0}^{K-1} NR^2 \left\{ \sum_{a=1}^{K-1} Q(a, b) \right\} \quad (18)$$

4 Variance is offered in Eq. (19), where φ is the mean of $Q(a, b)$.

$$\text{variance} = \sum_{x=1}^{K-1} \sum_{a=1}^{K-1} (Q(a, b))^2 - \varphi^2 \quad (19)$$

5 Sum Average is given in Eq. (20).

$$\text{Sum average} = \sum_{a=0}^{2K-1} aQ_{x+y}(a) \quad (20)$$

6 Angular moment is given in Eq. (21).

$$\text{Angular moment} = \sum_{k=1}^{H-1} \sum_{l=1}^{H-1} R(l, m)^2 \quad (21)$$

7 Inverse difference moment is defined in eq. (22), where $M-L = NR$.

$$\text{IDM} = \sum_{x=1}^{K-1} \sum_{a=1}^{K-1} \frac{1}{1} + (M-L)^2 Q(a, b) \quad (22)$$

The extracted GLCM features are denoted as fl_{GLCM} . Moreover, the overall extracted feature is indicated as Im_{fea} and it is given in Eq. (23).

$$Im_{fea} = fl_{ed} + fl_{sh} + fl_{co} + fl_{GLCM} \quad (23)$$

6. Pest detection by optimized hybrid long short term memory and recurrent neural network

The extracted features Im_{fea} are subjected to detection process via optimized hybrid classifier (LSTM and RNN). Here, the extracted features are subjected directly to both the classifiers. Both the classifiers are executed parallely and the final results from them are averaged to determine the final classified results.

6.1. LSTM**a

The extracted features (Im_{fea}) are subjected to the LSTM for the detection purpose. The LSTM [34] formation consists sequences of persistent LSTM cells. The LSTM cells consisted of 3 units which indicates the “forget gate, the input gate, and the output gate”. These elements allow the LSTM memory cells to suggest the information for extensive time duration and to stock up. Assume H and CS as the hidden and cell state. (H_t, CS_t) and (Z_t, CS_{t-1}, H_{t-1}) represents the output and input layers correspondingly. At time t , the forget gate, the output and input gates are denoted as O_t, IP_t, G_t correspondingly. The LSTM cell primarily uses G_t to filter the data. The modelling of G_t is determined in Eq. (24). Here, (We_{HG}, J_{HG}) and (We_{IPG}, J_{IPG}) portrays the bias parameter and weight matrix.

$$G_t = \kappa(We_{IPG}Z_t + J_{IPG} + We_{HG}H_{t-1} + J_{HG}) \quad (24)$$

Consequently, the activation function of gate (κ) is elected as sigmoid operation. Next, the LSTM cell makes use of the input gate to integrate the proper data as given in Eq. (25), Eq. (26) and Eq. (27).

$$X_t = \tanh(We_{IPX}Z_t + J_{IPX} + We_{HX}H_{t-1} + J_{HX}) \quad (25)$$

$$IP_t = \kappa(We_{IPI}Z_t + J_{IPI} + We_{HIP}H_{t-1} + J_{HIP}) \quad (26)$$

$$CS_t = G_t CS_{t-1} + IP_t X_t \quad (27)$$

Table 3
Feature Length Of Colour Feature.

S.No.	Features	Parameter	Length
1.	L- Channel	Standard Deviation	1
		Mean	1
2.	V-Channel	Standard Deviation	1
		Mean	1
3.	H- Channel	Standard Deviation	1
		Mean	1
4.	R-Channel	Standard Deviation	1
		Mean	1

In Eq. (25) to Eq. (27), (W_{HX}, J_{HX}) and (W_{IPX}, J_{IPX}) denotes to the weight matrices and bias parameters, which map the hidden and input layers to cell gate. (W_{HIP}, J_{HIP}) and (W_{IPIP}, J_{IPIP}) represent the weight and bias parameters which map the hidden and input layers to IP_t correspondingly. Finally, the LSTM obtains hidden layer (output) from output gate as given in Eq. (28) and (29), wherein, (W_{HO}, J_{HO}) as well as (W_{IPO}, J_{IPO}) indicates weight and bias parameters for mapping the hidden and input layers to O_t correspondingly.

$$O_t = \kappa(W_{IPO}Z_t + J_{IPO} + W_{HO}H_{t-1} + J_{HO}) \quad (28)$$

$$H_t = O_t \tanh(CS_t) \quad (29)$$

The output of LSTM is denoted as Out_{LSTM} .

6.2. Optimized RNN

The extracted features Im_{fea} are given as the input of the RNN framework. In addition, the RNN [36] includes output layer, hidden layer, and an input layer, in which each layer consists of neurons. Further, the input units IU are present in the input layer that has the sequence of vectors with time T , for instance $\{..., RP_{T-1}, RP_T, RP_{T+1}, ...\}$, in which $RP_T = (RP_1, RP_2, ..., RP_{IN})$. In the fully convolutional RNN, each input units are linked with the each hidden unit of the hidden layer, and it is specified by the weight matrix W_{th} . Further, the hidden layer HG includes the hidden units with $JS_T = (JS_1, JS_2, ..., JS_{HG})$ that are linked to each other by the recurrent links in the matrix W_{hh} . Similarly, the hidden layer of the RNN is given in Eq. (30), where, $AF_{ht}()$ and BF_{ht} specifies the activation function and the bias vector of the hidden units, correspondingly.

$$HM_T = AF_{ht}(W_{th}RP_T + W_{hh}HM_{T-1} + BF_{ht}) \quad (30)$$

Further, the hidden units are associated to the output layer by the weight matrix W_{ho} . Moreover, the output layer includes SL units as $OQ_T = (OQ_1, OQ_2, ..., OQ_{SL})$ in Eq. (31), where, $AF_o()$ and BF_o refers to the bias vector and the activation function of output units, respectively.

$$OQ_T = AF_o(W_{ho}HM_T + BF_o) \quad (31)$$

In addition, the RNN has different weight parameters including the weight matrix W_1 with hidden-to-hidden recurrent connections (i.e.), exist among the nodes of the hidden layer, W_2 connected to the layer and hidden the output layer, and W_3 connects among the hidden layer and input layer. All these parameters (WM_3, WM_1, WM_2) are shared across time. The following steps of the RNN frameworks are as follows:

Step 1: The weight matrices are given as W_3, W_1, W_2 , and the bias function BZ_1, BZ_2 are initialized with zeros, and the weights are then updated by the proposed SITSA algorithm. The solution encoding and the algorithmic description is given in the subsequent section.

Step 2: The speech emotion recognition is computed by the Forward propagation process. The RNN forward pass is given in Eq. (32) to Eq. (35), correspondingly. The softmax function is provided as a post-processing step to obtain the normalized probabilities of output as D .

$$SR(T) = BZ_1 + W_3 \cdot UL(T) + W_1 \cdot HM(T-1) \quad (32)$$

$$HM(T) = \tanh(SR(T)) \quad (33)$$

$$JS(T) = BZ_2 + HM(T) \cdot W_2 \quad (34)$$

$$D(T) = \text{softmax}(JS(T)) \quad (35)$$

Step 3: The loss function is determined in Eq. (36).

$$Loss = - \sum_{BZ_2=1}^{NT} ZI_{obs,cls} \cdot \log(MS_{obs,cls}) \quad (36)$$

In Eq. (36), NT specifies the count of possible class labels, ZI indicates the binary indicator that checks whether the class label cls is classified

correctly for the observation obs .

Step 4: Compute the gradients through the back-propagation.

Thus, the final output obtained from the RNN is denoted as Out_{RNN} . The final classification output is denoted as Out , and it is expressed in Eq. (37).

$$Out = \frac{Out_{LSTM} + Out_{RNN}}{2} \quad (37)$$

Classifier parameters are the batch-size = 128, epochs = 10 and learning rate = 0.01.

7. RNN weight Optimization by Self improved tunicate Swarm Optimization Algorithm

7.1. Solution encoding and objective function

As mentioned, the weights of RNN are optimally tuned using the proposed SITSA method. Fig. 2 illustrates the input solution to the proposed SITSA model. Here, the total number of weights in RNN is indicated as N . The objective function of the implemented method is given in Eq. (38), where *accuracy* indicates the detection accuracy.

7.2. Proposed SITSA model

Even though, the conventional TSA [26] model has the ability to find the location of food source pre sent in the sea; still, it has no idea regarding the food source obtained in the search space. This becomes the issue while solving optimization problems. For overcoming this scenario, the SITSA model is proposed in this work. Generally, the self-improvement is proved to be capable in the existing optimization algorithms [27 28 29 30 31]. In TSA, the two tunicate behaviors are employed to find the food source. Furthermore, the two behaviors of TSA include the swarm intelligence and jet propulsion.

Jet propulsion behavior: In addition, a tunicate must satisfy the following 3 conditions including “avoid the conflicts among the search agents, remains close to the best search agent, and movement towards the position of best search agent”. Still, the swarm behavior updated the other search agent’s position on the basis of best optimal solution. The 3 conditions of the jet propulsion behavior is specified as follows.

(i) Avoid the conflicts between search agents: The $X\vec{L}$ vector is employed to compute the new search agents position for avoiding the conflicts among the search agents, and it is given in Eq. (39).

$$X\vec{L} = \frac{Y\vec{L}}{Z\vec{L}} \quad (39)$$

Where,

$$Y\vec{L} = n_2 + n_3 - E\vec{O} \quad (40)$$

$$E\vec{O} = 2 \cdot n_1 \quad (41)$$

In Eq. (40) and Eq. (41), $E\vec{O}$ indicates the water flow advection in deep ocean, $Y\vec{L}$ represents the gravity force, and the variables n_1, n_2 , and

$$Obj = \max(\text{accuracy})$$



Fig. 2. Solution Encoding.

n_3 refers to the random number ranges among [0, 1]. \vec{ZL} specifies the social forces among the search agents, and it is given in Eq. (42).

$$\vec{ZL} = [B_{\min} + n_1 \cdot B_{\max} - B_{\min}] \quad (42)$$

In Eq. (42), B_{\max} and B_{\min} denotes the subordinate and initial speeds for making the social interaction. Further, the values of B_{\min} is 1, and B_{\max} is 4, correspondingly.

(ii) Movement towards the best neighbour's direction: The search agents move towards the best neighbour's direction once after the conflict avoided between the neighbours.

$$D\vec{P} = |H\vec{R} - rand \cdot \vec{B}_{sl}(w)| \quad (43)$$

In Eq. (43), w denotes the current iteration, $D\vec{P}$ portrays the distance among the food source and tunicate (i.e.), search agent, $H\vec{R}$ refers to the position of food source, the vector $\vec{B}_{sl}(w)$ specifies the tunicate position and $rand$ indicates the random number lies among [0, 1].

(iii) Proposed Converge towards the best search agent: Conventionally, the search agent could sustain the positions towards the food source (i.e.) best search agent. However, as per the proposed SITSA method, the positions are updated with levy update as given in Eq. (44).

$$\vec{B}_{sl}(w)' = \begin{cases} H\vec{R} + X\vec{L} \cdot D\vec{P} + Levy(\beta) & \text{if } rk \geq 0.5 \\ H\vec{R} + X\vec{L} \cdot D\vec{P} & \text{if } rk < 0.5 \end{cases} \quad (44)$$

$\vec{B}_{sl}(w)'$ specifies the updated position of tunicate in terms of the $H\vec{R}$ food source position.

If $rk < pr$, then

$$\vec{B}_{sl}(w) = B_{sl}^{md} + f_{x1} \times (u_{q1} * GH_{best} - u_{q2} * GH_{kg}^{md}) + f_{x2} \times \rho_1 \times \left(\frac{u_{q3} * (GH_{2no}^{md} - GH_{1no}^{md}) + u_{q2} * (GH_{rk1}^{md} - GH_{rk2}^{md})}{2} \right) \quad (45)$$

Else,

$$\vec{B}_{sl}(w) = GH_{best} + f_{x1} \times (u_{q1} * GH_{best} - u_{q2} * GH_{kg}^{md}) + f_{x2} \times \rho_1 \times \left(\frac{u_{q3} * (GH_{2no}^{md} - GH_{1no}^{md}) + u_{q2} * (GH_{rk1}^{md} - GH_{rk2}^{md})}{2} \right) \quad (46)$$

Where, B_{sl}^{md} portrays the current position of tunicate, GH_{best} indicates the best position, pr denotes the probability ($pr = 0.3$), rk specifies the random value $\in (0, 1)$, f_{x1}, f_{x2} indicates the uniformly distributed random values $\in (-1, 1)$, GH_{rk1}^{md} and GH_{rk2}^{md} specifies the two random solutions selected from population, ρ_1 indicates the balance in exploration and exploitation process, $rand$ refers to the random number, GH_{1no}^{md} and GH_{2no}^{md} denotes the random solution and it is determined in Eq. (47).

$$GH_{1no}^{md}, GH_{2no}^{md} = LB + rand(dim) * (UB - LB) \quad (47)$$

In Eq. (47), LB indicates the lower bound, UB denotes the upper bound, dim specifies the dimension, n and m refers to the coordinates of solution $no = 1, 2, \dots, NO$ and $md = 1, 2, \dots, dim$. Furthermore, u_{q1}, u_{q2} , and u_{q3} are calculated as per Eq. (48), Eq. (49), and Eq. (50).

$$u_{q1} = LM_1 * 2 * rand + (1 - LM_1) \quad (48)$$

$$u_{q2} = LM_1 * rand + (1 - LM_1) \quad (49)$$

$$u_{q3} = LM_1 * rand + (1 - LM_1) \quad (50)$$

Where, LM_1 and LM_2 are the binary parameters. w_{kg}^{md} is determined as in Eq. (51).

$$w_{kg}^{md} = LM_2 * w_{sl}^{md} + (1 - LM_2) * rand \quad (51)$$

Swarm behaviour: For simulating the swarm behaviour of tunicate, it saves the other search agent's positions and the first two optimal best solutions are updated based on the best search agent's position. Furthermore, the swarm behaviour of tunicate is determined as in Eq. (52).

$$\vec{B}_{sl}(\vec{w} + 1) = \frac{\vec{B}_{sl}(\vec{w}) + \vec{B}_{sl}(\vec{w} + 1)}{2 + n_1} \quad (52)$$

Algorithm 1 describes the pseudo code of the proposed SITSA scheme.

Algorithm 1: Pseudo code of Proposed SITSA Model

Step 1: Initialization of the tunicate population \vec{B}_{sl}

Step 2: Choose the total number of iterations and initial parameters.

Step 3: The fitness value for each search agent is determined.

Step 4: The best search agent is identified after the fitness evaluation.

Step 5: Each search agent's position is updated as per Eq. (52).

Step 6: The updated search agent is adjusted away from the boundary in a specified search space.

Step 7: The fitness value of updated search agent is calculated. The \vec{B}_{sl} is updated using proposed update evaluation as in Eq. (44).

Step 8: The algorithm end only if the stopping criterion is satisfied. Else, repeat the steps from 5 to 8.

Step 9: Returns the so far best optimal solution is.

8. Results and discussion

8.1. Simulation procedure

The adopted pest detection with hybrid classifier + SITSA model was executed in PYTHON and the outcomes were verified. The performance of the adopted hybrid classifier + SITSA model with pest detection was computed over the conventional schemes such as SVM [37], NN [38], RF [41], DBN [32], hybrid classifier + WOA [39], hybrid classifier + EHO [40], hybrid classifier + TSA [26], hybrid classifier + D-NU [35], hybrid classifier + BOA [42] and hybrid classifier [44] + PSO correspondingly. Furthermore, the performance was computed by varying the training percentage such as 50, 60, 70, 80, and 90 for different performance measures such as "accuracy, sensitivity, specificity, precision, FMS, Thread score, FDR, FNR, FPR, FOR, NPV, and MCC", respectively. The sample images, pre-processed images and segmented images of the proposed work are illustrated in Fig. 3.

8.2. Dataset description

The dataset including the videos of pests like: *Heliothis armigera* (Cotton bollworm) and *Leptocorisa acuta* (rice bug) were manually collected. The cotton bollworm image consists of 34 videos and the rice bug image consists of 36 videos. Average of 100 frames per video is considered.

8.3. Performance analysis

The performance analysis of the proposed hybrid classifier + SITSA model is compared to the existing schemes like SVM, NN, RF, DBN, hybrid classifier + WOA, hybrid classifier + EHO, hybrid classifier + TSA, hybrid classifier + D-NU, hybrid classifier + BOA and hybrid classifier + PSO, respectively in terms of certain metrics, and it is represented in Figs. 4, 5, and 6. Similarly, the positive measures such as sensitivity, accuracy, precision and specificity of the proposed hybrid classifier + SITSA model shows superior outcomes than other traditional methods in detecting the pest. Moreover, the accuracy of hybrid classifier + SITSA model for training percentage 90 is 3.34 %, 3.06 %, 3 %, 2.79 %, 2.66 %, 2.11 %, 2.05 %, 1.98 %, 2.52 % and 3.71 % better than other conventional schemes like SVM, NN, RF, DBN, hybrid classifier +

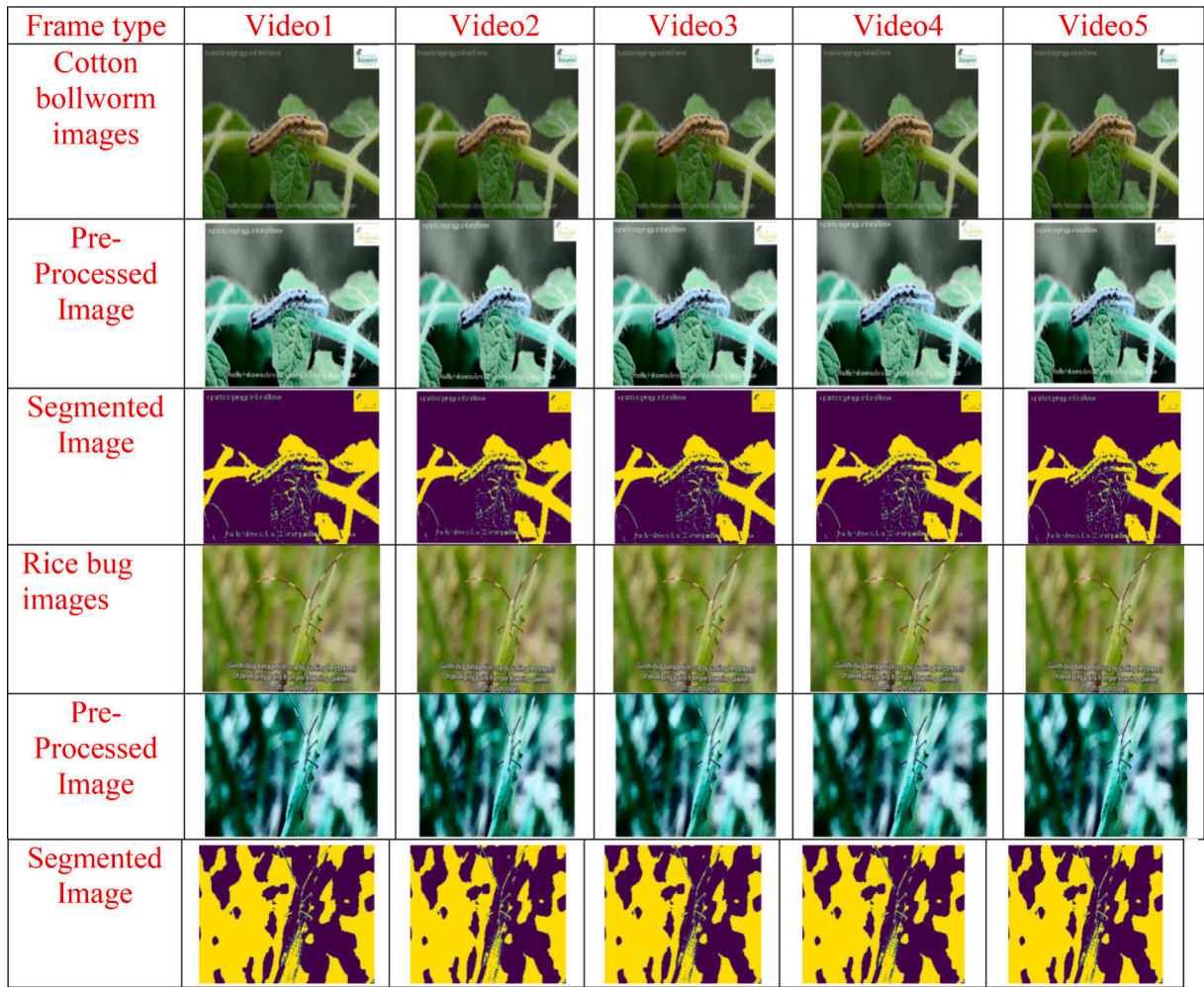


Fig. 3. Sample images, pre-processed images and segmented images of the proposed work.

WOA, hybrid classifier + EHO, hybrid classifier + TSA, hybrid classifier + D-NU, Hybrid classifier + BOA and Hybrid classifier + PSO, correspondingly as shown in Fig. 4(a). The adopted hybrid classifier + SITSA model attains higher sensitivity (~ 75.81) in detected results when compared over the existing schemes like SVM (~ 63.20), NN (~ 63.39), RF (~ 63.52), DBN (~ 69.34), hybrid classifier + WOA (~ 70.20), hybrid classifier + EHO (~ 70.31), hybrid classifier + TSA (~ 70.76), hybrid classifier + D-NU (~ 73.74), hybrid classifier + BOA (~ 70) and hybrid classifier + PSO (~ 72.14), respectively in Fig. 4(b) for training percentage 50. Furthermore, the proposed hybrid classifier + SITSA model holds maximum specificity for training percentage 80 that is 9.01 %, 7.26 %, 5.40 %, 4.21 %, 3.44 %, 2.90 %, 2.68 %, 2.15 %, 8.25 % and 6.24 % superior to the existing approaches like SVM, NN, RF, DBN, hybrid classifier + WOA, hybrid classifier + EHO, hybrid classifier + TSA, hybrid classifier + D-NU, hybrid classifier + BOA and hybrid classifier + PSO, respectively as given in Fig. 4(c). Additionally, the adopted hybrid classifier + SITSA model attains higher precision (~ 96.40); whereas, the traditional schemes attains lower precision value for SVM, NN, RF, DBN, hybrid classifier + WOA, hybrid classifier + EHO, hybrid classifier + TSA, hybrid classifier + D-NU, hybrid classifier + BOA and hybrid classifier + PSO, respectively for training percentage 60 in Fig. 4(d). The observed enhancement shows the impact of proposed SITSA model on training the classifier in a better way.

Fig. 5 illustrates the negative measures like FPR, FNR, FDR, and FOR of the adopted hybrid classifier + SITSA model and the existing models. The adopted hybrid classifier + SITSA model attains less FPR (~ 4.009) which is the better performance; whereas, the traditional schemes

attains high FPR as SVM (~ 27.64), NN (~ 25.03), RF (~ 25.03), DBN (~ 22.40), hybrid classifier + WOA (~ 14.20), hybrid classifier + EHO (~ 8.50), hybrid classifier + TSA (~ 6.41), hybrid classifier + D-NU, Hybrid classifier + BOA and Hybrid classifier + PSO, (~ 6.20), respectively for training percentage 60 in Fig. 5(a). The adopted hybrid classifier + SITSA model holds minimum FNR value that is 49.21 %, 48.85 %, 48.74 %, 42.70 %, 38.98 %, 35.28 %, 20.08 %, 18.13 %, 25.26 % and 38.15 % than other traditional models like SVM, NN, RF, DBN, hybrid classifier + WOA, hybrid classifier + EHO, hybrid classifier + TSA, hybrid classifier + D-NU, Hybrid classifier + BOA and Hybrid classifier + PSO, respectively for training percentage 80 in Fig. 5(b). Moreover, the FDR of the adopted hybrid classifier + SITSA model is 75.20 %, 72.60 %, 72.31 %, 53.20 %, 49 %, 40.33 %, 37.08 %, 30.88 %, 50.75 % and 63.2 % better than the other conventional models such as SVM, NN, RF, DBN, hybrid classifier + WOA, hybrid classifier + EHO, hybrid classifier + TSA, hybrid classifier + D-NU, Hybrid classifier + BOA and Hybrid classifier + PSO, respectively for training percentage 70 in Fig. 5 (c). Further, the FOR of the proposed hybrid classifier + SITSA model achieves superior outcomes (~ 5.27) than other existing models like SVM, NN, RF, DBN, hybrid classifier + WOA, hybrid classifier + EHO, hybrid classifier + TSA, hybrid classifier + D-NU, Hybrid classifier + BOA and Hybrid classifier + PSO, respectively for training percentage 90 in Fig. 5(d). Thus, the improvement of the proposed hybrid classifier + SITSA model is proved by the obtained results.

The other measures analysis such as NPV, MCC, FMS and thread score of the adopted hybrid classifier + SITSA model and existing models are represented in Fig. 6. From the graph, it is shown clearly that

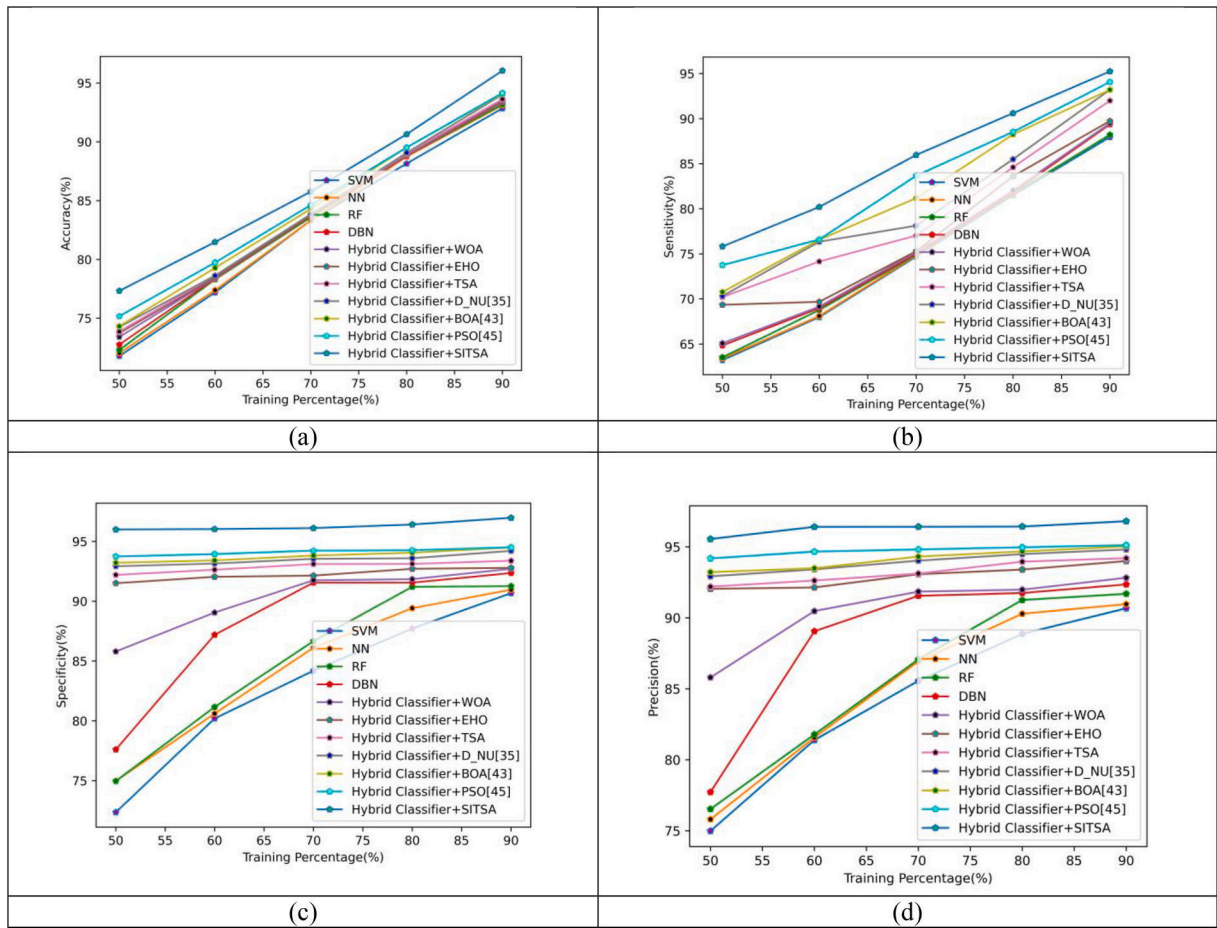


Fig. 4. Performance analysis of the proposed hybrid classifier + SITSA model over other traditional schemes for (a) accuracy (b) sensitivity (c) specificity (d) precision.

the NPV of the proposed MCSO hybrid classifier + SITSA model holds a value (~ 84.53) for training percentage 70; whereas, the compared existing models like SVM, NN, RF, DBN, hybrid classifier + WOA, hybrid classifier + EHO, hybrid classifier + TSA, hybrid classifier + D-NU, Hybrid classifier + BOA and Hybrid classifier + PSO, respectively attains lower values as per Fig. 6(a). In addition, the FMS of adopted hybrid classifier + SITSA model at training percentage 60 is 5.89 %, 5.83 %, 4.09 %, 3.48 %, 3.38 %, 3.25 %, 3.22 %, 1.89 %, 4.23 % and 5.08 % superior to other traditional scheme like SVM, NN, RF, DBN, hybrid classifier + WOA, hybrid classifier + EHO, hybrid classifier + TSA, hybrid classifier + D-NU, Hybrid classifier + BOA and Hybrid classifier + PSO, respectively in Fig. 6(b). Likewise, the adopted hybrid classifier + SITSA model attains maximum MCC (~ 92.32) for training percentage 90; whereas, the traditional schemes attains low MCC values such as SVM (~ 87.35), NN (~ 87.79), RF (~ 87.88), DBN (~ 88.02), hybrid classifier + WOA (~ 88.42), hybrid classifier + EHO (~ 89.09), hybrid classifier + TSA (~ 89.26), and hybrid classifier + D-NU (~ 89.36), Hybrid classifier + BOA (~ 79.09) and Hybrid classifier + PSO (~ 80.09), respectively in Fig. 6(c). The thread score of adopted hybrid classifier + SITSA model at training percentage 80 is 4.89 %, 4.02 %, 3.98 %, 3.79 %, 3.71 %, 2.50 %, 2.46 %, 2.43 %, 4.21 % and 5.32 % better than other existing schemes like as SVM, NN, RF, DBN, hybrid classifier + WOA, hybrid classifier + EHO, hybrid classifier + TSA, hybrid classifier + D-NU, Hybrid classifier + BOA and Hybrid classifier + PSO, correspondingly in Fig. 6(d). Thus, the performance of adopted hybrid classifier + SITSA model has shown enhancement than other existing models.

8.4. Overall performance analysis

The overall performance analysis of the adopted hybrid classifier + SITSA model over other traditional models for different training percentages concerning accuracy measure is determined in Table 4. From the table, the adopted hybrid classifier + SITSA model have proven its pest detection ability for all training percentages than other traditional models such as SVM, NN, RF, DBN, hybrid classifier + WOA, hybrid classifier + EHO, hybrid classifier + TSA, and hybrid classifier + D-NU, hybrid classifier + BOA and hybrid classifier + PSO, correspondingly. Similarly, the proposed hybrid classifier + SITSA model attains 3.90 %, 3.81 %, 3.74 %, 3.65 %, 3.49 %, 3.49 %, 2.70 %, 2.13 %, 4.67 % and 4.24 % better accuracy value than other traditional models like SVM, NN, RF, DBN, hybrid classifier + WOA, hybrid classifier + EHO, hybrid classifier + TSA, hybrid classifier + D-NU, hybrid classifier + BOA and hybrid classifier + PSO, correspondingly for training percentage 60. Furthermore, the proposed hybrid classifier + SITSA model attains maximum accuracy values (~ 96.04483) for training percentage 90 than other traditional models like SVM, NN, RF, DBN, hybrid classifier + WOA, hybrid classifier + EHO, hybrid classifier + TSA, and hybrid classifier + D-NU, respectively in Table 4. The outcomes have summarized that the adopted hybrid classifier + SITSA model performance is improved over the traditional models. Table 4 shows the overall performance analysis.

8.5. Statistical analysis

The statistical analysis of the proposed hybrid classifier + SITSA scheme over other existing models concerning accuracy measure is

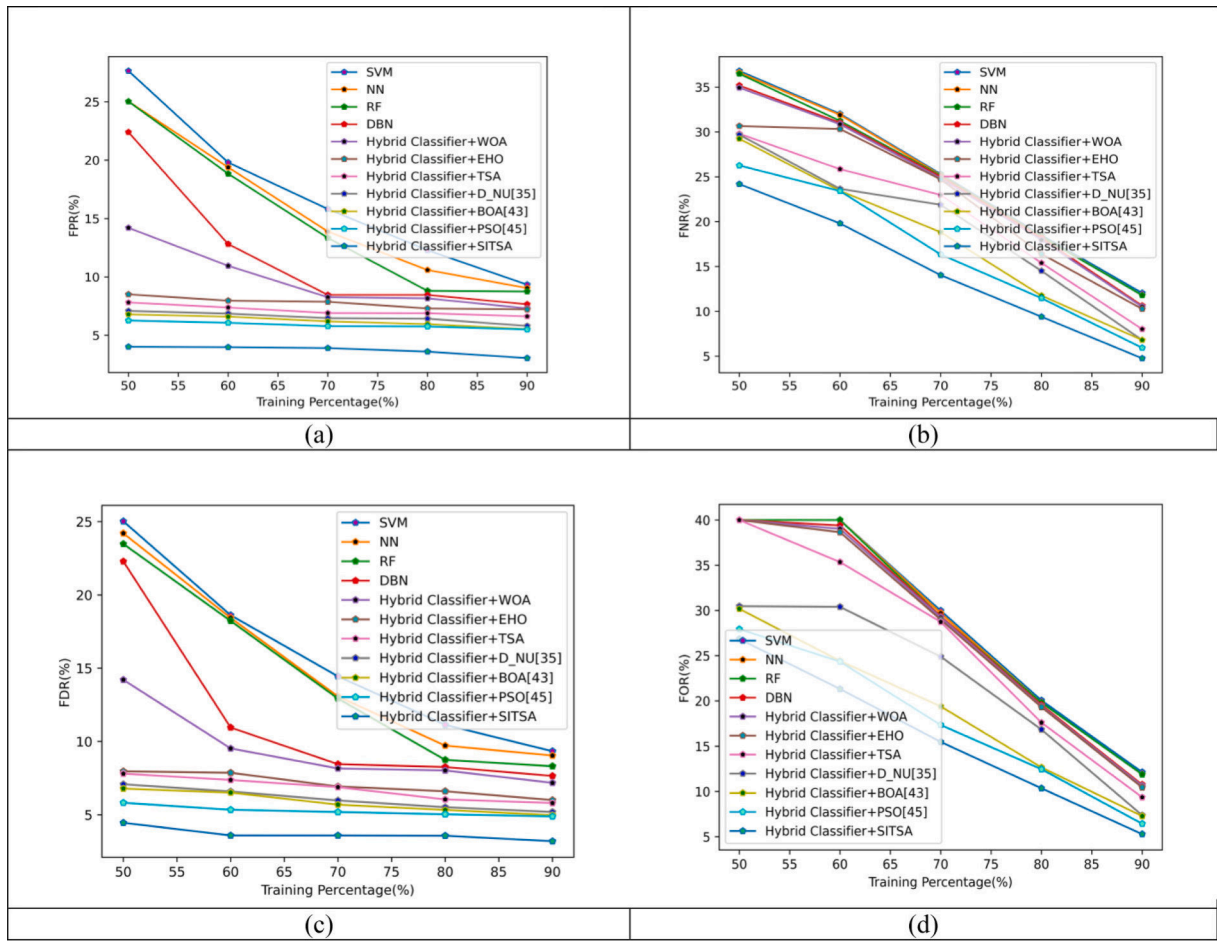


Fig. 5. Performance analysis of the adopted hybrid classifier + SITSA model over other traditional schemes for (a) FPR (b) FNR (c) FDR (d) FOR.

illustrated in Table 5. The meta-heuristic algorithms are stochastic; therefore, the algorithms are executed several times to determine the objective of the work by evaluating different case scenarios. Moreover, the adopted hybrid classifier + SITSA model has shown superior performance under best-case scenario that is 3.34 %, 3.07 %, 3 %, 2.80 %, 2.67 %, 2.11 %, 2.05 %, 1.98 %, 3.43 % and 4.21 % better than the traditional models like SVM, NN, RF, DBN, hybrid classifier + WOA, hybrid classifier + EHO, hybrid classifier + TSA, and hybrid classifier + D-NU, hybrid classifier + BOA and hybrid classifier + PSO, respectively. The mean performance of the proposed method in terms of accuracy measure holds better outcomes (86.24918) than other traditional models like SVM, NN, RF, DBN, hybrid classifier + WOA, hybrid classifier + EHO, hybrid classifier + TSA, and hybrid classifier + D-NU, respectively. In addition, the proposed model attains a maximum value (77.32367) at worst-case scenario; whereas, the existing schemes hold minimum values concerning accuracy measure such as SVM (~71.7791), NN (~72.03988), RF (~72.30066), DBN (~72.75702), hybrid classifier + WOA (~73.40897), hybrid classifier + EHO (~73.73494), hybrid classifier + TSA (~74.32169), hybrid classifier + D-NU (~75.16922), respectively, hybrid classifier + BOA (~64.21) and hybrid classifier + PSO (~74.21). Consequently, the enhancement of the proposed hybrid classifier + SITSA model has been validated effectively. Table 5 shows the statistical analysis.

8.6. Convergence analysis

Fig. 7 represents the convergence analysis of the proposed Hybrid Classifier + SITSA method over other traditional models for varied iterations that range from 0 to 50. On observing the graph, it is shown that

the gradual decrement of the cost function with increased iterations. The convergence of the adopted Hybrid Classifier + SITSA method at the 40th iteration is 64 %, 85 %, and 95.7 % better than the existing model like Hybrid Classifier + WOA, Hybrid Classifier + EHO, Hybrid Classifier + TSA, Hybrid classifier + BOA, and Hybrid classifier + PSO corresponding concerning minimized error.

8.7. Practical implications

Correct identification of a pest allows us to determine basic information about it, including its life cycle and the time that it is most susceptible to being controlled. Regularly monitor the pest population and/or damage to determine whether control measures are necessary and, if so, when to begin the control measures. Agricultural employees can determine whether or not to use our method based on the classification result. Spray or don't spray in this area, and give instructions for varied dosing/treatment that is curative. They can also assess the current state of the crop and forecast crop yields in this region.

9. Conclusion

The *Heliothis armigera* (Cotton bollworm) and *Leptocoris acuta* (rice bug) have been detected using this model, which has three primary phases: (i) Pre-processing; (ii) Object tracking and segmentation; (iv) Feature extraction; (v) Classification. The input video frame (pictures) was first subjected to a pre-processing phase, during which the video frames were pre-processed. Object tracking and segmentation were performed on the pre-processed images. The FCM technique was used to segment the foreground and background in this case. The suggested

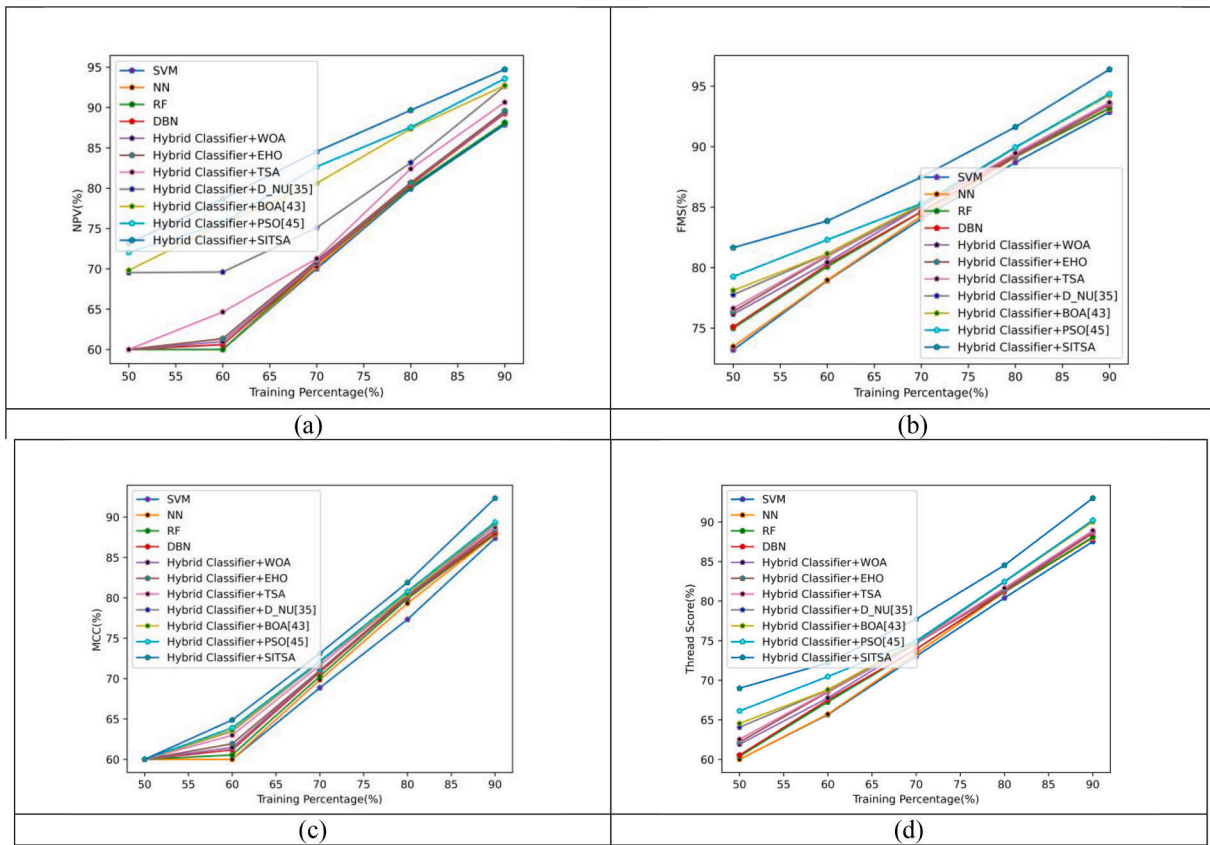


Fig. 6. Performance analysis of the adopted hybrid classifier + SITSA model over other traditional schemes for (a) NPV (b) FMS (c) MCC (d) Thread score.

Table 4

overall performance analysis of adopted and existing schemes for various training percentage.

Methods	Training percentage				
	50	60	70	80	90
SVM [37]	71.77	78.29	83.31	88.14	92.83
NN [38]	72.03	78.36	83.31	88.72	93.09
RF [41]	72.30	78.42	83.53	88.79	93.162
DBN [32]	72.75	78.49	83.70	88.86	93.35
Hybrid classifier + BOA [42]	73.21	77.35	82.50	88.65	92.25
Hybrid classifier + PSO [44]	74.25	78.15	83.25	88.70	92.80
Hybrid classifier + WOA [39]	73.40	78.62	83.77	88.92	93.48
Hybrid classifier + EHO [40]	73.73	78.62	83.84	88.99	94.01
Hybrid classifier + TSA [26]	74.32	79.27	84.29	89.51	94.07
Hybrid classifier + D-NU [35]	75.16	79.73	84.62	89.51	94.14
ProposedHybridclassifier + SITSA	77.32	81.47	85.76	90.63	96.04

GLCM based texture features, color, edge, and form-based characteristics are derived from the segmented pictures. Furthermore, the collected features were fed into a detection procedure that utilized hybrid classifiers like LSTM and RNN. RNN training was used to achieve exact detection results. Finally, the performance of the proposed scheme was compared over the other existing schemes concerning various metrics like FDR, specificity, accuracy, precision, FNR, sensitivity, FPR, Thread score, FMS, FOR, NPV, and MCC, correspondingly. On observing the graph, the adopted hybrid classifier + SITSA model attains higher sensitivity (~ 75.81) in detected results when compared over the existing schemes like SVM (~ 63.20), NN (~ 63.39), RF (~ 63.52), DBN (~ 69.34), hybrid classifier + WOA (~ 70.20), hybrid classifier + EHO (~ 70.31), hybrid classifier + TSA (~ 70.76), hybrid classifier + D-NU (~ 73.74), hybrid classifier + BOA (~ 70) and hybrid classifier + PSO (~ 72.14), respectively for training percentage 50. The adopted hybrid classifier +

Table 5

Statistical analysis with respect to accuracy: Proposed vs Conventional models.

Methods	Mean	Median	Standard deviation	Worst	Best
SVM [37]	82.87	83.31	7.36	71.77	92.82
NN [38]	83.10	83.31	7.43	72.03	93.04
RF [41]	83.25	83.57	7.37	72.30	93.16
DBN [32]	83.43	83.70	7.29	72.75	93.35
Hybrid classifier + WOA [39]	83.64	83.77	7.13	73.40	93.48
Hybrid classifier + EHO [40]	83.84	83.84	7.20	73.73	94.01
Hybrid classifier + TSA [26]	84.29	84.29	7.03	74.32	94.07
Hybrid classifier + D-NU [35]	86.63	84.62	6.74	75.16	94.14
Hybrid classifier + SITSA	86.24	85.76	6.60	77.32	96.04

SITSA model holds minimum FNR value that was 49.21 %, 48.85 %, 48.74 %, 42.70 %, 38.98 %, 35.28 %, 20.08 %, 18.13 %, 25.26 % and 38.15 % than other traditional models like SVM, NN, RF, DBN, hybrid classifier + WOA, hybrid classifier + EHO, hybrid classifier + TSA, hybrid classifier + D-NU, hybrid classifier + BOA and hybrid classifier + PSO, respectively for training percentage 80. Moreover, the adopted hybrid classifier + SITSA model has shown superior performance under best case scenario was 3.34 %, 3.07 %, 3 %, 2.80 %, 2.67 %, 2.11 %, 2.05 %, 1.98 %, 3.43 % and 4.21 % better than the traditional models like SVM, NN, RF, DBN, hybrid classifier + WOA, hybrid classifier + EHO, hybrid classifier + TSA, and hybrid classifier + D-NU, hybrid classifier + BOA and hybrid classifier + PSO, respectively. In the future, we will use data augmentation technology to increase the amount of data points in classes where there are few samples. Furthermore, in

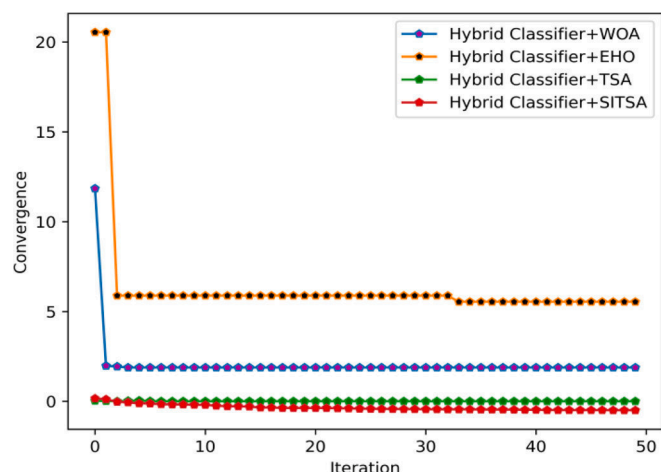


Fig. 7. Convergence analysis of proposed method over existing methods.

order to put our pest detection approach into practice, we will incorporate model onto a mobile terminal, including IOS platforms and Android. This will aid in the promotion of agricultural productivity.

Declaration of Competing Interest

The authors declare that they have no known competing financial interests or personal relationships that could have appeared to influence the work reported in this paper.

References

- [1] L.J. Shifeng, D.H. Wang, AF-RCNN: An anchor-free convolutional neural network for multi-categories agricultural pest detection, *Comput. Electron. Agric.*, 174, Art. no. 105522 (2020) (Cover date: July 2020).
- [2] F.W. Rujing, W.L. Liu, Fusing multi-scale context-aware information representation for automatic in-field pest detection and recognition, *Comput. Electron. Agric.*, 169, Art. no. 105222 (2020) (Cover date: February 2020).
- [3] K.L. Roldán-Serrato, J.A.S. Escalante-Estrada, M.T. Rodríguez-González, Automatic pest detection on bean and potato crops by applying neural classifiers, *Engineering in Agriculture, Environ. Food* 11 (4) (2018) 245–255. Cover date: October 2018.
- [4] Y.S. Xuanxin, L.Z. Chen, Automatic in-trap pest detection using deep learning for pheromone-based *Dendroctonus valens* monitoring, *Biosyst. Eng.* 176 (2018) 140–150. Cover date: December 2018.
- [5] L. Liu, et al., PestNet: An End-to-End Deep Learning Approach for Large-Scale Multi-Class Pest Detection and Classification, *IEEE Access* 7 (2019) 45301–45312, <https://doi.org/10.1109/ACCESS.2019.2909522>.
- [6] C.J. Chen, Y.Y. Huang, Y.S. Li, C.Y. Chang, Y.M. Huang, An AIoT Based Smart Agricultural System for Pests Detection, *IEEE Access* 8 (2020) 180750–180761, <https://doi.org/10.1109/ACCESS.2020.3024891>.
- [7] M.G. Selvaraj, A. Vergara, H. Ruiz, et al., AI-powered banana diseases and pest detection, *Plant Methods* 15 (2019) 92, <https://doi.org/10.1186/s13007-019-0475-z>.
- [8] B. Shen, J. Chang, C. Wu, et al., Local zoom system for agricultural pest detection and recognition, *Appl. Phys. B* 124 (2018) 219, <https://doi.org/10.1007/s00340-018-7089-4>.
- [9] T. Mu, et al., Detection of Pesticide Residues Using Nano-SERS Chip and a Smartphone-Based Raman Sensor, *IEEE J. Sel. Top. Quant. Electron.* 25 (2) (2019) 1–6, <https://doi.org/10.1109/JSTQE.2018.2869638>.
- [10] A. Sanz-Aguilar, I. Cortés, I. Gascón, et al., Modelling pest dynamics under uncertainty in pest detection: the case of the red palm weevil, *Biol. Invasions* 22 (2020) 1635–1645, <https://doi.org/10.1007/s10530-020-02208-6>.
- [11] M.K. Hadi, M.S.M. Kassim, A. Wayayok, Development of an Automated Multidirectional Pest Sampling Detection System Using Motorized Sticky Traps, *IEEE Access* 9 (2021) 67391–67404, <https://doi.org/10.1109/ACCESS.2021.3074083>.
- [12] S.D. Mahalakshmi, K. Vijayalakshmi, Agro Suraksha: pest and disease detection for corn field using image analysis, *J. Ambient Intell. Human Comput.* (2020), <https://doi.org/10.1007/s12652-020-02413-0>.
- [13] Y.V. Prabhu, J.S. Parab, R.S. Gad, et al., Farmer-friendly portable system for diagnosis of pest attack in cashew trees, *CSIT* 6 (2018) 215–219, <https://doi.org/10.1007/s40012-018-0198-8>.
- [14] C.R.R. Preetom, S.A.A. Wasif, Identification and recognition of rice diseases and pests using convolutional neural networks, *Biosyst. Eng.* 194 (2020) 112–120. Cover date: June 2020.
- [15] Y.L. Hanxiang, W.H. Moon, Crop pest recognition in natural scenes using convolutional neural networks, *Comput. Electron. Agric.*, 169, Art. no. 105174 (2020) (Cover date: February 2020).
- [16] M. John, K.L.D. Stringer, Optimising the seasonal deployment of surveillance traps for detection of incipient pest invasions, *Crop Prot.* 123 (2019) 36–44. Cover date: September 2019.
- [17] Z.B. Bahareh, J. Yousef, Abbaspour-Gilandeh, Detection of sunn pest-damaged wheat samples using visible/near-infrared spectroscopy based on pattern recognition, *Spectrochimica Acta Part A: Mol. Biomol. Spectrosc.* 203 (2018) 308–314. Cover date: 5 October 2018.
- [18] J.P. Lemos, E.R. Capobianco, G.A.K. Dezotti, Automated acoustic detection of a cicadid pest in coffee plantations, *Comput. Electron. Agric.*, 169, Art. no. 105215 (2020) (Cover date: February 2020).
- [19] Y.Y.X. Cheng, Y. Zhang, Deep recursive super resolution network with Laplacian Pyramid for better agricultural pest surveillance and detection, *Comput. Electron. Agric.*, 150, (2018) 26–32 (Cover date: July 2018).
- [20] E. Castela, T.B. Brandoli, M.H. Pistori, Detection and classification of soybean pests using deep learning with UAV images, *Comput. Electron. Agric.* 1 (179) (2020). Art. no. 105836 Cover date: December 2020.
- [21] B.N. Kobra, F. Seyed, H. Goldansaz, Detection of different densities of *Ephestia kuehniella* pest on white flour at different larvae instar by an electronic nose system, *J. Stored Prod. Res.* 84 (2019). Art. no. 101522 Cover date: December 2019.
- [22] Q.J. WangSheng-Yu, Z.H.Q. Wang, Pest24: A large-scale very small object data set of agricultural pests for multi-target detection, *Comput. Electron. Agric.* 175 (2020) (Cover date: August 2020) Article 105585.
- [23] Y. Ai, C. Sun, J. Tie, X. Cai, Research on Recognition Model of Crop Diseases and Insect Pests Based on Deep Learning in Harsh Environments, *IEEE Access* 8 (2020) 171686–171693, <https://doi.org/10.1109/ACCESS.2020.3025325>.
- [24] T. Kasinathan, S.R. Uyyala, Machine learning ensemble with image processing for pest identification and classification in field crops, *Neural Comput. Appl.* (2021), <https://doi.org/10.1007/s00521-020-05497-z>.
- [25] Y. Chen, C. Hsu, Lo C (2020) An Entire-and-Partial Feature Transfer Learning Approach for Detecting the Frequency of Pest Occurrence, *IEEE Access* 8 (2020) 92490–92502, <https://doi.org/10.1109/ACCESS.2020.2992520>.
- [26] S. Kaur, L.K. Awsthi, A.L. Sangal, G. Dhiman, Tunicate Swarm Algorithm: A new bio-inspired based metaheuristic paradigm for global optimization, *Eng. Appl. Artif. Intel.* 90 (2020).
- [27] B.R. Rajakumar, Impact of Static and Adaptive Mutation Techniques on Genetic Algorithm, *Int. J. Hybrid Intell. Syst.* 10 (1) (2013) 11–22, <https://doi.org/10.3233/HIS-120161>.
- [28] B.R. Rajakumar, Static and Adaptive Mutation Techniques for Genetic algorithm: A Systematic Comparative Analysis, *Int. J. Comput. Sci. Eng.* 8 (2) (2013) 180–193, <https://doi.org/10.1504/IJCSE.2013.053087>.
- [29] S.M. Swamy, B.R. Rajakumar, I.R. Valarmathi, Design of Hybrid Wind and Photovoltaic Power System using Opposition-based Genetic Algorithm with Cauchy Mutation, *IET Chennai Fourth International Conference on Sustainable Energy and Intelligent Systems (SEISCON 2013)*, Chennai, India (2013), DOI: 10.1049/ic.2013.0361.
- [30] A. George, B.R. Rajakumar, APOGA: An Adaptive Population Pool Size based Genetic Algorithm, *AASRI Procedia - 2013 AASRI Conference on Intelligent Systems and Control (ISC 2013)*, 4 (2013), 288–296, DOI: <https://doi.org/10.1016/j.aasri.2013.10.043>.
- [31] B.R. Rajakumar, A. George, A New Adaptive Mutation Technique for Genetic Algorithm, In proceedings of IEEE International Conference on Computational Intelligence and Computing Research (ICICR), 1-7 (2012), Dec 18-20, Coimbatore, India, DOI: 10.1109/ICICR.2012.6510293.
- [32] L.J. Kao, C.C. Chiu, Application of integrated recurrent neural network with multivariate adaptive regression splines on SPC-EPC process, *J. Manuf. Syst.* 57 (2020) 109–118.
- [33] M.M. Yamunadevi, S.S. Ranjani, Efficient segmentation of the lung carcinoma by adaptive fuzzy-GLCM (AF-GLCM) with deep learning based classification, *J. Ambient Intell. Human Comput.* 12 (2021) 4715–4725, <https://doi.org/10.1007/s12652-020-01874-7>.
- [34] S. Nascimento, B. Mirkin, F. Moura-Pires, A Fuzzy Clustering Model of Data and Fuzzy c-Means, <http://citeseerx.ist.psu.edu>.
- [35] X. Zhou, J. Lin, Z. Zhang, Z. Shao, H. Liu, Improved itracker combined with bidirectional long short-term memory for 3D gaze estimation using appearance cues, *Neuro computing* In press, corrected proof (2019), Available online.
- [36] M.D. Chodey, Neural Network based Pest Detection with K-Means Segmentation: Impact of Improved Dragonfly Algorithm, In communication.
- [37] H.Z. Wang, G.B. Wang, G.Q. Li, J.C. Peng, Y.T. Liu, Deep belief network based deterministic and probabilistic wind speed forecasting approach, *Appl. Energy* 182 (2016) 80–93.
- [38] E. Avci, A new intelligent diagnosis system for the heart valve diseases by using genetic-SVM classifier, *Expert Syst. Appl.* 36 (7) (2009) 10618–10626.
- [39] K. Golhani, S.K. Balasundram, G. Vadmalai, B. Pradhan, A review of neural networks in plant disease detection using hyperspectral data, *Inform. Process. Agric.* 5 (3) (2018) 354–371.
- [40] S. Mirjalili, A. Lewis, The Whale Optimization Algorithm, *Adv. Eng. Softw.* 95 (2016) 51–67.
- [41] M.A. Elhossaini, R.A. El Sehiemy, Y.I. Rashwan, X.Z. Gao, On the performance improvement of elephant herding optimization algorithm, *Knowl.-Based Syst.* 166 (2019) 58–70.

- [42] Z. Xu, X. Huang, L. Lin, et al., BP neural networks and random forest models to detect damage by *Dendrolimus punctatus* Walker, *J. For. Res.* 31 (2020) 107–121, <https://doi.org/10.1007/s11676-018-0832-1>.
- [43] Y. Chen, Crowd Behaviour recognition using Enhanced Butterfly Optimization Algorithm based Recurrent Neural Network, *Multimedia Res.* 3 (3) (2020).
- [44] A. Sarkar, Optimization Assisted Convolutional Neural Network for Facial Emotion Recognition, *Multimedia Res.* 3 (2) (2020).
- [45] R. Cristin, N.R.G. Merlin, L. Ramanathan, S. Vimala, Image Forgery Detection Using Back Propagation Neural Network Model and Particle Swarm Optimization Algorithm, *Multimedia Research* 3 (1) (2020) 21–32.
- [46] J.B. Shaik, V. Ganesh, Deep Neural Network and Social Ski-Driver Optimization Algorithm for Power System Restoration with VSC - HVDC Technology, *J. Comput. Mech., Power Syst. Control* 3 (1) (2020) 1–9.
- [47] K. Gaddala, P.S. Raju, Enhanced Self Adaptive Bat Algorithm for Optimal Location of Unified Power Quality Conditioner, *J. Comput. Mech., Power Syst. Control* 2 (3) (2019) 28–38.
- [48] S.B. Chandanapalli, E.S. Reddy, D.R. Lakshmi, Convolutional Neural Network for Water Quality Prediction in WSN, *J. Netw. Commun. Syst.* 2 (3) (2019) 40–47.
- [49] V. Bhagyalakshmi, Ramchandra, D. Geeta, Arrhythmia Classification Using Cat Swarm Optimization Based Support Vector Neural Network, *J. Netw. Commun. Syst.* 1 (1) (2018) 28–35.



iJRASET

International Journal For Research in
Applied Science and Engineering Technology



INTERNATIONAL JOURNAL FOR RESEARCH

IN APPLIED SCIENCE & ENGINEERING TECHNOLOGY

Volume: 12 **Issue:** V **Month of publication:** May 2024

DOI: <https://doi.org/10.22214/ijraset.2024.61732>

www.ijraset.com

Call: ☎ 08813907089

E-mail ID: ijraset@gmail.com

Internet of Things(IoT) Application for Crop Prediction and Fertilizer Suggestion Using Machine Learning Techniques

Asha Jyothi¹, Abhishek S M², Atukuri Saivinay³, Chandrashekar Reddy V⁴, E S Tejas⁵

¹Assistant Professor, ^{2, 3, 4, 5}Student, Department of Artificial Intelligence and Machine Learning, Ballari Institute of Technology and Management, India

Abstract: Agriculture serves as the primary source of income globally, particularly in regions like the Indian subcontinent. However, modern challenges such as unpredictable weather patterns, water scarcity, and market fluctuations necessitate the adoption of advanced farming techniques. Soil fertility depletion, caused by various factors, further exacerbates these challenges, leading to decreased crop yields. To solve these problems, our project utilizes modern technology, specifically leveraging machine learning techniques. By integrating an NPK sensor with a web application, our goal is to give farmers practical insights into their soil's nutrient composition. Upon collecting nitrogen, phosphorus, potassium, and pH levels from the soil, these values are entered into the application. Compared to traditional farming methods, our project offers several advantages. Firstly, it empowers farmers with accurate and timely information about their soil's nutrient levels, giving them the ability to make wise decisions. Secondly, by the use of machine learning methods, our system provides personalized recommendations that address the particular needs of each farmer's soil. Overall, our project aims to enhance agricultural productivity and sustainability by bridging the gap between traditional farming practices and modern technology.

Keywords: Machine learning Techniques, Internet of things, web application, Logistic Regression, Crop Recommendation.

I. INTRODUCTION

In the landscape of modern agriculture, Technology integration is becoming more and more common., offering innovative solutions to solve the challenges faced by farmers worldwide. Our project centres around leveraging technology, specifically the Internet of Things (IoT) and web applications, to streamline and optimize crop and fertilizer recommendations based on soil nutrient analysis. The process begins with the deployment of NPK sensors, which are able to measure nitrogen, phosphorus, potassium, and pH levels in the soil. These sensors serve as the foundational element in our project, providing real-time data on the nutrient composition of the soil. Upon collecting the soil nutrient data, the information is then fed into a user-friendly web application, designed to provide farmers with actionable insights and recommendations tailored to their specific agricultural needs. The application offers two primary functionalities: crop recommendation and fertilizer recommendation. These options empower farmers to make knowledgeable choices about soil management techniques and crop selection, ultimately enhancing agricultural productivity and sustainability. A major development in the world of agriculture is the incorporation of technology into farming operations, offering farmers access to valuable data and insights that can inform decision-making processes. Making use of web applications and Internet of Things sensors, our project aims to empower farmers with the tools and information they need to maximize crop yields, optimize resource utilization, and promote long-term sustainability in agriculture.

II. LITERATURE REVIEW

Paper [1]: The paper titled "Internet of Things (IoT) assisted Context-Aware Fertilizer Recommendation". It considers variables including crop kind, soil type, and soil fertility to satisfy the requirement for real-time context-awareness in fertilizer recommendation. The study suggests an Internet of Things-based approach to real-time mapping of soil fertility that gets beyond the difficulties and expensive nature of conventional techniques. When compared to conventional soil chemical analysis, the system's accuracy is validated through practical implementation in crop fields. The most precise machine learning model for context-aware fertilizer recommendation is the Gaussian Naïve Bayes (GNB) model. To improve sustainability and profitability in agriculture, this research provides a framework for the integration of IoT and machine learning.

Paper [2]: The paper titled "Artificial Intelligence-Based Crop Suggestion System" tackles the urgent problem of India's farmers choosing the wrong crops, which results in low incomes and a desire to leave the agricultural industry. It offers a method based on machine learning algorithms to make crop recommendations based on a variety of environmental and financial factors, including temperature, rainfall, soil properties, and more.

This method forecasts yields, examines profitability, and recommends appropriate crops. Crop selection is done using a different types of machine learning methods, such as Decision Tree Learning and Artificial Neural Networks. The study highlights the importance of data mining and machine learning in assisting farmers in making knowledgeable crop decisions., which improves agricultural sustainability and financial viability.

Paper [3]: The paper titled "Crop, Fertilizer, & Irrigation Recommendation using the Machine Learning Techniques" emphasizes the use of agriculture to the economy as well as the difficulties farmers encounter because of weather fluctuations, a lack of water, and problems with soil fertility. It underlines the necessity of utilizing contemporary technology to offer practical solutions to these issues. Crop yield prediction is advised to use machine learning, which offers different methods such as regression, clustering, classification, and prediction.

To predict agricultural productivity, a variety of methods can be used, such as Naïve Bayes, support vector machines, decision trees, and artificial neural networks. The research aims to examine how different machine learning algorithms may be used to forecast crop yield and recommend fertilizers, thereby supporting efficient crop management. We'll focus on supervised learning techniques and big data computing.

Paper [4]: The paper "Crop prediction using machine learning" addresses the pressing issue of declining agricultural productivity in India due to unpredictable climatic changes. This decline threatens the livelihoods of farmers and national food security. The study proposes a solution leveraging machine learning, specifically Naive Bayes, to predict suitable crops for cultivation. By collecting seed data and considering crucial parameters like temperature, humidity, and moisture content, the model assists farmers, especially beginners, in making informed decisions about crop selection. Additionally, the development of a user-friendly mobile application for Android facilitates easy access to the prediction process, encouraging user engagement and adoption of the technology in agricultural practices.

III. MOTIVATION

Our project revolves around harnessing technology to empower farmers with real-time soil insights. Using a specialized sensor, we delve into the soil, uncovering its nutrient secrets - nitrogen, phosphorus, potassium, and pH levels. This data is then fed into a user-friendly web application, offering farmers two invaluable tools: crop recommendations and fertilizer suggestions. With crop recommendations, Farmers receive customized guidance on which plants are ideal for the particular composition of their soil, optimizing yields and sustainability.

Meanwhile, fertilizer suggestions provide guidance on how to enhance soil fertility, promoting healthier crops and reducing environmental impact.

IV. OBJECTIVE

- 1) *Enhance Crop Selection:* The primary objective is to employ Machine Learning and IoT to provide data-driven recommendations for optimal crop selection, considering soil conditions, climate, and previous historical data. This will increase agricultural productivity and assist farmers in making wise selections.
- 2) *Optimize Fertilizer Application:* The project aims to recommend precise fertilizer application strategies, reducing waste and its negative effects on the environment while making sure crop nutrient requirements are efficiently supplied.
- 3) *Improve Resource Efficiency:* By integrating technology, the project strives to enhance resource utilization, reducing water, energy, and fertilizer wastage, thereby increasing agricultural sustainability.
- 4) *Increase Productivity:* The system will work towards maximizing crop yield and, in turn, the economic well-being of farmers through better decision-making.
- 5) *Sustainable Agriculture:* In order to balance output with environmental responsibility, sustainable farming practices must be promoted, contributing to global food security and ecological well-being.

V. METHODOLOGY

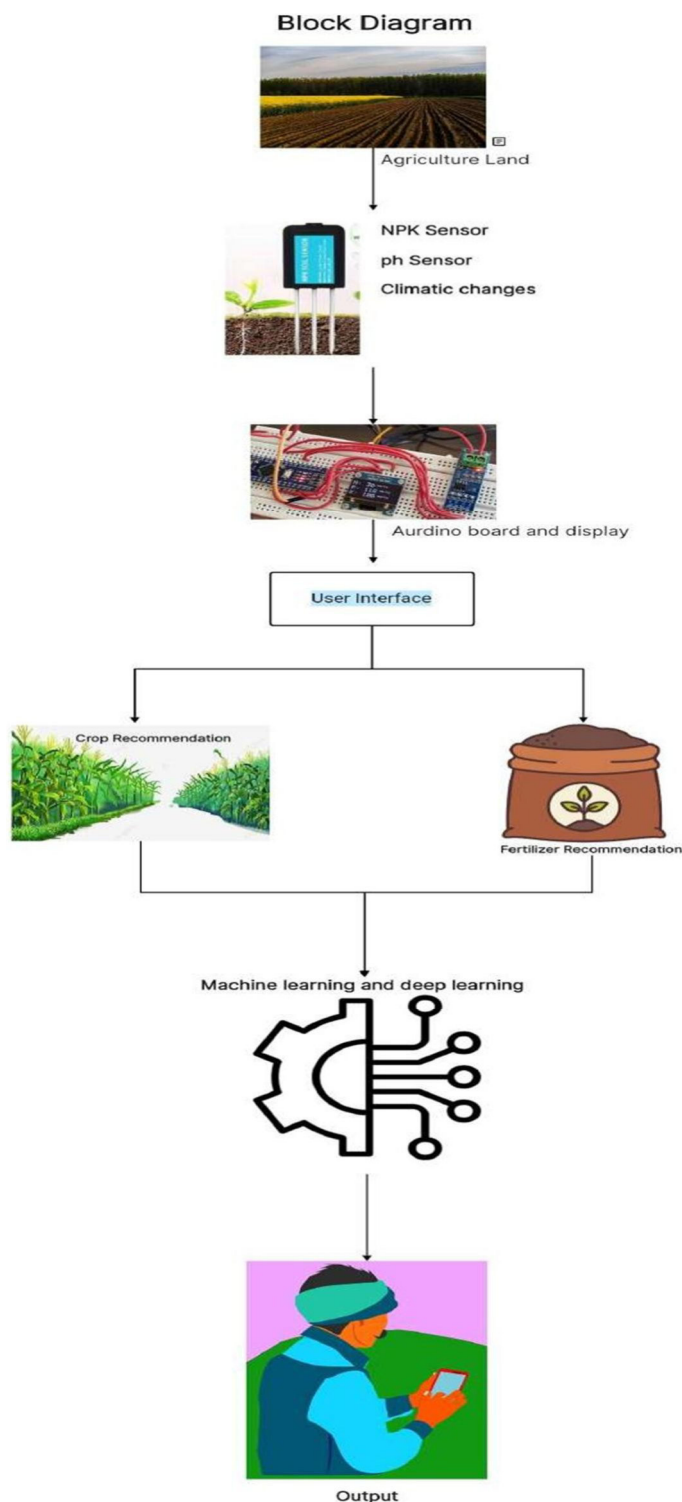


Fig 5.1 Block Diagram

Fig 5.1 Represents by considering agricultural land, and we're using sensors like NPK (Nitrogen, Phosphorus, Potassium) and pH sensors to measure the levels of these elements in the soil. The results are then shown on an OLED display. After obtaining these values, users can enter these into our web application. The application provides crop and fertilizer recommendations based on the soil's nutrient levels. This aids farmers in selecting the best crops to plant and fertilizers to utilize for maximum production.

VI. RESULTS

A. Home Page of The User Interface

The user interface of the home page is displayed in Fig. 6.1.



Fig 6.1 Project Home page

B. Services Page

The user interface displays the services that are available to the user in Fig. 6.2.

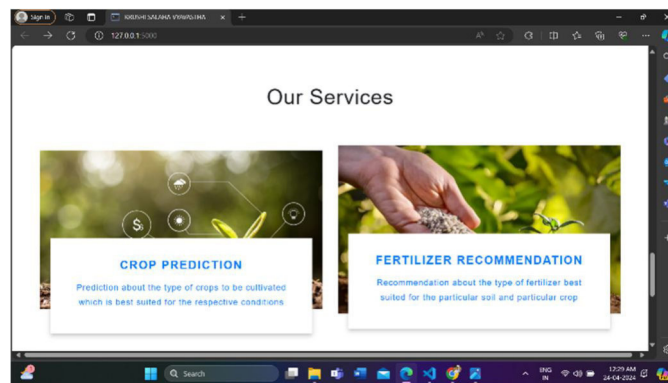


Fig 6.2 Services page

C. Crop Prediction

The user interface for entering values to obtain crop recommendations is depicted in Fig. 6.3.

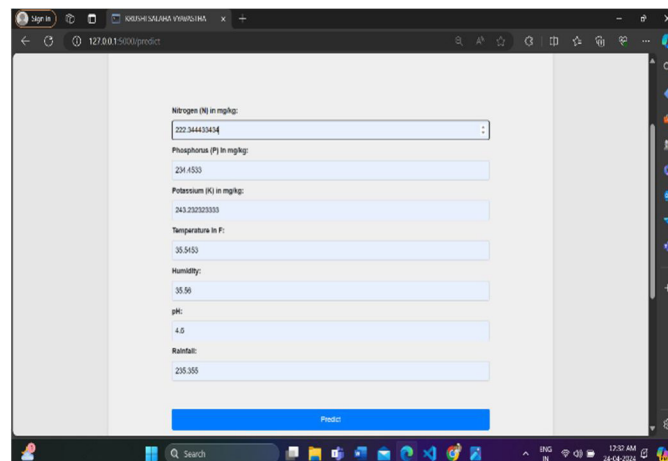


Fig 6.3 Crop Prediction

D. Predicted Crop

The crop recommendation result is shown in the user interface in Fig. 6.4.

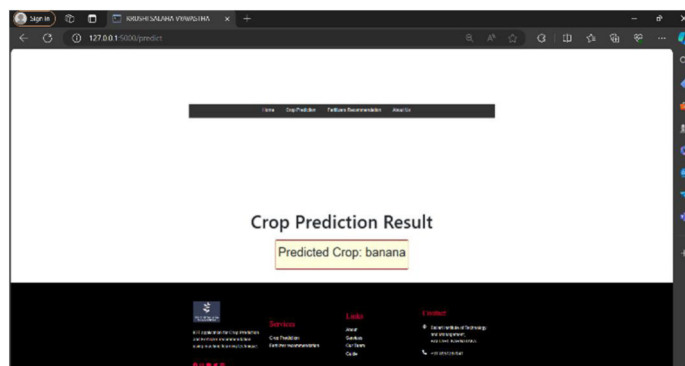


Fig 6.4 Predicted Crop

E. Fertilizer Recommendation

The user interface for entering values to obtain Fertilizer recommendations is depicted in Fig. 6.5.

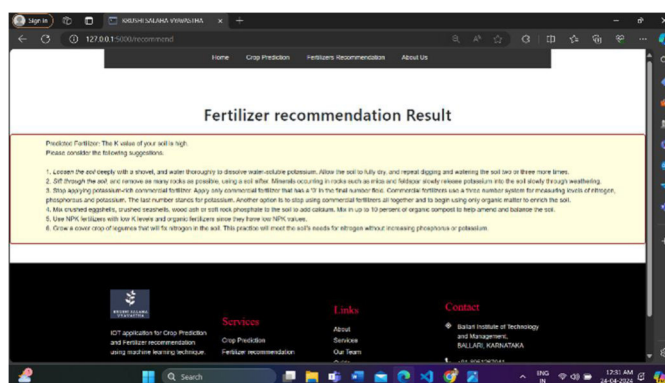


Fig 6.5 Fertilizer Recommendation

F. Recommended Fertilizer

The Fertilizer recommendation result is shown in the user interface in Fig. 6.6.

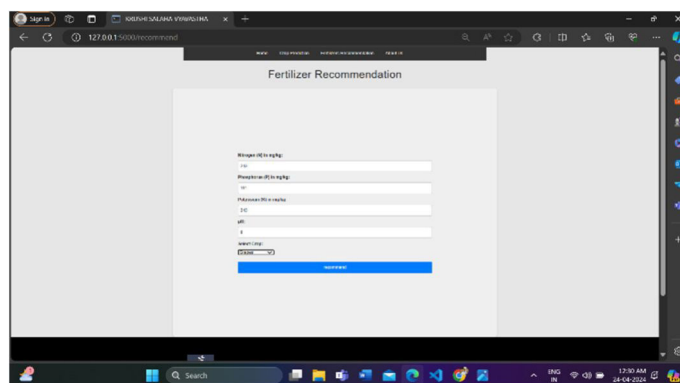


Fig 6.6 Recommended Fertilizer

VII. FUTURE SCOPE

- 1) The project will combine models of machine learning with IoT data streams to provide dynamic fertilizer and crop recommendations that optimize nutrient application and minimize environmental impact.
- 2) The project will focus on recommending crops suitable for cultivation in the specific geographical region where the IoT sensor network is deployed.

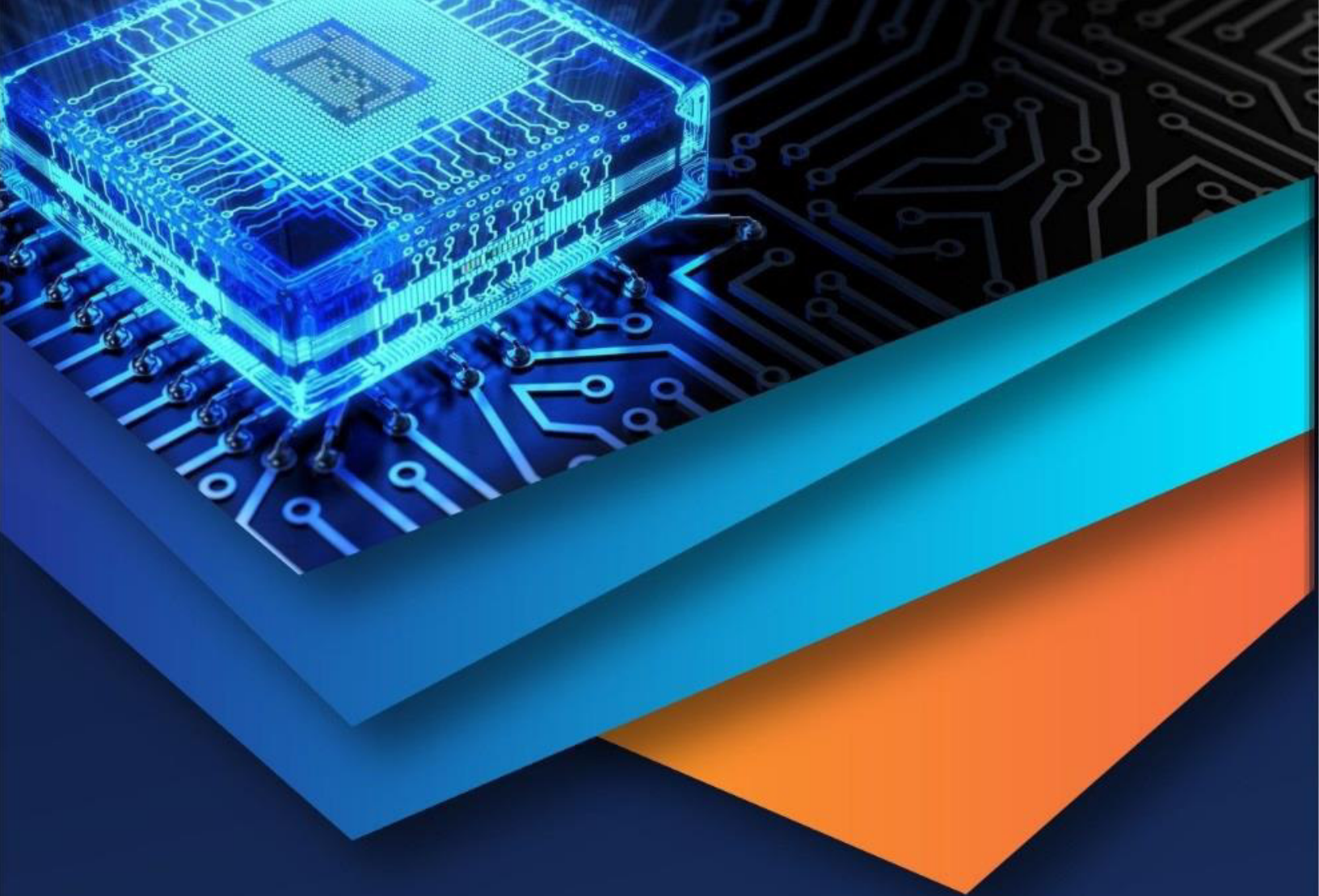
- 3) The crop recommendation system will be limited to recommending a select number of major crops commonly grown in the target region.
- 4) The accuracy of crop and fertilizer recommendations may be affected by the quality and completeness of input data, including soil samples, weather data, and historical crop yields.
- 5) The fertilizer recommendation system will give suggestions for the type and quantity of fertilizers based on the specific crop selection and real-time data from the IoT sensor network.

VIII. CONCLUSION

In conclusion, our project leverages advanced sensor technology and web-based analytics to offer tailored agricultural solutions, enhancing soil management and crop production. By incorporating an NPK sensor to assess soil fertility levels, our system provides critical data points on nitrogen, phosphorous, and potassium and soil pH values. This data-driven approach enables precise crop and fertilizer recommendations through an intuitive web application. Users can choose between optimizing crop selection or improving soil nutrient profiles via customized fertilizer suggestions. Our system not only promotes optimal resource use but also supports sustainable agricultural practices by allowing farmers to adjust inputs based on real-time soil conditions, thus minimizing environmental impact. The combination of machine learning and technology tools in our project aims to revolutionize traditional farming techniques, improve yields, and offer a scalable solution adaptable across various agricultural settings. Overall, this project represents a significant step forward in the pursuit of sustainable agriculture powered by smart technologies.

REFERENCES

- [1] A. Khan, M. Faheem, R. N. Bashir, C. Wechtaisong and M. Z. Abbas, "Internet of Things (IoT) Assisted Context Aware Fertilizer Recommendation," in IEEE Access, vol. 10, pp. 129505-129519, 2022, doi: 10.1109/ACCESS.2022.3228160.
- [2] P. A, S. Chakraborty, A. Kumar and O. R. Pooniwalla, "Intelligent Crop Recommendation System using Machine Learning," 2021 5th International Conference on Computing Methodologies and Communication (ICCMC), Erode, India, 2021, pp. 843-848, doi: 10.1109/ICCMC51019.2021.9418375.
- [3] Ajmera, A., Bhandari, M., Jain, H. K., & Agarwal, S. (2022). Crop Fertilizer & Irrigation Recommendation using Machine Learning Techniques. International Journal for Research in Applied Science & Engineering Technology.
- [4] Kalimuthu, M., Vaishnavi, P. and Kishore, M., 2020, August. Crop prediction using machine learning. In 2020 third international conference on smart systems and inventive technology (ICSSIT) (pp. 926-932). IEEE.



10.22214/IJRASET



45.98



IMPACT FACTOR:
7.129



IMPACT FACTOR:
7.429



INTERNATIONAL JOURNAL FOR RESEARCH

IN APPLIED SCIENCE & ENGINEERING TECHNOLOGY

Call : 08813907089  (24*7 Support on Whatsapp)

A Bootstrapped Volatile Key Management Scheme For Efficient And Secured Data Transmission In WSNs

Girija Vani Gurram¹, Phanindra Reddy Kannari², Noorullah Shariff C³

1 Associate Professor, Department of Electronics & Communication Engineering, BITM, Ballari.

2 Associate Professor, Department of Artificial Intelligence & Machine Learning, BITM, Ballari.

3 Professor, Department of Artificial Intelligence & Machine Learning, BITM, Ballari.

Abstract— The recent era has witnessed several advances in Wireless Sensor Networks (WSNs), with few resources presents unprecedented challenges for secured data transmission in an ever-unsecured broadcast network. The situation is more challenging when adversaries are equipped with sophisticated resources having direct access to sensor nodes. Nevertheless, there exists several cryptographic techniques used for node authentication, authorization, data confidentiality, integrity, and other security related services. This paper contributes to novel network security strategies to prevent network compromise. The proposed strategies attempt to boost data integrity, reliability and secure data transmissions. The proposal identifies the strategically important nodes (SIN) in implementing network security measures using volatile symmetric-key management scheme (KMS).

The scheme involves four phases: The first phase involves strategically important nodes (SIN) designation using Grey Wolf Optimization (GWO). Usually, hackers find it difficult to guess and access the keys that are selected on a random basis. To further increase the key protection, the scheme introduces a limited lifespan master key (LLM_K). Secondly, to secure the KMS, this phase utilizes SHA for LLM_K distribution, and paired node prediction. Next phase performs secret key generation with a gradient approach and the key sharing is performed using Supersingular Isogeny Diffie-Hellman algorithm. The last phase is responsible for the dynamic S-Box generation using the Blowfish algorithm. The generated S-Box are subsequently shuffled to enhance the cryptographic process offering immunity towards attacks.

To evaluate the effectiveness of this approach, the proposed KMS is compared with relevant methods on various performance metrics. The results demonstrate that the proposed scheme achieves notable performance improvements over other methods.

Index Terms— Volatile key management, WSNs, GWO, SIDH, Blow fish Algorithm, Dynamic S-Box generation.

I. INTRODUCTION

Wireless Sensor Networks have been gaining popularity over a few decades due to their low-cost, low-power, scalable and ease of deployments. However, these networks has been facing serious security challenges based on design due to the limited computational resources and their minimal battery life [1]. Its architecture comprises of numerous nodes that ranges from 100s to 1000s, deployed in a network. The sensor nodes

are used for sensing the data that is generated from surroundings and route it back to the base station via hopping techniques. However, these nodes have poor energy and memory resources. Several routing protocols have been devised to improve the network's lifetime and compensate for resource insufficiencies. The wireless structure is prone to various attacks, that would easily alter the sensed data which affects the confidentiality of the network data as well. Hence, data integrity and authentication might be compromised, thus securing against the vulnerabilities using various secure routing protocols and cryptographic techniques are mandatory for the appropriate functioning of the WSNs.

The sensors present in WSNs should share their keys to ensure the secure data transmission among the sensor nodes. In WSN, the key management schemes involves network formation and network initialization. The network formation follows either shared key or key establishment approach. Under the shared key approach, two nodes attempt to discover a public key, whereas in key establishment approach, several SNs establish a common key for secure communication. Various approaches are developed for key establishment and with resource scarcity, designing or structuring key distribution is an interesting task. Some of the KMS discussed in [2] are Public key cryptography, Randomized key distribution, Global master key and transitory master key. As security services like confidentiality, data integrity, etc must be enforced, cryptographic keys are to be utilized. This is where key management performs vital part in WSNs. The volatile key management is gaining traction in recent days due to the limited life span, preventing unauthorized access to the keys. The key management comprises of Symmetric, Asymmetric and Hybrid schemes [3], as shown in the figure 1. To establish volatile keys, a symmetric key management scheme [4] is essential to facilitate the keys between neighboring nodes without using any key ring or pools.

The initialization stage allows a pair of nodes to exchange a plain text message, with the plain text message being encrypted and the encrypted nonce is used by the network node, where a LLMK should only be inserted into some potential nodes (SINs). These SINs ensure the security of the LLMK from the attackers to expose the used key for any given node directly after the deployment process, even if the attacker captures few network nodes. The technique also ensures that the LLMK reaches every node in the network enabling network connectivity.

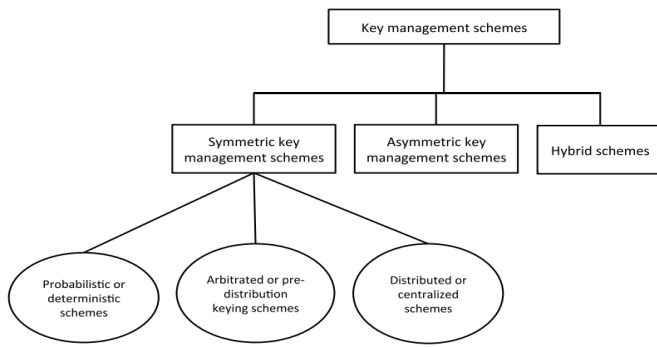


Figure 1: Key Management Scheme – A Hierarchy

The proposed work applies a volatile key management scheme to generate the LLM_K , SIN node designation using an optimization algorithm, a hashing algorithm to distribute volatile key and finally cryptographic techniques to ensure secure data communication using the shared keys.

The paper discusses the existing security and KMS of WSNs in section 2. The methodology and implementation along with respective algorithms are explained in section 3. The performance analysis and the results discussed in section 4. Section 5 provides conclusion and future enhancements.

II. RELATED WORKS

The design of secure and efficient routing protocols for WSNs is an active area of research due to the unique security challenges presented by these resource-constrained networks. The attacks against WSNs can be categorized into two types namely active attacks and passive attacks [5]. There exists a plethora of security mechanisms for secure data transmission, data aggregation, using key exchange and key management schemes. However, the complex broadcast channel impairments and limited resources weakened the full-fledged implement of a given security mechanism in WSNs. This section discusses various existing approaches that attempted to provide secure key exchanges, and transmission in WSNs.

A. Key Management schemes:

Several research works present the vulnerabilities and complicated nature of WSNs against attacks, for the network utilizing a random pairwise key distribution scheme. The random key distribution schemes experience various issues while assigning the secured keys to sensor nodes, prior to network deployment. [6] investigated that whether resiliency could be achieved in WSNs beneath random pairwise key redistribution scheme. This work presented certain conditions on model parameters such that the network would be un-splitable and unassailable, with maximum probability as the 'n' nodes increase. These ideas were developed against an intruder who possessed enough computing resources and good knowledge about network topology, however, with an assumption that only a fraction of sensor nodes are compromised. This research also proved that cryptographic keys should ensure un-splitability and unassailability under the pairwise key distribution method.

More importantly, compromised sensor nodes in military surveillance or disaster management applications across horizontal and vertical security landscapes is unacceptable. However, a deployment based key distribution scheme had been developed for cellular model in WSN for thwarting attacks [7]. The key distribution model is utilized in all those networks where the random selection of small subset of keys is chosen from the collection of key pools. At least, there should exist one common key from key pool for the secured connection among the nodes. The secured communication link relies on the length and strength of keys used for the connection establishment. The major focus of this research centered around node density, neighbor influence factor, sink node placement, gradient distance and application types on nodes to construct the attack matrix of each mobile cell. An efficient key management strategy along with secured data aggregation over Dynamic WSN had been implemented in [8]. This research work utilized a Key Generation Center (KGC) for dealing with partial private keys. This research work addresses escrow issue with the help of KGC.

The sensor nodes in WSNs would share their keys for secured data transfer. The demand of designing an energy optimized key establishment/distribution in WSNs is increasing due to the limited resources of sensor nodes. Various polynomial based key distribution scheme had been proposed in WSNs to provide a light weighted solution for devices with limited resources. These polynomial – based approaches are highly susceptible toward sensor attacks. Sometimes, the intruders compromise the security system by capturing a fixed number of sensor nodes. [9] developed a polynomial based key management scheme together with probabilistic security that minimizes the security risk of attacks along with minimized computational overhead and memory resources.

To establish a secured data transmission over WSN, several literatures suggested a protocol namely Multi-level Key Management protocol. Under this protocol, every single transmission was undertaken based on available secured key. The research work by [10] developed a protocol for key management referred as MSKM protocol, to perform protected communiqué in the clustered WSNs. This framework implemented in three phases consists of 1) Key Generation 2) Pre-deployment 3) Key Authentication and verification. The key generation is responsible to ensure the secrecy of communication and the necessary keys are generated using homomorphic encryption model. In pre-deployment, node's identity is established. The last phase, a mathematical model had been constructed along with various factors like random numbers, dynamic passwords, etc.

The secured key generation in physical layer (PL-SKG – Physical Layer Secure Key Generation) has some potential benefits to improve the network security posture. This scheme strengthens the security-based protocols by minimizing the quantity of key materials needed for deployment. This scheme is extremely useful in limited resources scenario and also in situations where designing of key management scheme is challenging. [11] discussed about the challenges in PL-SKG scheme, and propose a unique key generation scheme which provided merits on potential and simplicity of correction codes.

The intruder might have unauthorized access which leads to eavesdropping, tampering of data, interception, and modification. Nevertheless, to improve efficacy of WSN, clustering methods are deployed, but sensor nodes' dynamic behavior with limited processing and storage makes secured transmission, a difficult one. To resolve this issue, effective key management is essential. [12] proposed a secured mechanism called as CAKE - Codeword Authenticated Key Exchange. It is completely based on one-way hashing with OTP and authentication. [13] developed a secured and provable key exchange protocol which is based on ECDH - Elliptical curve Diffie-Hellman for WSNs. Elliptical curve schemes are standard protocol for establishing shared keys. This implementation handles even a lack of authentication related attacks namely Man-in-the-Middle Attack. Enhanced energy utilization is the most primary factor. Thus an efficient method for securing energy in data transfer using Hierarchical and Dynamic ECC[14] had been proposed. LEACH – Low Energy Adaptive Clustering Hierarchy had been utilized for selecting dynamic cluster heads. Here the key management scheme consisted of three phases namely key – computation, key – exchange and, node authentication.

B. Pair- Node Authentication:

Since WSN is widely applied in critical applications like military surveillance, health care monitoring, etc., the vulnerability of handling the data creates high risk. Since, it is mandatory to maintain confidentiality during data transmission and the data should be authenticated in all aspects. [15] stated that the memory and energy restraints of certain sensor nodes for military applications need light weight cryptographic schemes and propose an asymmetric key cryptographic scheme. The scheme uses the base idea called Elliptic Curve Cryptography and as well use Identity Based Public Key Cryptography.

Here, no permission is provided to third-party thereby in single transmission authentication is accomplished. Thus it is benefitted in a way that the receiving party need not to be active in receiving authenticated message, which decreases the encryption and decryption time without compromising the security level.

When considering large scale scenario of IoT, the trusted authority would be joined by a remote server. This remote server would be accessed through a domestic gateway by using different users to bootstrap the keys that are engaged in secure transmission. But all these users might not fully trust the remote server, especially when they are holding private key of their sensor nodes. So to handle this issue, [16] developed an escrow less and light weighted authenticated key Agreement technique (AKA) for WSNs. Various applications like medical monitoring in healthcare institutions needs highly secured WSN network. To promote that, [17] developed an user authentication scheme and secured data transmission of health care data. This research work discussed various secure transmission schemes like identity-based authentication, mutual authentication, decentralization, multi-routes transmission.

C. Cryptography:

Cryptography can be defined as the study or practice of several techniques that are involved in secure transmission of data even in the presence of intruders or adversaries. Usually, cryptographic techniques are about developing and analyzing various protocols that tries to stop or prevent third party adversaries or unauthorized public from viewing or intercepting private or sensitive messages. There are several aspects which are major parts of modern cryptography such as data integrity, confidentiality, non-repudiation and authentication. As cryptography shows continuous progress and new advances, WSNs utilized its techniques to improve the security landscape. The cryptography techniques utilized by WSNs are 1) Elliptic Curve Cryptography, 2) Pairing-based cryptography, 3) Identity based Cryptography.

As WSNs found its wide range of applications, subsequently, outsiders reach to access the sensitive data by directly interacting with sensor nodes increase substantially. Since, WSNs are fragile to attacks, it is essential to provide security to critical or sensitive data such that it should be available only to legitimate users. A scheme based on two factor authentication combined with smart card and password is used to enhance security. But several two factor authentication protocols have been suggested. [18] proposed a 2 factor authentication protocol that is based on ECC for WSN by considering privacy awareness. This novel protocol accomplished several features for real life applications without compromising efficiency.

[19] developed an algorithm which combined a method of merging of both symmetric and asymmetric methodologies such as AES – Advanced Encryption Standard and RSA – Rivest – Shamir – Adleman Algorithm followed by LZW – Lempel – Ziv- Welch compression. The primary objective of this mechanism is to encrypt the plain text via AES which led into faster symmetric encryption. The secondary objective includes encryption of plain text through RSA which leads to the development of secured data process. The last objective is to perform LZW compression. A reversal process of the algorithm at receiver performs decompression and finally the decryption step.

Though there are several techniques proposed, these mechanisms faced below short-comes in certain circumstances. They are as follows,

- Most of the existing methods used random number of node selection in order to share the master key before deployment. This might result in selection of malicious nodes, which in turn resulted in poor security.
- Some of the techniques used AES, which possess simple encryption process. So, an adversary with enough connected resources can easily break AES encryption.
- Most of the existing methods follow non-volatile approach in managing keys. This resulted in increased life span of master key. Master key with high life span would give chance for intrusion.

The proposed security mechanisms attempts to overcome the above-mentioned limitations.

III. PROPOSED WORK

The proposed scheme block diagram is depicted in the figure 2. It involves four modules namely 1) SIN prediction, 2) LLM_K distribution and pair node prediction, 3) Key generation 4) Dynamic S-Box generation. To enhance the security of sensitive data against adversaries, a volatile key management scheme has been implemented. A master key with shorter life span (LLM_K) gets shared with certain nodes and these nodes are paired up with neighboring nodes for performing data transmission. As mentioned, the master key is inserted into few nodes that are selected using objective function by GWO algorithm. Then, these selected node pairs are ready to transmit data after authentication. The authentication is done between the node which holds the LLM_K with broadcast message and the receiver node that got paired.

The concept of volatile key technique is presented briefly in the following part. This concept is utilized in the proposed work for exploiting some of the basic operations by providing permissions to respond to certain problems and the security measures in WSNs. The symbols utilized in the equations of proposed work are described in Table 1.

Every node present in the network is preloaded by preliminary functions and data before the deployment of nodes. This helps in sharing the common keys among the adjacent neighbor nodes. Further, keys are established separately for each pair of adjacent neighbor nodes in a secured manner through the usage of primary configuration where MAC is utilized before initiating the secured communication in the perspective of authenticated channel. Preliminary data comprises of pseudo random (PR) functions, finite groups that comprise of LLM_K (can be inserted only in certain nodes) and

the prime numbers as shown in Table.2. Volatile Key is denoted as LLM_K in the proposed work as the master key that would appear in few nodes.

Table 1. Notations and Description

Notation	Description
N	Total number of nodes deployed
n_a	a^{th} node in network
ID_a	Identifier for node a
$S_a \rightarrow \text{type}, * :$	Node S_a distributes the message M to each node within the radio communication range
NReq NResp	Pairwise key request and pairwise key response among the nodes
nonce _a	Random number produced by S_a
X_a	Random group chosen by S_a
LLM_K	Limited life Master Volatile Key for the secure sharing of nonce _a to n_a, n_b
$f(\text{int}, \text{int})$	function that produces Pseudo-random numbers upon accepting 2 integral types as arguments
K_{ab}	Pairwise secret key for n_a and n_b
Counter	Utilized for restricting a data replay attack; is an alternative to nonce
$K_e(M)$ and $K_d(M)$	Encryption (e), Decryption (d) of message 'm' using the key K

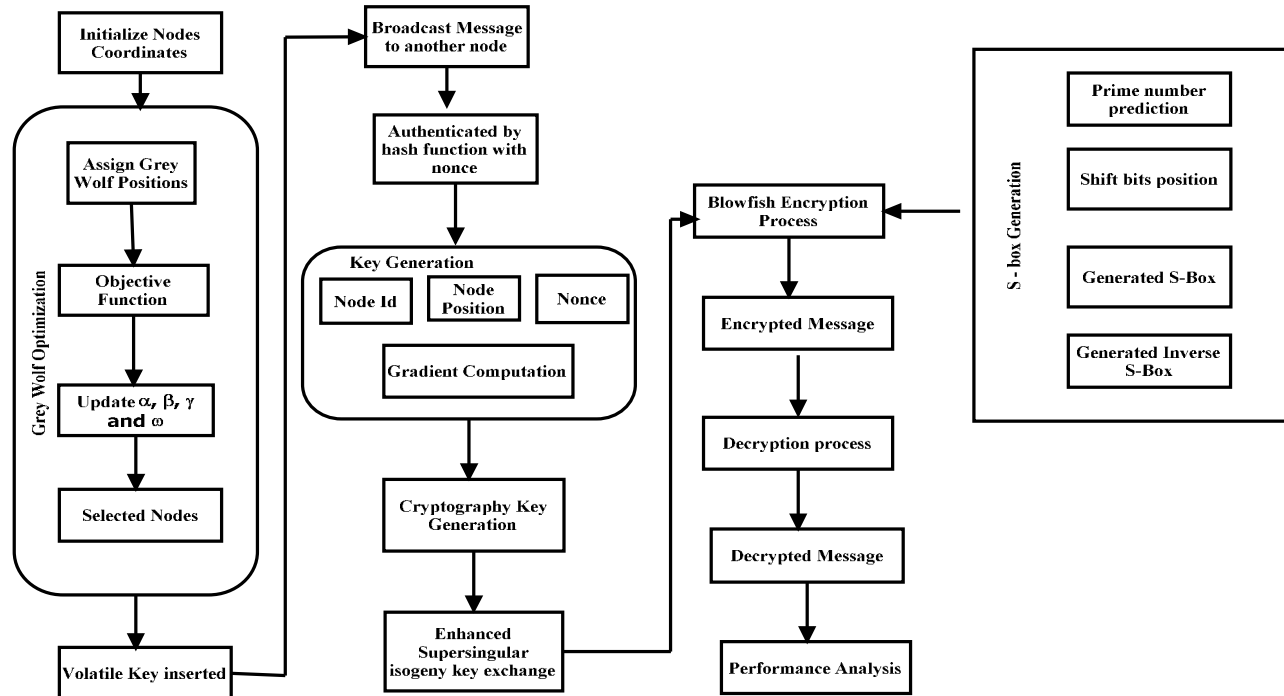


Figure 2: Proposed Scheme Block Diagram

A. LLM_K-Node Prediction using GWO:

Previously, the Master Keys (MKs) selection from the key pool has allowed the intruders to predict the MKs resulting into compromised node, network or communications. Thus, to handle this, proposed scheme utilizes optimization algorithm named GWO. The methodology of GWO algorithm is entirely based on hunting nature of wolves. Out of four, only three wolves are included in the hunting process. The decisions like hunting time, sleeping time are determined by wolf α . Thus, α wolf is designated as the leader of the wolf pack. The second and third β and δ wolves respectively support α in making decisions. The last ω wolf is allowed only for eating hence these are not imperative in process of hunting. Initially, all the nodes are initialized with the basic node configuration data. Later, based on objective function, α , β , δ and ω positions are updated. The objective function, based on estimating the information measure that is correlated among the nodes, can be formulated as below,

$$Fit_{val} = (a_1 * b_1) * (a_2 * b_2) * (a_3 * b_3) \quad (1)$$

$$\text{Where, } b_1 = \frac{\sum_{j=1}^N D_{ij}}{C_i^n}$$

$$b_2 = \frac{E_0}{C_i^n}$$

$$b_3 = \frac{1}{C_i^n}$$

// b_1 , b_2 and b_3 are energy-based coefficients

$a_1 = 0.5$, $a_2 = 0.2$, $a_3 = 1 - a_1 - a_2$ // Coefficient parameters

$$D_{ij} = \sqrt{(X_i - X_j)^2}$$

$$C_i^n = \text{size}(C_n) \quad \text{if } D_{ij} < \text{Cover}_{area}$$

// C_i^n - node number which are covered by i^{th} node

// Cover_{area} - coverage area of an i^{th} node

The above fitness function is formulated based on distance and energy constraints.

The initialized α , β , δ and ω wolves along with scores and its positions are updated respectively using the following functions:

For alpha wolves,

$$\alpha_{wolves}^{score} = Fit_{val}, \alpha_{wolves}^{pos} = X_i, \quad \text{if } Fit_{val} < \alpha_{wolves}^{score} \quad (2)$$

For beta wolves,

$$\beta_{wolves}^{score} = Fit_{val}, \beta_{wolves}^{pos} = X_i, \quad \text{if } Fit_{val} > \alpha_{wolves}^{score} \text{ \& \& } Fit_{val} < \beta_{wolves}^{score} \quad (3)$$

For delta wolves,

$$\delta_{wolves}^{score} = Fit_{val}, \delta_{wolves}^{pos} = X_i, \quad \text{if } Fit_{val} > \alpha_{wolves}^{score} \text{ \& \& } Fit_{val} > \beta_{wolves}^{score} \text{ \& \& } Fit_{val} < \delta_{wolves}^{score}$$

$$\delta_{wolves}^{score} = Fit_{val}, \delta_{wolves}^{pos} = X_i \quad (4)$$

For omega wolves,

$$\begin{aligned} &\text{if } Fit_{val} > \alpha_{wolves}^{score} \text{ \& \& } Fit_{val} > \beta_{wolves}^{score} \text{ \& \& } Fit_{val} > \delta_{wolves}^{score} \text{ \& \& } Fit_{val} > \omega_{wolves}^{score} \\ &\omega_{wolves}^{score} = Fit_{val}, \omega_{wolves}^{pos} = X_i \end{aligned} \quad (5)$$

Where X_i represents position updation based on upper bound and lower bound, explained by equation (11). The overall updating of all types of wolves can be formulated as below,

$$X_1 = \alpha_{wolves}^{pos} - \left(\frac{A}{|C * (\alpha_{wolves}^{pos} - X_i)|} \right) \quad (6)$$

$$\begin{aligned} &\text{Where } a = 2 - it * \left(\frac{2}{iter} \right) \\ &A = (2 * a * rand(1,1)) - a \\ &C = 2 * rand(1,1) \end{aligned}$$

Similar process is applied for all wolves and X_2, X_3, X_4 .

$$X_i = \frac{(X_1 + X_2 + X_3 + X_4)}{4} \quad (7)$$

Finally, α position is converged and provides a solution which guarantees, the attacker cannot utilize the LLM_K from SINs instantly after deployment. The final solution, that contain designated SINs and normal node can be obtained by the below equation 8. SINs are estimated based on the updating wolves' positions, the process is repeated for all iterations by updating the wolves position,

$$Best_{Agent} = \alpha_{wolves}^{pos} \quad \alpha_{wolves}^{score} > Fit_{val} \quad (8)$$

$$X_i = \frac{(X_1 + X_2 + X_3 + X_4)}{4}$$

The process of identifying SINs using GWO is given in algorithm 1.

Algorithm 1: SIN Identification using GWO

Input: Total number of nodes N

Output: Identified Master Node M_N , Normal Node N_N

Procedure:

Step 1:

Initialize the wolves (Sensor Nodes) position randomly from, $X_i (i = 1, 2, \dots, N)$ $X_j (i = 1, 2, \dots, N)$

Maximum iteration, $iter = 500$

Lower Bound, $lb = -100$

Upper Bound, $ub = 100$

Initialize $\alpha_{wolves}^{score}, \beta_{wolves}^{score}, \delta_{wolves}^{score}$ and ω_{wolves}^{score}

Step 2: iterate the process to maximum iterations,

While $it < iter$

$$Flag_{up}^i = \begin{cases} 1 & X_i > ub \\ 0 & else \end{cases}$$

$$Flag_{Lb}^i = \begin{cases} 1 & X_i < lb \\ 0 & \text{else} \end{cases}$$

Update the position based on the updating ub and lb

$$X_i = X_i * (Flag_{up} - Flag_{Lb}) + (ub * Flag_{up}) + (lb * Flag_{Lb}) \quad (11)$$

$$X_j = X_j * (Flag_{up} - Flag_{Lb}) + (ub * Flag_{up}) + (lb * Flag_{Lb})$$

Step 3:

Execute the objective function based on the estimation of information measure, correlation among the nodes, using equation (1).

Step 4:

Update α , β , δ and ω wolves score and position, using equation (2 – 5).

Step 5: Update position of all wolves, using equation (6).

Iterate the process for all wolves and estimate, using equation (7).

Step 6: Best agents are estimated based on the updating wolves' positions, using equation (8).

End while

Step 7: This process is repeated for all iterations and the final solution identifies strategically important nodes (SIN).

B. Pair node prediction, volatile key (LLM_K) and shared key generation using Secure Hash Algorithm (SHA):

The SINs and neighbor nodes, that are ready for transmission, are authenticated. The authentication is done through SHA, which involves generating the nonce message and shared key for the node which holds the volatile key and the node involved in communication. The volatile key has been generated for a SIN along with limited key's lifetime. Limited Life Volatile Master key (LLM_K) generation can be formulated as below,

$$LLM_K = \{M_N^{id}, rand_{0 \text{ to } 1}, randint_{1 \text{ to } 10}\} \quad (12)$$

Where M_N^{id} – Master node Id,

$rand$ – random value generated between 0 to 1

$randint$ - random value generated between 1 to 10

After volatile key generation, the master node sends the request message NReq to the adjacent neighbor nodes along with prime number which is selected from the prime number group (in table 2).

$$Pair_{node} = N_N^{id} \{neighbor \text{ node list}\} \quad (13)$$

where N_N^{id} = Neighbor node.

Table. 2 Prime Number Groups

Group	Prime Numbers			
A	P1	P2	P3	P4
B	P1	P5	P6	P7
C	P2	P5	P8	P9
D	P3	P6	P8	P10
E	P4	P7	P9	P10

Further, among the various neighbor nodes around the SIN, only one node is designated as a pair node. A finite number

of prime numbers are selected in a random manner and are partitioned into groups in such a manner that every intersection among two separate groups comprise of at least one prime number. Through this the process of key computation is distributed among two adjacent nodes, where each node S_a and S_b do randomly select one group. The intersection of these groups is represented as common prime number which are selected by S_a and S_b .

The neighbor node S_b generates nonce message by employing hash algorithm by considering the prime numbers. There exist five different available hash functions such as 160, 224, 256, 384, and 512 bit combinations. Out of these only one hash function is selected at any point of time.

$$nonce_b = hash(X_b)$$

The SHA is used for authentication and generates a cryptographic message digest algorithm which is similar to MD4 group of hash functions. A hash function can be defined as a function which takes the variable of size m as input and generates fixed-size string output, commonly known as hash value h (i.e. $h=H(m)$). Hash functions along with these properties have various computational uses. However, when it is employed in cryptography these functions requires, a) the input data 'x' of any length, b) The fixed length output, c) $H(x)$ can be easy for computing some given value of x , d) $H(x)$ is a unique function.

Algorithm II: Secure Hash Algorithm

Input: Common Prime number, ID_a and ID_b

Output: Predicted SINs message security

Procedure:

Step 1: Initialize variables:

$$m_{len}=64$$

$$m_{fact}=1$$

$$\rho_{pad}=64 \quad //pad \text{ zero}$$

$$h0 := 0x67452301$$

$$h1 := 0xEFCDAB89$$

$$h2 := 0x98BADCFE$$

$$h3 := 0x10325476$$

$$h4 := 0xC3D2E1F0$$

Step 2: Pre-processing:

ml = message length in bits (always a multiple of the number of bits in a character).

$$m_{size}=512*(m_{fact});$$

$$m_d=sign(rand(1, m_{len})-0.5)+1)*0.5;$$

$$\text{for } uu=1: m_{len}$$

$$m_d(uu)=mod(uu,2)$$

End

Let initialize the message input,


```

msginp = message_input;
for ii = 1: length(msginp)
    mstr(ii) = strcat(
        mstr, dec2bin(hex2dec(msginp(ii), 4)))
End
mstr = mstr(1: mlen)
mraw_512 = char();
blknum = fix(length(mstr)/512 * mfact)
If (mod(length(mstr)), 512, mfact) == 0
    blknum = blknum - 1
End
exndnum = 512 * mfact * (blknum + 1) - mod(length(mstr))
for k = 1: 128 * (blknum + 1) * mfact
    mraw_512 = strcat(mraw_512, dec2hex(bin2dec(mstr)4 *
        (k - 1) + 1: 4 * k))
end
while (mod(diff_k, 512 * mfact))
    int_k = int_k + 1
    diff_k = abs(int_k + 1 - 448 * mfact)
Step 4: Process the message m in consecutive 512bit chunks
    for each chunk
        break chunk into sixteen 32-bit big-endian words w[i], 0 ≤ i
        ≤ 15;
Step 5: Extend the sixteen 32-bit words into eighty 32-bit
        words:
        for i from 17 to 80
            w[i] := (w[i-3] xor w[i-8] xor w[i-14] xor w[i-16])
        leftrotate
Step 6: Initialize hash value for this chunk:
        a := h0
        b := h1
        c := h2
        d := h3
        e := h4
        Main loop:
        for i from 0 to 80
            if 0 ≤ i ≤ 20 then
                f := (b and c) or ((not b) and d)
                k := 0x5A827999

```

```

            else if 21 ≤ i ≤ 40
                f := b xor c xor d
                k := 0x6ED9EBA1
            else if 41 ≤ i ≤ 60
                f := (b and c) or (b and d) or (c and d)
                k := 0x8F1BBCDC
            else if 61 ≤ i ≤ 80
                f := b xor c xor d
                k := 0xCA62C1D6
            temp := (a leftrotate 5) + f + e + k + w[i]
            e := d
            d := c
            c := b leftrotate 30
            b := a
            a := temp

```

Step 7: Add this chunk's hash to result (Authenticated message)
so far:

```

h0 = mod(bin2dec(h0) + bin2dec(a'), 4294967296);
h1 = mod(bin2dec(h1) + bin2dec(b'), 4294967296);
h2 = mod(bin2dec(h2) + bin2dec(c'), 4294967296);
h3 = mod(bin2dec(h3) + bin2dec(d'), 4294967296);
h4 = mod(bin2dec(h4) + bin2dec(e'), 4294967296);
H0 = dec2hex(h0, 32)
H1 = dec2hex(h1, 32)
H2 = dec2hex(h2, 32)
H3 = dec2hex(h3, 32)
H4 = dec2hex(h4, 32)

```

A_{mes} = strcat(H0, H1, H2, H3, H4)

Step 8: Verified authentication message by SIN node which is generated and received from the chosen pair node.

Shared key generation

Shared key is generated at S_b and is denoted as K_{ab}.

$$K_{ab} = f(\text{nonce}_b, ID_a, ID_b, S_a^x, S_a^y, S_b^x, S_b^y)$$

Where, S_a^x, S_a^y, S_b^x, S_b^y are the two-dimensional coordinates of SIN node and pair node location respectively.

Pair node sends a response message NResp to the SIN along with hash function and selected prime number group.

$$NRep_b = \{\text{hash}_{f_{unc}}, X_b\}$$

SIN upon receiving this response message, then generates nonce at S_a. Further, the shared key using generated nonce nonce_a is generated using chosen hash function and common prime number.

$$\text{nonce}_a = \text{hash}(X_a)$$

Next, the SIN encrypts the volatile key LLM_k using generated shared key K_{ab} .

$$E(LLM_k) = E_f(K_{ab})$$

C. Key generation using gradient approach and Key sharing using Super-singular Isogeny Diffie Hellmann (SIDH):

Encrypted volatile key LLM_k is transmitted to S_b using super singular Diffie Hellmann algorithm.

SIDH:

This cryptographic algorithm has been utilized for establishing a secret key among dual parties under the uncertain and unreliable transmission channel. It has been designed in such a way that it resists cryptanalytic attack caused by an intruder. It claims as one of the small key sizes along with compression. The public key with 2699 bit is utilized at 128 bit quantum security level. This SIDH establishes a set of super singular elliptic curves along with their isogenies. An isogeny (ϕ) between elliptic curves E, E' can be defined in equation 14,

$$\phi: E \rightarrow E' \quad (14)$$

The SIDH can be set up as the prime of the form as,

$$p = l_A^{e_A} \cdot l_B^{e_B} \cdot f \mp 1 \quad (15)$$

Where $l_A, l_B \rightarrow$ small primes,

$e_A, e_B \rightarrow$ Exponents,

$f \rightarrow$ small co-factor

Thus, the curve has two large subgroups such as $E[l_A^{e_A}]$ and $E[l_B^{e_B}]$, that are assigned for paired nodes respectively. Each node starts the protocol by choosing a random cyclic subgroup (secretly) and compute the corresponding secret (isogeny). The efficiency of the SIDH can be analyzed during key exchange among the paired nodes, where each of them transmits information of two co-efficients ($\text{mod } p^2$) which in turn defined two elliptic curve points and an elliptic curve. Each elliptic curve needs $\log_2 p^2$ bits. Hence for two curve points, it amounts to $8\log_2 p^2 + 4$ bits, which is 6144 bits for 768 bit modulus p . But it can be reduced to 2640(330 bytes) using compression techniques. Along with compression methods, SIDH has same bandwidth constraint as 3072 – bit Diffie-Hellman exchange. Thus, it makes the SIDH applicable to schemes that have smaller memory space requirements.

Algorithm III: Key generation using SIDH and Key-sharing using SIDH

Input: Authentication Message M , pair nodes $Id PN^{id}$, Pair node position PN_x and PN_y

Output: Secret Key K

Procedure:

Step1: consider the authentication message as nonce.
Nonce = double(M) // convert the authentication message into integer format.

Step 2: Combine this information and perform gradient computation,

$$C = \{PN^{id}, PN_x, PN_y, Nonce\}$$

$$G = \frac{\partial C}{\partial x} i + \frac{\partial C}{\partial y} j \quad (16)$$

Step 3: Form the secret key based on the unique estimated gradient,

$$K = \text{unique}(G)$$

Step 4: Share the generated secret key to the pair node via Super singular Isogeny Diffie Hellman algorithm,

$$\text{Receiver}_{key} = \text{SIDH}(K) \quad (17)$$

Decrypt volatile key LLM_k at S_b ,

$$D(LLM_k) = D_f(K_{ab})$$

D. Blow Fish Algorithm based generated Dynamic S-Box using Key

Blow Fish Algorithm:

Blowfish is said to be a 64 – bit block cipher, lightweight, and highly secured algorithm[20]. It can be implemented through software or hardware implementation. The confidentiality of key encryption is utmost significant in case of symmetric ciphers (i.e. Blowfish). Hardware implementation of blowfish has higher advantages than software implementation viz., rapid processing, minimal delay and extremely secured. It is one such employment of hardware which uses hard-wired components. In this blow fish algorithm, XOR operation is represented by the symbol \oplus . Almost 18 sub keys are required to execute this algorithm, along with non-linear function F. This F function utilizes 4 Dynamic S-Boxes or substitution boxes, each containing 256 [32-bit] entries. The S- boxes are generated using the algorithm IV.

Algorithm IV: Blow Fish Algorithm based generated Dynamic S-Boxes using Key K.

Input: Secret Key K

Output: P_{arr}, S_{box}

Procedure:

Step 1: Convert hexadecimal key into decimal format,

$$K_1 = \text{hex2dec}(K) \quad // \text{hexadecimal to decimal}$$

Step 2: Convert decimal to binary format and concatenate each adjacent rows of the key element to horizontal arrangement,

$$K_2 = \text{horzcat}(\text{dec2bin}(K_1)) \quad // \text{horzcat – horizontal wise concatenation of two vectors, dec2bin – decimal to binary conversion.}$$

Step 3: Initialize P-array and Dynamic S-Box using random values and updated key matrix,

$$P_{arr} = \text{horzcat}(\text{dec2bin}(\text{hex2dec}(\text{rand})))$$

$$S_{box} = \text{horzcat}(\text{dec2bin}(\text{hex2dec}(\text{Txt}_{file})))$$

$$P_{arr} = P_{arr} \oplus K_2 \quad // \oplus - \text{bitwise XOR operation}$$

$$S_{box} = S_{box} \oplus K_2$$

Generated s box with the dimension of $S_{box}[4][256]$

Blow Fish Encryption & Decryption:

Here the block size of the proposed cipher is 64 – bits, which will encrypt the block ‘x’ and then is also decrypted.

Algorithm V: Blow Fish Algorithm based Encryption and Decryption.

Input: Plain text MeS_{PT}

Output: Encrypted Text $Crypt_T$, Decrypted Text $Decrypt_T$

Step 1: Perform blow fish encryption process,

Let $L = MeS_{PT}(1:4)$ // Consider 1 to 4 bits

$R = MeS_{PT}(5:8)$ // Consider 5 to 8 bits

for (int $i = 0$; $i < 16$; $i += 2$) {

$L = L \oplus P_{arr}[i];$
 $R = R \oplus MeS_{PT}(L);$
 $R = R \oplus P_{arr}[i+1];$
 $L = L \oplus MeS_{PT}(R);$

$L = L \oplus P_{arr}[16];$
 $R = R \oplus P_{arr}[17];$
 $Crypt_T = swap(L, R);$

Step 2: Perform blow fish decryption process,

Let $L = MeS_{PT}(1:4)$ // Take 1 to 4 bits

$R = MeS_{PT}(5:8)$ // Take 5 to 8 bits

for (int $i = 16$; $i > 0$; $i -= 2$) {

$L = L \oplus P_{arr}[i+1];$
 $R = R \oplus MeS_{PT}(L);$
 $R = R \oplus P_{arr}[i];$
 $L = L \oplus MeS_{PT}(R);$

$L = L \oplus P_{arr}[1];$
 $R = R \oplus P_{arr}[0];$

$Decrypt_T = swap(L, R);$

It is noted that, these substitution-boxes are generated for every encryption, thus, the schemes dynamic nature increases the difficulty for the attacker in predicting the keys.

IV. PERFORMANCE ANALYSIS

This section analyzes the proposed scheme's performance using the following key metrics:

- **SIN (LLM_k) nodes vs. Node Density:** The impact of node density on the master key's (LLM_k) lifetime, where the Sensor nodes are randomly deployed within an 300m*300m simulation area is investigated. Considering the three different random deployment scenarios, the LLM_k is inserted into the central nodes and border nodes in the WSN. This enables to observe the scheme's behavior at time 't' and determine how node location affects execution time, security attributes and resource utilization.
- **Delay Time vs. Number of Neighbor Nodes:** This analysis explores the relationship between the number of neighboring nodes and the delay experienced in the key distribution process with varying node density.
- **Energy Consumption Overhead:** The energy consumption of the proposed scheme compared to existing solutions is evaluated.

SIN vs. Node Density (Detailed Analysis):

Deployment Scenario 1

The first scenario focuses on randomly deploying the SNs and assessing the influence of parameters on the execution time of the proposed keying technique. Here, a low execution time is associated with the initial position and number of nodes holding the master key. As shown in figure 3, the proposed scheme efficiently performs the keying process across the entire network within 400ms. Additionally, out of 100 nodes, 94 successfully receive the volatile key, resulting in significantly higher key availability and key distribution in the WSN compared to the previous Self-VKS scheme [21].

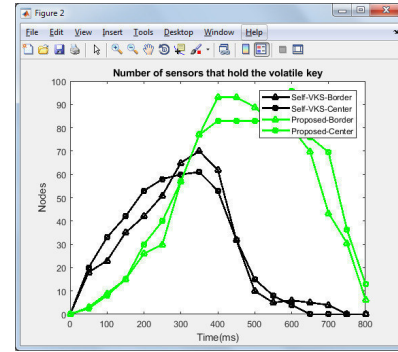


Figure 3 LLM_k vs node density – deployment scenario #1

ii. Deployment Scenario 2

As illustrated in figure 4, the proposed scheme efficiently completes the keying process throughout the network within 410 milliseconds. Furthermore, 88 out of 100 nodes successfully receive the volatile key, achieving a superior level of key availability within the network compared to the prior Self-VKS scheme [21].

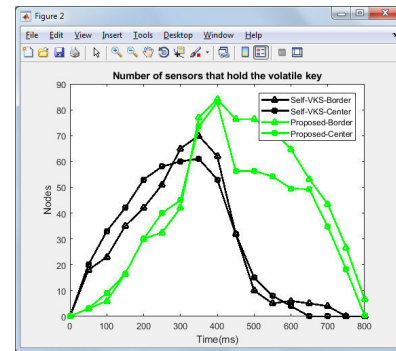


Figure 4. LLM_k vs node density – deployment scenario #2

i. Deployment Scenario #3

As shown in figure 5, the proposed scheme efficiently performs the keying process throughout the network within 405 milliseconds. Additionally, 91 out of 100 nodes successfully receive the volatile key, demonstrating a significantly higher level of key availability compared to the prior Self-VKS scheme [21].

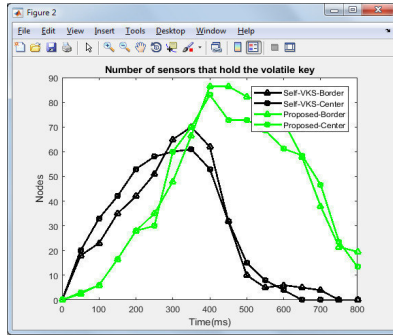


Figure 5. LLM_K vs node density – deployment scenario #3

1) LLM_K lifetime Vs node density

This section examines the impact of node density on the lifetime of volatile keys within the Wireless Sensor Network (WSN). Traditional approaches to secure communication in WSNs incur significant collision management overhead due to the broadcast nature of the communication channel and processing time associated with volatile key communication. To address this challenge, prior works have resorted to extending the key lifetime to around 25 seconds [21].

In contrast, the proposed scheme eliminates the need for extended key lifetimes. Each node (i^{th} node) can successfully communicate the volatile key to its 'n' neighboring nodes within the WSN before the key expires, achieving this feat within a 10-second time interval. Figures 6 to 8 visually depict the relationship between volatile key lifetime and time within the WSN with respect to the node density.

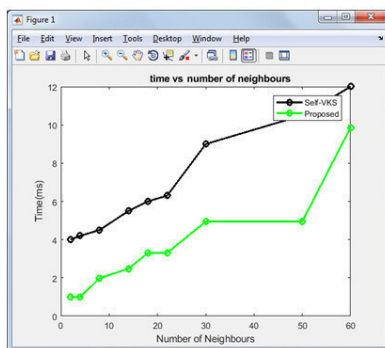


Figure 6. LLM_K lifetime vs node density – for deployment scenario #1

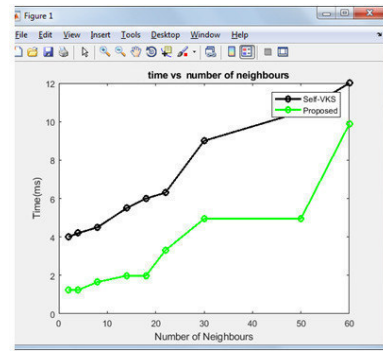


Figure 7. LLM_K lifetime vs node density – for deployment scenario #2

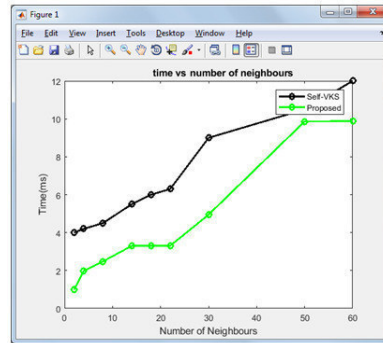


Figure 8. LLM_K lifetime vs node density – for deployment scenario #3

2) Energy consumption overhead

Energy Efficiency Analysis:

The proposed scheme minimizes energy consumption during session establishment between SNs due to several factors. Unlike traditional approaches, not all SNs in the Wireless Sensor Network (WSN) need to generate and encrypt nonces before the keying process begins. This significantly reduces energy expenditure.

The total energy consumption for the network can be expressed as $E_m = (k + 1)N$, where E_m represents the energy spent as a function of the number of messages sent (N) and k denotes the average number of neighbors between each node pair [21]. This formula highlights the impact of several factors on energy efficiency:

- **Node Density (N):** As 'N' increases the total number of messages transmitted increase as well, thus resulting into spending more energy per node.
- **Packet Size:** Larger packet sizes contribute to increased energy consumption.
- **Encryption/Decryption Cost:** The choice of encryption and decryption algorithms and their key size significantly affect node energy and other resource usage.

During the keying process, each sensor transmits a discovery message and receives a maximum of k messages from its neighbors. Based on these calculations, the average energy consumption per sensor (E_m) can be estimated as $(k + 1)$ [21].

V. CONCLUSION

This proposal presents a novel key management scheme (KMS) designed for dynamically scalable, secure data communications in Wireless Sensor Networks (WSNs). The suggested deterministic technique makes use of an encrypted nonce that corresponds to a plain text message. Because of this, nodes may effectively continue the key formation process even in situations when initially just a portion of nodes have the master key. Through this approach, the number of messages needed for key establishment is minimized, resulting in a considerable reduction of data transmission energy usage. In addition, capacity and processing demands on sensor nodes are substantially reduced. Critical sensor node behaviors including dynamic node movement, secure node addition, and key renewal are all fully covered by the method. The efficiency of the scheme in terms of keying time and robustness against different WSN assaults is shown by a thorough security study.

VI. FUTURE SCOPE

Asynchronous Duty cycles:

It is suggested that asynchronous sensor duty cycles be investigated for optimal energy use and routing effectiveness.

Relevance to IoT:

The incorporation of IoT into WSNs increases the ubiquitous nature of sensor networks. Future study might be beneficial in evaluating the suggested key management, routing, and security systems in the context of Internet of Things applications with a consideration of devices with limited resources.

Considering Dynamic Networks:

The existing technique for managing symmetric volatile keys requires a static network design with fixed placements for sensor nodes. Future research should focus on creating and assessing these techniques for dynamic network topologies on mobility of nodes in heterogeneous environments.

Enhanced Security with Surveillance Nodes:

Adding "surveillance nodes" to the typical network deployment plan might bolster WSN security. These nodes would monitor network traffic, including potentially harmful behavior. Through the identification and elimination of bad actors, surveillance nodes establish connections only with securely configured nodes. Moreover, it is promising to use artificial intelligence techniques in these monitoring nodes for compromised node rehabilitation and recovery.

REFERENCES

- [1] A. Rani and S. Kumar, "A survey of security in wireless sensor networks," in *2017 3rd International Conference on Computational Intelligence & Communication Technology (CICCT)*, 2017, pp. 1-5.
- [2] F. Gandino, C. Celozzi, and M. Rebaudengo, "A key management scheme for mobile wireless sensor networks," *Applied Sciences*, vol. 7, p. 490, 2017.
- [3] P. Singh and N. S. Gill, "A Survey on Key management Schemes in Wireless Ad Hoc Networks," *International Journal of Applied Engineering Research*, vol. 13, pp. 268-272, 2018.
- [4] A. Laouid, M.-L. Messai, A. Bounceur, R. Euler, A. Dahmani, and A. Tari, "A dynamic and distributed key management scheme for wireless sensor networks," in *Proceedings of the International Conference on Internet of things and Cloud Computing*, 2016, p. 70.
- [5] M. Elhoseny and A. E. Hassanien, "Secure data transmission in WSN: an overview," in *Dynamic Wireless Sensor Networks*, ed: Springer, 2019, pp. 115-143.
- [6] O. Yagan and A. M. Makowski, "Wireless sensor networks under the random pairwise key predistribution scheme: Can resiliency be achieved with small key rings?," *IEEE/ACM Transactions on Networking (TON)*, vol. 24, pp. 3383-3396, 2016.
- [7] P. Ahlawat and M. Dave, "Deployment Based Attack Resistant Key Distribution with Non Overlapping Key Pools in WSN," *Wireless Personal Communications*, vol. 99, pp. 1541-1568, 2018.
- [8] P. A. R. B. P. Shraddha Deshmukh, Harshad Nakade, "Implementation of Effective Key Management Strategy with Secure Data Aggregation in Dynamic Wireless Sensor Network," *International Journal of Scientific Research in Computer Science, Engineering and Information Technology (IJSRCSEIT)*, vol. 4, pp. 358-364, March-April 2018.
- [9] A. Albakri, L. Harn, and S. Song, "Hierarchical Key Management Scheme with Probabilistic Security in a Wireless Sensor Network (WSN)," *Security and Communication Networks*, vol. 2019, 2019.
- [10] R. V. Saraswathi, L. P. Sree, and K. Anuradha, "Multi-stage Key Management Scheme for Cluster based WSN," *International Journal of Communication Networks and Information Security*, vol. 10, p. 552, 2018.
- [11] K. Moara-Nkwe, Q. Shi, G. M. Lee, and M. H. Eiza, "A novel physical layer secure key generation and refreshment scheme for wireless sensor networks," *IEEE Access*, vol. 6, pp. 11374-11387, 2018.
- [12] P. S. Mehra, M. N. Doja, and B. Alam, "Codeword Authenticated Key Exchange (CAKE) light weight secure routing protocol for WSN," *International Journal of Communication Systems*, vol. 32, p. e3879, 2019.
- [13] U. Iqbal and S. Shafi, "A provable and secure key exchange protocol based on the elliptical curve diffe-

- hellman for wsn," in *Advances in Big Data and Cloud Computing*, ed: Springer, 2019, pp. 363-372.
- [14] C. G. Krishnan, K. Sivakumar, and E. Manohar, "An Enhanced Method to Secure and Energy Effective Data Transfer in WSN using Hierarchical and Dynamic Elliptic Curve Cryptosystem," in *2018 International Conference on Smart Systems and Inventive Technology (ICSSIT)*, 2018, pp. 1-7.
 - [15] D. Suhag, S. S. Gaur, and A. Mohapatra, "A proposed scheme to achieve node authentication in military applications of wireless sensor network," *Journal of Statistics and Management Systems*, vol. 22, pp. 347-362, 2019.
 - [16] M. A. Simplicio Jr, M. V. Silva, R. C. Alves, and T. K. Shibata, "Lightweight and escrow-less authenticated key agreement for the internet of things," *Computer Communications*, vol. 98, pp. 43-51, 2017.
 - [17] C.-H. Liu and Y.-F. Chung, "Secure user authentication scheme for wireless healthcare sensor networks," *Computers & Electrical Engineering*, vol. 59, pp. 250-261, 2017.
 - [18] Q. Jiang, N. Kumar, J. Ma, J. Shen, D. He, and N. Chilamkurti, "A privacy-aware two-factor authentication protocol based on elliptic curve cryptography for wireless sensor networks," *International Journal of Network Management*, vol. 27, p. e1937, 2017.
 - [19] Y. Alkady, M. I. Habib, and R. Y. Rizk, "A new security protocol using hybrid cryptography algorithms," in *2013 9th International Computer Engineering Conference (ICENCO)*, 2013, pp. 109-115.
 - [20] M. Suresh and M. Neema, "Hardware implementation of blowfish algorithm for the secure data transmission in Internet of Things," *Procedia Technology*, vol. 25, pp. 248-255, 2016.
 - [21] A. Laouid et al., "A self-managing volatile key scheme for wireless sensor networks," *J. Ambient Intell. Humaniz. Comput.*, vol. 10, no. 9, pp. 3349-3364, 2019, doi: 10.1007/s12652-018-0772-9.

See discussions, stats, and author profiles for this publication at: <https://www.researchgate.net/publication/382180451>

LEUKEMIA DISEASE: OVERVIEW AND DETECTION APPROACHES

Article · July 2024

CITATIONS
0

READS
93


4 authors:



Tabasum Guledgudd
SECAB INSTITUTE OF ENGINEERING AND TECHNOLOGY

1 PUBLICATION 0 CITATIONS


SEE PROFILE



Noorullah Shariff C
Ballari Institute of Technology and Management

6 PUBLICATIONS 87 CITATIONS

SEE PROFILE



S. A. Quadri
Universiti Sains Malaysia

57 PUBLICATIONS 247 CITATIONS

SEE PROFILE



Sayed Abdulhayan
P.A.College of Engineering

6 PUBLICATIONS 12 CITATIONS

SEE PROFILE

LEUKEMIA DISEASE: OVERVIEW AND DETECTION APPROACHES

Tabasum Guledgudd^{1*}, Noorullah Shariff C², S.A. Quadri³ and Sayed Abdulhayan⁴

¹ Department of Electronics and Communication Engineering, SECAB IET Vijayapura, India.

² Department of AIML, BITM, Bellary, India.

³ Department of Computer Science & Engineering, SECAB IET Vijayapura, India.

⁴ Department of Computer Science and Engineering, P A College of Engineering, Mangalore,

*Corresponding Author: Tabasum Guledgudd

Keywords: Leukemia, WBC, Complete blood count, CML - Chronic Myeloid Leukemia, Acute Lymphoblastic Leukemia, Clustering.

Abstract: Leukemia, a complex hematologic malignancy, presents a formidable challenge in oncology due to its diverse subtypes and intricate diagnostic landscape. This paper provides an extensive literature review encompassing the classification of leukemia and exploration of various diagnostic approaches. Various methods such as blood tests, bone marrow aspiration, cytogenetic analysis, molecular testing, flow cytometry, and imaging tests are examined alongside recent advancements in diagnostic technologies. The review synthesizes studies highlighting the efficacy of innovative detection methodologies, including terahertz radiation, machine learning algorithms, deep learning models, and image processing techniques, in leukemia diagnosis. Furthermore, the paper presents an approach that utilizes pathological report analysing blood parameters and identifying correlations with different leukemia types using clustering techniques.

1. Introduction:

Cancer is characterized by uncontrolled cell growth, division, and invasion into other tissues due to genetic mutations. Mutated cells replicate uncontrollably, forming cancerous tissues responsible for further proliferation. Symptoms arise from cancerous cells invading other tissues, a process known as metastasis, spreading cancer throughout the body and impairing organ function. While cancer can affect individuals of any age, most types are more prevalent in older individuals due to accumulated DNA damage. Cancer is a leading cause of death in developed countries, driving extensive research in oncology for effective treatment strategies(<https://en.wikipedia.org/wiki/Cancer>).

There is no sure cure for cancer. It can only be cured if all of the cancerous cells are cut out or killed in place. This means that the earlier the cancer is treated, the better the chances are for

a cure (because the cancer cells may not have had enough time to copy themselves and spread so much that the person cannot be cured). There are many different types of cancer, and each has its own symptoms and causes. Even with the same type of cancer, different people may have different symptoms, and may react to treatments differently; their cancer also may grow or spread at different speeds. Treatment has to be a good fit to both the type of cancer and the individual patient who has the cancer.

The paper is organized such that section 2 deals with Leukemia and WBC classes, section 3 emphasis literature review, section 4 presents proposed methodology followed by the conclusion.

2. Leukemia

Leukemia, or leukaemia, denotes a malignancy affecting white blood cells and bone marrow, characterized by an overproduction of leukocytes. Its severity and prognosis vary depending on the leukemia subtype. In 2000, approximately 256,000 individuals globally developed leukemia, with about 209,000 succumbing to the disease. The majority of cases, around 90%, occur in adults(<https://en.wikipedia.org/wiki/Leukemia>).

Blood comprises various types of cells, including white blood cells (monocytes, lymphocytes, neutrophils, eosinophils, basophils, and macrophages), red blood cells (erythrocytes), and platelets.

White blood cells are produced by different tissues in the body. Around 60 to 70 percent of white cells, known as granulocytes, are generated in the bone marrow in adults. Lymphocytes, accounting for 20 to 30 percent, are produced in lymphatic tissues like the thymus, spleen, and lymph nodes. Monocytes, comprising 4 to 8 percent of white cells, are produced in reticuloendothelial tissues such as the spleen, liver, and lymph nodes. An average healthy adult has between 4,500 and 11,000 white blood cells per cubic millimetre of blood, with fluctuations occurring throughout the day.

2.1 WBC Classes

White blood cells are categorized into major classes:

Lymphocytes, further divided into B cells and T cells, play a crucial role in recognizing and eliminating foreign agents from the body. B lymphocytes produce antibodies to destroy

foreign microorganisms, while T cells identify and destroy virally infected or cancerous cells. Natural killer (NK) cells also contribute to this process.

Granulocytes, the most abundant white cells, combat large pathogens like protozoans and helminths, and play a role in allergy and inflammation. They contain cytoplasmic granules with potent chemicals and are subdivided into neutrophils, eosinophils, and basophils based on their dye uptake in the laboratory.

Monocytes, constituting 4 to 8 percent of white blood cells, transform into macrophages at sites of infection. Macrophages act as scavengers, phagocytosing microorganisms and cellular debris, and play a key role in the immune response by presenting antigens to T lymphocytes. Figure 2.1 summarizes various classification of WBC(https://en.wikipedia.org/wiki/White_blood_cell).

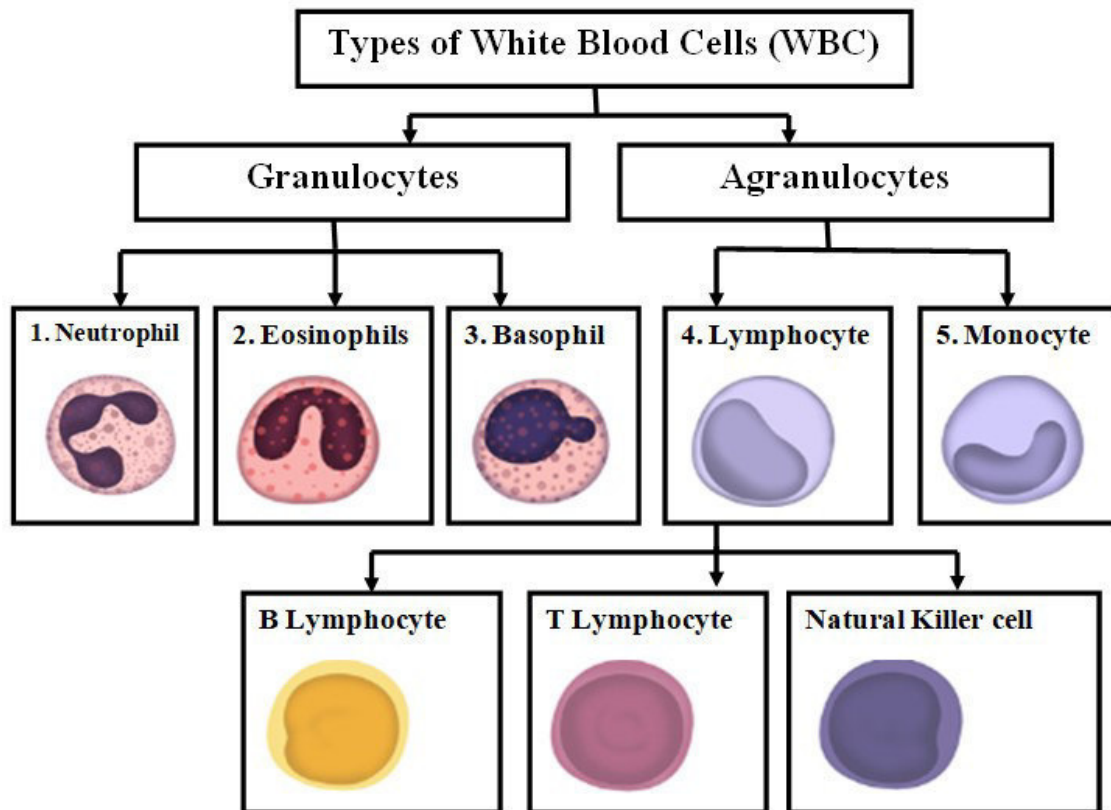


Figure 2.1: WBC Classification

Acute type of Leukemia shows rapid growth or spread of cancer. Chronic type of Leukemia shows slow growth or spread of cancer. ALL- Acute Lymphoblastic Leukemia. Common in children and more in male. It indicates Non-specific esterase (NSE). Symptoms have low HB

and platelets. There is presence of lymphoblast. AML- Acute myeloblastic Leukemia Common in adults. There is presence of Auer rods in blast cells. It indicates Non-specific esterase (NSE). Symptoms have low platelets. There is presence of myeloblast cells. CLL- Chronic lymphoblastic Leukemia. It indicates slow progression. It's mostly seen in 60 years and above WBC count is high. Platelets count low. There will be presence of smear cells. CML- Chronic myeloblastic Leukemia. There is presence of myeloid cells. WBC has Neutrophil, Monocyte, Basophil and Eosinophil. High WBC count in blood report.

ALL is characterized by the rapid proliferation of immature lymphocytes, leading to symptoms such as fatigue, pale skin, fever, bruising, and enlarged lymph nodes. CLL, on the other hand, is marked by excessive lymphocyte production, often progressing gradually over years. Initial stages may be asymptomatic, while later stages may manifest as non-painful lymph node swelling, fatigue, fever, night sweats, or weight loss. AML involves the rapid growth of abnormal myeloid cells, leading to symptoms like fatigue, shortness of breath, bruising, and increased infection risk. Diagnosis typically involves bone marrow aspiration and specific blood tests.

Treatment for leukemia varies depending on the subtype and individual factors. Chemotherapy is commonly used to induce remission, followed by additional therapies such as radiation or stem cell transplant. Targeted therapies may also be employed based on genetic mutations present in the cancer cells. Overall, collaborative efforts among researchers, clinicians, and patients are essential in improving outcomes and advancing leukemia treatment strategies.

3. Literature Review

In the diagnosis of leukemia, a variety of diagnostic techniques are utilized to accurately identify different types of the Leukemia types. These methods encompass:

1. Blood Tests: Complete blood count (CBC) and peripheral blood smear examination to identify abnormal blood cell counts and morphology.
2. Bone Marrow Aspiration and Biopsy: Direct examination of bone marrow cells for abnormalities in cell morphology and proliferation.
3. Cytogenetic Analysis: Examination of chromosomal abnormalities, such as translocations, using techniques like karyotyping and fluorescence in situ hybridization (FISH).

4. Molecular Testing: Polymerase chain reaction (PCR) to detect specific genetic mutations, like BCR-ABL1 in chronic myeloid leukemia (CML) or FLT3 mutations in acute myeloid leukemia (AML).
5. Flow Cytometry: Immunophenotyping of leukemia cells based on cell surface markers to classify leukemia subtypes and assess their immunophenotypic profiles.
6. Imaging Tests: X-rays, computed tomography (CT), magnetic resonance imaging (MRI), or positron emission tomography (PET) scans to detect organ enlargement or infiltration by leukemia cells.

Each method has its advantages and may be used alone or in combination to achieve an accurate diagnosis of leukemia. We have presented a brief review of the same in the below section.

Cheon et al. [1] used terahertz radiation to detect and manipulate DNA methylation in blood cancer cell lines, suggesting its potential in cancer treatment. Xing and Yilin [2] enhanced the KNN algorithm for medical health big data classification, improving efficiency and accuracy. Safuan et al. [3] proposed a CNN algorithm to automate White Blood Cell (WBC) detection, with VGG showing superior performance.

Nighat et al. [4] introduced an IoMT-based framework for leukemia detection, enabling real-time testing and diagnosis. Jabeen et al. [5] developed a method for early leukemia detection using image analysis, offering a rapid, cost-effective alternative. Hossain et al. [6] proposed a Faster-RCNN-based system for early leukemia detection in Bangladesh, integrating with smartphones for rural areas. Genovese et al. [7] introduced a machine learning-based approach for enhancing blood sample images and classifying ALL from normal samples.

Pałczyński et al. [8] developed an optimized neural network architecture for acute lymphoblastic leukemia diagnosis, achieving high accuracy. Aftab et al. [9] focused on Acute Leukemia detection using deep transfer learning, achieving high accuracy. Atteia et al. [10] introduced a Bayesian-optimized CNN for acute lymphoblastic leukemia detection, achieving superior classification accuracy.

Zhong et al. [11] developed an AI model for acute leukemia diagnosis using multiparameter flow cytometry, showing promising clinical application. Genovese et al. [12] presented a method for detecting ALL using histopathological transfer learning, showing enhanced accuracy. Khademi et al. [13] explored nanotechnology-based diagnostics and therapeutics for acute lymphoblastic leukemia, revealing promising applications.

Desi et al. [14] introduced an automated optical image processing system for blood disorder identification, enhancing accuracy and processing time. Hossain et al. [15] focused on early leukemia prediction using a supervised machine learning model, achieving high accuracy. Arnya et al. [16] assessed leukemia detection using machine learning classifiers, with Naïve Bayes showing the highest accuracy. Diana et al. [17] automated leukocyte classification using deep learning, surpassing the Naive Bayes Classifier in accuracy. Jusman et al. [18] developed a system program for early leukemia detection using image processing, achieving high accuracy. Kumar et al. [19] utilized microscopy image processing software for acute lymphoblastic leukemia detection, enhancing diagnostic accuracy.

Della et al. [21] investigated various molecular methods for minimal residual disease evaluation in acute lymphoblastic leukemia, suggesting potential advantages of new molecular approaches. Varadarajan et al. [22] explored novel therapeutic approaches for relapsed acute lymphoblastic leukemia post allogeneic hematopoietic cell transplantation in adult patients.

Hoffmann et al. [23] developed Cinderella, an XAI method for measuring haemodilution and minimal residual disease in acute myeloid leukemia.

Devi et al. [24] introduced the GBHSV-Leuk method for acute lymphoblastic leukemia detection, achieving high accuracy. Hossain et al. [25] proposed a supervised machine learning model for leukemia detection, achieving high accuracy and generating explainable rules. Ananth et al. [26] developed a small image processing method for leukemia detection, showing greater effectiveness than previous methods. Sridhar et al. [27] employed deep learning techniques for early leukemia detection, achieving notable accuracy.

Das et al. [28] systematically analysed segmentation and classification approaches for acute lymphoblastic leukemia detection, emphasizing the efficacy of deep learning. Hoffmann et al. [29] investigated the potential of MPFC data from chronic lymphocytic leukemia samples to predict outcomes using XAI. Molin et al. [30] developed CircFusion, a software tool for detecting linear fusion transcripts and f-circRNAs in cancer cells with rearranged genomes.

Hoffmann Khalil et al. [31] studied CD200 expression in leukemic B cells and its correlation with clinical findings in acute lymphoblastic leukemia patients. Liu [32] explored SETD2 expression in acute myeloid leukemia patients, revealing its association with treatment response and survival outcomes.

Tiago et al. [33] highlighted the potential of DNA methylation-based tests in molecular cancer early detection (MCED), particularly in combination with AI. Pier et al. [34] examined the relationship between physical activity and mental health outcomes among adolescents during the COVID-19 pandemic. Mansoor et al. [35] investigated gamma-tocotrienol as a potential inhibitor for the BCR-ABL1 fusion protein in leukemia therapy.

Sakthivel et al. [36] proposed an approach for classifying Acute Lymphoblastic Leukemia (ALL) and Multiple Myeloma (MM) using image processing techniques. Rawal et al. [37] fabricated Ag/Au thin film electrodes for monitoring serum albumin levels as a prognostic biomarker for blood cancer. The summary of the same has been provided in the table 3.1.

Table 3.1: Literature Review Summary

SI.NO. (References)	TITLE	SAMPLE COLLECTION	TECHNIQUES/METHODS	TYPES OF LEUKEMIA	ACCURACY
[1]	Detection and manipulation of methylation in blood cancer DNA using terahertz radiation	BLOOD	Terahertz radiation and Terahertz time-domain spectroscopy	Blood cancer	10% to 70%
[2]	Medical Health Big Data Classification Based on KNN Classification Algorithm	Hospital, Public health and community healthcare data base	KNN algorithm based on cluster denoising and density cropping	Blood cancer	Single-category classification and multi-category classification
[3]	Investigation of white blood cell biomarker model for acute lymphoblastic leukemia detection based on convolutional neural network	Immature White Blood Cells (WBCs) called lymphoblast	Convolutional Neural Network (CNN)	Acute Lymphoblastic Leukemia (ALL)	99.13%
[4]	IoT-Based Automated Detection and Classification of Leukemia Using Deep Learning	Bone marrow and/or blood	Dense Convolutional Neural Network (DenseNet-121) and Residual Convolutional Neural Network (ResNet-34)	Acute or chronic Leukemia & ALL, AML	99.91% and 99.96%
[5]	Leukemia Detection Mechanism through Microscopic Image and ML Techniques	Blood components (Neutrophils, Eosinophils, Basophils, Lymphocytes and Monocytes)	Faster-RCNN machine learning algorithm	Acute Lymphocytic Leukemia (ALL)	90%
[6]	Acute lymphoblastic leukemia detection based on adaptive unsharping and deep learning	Peripheral blood samples	Deep Learning, CNN	Acute Lymphoblastic (or Lymphocytic) Leukemia (ALL)	96.84%

[7]	Executing Spark BigDL for Leukemia Detection from Microscopic Images using Transfer Learning	Bone marrow & blood cells	1. BigDL library using apache spark framework 2. Convolutional Neural Network (CNN) architecture GoogleNet deep transfer learning	Acute Myeloid Leukemia (AML), Acute Lymphocytic Leukemia (ALL), Chronic Myeloid Leukemia (CML) and Chronic Lymphocytic Leukemia (CLL)	1)97.33% and 94.78% 2)96.42% and 92.69%
[8]	Histopathological Transfer Learning for Acute Lymphoblastic Leukemia Detection	Blood samples	1) BigDL library using apache spark framework 2) CNN deep learning model Deep Learning, CNN Transfer Learning, Histopathology	Acute Lymphoblastic (or Lymphocytic) Leukemia (ALL)	1)97.33% and 94.78% 2)96.42% and 92.69% training and validation
[9]	IoT Application of Transfer Learning in Hybrid Artificial Intelligence Systems for Acute Lymphoblastic Leukemia Classification	Bone marrow	MobileNet v2 encoder pre-trained on the ImageNet dataset and machine learning algorithms, XGBoost, Random Forest, and Decision Tree algorithms	Acute lymphoblastic leukemia	97.4%.
[10]	BO-ALLCNN: Bayesian-Based Optimized CNN for Acute Lymphoblastic Leukemia Detection in Microscopic Blood Smear Images	Lymphocytes in the blood or bone marrow, blood smear	Bayesian-based optimized convolutional neural network (CNN)	Acute lymphoblastic leukemia (ALL)	100%
[11]	Diagnosis of Acute Leukemia by Multiparameter Flow Cytometry with the Assistance of Artificial Intelligence	Peripheral blood (PB) and bone marrow (BM) specimens, and cytogenetic and molecular data	AI assisted multiparameter flow cytometry (MFC) diagnosis	Acute leukemia	Not mentioned
[12]	Analysis of IoT based Leukemia Detection Techniques	Blood cells (leucocytes)	Convolutional neural networks (CNNs), deep learning, image processing, and machine learning	Acute lymphoblastic leukemia (ALL)	Not mentioned
[13]	Diagnosis of Acute Leukemia by Multiparameter Flow Cytometry with the Assistance of Artificial Intelligence	Peripheral blood (PB) and bone marrow (BM) specimens, and cytogenetic and molecular data	AI assisted multiparameter flow cytometry (MFC) diagnosis	Acute leukemia	Not mentioned
[14]	Identification of critical hemodilution by artificial intelligence in bone marrow assessed for minimal residual disease analysis in acute myeloid leukemia: The Cinderella method	Bone marrow (BM) & peripheral blood (PB)	Explainable artificial intelligence (XAI) Cinderella, flow cytometry	Acute myeloid leukemia	Not mentioned
[15]	A Systematic Literature Review on Leukemia Prediction Using Machine Learning	Marrow of bones	Machine Learning	Leukemia	Not mentioned

[16]	An Advanced Low-cost Blood Cancer Detection System	Blood Cancer, white blood cells, immature cells	Histogram levelling, Thresholding, straight difference expanding, and morphological techniques	Blood Cancer	Not mentioned
[17]	Enhanced Machine learning algorithms Lightweight Ensemble Classification of Normal versus Leukemic Cells	Blood, bone marrow	Machine learning algorithms, conventional neural network topologies, computer-aided diagnostic (CAD) models, deep learning model, ML calculations, especially DL, in CAD frameworks, entire slide imaging (WSI)	leukemia	Not mentioned
[18]	A Systematic Review on Recent Advancements in Deep and Machine Learning Based Detection and Classification of Acute Lymphoblastic Leukemia	Bone marrow and affects white blood cells (WBCs)	Deep and machine learning-based, artificial intelligence, signal and image processing-based techniques, conventional machine learning-based techniques, and deep learning-based techniques, Convolutional Neural Network (CNN), Recurrent Neural Network (RNN), and the Autoencoder	Acute Lymphoblastic Leukemia	Not mentioned
[19]	Symptom Based Explainable Artificial Intelligence Model for Leukemia Detection	Bone marrow & blood cells	Machine learning model, explainable supervised model, Apriori algorithm, decision tree model proposed in our experiments has achieved 97.45% of accuracy, 0.63 of Mathew's Correlation Coefficient (MCC) and 0.783 of area under Receiver Operating Characteristic (ROC) curve on the test set.	Leukemia	Not mentioned
[20]	Gaussian Blurring Technique for Detecting and Classifying Acute Lymphoblastic Leukemia Cancer Cells from Microscopic Biopsy Images	Peripheral blood samples	Gaussian Blurring Technique, GBHSV-Leuk method	Acute Lymphoblastic Leukemia Cancer	Not mentioned
[21]	Optimizing Molecular Minimal Residual Disease Analysis in Adult Acute Lymphoblastic Leukemia	Neoplastic cells, blood components	MRD in ALL are polymerase chain reaction (PCR) amplification-based approaches	Adult Acute Lymphoblastic Leukemia	Not mentioned
[22]	Post-Hematopoietic Cell Transplantation Relapsed Acute Lymphoblastic Leukemia: Current Challenges and Future Directions	T-cell	Allogeneic hematopoietic cell transplantation (allo-HCT), cellular immunotherapy	Acute Lymphoblastic Leukemia	Not mentioned

[23]	Prediction of Clinical Outcomes with Explainable Artificial Intelligence in Patients with Chronic Lymphocytic Leukemia	Genetic analysis	Artificial intelligence; ALPODS; flow cytometry	Chronic Lymphocytic Leukemia	CD4+ T-cell population enhanced the predictive ability of the CLL-IPI (AUC 0.83; 95% CI 0.77–0.90; $p < 0.0001$).
[24]	Prognostic Role of CD200 in Acute Lymphoblastic Leukemia Patients	Complete blood count , BM aspiration, immunophenotyping of blast cells, and CD200 expression	CD200 expression shows a significant correlation with total leucocytic count and haemoglobin level ($p = 0.001, 0.03$, respectively).	Acute Lymphoblastic Leukemia	Not mentioned
[25]	SETD2 detection may reveal response to induction therapy and survival profile in acute myeloid leukemia patients	Bone marrow (BM) samples	SETD2 expression with disease risk, features, treatment response, and survival profile, CD200 expression shows a significant correlation with total leucocytic count and haemoglobin level ($p = 0.001, 0.03$, respectively).	Acute myeloid leukemia	Not mentioned
[26]	Shifting the Cancer Screening Paradigm: The Rising Potential of Blood-Based Multi-Cancer Early Detection Tests	Tumor-related markers	Multicancer early detection (MCED) tests, artificial intelligence, liquid biopsy; biomarkers, DNA methylation-based tests	Cancer	Not mentioned
[27]	Updating the Clinical Application of Blood Biomarkers and Their Algorithms in the Diagnosis and Surveillance of Hepatocellular Carcinoma: A Critical Review	Tumor biomarkers	α -FP biomarker with/without ultrasonography, combining α -FP with novel biomarkers can enhance HCC detection sensitivity, Lens culinaris agglutinin-reactive fraction of Alpha-fetoprotein (α -FP), α -FP-L3, Des- γ -carboxy-prothrombin (DCP or PIVKA-II), and the GALAD score, are being used more frequently in the diagnosis and prognosis of HCC	Hepatocellular Carcinoma, liver cancer is hepatocellular carcinoma (HCC)	Not mentioned
[28]	Antigen Receptors Gene Analysis for Minimal Residual Disease Detection in Acute Lymphoblastic Leukemia: The Role of High Throughput Sequencing.	Residual leukemic blast prognostic indicator, minimal residual disease	High throughput sequencing (HTS), MRD monitoring with emphasis on the use of HTS	Acute Lymphoblastic Leukemia	Not mentioned

[29]	Artificial Intelligence Assisted Pharmacophore Design for Philadelphia Chromosome-Positive Leukemia with Gamma-Tocotrienol: A Toxicity Comparison Approach with Asimina	Philadelphia chromosome, high level Ph+	Deep learning artificial intelligence (AI) drug design, AIGT's (Artificial Intelligence Gamma-Tocotrienol) drug-likeness analysis	Chronic Myeloid Leukemia (CML)	Not mentioned
[30]	Discovery of fusion circular RNAs in leukemia with KMT2A::AFF1 rearrangements by the new software CircFusion	Chromosomal translocations in cancer genomes	Genomes with chromosomal rearrangements, fusion circular RNAs (f-circRNAs), PML::RAR α and KMT2A::MLLT3	Leukemia	Not mentioned
[31]	Electrochemical and Optical Analysis of Various Compositions of Au and Ag Layers for Blood Cancer Prognosis	Prognostic biomarker of blood	Electrochemical and optical analysis, Ag/Au thin film electrode	Leukemia	Not mentioned
[32]	An Optimized Single Nucleotide Polymorphism-Based Detection Method Suggests That Allelic Variants in the 3' Untranslated Region of RRAS2 Correlate with Treatment Response in Chronic Lymphocytic Leukemia Patients	RS8570 position in the 3'-untranslated region of RRAS2	Single qPCR method, RRAS2 Correlate, polymerase chain reaction (PCR)	Chronic Lymphocytic Leukemia	Not mentioned
[33]	Machine Learning Driven Dashboard for Chronic Myeloid Leukemia Prediction using Protein Sequences	Protein Sequences, hematopoietic progenitor cells, mutated genes like BCL2, HSP90, PARP, and RB	Machine Learning and Data Science, feature extraction of Di-peptide Composition (DPC), Amino Acid Composition (AAC), and Pseudo amino acid composition (Pse-AAC), Support Vector Machine (SVM), XGBoost, Random Forest (RF), K Nearest Neighbour (KNN), Decision Tree (DT), and Logistic Regression (LR)	Chronic Myeloid Leukemia	94%
[34]	Automated Leukemia Screening and Sub-types Classification Using Deep Learning	Blood and bone marrow, complete blood count test	FAB classification, i.e., L1, L2, and L3 types, microscopic inspection of blood smears and bone marrow aspiration	Leukemia and ALL	96.06%
[35]	Hematologic Cancer Detection Using White Blood Cancerous Cells Empowered with Transfer Learning and Image Processing	Immature lymphocytes, monocytes, neutrophils, and eosinophil cells	Deep learning, AlexNet, MobileNet, and ResNet	Lymphoma and Leukemia	97.30%

[36]	Applications of Machine Learning in Chronic Myeloid Leukemia	Myeloid cells in the bone marrow, neutrophils	Artificial intelligence; chronic myeloid leukemia; machine learning; convolutional neural networks; hemoglobinopathies	Chronic myeloid leukemia (CML)	Not mentioned
[37]	Automated Acute Lymphoblastic Leukemia Detection Using Blood Smear Image Analysis	Blood cells of bone marrow	Image processing and artificial intelligence methods. Machine learning– and deep learning	Acute lymphoblastic leukemia (ALL)	Not mentioned

4. Proposed methodology

In our proposal approach, we outline a methodology for analysing blood reports sourced from the pathological department, focusing on various blood parameters to discern correlations with different types of blood cancers, such as Chronic Myeloid Leukemia (CML), Acute Myeloid Leukemia (AML), Non-Hodgkin's Lymphoma (NHL), and Normal Leukocyte (NL). Our proposed method leverages the clustering concept of the K-means algorithm to conduct an in-depth analysis aimed at identifying similarities among these parameters for each type of blood cancer. By employing this approach, we aim to group similar features together, providing valuable insights into potential patterns and relationships within the dataset. The proposed methodology is illustrated in the Figure 4.1.

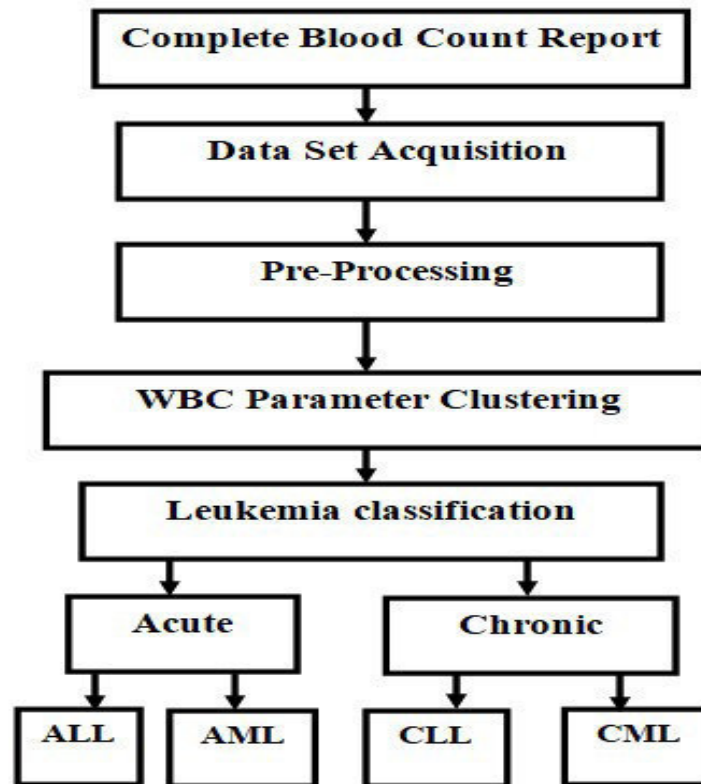


Figure 4.1: Proposed methodology for Leukemia classification

5. Conclusion: Blood cancer poses unique challenges due to its varied subtypes and diagnostic intricacies. This paper has tried to present an overview of leukemia classification and diagnostic methodologies, evaluating various detection approaches, and presented research contributions. The literature review analysed traditional diagnostic techniques alongside recent advancements such as terahertz radiation and machine learning algorithms, stating their potential in enhancing diagnostic accuracy. Furthermore, we are proposing an approach that utilizes clustering techniques to uncover patterns within the dataset, aiming to provide insights that could potentially enhance patient outcomes and inform treatment strategies.

References

1. Cheon, Hwayeong, Jin Ho Paik, Moran Choi, Hee-Jin Yang, and Joo-Hiuk Son. "Detection and manipulation of methylation in blood cancer DNA using terahertz radiation." *Scientific reports* 9, no. 1 (2019): 6413.
2. Xing, Wenchao, and Yilin Bei. "Medical health big data classification based on KNN classification algorithm." *IEEE Access* 8 (2019): 28808-28819.

3. Safuan, Syadia Nabilah Mohd, Mohd Razali Md Tomari, Wan Nurshazwani Wan Zakaria, Mohd Suriani. "Investigation of white blood cell biomaker model for acute lymphoblastic leukemia detection based on convolutional neural network." *Bulletin of Electrical Engineering and Informatics* 9, no. 2 (2020): 611-618.
4. Nighat, Misba Sikandar, Ikram Ud Din, Ahmad Almogren, and Sikandar Ali. "IoMT-based automated detection and classification of leukemia using deep learning." *Journal of healthcare engineering* 2020 (2020): 1-12.
5. Hossain, Mohammad Akter, Mubtasim, Muntasir, AKM, Islam, and Ashir Ahmed. "Leukemia detection mechanism through microscopic image and ML techniques." In *2020 IEEE REGION 10 CONFERENCE (TENCON)*, pp. 61-66. IEEE, 2020.
6. Aftab, Muhammad Omer, Mazhar Javed Awan, Shahid Khalid, Rabia Javed, and Hassan Shabir. "Executing spark BigDL for leukemia detection from microscopic images using transfer learning." In *2021 1st International Conference on Artificial Intelligence and Data Analytics (CAIDA)*, pp. 216-220. IEEE, 2021.
7. Genovese, Angelo, Mahdi S. Hosseini, Vincenzo Piuri, Konstantinos N. Plataniotis, and Fabio Scotti. "Acute lymphoblastic leukemia detection based on adaptive unsharpening and deep learning." In *ICASSP 2021-2021 IEEE International Conference on Acoustics, Speech and Signal Processing (ICASSP)*, pp. 1205-1209. IEEE, 2021.
8. Pałczyński, Krzysztof, Sandra Śmigiel, Marta, Sławomir Bujnowski, and Zbigniew Lutowski. "IoT application of transfer learning in hybrid artificial intelligence systems for acute lymphoblastic leukemia classification." *Sensors* 21, no. 23 (2021): 8025.
9. Kumar, T. Ananth, K. Suresh Kumar, and A. Jayakumar. "Analysis of IoT based Leukemia Detection Techniques." (2022).
10. Atteia, Ghada, Amel A. Alhussan, and Nagwan Abdel Samee. "Bo-allcnn: Bayesian-based optimized cnn for acute lymphoblastic leukemia detection in microscopic blood smear images." *Sensors* 22, no. 15 (2022): 5520.
11. Zhong, Pengqiang, Mengzhi Hong, Huanyu He, Jiang Zhang, Yaoming Chen, Zhigang Wang, Peisong Chen, and Juan Ouyang. "Diagnosis of Acute Leukemia by Multiparameter Flow Cytometry with the Assistance of Artificial Intelligence." *Diagnostics* 12, no. 4 (2022): 827.
12. Hoffmann, Joerg, Michael C., Malte von Bonin, , Alfred Ultsch, and Cornelia Brendel. "Identification of critical haemodilution by artificial intelligence in bone

- marrow assessed for minimal residual disease analysis in acute myeloid leukemia: The Cinderella method." *Cytometry Part A* 103, no. 4 (2023): 304-312.
13. Khademi, Reyhane, Zahra Mohammadi, Saghazadeh, and Rezaei. "Nanotechnology-based diagnostics and therapeutics in acute lymphoblastic leukemia: a systematic review of preclinical studies." *Nanoscale Advances* (2023).
14. Hossain, Mohammad Akter, AKM Muzahidul Islam, , and Ashir Ahmed. "Symptom based explainable artificial intelligence model for leukemia detection." *IEEE Access* 10 (2022): 57283-57298.
15. Malik, Saroosh, Arslan Iftikhar, Faheem Haider Tauqeer, Muhammad Adil, and Sheeraz Ahmed. "A Systematic Literature Review on Leukemia Prediction Using Machine Learning." *Journal of Computing & Biomedical Informatics* 3, no. 02 (2022): 104-123.
16. Ananth, Christo, K. Mystica, M. Sridharan, S. Aaron James, and T. Ananth Kumar. "An Advanced Low-cost Blood Cancer Detection System." *International Journal of Early Childhood Special Education* 14, no. 5 (2022).
17. Sridhar, K., Ajay Reddy Yeruva, Dixit, Aatif Jamshed, and Ravi Rastogi. "Enhanced Machine learning algorithms Lightweight Ensemble Classification of Normal versus Leukemic Cel." *Journal of Pharmaceutical Negative Results* (2022): 496-505.
18. Das, Pradeep Kumar, V. A. Diya, Panda, and Ajith. "A systematic review on recent advancements in deep & machine learning based detection and classification of acute lymphoblastic leukemia." *IEEE access* (2022).
19. Hossain, Mohammad Akter, AKM Ahmed. "Symptom based explainable artificial intelligence model for leukemia detection." *IEEE Access* 10 (2022): 57283-57298.
20. Devi, Tulasi Gayatri, Nagamma Patil, Sharada Rai, and "Gaussian blurring technique for detecting and classifying acute lymphoblastic leukemia cancer cells from microscopic biopsy images." *Life* 13, no. 2 (2023): 348.
21. Della Starza, Irene, Lucia Anna De Novi, Loredana Elia, Vittorio Bellomarino, Marco Beldinanzi, Roberta Soscia, Deborah Cardinali, Sabina Chiaretti, Anna Guarini, and Robin Foà. "Optimizing molecular minimal residual disease analysis in adult acute lymphoblastic leukemia." *Cancers* 15, no. 2 (2023): 374.
22. Varadarajan, Indumathy, Eric Pierce, Chaer, and Michael Keng. "Post-Hematopoietic Cell Transplantation Relapsed Acute Lymphoblastic Leukemia: Current Challenges and Future Directions." *OncoTargets and Therapy* (2023): 1-16.

23. Hoffmann, Joerg, Semil Eminovic, Christian Wilhelm, Stefan W. Krause, Andreas Neubauer, Michael C. Thrun, Alfred Ultsch, and Cornelia Brendel. "Prediction of Clinical Outcomes with Explainable Artificial Intelligence in Patients with Chronic Lymphocytic Leukemia." *Current Oncology* 30, no. 2 (2023): 1903-1915.
24. Khalil, Mohamed, Nahla Elsharkawy, Mona Mohsen Elmawardy, and Mahmoud Aly Ayoub. "Prognostic role of CD200 in acute lymphoblastic leukemia patients." *Diagnostics* 13, no. 2 (2023): 325.
25. Liu, Hui. "SETD2 detection may reveal response to induction therapy and survival profile in acute myeloid leukemia patients." *Hematology* 28, no. 1 (2023): 2161194.
26. Brito-Rocha, Tiago, Vera Constâncio, Rui Henrique, and Carmen Jerónimo. "Shifting the cancer screening paradigm: the rising potential of blood-based multi-cancer early detection tests." *Cells* 12, no. 6 (2023): 935.
27. Shahini, Endrit, Giuseppe Claudio Tiribelli, Raffaele Cozzolongo, and Gianluigi Giannelli. "Updating the Clinical Application of Blood Biomarkers and Their Algorithms in the Diagnosis and Surveillance of Hepatocellular Carcinoma: A Critical Review." *International Journal of Molecular Sciences* 24, no. 5 (2023): 4286.
28. Piccaluga, Pier Paolo, Stefania Paolini, and Giuseppe Visani. "Antigen Receptors Gene Analysis for Minimal Residual Disease Detection in Acute Lymphoblastic Leukemia: The Role of High Throughput Sequencing." *Hemato* 4, no. 1 (2023): 42-55.
29. Naveed, Muhammad, Muhammad Aqib Shabbir, Metab Alharbi, Abdulrahman Alsahammari, and Abdullah F. Alasmari. "AI Assisted Pharmacophore Design for Philadelphia Chromosome-Positive Leukemia with Gamma-Tocotrienol: A Toxicity Comparison Approach with Asciminib." *Biomedicines* 11, no. 4 (2023): 1041.
30. Molin, Anna, Caterina Tretti Parenzan, Cristina Borin, Elena Boldrin, Lueder H. Meyer, Geertruij Te Kronnie, Silvia Bresolin, and Stefania Bortoluzzi. "Discovery of fusion circular RNAs in leukemia with KMT2A:: AFF1 rearrangements by the new software CircFusion." *Briefings in Bioinformatics* 24, no. 1 (2023): bbac589.
31. Farahdina, Ulya, Amastasia Salsabila Muliawati, Hari, Darsono Darsono, Nasori, and Agus Rubiyanto. "Electrochemical and Optical Analysis of Various Compositions of Au and Ag Layers for Blood Cancer Prognosis." *Coatings* 13, no. 1 (2023): 186.
32. Hortal, Alejandro, Marta Lacuna, Claudia Cifuentes, Miguel Alcoceba, Xosé R. Bustelo, Marcos González, and Balbino Alarcón. "An Optimized Single Nucleotide Polymorphism-Based Detection Method Suggests That Allelic Variants in the

- 3'Untranslated Region of RRAS2 Correlate with Treatment Response in Chronic Lymphocytic Leukemia Patients." *Cancers* 15, no. 3 (2023): 644.
33. Ahmad, W.; Iqbal, M.; Amin, Shahzad, A.R. Machine Learning Driven Dashboard for Chronic Myeloid Leukemia Prediction using Protein Sequences. *Preprints* 2023, 2023120053. <https://doi.org/10.20944/preprints202312.0053.v1>
34. Penmetsa, Venkat, Lachin Fernando, and Sindhu Ghanta. "Improving AML Diagnosis Precision: Deep Learning-Based Classification of Leukocyte Morphology and Malignancy." In *2023 International Conference on Machine Learning and Applications (ICMLA)*, pp. 2119-2124. IEEE, 2023.
35. Mansor, Muhammad, Farah Hanan Mohd Faudzi, Syahrul Affandi Saidi, Mohd Aminudin Jamlos, Noor Anida Abu Talib, and Ahmad Kadri Junoh. "Leukemia Blood Cells Detection using Neural Network Classifier." *Journal of Advanced Research in Applied Sciences and Engineering Technology* 33, no. 1 (2023): 152-162.
36. Sakthivel, M., Md Sakiul Islam Sudman, K. Ravishankar, Bhagyalakshmi Avinash, Anup Kumar, and Muruganantham Ponnusamy. "Medical Image Analysis of Multiple Myeloma Diagnosis Using CNN and KNN Based Approach." In *2023 International Conf. on Self Sustainable AI Systems (ICSSAS)*, pp. 92-97. IEEE, 2023
37. Rawal, Kartik, Advika Parthvi, Dilip Kumar Choubey, and Vaibhav Shukla. "Prediction of leukemia by classification and clustering techniques." In *Machine Learning, Big Data, and IoT for Medical Informatics*, pp. 275-295. Academic Press, 2021.



iJRASET

International Journal For Research in
Applied Science and Engineering Technology



INTERNATIONAL JOURNAL FOR RESEARCH

IN APPLIED SCIENCE & ENGINEERING TECHNOLOGY

Volume: 12 Issue: V Month of publication: May 2024

DOI: <https://doi.org/10.22214/ijraset.2024.61392>

www.ijraset.com

Call:  08813907089

E-mail ID: ijraset@gmail.com

GreenRoute Ballari: A Hybrid Approach for Optimizing Waste Collection Routes Using K-Means Clustering and Genetic Algorithm

Manasa Bellamkonda¹, Dinesh N², K Pravallika³, Zaheed Hussain⁴, Noorullah Shariff C⁵

^{1, 2, 3, 4, 5}Department of Artificial Intelligence and Machine Learning, Ballari Institute of Technology and Management, Ballari, Karnataka, India

Abstract: *The exponential growth of the population in Ballari has exacerbated the challenge of municipal waste management, necessitating the development of efficient waste collection strategies to address environmental and social concerns. In response to that our system introduces a hybrid approach that employs K-means clustering and Genetic Algorithm, for optimizing waste collection routes tailored to the unique waste generation profiles of the region. By utilizing Geographic Information System (GIS) data that is in the form of GeoJSON files containing the spatial distribution of waste collection points, we propose a methodology that combines K-means clustering and Genetic Algorithm to develop intelligent and fuel-efficient routes. Our system not only benefits municipal authorities in resource deployment and planning but also aids waste carrier vehicle drivers in prioritizing routes. Our findings contribute to the transformation of Ballari City towards eco-friendly and smart urban development.*

Keywords: *Waste Management, Route Optimization, Genetic Algorithm, K-Means Clustering, Urban Logistics.*

I. INTRODUCTION

The ever-growing problem of waste generation, particularly plastic waste, poses a significant environmental and economic threat to Ballari, Karnataka, as it does in many urban centers worldwide. Traditional methods often rely on static routes, leading to inefficiencies such as unnecessary travel distances, increased fuel consumption, and higher operational costs [4]. While GIS-based route optimization offers promise [2], a deeper understanding of how factors like waste composition, collection frequency, and truck design interact with each other is essential for even greater optimization [3, 5]. The GreenRoute Ballari proposes a novel system to address these challenges by leveraging machine learning and advanced route optimization techniques. This approach builds upon existing research on factors affecting route optimization. Unlike traditional methods that rely on static data, our system utilizes machine learning to predict waste volume and composition at collection points dynamically. This allows for a more data-driven and adaptable approach to route planning, similar to the work by Sutana (2021) who emphasizes the importance of dynamic factors in waste management systems [1]. As of March 2023, the Ballari City Corporation has 39 wards. 600 Pourakarmikas work day and night to make Ballari clean. Each ward is assigned nearly 2 vehicles if the ward is small, else 3-4 vehicles if the ward is huge. Large 12-ton vehicles carry the collected waste out of the city from the collection point near Stadium Road in the city. These large vehicles make 2-3 trips daily to dump all the waste, as Ballari daily puts up nearly 180 tonnes of waste.

A. Green Route Ballari factors in these Specifics, Including

- 1) *Limited Vehicle Availability:* The system considers the number of collection vehicles available in each ward (2-4).
- 2) *Dynamic Waste Prediction:* Machine learning algorithms predict waste volume and composition for each collection point, optimizing routes based on real-time data.
- 3) *Time Window Constraints:* The system accounts for designated collection times in each ward to ensure efficient scheduling.
- 4) *Unique Traffic Patterns and Road Conditions:* GreenRoute Ballari incorporates Ballari's unique traffic patterns and road conditions to optimize routes for faster collection times.

B. By optimizing routes based on these factors, Green Route Ballari aims to achieve significant benefits for Ballari

- 1) *Reduced Fuel Consumption:* Optimized routes minimize travel distances, leading to substantial fuel cost savings for the Ballari Municipal Corporation or private waste collection companies.

- 2) *Improved Operational Efficiency*: More efficient routes allow for faster collection times and better utilization of collection vehicles, reducing overall operational costs.
- 3) *Environmental Sustainability*: Reduced fuel consumption translates to lower greenhouse gas emissions, contributing to a cleaner Ballari.
- 4) *Unlocking Economic Opportunities*: By accurately predicting waste composition, Green Route Ballari can help identify waste segregation and resource recovery opportunities, particularly valuable wet waste that can benefit farmers.

C. The GreenRoute Ballari system Caters to a Diverse Audience within the waste Collection Management Ecosystem

- 1) *Waste Management Authorities*: Gain real-time data and insights to optimize waste collection strategies and ensure regulatory compliance.
- 2) *Fleet Managers*: Utilize the system to monitor and manage the waste collection fleet, optimize routes, and schedule vehicle maintenance.
- 3) *Waste Collection Drivers*: Receive optimized routes through a user-friendly interface, facilitating navigation and communication with the system.
- 4) *System Administrators*: Maintain the system, manage user access, and troubleshoot any technical issues.
- 5) *Government Officials*: Leverage data-driven insights for informed decision-making regarding waste management policies and resource allocation.

D. GreenRoute Ballari's key Features Include

- 1) *Data Storage and Analysis*: Stores and analyses historical and real-time data to generate route optimization strategies and operational insights.
- 2) *Machine Learning for Waste Prediction*: Employs machine learning algorithms to predict waste volume and composition at collection points, enabling dynamic route planning.
- 3) *Genetic Algorithm for Route Optimization*: Utilizes a GA to optimize waste collection routes based on dynamic waste prediction and collection point data.
- 4) *Mapping Integration*: Optimized routes are visually displayed to drivers through integration with mapping services like MapBox API, aiding navigation.
- 5) *User Interface*: User-friendly interfaces for municipal administrators and drivers display optimized routes, collection points, and real-time updates.
- 6) *Security Measures*: Secure communication protocols ensure the confidentiality of route information sent to drivers.

By implementing the GreenRoute Ballari project, Ballari can move towards a more efficient, cost-effective, and sustainable waste management system, paving the way for a cleaner, healthier, and more resource-conscious future.

II. LITERATURE REVIEW

SL.NO	Title	Author	Findings
[1]	A Genetic Algorithm Approach for Waste Collection Using Multi-trip Multi-period Capacitated Vehicle Routing Problem with Time Windows (MCVRPTW)	Nur Layli Rachmawati, Yelita Anggiane Iskandar, Dian Permana Putri, Mirna Lusiani	The main findings of the study include the successful application of the Genetic Algorithm (GA) to optimize waste collection routes, resulting in significant cost savings of around 30% compared to existing conditions. The study also highlights the importance of route optimization in waste management to improve overall operational efficiency and reduce transportation costs.

[2]	Waste Collection Area Generation Using a 2 Stage Cluster Optimization Process and GIS Data	Tyler Parsons, Jaho Seo, Dan Livesey	The proposed clustering techniques improved the balance of dwelling units in collection areas by 87.75% compared to the current arrangement. There was a 38.04% and 37.54% improvement in simulated statistics for Week 1 and Week 2 collections, respectively.
[3]	Route optimization for city cleaning vehicle	Łukasz Wojciechowski, Tadeusz Cisowski, Arkadiusz Małek	This paper represents the route optimization solution for vehicles collecting waste, aiming to determine the driving order across the city lanes. Also, this paper uses multi-criteria optimization for the collection and disposal of municipal waste which combines various methods into one hybrid computational process.
[4]	Optimal Route Recommendation for Waste Carrier Vehicles for Efficient Waste Collection: A Step Forward Towards Sustainable Cities	Shabir Ahmad, Faisal Jamil, Naeem Iqbal, Dohyeun Kim	This paper proposes an optimal route recommendation system for waste carrier vehicles to collect waste efficiently based on the behavior of people in specific grid locations. Its objective is to minimize the distance traveled by carrier vehicle which in turn minimizes fuel consumption and maximize waste collection by utilizing historical data and predictive algorithms.
[5]	Interactions of residential waste composition and collection truck compartment design on GIS route optimization	Hoang Lan Vu, Kelvin Tsun, Wai Ng, Bahareh Fallah, Amy Richter, Golam Kabir	Waste density and collection frequency significantly impact travel distances and time in waste collection. Increasing truck capacity and using dual-compartment trucks can lead to substantial savings. The optimal volume ratio of truck compartments is 50:50.

III.METHODOLOGY

This section presents a methodology for optimizing waste collection routes in Ballari City using a combination of K-means clustering and Genetic Algorithm. The main aim of the system is to optimize the total distance traveled by waste collection vehicles while considering capacity constraints. Initially, the system utilizes Geographic Information System (GIS) data that is in the form of GeoJSON files containing the spatial distribution of waste collection points. Further, K-Means Clustering is employed to group these points into clusters, representing potential stops for waste collection vehicles. Subsequently, the Genetic Algorithm is applied to generate optimized routes for waste collection vehicles within each cluster, by considering vehicle capacity limitations. The proposed methodology aims to improve the effectiveness of waste collection operations, leading to improved resource utilization, reduced fuel consumption, and lower emissions.

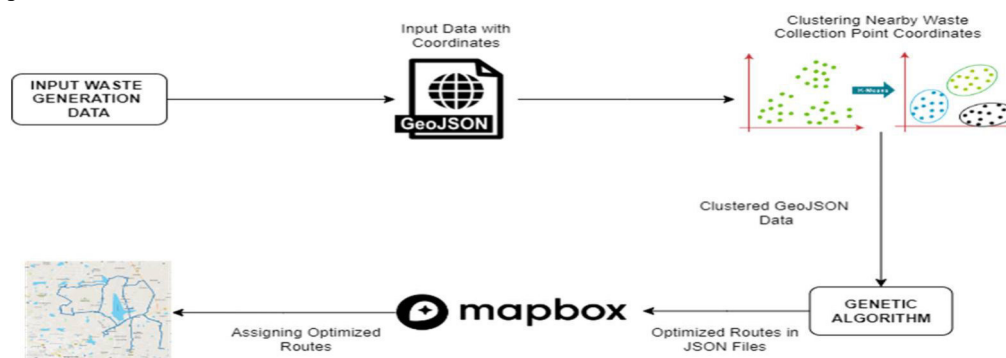


Fig. 1 Block diagram representing vehicle route optimization methodology

A. Data Collection and Clustering Using K-Means Clustering Algorithm

The input data consists of spatial information about waste generation zones, including zone identifiers, zone names, population, and waste generation volumes. To prepare the data for route optimization, the coordinates of waste generation zones are extracted from the GeoJSON files. K-Means Clustering is then applied to group these coordinates into clusters, each representing a potential stop for waste collection vehicles. Here, the predetermined number of clusters is based on the availability of waste collection vehicles.

B. Genetic Algorithm for Route Optimization

The Genetic Algorithm is employed to optimize the routes for waste collection within each cluster. The Genetic Algorithm undergoes the following sequence of steps:

- 1) *Initialization:* An initial population of routes is generated. Each route represents a sequence of waste collection points within a cluster, ensuring that each point is visited exactly once
- 2) *Fitness Evaluation:* The fitness of each route is evaluated based on the total distance traveled. The distance matrix between waste collection points is computed using geographical coordinates. Lower total distances indicate fitter routes
- 3) *Selection:* The parent routes for the next generation are chosen based on their fitness level. This selection process employs a mechanism such as tournament selection or roulette wheel selection to identify the fittest individuals within the population.
- 4) *Crossover:* The crossover is applied to selected parent routes to generate offspring. The crossover point is selected randomly, and segments of routes beyond the crossover point are swapped between parents to create new routes.
- 5) *Mutation:* The mutation is introduced to maintain genetic diversity within the population. Randomly selected genes (waste collection points) in individual routes are swapped or altered with a certain probability.
- 6) *Replacement:* Here, the newly generated optimized routes through crossover and mutation are replaced by the least optimal routes. Such that this ensures that the most optimal routes are evolved over successive generations.
- 7) *Termination:* The algorithm terminates after a predefined number of generations or when a convergence criterion is met. The best-performing routes found during the optimization process are selected as the final solution.

C. Route Assignment to Vehicles

Once optimized routes are derived for every cluster, the routes need to be assigned to available waste collection vehicles while adhering to capacity constraints. The waste generation volume of each waste collection point is considered in this step. Points are assigned to vehicles based on their proximity to each other and the capacity of the vehicles. A vehicle's capacity is determined by the maximum volume of waste it can carry. The assignment process ensures that each vehicle's capacity is not exceeded, and waste collection points are efficiently distributed among vehicles.

IV. RESULTS AND DISCUSSIONS

In this section, the outcomes of the GreenRoute Ballari project are illustrated that are obtained by applying a combination of K-means clustering and Genetic algorithm to the waste collection input data points, we obtained optimized waste collection routes for various areas across Ballari City. The specific coordinate data used for mapping is simulated due to the unavailability of Ballari's precise data. The below figures present the visual representation of optimized routes for waste collection using MapBox API.



Fig. 2 Vehicle 1 route

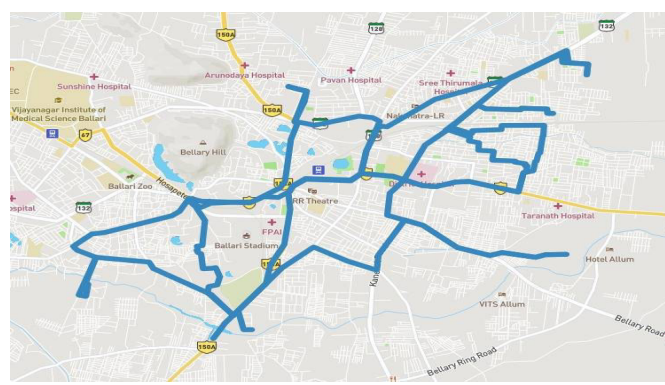


Fig. 3 Vehicle 2 route

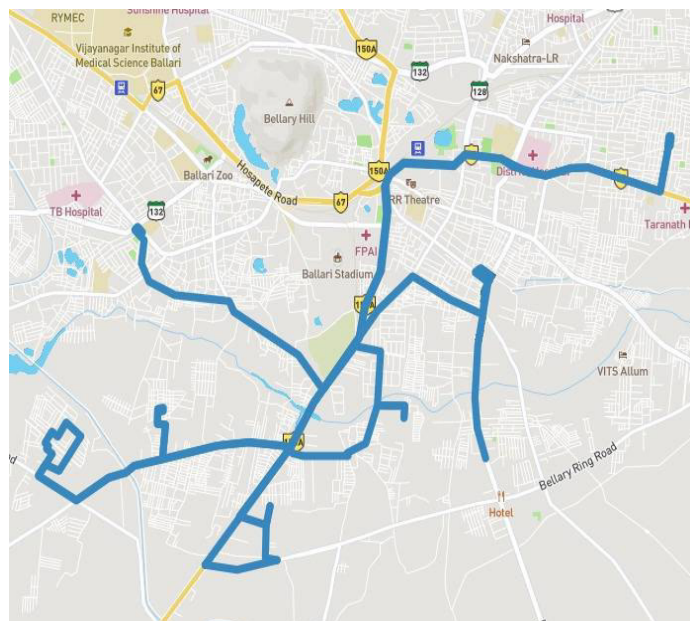


Fig. 4 Vehicle 5 route

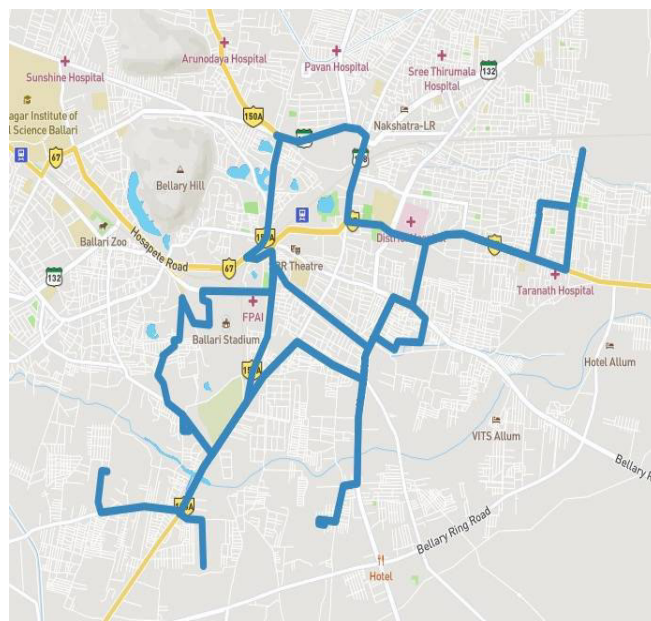


Fig. 5 Vehicle 7 route

A. Route Optimization Results

Implementing K-means clustering and Genetic Algorithm yielded optimized waste collection routes tailored to the specific spatial distribution of waste generation points in the study area. Here are the key findings:

- 1) *Reduced Travel Distances:* The optimized routes significantly reduced the total travel distances compared to traditional static routes, resulting in more fuel-efficient and cost-effective waste collection operations.
- 2) *Improved Operational Efficiency:* By minimizing travel distances and optimizing stop sequences, the waste collection vehicles were able to complete their routes more efficiently, leading to reduced operational costs and increased productivity.
- 3) *Dynamic Adaptation:* Applying machine learning to predict the waste allowed the system to dynamically adapt to changing waste generation patterns, ensuring that the routes remained optimal and responsive to real-time conditions.

B. Mapping Results

Despite using coordinate data from Ballari for visualization purposes, the mapping of optimized routes using MapBox API provided insightful representations of the optimized waste collection routes. The map displayed:

- 1) *Clustered Collection Points:* The distinct clusters of waste collection points across Ballari City were represented by K-means clustering.
- 2) *Optimized Routes:* The optimized routes that are generated from the Genetic Algorithm are overlaid on the map, depicting the order of waste collection points within each cluster. These routes are optimized to minimize travel distances and adhere to capacity constraints.
- 3) *Visualization of Efficiency Gains:* Through the map interface, stakeholders could observe the spatial distribution of waste collection activities and the efficiency gains achieved through route optimization.

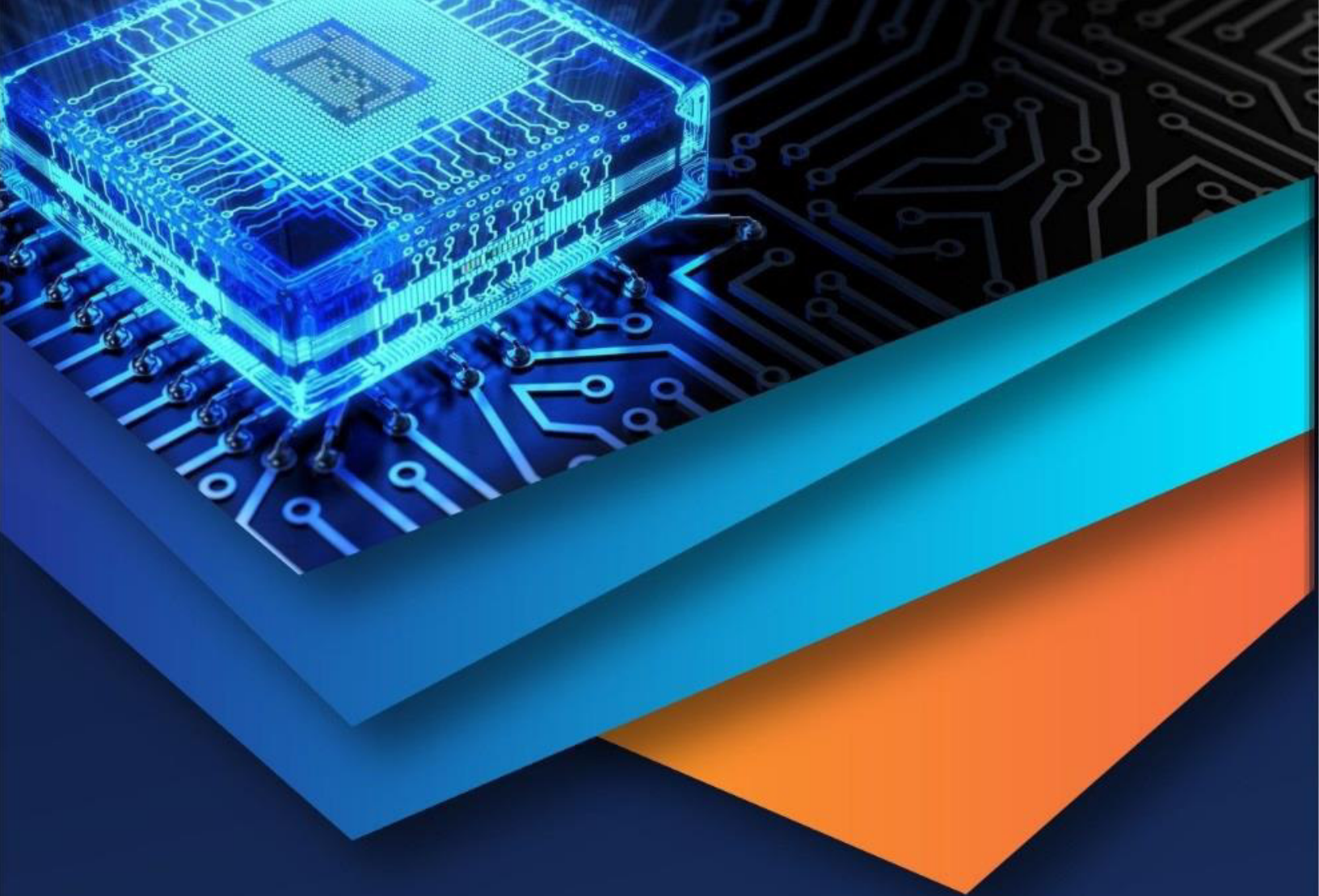
V. CONCLUSIONS

The effective management of municipal waste poses a significant challenge in the transformation of Ballari City towards eco-friendly and smart urban development. In this paper, we have proposed a system to optimize waste collection routes across Ballari City. In response to that, a combination of K-means clustering and genetic algorithms are used to obtain optimized routes using the waste collection points as input data. This approach aims to minimize travel distance, reduce fuel costs, and optimize time allocated for waste collection. The proposed system is beneficial for waste carrier truck drivers to prioritize the routes for waste collection. Additionally, the system benefits municipal authorities by enhancing resource deployment and planning. In conclusion, the system represents a significant step towards the sustainable development of Ballari City.



REFERENCES

- [1] S. Ahmad, Imran, F. Jamil, N. Iqbal, and D. Kim, "Optimal route recommendation for waste carrier vehicles for efficient waste collection: A step forward towards sustainable cities," IEEE Access, vol. 8, 2021, doi: 10.1109/ACCESS.2021.2988173.
- [2] T. Parsons, J. Seo, and D. Livesey, "Waste Collection Area Generation Using a 2 Stage Cluster Optimization Process and GIS Data," IEEE Access, vol. 11, pp. 11849-11859, 2023, doi: 10.1109/ACCESS.2023.3241626.
- [3] Ł. Wojciechowski, T. Cisowski, and A. Małek, "Route optimization for city cleaning vehicle," Open Engineering, vol. 11, no. 1, 2021, doi: 10.1515/eng-2021-0049.
- [4] H. L. Vu, K. T. W. Ng, B. Fallah, A. Richter, and G. Kabir, "Interactions of residential waste composition and collection truck compartment design on GIS route optimization," Waste Management, vol. 102, 2020, doi: 10.1016/j.wasman.2019.11.028.
- [5] N. L. Rachmawati, Y. A. Iskandar, D. P. Putri, and M. Lusiani, "A Genetic Algorithm Approach for Waste Collection Using Multi-trip Multi-period Capacitated Vehicle Routing Problem with Time Windows (MCVRPTW)," 2023. doi: 10.46254/an13.20230217.



10.22214/IJRASET



45.98



IMPACT FACTOR:
7.129



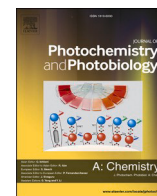
IMPACT FACTOR:
7.429



INTERNATIONAL JOURNAL FOR RESEARCH

IN APPLIED SCIENCE & ENGINEERING TECHNOLOGY

Call : 08813907089  (24*7 Support on Whatsapp)



Imidazole-centred cupric ions sensor: Experimental validation, theoretical understanding, and zebrafish bioimaging

Keshav Kumar Harish^{a,1}, Aravind R. Nesaragi^{b,c,*}, Naveen Kumar Kalagatur^d, Praveen Naik^e, Mahendra Madegowda^{a,*}, Anup Pandith^{f,*}, Kholood A. Dahlous^g, Saikh Mohammad^g, H.P. Shivarudrappa^h, T.M. Sharanakumarⁱ, H. Guddappa^j

^a Department of Studies in Physics, University of Mysore, 570005 Karnataka, India

^b Centre for Nano and Material Sciences, Jain (Deemed-to-be University), Jain Global Campus, Kanakapura, Bangalore, 562112 Karnataka, India

^c Department of Chemistry, Indian Institute of Technology, Dharwad 580007, Karnataka, India

^d DRDO-BU, Centre for Life Sciences, Coimbatore 641 046, Tamil Nadu, India

^e Department of Chemistry, Nitte Meenakshi Institute of Technology, Yelahanka, Bengaluru 560064, Karnataka, India

^f International Ph.D. Program in Biomedical Engineering (IPBME), College of Biomedical Engineering, Taiping Medical University, Taiping 11031, Taiwan

^g Department of Chemistry, College of Science, King Saud University, Riyadh 11451, Saudi Arabia

^h College of Pharmacy and Integrated Research Institute for Drug Development, Dongguk University, Goyang 10325, South Korea

ⁱ Department of Chemistry, Ballari Institute of Technology and Management, Ballari 583104, Karnataka, India

^j Department of Chemistry, ATME College of Engineering, Mysuru 570028, Karnataka, India

ARTICLE INFO

Keywords:

Bio-imaging
Coumarin
Cytotoxicity
Cu²⁺ sensor
Imidazole
Zebrafish

ABSTRACT

In this study, we have developed an imidazole centered fluorescent probe 3-(2-(2-(5-bromo-2-hydroxyphenyl)-4,5-diphenyl-1H-imidazol-1-yl)thiazol-4-yl)-6-chloro-2H-chromen-2-one (SICT), achieving exceptional selectivity for Cu²⁺ ion detection. These probes exhibit rapid responsiveness (109 nM detection limit) and strong binding constants ($0.214 \times 10^5 \text{ M}^{-1}$). Employing an aqueous ethanol system, we assessed their sensing capabilities through both *in vitro* and *in vivo* studies, using zebrafish as our model organism. Notably, the SICT probe displays a high quantum yield of 0.62 and follows a 1:1 binding mechanism with Cu²⁺ ions, validated by Job's plot and ESI-Mass spectrum analyses. Furthermore, our probe demonstrates minimal cytotoxicity in both *in vitro* (MDA-MB-231 cells) experiments. These promising results motivate us to apply the SICT probe for intracellular Cu²⁺ ion tracking in zebrafish embryos, showcasing its potential in diverse fields like biomedicine and environmental monitoring.

1. Introduction

In recent years, the presence of toxic heavy metal ions has emerged as a pressing concern, posing significant threats to the environment and public health. Among these hazardous species, copper ions (Cu²⁺) hold a unique position as both an essential micronutrient for humans and a potential source of toxicity when present in excessive concentrations, notably in natural aqueous environments [1–3]. Cu²⁺ plays a pivotal role in various biological processes, encompassing bone formation, connective tissue development, and cellular respiration, yet its overabundance can lead to various health-related complications [4–8].

Regulatory bodies such as the World Health Organization (WHO) and the U.S. Environmental Protection Agency (EPA) have, therefore, established stringent guidelines stipulating maximum permissible Cu²⁺ concentrations in drinking water to safeguard human well-being [9]. Consequently, there is an increasing demand for developing efficient sensing probes with high selectivity and sensitivity, mainly aimed at detecting trace Cu²⁺ ions in complex matrices such as drinking water and agricultural products. To address this challenge, the scientific community has shown a growing interest in the design and synthesis of fluorescent chemosensors, seeking to provide robust solutions for the sensitive detection of metal ions within both environmental and

* Corresponding authors at: Centre for Nano and Material Sciences, Jain (Deemed-to-be University), Jain Global Campus, Kanakapura, Bangalore, 562112 Karnataka, India (A.R. Nesaragi); Department of Studies in Physics, University of Mysore – 570005, Karnataka, India (M. Madegowda); International Ph.D. Program in Biomedical Engineering (IPBME), College of Biomedical Engineering, Taiping Medical University, Taiping – 11031, Taiwan (A. Pandith).

E-mail addresses: nesaragiaravind@gmail.com (A.R. Nesaragi), mahendra@physics.uni-mysore.ac.in (M. Madegowda), anupandith@tmu.edu.tw (A. Pandith).

¹ Indicates both the authors contributed equally to this manuscript.

biochemical contexts.

This endeavor explores novel recognition unit-fluorophore interactions, aiming to balance selectivity, sensitivity, and response time. Among the various detection methodologies available, ion-induced chemo-sensors have emerged as a particularly appealing approach due to their capacity for selective detection and rapid response times [10]. However, the design and construction of fluorescence-based turn-on and turn-off sensors remain intricate, given the tendency of biologically essential ions to quench Fluorescence. While numerous fluorescence chemo sensors have recently been proposed for selective metal ion detection, the literature still lacks comprehensive examples of selective Cu^{2+} ion sensing. Previous research has introduced various strategies, ranging from rhodamine B derivatized turn-off-on chemo sensors to thiophene-based Schiff base sensors and coumarin-quinoline-based sensors. These include a rhodamine B derivatized turn-off-on chemo-sensor designed by Zhihong Xu et al., demonstrating high sensitivity and selectivity for Cu^{2+} [11]. Suganya et al. introduced a thiophene-based Schiff base fluorescent sensor, exhibiting a colorimetric shift from yellow to colourless and a fluorescence 'turn-on' response upon encountering Cu^{2+} ions [12]. Yunling Gao et al. reported an innovative coumarin-quinoline-based sensor with a 1:1 binding stoichiometry, switching off in the presence of Cu^{2+} ions and effectively identifying Cu^{2+} in live breast cancer MCF-7 cells [13]. Hazem et al. presented an imidazole-based fluorescent sensor capable of detecting Cu^{2+} and bi-thiols in aqueous solutions, with increasing Cu^{2+} concentrations causing a red-shift in absorption and a transition from colourlessness to blue [14]. Araghni et al. introduced a turn-off-responsive 2,4,5-Tris(2-pyridyl)imidazole molecule for dual sensing of Hg^{2+} and Cu^{2+} ions in a HEPES buffer medium [15]. Additionally, Ayya et al. reported a ratio metric turn-on/turn-off benzothiazole-based chemo sensor, offering highly selective and sensitive detection of metal ions, including Zn^{2+} , Cu^{2+} , and Ni^{2+} [16]. Nevertheless, many of these sensors exhibit limitations, including insufficient selectivity, weak fluorescence outputs, and constrained applicability in living systems.

Despite these advancements, many described sensors face limitations, such as reduced selectivity towards Cu^{2+} ions, decreased fluorescence signals, and limited applicability in living systems, presenting ongoing challenges in developing reliable iron chemosensor. In this study, we introduce a novel imidazole coumarin-thiazole-based chemo sensor [17–19], 3-(2-(2-(5-Bromo-2-hydroxyphenyl)-4,5-diphenyl-1H-imidazol-1-yl)thiazol-4-yl)-6-chloro-2H-chromen-2-one (SICT), designed for efficient Cu^{2+} metal ion detection. We comprehensively analyze SICT's binding properties with various metal ions using UV absorption, fluorescence spectra, and pH-dependent studies. Supporting Density Functional Studies (DFT) is also performed to validate the sensor's behaviour. Our findings establish SICT as a promising compound for Cu^{2+} metal ion detection, addressing existing challenges in developing reliable iron chemosensors.

2. Experimental section

2.1. Synthesis of chemosensor 3-(2-(2-(5-bromo-2-hydroxyphenyl)-4,5-diphenyl-1H-imidazol-1-yl)thiazol-4-yl)-6-chloro-2H-chromen-2-one (SICT)

Mixture of 1,2-diphenylethane-1,2-dione (1.0 mmol, 0.210 g), 5-bromosalicylaldehyde (1.0 mmol, 0.20 g), 3-(2-aminothiazol-5-yl)-6-chloro-2H-chromen-2-one (1.0 mmol, 0.277 g) (4) and ammonium acetate (1.0 mmol, 0.077 g) were taken in an equimolar concentration and dissolved in acetic acid (~10 mL). The reaction mixture was ultrasonicated (~20 min) and refluxed for about 6 h. After the reaction, as monitored by TLC, the resultant mixture was cooled to room temperature and poured into crushed ice. The obtained crude product was purified through column chromatography to get the desired light yellowish solid (Yield: 94 %); ^1H NMR (400 MHz, $\text{DMSO}-d_6$) δ (ppm): δ 9.47 (s, 1H, Ar-H), 8.35 (s, 1H, Ar-H), 7.83 (m, 2H, Ar-H), 7.63–7.55 (m, 3H, Ar-H), 7.47–7.37 (m, 9H, Ar-

H), 7.28 (m, 2H, Ar-H), 6.98 (d, $J = 8.8$ Hz, 1H, Ar-H). ^{13}C NMR (100 MHz, $\text{DMSO}-d_6$) δ (ppm): 166.17, 164.25, 154.15, 154.57, 151.25, 146.38, 144.95, 144.11, 136.40, 135.16, 134.78, 134.16, 133.56, 132.33, 131.10, 129.94, 129.87, 129.60, 129.48, 128.26, 126.87, 126.22, 119.83, 118.58, 118.02, 116.83, 116.78, 116.42. MS m/z : 651 (M^+), 653 ($\text{M}+2$), 655 ($\text{M}+4$). Elem. Anal. Calcd for $\text{C}_{33}\text{H}_{19}\text{N}_3\text{O}_3\text{BrClS}$ (%): Calcd. C, 60.70; H, 2.93; N, 6.44; Found: C, 60.73; H, 2.98; N, 6.48.

3. Results and discussion

3.1. Chemistry

One of the starting material 3-(2-aminothiazol-5-yl)-6-chloro-2H-chromen-2-one (1) was synthesized according to the reported method with slight modification (ESI) [20]. The chemosensor 3-(2-(2-(5-bromo-2-hydroxyphenyl)-4,5-diphenyl-1H-imidazol-1-yl) thiazol-4-yl)-6-chloro-2H-chromen-2-one (SICT) has been developed by a straight forward synthetic strategy (Scheme 1). An equimolar mixture of 1,2-diphenylethane-1,2-dione, 5-bromosalicylaldehyde, 3-(2-aminothiazol-5-yl)-6-chloro-2H-chromen-2-one, ammonium acetate was ultrasonicated in ethanol in a one pot manner. The reaction mixture was refluxed to obtain the desired product in a high yield (88 %). The synthesized blue light emitting imidazole-coumarin thiazole-based fluorophore was used as chemosensor for metal ion sensing. The highly selective sensing ability of SICT prompted us to carry out a detailed study on metal ion sensing *in vitro* and *in vivo*.

3.2. Photochemistry

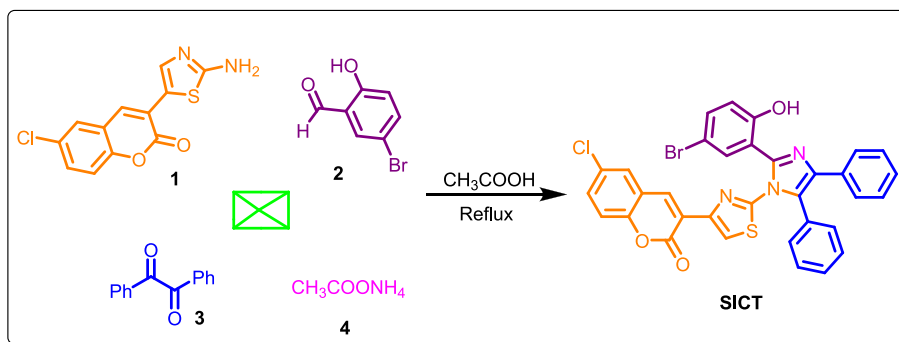
3.2.1. UV-Vis absorption studies

The selectivity of the fluorophore SICT towards various metal ions was assessed using UV-Vis absorption measurements. Electronic absorption spectra of SICT were recorded in the presence of different metal ions, including Al^{3+} , Cr^{3+} , Ga^{3+} , In^{3+} , Ca^{2+} , Cd^{2+} , Co^{2+} , Fe^{2+} , Mn^{2+} , La^{2+} , Na^{2+} , Sr^{2+} , Pb^{2+} , Mg^{2+} , Zn^{2+} and Ni^{2+} , all in an aqueous acetonitrile solution at physiological pH 7.2 conditions. Notably, distinctive changes were observed in the absorption spectra of SICT when Cu^{2+} ions were introduced, unlike the responses observed with the other metal ions under investigation (Fig. 1a). Specifically, SICT exhibited a unique responsiveness to Cu^{2+} ions compared to all other metal ions, which can be attributed to the formation of complexes through ligand-to-metal charge transfer (LMCT), involving the transfer of electrons from SICT to Cu^{2+} ions. The plot shows that SICT, combined with all other metal ions, resulted in a peak at 348 nm. However, when Cu^{2+} ions were introduced, the peak at 348 nm diminished, and a new peak emerged at 428 nm, indicative of the complexation between SICT and Cu^{2+} ions (Fig. 1a).

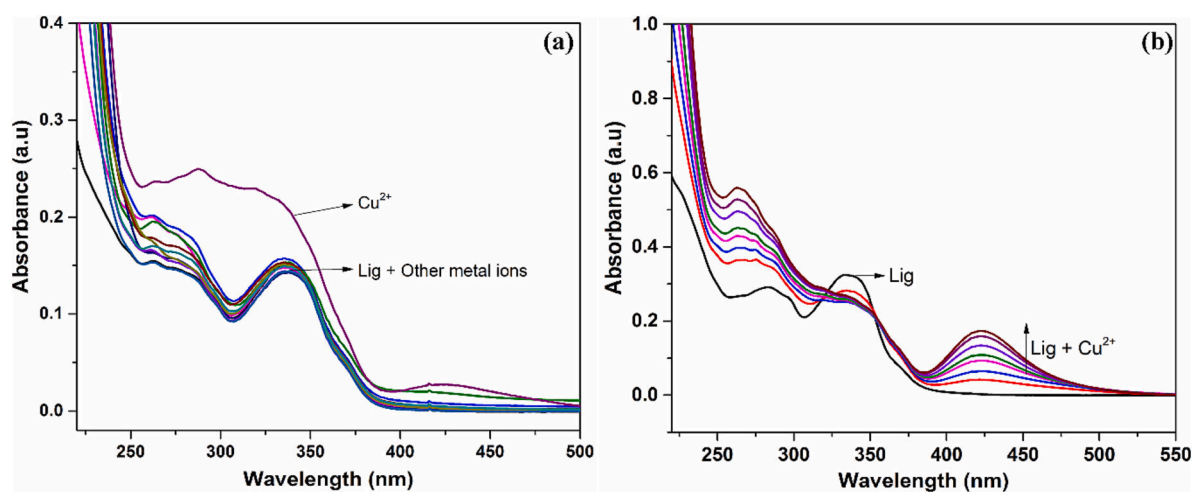
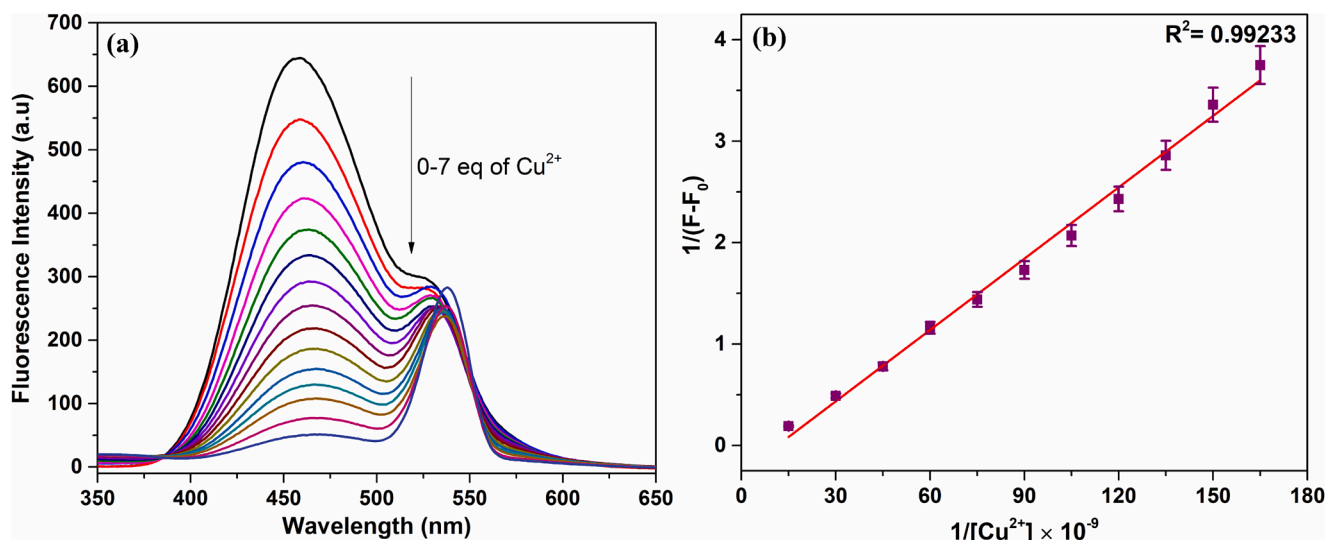
Furthermore, titration studies were conducted by recording UV-Visible absorption spectra of the chemosensor at different concentrations of Cu^{2+} ions, progressing until spectral changes ceased (up to 10 equivalents). The absorption data revealed that as Cu^{2+} concentration increased, the peak at 348 nm gradually diminished, while the peak at 280 nm gradually shifted towards 264 nm. Most significantly, a new peak began to appear at 448 nm with increasing Cu^{2+} concentration (Fig. 2b). Once the complexation between SICT and Cu^{2+} reached saturation, the rising absorbance at 448 nm remained stable. These findings illustrate the versatile interaction between the sensor SICT and the specific metal ion Cu^{2+} in various media. Consequently, in line with the results from the absorption studies, SICT demonstrates exceptional sensitivity and selectivity towards Cu^{2+} metal ions across a range of conditions.

3.2.2. Fluorescence emission studies

To evaluate the fluorescence quenching efficiency of SICT, fluorescence titrations were conducted at varying concentrations of Cu^{2+} . The fluorescence intensity of SICT (6×10^{-6} M) exhibited a gradual decrease



Scheme 1. Schematic representation for the synthesis of SICT.

Fig. 1. Absorption spectra of SICT (6 μM) in the presence of various metal ions (a) and (b) UV-Vis titration experiments of SICT with Cu²⁺ in acetonitrile: water (7:3, v/v) system.Fig. 2. Steady-state fluorescence spectra of SICT (6 μM) in acetonitrile: water (7:3) mixture at various Cu²⁺ concentrations (a). Benesi-Hildebrand linear analysis plot of SICT with different concentrations of Cu²⁺ ions (b).

upon the incremental addition of Cu²⁺ ions within the range of 0–10 equivalents, as illustrated in Fig. 2a. This decline in intensity can be attributed to the formation of coordination bonds between SICT and Cu²⁺ ions, involving the donation of lone electron pairs from the two imine groups (one from the imidazole and the other from the thiazole

core) to the vacant 3d orbitals of the Cu²⁺ ions. The fluorescence intensity reduction continues until ten equivalents of Cu²⁺ ions are added, at which point it stabilizes. The quenching of SICT's fluorescence intensity upon binding with Cu²⁺ ions can be ascribed to the paramagnetic nature of SICT-Cu²⁺ complexes [21,22]. This switch-off fluorescence

mechanism of **SICT**, induced by coordination with Cu^{2+} , results from intramolecular charge transfer and ligand-to-metal charge transfer processes. Notably, the intensity at 460 nm exhibits a linear decline ($R^2 = 0.99233$) as the concentration of Cu^{2+} ions increases (Fig. 2b), suggesting the potential utility of the **SICT** chemosensor for the quantitative assessment of Cu^{2+} ions, with a limit of detection (LOD) of 109 nM. The binding constant of **SICT** with Cu^{2+} in the aqueous ethanol medium was determined to be $27 \times 10^5 \text{ M}^{-1}$, affirming the strong interaction between **SICT** and Cu^{2+} ions.

The selectivity of the chemosensor greatly influences the accuracy of fluorescence detection. To further assess the specificity of the chemosensor, we analyzed the fluorescence intensity in the presence of various metal ions. When excited at 280 nm, the fluorophore **SICT** exhibited a strong fluorescence emission peak at 460 nm (Fig. 3a). However, no significant changes were observed in the fluorescence emission of **SICT** when it was exposed to various metal ions, including Al^{3+} , Cr^{3+} , Ga^{3+} , In^{3+} , Ca^{2+} , Cd^{2+} , Co^{2+} , Fe^{2+} , Mn^{2+} , La^{2+} , Na^{2+} , Sr^{2+} , Pb^{2+} , Mg^{2+} , Zn^{2+} and Ni^{2+} in an aqueous ethanol solution. Only Cu^{2+} ions induced a substantial difference in the emission intensity of **SICT**. The remarkable reduction in fluorescence intensity observed in the presence of Cu^{2+} ions highlights the exceptional selectivity of **SICT** for Cu^{2+} metal ions in an aqueous acetonitrile solution. The fluorescence intensity was significantly diminished, leading to Fluorescence quenching upon adding Cu^{2+} ($3.0 \times 10^{-6} \text{ molL}^{-1}$ of Cu^{2+} ion).

A competitive binding study was conducted to evaluate the sensitivity of **SICT** exclusively to Cu^{2+} ions amidst the presence of competing metal ions. In this study, the chemosensor **SICT** ($6 \times 10^{-6} \text{ M}$) was exposed to 10 equivalents of Cu^{2+} ions while being simultaneously treated with an equivalent quantity of other metal ions, and the outcomes of this study are illustrated in Fig. 3b. Notably, the preference for Cu^{2+} ion recognition remained unaffected despite other metal ions vying for binding concurrently. **SICT** demonstrated robust anti-interference properties, ensuring its ability to selectively recognize Cu^{2+} ions more precisely than competing metal ions. The results from the fluorescence studies further underscore the sensitive and selective nature of **SICT**'s response to Cu^{2+} ions, evidenced by the substantial fluorescence turn-off signal observed in the aqueous ethanol environment.

Further, to assess the stability of **SICT** over time, fluorescence analysis was performed (Fig. 4a). Emission spectra of **SICT** were recorded at various time intervals, and even after 10 min, the emission spectra remained consistent with the initial observations. Consequently, it can be confidently affirmed that the sensor (**SICT**) maintains stability and is not susceptible to self-quenching. Fluorescence investigations over time were carried out to explore the time-dependent sensor response to Cu^{2+}

further (Fig. 4b). After introducing 5.0 equivalents of Cu^{2+} into the **SICT** sensor, emission spectra were recorded at 0 min (baseline), 2, 4, 6, 8, and 10 min. The emission profiles and extent of quenching remained consistent between 2 and 8 min and remained stable even after 10 min. These combined observations, coupled with the results from titration studies, conclude that **SICT** exclusively responds to an increased concentration of Cu^{2+} ions and maintains a consistent response level, irrespective of variations in duration.

3.2.3. Influence of pH on fluorescence

Understanding the pH sensitivity of Fluorescence in near-neutral and mildly acidic/basic environments is crucial for environmental and biological research applications. We examined how the fluorescence output of the chemosensor **SICT** towards Cu^{2+} ions changed with varying pH levels, as pH plays a pivotal role in the fundamental principles of sensing (Fig. 5). To assess pH sensitivity, we conducted experiments using phosphate buffer saline (PBS) with **SICT** ($6 \mu\text{M}$) and Cu^{2+} ions ($3 \mu\text{M}$) within the pH range of 3–10. The pH investigation revealed that **SICT** effectively binds to Cu^{2+} ions across a wide pH spectrum, including acidic, neutral, and basic conditions (pH 3–10). Fascinatingly, the most substantial fluorescence quenching was observed at pH 7, corresponding to the physiological pH among all the pH ranges tested. This finding underscores the adaptability of **SICT** as a chemosensor, as it maintains its responsiveness to Cu^{2+} ions under a broad range of pH conditions, with particularly notable performance at the physiological pH level.

3.2.4. Binding mode studies

To gain further insights into the binding mode between **SICT** and Cu^{2+} ions, we employ the Job's plot method, which revealed a 1:1 binding stoichiometry (Fig. 6) using the continuous variation method. Additionally, in the mass spectrum, a peak at $m/z = 651$ disappeared upon adding one equivalent of Cu^{2+} , and a new peak emerged at $m/z = 713$, corresponding to $[\text{SICT} + \text{Cu}^{2+}]$ (Fig. S2).

The binding constants (K_a and K_b) of the **SICT**- Cu^{2+} complex was determined using the modified Stern-Volmer equation [23], as depicted below, with the aid of a Stern-Volmer plot

$$F_0/\Delta F = 1/fa + 1/(faK_a[Q])$$

Here, F_0 and F represent the initial fluorescence intensity in the absence and presence of the quencher, respectively. K_a is the Stern-Volmer constant, denoting the association constant of Cu^{2+} with **SICT**, $[Q]$ is the concentration of the quencher, and fa represents the initial fluorescence fraction in which the quencher is accessible. Through this method, the binding constant for the **SICT**- Cu^{2+} complex was determined to be

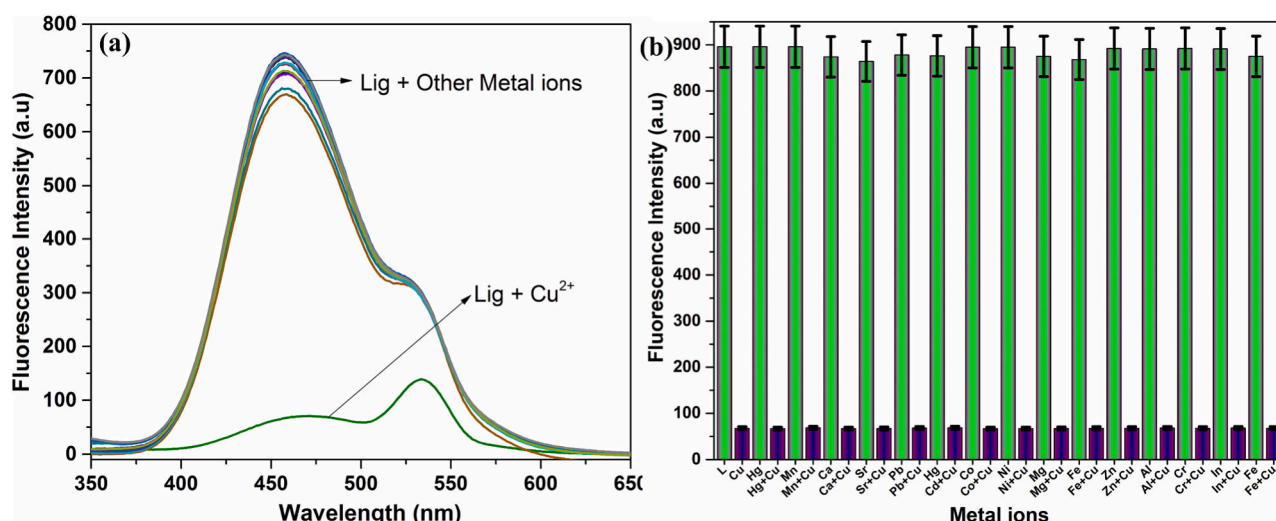


Fig. 3. Fluorescence spectra of **SICT** ($6 \mu\text{M}$) with various metal ions (a). Interference studies of **SICT** and Cu^{2+} with different metal ions (b).

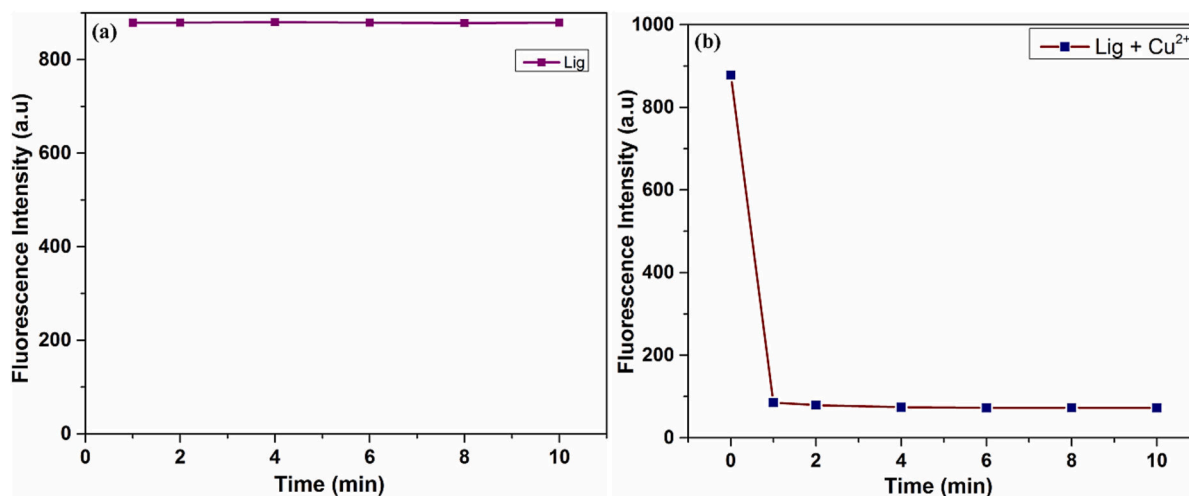


Fig. 4. Time-dependent fluorescence studies of SICT (6 μM) in the absence (a) and presence of Cu^{2+} ions (b).

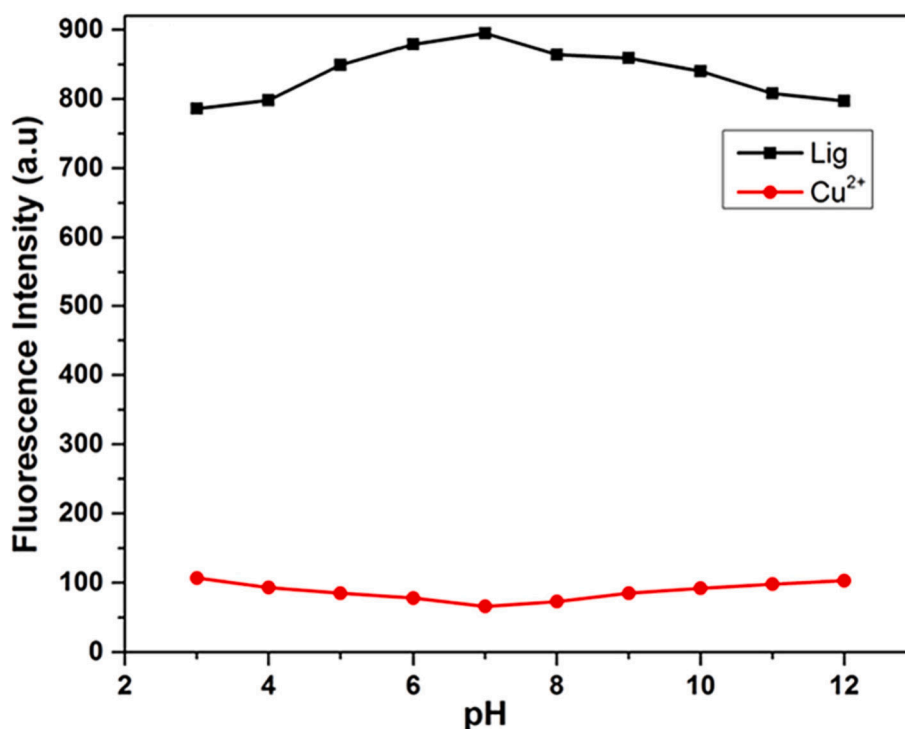


Fig. 5. Fluorescence studies of SICT (6 μM) in the absence and presence of Cu^{2+} ions at different pH levels.

$27 \times 10^5 \text{ M}^{-1}$. These results underscore the selectivity of SICT for copper ions and suggest that the formation of the SICT- Cu^{2+} complex is highly favorable and spontaneous.

3.3. DFT calculations

3.3.1. Geometry optimization

The minimum energy conformer of the chemosensor SICT was obtained by optimizing its geometry in the ground state using Gaussian 09 software. In the computed DFT values, no imaginary wave number modes were detected, and all were found to be positive, indicating the presence of the true minimum energy conformer. Fig. 7a and 7b illustrate the optimized structure of SICT. The bond lengths and angles obtained in this optimization were compared with experimental data reported in the literature, and the results are summarized in Tables S1 and S2. For reference, the C-C bond lengths in a benzene ring typically

fall around 1.395 Å [24,25]. Experimental X-ray results have reported C=O bond lengths of approximately 1.224 Å and 1.227 Å [26], consistent with the DFT-calculated values of 1.224 Å for SICT. The C-C bond lengths in the present molecule, SICT, ranged from 1.3 Å to 1.4 Å, while the C=O bond length was determined to be 1.209 Å. These values align with previous findings [27–29]. Additionally, the thiazole moiety's S-C and N-C bond lengths are typically around 1.743 Å and 1.390 Å, respectively, as reported by experimental XRD [33]. In SICT, the theoretical S-C and N-C bond lengths in the thiazole moiety were calculated to be 1.7 Å and 1.39 Å, respectively, closely matching the reported experimental values.

Moreover, the C-N bond lengths within the imidazole core of SICT (ranging from 1.39 Å to 1.4 Å) fall within the same range as those reported in the literature [30]. It is observed from the optimized structures of SICT and SICT- Cu^{2+} complex (Fig. 7) that there is a slight modification in bond lengths of SICT after binding with Cu^{2+} ion. The S-C bond

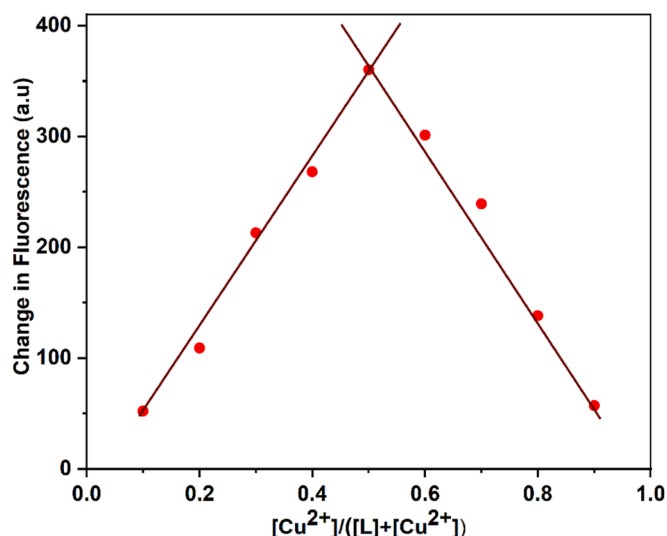


Fig. 6. Job's graph for SICT with different concentration of Cu²⁺ ions.

length is changed to 1.823 Å and 1.785 Å from 1.753 Å and 1.723 Å after complexation. Overall, all other bond lengths and angles calculated through DFT are in good agreement with the literature data, validating the accuracy of the computational model.

3.3.2. Molecular electrostatic potential (MESP) plot

To further understand the molecular reactivity and interaction, the molecular electrostatic potential map (MESP) was employed, as shown in Fig. 8. The MESP provides insights into nucleophilic and electrophilic regions within the molecule, aiding in interpreting its chemical behaviour. The MESP is generated from the electron density distribution within the molecule, calculated at the B3LYP level using a 6-311++G (d, p) basis set. It provides valuable insights into the electrophilic and nucleophilic regions within the molecule. To gain a deeper understanding of the bonding interaction between SICT and Cu²⁺, the SICT-Cu²⁺ complex was theoretically calculated using the B3LYP/LANL2DZ relativistic pseudo-potential basis set.

Fig. 8 illustrates the MESP plot for both SICT and the SICT-Cu²⁺ complex, along with their corresponding colour gradient scheme. In the colour spectrum used, potential values range from negative to positive, with the deepest red indicating the negative regions (electrophilic reactivity) and the deepest blue representing the positive regions

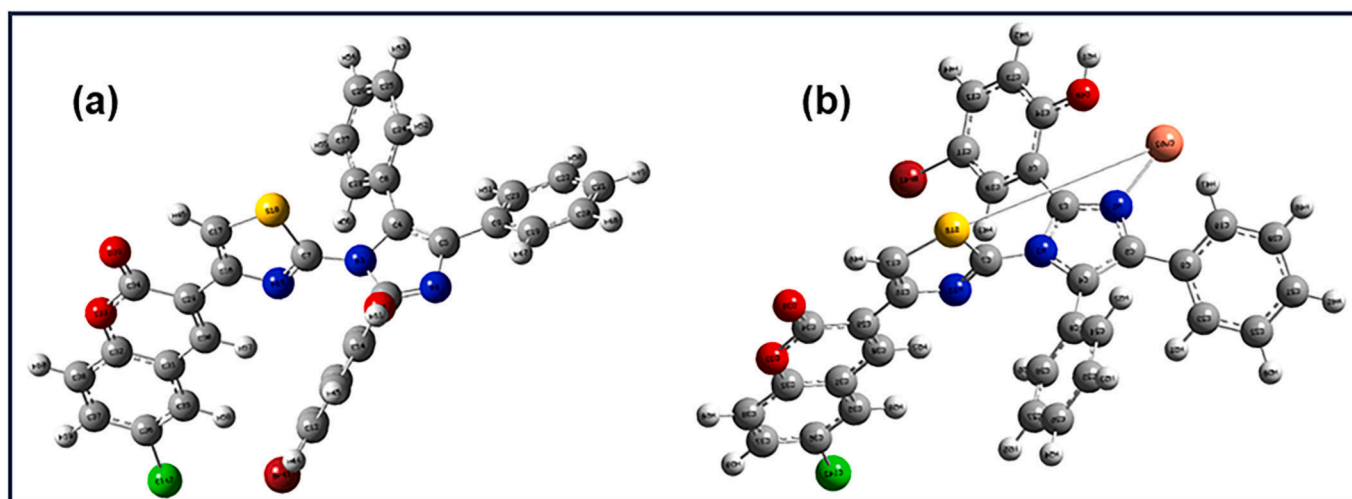


Fig. 7. Optimized geometry for the a) SICT and b) SICT-Cu²⁺ complex.

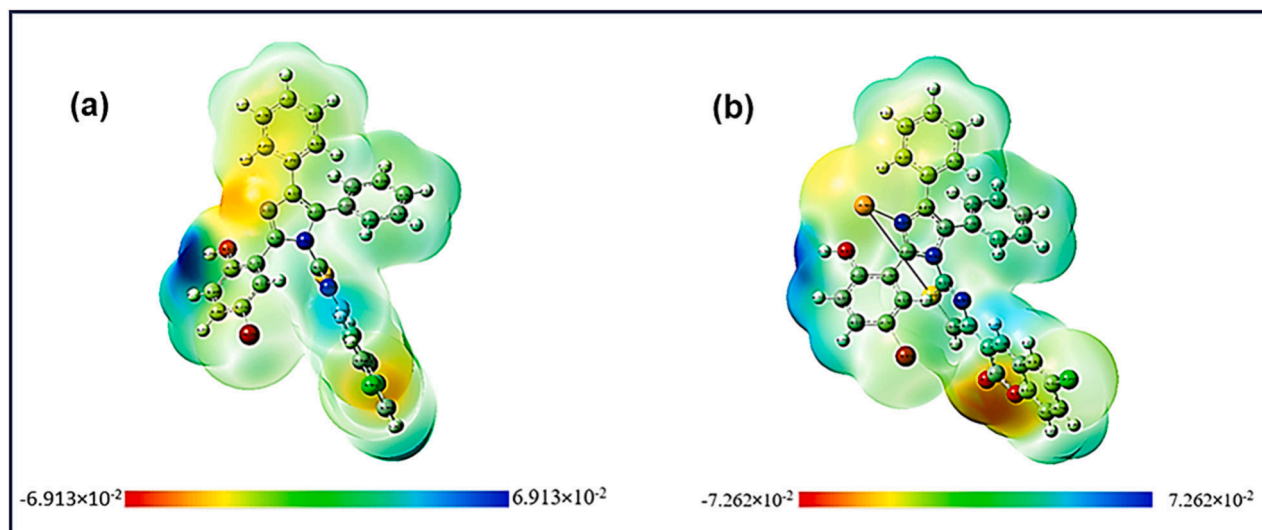


Fig. 8. Molecular electrostatic potential map of a) SICT and b) SICT-Cu²⁺ complex with colour range of $\pm 6.913 \times 10^{-2}$ (SICT) and $\pm 7.262 \times 10^{-2}$ (SICT-Cu²⁺).

(nucleophilic reactivity). Analysing the MESP plot (Fig. 8), we observe that the negative regions in **SICT** are primarily centred around atoms N1, O33, and O39, with electronegativity values of 0.300, -0.273 , and -0.128 , respectively. As a result, there are two potential sites where Cu^{2+} ions can engage in electrophilic interactions: one with the nitrogen atom in the imidazole moiety of **SICT** and the other with the sulphur atom in the thiazole ring, at approximately 2.00 \AA (N-Cu). The absence of negative frequencies in frequency calculations and stability studies confirms that the complex represents a stable local energy minimum.

Upon coordination with Cu^{2+} , the negative charge on N1 (-0.285) increases, while the positive charges on S18 (0.346) and N32 (0.124) atoms in the **SICT-Cu** $^{2+}$ complex also increase. Additionally, it is observed that after binding with the Cu^{2+} ion, the charge on O33 in **SICT** becomes -0.286 , indicating a shift of charge from the ligand's nitrogen atoms to the Cu^{2+} ion (-0.064). These findings provide valuable insights into the electronic structure and charge distribution within the **SICT-Cu** $^{2+}$ complex, shedding light on the nature of their bonding interaction.

3.3.3. UV-Vis absorption transitions

The UV-Vis spectra of **SICT** were obtained through TD-DFT calculations, considering ethanol as the solvent. Table 1 provides key excitation properties, including oscillator strength (f), excitation energy (eV), and excitation wavelength (nm). These properties are summarized in the table, giving insights into the electronic transitions within **SICT**. Fig. 9 compares the theoretical and experimental UV-Vis absorption spectra of **SICT**. The calculated absorption wavelengths were determined to be 269.823 nm and 313.545 nm . Remarkably, experimental measurements closely matched the theoretical calculations, with peak absorption levels observed at 265.124 nm and 294.042 nm , as depicted in Fig. 9. Table 1 further discloses that the excitation at 294.042 nm accounts for a significant portion (90 %) of **SICT**'s electronic transition from the ground state HOMO-1 to the excited state LUMO, with an oscillator strength of 0.709 . Similarly, the transition from HOMO to LUMO, represented by the excitation wavelength at 265.124 nm , contributes to 84 % of the electronic transition with an oscillator strength of 0.017 . These findings shed light on the dominant electronic transitions within **SICT**, providing valuable insights into its UV-Vis absorption properties.

3.3.4. Frontier molecular orbital (FMO) analysis

To get the insights into the binding nature between **SICT** and Cu^{2+} , theoretical calculations were conducted for both **SICT** and the **SICT-Cu** $^{2+}$ complex. Frontier molecular orbital (FMO) analysis was employed to investigate various optical, chemical, and electronic properties of the molecules, and these calculations were carried out at the same level of theory used for the optimized structures [31–33]. Figs. 10, 11a, and 11b display the plots for HOMO-1, HOMO, LUMO, and LUMO+1 of both **SICT** and the **SICT-Cu** $^{2+}$ complex, along with their respective energy gaps. From the FMO plots (Fig. 10), it is evident that in the **SICT** molecule, the HOMO is primarily located on the 4-bromo-2-(4,5-diphenyl-1H-imidazol-2-yl)phenol moieties, while the LUMO is situated on the thiazole and chromen-2-one moieties. This suggests a charge transfer from the imidazole moiety to the thiazole and chromen-2-one moieties. The calculated energies of the HOMO and LUMO for **SICT**

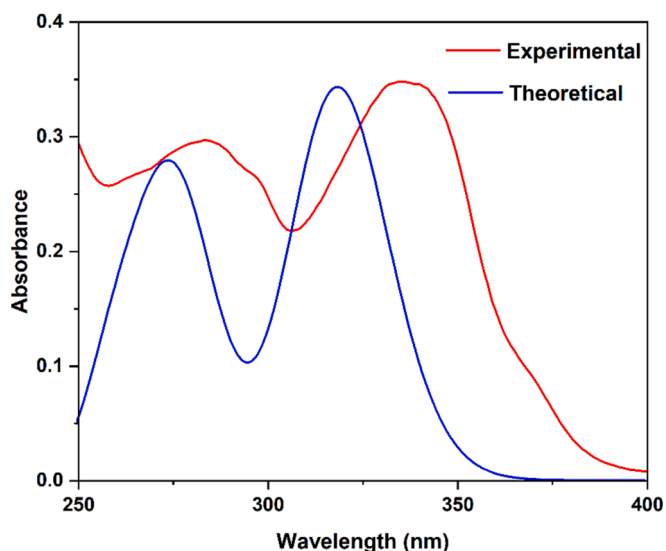


Fig. 9. Comparison of experimental and theoretical UV-Visible absorption spectra of **SICT**.

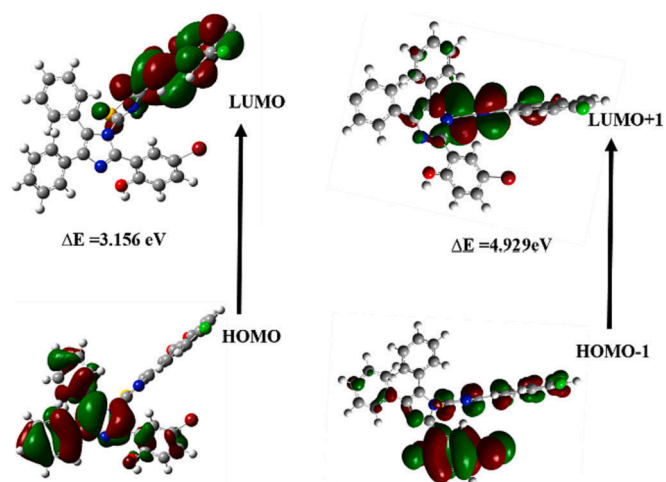


Fig. 10. FMO orbital surfaces of **SICT**.

are -5.857 eV and -2.701 eV , respectively, resulting in an energy gap of 3.156 eV . It is worth noticing that organic compounds with smaller HOMO-LUMO energy gaps are of particular interest due to their unique optoelectronic properties. A larger HOMO-LUMO energy gap implies greater stability, reduced reactivity, and increased hardness of the molecule.

Table 2 provides values for various global reactivity parameters, including electronegativity, chemical potential, softness, chemical hardness, and electrophilicity index. **SICT** exhibits a global chemical hardness of 1.578 eV and an electronegativity of 4.279 eV , indicating its ability to attract electron pairs. The electrophilicity index for **SICT** is calculated as 5.785 eV , signifying its strong electron-attracting capability. In the **SICT-Cu** $^{2+}$ complex, the HOMO of the complex is found in the 151st alpha orbital and 150th beta orbital, while the LUMO is in the 152nd alpha orbital and 151st beta orbital, as shown in Fig. 10a and 10b. Upon binding, the alpha and beta molecular orbital energy gaps for the **SICT-Cu** $^{2+}$ complex decrease to 0.292 eV and 3.068 eV , respectively. This suggests the complex is more reactive upon binding than the isolated analyte. The values for softness, electronegativity, and electrophilicity indexes of the **SICT-Cu** $^{2+}$ complex show slight changes, as indicated in Table 2.

Table 1

Theoretically calculated absorption wavelengths λ (nm), excitation energies E (eV), major contributions, and oscillator strengths (f) using TD-DFT/CAM-B3LYP/6-311++G (d, p) method in aqueous solution.

Molecule	Wavelength λ (nm)		E (eV)	F (a. u.)	Major contribution
	Experimental	DFT			
SICT	294.042	313.545	3.892	0.709	H-1->LUMO (90 %)
	265.124	269.823	4.561	0.017	HOMO->LUMO (84 %)

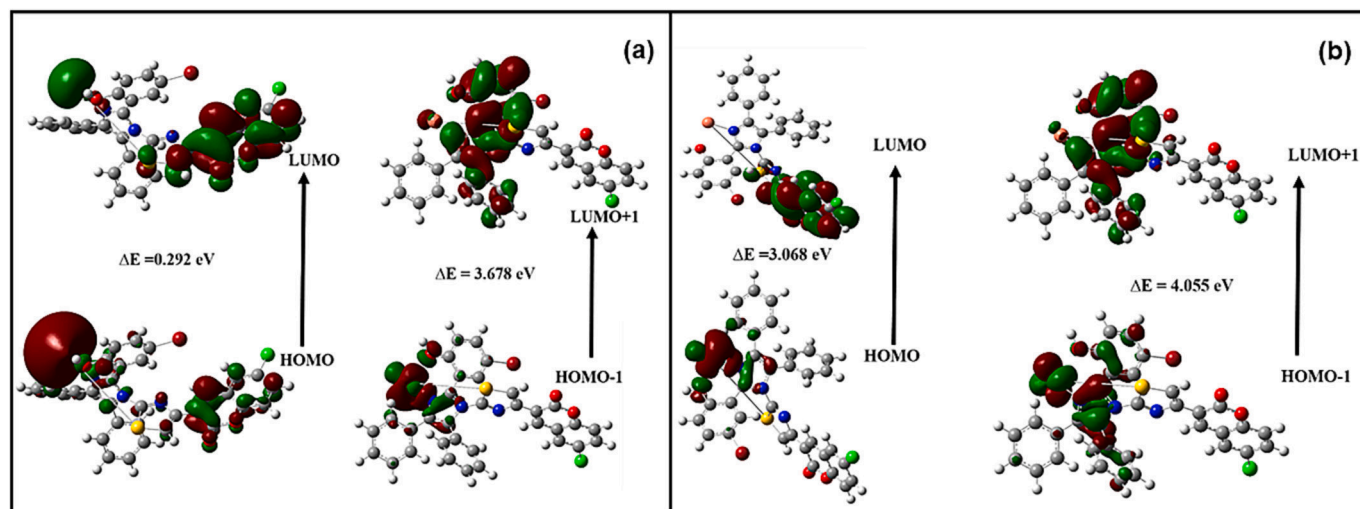


Fig. 11. Computational FMO orbital surfaces of (a) alpha SICT-Cu^{2+} and (b) beta SICT-Cu^{2+} molecular orbitals.

Table 2

Global chemical reactivity descriptors parameters of SICT and SICT-Cu^{2+} complex.

Molecule Properties	SICT	SICT-Cu^{2+}	
		Alpha orbitals	Beta orbitals
Energy in a. u.	-5091.900	-1892.939	
E_{HOMO} in eV	-5.857	-3.097	-5.625
E_{LUMO} in eV	-2.701	-2.805	-2.557
$E_{\text{HOMO-1}}$ in eV	-6.563	-5.735	-6.099
$E_{\text{LUMO+1}}$ in eV	-1.634	-2.057	-2.044
$\Delta E_{\text{LUMO-HOMO}}$ in eV	3.156	0.292	3.068
Ionization potential(I)	5.857	3.097	5.625
Electron affinity (A)	2.701	2.805	2.557
Global Hardness (η)	1.578	0.146	1.534
Softness (S)	0.316	3.424	0.162
Chemical potential (μ)	-4.279	-2.951	-4.091
Electronegativity (χ)	4.279	2.951	4.091
Electrophilicity (Ψ)	5.785	29.823	2.711

3.3.5. *In vitro* and *in vivo* cytotoxicity and bioimaging analysis

In vitro and *in vivo* cytotoxicity and bioimaging analysis was carried out in MDA-MB-231 cells and D. Rerio embryos, respectively [10,34]. The *in vitro* toxicity in MDA-MB-231 cells and the morphological observations were assessed by MTT assay. The MTT assay was conducted to reveal the cytotoxicity effect of the probe and dose-dependently affected the viability of the cells, as depicted in Fig. S4. The IC_{50} value of SICT was determined to be $12.5 \pm 0.15 \mu\text{M}$. The microscopic observations revealed the dose-dependent change in morphology of the cells. From Fig. 12, it can be seen that the probe has a dose-dependent effect on the cells. The detrimental cell damage was found after $12.5 \mu\text{M}$ of concentration. From the microscopic image, the damage to the cell membrane has been caused at a higher concentration. However, probes at lower concentrations than their IC_{50} values didn't show detrimental effects in morphological observation.

The cytotoxicity along with bioimaging studies were conducted using cell line MDA-MB-231 at $5.0 \mu\text{M}$ fixed concentration of the chemosensor SICT . It was observed that on incubation with different

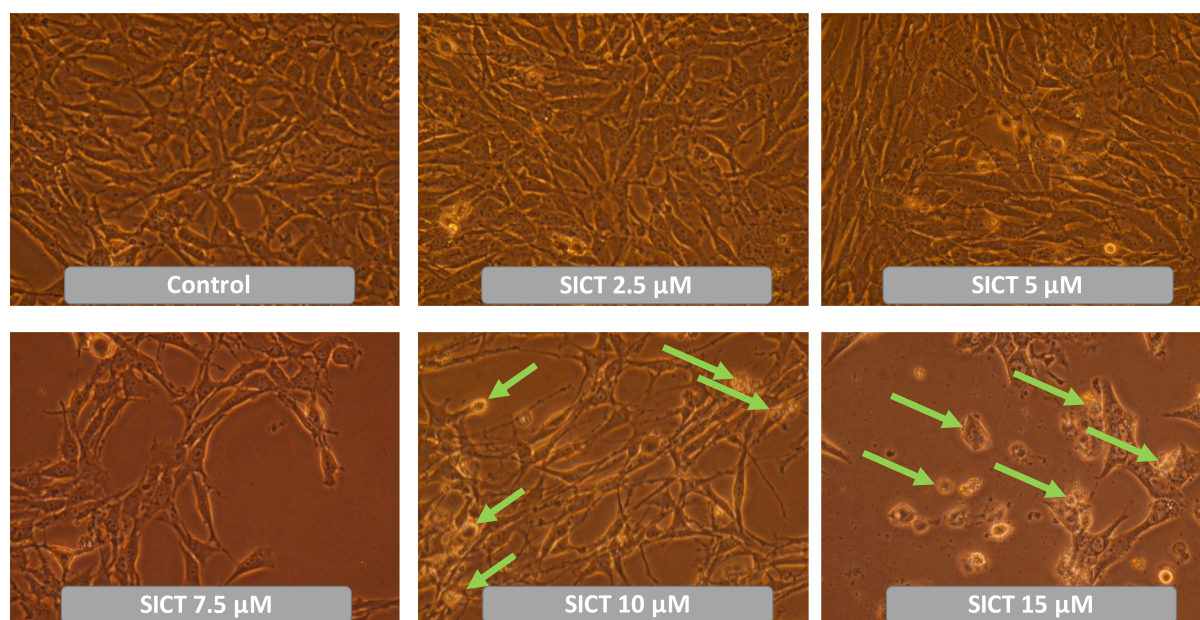


Fig. 12. Effect of SICT on the morphology of the MDA-MB-231 cells observed by bright-field microscopy. The arrows show the detrimental impact, such as disruption of a monolayer of cells, rupturing of cells, leakage of cellular debris, and formation of apoptotic bodies. Images were captured at 400x magnification.

concentrations of Cu^{2+} , there was no change in the cell stability or morphology. There was no cell death observed, and from Fig. S5, it is evident that on increasing the concentration of Cu^{2+} from 60 nM to 120 nM, the fluorescence intensity was found to be reduced. These results manifest that **SICT** can bind to Cu^{2+} effectively even inside the cell system.

To further investigate the impact of **SICT** in a living system, we conducted *in vivo* cytotoxicity and bioimaging analyses using D. Rerio embryos. The *in vivo* cytotoxicity assessment of the probe was carried out on embryos at 24, 48, 72, and 96 h post-fertilization (hpf), as depicted in Figs. S6 and S7. We exposed the embryos to different concentrations of the chemosensor **SICT** to study its effect on their development. We assessed developmental defects and mortality as indicators of cytotoxicity. In most survival experiments, embryos were exposed to varying concentrations of **SICT**. We observed minimal cytotoxicity even at higher probe concentrations (20 μM). Even at this concentration, embryos had no observable deformations, and their growth appeared normal without any defects. No embryo deaths were recorded during these phases. Although slight cytotoxicity was observed after 20 μM , no deformations or deaths were noted up to 72 hpf. Mortality was only recorded beyond 72 hpf with a concentration of 20 μM . This suggests that concentrations of up to 20 μM exhibit low cytotoxicity in zebrafish embryos and can be used as a fluorescent probe for bioimaging studies.

Furthermore, the bioimaging studies were conducted by exposing **SICT** to embryos to demonstrate the chemosensor's uptake ability. As shown in Fig. 13, blue emission from **SICT** was clearly observed in the zebrafish. The sensor **SICT** remained stable for an extended period with consistent fluorescence intensity, even at 96 hpf. This indicates that the probe persisted in the embryo for an extended duration, from 24 hpf, and entered through passive diffusion, either by ingestion or absorption. **SICT** was selectively accumulated in the heart, pericardium, common caudal vein, posterior caudal vein, and eyes. This selective accumulation in different parts of the zebrafish suggests tissue-dependent affinity of the chemosensor. The fluorescence intensity remained constant from 24 hpf to 96 hpf, indicating that **SICT** entered the circulatory system, which

is essential for probe transport in zebrafish. These results collectively demonstrate that **SICT** can be utilized for bioimaging studies.

Moreover, we investigated the *in vivo* Cu^{2+} sensing ability of the sensor **SICT** in zebrafish. We incubated embryos with different concentrations of Cu^{2+} . As shown in Fig. 13, the fluorescence intensity gradually decreased with increasing uptake of Cu^{2+} ions. Initially, a decrease in fluorescence intensity was observed in the pericardial vein, indicating the uptake of Cu^{2+} and its entry into the circulatory system. This was followed by a reduction in fluorescence intensity in the sac.

Interestingly, the fluorescence intensity in the eyes decreased more slowly compared to other parts of the zebrafish, suggesting that copper reached the eyes later in the process. These results confirm that the chemosensor enters selectively into different parts of the zebrafish, and probe **SICT** holds excellent potential for bioimaging in mammalian tissues. Furthermore, we compared the sensing ability and adaptability of **SICT** with other reported turn-off sensors for Cu^{2+} , as summarized in Table 3.

4. Conclusions

In conclusion, we have developed a straightforward one-pot synthetic method to produce the probe **SICT** (3-(2-(2-(5-bromo-2-hydroxyphenyl)-4,5-diphenyl-1H-imidazol-1-yl)thiazol-4-yl)-2H-chromen-2-one) for the selective detection of Cu^{2+} ions. The probe exhibited remarkably low cytotoxicity, with an IC_{50} value of $12.5 \pm 0.15 \mu\text{M}$. **SICT** demonstrated impressive sensitivity in aqueous acetonitrile medium, with a detection limit in the nanomolar range (109 nM), underscoring its high sensitivity. The 1:1 binding mode of **SICT** with Cu^{2+} was verified through Job's plot, ESI-Mass analysis, and DFT studies. Bioimaging experiments conducted in zebrafish and human cancer cells yielded highly promising results, suggesting the potential utility of the **SICT** ligand for detecting Cu^{2+} ions in both *in vitro* and *in vivo* systems. This work contributes to developing practical tools for copper ion sensing, with applications in various fields, including environmental monitoring and biomedical research.

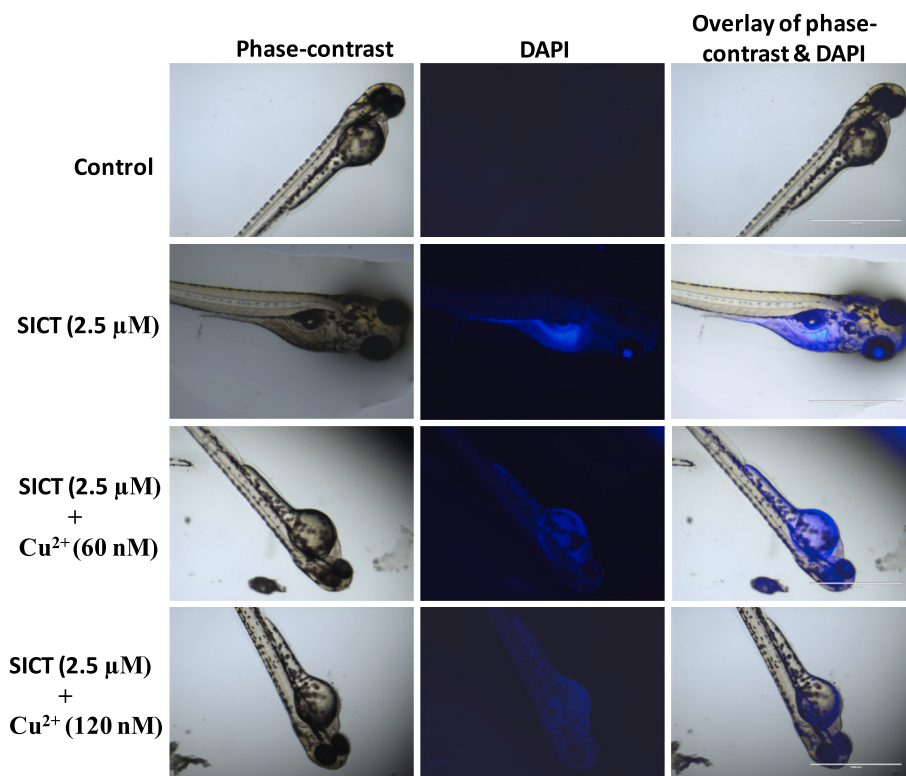


Fig. 13. Fluorescence images of live zebrafish larvae for **SICT**.

Table 3Comparison of reported Cu²⁺ sensors with SICT.

Sensor	Type of Sensor	Binding constant (M ⁻¹)	LOD	Media	Application	References
Schiff base	Turn Off	1.29 × 10 ³	–	DMSO:H ₂ O (4:1) v/v	Metal ion Sensor	[35]
Schiff base	Turn Off	0.619 × 10 ⁷	0.302 μM	Ethanol-water medium (1:9) v/v	Metal ion Sensor and real water sample analysis	[36]
Quinoline-Conjugated Calixarene	Turn Off	1.97 × 10 ⁴	350 μM,	1 % of water-Tetra hydrofuran	Metal ion Sensor	[37]
Schiff base	Turn Off	1.43 × 10 ⁵	0.65 μM	DMSO/H ₂ O solution (1:10)	Metal ion Sensor	[38]
2-Mercapto-4-methyl-5-thiazoleacetic acid	Turn Off	1.48 × 10 ⁵	0.5 pg/L	Double distilled water	Metal ion Sensor and real water sample analysis	[39]
Benzothiadiazole	Turn Off	–	0.11 μM	DMF	Fluorescence imaging	[40]
Imidazole	Turn Off	–	3.7 μM	Water/ACN (9:1) v/v	Fluorescence imaging	[14]
Pyridyl Imidazole	Turn Off	1.53 × 10 ⁴	0.77 μM	Ethanol-water	Fluorescence imaging + Real water sample analysis	[15]
Benzo-thiazole	Turn Off	6.0 × 10 ¹⁰	0.34 ppm	1:1 ratio of DMSO and CHCl ₃	Fluorescence imaging	[16]
Schiff base	Turn On	2.83 × 10 ⁴	3.42 μM	DMSO/H ₂ O (1:9)	Real water sample analysis	[11]
Schiff base	Turn On	4.23 10 ⁵	418 μM	ACN/H ₂ O 1.5 × 10 ⁻² /2.5 × 10 ⁻⁵	Fluorescence imaging	[12]
Coumarin-Quinoline	Turn On	3.65 × 10 ³	2.5 μM	H ₂ O/DMSO (9:1)v/v	Fluorescence imaging	[13]
Imidazole-Chromene	Turn off	27 × 10 ⁵	109 × nM	ACN/H ₂ O (7:3) v/v	Fluorescence live cell imaging + Zebrafish imaging	Present

CRedit authorship contribution statement

Keshav Kumar Harish: Writing – review & editing, Software, Methodology, Data curation. **Aravind R. Nesaragi:** Writing – review & editing, Writing – original draft, Visualization, Validation, Software, Methodology, Formal analysis, Data curation, Conceptualization. **Naveen Kumar Kalagatur:** Visualization, Validation, Data curation. **Praveen Naik:** Visualization, Validation, Formal analysis. **Mahendra Madegowda:** Writing – review & editing, Resources, Investigation, Formal analysis. **Anup Pandith:** Visualization, Validation, Formal analysis. **Kholood A. Dahlous:** Visualization, Validation, Funding acquisition, Formal analysis. **Saikh Mohammad:** Visualization, Validation, Funding acquisition, Formal analysis. **H.P. Shivarudrappa:** Formal analysis, Validation, Visualization. **T.M. Sharanakumar:** Formal analysis, Validation, Visualization. **H. Guddappa:** Visualization, Validation, Formal analysis.

Declaration of competing interest

The authors declare that they have no known competing financial interests or personal relationships that could have appeared to influence the work reported in this paper.

Data availability

The data that support the findings of this study are available in the [Supporting Information](#) of this article

Acknowledgements

The authors acknowledge DRDO-BU, Centre for Life Sciences, Coimbatore, Tamil Nadu for carrying out bio-imaging studies. This work was funded by the Researchers Supporting Project Number (RSP2023R388) King Saud University, Riyadh, Saudi Arabia.

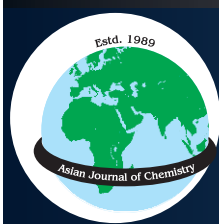
Appendix A. Supplementary data

Supplementary data to this article can be found online at <https://doi.org/10.1016/j.jphotochem.2024.115565>.

References

- [1] N. Murugan, M. Prakash, M. Jayakumar, A. Sundaramurthy, A.K. Sundramoorthy, Green synthesis of fluorescent carbon quantum dots from Eleusine coracana and their application as a fluorescence 'turn-off' sensor probe for selective detection of Cu²⁺, *Appl. Surf. Sci.* 476 (2019) 468–480.
- [2] L.B. Björklund, G.M. Morrison, Determination of copper speciation in freshwater samples through SPE-spectrophotometry, *Anal. Chim. Acta* 343 (1997) 259–266.
- [3] A.R. Nesaragi, R.R. Kamble, S.R. Hoolageri, S. Dixit, S.D. Joshi, S. Vootla, V. M. Kumbhar, Microwave-assisted copper (I) catalyzed a 3 cascade coupling of imidazo [1, 2-a] pyridines via C-H bond functionalization as selective COX-2 inhibitors and antioxidants, and in silico studies, *New J. Chem.* 47 (2023) 9401–9413.
- [4] W. Dong, R. Wang, X. Gong, W. Liang, L. Fan, S. Song, C. Dong, A ratiometric and far-red fluorescence "off-on" sensor for sequential determination of copper (II) and L-histidine based on FRET system between N-acetyl-L-cysteine-capped AuNCs and N, S, P co-doped carbon dots, *Microchim. Acta* 187 (2020) 1–12.
- [5] F. Li, R. Sa, Formation of cu 3, 4 (TCA), making the TCA complex a highly selective probe for Cu²⁺ detection: a TDDFT study, *J. Mater. Chem. C* 7 (2019) 2443–2456.
- [6] Y. Xu, Y. Hou, Y. Wang, Y. Wang, T. Li, C. Song, N. Wei, Q. Wang, Sensitive and selective detection of Cu²⁺ ions based on fluorescent ag nanoparticles synthesized by R-phycoerythrin from marine algae *Porphyra yezoensis*, *Ecotoxicol. Environ. Saf.* 168 (2019) 356–362.
- [7] R. Danzeisen, M. Araya, B. Harrison, C. Keen, M. Solioz, D. Thiele, H.J. McArdle, How reliable and robust are current biomarkers for copper status? *Br. J. Nutr.* 98 (2007) 676–683.
- [8] M. Araya, M. Olivares, F. Pizarro, Copper in human health, *International Journal of Environment and Health* 1 (2007) 608–620.
- [9] Y.B. Barot, V. Anand, R. Mishra, Di-triphenylamine-based AIE active schiff base for highly sensitive and selective fluorescence sensing of Cu²⁺ and Fe³⁺, *J. Photochem. Photobiol. A Chem.* 426 (2022) 113785.
- [10] A.R. Nesaragi, C.H. Ravikumar, N.K. Kalagatur, S.R. Hoolageri, K.M.M. Pasha, R. G. Balakrishna, S.A. Patil, In vitro and in vivo nanomolar Hg²⁺ detection in live cells and zebrafish, theoretical studies, *J. Photochem. Photobiol. A Chem.* 445 (2023) 115079.
- [11] Z. Xu, L. Zhang, R. Guo, T. Xiang, C. Wu, Z. Zheng, F. Yang, A highly sensitive and selective colorimetric and off-on fluorescent chemosensor for Cu²⁺ based on rhodamine B derivative, *Sens. Actuators B* 156 (2011) 546–552.
- [12] S. Suganya, S. Velmathi, D. MubarakAli, Highly selective chemosensor for nano molar detection of Cu²⁺ ion by fluorescent turn-on response and its application in living cells, *Dyes Pigm.* 104 (2014) 116–122.
- [13] Y. Gao, J. Shu, C. Zhang, X. Zhang, H. Chen, K. Yao, A fluorescence on-off sensor for cu 2+ and its resultant complex as an off-on sensor for cr 3+ in aqueous media, *RSC Adv.* 5 (2015) 74629–74637.
- [14] H.E. Okda, S. El Sayed, I. Otri, R.C.M. Ferreira, S.P.G. Costa, M.M.M. Raposo, R. Martinez-Manez, F. Sancenon, A simple and easy-to-prepare imidazole-based probe for the selective chromo-fluorogenic recognition of biothiols and cu (II) in aqueous environments, *Dyes Pigm.* 162 (2019) 303–308.
- [15] A. Bhattacharya, S. Mahata, A. Bandyopadhyay, B.B. Mandal, V. Manivannan, Application of 2, 4, 5-tris (2-pyridyl) imidazole as 'turn-off' fluorescence sensor for cu (II) and hg (II) ions and in vitro cell imaging, *Luminescence* 37 (2022) 883–891.
- [16] C.A.S. Pothulapadu, A. Jayaraj, S. N. R.N. Priyanka, G. Sivaraman, Novel benzothiazole-based highly selective ratiometric fluorescent turn-on sensors for Zn²⁺ and colorimetric chemosensors for Zn²⁺, Cu²⁺, and Ni²⁺ ions, *ACS, Omega* 6 (2021) 24473–24483.

- [17] S.R. Hoolageri, A.R. Nesaragi, R.R. Kamble, S. Dixit, S. Vootla, S.D. Joshi, S. J. Shaikh, Green synthesis of novel triazolothiadiazine-coumarins catalyzed by agro waste extract: an approach towards in-silico and in-vitro anti-fungal activity, *ChemistrySelect* 7 (2022) e202200077.
- [18] A.R. Nesaragi, R.R. Kamble, P.K. Bayannavar, V. Metre, M.Y. Kariduraganavar, S. B. Margankop, D. Joshi, V.M. Kumbar, Microwave facilitated one-pot three component triazoles: antimicrobial evaluation, molecular docking and in silico ADME studies, *Synth. Commun.* 51 (2021) 3460–3472, <https://doi.org/10.1080/00397911.2021.1980806>.
- [19] A.R. Nesaragi, R.R. Kamble, S. Dixit, B. Kodasi, S.R. Hoolageri, P.K. Bayannavar, J. P. Dasappa, S. Vootla, S.D. Joshi, V.M. Kumbar, Green synthesis of therapeutically active 1, 3, 4-oxadiazoles as antioxidants, selective COX-2 inhibitors and their in silico studies, *Bioorg. Med. Chem. Lett.* 43 (2021) 128112.
- [20] S.R. Hoolageri, R.R. Kamble, A.R. Nesaragi, L. Bheemayya, V.B. Nadoni, S. Dixit, S. Vootla, S.D. Joshi, Cu (I) catalyzed A3 cascade coupling via C-H functionalization followed by cyclization: synthesis, in silico, in vitro, and toxicity studies of imidazo[2,1-b]thiazoles, *Appl. Organomet. Chem.* 36 (2022) 1–19, <https://doi.org/10.1002/aoc.6801>.
- [21] S. Sharma, K.S. Ghosh, Overview on recently reported fluorometric sensors for the detection of copper ion based on internal charge transfer (ICT), paramagnetic effect and aggregation induced emission (AIE) mechanisms, *J. Mol. Struct.* 1237 (2021) 130324.
- [22] Y. Qu, Y. Wu, C. Wang, K. Zhao, H. Wu, A selective fluorescence probe for copper (II) ion in aqueous solution based on a 1, 8-naphthalimide schiff base derivative, *Zeitschrift Für Naturforschung B* 74 (2019) 665–670.
- [23] K. Kur-Kowalska, M. Przybyl, E. Miller, The study of phenylboronic acid optical properties towards creation of a glucose sensor, (2014).
- [24] T.S. Yamuna, H.S. Yathirajan, J.P. Jasinski, A.C. Keeley, B. Narayana, B.K. Sarojini, (2E)-1-(4-chlorophenyl)-3-(4-nitrophenyl) prop-2-en-1-one, *acta crystallographica section E: structure reports*, Online 69 (2013) o790–o791.
- [25] H.A. Khamees, M. Jyothi, S.A. Khanum, M. Madegowda, Synthesis, crystal structure, spectroscopic characterization, docking simulation and density functional studies of 1-(3, 4-dimethoxyphenyl)-3-(4-fluorophenyl)-propan-1-one, *J. Mol. Struct.* 1161 (2018) 199–217.
- [26] T.A. De Toledo, L.E. Da Silva, A.M.R. Teixeira, P.T.C. Freire, P.S. Pizani, Characterization of meldrum's acid derivative 5-(5-Ethyl-1, 3, 4-thiadiazol-2-ylamino) methylene-2, 2-dimethyl-1, 3-dioxane-4, 6-dione by raman and FT-IR spectroscopy and DFT calculations, *J. Mol. Struct.* 1091 (2015) 37–42.
- [27] N.A. Dlala, Y. Bouazizi, H. Ghalla, N. Hamdi, DFT calculations and molecular docking studies on a chromene derivative, *J. Chem.* 2021 (2021) 1–17.
- [28] M. El Gaafary, T. Syrovets, H.M. Mohamed, A.A. Elhenawy, A.M. El-Agrody, A. El-Galil, E. Amr, H.A. Ghabbour, A.A. Almhazia, Synthesis, cytotoxic activity, crystal structure, DFT studies and molecular docking of 3-Amino-1-(2, 5-dichlorophenyl)-8-methoxy-1 H-benzo [f] chromene-2-carbonitrile, *Crystals* 11 (2021) 184.
- [29] R.M. Okasha, A.M. Fouda, M.A. Bajaber, H.A. Ghabbour, A.-E.-G.-E. Amr, A. M. Naglah, A.A. Almhazia, A.A. Elhenawy, A.M. El-Agrody, The crystal structure of 3-Amino-1-(4-chlorophenyl)-9-Methoxy-1 H-benzo [f] Chromene-2-carbonitrile: antimicrobial activity and docking studies, *Crystals* 12 (2022) 982.
- [30] R. Ramachandran, M. Rani, S. Senthana, Y.T. Jeong, S. Kabilan, Synthesis, spectral, crystal structure and in vitro antimicrobial evaluation of imidazole/benzotriazole substituted piperidin-4-one derivatives, *Eur. J. Med. Chem.* 46 (2011) 1926–1934.
- [31] N. Piliccode, N.K. M. M. Acharya, P. Naik, S.M. N. A.V. Adhikari, New blue light emitting cyanopyridine based conjugated polymers: from molecular engineering to PLED applications, *J Photochem Photobiol A Chem* 378 (2019) 38–45.
- [32] P. Naik, D.D. Babu, G.K. Jayaprakash, A computational approach for screening carbazole based organic dyes as potential photosensitizers for DSSCs application, *Results Chem.* 6 (2023) 101000.
- [33] P. Naik, N. Piliccode, K.S. Keremane, M. Acharya, A.V. Adhikari, Synthesis, optical, electrochemical, and computational investigation of new cyanopyridine-centered organic dyads, *Opt. Mater. (Amst)* 142 (2023) 114002.
- [34] N.K. Kalagatur, E.F. Abd Allah, S. Poda, K. Kadirvelu, A. Hashem, V. Mudili, C. Siddaiah, Quercetin mitigates the deoxynivalenol mycotoxin induced apoptosis in SH-SY5Y cells by modulating the oxidative stress mediators, *Saudi Journal of Biological Sciences* 28 (2021) 465–477.
- [35] B.N. Revanna, M. Madegowda, J. Rangaswamy, N. Naik, A novel Schiff base derivative as a fluorescent probe for selective detection of Cu²⁺ ions in buffered solution at pH 7.5: Experimental and quantum chemical calculations, *J. Mol. Struct.* 1254 (2022) 132327.
- [36] N.R. Divyashree, H.D. Revanasiddappa, N.R. Bhavya, M. Mahendra, B. Jayalakshmi, C. Shivamallu, S.P. Kollur, Azaneylylidene-based tetradentate Schiff base as a new “ON-OFF” fluorescent probe for the detection of Cu (II) ion: synthesis, characterization and real sample analysis, *Spectrochim. Acta A Mol. Biomol. Spectrosc.* 292 (2023) 122435.
- [37] S. Sayin, Synthesis of new quinoline-conjugated calixarene as a fluorescent sensor for selective determination of Cu²⁺ ion, *J. Fluoresc.* 31 (2021) 1143–1151.
- [38] P. Aussawaponpaisan, P. Nusuwan, P. Tongraung, P. Jittangprasert, K. Pumsa-ard, M. Kuno, Fluorescent chemosensor for Cu²⁺ based on Schiff base-naphthalene-2-ol, *Mater. Today: Proc.* 4 (2017) 6022–6030.
- [39] N. Vasimalai, S.A. John, Off-on and on-off chemosensors for ultratrace mercury (II) and copper (II) using functionalized thiazole and cadmium sulfide nanoparticles fluorophores, *Sens. Actuators B* 190 (2014) 800–808.
- [40] X.-M. Tian, S.-L. Yao, J. Wu, H. Xie, T.-F. Zheng, X.-J. Jiang, Y. Wu, J. Mao, S.-J. Liu, Two benzothiadiazole-based fluorescent sensors for selective detection of Cu²⁺ and OH⁻ ions, *Polyhedron* 171 (2019) 523–529.



Gas Chromatographic Technique Employed for Catalytic Investigation of Novel Phthalocyanines

T.M. SHARANAKUMAR^{1,*}, A. SUNILKUMAR², M.N. SOMASHEKAR³, B. CHETHAN⁴, T. NAVEEN KUMAR⁵ and C.R. RAVIKUMAR^{6,*}

¹Department of Chemistry, Ballari Institute of Technology and Management, Jnana Gangotri Campus, Bellary-583104, India

²Department of Physics, Ballari Institute of Technology and Management, Jnana Gangotri Campus, Bellary-583104, India

³Department of Chemistry, S.S. Margol Degree College of Arts, Science and Commerce, Shahabad Rural-585228, India

⁴Department of Physics, Indian Institute of Science, Bengaluru-560012, India

⁵Department of PG Chemistry, Surana College (Autonomous Institute), Bangalore-560004, India

⁶Research Centre, Department of Chemistry, East-West Institute of Technology (Affiliated to Visvesvaraya Technological University) Bangalore-560091, India

*Corresponding authors: E-mail: sharanbk199@gmail.com; ravicr128@gmail.com

Received: 2 May 2023;

Accepted: 8 June 2023;

Published online: 6 July 2023;

AJC-21298

The primaquine substituted Fe(II) phthalocyanine (PQFePc) and Co(II) phthalocyanine (PQCoPc) catalysts were prepared by using amide linkage method. The physical and chemical properties have been investigated by FTIR, mass, UV-Vis, TGA, XRD and elemental analysis. The catalytic oxidation of benzyl alcohol was determined by PQFePc and PQCoPc complexes by varying parameters like temperature, oxidant/catalytic ratio and substance/catalyst ratio. The optimization of catalytic oxidation reaction has been effectively achieved for the determination of benzyl alcohol (Bzalc) to benzaldehyde (Bzald). The PQCoPc and PQFePc exhibited excellent catalytic behaviour for the oxidation of benzyl alcohol obtaining high yield and good selectivity.

Keywords: Primaquine, Catalytic oxidation, Benzyl alcohol, Phthalocyanines.

INTRODUCTION

The invention of phthalocyanine has dragged greater attention in various technological applications due to its solubility in organic solvents and water [1]. Phthalocyanine exhibits good chemical, electrochemical and physical properties by suitable modifications in the structure [2]. The phthalocyanines are widely used in the field of sensors, supercapacitors, electro-catalytic, catalytic studies [3-7], semiconductors, nonlinear optical materials, liquid crystals, molecular conductors, nano-technology [8-13], photosensitizers [14] and in addition, as a catalyst in the chemical reactions [15-17]. Primaquine ligand is an 8-aminoquinoline derivative in the Class-I of the biopharmaceutical classification system [18]. Primaquine phosphate salt exhibits antiparasitic activity which acts on the secondary tissue schizonts and hypnozoites, which reveals the outstanding activity of exo-erythrocytic antimalarial agent [19]. In this view, we have chosen primaquine compound for the substitution with phthalocyanine ring for further studies.

In recent years, researchers in both academia and chemical industries have focused on improving the catalytic process by which benzyl alcohol is transformed into benzaldehyde [20,21]. The benzaldehyde is an important raw material for the preparation of dyestuff, perfumery and agrochemical sectors [22,23].

Earlier, Aktas *et al.* [24] reported the benzyl alcohol oxidation using fluoro-substituted iron(II), cobalt(II) phthalocyanines has determined the oxidation of benzyl alcohol to benzaldehyde using *tert*-butyl hydroperoxide (tBuOOH, TBHP) as oxidant. The determination of new material for the detection of highly effective benzyl alcohol to benzaldehyde is an never ending process in this context, primaquine substituted Fe(II) phthalocyanine (PQFePc) and Co(II) phthalocyanine (PQCoPc) complexes were synthesized. These complexes characterized by mass, FTIR, UV-visible, XRD, elemental analysis and thermogravimetric methods. A novel gas chromatographic (GC) technique has been adopted for the catalytic oxidation of benzyl alcohol with PQFePc and PQCoPc catalysts. The catalytic activities of PQCoPc and PQFePc were confirmed by varying

the parameters such as temperature, oxidant/catalytic ratio and substance/catalyst ratio. The overall results revealed that the synthesized compounds act as good catalyst for oxidation of benzyl alcohol into benzaldehyde reaction.

EXPERIMENTAL

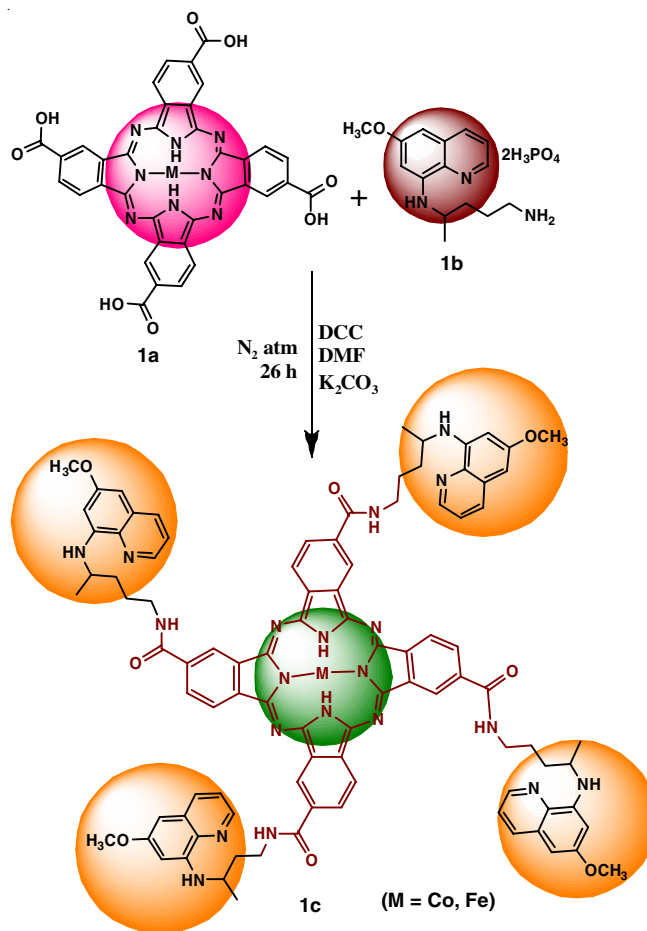
All the utilized chemicals, solvents and reagents were procured for the Sigma-Aldrich Chemie GmbH, Sternheim, Germany. Nitrogen atmosphere was used during the reaction. A few chemicals like NaOH, HCl, KOH were prepared by using oxygen-free distilled water. The primaquine substituted Fe(II) phthalocyanine (PQFePc) and Co(II) phthalocyanine (PQCoPc) were synthesized by following the procedure reported earlier [25,26].

The FT-IR measurements were carried out on a Perkin Elmer-1600 FTIR instrument on A Perkin-Elmer Lambda 25 instrument was used to record UV-vis spectra. The crystal structure evaluation was carried out on Bruker D8 diffractometer CuK α radiation source and the thermal stability of PQFePc and PQCoPc was investigated by thermogravimetric analysis using STA6000 system in the 20 to 1000 °C temperature range with the sweep rate of 20 °C min⁻¹ under blowing rate of 20 mL min⁻¹ oxygen and GC Agilent technologies 7820A equipment was used for GC measurement.

Synthesis of primaquine bisphosphate substituted Co(II) phthalocyanine (PQCoPc): A mixture of primaquine bisphosphate (0.07 mmol) with tetracarboxy-Co(II) phthalocyanine (CoTcPc) (0.0175 mmol), K₂CO₃ (0.06 mmol), DCC (15 mg) and DMF 40 mL in 250 mL round bottom flask was agitated under N₂ atmosphere for 26 h at 28 °C (**Scheme-I**). The obtained green coloured material was then filtered and washed with warm water as well as ethanol and finally rinsed with oxygen-free distilled water then dried at 45 °C (yield = 45%).

Synthesis of primaquine bisphosphate substituted Fe(II) phthalocyanine (PQFePc): A mixture of primaquine bisphosphate (0.06 mmol), tetracarboxylic-Fe(II)-phthalocyanine (FeTcPc) (0.015 mmol), K₂CO₃ (0.05 mmol), N,N'-dicyclohexylcarbodiimide (DCC, 15 mg) and DMF 40 mL in 250 mL round bottom flask was agitated under N₂ atmosphere for about 26 h at 28 °C (**Scheme-I**). The resulting green coloured material was filtered and washed by ethanol and distilled water. At the last, the obtained PQFePc complex was dried at 45 °C (yield = 55%).

Oxidation of benzyl alcohol: The oxidation reaction was conducted by using a thermostat schlenk vessel fitted with a stirrer and a condenser. Initially, oxygen was removed by passing nitrogen gas into the mixture containing benzyl alcohol (2.12 mol), catalyst (2.12 mol) and solvent (0.02 L). Later this mixture



Scheme-I: Preparation route of PQCoPc and PQFePc complexes

was stirred (2-3 min) in a Schlenk's vessel maintained at 50 °C. The oxidant *tert*-butyl hydroperoxide (TBHP, 2.23 mol) was added to this mixture with constant stirring. The samples (0.0006 L) were drawn at regular time intervals; at least twice, each sample was injected into GC (1.5 μ L each time). The obtained products, consumed substrates and conversion were monitored by GC method.

RESULTS AND DISCUSSION

Elemental analysis: Vario EL (III) CHNS analyzer used for elemental analysis of the synthesized compounds. The primaquine, PQCoPc and PQFePc complexes, were examined by decomposing a well known quantity of the complexes mixed with H₂SO₄ and HNO₃, followed evaporation and calcinations. The results are shown in Table-1.

Mass spectral studies: The mass by charge ratio [M+2] of prepared compounds was measured by mass spectra Fig. 1. The theoretical value of PQFePc was found to be 1697.75 and

TABLE-1
ELEMENTAL ANALYSIS OF THE LIGAND AND ITS METAL COMPLEXES

Ligand/ complexes	m.f.	m.w.	Colour	Elemental analysis (%): Calcd. (found)				
				C	H	N	O	M
Ligand	C ₁₅ H ₂₁ N ₃ O	259.35	Violet blue	69.47 (69.45)	8.16 (8.12)	16.20 (16.21)	6.17 (6.12)	–
[Co(L) ₄]	C ₉₅ H ₉₂ N ₂₀ O ₈ Co	1698.67	Green	67.09 (67.08)	5.45 (5.42)	16.47 (16.45)	7.53 (7.51)	3.46 (3.44)
[Fe(L) ₄]	C ₉₅ H ₉₂ N ₂₀ O ₈ Fe	1697.75	Green	67.21 (67.18)	5.46 (5.44)	16.50 (16.47)	7.54 (7.52)	3.29 (3.28)

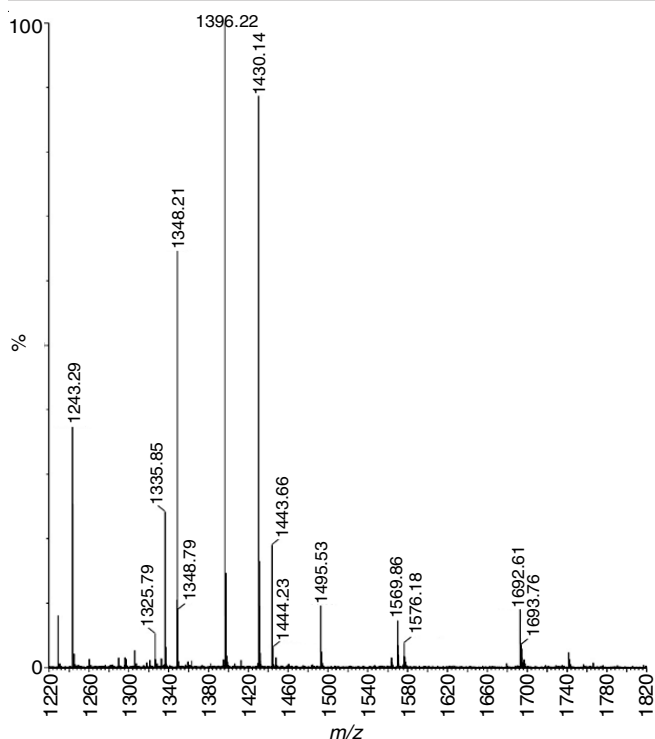


Fig. 1. Mass spectra of PQFePc complex

the experimental result is 1693.76. It clearly shows the confirmation of the prepared compound.

FT-IR spectral studies: The FTIR spectra confirmed the functional groups present in the range between 4000 to 600 cm^{-1} [27]. The FTIR spectra of the PQCoPc and PQFePc (Fig. 2a-b) shows the broad and intense peak in the range of 3600 to 3000 cm^{-1} ($-\text{OH}$ and $-\text{NH}_2$). The peaks at 3420.43 and 3432.72 cm^{-1} corresponds to $-\text{COOH}$ group of CoTcPc and FeTcPc, respectively appears in the range of 3300 to 2500 cm^{-1} . However in Fig. 2a (line blue) and 2b (line brown), the peak for $-\text{COOH}$ group disappears with the appearance of new peak pertaining to amide group formation (PQCoPc) at 3327.65 cm^{-1} and (PQFePc) at 3334.54 cm^{-1} ($-\text{CONH}$). The presence of narrow peak between 2932 and 2878 cm^{-1} is due to the vibr-

ation of C-H bond. Finally, the bands at 2236 cm^{-1} , 1653 cm^{-1} corresponds to C=C group, whereas 1629.29 and 1616.36 cm^{-1} corresponds to C-O group. Moreover, the peaks at 1242.72 and 1239.33 cm^{-1} corresponds to $-\text{C-N}$ group, while the peaks at 1082 and 1084.54 cm^{-1} corresponds to the C=N group, respectively.

UV-visible spectral studies: The UV-Vis spectra of the PQCoPc, CoTcPc PQFePc and FeTcPc complexes exhibits a well distinguished two strong absorption Q and B bands in the range of 300-800 nm (Fig. 3). The Q-band was observed at 680-720 nm, which is due to the excitation of the electrons from π to π^* (HOMO to LUMO) level in the complexes, similarly, the B-band was observed at 300-350 nm [28,29]. The lower state electronic absorption spectra of the compounds showed characteristics absorption Q-band region at 687.13 nm for PQCoPc compound, 711.54 nm for CoTcPc compound, 707.98 nm for PQFePc compound and 699 nm for FeTcPc compound in DMF. The B-band absorption of phthalocyanines of PQCoPc, CoTcPc, PQFePc and FeTcPc were observed at 384.80, 374.29, 319.86 and 328.95 nm, respectively [28,29]. These findings demonstrate that the aggregation behaviour was satisfactory in the DMF solvent.

Thermal studies: Fig. 4 represents the TGA plots of the PQCoPc and PQFePc complexes involves two-step reactions. In the first step, the PQCoPc and PQFePc undergo degradation and decomposition of the substituents take place at the temperature range of 150-300 $^{\circ}\text{C}$, while in the second step, phthalocyanine ring is broken, finally, metal is converted into metal oxide at 500-550 $^{\circ}\text{C}$ [29]. The PQCoPc and PQFePc complexes exhibited a good thermal stability upto nearly 550 $^{\circ}\text{C}$, confirms that the melting points of the PQCoPc and PQFePc complexes are greater than 500 $^{\circ}\text{C}$. Consequently, the PQCoPc and PQFePc complexes are used in electrochemical and chemical reactions.

XRD studies: The diffraction patterns of PQCoPc and PQFePc complexes (Fig. 5a-b) shows the broad peaks with different diffused intensity, where the intensity of peak increases by primaquine group. The less intense and short peaks were observed at 2θ values of 12 $^{\circ}$, 13 $^{\circ}$, 21 $^{\circ}$, 35 $^{\circ}$, 36 $^{\circ}$, 38 $^{\circ}$, 48 $^{\circ}$ and 55 $^{\circ}$ for PQCoPc and 13 $^{\circ}$, 14 $^{\circ}$, 16 $^{\circ}$, 20 $^{\circ}$, 35 $^{\circ}$, 37 $^{\circ}$, 38 $^{\circ}$, 50 $^{\circ}$ and 55 $^{\circ}$

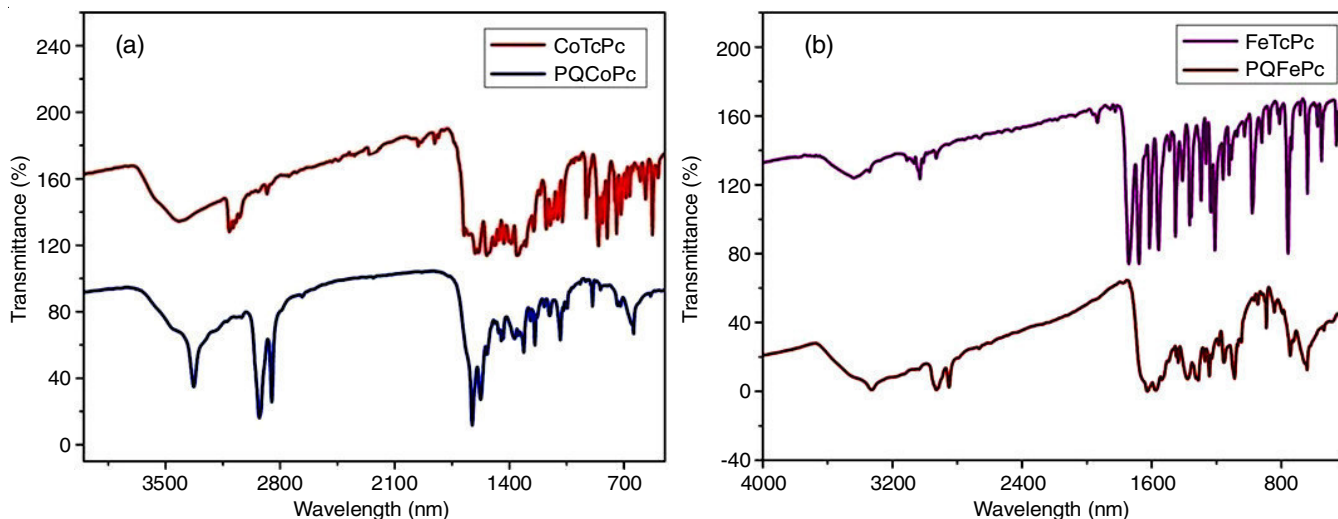


Fig. 2. FT-IR spectra of (a) PQCoPc with CoTcPc complex (b) PQFePc with FeTcPc complex

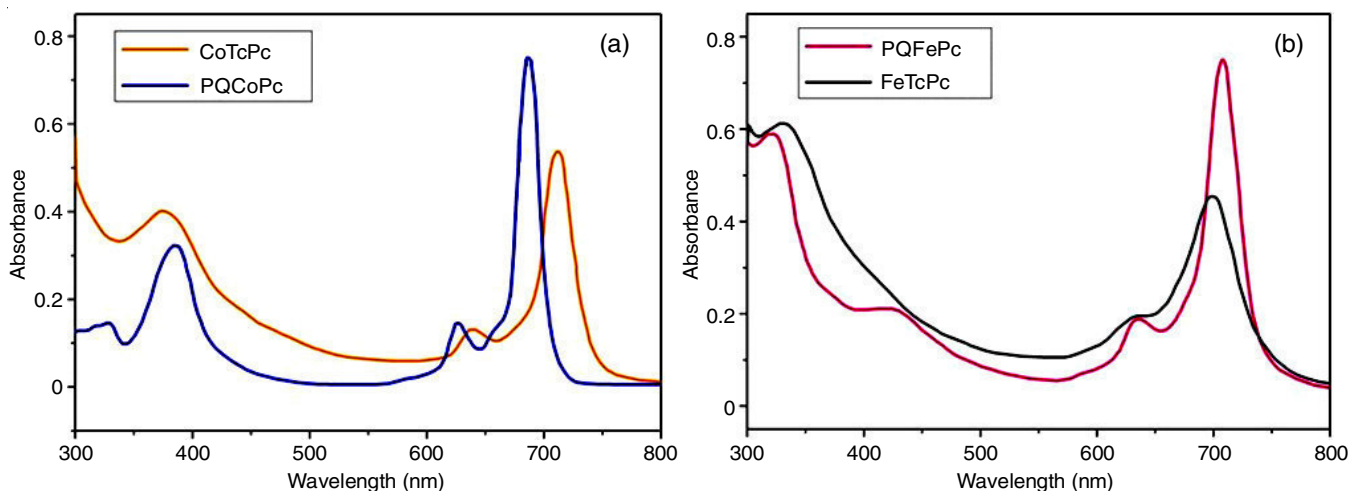


Fig. 3. UV-visible spectra of (a) PQCoPc with CoTcPc complex (b) PQFePc with FeTcPc complex

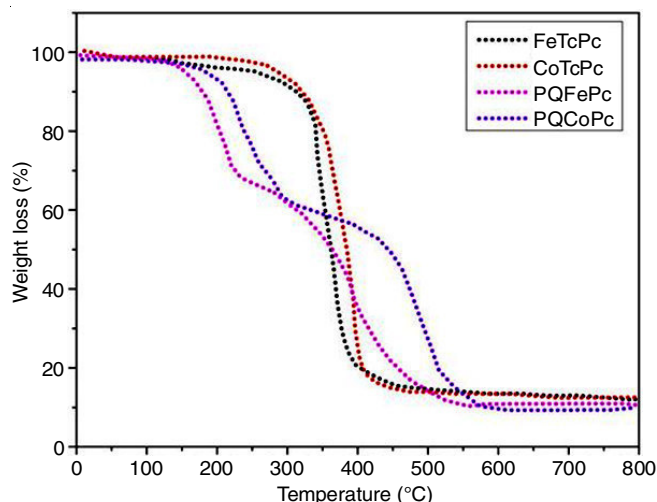


Fig. 4. TGA plots of PQCoPc, PQFePc, CoTcPc and FeTcPc complexes

for PQFePc. The high intense and sharp peaks were observed at 2θ values of 11° , 27° , 28° , 30° and 45° for PQCoPc and 12° , 27° , 28° , 30° and 46° for PQFePc. This indicates that PQCoPc and PQFePc complexes were crystalline nature.

Aggregation behaviour of PQCoPc complex: The aggregation behaviour of PQCoPc was studied by the UV-Vis absorption method. This complex exhibited good aggregation because of its 18π -electron structure. The major factors affecting the aggregation are concentration, temperature, solubility and substituents. The two types of aggregation observed are H-type and J-type [30]. The PQCoPc complex exhibited less of J-type aggregation but more of H-type aggregation in solvents.

The PQCoPc complex aggregation studies were performed by using different concentrations of DMF solvents (Fig. 6a). The Q-band intensity increased with the concentration of DMF solvent. The PQCoPc complex aggregation studies were performed by using different solvents like DMSO, EtOAc, CHCl_3 , THF and DMF (Fig. 6b). The Q-band intensity increased with DMF solvent. The aggregation studies of the PQCoPc complex were measured in the concentration range from 12×10^{-6} to $6 \times 10^{-6} \text{ mol dm}^{-3}$. The PQCoPc complex exhibited high coordinating ability and solubility in DMF and DMSO solvents. Therefore, more aggregation took place in these two solvents but less aggregation was observed in EtOAc and CHCl_3 solvents.

The above overall results showed that the aggregation of PQCoPc complex was better in DMF solvent. It increased the

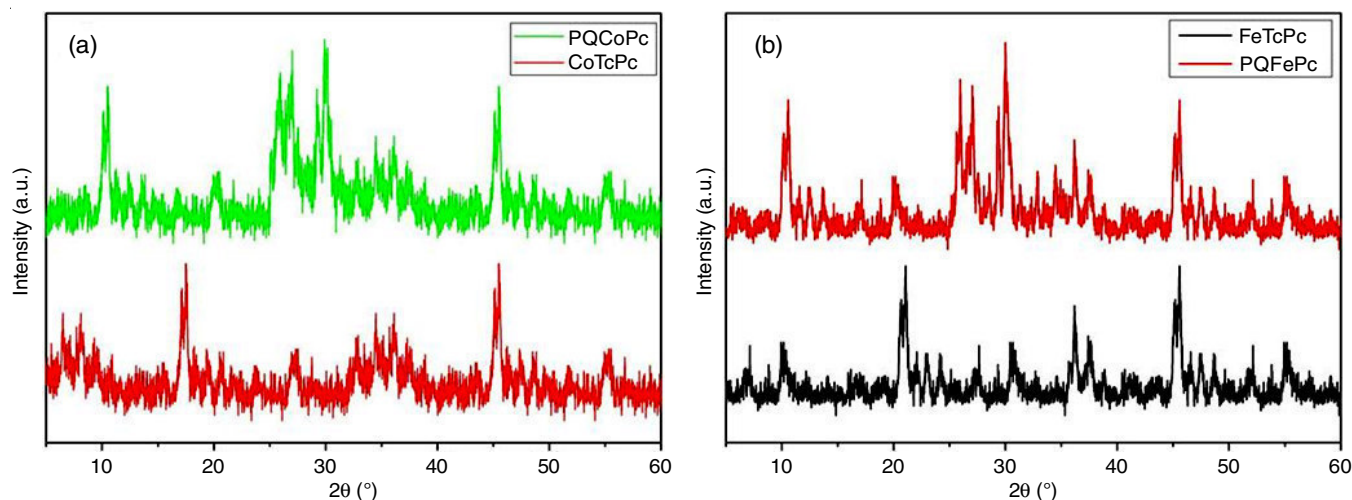


Fig. 5. P-XRD spectra of (a) PQCoPc with CoTcPc complex (b) PQFePc with FeTcPc complex

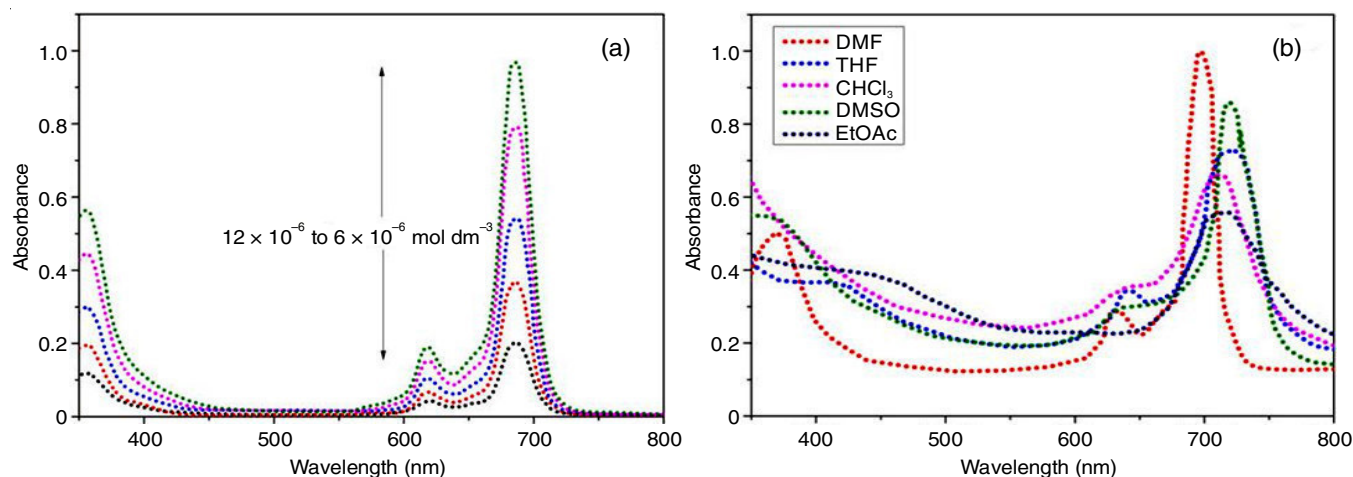


Fig. 6. Aggregation behaviour of (a) DMF solvents with different concentration (b) PQCoPc with different solvents (DMF, THF, CHCl_3 , DMSO and EtOAc)

absorption of Q-band by an increase of the concentration of DMF solvent.

Catalytic studies: Oxidation of benzyl alcohol was performed in presence of PQCoPc and PQFePc complexes as catalysts using gas chromatographic method and applied by various parameters of catalytic oxidation reactions *e.g.*, the percentage conversion and selectivity of products have been studied. The catalytic oxidation was performed by using various oxidants and auxiliary chemicals to reach good yields. In the oxidation reaction, benzyl alcohol was converted into various organic products. The major product is benzaldehyde (Bzald) and the minor products are benzoquinone (BzQn) and benzoic acid (BzAc). The peripherally substituents play an important role in the catalytic reaction [24].

The catalytic oxidations of benzyl alcohol to benzaldehyde were carried out in the presence and absence of PQCoPc and PQFePc catalysts and suitable oxidant at 50°C (Table-1). The catalytic oxidation reaction was found to give low yield of benzaldehyde in absence of catalyst. But, in presence of catalyst, an excellent yield (98%) was recorded after 3 h. There is no product formed (Table-2) when the catalytic oxidation was performed in absence of an oxidant. These results proved that the oxidation of benzyl alcohol, PQCoPc and PQFePc catalyst and oxidants are required and the present synthesized compounds have important role in the oxidation of benzyl alcohol.

Effect of substrate concentration: The transformation of benzyl alcohol to benzaldehyde was increased with the continuous reaction and yielded maximum conversion of 98% for PQCoPc and 95% for PQFePc after the reaction continued for 210 min and remains ideal with a slight increase as shown in Table-1. On the other hand, as the reaction precedes further oxidation of benzaldehyde to benzoic acid leads to decreased selectivity. From these results, 210 min was chosen as the optimal reaction time for conversion and selectivity of catalytic oxidation reaction of benzaldehyde to benzoic acid.

The conversion of benzyl alcohol to various organic products by uneven addition of the substrate/catalyst in a molar ratio varying from 600 to 1600 at 45°C is shown in Table-2. The obtained data shows that as the substrate/catalyst ratio is increased, the conversion of benzyl alcohol was found to decrease. The high mass of the substrate and low mass of the catalyst exhibits low conversion of benzyl alcohol due to fewer catalytic sites. From these result, it can be concluded that 600/1 substrate/catalyst ratio is ideal for the efficient conversion of benzyl alcohol (98% for PQCoPc and 95% for PQFePc) when compared to ratios reported in the previous studies [31,32].

Effect of oxidants concentration: Table-3 shows oxidation effects of benzyl alcohol with PQCoPc and PQFePc with the varied molar ratio of substrate/oxidant. If the ratio of TBHP/benzyl alcohol was increased from 0.83 to 3.3, the conversion

TABLE-2
OXIDATION OF BENZYL ALCOHOL WITH PQCoPc AND PQFePc BY VARYING OF QUANTITY OF SUBSTRATE

Substrate/ catalyst	Catalyst	Aldehyde (Bzald)	Quinine (BzQn)	Acid (BzAc)	Total conv. (%)	TON (mole of product/mole of catalyst)	TOF (h^{-1}) (mole of product/ mole of catalyst \times time)
600/1	1c	82	8	8	98	584	196
	2c	79	9	7	95	566	190
800/1	1c	66	8	7	81	642	214
	2c	70	9	7	86	682	228
1000/1	1c	58	8	6	72	712	238
	2c	55	9	7	71	702	234
1200/1	1c	48	6	6	60	710	238
	2c	46	7	6	59	698	234
1600/1	1c	33	5	6	46	722	242
	2c	33	6	5	44	690	230
600/1	Absence of catalyst	—	—	—	—	—	—

TABLE-3
OXIDATION OF BENZYL ALCOHOL WITH PQCoPc AND PQFePc WITH VARIOUS AMOUNTS OF OXIDANTS

Oxidant/ catalyst	Catalyst	Aldehyde (Bzald)	Quinine (BzQn)	Acid (BzAc)	Total conv. (%)	TON (mole of product/ mole of catalyst)	TOF (h ⁻¹) (mole of product/ mole of catalyst × time)
500/1	1c	84	5.9	8.1	98	584	196
	2c	83	4.3	7.7	95	566	190
800/1	1c	79	3.2	3.8	86	500	168
	2c	74	4.2	4.8	83	518	174
1200/1	1c	76	2.7	2.3	81	476	160
	2c	70	3.2	3.8	77	464	156
1600/1	1c	61	6.3	4.7	72	380	128
	2c	59	4.9	4.1	68	362	122
2000/1	1c	54	7.6	7.4	69	308	104
	2c	50	5.1	4.9	60	260	88
Without oxidant	Without catalyst	–	–	–	–	–	–

rate of benzyl alcohol was decreased from 98% to 52% for PQCoPc and 95% to 44% for PQFePc complexes. When the substrate and oxidant ratio increased to 0.83 benzyl alcohol conversion reaches 98% for PQCoPc and 95% for PQFePc, it exhibits high turnover number (TON) and turnover frequency (TOF) values of 584, 196 for PQCoPc and 566, 190 for PQFePc, respectively. The above result corroborates that a decrease in benzyl alcohol conversion rate is inversely related to the amount of TBHP oxidant [33]. The PQCoPc selectivity for benzaldehyde is 84%, while the PQFePc's selectivity is 83% at this oxidant content. Therefore, all these results revealed that the molar ratio of TBHP:benzyl alcohol of 0.83 was ideal with high conversion rate and selectivity.

Effect of temperature: The oxidation of benzyl alcohol was performed at various temperatures ranging from 25 to 90 °C in the presence of PQCoPc and PQFePc catalysts. A drastic change was observed in the conversion of benzyl alcohol (Table-4). It can be observed that as the temperature increased from 25 to 50 °C, the rate of conversion of benzyl alcohol increases from 61% to 98% for PQCoPc and 58% to 95% for PQFePc.

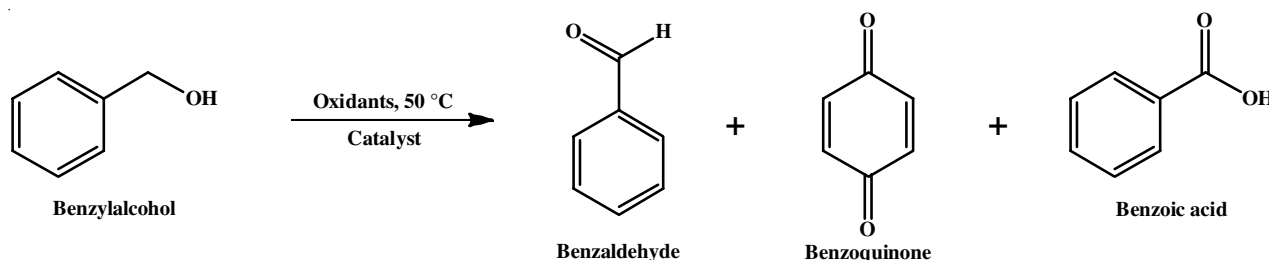
When temperature was increased above 50 °C, benzaldehyde selectivity was found to be decreased slightly. This decrease in selectivity of benzaldehyde can be attributed, as before, to the loss of benzyl alcohol [24]. Therefore, 50 °C is the ideal temperature for producing a good yield of benzaldehyde.

Oxidant effect: The catalytic oxidation of benzyl alcohol (**Scheme-II**) was conducted with PQCoPc and PQFePc by various oxidants hydrogen peroxide (H₂O₂) and *meta*-chloroperbenzoic acid (*m*-CPBA), which produces fewer yields of both PQCoPc and PQFePc complexes as shown in Table-5. The reaction of PQCoPc and PQFePc yields brown products from green colour in the presence of *m*-CPBA and H₂O₂. The colour changes due to PQCoPc and PQFePc were degraded immediately with H₂O₂ and *m*-CPBA. All of these findings suggest that TBHP is an effective oxidant for selectively converting benzaldehyde. In the presence of TBHP oxidant, the colour of both complex becomes light green from green.

The PQCoPc catalyst showed good catalytic effect with the highest conversion, TON and TOF values compared with the PQFePc catalyst. The catalytic activity also varies with the

TABLE-4
OXIDATION OF BENZYL ALCOHOL WITH PQCoPc AND PQFePc BY VARYING OF TEMPERATURE

Temp. (°C)	Catalyst	Aldehyde (Bzald)	Quinine (BzQn)	Acid (BzAc)	Total conv. (%)	TON (mole of product/ mole of catalyst)	TOF (h ⁻¹) (mole of product/ mole of catalyst × time)
25	1c	56	3	2	61	356	120
	2c	50	5	3	58	392	132
50	1c	83	8	7	98	584	196
	2c	81	7	7	95	566	190
70	1c	62	5	3	70	368	124
	2c	55	7	6	68	362	122
90	1c	46	4	2	52	302	102
	2c	40	6	4	50	290	98



Scheme-III: Benzyl alcohol oxidation reaction

TABLE-5
OXIDATION OF BENZYL ALCOHOL WITH PQCoPc AND PQFePc BY VARIOUS OXIDANTS

Oxidant	Catalyst	Aldehyde (Bzald)	Quinine (BzQn)	Acid (BzAc)	Total conv. (%)	TON (mole of product/mole of catalyst)	TOF (h ⁻¹) (mole of product/mole of catalyst × time)
TBHP	1c	82	8	8	98	588	200
	2c	79	9	8	96	570	194
H ₂ O ₂	1c	56	12	-	68	396	136
	2c	55	9	-	64	380	130
<i>m</i> -CPBA	1c	36	10	6	52	300	104
	2c	27	8	7	42	236	84

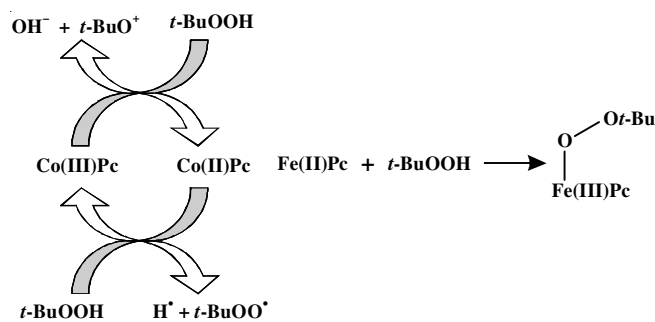
TABLE-6
COMPARISON STUDY OF VARIOUS CATALYSTS WITH PQCoPc AND PQFePc CATALYSTS

Catalyst	Reaction time	Reaction temperature (°C)	Oxidant	Conversion (%)	Ref.
CuPc ^A	0.5 h	70	TBAOX	25.0	[34]
CoPc ^B	5.5 h	70	TBHP	26.6	[35]
PdPc ^B	24 h	50	<i>m</i> -CPBA	31.3	
MnTEPyP ^C	4 h	60	TBHP	47.0	[36]
CuTPP ^D	40 min	60	O ₂	40 (in toluene) 35 (in benzene)	[37]
PQFePc	3 h	50	TBHP	98	Present work
PQCoPc	3 h	50	TBHP	96	

^APc = Un-substituted phthalocyanine; ^BPc = perfluoroalkylphthalocyanine; ^CTEPyP = water soluble metalporphyrins; ^DTPP = copper meso-tetraphenylporphyrin

transition metals present in the phthalocyanine ring [22]. Thus, it is concluded that PQCoPc catalyst exhibits more oxidation reaction compared with PQFePc catalyst (PQCoPc > PQFePc).

Comparison study of various catalysts with PQCoPc and PQFePc Catalysts for oxidation of benzyl alcohol: In present work, the reaction mechanism of PQCoPc and PQFePc with TBHP gives an active species. When phthalocyanine was compared to a porphyrin molecule with the same oxidation state of the central metal atom, phthalocyanine shows good stability and exhibits a strong oxidizing ability. When oxidant as TBHP, in the first step formation of PcCo(III)-OO*t*-Bu or PcFe(III)-OO*t*-Bu. Normally, peroxides react with porphyrin Fe complex *via* homolytic cleavage of the O-O bond to form porphyrin Fe^{IV=O} or porphyrin Fe^{V=O} species. It indicates that porphyrin Fe would be reacting with *t*-BuOOH, similarly, the PQFe^{IV=O} or PQFe^{V=O} reaction takes place in **Scheme-III** [38,39]. The catalytic oxidation of benzyl alcohol using different catalyst and their comparative data are presented in Table-6.



Scheme-IV: Red-ox reactions involving as *t*-BuOOH

Conclusion

In present work, the synthesis, characterization and the catalytic properties of two novel peripherally tetrasubstituted

phthalocyanine compounds in association with primaquine functionalized groups *i.e.* Fe(II) phthalocyanine (PQFePc) and Co(II) phthalocyanine (PQCoPc) were conducted. All the synthesized compounds were characterized by FTIR, UV-visible, mass, XRD, elemental analysis and thermogravimetric studies. The PQFePc and PQCoPc complexes show good aggregation behaviour in DMF and DMSO solvents. The catalytic activities of PQCoPc and PQFePc were executed for the oxidation of benzyl alcohol with various oxidants by varying the temperature, oxidant/catalytic ratio and substrate/catalyst ratio affect. The oxidation reactions were carried out to determine the optimum conditions of catalysts. Both PQCoPc and PQFePc complexes showed good catalytic activity for the oxidation of benzyl alcohol with high benzaldehyde selectivity by using *tert*-butyl hydroperoxide (TBHP) as an oxidant. In conclusion, these catalytic works are expedient, time saving and determined to be the best oxidation conditions with high turnover number (TON) and turnover frequency (TOF) values.

ACKNOWLEDGEMENTS

One of the authors, TMS expresses his gratitude to BITM College, Ballari and V.S.K. University, Ballari, India for providing the research facilities and spectral analysis, respectively.

CONFLICT OF INTEREST

The authors declare that there is no conflict of interests regarding the publication of this article.

REFERENCES

1. Z. Biyiklioglu, I. Acar and H. Kantekin, *Inorg. Chem. Commun.*, **11**, 630 (2008); <https://doi.org/10.1016/j.inoche.2008.02.030>
2. I. Acar, S. Topçu, Z. Biyiklioglu and H. Kantekin, *Color. Technol.*, **259**, 4 (2013); <https://doi.org/10.1111/cote.12031>

3. T.M. Sharanakumar, Mounesh, N.Y.P. Kumar, K.R.V. Reddy and Suresh, *Rasayan J. Chem.*, **13**, 2133 (2020); <https://doi.org/10.31788/RJC.2020.1345876>
4. B. Sanna Jilani, C.D. Mruthyunjayachari, P. Malathesh, Mounesh, T.M. Sharanakumar and K.R.V. Reddy, *Sens. Actuators B Chem.*, **301**, 127078 (2019); <https://doi.org/10.1016/j.snb.2019.127078>
5. S. Mounesh, T.M. Sharan Kumar, N.Y. Praveen Kumar, K.R.V. Reddy, K.B. Chandrakala, L. Arunkumar and C.C. Vidyasagar, *RSC Adv.*, **11**, 16736 (2021); <https://doi.org/10.1039/D1RA01815A>
6. P.K. Mounesh, N.Y. Praveenkumar, T.M. Sharankumar and K.R. Venugopal Reddy, *Electrochem. Sci. Adv.*, **2**, e2100006 (2021); <https://doi.org/10.1002/elsa.202100006>
7. N.Y. Praveen Kumar, Mounesh, T.M. Sharanakumar and K.R. Venugopala Reddy, *Chem. Pap.*, **75**, 2683 (2021); <https://doi.org/10.1007/s11696-021-01523-z>
8. T. Inabe and K. Morimoto, *Synth. Met.*, **86**, 1799 (1997); [https://doi.org/10.1016/S0379-6779\(97\)80909-5](https://doi.org/10.1016/S0379-6779(97)80909-5)
9. A.S. Komolov and P.J. Moller, *Synth. Met.*, **138**, 119 (2003); [https://doi.org/10.1016/S0379-6779\(02\)01286-9](https://doi.org/10.1016/S0379-6779(02)01286-9)
10. X. Zhang, J. Song, C. Zhou, L. Zhou and M. Gong, *J. Lumin.*, **149**, 69 (2014); <https://doi.org/10.1016/j.jlumin.2014.01.012>
11. A. Kumar, J. Brunet, C. Varenne, A. Ndiaye, A. Pauly, M. Penza and M. Alvisi, *Sens. Actuators B Chem.*, **210**, 398 (2015); <https://doi.org/10.1016/j.snb.2015.01.010>
12. Q.T. Ozmen, K. Goksen, A. Demir, M. Durmus and O. Koysal, *Synth. Met.*, **162**, 2188 (2012); <https://doi.org/10.1016/j.synthmet.2012.10.013>
13. O.M. Bankole, J. Britton and T. Nyokong, *Polyhedron*, **88**, 73 (2015); <https://doi.org/10.1016/j.poly.2014.12.020>
14. D. Çakir, C. Göl, V. Çakir, M. Durmus, Z. Biyiklioglu and H. Kantekin, *J. Lumin.*, **159**, 79 (2015); <https://doi.org/10.1016/j.jlumin.2014.10.044>
15. C. Colomban, E.V. Kudrik, P. Afanasiev and A.B. Sorokin, *Catal. Today*, **235**, 14 (2014); <https://doi.org/10.1016/j.cattod.2014.03.016>
16. C.G. Chao and D.E. Bergbreiter, *Catal. Commun.*, **77**, 89 (2016); <https://doi.org/10.1016/j.catcom.2016.01.022>
17. A. Aktas, E.T. Saka, Z. Biyiklioglu, I. Acar and H. Kantekin, *J. Organomet. Chem.*, **745-746**, 18 (2013); <https://doi.org/10.1016/j.jorganchem.2013.07.013>
18. A. Nair, B. Abrahamsson, D.M. Barends, D.W. Groot, S. Kopp, J.E. Polli, V.P. Shah and J.B. Dressman, *J. Pharm. Sci.*, **101**, 936 (2012); <https://doi.org/10.1002/jps.23006>
19. C.S. Chu, A.P. Phyto, K.M. Lwin, H.H. Win, T. San, A.A. Aung, R. Raksapradee, V.I. Carrara, G. Bancone, J. Watson, K.A. Moore, J. Wiladphaingern, S. Proux, K. Sriprawat, M. Winterberg, P.Y. Cheah, A.L. Chue, J. Tarning, M. Imwong, F. Nosten and N.J. White, *Clin. Infect. Dis.*, **67**, 1543 (2018); <https://doi.org/10.1093/cid/ciy319>
20. M.P. Chaudhari and S.B. Sawant, *Chem. Eng. J.*, **106**, 111 (2005); <https://doi.org/10.1016/j.cej.2004.07.014>
21. S. Tsuruya, H. Miyamoto, T. Sakae and M. Masai, *J. Catal.*, **64**, 260 (1980); [https://doi.org/10.1016/0021-9517\(80\)90501-1](https://doi.org/10.1016/0021-9517(80)90501-1)
22. R.A. Sheldon and J.K. Kochi, *Metal-Catalyzed Oxidation of Organic Compounds*, Academic: New York (1981).
23. M. Hudlicky, *Oxidations in Organic Chemistry*, ACS Monograph Series 186, American Chemical Society, Washington, p. 174 (1990).
24. A. Aktas, I. Acar, E.T. Saka, Z. Biyiklioglu and H. Kantekin, *J. Incl. Phenom. Macrocycl. Chem.*, **86**, 183 (2016); <https://doi.org/10.1007/s10847-016-0650-z>
25. K.M. Pradeep, K.R. Venugopala Reddy, M.N.K. Harish, B. Chidananda, B.J. Madhu, C.D. Mruthyunjayachari and S.D. Ganesh, *Synth. Met.*, **185-186**, 79 (2013); <https://doi.org/10.1016/j.synthmet.2013.09.009>
26. T.M. Sharanakumar, K.R. Venugopala Reddy, Mounesh, N.Y. Praveen Kumar, Suresh and N.H.M. Nandinibaby, *J. Indian Chem. Soc.*, **98**, 100139 (2021); <https://doi.org/10.1016/j.jics.2021.100139>
27. Mounesh and K.R. Venugopala Reddy, *Anal. Chim. Acta*, **1108**, 98 (2020); <https://doi.org/10.1016/j.aca.2020.02.057>
28. Mounesh, K.R. Venugopal Reddy and Fasiulla, *Anal. Chem. Lett.*, **10**, 137 (2020); <https://doi.org/10.1080/22297928.2020.1760132>
29. Mounesh, P. Malathesh, N.Y. Praveen Kumara, C.D. Mruthyunjayachari, B.S. Jilani and K.R. Venugopala Reddy, *Heliyon*, **5**, e01946 (2019); <https://doi.org/10.1016/j.heliyon.2019.e01946>
30. M. Grossman, G. Glosser, J. Kalmanson, J. Morris, M.B. Stern and H.I. Hurtig, *J. Neurol. Sci.*, **184**, 123 (2001); [https://doi.org/10.1016/S0022-510X\(00\)00491-3](https://doi.org/10.1016/S0022-510X(00)00491-3)
31. A. Aktas, I. Acar, Z. Biyiklioglu, E.T. Saka and H. Kantekin, *Synth. Met.*, **198**, 212 (2014); <https://doi.org/10.1016/j.synthmet.2014.10.022>
32. V. Çakir, E.T. Saka, Z. Biyiklioglu and H. Kantekin, *Synth. Met.*, **197**, 233 (2014); <https://doi.org/10.1016/j.synthmet.2014.09.022>
33. S.R. Ali, V.K. Bansal, A.A. Khan, S.K. Jain and M.A. Ansari, *J. Mol. Catal. Chem.*, **303**, 60 (2009); <https://doi.org/10.1016/j.molcata.2008.12.020>
34. A. Rezaeifard, M. Jafarpour and A. Naeimi, *Catal. Commun.*, **16**, 240 (2011); <https://doi.org/10.1016/j.catcom.2011.09.039>
35. M. Ozer, F. Yilmaz, H. Erer, I. Kani and O. Bekaroglu, *Appl. Organomet. Chem.*, **23**, 55 (2009); <https://doi.org/10.1002/aoc.1471>
36. Q.G. Ren, S.Y. Chen, X.T. Zhou and H.B. Ji, *Bioorg. Med. Chem.*, **18**, 8144 (2010); <https://doi.org/10.1016/j.bmc.2010.10.026>
37. R. Rahimi, E. Gholamrezapor and M.R. Naimi-jamal, *Inorg. Chem. Commun.*, **14**, 1561 (2011); <https://doi.org/10.1016/j.inoche.2011.05.056>
38. A. Aktas, I. Acar, E.T. Saka and Z. Biyiklioglu, *J. Organomet. Chem.*, **815-816**, 1 (2016); <https://doi.org/10.1016/j.jorganchem.2016.04.025>
39. A.B. Sorokin, S. Mangematin and C. Pergrale, *J. Mol. Catal. Chem.*, **182-183**, 267 (2002); [https://doi.org/10.1016/S1381-1169\(01\)00486-1](https://doi.org/10.1016/S1381-1169(01)00486-1)

DESIGN, SYNTHESIS, MOLECULAR DOCKING, AND ANTIMICROBIAL STUDY ON NAPHTHOFURAN DERIVATIVES

S.M. Raghavendra^{1,3}, M.N. Kumaraswamy², K.M. Nagarsha³,
T.M. Sharanakumar⁴, Praveen C. Ramamurthy⁵ and K.P. Latha^{3,✉}

¹Department of Chemistry, Sir M V Govt. Science College, Bhadravathi-577 303,
Karnataka, India

²Department of Chemistry, Government First Grade College, Kadur-577 548, Karnataka, India

³Department of Chemistry, Sahyadri Science College, Shivamogga-577 203, Karnataka India

⁴Department of Chemistry, Ballari Institute of Technology and Management, Ballari-583104,
Karnataka, India

⁵Department of Materials Engineering, Indian Institute of Science, Bengaluru-560 012,
Karnataka, India

✉Corresponding Author: lathakpssc@gmail.com

ABSTRACT

The ethyl-naphtho[2,1-*b*]furon-2-carboxylate 2, hydrazine hydrate in the presence of a catalytic quantity of conc. HCl in ethanol was refluxed at 30 °C to get the naphtho[2,1-*b*]furan-2-carbohydrazide 3. The reaction of aromatic acids with methanol in the presence of an acid catalyst gives esters, these esters on treatment with hydrazine hydrazide produce acid hydrazides 4a-f. These acid hydrazides 4a-f, in reaction with carbon disulphide produces 2-(substituted)phenylhydrazine-potassiumcarbodithioate 5a-f. The reaction of 5a-f with compound 3 in ethanol produces *N*-[3-phenyl-5-sulphonyl-4H-1,2,4-triazole-4-yl]-naphtho[2,1-*b*]furan-2-carboxamide 6a-f. Elemental analysis, FTIR, NMR, and mass spectral analyses have been used to characterize the synthesized compounds. They have also been applied to research on antimicrobial studies and have also done the docking investigation of the synthesized compounds with the various biological molecules to get excellent results.

Keywords: Naphthofuran, Triazole, Molecular Docking, Antibacterial Activity, Antifungal Activity, Hydrazine Hydrazide.

RASAYAN J. Chem., Vol. 16, No. 3, 2023

INTRODUCTION

Synthetic chemistry plays an important role in the blooming of drug discoveries. Large numbers of the consolidated heterocycles and bi-heterocycles including naphthofuran have accounted for a wide range of pharmacological activities.¹⁻⁴ Naphthofuran cores are key primary moieties found in countless organically significant normal products.⁵⁻⁶ Naphthofuran subsidiaries have been isolated from different natural sources, such as *Fusarium*, *Oxysporum*, *Gossipium barbandanse*, and so on, and are notable for different natural exercises like antitumor, antifertility, mutagenic, development inhibitory, and osterogenic.⁷⁻⁹ The literature review revealed that the prepared subsidiaries of naphtho[2,1-*b*]furans show an extensive variety of pharmacological and biological action.¹⁰⁻¹⁴ Recently, reviews on derivatives of arene ring-fused furans exhibit very potent and diverse pharmacological activities.¹⁵⁻¹⁶ The literature survey reveals the importance of triazoles, which shows magnificent biological medicinal properties. Due to their numerous biological functions, the substituted triazoles are a very significant class of chemicals that have attracted the interest of numerous chemists and biologists in the domains of organic synthesis, medicine, and pharmaceuticals. like antitubercular, antimicrobial, anticonvulsant, antibacterial antifungal, and anticancer.¹⁷⁻²¹ The effectiveness of substituted triazoles as antibacterial and antitubercular medicines has been supported by a substantial body of research in recent years. Biheterocyclic compounds involving 1,2,4-triazole derivatives designed with a new approach have efficient antitubercular and Antimicrobial qualities.²² Substituted alkyl and aryl derivatives encompassing 1,2,4-triazole moiety are used as very effective antifungal drugs.²³ In these years, 1,2,4-Triazole hybrids have been found as potential

antibacterial agents against both drug-sensitive and drug-resistant pathogens.²⁴ Thus, naphthofuran derivatives show diverse pharmacological activities.²⁵⁻²⁷ In view of the several biological activities of heterocyclic compounds comprising the naphthofuran entity, our present investigation describes to formulation and synthesis of different derivatives of naphthofurans and to study their antimicrobial activities as per the scheme given below. The derivatives of title compounds were confirmed by elemental analysis, UV-Visible, FT-IR, NMR, and Mass Spectral studies.

EXPERIMENTAL

Chemicals and Instruments

All of the chemicals and reagents were purchased from Sigma Aldrich. Double distilled water is used to prepare all the required compounds. The synthesized compounds' functional groups were investigated using FTIR spectra in the 4000-300 cm^{-1} range with an FTIR Frontier Perkin Elmer instrument. With the Agilent VNMRS-400 NMR instrument, the ^1H -NMR spectrum was detected. The molecular weight of the molecule was calculated by using Water's SYNAPT G2 QTOF LCMS equipment.

Synthesis of 2-hydroxy-1-naphthaldehyde (1)

The 2-Naphthol (0.05 M) was dissolved in 20 mL of ethanol, then add sodium hydroxide (0.26 M) was in 25 mL water the solution was stirred in the reaction vessel and simultaneously add dropwise 4.3 mL of chloroform, then the reaction mixture was stirred for 2 h to get the required product. The product was poured into ice-cold water and neutralized with dilute HCl, the solid product separates and it is filtered and dried²⁵ Scheme-1.

Synthesis of ethyl naphtho[2,1-*b*]furan-2-carboxylate (2)

The compound **1** (0.04 M), N,N-dimethyl formamide (30 mL), ethyl-chloroacetate (0.04 M), and anhydrous K_2CO_3 (0.95 M) were added in the reaction vessel and refluxed in water bath for 26 h. The reaction mixture was filtered and the filtrate was concentrated by distillation and then transferred into ice-cold water, the solid product separates and was filtered and dried Scheme-1.

Synthesis of naphtho[2,1-*b*]furan-2-carbohydrazide (3)

The compound **2** (0.02 M), catalytic quantity of conc. HCl and hydrazine hydrate (0.04 M), and absolute ethanol (30 mL) were refluxed for 2 h in a water bath. Then the product was cooled at 28 $^\circ\text{C}$, the solid product was obtained and it is filtered and dried Scheme-1.

Synthesis of substituted acid hydrazides (4a-f)

A solution of aromatic acid (0.03 M) in methanol (60 mL), for this solution add a few drops of conc. sulphuric acid and reflux the reaction mixture for 18 h at 40 $^\circ\text{C}$. Then add hydrazine hydrate (3 mL 0.06 M) and the reaction mixture was refluxed for 12 h. The excess methanol was eliminated under reduced pressure and the reaction mixture was transferred into ice-cold water. The separated solid product is obtained and it is filtered and dried²⁵⁻²⁶ Scheme-1.

Synthesis of 2-(substituted)phenylhydrazine-potassiumcarbodithioate (5a-f)

To a solution of **4a** (0.02 M) in ethanol (30 mL), carbon disulphide (1.5 mL, 0.026 M), and KOH (0.025 M) were added and stirred for 20 h at 28 $^\circ\text{C}$. The solid product was obtained and it is filtered, and washed with diethyl ether to get the required **5a** compound. The same methodology was used for the synthesis of **5b-f** from **4b-f**²⁷ Scheme-1.

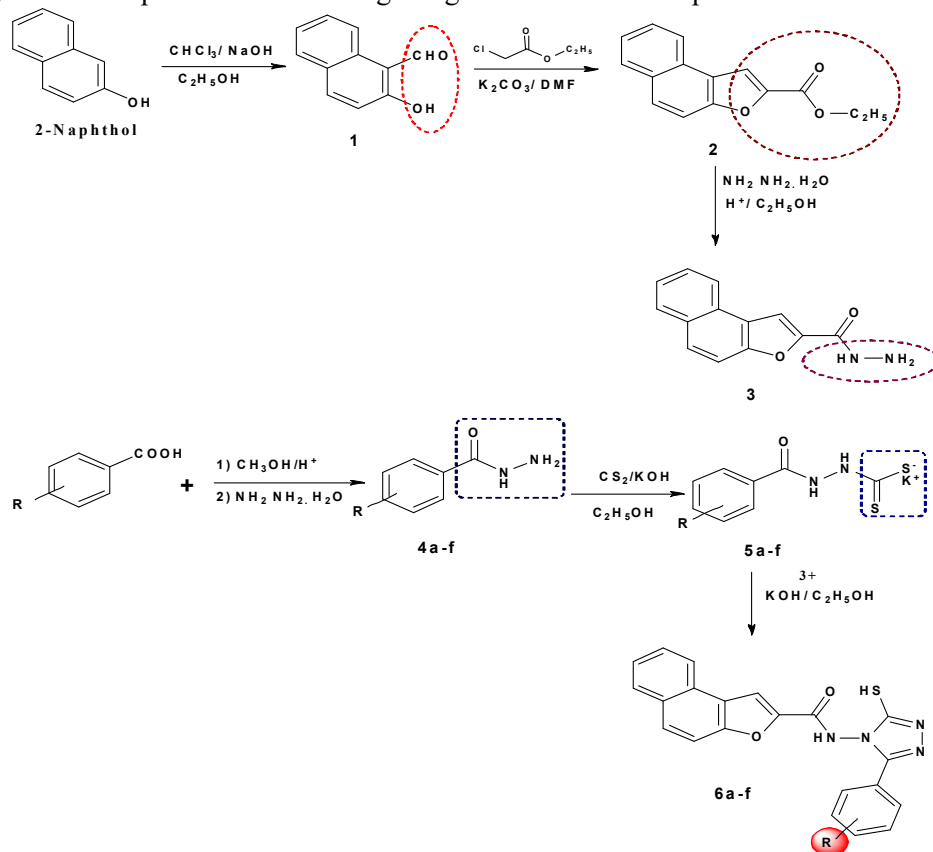
Synthesis of *N*-[3-phenyl-5-sulphanyl-4H-1,2,4-triazol-4-yl]-naphtho[2,1-*b*]furan-2-carboxamide (6a-f)

The compound **3** (0.02 M) and phenyl hydrazine-potassium carbodithioate aromatic acid hydrazide **5a** (0.02 M) were refluxed at 60 $^\circ\text{C}$ in a water bath for 6 h. The obtained product was transferred into ice-cold water and neutralized with conc. HCl. The precipitated triazole was filtered and purified from ethanol, the same methodology was used for the synthesis of **6b-f** Scheme-1.

RESULTS AND DISCUSSION

Spectral Characterization

All the synthesized compounds were characterized using FTIR, Mass, and NMR Spectroscopy techniques. The FTIR spectra of 2 show an absorption band at 1733 cm^{-1} due to the carbonyl group of ester Fig.-1. In $^1\text{H-NMR}$ spectra (CDCl_3), a triplet at δ 1.6 due to $-\text{CH}_3$ protons, a quartet at δ 4.6 due to $-\text{CH}_2$ protons, and a multiplet at δ 7.5-8.1 integrating for seven aromatic protons were confirmed Fig.-4.



Scheme-1: Synthetic Route of Naphthofuran Derivatives (6a-f)

The FTIR spectra of 3 show an absorption band at $3303\text{--}2968\text{ cm}^{-1}$ due to amino and an absorption band at 1656 cm^{-1} due to carbonyl group Fig.-2. $^1\text{H-NMR}$ spectra of 3 show a broad singlet at δ 4.6, 1H, NH, (D_2O exchangeable), multiplet δ 7.4-8.6, for seven aromatic protons, and a singlet at δ 9.8 for two amino group protons. The FTIR spectra of 4d show an absorption band at $3300\text{--}2970\text{ cm}^{-1}$ due to the amino group and an absorption band at 1652 cm^{-1} due to the carbonyl group. $^1\text{H-NMR}$ spectra of 4d show a broad singlet at δ 3.8, 3H, for methoxy, singlet at δ 4.1, 1H, NH, (D_2O exchangeable), multiplet δ 6.5-6.9 for four aromatic protons and a singlet at δ 9.1 for two amino protons. The FTIR (KBr) spectrum of 6a shows an absorption band at 1667 cm^{-1} due to carbonyl group. $^1\text{H-NMR}$ spectra (DMSO-d_6) of 6a shows a singlet at δ 6.95, 1H, SH, singlet at δ 12.12, 1H, NH, multiplet δ 7.2-8.5, for twelve aromatic protons. The Mass spectral analysis indicates the m/z 386. The FTIR (KBr) spectrum of 6b shows an absorption band at 1668 cm^{-1} due to carbonyl group. $^1\text{H-NMR}$ spectra (DMSO-d_6) of 6b shows a broad singlet δ 5.8, 1H, OH, singlet at δ 6.95, 1H, SH, singlet at δ 12.10, 1H, NH, multiplet δ 7.3-8.4, for eleven aromatic protons. The Mass spectral analysis indicates the m/z 402. The FTIR (KBr) spectrum of the 6c shows an absorption band at 1666 cm^{-1} is due to the C=O group. $^1\text{H-NMR}$ spectra (DMSO-d_6) of 6c shows a singlet at δ 6.97, 1H, SH, singlet at δ 12.21, 1H, NH, multiplet δ 7.4-8.6, for eleven aromatic protons. The Mass spectral analysis indicates the m/z 431. The FTIR (KBr) spectrum of the 6d shows an absorption band at 1667 cm^{-1} due to the carbonyl group and 3284.61 cm^{-1} due to the $-\text{NH}$ group Fig.-3. $^1\text{H-NMR}$ spectra (DMSO-d_6) of 6d shows a singlet at δ 3.8, 3H, OCH_3 , singlet at δ 7.05, 1H, SH, singlet at δ 12.2, 1H, NH, multiplet δ 7.6-8.6, for eleven

aromatic protons Fig.-5. The Mass spectral analysis indicates the m/z 416 Fig.-6. The FTIR (KBr) spectrum of 6e absorption band at 1669 cm^{-1} due to carbonyl group. $^1\text{H-NMR}$ spectra (DMSO-d_6) of 6e show a singlet at δ 6.98, 1H, SH, singlet at δ 12.23, 1H, NH, multiplet δ 7.6-8.7, for eleven aromatic protons. The Mass spectral analysis indicates the m/z 421. The FTIR (KBr) spectrum of 6f absorption band at 1669 cm^{-1} due to carbonyl group. $^1\text{H-NMR}$ spectra (DMSO-d_6) of 6f show a singlet at δ 1.7, 3H, CH_3 singlet at δ 7.05, 1H, SH, singlet at δ 12.01, 1H, NH, multiplet δ 7.5-8.6, for eleven aromatic protons. The Mass spectral analysis indicates the m/z 400.

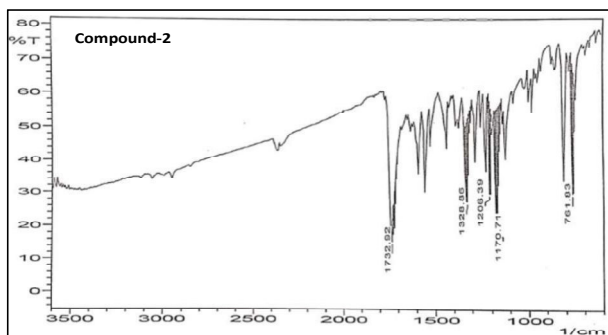


Fig.-1: FTIR Spectra of Compound 2

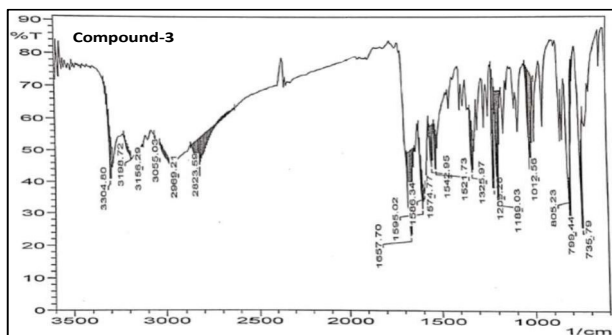


Fig.-2: FTIR Spectra of Compound 3

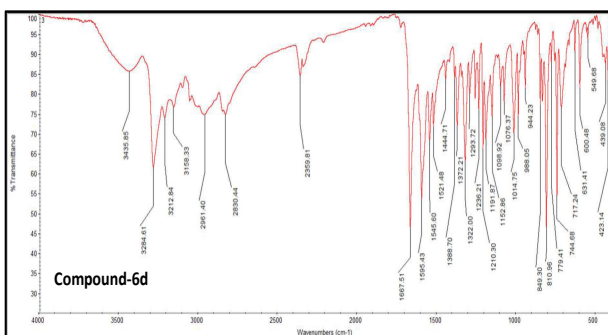


Fig.-3: FTIR Spectra of Compound 6d

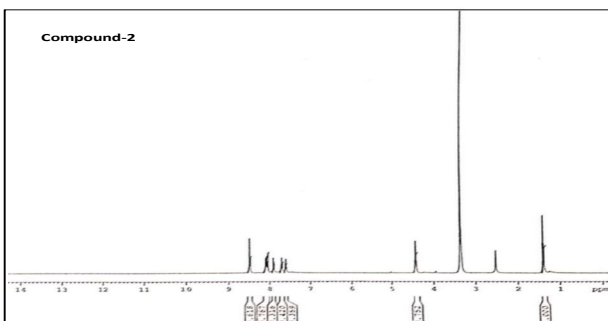


Fig.-4: NMR Spectra of Compound 2

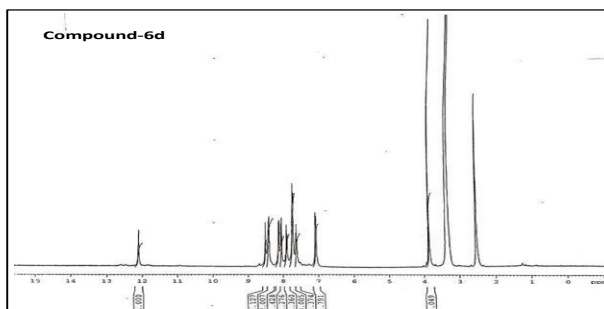


Fig.-5: NMR Spectra of Compound 6d

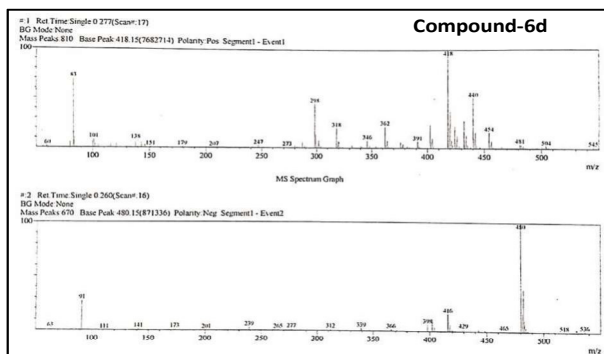


Fig.-6: Mass Spectra of Compound 6d

Elemental Analysis

Table-1: Elemental Data of Newly Synthesized Compounds

Comp.	R	M.p. °C	Yield (%)	Mol. formula	Clad (Found) %		
					C	H	N
1	-----	81	64	C ₁₂ H ₁₀ O ₂	-----	-----	-----
2	----	102	65	C ₁₅ H ₁₂ O ₃	-----	-----	-----
3	----	268	66	C ₁₃ H ₁₀ N ₂ O ₂	-----	-----	-----
4a	H	114	73	C ₇ H ₈ N ₂ O	-----	-----	-----
4b	2-OH	139	67	C ₇ H ₈ N ₂ O ₂	-----	-----	-----
4c	3-NO ₂	146	65	C ₇ H ₇ N ₃ O ₃	-----	-----	-----
4d	4-OCH ₃	198	69	C ₈ H ₁₀ N ₂ O ₂	-----	-----	-----
4e	4-Cl	159	70	C ₇ H ₇ ClN ₂ O ₂	-----	-----	-----
4f	4-CH ₃	119	69	C ₈ H ₁₀ N ₂ O	-----	-----	-----
6a	H	260	68	C ₂₁ H ₁₄ N ₄ O ₂ S	65.27 64.34	3.65 3.41	14.50 13.89
6b	2-OH	279	63	C ₂₁ H ₁₄ N ₄ O ₃ S	62.68 61.83	3.51 3.21	13.92 12.97
6c	3-NO ₂	294	65	C ₂₁ H ₁₃ N ₅ O ₄ S	58.46 57.55	3.04 2.74	16.23 15.16
6d	4-OCH ₃	273	68	C ₂₂ H ₁₆ N ₄ O ₃ S	63.45 62.53	3.87 3.57	13.45 13.27
6e	4-Cl	268	67	C ₂₁ H ₁₃ ClN ₄ O ₂ S	59.93 58.87	3.11 2.66	13.31 12.19
6f	4-CH ₃	286	64	C ₂₂ H ₁₆ N ₄ O ₂ S	65.98 64.81	4.03 3.59	13.99 12.89

Biological Activity of Synthesized Compounds

Antimicrobial Activity

The cup-plate technique was used to test the in vitro antibacterial activity against cultures of six bacteria and two fungi that had been grown for 24h.²⁸ The compounds 6a-f have been determined for their antibacterial activity against *S. aureus*, *S. epidermidis*, *B. cereus*, *P. aeruginosa*, *V. cholerae*, and *E. coli* and antifungal activity against *A. aureus* and *A. fumigatus*. Standards for antibacterial and antifungal

activity were *chloramphenicol* and *fluconazole*, respectively. The substances were tested against all species in DMF at a different concentration of 25, 50, 100 $\mu\text{g/ml}$. After incubation for 48 hours at 30 $^{\circ}\text{C}$ for antifungal activity and 24 hours at 25 $^{\circ}\text{C}$ for antibacterial activity, the zone of inhibition was compared to the reference medication. The outcomes are shown in Table-2 and Table-3.

Table-2: Antibacterial Activity of Compounds 6a-f

Compound	Concentration in $\mu\text{g/ml}$	Growth inhibition against <i>bacteria</i> in mm					
		<i>S.aureus</i>	<i>S.epidermidis</i>	<i>B. cereus</i>	<i>P.aeruginosa</i>	<i>V.cholerae</i>	<i>E.coli</i>
6a	25	15.26 \pm 0.23	15.28 \pm 0.26	13.48 \pm 0.21	14.26 \pm 0.14	16.48 \pm 0.27	14.88 \pm 0.46
	50	18.21 \pm 0.01	17.29 \pm 0.27	16.57 \pm 0.06	18.26 \pm 0.13	19.24 \pm 0.31	17.25 \pm 0.04
	100	23.23 \pm 0.12	19.26 \pm 0.21	21.26 \pm 0.01	21.24 \pm 0.13	22.57 \pm 0.32	19.52 \pm 0.26
6b	25	13.44 \pm 0.25	13.18 \pm 0.26	14.48 \pm 0.20	14.12 \pm 0.13	14.42 \pm 0.27	13.79 \pm 0.46
	50	15.92 \pm 0.08	16.26 \pm 0.27	15.88 \pm 0.05	16.23 \pm 0.13	17.42 \pm 0.38	14.88 \pm 0.04
	100	18.59 \pm 0.13	20.13 \pm 0.23	19.56 \pm 0.00	20.22 \pm 0.13	19.25 \pm 0.32	19.45 \pm 0.23
6c	25	15.43 \pm 0.05	16.83 \pm 0.16	17.49 \pm 0.16	16.58 \pm 0.22	17.02 \pm 0.21	15.68 \pm 0.19
	50	19.46 \pm 0.08	18.35 \pm 0.30	21.48 \pm 0.05	19.26 \pm 0.22	18.23 \pm 0.04	15.25 \pm 0.19
	100	25.46 \pm 0.32	23.98 \pm 0.35	27.45 \pm 0.02	23.15 \pm 0.22	26.25 \pm 0.25	24.55 \pm 0.09
6d	25	10.26 \pm 0.13	10.87 \pm 0.35	11.86 \pm 0.25	11.26 \pm 0.26	13.22 \pm 0.05	12.36 \pm 0.15
	50	15.25 \pm 0.16	13.48 \pm 0.15	14.84 \pm 0.18	14.27 \pm 0.15	14.89 \pm 0.12	13.47 \pm 0.23
	100	20.15 \pm 0.58	20.77 \pm 0.26	23.43 \pm 0.14	18.45 \pm 0.11	21.58 \pm 0.13	21.85 \pm 0.15
6e	25	15.85 \pm 0.14	15.85 \pm 0.03	14.78 \pm 0.02	14.32 \pm 0.15	16.23 \pm 0.07	16.43 \pm 0.12
	50	19.55 \pm 0.55	19.24 \pm 0.01	18.54 \pm 0.07	18.21 \pm 0.16	18.45 \pm 0.05	18.34 \pm 0.23
	100	26.25 \pm 0.13	23.12 \pm 0.06	28.21 \pm 0.14	22.22 \pm 0.07	26.88 \pm 0.24	24.83 \pm 0.02
6f	25	16.78 \pm 0.26	14.90 \pm 0.12	13.25 \pm 0.02	13.23 \pm 0.22	15.47 \pm 0.07	12.90 \pm 0.23
	50	19.45 \pm 0.23	18.51 \pm 0.09	16.24 \pm 0.20	16.22 \pm 0.13	17.58 \pm 0.03	18.21 \pm 0.24
	100	21.53 \pm 0.19	20.52 \pm 0.05	22.82 \pm 0.03	19.25 \pm 0.15	22.17 \pm 0.05	20.62 \pm 0.13
Control	100	-	-	-	-	-	-
Std	100	27.13 \pm 0.02	25.04 \pm 0.32	30.06 \pm 0.44	24.01 \pm 0.02	28.28 \pm 0.15	26.12 \pm 0.21

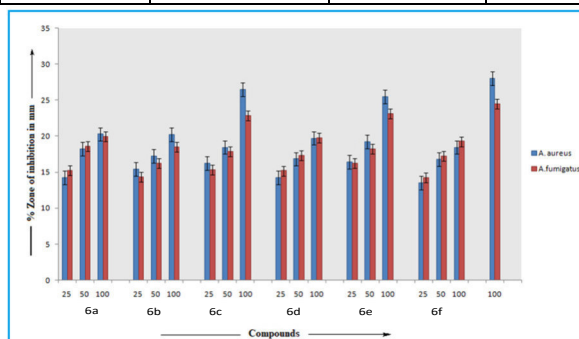


Fig.-7: Graphical Representation Chart of Antibacterial Activity of Compounds 6a-f

Table-3: Antifungal Activity of Compounds 6a-f

Compound	Concentration in $\mu\text{g/ml}$	Growth inhibition against <i>fungicides</i> in mm	
		<i>A.aureus</i>	<i>A.fumigatus</i>
6a	25	14.35 \pm 0.26	15.25 \pm 0.23
	50	18.25 \pm 0.32	18.58 \pm 0.23
	100	20.28 \pm 0.25	29.99 \pm 0.22
6b	25	15.42 \pm 0.18	14.30 \pm 0.18
	50	17.23 \pm 0.22	16.29 \pm 0.18
	100	20.25 \pm 0.35	18.55 \pm 0.19
6c	25	16.23 \pm 0.18	15.30 \pm 0.15
	50	18.45 \pm 0.18	17.90 \pm 0.08
	100	26.45 \pm 0.05	22.85 \pm 0.05

6d	25	14.25±0.18	15.20±0.15
	50	16.85±0.25	17.35±0.28
	100	19.73±0.25	19.78±0.18
6e	25	16.45±0.15	16.26±0.08
	50	19.25±0.26	18.27±0.07
	100	25.45±0.15	23.13±0.03
6f	25	13.55±0.03	14.24±0.15
	50	16.74±0.23	17.29±0.14
	100	18.48±0.14	19.25±0.02
Control	100	-	-
Std	100	28.06±0.13	24.51±0.16

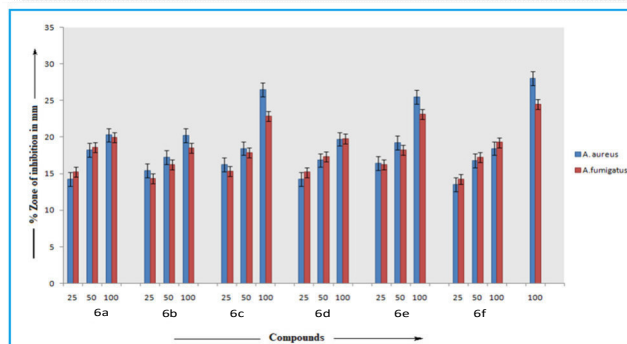


Fig.-8: Graphical Representation of Antifungal Activity of Compounds 6a-f

The zone of inhibition against the test organisms is measured and comparing it to a standard reference, the antibacterial activity and antifungal activities were assessed. The inhibitory zones that were found are shown in Table-2 and Table-3. This led to the excellent zone of inhibition in the main screening against the bacterial and fungal strains and also, as shown in Fig-7 and Fig-8. It was shown that the existence of electron-withdrawing groups bound to the Naphthofuran ring had a significant impact on the antibacterial activity. For instance, the compounds 6c and 6e had increased activity as a result of having nitro and chloro substituents in their structures, which showed that all of the examined compounds in this series had outstanding antibacterial activity.

Molecular Docking Studies

The docking of molecules examinations was ultimately completed using the described methodology.^{29,30} The antitubercular receptor (PDB code: 2MBR), whose crystal structure was got from the Protein Data Bank (PDB: <http://www.rcsb.org/pdb>), had been subjected to In-silico molecular docking. The water molecules and heteroatoms were removed before screening. The protein preparations module of the HEX modeling package 8.0 was used for constructing the receptor structure before it was used in the docking investigation. Except for the water molecules that were 5 Å away from the ligand, During the production of the protein, all hetero and water molecules from the crystal structure were taken out. Utilizing discovery studio 3.2, the three-dimensional configurations of each ligand and the receptor binding interactions were visualized to optimize the quality. All molecules were docked at the receptor's active binding sites. The outcomes of the in silico molecular docking process offer crucial insight into the potential affinity of the newly developed drugs for the active regions of the receptor. We used the docking values that were acquired to guide our wet study of antimicrobial activity. All derivatives demonstrated improved binding interaction with receptors nearby through hydrogen bonds, alkyl, pi-alkyl, Vander walls, and other interactions with a range of amino acids of the receptor, potentially limiting the receptor's ability to cause bacterial infections. The binding energy of all the complexes showed prominent binding interactions, with E. Coli murbenzyme receptor by the key of amino acid residues ARG327, TRP89, PHE328, VAL52, VAL326, ILE110, ASN51, GLN120, GLU325, GLU334, LEU107, LEU104, ILE122, VAL132, LEU178, LEU53, and VAL326. To identify the interaction positions, which will be the potential ligand binding sites in each scenario, the hydrophobic and hydrophilic spheres are used. Finally,

Interactions

- van der Waals
- Unfavorable Bump
- Conventional Hydrogen Bond
- π -Anion
- π -Sigma
- π -Alkyl

Interactions

- Unfavorable Bump
- Conventional Hydrogen Bond
- Carbon-Hydrogen Bond
- Pi-delta
- Pi-pi

Residues

- N-Oxide Hydrogen Bond
- Aligine
- Alkil
- Pi-alkil

1620
ANTIMICROBIAL STUDY ON NAPHTHOFURAN DERIVATIVES S.M. Raghavendra *et al.*

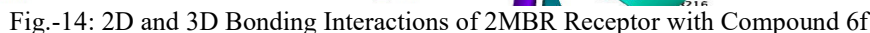
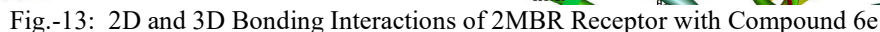


Table-4: Binding Energies of Compound 6(a-f) with 2MBR Receptor

CONCLUSION

1621

On the basis of their antibacterial activity and antifungal activity, the newly synthesized compounds were assessed. Each substance demonstrated a considerable level of antibacterial action by studying their molecular docking studies.

ACKNOWLEDGMENTS

One of the authors S.M. Raghavendra thanks the Department of Chemistry, Sir M V Govt. Science College, Bommanakatte, Bhadravathi and Sahyadri Science College, Kuvempu University, Shivamogga for providing facilities and encouragement.

CONFLICT OF INTERESTS

The authors declare that there is no conflict of interest.


AUTHOR CONTRIBUTIONS

All the authors contributed significantly to this manuscript, participated in reviewing/editing, and approved the final draft for publication.

S. M. Raghavendra  <https://orcid.org/0000-0003-3482-5206>

M. N. Kumarswamy  <https://orcid.org/0000-0003-4378-6794>

K. M. Nagarsha  <https://orcid.org/0000-0003-4743-5477>

T. M. Sharanakumar  <https://orcid.org/0000-0002-6427-9130>

Praveen C. Ramamurthy  <https://orcid.org/0000-0003-1880-5889>

K. P. Latha  <https://orcid.org/0000-0001-8464-9613>

Open Access: This article is distributed under the terms of the Creative Commons Attribution 4.0 International License (<http://creativecommons.org/licenses/by/4.0/>), which permits unrestricted use, distribution, and reproduction in any medium, provided you give appropriate credit to the original author(s) and the source, provide a link to the Creative Commons license, and indicate if changes were made.

REFERENCES

1. A.N. Mayekar, H.S. Yathirajan, B. Narayana, B.K. Sarojini, N.S. Kumari, *International Journal of Chemistry*, **2(1)**, 38(2010), <https://doi.org/10.1155/2012/530392>
2. Wei Hou, Hongtao Hu, *Journal of Medicinal Chemistry*, **65(6)**, 4436(2022), <https://doi.org/10.1021/acs.jmedchem.1c01859>
3. Upare Abhay Atmaram, Selvaraj Mohana Roopan, *Applied Microbiology and Biotechnology*, **106**, 3489(2022), <https://doi.org/10.1007/s00253-022-11969-0>
4. N.C. Desai, G.M. Kotadiya, A.R. Trivedi, V.M. Khedkar, P.C. Jha, Design, *Medicinal Chemistry Research*, **25(11)**, 2698(2016), <https://doi.org/10.1007/s00044-016-1683-y>
5. Ahmed M, Abdelfattah, Ahmed E.M. Mekky, SherifM, H. Sanad, *Synthetic Communications*, **11-12(52)**, 1421(2022), <https://doi.org/10.1080/00397911.2022.2095211>
6. B. Sadek, K.M. Fafelelbom, *Molecules*, **16(6)**, 4339(2011), <https://doi.org/10.3390/molecules16064339>
7. S. Dash, B.A. Kumar, J. Singh, B.C. Maiti, T.K. Maity, *Medicinal Chemistry Research*, **20(8)**, 1206(2011), <https://doi.org/10.1007/s00044-010-9455-6>
8. A. Özdemir, B. Sever, M.D. Altıntop, H.E. Temel, O. Athi, M. Baysal, F. Demirci, *Molecules*, **22(7)**, 1(2017), <https://doi.org/10.3390/Molecules22071109>
9. A. Mazumder, M. Shaharyar, *Biomed Research International*, **2014**, Article ID 491492(2014) <http://dx.doi.org/10.1155/2014/491492>
10. R. Iqbal, M. Zareef, S. Ahmed, J.H. Zaidi, M. Arfan, M. Shafique, N.A. Al-Masoudi, *Journal of the Chinese Chemical Society*, **53**, 689(2006), <https://doi.org/10.1002/jccs.200600091>
11. K.C. Ravindra, H.M. Vagdevi, V.P. Vaidya, B. Padmashali, *Indian Journal of Chemistry*, **45B**, 2506(2006).
12. S. Bansal, M. Bala, S.K. Suthar, S. Choudhary, S. Bhattacharya, V. Bhardwaj, S. Singla, A. Joseph, *European Journal of Medicinal Chemistry*, **80**, 167(2014), <https://doi.org/10.1016/j.ejmech.2014.04.045>
13. M. Amir, K. Saifullah, W. Akhter, *Indian Journal of Chemistry*, **50B**, 1107(2011)

14. A. A. Siddiqui, M. Islam, S. Kumar, *Der Pharmacia Lettre*, **2(2)**, 319(2010).
15. D. Dewangan, A. Pandey, T. Sivakumar, R. Rajavel, R.D, Dubey, *International Journal of ChemTech Research*, **2(3)**, 1397(2010).
16. N.C. Desai, A.R. Trivedi, H.V. Vaghani, H.C. Somani, K.A. Bhatt, *Medicinal Chemistry Research*, **25(2)**, 329(2016), <https://doi.org/10.1007/s00044-015-1485-7>
17. D.B. Suresh, D.R. Jamatsing, S.K. Pravin, S.B. Ratnamala, *Mod Chem Appl*, **4(4)**, 1(2016), <https://doi.org/10.4172/2329-6798.1000193>
18. N. Mihailović, V. Marković, I.Z. Matić, N.S. Stanisavljević, Z.S. Jovanović, S. Trifunović, L. Joksović, *RSC Advances*, **7**, 8550(2017), <https://doi.org/10.1039/C6RA28787E>
19. M.A. Sindhe, Y.D. Bodke, R. Kenchappa, S. Telkar, A. Chandrashekar, *Journal of Chemical Biology*, **9**, 79(2016), <https://doi.org/10.1007/s12154-016-0153-9>
20. Murugan, K.M. Manisha Shukla, A.K. Geetha, Ashwini, Vishal Singh, Scholars Research Library, *Der Pharma Chemica*, **3(4)**, 509(2011).
21. T. M. Sharanakumar, Mounesh, N. Y. Praveen Kumar, K. R. Venugopala Reddy, Suresh, *Rasayan Journal of Chemistry*, **13(4)**, 2133(2020), <http://dx.doi.org/10.31788/RJC.2020.1345876>
22. T. M. Sharanakumar, Mounesh, Suresh, N. Y. Praveen Kumar, N. H. M. Nandinibaby, K. R. Venugopala Reddy, *Journal of Indian Chemical Society*, **98(10)**, 100139(2021), <https://doi.org/10.1016/j.jics.2021.100139>
23. İlkay Küçükgülzel, Sevim Rollas, and Adile Çevikbaş, *Drug Metabolism and Drug Interactions*, **12**, 151(1995), <https://doi.org/10.1515/DMDI.1995.12.2.151>
24. F. Gao, T. Wang, J. Xiao, G. Huang, *European Journal of Medicinal Chemistry*, **173**, 274(2019), <https://doi.org/10.1016/j.ejmech.2019.04.043>
25. M.N. Kumaraswamy, V.P. Vaidya, C. Chandrasekhar, D.A. Prathima Mathias, H. Shivakumar, K.M. Mahadevan, *Research Journal of Pharmaceutical, Biological and Chemical Sciences*, **4(1)**, 90(2013).
26. M.N. Kumaraswamy, V.P. Vaidya, C. Chandrasekhar, D.A. Prathima Mathias, H. Shivakumar, K.M. Mahadevan, *International Journal of Pharmaceutical, Chemical and Biological Sciences*, **3(2)**, 281(2013).
27. M.N. Kumaraswamy, V.P. Vaidya, C. Chandrasekhar, D.A. Prathima Mathias, H. Shivakumar, K.M. Mahadevan, *International Journal of Pharmaceutical and Chemical Sciences*, **2(1)**, 159(2013).
28. K. S. Meghashree, K. P. Latha, *Plant Archives*, **20**, 2920(2020).
29. Mohammed Shafeeulla R., Krishnamurthy G., Bhojyanaik H.S., Shivarudrappa H.P., Yallappa Shiralgi, *BSU. J. BAS.*, **6(1)**, 1(2017)
30. Mohammed Shafeeulla, Krishnamurthy, H. S. Bhojyanaik, Manjuraj T., *Journal of the Turkish Chemical Society Section A: Chemistry*, **4(3)**, 787(2016), <https://doi.org/10.18596/jotcsa.309261>

[RJC-8459/2023]



New thiophene-1,3,4-oxadiazole-thiazolidine-2,4-dione hybrids: Synthesis, MCF-7 inhibition and binding studies

Manasa A. Doddagaddavalli^a, Veerendra Kumar A. Kalalbandi^b,
Jaldappagari Seetharamappa^{a,*}, Shrinivas D. Joshi^c

^a Department of Chemistry, Karnatak University, Dharwad 580 003, India

^b Department of Chemistry, Ballari Institute of Technology and Management, Ballari 583 104, India

^c Department of Pharmaceutical Chemistry, SET's College of Pharmacy, Dharwad 580 002, India

ARTICLE INFO

Keywords:

MTT assay

ROS assay

MCF-7 cell lines

Binding studies

Thiophene -1,3,4-oxadiazole-thiazolidine-2,4-dione

ABSTRACT

Two synthetic methods were proposed for the preparation of a new series of thiophene-1,3,4-oxadiazole-thiazolidine-2,4-dione hybrids (**TOT-1 to 15**) and their structures were elucidated based on spectral data. Studies on cytotoxicity, ROS, cellular uptake and interactions of TOT-14 with calf thymus DNA were carried out. Anticancer activity of compounds, **TOT-1 to 15** on breast cancer (MCF-7) cell lines was investigated. The IC₅₀ values for the standard, epirubicin hydrochloride and TOT-12, 13, 14 and 15 were found to be 6.78, 5.52, 6.53, 4.83 and 5.57 µg/mL, respectively. Notably, **TOT-14** exhibited a remarkable antiproliferative activity with a strikingly selective inhibitory effect compared to standard. This specific selectivity could be attributed to the synergistic effect of increased cellular uptake and generation of higher ROS in cancer cells after irradiation. The binding constant of $4.25 \times 10^3 \text{ M}^{-1}$ indicated the moderate interaction between TOT-14 and ct-DNA. The docking score of TOT derivatives was substantially identical to the docking score of epirubicin hydrochloride. The designed molecules complied with the requirements for drug-likeness and ADME.

1. Introduction

The most frequent kind of cancer suffered by women and the main factor in cancer-related mortality is the breast cancer (BC). Currently, the situation in BC is alarming, endangering the health and quality of life of women severely. With a 15 % lifetime risk, around 2.3 million cases are diagnosed globally each year [1].

According to the World Health Organisation, BC develops in the epithelial cells of the ducts (85 %) or lobules (15 %) of the glandular tissues of the breast [2]. The malignant development is initially restricted to the duct or lobule, with no symptoms and no spread potential. It will eventually infiltrate the surrounding breast tissue or other organs in the body [3]. When a woman perishes from breast cancer, it is usually as a result of extensive metastases.

The greatest challenge in developing a new anti-cancer drug is to find out the therapeutic strategy that can attenuate malignant cells without damaging healthy cells. Besides this, the unwanted side effects of existing cancer treatment, as well as the multidrug resistance, have increased the difficulties in researching alternative anticancer

medicines, with lower toxicity to normal tissue and less tumour cell resistance [4]. To overcome these concerns, an alternative strategy for the design of a hybrid molecule that contains more than a single pharmacophore may be proposed to hit multiple cancer hallmarks and achieve the desired pharmacological effectiveness.

In general, heterocycles constitute the foundation of most of drugs. Notably, heterocycles with 1,3,4-oxadiazole rings define a class of compounds with exceptional biological activities including remarkable high cytostatic potential [5]. Most of the currently available medications also have pharmacophore composed of 1,3,4-oxadiazole ring. For example, raltegravir, an HIV integrase inhibitor, is used to treat AIDS in combination with other antiretroviral medications [6]. Tiodazosin, a 2-adrenoceptor presynaptic antagonist, is used to treat hypertension while nesipidil is also used as an antihypertensive drug [7]. Fenadiazole is a sedative and hypnotic drug that can be used to treat insomnia and anxiety [8]. Zibotentan is recommended for the treatment of cancer of the colon, breast, ovary, lung, and, in especially, prostate [9]. Besides these significant biological properties, 1,3,4-oxadiazoles and its derivatives are also known to have anti-proliferative properties through a

* Corresponding author.

E-mail address: drjseetharamappa@kud.ac.in (J. Seetharamappa).

<https://doi.org/10.1016/j.bioorg.2023.107003>

Received 20 October 2023; Accepted 23 November 2023

Available online 25 November 2023

0045-2068/© 2023 Elsevier Inc. All rights reserved.

number of different pathways, including the inhibition of growth factors, enzymes, kinases, and other molecules. Structures of 1,3,4-oxadiazole-containing compounds which are available in the market are represented in Fig. 1.

On the other hand, 2,4-thiazolidinediones, which were first introduced in the late 1990 s, are oral hypoglycemic medicines that have gained worldwide attention due to their varied biological profile [10] which include anti-hyperglycemic [11,12], anti-oxidant [13], anti-inflammatory [14], anti-cancer [15–18], anti-obesity [19], anti-malarial [20] and anti-microbial [21,22] actions. In preclinical and clinical evaluation phases, derivatives of thiazolidinedione (TZD) have shown promise as anticancer agents. Structures I, II and III in Fig. 2 represent 2,4-thiazolidinediones moieties with anticancer activity.

The development of hybrid drugs has led to better treatment for a number of illnesses including cancer. Through a variety of mechanisms, hybrid molecules with two or more pharmacophores have the ability to overcome drug resistance while simultaneously reducing the risk of side effects [23]. In view of aforementioned discussion and in the quest of designing new anticancer agents, we have envisaged to synthesize hybrid molecules containing 1,3,4-oxadiazole and thiazolidine-2,4-dione moieties due to their remarkable biological activities.

In this paper, the synthesis of a novel family of thiophene-1,3,4-oxadiazole-thiazolidine-2,4-dione derivatives with a distinct aldehyde moiety was demonstrated. The single crystal X-ray crystallographic studies of the intermediate TOT were deliberated. *In vitro* anticancer capabilities of these compounds against MCF-7 breast cancer cell lines have been investigated. Anticancer drugs' effectiveness depends heavily on ROS [24]. The significance of ROS in the anticancer mechanism of novel thiophene-1,3,4-oxadiazole-thiazolidine-2,4-dione hybrid compounds was examined in this study. Contrary to analytical methods like high-performance liquid chromatography, the uptake of luminous model pharmaceuticals could be evaluated on a single-cell level using confocal fluorescence microscopy, allowing real-time monitoring of the intracellular spatial distribution of the model drug [25]. The *in vitro* cellular uptake behaviour of compounds, TOT 12, 13, 14 and 15 by MCF-7 cell lines was investigated using laser scanning confocal

microscope to confirm whether they could be efficiently internalised into tumour cells.

DNA-drug interaction studies are extremely useful and necessary for the development of innovative and more effective medications with fewer adverse effects. Hence, to understand the mechanism of interaction of a highly potent anticancer agent, TOT-14 with ct-DNA, we have accomplished fluorescence quenching studies using ethidium bromide as a biomarker. Further, *in-silico* technique offers a platform for testing the efficacy of putative therapies against molecular targets, assisting in the selection of those with the greatest potential activity for additional *in vitro* and *in vivo* testing. So, we have proposed TOT and its 15 derivatives presented in this study as novel prospective drugs for the treatment of breast cancer.

2. Results and discussion

2.1. Chemistry

2.1.1. Synthetic protocol

Following the pathway depicted in Scheme 1, fifteen compounds (TOT 1–15) were synthesized. N'-(2-chloroacetyl)thiophene-2-carbohydrazide (2) was prepared by the addition of chloroacetyl chloride to thiophene-2-carbohydrazide in ethyl acetate. Further, cyclization of compound 2 took place in the presence of POCl₃ to yield 2-(chloromethyl)-5-(thiophen-2-yl)-1,3,4-oxadiazole (TO). The compounds (TOT-1 to 15) were synthesized by two methods. In the first approach, 3-((5-(thiophen-2-yl)-1,3,4-oxadiazol-2-yl)methyl)thiazolidine-2,4-dione (TOT) was obtained by the condensation of TO with potassium salt of thiazolidine-2,4-dione in the presence of DMF at 60 °C. Further, TOT 1–15 were obtained by the Knoevenagel condensation reaction in ethanol medium between various substituted aldehydes and TOT in the presence of a catalytic amount of piperidine. In all the cases, the product was precipitated out from the reaction mixture. In the second method, the derivatives of TZD (1–15) were synthesized by Knoevenagel condensation reaction between TZD and various substituted aldehydes. In the next step TZD (1–15) were treated with TO in the presence of

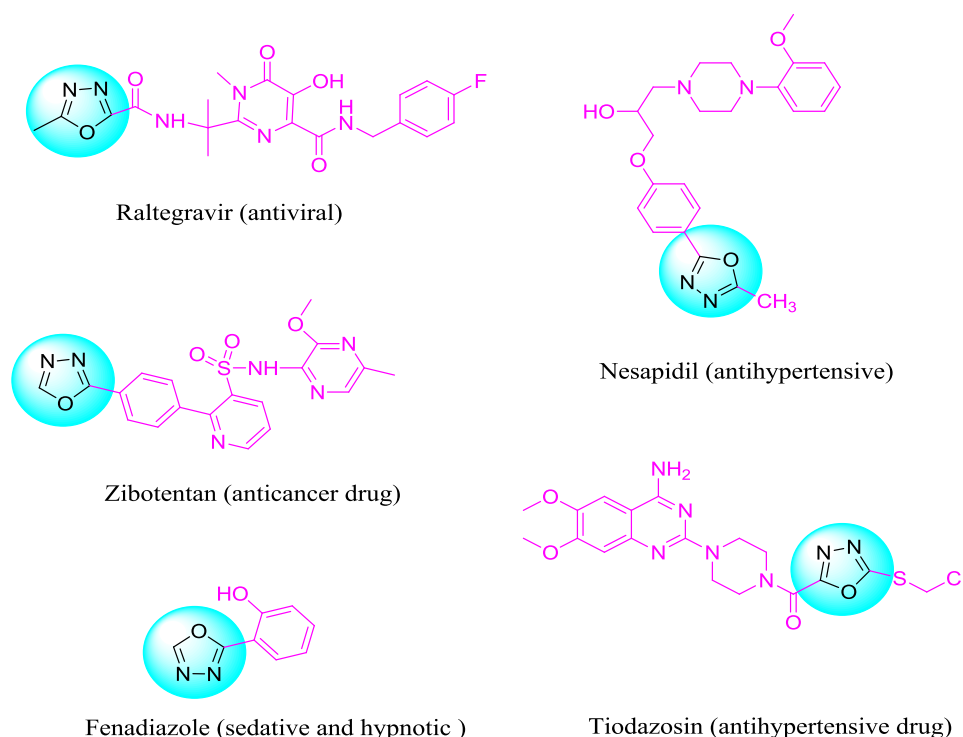


Fig. 1. Structures of drugs containing 1,3,4-oxadiazole.

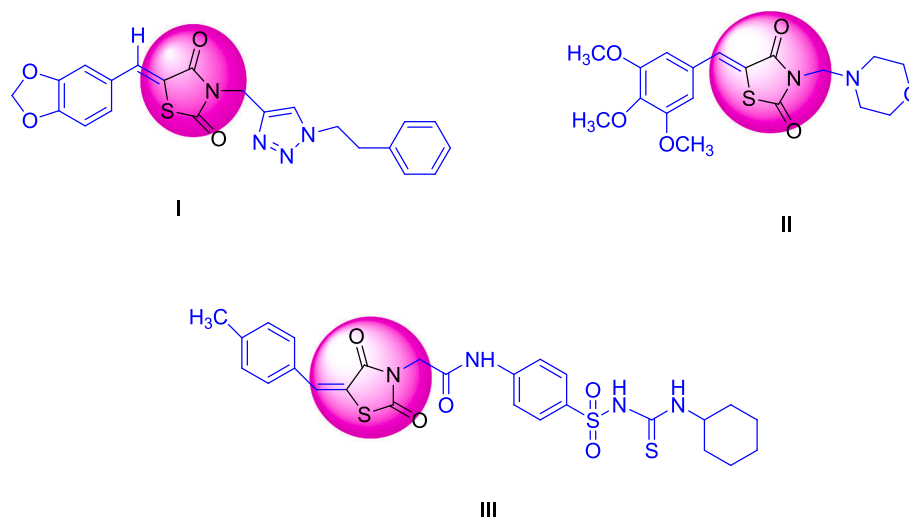
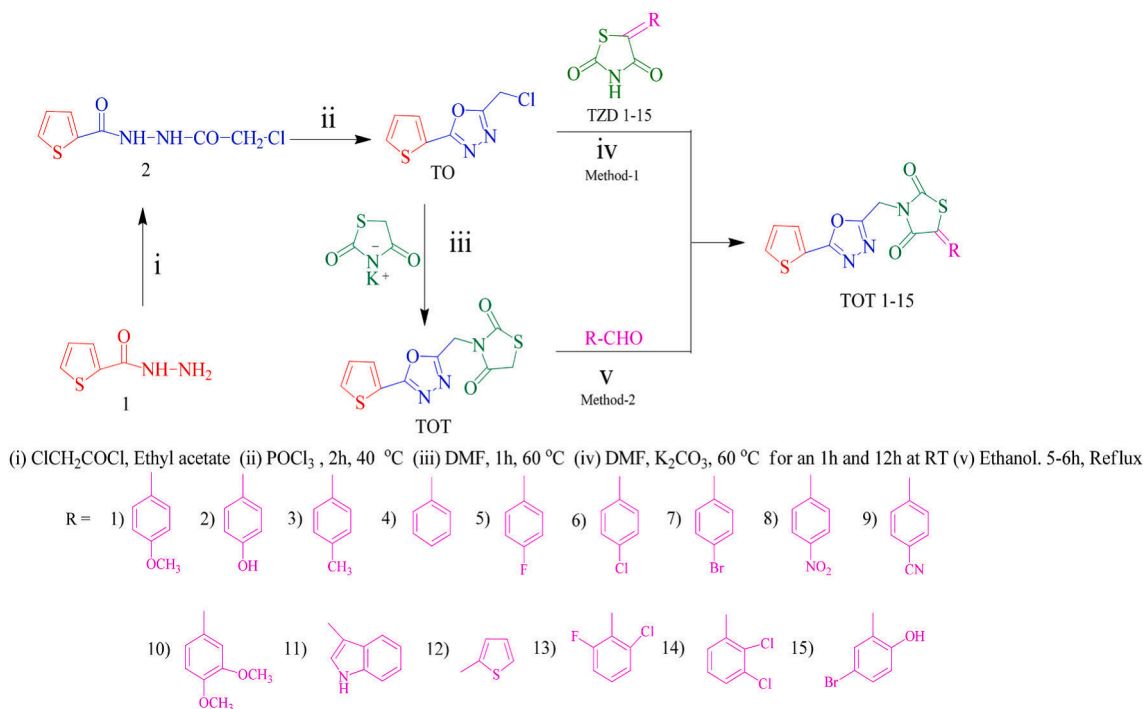


Fig. 2. Thiazolidine-2,4-diones moieties as anticancer agents.



Scheme 1. Synthesis of 3-((5-(thiophen-2-yl)-1,3,4-oxadiazol-2-yl)methyl)thiazolidine-2,4-dione aldehyde derivatives (TOT 1–15).

DMF and K_2CO_3 to get **TOT 1–15**.

In continuation of our research work on synthesis of thiazolidine-dione derivatives, we have followed method-1 [26] to synthesize the title compounds. However, we failed to get good yields of some of the derivatives, notably the compounds that contained halogen groups. This might be due to the formation of by-product, N-(((Z)-(2-oxo-2-(thiophen-2-yl)ethyl)diazenyl)methylene)piperidine-1-carboxamide (BS) in larger yield. The structure of BS was elucidated based on ^1H and ^{13}C NMR and mass spectral data. Formation of BS might be attributed to decyclization of oxadiazole ring and thiazolidine-dione ring by the addition of piperidine to the reaction mixture [27]. Thus, we have employed method-2 to synthesize the title compounds in good yields. Further, we have witnessed good yields with respect to title compounds containing halogen groups. However, purity of the synthesized compounds was found to be satisfactory in method-1 as these were precipitated from the reaction mixture. The lesser purity of compounds that

were prepared in method-2 might be attributed to the use of DMF as solvent and prolonged reaction time. Nevertheless, both the synthetic approaches were found to be competent in yielding the title compounds. The comparison of two methods is depicted in Table 1.

2.1.2. Characterization of the synthesized compounds by spectral methods

The structural elucidation of synthesized hybrids, **TOT 1–15**, was established using FT-IR, LCMS, ^1H , and ^{13}C NMR spectroscopic data. The FT-IR spectra of compounds **TOT 1–15**, revealed the presence of two sharp bands due to the carbonyl stretching vibration of the thiazolidine-dione in the range of $1733\text{--}1758\text{ cm}^{-1}$ and $1677\text{--}1700\text{ cm}^{-1}$. The peak in the range of $1310\text{--}1345\text{ cm}^{-1}$ indicated C—O stretching in oxadiazole ring and the bands noticed at $2923\text{--}2932\text{ cm}^{-1}$ and $3004\text{--}3015\text{ cm}^{-1}$ were attributed to C—H stretching of methylene group between oxadiazole and thiazolidine-dione rings. The ^1H NMR spectrum revealed two singlets at $5.14\text{--}5.17\text{ ppm}$ and $7.96\text{--}8.23\text{ ppm}$ for CH_2 protons bound to

Table 1

Comparison of two methods used for the synthesis of TOT 1-15.

Compound	Method 1				Method 2			
	Time (h)	Temp. (C)	Yield (%)	Purity (TLC)	Time (h)	Temp. (C)	Yield (%)	Purity (TLC)
TOT-1	5	75–80	70	>98	12	RT	95	>85
TOT-2	6	75–80	60	>98	12	RT	90	>85
TOT-3	6	75–80	70	>98	12	RT	95	>85
TOT-4	6	75–80	65	>98	12	RT	95	>85
TOT-5	5	75–80	30	>98	12	RT	90	>85
TOT-6	5	75–80	40	>98	12	RT	90	>85
TOT-7	5	75–80	60	>98	12	RT	90	>85
TOT-8	6	75–80	40	>98	12	RT	90	>85
TOT-9	6	75–80	50	>98	12	RT	95	>85
TOT-10	5	75–80	70	>98	12	RT	95	>85
TOT-11	5	75–80	80	>98	12	RT	95	>85
TOT-12	5	75–80	80	>98	12	RT	95	>85
TOT-13	6	75–80	20	>98	12	RT	90	>85
TOT-14	6	75–80	30	>98	12	RT	90	>85
TOT-15	6	75–80	40	>98	12	RT	90	>85

the oxadiazole ring and the thiazolidindione ring, and = C–H of aldehyde attached to thiazolidindione ring, respectively. The study of ^{13}C NMR spectrum indicated two distinct peaks due to CH_2 and = C–H carbons at 35.1–36.4 ppm and 159.5–161.5 ppm, as well as two carbonyl peaks at 166.6–167.5 and 164.7–165.4 ppm, respectively. Rest of the carbons were resonated as expected. The mass spectra of compounds showed the molecular ion peak according to their respective molecular masses of compounds. Thus, mass spectral data confirmed the proposed formulae of compounds.

2.2. X-ray crystallographic studies

Single crystals of the intermediate TOT were obtained by slow evaporation of its dichloromethane solution. From X-ray crystallographic data, it was observed that TOT crystal belonged to the monoclinic crystal system with a space group of $P2_1/c$. The unit cell parameters of TOT were as follows: $a = 14.9294(6)$ Å, $b = 4.9313(2)$ Å, $c = 16.8470(7)$ Å and $\alpha = \gamma = 90^\circ$, $\beta = 105.434(3)^\circ$. The complete crystallographic details are given in Table 2. The ORTEP image of

Table 2

X-ray crystallographic data of TOT and structural refinement.

Chemical formula	$\text{C}_{10}\text{H}_7\text{N}_3\text{O}_3\text{S}_2$
Molecular mass	281.31
Crystal system, space group	Monoclinic, $P2_1/c$
Temperature (K)	296
a, b, c (Å)	14.9294 (6), 4.9313 (2), 16.8470 (7)
α, γ ($^\circ$)	90
β ($^\circ$)	105.434 (3)
V (Å ³)	1195.57 (9)
Z	4
Radiation type	$\text{Mo K}\alpha$
μ (mm ^{−1})	0.45
Crystal size (mm)	$0.21 \times 0.19 \times 0.18$
Diffractometer	Bruker SMART X2S benchtop
Absorption correction	Multi-scan SADABS2012/1 (Bruker, 2012) was used for absorption correction. $wR2(\text{int})$ was 0.1095 before and 0.0453 after correction. The Ratio of minimum to maximum transmission is 0.8573. The $\square/2$ correction factor is 0.0015.
T_{\min}, T_{\max}	0.640, 0.746
No. of measured, independent and observed [$I > 2\sigma(I)$] reflections	13874, 3632, 2036
R_{int}	0.035
$(\sin \theta/\lambda)_{\text{max}}$ (Å ^{−1})	0.718
$R[F^2 > 2\sigma(F^2)], wR(F^2), S$	0.055, 0.185, 1.07
No. of reflections	3632
No. of parameters	164
H-atom treatment	H-atom parameters constrained
$\Delta\rho_{\text{max}}, \Delta\rho_{\text{min}}$ (e Å ^{−3})	0.32, −0.45

compound TOT with 50 % probability is shown in Fig. 3. The crystal structure has been deposited at the Cambridge Crystallographic Data Centre (deposition number: CCDC 2262173).

Four molecules were packed in a unit cell and it crystallized in centro symmetric lattice. Weak intermolecular hydrogen bonds existed between both hydrogen atoms of methylene group and nitrogen atom of oxadiazole ring with a bond distance of 2.697 and 2.653 Å. Another hydrogen bond between sulphur atom of thiazolidine-2,4-dione ring and hydrogen atom of the other thiazolidine-2,4-dione ring with a bond distance of 2.915 Å was observed. The intermolecular hydrogen bonds between the molecules are embodied in Fig. 4. From the crystallographic data, it was evident that the molecule was not planar in space, the plane of thiazolidine-2,4-dione ring making a dihedral angle of 84.52° with the plane of 1,3,4-oxadiazole.

2.3. Biological evaluation

2.3.1. Cell cytotoxicity (MTT) assay

MTT colorimetric evaluation was used to assess the *in vitro* anticancer activity of all synthesized compounds (TOT 1–15) against MCF-7 (human breast adeno carcinoma) cell line. Epirubicin hydrochloride was used as a standard. The corresponding IC_{50} values were tabulated in Table 3. Among the studied compounds, TOT 12 to 15 surpassed the IC_{50} value of epirubicin hydrochloride ($6.78 \mu\text{g/mL}$) with IC_{50} values of 5.57, 6.53, 4.83, and $5.57 \mu\text{g/mL}$ against MCF-7 cell lines, respectively. The remarkable activity of these compounds might be attributed to the presence of electron withdrawing groups at *ortho* and/or *meta* position of phenyl ring. However, the analogous functionalities at para position of the phenyl group did not make a significant contribution towards the activity. Further, the di substitution of an electron-withdrawing halogen at the *ortho* and *meta* positions of the phenyl ring might also be a contributing factor for TOT 14's higher potential. Additionally, compounds TOT-2, 7 and 8 also showed good to moderate activity with respect to that of the standard. These findings demonstrated that the hybrid molecules showed synergistic effects for cell cytotoxicity (MTT) action. Fig. 5 represents the pictorial representation of MTT assay results for compounds TOT 1–15 and epirubicin hydrochloride against MCF-7 cell lines.

2.3.2. ROS production in MCF-7 cells with certain TOT derivatives

Reactive oxygen species (ROS) at physiological levels are essential signalling molecules that regulate a variety of biological processes, altering host defence, gene expression, and cell proliferation [28]. The results of MTT assay revealed that TOT 12–15 exhibited the strong anticancer effect on MCF-7 breast cancer cells. The fluorescence intensity for MCF-7 cells with and without TOT 12–15 was measured, and the fluorescence intensity upon irradiation with aforementioned

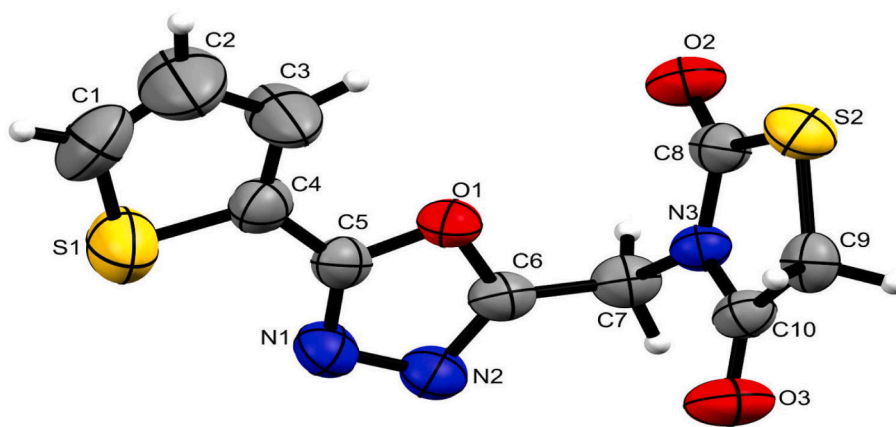


Fig. 3. ORTEP image of TOT by X-ray molecular structure with 50% probability.

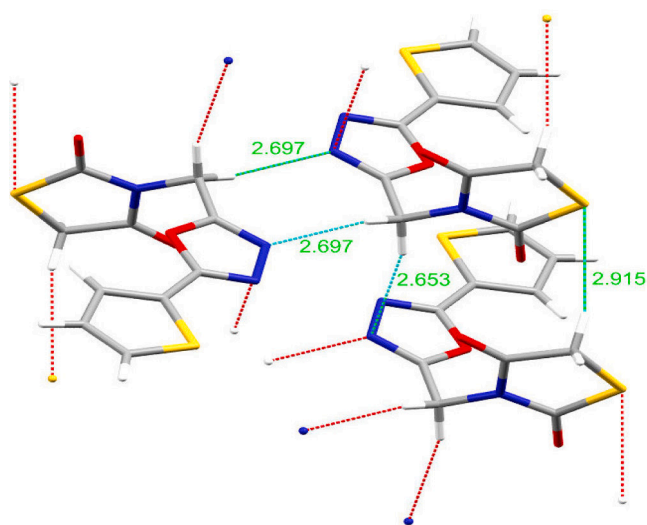


Fig. 4. Green dotted lines represent intermolecular hydrogen bonding (weak).

Table 3

In vitro anticancer activity of TOT 1–15.

Compound	IC ₅₀ (μg/mL)
TOT-1	>25
TOT-2	10.93 ± 1.05
TOT-3	18.43 ± 1.07
TOT-4	19.27 ± 1.10
TOT-5	20.19 ± 1.14
TOT-6	>25
TOT-7	9.98 ± 0.99
TOT-8	11.04 ± 0.95
TOT-9	>25
TOT-10	>25
TOT-11	23.67 ± 0.95
TOT-12	5.52 ± 1.00
TOT-13	6.53 ± 1.25
TOT-14	4.83 ± 1.30
TOT-15	5.57 ± 0.79
Epirubicin hydrochloride (Standard)	6.78 ± 1.10

compounds and CellROX Deep Red was appreciably increased (Fig. 6). This indicated that the quantity of ROS produced in TOT 12–15 treated MCF-7 cells was greater than that in unincubated MCF-7 cells. MCF-7 cells treated with TOT 12–15 were bulged compared to control due to increase in ROS production indicating that the synthesized compounds were able to eradicate cancer cells. The increased concentration of ROS

MTT assay for MCF-7 Cell lines

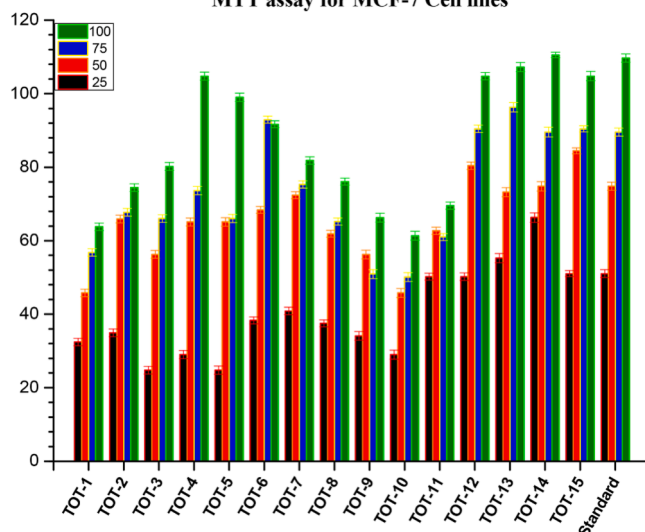


Fig. 5. MTT assay of synthesised compounds TOT 1–15 with epirubicin hydrochloride for MCF-7 cell lines (Anticancer activity).

indicated that the compounds TOT 12–15 acted on MCF-7 cell lines by triggering the intrinsic apoptotic pathway [29]. The percentage of relative ROS increased cells in compounds with respect to control is shown in Fig. 7.

2.3.3. Cellular uptake and confocal fluorescence assay

Cellular uptake plays an important role in a drug's bioactivity so that internalization and accumulation of the drug into cancer cells is crucial for the therapeutic effect against tumours. For this reason, the *in vitro* cellular uptake behaviour of compounds TOT 12–15 in MCF-7 cell lines was largely investigated using laser scanning confocal microscope to confirm whether they could be efficiently internalized into tumour cells. Green fluorescence was noticed in MCF-7 cells after 2 h of treatment with compounds TOT 12–15, as illustrated in Fig. 8. This suggested effective internalization of compounds. The observed fluorescence inside the cells was considerably increased in compounds TOT 12 and 14 compared to that in TOT 13 and 15, demonstrating that compounds TOT 12 and 14 had a significant rise in green emission indicating effective internalization. These compounds showcased the damage in cytoplasm and exhibited good anticancer activity.

2.3.4. Assay for electrophoretic mobility shift of pUC19-DNA

An electrophoretic mobility shift assay (EMSA) was used to analyse

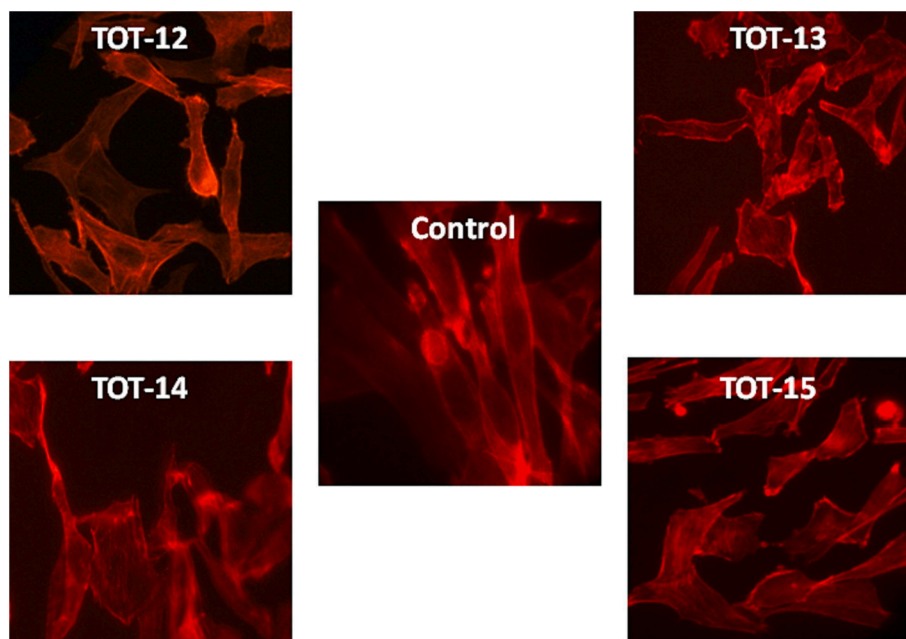


Fig. 6. Deep red staining fluorescence pictures. ROX-L: Incubate cells for 1 h in the dark with Cell ROX Deep Red, then irradiate (532 nm, 1 min, 20 mW/cm²); TOT 12,13,14,15 + ROX-L: Co-incubate cells for 1 h in the dark with TOT 11, 12, 13, 14, 15, and Cell ROX Deep Red, then irradiate (532 nm, 1 min, 20 mW/cm²).

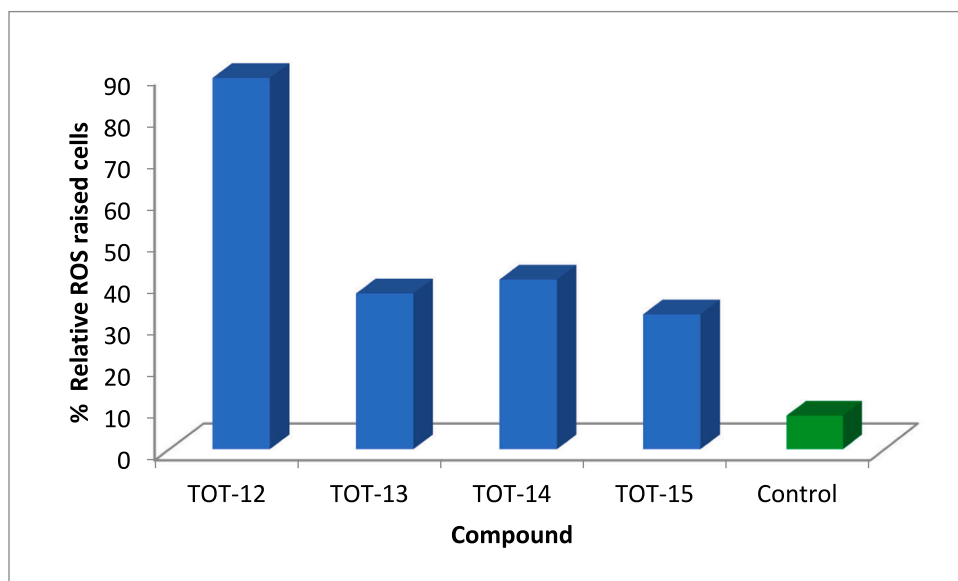


Fig. 7. The percentage of relative ROS raised cells in compounds TOT 12, 13, 14, 15 and the control.

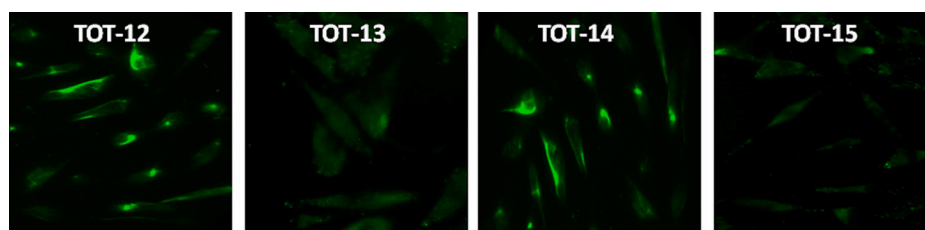


Fig. 8. Intracellular fluorescence images of compounds in MCF-7 cells after incubating with TOT 12, 13, 14, 15 (5 μM) via confocal fluorescence imaging.

the influence of the synthesized compounds on the characteristics of plasmid DNA. In general, the compound of interest was exposed to plasmids of supercoiled DNA. Single-strand breaks induced the

production of open circular DNA (oc-DNA), whereas double-strand breaks resulted in the formation of linear DNA, both of which might be distinguished from super coiled DNA (sc-DNA) by gel electrophoresis

[30].

By quantifying the sc and oc agarose gel DNA bands, it was possible to assess the generation of oc-DNA by treatment with $\text{NiCl}_2/\text{H}_2\text{O}_2$ and its suppression by the chosen TOT derivatives (Fig. 9). While treatment with the ethidium bromide, a positive intercalating control, inhibited the synthesis of oc-DNA by less than 50 %. The more suppression of oc-DNA production by TOT derivatives was seen for compound **TOT-13** & **14**, indicating that the compounds under study have interacted with DNA.

2.4. Binding studies

DNA is a physiologically important macromolecule that plays an important part in cellular advancement such as replication, transcription, and translation. These pathways are critical for cell survival and growth. As a result, cellular DNA is the most significant pharmacological target of a variety of medications. So, DNA-drug interaction studies are extremely useful and necessary for the development of innovative and more effective medications with fewer adverse effects [31,32]. **TOT-14**, a more potent anticancer agent among the synthesized compounds, was selected to comprehend the interaction with ct-DNA.

2.4.1. Interaction of TOT-14 with ct-DNA using fluorescent probe ethidium bromide (EB) as a probe

Fluorescence spectroscopy is useful and efficient tool for the investigation of a small molecule-DNA binding. Since, ct-DNA shows only weak fluorescence, we used a well-known fluorescence probe, EB. EB intercalates into ct-DNA base pairs, increasing the intensity of ct-DNA emission. The addition of **TOT-14** resulted in a substantial decrease in the emission intensity of ct-DNA-EB without a shift in the emission wavelength suggesting the change in the environment around ct-DNA.

$$F_0/F = 1 + K_{sv}[Q] = 1 + K_q\tau_0[Q] \quad (1)$$

where, F and F_0 are the fluorescence intensities in the presence and absence of a quencher, K_{sv} is the Stern–Volmer quenching constant, K_q is the bimolecular quenching constant, τ_0 is the average lifespan of the fluorophore in the absence of a quencher and [Q] is the concentration of the quencher.

2.4.2. Evaluation of binding constant

The determination of binding constant of a drug-macromolecule system offers information on the binding affinity of a specific drug towards that macromolecule. The binding constant (K) of **TOT-14**-ct-DNA-EB system and the number of **TOT-14** molecules (n) per ct-DNA base pair in the interaction were calculated using the following equation:

$$\log(F_0 - F)/F = \log K + n\log[Q] \quad (2)$$

The intercept and slope of the $\log [(F_0 - F)/F]$ vs. $\log [Q]$ plot yielded the values of K and n, respectively and the relevant values are given in Table 4. **TOT-14** showed a moderate binding with ct-DNA as evident from K value which is in the order of 10^3 . The value of n near to unity suggested that each combination had one independent class of binding

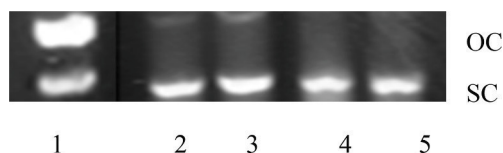


Fig. 9. Treatment of pUC19 DNA with $\text{NiCl}_2/\text{H}_2\text{O}_2$ and ethidium bromide. Agarose gel electrophoresis was used to find the pUC plasmid DNA that was super coiled (SC) and open circular (OC). Lane 1: pUC19 DNA was treated for 1 h with 50 μM NiCl_2 and 0.5 mM H_2O_2 , then for 1 h with 2 mM ethidium bromide. Lane 2–5: After being incubated with $\text{NiCl}_2/\text{H}_2\text{O}_2$ for 1 h, pUC 19 DNA was treated with 2 mM of **TOT-12**, **13**, **14**, **15**.

Table 4

The binding constant (K), Stern-Volmer constant (K_{sv}) and quenching rate constant of ct-DNA (K_q) for **TOT-14**-ct-DNA system.

System	K, 10^3 (Lmol $^{-1}$)	K_{sv} , 10^6 (Lmol $^{-1}$)	K_q , 10^{15} (Lmol $^{-1}$ s $^{-1}$)
TOT-14 -ct-DNA	4.25	4.00	4.96

sites on ct-DNA. The fluorescence spectra and Stern-Volmer plot for ct-DNA-**TOT-14**-EB are illustrated in Fig. 10.

2.5. Molecular docking studies

To investigate the mechanism of anticancer activity and detailed intermolecular interactions between the synthesized compounds, molecular docking studies were performed on the binary and ternary crystal structures of a novel inhibitor of 17 beta-HSD type 1, a lead compound for breast cancer therapy (PDB ID 3HB5, 2.00 Å X-ray resolution) [33] using the Surflex-dock programme of sybyl-X 2.0 software. All the inhibitors were docked into the active site of enzyme as shown in Fig. 11A and B. The predicted binding energies of the compounds are listed in Table 5. The docking study revealed that all the compounds have showed good docking score against breast cancer protein.

As depicted in Fig. 12(A-C), compound **TOT-13** makes three hydrogen bonding interactions at the active site of the enzyme (PDB ID: 3HB5). Among these an interaction was through nitrogen atom present at 4th position of 1,3,4-oxadiazole ring with hydrogen atom of ASN152 (N—H-ASN152, 2.34 Å), oxygen atom present at the 2nd position of thiadiazolidine-2,4-dione ring makes two interactions with hydrogen atoms of SER142 and GLY144 (O—H-SER142, 2.70 Å; O—H-GLY144, 2.05 Å).

As depicted in Fig. 13(A-C), compound **TOT-4** makes three hydrogen bonding interactions at the active site of the enzyme (PDB ID: 3HB5). Among these an interaction was through nitrogen atom present at 4th position of 1,3,4-oxadiazole ring with hydrogen atom of ASN152 (N—H-ASN152, 2.30 Å), oxygen atom present at the 2nd position of thiadiazolidine-2,4-dione ring makes two interactions with hydrogen atoms of SER142 and GLY144 (O—H-SER142, 2.75 Å; O—H-GLY144, 2.04 Å). The interaction of epirubicin with protein active sites shows ten bonding interactions and the docked view of the same has been depicted in Fig. 14(A-C). Fig. 15(A&B) represents the hydrophobic and hydrophilic amino acids which are surrounded to the studied compounds **TOT-13** & **4**.

All the compounds showed consensus score in the range of 7.15–5.01, indicating the summary of all forces of interaction between ligands and the protein. We noticed that the studied compounds have shown similar type of interactions with amino acid residues (ASN152, SER142 and GLY144) as that of epirubicin drug. These scores indicated that the molecules preferentially bound to protein in comparison to the reference drug, epirubicin hydrochloride (Table 5). Thus, **TOT-1**–**15** compounds are proposed to exhibit epirubicin type biological activity.

2.6. ADME studies

The Lipinski analysis makes use of physico-chemical characteristics to forecast how much an oral medicinal agent would resemble a medication. This rule-of-five illustrates how physico-chemical and pharmacokinetics indices are related. According to Lipinski's rule, an orally active drug-like compound should not have more than one infraction of the following standards: molecular weight not exceeding 500 Da, octanol–water partition coefficient (log P) not exceeding 5, hydrogen bond donors not exceeding 5, and hydrogen bond acceptors not exceeding 10 [34]. All the synthesized compounds, **TOT-1**–**15** followed Lipinski rule of five. Therefore, they have the potential to be developed into medications that can be taken orally. Table 6 consists of some important physico-chemical characteristics of synthesized compounds.

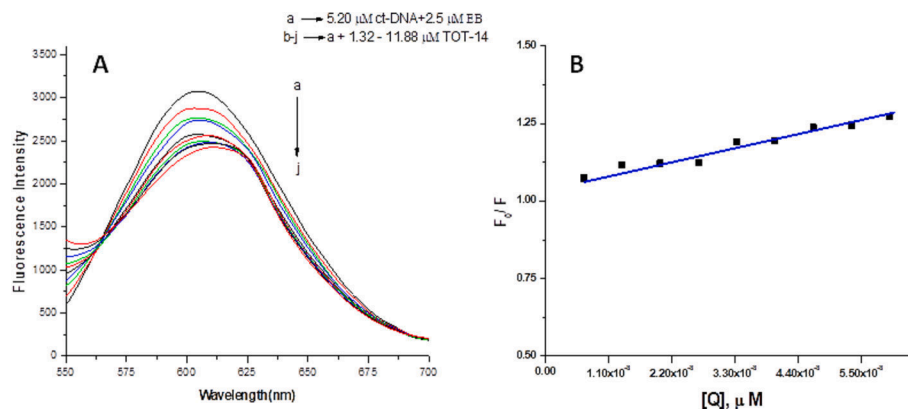


Fig. 10. A: Fluorescence spectra of ct-DNA-EB in the presence and absence of TOT 14 (1.32–11.88 μ M). The concentration of ct-DNA (5.20 μ M). B: Stern- Volmer plot for ct- DNA-EB in the presence of compound TOT-14.

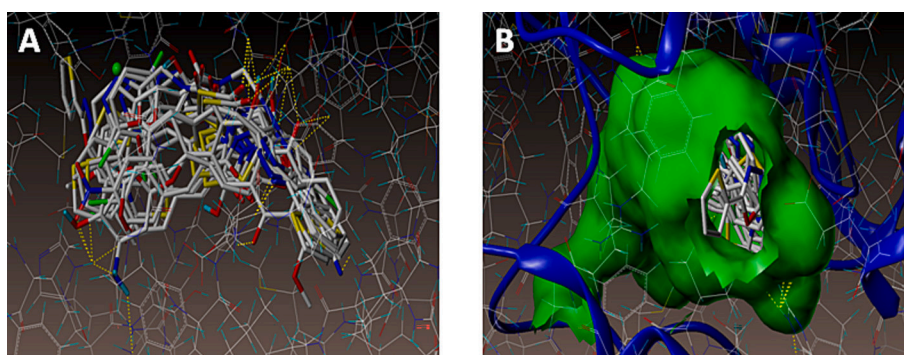


Fig. 11. Docked view of all the compounds at the active site of the enzyme PDB ID: 3HB5.

Table 5

Surflex docking score (kcal/mol) of TOT 1–15.

Compound	C Score ^a	Crash Score ^b	Polar Score ^c	D Score ^d	PMF Score ^e	G Score ^f	Chem Score ^g
Epirubicin	7.15	−1.08	0.00	−118.330	−85.106	−285.475	−32.832
13	6.49	−1.06	0.73	−110.859	−75.748	−242.440	−31.473
4	6.33	−1.66	0.08	−123.167	−81.585	−259.347	−31.666
9	5.90	−1.40	0.00	−154.786	−76.591	−252.504	−29.033
14	5.90	−1.32	0.02	−116.866	−62.699	−261.064	−33.931
12	5.86	−1.66	0.04	−112.898	−56.421	−276.849	−30.924
5	5.78	−0.95	0.00	−98.641	−80.757	−236.808	−29.656
7	5.55	−2.34	0.24	−115.913	−77.342	−275.436	−31.549
8	5.53	−1.48	0.35	−113.504	−86.515	−268.910	−29.431
15	5.46	−2.19	0.78	−168.428	−77.398	−274.080	−32.651
1	5.40	−1.41	0.70	−109.335	−65.457	−248.698	−33.664
3	5.26	−1.36	0.02	−101.227	−83.918	−257.475	−31.246
10	5.25	−1.09	0.74	−98.497	−67.557	−242.922	−32.458
2	5.12	−1.08	1.10	−120.440	−88.642	−199.723	−25.279
6	5.03	−1.16	0.00	−155.876	−74.196	−250.753	−31.265
11	5.01	−1.86	0.91	−229.965	−108.187	−399.044	−43.485

^a C Score (Consensus Score) integrates a number of popular scoring functions for ranking the affinity of ligands bound to the active site of a receptor and reports the output of total score.

^b Crash-score revealing the inappropriate penetration into the binding site. Crash scores close to 0 are favorable. Negative numbers indicate penetration.

^c Polar indicating the contribution of the polar interactions to the total score. The polar score may be useful for excluding docking results that make no hydrogen bonds.

^d D-score for charge and van der Waals interactions between the protein and the ligand.

^e PMF-score indicating the Helmholtz free energies of interactions for protein–ligand atom pairs (Potential of Mean Force, PMF).

^f G-score showing hydrogen bonding, complex (ligand–protein), and internal (ligand–ligand) energies.

^g Chem-score points for H-bonding, lipophilic contact, and rotational entropy, along with an intercept term.

3. Conclusions

Thiophene-1,3,4-oxadiazole-thiazolidine-2,4-dione hybrids were synthesized in high yields using the Knoevenagel condensation method.

IR, ¹H NMR, ¹³C NMR and mass spectral data were used to characterize the synthesized molecules. Single crystals of the intermediate compound, TOT were developed and its crystallographic data was collected and refined to deduce the structure of compound. The findings of

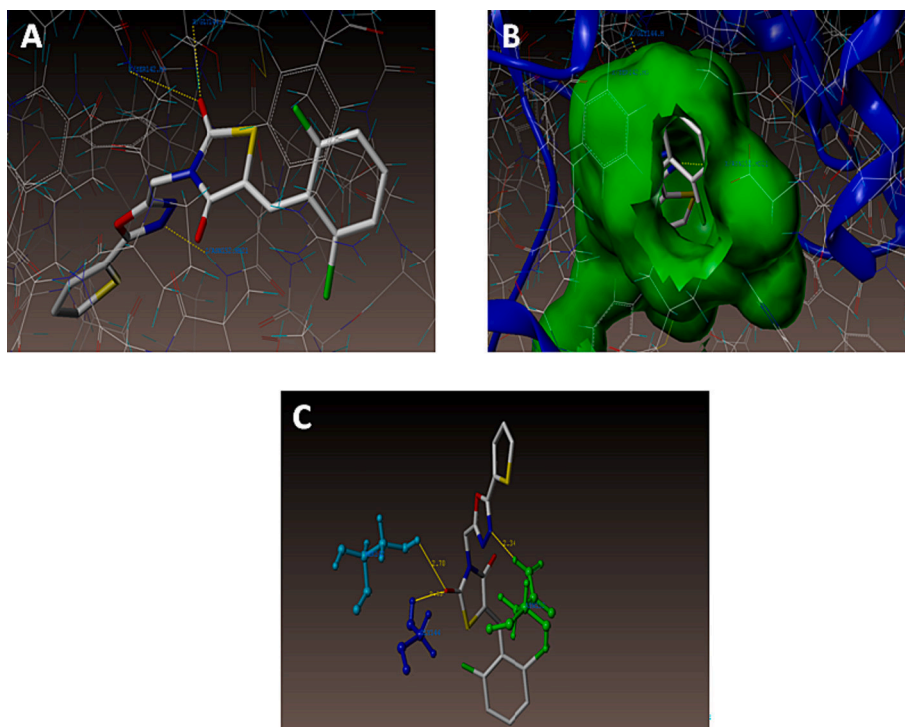


Fig. 12. Docked view of the compound TOT-13 at the active site of the enzyme PDB: 3HB5.

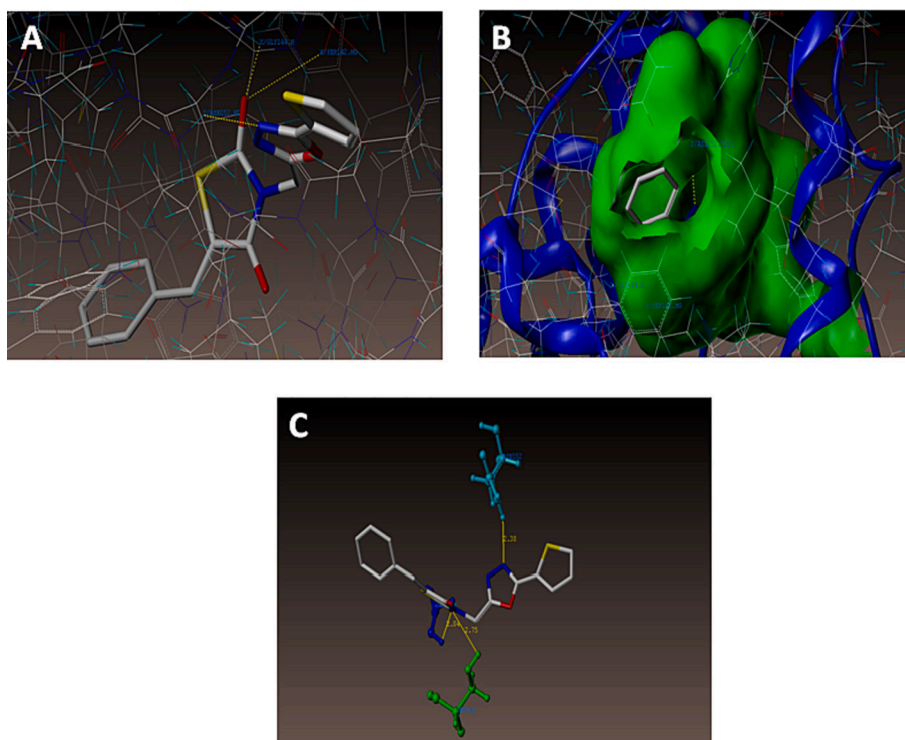


Fig. 13. Interaction of the compound TOT-4 at the binding site of the enzyme (PDB ID: 3HB5).

anticancer activity of novel derivatives (TOT 1–15) against MCF-7 breast cancer cell lines demonstrated that the series' TOT-14 (IC_{50} : 4.83 $\mu\text{g/mL}$), TOT-12 (IC_{50} : 5.52 $\mu\text{g/mL}$), TOT-13 (IC_{50} : 6.53 $\mu\text{g/mL}$), and TOT-15 (IC_{50} : 5.57 $\mu\text{g/mL}$) compounds could be considered as promising anticancer agents. The cytotoxicity results revealed that all of the synthesized compounds showed reduced toxicity. Further, the findings showed that the increased capacity of cancer cell lines to generate ROS

explained the selective photocytotoxicity to tumour cells. The results of *in vitro* cellular uptake behaviour of compounds TOT 12, 13, 14 and 15 in MCF-7 cell lines described that compounds TOT 12 and 14 had a significant rise in green emission indicating effective internalization. The outcome of DNA studies revealed the more suppression of oc-DNA production by TOT derivatives for compound TOT 13&14, indicating that the compounds under study have interacted with DNA. The more

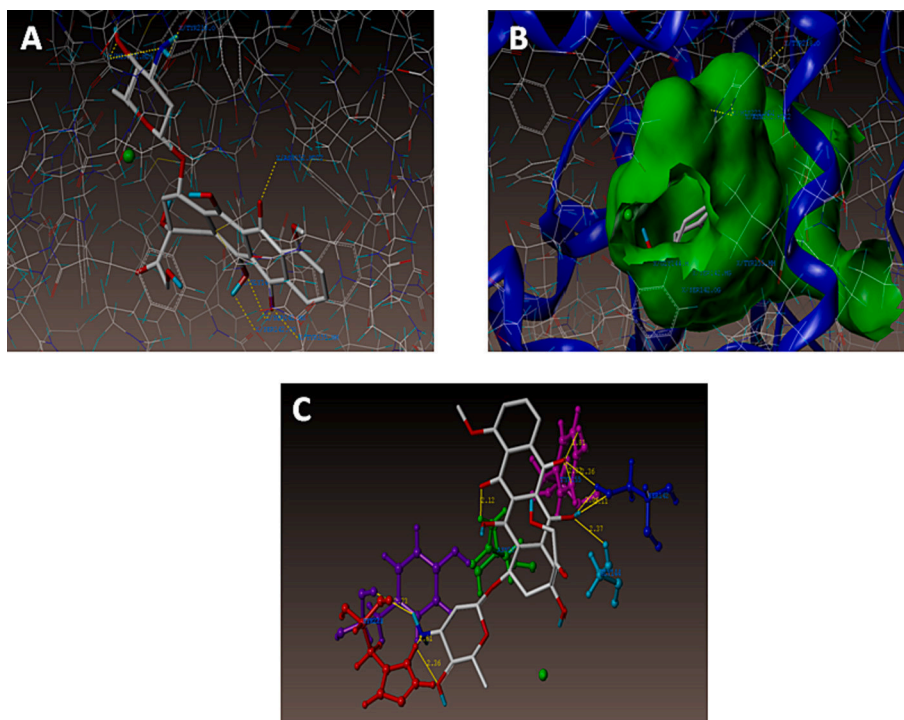


Fig. 14. Interaction of epirubicin at the binding site of the enzyme (PDB ID: 2HB5).

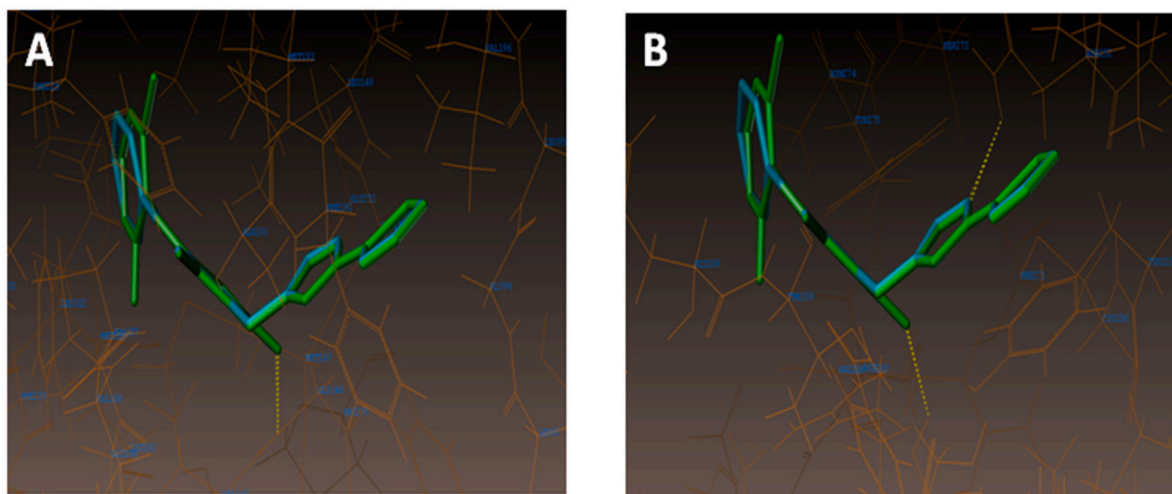


Fig. 15. A) Hydrophobic amino acids surrounded to compounds **TOT-13** (green colour) and **TOT-4** (cyan colour). B) Hydrophilic amino acids surrounded to **TOT-13** and **TOT-4**.

potent anticancer agent, **TOT-14** among the synthesized compounds was selected to study the interaction with ct-DNA using fluorescence spectroscopy under physiological conditions. The addition of **TOT-14** resulted in a substantial decrease in ct-DNA-EB emission intensity without a shift exhibiting moderate binding with ct-DNA. Molecular docking investigations showed hydrogen bonding interactions with the target protein. **TOT 1–15** compounds potency, selectivity and minimal cytotoxicity led to increased anticancer progress. Molecular docking studies revealed that TOT derivatives have substantially identical docking scores to common chemotherapeutic drug, epirubicin hydrochloride. Thus, the synthesized **TOT 1–15** compounds met the expectations for drug-likeness and ADME.

4. Experimental section

4.1. Materials and methods

All the starting materials and reagents were of analytical grade and were purchased from Spectrochem, sd-fine, TCI, Sigma Aldrich and HiMedia (India) and used without further purification. ^1H and ^{13}C NMR spectra were recorded in CDCl_3 , $\text{DMSO}-d_6$ and dichloromethane (DCM) on a 400 MHz FT-NMR Spectrometer (JEOL JNM-EC400S). Chemical shifts (δ) were reported in ppm relative to TMS, whereas coupling constants (J) were given in Hz. IR spectra were obtained on a Nicolet, 5700 FT-IR spectrophotometer using KBr optics. Mass spectra were recorded on a Waters Xevo G2-XS QT (LC-MS/ESI-MS). Bruker SMART APEX II diffractometer was used to generate high resolution X-ray diffraction data.

Table 6

Swiss ADME's prediction of the physico-chemical characteristics of TOT derivatives.

Comp.	MF	MW	RB	HBA	HBD	LogP	BS	TPSA	LV
TOT-1	C ₁₈ H ₁₃ N ₃ O ₄ S ₂	399.44	5	6	0	3.13	0.55	139.07	0
TOT-2	C ₁₇ H ₁₁ N ₃ O ₄ S ₂	385.42	4	6	1	2.74	0.55	150.07	0
TOT-3	C ₁₈ H ₁₃ N ₃ O ₃ S ₂	383.44	4	5	0	3.47	0.55	129.84	0
TOT-4	C ₁₇ H ₁₁ N ₃ O ₃ S ₂	369.42	4	5	0	2.99	0.55	129.84	0
TOT-5	C ₁₇ H ₁₀ FN ₃ O ₃ S ₂	387.41	4	6	0	3.43	0.55	129.84	0
TOT-6	C ₁₇ H ₁₀ ClN ₃ O ₃ S ₂	403.86	4	5	0	3.65	0.55	129.84	0
TOT-7	C ₁₇ H ₁₀ BrN ₃ O ₃ S ₂	448.31	4	5	0	3.76	0.55	129.84	0
TOT-8	C ₁₇ H ₁₀ N ₄ O ₃ S ₂	414.42	5	7	0	2.56	0.55	175.66	0
TOT-9	C ₁₈ H ₁₀ N ₄ O ₃ S ₂	394.43	4	6	0	2.9	0.55	153.63	0
TOT-10	C ₁₉ H ₁₅ N ₃ O ₅ S ₂	429.47	6	7	0	3.1	0.55	148.3	0
TOT-11	C ₁₉ H ₁₂ N ₄ O ₃ S ₂	408.45	4	5	1	3.25	0.55	145.63	0
TOT-12	C ₁₅ H ₉ N ₃ O ₃ S ₃	375.45	4	5	0	3.12	0.55	158.08	0
TOT-13	C ₁₇ H ₉ ClFN ₃ O ₃ S ₂	421.85	4	6	0	3.96	0.55	129.84	0
TOT-14	C ₁₇ H ₉ Cl ₂ N ₃ O ₃ S ₂	438.31	4	5	0	4.15	0.55	129.84	0
TOT-15	C ₁₇ H ₁₀ BrN ₃ O ₄ S ₂	464.31	4	6	1	3.36	0.55	150.07	0

MF- Molecular Formula; **MW**- Molecular Weight; **RB**-Number of Rotatable Bonds; **HBA**- Number of H-bond Acceptor; **HBD**- Number of H-bond Donor; **LogP**- partition coefficient between *n*-octanol and water; **BS**- Bioavailability Score; **TPSA**- topological polar surface area; **LV**- Lipinski's Violation.

4.2. Chemistry

As depicted in Scheme 1, thiophene-2-carbohydrazide is used as a starting material to prepare the key intermediate 2-(chloromethyl)-5-(thiophen-2-yl)-1,3,4-oxadiazole (TO) via two steps i.e, amidation and cyclization according to the reported procedures [35]. Final products were obtained by two different methods. In method-1, TO was coupled with potassium salt of thiazolidine-2,4-dione(TZD) to give 3-((5-(thiophen-2-yl)-1,3,4-oxadiazol-2-yl)methyl)thiazolidine-2,4-dione (TOT). Further, various substituted aldehydes were used to obtain final products (TOT 1–15) via Knoevenagel condensation and by-product N-(((Z)-2-oxo-2-(thiophen-2-yl)ethyl)diazenyl)methylene)piperidine-1-carboxamide (BS). In Method-2, primarily different substituted aldehydes were treated with thiazolidinedione (TZD) through Knoevenagel condensation. Further, various aldehyde derivatives of TZD were coupled with TO to get final products TOT 1–15. All the TOT derivatives were characterized by IR, ¹H NMR, ¹³C NMR and mass spectra. Structure of TOT was confirmed by single crystal XRD. Purity of analogues was determined to be above 95 % by liquid chromatography mass spectrometry.

4.2.1. Synthesis of N'-(2-chloroacetyl)thiophene-2-carbohydrazide (2)

Thiophene-2-carbohydrazide (10 mmol, 1.42 g) was dissolved in ethyl acetate (20 mL) and chloroacetylchloride (10 mmol, 0.80 mL) was added slowly. The reaction mixture was stirred at room temperature for 1 h where pale pink precipitate was formed. After completion of the reaction, the product was filtered and dried. Melting point: 68–70 °C.

4.2.2. Synthesis of 2-(chloromethyl)-5-(thiophen-2-yl)-1,3,4-oxadiazole (TO)

Compound 2 was heated at 40 °C with phosphorus oxychloride for 2 h. Excess of POCl₃ was recovered by distillation and the reaction mixture was cooled to room temperature. The reaction mixture was then quenched with ice and stirred continuously to get the solid product (TO). It was further filtered and dried. Melting point: 70–72 °C.

4.2.3. General procedure for the synthesis of 3-((5-(thiophen-2-yl)-1,3,4-oxadiazol-2-yl)methyl)thiazolidine-2,4-dione aldehyde derivatives (TOT 1–15)

Method –1.

To a solution of TO (5 mmol, 1.0 g) in DMF (5 mL), potassium salt of thiazolidine-2,4-dione (TZD) (5 mmol, 0.77 g) was added and heated to about 60 °C for an hour. After completion of reaction, the mixture was quenched with water and product was extracted with dichloromethane. The organic layer was dried over anhydrous sodium sulphate, filtered and concentrated under reduced pressure to obtain 3-((5-(thiophen-2-

yl)-1,3,4-oxadiazol-2-yl)methyl)thiazolidine-2,4-dione (TOT).

Pale Yellow solid; Yield: 90 %; mp: 88–90 °C. **FT-IR** (KBr, cm⁻¹) 3099 (Ar C–H), 1758, 1676 (C=O), 1601 (C=C), 1494, 1575 (C=N), 3004, 2967 (C–H, methylene), 1038, 750, 713 (C–S), 1339 (C–O); ¹H NMR (400 MHz, DMSO-D₆) δ 7.92 (d, *J* = 4.9 Hz, 1H), 7.75 (d, *J* = 3.1 Hz, 1H), 7.25 (t, *J* = 4.3 Hz, 1H), 4.98 (s, 2H), 4.29 (s, 2H). ¹³C NMR (101 MHz, DMSO-D₆) δ 172.2, 171.6, 161.4, 161.1, 132.4, 131.1, 129.3, 124.4, 35.9, 34.6. Mass calculated for C₁₀H₇N₃O₃S₂ is 280.9929; **LCMS** (ES +) *m/z*: 282.0255 [M + H⁺].

Substituted aldehyde (1 mmol) with TOT (1 mmol, 0.15 g) in EtOH (5 mL) with catalytic amount of piperidine was refluxed for 6–12 h to get derivatives of TOT.

Method- 2

Synthesis of aldehyde derivative of TZD: To a solution of TZD (10 mmol) and different aldehyde (10 mmol) in EtOH (10 mL), catalytic amount of piperidine was added slowly at room temperature. The reaction mixture was refluxed for 12 h with stirring. The completion of the reaction was monitored by TLC. After completion of the reaction, the mixture was poured to water and then sodium meta bisulphite was added to remove excess of aldehyde. Thus, the obtained solid was then filtered and dried.

To a stirred solution of aldehyde derivative of TZD (5 mmol) in DMF (5 mL), K₂CO₃ (5 mmol) was added and heated to 40 °C for 1 h. To this, TO (5 mmol) was added and continued heating for another 1 h. Further, the reaction mixture was stirred for 12 – 24 h at room temperature to obtain the product.

4.2.3.1. Z)-5-(4-methoxybenzylidene)-3-((5-(thiophen-2-yl)-1,3,4-oxadiazol-2-yl)methyl)thiazolidine-2,4-dione (TOT-1). Yellow solid; Yield: 85 %; mp: 171–173 °C. **FT-IR** (KBr, cm⁻¹) 3101 (Ar C–H), 1756, 1698 (C=O), 1605 (C=C), 1492, 1513 (C=N), 3004, 2925 (C–H, methylene), 1032, 723 (C–S), 1339 (C–O), 1254 (C–OCH₃). ¹H NMR (400 MHz, DMSO-D₆) δ 7.93 (dd, *J* = 6.7, 5.5 Hz, 2H), 7.77 (d, *J* = 3.7 Hz, 1H), 7.60 (d, *J* = 8.6 Hz, 2H), 7.25 (dd, *J* = 4.9, 3.7 Hz, 1H), 7.09 (d, *J* = 8.6 Hz, 2H), 5.14 (s, 2H). ¹³C NMR (101 MHz, DMSO-D₆) δ 166.6, 164.7, 161.5, 159.5, 134.5, 132.0, 130.1, 129.7, 127.8, 125.1, 124.2, 117.0, 114.4, 55.2, 35.1. Mass calculated for C₁₈H₁₃N₃O₄S₂ is 399.0347; **LCMS** (ES +) *m/z*: 400.0322 [M + H⁺].

4.2.3.2. Z)-5-(4-hydroxybenzylidene)-3-((5-(thiophen-2-yl)-1,3,4-oxadiazol-2-yl)methyl)thiazolidine-2,4-dione (TOT-2). Yellow solid; Yield: 80 %; mp: 174–176 °C. **FT-IR** (KBr, cm⁻¹) 3098 (Ar C–H), 1745, 1696 (C=O), 1593 (C=C), 1489, 1518 (C=N), 3004, 2924 (C–H, methylene), 10044, 738, 722 (C–S), 1342 (C–O), 1261 (C–OH). ¹H NMR (400 MHz, DMSO-D₆) δ 10.39 (s, 1H), 7.92–7.88 (m, 2H), 7.76 (d, *J* = 2.4 Hz, 1H), 7.49 (d, *J* = 7.9 Hz, 2H), 7.25 (d, *J* = 3.7 Hz, 1H), 6.90 (d, *J* = 8.6

H₂, 2H), 5.14 (s, 2H). ¹³C NMR (101 MHz, DMSO-D₆) δ 167.5, 165.4, 161.4, 161.2, 160.9, 135.1, 133.4, 132.4, 131.1, 129.3, 124.4, 124.2, 117.0, 116.4, 36.2. Mass Calculated for C₁₇H₁₁N₃O₄S₂ is 385.0191; LCMS(ES +) *m/z*: 385.9902 [M + H⁺].

4.2.3.3. (Z)-5-(4-methylbenzylidene)-3-((5-(thiophen-2-yl)-1,3,4-oxadiazol-2-yl)methyl)thiazolidine-2,4-dione (TOT-3). Yellow solid; Yield: 80 %; mp: 169–171 °C. FT-IR (KBr, cm⁻¹) 3099 (Ar C—H), 1751, 1687 (C=O), 1599 (C=C), 1490, 1509 (C=N), 3004, 2924 (C—H, methylene), 1040, 724, 705 (C—S), 1341 (C—O), 3080 (C—H, methyl); ¹H NMR (400 MHz, DMSO-D₆) δ 7.95–7.91 (m, 2H), 7.77 (d, *J* = 3.1 Hz, 1H), 7.52 (d, *J* = 8.6 Hz, 2H), 7.34 (d, *J* = 7.9 Hz, 2H), 7.25 (t, *J* = 4.6 Hz, 1H), 5.15 (s, 2H), 2.34 (s, 3H). ¹³C NMR (101 MHz, DMSO-D₆) δ 166.6, 164.7, 161.3, 159.4, 141.5, 134.7, 130.1, 129.9, 129.7, 129.5, 127.7, 124.1, 118.8, 35.1, 20.8. Mass calculated for C₁₈H₁₃N₃O₃S₂ is 383.0398; LCMS(ES +) *m/z*: 384.0706.9902 [M + H⁺].

4.2.3.4. (Z)-5-benzylidene-3-((5-(thiophen-2-yl)-1,3,4-oxadiazol-2-yl)methyl)thiazolidine-2,4-dione (TOT-4). Yellow solid; Yield: 76 %; mp: 168–170 °C. FT-IR (KBr, cm⁻¹) 3106 (Ar C—H), 1758, 1689 (C=O), 1608 (C=C), 1492, 1505 (C=N), 3004, 2925 (C—H, methylene), 1038, 740, 727 (C—S), 1338 (C—O). ¹H NMR (400 MHz, DMSO-D₆) δ 7.99 (s, 1H), 7.92 (d, *J* = 4.3 Hz, 1H), 7.77 (d, *J* = 3.7 Hz, 1H), 7.63 (d, *J* = 6.7 Hz, 2H), 7.55–7.48 (m, 2H), 7.25 (dd, *J* = 4.7, 3.8 Hz, 1H), 5.15 (s, 2H). ¹³C NMR (101 MHz, DMSO-D₆) δ 167.3, 165.3, 161.5, 161.1, 134.6, 133.3, 132.4, 131.5, 131.1, 130.8, 130.0, 129.3, 124.4, 121.2, 36.2. Mass calculated for C₁₇H₁₁N₃O₃S₂ is 369.0242; LCMS(ES +) *m/z*: 370.0542 [M + H⁺].

4.2.3.5. (Z)-5-(4-fluorobenzylidene)-3-((5-(thiophen-2-yl)-1,3,4-oxadiazol-2-yl)methyl)thiazolidine-2,4-dione (TOT-5). Yellow solid; Yield: 82 %; mp: 174–176 °C. FT-IR (KBr, cm⁻¹) 3103 (Ar C—H), 1736, 1682 (C=O), 1611 (C=C), 1505, 1572 (C=N), 3008, 2924 (C—H, methylene), 1038, 743, 717 (C—S), 1320 (C—O), 1240 (C—F). ¹H NMR (400 MHz, DMSO-D₆) δ 8.00 (s, 1H), 7.92 (dd, *J* = 4.9, 1.2 Hz, 1H), 7.76 (q, *J* = 1.6 Hz, 1H), 7.70 (dd, *J* = 8.6, 5.5 Hz, 2H), 7.38 (t, *J* = 8.9 Hz, 2H), 7.25 (dd, *J* = 5.2, 4.0 Hz, 1H), 5.15 (s, 2H). ¹³C NMR (101 MHz, DMSO-D₆) δ 167.2, 165.2, 162.4, 161.5, 161.1, 133.5, 133.4, 133.3, 132.4, 131.1, 130.0, 129.3, 124.4, 120.9, 117.3, 117.1, 36.3. Mass Calculated for C₁₇H₁₀FN₃O₃S₂ is 387.0148; LCMS(ES +) *m/z*: 388.0436 [M + H⁺].

4.2.3.6. (Z)-5-(4-chlorobenzylidene)-3-((5-(thiophen-2-yl)-1,3,4-oxadiazol-2-yl)methyl)thiazolidine-2,4-dione (TOT-6). Yellow solid; Yield: 80 %; mp: 175–177 °C. FT-IR (KBr, cm⁻¹) 3088 (Ar C—H), 1751, 1693 (C=O), 1607 (C=C), 1490, 1506 (C=N), 3008, 2923 (C—H, methylene), 1040, 733, 723 (C—S), 1338 (C—O), 733 (C—Cl). ¹H NMR (400 MHz, DMSO-D₆) δ 7.98 (s, 1H), 7.91 (d, *J* = 4.3 Hz, 1H), 7.76 (d, *J* = 2.4 Hz, 1H), 7.62 (dd, *J* = 23.2, 8.6 Hz, 4H), 7.25 (t, *J* = 4.3 Hz, 1H), 5.15 (s, 2H). ¹³C NMR (101 MHz, DMSO-D₆) δ 167.0, 165.2, 161.5, 161.0, 136.1, 133.2, 132.4, 132.2, 131.1, 130.0, 129.3, 124.4, 122.0, 44.9, 36.3, 25.9. Mass calculated for C₁₇H₁₀ClN₃O₃S₂ is 402.9852; LCMS(ES +) *m/z*: 403.9757 [C₁₇H₁₀³⁵ClN₃O₃S₂, M + H⁺] 405.9733 [C₁₇H₁₀³⁷ClN₃O₃S₂, M + H⁺].

4.2.3.7. (Z)-5-(4-bromobenzylidene)-3-((5-(thiophen-2-yl)-1,3,4-oxadiazol-2-yl)methyl)thiazolidine-2,4-dione (TOT-7). Yellow solid; Yield: 82 %; mp: 177–179 °C. FT-IR (KBr, cm⁻¹) 3088 (Ar C—H), 1752, 1693 (C=O), 1605 (C=C), 1488, 1507 (C=N), 3008, 2924 (C—H, methylene), 1040, 733, 722 (C—S), 1324 (C—O), 1073 (C—Br). ¹H NMR (400 MHz, DMSO-D₆) δ 7.96 (s, 1H), 7.92 (d, *J* = 4.0 Hz, 1H), 7.77–7.72 (m, 3H), 7.57 (d, *J* = 8.6 Hz, 2H), 7.25 (t, *J* = 4.6 Hz, 1H), 5.15 (s, 2H). ¹³C NMR (101 MHz, DMSO-D₆) δ 167.0, 165.2, 161.5, 161.0, 133.3, 133.0, 132.5, 132.4, 131.1, 129.3, 125.0, 124.4, 122.1, 36.3. Mass calculated for C₁₇H₁₀BrN₃O₃S₂ is 446.9347; LCMS(ES +) *m/z*: 447.9244 [C₁₇H₁₀⁷⁹BrN₃O₃S₂ + H⁺] 449.9235 [C₁₇H₁₀⁸¹BrN₃O₃S₂ + H⁺].

4.2.3.8. (Z)-5-(4-nitrobenzylidene)-3-((5-(thiophen-2-yl)-1,3,4-oxadiazol-2-yl)methyl)thiazolidine-2,4-dione (TOT-8). Light brown solid; Yield: 78 %; mp: 176–178 °C. FT-IR (KBr, cm⁻¹) 3106 (Ar C—H), 1745, 1690 (C=O), 1609 (C=C), 1489, 1572 (C=N), 3008, 2925 (C—H, methylene), 1033, 751, 734 (C—S), 1345 (C—O), 1508, 1345 (N—O). ¹H NMR (400 MHz, DMSO-D₆) δ 8.32 (d, *J* = 7.9 Hz, 2H), 8.09 (s, 1H), 7.92–7.87 (m, 3H), 7.77 (s, 1H), 7.25 (s, 1H), 5.17 (s, 2H). ¹³C NMR (101 MHz, DMSO-D₆) δ 166.8, 165.0, 161.5, 160.9, 148.3, 139.6, 132.4, 131.8, 131.7, 131.1, 129.3, 125.6, 124.9, 124.4, 36.3. Mass calculated for C₁₇H₁₀N₄O₅S₂ is 414.0093; LCMS(ES +) *m/z*: 415.0106 [M + H⁺].

4.2.3.9. (Z)-4-((2,4-dioxo-3-((5-(thiophen-2-yl)-1,3,4-oxadiazol-2-yl)methyl)thiazolidin-5-ylidene)methyl)benzonitrile (TOT-9). Light Yellow solid; Yield: 78 %; mp: 164–166 °C. FT-IR (KBr, cm⁻¹) 3097 (Ar C—H), 1758, 1700 (C=O), 1613 (C=C), 1487, 1567 (C=N), 3015, 2925 (C—H, methylene), 1036, 738, 723 (C—S), 1335 (C—O), 2228 (C≡N). ¹H NMR (400 MHz, DMSO-D₆) δ 8.04 (s, 1H), 7.97 (d, *J* = 8.6 Hz, 2H), 7.92 (d, *J* = 4.9 Hz, 1H), 7.80–7.76 (m, 3H), 7.25 (t, *J* = 4.3 Hz, 1H), 5.16 (s, 2H). ¹³C NMR (101 MHz, DMSO-D₆) δ 166.9, 165.0, 161.5, 160.9, 137.8, 133.7, 132.4, 132.4, 131.1, 129.3, 124.9, 124.4, 118.9, 113.0, 36.3. Mass calculated for C₁₈H₁₀N₄O₃S₂ is 394.0194; LCMS(ES +) *m/z*: 395.0457 [M + H⁺].

4.2.3.10. (Z)-5-(3,4-dimethoxybenzylidene)-3-((5-(thiophen-2-yl)-1,3,4-oxadiazol-2-yl)methyl)thiazolidine-2,4-dione (TOT-10). Bright Yellow solid; Yield: 90 %; mp: 158–160 °C. FT-IR (KBr, cm⁻¹) 3111 (Ar C—H), 1733, 1686 (C=O), 1591 (C=C), 1471, 1591 (C=N), 3008, 2929 (C—H, methylene), 1036, 771, 737 (C—S), 1310 (C—O), 1274 (C—OCH₃). ¹H NMR (400 MHz, DMSO-D₆) δ 7.92 (t, *J* = 4.3 Hz, 2H), 7.76 (d, *J* = 2.4 Hz, 1H), 7.26–7.20 (m, 3H), 7.11 (d, *J* = 9.2 Hz, 1H), 5.15 (s, 2H), 3.80 (d, *J* = 7.9 Hz, 6H). ¹³C NMR (101 MHz, DMSO-D₆) δ 167.3, 165.3, 161.4, 161.1, 151.8, 149.5, 135.0, 132.4, 131.1, 129.3, 126.0, 124.6, 124.4, 117.9, 114.1, 112.7, 56.3, 56.1, 36.2. Mass Calculated for C₁₉H₁₅N₃O₅S₂ is 429.0453; LCMS(ES +) *m/z*: 430.0692 [M + H⁺].

4.2.3.11. (Z)-5-((1H-indol-3-yl)methylene)-3-((5-(thiophen-2-yl)-1,3,4-oxadiazol-2-yl)methyl)thiazolidine-2,4-dione (TOT-11). Yellow solid; Yield: 88 %; mp: 193–195 °C. FT-IR (KBr, cm⁻¹) 3114 (Ar C—H), 1733, 1677 (C=O), 1597 (C=C), 1489, 1577 (C=N), 3008, 2924 (C—H, methylene), 1040, 748, 732 (C—S), 1328 (C—O), 3282 (N—H). ¹H NMR (400 MHz, DMSO-D₆) δ 12.24 (s, 1H), 8.23 (s, 1H), 7.93–7.90 (m, 2H), 7.83 (s, 1H), 7.78 (d, *J* = 3.7 Hz, 1H), 7.48 (d, *J* = 7.9 Hz, 1H), 7.26–7.16 (m, 3H), 5.15 (s, 2H). ¹³C NMR (101 MHz, DMSO-D₆) δ 167.2, 165.1, 161.4, 136.8, 132.4, 131.1, 130.1, 129.3, 127.4, 127.3, 124.4, 123.8, 121.8, 119.0, 113.3, 113.0, 110.9, 36.2. Mass Calculated for C₁₉H₁₂N₄O₃S₂ is 408.0351; LCMS(ES +) *m/z*: 409.0596 [M + H⁺].

4.2.3.12. (Z)-3-((5-(thiophen-2-yl)-1,3,4-oxadiazol-2-yl)methyl)-5-(thiophen-2-yl)methylene)thiazolidine-2,4-dione (TOT-12). Yellow solid; Yield: 86 %; mp: 154–156 °C. FT-IR (KBr, cm⁻¹) 3100 (Ar C—H), 1745, 1685 (C=O), 1595 (C=C), 1491, 1563 (C=N), 3008, 2924 (C—H, methylene), 1040, 730, 718 (C—S), 1324 (C—O). ¹H NMR (400 MHz, DMSO-D₆) δ 8.27 (s, 1H), 8.05 (d, *J* = 4.9 Hz, 1H), 7.93–7.91 (m, 1H), 7.77–7.73 (m, 2H), 7.27 (dt, *J* = 16.9, 4.4 Hz, 2H), 5.14 (s, 2H). ¹³C NMR (101 MHz, DMSO-D₆) δ 166.6, 165.0, 161.5, 161.1, 137.4, 136.1, 134.6, 132.4, 131.1, 129.7, 129.3, 127.9, 124.4, 118.3, 36.3. Mass Calculated for C₁₅H₉N₃O₃S₃ is 374.9806; LCMS(ES +) *m/z*: 376.0310 [M + H⁺].

4.2.3.13. (Z)-5-(2-chloro-6-fluorobenzylidene)-3-((5-(thiophen-2-yl)-1,3,4-oxadiazol-2-yl)methyl)thiazolidine-2,4-dione (TOT-13). Yellow solid; Yield: 82 %; mp: 152–154 °C. FT-IR (KBr, cm⁻¹) 3088 (Ar C—H), 1753, 1698 (C=O), 1600 (C=C), 1491, 1568 (C=N), 3008, 2926 (C—H, methylene), 1038, 758, 722 (C—S), 1329 (C—O), 722 (C—Cl), 1376 (C—F). ¹H NMR (400 MHz, DMSO-D₆) δ 7.92–7.76 (m, 3H), 7.56–7.37 (m, 3H), 7.25 (t, *J* = 4.0 Hz, 1H), 5.14 (s, 2H). ¹³C NMR (101 MHz, DMSO-D₆) δ

166.7, 164.4, 161.5, 160.9, 158.3, 134.6, 133.5, 132.4, 131.1, 129.3, 126.8, 126.0, 124.4, 120.6, 116.1, 115.9, 36.4. Mass Calculated for $C_{17}H_9ClF_3N_3O_3S_2$ is 420.9758; **LCMS**(ES +) m/z : 422.0007 [$C_{17}H_9^{35}ClF_3N_3O_3S_2 + H^+$] 423.9959 [$C_{17}H_9^{37}ClF_3N_3O_3S_2 + H^+$].

4.2.3.14. (Z)-5-(2,3-dichlorobenzylidene)-3-((5-(thiophen-2-yl)-1,3,4-oxadiazol-2-yl)methyl)thiazolidine-2,4-dione (TOT-14). Orange solid; Yield: 74 %; mp: 150–152 °C. **FT-IR** (KBr, cm^{-1}) 3107 (Ar C—H), 1751, 1698 (C=O), 1600 (C=C), 1491, 1570 (C=N), 3008, 2927 (C—H, methylene), 1047, 784, 720 (C—S), 1325 (C—O), 720 (C—Cl). **1H NMR** (400 MHz, DMSO- D_6) δ 8.04 (s, 1H), 7.92 (d, $J = 4.3$ Hz, 1H), 7.76 (dd, $J = 8.3, 2.1$ Hz, 2H), 7.55–7.50 (m, 2H), 7.25 (dd, $J = 4.9, 3.7$ Hz, 1H), 5.16 (s, 2H). **^{13}C NMR** (101 MHz, DMSO- D_6) δ 166.9, 164.8, 162.8, 161.5, 160.9, 133.9, 133.6, 132.8, 132.4, 131.1, 130.7, 129.5, 129.3, 128.1, 127.2, 124.4, 36.3. Mass Calculated for $C_{17}H_9Cl_2N_3O_3S_2$ is 436.9462; **LCMS**(ES +) m/z : 422.0007 [$C_{17}H_9^{35}Cl_2N_3O_3S_2 + H^+$] 423.9959 [$C_{17}H_9^{37}Cl_2N_3O_3S_2 + H^+$].

4.2.3.15. (Z)-5-(4-bromo-2-hydroxybenzylidene)-3-((5-(thiophen-2-yl)-1,3,4-oxadiazol-2-yl)methyl)thiazolidine-2,4-dione (TOT-15). Yellow solid; Yield: 70 %; mp: 168–170 °C. **FT-IR** (KBr, cm^{-1}) 3110 (Ar C—H), 1743, 1693 (C=O), 1601 (C=C), 1424, 1565 (C=N), 3008, 2932 (C—H, methylene), 1039, 738, 717 (C—S), 1321 (C—O), 1424 (C—Br), 1247 (C—OH). **1H NMR** (400 MHz, DMSO- D_6) δ 10.99 (s, 1H), 8.00 (s, 1H), 7.92 (d, $J = 4.9$ Hz, 1H), 7.77 (d, $J = 3.7$ Hz, 1H), 7.45 (td, $J = 9.2, 2.4$ Hz, 2H), 7.25 (t, $J = 4.3$ Hz, 1H), 6.91 (d, $J = 8.6$ Hz, 1H), 5.14 (s, 2H). **^{13}C NMR** (101 MHz, DMSO- D_6) δ 167.2, 165.3, 161.4, 161.1, 156.9, 135.5, 132.4, 131.4, 131.1, 129.3, 128.7, 124.4, 122.5, 121.6, 118.9, 111.1, 36.2. Mass calculated for $C_{17}H_9BrN_3O_4S_2$ is 462.9296; **LCMS**(ES +) m/z : 464.0549 [$C_{17}H_9^{79}BrN_3O_4S_2 + H^+$] 465.9527 [$C_{17}H_9^{81}BrN_3O_4S_2 + H^+$].

4.3. Single crystal X-ray crystallographic studies

X-ray crystallographic data was collected on a Bruker APEX-II CCD X-ray diffractometer. The structural analysis was performed on a computer with the *SHELXT* 2018/2 [36], *SHELXL* 2018/3 [37] and *Olex2* 1.5 [38] program package. Monochromated (doubly curved silicon crystal) M_o - K_{α} radiation (0.7107 Å) from a sealed microfocus tube was used to evaluate intensity. The generator was tuned to 50 kV and 1 mA. Six sets of Omega scans at various Phi values were used to obtain data. The breadth of the frame was 0.5°. For preliminary unit cell determination, the APEX2 software was employed. SAINT was used for the determination of integrated intensities and unit cell refinement. SADABS was used to adjust the data for absorption effects using the multi-scan approach [39]. The structure was resolved using *ShelxT* in the *Olex* 2.0 [38] package and polished using full-matrix least squares based on F^2 in *ShelxL* [40]. CCDC 2221637 contains the supplementary crystallographic data for the said compound.

4.4. Biological evaluation

4.4.1. Cell growth

MCF-7 (human breast cancer cell line) was cultured in Dulbecco's Modified Eagle Medium (DMEM) containing 10 % fetal bovine serum, 100 μ g/mL penicillin and 100 μ g/mL streptomycin antibiotics. The cells were incubated under 5 % CO_2 at 37 °C. After the cells grew well, the logarithmic growth phase cells were digested with trypsin to prepare the cell suspension for further biological assays. **TOT 12–15** were placed at 24 °C upon dissolving in dimethyl sulphoxide (DMSO) at storage concentration.

4.4.2. Cell cytotoxicity (MTT) assay

Using the MTT assay (3-(4, 5-dimethylthiazol-2-yl)-2, 5-diphenyltetrazolium bromide), the human breast cancer cell lines (MCF-7) were

seeded in 96 wells plate containing 100 μ L of DMEM (high glucose) medium, and allowed to grow. After 2 days, 100, 75, 50 and 25 μ g/mL of sample were dissolved in 500 μ L of 80 % chloroform and 20 % methanol. Then, these cells were treated with varying doses of samples and observed after 4 h. 10 μ L of MTT reagent was added to the 96 wells plate and left for 3 to 4 h. After that, the medium was removed from 96 wells plate and 50 μ L of 100 % DMSO was added to each well and shaken for 10 s. Then, absorbance was measured at 570 nm using a multi-well plate reader. Each concentration was repeated in three wells and the same experimental conditions were maintained for all testing procedures. The MTT assays were repeated three times for each cell line. The results were expressed as IC_{50} values (mean, $n = 3$) with standard deviation, which was defined as the concentration at which 50 % survival of cells was discerned. Epirubicin hydrochloride was co-assayed as positive control.

4.4.3. Cellular uptake and confocal fluorescence imaging of MCF-7 cells

Cellular uptake assay was carried out to investigate the mechanism of cytotoxicity in cancer cells. MCF-7 cells was cultured in DMEM medium supplemented with 10 % fetal bovine serum (FBS) in an atmosphere of 5 % CO_2 and 95 % air at 37 °C [41]. Before imaging, the cells were incubated with RPMI-1640 containing **TOT 12, 13, 14 and 15** in the dark at 37 °C for incubation time (2 h). The fluorescence images of **TOT 12, 13, 14 and 15** incubated cells were collected upon excitation at 460 nm with an emission band path of 400–600 nm. All of the images were captured using a Zeiss LSM710 laser scanning confocal microscope.

4.5. Steady state fluorescence quenching spectral measurements

A stock solution of **TOT-14** (5 mM) was prepared by dissolving the appropriate amount of it in DMSO and diluted with millipore water to get a concentration of 100 μ M. A stock solution of ct-DNA was prepared by dissolving ct-DNA in phosphate buffer (pH 7.4). A stock solution of ethidium bromide solution (250 μ M) was prepared. The purity of ct-DNA was determined by comparing the absorbance at 260 nm to that at 280 nm. This ratio was determined to be 1.86, suggesting that the ct-DNA was adequately protein-free. The concentration of ct-DNA was determined spectrophotometrically at 260 nm using a molar extinction coefficient of 6600 $L\ mol^{-1}\ cm^{-1}$ [42]. All of the chemicals utilised were of analytical quality.

All fluorescence spectra were recorded on a Agilent Technologies Carry Eclipse fluorescence spectrophotometer equipped with a Xenon flash lamp and a Cary single cell peltier to maintain the constant temperature. The excitation and emission slit widths was set at 5 nm.

4.6. Molecular docking

Molecular docking was used to clarify the binding mode of the compound to provide straight forward information for further structural optimization.

Binary and ternary crystal structures of a novel inhibitor of 17 beta-HSD type 1, a lead compound for breast cancer therapy (PDB ID 3HB5, 2.00 Å X-ray resolution) was extracted from the Brookhaven Protein Database (PDB <http://www.rcsb.org/pdb>). The proteins were prepared for docking by adding polar hydrogen atom with Gasteiger-Huckel charges and water molecules were removed. The 3D structure of the ligands was generated by the SKETCH module implemented in the SYBYL program (Tripos Inc., St. Louis, USA) and its energy-minimized conformation was obtained with the help of the Tripos force field using Gasteiger-Huckel [43] charges and molecular docking was performed with Surflex-Dock program that is interfaced with Sybyl-X 2.0. [44] and other miscellaneous parameters were assigned with the default values given by the software.

Declaration of competing interest

The authors declare that they have no known competing financial

interests or personal relationships that could have appeared to influence the work reported in this paper.

Data availability

Data will be made available on request.

Acknowledgements

The authors would like to thank the SAIF and USIC of Karnatak University in Dharwad for instrumental facilities. One of the authors expresses gratitude to the DST-KSTePs, Govt. of Karnataka, for awarding the Fellowship to carry out the research work. Thanks are also due to Dr. Satish Bhat, Department of Chemistry, Karnatak University, Dharwad for his insightful conversation and discussion on the X-ray crystallographic data. We gratefully acknowledge Dr. Avinash Prakash, Alekya Agro Solutions, Mysore, for biological studies. The supplemental crystallographic data for the compound TOT was deposited in CCDC 2262173, which could be downloaded for free from the Cambridge Crystallographic Data Centre, www.ccdc.cam.ac.uk/data_request/cif.

Appendix A. Supplementary data

Supplementary data to this article can be found online at <https://doi.org/10.1016/j.bioorg.2023.107003>.

References

- [1] A. Stanislawek, Breast Cancer—Epidemiology, Risk Factors, Classification, Prognostic Markers, and Current Treatment Strategies—An Updated Review (2021) 1–30.
- [2] Y. Feng, M. Spezia, S. Huang, C. Yuan, Z. Zeng, L. Zhang, X. Ji, W. Liu, B. Huang, W. Luo, B. Liu, Y. Lei, S. Du, A. Vuppalapati, H.H. Luu, R.C. Haydon, T.C. He, G. Ren, Breast cancer development and progression: Risk factors, cancer stem cells, signaling pathways, genomics, and molecular pathogenesis, *Genes Dis.* 5 (2018) 77–106, <https://doi.org/10.1016/j.gendis.2018.05.001>.
- [3] J. Makki, Diversity of breast carcinoma: Histological subtypes and clinical relevance, *Clin. Med. Insights Pathol.* 8 (2015) 23–31, <https://doi.org/10.4137/CPath.s31563>.
- [4] B.Z. Sibuh, S. Khanna, P. Taneja, P. Sarkar, N.K. Taneja, Molecular docking, synthesis and anticancer activity of thiosemicarbazone derivatives against MCF-7 human breast cancer cell line, *Life Sci.* 273 (2021), 119305, <https://doi.org/10.1016/j.lfs.2021.119305>.
- [5] G. Housman, S. Byler, S. Heerboth, K. Lapinska, M. Longacre, N. Snyder, S. Sarkar, Drug resistance in cancer: An overview, *Cancers (Basel)* 6 (2014) 1769–1792, <https://doi.org/10.3390/cancers6031769>.
- [6] M. Sharma, S.L. Walmsley, Raltegravir as antiretroviral therapy in HIV/AIDS, *Expert Opin. Pharmacother.* 15 (2014) 395–405, <https://doi.org/10.1517/14656566.2014.868884>.
- [7] M.M. Alam, 1,3,4-oxadiazole as a potential anti-cancer scaffold: A review, *Biointerface Res. Appl. Chem.* 12 (2022) 5727–5744, <https://doi.org/10.33263/BRIAC124.57275744>.
- [8] S.S. Thakkar, P. Thakor, H. Doshi, A. Ray, 1,2,4-Triazole and 1,3,4-oxadiazole analogues: Synthesis, MO studies, in silico molecular docking studies, antimalarial as DHFR inhibitor and antimicrobial activities, *Bioorg. Med. Chem.* 25 (2017) 4064–4075, <https://doi.org/10.1016/j.bmc.2017.05.054>.
- [9] K. Fizazi, C.S. Higano, J.B. Nelson, M. Gleave, K. Miller, T. Morris, F.E. Nathan, S. McIntosh, K. Pemberton, J.W. Moul, Phase III, randomized, placebo-controlled study of docetaxel in combination with zibotentan in patients with metastatic castration-resistant prostate cancer, *J. Clin. Oncol.* 31 (2013) 1740–1747, <https://doi.org/10.1200/JCO.2012.46.4149>.
- [10] M.J. Naim, M.J. Alam, F. Nawaz, V.G.M. Naidu, S. Aaghaz, M. Sahu, N. Siddiqui, O. Alam, Synthesis, molecular docking and anti-diabetic evaluation of 2,4-thiazolidinedione based amide derivatives, *Bioorg. Chem.* 73 (2017) 24–36, <https://doi.org/10.1016/j.bioorg.2017.05.007>.
- [11] B.C.C. Cantello, M.A. Cawthorne, G.P. Cottam, P.T. Duff, D. Haigh, R.M. Hindley, C.A. Lister, S.A. Smith, P.L. Thurlby, [ω-(Heterocyclylamino)alkoxy]benzyl]-2,4-thiazolidinediones as Potent Antihyperglycemic Agents, *J. Med. Chem.* 37 (1994) 3977–3985, <https://doi.org/10.1021/jm00049a017>.
- [12] T.V. Metre, B. Kodasi, P.K. Bayannavar, L. Bheemayya, V.B. Nadoni, S. R. Hoolageri, A.K. Shettar, S.D. Joshi, V.M. Kumbar, R.R. Kamble, Coumarin-4-yl-1,2,3-triazol-4-yl-methyl-thiazolidine-2,4-diones: Synthesis, glucose uptake activity and cytotoxic evaluation, *Bioorg. Chem.* 130 (2023), 106235, <https://doi.org/10.1016/j.bioorg.2022.106235>.
- [13] M. Shahnaz, Synthesis, Characterization of 2,4 -Thiazolidinedione Derivatives and Evaluation of Their Antioxidant Activity, *J. Drug Deliv. Ther.* 3 (2013) 96–101, <https://doi.org/10.22270/jddt.v3i6.714>.
- [14] C. Prabhakar, G. Madhusudhan, K. Sahadev, C. Maheedhara Reddy, M.R. Sarma, G. Om Reddy, R. Chakrabarti, C. Seshagiri Rao, T. Dileep Kumar, R. Rajagopalan, Synthesis and biological activity of novel thiazolidinediones, *Bioorganic Med. Chem. Lett.* 8 (1998) 2725–2730, [https://doi.org/10.1016/S0960-894X\(98\)00485-5](https://doi.org/10.1016/S0960-894X(98)00485-5).
- [15] H.N. Hafez, A.R.B.A. El-Gazzar, Synthesis and antitumor activity of substituted triazolo[4,3-a]pyrimidin-6-sulfonamide with an incorporated thiazolidine moiety, *Bioorganic Med. Chem. Lett.* 19 (2009) 4143–4147, <https://doi.org/10.1016/j.bmcl.2009.05.126>.
- [16] Y. Chinthala, A. Kumar Domatti, A. Sarfaraz, S.P. Singh, N. Kumar Arigari, N. Gupta, S.K.V.N. Satya, J. Kotes Kumar, F. Khan, A.K. Tiwari, G. Paramjit, Synthesis, biological evaluation and molecular modeling studies of some novel thiazolidinediones with triazole ring, *Eur. J. Med. Chem.* 70 (2013) 308–314, <https://doi.org/10.1016/j.ejmech.2013.10.005>.
- [17] H. El-Kashef, G. Badr, N. Abo El-Maali, D. Sayed, P. Melnyk, N. Lebegue, R. Abd El-Khalek, Synthesis of a novel series of (Z)-3,5-disubstituted thiazolidine-2,4-diones as promising anti-breast cancer agents, *Bioorg. Chem.* 96 (2020), 103569, <https://doi.org/10.1016/j.bioorg.2020.103569>.
- [18] M.A. Abdelgawad, K. El-Adl, S.S.A. El-Hddad, M.M. Elhady, N.M. Saleh, M. M. Khalifa, F. Khedr, M. Alswah, A.A. Nayl, M.M. Ghoneim, N.E.A. Abd El-Sattar, Design, Molecular Docking, Synthesis, Anticancer and Anti-Hyperglycemic Assessments of Thiazolidine-2,4-diones Bearing Sulfonylthiourea Moieties as Potent VEGFR-2 Inhibitors and PPAR γ Agonists, *Pharmaceuticals* 15 (2022) 1–23, <https://doi.org/10.3390/ph15020226>.
- [19] B.R. Bhattacharai, B. Kafle, J.S. Hwang, S.W. Ham, K.H. Lee, H. Park, I.O. Han, H. Cho, Novel thiazolidinedione derivatives with anti-obesity effects: Dual action as PTP1B inhibitors and PPAR- γ activators, *Bioorg. Med. Chem. Lett.* 20 (2010) 6758–6763, <https://doi.org/10.1016/j.bmcl.2010.08.130>.
- [20] N. Sunduru, K. Srivastava, S. Rajakumar, S.K. Puri, J.K. Saxena, P.M.S. Chauhan, Synthesis of novel thiourea, thiazolidinedione and thioparabanic acid derivatives of 4-aminoquinoline as potent antimalarials, *Bioorg. Med. Chem. Lett.* 19 (2009) 2570–2573, <https://doi.org/10.1016/j.bmcl.2009.03.026>.
- [21] C.G. Bonde, N.J. Gaikwad, Synthesis and preliminary evaluation of some pyrazine containing thiazolines and thiazolidinediones as antimicrobial agents, *Bioorganic, Med. Chem.* 12 (2004) 2151–2161, <https://doi.org/10.1016/j.bmc.2004.02.024>.
- [22] N.C. Desai, H.M. Satodiya, K.M. Rajpara, V.V. Joshi, K. Bhatt, H.V. Vaghani, Synthesis and Evaluation of N-Substituted Thiazolidine-2,4-dione Containing Pyrazole as a Potent Antimicrobial Agents, *Anti-Infective Agents* 12 (2014) 85–94, <https://doi.org/10.2174/22113525113119990117>.
- [23] S. Nayak, S.L. Gaonkar, E.A. Musad, A.M.A.L. Dawasr, 1,3,4-Oxadiazole-containing hybrids as potential anticancer agents: Recent developments, mechanism of action and structure-activity relationships, *J. Saudi Chem. Soc.* 25 (2021), 101284, <https://doi.org/10.1016/j.jscs.2021.101284>.
- [24] D. Sypniewski, N. Szkaradek, T. Loch, A.M. Waszkielewicz, A. Gunia-Krzyzak, D. Matczyńska, D. Sołtysik, H. Marona, I. Bednarek, Contribution of reactive oxygen species to the anticancer activity of aminoalkanol derivatives of xanthone, *Invest. New Drugs* 36 (2018) 355–369, <https://doi.org/10.1007/s10637-017-0537-x>.
- [25] A. Zeghimi, J.M. Escoffre, A. Bouakaz, Role of endocytosis in sonoporation-mediated membrane permeabilization and uptake of small molecules: A electron microscopy study, *Phys. Biol.* 12 (2015), <https://doi.org/10.1088/1478-3975/12/6/066007>.
- [26] M.A. Doddagaddavalli, V.K.A. Kalalbandi, J. Seetharamappa, Synthesis, characterization, crystallographic, binding, in silico and antidiabetic studies of novel 2,4-thiazolidinedione-phenothiazine molecular hybrids, *J. Mol. Struct.* 1276 (2023), 134625, <https://doi.org/10.1016/j.molstruc.2022.134625>.
- [27] M.A. Doddagaddavalli, S.S. Bhat, J. Seetharamappa, Characterization, Crystal Structure, Anticancer and Antioxidant Activity of Novel N-(2-Oxo-2-(10H-Phenothiazin-10-Yl) Ethyl)Piperidine-1-Carboxamide, *J. Struct. Chem.* 64 (2023) 131–141, <https://doi.org/10.1134/S0022476623010092>.
- [28] K. Bedard, K.H. Krause, The NOX family of ROS-generating NADPH oxidases: Physiology and pathophysiology, *Physiol. Rev.* 87 (2007) 245–313, <https://doi.org/10.1152/physrev.00044.2005>.
- [29] F. Qi, H. Yuan, Y. Chen, Y. Guo, S. Zhang, Z. Liu, W. He, Z. Guo, BODIPY-based monofunctional Pt (II) complexes for specific photocytotoxicity against cancer cells, *J. Inorg. Biochem.* 218 (2021), 111394, <https://doi.org/10.1016/j.jinorgbio.2021.111394>.
- [30] M. Stahlberger, O. Steinlein, C.R. Adam, M. Rotter, J. Hohmann, M. Nieger, B. Köberle, S. Bräse, Fluorescent annulated imidazo[4,5-c]isoquinolines via a GBB-3CR/imidoylation sequence - DNA-interactions in pUC-19 gel electrophoresis mobility shift assay, *Org. Biomol. Chem.* 20 (2022) 3598–3604, <https://doi.org/10.1039/d2ob00372d>.
- [31] A. Subastri, C.H. Ramamurthy, A. Suyavaran, R. Mareeswaran, P. Lokeshwara Rao, M. Harikrishna, M. Suresh Kumar, V. Sujatha, C. Thirunavukkarasu, Spectroscopic and molecular docking studies on the interaction of trolox with DNA, *Int. J. Biol. Macromol.* 78 (2015) 122–129, <https://doi.org/10.1016/j.ijbiomac.2015.03.036>.
- [32] C.Z. Yang, C.Y. Liang, D. Zhang, Y.J. Hu, Deciphering the interaction of methotrexate with DNA: Spectroscopic and molecular docking study, *J. Mol. Liq.* 248 (2017) 1–6, <https://doi.org/10.1016/j.molliq.2017.10.017>.
- [33] S. Akash, A. Kumer, M.M. Rahman, T. Bin Emran, R. Sharma, R.K. Singla, F. A. Alhumaydhi, M.U. Khandaker, M.N. Park, A.M. Idris, P. Wilairatana, B. Kim, Development of new bioactive molecules to treat breast and lung cancer with natural myricetin and its derivatives: A computational and SAR approach, *Front. Cell. Infect. Microbiol.* 12 (2022) 1–13, <https://doi.org/10.3389/fcimb.2022.952297>.

- [34] C.A. Lipinski, Lead- and drug-like compounds: The rule-of-five revolution, *Drug Discov. Today Technol.* 1 (2004) 337–341, <https://doi.org/10.1016/j.ddtec.2004.11.007>.
- [35] Y. Guo, T. Xu, C. Bao, Z. Liu, J. Fan, R. Yang, S. Qin, Design and synthesis of new norfloxacin-1,3,4-oxadiazole hybrids as antibacterial agents against methicillin-resistant *Staphylococcus aureus* (MRSA), *Eur. J. Pharm. Sci.* 136 (2019), 104966, <https://doi.org/10.1016/j.ejps.2019.104966>.
- [36] I. Usón, G.M. Sheldrick, An introduction to experimental phasing of macromolecules illustrated by SHELX; New autotracing features, *Acta Crystallogr. Sect. D Struct. Biol.* 74 (2018) 106–116, <https://doi.org/10.1107/S2059798317015121>.
- [37] G.M. Sheldrick, Crystal structure refinement with SHELXL, *Acta Crystallogr. Sect. C Struct. Chem.* 71 (2015) 3–8, <https://doi.org/10.1107/S2053229614024218>.
- [38] O.V. Dolomanov, L.J. Bourhis, R.J. Gildea, J.A.K. Howard, H. Puschmann, OLEX2: a complete structure solution, refinement and analysis program, *J. Appl. Crystallogr.* 42 (2009) 339–341.
- [39] S. Bruker, and SAINT-plus (Version 6.45 A), Bruker AXS Inc, Madison, Wisconsin, USA. (2014).
- [40] G.M. Sheldrick, XS. version 2013/1, Georg-August-Universität Göttingen, Germany, 2013; b) GM Sheldrick, *Acta Crystallogr., Sect. A.* 71 (2015) 3–8.
- [41] W. Chen, S. Shen, L. Dong, J. Zhang, Q. Yang, Selective inhibition of β -N-acetylhexosaminidases by thioglycosyl-naphthalimide hybrid molecules, *Bioorganic, Med. Chem.* 26 (2018) 394–400, <https://doi.org/10.1016/j.bmc.2017.11.042>.
- [42] S.K. Pawar, Intercalation of a flavonoid, silibinin into DNA base pairs: Experimental and Intercalation of a flavonoid, silibinin into DNA base pairs, Experimental and Theoretical Approach (2019), <https://doi.org/10.1002/jmr.2812>.
- [43] P. Baby Sudha Lakshmi, D. Ramchandran, C. Rambabu, Spectrophotometric determination of ezetimibe, *E-J. Chem.* 7 (2010) 101–104, <https://doi.org/10.1155/2010/238140>.
- [44] S.D. Joshi, S.R. Dixit, U.A. More, K.V.S.N. Raju, R. Narayan, T.M. Aminabhavi, V. H. Kulkarni, 3D-QSAR and molecular docking studies of 1,3,4-oxadiazoles containing substituted phenoxy fragment as inhibitors of enoyl-acyl carrier protein reductase from *Escherichia coli*, *Med. Chem. Res.* 23 (2014) 4542–4558, <https://doi.org/10.1007/s00044-014-1013-1>.



Cite this: DOI: 10.1039/d3nj01922e

Fluorenone–thiazolidine-4-one scaffolds as antidiabetic and antioxidant agents: design, synthesis, X-ray crystal structures, and binding and computational studies†

Manasa A. Doddagaddavalli,^a Veerendra Kumar A. Kalalbandi,^b T. R. Ravi Naik,^c Shrinivas D. Joshi^d and Jaldappagari Seetharamappa  ^{*,a}

Using 2-(9*H*-fluoren-9-ylidene)hydrazinylthiazol-4(5*H*)-one and substituted benzaldehydes, a new library of fluorenone–thiazolidine-4-one scaffolds (**5a–u**) were synthesized and characterized using FT-IR, ¹H NMR, ¹³C NMR and mass spectral data. Single crystals of compound **5s** were developed and crystallographic data were collected. Hirshfeld surface evaluation was used to investigate the intermolecular interactions that exist within the crystals. The synthesized compounds were screened for *in vitro* antioxidant and anti-diabetic properties by DPPH scavenging activity and α -glucosidase inhibition, respectively. Compounds **5a–l** exhibited promising DPPH scavenging activity. Compound **5l** showed an IC₅₀ value of 27.70 \pm 0.8 μ M, which is 4.25-fold greater as compared to that of the standard, gallic acid (an IC₅₀ value of 117.92 \pm 2.8 μ M). Compound **5g** exhibited good α -glucosidase inhibition with an IC₅₀ value of 114.58 \pm 1.6 μ M, which is less than that of the standard inhibitor, acarbose, with an IC₅₀ value of 115.49 \pm 2.2 μ M. The mechanism of binding of compound **5g** with human serum albumin (HSA) and calf thymus DNA (Ct-DNA) was studied by fluorescence spectroscopy. Furthermore, the ADME properties of the designed compounds were studied using the SwissADME online tool. The molecular docking studies of the compounds were performed against acid- α -glucosidase, in complex with 1-deoxynojirimycin (PDB ID: 5NN5).

Received 27th April 2023,
Accepted 5th June 2023

DOI: 10.1039/d3nj01922e

rsc.li/njc

Introduction

Diabetes mellitus (DM) is a chronic disease characterized by dyslipidemia and high blood sugar levels, which are primarily caused by environmental and hereditary factors. Additionally, there are two forms, *viz.*, insulin-dependent diabetes mellitus (IDDM) and non-insulin-dependent diabetes mellitus (NIDDM). NIDDM, often known as type 2 diabetes (T2DM), affects more than 90% of diabetic individuals. T2DM is presently incurable and is considered as deadly illness with a high prevalence of morbidity and disability.¹ It can cause long-term

harmful effects on organs such as the kidneys, liver, eyes, nerves, heart, and veins. Some of these organs can even fail and may lead to death.²

The typical course of therapy focuses mostly on controlling and lowering the blood sugar level to return to the normal range. However, there are many approaches to control the effect of T2DM. The primary mechanisms in both conventional medicine and western medicine involve lowering of blood sugar levels by stimulating pancreatic β -cells, blocking hormones that increase blood sugar, enhancing the affinity and sensitivity of insulin receptors, reducing glycogen release, enhancing glucose utilization in many tissues and organs, eradicating free radicals, increasing resistance to lipid peroxidation, correcting lipid and protein metabolic disorders, and enhancing the general health.³

Feasting diets that are rich in carbohydrates could activate the high blood glucose level due to the rapid absorption of carbohydrates by the small intestine. This phenomenon is aided by the sugar hydrolysing enzymes such as α -glucosidase which reside in the epithelial mucosa of the small intestine. One crucial therapeutic strategy to manage diabetes is to decrease postprandial hyperglycemia, which can be regulated

^a Department of Chemistry, Karnatak University, Dharwad-580 003, India.
E-mail: drjseetharamappa@kud.ac.in

^b Department of Chemistry, Ballari Institute of Technology and Management, Ballari-583 104, India

^c Department of P.G. Studies in Chemistry, Veerashaiva College, Ballari-583104, India

^d Department of Pharmaceutical Chemistry, SET's College of Pharmacy, Dharwad-580 002, India

† Electronic supplementary information (ESI) available. CCDC 2221637 (**5s**). For ESI and crystallographic data in CIF or other electronic format see DOI: <https://doi.org/10.1039/d3nj01922e>

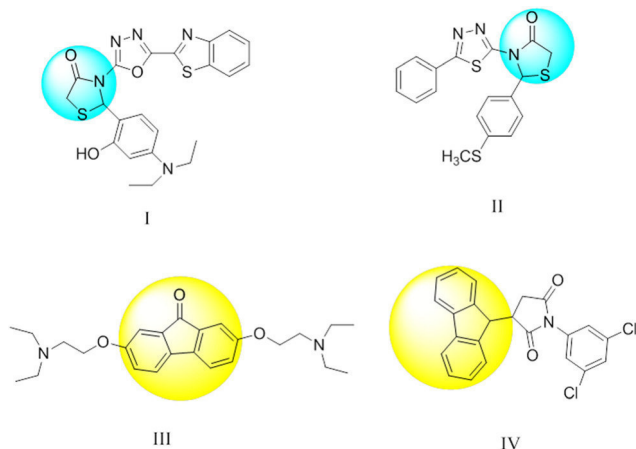


Fig. 1 Drug moieties of structurally related fluorenone and thiazolidine-4-one.

by prolonging the absorption of glucose by inhibition of the carbohydrate-hydrolyzing enzymes, α -amylase and α -glucosidase in the digestive tract.⁴ α -Glucosidase is essential in hydrolyzing the 1,4- α -glucopyranoside bonds to harvest α -glucose.⁵ The small intestine's ability to absorb carbohydrates could be delayed by inhibition of α -glucosidase, which would also lower postprandial blood glucose levels.⁶ Additionally, α -glucosidase inhibitors have been promoted as T2DM treatment medications. Consequently, it was proposed that one of the most promising strategies for the therapy of diabetes was the inhibition of the α -glucosidase enzyme.⁷

Thiazolidinones, which raise insulin sensitivity and improve glycemic control, are increasingly being used to treat T2DM. The heterocyclic compounds, namely, thiazolidine-4-one and its derivatives that contain a carbonyl group in the fourth position, are crucial components of many synthetic medications with a range of biological functions.⁸ For instance, thiazolidine-4-one-based hybrids **I** and **II** (Fig. 1) have been found to be powerful PPAR δ agonists and α -glucosidase inhibitors for the treatment of T2DM. The widespread use of the thiazolidine-4-one ring, on the other hand, has exhibited a wide range of biological activities including anticancer,^{9–13} anti-tuberculosis,¹⁴ antiviral,¹⁵ antimicrobial,¹⁶ antimycobacterial,¹⁷ and anti-HIV.^{18,19}

Furthermore, biologically active molecule hybridization is a potent drug discovery approach that has been used to treat a number of ailments. In this context, we have designed scaffolds of thiazolidine-4-one and fluorenone. Fluorenone is a polysubstituted benzene derivative that plays a significant role in the fields of medicinal chemistry and materials sciences. Fluorenone scaffolds are extensively found in a variety of physiologically significant compounds including antinociceptive,²⁰ anticancer,²¹ antimicrobial,²² antitubercular,²³ and antiviral²⁴ compounds. For instance, fluorenone based hybrids **III** and **IV** with anticancer and antitubercular activity, respectively, are given in Fig. 1.

To continue our investigation on the thiazolidine-4-one scaffold and in the light of the aforementioned results, we have

hybridised the biologically active compound thiazolidine-4-one with the fluorenone moiety in this study. The newly synthesized libraries of compounds (**5a–5u**) were characterized using FT-IR, ¹H NMR, ¹³C NMR and mass (LC-MS) spectral data. Single crystals of compound **5s** were developed and crystallographic data were collected. The said compound was crystallised in the triclinic space group of *P* $\bar{1}$. It is hypothesized that the antidiabetic and antioxidant potentials of compounds are directly related. Research studies have demonstrated that the compound with a stronger glucose-lowering impact also had a high antioxidant capacity. We have compared the synthesized compounds' ability to inhibit α -glucosidase activity with that of the standard, acarbose, and the DPPH radical scavenging activity to that of the standard, gallic acid. Furthermore, molecular docking studies are supportive in positioning the optimized 3D structure of a small ligand into a receptor structure in a variety of orientations, conformations, and locations. This strategy can be used to create novel and effective drugs. As a result, molecular docking studies of the more effective α -glucosidase inhibitor compounds were performed.

Studies on bioactive molecule–protein binding are crucial from a theoretical and practical perspective because they help us understand the processes underlying drug disposition and elimination, as well as how different pathological conditions or concurrent medications affect the drug delivery and its effectiveness. The primary plasma protein, human serum albumin (HSA), serves as a store and carrier for several endogenous (fatty acids, bilirubin, *etc.*) and exogenous (drugs, nutrients, *etc.*) compounds in the blood. The drug's ability to bind to HSA regulates its free, active concentration and may have a significant impact on its overall pharmacodynamic and pharmacokinetic characteristics. Understanding the characteristics of a bioactive compound and its mechanism of action in the body requires the investigation of the mechanism of binding between the ligand (**5g**) and serum albumin. So, the mechanism of interaction of **5g** with HSA was studied using a fluorescence spectroscopic method.

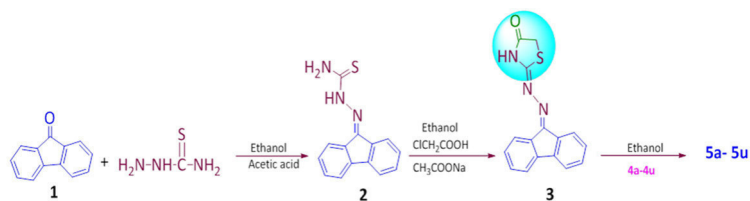
The interaction of a bioactive compound with DNA is an important aspect of pharmacology. The binding study helps in the understanding of drug action and the development of efficient and precisely targeted medications with less adverse effects. Thus, with the interest in exploring the binding mechanism of the selected bioactive compound (**5g**) with calf thymus DNA (Ct-DNA), a fluorescence spectroscopic method was adopted.

Results and discussion

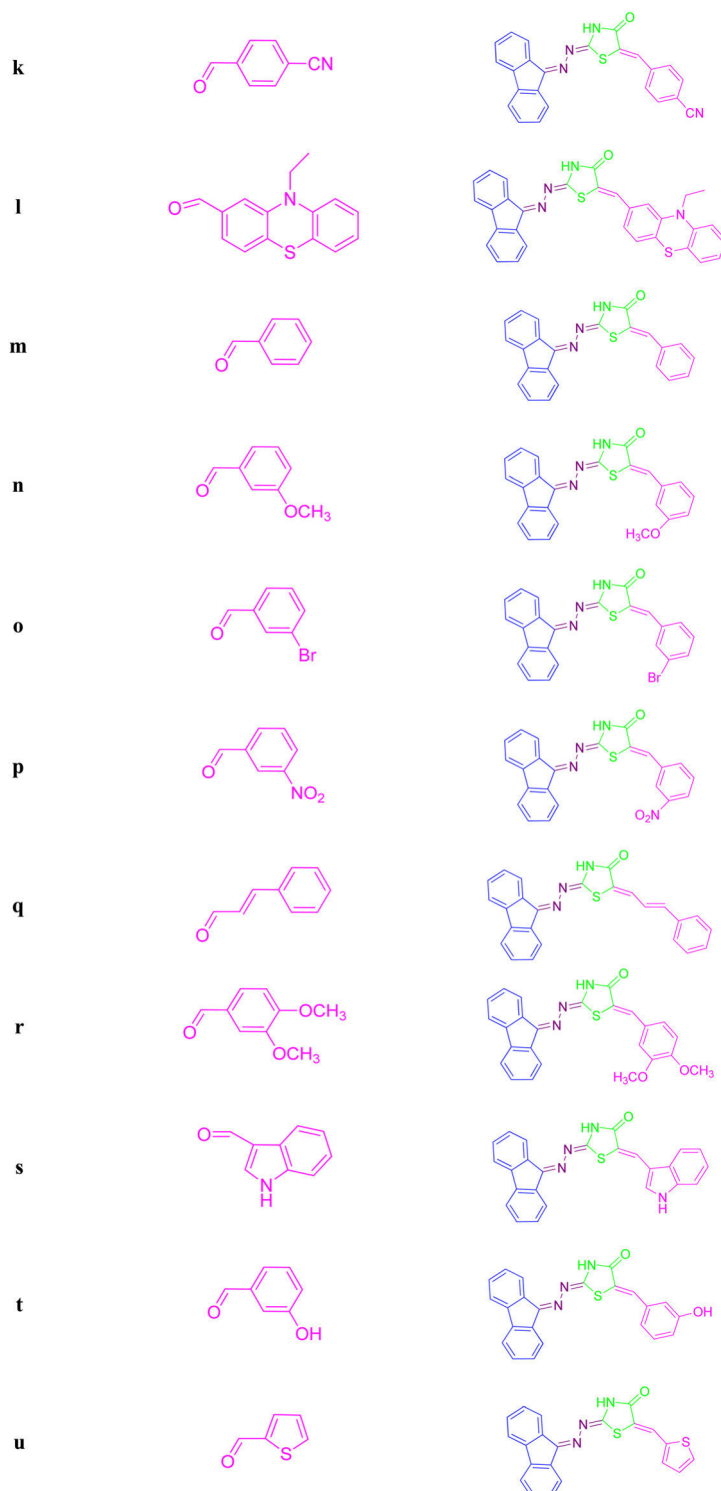
Chemistry

The procedure depicted in Scheme 1 was employed to synthesize the target and intermediate compounds.

9H-Fluoren-9-one (**1**) reacted with thiosemicarbazide in ethanol and a catalytic amount of acetic acid to yield 2-(9H-fluoren-9-ylidene)hydrazinecarbothioamide (**2**).^{25,26} The structure of **2** was confirmed on the basis of spectral data where the IR spectrum of compound **2** showed bands at 1279, 3263 and



Derivatives	Compound 4	Compound 5
a		
b		
c		
d		
e		
f		
g		
h		
i		
j		



Scheme 1 Synthetic route for the preparation of compounds (**5a–5u**).

3411 cm^{-1} due to $\text{C}=\text{S}$ and NH_2 groups, respectively, while the ^1H NMR spectrum showed a singlet at 11.68 ppm characteristic of the NH_2 group.

The treatment of **2** with chloroacetic acid in the presence of sodium acetate and ethanol yielded 2-(2-(9H-fluoren-9-ylidene)hydrazinyl)thiazol-4(5H)-one (**3**). This compound on

reaction with different aromatic aldehydes, **4a–4u**, yielded corresponding compounds, **5a–5u**, by the Knoevenagel condensation reaction.^{27,28}

The structures of the newly synthesised compounds were proposed using FT-IR, ^1H and ^{13}C NMR spectral data and then confirmed using mass spectral data. For instance, the

Table 1 Crystallographic refinement data for compound **5s**

Chemical formula	C ₂₅ H ₁₆ N ₄ OS·C ₂ H ₆ O
<i>M_r</i>	466.54
Crystal system, space group	Triclinic, <i>P</i> $\bar{1}$
Temperature (K)	296
<i>a</i> , <i>b</i> , <i>c</i> (Å)	9.5263 (4), 10.9713 (6), 11.9081 (6)
α , β , γ (°)	67.572 (2), 76.947 (3), 83.014 (3)
<i>V</i> (Å ³)	1119.85 (10)
<i>Z</i>	2
Radiation type	MoK α
μ (mm ⁻¹)	0.18
Crystal size (mm)	0.19 × 0.19 × 0
Diffractometer	Bruker APEX-II CCD
Absorption correction	Multi-scan SADABS2012/1 (Bruker, 2012) was used for absorption correction. <i>wR₂</i> (int) was 0.1009 before and 0.0480 after correction. The ratio of minimum to maximum transmission is 0.9277. The $\lambda/2$ correction factor is 0.0015
<i>T_{min}</i> , <i>T_{max}</i>	0.691, 0.745
No. of measured, independent and observed [<i>I</i> > 2 σ (<i>I</i>)] reflections	15 443, 4153, 3185
<i>R_{int}</i>	0.036
(<i>sin</i> θ / λ) _{max} (Å ⁻¹)	0.606
Refinement	
<i>R</i> [<i>F</i> ² > 2 σ (<i>F</i> ²)], <i>wR</i> [<i>F</i> ²], <i>S</i>	0.049, 0.123, 1.04
No. of reflections	4153
No. of parameters	309
H-atom treatment	H-atom parameters constrained
Δ _{max} , Δ _{min} (e Å ⁻³)	0.28, -0.29

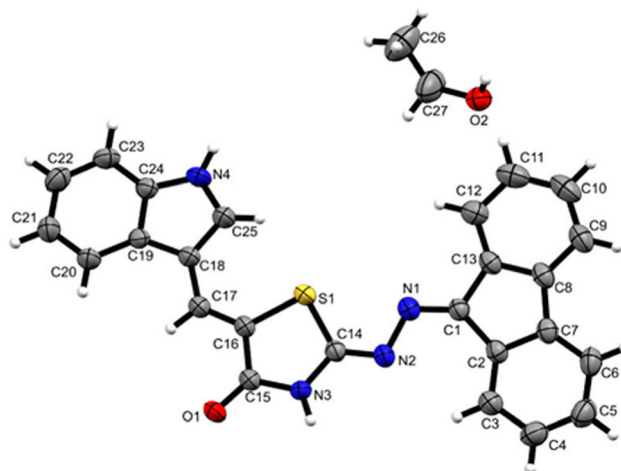
characterization of a methoxy substituted compound (**5a**) is discussed here. The FT-IR spectrum of **5a** displayed bands at 3412 cm⁻¹ corresponding to N-H stretching, 1719 cm⁻¹ assignable to carbonyl (C=O) stretching, 1252 cm⁻¹ due to C-OCH₃ stretching and 1639 and 1606 cm⁻¹ assignable to C=N stretching. The ¹H NMR spectrum showed three characteristic peaks. The singlet peaks at 12.91, 7.64 and 3.80 ppm corresponded to -NH-, =CH- (aldehydes) and -OCH₃ protons, respectively. The peaks around 7–9 ppm due to aromatic protons were observed. In ¹³C NMR spectra, a peak attributed to methoxy carbon was observed at 55.83 ppm. The characteristic peak of the carbonyl group appeared at 167.79 ppm. The peaks attributed to benzene ring carbons were observed between 121.11 and 140.97 ppm. The peak observed at 142.1 ppm was attributed to =CH- formed by the condensation of aldehydes and the methylene group of the thiazolidine-4-one ring. The peak at 163.01 ppm was assigned to the carbon of C=N in the fluorenone ring and the peak at 160.15 ppm was attributed to the carbon of C=N in the thiazolidine-4-one ring. Furthermore, the mass spectrum showed a molecular ion peak at *m/z* 412.09 corresponding to [*M* + 1] that confirmed the formation and purity of the compound. Similarly, the structures of all other derivatives were elucidated and the spectral data of the derivatives are given in the Experimental section.

X-ray crystallographic studies

Compound **5s** was crystallized in the triclinic crystal system with a space group of *P* $\bar{1}$ and the unit cell parameters were namely *a* = 9.5263 (4) Å, *b* = 10.9713 (6) Å, *c* = 11.9081 (6) Å, α = 67.572° (2), β = 76.947° (3) and γ = 83.014° (3), and the unit cell volume was 1119.85 (10) Å³. The crystallographic refinement data of compound **5s** are given in Table 1. The compound consisted of two molecules in the unit cell. The crystal structure

was deposited at the Cambridge Crystallographic Data Centre (deposition number CCDC 2221637†).

The ORTEP view at 30% ellipsoidal probability of compound **5s** is shown in Fig. 2. Intermolecular interactions were responsible for the formation of crystalline solids; particularly the classical and non-classical hydrogen bonds played a key role. The hydrogen bond geometrical parameters of compound **5s** are presented in Fig. 3 and Table 2. Two intermolecular hydrogen bonds aid the structural stability of the molecule. One H-bond was observed at a bond distance of 2.833 Å between the hydrogen of the thiazolidine-4-one ring and the oxygen of ethanol (O2), while the other H-bond was observed at a distance of 2.849 Å between the hydrogen of the hydroxyl of ethanol (H2) and the oxygen atom of the carbonyl of the thiazolidine-4-one

Fig. 2 ORTEP view of compound **5s** at the 30% ellipsoidal probability.

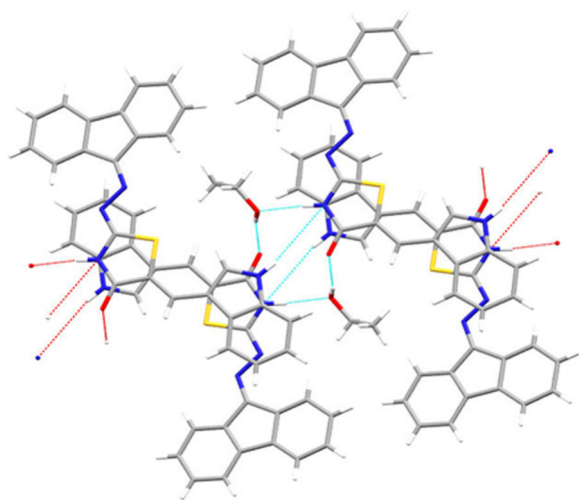


Fig. 3 Intermolecular hydrogen bonding shown using dotted lines [N3–H3...O2 and O2–H2...O1] in compound **5s**.

Table 2 Data related to observed intermolecular hydrogen bond formation in compound **5s**

D–H...A	D–H (Å)	H...A (Å)	D...A (Å)	D–H...A (°)
N3–H3...O2 ⁱ	0.86	1.98	2.833 (2)	173.3
O2–H2...O1 ⁱⁱ	0.82	2.06	2.849 (2)	161.7

ring (O1). Table 2 depicts the intermolecular hydrogen bonding characteristics. Bond lengths and bond angles of **5s** were found to be within typical limits. Furthermore, the phenyl ring of the indole group makes a dihedral angle of 16.24(1) with the phenyl ring of fluorenone.

Hirshfeld surface analysis

Using the crystal explorer 2.1 tool, a Hirshfeld surface study of compound **5s** was performed to examine the strength and position of intermolecular interactions.²⁹ Various colours on the Hirshfeld surface, such as white, red and blue, were allocated based on the distance and interactions to the van der Waals radius.³⁰ Fig. 4 depicts the Hirshfeld surfaces of compound **5s**, which have been mapped onto d_{norm} (Fig. 4a), d_i (Fig. 4b) and d_e (Fig. 4c).

Using fingerprint plot (FP) analysis, the effect of each intermolecular interaction on the stability of **5s** crystals was predicted and the same is shown in Fig. 5. It was observed that the C...H/H...C (Fig. 5b) intermolecular interactions contributed 18.4%. The intermolecular interactions in O...H/H...O (Fig. 5c) and C...N/N...C (Fig. 5d) contributed 9.6% and 4.1%, respectively. The N...H/H...N (Fig. 5e) and C...S/S...C (Fig. 5f) interactions 3.3% and 3.0%, respectively.

Biological activity

Antioxidant activity

The antioxidant properties of hybrids **5a–u** were quantified by assessing their capacity to scavenge free radicals using

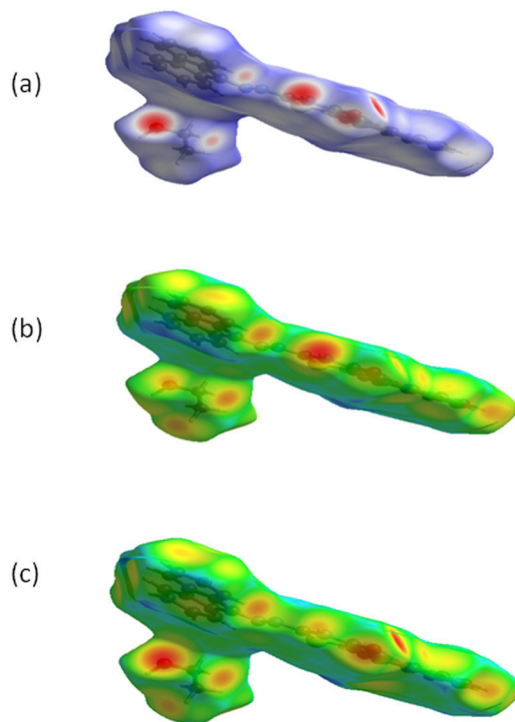


Fig. 4 Hirshfeld surface analysis of compound **5s** by (a) d_{norm} , (b) d_i and (c) d_e mapping.

2,2-diphenyl-1-picrylhydrazyl (DPPH). The findings recorded in Table 3 indicated that several of these synthesized compounds showed good antioxidant activity. With an IC_{50} value of $27.70 \pm 0.8 \mu\text{M}$, compound **5l** displayed better DPPH radical scavenging activity which was 4.25-fold greater than that of gallic acid with an IC_{50} value of $117.92 \pm 2.8 \mu\text{M}$. Compounds **5a–5k** showed significant activity with IC_{50} values ranging from 35.46 ± 0.8 to $112.40 \pm 1.5 \mu\text{M}$. Compounds **5m–5u** exhibited moderate activity. In general, the aforementioned results suggested that the derivatives having substitution at *ortho* and *para* positions exhibited significant antioxidant properties compared to *meta* substituted derivatives. In particular, the electron withdrawing groups such as nitro, cyano and halogen groups at *ortho* and *para* positions showed good antioxidant properties, whereas the electron releasing groups such as methyl, hydroxyl and methoxy groups at *ortho* and *para* positions exhibited good activity but compounds with substituents at the *meta* position showed less antioxidant activity. The graph of DPPH radical scavenging activity *versus* each compound is given in Fig. 6.

Antidiabetic activity

Using acarbose as the positive control, the *in vitro* enzyme assay was used to evaluate the α -glucosidase inhibitory activity of all the target compounds, fluorenone-thiazolidine-4-one molecular hybrids (**5a–u**). The IC_{50} values of these compounds are shown in Table 3. Among these compounds, **5g** exhibited better inhibition of the α -glucosidase enzyme with an IC_{50} value of $114.58 \pm 1.8 \mu\text{M}$ which was closer to that of acarbose with an IC_{50} value of $115.49 \pm 2.2 \mu\text{M}$ while compounds **5h** and **5t**

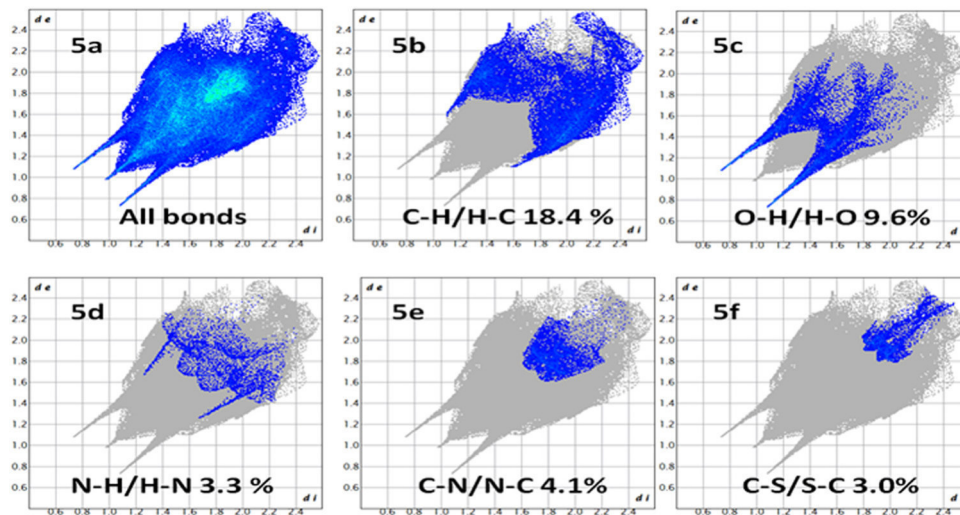


Fig. 5 Fingerprint plot of the proportion of short-range action on the Hirshfeld surface in compound **5s**.

showed IC_{50} values of 118.66 ± 1.7 and 116.45 ± 1.9 μM respectively. These findings indicated that the compounds with hydroxyl groups exhibited good antidiabetic activity. However, compound **5h** displayed a modest decrease in the activity compared to **5g** and **5t** due to the presence of the bromo group adjacent to the hydroxyl group. Furthermore, compounds with electron withdrawing groups exhibited good to moderate α -glucosidase inhibition. However, compound **5j** also exhibited good to moderate activity though it has electron releasing groups among all the compounds. The graph of the α -glucosidase inhibition against each compound is recorded in Fig. 7.

Structure–activity relationship (SAR) studies

Various aldehydes (**4a–u**) which include substituted benzaldehydes (mono- and di-substituted) and heterocyclic benzaldehydes (1*H*-indole-3-carbaldehyde, thiophene-2-carbaldehyde and 10-ethyl-10*H*-phenothiazine-2-carbaldehyde) were used to synthesize compounds **5a–u**. For DPPH radical scavenging activity, *para*-substituted aldehyde and disubstituted aldehyde containing compounds exhibited good activity compared to *meta*-substituted aldehyde containing compounds. Out of the three heterocyclic aldehyde derivatives, only phenothiazine-containing derivative **5l** showed promising activity. On the other hand, for α -glucosidase inhibition activity, compounds with hydroxyl groups displayed good activity when compared to others. However, mono-halogen-substituted compounds exhibited appreciable inhibition but di-halogen-substituted compounds showed less inhibition. Even heterocyclic aldehyde containing compounds did not show any impact on inhibition. A schematic representation of the plausible SAR of the synthesized molecules is shown in Fig. 8.

Binding studies

Drug–protein interactions are critical because most medications are extensively and reversibly bound to serum albumin

and are predominantly administered as a complex with protein. The form and extent of the drug–protein interaction have a significant influence on the drug's biological activity. The binding variables are significant in researching pharmaceutical pharmacology and creating dosage formulations. Since serum albumin is the major binding protein for pharmaceuticals and other physiological substances, we have utilized HSA as a model for the investigation of *in vitro* drug–protein interactions.³¹

Interactions of compound **5g** with HSA

The best method to study the interaction of a bioactive compound with HSA is fluorescence spectroscopy because it is more sensitive compared to other optical techniques. The intrinsic fluorescence of HSA is caused by three amino acid residues, *viz.*, tryptophan (Trp), tyrosine (Tyr), and phenylalanine (Phe). However, the fluorescence of HSA is almost contributed by Trp alone because Phe has a very low quantum yield while the fluorescence of Tyr is nearly completely quenched if it is ionised or located near an amino group or a carboxyl group. When small molecules bind to HSA, the intrinsic fluorescence intensity of HSA changes.³² So, fluorescence spectra of HSA in the range of 300–500 nm were recorded upon excitation at 295 nm and in the presence and absence of compound **5g**. To a fixed concentration of HSA (4.16 μM), varied amounts of compound **5g** (0.66 to 8.58 μM) were successively added and the corresponding fluorescence quenching spectra of HSA were recorded and are shown in Fig. 9A.

Evaluation of the quenching mechanism and binding constant

The fluorescence quenching data can be used to calculate the binding characteristics of **5g**-HSA, *viz.*, the Stern–Volmer quenching constant, number of binding sites and binding constant. The following equation is used to calculate the Stern–Volmer quenching constant.

$$F_0/F = 1 + K_{sv} [Q] = 1 + K_q \tau_0 [Q] \quad (1)$$

Table 3 *In vitro* antidiabetic and antioxidant activities of synthesized compounds **5a–5u**

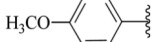
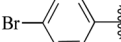
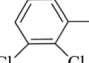
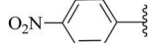
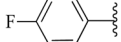
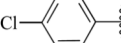
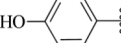
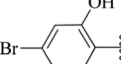
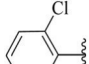
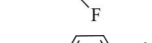
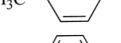
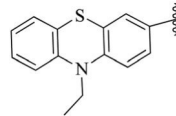
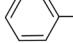
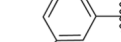
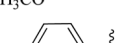
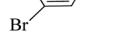
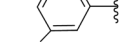
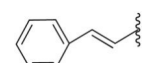
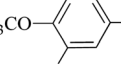
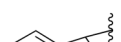
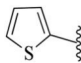
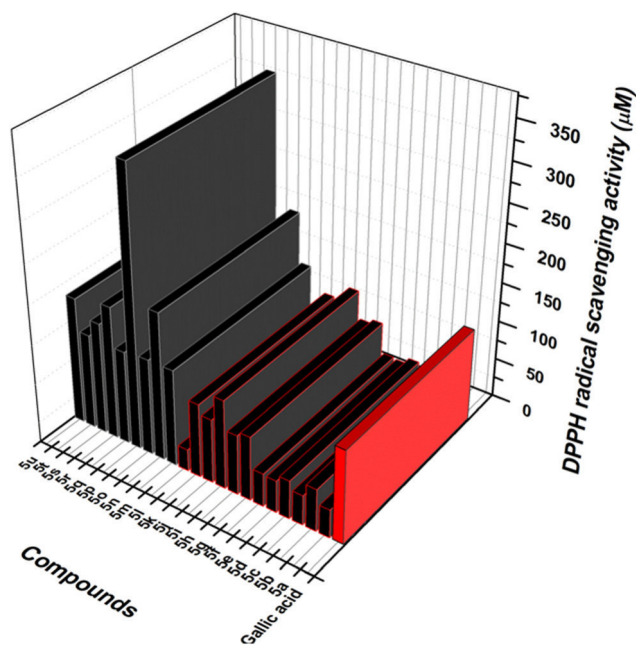
Compound	Substituent (R)	Antidiabetic activity α -glucosidase (IC ₅₀ μ M)	Antioxidant activity DPPH (IC ₅₀ μ M))
5a		206.64 \pm 2.5	35.46 \pm 0.8
5b		165.00 \pm 2.3	53.42 \pm 0.7
5c		158.15 \pm 1.8	37.84 \pm 0.6
5d		148.13 \pm 2.6	48.38 \pm 1.1
5e		142.45 \pm 1.2	40.58 \pm 0.9
5f		175.58 \pm 1.6	42.00 \pm 1.8
5g		114.58 \pm 1.8	81.27 \pm 1.3
5h		118.66 \pm 1.7	75.78 \pm 1.7
5i		136.39 \pm 1.7	112.40 \pm 1.5
5j		131.36 \pm 2.4	81.09 \pm 1.2
5k		154.16 \pm 2.3	92.97 \pm 1.1
5l		151.66 \pm 1.8	27.70 \pm 0.8
5m		184.14 \pm 2.1	121.98 \pm 1.1
5n		213.50 \pm 2.4	186.98 \pm 1.2
5o		169.96 \pm 1.8	121.76 \pm 1.8
5p		140.55 \pm 2.3	350.38 \pm 1.8
5q		197.18 \pm 1.6	118.36 \pm 2.1
5r		228.43 \pm 1.7	168.20 \pm 2.3
5s		156.10 \pm 2.2	141.07 \pm 1.8
5t		116.45 \pm 1.9	119.78 \pm 1.7

Table 3 (continued)

Compound	Substituent (R)	Antidiabetic activity α -glucosidase (IC ₅₀ μ M)	Antioxidant activity DPPH (IC ₅₀ μ M))
5u		227.75 \pm 1.8	160.47 \pm 2.1
Standard	Acarbose	115.49 \pm 2.2	—
	Gallic acid	—	117.92 \pm 2.8

Data represented in terms of mean \pm standard error of three independent experiments.

**Fig. 6** Graph of IC₅₀ values in μ M of DPPH scavenging activity for compounds **5a–5u**.

where F_0 and F are the fluorescence intensities in the absence and presence of the quencher, K_{sv} is the Stern–Volmer quenching constant, K_q is the bimolecular quenching constant and $[Q]$ is the concentration of the quencher and τ_0 is the average lifetime of the fluorophore (HSA) in the absence of the quencher. It is known that the average lifetime of HSA without the quencher is in the order of 1×10^{-9} s based on lifetime experiments.³³ The Stern–Volmer plots of F_0/F versus $[Q]$ are displayed in Fig. 9B. The values of K_{sv} and K_q are recorded in Table 4. The observed values of K_q were higher than the bimolecular limiting diffusion rate constant of $2.0 \times 10^{10} \text{ M}^{-1} \text{ s}^{-1}$, thereby confirming that the fluorescence of HSA was quenched by the static quenching mechanism.³⁴

The following equation was used to calculate the values of the binding constant (K) and the number of binding sites:

$$\log[(F_0 - F)/F] = \log K + n \log [Q] \quad (2)$$

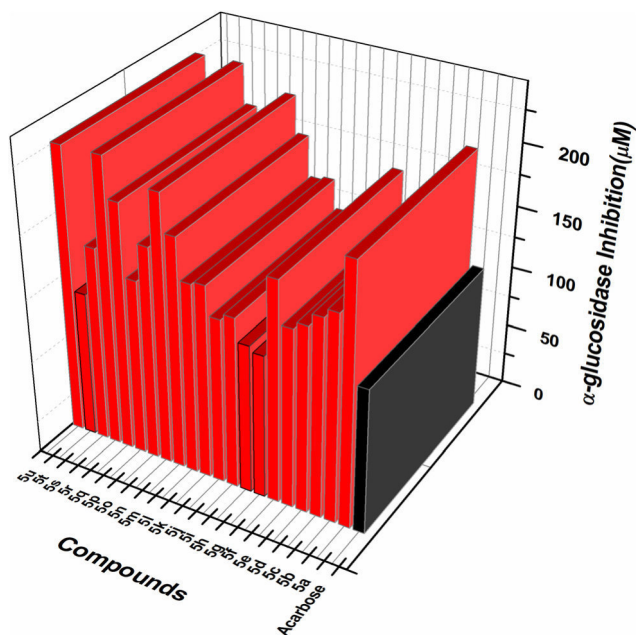


Fig. 7 Graph of IC_{50} values in μM of α -glucosidase inhibition for compounds **5a–5u**.

The binding constant of **4g**-HSA was calculated from the intercept of the $\log(F_0 - F)/F$ vs. $\log[Q]$ plot and found to be $1.01 \times 10^4 M^{-1}$. The value of n was obtained from the slope of the plot and calculated to be 0.861. This indicated that one molecule of compound **5g** was bound to one HSA molecule.

Studies on binding of compound **5g** with calf thymus DNA (ctDNA)

DNA is a well-known biomacromolecule with significant biological relevance since it is involved in the transcription and translation of genetic information in living cells. These are thought to be essential for cell survival and proliferation. Because of its biological significance, it is regarded as the most important pharmacological target for many drugs. A large number of tiny molecules bind to DNA. Conformational changes may occur in DNA as a result of binding. Studies on the interactions between drugs and DNA assist in comprehending

the molecular basis of a drug's action and in developing innovative and effective drugs with fewer adverse effects and greater therapeutic results.³⁵

Steady state quenching measurements

The concentration of ct-DNA was determined by recording absorbance at 260 nm and using a molar extinction coefficient ($L M^{-1} cm^{-1}$) of 6600. The purity of DNA was determined by comparing the absorbance at 260 nm to that at 280 nm. In the present study, the value of A_{260}/A_{280} was observed to be greater than 1.8, suggesting that the DNA was sufficiently free of protein. Since ctDNA is non-fluorescent, we have monitored the interaction of ctDNA with **5g** using a well known fluorescent probe, ethidium bromide. To a fixed concentration of ctDNA ($1.38 \mu M$) and ethidium bromide ($0.83 \mu M$), various concentrations of **5g** (0.6 to $6.0 \mu M$) were added and fluorescence spectra in the range of 560–660 nm were recorded upon excitation at 510 nm. The corresponding results are shown in Fig. 10A.

The values of the Stern-Volmer quenching constant and binding constant were calculated from the intercept of the plots of F_0/F vs. $[Q]$ and $\log(F_0 - F)/F$ vs. $\log[Q]$ respectively using equations 1 and 2. Fluorescence quenching and Stern-Volmer plots are given in Fig. 10A and B, respectively. The values of K_{sv} , K_q , K and n are tabulated in Table 4.

Circular dichroism studies

CD spectroscopy is commonly used to monitor the conformation and stability of proteins in solution. CD investigates the secondary structure of proteins because the peptide bond is asymmetric. Molecules lacking a plane of symmetry exhibit CD effects. CD offers highly accurate estimate of the percentage of α -helices, β -sheets, and disorderly formed (random coil) residues in a protein structure. We have performed CD spectral investigations of HSA ($2.08 \mu M$) in the presence of different concentrations of compound **5g** to understand the conformational changes brought about by compound **5g** (1.98 – $5.94 \mu M$). The α -helical structure of HSA was indicated by two peaks in the CD spectrum at 208 nm and 222 nm. CD spectra of HSA in the presence of compound **5g** showed a modest drop at both wavelengths without a shift in the peak position, suggesting

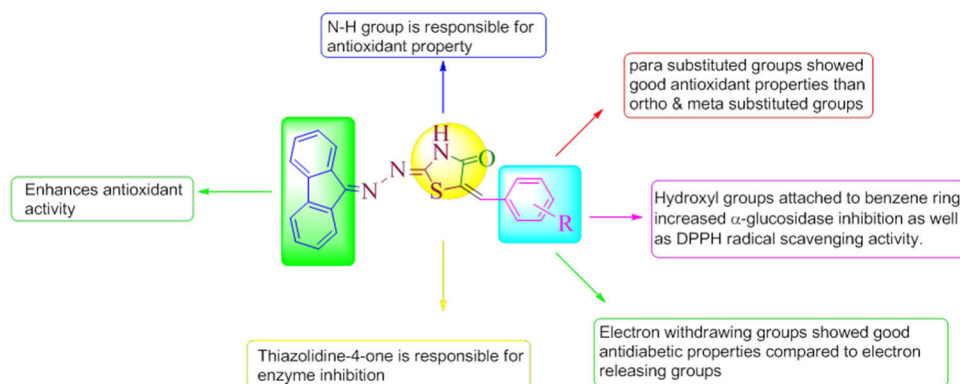


Fig. 8 Plausible structure–activity relationship trends of the synthesized compounds.

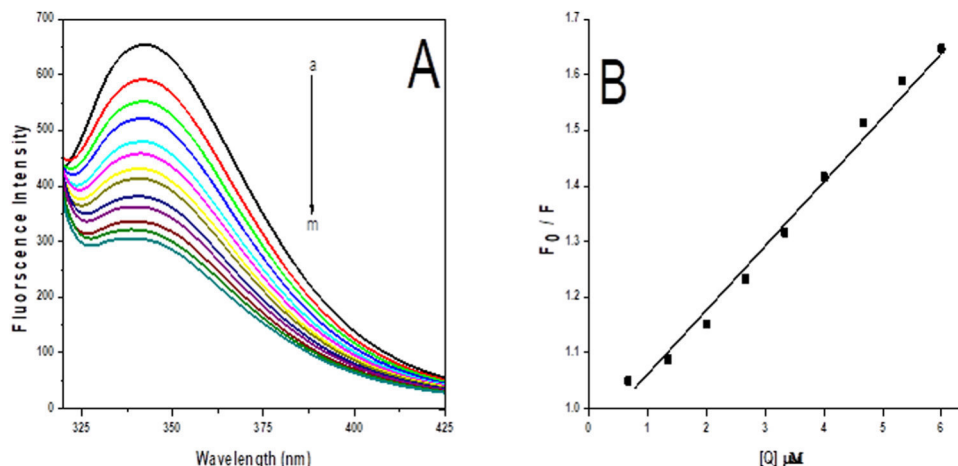


Fig. 9 (A) Fluorescence spectra of HSA (a: 4.16 μM) in the absence and presence of compound **5g** (b–m: 0.66 to 8.58 μM) at 298 K and (B) Stern–Volmer plot for HSA in the presence of compound **5g**.

Table 4 Stern–Volmer quenching constant (K_{SV}), quenching rate constant (K_q), binding constant (K), and the number of binding site (n) values for the interactions of **5g**–HSA and **5g**–ctDNA

System	$K_{SV}, 10^4$ (L mol^{-1})	$K_q, 10^{13}$ ($\text{L mol}^{-1} \text{s}^{-1}$)	$K, 10^4$ (L mol^{-1})	n
5g –HSA	4.96	4.96	1.01	0.861
5g –ctDNA	9.44	9.44	6.42	0.972

the interaction between **5g** and HSA. The unfolding of the peptide strand was controlled by the negative ellipticity point in the α -helical content. Using information from the CD spectra of HSA in the presence of compound **5g**, it was possible to determine the proportion of α -helical content of HSA. In the present study, the α -helicity of HSA decreased from 59.6% to 49.8% in the presence of **5g** (0 to 5.94 μM) in phosphate buffer of pH 7.4. Furthermore, the shape of the CD curves remained nearly unchanged, indicating that the structure of HSA was

predominantly α -helical even after binding to compound **5g**. Fig. 11 depicts the CD spectra of HSA in the presence and absence of different amounts of compound **5g**. The contents of the secondary structure of HSA in the presence and absence of **5g** are shown in Table 5.

Docking study of potent inhibitors

The crystal structure of human lysosomal acid-alpha-glucosidase, GAA, in complex with 1-deoxynojirimycin (PDB ID: 5NN5) was obtained from the PDB (<https://www.rcsb.org/pdb>). The proteins were prepared for docking by adding polar hydrogen atoms with Gasteiger–Huckel charges and water molecules were removed. The 3D structure of the ligand was generated using the SKETCH module implemented in the SYBYL program (Tripos Inc., St. Louis, USA) and its energy-minimized conformation was obtained with the help of the Tripos force field using Gasteiger–Huckel charges.³⁶ Molecular docking was performed using the Surflex-Dock program that is

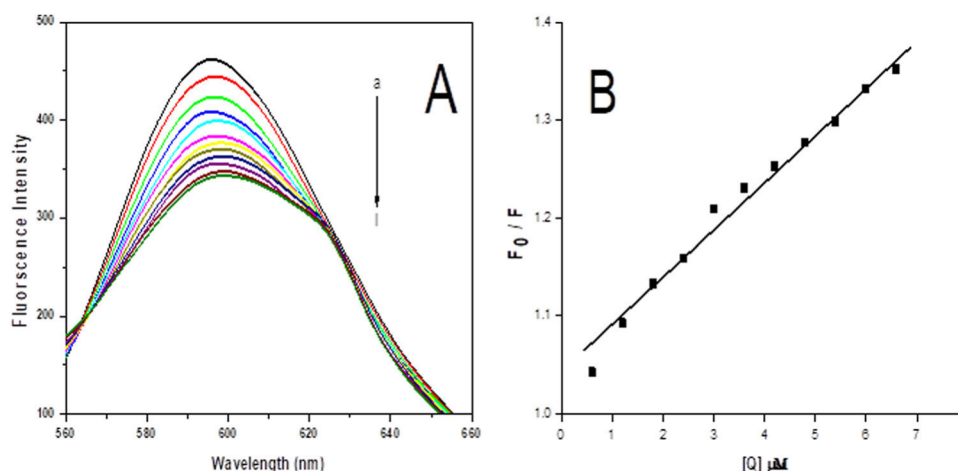


Fig. 10 (A) Fluorescence spectra of ctDNA (a: 1.38 μM), ethidium bromide (0.83 μM) in the absence and presence of compound **5g** (b–l: 0.6 to 6.0 μM) at 298 K and (B) Stern–Volmer plot for ctDNA in the presence of compound **5g**.

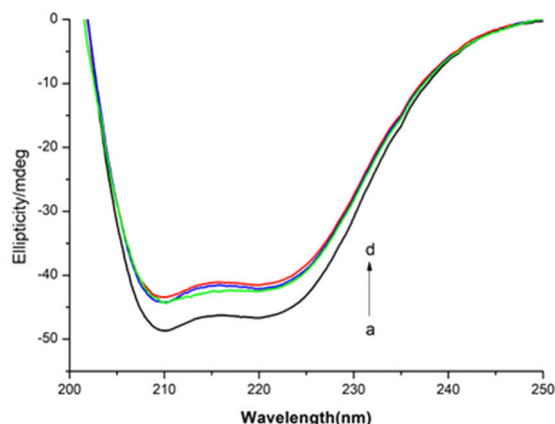


Fig. 11 CD spectra of HSA in the presence of compound **5g**. The concentration of HSA was kept constant (a: 2.08 μ M) and that of compound **5g** was varied (b–d: 1.98–5.94 μ M).

Table 5 Contents of α -helices and β -sheets of HSA in the presence of compound **5g**

Concentration of HSA (μ M)	Concentration of 5g (μ M)	α -Helix (%)	β -Sheet (%)	Turn (%)	Others (%)
2.08	0.0	59.6	22.8	2.3	15.4
	1.98	54.3	21.3	4.3	20.1
	3.96	53.1	16.0	5.5	25.4
	5.94	49.8	17.9	4.3	28.0

interfaced with Sybyl-X 2.0³⁷ and other miscellaneous parameters were assigned with the default values given by the software.

A molecular docking study was carried out to support the interaction and preferred binding mode of the compound with protein. All the inhibitors were docked into the active site of protein as shown in Fig. 12A and B. The predicted binding energies of the compounds are listed in Table 6.

As depicted in Fig. 13A–C, compound **5g** makes six hydrogen bonding interactions at the active site of the enzyme (PDB ID: 5NN5), the hydrogen atom of NH present at the 3rd position of the thiazolidine ring makes hydrogen bonding interaction with the oxygen of ASP282 (NH–O–ASP282, 1.952 Å), the oxygen atom of the carbonyl group present at the 4th position of the thiazolidine ring makes two hydrogen bonding interactions with the hydrogen atoms of ARG600 (O–H–ARG600, 2.50 Å; 2.63 Å),

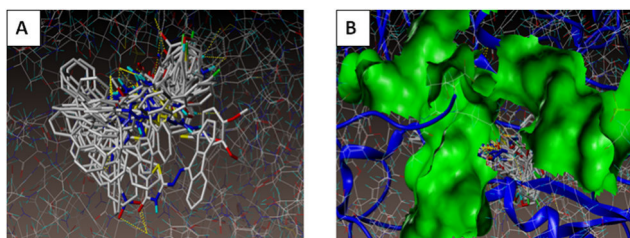


Fig. 12 Docked view of all the compounds at the active site of human lysosomal acid- α -glucosidase protein, PDB ID: 5NN5, at different poses A and B.

the hydrogen atom of the hydroxyl group present at the 4th position of the benzylidene ring which is present on the 5th position of the thiazolidine ring makes hydrogen bonding interactions with the oxygen atoms of ASP404 (OH–O–ASP404, 2.57 Å; 1.98 Å) and the nitrogen atom of the hydrazinylidene group present at the 9th position of the fluorenylidene ring makes hydrogen bonding interaction with the hydrogen of ED01033 (N–H–ED01033, 2.75 Å).

As depicted in Fig. 14A–C, compound **5t** makes two hydrogen bonding interactions at the active site of the enzyme (PDB ID: 5NN5), the hydrogen atom of the hydroxyl group present at the 3rd position of the benzylidene ring which is present on the 5th position of the thiazolidine ring makes hydrogen bonding interaction with the oxygen atom of ASP518 (OH–O–ASP518, 1.78 Å) and the oxygen atom of the hydroxyl group present at the 3rd position of the benzylidene ring which is present on the 5th position of the thiazolidine ring makes hydrogen bonding interaction with the hydrogen atom of ASP518 (HO–H–TRP481, 1.90 Å).

The interaction of the ligand with α -glucosidase protein active sites shows six bonding interactions and the docked view of the same has been depicted in Fig. 15A–C.

The docking results revealed that the synthesized compounds were well accommodated in the binding pockets of α -glucosidase. The synthesized compounds were bound to the protein in a similar manner to that of ligand_5NN5. The compounds have the same H-bonding interactions with the same amino acids ASP404, ASP518 and TRP481 as that of ligand_5NN5. Fig. 16A and B present the hydrophobic and hydrophilic amino acids surrounding the studied molecules, **5g** and **5t**.

Pharmacokinetic properties

The SwissADME web tool is a free software program used to forecast the absorption, distribution, metabolism and elimination of molecules. All these are important factors in deciding whether or not to conduct additional clinical trials. It considers six crucial physicochemical characteristics such as size, polarity, lipophilicity, flexibility and saturation.³⁸ By using SwissADME, we have calculated the physicochemical characteristics of the synthesised compounds, **5a–5u**. The predicted physicochemical characteristics included molecular weight (M_w), the number of rotatable bonds, the number of hydrogen bond acceptors and donors, and XLogP3. Notably, the ligands' "drug-likeness" was evaluated using a number of pertinent test filters related to medicinal chemistry.³⁹ Lipinski and his colleagues predicted that when there are more than five hydrogen bond donors and ten hydrogen bond acceptors, a molecular weight greater than 500 and a calculated $\log P$ ($C\log P > 5$), poor absorption or permeation is more likely.⁴⁰ The predicted physicochemical results (Table 7) indicated that most of the compounds followed Lipinski's rule of five.

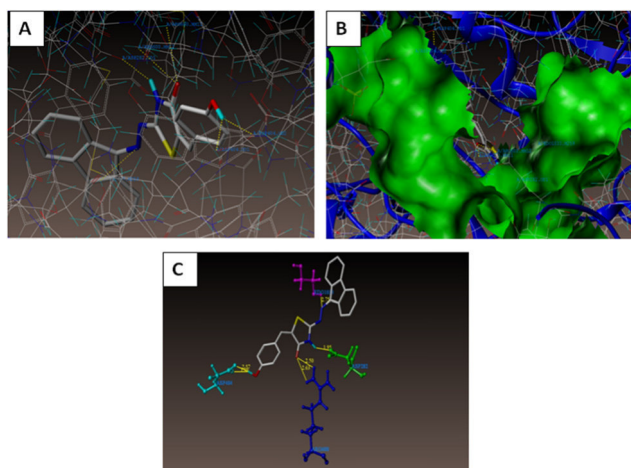
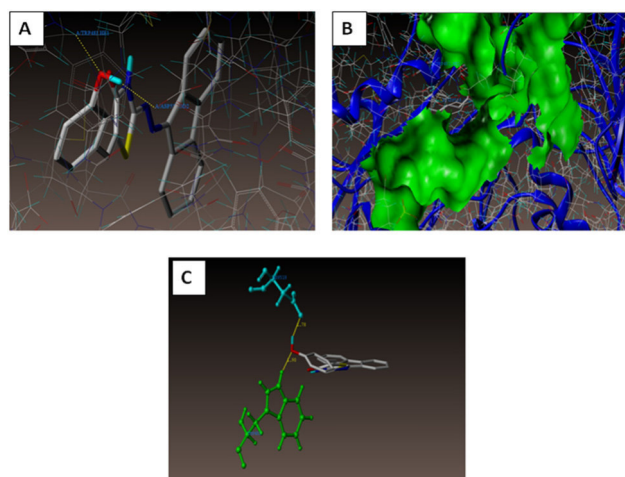
Toxicity prediction

In silico approaches provide major advantages to both regulatory demands and requirements for risk assessments as well as

Table 6 Surflex docking score (kcal mol⁻¹) of the compounds for α -glucosidase protein (PDB ID: 5NN5)

Compound	C score ^a	Crash score ^b	Polar score ^c	D score ^d	PMF score ^e	G score ^f	Chem score ^g
Ligand_5NN5	5.82	-1.91	4.24	-111.500	-112.064	-153.924	-20.140
5a	3.19	-2.96	1.73	-135.478	-118.632	-286.226	-41.223
5b	2.31	-0.94	0.87	-96.313	-55.096	-169.049	-29.207
5c	2.26	-1.92	0.61	-144.775	-90.396	-239.346	-36.292
5d	1.06	-1.24	0.00	-77.822	-72.677	-116.265	-21.624
5e	3.39	-1.35	0.01	-109.009	-80.376	-188.862	-29.759
5f	2.46	-0.86	1.79	-85.523	-65.505	-126.243	-26.782
5g	3.15	-0.78	2.86	-100.655	-96.382	-172.575	-29.637
5h	1.84	-0.92	1.60	-100.419	-77.043	-179.768	-25.177
5i	3.04	-1.86	0.80	-120.485	-88.429	-183.372	-30.681
5j	3.17	-1.11	1.04	-88.747	-67.650	-158.158	-30.249
5k	1.08	-4.38	0.09	-149.331	-126.118	-263.842	-39.995
5l	2.20	-0.93	0.00	-104.750	-74.080	-183.166	-26.034
5m	3.46	-1.20	0.00	-113.708	-88.372	-205.195	-30.621
5n	3.33	-0.89	2.03	-114.319	-108.047	-226.227	-30.124
5o	1.91	-0.89	0.88	-90.575	-87.186	-150.783	-30.107
5p	2.33	-3.94	0.61	-154.066	-119.330	-253.899	-39.634
5q	3.97	-0.61	2.50	-100.468	-84.825	-197.872	-35.131
5r	1.15	-0.84	0.00	-95.252	-52.035	-149.468	-21.884
5s	4.20	-0.75	1.26	-143.785	-98.086	-207.118	-31.242
5t	2.96	-1.85	1.18	-129.091	-83.154	-214.806	-36.970
5u	2.13	-0.85	0.00	-151.098	-95.521	-202.660	-31.194

^a C score (consensus score) integrates a number of popular scoring functions for ranking the affinity of ligands bound to the active site of a receptor and reports the output of the total score. ^b Crash-score revealing the inappropriate penetration into the binding site. Crash scores close to 0 are favorable. Negative numbers indicate penetration. ^c Polar indicating the contribution of the polar interactions to the total score. The polar score may be useful for excluding docking results that make no hydrogen bonds. ^d D-score for charge and van der Waals interactions between the protein and the ligand. ^e PMF-score indicating the Helmholtz free energies of interactions for protein-ligand atom pairs (Potential of Mean Force, PMF). ^f G-score showing hydrogen bonding, complex (ligand-protein), and internal (ligand-ligand) energies. ^g Chem-score points for H-bonding, lipophilic contact, and rotational entropy, along with an intercept term.

**Fig. 13** Docked view of compound **5g** at the active site of the enzyme PDB: 5NN5 in different poses (A–C).**Fig. 14** Docked view of compound **5t** at the active site of the enzyme PDB: 5NN5 in different poses (A–C).

the pharmaceutical sector to analyse the safety profile of a compound. This has been made feasible by advancements in the field of computational research.⁴¹ To forecast the toxicity parameters, we have used the ProTox-II web servers. ProTox-II analysis divides compounds into several toxicity classes. All the synthesized compounds (**5a–5u**) were screened for cytotoxicity. The results showed that none of the compounds exhibited cytotoxicity. All the synthesized compounds belonged to class IV with $300 < LD_{50} \leq 2000$. The LD_{50} values are given in mg kg⁻¹.

Most of the synthesized compounds have an LD_{50} value of 1400 mg kg⁻¹ with about 54.26% prediction accuracy. As a result, we conclude from the data that these compounds could be employed as safe lead molecules (Table 8).

Conclusions

A series of novel fluorenone-thiazolidine-4-one derivatives **5a–5u** were designed and synthesized. The structures of the

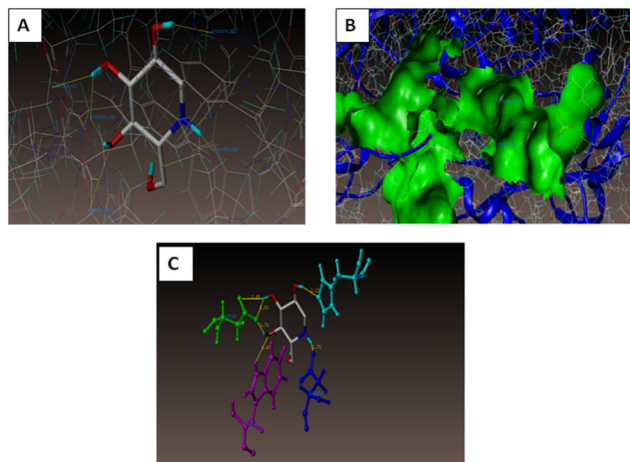


Fig. 15 Docked view of ligand_5NN5 at the active site of the enzyme PDB: 5NN5 in different poses (A–C).

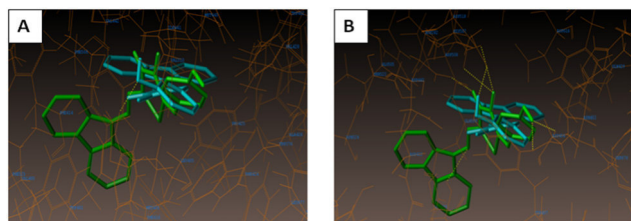


Fig. 16 (A) Hydrophobic amino acids surrounding compound **5g** (green colour) and **5t** (cyan colour). (B) Hydrophilic amino acids surrounding compounds **5g** and **5t**.

synthesized molecules were elucidated using FTIR, ^1H NMR, ^{13}C NMR and mass spectral data. Single crystals of compound

5s were developed and their structure refinement data were obtained. Compound **5s** crystallized in the triclinic space group of $P\bar{1}$. Furthermore, the ability of the synthesised compounds to scavenge DPPH radicals and inhibit α -glucosidase was evaluated. The results revealed that the compounds with hydroxyl functional groups at the *para* and *meta* positions of thiazolidine-4-one demonstrated greater α -glucosidase inhibition. Furthermore, compounds containing halogen groups like fluoro, chloro, and bromo groups exhibited a moderate α -glucosidase inhibitory effect. The findings showed that α -glucosidase inhibition increased with an increase in the number of halogen groups. With an increase in the number of substituted methoxy functional groups, inhibition was decreased. The DPPH scavenging activity of compounds **5a–l** was promising. The IC_{50} value of compound **5l** was calculated to be $27.70\ \mu\text{M}$. In general, the DPPH scavenging activity results suggested that the derivatives having substitution at the *ortho* and *para* positions exhibited significant antioxidant properties compared to the *meta* substituted derivatives. In particular, the electron withdrawing groups such as nitro, cyano and halogen groups at the *ortho* and *para* positions showed good antioxidant properties, whereas the electron releasing groups such as methyl, hydroxyl and methoxy groups at the *ortho* and *para* positions exhibited good activity but at the *meta* position they showed less antioxidant activity. A fluorescence spectroscopic technique was adopted to study the interaction of HSA and ctDNA with compound **5g** that displayed more potent α -glucosidase inhibition. Fluorescence quenching data revealed that the binding constant (K) of compound **5g**-HSA was $1.01 \times 10^4\ \text{L mol}^{-1}$ and that of **5g**-ctDNA was $6.42 \times 10^4\ \text{L mol}^{-1}$, indicating moderate binding affinity. According to ADME predictions, most of the compounds followed Lipinski's rule of five to develop into "drug-like" molecules. The present study

Table 7 SwissADME predicted pharmacokinetic profile for fluorenone–thiazolidine-4-one hybrids

Comp.	M_F	M_W	NRB	NHBA	NHBD	$\log P$	GIA	BAS	SA	LV
5a	$\text{C}_{24}\text{H}_{17}\text{N}_3\text{O}_2\text{S}$	411.48	3	4	1	3.73	High	0.55	3.77	0
5b	$\text{C}_{23}\text{H}_{14}\text{BrN}_3\text{OS}$	460.35	2	3	1	3.87	High	0.55	3.74	0
5c	$\text{C}_{23}\text{H}_{13}\text{Cl}_2\text{N}_3\text{OS}$	450.34	2	3	1	3.89	High	0.55	3.79	1
5d	$\text{C}_{23}\text{H}_{14}\text{N}_4\text{O}_3\text{S}$	426.45	3	5	1	2.77	High	0.55	3.74	0
5e	$\text{C}_{23}\text{H}_{14}\text{FN}_3\text{OS}$	399.44	2	4	1	3.58	High	0.55	3.72	0
5f	$\text{C}_{23}\text{H}_{14}\text{ClN}_3\text{OS}$	415.89	2	3	1	3.77	High	0.55	3.71	0
5g	$\text{C}_{23}\text{H}_{15}\text{N}_3\text{O}_2\text{S}$	397.45	2	4	2	3.12	High	0.55	3.72	0
5h	$\text{C}_{23}\text{H}_{14}\text{BrN}_3\text{O}_2\text{S}$	476.35	2	4	2	3.5	High	0.55	3.8	0
5i	$\text{C}_{23}\text{H}_{13}\text{ClFN}_3\text{OS}$	433.89	2	4	1	3.73	High	0.55	3.81	1
5j	$\text{C}_{24}\text{H}_{17}\text{N}_3\text{OS}$	395.48	2	3	1	3.65	High	0.55	3.86	0
5k	$\text{C}_{24}\text{H}_{14}\text{N}_4\text{OS}$	406.46	2	4	1	3.45	High	0.55	3.82	0
5l	$\text{C}_{31}\text{H}_{22}\text{N}_4\text{OS}_2$	530.66	3	3	1	4.46	Low	0.17	4.39	2
5m	$\text{C}_{23}\text{H}_{15}\text{N}_3\text{OS}$	381.45	2	3	1	3.14	High	0.55	3.74	0
5n	$\text{C}_{24}\text{H}_{17}\text{N}_3\text{O}_2\text{S}$	411.48	3	4	1	3.75	High	0.55	3.8	0
5o	$\text{C}_{23}\text{H}_{14}\text{BrN}_3\text{OS}$	460.35	2	3	1	3.83	High	0.55	3.75	0
5p	$\text{C}_{23}\text{H}_{14}\text{N}_4\text{O}_3\text{S}$	426.45	3	5	1	3.00	High	0.55	3.8	0
5q	$\text{C}_{25}\text{H}_{17}\text{N}_3\text{OS}$	407.49	3	3	1	3.64	High	0.55	3.98	1
5r	$\text{C}_{25}\text{H}_{19}\text{N}_3\text{O}_3\text{S}$	441.5	4	5	1	3.96	High	0.55	3.94	0
5s	$\text{C}_{25}\text{H}_{16}\text{N}_4\text{OS}$	420.49	2	3	2	2.98	High	0.55	3.77	0
5t	$\text{C}_{23}\text{H}_{15}\text{N}_3\text{O}_2\text{S}$	397.45	2	4	2	3.08	High	0.55	3.74	0
5u	$\text{C}_{21}\text{H}_{13}\text{N}_3\text{OS}_2$	387.48	2	3	1	3.33	High	0.55	3.72	0

MF – molecular formula; M_W – molecular weight; NRB – number of rotatable bonds; NHBA – number of H-bond acceptors; NHBD – number of H-bond donors; $\log P$ – partition coefficient between *n*-octanol and water; GIA – gastrointestinal absorption; BAS – bioavailability score; SA – synthetic accessibility; LV – Lipinski's violation.

Table 8 Toxicity prediction results of compounds 5a–5u

Compound	Predicted LD ₅₀ (mg kg ⁻¹)	Predicted toxicity class	Predicted cytotoxicity	Probability	Average similarity (%)	Prediction accuracy (%)
5a	1000	IV	Inactive	0.76	43.08	54.26
5b	1400	IV	Inactive	0.74	43.48	54.26
5c	1400	IV	Inactive	0.81	42.76	54.26
5d	1400	IV	Inactive	0.85	42.04	54.26
5e	1400	IV	Inactive	0.80	43.44	54.26
5f	1400	IV	Inactive	0.81	44.43	54.26
5g	1400	IV	Inactive	0.74	43.98	54.26
5h	1400	IV	Inactive	0.65	41.61	54.26
5i	1400	IV	Inactive	0.81	40.50	54.26
5j	1400	IV	Inactive	0.83	45.06	54.26
5k	1400	IV	Inactive	0.82	43.82	54.26
5l	1150	IV	Inactive	0.78	39.67	23
5m	1400	IV	Inactive	0.82	43.82	54.26
5n	1000	IV	Inactive	0.76	42.92	54.26
5o	1400	IV	Inactive	0.76	43.06	54.26
5p	1400	IV	Inactive	0.85	41.79	54.26
5q	350	IV	Inactive	0.82	41.39	54.26
5r	1000	IV	Inactive	0.69	42.97	54.26
5s	1400	IV	Inactive	0.79	42.15	54.26
5t	1400	IV	Inactive	0.74	44.04	54.26
5u	1400	IV	Inactive	0.82	39.88	23

indicated that compound **5g** demonstrates promising α -glucosidase inhibition and so, it could be employed as a lead molecule in the creation of novel anti-diabetic medications. Furthermore, the majority of compounds demonstrated promising DPPH scavenging activity and could be used as antioxidants.

Experimental section

Materials and methods

All starting materials and reagents were of analytical grade purchased from Spectrochem, sd-fine, TCI, Sigma Aldrich and HiMedia (India) and used without further purification. Melting points were obtained in open capillary tubes using a system obtained from Concord Instruments (P) Ltd, Bangalore, and are presented as uncorrected values. ¹H and ¹³C NMR spectra were recorded in DMSO-d₆ on a FT-NMR Spectrometer (400 MHz) JEOL JNM-EC400S. Chemical shifts (δ) are reported in ppm relative to TMS, whereas coupling constants (*J*) are given in Hz. IR spectra were obtained on a Nicolet 5700 FT-IR spectrophotometer using KBr optics. Mass spectra were recorded on a Waters Xevo G2-XS QT (LC-MS/ESI-MS) system. A Bruker SMART APEX II diffractometer was used to generate high-resolution X-ray diffraction data. The antidiabetic and antioxidant assessment was carried out at the Alekya Agro Solutions, Mysore, Karnataka, India.

Single crystal measurements

Crystal data were collected on Bruker APEX-II CCD crystallographic equipment. The structural analysis was performed on a computer with the *SHELXT* 2018/2,⁴² *SHELXL* 2018/3⁴³ and Olex2 1.5⁴⁴ program packages. Monochromated (doubly curved silicon crystal) Mo-K α radiation (0.7107 Å) from a sealed micro-focus tube was used to evaluate the intensity. The generator was tuned to 50 kV and 1 mA. Six sets of Omega scans at various Phi values were used to obtain data. The breadth of the frame was

0.5°. For preliminary unit cell determination, APEX2 software was employed. SAINT was used for the determination of integrated intensities and unit cell refinement. SADABS was used to adjust the data for absorption effects using the multi-scan approach.⁴⁵ The structure was resolved using ShelxT in the Olex2.0⁴⁴ package and polished using full-matrix least squares based on F² in ShelxL.⁴⁶ CCDC 2221637† contains the supplementary crystallographic data for the said compound.

Steady state fluorescence quenching spectral measurements

Fluorescence spectra were recorded on an Agilent Technologies Carry Eclipse fluorescence spectrophotometer equipped with a xenon flash lamp and a Cary single cell Peltier to maintain a constant temperature. The excitation and emission slit widths were set at 5 nm.

Circular dichroism measurements

A JASCO J-1500 CD spectrometer was used to record the CD spectra of HSA in the presence and absence of compound **5g** in the range of 200–250 nm at 25 °C using 0.1 cm path length cuvettes. The content of α -helices and β -sheets of HSA in the presence and absence of compound **5g** was calculated using the inbuilt software CD Multivariate SSE.

General procedure for the synthesis of 2-(2-(9H-fluoren-9-ylidene)hydrazinyl)thiazol-4(5H)-one (compound 3). A mixture of compound **2** (0.255 g, 1 mmol), chloroacetic acid (0.094 g, 1 mmol) and sodium acetate (0.082 g, 1 mmol) was dissolved in ethanol (10 mL). The reaction mixture was refluxed for 8 h to precipitate out compound **3**. The yellow solid was filtered, washed and recrystallized with ethanol. Yellow solid; mp: 222–224 °C. FT-IR (KBr, cm⁻¹) 3436 (N-H), 3062 (Ar C-H), 1721 (C=O), 1630, 1601 (C=N), 1558 (C=C), 806 (C-S). ¹H-NMR (400 MHz, DMSO-d₆) δ (ppm) 12.28 (s, 1H), 8.57 (d, *J* = 7.6 Hz, 1H), 7.81–7.70 (m, 3H), 7.46–7.29 (m, 4H), 3.95 (s, 2H). ¹³C-NMR (101 MHz, DMSO-d₆) δ (ppm) 174.6 (C=O), 168.9 (C=N in the fluorenone ring), 156.5 (C=N in the thiazolidine-4-one

ring), 141.8, 140.7, 136.6, 131.8, 131.6, 131.3, 130.3, 128.7, 122.4, 120.9, 33.7 (–CH₂–). LC-MS (*m/z*): [M + 1] 294.1168.

General procedure for the synthesis of 2-(2-(9H-fluoren-9-ylidene)hydrazinyl)thiazol-4(5H)-one derivatives (5a–5u). A mixture of compound (3) (0.5 g, 1.7 mmol), aromatic aldehydes (4a–4u) (1.7 mmol), and a catalytic amount of piperidine was added to ethanol. The resultant mixture was refluxed for 12 h and allowed to cool. The precipitate obtained was collected, dried, and recrystallized from ethanol.

(2Z,5Z)-2-((9H-Fluoren-9-ylidene)hydrazono)-5-(4-methoxybenzylidene)thiazolidin-4-one (5a). Yellow solid; yield: 0.49 g, 70%; mp: 218–220 °C. FT-IR (KBr, cm^{–1}) 3412 (N–H), 3062 (Ar C–H), 1719 (C=O), 1639, 1606 (C=N), 1567 (C=C), 805 (C–S), 1259 (C–OCH₃). ¹H-NMR (400 MHz, DMSO-d₆) δ (ppm) 12.91 (s, 1H), 8.59 (d, *J* = 7.6 Hz, 1H), 7.83 (dd, *J* = 12.2, 7.6 Hz, 3H), 7.64 (s, 1H), 7.51–7.45 (m, 3H), 7.35 (t, *J* = 7.2 Hz, 2H), 7.25 (t, *J* = 9.5 Hz, 2H), 7.04 (dd, *J* = 8.0, 1.9 Hz, 1H), 3.80 (s, 3H). ¹³C-NMR (101 MHz, DMSO-d₆) δ (ppm) 167.8 (C=O), 163.0 (C=N in the fluorenone ring), 160.2 (C–O), 157.7 (C=N in the thiazolidine-4-one ring), 142.1 (=CH–), 141.0, 136.3, 135.4, 132.3, 131.8, 131.5, 131.0, 130.5, 130.4, 128.9, 123.7, 122.8, 122.2, 121.1, 116.3, 55.8 (–OCH₃). LC-MS (*m/z*): [M + 1] 412.1575.

(2Z,5Z)-2-((9H-Fluoren-9-ylidene)hydrazono)-5-(4-bromobenzylidene)thiazolidin-4-one (5b). Yellow solid; yield: 0.61 g, 78%; mp: 220–222 °C. FT-IR (KBr, cm^{–1}) 3448 (N–H), 3062 (Ar C–H), 1697 (C=O), 1630, 1584 (C=N), 1555 (C=C), 801 (C–S), 1485 (C–Br). ¹H-NMR (400 MHz, DMSO-d₆) δ (ppm) 12.94 (s, 1H), 8.57 (t, *J* = 8.0 Hz, 1H), 7.82 (t, *J* = 8.0 Hz, 3H), 7.72 (t, *J* = 8.8 Hz, 2H), 7.62 (d, *J* = 5.3 Hz, 3H), 7.50–7.42 (m, 2H), 7.34 (q, *J* = 7.4 Hz, 2H). ¹³C-NMR (101 MHz, DMSO-d₆) δ (ppm) 167.0 (C=O), 163.0 (C=N in the fluorenone ring), 157.7 (C=N in the thiazolidine-4-one ring), 142.1 (=CH–), 141.0, 136.3, 133.3, 132.8, 132.3, 131.8, 131.5, 130.3, 129.1, 128.8, 124.3, 123.9, 122.8, 121.1. LC-MS (*m/z*): [M + 1] 462.0114.

(2Z,5Z)-2-((9H-Fluoren-9-ylidene)hydrazono)-5-(2,3-dichlorobenzylidene)thiazolidin-4-one (5c). Yellow solid; yield: 0.52 g, 68%; mp: 222–224 °C. FT-IR (KBr, cm^{–1}) 3414 (N–H), 3063 (Ar C–H), 1706 (C=O), 1633, 1602 (C=N), 1556 (C=C), 805 (C–S), 731 (C–Cl). ¹H-NMR (400 MHz, DMSO-d₆) δ (ppm) 13.10 (s, 1H), 8.56 (d, *J* = 7.6 Hz, 1H), 7.85–7.72 (m, 6H), 7.58 (t, *J* = 8.0 Hz, 1H), 7.51–7.44 (m, 2H), 7.34 (q, *J* = 7.6 Hz, 2H). ¹³C-NMR (101 MHz, DMSO-d₆) δ (ppm) 167.0 (C=O), 161.7 (C=N in the fluorenone ring), 158.3 (C=N in the thiazolidine-4-one ring), 142.2 (=CH–), 136.1, 134.8, 132.4, 132.3, 132.2, 131.9, 131.7, 129.4, 128.8, 128.6, 128.2, 125.5, 122.8, 121.0. LC-MS (*m/z*): [M + 1] 452.0662.

(2Z,5Z)-2-((9H-Fluoren-9-ylidene)hydrazono)-5-(4-nitrobenzylidene)thiazolidin-4-one (5d). Yellow solid; yield: 0.48 g 66%; mp: 216–218 °C. FT-IR (KBr, cm^{–1}) 3416 (N–H), 3062 (Ar C–H), 1691 (C=O), 1631, 1603 (C=N), 1557 (C=C), 802 (C–S), 1514, 1340 (N–O). ¹H-NMR (400 MHz, DMSO-d₆) δ (ppm) 8.65 (d, *J* = 7.6 Hz, 1H), 8.31 (d, *J* = 9.2 Hz, 2H), 7.90 (d, *J* = 9.2 Hz, 2H), 7.81 (dd, *J* = 11.8, 7.2 Hz, 4H), 7.51 (s, 1H), 7.42 (q, *J* = 7.9 Hz, 2H), 7.34 (s, 2H). ¹³C-NMR (101 MHz, DMSO-d₆) δ (ppm) 170.1 (C=O), 167.6 (C=N in the fluorenone ring), 154.7 (C=N in the thiazolidine-4-one ring), 153.4, 147.7 (C–NO₂), 146.8 (=CH–),

142.4, 141.2, 140.3, 137.2, 131.7, 131.0, 130.8, 130.5, 129.7, 128.7, 128.6, 128.4, 124.7, 123.4, 122.0, 121.0. LC-MS (*m/z*): [M + 1] 427.0906.

(2Z,5Z)-2-((9H-Fluoren-9-ylidene)hydrazono)-5-(4-fluorobenzylidene)thiazolidin-4-one (5e). Orange solid; yield: 0.46 g, 68%; mp: 220–222 °C. FT-IR (KBr, cm^{–1}) 3417 (N–H), 3062 (Ar C–H), 1692 (C=O), 1633, 1604 (C=N), 1557 (C=C), 804 (C–S), 1351 (C–F). ¹H-NMR (400 MHz, DMSO-d₆) δ (ppm) 8.59 (d, *J* = 7.3 Hz, 1H), 7.80 (dd, *J* = 12.5, 7.6 Hz, 3H), 7.75–7.72 (m, 2H), 7.63 (s, 1H), 7.47 (td, *J* = 15.1, 6.9 Hz, 3H), 7.39–7.32 (m, 3H), 7.01 (d, *J* = 8.6 Hz, 1H). ¹³C-NMR (101 MHz, DMSO-d₆) δ (ppm) 167.8 (C=O), 163.0 (C=N in the fluorenone ring), 162.8 (C=N in the thiazolidine-4-one ring), 154.0 (C–F), 142.1 (=CH–), 141.0, 138.4, 136.3, 133.0, 132.9, 132.3, 131.8, 131.5, 130.7, 130.3, 129.4, 128.8, 122.8, 121.1, 117.1, 116.9. LC-MS (*m/z*): [M + 1] 401.1259.

(2Z,5Z)-2-((9H-Fluoren-9-ylidene)hydrazono)-5-(4-chlorobenzylidene)thiazolidin-4-one (5f). Orange solid; yield: 0.50 g, 70%; mp: 218–220 °C. FT-IR (KBr, cm^{–1}) 3448 (N–H), 3062 (Ar C–H), 1698 (C=O), 1632, 1601 (C=N), 1555 (C=C), 815 (C–S), 732 (C–Cl). ¹H-NMR (400 MHz, DMSO-d₆) δ (ppm) 8.65 (d, *J* = 6.9 Hz, 1H), 7.81 (q, *J* = 6.6 Hz, 3H), 7.68 (d, *J* = 8.4 Hz, 2H), 7.56 (d, *J* = 9.2 Hz, 2H), 7.42 (q, *J* = 7.9 Hz, 3H), 7.33 (t, *J* = 7.2 Hz, 3H). ¹³C-NMR (101 MHz, DMSO-d₆) δ (ppm) 167.7 (C=O), 163.2 (C=N in the fluorenone ring), 162.8 (C=N in the thiazolidine-4-one ring), 141.6 (=CH–), 140.6, 136.8, 134.3, 133.7, 131.9, 131.6, 131.6, 131.1, 130.0, 129.7, 128.7, 128.6, 127.0, 122.4, 120.9. LC-MS (*m/z*): [M + 1] 416.1017.

(2Z,5Z)-2-((9H-Fluoren-9-ylidene)hydrazono)-5-(4-hydroxybenzylidene)thiazolidin-4-one (5g). Yellow solid; yield: 0.54 g, 80%; mp: 220–222 °C. FT-IR (KBr, cm^{–1}) 3416 (N–H), 3062 (Ar C–H), 1697 (C=O), 1635, 1604 (C=N), 1580 (C=C), 822 (C–S), 1 275 (C–OH), 3206 (O–H). ¹H-NMR (400 MHz, DMSO-d₆) δ (ppm) 12.75 (s, 1H), 10.26 (s, 1H), 8.59 (t, *J* = 6.1 Hz, 1H), 7.85–7.78 (m, 3H), 7.57–7.33 (m, 7H), 6.93 (t, *J* = 3.4 Hz, 2H); ¹³C-NMR (101 MHz, DMSO-d₆) δ (ppm) 168.1 (C=O), 163.5 (C=N in the fluorenone ring), 160.1 (C=N in the thiazolidine-4-one ring), 157.2 (C–OH), 142.0 (=CH–), 140.9, 136.4, 132.9, 132.2, 131.6, 131.6, 131.1, 130.3, 128.8, 125.0, 122.8, 121.1, 118.8, 116.8. LC-MS (*m/z*): [M + 1] 398.0984.

(2Z,5Z)-2-((9H-Fluoren-9-ylidene)hydrazono)-5-(4-bromo-2-hydroxybenzylidene)thiazolidin-4-one (5h). Orange solid; yield: 0.42 g, 62%; mp: 216–218 °C. FT-IR (KBr, cm^{–1}) 3416 (N–H), 3062 (Ar C–H), 1698 (C=O), 1632, 1604 (C=N), 1557 (C=C), 815 (C–S), 1431 (C–Br), 1250 (C–OH). ¹H-NMR (400 MHz, DMSO-d₆) δ (ppm) 12.87 (s, 1H), 10.78 (s, 1H), 8.59 (d, *J* = 7.3 Hz, 1H), 7.84–7.76 (m, 4H), 7.56 (d, *J* = 1.8 Hz, 1H), 7.47 (dd, *J* = 19.0, 7.9 Hz, 3H), 7.35 (t, *J* = 7.0 Hz, 2H), 6.92 (d, *J* = 9.2 Hz, 1H). ¹³C-NMR (101 MHz, DMSO-d₆) δ (ppm) 167.7 (C=O), 162.5 (C=N in the fluorenone ring), 160.1 (C–OH), 156.7 (C=N in the thiazolidine-4-one ring), 142.1 (=CH–), 141.0, 136.3, 134.5, 132.3, 131.8, 131.6, 131.0, 130.9, 130.4, 128.9, 124.3, 123.5, 123.4, 122.7, 121.1, 118.7, 111.0 (C–Br). LC-MS (*m/z*): [M + 1] 475.1200.

(2Z,5Z)-2-((9H-Fluoren-9-ylidene)hydrazono)-5-(2-chloro-6-fluorobenzylidene)thiazolidin-4-one (5i). Yellow solid; yield:

0.44 g, 60%; mp: 216–218 °C. FT-IR (KBr, cm^{-1}) 3416 (N–H), 3056 (Ar C–H), 1708 (C=O), 1639, 1606 (C=N), 1563 (C=C), 802 (C–S), 723 (C–Cl), 1345 (C–F). $^1\text{H-NMR}$ (400 MHz, DMSO-d_6) δ (ppm) 13.03 (s, 1H), 8.55 (d, $J = 6.9$ Hz, 1H), 7.80 (q, $J = 7.6$ Hz, 2H), 7.70 (d, $J = 6.9$ Hz, 1H), 7.54 (d, $J = 13.7$ Hz, 2H), 7.49–7.46 (m, 2H), 7.42 (d, $J = 9.9$ Hz, 2H), 7.32 (td, $J = 14.7, 7.4$ Hz, 2H). $^{13}\text{C-NMR}$ (101 MHz, DMSO-d_6) δ (ppm) 166.7 (C=O), 162.2 (C=N in the fluorenone ring), 160.9 (C=N in the thiazolidine-4-one ring), 158.0 (C–F), 142.1 (=CH–), 141.0, 136.2, 134.5, 132.9, 132.4 (C–Cl), 131.8, 131.5, 131.3, 130.4, 128.9, 126.6, 122.8, 121.7, 121.1, 116.0, 115.8. LC-MS (m/z): [M + 1] 436.0917.

(2Z,5Z)-2-((9H-Fluoren-9-ylidene)hydrazono)-5-(4-methylbenzylidene)thiazolidin-4-one (5j). Yellow solid; yield: 0.48 g, 72%; mp: 216–218 °C. FT-IR (KBr, cm^{-1}) 3416 (N–H), 3054 (Ar C–H), 1698 (C=O), 1637, 1599 (C=N), 1551 (C=C), 811 (C–S). $^1\text{H-NMR}$ (400 MHz, DMSO-d_6) δ (ppm) 12.85 (s, 1H), 8.59 (d, $J = 7.6$ Hz, 1H), 7.81 (dd, $J = 12.2, 7.6$ Hz, 3H), 7.62–7.55 (m, 3H), 7.46 (q, $J = 7.9$ Hz, 2H), 7.35 (t, $J = 7.6$ Hz, 4H), 2.33 (s, 3H). $^{13}\text{C-NMR}$ (101 MHz, DMSO-d_6) δ (ppm) 167.9 (C=O), 163.1 (C=N in the fluorenone ring), 157.5 (C=N in the thiazolidine-4-one ring), 142.0 (=CH–), 141.0, 140.7, 136.4 (C–CH₃), 132.2, 131.7, 131.6, 131.3, 130.6, 130.5, 130.4, 128.8, 122.8, 122.1, 121.1, 21.7 (–CH₃). LC-MS (m/z): [M + 1] 396.1203.

4-((Z)-2-((9H-Fluoren-9-ylidene)hydrazono)-4-oxothiazolidin-5-ylidene)methyl benzonitrile (5k). Orange solid; yield: 0.44 g, 64%; mp: 216–218 °C. FT-IR (KBr, cm^{-1}) 3422 (N–H), 3062 (Ar C–H), 1721 (C=O), 1638, 1600 (C=N), 1561 (C=C), 812 (C–S), 2222 (C≡N). $^1\text{H-NMR}$ (400 MHz, DMSO-d_6) δ (ppm) 8.58 (d, $J = 7.6$ Hz, 1H), 7.95 (d, $J = 8.4$ Hz, 2H), 7.83–7.78 (m, 5H), 7.66 (s, 1H), 7.46 (q, $J = 7.6$ Hz, 2H), 7.34 (td, $J = 7.2, 3.8$ Hz, 2H). $^{13}\text{C-NMR}$ (101 MHz, DMSO-d_6) δ (ppm) 168.7 (C=O), 168.0 (C=N in the fluorenone ring), 160.1 (C=N in the thiazolidine-4-one ring), 142.0 (=CH–), 141.0, 138.7, 136.3, 135.2, 133.5, 132.3, 131.8, 131.5, 130.9, 130.4, 129.9, 128.9, 128.8, 127.9, 127.5, 122.8, 121.1, 119.1 (C≡N), 111.9 (C–CN). LC-MS (m/z): [M + 1] 407.1040.

(2Z,5Z)-2-((9H-Fluoren-9-ylidene)hydrazono)-5-((10-ethyl-10H-phenothiazin-3-yl) methylene)thiazolidin-4-one (5l). Orange solid; yield: 0.69 g, 76%; mp: 218–220 °C. FT-IR (KBr, cm^{-1}) 3402 (N–H), 3062 (Ar C–H), 1682 (C=O), 1630, 1596 (C=N), 1571 (C=C), 801 (C–S). $^1\text{H-NMR}$ (400 MHz, DMSO-d_6) δ (ppm) 12.80 (s, 1H), 8.61 (d, $J = 7.3$ Hz, 1H), 7.84–7.79 (m, 3H), 7.52–7.43 (m, 4H), 7.38–7.30 (m, 3H), 7.20–7.10 (m, 3H), 7.02 (d, $J = 7.9$ Hz, 1H), 6.94 (t, $J = 7.3$ Hz, 1H), 3.94 (q, $J = 6.9$ Hz, 2H), 1.30 (t, $J = 6.7$ Hz, 3H). $^{13}\text{C-NMR}$ (101 MHz, DMSO-d_6) δ (ppm) 167.2 (C=O), 155.8 (C=N in the fluorenone ring), 155.6 (C=N in the thiazolidine-4-one ring), 147.5, 145.6 (C–N, PTZ), 143.7 (=CH–), 141.7, 140.6, 136.8, 131.6, 131.1, 130.1, 129.9, 129.0, 128.7, 128.6, 128.4, 128.0, 127.6, 123.5, 122.4, 122.3, 121.0, 116.2, 42.0 (–CH₂–), 13.0 (–CH₃). LC-MS (m/z): [M + 1] 531.1898.

(2Z,5Z)-2-((9H-Fluoren-9-ylidene)hydrazono)-5-benzylidenethiazolidin-4-one (5m). Yellow solid; yield: 0.48 g, 74%; mp: 220–222 °C. FT-IR (KBr, cm^{-1}) 3417 (N–H), 3062 (Ar C–H), 1695 (C=O), 1637, 1605 (C=N), 1560 (C=C), 803 (C–S). $^1\text{H-NMR}$ (400 MHz, DMSO-d_6) δ (ppm) 12.91 (s, 1H), 8.59 (d, $J = 6.9$ Hz, 1H), 7.82 (dd, $J = 11.1, 7.2$ Hz, 3H), 7.67 (d, $J = 6.1$ Hz, 3H),

7.54 (d, $J = 6.9$ Hz, 2H), 7.48 (d, $J = 16.8$ Hz, 3H), 7.36 (d, $J = 6.9$ Hz, 2H). $^{13}\text{C-NMR}$ (101 MHz, DMSO-d_6) δ (ppm) 167.9 (C=O), 165.2 (C=N in the fluorenone ring), 163.1 (C=N in the thiazolidine-4-one ring), 157.6, 142.1 (=CH–), 141.0, 136.4, 134.1, 132.3, 132.2, 131.8, 131.5, 130.6, 130.4, 129.9, 128.8, 123.3, 122.8, 122.0, 121.1. LC-MS (m/z): [M + 1] 382.1517.

(2Z,5Z)-2-((9H-Fluoren-9-ylidene)hydrazono)-5-(3-methoxybenzylidene)thiazolidin-4-one (5n). Yellow solid; yield: 0.56 g, 80%; mp: 218–220 °C. FT-IR (KBr, cm^{-1}) 3413 (N–H), 3062 (Ar C–H), 1719 (C=O), 1638, 1606 (C=N), 1567 (C=C), 806 (C–S), 1260 (C–OCH₃). $^1\text{H-NMR}$ (400 MHz, DMSO-d_6) δ (ppm) 12.89 (s, 1H), 8.58 (d, $J = 6.9$ Hz, 1H), 7.79 (q, $J = 6.4$ Hz, 3H), 7.62 (s, 1H), 7.45 (d, $J = 5.3$ Hz, 3H), 7.33 (t, $J = 6.9$ Hz, 2H), 7.26–7.21 (m, 2H), 6.96–7.08 (1H), 3.79 (s, 3H). $^{13}\text{C-NMR}$ (101 MHz, DMSO-d_6) δ (ppm) 167.8 (C=O), 163.0 (C=N in the fluorenone ring), 160.1 (C–OCH₃), 157.7 (C=N in the thiazolidine-4-one ring), 142.1 (=CH–), 141.0, 136.4, 135.4, 132.2, 131.7, 131.6, 130.9, 130.4, 128.8, 123.7, 122.8, 122.2, 121.1, 116.3, 116.1, 55.8 (–OCH₃). LC-MS (m/z): [M + 1] 412.1118.

(2Z,5Z)-2-((9H-Fluoren-9-ylidene)hydrazono)-5-(3-bromobenzylidene)thiazolidin-4-one (5o). Yellow solid; yield: 0.58 g, 74%; mp: 216–218 °C. FT-IR (KBr, cm^{-1}) 3416 (N–H), 3062 (Ar C–H), 1691 (C=O), 1631, 1603 (C=N), 1557 (C=C), 802 (C–S), 1043 (C–Br). $^1\text{H-NMR}$ (400 MHz, DMSO-d_6) δ (ppm) 12.95 (s, 1H), 8.58–8.52 (m, 1H), 7.86–7.78 (m, 4H), 7.69–7.63 (m, 3H), 7.48 (dt, $J = 17.9, 8.3$ Hz, 3H), 7.34 (t, $J = 7.6$ Hz, 2H). $^{13}\text{C-NMR}$ (101 MHz, DMSO-d_6) δ (ppm) 167.7 (C=O), 163.1 (C=N in the fluorenone ring), 157.7 (C=N in the thiazolidine-4-one ring), 142.2 (=CH–), 141.3, 136.2, 133.5, 132.9, 132.4, 131.7, 131.6, 130.4, 129.3, 128.9, 124.4, 123.8, 122.7 (C–Br), 121.2. LC-MS (m/z): [M + 1] 462.1121.

(2Z,5Z)-2-((9H-Fluoren-9-ylidene)hydrazono)-5-(3-nitrobenzylidene)thiazolidin-4-one (5p). Yellow solid; yield: 0.61 g, 84%; mp: 216–218 °C. FT-IR (KBr, cm^{-1}) 3452 (N–H), 3062 (Ar C–H), 1695 (C=O), 1637, 1604 (C=N), 1562 (C=C), 802 (C–S), 1529, 1351 (N–O). $^1\text{H-NMR}$ (400 MHz, DMSO-d_6) δ (ppm) 8.66 (d, $J = 7.6$ Hz, 1H), 8.48 (s, 1H), 8.12 (dd, $J = 30.5, 7.6$ Hz, 2H), 7.82–7.74 (m, 4H), 7.51 (s, 1H), 7.43–7.31 (m, 5H). $^{13}\text{C-NMR}$ (101 MHz, DMSO-d_6) δ (ppm) 174.1 (C=O), 153.0 (C=N in the fluorenone ring), 152.9 (C=N in the thiazolidine-4-one ring), 148.8 (C–NO₂), 141.1 (=CH–), 140.1, 137.6, 135.7, 133.1, 131.7, 131.0, 130.2, 129.6, 128.4, 124.0, 123.2, 121.8, 120.8. LC-MS (m/z): [M + 1] 427.1414.

(2Z,5Z)-2-((9H-Fluoren-9-ylidene)hydrazono)-5-((E)-3-phenylallylidene)thiazolidin-4-one (5q). Yellow solid; yield: 0.51 g, 74%; mp: 220–222 °C. FT-IR (KBr, cm^{-1}) 3416 (N–H), 3062 (Ar C–H), 1691 (C=O), 1631, 1603 (C=N), 1557 (C=C), 802 (C–S), 2854 (C–H). $^1\text{H-NMR}$ (400 MHz, DMSO-d_6) δ (ppm) 12.70 (s, 1H), 8.58 (d, $J = 7.9$ Hz, 1H), 7.85–7.78 (m, 3H), 7.67 (d, $J = 6.7$ Hz, 1H), 7.48–7.35 (m, 9H), 7.24–7.06 (m, 2H). $^{13}\text{C-NMR}$ (101 MHz, DMSO-d_6) δ (ppm) 168.2 (C=O), 160.1 (C=N in the fluorenone ring), 158.4 (C=N in the thiazolidine-4-one ring), 144.8, 143.2 (=CH–), 141.0, 138.7, 136.3, 135.2, 133.4, 132.2, 131.8, 131.6, 130.8, 130.4, 129.9, 128.7, 128.4, 127.8, 127.4, 125.3, 122.7, 121.1, 119.1. LC-MS (m/z): [M + 1] 408.2130.

(2Z,5Z)-2-((9H-Fluoren-9-ylidene)hydrazono)-5-(3,4-dimethoxybenzylidene)thiazolidin-4-one (5r). Yellow solid; yield: 0.63 g,

84%; mp: 220–222 °C. FT-IR (KBr, cm^{-1}) 3416 (N–H), 3062 (Ar C–H), 1692 (C=O), 1635, 1600 (C=N), 1559 (C=C), 802 (C–S), 1309 (C–OCH₃). ¹H-NMR (400 MHz, DMSO-*d*₆) δ (ppm) 12.80 (s, 1H), 8.59 (d, *J* = 7.6 Hz, 1H), 7.82 (dd, *J* = 12.2, 7.6 Hz, 3H), 7.63 (s, 1H), 7.46 (t, *J* = 7.4 Hz, 2H), 7.37–7.27 (m, 4H), 7.15 (d, *J* = 8.4 Hz, 1H), 3.81 (s, 6H). ¹³C-NMR (101 MHz, DMSO-*d*₆) δ (ppm) 168.0 (C=O), 163.4 (C=N in the fluorenone ring), 157.3 (C=N in the thiazolidine-4-one ring), 151.0 (=CH–), 149.4 (C–OCH₃), 142.0, 140.9, 136.4, 132.1, 131.6, 131.6, 130.9, 130.3, 128.8, 126.8, 123.5, 122.7, 121.1, 120.4, 114.4, 112.6, 56.1 (–OCH₃). LC-MS (*m/z*): [*M* + 1] 442.0700.

(2*Z*,5*Z*)-5-((1*H*-Indol-3-yl)methylene)-2-(2-(9*H*-fluoren-9-ylidene)hydrazono)thiazolidin-4-one (5s). Yellow solid; yield: 0.57 g, 80%; mp: 218–220 °C. FT-IR (KBr, cm^{-1}) 3416 (N–H), 3062 (Ar C–H), 1692 (C=O), 1635, 1600 (C=N), 1558 (C=C), 802 (C–S), ¹H-NMR (400 MHz, DMSO-*d*₆) δ (ppm) 12.63 (s, 1H), 12.06 (s, 1H), 8.62 (d, *J* = 7.6 Hz, 1H), 7.94–7.70 (m, 7H), 7.51–7.45 (m, 3H), 7.36 (q, *J* = 7.1 Hz, 2H), 7.20 (td, *J* = 15.3, 7.9 Hz, 2H). ¹³C-NMR (101 MHz, DMSO-*d*₆) δ (ppm) 168.0 (C=O), 163.7 (C=N in the fluorenone ring), 156.8 (C=N in the thiazolidine-4-one ring), 141.9 (=CH–), 140.9, 136.7, 136.5, 132.1, 131.6, 131.5, 130.3, 129.0, 128.8, 128.7, 127.4, 123.5, 123.0, 122.8, 121.4, 121.1, 118.8, 116.2, 112.9, 111.2. LC-MS (*m/z*): [*M* + 1] 421.1141.

(2*Z*,5*Z*)-2-((9*H*-Fluoren-9-ylidene)hydrazono)-5-(3-hydroxy-benzylidene)thiazolidin-4-one (5t). Yellow solid; yield: 0.67 g, 82%; mp: 218–220 °C. FT-IR (KBr, cm^{-1}) 3416 (N–H), 3062 (Ar C–H), 1694 (C=O), 1632, 1602 (C=N), 1558 (C=C), 802 (C–S), 1255 (C–OH), 3159 (O–H). ¹H-NMR (400 MHz, DMSO-*d*₆) δ (ppm) 12.78 (s, 1H), 10.39 (s, 1H), 8.60 (d, *J* = 7.9 Hz, 1H), 7.91 (s, 1H), 7.84–7.76 (m, 4H), 7.53 (d, *J* = 6.7 Hz, 1H), 7.46 (q, *J* = 8.2 Hz, 2H), 7.34 (t, *J* = 7.6 Hz, 2H), 7.30–7.25 (m, 1H), 6.97 (q, *J* = 8.6 Hz, 2H). ¹³C-NMR (101 MHz, DMSO-*d*₆) δ (ppm) 168.2 (C=O), 163.4 (C=N in the fluorenone ring), 160.1 (C=N in the thiazolidine-4-one ring), 157.3 (C–OH), 142.1 (=CH–), 140.8, 136.6, 132.8, 132.4, 131.2, 131.5, 131.3, 130.1, 128.9, 125.1, 122.9, 121.0, 118.7, 116.9. LC-MS (*m/z*): [*M* + 1] 398.1204.

(2*Z*,5*Z*)-2-((9*H*-Fluoren-9-ylidene)hydrazono)-5-(thiophen-2-ylmethylene)thiazolidin-4-one (5u). Yellow solid; yield: 0.49 g, 74%; mp: 214–216 °C. FT-IR (KBr, cm^{-1}) 3458 (N–H), 3062 (Ar C–H), 1741 (C=O), 1635, 1594 (C=N), 1557 (C=C), 804 (C–S). ¹H-NMR (400 MHz, DMSO-*d*₆) δ (ppm) 12.87 (s, 1H), 8.58 (d, *J* = 6.9 Hz, 1H), 7.99 (d, *J* = 5.3 Hz, 1H), 7.94 (s, 1H), 7.85–7.79 (m, 3H), 7.67 (d, *J* = 3.1 Hz, 1H), 7.48 (q, *J* = 7.4 Hz, 2H), 7.36 (q, *J* = 7.1 Hz, 2H), 7.28 (t, *J* = 4.2 Hz, 1H). ¹³C-NMR (101 MHz, DMSO-*d*₆) δ (ppm) 167.6 (C=O), 162.8 (C=N in the fluorenone ring), 157.5 (C=N in the thiazolidine-4-one ring), 142.1 (=CH–), 141.0, 138.3, 136.4, 134.4, 132.9, 132.2, 131.7, 131.5, 130.3, 129.4, 128.9, 123.8, 122.7, 121.1, 120.9 (=CH–). LC-MS (*m/z*): [*M* + 1] 388.0960.

Pharmacological assays

In vitro antioxidant assay

Free radical scavenging activity assay 1,1-diphenyl-2-picrylhydrazyl (DPPH) assay. The DPPH radical scavenging assay, as

described by Wong *et al.*,⁴⁷ was used to examine the ability of the synthesized compounds to scavenge free radicals. The ability of the synthesized compounds to donate hydrogen atoms was tested by decolorizing a methanol solution of 1,1-diphenyl-2-picrylhydrazyl (DPPH). In the presence of the anti-oxidant, DPPH generates a violet/purple colour in methanol solution which fades to yellow colour. 1 mL of each compound at different concentrations was added to 3 mL of DPPH (0.1 mM) methanolic solution. The tubes were vigorously shaken and left to stand for 30 min at room temperature in the dark before measuring changes in absorbance at 517 nm. The DPPH radical scavenging activity of gallic acid was measured for comparison. All tests were run in triplicate, and the mean values were shown in the graph. The following formula was used to calculate the percentage of inhibition:

$$\% \text{ DPPH radical scavenging activity} = [(A_0 - A_1)/A_0] \times 100$$

where *A*₀ is the absorbance of the control (no test sample) and *A*₁ is the absorbance of the test samples.

The IC₅₀ values (the concentration required to scavenge 50% of free radicals) were calculated from the plot of % inhibition *versus* sample solution concentration.

In vitro antidiabetic assay

α -Glucosidase inhibitory activity. Li *et al.* (2004) assessed the inhibitory activity against α -glucosidase.⁴⁸ A reaction mixture containing 500 μ L of phosphate buffer (100 mM, pH = 6.8), 200 μ L of α -glucosidase solution (0.6 U mL^{−1}), and various concentrations of test samples ranging from 25 to 100 μ g and a control sample were pre-incubated for 5 min with a series of synthesised compounds 5a–5u in a test tube. 10 mM *p*-Nitrophenyl- α -D-glucopyranoside (*p*-NPG) was used to initiate the reaction, which was then stopped after 15 min at 37 °C by heating on a water bath. The amount of released glucose was calculated. The amount of liberated glucose was measured at 400 nm on a UV spectrophotometer. The amount of liberated glucose is directly proportional to the enzyme activity. The assay methods were carried out three times. The compound's inhibitory activity and IC₅₀ were calculated.

$$\% \text{ Inhibitory activity} = [(A_s - A_c)/A_s] \times 100$$

where *A*_s is the absorbance when the test material is present and *A*_c is the absorbance of the control.

Conflicts of interest

The authors declare that they have no conflict of interest.

Acknowledgements

The authors thank the SAIF and USIC, Karnatak University, Dharwad, for instrumental facilities. One of the authors (MD) thanks the DST-KSTePs, Govt. of Karnataka, for awarding the fellowship to carry out this work. We thank Dr Satish Bhat, Department of Chemistry, Karnatak University, Dharwad, for

his fruitful discussion and assistance in X-ray crystallographic studies. Thanks are also due to Dr Avinash Prakash, Alekya Agro Solutions, Mysore, for biological activities.

References

- 1 Y. Zhu, J. Zhao, L. Luo, Y. Gao, H. Bao, P. Li and H. Zhang, *Eur. J. Med. Chem.*, 2021, **223**, 113665.
- 2 N. Sylla, A. Bouyahya, D. Taha, N. Dakka and H. Elhajji, *Biocatal. Agric. Biotechnol.*, 2021, **36**, 102126.
- 3 M. Jung, M. Park, H. C. Lee, Y.-H. Kang, E. S. Kang and S. K. Kim, *Curr. Med. Chem.*, 2006, **13**, 1203–1218.
- 4 F. Hasaninezhad, Z. Tavaf, F. Panahi, M. Nourisefat, A. Khalafi-Nezhad and R. Yousefi, *J. Diabetes Metab. Disord.*, 2020, **19**, 1505–1515.
- 5 J. H. Kim, H. Y. Kim and C. H. Jin, *Bioorg. Chem.*, 2019, **87**, 803–809.
- 6 S. A. Ross, E. A. Gulve and M. Wang, *Chem. Rev.*, 2004, **104**, 1255–1282.
- 7 S. R. Joshi, E. Standl, N. Tong, P. Shah, S. Kalra and R. Rathod, *Expert Opin. Pharmacother.*, 2015, **16**, 1959–1981.
- 8 J. A. Abdullah, B. J. M. Aldahham, M. A. Rabeea, F. A. Asmary, H. M. Alhajri and M. A. Islam, *J. Mol. Struct.*, 2021, **1223**, 129311.
- 9 K. Appalanaidu, R. Kotcherlakota, T. L. Dadmal, V. S. Bollu, R. M. Kumbhare and C. R. Patra, *Bioorganic Med. Chem. Lett.*, 2016, **26**, 5361–5368.
- 10 H. K. Mahmoud, H. A. Abdelhady, M. M. Elaasser, D. Z. H. Hassain and S. M. Gomha, *Polycycl. Aromat. Compd.*, 2022, **42**, 7232–7246.
- 11 A. S. Abouzied, J. Y. Al-humaidi, A. S. Bazaid, H. Qanash, N. K. Binsaleh, A. Alamri, S. M. Ibrahim and S. M. Gomha, *Molecules*, 2022, **27**, 6368.
- 12 S. M. Gomha, S. M. Riyadh, B. Huwaimel, M. E. M. Zayed and M. H. Abdellattif, *Molecules*, 2022, **27**, 4639.
- 13 G. F. Aljohani, T. Z. Abolibda, M. Alhilal, J. Y. Al-Humaidi, S. Alhilal, H. A. Ahmed and S. M. Gomha, *J. Taibah Univ. Sci.*, 2022, **16**, 1005–1015.
- 14 T. S. Chitre, K. D. Asgaonkar, P. B. Miniyar, A. B. Dharme, M. A. Arkile, A. Yeware, D. Sarkar, V. M. Khedkar and P. C. Jha, *Bioorganic Med. Chem. Lett.*, 2016, **26**, 2224–2228.
- 15 V. A. Barbosa, P. Baréa, R. S. Mazia, T. Ueda-Nakamura, W. F. da Costa, M. A. Foglio, A. L. T. Goes Ruiz, J. E. de Carvalho, D. B. Vendramini-Costa, C. V. Nakamura and M. H. Sarragiotto, *Eur. J. Med. Chem.*, 2016, **124**, 1093–1104.
- 16 R. M. Kassab, S. M. Gomha, S. A. Al-Hussain, A. S. Abo Dena, M. M. Abdel-Aziz, M. E. A. Zaki and Z. A. Muhammad, *Arab. J. Chem.*, 2021, **14**, 103396.
- 17 H. K. Mahmoud, A. R. Sayed, M. M. Abdel-Aziz and S. M. Gomha, *Med. Chem.*, 2022, **18**, 1100–1108.
- 18 R. Suryawanshi, S. Jadhav, N. Makwana, D. Desai, D. Chaturbhuj, A. Sonawani, S. Idicula-Thomas, V. Murugesan, S. B. Katti, S. Tripathy, R. Paranjape and S. Kulkarni, *Bioorg. Chem.*, 2017, **71**, 211–218.
- 19 L. Gummidi, N. Kerru, O. Ebenezer, P. Awolade, O. Sanni, M. S. Islam and P. Singh, *Bioorg. Chem.*, 2021, **115**, 105210.
- 20 A. I. Siutkina, N. M. Igidov, M. V. Dmitriev, R. R. Makhmudov and V. V. Novikova, *Russ. J. Gen. Chem.*, 2019, **89**, 1026–1032.
- 21 P. J. Perry, M. A. Read, R. T. Davies, S. M. Gowan, A. P. Reszka, A. A. Wood, L. R. Kelland and S. Neidle, *J. Med. Chem.*, 1999, **42**, 2679–2684.
- 22 S. R. Choi, M. A. Larson, S. H. Hinrichs and P. Narayanasamy, *Bioorganic Med. Chem. Lett.*, 2016, **26**, 1997–1999.
- 23 T. Matviiuk, F. Rodriguez, N. Saffon, S. Mallet-Ladeira, M. Gorichko, A. L. De Jesus Lopes Ribeiro, M. R. Pasca, C. Lherbet, Z. Voitenko and M. Baltas, *Eur. J. Med. Chem.*, 2013, **70**, 37–48.
- 24 E. R. Andrews, R. W. Fleming, J. M. Grisar, J. C. Kihm, D. L. Wenstrup and G. D. Mayer, *J. Med. Chem.*, 1974, **17**, 882–886.
- 25 S. M. Gomha, H. A. Abdelhady, D. Z. H. Hassain, A. H. Abdelmonsef, M. El-Naggar, M. M. Elaasser and H. K. Mahmoud, *Drug Des. Devel. Ther.*, 2021, **15**, 659–677.
- 26 M. Abdalla, S. Gomha, M. Abd El-Aziz and N. Serag, *Turkish J. Chem.*, 2016, **40**, 441–453.
- 27 K. M. Darwish, I. Salama, S. Mostafa, M. S. Gomaa and M. A. Helal, *Eur. J. Med. Chem.*, 2016, **109**, 157–172.
- 28 P. Sharma, T. Srinivasa Reddy, D. Thummuri, K. R. Senwar, N. Praveen Kumar, V. G. M. Naidu, S. K. Bhargava and N. Shankaraiah, *Eur. J. Med. Chem.*, 2016, **124**, 608–621.
- 29 P. R. Spackman, M. J. Turner, J. J. McKinnon, S. K. Wolff, D. J. Grimwood, D. Jayatilaka and M. A. Spackman, *J. Appl. Crystallogr.*, 2021, **54**, 1006–1011.
- 30 H. F. Clausen, M. S. Chevallier, M. A. Spackman and B. B. Iversen, *New J. Chem.*, 2010, **34**, 193–199.
- 31 J. Seetharamappa and B. P. Kamat, *Chem. Pharm. Bull.*, 2004, **52**, 1053–1057.
- 32 S. K. Pawar, R. Punith, R. S. Naik and J. Seetharamappa, *J. Biomol. Struct. Dyn.*, 2016, **35**, 3205–3220.
- 33 R. Naik and S. Jaldappagari, *J. Mol. Liq.*, 2019, **293**, 111492.
- 34 C. B. Pradeep Kumar, B. S. Prathibha, K. N. N. Prasad, M. S. Raghu, M. K. Prashanth, B. K. Jayanna, F. A. Alharthi, S. Chandrasekhar, H. D. Revanasiddappa and K. Yogesh Kumar, *Bioorganic Med. Chem. Lett.*, 2021, **36**, 127810.
- 35 S. Pawar, R. Tandel, R. Kunabevu and S. Jaldappagari, *J. Biomol. Struct. Dyn.*, 2019, **37**, 846–856.
- 36 J. Gasteiger and M. Marsili, *Tetrahedron*, 1980, **36**, 3219–3228.
- 37 V. Desai, S. Desai, S. N. Gaonkar, U. Palyekar, S. D. Joshi and S. K. Dixit, *Bioorg. Med. Chem. Lett.*, 2017, **27**, 2174–2180.
- 38 Y. Isyaku, A. Uzairu and S. Uba, *Heliyon*, 2020, **6**, e03724.
- 39 N. R. Jabir, S. Shakil, S. Tabrez, M. S. Khan, M. T. Rehman and B. A. Ahmed, *J. Biomol. Struct. Dyn.*, 2021, **39**, 5083–5092.
- 40 D. Kaminskyy, A. Kryshchshyn and R. Lesyk, *Eur. J. Med. Chem.*, 2017, **140**, 542–594.
- 41 P. Banerjee, A. O. Eckert, A. K. Schrey and R. Preissner, *Nucleic Acids Res.*, 2018, **46**, W257–W263.
- 42 I. Usón and G. M. Sheldrick, *Acta Crystallogr., Sect. D: Struct. Biol.*, 2018, **74**, 106–116.

- 43 G. M. Sheldrick, *Acta Crystallogr., Sect. C: Struct. Chem.*, 2015, **71**, 3–8.
- 44 O. V. Dolomanov, L. J. Bourhis, R. J. Gildea, J. A. K. Howard and H. Puschmann, *J. Appl. Crystallogr.*, 2009, **42**, 339–341.
- 45 S. Bruker, Bruker AXS Inc., Madison, Wisconsin, USA, 2015.
- 46 G. M. Sheldrick, *Acta Crystallogr., Sect. A: Found. Adv.*, 2015, **71**, 3–8.
- 47 C. C. Wong, H. Bin Li, K. W. Cheng and F. Chen, *Food Chem.*, 2006, **97**, 705–711.
- 48 Y. Li, G. Peng, Q. Li, S. Wen, T. Hsun-Wei Huang, B. D. Roufogalis and J. Yamahara, *Life Sci.*, 2004, **75**, 1735–1746.

Microwave-assisted synthesis and characterizations of nanosized copper ferrite and barium titanate for antimicrobial applications

Arunkumar Lagashetty^{a*}, K. Devendra^a, M. Sandhyarani^a, J. Rajeshwari^a, Galeppa^a, K.H. Lakshmidhevi^a, B. B. Hajara^a, Veena V^b, Preeti R.K^c and Sangappa K. Ganiger^d

^aDepartment of Chemistry, Vijayanagara Sri Krishnadevaraya University, Ballari, 583105, Karnataka, India

^bDepartment of Chemistry, Ballari Institute of Technology and Management, Ballari, 583105, Karnataka, India

^cDepartment of Zoology, Gulbarga University, Kalaburagi, 585103, Karnataka, India

^dDepartment of Physics, Government Engineering College, Huvinahadagali, 583219, Karnataka, India

CHRONICLE

Article history:

Received March 20, 2023

Received in revised form

June 17, 2023

Accepted October 9, 2023

Available online

October 12, 2023

Keywords:

Bimetallic oxides

BaTiO₃

CuFe₂O₄

XRD

SEM

FT-IR

DX

ABSTRACT

Science and technology of nanosized bimetallic oxide nanomaterials records the various properties and applications. Especially biomedical applications are viewed in particular due to its nanosized particle size. The present experimentation is reporting the microwave-assisted synthesis of nanosized bimetallic oxides like copper ferrite (CuFe₂O₄) and barium titanate (BaTiO₃) by solid state combustion route using poly (vinyl alcohol) (PVA) as a fuel. The structural and morphological characterizations of the bimetallic oxide nanomaterials are performed out by X-ray diffraction (XRD) and scanning electron micrograph (SEM) tools respectively. These analyses report the crystalline nature of both samples. EDX spectral study is also undertaken to know the existence of different metals in the above-mentioned samples. Bonding nature of the bimetallic oxide samples were readied by Fourier transfer infrared (FT-IR) instrumentation. The study reviewed the varied vibrational modes confirms the phase formation of the samples. UV-Vis and thermal study of these bimetallic oxide samples are also studied extensively to know the thermal and absorption behavior respectively. TGA of both the samples are traced and are showing decomposition at rapid rate. In addition, the maximum absorption peaks due to $\pi - \pi^*$ transition confirms the sample formation. Antimicrobial activity of the prepared oxide samples was studied for antibacterial and antifungal behavior. Both samples showing considerable activity against various bacteria and fungi.

© 2024 by the authors; licensee Growing Science, Canada.

1. Introduction

Nanoscience is popularly defining by designing the functional materials at the nanoscale for its potential applications in various fields¹⁻³. The reasons why nanoscale materials have become so important, because of its easy scale up synthesis, improved properties and need based applications⁴⁻⁶. Based on technology of nanomaterials is feathered to cover the design, utilization and construction of functional nanomaterials with at least one characteristic dimension⁷⁻⁸. Nanosized novel materials can be refigured to improve physical, chemical and biological properties in comparison with micro materials⁹⁻¹¹. The reason behind such interesting development and useful behavior of these materials is due to structural features with intermediate in between isolated atoms and bulky materials. Hence, the objects may display physical substantially different from those displayed by either atoms or bulk materials lead to new technological opportunities as well as new challenges¹²⁻¹⁴. Bimetallic oxide nanomaterials are most important and are widely studied solid materials at nanoscale for various new properties for substantial applications¹⁵⁻¹⁶. Especially, nanosized transition metal oxides have attracted much due to their outer electron configuration and are applied widely in various reactions for their structural properties such as high surface area, variable pore size, and stability¹⁷⁻¹⁹. The current study materials like nanosized copper ferrite and barium ferrite materials falls under the same category and one can find superficial properties as well as applications in various fields.

* Corresponding author.

E-mail address arun.lagashetty@gmail.com (A. Lagashetty)

CuFe_2O_4 is a spinel type of oxide material which has high chemical stability, high thermal stability, high mechanical resistance and low surface acidity. In addition, this spinel material is suitable for various applications, such as high-density storage media, ferromagnetic fluids, catalysts, magnetic drug delivery systems, magnetic separation, magnetic resonance tomography, gas sensors, and another applications²⁰⁻²³. Copper based ferrite materials are having strong magnetic properties, relatively low conductivity, low eddy currents and dielectric losses. In continuation, it also shows the high permeability properties²⁴⁻²⁵. Similarly, barium titanate is one of the perovskite materials which can find various electronic and biological applications²⁶⁻²⁷. The ferroelectric and hydroelectric properties of barium ferrite are highly useful in manufacture of some varieties un-cooled sensors which are used in thermal cameras. Large crystals of barium ferrite are used in electronic precursors like capacitors, electrochemical transducers, and nonlinear optical tools.²⁸⁻²⁹ Recently, barium based titanate nanoparticles have been employed as nanocarriers for drug delivery in the body system³⁰⁻³¹. It naturally occurring in barium-based perovskites and is very rare natural analogue of barium titanate found as micro inclusions in benitoite. In consideration of these including remarks, the present experimentation is reporting the synthesis of nanosized copper ferrite and barium titanate perovskite nanomaterials by self-propagating combustion route using PVA as a fuel. These bimetallic oxide nanomaterials were well characterized by various characterization tools for their phase formation. Antimicrobial activity studies of these prepared oxide materials are undertaken to know its antimicrobial behavior towards various bacteria and fungi.

2. Experimental

2.1 Materials and Methods

The chemicals used in the experimentation are of AR grade and are purchased from Merck (Mumbai, India) and are used with further purification. Properly rinsed glass wares with chromic acid are used in the experimentation for purity of the reaction product. Microwave-assisted self-propagating combustion route was adopted for the synthesis of barium titanate and copper ferrite nanomaterials using polymer as a fuel. For antimicrobial activity, nutrient agar (NA) and potato dextrose agar (PDA) media were purchased from Hi Media. The bacterial strains were of microbial type culture collection, procured from Institute of Microbial Technology, Chandigarh, India.

2.2 Synthesis of the copper oxide and iron oxide nanomaterials

Copper sulphate was thoroughly mixed with PVA in the weight ratio 1:5 and grounded well in a pestle and mortar. The resultant solid is transferred into China dish and was heated in an open air atmosphere until the completion of evolved carbonaceous fumes. The reaction undergoes self-propagating combustion reaction in presence of polymer fuel. Incomplete reaction product is transferred into a silica crucible and was ignited at around 800°C in muffle furnace. It was observed that, initially PVA melted, then frothed and finally ignited to give copper oxide as a residue³². Similar procedure was adopted for the synthesis of iron oxide nanomaterials by use of ferrous sulphate as a precursor material with same polymer fuel.

2.3 Synthesis of Copper ferrite and Barium titanate

Equimolar quantity of as prepared nanosized copper oxide and iron oxide was grinded well with PVA in the weight ratio of 1:1:5 in a pestle and mortar. The mixture was transferred into a crucible and was burnt initially on electric oven for complete evolution of fumes. Then, it is transferred to microwave oven for complete calcinations process. The sample was calcined on microwave oven having 2.45GHz frequency and power is 800w for about 15 minutes. During burning, the approximate temperature maintained around 1200°C. The reaction mixture burns suitably and leaving behind a solid copper ferrite as a crystalline product. Similar procedure is used for the synthesis of nanosized barium titanate nanomaterials sample. The obtained bimetallic oxide samples are shown in figure 1. Possible reactions involved in the combustion process are given below. The complete synthetic scheme of both the bimetallic oxides is given in **Scheme 1**.

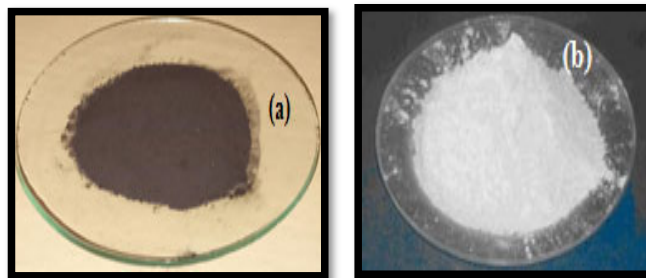
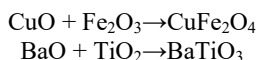
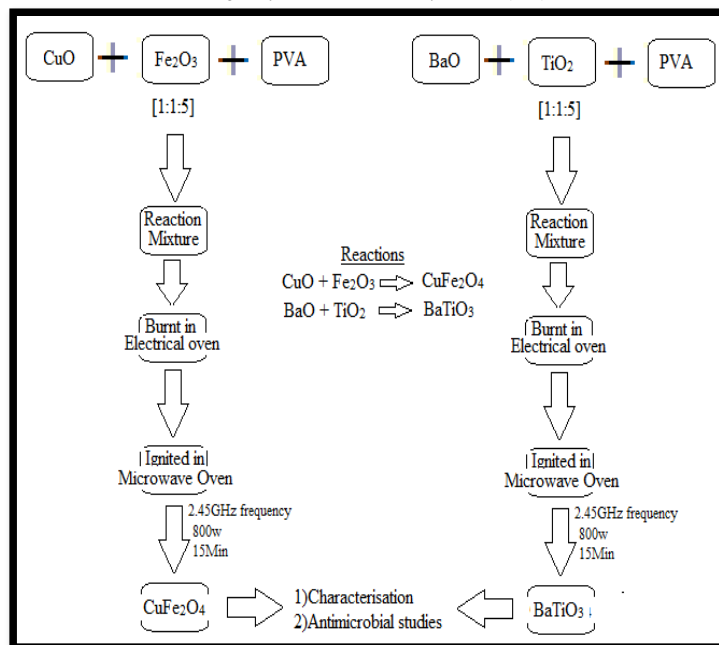


Fig. 1. Optical image of (a) CuFe_2O_4 nanomaterials (b) BaTiO_3 nanomaterials



Scheme 1. Synthetic scheme of Copper ferrite and Barium titanate nanomaterials

2.3.1 Antibacterial activity

Antibacterial activity of as prepared copper ferrite and barium titanate nanomaterial samples were performed by agar well diffusion method (Zhang *et al.*, 2009) with minor modifications³³. Petri dishes were prepared by inserting 20 ml sterilized NA media under regular condition and allowed to solidify. After media solidification, 100 μ l of standard test microbial inoculums of gram-positive bacteria like *S. aureus*, *B. subtilis* and gram-negative bacteria like *S. Typhi*, and *Pseudomonas aeruginosa* were spread uniformly by use of sterile cotton swabs. 6 mm diameter agar is drawn from plate to form a well using sterile cork borer. Standard antibiotic gentamycin was considered and used as positive control, DMSO as negative control. After keeping at 4 $^{\circ}$ C for 4 hours for the diffusion of antibacterial metabolites, thereafter plates were incubated at 37 $^{\circ}$ C for 24 h. The antibacterial effect was estimated by taking a record of the growth inhibition zones in millimeters. The whole experiment was conducted in triplicate for proper confirmation of the activity.

2.3.2 Antifungal activity

Antifungal activity of prepared samples was studied by agar well diffusion method (Zhang *et al.*, 2009) with required minor modifications³³. Petri dishes were prepared by pouring 20 ml of PDA sterilized media under aseptic condition and allowed the same solidification. Soon after the solidification of the media, 100 μ l of standardized test *Aspergillus niger* and *Fusarium* was spread uniformly using sterile L-shaped loop. 6 mm diameter agar is drawn from plate to form a well using sterile cork borer for its spreading the sample. Antifungal Nystatin was used as positive control and DMSO as a negative control for the activity results. Samples kept at 4 $^{\circ}$ C for 4 hours for the diffusion of antibacterial metabolites, thereafter plates were incubated in reaction incubator at 28 $^{\circ}$ C for 72 h. The obtained diameter of the inhibition zone around the prepared well is measured in mm and the average of three best repeated agar discs were taken in to account to assess the strength of antifungal activity of the samples.

2.3.3 Characterization Techniques

The powder X-ray diffraction patterns of the samples were catalogued using JEOL JDX-8P diffractometer using CuK α radiation (1.54 \AA) at 30 kV. The Fourier transform infrared (FTIR) spectra of the samples were recorded on a Perkin-Elmer FT-IR (Model No. 1000) in the range 4000-400 cm^{-1} at a resolution of 4 cm^{-1} . JEOL JSM-6380 LA scanning electron microscope with energy dispersive micro analysis of X-Ray (EDAX) is used to study particle morphology with metal confirmation of the sample. The absorption behavior of the sample was carried out by UV visible spectrophotometric measurements using Elico spectrophotometer. Technai-20 Philips transmission electron microscope operated at 190 KeV to carry out TEM images. Mettler Toledo star tool was used to trace the thermal characterization.

3. Results and discussion

3.1 FT-IR study

Fig. 2(a-b) shows FT-IR spectra of combustion derived copper ferrite and barium titanate samples respectively. The metal-oxygen bonding and nature of the synthesized bimetallic oxide samples were carried out by infrared study. Generally

metal oxides give absorption bands below 1000cm^{-1} arising from inter-atomic vibrations³⁴. It is observed in both spectra that, the peak at 3500cm^{-1} corresponds to absorption of moisture content. Further, the vibration band observed at 1050cm^{-1} is due to some overtones. Peaks below 1000cm^{-1} corresponds to Metal-oxygen vibrational modes and metal-metal vibration modes of the readied sample confirm the phase formation of prepared bimetallic oxide samples³⁵.

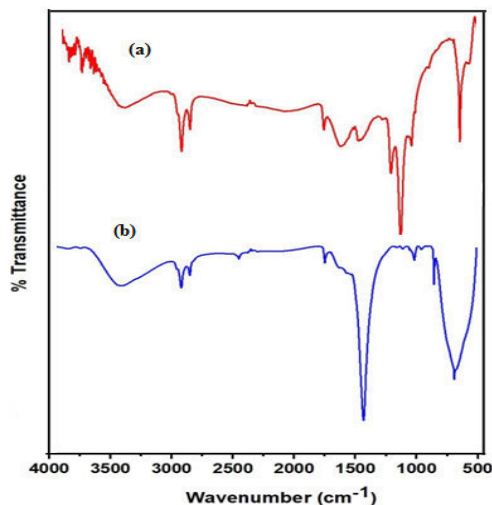


Fig. 2. FT-IR of (a) CuFe_2O_4 nanomaterials (b) BaTiO_3 nanomaterials

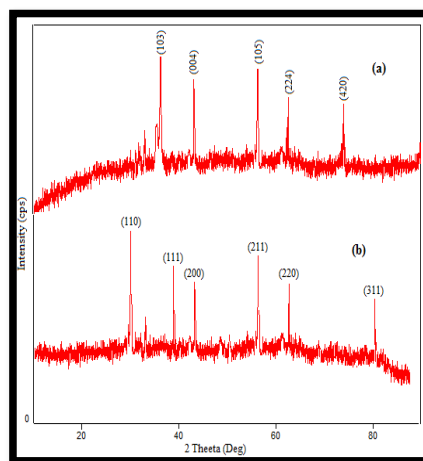


Fig. 3. Indexed XRD pattern (a) CuFe_2O_4 nanomaterials (b) BaTiO_3 nanomaterials

3.2 XRD Study

XRD system was used to know the crystallinity and phase structure of the as-synthesised bimetallic oxide samples. **Fig. 3(a-b)** represents the indexed XRD pattern of as synthesized copper ferrite and barium titanate nanomaterials respectively. According to the XRD pattern, obtained 2θ values and (hkl) values of both samples are indexed in accordance with standard JCPDS values and are tabulated in table-1. Both patterns show the presence of highly intense Bragg's reflections indicates the crystalline nature of both samples. It is also illustrating that, at higher temperature samples showing stable structure. The intensity of peaks in the pattern are sharp indicates the high crystalline nature of both the samples. These patterns not demonstrating monometallic oxide reflections which are utilized for bimetallic oxide sample preparation. It is observed from the table and indexed pattern, the most of the 2θ (or d-spacing) value of the sample acceptably matches with literature data of the copper ferrite (JCPDS card No. 34-0425) and barium titanate (JCPDS card No.79-2264) confirms the formation of CuFe_2O_4 and BaTiO_3 nanomaterials respectively with single crystalline phase. Further, the existence of the indexed major lattice planes in the pattern supports the sample formation. The broadening and sharp peaks indicate the reduced particle size and high crystallinity of the samples. It is also noticed that, at the higher temperature the removal of extra undefined phases. Purity of the samples analyzed in the pattern by the absence of the other reflection³⁶.

Table 1. XRD data of BaTiO_3 and CuFe_2O_4 samples

Sl.No	CuFe_2O_4		BaTiO_3	
	Observed 2θ values	(hkl)	Observed 2θ values	(hkl)
1	35.02	(103)	32.33	(110)
2	43.10	(004)	39.43	(111)
3	56.11	(105)	46.82	(200)
4	62.00	(224)	57.64	(211)
5	73.33	(420)	67.50	(220)
6	-----	---	80.05	(311)

3.3 EDX Study

The EDX analyses of the bimetallic oxide samples were performed to clarify its elemental compositions. **Fig. 4 (a-b)** shows the EDX pattern of combustion derived CuFe_2O_4 and BaTiO_3 nanomaterials respectively. The chemical constituents like presence of Cu, Fe, and O elemental segments are observed at respective position in the EDX pattern of copper ferrite (**Fig. 4(a)**) confirms the formation of the said sample. Similarly, the reflections of Ba, Ti and O elemental segments in the EDX pattern of barium titanate (**Fig. 4(b)**) signify the formation of sample. No other elemental reflections other than the above observed indicates the purity of the prepared samples.

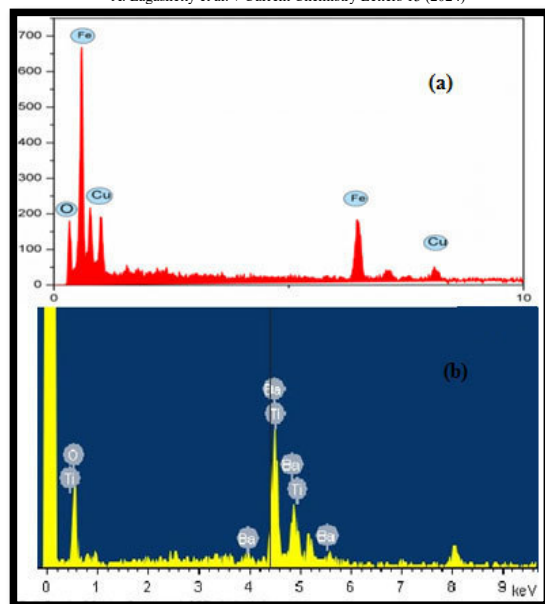


Fig. 4. EDX pattern of (a) CuFe_2O_4 (b) BaTiO_3 nanomaterials

3.4 SEM study

The surface morphology of the prepared nanomaterial was examined through SEM instrumentation. Figure 5(a-b) shows SEM images of CuFe_2O_4 and BaTiO_3 nanomaterials respectively. Several cracks are observed due to the existence of the voids, which originates from the pore boundaries and then propagate to maximum compression direction. The grain morphology, uniformity, homogeneity, and their distribution have been observed. Copper ferrite particles showed large grains stuck to each other in an irregular and non-uniform manner is observed in **Fig. 5(a)**. The SEM image of barium titanate (**Fig. 5(b)**) shows that the particles fall in the nano-orange with fine, spherical shaped particles with regular arrangement. Some particles show clear close compactness of the particles indicated the very crystalline nature and also lead to applicable morphology. It is also noticeable that the particle sizes differed from the crystalline sizes due to polycrystalline agglomeration with a single crystal. These results are in close consideration with XRD results in terms of its crystalline behavior.

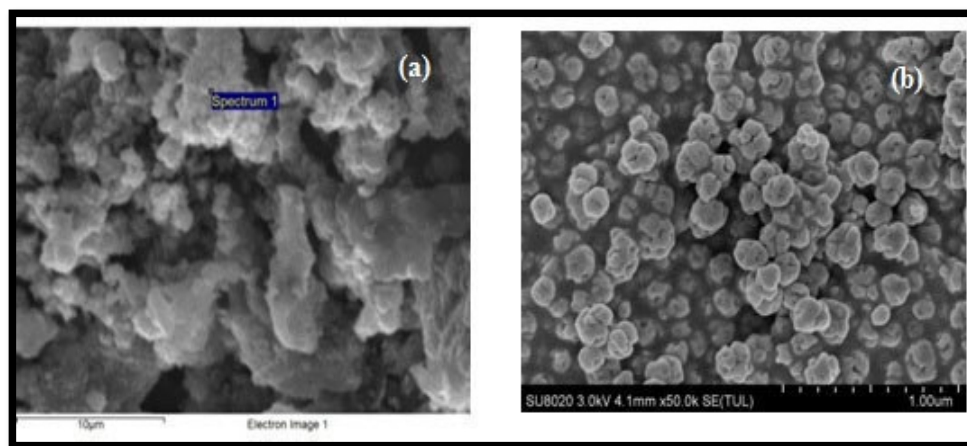


Fig. 5. SEM image of (a) CuFe_2O_4 (b) BaTiO_3 nanomaterials

3.4 TEM Study

Particle morphology and its size of the combustion derived CuFe_2O_4 and BaTiO_3 nanomaterials samples was studied by TEM instrumentation and its images are represented in **Fig. 6(a-b)**, respectively. **Fig. 6(a)** shows the crystalline nature of the sample and is in accordance with XRD results. It is also highlighting particle netting falls under nano size range diameters. However, the image further reveals that some particles are spherical, and some are irregular particles nature in agreement with SEM results.

Similarly, barium titanate nanomaterials also show crystalline behavior and its SEM image is given in figure 6(b). In addition, particle agglomeration with particle compactness is also viewed in the said image.

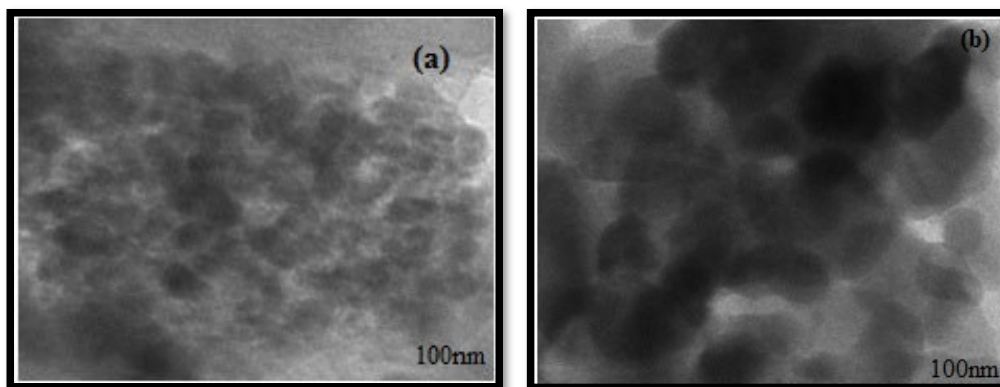


Fig. 6. TEM image of (a) CuFe_2O_4 (b) BaTiO_3 nanomaterials

3.5 Thermal Study

TGA study is carried out to view the sequential weight loss and subsequent transformation due to heat treatment of the samples. **Fig. 7(a-b)** shows the TGA traces of CuFe_2O_4 and BaTiO_3 samples respectively. It is observed from **Fig. 7(a)** that the three-step decomposition under exited temperature range 100-500°C, 500-650°C and 650-1000°C. Copper ferrite sample shows the initial weight loss in the range 100-500°C is due to water evaporation. Further, the sample decomposes continuously as the temperature rises and shows a sharp weight loss in the range 500°C-650°C due to further decomposition of residual precursor oxides present in the sample. Above 900°C, no weight loss was observed indicates the decomposition of the phases of the sample. Similar features are observed in barium titanate sample. TGA trace of barium titanate sample (**Fig. 7(b)**) is also showing significant three step weight loss in the temperature range 100-400°C, 400-500°C and 500-800°C. The initial weight loss is due to evaporation of water and second loss is due to further residual oxides decomposition and third loss is due to decomposition of complete phase of the sample.³⁷⁻³⁸

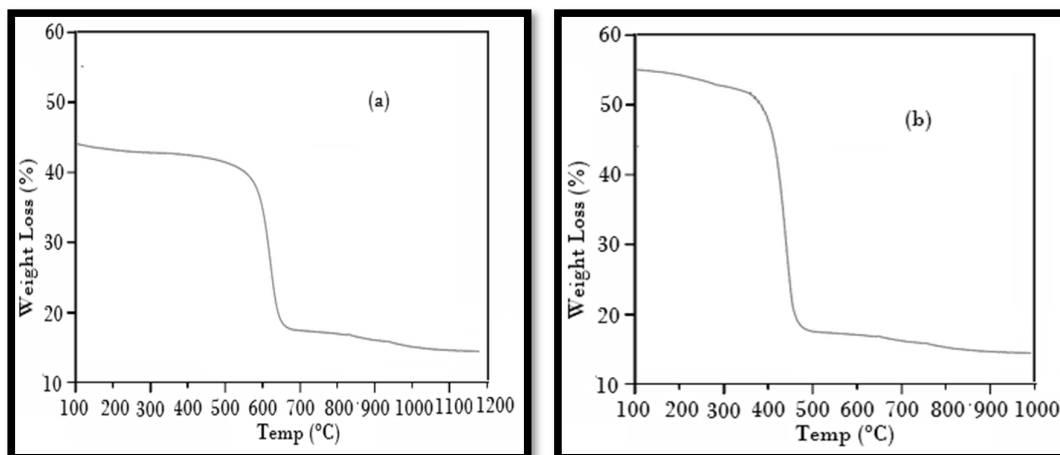


Fig. 7. TGA trace of (a) CuFe_2O_4 (b) BaTiO_3 nanomaterials

3.6 UV-Vis study

Optical properties of bimetallic samples were well studied by UV-Vis spectroscopic analysis. The absorption spectra of CuFe_2O_4 and BaTiO_3 samples are shown in **Fig. 8(a-b)**, respectively. It is observed from UV-Vis absorption spectra of CuFe_2O_4 that, a single and maximum strong surface Plasmon resonance band (λ_{max}) at 350nm is assigned to the characteristics phase of CuFe_2O_4 . Similarly, a single maximum strong surface Plasmon resonance band (λ_{max}) at 310nm (in **Fig. 8(b)**) is observed due to excitation of electron from valence band to conduction band and the characteristics phase of BaTiO_3 sample. Both samples show the broad Plasmon bands with an absorption tail in the higher wavelength.

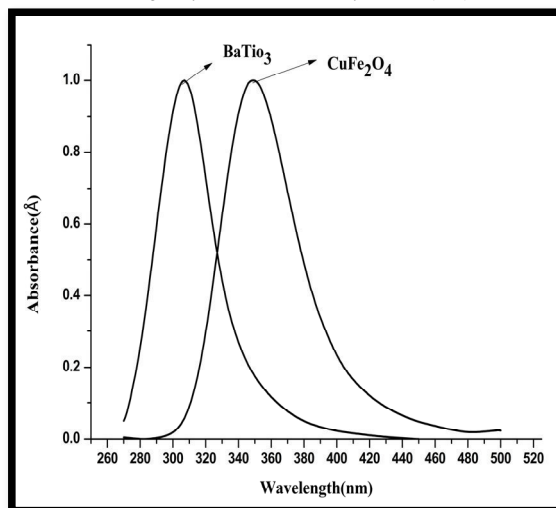


Fig. 8. UV-Vis spectra of CuFe_2O_4 and BaTiO_3 nanomaterials

3.7 Antibacterial activity

Observed antibacterial results of the prepared BaTiO_3 and CuFe_2O_4 samples are given in **Table 2** and results are represented graphically in **Fig. 9**. It is observed from the table that; the samples show good activity at higher concentration in comparison with standard drug.

Table 2. Antibacterial results of BaTiO_3 and CuFe_2O_4 samples

Sl.No	Name of the samples	Conc. ($\mu\text{g/ml}$)	<i>S. aureus</i> (mm)	<i>B. subtilis</i> (mm)	<i>S. Typhi</i> (mm)	<i>Pseudomonas A</i> (mm)
1	BaTiO_3	25	0	0	0	0
	CuFe_2O_4		0	0	0	0
2	BaTiO_3	50	3	4	4	4
	CuFe_2O_4		4	6	5	5
3	BaTiO_3	75	9	10	9	10
	CuFe_2O_4		10	10	10	11
4	BaTiO_3	100	12	12	12	13
	CuFe_2O_4		12	13	12	12
5	BaTiO_3	200	12	13	13	13
	CuFe_2O_4		14	14	14	14
6	Gentamycin (Standard)	100	15mm	15	15	15

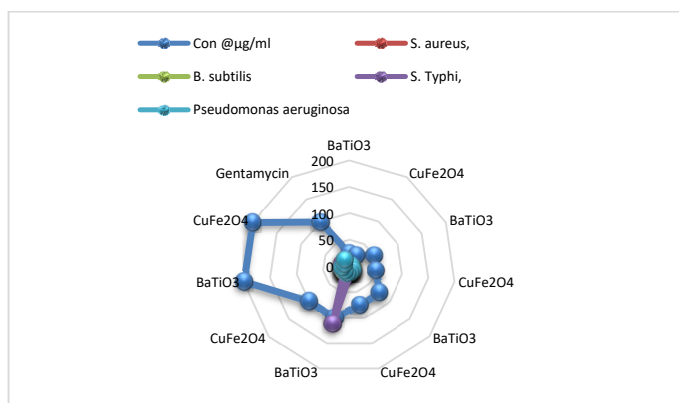


Fig. 9. Graphical representation of antibacterial activity of CuFe_2O_4 BaTiO_3 nanomaterials

In addition, both the samples show the same activity range for all bacteria at the same concentration. The increasing use of nanoparticles (NPs) in medicine has led to an enhanced number of studies declaring the potential antibacterial mechanisms of NPs against bacteria. The nanosized sample materials are made in contact with bacterial cells to achieve their antibacterial functional performance. The acceptable forms of contact include electrostatic attraction³⁹ van der Waals forces⁴⁰, receptor–ligand⁴¹ and hydrophobic interactions⁴². From the mentioned figure, it is also observed that antimicrobial activity was performed to understanding the molecular biology mechanism associated with the bactericidal action of BaTiO_3 and CuFe_2O_4 nanomaterials. In comparison, CuFe_2O_4 nanomaterials exhibited good antibacterial results compared to nanosized BaTiO_3 sample. The reason is that the combination of copper and iron oxide nanomaterials can adhere to the

surface of bacterial cells to produce ROS and damage the composition as well as structure of the cell membrane⁴³. There by interfering with the function of the cell membrane and causing leakage of cellular contents, resulting in bacterial death.

3.8 Antifungal activity

The growths of the tested fungal species were significantly inhibited by the synthesized nanoparticles. From the obtained results it is confirming that the MIC of the tested fungal species was at $100 \mu\text{g mL}^{-1}$. The observed antifungal activity results are given in table-3 and results are represented graphically in figure 10. The table clearly indicated that the CuFe_2O_4 nanomaterials exhibited good antifungal activity compared to BaTiO_3 nanomaterials. Both the samples show good antifungal activity at higher concentration in comparison with standard drug. Further, both fungi show the same activity range for respective concentration. CuFe_2O_4 nanomaterials would allow a higher level of penetration of free radicals or ions causing cell death at lower concentrations⁴⁴. Nanomaterials with the smaller size can interact quickly with the cell wall and membrane causing leakage of genetic materials, proteins, and minerals that finally result in cell death⁴⁵.

Table 3. Antifungal activity results of BaTiO_3 and CuFe_2O_4 samples

Sl. No.	Sample	Conc. ($\mu\text{g/ml}$)	Anti-fungal <i>Aspergillus niger</i> (mm)	<i>Fusarium. S</i> (mm)
1	BaTiO_3	25	4	5
	CuFe_2O_4		4	5
2	BaTiO_3	50	6	6
	CuFe_2O_4		6	6
3	BaTiO_3	75	7	9
	CuFe_2O_4		8	11
4	BaTiO_3	100	9	10
	CuFe_2O_4		9	12
5	BaTiO_3	200	11	10
	CuFe_2O_4		10	11
6	Nystatin (standard)	100	12	12

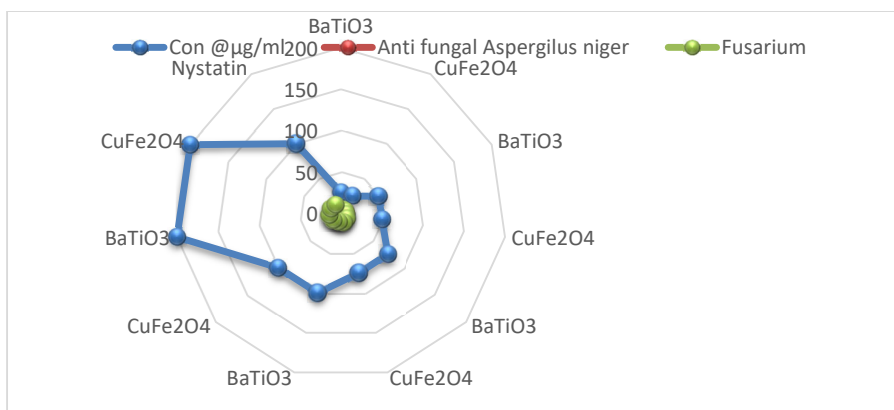


Fig. 10. Graphical representation of antifungal activity of CuFe_2O_4 and BaTiO_3 nanomaterials

4. Conclusions

The successful synthesis of nanosized copper ferrite and barium titanate is achieved by combustion route with PVA as a fuel. This self-propagating solid state combustion reaction achieved the phase formation of bimetallic oxide samples with simple experimentation. This method may be one of the prominent routes for the synthesis of other bimetallic oxide nanomaterials like perovskites. The synthesized nanoparticles showed potent antibacterial and antifungal activities against the tested pathogens. Consequently, the synthesized CuFe_2O_4 nanoparticles showed better activity compared to BaTiO_3 nanomaterials. Results of the current study reflect that CuFe_2O_4 can be better explored soon for various biomedical, industrial, and agricultural applications. Moreover, the high yield of the copper ferrite nanoparticles achieved in the present study could open up the way for the manufacture of nanoparticles at an industrial scale using a cost-effective and eco-friendly methodology.

Acknowledgement

Authors thank DST-FIST (SR/FST/CSI-003/2016) grant provided for instruments and infrastructure facilities to VSK University, Ballari. Thanks are due to Prof. A.Venkataraman, Professor, Department of Chemistry, Gulbarga University, Kalaburagi, Karnataka, India for useful discussion in spectral analysis.

References

1. Ngonidzashe Masunga., Olga Kelebogile Mmesile., Kebede K. Kefeni., Bhokie B. Mamba. **(2019)** Recent advances in copper ferrite nanoparticles and nanocomposites synthesis, magnetic properties and application in water treatment: Review, *J. Env.Chem.Engg.* 7(3), 103179.
2. Faten Haithum Mulud., Najat A., Dahham., Ibrahim F., Waheed. **(2020)** Synthesis and characterization of copper ferrite nanoparticles, *IOP Conf. Ser. Mater. Sci. Eng.* 928, 072125.
3. Pragnesh Dave N., Thakkar R., Ruksana Sirach., Shalini Chaturvedi. **(2022)** Effect of copper ferrite (CuFe_2O_4) in the thermal decomposition of modified nitrotriazolone, *Mater. Adv.*, 3, 5019 – 5026.
4. Tarun Kumar Barik., Gopal Chandra Maity., Pallavi Gupta., Mohan L., Tuhin Subhra Santra. **(2021)** Nanomaterials: An Introduction, *Nanomaterials and their Biomedical Applications*, 1, 27.
5. Velinov N., Petrova T., Ivanovna., Tsoncheva T., Kovacheva D., Mitov I. **(2021)** Synthesis Mossbauer study and catalytic properties of Cu-Ni-Fe- oxide/nitride mixed-phase materials, *Hyperfine Interact.*, 242, 1-12.
6. Wang W., Guo S., Zhang D., Yang Z. **(2019)** One-pot hydrothermal synthesis of reduced graphene oxide/zinc ferrite nano hybrids and its catalytic activity on the thermal decomposition of ammonium perchlorate, *Journal Saudi Chem. Soc.*, 23, 133-140.
7. Pham T. N., Huy T. Q. **(2020)** Spinel ferrite (AF_2O_4)-based hetero-structured designs for lithium-ion battery environmental monitoring and biomedical applications, *RSC*, 10, 31622-31631.
8. Chen Q. W. D., Wang R., Shen G. **(2015)** Ternary oxide nanostructured materials for supercapacitors a review, *J. Mater. Chem. A*, 3, 10158 – 10173.
9. Yang Z., Zhang Z., Jiang Y., Chi M., Nie G., Lu X., Wang C. **(2016)** Palladium nanoparticles modified electro spun CoFe_2O_4 nanotubes with enhanced peroxidase-like activity for colorimetric detection of hydrogen peroxide, *RSC Adv*, 6, 33636 -33642.
10. Abu-Hani A. F. S., Mahmoud S. T., Awwad F., Ayesh A. I. **(2017)** Design fabrication and characterization of portable gas sensors based on spinel ferrite nanoparticles embedded in organic membranes, *Sens. and Actuators, B*, 214, 1179 – 1187.
11. Peebles B., Goornavar V., Peebles C., Spence D., Parker V., Bell C., Biswal D., Ramesh G. T., Pradhan A. K. **(2014)** Structural, stability, magnetic, and toxicity studies of nanocrystalline iron oxide and cobalt ferrites for biomedical applications, *J. Nano part. Res.*, 16, 2290.
12. Kim H., Lee J. W., Byun D., Choi W. **(2018)** Coaxial-nanostructured MnFe_2O_4 nanoparticles on polydopamine-coated MWCNT for anode materials in rechargeable batteries, *Nanoscale*, 10, 18949 – 18960.
13. Galvao W. S., Neto D. M. A., Freire R. M., Fachine P. B. A. **(2015)** Super-Paramagnetic nanoparticles with spinel structure: A Review of synthesis and biomedical applications, *Solid State Phenom.*, 241, 139 – 176.
14. Kumar M., Singh Dosanjh H., Sonika Singh J., Monir K., Singh H. **(2020)** Review on magnetic nano ferrites and their composites as alternatives in waste water treatment: synthesis, modifications and applications, *Environ. Sci. Water Res. Technol.*, 6, 491 – 514.
15. Elango Balaji T., Himadri Tanaya Das., Maiyalagan T. **(2021)** Recent trends in bimetallic oxides and their composites as electrode materials for super-capacitor applications, *Electro Chem.* 8(10), 1723 – 1717.
16. Diaz C., Valenzuela M. L., Laguna-Bercero M. A. **(2022)** Solid-state preparation of metal and metal oxides nanostructures and their application in environmental remediation, *Int. J. Mol. Sci.* 23, 1093.
17. Diaz C., Valenzuela M. L., Garcia C., Campa De la R., Soto A. P. **(2017)** Solid-state synthesis of pure and doped lanthanides oxide nanomaterials by using polymer templates. Study of their luminescent properties. *Mater. Lett.* 209, 111 – 114.
18. Ray C., Pai T. **(2017)** Recent advances of metal–metal oxide nanocomposites and their tailored nanostructures in numerous catalytic applications, *J. Mater. Chem.*, 5, 9465 – 9478.
19. Yattinahalli S. S., Kapatkar S. B., Ayachith N. H. **(2013)** Synthesis and structural characterisation of nanosized nickel ferrite, *International Journal of Self Propagating High Temperature Synthesis*, 22, 147-150.
20. Maleki A., Hajizadeh Z., Salehi P. **(2019)** Mesoporous halloysite nanotubes modified by CuFe_2O_4 spinel ferrite nanoparticles and study of its application as a novel and efficient heterogeneous catalyst in the synthesis of pyrazolopyridine derivatives, *Sci. Rep.* 9, 5552.
21. Mirzaei M., Habibi M. H., Sabzyan H. **(2022)** Synthesis characterization and dye degradation photocatalytic activity of the nano-size copper iron binary oxide, *Environ Sci. Pollut. Res.*, 29, 9173 – 9192.
22. Kamel A. H., Hassan A. A., Amr A. E., El-Shalakany H. H., Al-Omar M. A. **(2020)** Synthesis and characterization of CuFe_2O_4 nanoparticles modified with Polythiophene: applications to mercuric ions removal, *Nanomaterials*, 10, 586 – 598.
23. Younes A., Kherrouba N., Bouamer A. **(2021)** Magnetic optical structural and thermal properties of copper ferrite nanostructured synthesized by mechanical alloying, *Micro Nano Lett.*, 16, 251 - 256; DOI; <https://doi.org/10.1049/mna2.12040>.
24. Qin Q., Liu Y., Li X., Suna T., Xu Y. **(2018)** Enhanced heterogeneous Fenton-like degradation of methylene blue by reduced CuFe_2O_4 , *RSC Adv*, 8, 1071.

25. Anandan S., Selvamani T., Asiri A. M., Wu J. J. (2017) Magnetic and catalytic properties of inverse spinel CuFe_2O_4 nanoparticles, *J. Mag. J. Mater*, 15, 437- 443.
26. Ahamed M., Akhtar M. J., Khan M. A. M., Alhadlaq H. A., Alshamsan A. (2020) Barium Titanate (BaTiO_3) nanoparticles exert cytotoxicity through oxidative stress in human lung carcinoma (A549) cells. *Nanomaterial's (Basel)*. 10(11), 2309.
27. Genchi G., Attilio Marino., Antonella Rocca., Mattoli V., Ciofani G. (2016) Barium titanate nanoparticles: promising multitasking vectors in nanomedicine, *Nanotechnology*, 27(23), 27 – 35.
28. Wen-Bo Li., Di Zhou., Ran Xu., Da-Wei Wang., Jin-Zhan Su., Li-Xia Pang., Wen-Feng Liuand., Guo-Hua Chen. (2019) BaTiO_3 -Based multilayers with outstanding energy storage performance for high temperature capacitor applications, *ACS Appl. Energy Mater*, 2(8), 5- 5506.
29. Huijing Yang., Weichao Bao., Zhilun Lu., Linhao Li., Hongfen Ji., Yuhe Huang., Fang fang Xu., Ge Wang., Dawei Wang. (2021) High-energy storage performance in BaTiO_3 -based lead-free multilayer ceramic capacitors, *Journal of Materials Research*, 36(6), 1285-1294.
30. Fakhar-e-Alam M., Samira Saddique., Nazia Hossain., Aamir Shahzad., Inaam Ullah., Amjad Sohail., Muhammad Junaid Iqbal Khan., Malik Saadullah. (2023) Synthesis characterization, and application of BaTiO_3 nanoparticles for anti-cancer activity, *Journal of Cluster Science*, 34, 1745-1755.
31. Jordan T., Mikaela O Brien A., Catalina-Paula., Spatarelu., Geoffrey P., Luke. (2020) Antibody-conjugated barium titanate nanoparticles for cell-specific targeting. *ACS Appl. Nano Mater*. 3, 2636 – 2646.
32. Arunkumar Lagashetty., Amrutha Pattar., Sangappa K Ganiger. (2019) Synthesis characterization and antibacterial study of Ag doped magnesium ferrite nanocompoiste, *Helvion* 5, e01760.
33. Zuhair S., Abeer A., Kassem Ragwa., Mohamed Farad., Shaimaa Khamis Mostafa., Gihan Salah Labib. (2022) Nano-carrier drug delivery systems: characterization, limitations, future perspectives and implementation of artificial intelligence, *Pharmaceutics*. 18, 14(4), 883.
34. Arunkumar Lagashetty., Sangappa K. Ganiger., Preeti R. K., Shashidhar Reddy., Malathesh Pari. (2020) Microwave-assisted green synthesis, characterization and adsorption study of metal oxide nanoparticles by *Ficus Benghalensis* plant leaf extract, *New Journal of Chemistry* 14(33), 14095 – 14102.
35. Mounesh T. M., Sharankumar N.Y., Praveen Kumar K. R., Venugopala Reddy K. B., Chandrakala., Arunkumar L., Vidyasagar C. C. (2021) Novel Schiff base cobalt (II) Phthalocyanine with appliance of MWCNTs: Enhanced electro-catalytic activity behaviour of α -amino acids, *RSC Advances*. 11, 16736-16746.
36. Arunkumar Lagashetty., Vibhav Mittin., Manjunath K. Patil., Sangappa K. Ganiger. (2020) Synthesis, Characterization and Studies of BaFe_2O_4 /PMMA nanocomposites, *Polymer Bulletin*, 78(10), 5905 – 5921.
37. Synkiewicz-Musialska B., Kulawik J., Czerwińska E., Pałka N. (2023) Novel copper borate ceramics with lithium-based sintering aids for LTCC terahertz applications, *J. Mater. Chem. C*, 11, 1863 – 1871.
38. Szwagierczak D., Synkiewicz-Musialska B., Kulawik., Czerwińska E., Pałka N., Bajurko P. (2020) Low temperature sintering of $\text{Zn}_4\text{B}_6\text{O}_{13}$ based substrates, their microstructure and dielectric properties up to the THz range, *Journal of Alloys and Compounds*, 819(5), 153025.
39. Chen Li H., Zhao Q. J., Urmila K. (2015) Enhancing the antimicrobial activity of natural extraction using the synthetic ultra-small metal nanoparticles. *Sci Rep*. 5, 11033.
40. Ilaria Armentano., Carla Renata Arciola., Elena Fortunati., Davide Ferrari., Samantha Mattioli., Concetta Floriana Amoroso., Jessica Rizzo., Jose M Kenny., Marcello Imbriani., Livia Visai. (2014) The interaction of bacteria with engineered nanostructured polymeric materials: a review. *Scientific World J*. 5, 410423.
41. Gao W., Thamphiwatana S., Angsantikul P., Zhang L. (2014) Nanoparticle approaches against bacterial infections. *Wires Nanomed Nanobi*. 6(6), 532 – 547.
42. Luan B., Huynh T., Zhou R. (2016) Complete wetting of graphene by biological lipids, *Nanoscale*, 8(10), 5750 - 5754; DOI: <https://doi.org/10.1039/C6NR00202A>
43. Foster H. A., Ditta, I. B., Varghese S., Steele A. (2011) Photocatalytic disinfection using titanium dioxide: spectrum and mechanism of antimicrobial activity. *Appl Microbiol Biotechnol*. 90(6), 1847 – 1868.
44. Ismail R. A., Suliman G.M., Abdurrahman S. A., Marzoog T. R. (2015) Antibacterial activity of magnetic iron oxide nanoparticles synthesized by laser ablation in liquid, *Mater. Sci. Eng. C*, 53, 286 – 297.
45. Hamilton D., Jones S. K., Orr Mallapragada., Narasimhan B., Canfield P. C., Prozorov R. (2007) Cobalt ferrite nano crystals: out-performing magneto tactic bacteria, *ACS Nano*, 1, 228 – 233.





Surface Functionalization of Silver Nanoparticles by 4-Amino, 3, 5-Dimercapto, 1, 2, 4 Triazole for Improved Intracellular Uptake and Biocompatibility

V. Veena¹ · K. H. Shivaprasad² · K. S. Lokesh² · H. Sharanagouda³

Accepted: 31 October 2023 / Published online: 30 November 2023

© The Author(s), under exclusive licence to Springer Science+Business Media, LLC, part of Springer Nature 2023

Abstract

In this study, novel chemically reduced silver nanoparticles (AgNPs) were functionalized with new 4-amino, 3, 5-dimercapto, 1, 2, 4 triazole (DMT) moiety. Nucleation and formation of the functionalized silver nanoparticles was monitored using UV–Vis absorption spectroscopy. UV/Vis-spectroscopy, zeta-potential, XRD, SEM, TEM, and FTIR analysis techniques confirmed the functionalization of AgNPs by DMT ligand having particle sizes 50–51 nm. The dimercapto-functionalized silver nanoparticles (DMT-AgNPs) showed high antibacterial activity against Gram-positive and Gram-negative bacteria. We found that the DMT-AgNPs had the potential to inhibit growth with cell cycle arrest and increased apoptosis of MCF-7 cancer cell in dose-dependent manner with an IC₅₀ value of 18.46% v/v. Our results showed that the DMT-AgNPs inhibited cancer cell line proliferation with a mechanism of action similar to that of other tubulin inhibitors. It is interestingly observed that the newly developed DMT-AgNPs are reliable safe and biocompatibility, hence could be used viable in the treatment of diseases with high accuracy in a patient-friendly manner compared to AgNPs and can be used as potent therapeutic agent in future.

Keywords Silver nanoparticles (AgNPs) · Dimercapto-triazole-functionalized silver nanoparticles (DMT-AgNPs) · Antibacterial · Anticancer properties

1 Introduction

Over the years, it has been witnessed an unprecedented growth in the area of nanotechnology and nanomedicine with the development of novel nanocomposites. These deal with manipulation of materials at atomic/molecular level [1] into a new range of products for advanced biomedical applications [2]. Nanomedicine field had visualized the next door for the ongoing development of theranostic systems like biological labeling, imaging [3], biosensing [4], antimicrobial activity [5], detection, designed as drugs carrier

genetic disorders, gene therapy, and DNA sequencing [6], and elimination of cancer cells before they form tumors [7]. In fact, nanocomposites of free metals, with their unique physical and chemical properties in combination with modern technology, play a tremendous role in overcoming many of the problems that conventional methods face in sensing, diagnosis, treatment, and detection of deadly diseases [8].

Among all metallic nanoparticles, silver nanoparticles (AgNPs) which possess higher level of therapeutic activity with lower toxicity rather than their counterparts (metal salts) have tremendous applications in photography [9], catalysis [10], biosensor [11], biomolecular detection [12], diagnostics [13], and particularly antimicrobial studies [14–16]. Thus, they are extensively used for developing unique therapeutic methodologies like treatment of multi-drug resistant microorganisms (bacteria, yeast, and fungi) [17], cancer treatments [18], drug delivery system, coating of medical equipments, food packaging materials, wound dressings bandages, gloves, textile fabrics [19, 20], wood flooring, and various wound healing gels to preventing infections due to their anti-microbial properties [21]. A number of methods were used in the past for the synthesis of AgNPs,

✉ V. Veena
veenaraj138@gmail.com; veena138n@gmail.com

¹ Department of Chemistry, Ballari Institute of Technology and Management, Ballari, India

² Department of Chemistry, Vijayanagara Sri Krishnadevaraya University, Ballari, India

³ Department of Processing and Food Engineering, College of Agricultural Engineering, University of Agricultural Sciences, Raichur, India

for example, reduction in solutions [22], radiation assisted [23] chemical and photo-reduction in reverse micelles [24], thermal decomposition of silver compounds [25], and recently via bio- or green-synthesis route [26, 27]. Chemical reduction is the most frequently applied method for the preparation of silver nanoparticles (AgNPs) as colloidal dispersions in water or organic solvents because chemical reduction of silver precursor salts in solution offers higher yield, easier production, and lower costs compared to other methods [28]. Reduction of silver (I) salts by chemical methods progress through a one-step process producing a colored sol as metal surface has free electrons in the conduction band and positively charged nuclei, thus forming long-lived clusters of AgNPs. Different shapes and sized AgNPs can be synthesized using several reducing agents [29–32].

Sodium borohydride reduction (a strong reductant) usually results in an average monodispersed smaller sized AgNPs while citrate (a weaker reductant) usually results poly-dispersed larger sized AgNPs due to slower reduction rate [33]. The smaller sized AgNPs formed using excess sodium borohydride are temporarily stabilized by BH_4^- species that forms a shell of excess borohydride anion around AgNPs. However, with time, this shell collapses due to the degradation of BH_4^- accompanied by hydrogen gas evolution [34], and nanoparticles start to aggregate. Therefore AgNPs synthesized by chemical reduction methods are often performed in the presence of stabilizers in order to prevent unwanted agglomeration of the colloids. AgNPs that are free from agglomeration make them ideal for research, development, and use in a variety of innovative applications. Thus, the great therapeutic potential of AgNPs which relies on the amazing chemo-physical versatility, which is achievable either by reducing the size in order to maximize the surface atoms number or surface modifications using certain appropriate ligands [35]. Ligands act like capping agents by forming a protective shell around nanoparticles. This stops further aggregation, thereby increasing the stability and make suitable for medical applications.

Ligands with certain functional groups like thiols, amines, phosphines, carboxylates, and polymers easily get conjugated to the noble metal nanoparticles through non-covalent and covalent interactions. Therefore, ligands can be successfully used as stabilizers/functionalizers to bring the surface modifications [35]. Ligand functionalization of AgNPs can be brought through a variety of techniques that includes physical adsorption, chemisorptions, electrostatic adsorption (electrostatic binding), and affinity-based (specific recognition and covalent coupling) method [36]. In fact, the key feature for nanoparticle functionalization is that their surface which is imperfect, results in defective sites corresponding to the vertices or edges and one non defective site (terrace or face) for binding of ligands [37, 38]. Defective and non defective sites have different electron densities and steric behavior and hence exhibit different reactivity with different functional groups

[37]. Thus, capping/functionalization of nanoparticles allows them to tune the material properties to promote their applications [39]. Recently, these immobilization techniques have been applied to bring biologically active ligands/drugs and nanoparticles together for advanced biomedical applications.

Heterocyclic chemistry always plays a major role in synthetic organic chemistry especially as efficient drug candidates. In fact, interestingly, more than 90% of new drug molecules, intermediates, other bio-molecules, and their derivatives in different forms are heterocyclic compounds [40]. Especially, interesting group of heterocyclic compounds such as triazole have been paid special attention due to their potential applications as medicinal agents, agro-chemicals, supramolecular ligands, biomimetic catalysts, etc. [41]. Both 1, 2, 4-triazoles and 1, 2, 3-triazoles and their derivatives in chemistry have wide spectrum of biological activities [41]. Indeed, among 1,2,4-triazole derivatives, mercapto and thione substituted ring structures are used in construction of promising novel bio-molecules that possess antiviral [42], antifungal [43], antibacterial [44], anti-inflammatory activity, anticonvulsant, antidepressant [45], and antitumor activities [46]. They also exhibit antimalarial, analgesic properties and owe in therapeutic applications as central nervous system stimulants [47]. Triazole is an electron rich system possessing aromaticity with five-membered ring structure containing three nitrogen and sulfur atoms. Thus, the unique structural arrangement endows triazole and its derivatives to readily bind with a variety of enzymes and receptors in biological system and display a broad spectrum of biological activities [48]. Greater pharmacological activities of triazole derivatives are also due to structural properties such as hydrogen bonding, reasonable dipole character, inflexibility, and their stability under in vivo environments [49]. Innovative biofunctional drug molecules can be produced using triazole moiety as a linker to combine different pharmacophore fragments which provides efficient pathway for developing new bioactive functional molecules [50].

Currently, researchers in scientific community are showing increasing interest to develop new routes, methods, and modifications for both synthesis and applications adjoining nanoparticles and heterocyclic moieties. In this context, introducing biologically active ligand functionality to the surface of AgNPs and deeper investigation of nanomaterial structures to test the biocompatibility are the critical aspects of the present study with an aim to improve its therapeutic applications. The current study reports the synthesis of 4-amino,3,5-dimercapto, 1,2,4 triazole (DMT) ligand-functionalized novel silver nanoparticles, characterization, and evaluation of antimicrobial and antitumor activity against MCF-7 cell lines that highlights its in vivo efficacy, so that the DMT-functionalized AgNPs can be considered for the biomedical applications and used in efficient drug delivery systems in near future.

2 Experimental Details

2.1 Chemicals, Cell Lines, and Microorganisms

All chemicals used were of laboratory grade and used without further purification. Purity of the compound was confirmed by the values given on the reagent bottles. The carbon disulphide (96%), hydrazine hydrate (97%), salicylaldehyde (98%), conc. H_2SO_4 (96%), hydrochloric acid (95%), acetic acid (97%), pyridine (96%), silver nitrate, sodium borohydride, and 3-(4,5-dimethylthiazole-2-yl)-2,5-diphenyltetrazolium bromide (MTT) were purchased from Sigma-Aldrich Ltd. The bacterial strains were procured from the Microbial Type Culture Collection, Institute of Microbial Technology, Chandigarh, India. The MCF-7 cell lines were obtained from National Centre for Cell Science, Pune, India. For cell culture, RPMI-1640 culture medium and fetal calf serum (FCS) were purchased from HiMedia.

2.2 Synthesis of AgNPs

The glasswares used for the preparation of AgNPs were cleaned with aquaregia (3:1 HCl/HNO_3), rinsed several times with double distilled water, and dried. AgNPs were synthesized by reducing silver nitrate with large excess of ice-cold sodium borohydride, which not only reduces the ionic silver but also stabilizes the formed nanoparticles [51, 52]. Thus, 30 mL of 0.002 M sodium borohydride (NaBH_4) was added to a flask incubated in dark, placed in an ice bath on a stir plate with a magnetic bead for about 20 min. Ice bath was used to slow down the reaction with a hope to gain better control over final particle size and shape. Two milliliters of 0.001 M silver nitrate (AgNO_3) was dripped into the NaBH_4 solution at approximately 1 drop per second with continuous stirring until; all AgNO_3 were reduced and clustered to form mono-dispersed

AgNPs as a transparent yellow colored solution in the aqueous medium.

2.3 Synthesis of AgNPs Using 4-Amino, 3,5-Dimercapto-1,2,4 Triazole (DMT) as Stabilizing Agent

4-Amino-3, 5-dimercapto-1, 2, 4-triazole (DMT) was prepared by using literature report [53, 54]. Thirty milliliters 0.001 M DMT solution was dripped to ice-cold AgNPs sol at approximately 1 drop per second using a syringe with continuous stirring. For complete stabilization and ligand exchange, the above prepared solution was kept at least for 18 h in dark with continuous stirring. The color of the solution turns to dark yellow from pale yellow (AgNPs), which indicated the formation of DMT-functionalized AgNPs (DMT-AgNPs) (Fig. 1).

2.4 Antimicrobial Assays

The antimicrobial susceptibility of newly synthesized DMT-AgNPs was evaluated using the disc diffusion method [55]. Muller Hinton agar media for antibacterial activity was prepared, sterilized, and aseptically transferred to Petri plates. These Petri plates containing media were solidified and later incubated overnight to confirm that the Petri plates are free from contamination. These Petri plates were first inoculated with test organisms and then disc-containing test samples were loaded. Zones of inhibition were measured using Hi media scale after 24 h of incubation at 37 °C. The comparative stability of discs containing gentamicin and nystatin was analyzed simultaneously to evaluate their antibacterial susceptibility. All the experiments were performed in triplicate, and results are recorded as mean \pm standard deviation.

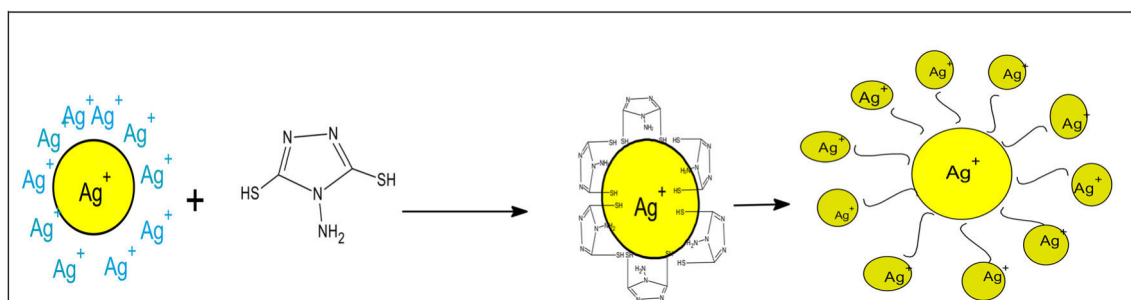


Fig. 1 Functionalization of AgNPs by 4-amino,3,5-dimercapto-1,2,4 triazole

2.5 In Vitro Study of Dimercapto-Triazole-Functionalized AgNPs (DMT-AgNPs)

The cytotoxicity study of synthesized DMT-AgNPs was tested on MCF-7 (breast cancer) cell lines by the reduction assay of tetrazolium salt (dye) [56]. The cells were cultured and then harvested such that 200 μL of each suspension contained approximately 15,000 cells. The cells were treated with 200 μL of increasing concentrations of DMT-AgNPs (0.1, 0.5, 1.0, 5.0, 10, and 20% v/v) from stock sol and incubated at 37 $^{\circ}\text{C}$ in 5% CO_2 atmosphere for 24 h and 48 h. Later, 200 μL of 10% MTT reagent was added to each well to get a final concentration of 0.5 mg/mL, and the plates were incubated at 37 $^{\circ}\text{C}$ in 5% CO_2 atmosphere for 24 h and 48 h. The resulting blue colored formazan product formed was dissolved in 100 μL dimethyl sulfoxide (DMSO) solvent, and the absorbance was measured at a wavelength of 570 nm. The absorbance of untreated cells was used as control (100% viable). Cis-platin was used as the standard anti-cancer drug for MCF-7 cell lines with an IC_{50} value of 25 $\mu\text{g/mL}$. Each experiment was performed in triplicate. The percentage growth inhibition was calculated, after subtracting the background and the blank. Concentration of test drug needed to inhibit cell growth by 50% (IC_{50}) was generated from the dose–response curve for the cell line.

3 Characterization

The formation of AgNPs and DMT-AgNPs were characterized by UV–visible spectrometer (Perkin Elmer, Lambda 35, Germany). Mean particle size and zeta potential (ξ) of the colloidal sol were investigated by dynamic light scattering (DLS) technique using a Zeta size analyzer (Nano ZS 90, Malvern Instruments Ltd., UK). Freeze-dried powders were

subjected to X-ray diffraction pattern analysis on a powder diffractometer (Rigaku theta-theta type) which was operated at 40 kV voltage, 30 mA current, 20 to 80 (2θ) range. Microphotographs were obtained using transmission electron microscope TEM (Philips model CM 200 instrument operated at an accelerating voltage at 200 kV) and scanning electron microscope SEM (Carl Zeiss Microscopy, EVO 10, Germany) in order to determine the size and morphology. Samples for analysis were prepared by placing drops of AgNPs and DMT-AgNPs solution on carbon-coated tape which was pasted on TEM and SEM grids and were then allowed to dry for 2 min, the extra solution was removed using a blotting paper. Further, secondary electron sputtering at an applied potential of 20 kV was adopted prior to the recording of SEM images. Fourier transform infrared (FTIR) spectra were recorded on a Vertex 70 spectrometer with KBr pellets (Bruker Corporation, Billerica, MA, USA). The cytotoxicity (MTT) assays were performed in 96-well plate, and absorbance was measured on microplate reader (Multiscan, Thermo Scientific).

4 Results and Discussion

4.1 UV–Visible Absorption Spectra Analysis

The formation of AgNPs and DMT-AgNPs by the reduction of the Ag^+ ions in solution was monitored by periodical sampling of aliquots of the reaction as a function of time and recording the UV–Visible spectrum in the range 200–600 nm operated at a resolution of 1 nm. Distilled water was used as blank.

The optical absorption spectra of metal nanoparticles are dominated by surface plasmon resonance at 420 nm for AgNPs, i.e., the energy of absorption depends on the degree of plasmon resonance which may shift either side of this

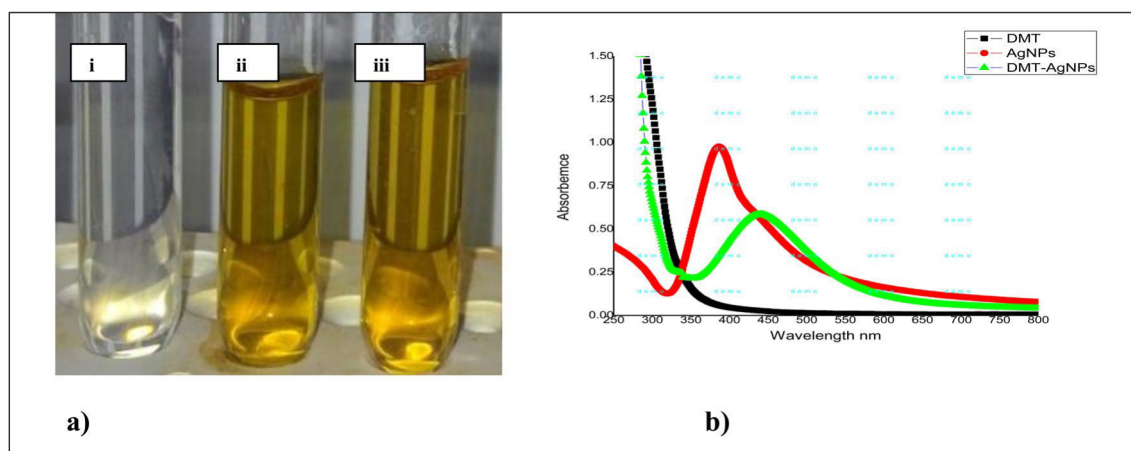


Fig. 2 **a** Color for (i)DMT, (ii)AgNPs, and (iii)DMT-AgNPs. **b** UV–Vis spectra of DMT, AgNPs, and DMT-AgNPs

value depending on the ratio of silver ions and zero-valent silver [57]. The spectroscopic observation indicates that the chrome yellow solution of AgNPs was formed (Fig. 2a) due to the reduction of Ag^+ to Ag^0 and the absorption peak at 420 nm for AgNPs shifted to longer wavelength (red shift) 440 nm which may be due to the increase in the particle size of DMT-AgNPs (Fig. 2b). There was no further aggregation, and the peak position was stable even after 18 h. The silver colloidal particles possess negative charge at first due to the adsorbed BH_4^- ions which dissolves slowly and later forms -SH capping [34]. The position and shape of the plasmon absorption of nanoparticles are strongly dependent on the particle size, dielectric constant, and surface adsorbed species which was further confirmed by zeta size and potential studies.

4.2 Particle Size and Zeta Potential (ξ) Analysis

Zeta potential (ξ) also known as surface potential along with the mean particle size distribution governs the other

characters such as, saturation solubility, dissolution velocity, physical stability, and even biological performances of synthesized nanoparticles [58]. Mean particle size and zeta potential of the colloidal AgNPs and DMT-AgNPs were measured directly after synthesis, using dynamic light scattering spectroscopy (DLS) (Fig. 3), and Table 1 gives the values of the obtained results.

The average particle size (z -average) was found to be 20–21 nm for uncapped AgNPs and 50–51 nm for DMT-AgNPs. Zeta potential of minimum +30 mV is required for the indication of stable AgNPs [59]. Zeta potential (ξ)/surface potential values measured were found to be –24.8 mV for AgNPs (Fig. 3a) and –27.1 mV for DMT-AgNPs (Fig. 3b), with a peak area of 100% intensity. The high negative value of zeta potential (ξ) and mobility values as seen from Table 1 supports long-term stability, good colloidal nature, and high dispersity of the synthesized AgNPs and DMT-AgNPs. The particle size of the synthesized nanoparticles was further confirmed by the XRD analysis.

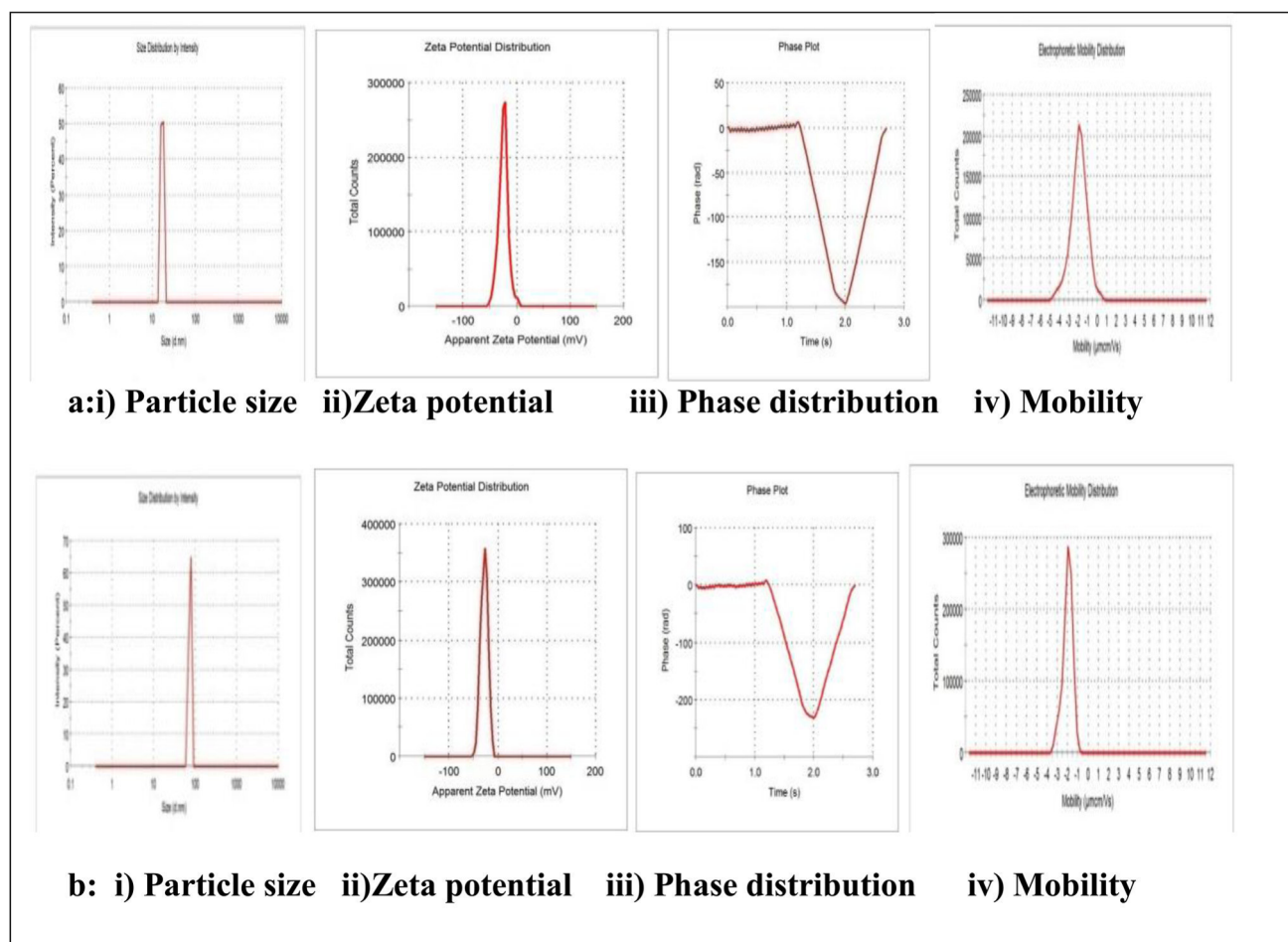


Fig. 3 Zeta particle size, phase distribution, and mobility images of **a** AgNPs and **b** DMT-AgNPs

4.3 XRD Analysis

The XRD diffraction peaks for the freeze-dried powders of the synthesized AgNPs and DMT-AgNPs areas are shown in Fig. 4. The X-ray diffraction peaks at 2θ values for both AgNPs (Fig. 4a) and DMT-AgNPs (Fig. 4b) are similar and showed peaks at 2θ values 38.012° , 45.17° , 62.489° , and 77.34° indexed as 111, 200, 220, and 311 planes of FCC of silver [60–62] at room temperature conditions. The lattices were identified by comparing the values for

interplanar spacing and relative intensities with the standard values of metal silver. The particle size of the synthesized nanoparticles were calculated using Debye-Scherrer's equation, $D = k \lambda / \beta \cos \theta$, where k is a constant value (0.96), λ is the wavelength of the X-ray, β is the full width at half maximum of the XRD peak (radians), and θ is Bragg's angle of the XRD peak. The particle size of the AgNPs was calculated to be 20–21 nm and for DMT-AgNPs 50–51 nm which were consistent with the zeta size values.

Table 1 Mean particle size diameter and zeta potential results of AgNPs and DMT-AgNPs

Sl. no	Parameters	AgNPs	DMT-AgNPs
1	Z-average (nm)	20–21	50–51
2	Zeta potential (mV)	–24.8	–27.1
3	Zeta quality	Phase and distribution data is good	Phase and distribution data meets the quality criteria
4	Electrophoretic mobility ($\mu\text{mcm/Vs}$)	–1.919	–2.200
5	Mobility deviation ($\mu\text{mcm/Vs}$)	0.8882	0.4831
6	Conductivity mS/cm	0.0993	0.188

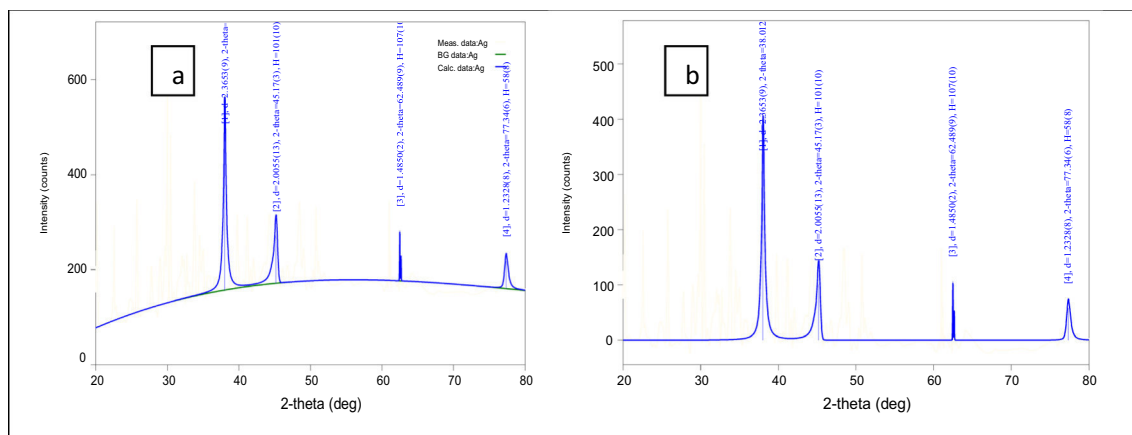


Fig. 4 XRD patterns of **a** AgNPs and **b** DMT-AgNPs

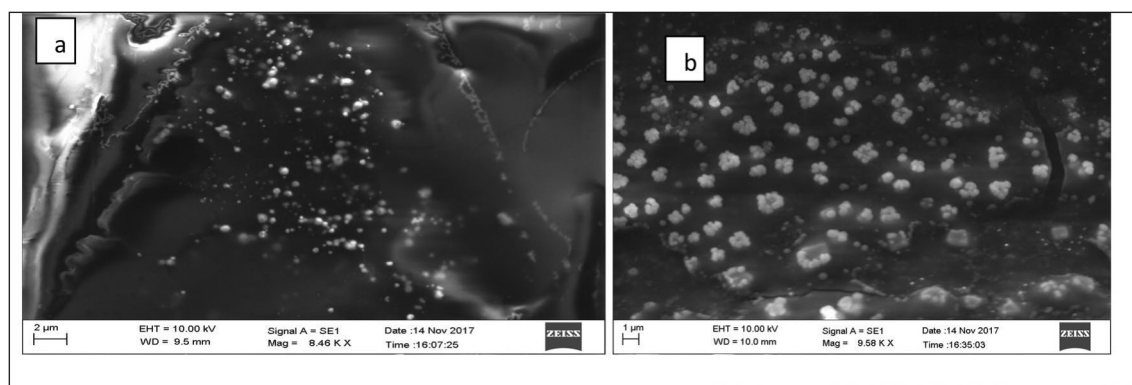


Fig. 5 SEM images of **a** AgNPs and **b** DMT-AgNPs

4.4 Scanning Electron Microscopy Analysis

Scanning electron microscopy has provided further insight into the morphology and size details of the synthesized nanoparticles. Micrographs of AgNPs and DMT-AgNPs are shown in Fig. 5a which shows SEM image with spherical AgNPs with uneven distribution of particles. The morphology of the DMT-AgNPs completely differs from AgNPs and are almost uniform and mono-dispersed without any aggregation (Fig. 5b). The separation between the nanoparticles indicates functionalization of nanoparticles by DMT which has been used as functionalizing agent.

4.5 TEM Analysis

The functionalization of DMT to AgNPs can be evidenced from the TEM studies which provide the exact size changes before and after capping AgNPs with DMT. The representative TEM picture recorded for the AgNPs and DMT-AgNPs deposited on a carbon coated copper tape

placed on TEM grid are shown in Fig. 6. Microphotographs show spherical particles of 20–21 nm (Fig. 6a) and 50–51 nm (Fig. 6b) for AgNPs and DMT-AgNPs without aggregation. The large variation in the size of AgNPs and DMT-AgNPs, i.e., difference of 30 nm, is due to the DMT which binds to AgNPs and brings the surface functionalization of nanoparticles. Both DMT-AgNPs and AgNPs are highly crystalline in nature, as seen from the selected area diffraction pattern recorded for the nanoparticles (Fig. 6a, b). Surface functionalization of AgNPs by functional groups present in the capping agent has been confirmed by FTIR studies.

4.6 Fourier Transform Infrared Spectroscopy (FTIR) Analysis

FTIR spectroscopy is useful in probing the chemical composition of the surface of the AgNPs and the local molecular environment of functionalizing agent DMT which has both free amine and thiol functional groups. There seems a

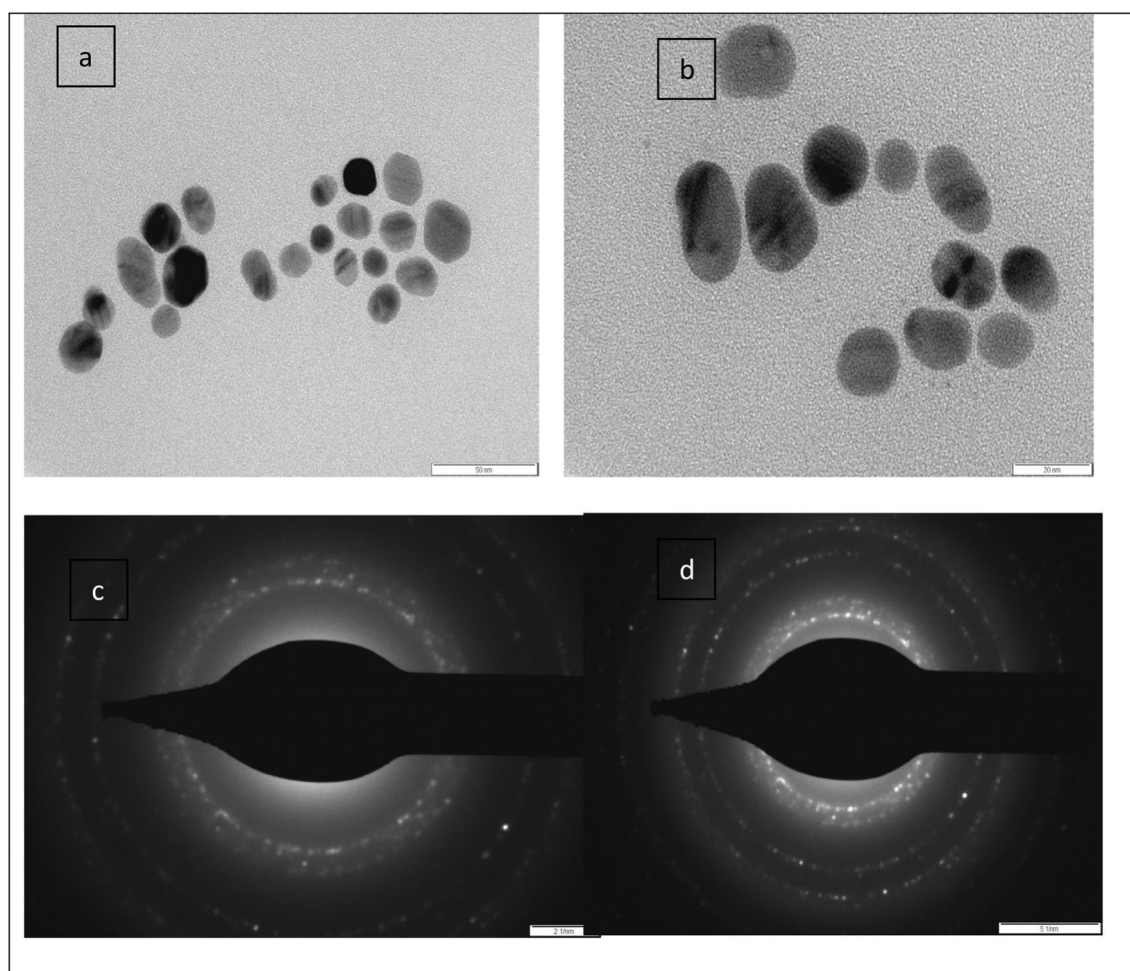


Fig. 6 TEM images of **a** AgNPs and **b** DMT-AgNPs and SAD pattern of **c** AgNPs and **d** DMT-AgNPs

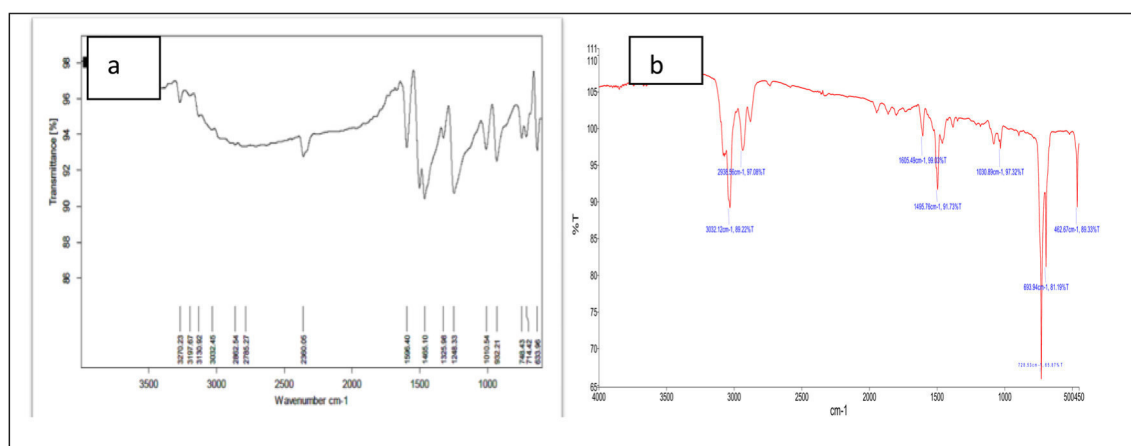


Fig. 7 **a** FT-IR Spectra of 4-amino-3,5-dimercapto-1,2,4-triazole(DMT). **b** DMT-AgNPs

competition between these two groups towards Ag as both groups have affinity for the novel AgNPs. The FTIR spectrum of AgNPs and DMT-AgNPs is as shown in Fig. 7. The purified freeze-dried powders of AgNPs were subjected to FTIR analysis to confirm the capping of DMT to AgNPs (Fig. 7). The broad band appearing at 3051 cm^{-1} can be assigned for C-H stretching vibration, small stretching band at 3276 cm^{-1} corresponds to NH_2 group, peak with bending vibration at 2360 cm^{-1} represents S-H (thiol) group, sharp stretching at 1596 cm^{-1} may be due to the presence of C=N bond, a sharp stretch at 1287 cm^{-1} can be assigned to C-N bond, and small stretching at 1010 cm^{-1} is assigned for N-N bond and the broad bending vibration at 1655 cm^{-1} for N-H group of DMT ligand. The IR spectrum of DMT-AgNPs (Fig. 7b) shows all the stretching and bending vibration of groups almost similar to ligand, except the peak around $1200\text{--}1300\text{ cm}^{-1}$ (Fig. 7b) indicating that S-H (thiol) group is involved in functionalization of DMT-AgNPs. Thus, the disappearance of the bending vibrations of the S-H (thiol) group and the decrease in intensity of the other bands are attributed to functionalization of AgNPs.

4.7 Antimicrobial Assays with Minimum Inhibitory Concentration

Antimicrobial activity study was performed to see the growth inhibitory effect of newly synthesized DMT-AgNPs on common laboratory microorganisms, using the standard method. The tabulated result (Table 2) reveals that DMT-AgNPs have higher antimicrobial activity compared to AgNPs. This might be due to their higher solubility (capping of polar groups) and higher diffusion potential of DMT-AgNPs. The DMT-AgNPs might get attached to the surface of the cell membrane and disturb its power function such as permeability and respiration, thus, inhibiting the growth of microbes (Fig. 8).

4.8 In Vitro Cytotoxicity Test Study of Dimercapto-Triazole-Functionalized AgNPs

In vitro cytotoxicity testing procedures reduces the use of animals [63] and hence increases the use of cultured tissues and cells [64] at laboratory keeping the animal environment safe (Fig. 9). The reduction of tetrazolium salts is now widely accepted as a reliable way to examine cell

Table 2 Antibacterial and antifungal activity of dimercapto-triazole-functionalized AgNPs

Sl. no	Test human pathogens	AgNPs 100 $\mu\text{g}/\text{disc}$	DMT-AgNPs 100 $\mu\text{g}/\text{disc}$	Gentamicin 100 $\mu\text{g}/\text{disc}$	Nystatin 100 $\mu\text{g}/\text{disc}$
1	<i>Candida albicans</i>	15 ± 0.52	22.0 ± 0.60	ND	22 ± 0.65
2	<i>Escherichia coli</i>	14 ± 0.68	18.6 ± 0.35	28 ± 0.45	ND
3	<i>Staphylococcus aureus</i>	13 ± 0.26	24.0 ± 0.64	33 ± 0.69	ND
4	<i>Bacillus subtilis</i>	27 ± 0.58	28 ± 0.60	31 ± 0.23	ND
5	Methicillin-resistant <i>Staphylococcus aureus</i>	00	11 ± 0.52	32 ± 0.45	ND
6	<i>Listeria monocytogenes</i>	00	09 ± 0.78	31 ± 0.63	ND
7	<i>Salmonella typhi</i>	06 ± 0.23	10 ± 0.84	30 ± 0.27	ND

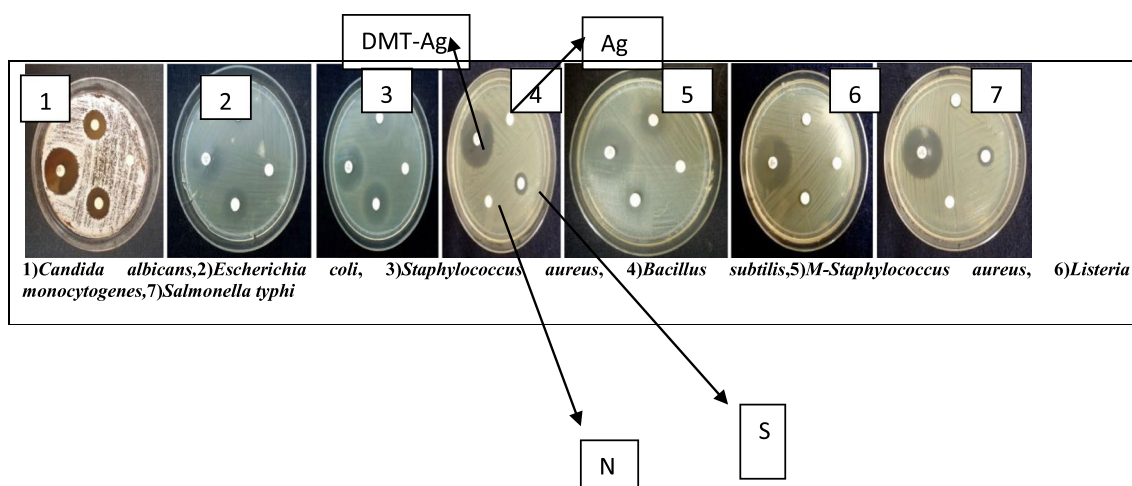
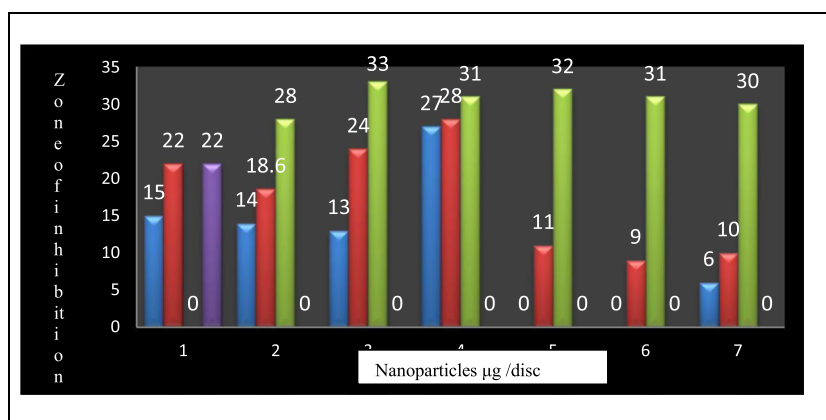


Fig. 8 Images of AgNPs and DMT-AgNPs showing inhibition zones for test human pathogens using gentamicin and nystatin as standards

Fig. 9 Graphical representation of antibacterial assay



proliferation [65]. The cytotoxicity assay measures the cell proliferation rate and, conversely, metabolic events that cause apoptosis or necrosis that lead to the reduction in cell viability. The cytomorphological changes for MCF-7 cell lines (Fig. 10) after 24 h of treatment along with their IC_{50} values with statistical studies are shown in Fig. 11a and its graphical representation in Fig. 11b.

Observations from Figs. 10 and 11 showed that the synthesized DMT-AgNPs show good results compared to AgNPs and chemotherapeutic drug Cis-platin against MCF-7 cell lines. We found that the DMT-AgNPs (Fig. 11) had the potential to inhibit growth of MCF-7 cancer cell in dose-dependent manner with an IC_{50} value of 18.46% v/v. The anticancer effect of AgNPs and DMT-AgNPs might be due to nano size, surface area, and surface functionalization factors which control bio-kinetics leading to reduction in cell viability. The action mode of DMT-AgNPs may be described as nanoparticles first make a breakthrough in the permeability of outer membrane, resulting in the leakage of cellular materials that cause cell decomposition

and death eventually. Secondly, DMT-AgNPs may enter the inner membrane and inactivate respiratory chain dehydrogenases or disruption of the mitochondrial respiratory chain leading to release of reactive oxygen species (ROS) and disturb (ATP) proteins, phosphate lipid synthesis, which in turn leads to DNA damage thus inhibiting respiration and growth of cells [66, 67]. Therefore, DMT-AgNPs result in increased cell proliferation rate compared to AgNPs.

5 Conclusion

The research work reports efficient, successful synthesis and characterization of DMT-AgNPs having spherical shapes with an average size of 50–51 nm. The DMT has two free groups, i.e., thiol and amine functional groups. Therefore, chemical reduction method was used to bring hydrophilic ligand functionalization of AgNPs. Ice bath used during the synthesis helps formation of AgNPs

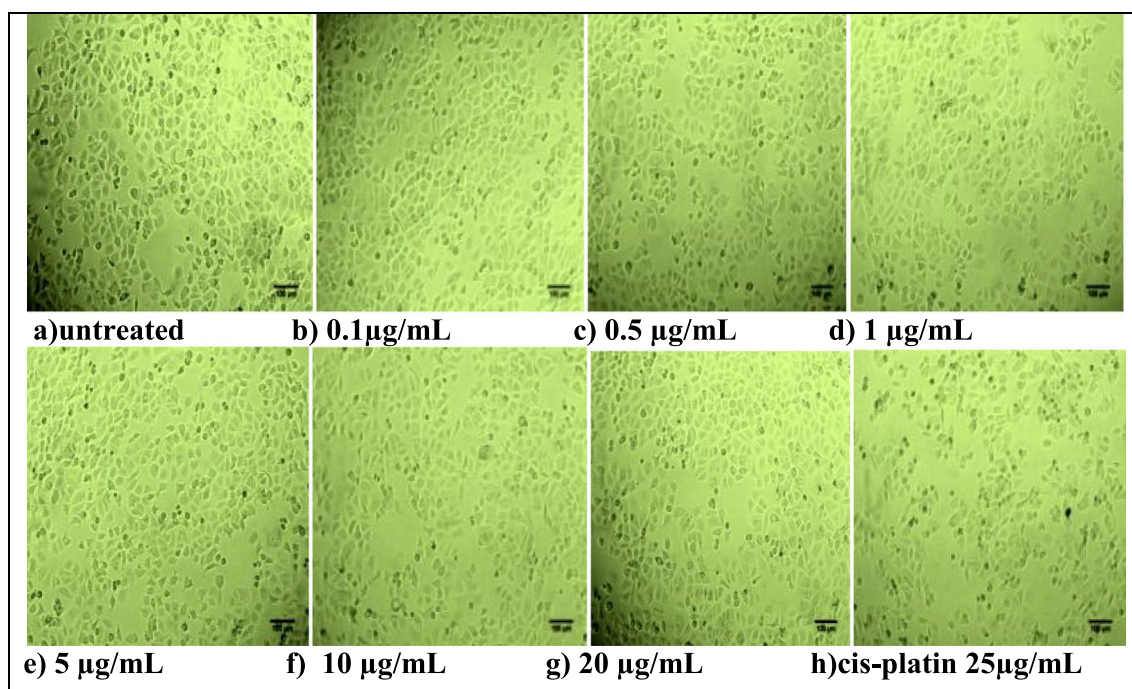


Fig. 10 Cytomorphological changes of MCF-7 cell line treated with colloidal AgNPs and DMT-AgNPs

with increased rate as individual atoms resulting in short time nucleation. In turn, this supported the formation of mono-dispersed particles as freshly generated atoms that get trapped by existing nuclei in a diffused-controlled growth mode and thus prevents new particle formation and no broad particle size distribution. Subsequent particle growth was influenced by the concentration of the reactants, the solvent, reducing agents, and specifically by the presence of a functionalizing agent. These DMT-AgNPs have certain advantages like ease for applicability in large-scale production, economically feasible, eco-friendly, and higher solubility (capping of polar groups) with higher

diffusion potential. Evaluation of antibacterial and antitumor study against MCF-7 cell lines explores the potential improvement in the biological activity of the DMT-AgNPs compared to AgNPs. Antimicrobial and anticancer study compiled the mobility of DMT-AgNPs into cells deciding their fate in a bioprocess and risk aspects for their applications. Conclusively, the results demonstrated that DMT-AgNPs can be used for the next generation biomedical applications.

Supplementary Information The online version contains supplementary material available at <https://doi.org/10.1007/s12668-023-01239-2>.

Acknowledgements The authors are thankful to Head, Department of Nanotechnology, UAS, Raichur, for providing the lab facilities for completion of synthesis and characterization work.

Funding We acknowledge DST-FIST (SR/FST/CSI-274/2016) grants for providing financial support.

Data Availability The capability of thiols to form disulfides—perhaps the most important bridging structure in nature—with cysteine subunits of endogenous proteins render them unique among functional groups that are utilized in nanotechnology.

i) By the formation of disulfide bonds thiolated NPs can be tightly bound to biological surfaces that exhibit cysteine-rich substructures such as the mucus gel layer, keratinized tissues and cell membranes.

ii) Similar to proteins that can alter their surface properties due to the reduction of disulfide bonds triggering conformational changes, thiolated NPs can alter their surface properties under reducing conditions. NPs that are PEG-coated via a disulfide linkage, for instance,

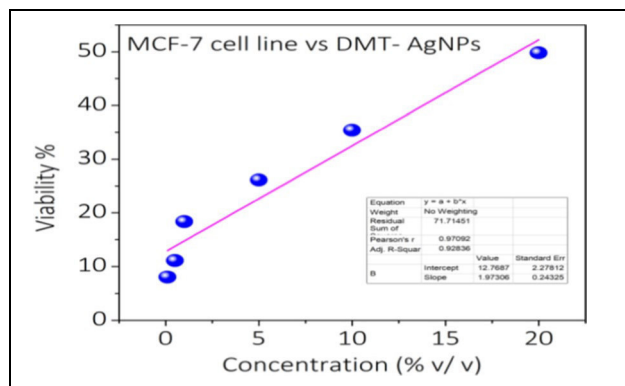


Fig. 11 Cell viability (%) of synthesized AgNPs and dimercapto-triazole-functionalized AgNPs against MCF-7 cell line

alter their surface under reducing conditions due to the release of this hydrophilic coating.

Declarations

Research Involving Humans and Animals Statement None.

Informed Consent None.

Conflict of Interest The authors declare no conflict of interests.

References

- Avouris, P. (1995). Manipulation of matter at the atomic and molecular levels. *Accounts of Chemical Research*, 28, 95–102.
- Salata, O. V. (2004). Applications of nanoparticles in biology and medicine. *Journal of Nanobiotechnology*, 2, 3.
- Nowostawska, M., Corr, S. A., Byrne, S. J., Conroy, J., Volkov, Y., & Gun'ko, Y. K. (2011). Porphyrin-magnetite nanoconjugates for biological imaging. *Journal of Nanobiotechnology*, 9, 13.
- Surendiran, A., Sandhiya, S., Pradhan, S. C., & Adithan, C. (2009). Novel applications of nanotechnology in medicine. *Indian Journal of Medical Research*, 130(6), 689–701.
- Holtz, R. D., Souza Filho, A. G., Brocchi, M., Martins, D., Durán, N., & Alves, O. L. (2010). Development of nanostructured silver vanadates decorated with silver nanoparticles as a novel antibacterial agent. *Nanotechnology*, 21, 185102.
- Thirumurgan, A., Tomy, N. A., Ganesh, R. J., & Gobikrishnan, S. (2010). Biological reduction of silver nanoparticles using plant leaf extracts and its effect an increased antimicrobial activity against clinically isolated organism. *Der Pharma Chemica*, 2(279), 284.
- Raghunandan, D., Ravishankar, B., Sharanbasava, G., Mahesh, D. B., Harsoor, V., Yalagatti, M. S., et al. (2011). Anti-cancer studies of noble metal nanoparticles synthesized using different plant extracts. *Cancer Nanotechnology*, 2(1–6), 57–65.
- Yeole, M. P., Dhole, S. N., & Kulkarni, N. S. (2013). Peptide nanomedicine in cancer treatment. *Asian Journal of Pharmaceutical and Clinical Research*, 6(2), 28–32.
- Albrecht, M. A., Evans, C. W., & Raston, C. L. (2006). *Green Chemistry*, 8, 417. <https://doi.org/10.1039/B517131H>
- Sun, T., & Seff, K. (1994). *Chemical Reviews*, 94, 857. <https://doi.org/10.1021/cr00028a001>
- Xiong, D. J., Chen, M. L., & Li, H. (2008). Synthesis of para-sulfonatocalix[4]arene-modified silver nanoparticles as colorimetric histidine probes. *Chemical Communications*, 7, 880–882. <https://doi.org/10.1039/B716270G>
- Duran, N., Marcato, P. D., Alves, O. L., De Souza, G. I. H., & Esposito, E. (2005). *Journal of Nanobiotechnology*, 3, 8. <https://doi.org/10.1186/1477-3155-3-8>
- Basu, S., Jana, S., Pande, S., & Pal, T. (2008). *Journal of Colloid and Interface Science*, 321, 288. <https://doi.org/10.1016/j.jcis.2008.02.015>
- Brigger, I., Dubernet, C., & Couvreur, P. (2004). *Advanced Drug Delivery Reviews*, 54, 631. [https://doi.org/10.1016/S0169-409X\(02\)00044-3](https://doi.org/10.1016/S0169-409X(02)00044-3)
- Guzman, M. G., Dille, J., & Godet, S. (2008). *World Academy of Science, Engineering and Technology*, 43, 357.
- Zhu, Z., Kai, L., & Wang, Y. (2006). *Materials Chemistry and Physics*, 96, 447. <https://doi.org/10.1016/j.matchemphys.2005.07.067>
- Lanje, A. S., Sharma, S. J., & Pode, R. B. (2010). Synthesis of silver nanoparticles: A safer alternative to conventional antimicrobial and antibacterial agents. *Journal of Chemical and Pharmaceutical*, 2, 478–483.
- Sriram, M. I., & Kanth, S. B. M. (2010). Antitumor activity of silver nanoparticles in Dalton's lymphoma ascites tumor model. *International Journal of Nanomedicine*, 5, 753–762. Res., 2010, 2(3):478–483.
- Peer, D., Karp, J. M., Hong, S., Farokhzad, O. C., Margalit, R., & Langer, R. (2007). Nanocarriers as an emerging platform for cancer therapy. *Nature Nanotechnology*, 2(12), 751–60.
- Bamrungsap, S., Zhao, Z., Chen, T., Wang, L., Li, C., Fu, T., & Tan, W. (2012). Nanotechnology in therapeutics: A focus on nanoparticles as a drug delivery system. *Nanomedicine (London)*, 7(8), 1253–71.
- Rai, M., Yadav, A., & Gade, A. (2009). Silver nanoparticles as a new generation of antimicrobials. *Biotechnology Advances*, 27, 76–83.
- Taleb, C., Petit, M., & Pileni, P. (1997). *Chemistry of Materials*, 9, 950. <https://doi.org/10.1021/cm960513y>
- Henglein, A. (2001). *Langmuir*, 17, 2329. <https://doi.org/10.1021/la001081f>
- Esumi, K., Tano, T., Torigoe, K., & Meguro, K. (1990). *Chemistry of Materials*, 2, 564. <https://doi.org/10.1021/cm00011a019>
- Zhu, J. J., Liu, S. W., Palchik, O., Koltypin, Y., & Gedanken, A. (2000). *Langmuir*, 16, 6396.
- Xie, J., Lee, J. Y., Wang, D. I. C., & Ting, Y. P. (2007). *ACS Nano*, 1, 429. <https://doi.org/10.1021/nn7000883>
- Sharma, V. K., Yngard, R. A., & Lin, Y. (2009). *Advances in Colloid and Interface Science*, 145, 83. <https://doi.org/10.1016/j.cis.2008.09.002>
- Zhang, X. F., Liu, Z. G., Shen, W., & Gurunathan, S. (2016). Silver nanoparticles: Synthesis, characterization, properties, applications, and therapeutic approaches. *International Journal of Molecular Sciences*, 17, 1534.
- Al-Thabaiti, S. A., Al-Nawaiser, F. M., Obaid, A. Y., Al-Youbi, A. O., & Khan, Z. (2008). *Colloids and Surfaces B: Biointerfaces*, 67, 230. <https://doi.org/10.1016/j.colsurfb.2008.08.022>
- Khan, Z., Al-Thabaiti, S. A., El-Mossalamy, E. H., & Obaid, A. Y. (2009). *Colloids and Surfaces B: Biointerfaces*, 73, 284. <https://doi.org/10.1016/j.colsurfb.2009.05.030>
- Won, H. I. I., Nersisyan, H., Won, C. W., Lee, J.-M., & Hwang, J.-S. (2010). *Chemical Engineering Journal*, 156, 459. <https://doi.org/10.1016/j.cej.2009.10.053>
- Pastoriza, I., & Lizmarzan, L. M. (2000). *Pure and Applied Chemistry*, 72, 83. <https://doi.org/10.1351/pac200072010083>
- Patil, R. S., Kokate, R. M., Jambhale, C., Pawar, S., Han, S., Kolekar, S., et al. (2012). One-pot synthesis of PVA-capped silver nanoparticles their characterization and biomedical application. *Advances in Natural Sciences: Nanoscience and Nanotechnology*, 3, 1–7.
- Nazeruddin, G., Prasad, N., Prasad, S., Garadkar, K., & Nayak, A. (2014). In-vitro bio-fabrication of silver nanoparticle using *Adhatoda vasica* leaf extract and its anti-microbial activity. *Physica E: Low-dimensional Systems and Nanostructures*, 61, 56–61.
- Caragheorghopol, A., & Chechik, V. (2008). *Physical Chemistry Chemical Physics*, 10, 5029.
- Wilson, R. (2008). The use of gold nanoparticles in diagnostics and detection. *Chemical Society Reviews*, 37, 2028–2045.
- Guo, R., Song, Y., Wang, G., & Murray, R. W. (2005). *Journal of the American Chemical Society*, 127, 2752.
- Hostetler, M. J., Templeton, A. C., & Murray, R. W. (1999). *Langmuir*, 15, 3782.
- Rai, M., Kon, K., Ingle, A., Duran, N., Galdiero, S., & Galdiero, M. (2014). Broad-spectrum bioactivities of silver nanoparticles:

- The emerging trends and future prospects. *Applied Microbiology and Biotechnology*, 98, 1951–1961.
40. Baumann, M., & Baxendale, R. (2013). *Beilstein Journal of Organic Chemistry*, 9, 2265.
 41. Lauria, A., Delisi, R., Mingoia, F., Terenzi, A., Martorana, A., Barone, G., & Almerica, A. M. (2014). *European Journal of Organic Chemistry*, 2014, 3289.
 42. Ferreira, M. L. G., Pinheiro, L. C. S., Santos-Filho, O. A., Pecanha, M. D. S., Sacramento, C. Q., Machado, V., Ferreira, V. F., Souza, T. M. L., & Boechat, N. (2014). *Medicinal Chemistry Research*, 23, 1501.
 43. Dai, Z. C., Chen, Y. F., Zhang, M., Li, S. K., Yang, T. T., Shen, L., Wang, J. X., Qian, S. S., Zhu, H. L., & Ye, Y. H. (2015). *Organic & Biomolecular Chemistry*, 13, 477.
 44. Quahrouh, A., Iqhachane, H., Taourite, M., Engels, J. W., Sedra, M. H., & Lazrek, H. B. (2014). *Archiv der Pharmazie*, 347, 748.
 45. Seelam, N., Shrivastava, S. P., Prasanthi, S., et al. (2016). Synthesis and in vitro study of some fused 1,2,4-triazole derivatives as antimycobacterial agents. *Journal of Saudi Chemical Society*, 20(4), 411–418.
 46. Ashwin, N., Garg, M., Mohan, C. D., Fuchs, J. E., Rangappa, S., Anusha, S., Swaroop, T. R., Rakesh, K. S., Kanojia, D., Madan, V., Bender, A., Koefer, H. P., & Basappa Rangappa, K. S. (2015). *Bioorganic & Medicinal Chemistry*, 23, 6157.
 47. Tratat, C., Haroun, M., Paparisva, A., et al. (2018). Design, synthesis and biological evaluation of new substituted 5-benzylideno-2-adamantylthiazol [3,2-b][1,2,4] triazol-6 (5H) ones. Pharmacophore models for antifungal activity. *Arabian Journal of Chemistry*, 11(4), 573–590.
 48. Stefanska, J., Szulczyk, D., Koziol, A. E., Mirosław, B., Kedzierska, E., Fidecka, S., & Struga, M. (2012). Disubstituted thiourea derivatives and their activity on CNS: Synthesis and biological evaluation. *European Journal of Medicinal Chemistry*, 55, 205–213. <https://doi.org/10.1016/j.ejmech.2012.07.020>
 49. Ali, A. A., & Al-Abdali, B. I. (2015). Synthesis and characterization of 4-(((3-mercapto-5-phenyl-4H-1,2,4-triazole-4-yl) imino) methyl)-2-methoxyphenol and its complexes with Zr (IV), Cd (II) and Sn (II) ions. *Iraqi Journal of Science*, 56(2B), 1274–1288.
 50. Lu, J., Ma, E., Liu, Y. H., Li, Y. M., Mo, L., & Zhang, Z. H. (2015). *RSC Advances*, 5, 59167.
 51. Creighton, J. A., Blatchford, C. G., & Albrecht, M. G. (1979). Plasma resonance enhancement of Raman scattering by pyridine adsorbed on silver or gold sol particles of size comparable to the excitation wavelength. *Journal of the Chemical Society, Faraday Transactions, II*(75), 790–798.
 52. Suh, J. S., DiLella, D. P., & Moskovits, M. (1983). Surface-enhanced Raman spectroscopy of colloidal metal systems: A two-dimensional phase equilibrium in p-aminobenzoic acid adsorbed on silver. *Journal of Physical Chemistry*, 87, 1540–1544.
 53. Sandstrom, J. (1961). *Acta Chemica Scandinavica*, 15, 1295.
 54. Guha, P. C., & De, S. C. (1924). *Journal of the Chemical Society*, 125, 1218.
 55. Pal, S., Kyung, Y., & Myong, S. J. (2007). *Applied and Environmental Microbiology*, 73(6), 1712–1720.
 56. Alley MC. *MTT cell proliferation assay instruction guide*. American Type Culture Collection, Manassas, VA. www.atcc.org
 57. Ghorbani, H. R., & Soltani, S. (2015). Antibacterial effects of silver nanoparticles on *Escherichia coli* and *Bacillus subtilis*. *Oriental Journal of Chemistry*, 31(1), 341–344.
 58. Soni, S., Patel, T., Thakar, B., Pandya, V., & Bharadia, P. (2012). Nanosuspension: An approach to enhance solubility of drugs. *Journal of Pharmaceutics and Cosmetology*, 2(9), 49–63.
 59. Sivaraman, D., Panneerselvam, P., Muralidharan, P., Prabhu, P. P., & Vijaya, K. R. (2013). Green synthesis, characterization and antimicrobial activity of the silver nanoparticles produced from Ipomea aquatic Forsk leaf extract. *International Journal of Science and Research*, 4(6), 2280–2285.
 60. Vigneshwaran, N., Kathe, A. A., Varadarajan, P. V., Nachane, R. P., & Balasubramanya, R. H. (2007). *Langmuir*, 23, 7113–7117.
 61. Varshney, R., Mishra, A. N., Bhadauria, S., & Gaur, M. S. (2009). *Digest Journal of Nanomaterials and Biostructures*, 4(2), 349–355.
 62. Sarkar, R., Kumbhakar, P., & Mitra, A. K. (2010). Green synthesis of silver nanoparticles and its optical properties. *Digest Journal of Nanomaterials and Biostructures*, 5(2), 491–496.
 63. Abraham, S. A., McKenzie, C., Masin, D., Ng, R., Harasym, T. O., Mayer, L. D., & Bally, M. B. (2004). In vitro and in vivo characterization of doxorubicin and vincristine encapsulated within liposomes through use of transition metal ion complexation and pH gradient loading. *Clinical Cancer Research*, 10, 728–738.
 64. Byrd, J. C., Lucas, D. M., Mone, A. P., Kitner, J. B., Drabick, J. J., & Grever, M. R. (2003). KRN5500: A novel therapeutic agent with in vitro activity against human B-cell chronic lymphocytic leukemia cells mediates cytotoxicity via the intrinsic pathway of apoptosis. *Blood*, 101, 4547–4550.
 65. Scudiere, D. A., Monks, A., Czerwinski, M., Shoemaker, R., II., & Boyd, M. R. (1986). Validation of an automated microculture tetrazolium assay (MTA) to assess growth and drug sensitivity of human tumor cell lines. *Proceedings of the American Association for Cancer Research*, 27, 389.
 66. Lanje, A. S., Sharma, S. J., & Pode, R. B. (2010). Synthesis of silver nanoparticles: A safer alternative to conventional antimicrobial and antibacterial agents. *Journal of Chemical and Pharmaceutical Research*, 2(3), 478–483.
 67. Solomon, S. D., Bahadory, M., Jeyarajasingam, A. V., Rutkowsky, S. A., & Boritz, C. J. (2007). *Chemical Education*, 84, 322. <https://doi.org/10.1021/ed084p322>

Publisher's Note Springer Nature remains neutral with regard to jurisdictional claims in published maps and institutional affiliations.

Springer Nature or its licensor (e.g. a society or other partner) holds exclusive rights to this article under a publishing agreement with the author(s) or other rightsholder(s); author self-archiving of the accepted manuscript version of this article is solely governed by the terms of such publishing agreement and applicable law.



Facile synthesis, characterization, insilico modelling, and bioinformatic study of dimercapto-triazole functionalized silver nanoparticles

V. Veena^a, K.H. Shivaprasad^b, H. Sharanagouda^c, Ganiger Sangappa K.^d,
Arunkumar Lagashetty^{b,*}

^a Department of Chemistry, Ballari Institute of Technology and Management, Ballari 583105, Karnataka, India

^b Department of Chemistry, Vijayanagara Sri Krishnadevaraya University, Ballari 583105, Karnataka, India

^c Department of Processing and Food Engineering, College of Agricultural Engineering, University of Agricultural Sciences, Raichur 584101, Karnataka, India

^d Department of Physics, Government Engineering College, Huvinahadagali 583219, Karnataka, India

ARTICLE INFO

Keywords:

AgNPs
DMT
Antibacterial
Anti-cancer
Molecular docking
Zeta-potential

ABSTRACT

Recent research reports that the increasing number of new bacterial infections are resistant to current antibiotics and have become a significant issue for public health. Silver nanoparticles (AgNPs) as bactericides, fungicides, and anti-cancer agents are notably promising, as evidenced by the recent investigation of scientific communications worldwide. Though biocompatible and non-toxic, they are unstable at higher ionic strengths, and even ambient light may cause nano-silver to aggregate. The aggregation can be overcome by surface functionalization. Thus, the current report is an attempt for biologically active dimercapto-triazole (DMT), which has both free thiol (R-SH) and amine(R-NH₂) groups were successfully used for the functionalization of AgNPs. Characterization techniques like UV/Vis-spectroscopy, zeta-potential, XRD, SEM, TEM, and FT-IR data confirmed the functionalization of AgNPs with the thiol (R-SH) group. The functionalized AgNPs have an average spherical particle size of 50–51 nm and a broad spectrum of activity for Gram-negative and Gram-positive bacteria and anti-cancer activity against MCF-7 cell lines with an IC₅₀ value of –18.681 % v/v. Molecular docking studies reviewing the best-fitting conformation of DMT-capped AgNPs with the highest binding energy for target proteins of cancer and bacteria reveal its biocompatibility.

Introduction

Recent research reviews that there is fast growth in nanotechnology, especially in nanomedicine, with the development of novel nanocomposite materials at the atomic/molecular level into a new range of products for advanced applications in the biomedical field [1,2]. Nanosized composite materials of free metals design nanomedicines with the implementation of modern technology, which has visualized the next door for the ongoing development of new theranostic systems [3–7]. Nanocomposites of this system have unique physical and chemical properties that play a tremendous role in overcoming many of the problems compared to conventional methods faced in sensing, diagnosing, treating, and detecting diseases [8]. AgNPs possess higher levels of therapeutic activity with lower toxicity and have tremendous applications in photography [9], catalysis [10], biosensors [11], biomolecular detection [12], diagnostics [13], and particularly anti-microbial studies [14–16]. Thus, it is extensively used for developing therapeutic

methodologies like treating multidrug-resistant microorganisms, drug delivery systems, coating medical equipment, food packaging materials, wound dressing bandages, and various wound healing gels to prevent infections due to their anti-microbial properties [17–21].

Literature reviews report that many researchers have experimented with various methods and have successfully synthesized AgNPs [22–27]. The chemical reduction method is the most preferred for synthesizing AgNPs as colloidal dispersion in solvents. In addition, the chemical reduction of silver salt in solution offers enhanced yield, a more straightforward reaction, and lower costs [28]. Reducing agents like ascorbic acid [29], hydrazine [30], ammonium formate [31], dimethyl formamide [32], sodium borohydride, and sodium citrate [33] are used to obtain different shapes of AgNPs. Sodium borohydride reduction usually results in mono-dispersed AgNPs, while citrate usually results from polydispersed AgNPs because of its slow reaction rate [34,35]. AgNPs synthesized by the chemical reduction method are preferred in the presence of stabilizers in order to prevent unwanted agglomeration

* Corresponding author.

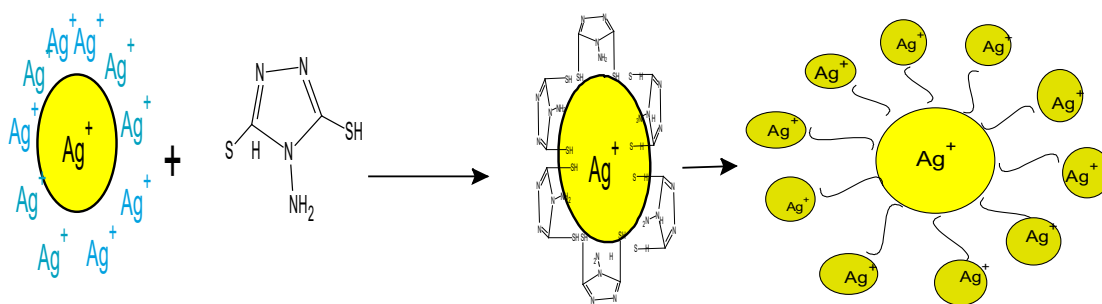
E-mail address: arun.lagashetty@vskub.ac.in (A. Lagashetty).

<https://doi.org/10.1016/j.rechem.2024.101351>

Received 27 December 2023; Accepted 29 January 2024

Available online 1 February 2024

2211-7156/© 2024 The Authors. Published by Elsevier B.V. This is an open access article under the CC BY license (<http://creativecommons.org/licenses/by/4.0/>).



Scheme 1. Functionalization of AgNPs by 4-amino, 3,5-dimercapto-1,2,4 triazole.

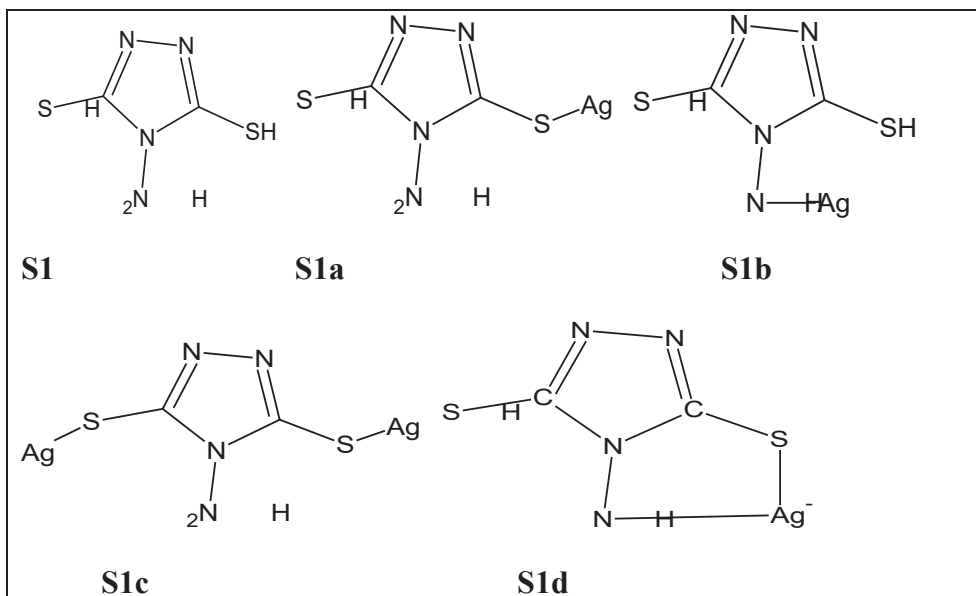


Fig. 1. The possible structures of AgNPs taken for *InsilicoiGem* Docking studies.

of the colloidal particles in the medium. In continuation, it reduces the size by surface modification using specific appropriate ligands for varied special applications [36]. Ligands in the modification can act like capping agents, which form a protective shell around AgNPs, and the protective shell stops the nanoparticles from further aggregation and increases their lifespan, which makes them more biocompatible.

Ligands substituted with functional groups are readily conjugated to the noble metal nanoparticles through non-covalent and covalent interactions that have been successfully reported [36]. Functionalisation of AgNPs with ligands can be brought through physisorption, chemisorption, electrostatic adsorption, and affinity-based methods [37]. The critical feature of AgNPs fictionalization is their surface, which is imperfect, resulting in defective sites corresponding to the vertices or edges and one non-defective site for the binding of ligands [38,39]. Defective and non-defective sites have different electron densities and steric behaviour, exhibiting different reactive natures with different functional groups [38]. Thus, the functionalisation of nanoparticles allows the material properties to promote their specified and simplified applications [40–42]. In modern drug design, molecular docking studies predict the possible structures of intermolecular complexes formed between two or more molecules. It also exhibits the best-fitting orientation of protein- ligand-nanoparticles that bind to a particular protein of interest to act as a drug receptor—the molecular docking design exercise to synthesize AgNPs intermolecular complexation. Functionalised AgNPs and their molecular docking study make a tremendous breakthrough in

nanomedicine to develop suitable formulations.

Nevertheless, introducing an appropriate functionality to the surface of AgNPs and a more profound investigation of nanomaterial structures are critical aspects of the present study to improve its therapeutic applications. 4-amino, 3, 5-mercapto, 1, 2, 4 triazoles (DMT) ligand has functionalized the synthesized AgNPs. Characterization and evaluation of anti-microbial and antitumor activity against MCF-7 cell lines is attempted to highlight its *in-vivo* efficacy. Later, the biological reports are compiled with the computational results obtained by molecular docking study. The binding mode interactions of proteins with functionalized AgNPs are expected to confirm the functionalization of AgNPs as engineered materials to assess the biological fate.

Experimental

Materials and methods

All chemicals used were of AR grade purchased from Sigma-Aldrich Ltd and are used without further purification. The bacterial strains were procured from the Institute of Microbial Technology (IMT) in Chandigarh, India. The MCF-7 cell lines were obtained from the National Centre for Cell Science, Pune, India. RPMI-1640 culture medium and fetal calf serum (FCS) were purchased from HI Media Chemicals. The glassware used was cleaned with aquaregia and rinsed with double distilled water.

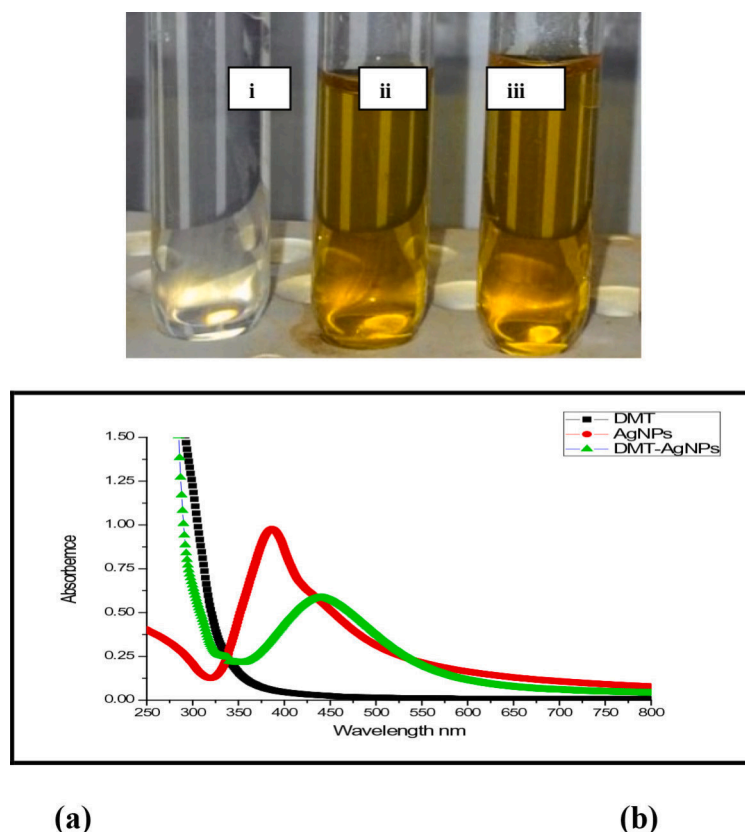


Fig. 2. A) colour for i) dmt, ii) agnps, and iii) dmt- agnps, b) uv-Vis spectra of DMT- AgNPs and DMT-AgNPs.

Synthesis of AgNPs

AgNPs were synthesized by reducing silver salt (AgNO_3) with a significant excess of ice-cold sodium borohydride as a reducing agent and stabilizer. [43,44]. The synthetic procedure was that 30 mL of 0.002 M sodium borohydride (NaBH_4) was added to a flask in an ice bath and incubated in a dark place. The flask's content was stirred thoroughly on a magnetic stirrer for about 20 min. An ice bath was used to slow down the reaction for better particle size control. 2 mL of 0.001 M AgNO_3 was dripped into the NaBH_4 solution at one drop per second with continuous stirring until complete AgNO_3 was reduced and clustered to form AgNPs as a transparent yellow-coloured solution in the aqueous medium.

Synthesis of functionalised AgNPs (DMT- AgNPs)

The functionalizing ligand 4-Amino-3, 5-dimercapto-1, 2, 4-triazole (DMT) was initially prepared by referring reported procedure [45]. Further, 30 mL 0.001 M DMT solution was dripped into ice-cold AgNP sol at approximately one drop per second using a syringe with continuous stirring. The above-prepared solution was kept in the dark for 18 h with continuous stirring for complete stabilization. The colour of the reaction solution turns dark yellow from pale yellow, indicating the formation of DMT-AgNPs, as shown in Scheme 1.

Antimicrobial assays

The disc diffusion method was used to evaluate the antimicrobial susceptibility of newly synthesized DMT-AgNPs [46]. Muller Hinton (MH) agar media for antibacterial activity was prepared, sterilized, and transferred to clean and dried petri plates. These plates containing media were solidified and incubated overnight to confirm that the petri plates were contamination-free. Later, petri plates were first inoculated

with test organisms, followed by a loaded disc. Zones of inhibition were measured after 24 hrs of incubation at 37 °C. The comparative stability of discs containing standard drugs like gentamicin and nystatin was analyzed simultaneously to evaluate their antibacterial susceptibility. All the experiments were exercised in triplicate for final confirmation, and results are recorded as mean \pm standard deviation.

In-vitro study of DMT-AgNPs

As reported in the literature, the cytotoxicity study of synthesized DMT-AgNPs was tested on MCF-7 cell lines by the reduction assay of tetrazolium salt [47]. The cells were cultured and then harvested, so 200 μL of each suspension contained approximately 15,000 cells. The cells were treated with 200 μL of increasing concentrations of the prepared DMT-AgNPs sample (0.1, 0.5, 1.0, 5.0, 10, 20 %v/v) from stock sol and incubated at 37 °C in 5 % CO_2 atmosphere for 24 h and 48 h. Later, 200 μL of 10 % MTT reagent was added to each well to get a final concentration of 0.5 mg/mL, and the plates were incubated at 37 °C in a 5 % CO_2 atmosphere for 24 h and 48 h. The resulting blue-coloured product was dissolved in 100 μL dimethyl sulfoxide (DMSO) solvent, and the absorption was measured at 570 nm wavelength. The absorbance of untreated cells was used as a control (100 % viable). Cis-platin was the standard anti-cancer drug for MCF-7 cell lines with an IC_{50} value of 25 $\mu\text{g/mL}$. Each experiment was performed in triplicate for final confirmation of the results. The percentage growth inhibition was calculated after subtracting the background and the blank. The concentration of the test drug needed to inhibit cell growth by 50 % (IC_{50}) was generated from the dose-response curve for the cell line.

Molecular docking

The structure-based molecular docking study for the prepared

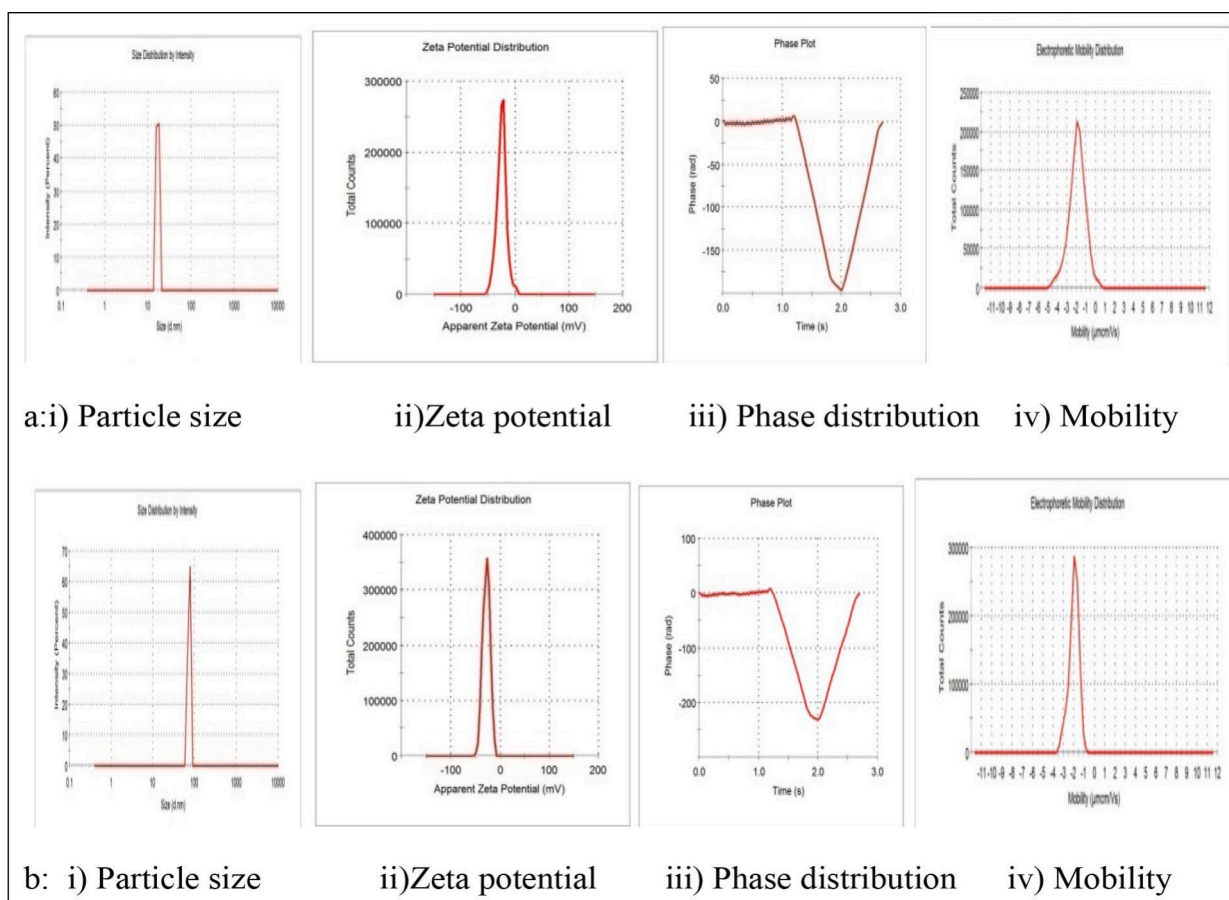


Fig. 3. Zeta Particle Size, phase distribution, and mobility images of a) AgNPs and b) DMT-AgNPs.

Table 1

Mean particle size diameter and zeta potential results of AgNPs and DMT-AgNPs.

Sl. No	Parameters	Samples	
		AgNPs	DMT-AgNPs
1.	Z-average (nm)	20–21	50–54
2.	Zeta potential (mV)	–24.8	–27.2
3.	Zeta quality	Phase and distribution data are good	Phase and distribution data meets the quality criteria
4.	Electrophoretic mobility ($\mu\text{cm}/\text{Vs}$)	–1.920	–2.201
5.	Mobility deviation ($\mu\text{cm}/\text{Vs}$)	0.8890	0.4833
6.	Conductivity mS/cm	0.0910	0.191

sample used iGEMDOCKV2.1 software [48] to study the protein–ligand interaction for all docking simulations. A set of few possible structures of DMT-AgNPs (shown in Fig. 1) were subjected to docking with bacteria β -lactamase *toho-1 Escherichia coli*-1iYS, *S.Aureus* ligase (PDB ID: 1JIJ), cancer FHA2 domain of RAD53 (PDB ID: 1K2N), Caspase-3 V266F (PDB ID: 5IAE) from the Protein Data Bank (RCSB) to study their antibacterial and anti-cancer activity. Canonical smiles were submitted to Corina's online 3D conversion server (https://www.mn-am.com/online_demos/corina_demo) to convert 2D structures into 3D structures. Further, the 3D structure of the sample was optimized for docking conformation study. The whole structure of the receptors was used for our molecular docking studies for the ligand S1 and DMT-AgNPs S1 (a–d). Further, the detailed interaction between the best functional group and its position with the target proteins was analyzed in the 3D visualization software PyMol [49].

Characterization

As syntheses, AgNPs and DMT-AgNPs were well characterized by various characterization tools. Perkin Elmer, Lambda 35, Germany: A UV–visible spectrometer tool was used to determine the absorbance. The mean particle size and Zeta potential (ξ) of the colloidal sol were investigated by dynamic light scattering (DLS) technique using a Zeta size analyzer (Nano ZS 90, Malvern Instruments Ltd., UK). Structural confirmation of the prepared samples was done by being subjected to X-ray diffraction pattern analysis on a powder diffractometer (Rigaku theta-theta type) operated at 40 KV voltage, 30 mA current, 20 to 80 (2θ) range. To determine the size and morphology, surface microphotographs were obtained using transmission electron microscope TEM (Philips model CM 200 instrument operated at an accelerating voltage at 200 KV) and scanning electron microscope SEM (Carl Zeiss Microscopy, EVO 10, Germany). Fourier transform infrared (FT-IR) spectra were recorded on a Vertex 70 spectrometer with KBr pellets (Bruker Corporation, Billerica, MA, USA). The cytotoxicity (MTT) assays were performed in a 96-well plate, and absorbance was measured on a microplate reader (Multiscan, Thermo Scientific).

Results and discussion

UV-Vis Study

The reduction of Ag salt solution to AgNPs and DMT-AgNPs was monitored by periodical sampling of aliquots of the reaction as a function of time and recording the UV–visible spectrum in the range 200–600 nm operated at a resolution of 1 nm. Double distilled water was used as a blank solution. A colour comparison of reaction products

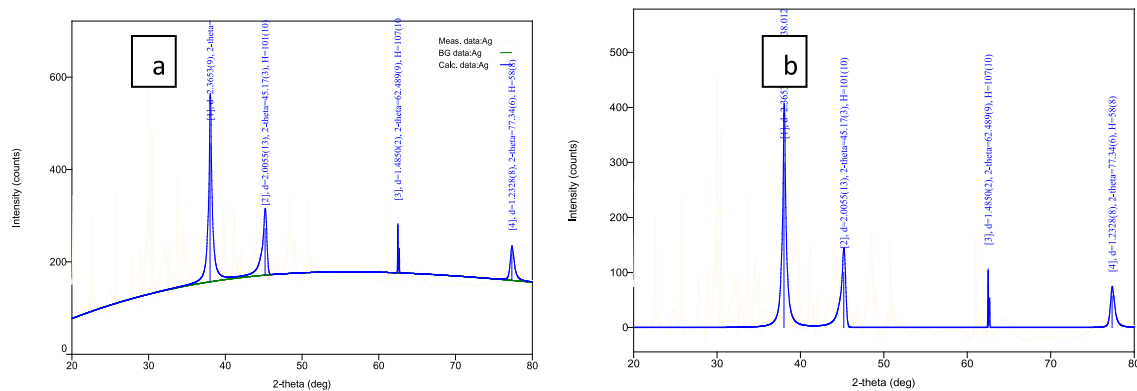


Fig. 4. XRD patterns of a) AgNPs and b) DMT-AgNPs.

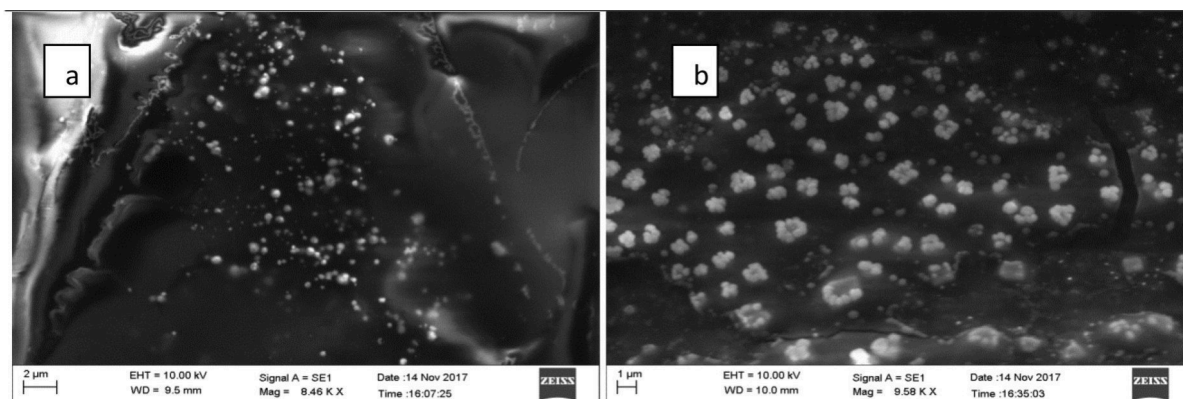


Fig. 5. SEM images of a) AgNPs, b) DMT-AgNPs.

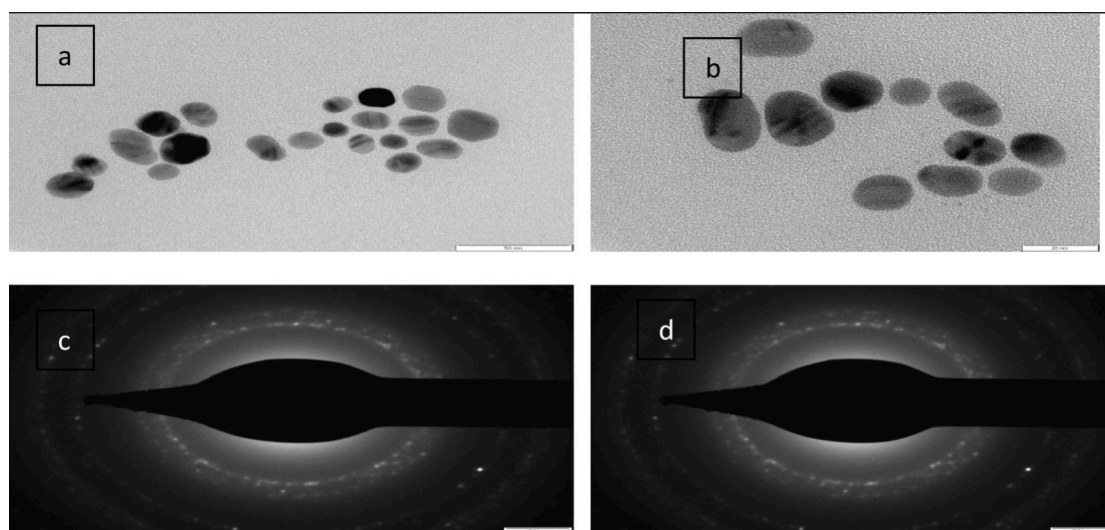


Fig. 6. TEM images of a) AgNPs and b) DMT-AgNPs c) SAD pattern of AgNPs d) SAD pattern of DMT-AgNPs.

concerning the standard solution and UV–vis spectrum of the samples is shown in Fig. 2. The optical absorption spectra of metal nanoparticles are dominated by surface plasmon resonance at 420 nm for AgNPs, i.e., the energy of absorption depends on the degree of plasmon resonance, which may shift either side of this value depending on the ratio of silver ions and zero-valent silver [50]. Fig. 2(a) shows that the pale yellow solution, due to the reduction of Ag^+ to Ag^0 and the absorption peak at

420 nm in UV–Vis spectra for AgNPs, shifted to a longer wavelength (red shift) of 440 nm, which may be due to the increase in the particle size of DMT-AgNPs (Fig. 2b). There was no further aggregation, and the peak position was stable after 18 h. The silver colloidal particles initially possess a negative charge due to the adsorbed BH_4^- ions, which dissolve slowly and later form -SH capping [35]. It is well understood that the position and shape of metal nanoparticles' plasmon absorption strongly

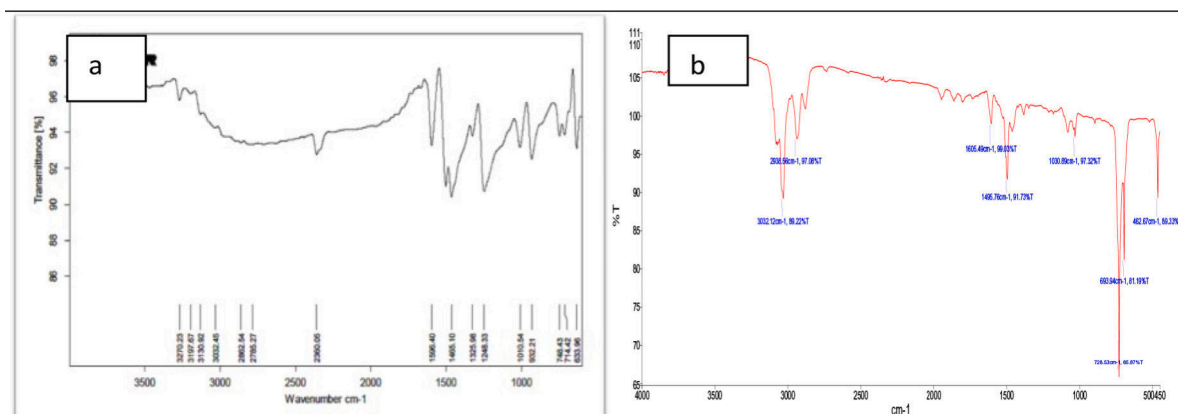


Fig. 7. FT-IR Spectrum of a) 4-amino-3,5-dimercapto-1,2,4-triazole(DMT) b) DMT- AgNPs.

Table 2

Antibacterial and antifungal activity of DMT- AgNPs sample.

Sl. No	Test Human Pathogens	AgNPs 500 µg/disc	DMT- AgNPs 500 µg/disc	Gentamicin 10 µg/disc	Nystatin 100 µg/disc
1.	<i>C. Albicans</i>	15 ± 0.51	22.0 ± 0.61	ND	22 ± 0.64
2.	<i>E. Coli</i>	14 ± 0.69	18.6 ± 0.36	28 ± 0.46	ND
3.	<i>S. Aureus</i>	13 ± 0.25	24.0 ± 0.65	33 ± 0.68	ND
4.	<i>B. subtilis</i>	27 ± 0.59	28 ± 0.61	31 ± 0.24	ND
5.	<i>M.Staphylococcus aureus</i>	00	11 ± 0.51	32 ± 0.46	ND
6.	<i>L. Monocytogenes</i>	00	09 ± 0.77	31 ± 0.64	ND
7.	<i>S. Typhi</i>	06 ± 0.24	10 ± 0.85	30 ± 0.28	ND

depend on their size, dielectric constant, and surface adsorption, further confirmed by Zeta size and potential studies, as discussed in the following section.

Particle size and zeta potential (ξ) analysis

Zeta potential and the mean particle size distribution govern the characteristics of synthesized metal nanoparticles, such as saturation solubility, dissolution velocity, physical stability, and biological performances [51]. Particle size and Zeta potential of the achieved colloidal AgNPs and DMT-AgNPs were measured directly using dynamic light scattering spectroscopy (DLS). Observed DLS figures are shown in Fig. 3, and their data is tabulated in Table 1. The z-average (average particle size) was 20–21 nm for AgNPs and 50–51 nm for DMT-AgNPs samples, respectively. Zeta potential (ξ) /surface potential values measured were found to be −24.8 mV for AgNPs (Fig. 3a) and −27.1 mV for DMT-AgNPs (Fig. 3b), with a peak area of 100 % intensity[52]. The high negative value of zeta potential and mobility values, as seen in Table 1, is supported by long-term stability, good colloidal nature, and high dispersity of the synthesized samples.

XRD analysis

The indexed XRD pattern of synthesized AgNPs and DMT-AgNPs samples is shown in Fig. 4. Both patterns show similar features with diffracting angles (2θ) at 38.012°, 45.17°, 62.489° and 77.34°. The indexing the reflections are (111), (200), (220), and (311) planes correspond to FCC of AgNPs in comparison with standard JCPDS 87–0720 data, which confirms the formation of monophasic AgNPs and

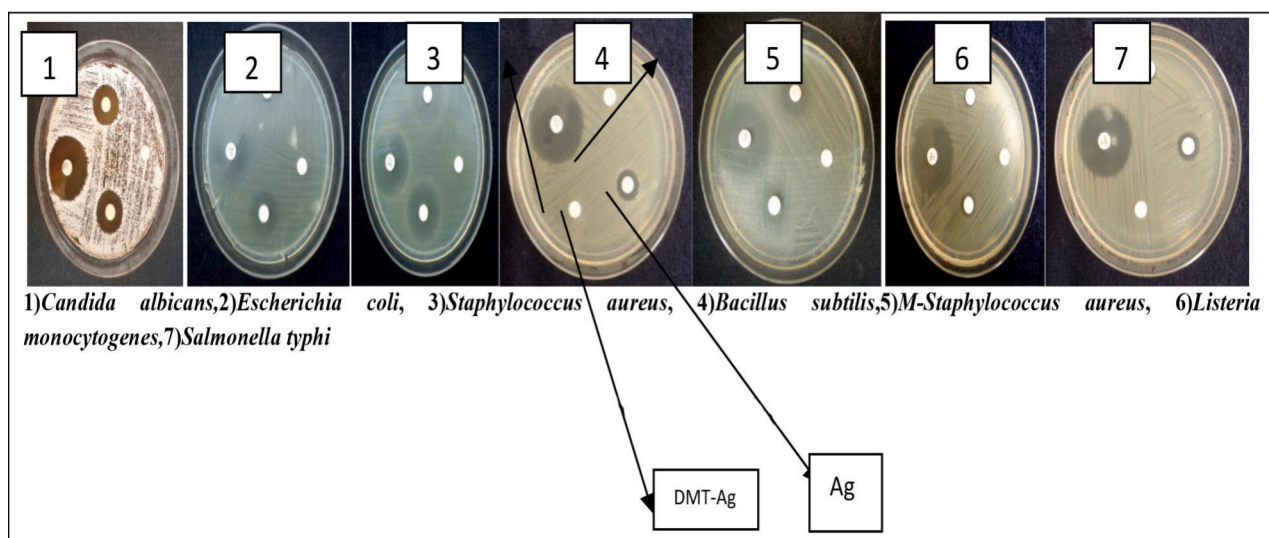


Fig. 8. ZOI Images of AgNPs and DMT-AgNPs forest human pathogens using Gentamicin and Nystatin as standards.

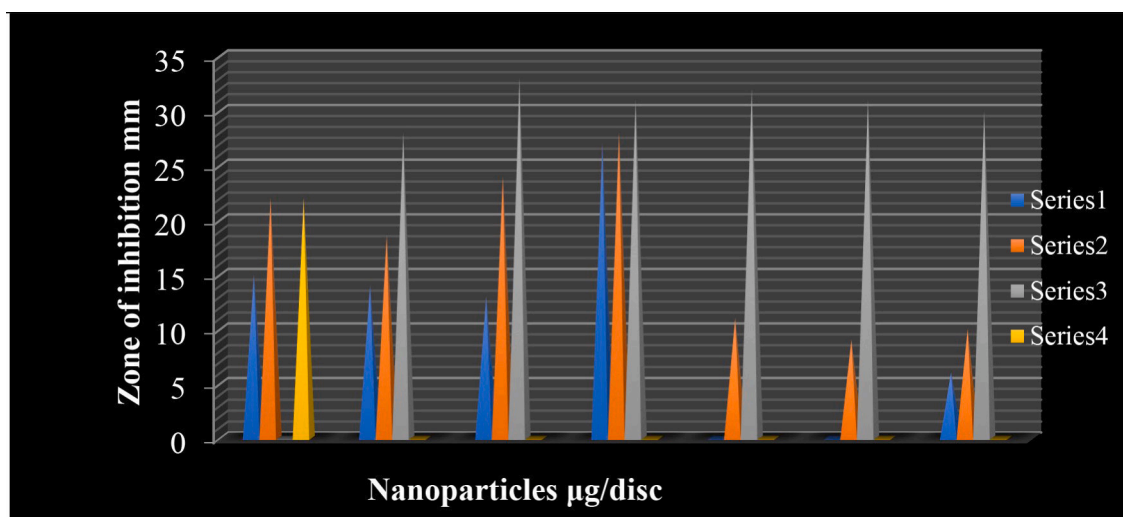


Fig. 9. Graphical representation of antibacterial assay.

DMT-AgNPs [53–55]. Unit cell parameters were identified by the XRD data's most minor square refinement. The obtained Bragg's reflections also indicate that both samples show crystalline nature. The lattices were identified by comparing the values for interlunar spacing and relative intensities with the reported standard values of silver metal. The particle size of the AgNPs sample was calculated using Debye-Scherrer's equation and is recorded as 20–21 nm and 50–51 nm for the DMT-AgNPs sample, consistent with the Zeta size values.

SEM study

The morphological study and size details of the as-synthesized samples were studied using a scanning electron microscope tool. Obtained SEM images of both AgNPs' and DMT-AgNPs' samples are shown in Fig. 5(a-b). Spherical-shaped AgNPs with uneven distribution of particles are observed in the AgNP images. Fine particle agglomeration retards the high surface area of the sample. A close, compact arrangement of the particles can be viewed in the image. The morphology of the DMT-AgNPs differs from AgNPs morphology and is almost uniform and mono-dispersed without any aggregation (Fig. 5b). It also notices the crystalline nature of fine particles with a free-procured particle arrangement. The separation between the nanoparticles indicates the functionalization of nanoparticles by DMT, which has been used as a functionalizing agent and may vary the morphology of the samples.

TEM study

The functionalization of DMT to AgNPs for enhanced properties can be evidenced from the TEM studies which provide the exact size and shape changes of AgNPs and capped AgNPs with DMT. The TEM image recorded for the AgNPs and DMT-AgNPs are shown in Fig. 6(a-b) and SAED images in Fig. 6(c-d) respectively. Microphotographs show spherical particles of 20–21 nm (Fig. 6a) and 50–51 nm (Fig. 6b) for AgNPs and DMT-AgNPs without aggregation. The large variation in the size of AgNPs and DMT-AgNPs i.e., a difference of 30 nm is due to the DMT which binds to AgNPs and brings the surface functionalization of nanoparticles. Both DMT-AgNPs and AgNPs are highly crystalline in nature as shown in the SAED pattern of the samples (Fig. 6c and 6d).

Fourier transform infrared spectroscopy analysis

FT-IR spectroscopy study is undertaken to know the chemical composition of the surface of the AgNPs and its functionalization with t

DMT which has both free amine and thiol functional groups. The FT-IR spectrum of AgNPs and DMT-AgNPs are shown in Fig. 7(a-b) respectively. The purified freeze-dried powders of AgNPs were subjected to FT-IR scanning to confirm the capping of DMT to AgNPs. The broadband appearing at 3051.34 cm^{-1} is due to C-H stretching vibration, the small stretching band at 3276.29 cm^{-1} corresponds to the NH_2 group, peak with bending vibration at 2360.28 cm^{-1} represents the S-H (thiol) group. In continuation, a sharp stretching at 1596.63 cm^{-1} maybe due to the presence of the C = N bond and a sharp stretch at 1287.20 cm^{-1} can be assigned to the C-N bond. A small stretching at 1010.54 cm^{-1} is assigned for the N-N bond and a broad bending vibration at 1655.63 cm^{-1} may be due to the N-H group of the DMT ligand. The FT-IR spectrum of DMT-AgNPs shows the stretching and bending vibration of groups almost similar to ligands except for the peak at the $1200\text{--}1300\text{ cm}^{-1}$ range which indicates the S-H (thiol) group is involved in the functionalization of DMT-AgNPs. Thus the disappearance of the bending vibrations of the S-H (thiol) group and the decrease in intensity of the other bands are attributed to functionalized AgNPs.

Antimicrobial assays with minimum inhibitory concentration

An antimicrobial behavior study was performed to see the growth inhibitory effect of synthesized AgNPs and DMT-AgNPs samples using the standard method. The obtained results are tabulated in Table 2 and the observed ZOI of the samples is shown in Fig. 8. The clear observation of the obtained results reveals that the sample DMT-AgNPs have higher antimicrobial activity compared to AgNPs. It may be due to their higher solubility (capping of polar groups) and higher diffusion potential of DMT-AgNPs. The functionalized sample might get attached to the surface of the cell membrane and disturb its power function such as permeability and respiration, thus inhibiting the growth of microbes. The representation of these results is shown in Fig. 9.

In vitro cytotoxicity test study of DMT-AgNPs

In-vitro cytotoxicity testing procedures reduce the use of animals and enforce to use of cultured tissues and cells [56,57] in the laboratory for a safe environment. The reduction of tetrazolium salts is widely accepted as a reliable way to examine cell proliferation [58]. The cytotoxicity assay measures the cell proliferation rate and metabolic events that cause apoptosis or necrosis. The cytomorphological changes for MCF-7 cell lines are shown in Fig. 10. After 24 h of treatment, their IC_{50} values with statistical studies are shown in Fig. 11a, and their graphical

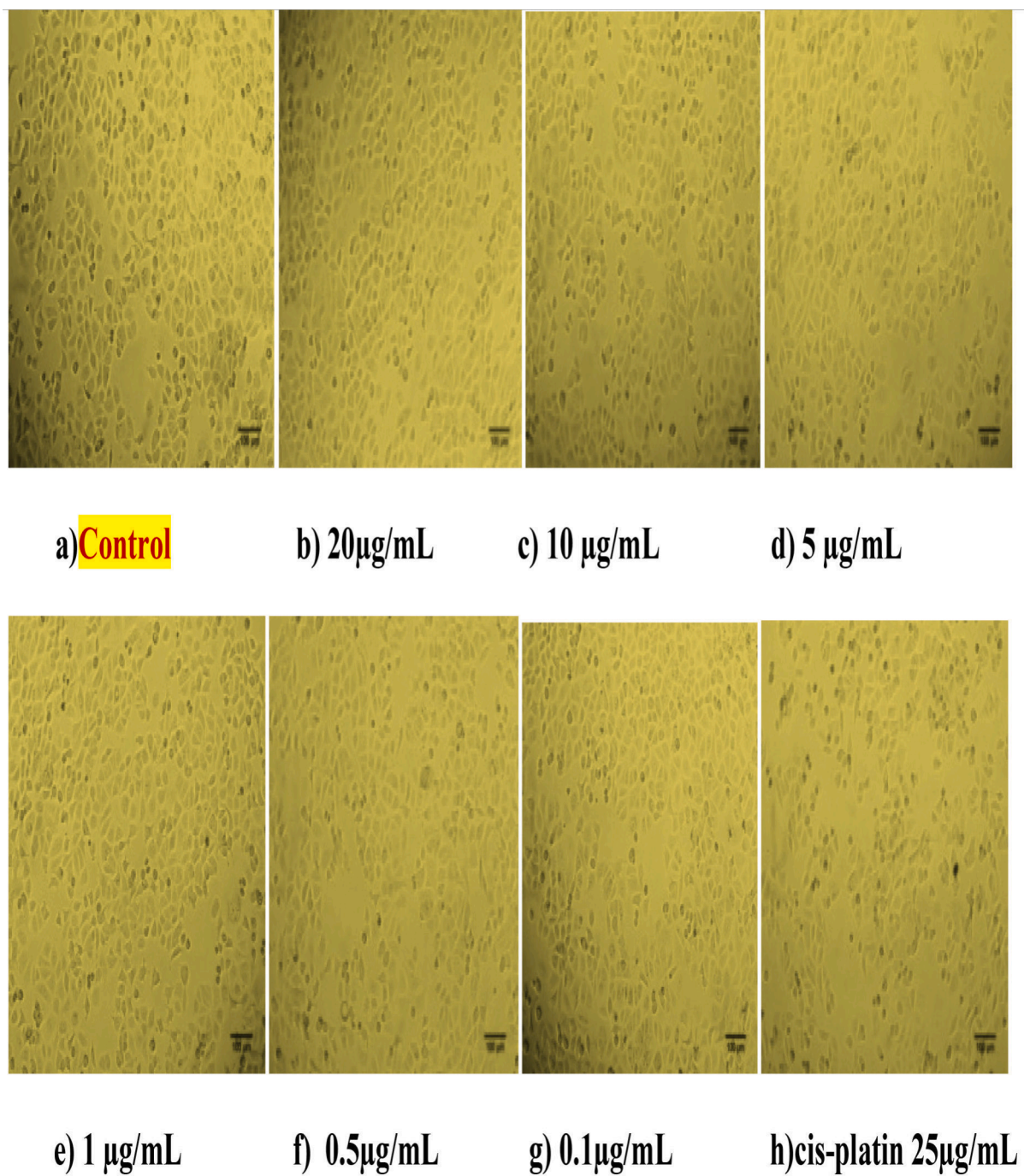


Fig. 10. Cytomorphological changes of MCF-7 cell line treated with colloidal AgNPs and DMT-AgNPs.

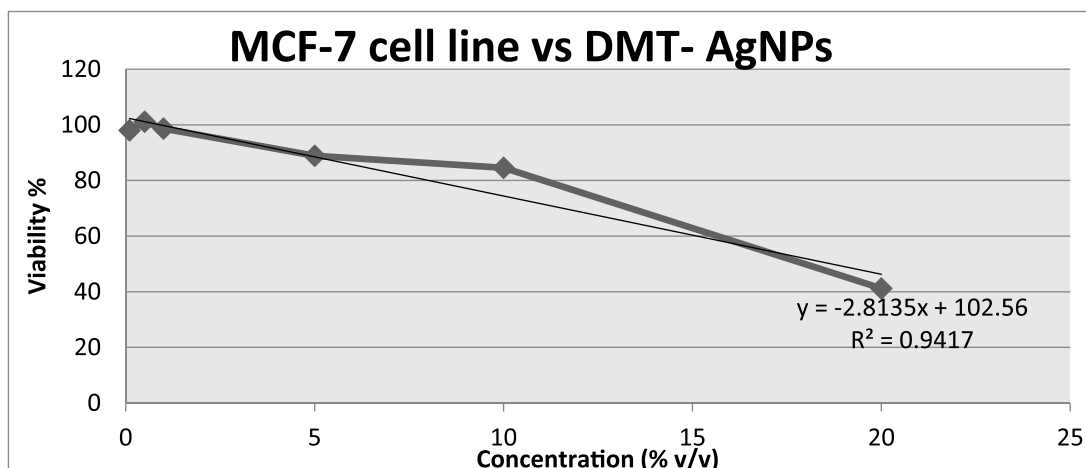


Fig. 11a. Statistical representation of *In vitro* cytotoxicity test study.

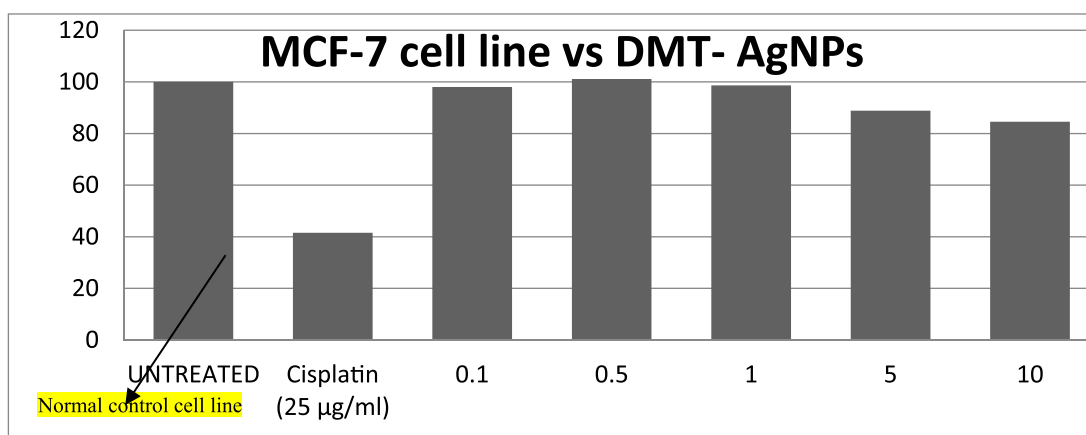


Fig. 11b. Graphical representation of *In vitro* cytotoxicity test study of a sample.

representation in Fig. 11b. Comparative observations from Fig. 10 and Fig. 11 indicate that the synthesized DMT-AgNPs show good results compared to plane AgNPs and chemotherapeutic drug Cis-platin against MCF-7 cell lines. The anticancer effect of AgNPs and DMT-AgNPs might be due to nano size, surface area, and surface functionalization factors which control bio-kinetics leading to a reduction in cell viability. The reacting mode of DMT-AgNPs may be described as Nano samples first making a breakthrough in the permeability of the outer membrane, resulting in the leakage of cellular materials that cause cell decomposition and death eventually. Further, the DMT-AgNPs sample may enter the inner cell membrane and inactivate or disruption of the mitochondrial respiratory chain leading to the release of Reactive Oxygen Species (ROS). This disturbs (ATP) proteins, and phosphate lipids synthesis, which in turn leads to DNA damage. It is inhibiting respiration and growth of cells [59]. Therefore DMT-AgNPs result in an increased cell proliferation rate compared to plane AgNPs.

Molecular docking study

Analyzing the results obtained from *in vitro* studies, it was thought worth performing molecular docking studies for the respective synthesized samples. The DMT ligand which has free thiol (-SH) and amine (-NH₂) groups may get attached to the AgNPs sample to bring the surface functionalization making them more bio-active. Hence, it was necessary to study the possible conformations, and binding energies and to inculcate both *in-silico* and *in-vitro* results. All four possible

conformations or target sites where AgNPs get attached to DMT ligand moiety and the standard drug (DMT) having 2D structure were converted to energy-minimized 3D structures. Finally, iGEMDOCK ranked for DMT- AgNPs were visualized in Fig. 12 with the binding pose by combining the pharmacological interactions and binding energy-based score function. The binding energies and residues involved in H-bonding are tabulated in Table 3.

In-silico studies revealed that the synthesized AgNPs and DMT-AgNPs showed good binding energy toward the targeted proteins as shown in Table 3. The S1b and S1c have a maximum binding energy for target proteins among all the designed possible conformations, which were taken for studies. S1b showed good antibacterial properties for 1iYS and 1JJJ target protein i, e-64.6292, and -65.7112.

The S1c possible conformations have a binding energy of -69.5458 for 5IAE and the S1b design possible conformations have a binding energy of -69.3362 for 1K2N cancer proteins when compared to standard drugs. It is the thiol group of DMT-AgNPs that alkylate the DNA resulting in obstruction of DNA replication and RNA translation or DNA-DNA cross-linking i.e. Guanine-Adenine or Guanine intrastrand and DNA-protein cross-links. Such crosslink proceeds through the S_N2 reaction mechanism leading to the disruption of DNA and RNA strands. These types of damages cannot be repaired by our body's cellular machinery and hence cells might undergo apoptosis mostly via the p53 pathway [60] acting as a good anticancer agent.

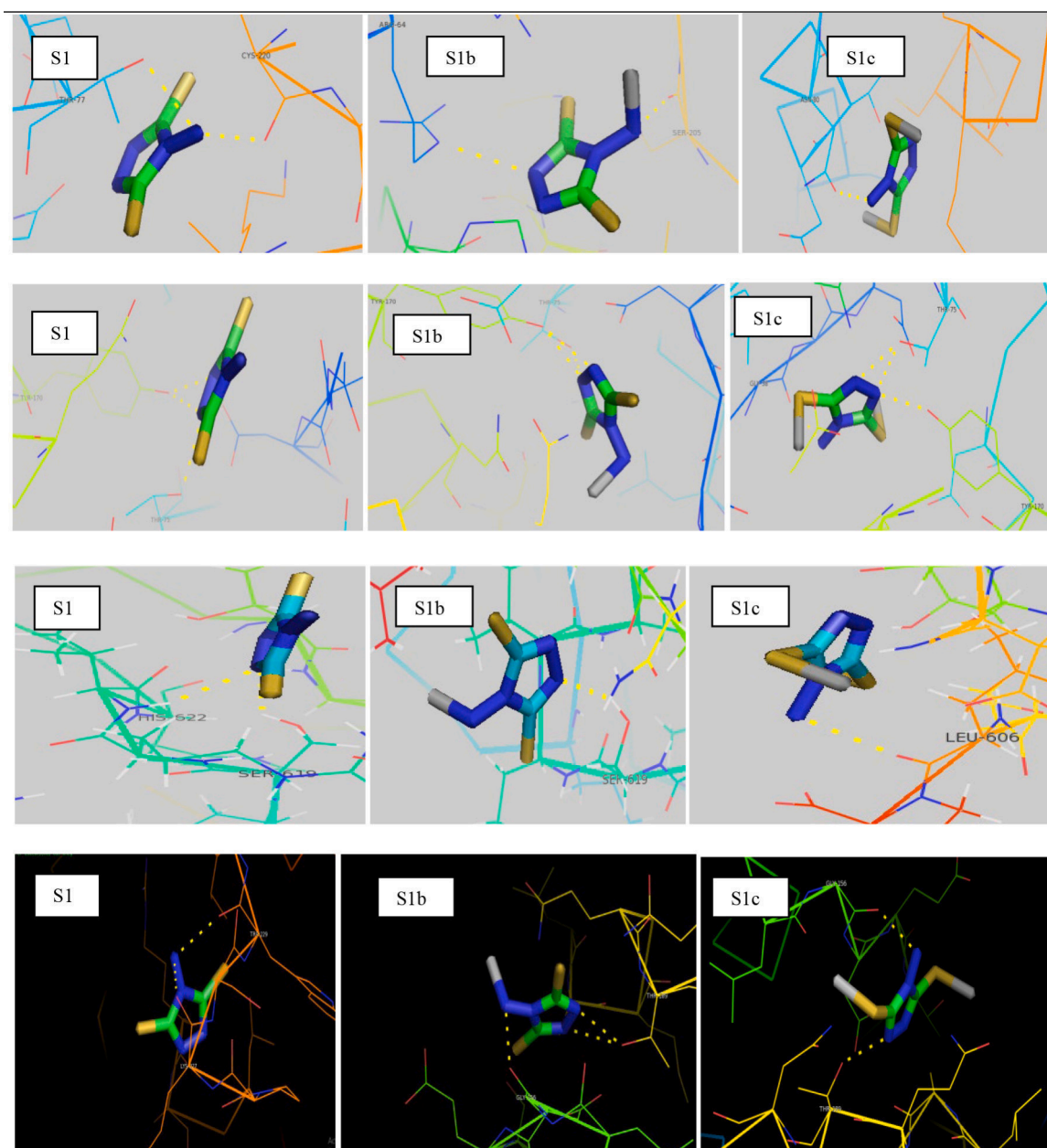


Fig. 12. The best and stable conformations of the synthesized DMT as standard drug molecule and DMT-AgNPs.

Table 3

Docking results of AgNPs and DMT-AgNPs.

Sl. No	Compound	β -lactamase toho-1 <i>Escherichia coli</i> - 1iYS	<i>S.Aureus</i> ligase-1JJJ	Caspase-3 V266F – 5IAE	FHA2 domain of RAD53- 1K2N
1.	S1	–61.5473	–62.1064	–63.1473	–60.2055
2.	S1a	–62.0388	–62.3817	–65.9447	–58.7761
3.	S1b	–64.6292	–65.7112	–67.1481	–69.3362
4.	S1c	–62.1103	–61.9892	–69.5458	–61.1364
5.	S1d	–60.8836	–49.0176	–46.0144	–39.6049
6.	Cpn (cisplatin)	–	–	–27.6801	–27.716
7.	Gmn (Gentamicin)	–98.2932	–91.5345	–	–

Conclusion

The present work reports an efficient chemical reduction method for the functionalization of AgNPs with DMT and is well characterized for its phase formation. Synthesized DMT-AgNPs have certain advantages like ease of applicability in large-scale production, economically feasible, eco-friendly, and higher solubility. Evaluation of biological study against MCF-7 cell lines explores the potential improvement in the biological activity of the DMT-AgNPs compared to AgNPs. A molecular docking study compiled the mobility of synthesized DMT-AgNPs samples into cells deciding their fate in a bioprocess and risk aspects for their application. Conclusively, the obtained results conclude that the DMT-AgNPs sample can be used for the next generation of biomedical applications.

Research data

The data that has been used is confidential.

CRedit authorship contribution statement

V. Veena: Writing – original draft, Conceptualization. **K.H. Shivaprasad:** Project administration, Supervision. **H. Sharanagouda:** Formal analysis. **Ganiger Sangappa K.:** Software, Writing – review & editing. **Arunkumar Lagashetty:** Software, Writing – review & editing.

Declaration of competing interest

The authors declare that they have no known competing financial interests or personal relationships that could have appeared to influence the work reported in this paper.

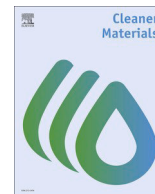
Acknowledgments

Authors acknowledge DST for a grant (DST-FIST (SR/FST/CSI-274/2016) providing financial support for this research work. Thanks are due to the Head, Department of Nanotechnology, UAS, Raichur, India for providing some laboratory facilities.

References

- [1] P. Avouris, Manipulation of matter at the atomic and molecular levels, *Accounts Chem. Res.* 28 (1995) 95–102, <https://doi.org/10.1021/ar00051a002>.
- [2] O.V. Salata, Applications of nanoparticles in biology and medicine. *J. Nanobiotechnol.* 30:2(1) (2004) 2–3, Doi: 10.1186/1477-3155-2-3.
- [3] M. Nowostawska, S. A. Corr, S. J. Byrne, J. Conroy, Y. Volkov, and Y. K. Gun'ko, Porphyrin-magnetite Nano conjugates for biological imaging. *J. Nanobiotechnol.* 8: 9(13) (2011) 9–13 Doi: 10.1186/1477-3155-9-13.
- [4] A. Surendiran, S. Sandhiya, SC Pradhan, C. Adithan Novel applications of nanotechnology in medicine. *Ind J Med Res.* 130(6) (2009) 689–701, Doi: 10.1111/j.1472-8206.2009.00692.x.
- [5] R. D. Holtz, A. G. Souza Filho, M. Brocchi, D. Martins, N. Durán, and O. L. Alves, Development of nanostructured silver vanadates decorated with silver nanoparticles as a novel antibacterial agent. *Nanotechnology* 7:21(18), 185102 (2010), Doi: 10.1088/0957-4484/21/18/185102.
- [6] S. Ahmed, U. Saif, M. Ahmad, B. Lal Sawmi, S. Ikram, Green synthesis of silver nanoparticles using *Azadirachta indica* aqueous leaf extract, *J. of Ration Resch. and Applied Sci.* 173 (2015) 1–7, <https://doi.org/10.1016/j.jrras.2015.06.006>.
- [7] D. Raghunandan B. Ravishankar, G. Sharanbasava D.B. Mahesh, V. Harsoor, Yalagatti MS, et al. Anti-cancer studies of noble metal nanoparticles synthesised using different plant extracts. *Cancer Nanotechnol* 2(1-6) (2011) 57–65, Doi: 10.1007/s12645-011-0014-8.
- [8] M.P. Yeole, S. Dhole, N. Kulkarni, Peptide nanomedicine in cancer treatment, *Asian J Pharm Clin Res* 6 (2) (2013) 28–32, <https://doi.org/10.3390/pharmaceutics14071378>.
- [9] M. Albrecht, A. Evans, C.W. Raston, C. L, *Green Chem.* 8 (2006) 417, <https://doi.org/10.1039/B517131H>.
- [10] T. Sun, K. Seff, Silver Clusters and Chemistry in Zeolites, *Cheminform.* 94 (1994) 857, <https://doi.org/10.1021/cr00028a001>.
- [11] D. Xiong, J.M. Chen, L. Li, H, *Chem Commun* (2008) 880, <https://doi.org/10.1039/B716270G>.
- [12] N. Duran, P. Marcato, D. Alves, O. L De Souza, G. I. H; Esposito, E. J. Nano biotechnology, 3(2005) 8, Doi: 10.1186/1477-3155-3-8.
- [13] S. Basu, S. Jana, S.Pande, T. Pal, *J. Colloid and Interface Sci.* 2008, 321, 288. Doi: 10.1016/j.jcis.2008.02.015.
- [14] I.Brigger, C. Dubernet, P. Couvreur, *Adv. Drug. Deliv. Rev.* 54 (2004) 631, Doi: 10.1016/S0169-409X (02)00044-3.
- [15] M.G. Guzman, J. Dille, S. Godet, *World Acad. Sci. Eng Technology.* 43 (2008) 357.
- [16] Z. Zhu, L. Kai, Y. Wang, *Mater. Chem. Phys.* 96 (2006) 447, <https://doi.org/10.1016/j.matchemphys.2005.07.067>.
- [17] S. Amruta Lanje, J. Satish, Sharma, B. Ramachandra Pode, Synthesis of silver nanoparticles: A safer alternative to conventional anti-microbial and antibacterial agents, *J. Chem. Pharm. Res.* 2 (3) (2010) 478–483.
- [18] M. Irulappan Sriram, Selvaraj Barath Mani Kanth. Antitumor activity of silver nanoparticles in Dalton's lymphoma ascites tumor model, *Int J Nanomed*, 5(2010) 753–762, Doi: 10.2147/IJN.S11727.
- [19] D. Peer, J. Karp, M. Hong, S. Farokhzad, O.C.R. Margalit, R. Langer, Nano carriers as an emerging platform for cancer therapy, *Nat, Nanotechnology.* 2 (12) (2007) 751–760, <https://doi.org/10.1038/nnano.2007.387>.
- [20] S. Bamrungsap Z. Zhao T. Chen L. Wang Li C. Fu T, Tan W, *Nanotechnology in therapeutics: a focus on nanoparticles as a drug delivery system.* *Nanomedicine (Lond).* 2012, 7(8):1253–71, Doi: 10.2217/nnm.12.87.
- [21] M. Rai, A. Yadav, A. Gade, Silver nanoparticles as a new generation of anti-microbials, *Biotechnol. Adv* 27 (1) (2009) 76–83, <https://doi.org/10.1016/j.biotechadv.2008.09.002>.
- [22] C. Taleb, M. Petit, P. Pileni, Synthesis of Highly Monodisperse Silver Nanoparticles from AOT Reverse Micelles: A Way to 2D and 3D Self-Organization, *Chem. Mater.* 9 (1997) 950, Doi: 10.1021/cm960513y.
- [23] A.Henglein, Reduction of Ag(CN)₂- on Silver and Platinum Colloidal Nanoparticles *Langmuir* 17 (2001) 2329–2333. Doi: 10.1021/la001081f.
- [24] K. Esumi, T. Tano, K. Torigoe, K.Meguro, Preparation and Characterisation of Bimetallic Pd-Cu Colloids by Thermal Decomposition of Their Acetate Compounds in Organic Solvents. *Chem. Mater.* 2(1990)564, Doi: 10.1021/cm00011a019.
- [25] J.J. Zhu, S.W. Liu, O. Palchik, Y. Koltypin, A. Gedanken, Shape-Controlled Synthesis of Silver Nanoparticles by Pulse Son Electrochemical Methods, *Langmuir* 16 (2000) 6396–6399, <https://doi.org/10.1002/chem.200400705>.
- [26] J. Xie, J. Lee, Y.D.I.C. Wang, Y.P. Ting, Identification of active biomolecules in the high yield synthesis of single-crystalline gold nameplates in algal solutions, *ACS Nano* 3 (4) (2007) 672–682, <https://doi.org/10.1021/nn7000883>.
- [27] V.K. Sharma, R.A. Yngard, Y. Lin, Silver nanoparticles: green synthesis and their anti-microbial activities, *Ads. Colloid Interface Sci.* 30 (145) (2009) 83–96, <https://doi.org/10.1016/j.cis.2008.09.002>.
- [28] X.F. Zhang, Z.G. Liu, W. Shen, S. Gurunathan, Silver Nanoparticles: Synthesis, Characterization, Properties, Applications, and Therapeutic Approaches, *Int. J. Mol. Sci.* 17 (9) (2016) 1534, <https://doi.org/10.3390/ijms17091534>.
- [29] S. A.Al-Thabaiti, F. M. Al- Nawaisar, A. Y. Obaid, A. O. Al- Youbi, Z. Khan, Formation and characterisation of surfactant stabilised silver nanoparticles: a kinetic study. *Colloids Surfs. B: Bio-interfaces* 67(2008) 230–237, Doi: 10.1016/j.colsurfb.2008.08.022.
- [30] .Zaheer , A O Al-Youbi Preparation and characterisation of silver nanoparticles by chemical reduction method *Colloids Surf B: Bio-interfaces* 1 (2011) 82(2), 513–517, Doi: 10.1016/j.colsurfb.2010.10.008.
- [31] C. W. Won, I; H, Nersisyan, H. L. Won, J.H. Lee, Refractory metal Nano powders: Synthesis and characterisation. *Curr. Opin. Solid State Mater. Sci.*, 114(3-4) (2010) 53–68, Doi: 10.1016/j.cossms.2009.10.001.
- [32] I. Pastoriza, L.M. Liz-marzan, Binary cooperative complementary nanoscale interfacial materials. Reduction of silver nanoparticles in DMF. Formation of monolayers and stable colloids, *J. Pure & ApplChem.* 72 (2000) 83–90, Doi: 10.1351/pac200072010083.
- [33] S.D. Solomon, M. Bahadory, A.V. Jeyarajasingam, S.A. Rutkowsky, C. Boritz, M. Lorraine, Synthesis and study of silver nanoparticles, *J. Chem. Edu.* 84 (2007) 322–341, <https://doi.org/10.1021/ed084p322>.
- [34] R.S. Patil Kokate, R.M. Jambhale C. Pawar S. Han S. Kolekar, One-pot synthesis of PVA-capped silver nanoparticles their characterization and biomedical application, *Adv Nat Sci Nanosci Nanotechnology.* 3(2012) 1-7. Doi: 10.1088/2043-6262/3/1/015013.
- [35] G. Nazeruddin, N. S. Prasad Prasad Garadkar K, Nayak A. *In-vitro* bio-fabrication of silver nanoparticle using *Adhathodavasic* leaf extract and its anti-microbial activity. *Phys. E.Low-dimens. syst Nanostruct.* 61 (2014) 56–61, Doi: 10.1016/j.physe.2014.02.023.
- [36] A. Carageorghieopol, V. Chechik, Mechanistic aspects of ligand exchange in Au Nanoparticles *Phys. Chem. Chem. Phys.* 10 (2008) 5029–5041, <https://doi.org/10.1039/B805551C>.
- [37] R. Wilson The use of gold nanoparticles in diagnostics and detection. *Chem Soc Rev.* 37(2008) 2028–2045. Doi: 10.1039/B712179M.
- [38] L.Dongli, L.Robert Donkers, Gangli Wang, Amanda S. Harper, Royce W. Murray, Electrochemistry and optical absorbance and luminescence of molecule-like Au38 nanoparticles, *J. Am Chem Soc* 19(2004) 126(19)6193–6199, Doi: 10.1021/ja049605b.
- [39] M.J. Hostetler, A.C. Templeton, R.W. Murray, Dynamics of Place-Exchange Reactions on Monolayer-Protected Gold Cluster Molecules, *Langmuir* 15 (1999) 3782–3789, <https://doi.org/10.1021/la981598f>.
- [40] M. Rai, K. Kon, A. Ingle, N. Duran, S. Galdiero, M. Galdiero, Broad-spectrum bioactivities of silver nanoparticles: The emerging trends and future prospects, *Appl. Microbiol. Biotechnology.* 98 (2014) 1951–1961, <https://doi.org/10.1007/s00253-013-5473-x>.
- [41] E. Katz, I. Willner, Integrated nanoparticle-biomolecule hybrid systems: synthesis, properties, and applications, *Angew Chem Int Ed Engl.* 43 (2004) 6042–6108, <https://doi.org/10.1002/anie.200400651>.
- [42] D.B. Kitchen, H. Decornez, J.R. Furr, J. Bajorath, Docking and scoring in virtual screening for drug discovery: methods and applications, *Nat Rev Drug Discov* 3 (11) (2004) 935–949, <https://doi.org/10.1038/nrd1549>.
- [43] J.A. Creighton, C.G. Blatchford, M.G. Albrecht. Plasma resonance enhancement of Raman scattering by pyridine adsorbed on silver or gold sol particles of size comparable to the excitation wavelength. *J. Chem Soc Faraday Trans II* 75 (1979) 790–8. Doi: 10.1039/F297975BA001.
- [44] J.S. Suh, D.P. DiLella, M. Moskovits, Surface-enhanced Raman spcopy of colloiodrosdal metal systems: a two-dimensional phase equilibrium in p-amino benzoic acid adsorbed on silver, *J. Phys Chem* 87 (1983) 1540–1544, Doi: 10.1021/J100232A018.
- [45] S. Pal, Y. Kyung, Myong Song Does the Antibacterial Activity of Silver Nanoparticles Depend on the Shape of the Nanoparticle? A Study of the Gram-Negative Bacterium *Escherichia coli*, *J. Appl Environ Microbiology* 73 (6) (2007) 1712–1720, <https://doi.org/10.1128/AEM.02218-06>.
- [46] MTT Cell Proliferation Assay Instruction Guide – ATCC, VA, USA www.atcc.org Alley, M. C.

- [47] Y. Ren, S. Long, S. Cao, Molecular Docking and Virtual Screening of an Influenza Virus Inhibitor That Disrupts Protein-Protein Interactions, *Viruses* 5;13(11) (2021) 2229–2234, <https://doi.org/10.3390/v13112229>.
- [48] M. A. Lill, M. L. Danielson, computer-aided drug design platform using Py. MoL.J. computer aided molecular discovery. 25 (2010) 13-19. Doi:10.1007/s10822-010-9395-8.
- [49] H.R. Ghorbani, S. Soltani. Antibacterial effects of silver nanoparticles on *Escherichia coli* and *Bacillus subtilis*. *Oriental Journal of Chemistry*. 31(1) (2015) 341–344. <https://doi.org/10.13005/OJC/310139>.
- [50] S. Soni, T. Patel, B. Thakar, V. Pandya, P. Bharadia Nano suspension: An approach to enhance solubility of drugs. *J Pharmaceut Cosmetol*. 2(9)(2012) 49-63, Doi: 10.4103/2231-4040.82950.
- [51] D. Sivaraman, P. Panneerselvam P.Muralidharan, P. Prabhu, R. Vijaya Kumar, Green synthesis, characterisation and anti-microbial activity of the silver nanoparticles produced from *Ipomea aquatica* Forsk leaf extract. *Int J Sci Res*, 4(6) (2013) 2280-2285, <https://doi.org/10.13040/IJPSR.0975-232.4> (6).2280-85.
- [52] N. Vigneshwaran, A. A. Kathe, P. V. Varadarajan, R. P. Nachane, and R. H. Balasubramanya, Biomimetic of silver nanoparticles by white rot fungus, *Phaenerochaete chrysosporium*, *Langmuir*, 23 (2007) 7113-7117, Doi: 10.1016/j.colsurfb.2006.07.014.
- [53] R. Varshney, A. N. Mishra, S. Bhadauria, M. S. Gaur, A novel microbial route to synthesise silver nanoparticles using fungus *Hormoconis resinae*, *Digest J Nanomater Biostructur*, 4(2) (2009) 349 – 355. Doi:10.1007/978-3-031-31111-6_17.
- [54] R. Sarkar, P. Kumbhakar, A. K. Mitra, Green Synthesis of Silver Nanoparticles and its Optical Properties, *Digest Journal of Nanomaterials and Biostructures*, 5(2) (2010) 491–496, Doi: 10.1016/J.JINDCROP.2014.08.030.
- [55] S.A. Abraham, C.McKenzie, D. Masin, Ng, R., Harasym, T.O., Mayer, L.D., Bally, M. B., Formation of transition metal-doxorubicin complexes inside liposomes, *BiochimBiophys Acta*, 20 (2002) 1565(1)41-54, Doi: 10.1016/s0005-2736(02)00507-2.
- [56] J. C. Byrd, T. Murphy, R. S. Howard, M. S. Lucas, A Goodrich, K. Park, M. Pearson, J. K. Waselenko, G Ling, M R Grever, A J Grillo-Lopez, J Rosenberg, L Kunkel, I W Flinn Rituximab using a thrice weekly dosing schedule in B-cell chronic lymphocytic leukemia and small lymphocytic lymphoma demonstrates clinical activity and acceptable toxicity, *J Clin Oncol*, 15; 19(8)(2001) 2153-64, <https://doi.org/10.1200/JCO.2001.19.8.2153>.
- [57] D. A. Scudiero, R. H. Shoemaker, K. D. Paull, A. Monks, S. Tierney, T. H. Nofziger, M. J. Currens, D. Seniff, M. R. Boyd, Evaluation of a soluble tetrazolium/formazan assay for cell growth and drug sensitivity in culture using human and other tumor cell lines *Cancer Res* 1;48(17) (1988) 4827-33, [https://doi.org/10.1016/0020-7519\(90\)90107-x](https://doi.org/10.1016/0020-7519(90)90107-x).
- [58] S. Amruta Lanje, J. Satish Sharma, B. Ramachandran, S. Pode, Raghu Mani Ningthoujam Synthesis and optical characterisation of copper oxide nanoparticle, *Adv Appl Sci Res* 1 (2) (2010) 36–40.
- [59] V. Probin, Y. A. Wang Bai, D. Zhou Busulfan Selectively Induces Cellular Senescence but Not Apoptosis in WI38 Fibroblasts via a p53-Independent but Extracellular Signal-Regulated Kinase38 Mitogen-Activated Protein Kinase-Dependent Mechanism, *J. pharmacol. Exp. Ther.* 319(2) (2006) 551-60, Doi: 10.1124/jpet.106.107771.
- [60] T. Iwamoto, Y. Hiraku. S. Oikawa, H. Mizutani, M. Kojima, S. Kawanishi DNA intrastrand cross-link at the 5'-GA-3' sequence formed by busulfan and its role in the cytotoxic effect, *Cancer Science*, 95;(5) (2004) 454-458, Doi: 10.1111/j.1349-7006.2004.tb03231.x.



Effect of collated fly ash, GGBS and silica fume on index and engineering properties of expansive clays as a sustainable landfill liner

Manikanta Devarangadi^{a,*}, Srikanth Vuppala^{b,2}, M. Uma Shankar^{c,3},
Mavinakere Eshwaraiah Raghunandan^{d,4}

^a Department of Civil Engineering, Ballari Institute of Technology & Management, Ballari, India

^b Research and Development Division, WIISE SRL SOCIETA' BENEFIT, Via dei Grottoni 67/16, Rome, 00149, Italy

^c Department of Environmental and Water Resources Engineering, Vellore Institute of Technology, Vellore, India

^d Senior Lecturer in Geomechanics, Department of Civil Engineering, School of Engineering, Monash University Malaysia, Bandar Sunway, Selangor Darul Ehsan, Malaysia

ARTICLE INFO

Keywords:

Expansive clay
Fly ash
GGBS
Landfill liner
Silica fume
Waste recycling

ABSTRACT

The effect of supplementary cementitious materials (SCMs) such as fly ash (FA), GGBS and silica fume (SF) on the geotechnical index and engineering properties of expansive clays (EC) are studied in this research work. This manuscript aims to determine the workability (consistency limits (CL)), swellability (free swell index (FSI)), compaction properties, strength characteristics (UCS) and hydraulic conductivity (HC) of varied eighteen mix proportions of FA-EC (P-series), FA-GGBS-EC (Q-series) and FA-GGBS-SF-EC (R-series) are experimentally studied as a bottom liner in landfills. From the test results, CL and FSI significantly decreased in P, Q and R series, this is due to the effect of flocculation, a process that increases the average particle size of mix blends and also depletion of the double-diffusive layer thickness of EC by promoting the Ca²⁺ ions in the pore water from SCMs. The compaction parameters such as optimum moisture content decreased in all the series, due to the higher flocculation of mixes. However, maximum dry unit weight increased in Q and R and decreased in the P series. The UCS values increased with an increase in optimum SCMs quantities and with curing intervals tested at 0, 7, 14 and 28 days. The higher UCS value is attained at 40 %FA with EC (i.e. P2), 60 %FA-GGBS with EC (i.e. Q3) and 60 %FA-GGBS-SF with EC (i.e. R3) in R-series which confirmed to be optimum due to the loss of cementation action/reduced cohesion in the matrix. In the case of HC, P2, Q3 and R3 mixes are confirmed to be optimum and fall under the criterion standards of landfill liner as per USEPA recommendation. Overall, this work proves to be a novelty and shows the feasibility of various collated SCMs blended with EC as landfill liner material, furthermore, these mixes are optimized to combine with EC to create a sustainable landfill liner that fits with the United Nations sustainable goals of 2030

1. Introduction

The earth's outer layer consists of soil which is referred to as the "skin of the earth", and mainly contributes to agriculture, but some soils are also great for use in construction and are still commonly employed today. In developing nations, the percentage of soil used in construction is bigger than in the West. There are several advantages of soil as a raw

material in construction. At the same time, there is an obvious negative influence on construction (Payá et al., 2020). For instance, soil in landfill liners leads to percolation and passage of waste into the earth's surface. To avoid seepage of leachate an engineered landfill liner is required. Apart from urbanization, industrialization, irrigation purposes and other cement-involved constructions raised cement production enormously (Huang et al., 2018).

* Corresponding author.

E-mail addresses: manikanta299@gmail.com (M. Devarangadi), srikanth.vuppala@seamthesis.com (S. Vuppala), mumashankar@vit.ac.in (M.U. Shankar), mavinakere.raghunandan@monash.edu (M.E. Raghunandan).

¹ ORCID: <https://orcid.org/0000-0002-1144-0939>.

² ORCID: <https://orcid.org/0000-0002-0487-0519>.

³ ORCID: <https://orcid.org/0000-0003-1473-3777>.

⁴ ORCID: <https://orcid.org/0000-0002-3212-0352>.

<https://doi.org/10.1016/j.clema.2024.100219>

Received 1 October 2023; Received in revised form 6 January 2024; Accepted 20 January 2024

Available online 24 January 2024

2772-3976/© 2024 The Author(s). Published by Elsevier Ltd. This is an open access article under the CC BY-NC-ND license (<http://creativecommons.org/licenses/by-nc-nd/4.0/>).

Because the cement manufacturing industry accounts for a significant portion of global CO₂ emissions, researchers have made and are continuing to work to increase cement plants' energy efficiency through improved production methods, the use of alternative fuels, and the application of cutting-edge carbon capture, utilization, and storage technologies (Zhu et al., 2022). To achieve the goal of carbon emission minimization through clinker replacement, the most significant and efficient approach is to add a significant amount of supplemental cementing materials (SCMs) to cement (Acordi et al., 2020; Benhelal et al., 2013; Silva et al., 2023). One of the more viable methods involves using industrial by-products such as cement kiln dust, red mud, waste wood ash, fly ash, and waste red mud as landfill liners (Al-Bakri et al., 2022).

The CO₂ emissions in the cement industry, and by-products of the cement industry together are one issue and the other hand which is quite important and directly linked to the landfill process is "Solid waste". The increasing global population needs have promoted the increasing amount of municipal waste. This waste must be treated according to national directives, the most suggested and common practices are a) recycle, b) burn, or c) deposit. The German Landfill Directive, which was passed in 2009 and the EU's environmental and technical standards that must adhere to legal requirements, recommends the essential and practicable qualitative criteria for constructed barriers (Beck-Broichsitter et al., 2019).

To safeguard the immediate area around the waste deposit site, landfill liners have been developed. Liner systems are therefore crucial to safeguarding groundwater and preventing the diffuse emission of greenhouse gases (i.e., methane). In order to inhibit the environmental effects of landfill leachate, landfills are designed with leachate barriers to prevent leachate from contaminating the underlying soil and groundwater (Nath et al., 2023; Wan et al., 2023). The barrier for leachate in general referred to as a "landfill liner" which is an impermeable liner that works to prevent the leachate from escaping the landfill system. Natural materials (such as clay and boulder marl) are frequently used to build landfills' top and bottom liners; however, they must adhere to technical standards (Emmanuel et al., 2020). Due to its affordability, effectiveness, convenient technology, and high capacity, engineered landfills have established themselves as the method of choice for disposing of municipal solid waste in various regions of the world (Chakradhar and Katoch, 2016; Feng et al., 2020). These landfills are in general constructed using clays with reference to local legal standards (Widomski et al., 2015).

Expansive clays, bentonite-sand mixes, laterite soils, etc. were blended with industrial by-products like fly ash (FA) (Mir and Sridharan, 2017), which also improved the engineering characteristics of the soils (Devarangadi and Shankar, 2021). The widespread application of these industrial by-products as lining materials produced excellent results. These industrial by-products have the ability to enhance the undesired geotechnical qualities of soils like expansive clays, dispersive clays, and soft marine clays, among others, by reducing their swelling-shrinkage parameters and enhancing the soil's strength, dry weight, and compressibility. The main disadvantage, however, is the spread of clays, which seriously harms pavement structures and is a big problem all over the world (Soltani et al., 2022; Widomski et al., 2015). High-plasticity characteristics were observed in these challenging soil exhibits. They can expand as a result of changes in seasonal and ambient moisture levels and absorb a lot of water. Silt, clay stones, residual soils, and sedimentary soils with smectite clay minerals and mica groups (such as montmorillonite, illite, and vermiculite) are expansive in character (Abbey et al., 2020). Especially expansive soils are well recognized for their behaviour in terms of volume change due to changes in water content (Koukousas et al., 2022). Clay-like minerals, such as montmorillonite, are found in expansive soils; these minerals' volumes change during wetting and drying. Structure, sidewalks, roadways, basement floors, pipes and even foundations could experience excessive strain from this volume change to be damaged. Clayey soils having a

significant specific surface area and strong cation exchange capacity are referred to as expansive soils. The difficulty for civil engineers is felt all across the world because expansive soils are present everywhere. Expansive soils may provide a natural hazard and cause significant structural damage if improperly managed (Devkota et al., 2022).

Desiccating these soils during the dry season causes shrinkage cracks, which make it easier for water to penetrate the soil and aggravate swelling. Soils undergo considerable volume changes due to this cycle of swelling and contracting, and finally lose their capacity to sustain weight. Additionally, unneeded stresses brought on by expansive soils' shrink-swell characteristics cause structural damage through heaving and differential settling. Due to the high-plasticity expansive soils that cover 20 % of the land surface in the United States (US), the issue is particularly severe there. The estimated annual damage from expansive soils in the US is estimated to be billions of dollars, outpacing the total damage from earthquakes, floods, hurricanes, and tornadoes. Urbanization has made land scarcely accessible, therefore, when choosing construction locations, it is frequently vital to take expansive soils into account. Chemical stabilization of these soils is a practical method for ensuring construction safety and achieving significant financial savings by lowering the expense of repair and rehabilitation (Ijaz et al., 2022). Cement and lime are the stabilising agents that are most frequently used to treat expansive soils. Numerous analyses of the stabilisation of expansive soils by cement and lime have been carried out over time by different scholars. However, the brittleness of soils that have been treated with cement and lime is often undesirable in situations where there are dynamic stresses, such as traffic loads on paving systems. (Mahedi et al., 2020).

Therefore, an innovative blend of collated FA, GGBS and Silica fume with EC could be the next-generation solution for geotechnical index issues raised in the construction sector and waste management sector. Looking at FA, GGBS, and Silica fume in this context, FA is originally formed from the coal's mineral matter into a fine powder, which consists of non-combustible materials in coal and a negligible amount of carbon that is left over after incomplete combustion. FA typically has a light brown colour and is primarily made up of glassy spheres the size of silt and clay. With respect to coal mix and plant operating conditions, FA properties vary greatly. Every year, almost 50 million tons of FA are recycled and reused in the US. FA is referred to as either cementations (Wei et al., 2018) or pozzolanic (Singh et al., 2021; Thomas et al., 2017). The specific characteristics of the FA, particularly in terms of cementations and pozzolanic, were described by Ghassemi and co-workers. A cementation material hardens when mixed with water. Pozzolanic materials will also harden when exposed to water, but only after being activated by an alkaline agent like lime. Some FAs help replace cement in concrete and numerous other construction needs because of these cementations and pozzolanic qualities. Fly ash is utilized in the production of concrete and cement, as well as in the production of road base, oil stabiliser, clean fill, filler for asphalt, and mineral filler (Ghassemi et al., 2004).

Gypsum, calcium hydrate, and limestone are among the active minerals that are present in GGBS abundantly, which is a by-product of the blast furnaces used to produce iron (Ghosh et al., 2023). Blast furnaces are fed with mixtures of iron ore, coke, and limestone and run at a temperature of roughly 1500 °C. When iron ore, coke and limestone melt in the blast furnace, molten iron and molten slag are two products created. Molten slag is lighter than molten iron and floats on top of it. The silicates and alumina make up the majority of the molten slag (Siddique, 2008). Slag is granulated by a process that involves cooling molten slag with high-pressure water jets. This causes the slag to rapidly cool, forming granular particles that are typically smaller than 5 mm. The granulated slag is then subjected to additional processing, including drying and grinding into a very fine powder known as "GGBS" in a rotating ball mill (Liu et al., 2023; Siddique and Bennacer, 2012).

Silica fume (SF) also known as micro-silica, is an amorphous (non-crystalline) polymorph of silicon dioxide. It is a by-product of the

reduction of high-purity quartz in electric arc furnaces using carbonate materials (such as coal, coke, and wood chips), and it has a particle size range of 0.1 m to 1 m. It is produced in the production of silicone and ferrosilicon alloys (Sumitha and Abraham, 2016). In the manufacturing of other silicon alloys such as ferrochrome, ferromanganese, ferromagnesium, and calcium silicon, it is also created as a byproduct. It is regarded as a high-performance, exceptionally reactive pozzolanic mineral additive because of its high silica concentration and extraordinary fineness. By altering the performance of the surface soil linings, Hussain, Al-Ameen, and Janna researched the permeability of silica fume and concluded that landfill liners are greatly enhanced with the inclusion of silica fume. The proportion of silica fume in the lining needs to be taken into account when designing the lining system because it will improve permeability (Hussain et al., 2021). Because GGBS, silica fume, and fly ash are waste materials with binding properties, they have drawn researchers' attention as potential candidates for inclusion in collated blends for lowering the environmental impact. On the contrary, mixing with EC makes for the most effective and sustainable landfill liner to solve the leachate problem. (Ahmad et al., 2022). Attempting to reduce waste and improve resources, energy, water, and human capital utilization efficiency is an approach to cleaner production (Gupt et al., 2023).

Several researchers worked on SCMs and their engineering properties, in some works either on properties alone or other applications as well. Lashari et al (2023) worked on the effect of silica fume and fly ash as cementitious material, the use of SF and FA as binary cementitious material (BCM) in roller compacted concrete (RCC) based on the hardened properties and embodied carbon of RCC. Singh et al (2020) investigated the effect of silica fume on the engineering properties of expansive soil, where this work is focused on the blend of FA, GGBS and SF on index and engineering properties of expansive clays and also investigated the suitability of landfill liner which is a sustainable approach to reach the SDG. Similar to the above work, other researchers worked on the mechanical, durability, and microstructure of concrete by incorporating Nano Silica (nS), carbon nanotubes, steel fibres and other sustainable pozzolanic materials (Golewski, 2023; Sumathi et al., 2023). Ahmad et al (2023) reviewed the durability and microstructure analysis of concrete made with volcanic ash (VA) and revealed that the durability of concrete improved considerably with the replacement of cement with VA due to pozzolanic activity and micro fillings and the typical optimum dose of VA ranges from 10 to 30 %. The dose optimization of FA is carried out by the authors in this work, which is a convincing approach concerning the above-cited research works.

It is important to discuss the synergistic effect of coal FA, and SF with other pozzolanic materials and nanomaterials, and the effects of these wastes on different mechanical and physical parameters. Wang et al (2020) researched on synergistic effects of nS (nano-silica) and FA blend to find the properties of cement-based composites. Golewski (2023a) thoroughly worked and described that FA has great potential to be used as a partial replacement for OPC, especially due to its physicochemical properties, fine grain size and impressive pozzolanic activity. In his extended work, Golewski (2023b) investigated on collated fly ash, silica fume and nS with ordinary Portland cement to check the mechanical properties and brittleness of concrete. This study utilized 5 % of nS; 10 % of SF; 0, 15, and 25 % of FA as a blend and the compressive strength (fcm) and splitting tensile strength (fctm) and the brittleness of these materials were analyzed.

While exploring the OPC, Golewski (2023c) studied the combined effect of siliceous FA, SF, and nS on the cement matrix morphology and size of microcracks and described that the addition of three FA, SF, and nS in combination (pozzolanic materials), modifies the microstructure of the cement matrix. The effect of the addition of FA on the control of water movement within the structure of the concrete was investigated (Golewski, 2023d), in another work, the early interfacial microstructures came from FA, SF and nS reacting with $\text{Ca}(\text{OH})_2$ was analyzed and also discussed reaction mechanism of three admixtures reacting with

cement hydration products and their effects on improving the interfacial microstructures, which significantly improved the performances of cement based composites (Wang et al., 2020). A detailed investigation was conducted to analyse the mechanical and durability features of a mixture of binary cement concrete modified with nanomaterials. In the context of the concrete matrix, the substitution of fractional cement content was carried out using nS (Kashyap et al., 2023). Wang et al (2023) reviewed the fabrication and properties of concrete containing industrial waste as well as the development of several environmentally friendly concretes. In brief, all the above literature states that using cementitious materials such as SF, FA, GGBS, nS and VA and other by-products to replace the concrete and increase the durability, strength and other physical-mechanical properties which leads to the production of sustainable and cleaner materials.

A useful byproduct of coal thermal power plants is fly ash (FA), GGBS and SF which are usually wasted and have been studied extensively with an optimization approach to blend with EC to produce a sustainable landfill liner. Waste management targets and their importance are described under one of the goals of the UN Sustainable Development Goals (SDGs) for 2030 (Pedersen, 2018). Growing populations and rising per capita consumption are the main causes for both environmental degradation and social unrest that have severely strained nations over the last two decades, therefore a sustainable and cleaner waste management approach is quite necessary for the leachate problem through a sustainable landfill liner (The-Sustainable-Development-Goals-Report-2023; UN-HABITAT, 2016; UN 2023 SDG Summit). By keeping in mind to reduce the burden on global CO_2 emissions control and increase the feasibility of solid waste management the collated fly ash, GGBS and silica fume on index and engineering properties of expansive clays has been studied extensively. This work would reduce the research gap and support the ongoing research where Hazardous waste landfills, municipal solid waste landfills, inert waste landfills, nuclear waste landfills and other miscellaneous toxic waste landfills will benefit.

2. Experimental (materials and methods)

2.1. Raw material characterization

The expansive clays (EC) used in this study were procured from a depth of 2 m in Ballari, India. The geotechnical properties of EC tested with ASTM standards are presented in Table 1. The EC consists of FSI and PI values of 120 % and 37 % respectively when tested with DIW, and it is designated as CH (inorganic clays of high plasticity) as per the USCS classification. The chemical and mineral composition of EC is depicted in Table 3.

The geotechnical properties of supplementary cementitious materials (SCMs) such as fly ash (FA), GGBS and silica fume (SF) and their tested ASTM standards are depicted in Table 2 and chemical compositions are displayed in Table 3. Fly ash was obtained from Bellary thermal power station, Karnataka, India which mainly comprises sand-silt mixtures and is non-plastic (NP). It is classified as class-F based on the sum

Table 1
Geotechnical properties of expansive clays (EC).

Property	Colour	ASTM standard	Expansive clay Blackish
Specific gravity		C188	2.68
Liquid limit (LL, %)		D4318-00	80
Plastic limit (PL, %)		D4318-00	43
Plasticity index (PI, %)		D4318-00	37
Shrinkage limit (SL, %)		D4943	14.8
Sand (%) (4.75–0.075 mm)		D422-63	2
Silt (%) (0.075–0.002 mm)		D422-63	28
Clay (%) (<0.002 mm)		D422-63	70
Free swell index (FSI, %)		D5890-02	120
USCS classification		D2487-06	CH
Optimum moisture content (%)		D698-07	30.29
Maximum dry density (kN/m^3)		D698-07	13.73

Table 2
Geotechnical properties of FA, GGBS and SF.

Property	ASTM standard	Fly ash	GGBS	Silica fume
Colour	–	Grey	Whitish	Whitish
Specific gravity	C188	2.20	2.86	2.19
Liquid limit (%)	D4318-00	Non-plastic	Non-plastic	Non-plastic
Plastic limit (%)	D4318-00	Non-plastic	Non-plastic	Non-plastic
Plasticity index	D4318-00	Non-plastic	Non-plastic	Non-plastic
Shrinkage limit (%)	D4943	–	–	–
Sand (%) (4.75–0.075 mm)	D422-63	32	1	–
Silt (%) (0.075–0.002 mm)	D422-63	68	99	–
Clay (%) (<0.002 mm)	D422-63	–	–	100
Free swell index	D5890-02	Non-swelling	Non-swelling	Non-swelling
USCS classification	D2487-06	–	–	–
Optimum moisture content (%)	D698-07	24.1	25.1	40.47
Maximum dry density (kN/m ³)	D698-07	13.05	16.44	11.77

of pozzolanic oxide content ($\sum P > 70\%$, as per ASTM 2005b (refer Table 3)). GGBS and SF were collected from chemical suppliers in Chennai, TN, India, which include fines and non-plastic. The value of $\sum P$ attained for GGBS and SF is 50.11 % and 97.70 % respectively. The SCMs resulted in non-swelling behaviour when permeated with DIW. Fig. 1 shows the raw materials' morphological (SEM) images. Fig. 1(a) shows the asymmetrically curved edges of the particles and the flaky texture of montmorillonite present in EC. FA particles are seen as spherical in Fig. 1(b) and GGBS/SF appear to be clear edges and angular in shape Fig. 1(c) and (d).

2.2. Test variables and quantities determined

The experimental campaign was conducted with three extensive series P, Q, and R-series respectively. According to the dry weight basis of the raw materials used in this investigation, the mixes were determined, and these results are shown in Table 4. Initially, to understand

the reference mix i.e. E100, it is determined for its geotechnical index and engineering properties. Further, in the P-series, FA was chosen as the first additive content which is varied from 0 % to 100 % by the dry weight with an interval of 20 % FA used in the mix blend. In the Q-series, FA and GGBS were equally proportionated and blended with expansive clay on a dry weight basis, the combined FA-GGBS used varied from 10 % to 50 % in the mix blends. Later in the R-series, GGBS-SF is equally proportionated with FA and blended with EC in the range of 0 %, 20 %, 40 %, 60 %, 80 % and 100 % by dry weight respectively, the combined GGBS-SF used is varied from 5 % to 25 % in the mix blends (refer to Table 4). Thus, a total of sixteen different combinations were chosen for this investigation, and the optimum was picked in each series as a landfill liner material. This is taken into consideration in accordance with the earlier literature, which states that industrial by-products are combined with different filler/binder contents before the best combination is chosen.

Experimental investigations such as consistency limits (LL and PL), FSI, standard Proctor compaction, UCS and HC tests were carried out for all the sixteen mix proportions. In performing LL and PL tests, the samples are subjected to equilibration with DIW (i.e. for 24 h period). Later in FSI and standard Proctor compaction, the samples are prepared instantaneously and a homogeneous mix is arrived in before performing the tests. In the case of UCS tests, the dimensions of the samples were prepared with the standard length-to-breadth ratio of 2:1. Further, the samples were stored in airtight polythene bags and stored in desiccators at their respective curing periods to sustain 100 % humidity. The consistency limits, FSI, compaction characteristics and UCS were tested in duplicate samples and the mean value was reported. Three trials of HC tests were performed for each specimen and the average HC of the three-test data was considered. On the whole, 16 LL and 16 PL tests, 16 FSI tests, 16 compaction tests, 16 HC tests and 64 UCS tests were performed in this research.

2.3. Experimental tests conducted

As mentioned in the above section the following tests as consistency limit Tests (LL and PL), free swell index tests (FSI), standard Proctor compaction characteristics, hydraulic conductivity tests (HC) and unconfined compressive strength (UCS) were performed. The whole method of sample preparation and procedure are accessible in our earlier work (Devarangadi and Shankar, 2021), however, the flowchart

Table 3
Chemical and mineral composition of expansive clay, fly ash, GGBS and silica fume.

Oxide (%)	Expansive clay	Fly ash	GGBS	Silica fume
Na ₂ O	8.41	0.30	0.17	0.20
MgO	1.66	1.40	6.92	0.50
Al ₂ O ₃	19.50	25.36	15.85	0.20
SiO ₂	60.79	50.78	33.59	97.00
P ₂ O ₅	–	–	0.02	–
SO ₃	1.68	–	1.56	0.15
K ₂ O	1.80	0.21	0.39	0.50
CaO	0.58	8.78	38.82	0.20
TiO ₂	0.70	0.24	0.78	–
MnO	–	–	1.00	–
Cr ₂ O ₃	–	–	–	–
Fe ₂ O ₃	4.64	10.37	0.67	0.50
Rb ₂ O	–	–	0.001	–
SrO	–	–	0.040	–
Y ₂ O ₃	–	–	0.006	–
ZrO ₂	–	–	0.024	–
BaO	–	–	0.083	–
LOI	0.23	2.40	–	–
$\Sigma P = \text{SiO}_2 + \text{Al}_2\text{O}_3 + \text{Fe}_2\text{O}_3$	84.93	86.51	50.11	97.70
Mineral phase composition	Quartz (SiO ₂), Calcite (CaCO ₃), Illite-smectite, Montmorillonite.	Mullite (3Al ₂ O ₃ ·2SiO ₂), Quartz (SiO ₂)	Akermanite (Ca ₂ MgSi ₂ O ₇), Merwinite (Ca ₃ Mg(SiO ₄) ₂), Diopside (CaMgSi ₂ O ₆)	Quartz (SiO ₂), Magnetite (Fe ₃ O ₄)

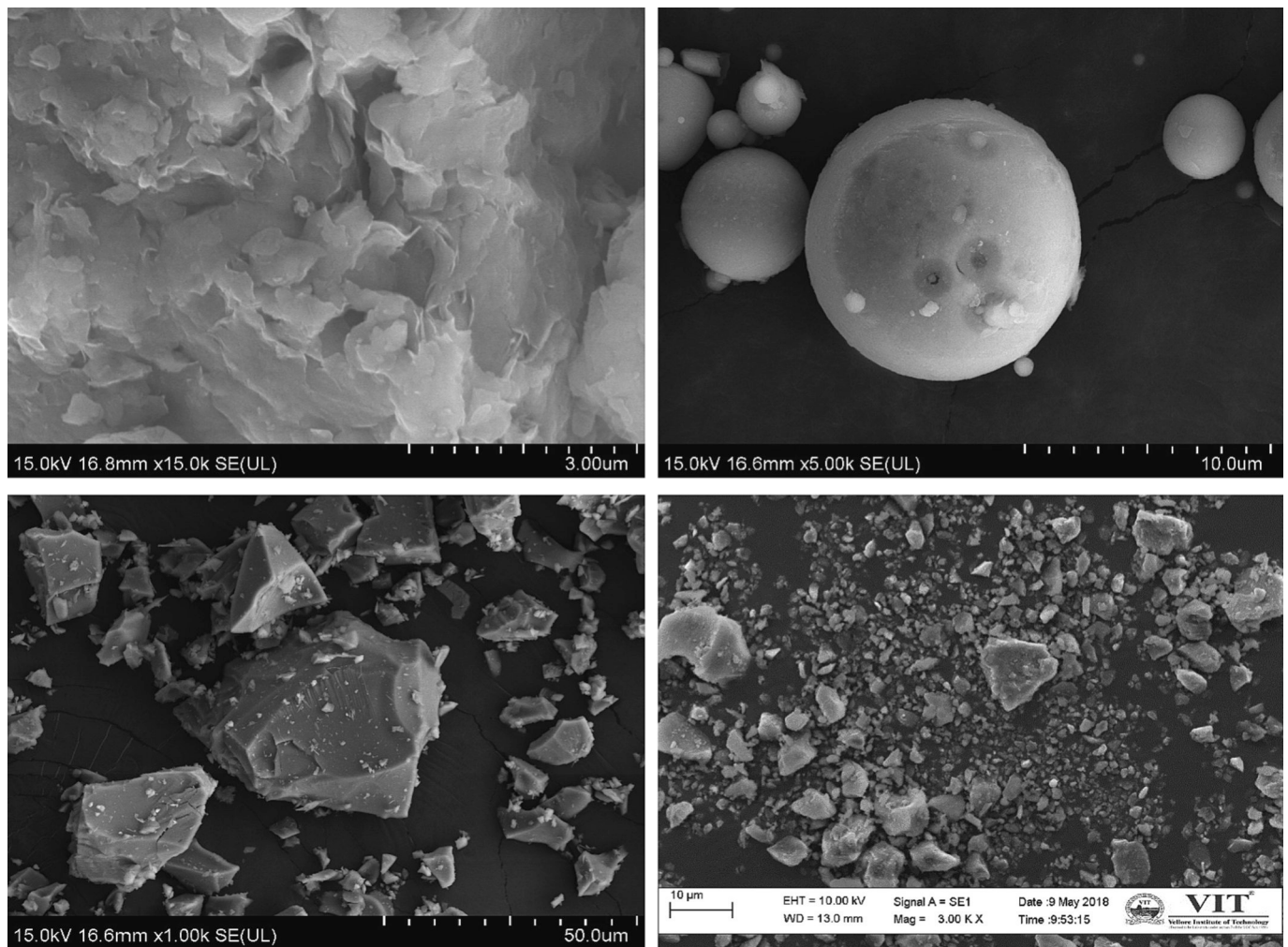


Fig. 1. Morphological SEM images of (a) expansive clay (b) fly ash (c) GGBS and (d) silica fume.

Table 4

Mix designations of raw materials by percentage dry weight.

Mix designation	Expansive clayby dry weight (%)	Supplementary cementitious materials by dry weight		
		Fly ash (%)	GGBS (%)	Silica fume (%)
<i>P-series</i>				
E100 (reference)	100	–	–	–
P1	80	20	–	–
P2	60	40	–	–
P3	40	60	–	–
P4	20	80	–	–
P5	–	100	–	–
<i>Q-series</i>				
Q1	80	10	10	–
Q2	60	20	20	–
Q3	40	30	30	–
Q4	20	40	40	–
Q5	–	50	50	–
<i>R-series</i>				
R1	80	10	5	5
R2	60	20	10	10
R3	40	30	15	15
R4	20	40	20	20
R5	–	50	25	25

below provides a fast summary of the tests and their standards. The pictures of the experimental program during preparation and testing are shown in Fig. 2.

3. Results and discussion

3.1. Effect of SCMs on FSI of expansive clays

The variation of FSI with the addition of FA on EC is represented in Fig. 3 i.e. P-series (E100, P1, P2, P3 and P4). The FSI of EC is 120 % upon the addition of FA, FSI values gradually reduced at 20 %, 40 %, 60 %, and 80 % FA contents with a declined ratio of 0.50 (i.e. $\Delta\text{FSI}\%$ to $\Delta\text{FA}\%$) when permeated with DIW. However, P5 (i.e. 100 % FA) has resulted in non-swelling behaviour with DIW. The above resulting decreased trend in the P-series is due to an increase in the average particle size of FA in mix blends and a decrease in the surface activity of mix blends (Devarangadi and Shankar, 2021; Shankar and Phanikumar, 2012). On the other hand, the partial replacement of FA with EC increases the cation exchange activity which further results in flocculation and increases the average particle size. This increased average particle size signified declining FSI values.

Fig. 3 depicts the variation of FSI with the addition of FA-GGBS on EC i.e. Q-series (E100, Q1, Q2, Q3 and Q4). With the addition of FA-GGBS in mix blends, FSI drastically reduced at 20 %, 40 %, 60 %, and 80 % FA-GGBS contents with a declined ratio of 0.38 (i.e. $\Delta\text{FSI}\%$ to $\Delta\text{FA-GGBS}\%$) when permeated with DIW. However, Q5 (i.e. 50 %FA-50 %GGBS) also



Fig. 2. (a) UCS testing of soil samples (Compaction of specimen to MDD and OMC, Inserting Sampler tube, Extraction of specimen to standard dimensions, Compression testing) (b) UCS samples stored in polythene bag for curing (c) FSI test (d) Hydraulic conductivity test.

resulted in non-swelling behaviour with DIW. The above-decreased trend in the Q-series is due to the combined pozzolanicity of FA-GGBS proportions with EC. Interestingly, an exchange of cations between sodium and calcium ions in EC and FA-GGBS mixes results in the effect of flocculation, a process that increases the average particle size of mix blends. Furthermore, this exchange of ions decreases the electrochemical/repulsive forces of the mix blends and yields decreased FSI values (Abu Seif, 2015).

Fig. 3 also illustrates the variation of FSI with the addition of FA-GGBS-SF on EC i.e. R-series (E100, R1, R2, R3 and R4). Interestingly, the addition of these combined SCMs with EC resulted in reduced FSI values at a higher decreased rate with DIW. Consequently, the declined ratio was found to be 0.31 (i.e. $\Delta\text{FSI}\%$ to $\Delta\text{FA-GGBS-SF}\%$), thereby signifying greater efficiency in the reduction of FSI values of EC. Also, R5 (i.e. 50 %FA-25 %GGBS = 25 %SF) resulted in non-swelling behaviour with DIW. This significant reduction in FSI values is mainly attributed to higher cementitious values of FA-GGBS-SF proportions with EC (Phanikumar and e, 2020). These tri-SCMs induced higher pozzolanicity and interexchange of ions when compared to P and Q-series respectively. This significantly impacted the increase in average particle size of mix proportions and obtained a higher reduction in FSI values.

3.2. Effect of SCMs on consistency limits of expansive clays

Table 5 displays the results of consistency limits including liquid

limit (LL), plastic limit (PL) and plasticity index ($\text{PI} = \text{LL} - \text{PL}$) of varied mix designs of EC against FA, GGBS and SF. The addition of FA in EC decreases the LL, PL and PI respectively. The PI of EC is 32.77 % upon the addition of FA, PI values gradually reduced at 20 %, 40 %, 60 %, and 80 % FA contents with a declined ratio of 0.24 (i.e. $\Delta\text{PI}\%$ to $\Delta\text{FA}\%$) when permeated with DIW. However, the SCMs related to mixes P5, Q5 and R5 resulted in non-plastic behaviour when experimented with DIW. A common fact that the declining ratio in PL was found to be three-fold lesser than that of LL i.e. $\Delta\text{PL}\%/\Delta\text{FA}\% = 0.06$ compared with $\Delta\text{LL}\%/\Delta\text{FA}\% = 0.30$. This observed monotonically decreasing trend of PI values in the P-series is mainly because of non-plastic, pozzolanicity, the particle size of FA and depletion of the double-diffusive layer thickness of EC by promoting the Ca^{2+} ions in the pore water from FA. As a result, PI decreased significantly with an increase in FA content in mix blends, indicating the transition towards non-plastic behaviour i.e. cohesionless packing of mix blends (also earlier reported by (Phani Kumar and Sharma, 2004; Shankar and Phanikumar, 2012; Sivapullaiah et al., 1996; Younus and Sreedeeep, 2012)).

Similarly, Table 5 displays the results of LL, PL and PI values of FA-GGBS mixes with EC. Importantly addition of varied FA-GGBS contents in EC resulted in the monotonically decreased trend of consistency limits when permeated with DIW. For instance, the PI values decreased from 24.65 % to 12.06 %, when the addition of equal proportions of FA-GGBS in EC increased from 0 % to 80 % respectively. A declined ratio of 0.16 (i.e. $\Delta\text{PI}\%$ to $\Delta\text{FA-GGBS}\%$) was observed with DIW as a permeant fluid.

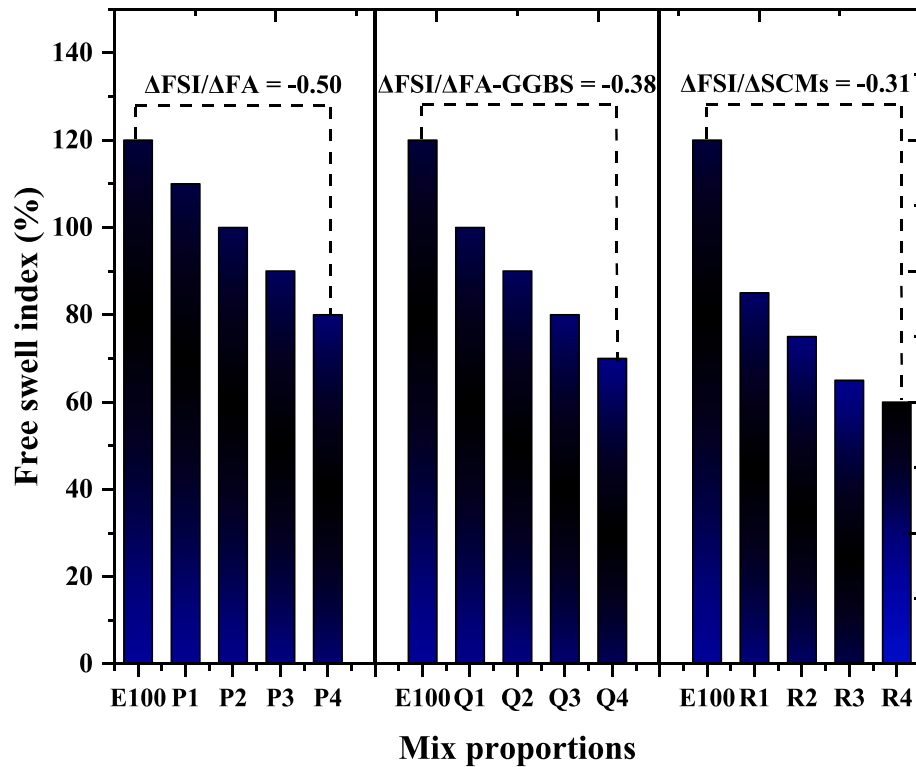


Fig. 3. Results of Free swell indexes.

Table 5
Results of consistency limits.

Mix designation	Consistency limits			Percentage decrease inΔPI (%) /ΔSCM's (%)
	LL (%)	PL (%)	PI (%)	
E100	64.89	32.12	32.77	−0.24
P1	56.57	29.87	26.7	
P2	49.2	28.79	20.41	
P3	43.89	27.82	16.07	
P4	40.6	26.75	13.85	
P5	Non-plastic			−0.16
Q1	51.33	26.68	24.65	
Q2	44.75	26.48	18.27	
Q3	40.85	25.29	15.56	
Q4	36.64	24.58	12.06	
Q5	Non-plastic			−0.13
R1	45.45	23.17	22.28	
R2	39.44	21.93	17.51	
R3	35.69	21.11	14.58	
R4	32.31	21.02	11.64	
R5	Non-plastic			

Appealingly, the declined ratio in LL and PL (i.e. $\Delta LL\%/\Delta FA-GGBS\% = 0.18$ and $\Delta PL\%/\Delta FA-GGBS\% = 0.02$) was found to be less when compared to the P-series. This is mainly due to the inclusion of GGBS in FA-EC, as a result, it increased the non-plasticity, pozzolanic, average particle size and depletion of DDL thickness. This hypothesis is further examined with the inclusion of SF in FA-GGBS against EC blends.

Interestingly, the consistency limits further decreased with the addition of SF in FA-GGBS against EC mixes, the results of LL, PL and PI are also represented in Table 3. A declined ratio of 0.13 (i.e. $\Delta PI\%/\Delta FA-GGBS-SF\%$) was observed with DIW as a permeant fluid used in this study. Interestingly, the declined ratio in LL and PL (i.e. $\Delta LL\%/\Delta FA-GGBS-SF\% = 0.16$ and $\Delta PL\%/\Delta FA-GGBS-SF\% = 0.02$) was found to be

less when compared to P-series and Q-series respectively. This significant declination of PI values is majorly due to the addition of SF content in the mix blends, SF facilitated the low plasticity in the FA-GGBS mixes against EC by increased flocculation effect and reduction in DDL thickness at higher rates.

Fig. 4 represents the location of all sixteen mix proportions used in this study on Casagrande's plasticity chart. The reference EC (i.e. E100) is located at the A-line and it is designated as CH (inorganic clays of high plasticity). In the P-series (i.e. EC with FA) and Q-series (i.e. EC with FA-GGBS), with the addition of FA and GGBS contents, the plasticity of E100 monotonically declined and noted a linear transition towards MH (i.e. inorganic silt with high plasticity) and ML (i.e. inorganic silt with low plasticity). Furthermore, in the R-series (i.e. EC with FA-GGBS-SF), the plasticity of E100 deputed to CL transition (i.e. inorganic clays of low to medium plasticity). Overall, the decrease in PI with the effect of these tri-SCMs (i.e. P, Q and R-series) resulted in a potential reduction of cohesion and undrained shear strength of E100.

3.3. Effect of SCMs on compaction characteristics of expansive clays

Fig. 5 illustrates the variation of MDUW-OMC of the design mixes used in this study. In the case of the P-series, the addition of FA increases against EC resulted in a decrease of optimum moisture content (OMC), which obtained a monotonically decreasing drift with a decreasing rate of $\Delta OMC\%/\Delta FA\% = -0.072$ (see Fig. 5a). In relative, the maximum dry unit weight (MDUW) resulted in a monotonically decreasing drift with a decreasing rate of $\Delta MDUW\%/\Delta FA\% = -0.007$ (see Fig. 5a). The reference E100 mix obtained an MDUW value of 13.74 kN/m^3 (corresponding to $OMC = 32.3\%$), upon the addition of FA at 20 %, 40 %, 60 %, 80 % and 100 % contents resulted in decreased MDUW = 13.61 kN/m^3 , 13.35 kN/m^3 , 13.28 kN/m^3 , 13.17 kN/m^3 and 13.04 kN/m^3 (corresponding to $OMC = 31.1\%$, 29.44% , 27.18% , 26.22% and 25.1%). In general, the decrease/increase in MDUW/OMC majorly depends on the type of fly ash used in the experimental program and its governing factors such as particle size gradation, carbon-iron contents, fineness

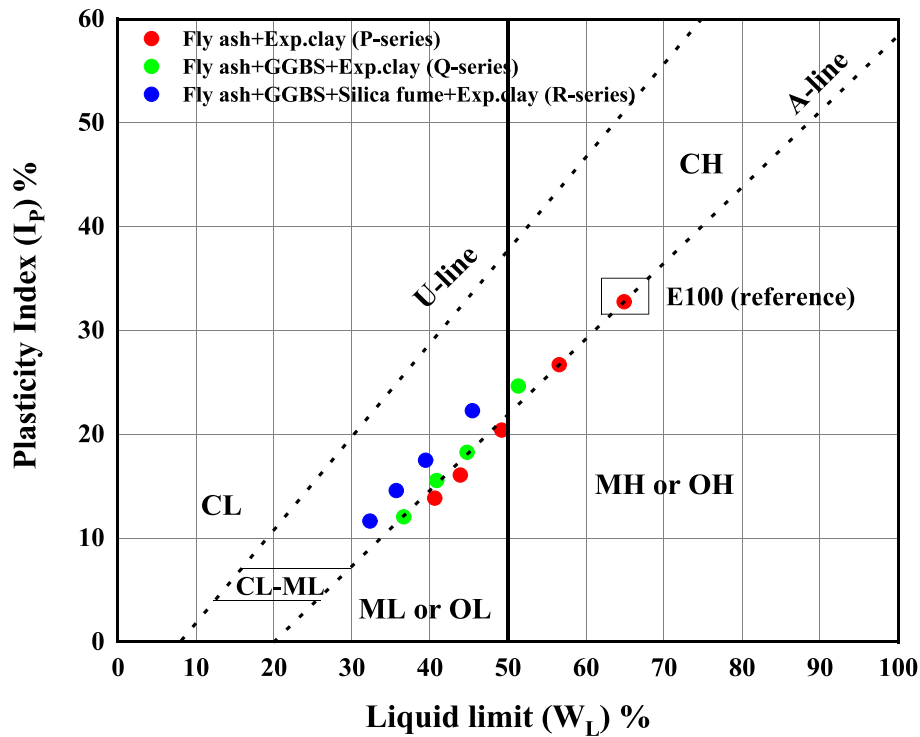


Fig. 4. Results of consistency limits in the USC plasticity chart.

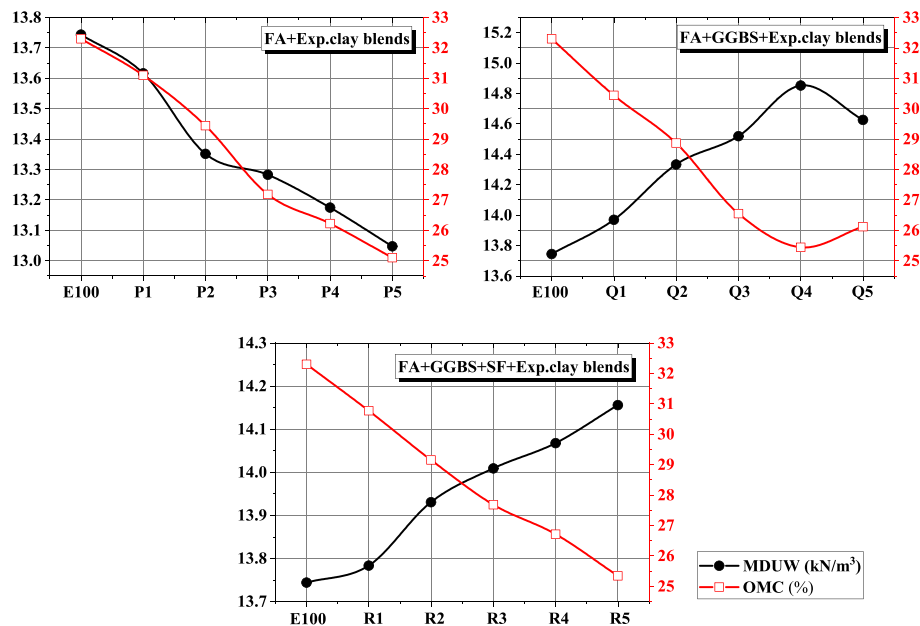


Fig. 5. Variation of MDUW and OMC of expansive clay blends.

and density etc. In this case, MDUW is reduced because of the high fineness and lower specific gravity/density of FA compared with EC. Also, the decline is due to the presence of hollow spherical particles, earlier reported by Das and Yudhbir (2006). On the other hand, the decrease in OMC is attributed to burnt carbon particles present in FA which decrease the water demand on surface absorption of FA-EC mixes (Joshi and Lohita, 1997).

Fig. 5b displays the variation of MDUW and OMC for the Q-series. It revealed that, with the addition of FA-GGBS at 20 %, 40 %, 60 %, 80 % and 100 % against EC, the MDUW increases (i.e. increasing rate of $\Delta\text{MDUW}\%/\Delta\text{FA-GGBS}\% = +0.008$) and OMC decreases (i.e. decreasing

rate of $\Delta\text{OMC}\%/\Delta\text{FA-GGBS}\% = -0.061$). The resultant increased MDUW is mainly attributed to the higher density of GGBS and its increased substitution with FA-EC resulted in higher flocculation of mix blends. Furthermore, the higher flocculation of these mixes can be compacted at lower water content which decreases the OMC values. It is a common fact that compaction effort is indirectly proportional to the percentage of clay and its resistance (Phanikumar and Sharma, 2007). The combined addition of FA-GGBS increased the average silt-size particles with EC and the clay resistance is reduced for the same compactive effort which increases the MDUW (Sharma and Sivapullaiah, 2016b).

In the same way, Fig. 5c represents the effect of FA-GGBS-SF on EC as

R-series (see Table 3). The addition of SF in FA-GGBS-EC blends increased their MDUW (i.e. increasing rate of $\Delta\text{MDUW}/\Delta\text{FA-GGBS-SF} \% = +0.004$) and decreased the OMC (i.e. decreasing rate of $\Delta\text{OMC}/\Delta\text{FA-GGBS-SF} \% = -0.069$). As mentioned earlier in the above case, the increase in MDUW is based on the effect of flocculation in the mixes which resulted in increased densities and reduced water contents. Interestingly, the addition of SF decreased the dry densities of the R-series compared with the Q-series. For instance, the rate of increase of MDUW in the Q-series (i.e. 0.008) is twofold times higher than R-series (i.e. 0.004). This is mainly due to its low denseness/specific gravity and increased fineness in mix blends after SF substitution. Hence, it confirms that the addition of tri-SCMs (i.e. FA-GGBS-SF) is ineffective in increasing the dry densities than FA-GGBS with EC mix blends. Moreover, this is also true with the corresponding MDUW of SCMs i.e. P5, Q5 and R5 which resulted in 13.04 kN/m^3 , 14.62 kN/m^3 and 14.15 kN/m^3 .

3.4. Effect of SCMs on UCS characteristics of expansive clays

The variation of UCS for sixteen mix proportions tested at different curing periods of 0, 7, 14 and 28 days were displayed in Fig. 6. In the P-series, as a result of FA inclusion, the UCS values of each mix increase with the increase in the curing period against 0, 7, 14 and 28 days respectively. The reference E100 resulted in UCS value of 155.78 kPa at 0 days, 158.05 kPa at 7 days, 163.55 kPa at 14 days and 165.32 kPa at 28 days curing period, this resulted in increased strength from 0 to 28 days curing period is negligible and the strength increment is only due to the possible effect of self-hardening under its own OMC and minimum effect of carbonation. With the addition of 20 % FA contents in EC, the UCS value increased from 163.55 kPa to 347.85 kPa at 0 to 28 days curing period. For 40 % FA content in EC, the UCS value increased from

224.44 kPa to 476.89 kPa at 0 to 28 days curing period. For 60 % FA content in EC, the UCS value increased from 166.14 kPa to 364.40 kPa at 0 to 28 days curing period. For 80 % FA content in EC, the UCS value increased from 142.37 kPa to 257.88 kPa at 0 to 28 days curing period. For 100 % FA content, the UCS value increased from 43.60 kPa to 73.60 kPa at 0 to 28 days curing period respectively.

However, a higher UCS value is attained at the P2 mix (i.e. 40 %FA-60 %EC) and thereafter the UCS values decrease with an increase in FA content, this was true for all the curing periods. The increase in UCS values is associated with (i) the production of cementitious hydrated products such as CSH, CAH, CASH etc. The amount of SiO_2 and Al_2O_3 present in EC has a tendency to react with free-lime (CaO) present in FA and OH^- ions present in pore water solution, liberating these cementitious hydrated products. This production process depends on the fineness of FA (SCMs), pH of pore solution, OH^- ions and presence of free-lime with respect to the replacement level of FA etc. Hence increasing the stabilization of the FA-EC matrix (Kumar and Sivapullaiah, 2016; Sharma and Sivapullaiah, 2016a; Sivapullaiah et al., 1998) (ii) interestingly, the free lime available in FA is utilized by EC for its cation exchange reactivity, results in increasing the $c-\phi$ (i.e. cohesion-internal friction parameters) (Prashanth et al., 2001) which further stabilizing the mix blends.

Hence, in this case, when the replacement level increases by more than 40 %FA content, the UCS values drift to a decreasing trend. This may be ascribed to poor cementitious reactivity between FA and EC and less improvement in $c-\phi$ (cohesion-internal friction parameters) of the matrix resulting in decreasing the UCS values. Similar studies were reported by several researchers (Kumar et al., 2007; Sabat and Bose, 2013; Sharma and Hymavathi, 2016). However, considerable studies have been performed by researchers in enhancing the higher strength of FA-

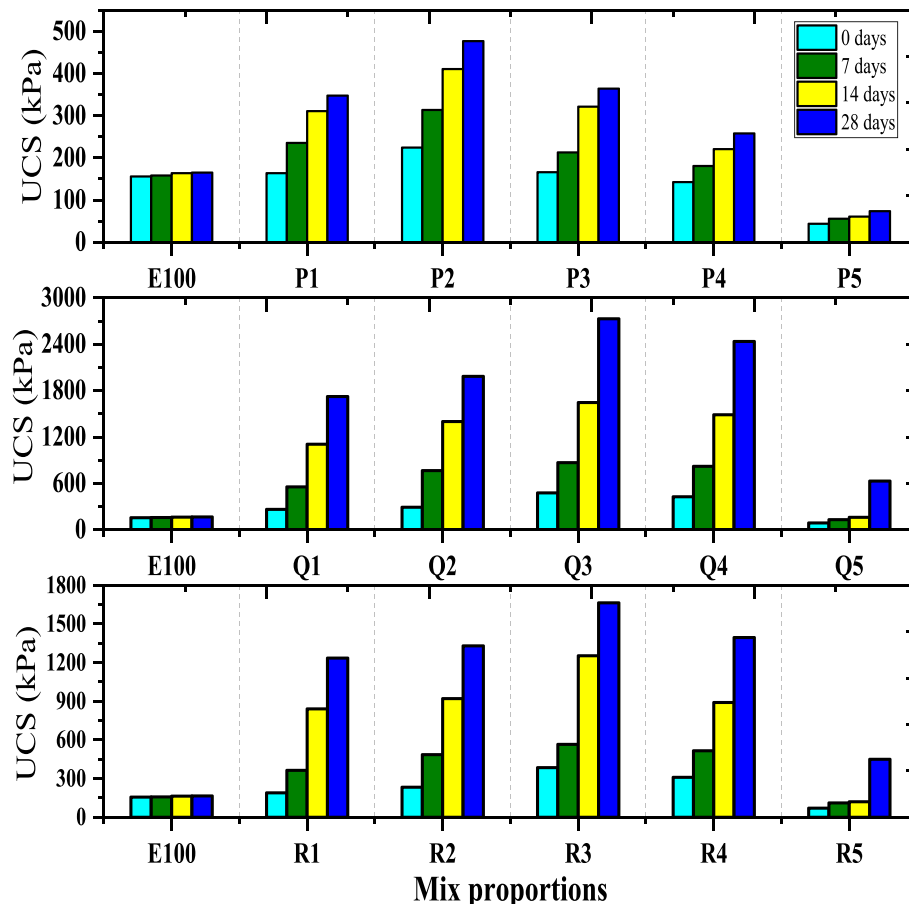


Fig. 6. Variation of UCS at 0, 7, 14 and 28 days curing period of expansive clay blends.

EC mix blends with additional binders such as cement, lime, gypsum clay etc. (Ganjian et al., 2004; Sharma and Sivapullaiah, 2017; Sivapullaiah and Moghal, 2011). In this work, the author's objective is to use only the SCMs and determine their efficacy without any additional binders. Overall, the recommended design criteria for UCS value for a liner in a landfill should be ≥ 200 kPa, to ensure stability because of increased overburden pressure (Daniel and Wu, 1993; Guney et al., 2008; Osinubi and Nwaiwu, 2006). In this series, mixes such as P1 mix at 7, 14 and 28 days, P2 mix at all curing periods, and P3 and P4 mix at 14 and 28 days curing period fall under the recommendations of UCS criteria.

The variation of FA-GGBS on EC is presented in Fig. 6 i.e. (refer to mixes, Q1 to Q5). The test results revealed that the addition of GGBS in FA-EC blends monotonically increases the UCS value for all the mix proportions and relative to curing periods from 0 to 28 days. For instance, with the addition of an equal proportionate of 20 %GGBS-FA contents in EC, the UCS value increased from 264.47 kPa to 1722.42 kPa at 0 to 28 days curing period. For 40 % GGBS-FA content in EC, the UCS value increased from 291.56 kPa to 1984.66 kPa at 0 to 28 days curing period. For 60 % GGBS-FA content in EC, the UCS value increased from 476.65 kPa to 2728.43 kPa at 0 to 28 days curing period. For 80 % GGBS-FA content in EC, the UCS value increased from 425.66 kPa to 2435.92 kPa at 0 to 28 days curing period. For 100 % GGBS-FA content, the UCS value increased from 130.22 kPa to 630.48 kPa at 0 to 28 days curing period respectively.

However, a higher UCS value is attained at the Q3 mix (i.e. 60 % GGBS-FA with 40 %EC) and thereafter the UCS values decrease with an increase in GGBS-FA contents, this was true for all the curing periods. As discussed, the technical reasons in the previous section, the influence of GGBS in this series is predominant in enhancing the UCS values with higher cementation action and $c-\phi$ improvement in the mix blends, resulting in higher UCS values when compared to P-series respectively. For instance, in case of P-series to Q-series, the UCS is increased by 395.16 % for Q1-mix at 28 days curing period, 316.17 % for Q2-mix at 28 days curing period, 648.75 % for Q3-mix at 28 days curing period, 843.43 % for Q4-mix at 28 days curing period and 756.63 % for Q5-mix at 28 days curing period respectively. In this series, mixes such as Q1, Q2, Q3, Q4 mixes at all curing periods and Q5 mix at 28 days curing period fall under the recommendations of UCS criteria.

The variation of FS on FA-GGBS-EC is presented in Fig. 6 i.e. (refer to mixes, R1 to R5). The test results revealed that the addition of SF in FAGGBS-EC blends monotonically increases the UCS value for all the mix proportions and relative to curing periods from 0 to 28 days. For instance, with the addition of 20 %SF-GGBS-FA contents in EC, the UCS value increased from 190.10 kPa to 1235.35 kPa at 0 to 28 days curing period. For 40 % SF-GGBS-FA content in EC, the UCS value increased from 233.12 kPa to 1330.57 kPa at 0 to 28 days curing period. For 60 % SF-GGBS-FA content in EC, the UCS value increased from 385.95 kPa to 1664.51 kPa at 0 to 28 days curing period. For 80 % SF-GGBS-FA content in EC, the UCS value increased from 310.32 kPa to 1394.60 kPa at 0 to 28 days curing period. For 100 % SF-GGBS-FA content, the UCS value increased from 70.88 kPa to 450.40 kPa at 0 to 28 days curing period respectively. The higher UCS value in this series resulted in R3-mix (i.e. 60 %GGBS-FA with 40 %EC) at all curing periods, thereafter the UCS values decreased with the addition of SCMs content with EC. This is due to the loss of cementation action and reduced cohesion in the matrix.

Interestingly, when compared with the Q-series, the UCS values decreased with the addition of SF in the mix blends. For instance, in the case of Q-series to R-series, the UCS is decreased by 28.28 % for R1-mix, 32.96 % for R2-mix, 38.99 % for R3-mix, 42.75 % for R4-mix and 28.56 % for R5-mix at 28 days curing period respectively. This monotonically decline trend is attributed to the lack of free lime available in SF for cementitious reactions. Since sufficient amounts of silicates are available in this series; free lime available in FA-GGBS attains a marginal effect to produce cementitious products to react with silicates present in SF (Sivapullaiah et al., 1998). In this series, mixes such as R1 at 7, 14 and

28 days curing period, R2, R3, and R4 mix at all curing periods and R5 mix at 28 days curing period fall under the recommendations of UCS criteria.

This section influences the specimen characteristics and consistency of the mix blends subjected to %strain failure of UCS at varied curing periods. Figs. 7–9 show the variation of %strain and UCS values for P-series, Q-series and R-series at 0, 7, 14 and 28 days respectively. In Fig. 7, the black line represents the deviation of %strain and the red line represents the deviation of UCS with FA-EC mix blends, similar interpretation is shown in Fig. 8 (i.e. FA-GGBS-EC mixes) and 9 (i.e. FA-GGBS-SF-EC mixes). It revealed that the %strain value decreases with an increase in SCMs content and curing period in P-series (refer Fig. 7), Q-series (refer Fig. 8) and R-series (refer Fig. 9). For instance, the E100 i.e. reference mix resulted in an %strain failure value of 10.12 % at 28 days UCS value, the resulted in failure consistency is the ductile type and represented a softening character. With the addition of FA, the %strain failure recorded for P1, P2, P3, P4 and P5 decreased to 3.88 %, 3.46 %, 3.7 %, 6.46 % and 4.05 % at 28 days UCS value, the resulting failure consistency is the brittle type and represented a hardening character. The decreased rate from E100 to P-series is reflected by 61.66 %, 65.81 %, 63.44 %, 36.17 % and 59.98 % respectively. Interestingly, the increase in %strain in the P3, P4 and P5 mix is mainly attributed to decreased cohesion and cementation between the particles which further decreases UCS values. Hence, this also concludes that the % strain values are inversely proportional to UCS values (refer to Fig. 7d); Similar findings can also be referred from Figs. 8 and 9. Therefore, the obtained strain value results agree with the UCS experiment findings.

3.5. Effect of SCMs on hydraulic conductivity (HC) of expansive clays

Fig. 10 demonstrates the deviation of HC with time for FA-EC mixes (i.e. P-series), permeated with DIW as test fluid. The test results revealed that (i) HC monotonically increases with an increase in FA addition with EC and (ii) HC of each individual mix decreases with time (refer Fig. 10). The reference mix E100, has resulted in a low HC value of $2.31\text{E}-10$ cm/s when permeated with DIW. After the addition of 20 %, 40 %, 60 %, 80 % and 100 % contents of FA with EC, the HC value increased to $7.45\text{E}-8$ cm/s, $8.75\text{E}-8$ cm/s, $6.41\text{E}-7$ cm/s, $7.54\text{E}-6$ cm/s and $4.84\text{E}-4$ cm/s respectively with DIW. This increasing drift in the P-series is because of (i) decreased maximum dry unit weights of mixes from P1 to P5, as the HC test is performed at their compactive optimum moisture contents. For instance, when FA content increases from 0 % to 100 %, the MDUW decreases from 13.74 kN/m^3 to 13.04 kN/m^3 , and corresponding HC values increase from $2.31\text{E}-10$ cm/s to $4.84\text{E}-4$ cm/s with DIW (Devarangadi and Masilamani, 2019; Phanikumar and Shankar, 2016). (ii) Replacement of fine particles of EC with silt-sized FA in the mix blends increases the marginal void space, thus resulting in increased HC (Prashanth et al., 2001). (iii) Even though considerable reactive silica is available in FA but the effect of alkaline activity is less due to lower amounts of free-lime available in FA. Furthermore, this leads to either insufficient cementation action or flocculation and later increases the HC of mixes (Sivapullaiah et al., 1998). Overall, 40 %FA with EC (i.e. P2 mix), is confirmed to be optimum and falls under the criterion standards of landfill liner as per USEPA recommendation for the type of EC used in this test program.

Fig. 11 demonstrates the deviation of HC with time for FA-GGBS-EC mixes (i.e. Q-series), permeated with DIW as test fluid. The test results revealed that (i) HC monotonically decreases up to the Q3 mix and thereafter the HC increases with an increase in FA-GGBS addition with EC (ii) HC of each mix decreases with time (refer Fig. 11). The reference mix E100, has resulted in a low HC value of $2.31\text{E}-10$ cm/s when permeated with DIW. After the addition of 20 %, 40 %, 60 %, 80 % and 100 % contents of FA-GGBS with EC, the resulting HC values are $5.86\text{E}-8$ cm/s, $3.54\text{E}-8$ cm/s, $2.14\text{E}-8$ cm/s, $2.7\text{E}-7$ cm/s and $9.65\text{E}-7$ cm/s respectively with DIW. This drift in the Q-series is because of decreased amounts of production of cementitious byproducts in mix Q4 and Q5.

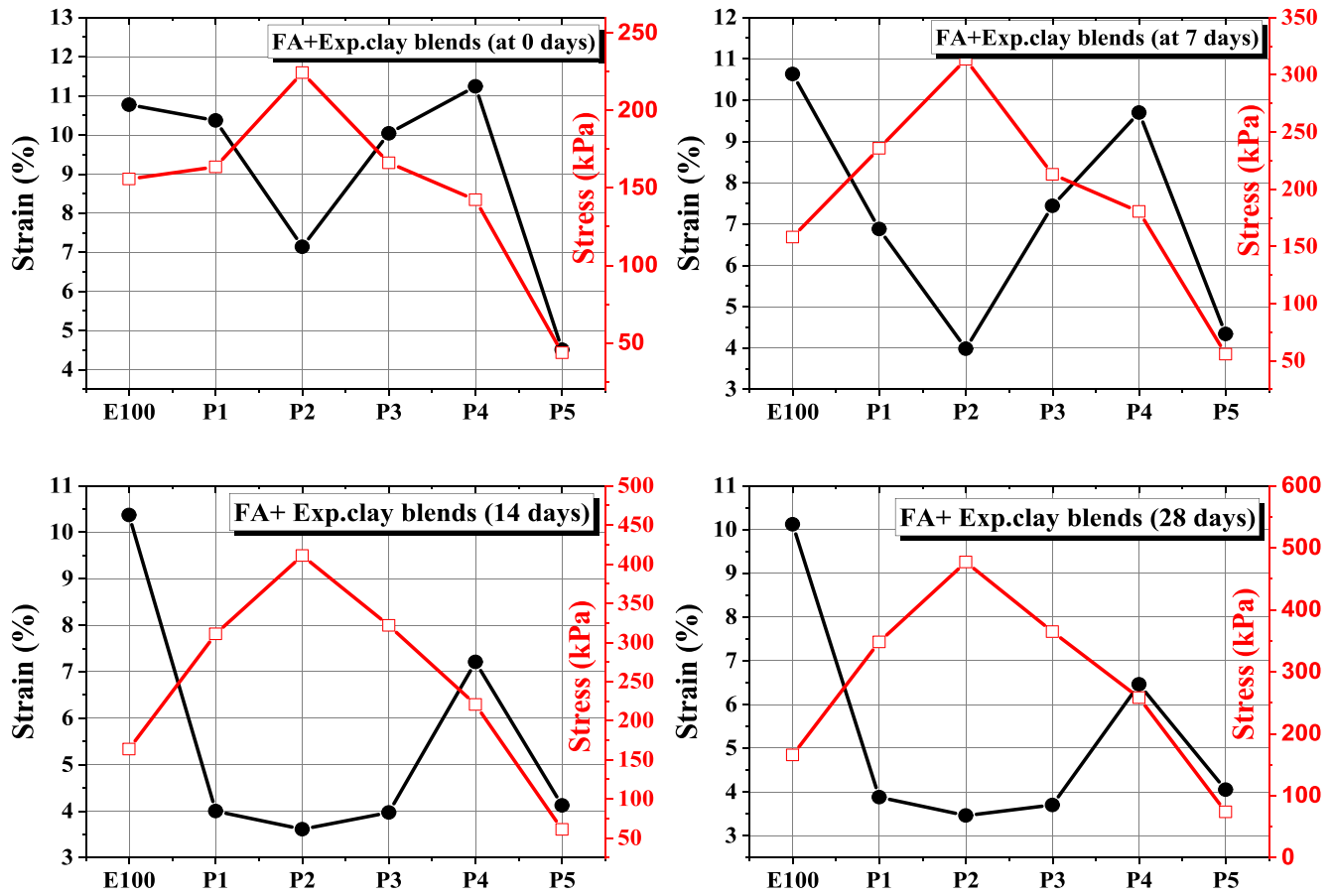


Fig. 7. Variation of stress–strain for FA-EC blends at various curing periods.

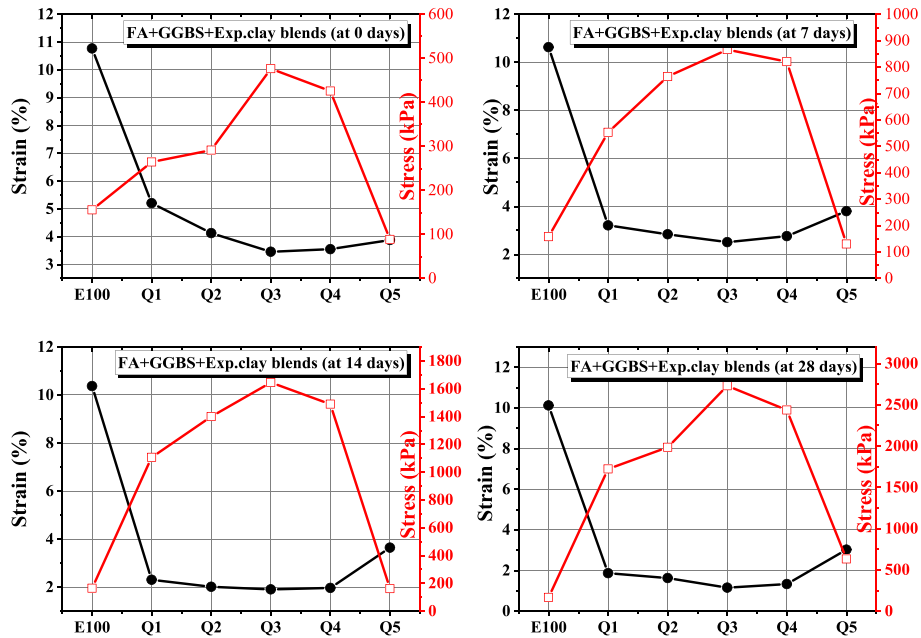


Fig. 8. Variation of stress–strain for FA-GGBS-EC blends at various curing periods.

Interestingly, from mix Q1 to Q3, sufficient hydration and cementation were achieved in the mix blends, henceforth resulting in decreased porosity, capillary channels and bleeding, which lowered the HC values. Overall, 60 %FA-GGBS with EC (i.e. Q3 mix), confirms to be optimum

and falls under the criterion standards of landfill liner as per USEPA recommendation for the type of EC used in this test program.

Fig. 12 demonstrates the deviation of HC with time for FA-GGBS-SF-EC mixes (i.e. R-series), permeated with DIW as test fluid. Similarly, the

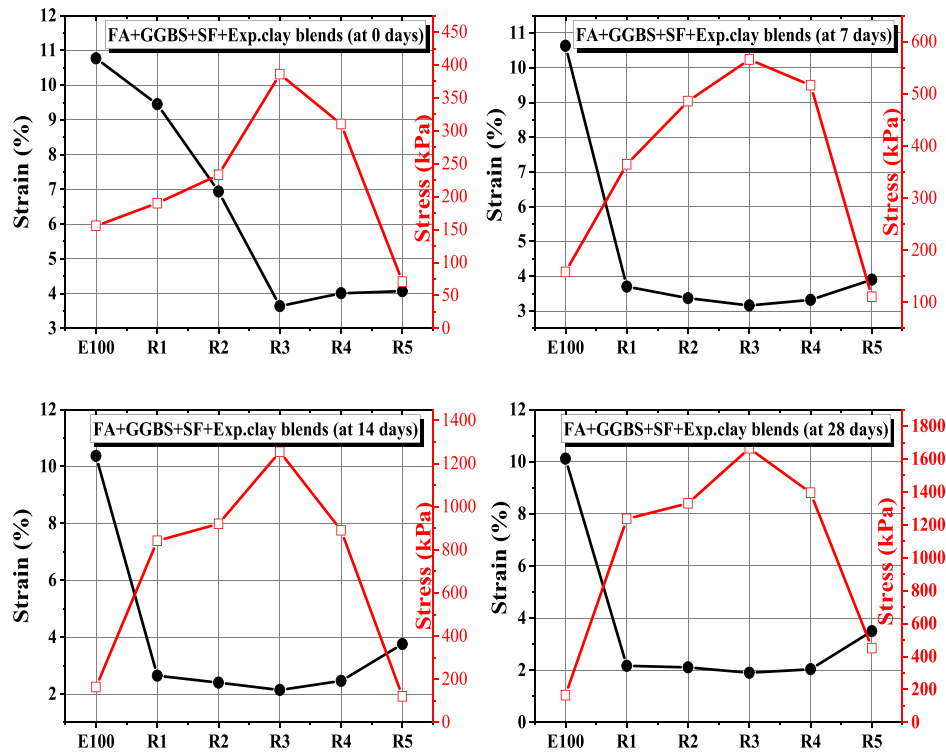


Fig. 9. Variation of stress-strain for FA-GGBS-SF-EC blends at various curing periods.

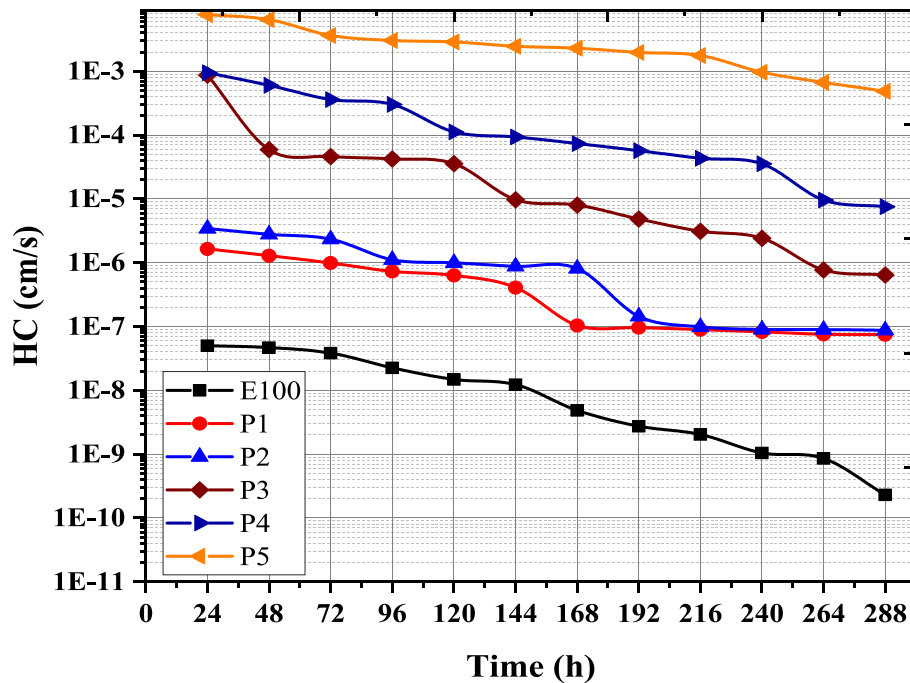


Fig. 10. Effect of HC with time on FA-EC blends permeated with DIW.

test results revealed that (i) HC monotonically decreases up to the R3 mix and thereafter the HC increases with an increase in FA-GGBS-SF addition with EC (ii) HC of each mix decreases with time (refer Fig. 12). The reference mix E100, has resulted in a low HC value of 2.31E-10 cm/s when permeated with DIW. After the addition of 20 %, 40 %, 60 %, 80 % and 100 % contents of FA-GGBS-SF with EC, the resulted HC values are 6.66E-8 cm/s, 4.87E-8 cm/s, 3.48E-8 cm/s, 6.85E-7 cm/s and 6.54E-6 cm/s respectively with DIW. As explained

earlier in the previous section, this drift in the R-series is also because of decreased amounts of production of cementitious byproducts in mix R4 and R5. Interestingly, from mix R1 to R3, sufficient hydration and cementation were achieved in the mix blends, thenceforth resulting in decreased porosity, capillary channels and bleeding, which lowered the HC values. Overall, 60 %FA-GGBS-SF with EC (i.e. R3 mix), is confirmed to be optimum and falls under the criterion standards of landfill liner as per USEPA recommendation for the type of EC used in this test program.

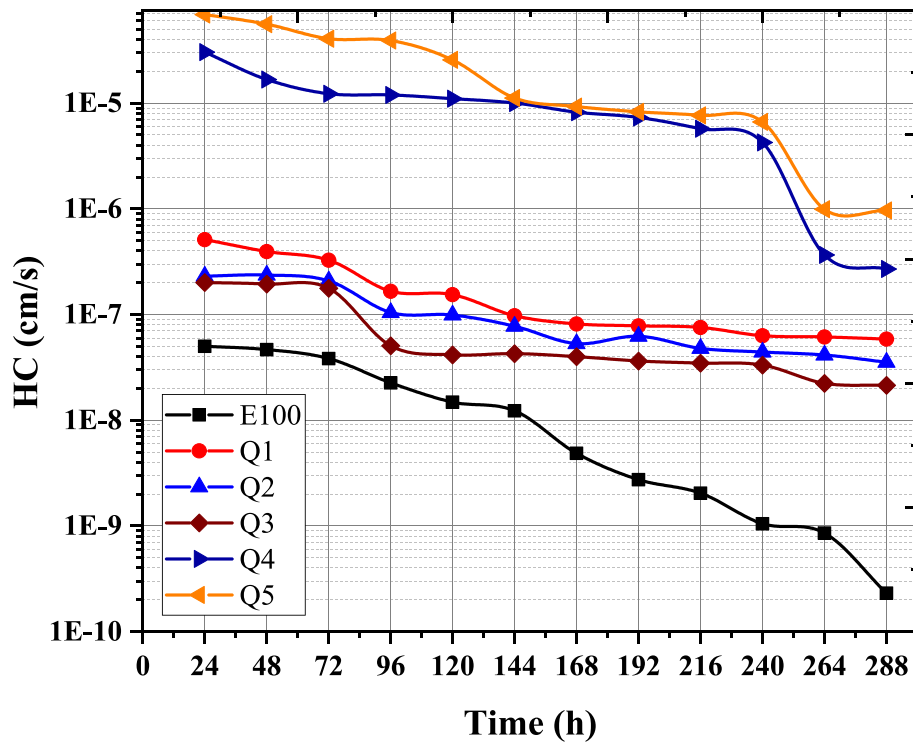


Fig. 11. Effect of HC with time on FA-GGBS-EC blends permeated with DIW.

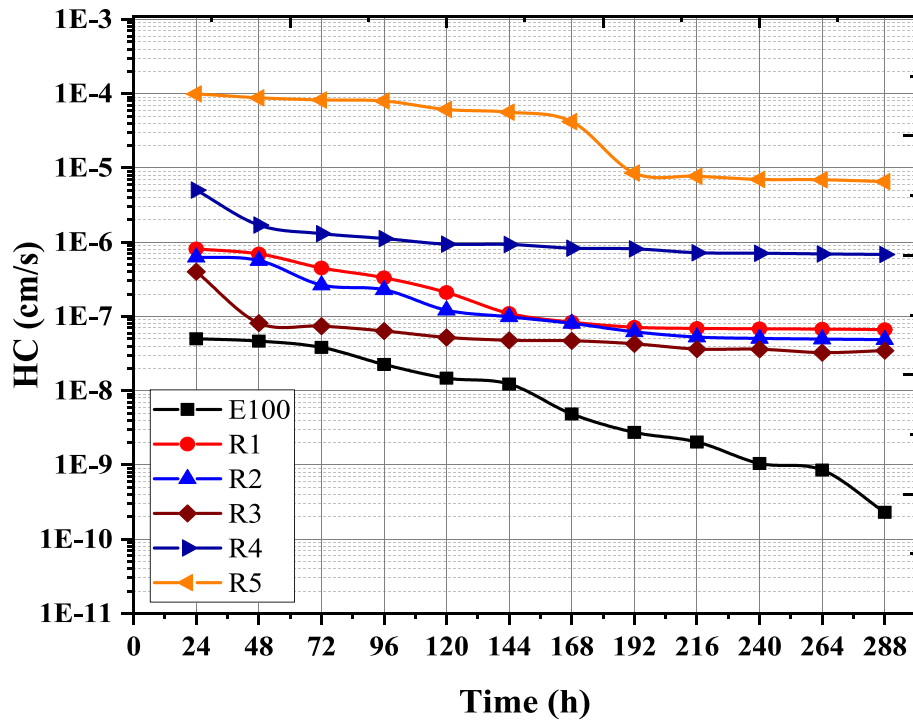


Fig. 12. Effect of HC with time on FA-GGBS-SF-EC blends permeated with DIW.

4. Correlations

This section presents the important correlations of FA-EC (i.e. P-series: Blue line), FA-GGBS-EC (Q-series: Red line) and FA-GGBS-SF-EC (R-series: Brown line) for the prediction of FSI, OMC, MDUW, UCS and HC with LL values, the regression analysis was performed using origin pro software. As mentioned, the correlations and regression analysis are

evaluated based on the LL value alone, because this property instruments the behaviour of all other indexes and engineering properties of EC. The regression parameters concerning to Pearson correlation coefficient (r) and the coefficient of determination (R^2) are depicted in Figs. 13–15. Thenceforth, the r value is used to identify the patterns in things, whereas, R^2 is used to identify the strength of the model.

4.1. Correlation of LL with FSI

Fig. 13 demonstrates the correlation between LL and FSI of tri-SCMs blended with EC. The r and R^2 values determined for all the series are obtained in the range of 98.61 % to 99.88 % and 96.32 % to 99.69 % of the confidence bound of LL with FSI values. The proposed model equations of LL with FSI values for P, Q, and R-series are given below (refer to Eqs. (1)–(3)).

$$Y = 18.99 + 1.59x \text{ for P – series} \quad (1)$$

$$Y = 9.50 + 1.73x \text{ for Q – series} \quad (2)$$

$$Y = 0.55 + 1.85x \text{ for R – series} \quad (3)$$

Where Y represents FSI and x is the LL value.

4.2. Correlation of LL with OMC

Fig. 14 demonstrates the correlation between LL and OMC of tri-SCMs blended with EC. The r and R^2 values determined for all the series are obtained in the range of 93.62 % to 97.96 % and 83.55 % to 94.63 % of the confidence bound of LL with OMC values. The proposed model equations of LL with FSI values for P, Q, and R-series are given below (refer to Eqs. (4)–(6)).

$$Y = 6.22 + 0.26x \text{ for P – series} \quad (4)$$

$$Y = 17.10 + 0.25x \text{ for Q – series} \quad (5)$$

$$Y = 22.15 + 0.16x \text{ for R – series} \quad (6)$$

where Y represents OMC and x is the LL value.

4.3. Correlation of LL with MDUW

Fig. 15 demonstrates the correlation between LL and MDUW of tri-SCMs blended with EC. The r and R^2 values determined for all the series are obtained in the range of 88.79 % to 98.90 % and 71.80 % to 97.09 % of the confidence bound of LL with OMC values. However, the r value is negative in Q and R-series, this is attributed to the two variables

that tend to move in the opposite direction. The proposed model equations of LL with MDUW values for P, Q, and R-series are given below (refer to Eqs. (7)–(9)).

$$Y = 12.21 + 0.024x \text{ for P – series} \quad (7)$$

$$Y = 14.32 - 0.009x \text{ for Q – series} \quad (8)$$

$$Y = 16.09 - 0.037x \text{ for R – series} \quad (9)$$

where Y represents MDUW and x is the LL value.

4.4. Correlation of LL with UCS

Fig. 16 displays the correlation of LL with UCS for all the series at varied curing periods of 0, 7, 14 and 28 days. The regression analysis was not performed with UCS, this is because (i) as the blends depicted distinctive variations and the possible analysis is difficult to interpret. (ii) Also, a few of the UCS values are well below the criterion limits (i.e. $UCS \leq 200$ kPa), hence regression may not be determined. However, the mixes were correlated, as per the UCS criterion, the unacceptable zone is pictured in the figures for the P, Q and R-series respectively. In the P-series, the highest UCS value was attained for mix P2 at an LL value of 49.2 % and the corresponding UCS value is 224.44 kPa, 313.56 kPa, 410.65 kPa and 476.89 kPa at 0, 7, 14 and 28 days curing period (refer to Fig. 16a). In the Q-series, the highest UCS value was attained for mix Q3 at an LL value of 40.85 % and the corresponding UCS value is 476.65 kPa, 866.70 kPa, 1644.59 kPa and 2728.43 kPa at 0, 7, 14 and 28 days curing period (refer to Fig. 16b). Furthermore, in the R-series, the highest UCS value was attained for mix R3 at an LL value of 35.69 % and the corresponding UCS value is 385.95 kPa, 565.49 kPa, 1254.2 kPa and 1664.51 kPa at 0, 7, 14 and 28 days curing period (refer to Fig. 16c) respectively.

4.5. Correlation of LL with HC

Fig. 17 displays the correlation of LL with HC for all the mix series used in this study. Similarly, the regression analysis was not performed with LL, this is because a few of the HC values are well below the criterion limits (i.e. $HC \leq 1E-07$ cm/s), hence regression was not

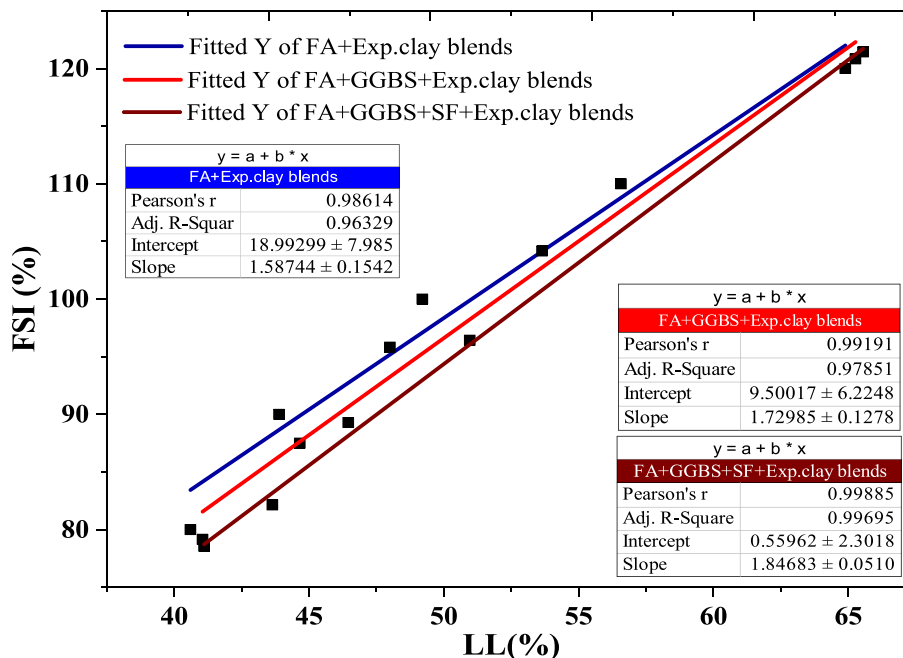


Fig. 13. Correlation of LL with FSI for SCM's and EC blends.

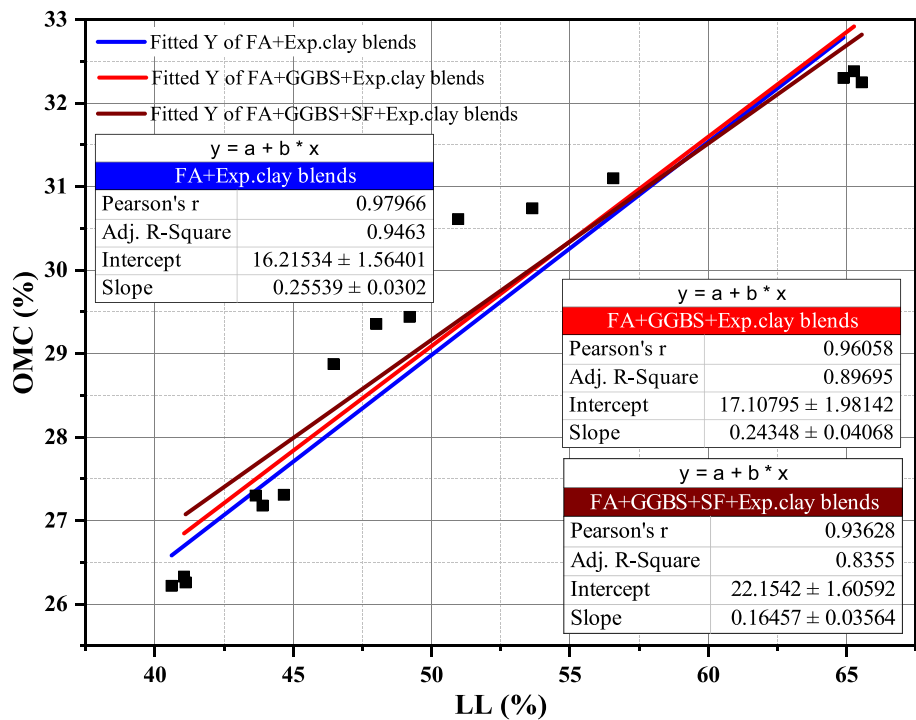


Fig. 14. Correlation of LL with OMC for SCMs and EC blends.

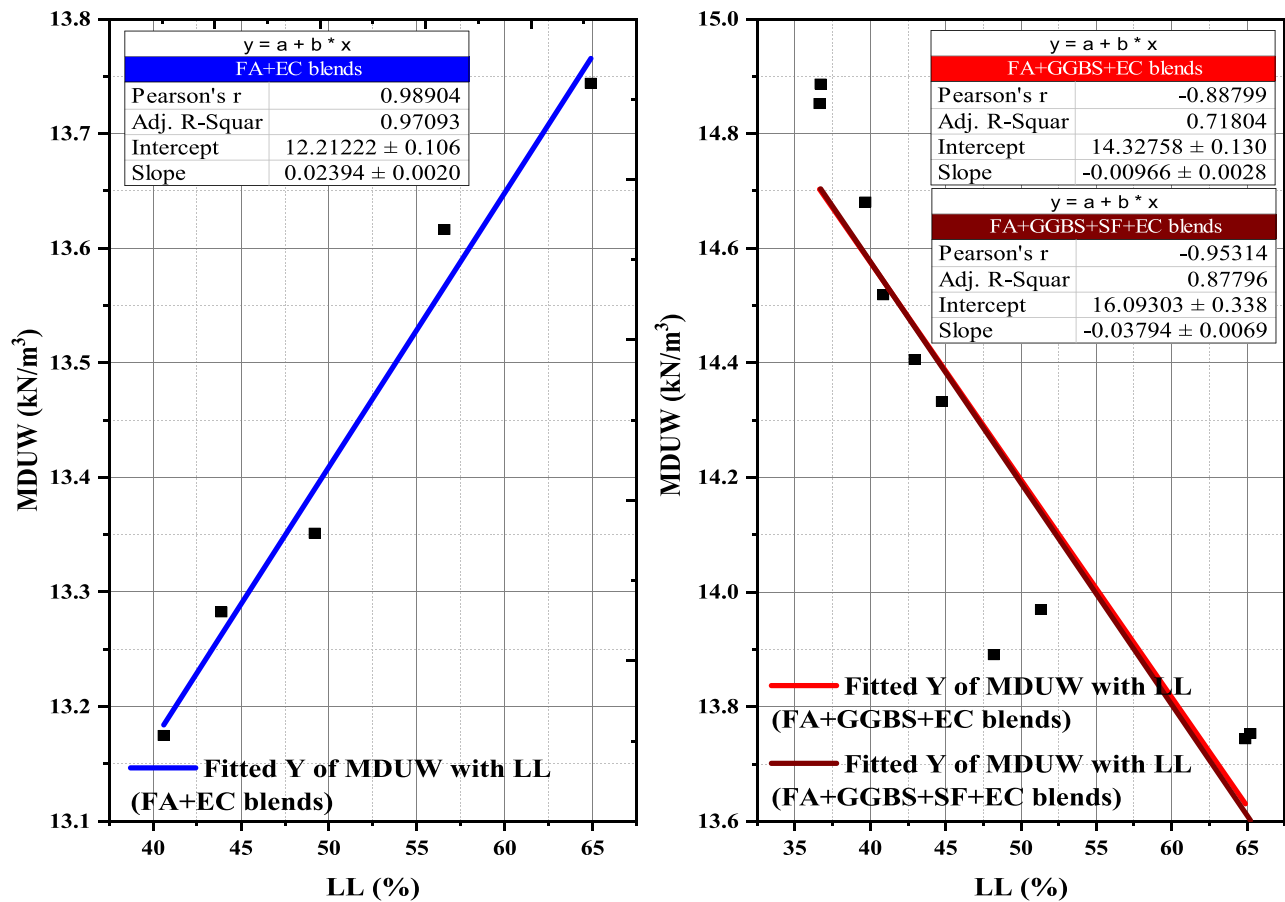


Fig. 15. Correlation of LL with MDUW for SCM's and EC blends.

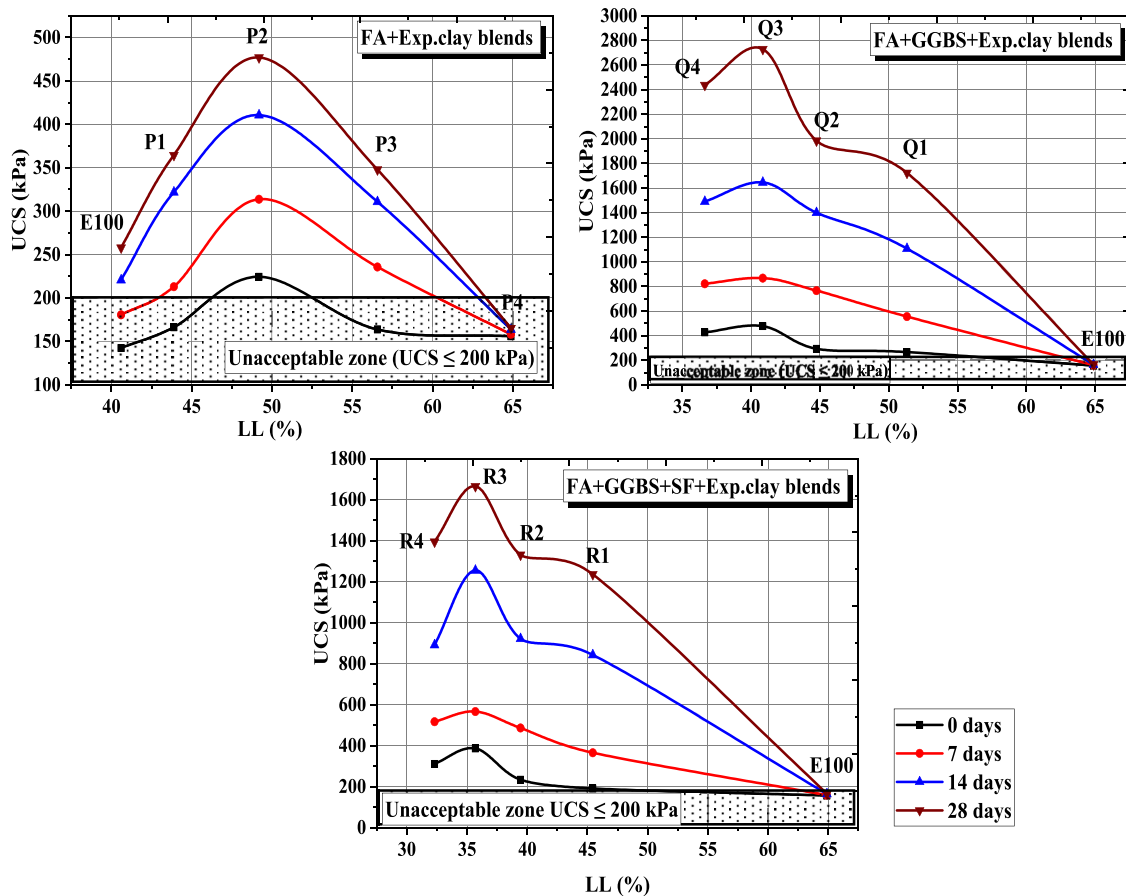


Fig. 16. Correlation of LL with UCS for SCM's and EC blends.

performed. However, the mixes were correlated, as per the HC criterion, the unacceptable zone is pictured in the figures for the P, Q and R-series respectively. This correlation termed as surrogate compatibility test (SCT) (earlier referred to by Lee et al. (2005)), is to observe the changes in the initial volume, which may also affect changes in the HC. These correlations examine the liner efficiency and predict the engineering characteristics of LL/FSI with HC infused with DIW. The figure revealed that LL values are inversely proportional to HC values, the higher the LL value, the lower the HC. For instance, the highest recorded LL value for E100 is 64.89 % and resulted in a lower HC value of $2.31\text{E-}10$ cm/s when permeated with DIW. The mixes P3, P4, Q4 and R4 resulted in the higher order (i.e. $\text{HC} \geq 1\text{E-}07$ cm/s) and corresponding LL values are 43.89 %, 40.6 %, 36.64 % and 32.31 % respectively.

5. Conclusions

This study investigates the effect of different types of SCMs (i.e. fly ash, GGBS and silica fume) and their combinations blended with expansive clays (EC) was investigated for the feasibility of landfill liner materials, overall sixteen mix proportions in three major series (i.e. P, Q, and R-series) were addressed in this research, furthermore, the optimum mix in each series was determined. From the test results, it can be concluded that as the addition of varied SCMs increases with EC in all the series, the consistency limits (i.e. liquid limit (LL), plastic limit (PL) and plasticity index (PI)) and FSI decreases when permeated with DIW. The consistency limits were largely decreased in R-series with the addition of SF in FA-GGBS against EC mixes, A declined ratio of -0.13 (i.e. $\Delta\text{PI}\%$ to $\Delta\text{FA-GGBS-SF}\%$) was observed with DIW as a permeant fluid used in this study. Consequently, the declined ratio was found to be -0.31 (i.e. $\Delta\text{FSI}\%$ to $\Delta\text{FA-GGBS-SF}\%$), thereby signifying greater efficiency in the reduction of FSI values of EC.

Interestingly, the addition of SF decreased the dry densities of the R-series compared with the Q-series. For instance, the rate of increase of MDUW in the Q-series (i.e. 0.008) is twofold times higher than the R-series (i.e. 0.004). Hence, it confirms that the addition of tri-SCMs (i.e. FA-GGBS-SF) is ineffective in increasing the dry densities than FA-GGBS with EC mix blends. The UCS increased with EC against certain quantities of SCMs addition with the curing period. The higher UCS values were recorded in the Q-series when compared to the R-series and P-series. This monotonically decline trend in R-series is attributed to the lack of freetime available in SF for cementitious reactions. Since sufficient amounts of silicates are available in this series; free lime available in FA-GGBS attains a marginal effect to produce cementitious products to react with silicates present in SF. The hydraulic conductivity decreased with EC against certain quantities of SCMs addition i.e. 40 %FA (i.e. for P2 mix in P-series), 60 %FA-GGBS (i.e. for Q3 mix in Q-series) and 60 %FA-GGBS-SF (i.e. for R3 mix in R-series) which resulted in the range of $8.75\text{E-}08$ cm/s, $2.14\text{E-}08$ cm/s and $3.48\text{E-}08$ cm/s respectively when permeated with DIW. This confirms to be optimum and falls under the criterion standards of landfill liner as per USEPA recommendation for the type of EC used in this test program.

Overall, in case of practical possibility, 40 % FA addition with EC, 30 % FA- 30 % GGBS with EC, and 30 % FA-15 % GGBS-15 % SF with EC prove to be the best and most advantageous SCM contents for designing as feasible landfill liner material, resulting in extremely low HC and higher UCS values as per the criterion limit indicated by USEPA (1993) i.e. $\text{HC} \leq 1\text{E-}07$ cm/s and $\text{UCS} \geq 200$ kPa. This study concludes that using FA, GGBS, and SF as landfill liners not only lowers the disposal issue but also enhances the engineering characteristics and geo-environmental requirements.

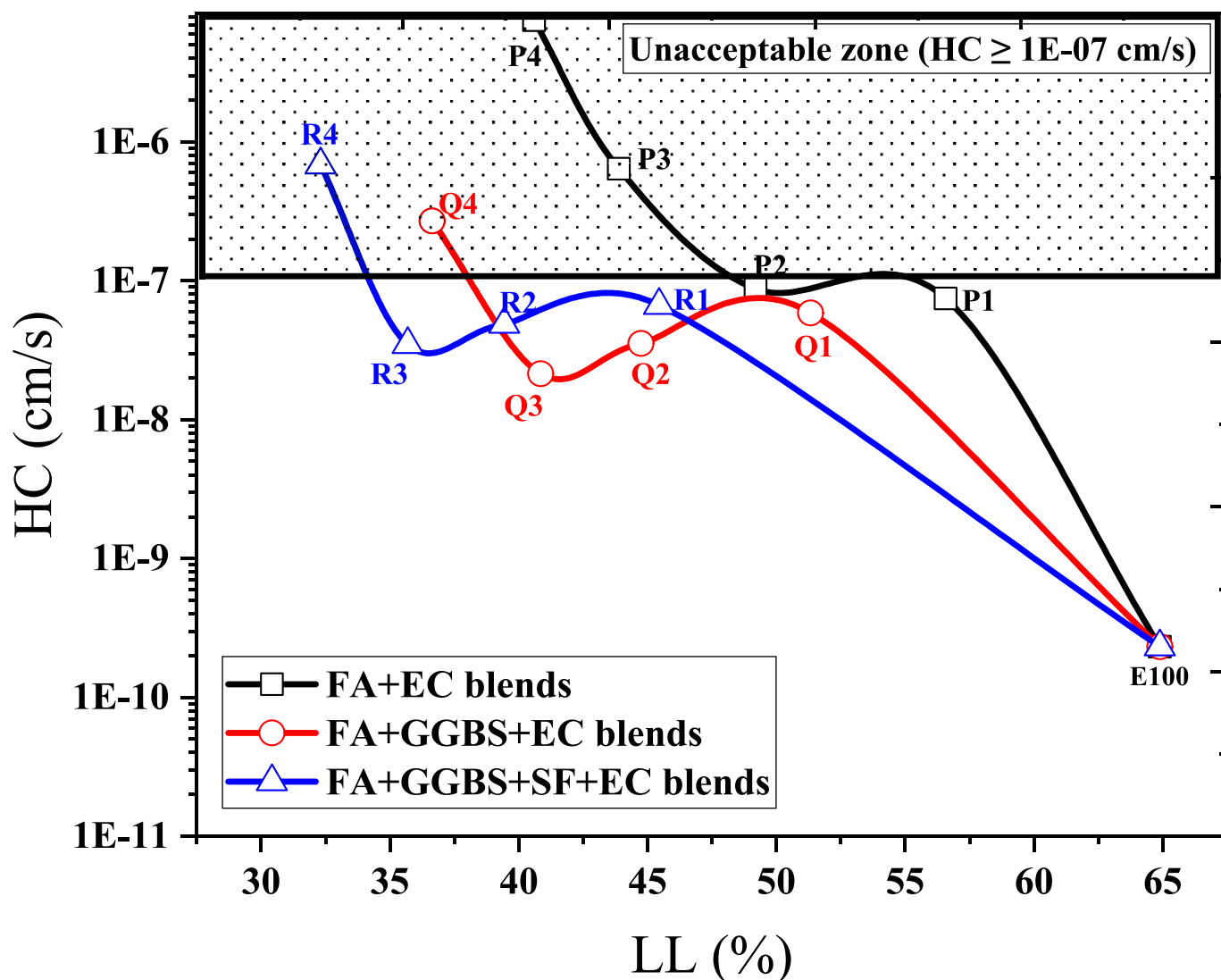


Fig. 17. Correlation of LL with HC for SCMs and EC blends.

CRediT authorship contribution statement

Manikanta Devarangadi: Conceptualization, Investigation, Methodology, Resources, Supervision, Writing – original draft. **Srikanth Vuppala:** Formal analysis, Writing – original draft. **M. Uma Shankar:** Resources. **Mavinakere Eshwaraiah Raghunandan:** Formal analysis.

Declaration of competing interest

The authors declare that they have no known competing financial interests or personal relationships that could have appeared to influence the work reported in this paper.

Data availability

Data will be made available on request.

Acknowledgments

The authors thank Ballari Institute of Technology and Management, Ballari, Karnataka for providing laboratory facility to conduct experiments and for the support extended in carrying out this research work.

References

- Abbey, S.J., Eyo, E.U., Ng'ambi, S., 2020. Swell and microstructural characteristics of high-plasticity clay blended with cement. *Bull. Eng. Geol. Environ.* 79, 2119–2130. doi: 10.1007/s10064-019-01621-z.
- Abu Seif, E.S.S., 2015. Efficiency of quicklime in reducing the swelling potential of pulverized expansive shale, Northern Jeddah, Saudi Arabia. *Bull. Eng. Geol. Environ.* 74, 637–650. <https://doi.org/10.1007/s10064-014-0658-9>.
- Acordi, J., Luza, A., Fabris, D.C.N., Raupp-Pereira, F., De Noni, A., Montedo, O.R.K., 2020. New waste-based supplementary cementitious materials: Mortars and concrete formulations. *Constr. Build. Mater.* 240, 117877 <https://doi.org/10.1016/j.conbuildmat.2019.117877>.
- Ahmad, J., Kontoleon, K.J., Majdi, A., Naqash, M.T., Deifalla, A.F., Ben Kahla, N., Islem, H.F., Qaidi, S.M.A., 2022. A Comprehensive Review on the Ground Granulated Blast Furnace Slag (GGBS) in Concrete Production. *Sustain.* 14 <https://doi.org/10.3390/su14148783>.
- Ahmad, J., Althoe, F., Abuhussain, M.A., Deifalla, A.F., Özkılıç, Y.O., Rahmawati, C., 2023. Durability and microstructure analysis of concrete made with volcanic ash: A review (Part II). *Sci. Eng. Compos. Mater.* 30 <https://doi.org/10.1515/secm-2022-0211>.
- Al-Bakri, A.Y., Ahmed, H.M., Hefni, M.A., 2022. Cement Kiln Dust (CKD): Potential Beneficial Applications and Eco-Sustainable Solutions. *Sustain.* 14 <https://doi.org/10.3390/su14127022>.
- Beck-Broichsitter, S., Gerke, H.H., Horn, R., 2019. Effect of compaction on soil physical properties of differently textured landfill liner materials. *Geosci.* 9, 1–20. <https://doi.org/10.3390/geosciences9010001>.
- Benhelal, E., Zahedi, G., Shamsaei, E., Bahadori, A., 2013. Global strategies and potentials to curb CO₂ emissions in cement industry. *J. Clean. Prod.* 51, 142–161. <https://doi.org/10.1016/j.jclepro.2012.10.049>.

- Chakradhar, V., Katoch, D.S.S., 2016. Study of fly ash in hydraulic barriers in landfills – a review. *Int. Ref. J. Eng. Sci.* 5, 32–38.
- Daniel, D.E., Wu, Y.-K., 1993. Compacted clay liners and covers for arid sites. *J. Geotech. Eng.* 119, 223–237.
- Das, S.K., Yudhbir, 2006. Geotechnical properties of low calcium and high calcium fly ash. *Geotech. Geol. Eng.* 24, 249–263.
- Devarangadi, M., Masilamani, U.S., 2019. Use of sawdust blended with bentonite and cement mixtures to retain diesel oil contaminants as a liner in a landfill. *Indian Geotech. J.* 1–20.
- Devarangadi, M., Shankar, M.U., 2021. Effect on engineering properties of ground granulated blast furnace slag admixed with laterite soil, cement and bentonite mixtures as a liner in a landfill. *J. Clean. Prod.* 329, 129757.
- Devkota, B., Karim, M.R., Rahman, M.M., Nguyen, H.B.K., 2022. Accounting for expansive soil movement in geotechnical design—a state-of-the-art review. *Sustain.* 14 <https://doi.org/10.3390/su142315662>.
- Emmanuel, E., Anggraini, V., Raghunandan, M.E., Asadi, A., 2020. Utilization of marine clay as a bottom liner material in engineered landfills. *J. Environ. Chem. Eng.* 8, 104048 <https://doi.org/10.1016/j.jece.2020.104048>.
- Feng, S.J., Zhao, Y., Zhang, X.L., Bai, Z.B., 2020. Leachate leakage investigation, assessment and engineering countermeasures for tunneling underneath a MSW landfill. *Eng. Geol.* 265, 105447 <https://doi.org/10.1016/j.enggeo.2019.105447>.
- Ganjian, E., Claisse, P. a, Tyrer, M., Atkinson, A., 2004. Selection of cementitious mixes as a barrier for landfill leachate containment. *ASCE J. Mater. Civ. Eng.* 16, 477–486. doi: 10.1061/(ASCE)0899-1561(2004)16:5(477).
- Ghassemi, M., Andersen, P.K., Ghassemi, A., Chianelli, R.R., 2004. Hazardous waste from fossil fuels. *Encycl. Energy* 3, 119–131. <https://doi.org/10.1016/b0-12-176480-x/00395-8>.
- Ghosh, D., Ma, Z.J., Hun, D., 2023. Effect of GGBFS slag on CSA-based ternary binder hydration, and concrete performance. *Constr. Build. Mater.* 386, 131554 <https://doi.org/10.1016/j.conbuildmat.2023.131554>.
- Golewski, G.L., 2023. Study of strength and microstructure of a new sustainable concrete incorporating pozzolanic materials. *Techno Press* 86, 431–441. <https://doi.org/10.12989/sem.2023.86.4.431>.
- Golewski, G.L., 2023a. Assessing of water absorption on concrete composites containing fly ash up to 30 % in regards to structures completely immersed in water. *Case Stud. Constr. Mater.* 19, e02337.
- Golewski, G.L., 2023b. Mechanical properties and brittleness of concrete made by combined fly ash, silica fume and nanosilica with ordinary Portland cement. *AIMS Mater. Sci.* 10, 390–404. <https://doi.org/10.3934/mat.2023021>.
- Golewski, G.L., 2023c. Concrete composites based on quaternary blended cements with a reduced width of initial microcracks. *Appl. Sci.* 13 <https://doi.org/10.3390/app13127338>.
- Golewski, G.L., 2023d. The effect of the addition of coal fly ash (CFA) on the control of water movement within the structure of the concrete. *Materials (basel)* 16. <https://doi.org/10.3390/ma16155218>.
- Guney, Y., Kopalal, S., Aydiş, A.H., 2008. Sepiolite as an alternative liner material in municipal solid waste landfills. *J. Geotech. Geoenviron. Eng.* 134, 1166–1180. doi: 10.1061/(ASCE)1090-0241(2008)134:8(1166).
- Gupt, C.B., Bordoloi, S., Sekharan, S., 2023. Contaminant retention affected by controlled and uncontrolled pH for fly ash-bentonite composites used as landfill liner material. *J. Clean. Prod.* 406, 136924 <https://doi.org/10.1016/j.jclepro.2023.136924>.
- Huang, W., Huang, Y., Lin, S., Chen, Z., Gao, B., Cui, S., 2018. Changing urban cement metabolism under rapid urbanization – a flow and stock perspective. *J. Clean. Prod.* 173, 197–206. <https://doi.org/10.1016/j.jclepro.2017.01.008>.
- Hussain, E.K., Al-Ameen, J., Janna, H., 2021. Surface soil enhancement for MSW lining by silica fume. *J. Phys. Conf. Ser.* 1895, 12046. doi: 10.1088/1742-6596/1895/1/012046.
- Ijaz, N., Ye, W., Rehman, Z. ur, Ijaz, Z., 2022. Novel application of low carbon limestone calcined clay cement (LC3) in expansive soil stabilization: An eco-efficient approach. *J. Clean. Prod.* 371, 133492. doi: 10.1016/j.jclepro.2022.133492.
- Joshi, R.C., Lohita, R.P., 1997. *Fly Ash in Concrete: Production, Properties and Uses*. CRC Press.
- Kashyap, V.S., Sancheti, G., Yadav, J.S., Agrawal, U., 2023. Smart sustainable concrete : enhancing the strength and durability with nano silica. *Smart Constr. Sustain. Cities* 1–17. <https://doi.org/10.1007/s44268-023-00023-1>.
- Koukousas, N., Tyrologou, P., Koutsovitis, P., Karapanos, D., Karkalis, C., 2022. 15 – Soil stabilization, in: Kar, K.K.B.T.-H. of F.A. (Ed.), . Butterworth-Heinemann, pp. 475–500. doi: 10.1016/B978-0-12-817686-3.00004-9.
- Kumar, A., Sivapullaiah, P.V., 2016. Ground granulated blast furnace slag amended fly ash as an expansive soil stabilizer. *Soils Found.* 56, 205–212. <https://doi.org/10.1016/j.sandf.2016.02.004>.
- Kumar, A., Walia, B.S., Bajaj, A., 2007. Influence of fly ash, lime, and polyester fibers on compaction and strength properties of expansive soil. *J. Mater. Civ. Eng.* 19, 242–248.
- Lashari, A.R., Kumar, A., Kumar, R., Rizvi, S.H., 2023. Combined effect of silica fume and fly ash as cementitious material on strength characteristics, embodied carbon, and cost of autoclave aerated concrete. *Environ. Sci. Pollut. Res.* 30, 27875–27883. <https://doi.org/10.1007/s11356-022-24217-9>.
- Lee, J.-M., Shackelford, C.D., Benson, C.H., Jo, H.-Y., Edil, T.B., 2005. Correlating index properties and hydraulic conductivity of geosynthetic clay liners. *J. Geotech. Geoenviron. Eng.* 131, 1319–1329.
- Liu, J.C., Hossain, M.U., Ng, S.T., Ye, H., 2023. High-performance green concrete with high-volume natural pozzolan: mechanical, carbon emission and cost analysis. *J. Build. Eng.* 68, 106087 <https://doi.org/10.1016/j.jobe.2023.106087>.
- Mahedi, M., Cetin, B., White, D.J., 2020. Cement, lime, and fly ashes in stabilizing expansive soils: performance evaluation and comparison. *J. Mater. Civ. Eng.* 32, 1–16. [https://doi.org/10.1061/\(asce\)mt.1943-5533.0003260](https://doi.org/10.1061/(asce)mt.1943-5533.0003260).
- Mir, B.A., Sridharan, A., 2017. Mechanical behaviour of fly-ash-treated expansive soil. *Proc. Inst. Civ. Eng. - Gr. Improv.* 172, 12–24. <https://doi.org/10.1680/jgrim.16.00024>.
- Nath, H., Kabir, M.H., Kafy, A.A., Rahaman, Z.A., Rahman, M.T., 2023. Geotechnical properties and applicability of bentonite-modified local soil as landfill and environmental sustainability liners. *Environ. Sustain. Indic.* 18, 100241 <https://doi.org/10.1016/j.indic.2023.100241>.
- Osinubi, K.J., Nwaiwu, C.M., 2006. Design of compacted lateritic soil liners and covers. *J. Geotech. Geoenviron. Eng.* 132, 203–213.
- Payá, J., Monzó, J., Roselló, J., Borrachero, M.V., Font, A., Soriano, L., 2020. Sustainable soil-compacted blocks containing blast furnace slag (Bfs) activated with olive stone biomass ash (oba). *Sustain.* 12, 1–15. <https://doi.org/10.3390/su12239824>.
- Pedersen, C.S., 2018. The un sustainable development goals (SDGs) are a great gift to business! *Proc. CIRP* 69, 21–24. <https://doi.org/10.1016/j.procir.2018.01.003>.
- Phani Kumar, B.R., Sharma, R.S., 2004. Effect of fly ash on engineering properties of expansive soils. *J. Geotech. Geoenviron. Eng.* 130, 764–767. [https://doi.org/10.1061/\(ASCE\)1090-0241\(2004\)130:7\(764\)](https://doi.org/10.1061/(ASCE)1090-0241(2004)130:7(764)).
- Phanikumar, B.R., e, R.R., 2020. Silica fume stabilization of an expansive clay subgrade and the effect of silica fume-stabilised soil cushion on its CBR. *Geomech. Geoenviron. Eng.* 15, 64–77.
- Phanikumar, B.R., Shankar, M.U., 2016. Studies on hydraulic conductivity of fly ash-stabilised expansive clay liners. *Geotech. Geol. Eng.* 34, 449–462.
- Phanikumar, B.R., Sharma, R.S., 2007. Volume change behavior of fly ash-stabilized clays. *J. Mater. Civ. Eng.* 19, 67–74.
- Prashanth, J.P., Sivapullaiah, P.V., Sridharan, A., 2001. Pozzolanic fly ash as a hydraulic barrier in land fills. *Eng. Geol.* 60, 245–252. [https://doi.org/10.1016/S0013-7952\(00\)00105-8](https://doi.org/10.1016/S0013-7952(00)00105-8).
- Sabat, A.K., Bose, B., 2013. Improvement in geotechnical properties of an expansive soil using fly ash-quarry dust mixes. *Electron. J. Geotech. Eng.* 18, 3487–3500.
- Shankar, M.U., Phanikumar, B.R., 2012. Correlation studies on index properties of fly ash-stabilised expansive clay liners. *Geomech. Geoenviron. Eng.* 7, 283–291. <https://doi.org/10.1080/17486025.2011.631036>.
- Sharma, R.K., Hymavathi, J., 2016. Effect of fly ash, construction demolition waste and lime on geotechnical characteristics of a clayey soil: a comparative study. *Environ. Earth Sci.* 75, 1–11.
- Sharma, A.K., Sivapullaiah, P.V., 2016a. Strength development in fly ash and slag mixtures with lime. *Proc. Inst. Civ. Eng. Improv.* 169, 194–205.
- Sharma, A.K., Sivapullaiah, P.V., 2016b. Ground granulated blast furnace slag amended fly ash as an expansive soil stabilizer. *Soils Found.* 56, 205–212. <https://doi.org/10.1016/j.sandf.2016.02.004>.
- Sharma, A.K., Sivapullaiah, P.V., 2017. Swelling behaviour of expansive soil treated with fly ash-GGBS based binder. *Geomech. Geoenviron. Eng.* 12, 191–200. <https://doi.org/10.1080/17486025.2016.1215548>.
- Siddique, R., 2008. In: *Ground Granulated Blast Furnace Slag BT - Waste Materials and by-Products in Concrete*. Springer, Berlin Heidelberg, Berlin, Heidelberg, pp. 1–39. https://doi.org/10.1007/978-3-540-74294-4_1.
- Siddique, R., Bennacer, R., 2012. Use of iron and steel industry by-product (GGBS) in cement paste and mortar. *Resour. Conserv. Recycl.* 69, 29–34. <https://doi.org/10.1016/j.resconrec.2012.09.002>.
- Silva, L.H.P., de Paiva, F.F.G., Tamashiro, J.R., Kinoshita, A., 2023. Potential of bamboo leaf ash as supplementary binder materials – a systematic literature review. *J. Build. Eng.* 71, 106547 <https://doi.org/10.1016/j.jobe.2023.106547>.
- Singh, P., Dash, H.K., Samantaray, S., 2020. Effect of silica fume on engineering properties of expansive soil. *Mater. Today Proc.* 33, 5035–5040. <https://doi.org/10.1016/j.matpr.2020.02.839>.
- Singh, M., Singh, J., Siddique, R., 2021. Bagasse ash. *Sustain. Concr. Made with Ashes Dust from Differ. Sources Mater. Prop. Appl.* 177–233 <https://doi.org/10.1016/B978-0-12-824050-2.00001-2>.
- Sivapullaiah, P.V., Moghal, A.A.B., 2011. Role of gypsum in the strength development of fly ashes with lime. *J. Mater. Civ. Eng.* 23, 197–206. [https://doi.org/10.1061/\(ASCE\)MT.1943-5533.0000158](https://doi.org/10.1061/(ASCE)MT.1943-5533.0000158).
- Sivapullaiah, P.V., Prashanth, J.P., Sridharan, A., 1996. Effect of fly ash on the index properties of black cotton soil. *Soils Found.* 28, 97–103. <https://doi.org/10.1248/cpb.37.3229>.
- Sivapullaiah, P.V., Prashanth, J.P., Sridharan, A., Narayana, B.V., 1998. Reactive silica and strength of fly ashes. *Geotech. Geol. Eng.* 16, 239–250. <https://doi.org/10.1023/A:1008889326269>.
- Soltani, A., Deng, A., Taheri, A., O'Kelly, B.C., 2022. Intermittent swelling and shrinkage of a highly expansive soil treated with polyacrylamide. *J. Rock Mech. Geotech. Eng.* 14, 252–261. <https://doi.org/10.1016/j.jrmge.2021.04.009>.
- Sumathi, A., Elavarasi, D., Karthikeyan, B., Shobana, P., Selvaraj, S.K., Dewangan, S., Molla, B., 2023. Mechanical, durability, and microstructure investigations on high-strength concrete incorporating nanosilica, multi-walled carbon nanotubes, and steel fibres. *Adv. Mater. Sci. Eng.* 2023 <https://doi.org/10.1155/2023/2164200>.
- Sumitha, Y., Abraham, R., 2016. Experimental Study on bentonite clay powder with silica fume and GGBS as partial replacement of cement in M40 grade concrete. *Int. J. Eng. Res.* 5, 339–343. <https://doi.org/10.17577/ijertv5is090235>.
- The-Sustainable-Development-Goals-Report-2023.pdf, n.d.
- Thomas, M., Jewell, R., Jones, R., 2017. 5 – Coal fly ash as a pozzolan, in: Robl, T., Oberlink, A., Jones, R.B.T.-C.C.P. (CCP's) (Eds.), . Woodhead Publishing, pp. 121–154. doi: 10.1016/B978-0-08-100945-1.00005-8.
- UN-HABITAT, 2016. *World Cities Report 2016; Urbanization And Development-Emerging Futures*. UN.

- USEPA, 1993. Solid Waste Disposal Facility Criteria. "Solid Waste Dispos. Facil. Criteria. Solid Waste Emerg. Response (5305)" EPA530-F-93- 017, United States Environ. Prot. Agency (USEPA), Washington, D.C., 1993.
- Wan, Y., Dong, Z., Cai, Y., Xue, Q., Liu, K., Liu, L., Guo, D., 2023. Geomembrane leaks detection and leakage correlation factor analysis of composite liner systems for fifty-five (55) solid waste landfills in China. *Environ. Technol. Innov.* 32, 103308 <https://doi.org/10.1016/j.eti.2023.103308>.
- Wang, J., Liu, M., Wang, Y., Zhou, Z., Xu, D., Du, P., Cheng, X., 2020. Synergistic effects of nano-silica and fly ash on properties of cement-based composites. *Constr. Build. Mater.* 262, 120737 <https://doi.org/10.1016/j.conbuildmat.2020.120737>.
- Wang, L., Zhang, P., Golewski, G., Guan, J., 2023. Editorial: Fabrication and properties of concrete containing industrial waste. *Front. Mater.* 10, 2022–2023. <https://doi.org/10.3389/fmats.2023.1169715>.
- Wei, Z., Wang, B., Falzone, G., La Plante, E.C., Okoronkwo, M.U., She, Z., Oey, T., Balonis, M., Neithalath, N., Pilon, L., Sant, G., 2018. Clinkering-free cementation by fly ash carbonation. *J. CO2 Util.* 23, 117–127. <https://doi.org/10.1016/j.jcou.2017.11.005>.
- Widomski, M.K., Stepniewski, W., Horn, R., Bieganski, A., Gazda, L., Franus, M., Pawłowska, M., 2015. Shrink-swell potential, hydraulic conductivity and geotechnical properties of clay materials for landfill liner construction. *Int. Agrophysics* 29, 365–375. <https://doi.org/10.1515/intag-2015-0043>.
- Younus, M.M., Sreedeeep, S., 2012. Reevaluation and modification of plasticity-based criterion for assessing the suitability of material as compacted landfill liners. *J. Mater. Civ. Eng.* 24, 1396–1402. [https://doi.org/10.1061/\(ASCE\)MT.1943-5533.0000522](https://doi.org/10.1061/(ASCE)MT.1943-5533.0000522).
- Zhu, H., Chen, W., Cheng, S., Yang, L., Wang, S., Xiong, J., 2022. Low carbon and high efficiency limestone-calcined clay as supplementary cementitious materials (SCMs): multi-indicator comparison with conventional SCMs. *Constr. Build. Mater.* 341 <https://doi.org/10.1016/j.conbuildmat.2022.127748>.



Application of index of entropy and Geospatial techniques for landslide prediction in Lunglei district, Mizoram, India

Jonmenjoy Barman^a, Syed Sadath Ali^b, Brototi Biswas^a, Jayanta Das^{c,*}

^a Department of Geography and Natural Resources, Mizoram University, Aizawl, 796004, India

^b Civil Engineering Department, Ballari Institute of Technology and Management, Ballari, India

^c Department of Geography, Rampurhat College, PO, Rampurhat, Dist- Birbhum, 731224, India

ARTICLE INFO

Keywords:

Landslide susceptibility
Remote sensing
Geographical information system
Index of entropy
Lunglei district

ABSTRACT

The present study focuses on developing a landslide susceptibility zonation (LSZ) using GIS-based bivariate statistical model in the Lunglei district of Mizoram. Initially, 17 factors were selected after calculating the multi-collinearity test for LSZ. A landslide inventory map was created based on 234 historic landslide events, which were randomly divided into training (70%) and testing (30%) datasets. Using the Index of Entropy (IOE) model, nine causative factors were identified as having significant weightage for LSZ: elevation, slope, aspect, curvature, normalized difference vegetation index, geomorphology, distance to road, distance to lineament, and distance to river. On the other hand, factors such as land use land cover, stream power index, terrain ruggedness index, terrain roughness, topographic wetness index, annual rainfall, topographic position index, and geology had negligible weightage. Based on the relative importance of the causative factors, two models were developed: scenario 1, which considered nine factors, and scenario 2, which considered all 17 factors. The results revealed that 16% and 14% of the district area were identified as very highly landslide prone in scenario 1 and scenario 2, respectively. The high susceptibility zone accounted for 26% and 25% of the area in scenario 1 and scenario 2, respectively. To assess the accuracy of the models, a receiver operating characteristic (ROC) curve and quality sum ratio method was performed using 30% of the testing landslide data and an equal number of non-landslide data points. The area under the curve (AUC) for scenario 1 and scenario 2 were 0.947 and 0.922, respectively, indicating higher efficiency for scenario 1. The quality sum ratios were 0.435 and 0.43 for scenario 1 and scenario 2, respectively. Based on these results, the LSZ mapping from scenario 1 is considered suitable for policymakers to address development and risk reduction associated with landslides.

1. Introduction

A landslide or landslip is a geological event that causes intense downward movement of earth materials along a surface plane under the influence of gravity force (Sarvothaman and Anandha, 2013). Varnes (1984) introduced landslide hazard as the chance of possible damaging phenomenon in a given time period within a given area. Landslides rank 3rd among other natural hazards on the basis of the degree of hazard worldwide (Basu and Pal, 2019). Huang and Zhao (2018) reported that 2620 fatal landslides claimed 32,322 human lives during 2004–2010 worldwide. Landslides not only damage life and property but sometimes damage the environment's stability (Chen and Chen, 2021). In India, 12.65% of the total land area is affected by landslides. It is very common in hilly regions where urbanization

is increasing rapidly (Barman et al., 2022a). Parkash (2011) divided India into three landslide-affected geographical regions; northeast India is one of them. A landslide is a combination of different conditioning factors. The factors that control landslide intensity and cause are broadly divided into two categories: (a) extrinsic variables that influence landslide susceptibilities, such as earthquakes and heavy rainfall, and (b) intrinsic variables, which are factors that contribute to landslide susceptibility (Dai et al., 2001). Landslide susceptibility zonation (LSZ) is the first step toward determining the distribution and risk of landslides (Trigila et al., 2015; Bui et al., 2012). The terminology "landslide susceptibility" can be explained as a likelihood measurement of the failure probability from a given known batch of environmental conditions (Guzzetti et al., 2005). The new development of GIS is an opportunity among scholars for landslide study. The

* Corresponding author.

E-mail addresses: jonmenjoybarman07@gmail.com (J. Barman), sayyu92@gmail.com (S.S. Ali), brototibiswas@gmail.com (B. Biswas), jayanta.daas@gmail.com (J. Das).

<https://doi.org/10.1016/j.nhres.2023.06.006>

Received 1 May 2023; Received in revised form 12 June 2023; Accepted 22 June 2023

Available online 23 June 2023

2666-5921/© 2023 National Institute of Natural Hazards, Ministry of Emergency Management of China. Publishing services provided by Elsevier B.V. on behalf of KeAi Communications Co. Ltd. This is an open access article under the CC BY-NC-ND license (<http://creativecommons.org/licenses/by-nc-nd/4.0/>).

approaches of LSZ are broadly classified into three fundamental clusters, namely quantitative physical or deterministic based; qualitative data-driven or statistical-based; and qualitative knowledge or heuristic-based (Li et al., 2016; Chen and Li, 2020).

The deterministic approaches mainly focus on the failure mechanism of a landslide (Zou et al., 2021). Statistical approaches are organized on the premise of the relationship between the existence of landslides and the terrain attributes responsible for their occurrence, while heuristic approaches are based on the landform investigation by an experienced geomorphologist (Ermini et al., 2005). The well-known methods used by the researcher are the analytical hierarchy process (Kumar and Anbalagan, 2016; Myronidis et al., 2016; Pourghasemi et al., 2012), the weight of evidence (Lee and Choi, 2004; Armaş, 2012; Neuhäuser et al., 2012), information value method (Achour et al., 2017; Sarkar et al., 2013; Farooq and Akram, 2021), frequency ratio (Akgun et al., 2008; Solaimani et al., 2013; Poudyal et al., 2010), support vector machine (Yao et al., 2008; Ballabio and Sterlacchini, 2012; Chen et al., 2016), logistic regression (Ayalew and Yamagishi, 2005; Hemasinghe et al., 2018; Bai et al., 2010), artificial neural network (Choi et al., 2010; Kawabata and Bandibas, 2009; Bragagnolo et al., 2020).

In the present study, a bivariate statistical approach i.e., Index of Entropy (IOE), is applied for LSZ in the Lunglei district of Mizoram. IOE is a statistical method that measures the maximum impact of a conditioning factor on landslide occurrences (Dam et al., 2022). The novelty of the method is that it considers Scenario 1 and Scenario 2 approaches based on parameter selection and weighting based on the Index of Entropy (IOE). Previous research by (Singh et al., 2021; Zhang et al., 2019; Shirani et al., 2018) successfully applied the index of entropy model to a variety of environmental conditions worldwide, but they did not utilize the parameter optimization technique. So, the present study aimed to determine the optimum landslide conditioning factors and prepare an LSZ mapping in the Lunglei district of Mizoram using 17 landslide conditioning factors along with 234 historic landslide events.

2. Material and methodology

2.1. Study area

The study area covers approximately 2014.49 km² and extends between 92° 42' E to 93° 10' E longitude and 22° 23' N to 23° 15' N latitude (Fig. 1). It is characterized by an undulating, dissected, and deep valley within the extended Himalayan range. Lunglei town, the second-largest urban center in Mizoram, is experiencing rapid urbanization, and slope cutting for road construction has made the area prone to landslides. The region receives heavy rainfall during the southwest monsoon season, with an average annual rainfall of 3204.7 mm (Rao et al., 2023). The tropic of cancer passes north of the district, and the annual average temperature ranges from 11 °C to 35 °C (Barman and Biswas, 2022). The mean relative humidity is 87%. The general topography of Lunglei District is highly diverse. The southwestern and western regions are characterized by relatively low and less prominent ridges, while the northern and eastern regions exhibit steep terrain with high relief. The entire Mizoram region is marked by dissected hills and valleys, which are common geomorphological features. Landslides occur frequently during the monsoon period, causing damage to the nutrient cycle, road networks, natural resources, and human life. Between 2017 and 2018, landslides resulted in the destruction of 39 fully or partially damaged houses and affected 58.06 lakh hectares of cropping areas (as per the District disaster management plan, 2019). Therefore, there is a need for a comprehensive landslide assessment at the district level in this area.

2.2. Database and background of the study

A landslide is a complex geological hazard. It is a systematic negative effect of different conditioning factors (Chen and Chen, 2021). There are no universal guidelines or regulations for the number of conditioning factors and their types. In the current study, conditional factors are

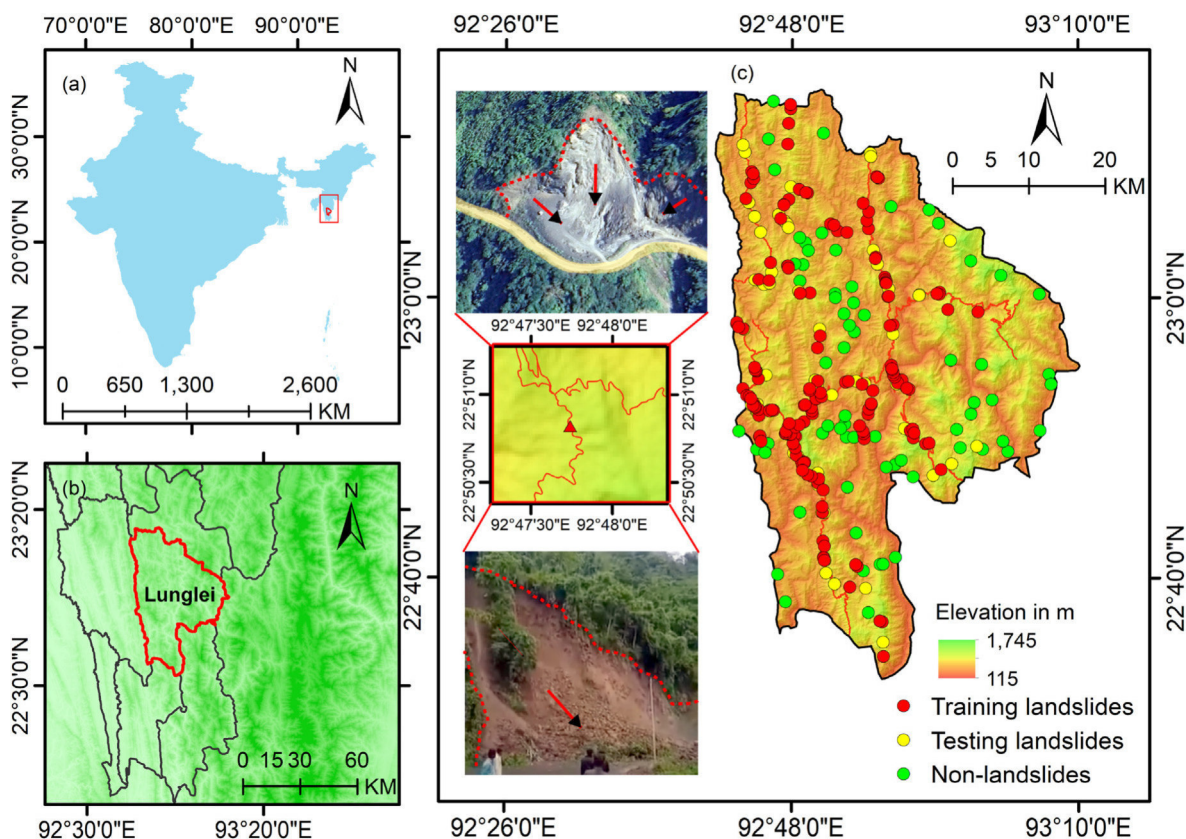


Fig. 1. Location of the study. (a) India, (b) Lunglei district in southern Mizoram, (c) Elevation in Lunglei district.

chosen based on the data availability and previous literature for the study area (Table 1). Different direct and indirect terrain attributes, namely elevation, slope, slope angle, curvature, relief amplitude, terrain ruggedness index, terrain roughness, and topographic wetness index, are extracted from the ASTER 30m digital elevation model (<https://search.earthdata.nasa.gov/search>). The hydrological factors, namely the distance to the river, are prepared from OSM (<https://www.openstreetmap.org>) through the Euclidean distance method, and rainfall distribution is prepared from a 0.5°0.5 high-resolution gridded Cru dataset (<https://crudata.uea.ac.uk/cru/data/hrg/>). The Bhukosh portal is used to collect tectonic factors such as lineament information (<https://bhukosh.gsi.gov.in/Bhukosh/MapView.aspx>). The geomorphology information is downloaded from the Bhukosh geo portal. The likely distance of human activities to a road is calculated using the OSM road network, and the land use/land cover map is prepared from Landsat 8 OLI (<https://earthexplorer.usgs.gov/>) using a training sample and the maximum likelihood method in a GIS environment (Table 2). A methodological flow chart is shown in Fig. 2.

2.3. Landslide conditioning factors

2.3.1. Elevation

Elevation has a positive relationship with landslide occurrence (Ayalew and Yamagishi 2005). The rainfall and temperature in a region are directly correlated with altitude. Height growth produces a steeper slope, which lowers the shear strength of the slope materials (Saranaathan et al., 2021). The elevation of the Lunglei district area is extracted from ASTER 30m Dem. Elevation in the study area ranges from 115 m to 1745 m, which is classified into five classes based on the natural breaking methods. The elevation classes are (a) 115–472.96 m, (b) 472.97–671.12 m, (c) 671.13–875.67 m, (d) 875.68–1131.35 m, and (e) 1131.36–1745 m. Most of the area (30%) ranged between elevations of 472.97 and 671.12 m.

Slope: The slope means the vertical elevational difference between two points with horizontal distances (Das et al., 2022). Theoretically, when the slope rises, shear stress increases, which raises the possibility of slope instability (Abedini and Tulabi, 2018). The slope map is driven from the ASTER 30 m DEM. The slope in the study area ranges between 0 and 73° and is classified into five classes. The slope classes are (a) 0–8°, (b) 8°–15°, (c) 15°–25°, (d) 25°–40°, and (e) 40°–73°. The maximum area of the study region (about 37%) falls under a 25–40° slope.

Aspect: The slope aspect indicates the slope's facing direction, which is a significant determinant of solar radiation, wind, and precipitation. Hence, it directly controls the types and intensities of vegetation cover and soil moisture (Guru et al., 2017). The slope direction of the area is divided into ten directions as (a) Flat (–1), (b) North (0–22.5), (c)

Northeast (22.5–67.5), (d) East (67.5–112.5), (e) Southeast (112.5–157.5), (f) South (157.5–202.5), (g) Southwest (202.5–247.5), (h) West (247.5–292.5), (i) Northwest (292.5–337.5), and (j) North (337.5–360). About 14% of the slopes are west-facing slopes.

Curvature: Curvature is an imagined line formed by intersecting random points on the earth's surface (Anbazhagan and Ramesh 2014). In the current study, a combination of both profile and plane curvature is considered. Flow direction, slope morphology, and many other geological structures directly depend on curvature. In the present study, zero values are considered flat regions, positive values are considered convex and negative values are considered concave regions. In the present study, the curvature is divided into three classes that are (a) –29.17–0, (b) flat (0), and (c) 0–31.35.

Stream power index (SPI): The stream power index provides an indication of energy dissipation against the bed and banks that is widely used as a proxy for sediment transportation and channel excavation rate (Johnson et al., 2009). It is measured as per (Moore and Grayson, 1991) according to Eq. (1).

$$SPI = A_s * \tan \beta \quad (1)$$

where, A_s is the contributing catchment area and β is the slope angle. As SPI is the product of catchment area and slope angle, a high SPI value indicated a larger catchment area and high slope angle which is reflect the high flow velocity and higher erosion risk. SPI for the current study is divided into five classes (a) < 0, (b) 1–10, (c) 11–20, (d) 21–30, and (e) 31–40.

Terrain ruggedness index (TRI): The TRI is employed to characterize the topography as smooth or rugged terrain, as well as the local change of slopes or surface curvatures (Dahal et al., 2008). Topographic heterogeneity or TRI is defined as the difference in height between adjacent pixels (Al-Najjar and Pradhan, 2021). It affects the hydrological and topographical factors to develop a landslide event. The terrain ruggedness index is prepared as Eq. (2). Based on the natural break method, TRI is divided into five classes: (a) 0–92, (b) 93–180, (c) 190–240, (d) 250–320, and (e) 330–710.

$$TRI = \sqrt{Abs(max^2 - min^2)} \quad (2)$$

Here, max and min are the maximum and minimum elevation of the define region respectively.

Terrain roughness (Rn): Elevational irregularity or variability of terrain within a terrain unit is called terrain roughness. The possibility of rock fall has a positive correlation with the terrain roughness (Fatemi Aghda et al., 2018). It is calculated using Eq. (3).

Table 1
Literature reviews for selection of conditioning factors for landslide susceptibility mapping.

References/Factors	Elevation	Slope	Aspect	Curvature	SPI	TRI	Rn	TPI	TWI	R	DTR	DTL	DTS	Geology	Geom	NDVI	LULC
Biswas et al. (2023)		✓	✓							✓	✓	✓	✓	✓	✓		✓
Roy et al. (2019)	✓	✓	✓		✓				✓	✓	✓	✓	✓	✓	✓	✓	✓
Youssef et al. (2015)	✓	✓	✓	✓						✓	✓	✓	✓	✓		✓	
Efiong et al., (2021)	✓	✓	✓	✓	✓			✓	✓		✓	✓	✓	✓			✓
Shahzad et al. (2022)	✓	✓	✓	✓				✓	✓	✓	✓	✓	✓	✓		✓	✓
Althuwaynee et al. (2012)	✓	✓	✓	✓	✓		✓			✓	✓	✓	✓			✓	✓
Mahalingam et al. (2016)	✓	✓					✓										
Al-Najjar et al. (2019)	✓	✓	✓	✓	✓	✓		✓			✓	✓	✓	✓			✓
Ullah et al. (2022)	✓	✓	✓	✓	✓	✓					✓	✓	✓			✓	✓
Pham et al. (2020)	✓	✓	✓	✓	✓	✓			✓								
García-Rodríguez and Malpica (2010)	✓	✓	✓				✓			✓							✓
Fatemi Aghda et al. (2018)		✓				✓					✓	✓	✓			✓	
Chang et al. (2016)	✓	✓	✓	✓		✓	✓										

Table 2
Spatial database used in the study.

Products	Thematic layer	Data source	Access date	Resolution/Scale	Type
GSI	DTL Geology Geom	Bhukosh (gsi.gov.in)	7/24/2022	1:50,000	Vector
ASTER DEM	Elevation Slope Aspect Curvature TRI Rn TWI SPI	Earthdata Search (nasa.gov)	7/25/2022	30 m	Raster
OSM	DTR DTS	BBBike extracts OpenStreetMap	7/24/2022	NA	Vector
Cru	R	High-resolution gridded datasets (uea.ac.uk)	7/26/2022	05° 0.5°	Gridded
Landsat 8 OLI	LULC NDVI	EarthExplorer (usgs.gov)	7/26/2022	30m	Raster

$$\text{Roughness} = \frac{(FS_{\text{mean}} - FS_{\text{min}})}{(FS_{\text{max}} - FS_{\text{min}})} \quad (3)$$

Where, FS_{mean} is the mean elevation of the define region, FS_{max} and FS_{min} are the minimum and maximum elevation of that region respectively. For the present study Rn is divided into five classes - (a) 0.11–0.3, (b) 0.31–0.43, (c) 0.44–0.5, (d) 0.51–0.58, and (e) 0.59–0.89.

Topographic position index (TPI): Altitudinal differences of a central point (Z_0) from average altitude (\bar{Z}) within a defined radius (R) is shown by TPI. It is formulated as Eqs. (4) and (5).

$$TPI = Z_0 - \bar{Z} \quad (4)$$

$$\bar{Z} = \frac{1}{n_R} \sum_{i \in R} Z_i \quad (5)$$

A positive TPI value indicates high land in the central point, while a negative TPI value indicates low land in the central point. In the study, the TPI of the district was classified into five groups (a) –10.2–1.4, (b) –1.3–0.5, (c) 0.4–0.3, (d) 0.4–1.2, and (e) 1.3–14.1.

Topographic wetness index (TWI): TWI identifies the source zone that has become saturated as a result of surface runoff under the impact of topographic conditions (Sema et al., 2017; Mitra et al., 2022). It is formulated as Eq. (6).

$$TWI = \ln \left(\frac{\alpha}{\tan \beta} \right) \quad (6)$$

where α is the upslope contributing area and β is the slope angle. Likewise, here $\alpha = \frac{A}{L}$, Amongst them A and L denote the total basin area and length of the contour. TWI is classified into five classes - (a) 2.47–5.68, (b) 5.69–7.48, (c) 7.49–9.28, (d) 9.29–11.86, and (e) 11.87–22.42.

Rainfall distribution (R): Rainfall is a dominant landslide controlling factor. During field studies, it has been observed that most of the landslides occurred in the rainy season. For the current study, the average annual rainfall of 2021 has been prepared by the IDW technique in GIS environment. It is classified into three classes (a) 360.6–370.4 cm, (b) 370.5–380 cm, and (c) 380.1–380.6 cm.

Distance to road (DTR): Road networks are the footprint of human activities and reflect the mobility of civilization (Basu and Pal, 2019). During the field study, it was discovered that the majority of slope failures occur along the roadside. For the current study, road network information is collected from open-source maps. The Euclidean distance method is implemented for measuring the distance from the road network. It is divided into the following categories: (a) 0–300 m, (b)

301–600 m, (c) 601–900 m, (d) 901–1200 m; (e) 1201–1500 m.

Distance to Lineament (DTL): Lineaments are underlain by linear geological expression. Lineaments have a direct influence on maximum landslides (Kaur et al., 2023). Kumar and Anbalagan (2019) reported that landslides are directly connected with the lineament vicinity. In the current study, a raster buffer by the Euclidean distance method is used for measuring the distance to the lineament. Further, it is classified into five classes (a) 0–300 m, (b) 301–600 m, (c) 601–900 m, (d) 901–1200 m, and (e) 1201–1500 m.

Distance to stream (DTS): It is assumed that along the river, the amount of saturation is quite high. The right conditions for a landslide include heavy rains followed by saturated soil on a steep slope or a quick rise in groundwater levels brought on by infiltration. Runoff near steep slopes may be increased by human activity in places with high drainage densities. As a result, landslides are more likely to occur in places with higher drainage density. Shear strength decreases with bank erosion and saturation areas. The distance from the river was measured using the Euclidean distance method and classified as (a) 0–500 m, (b) 501–1000 m, (c) 1001–1500 m, (d) 1501–2000 m, and (e) 2001–2500 m in the study.

Geology: Similar to geomorphology, geology is another significant landslide-controlling factor. The main geological groups, namely Surma and Bhuvan, cover the entire district. The Suma group covers the majority of the district, but the Bhuvan group only covers a small portion of the district in the east.

Geomorphology (Geom): The entire Lunglei district is covered with hills and valleys. Geomorphologically the whole district is divided into three geomorphological divisions, namely: (a) Highly dissected structural hills and valleys, (b) Moderately dissected structural hills and valleys, and (c) Riverian areas. The maximum area of the study region (about 1066.4937 km²) is covered with moderately dissected structural hills and valleys, while only a small part (about 19.0683 km²) comes under the riverine area.

Normalized Differences Vegetation Index (NDVI): NDVI is a representation of vegetation density that indirectly controls landslide distribution, type and magnitude (Hong et al., 2016). The NDVI map is prepared through raster calculator in GIS environment by Eq. (7).

$$NDVI = (NIR - Red) / (NIR + Red) \quad (7)$$

where NIR and Red are the near-infrared and red bands, respectively. Landsat 8 OLI satellite imagery is used for measuring NDVI. It is further divided into five classes (a) ≤ 0 , (b) 0–0.2, (c) 0.2–0.4, (d) 0.4–0.6, and (e) ≥ 0.6 .

Land use and land cover (LULC): Land use and land cover types determine different natural hazards like floods, soil erosion, surface structure characteristics, and precipitation infiltration (Hong et al., 2016). In general, dense vegetation-covered areas have less potential for landslides and soil erosion, whereas bare land and built-up areas have more potential for landslides. Landsat 8 OLI satellite images have been classified by the supervised maximum likelihood classification method for assessing the land use land cover. The study validates the LULC map using Kappa statistics calculated from 100 randomly selected points obtained through stratified random sampling. The resulting Kappa statistic of 0.844 indicates a significant agreement between observed LULC classifications and the prepared LULC map. This robust Kappa value exceeds chance agreement, demonstrating the consistent and reliable nature of the LULC classifications in this study. There are mainly five land use and land cover classes found in the Lunglei district, namely buildup areas, Jhum land, water bodies, sparse vegetation, and dense vegetation. Sparse vegetation encompasses most of the land (59.42%), followed by dense vegetation (25.88%), Jhum land (13.30%), buildup areas (1.07%), and water bodies (0.37%).

All the conditioning factors are mentioned in Fig. 3.

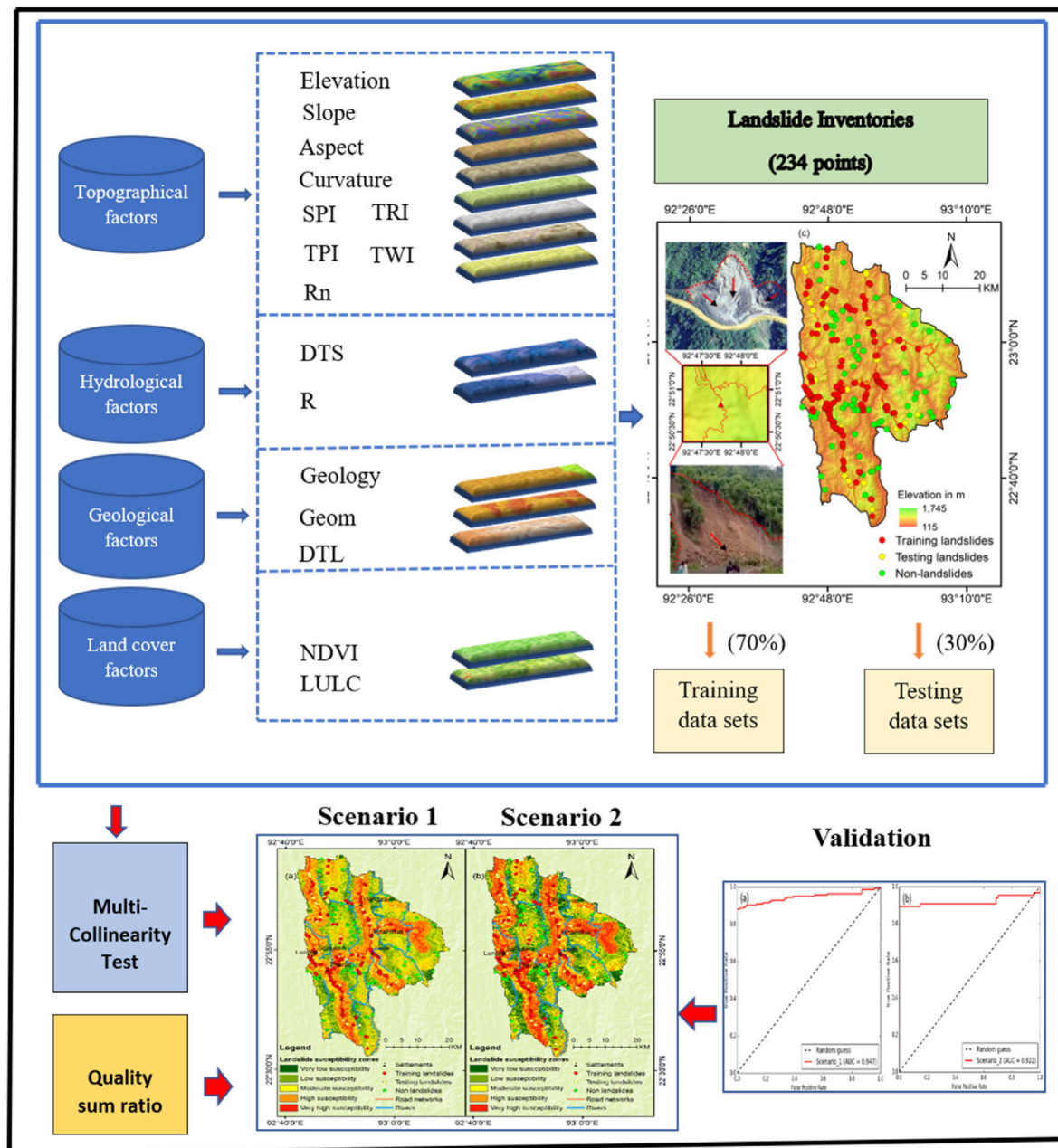


Fig. 2. Methodological flow chart of the study.

2.4. Multicollinearity test

Multicollinearity can be explained as the presence of near-linear familiarity among the landslide-triggering factors (Das et al., 2023). The present multi-collinearity problem will minimize the prediction accuracy and even lead to model failure (Zhou et al., 2021). So, it is important to consider the existence of multi-collinearity among the conditioning factors before the analysis of landslide susceptibility. To manage multi-collinearity in landslide susceptibility analysis, it is important to identify its sources. There is a different source of multi-collinearity in the susceptibility analysis. It may be from the sample collection; it may be from the outlier value of the conditioning factor (Lee et al., 2018). It is a critical challenge to minimize the value of an outlier statistically. Most of the multi-collinearity problems come from that source. Different methodologies have been discovered to identify the existence of multi-collinearity in literature (Li et al., 2020; Pradhan and Sameen 2017), namely variance inflation factors (VIFs), tolerance (TOL), gain

ratio method, principal component analysis (PCA), Pearson's correlation coefficient etc. In the present study, the TOL and VIFs have been used to detect the multi-collinearity among the conditioning factors. The TOL and VIFs are calculated using Eqs. (8) and (9) respectively.

$$\text{Tolerance} = 1 - R_j^2 \quad (8)$$

$$\text{VIF} = \left[\frac{1}{\text{Tolerance}} \right] \quad (9)$$

For j th independent variable, R_j^2 represents the coefficient of determination. A TOL value of less than 0.1 and a VIF value greater than 10 indicate the presence of multicollinearity (Mittra and Das, 2023).

2.5. Landslide inventory

Knowledge about the spatial distribution of past landslides is an

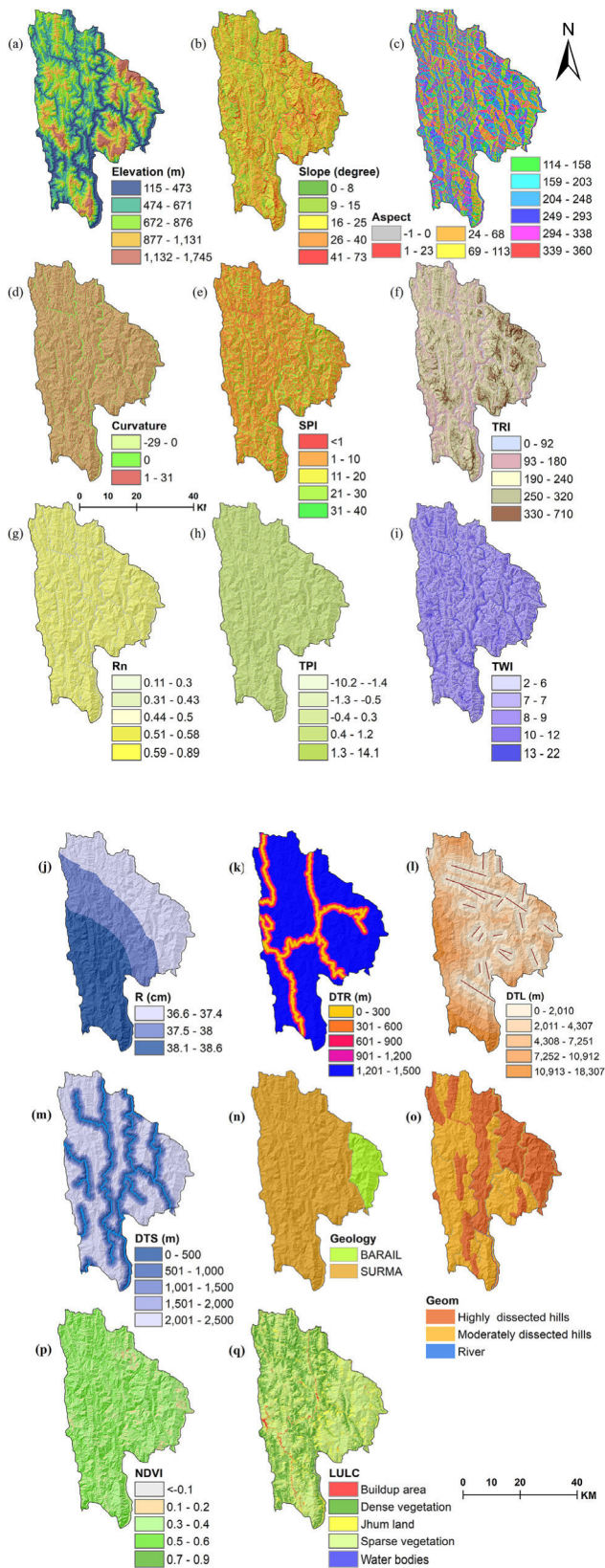


Fig. 3. Landslide conditioning factors (a) Elevation, (b) Slope, (c) Aspect, (d) Curvature, (e) Stream power index (SPI), (f) Topographic ruggedness index (TRI), (g) Terrain roughness, (h) Topographic position index (TPI), (i) Topographic wetness index (TWI), (j) Rainfall (R), (k) Distance to road (DTR), (l) Distance to lineament (DTL), (m) Distance to stream (DTS), (n) Geology, (o) Geomorphology (Geom), (p) Normalized difference vegetation index (NDVI), and (q) Land use land cover (LULC).

essential part of a landslide prediction study. The landslide inventory is the location of existing landslides. It helps to know the nature, characteristics, and morphology of existing landslides. In every bivariate approach, landslide inventory is classified into training and testing inventory. Training inventories are used for model prediction, and testing inventories are used for model accuracy testing. More than 300 historical landslide occurrences of the study area were downloaded from the Bhukosh portal (<https://bhukosh.gsi.gov.in/Bhukosh/Public>) and the Nasa landslide portal (<https://gpm.nasa.gov/landslides/index.html>). After obtaining the landslide data, we conducted a rigorous verification process, which involved field investigations and cross-referencing with Google Earth Pro. Through these methods, we ensured the accuracy and reliability of the data. Following the verification process, we selected a total of 234 landslide locations for our analysis. These locations were then divided into training and testing datasets, with 70% allocated for training and 30% for testing. Additionally, to validate the model, we included 70 non-landslide points from safe landslide zones. This comprehensive approach allows us to evaluate the model's performance effectively.

2.6. Index of entropy assessment

Initially, the entropy method was used to determine the thermodynamic status of a system, especially in the Boltzmann principle, to show the one-to-one relationship with the degree of disorder (Pourghasemi et al., 2012). Shannon later modified it to entropy information theory. The self-information-related value measures how much knowledge or levels of surprise are connected to a specific result. This outcome is known as a random variable. The Shannon entropy measures how "informative" or "surprising" the entire random variable would be after averaging all of its conceivable outcomes. Generally, entropy is used to measure uncertainty, instability, disorder, and imbalance in a system (Youssef et al., 2015). It is also used to measure a system's relevant conditioning factor or parameters (Constantin et al., 2011). Wang et al. (2016) defined the entropy of a landslide as the extent of different landslide conditioning factors for landslide development. Different morphometric parameters provide supplementary entropy in the index system. Thus, the entropy method is used to calculate the objective weight of an index system (Pourghasemi et al., 2012). The information coefficient represents the objective weight (W_j) and is calculated as Eqs. (10)–(16).

$$E_{ij} = \frac{m}{n} \quad (10)$$

$$(E_{ij}) = \frac{E_{ij}}{\sum_{j=1}^n E_{ij}} \quad (11)$$

where, m and n represented the domain and landslide percentage gradually and E_{ij} is the probability density for class S_j of j. Here, H_j and H_{jmax} are two entropy value for class S_j known as informative and surprising.

$$H_j = - \sum_{i=1}^{S_j} (E_{ij}) \log_2 (E_{ij}), j = 1, 2, \dots, n \quad (12)$$

$$H_{jmax} = \log_2 S_j, S_j = \text{no. of classes} \quad (13)$$

Again, W_j is the corresponding weight for coefficient I_j.

$$I_j = \frac{H_{jmax} - H_j}{H_{jmax}} I = (0, 1), j = 1, 2, \dots, n \quad (14)$$

$$W_j = I_j E_{ij} \quad (15)$$

$$Y_{IOE} = \sum_i^n \frac{z}{m_i} \times C \times W_j \quad (16)$$

where, Y_{IOE} is the sum of I is the count of map parameters (1,2,3,, n), Z is the highest number of the class. m_i is the class number in the map parameter, C is the value after secondary classification and W_j is the weight of each conditioning factor.

2.7. Validation

In general, a pure landslide susceptibility validation is possible only if a new landslide event happens after the creation of the susceptibility map (Neuhäuser and Terhorst 2007). In real life, it is unacceptable because of the "wait and see" strategy. It is problematic to estimate the accuracy of the susceptibility model. However, the prediction accuracy of the present study has been measured through the receiver operating characteristics (ROC) curve and the statistical measure Quality sum.

A ROC is a useful measure for representing the probabilistic and deterministic quality of detection. The graphical plot of ROC describes the "fraction of true positives out of the positives versus the fraction of false positives out of the negatives for a binary classifier system as its discrimination threshold is varied" (Devkota et al., 2013). On the 'X' axis and the 'Y' axis, the ROC plot shows 1-specificity and sensitivity, respectively. Sensitivity (TP rate) denotes the proportion of pixels truly classified as landslides in the prediction map, while specificity (TN rate) denotes the proportion of non-landslide pixels truly classified as non-landslide in the prediction map. The sensitivity and specificity are measured as Eqs. (17) and (18).

$$\text{Sensitivity} = TP / (TP + FN) \quad (17)$$

$$\text{Specificity} = TN / (TN + FP) \quad (18)$$

where, TP is true positive, FN is false negative, TN is true negative and FP is false positive.

The desirability function of LSZ predicting methods is checked by the quality sum (Q_s) index. Q_s value is measured following Eq. (19) followed by (Roy et al., 2019).

$$Q_s = \sum_{i=1}^n ((R_d - 1)^2 * P) \quad (19)$$

where R_d is the density ratio of the landslide classes, which is calculated using Eq. (19) and P is the area ratio by landslide susceptible area to the total area.

$$R_d = \frac{M_i}{S_i} / \frac{\sum M_i}{\sum S_i} \quad (20)$$

In Eq. (20), M_i is the pixels count in the domain and S_i count of landslide-affected pixels in the domain. Higher the Q_s value range indicates more desirability and less value of Q_s indicates less desirability.

3. Results

3.1. Multicollinearity

The presence of collinearity among the conditioning factors is examined through TOL and VIF in SPSS v23. Table 3 shows the TOL and VIF of all factors. The TOL value for the conditioning factor ranges between 0.308 (TPI) and 0.998 (LULC) and the VIF value ranges between 3.252 (TPI) and 1.002 (LULC). It indicates all the conditioning factors are free from multi-collinearity problem.

3.2. Relationship of conditioning factors and past landslides

The relationship between landslide and landslide conditioning factors

is evaluated by the weight (W_{ij}) of factors measured by the index of entropy. Table 4 shows the weights of landslide factors. As a result, nine conditioning factors have significant contribution weight in landslide susceptibility and others haven't significant weight in landslide susceptibility. Among the factors, DTR was ranked first followed by NDVI, Geom, elevation, curvature, slope, DTL, aspect and DTS. While the SPI, TPI, Rn, TPI, TWI, geology and LULC haven't significant weight (Fig. 4).

The Entropy model not only measures the overall weight score of conditioning factors, but it also considers the distinct probability (E_{ij}) of each sub-class of factors. Elevation in the study area ranges between 115 m and 1745 m and has the highest E_{ij} found between 1131.36 m and 1745 m, followed by 875.68 m and 1131.35 m, 671.13 m and 875.67 m, 472.97 m and 671.12 m, and 115 m and 472.96 m. It is stated that landslide probability increases with increasing elevation. Similarly, the slope of the study area extends from 0 to 73°. The highest E_{ij} value was found between slope ranges 25°–40° and 40°–73°, followed by 15°–25°, 8°–15°, and 0–8°. It also demonstrated that the likelihood of a landslide increases proportionally with slope. Aspect is considered an important conditioning factor. It claims that the likelihood of a landslide is greatest on slopes facing northwest, followed by west and southwest. Most of the cases of landslides in Lunglei district are rainfall-induced, that is, by the influence of the south-west monsoon. Curvature is classified into concave, flat, and convex. In the area, convex slopes have the highest probability of landslide, followed by concave and flat.

Three distance parameters, namely DTR, DTL and DTS play significant roles in landslide occurrences. DTR shares a significant footprint among distance parameters (Fig. 5). An inverse relationship, i.e., the probability of landslide decreased with increasing distance from the road. Landslide probability is highest within 0–300 m of the road in the Lunglei district, followed by 901–1200 m, 601–900 m and 301–600 m. There is no landslide reported beyond 1200 m. An opposite relationship is found with the river. Landslide probability is highest within a distance of 1501–2500 m from rivers in the area. It is found that landslide probability is increased with an increasing lineament distance. The likelihood of a landslide is greatest between 1201 m and 1500 m from lineaments.

The geomorphology of the district is very generalized. Mainly moderate dissected hills and valleys have high chance of landslide occurrences, whereas river bodies have a low possibility of landslide occurrences. The NDVI, play an important role in landslide occurrence. Landslides are most likely in the range of NDVI between 0 and 0.2, followed by 0.2–0.4 and 0.4–0.6. There is no possibility of landslide occurrences if an NDVI value is found to be less than 0 and more than 0.6.

3.3. Landslide susceptibility

The model index of entropy is the most commonly used bivariate

Table 3
Multi-collinearity test by tolerance and VIF.

Factors	Tolerance	VIF
Elevation	0.524	1.907
Slope	0.325	3.077
Aspect	0.924	1.082
Curvature	0.356	2.808
SPI	0.867	1.154
TRI	0.521	1.92
Rn	0.768	1.303
TPI	0.308	3.252
TWI	0.743	1.345
R	0.702	1.319
DTR	0.924	1.082
DTL	0.874	1.145
DTS	0.777	1.287
Geology	0.754	1.327
Geom	0.815	1.227
NDVI	0.884	1.131
LULC	0.998	1.002

Table 4
Spatial association of each conditioning factor and landslide by IOE co-efficient.

Factors	Sub-classes	% of A	% of B	Eij	(Eij)	Pij	Hj	Hj max	Ij	Pj	Wj
Elevation	115–472.96	18.03	7.19	0.40	0.06	−0.25	2.00	2.32	0.14	1.29	0.18
	472.97–671.12	30.94	16.77	0.54	0.08	−0.30					
	671.13–875.67	27.56	28.74	1.04	0.16	−0.42					
	875.68–1131.35	16.21	26.95	1.66	0.26	−0.50					
	1131.36–1745	7.25	20.36	2.81	0.44	−0.52					
Slope	0–8	8.35	2.99	0.36	0.08	−0.29	2.10	2.32	0.09	0.90	0.08
	8–15	14.65	5.39	0.37	0.08	−0.30					
	15–25	35.32	31.74	0.90	0.20	−0.46					
	25–40	36.62	52.69	1.44	0.32	−0.53					
	40–73	5.06	7.19	1.42	0.32	−0.53					
Aspect	−1	2.10	0.00	0.00	0.00	0.00	3.09	3.32	0.07	0.86	0.06
	0–22.5	5.23	2.99	0.57	0.07	−0.26					
	22.5–67.5	13.07	13.77	1.05	0.12	−0.37					
	67.5–112.5	13.91	10.18	0.73	0.09	−0.30					
	112.5–157.5	11.48	10.78	0.94	0.11	−0.35					
	157.5–202.5	10.43	11.98	1.15	0.13	−0.39					
	202.5–247.5	13.77	16.77	1.22	0.14	−0.40					
	247.5–292.5	14.02	17.37	1.24	0.14	−0.40					
	292.5–337.5	11.21	14.37	1.28	0.15	−0.41					
	337.5–360	4.79	1.80	0.37	0.04	−0.20					
Curvature	−29.17–0	47.23	47.90	1.01	0.44	−0.52	1.34	1.58	0.16	0.77	0.12
	0	6.04	1.20	0.20	0.09	−0.30					
	0–31.35	46.73	50.90	1.09	0.47	−0.51					
	<0	13.53	12.18	0.00	0.19	−0.46					
SPI	1–10	58.31	57.05	0.00	0.21	−0.47	2.27	2.32	0.02	0.00	0.00
	11–20	19.67	22.44	0.00	0.24	−0.50					
	21–30	6.04	7.05	0.00	0.25	−0.50					
	31–40	2.45	1.28	0.00	0.11	−0.35					
TRI	0–92	4.62	0.60	0.00	0.02	−0.13	1.81	2.32	0.22	0.00	0.00
	93–180	26.29	10.18	0.00	0.07	−0.27					
	190–240	36.86	28.74	0.00	0.14	−0.40					
	250–320	24.71	40.12	0.00	0.29	−0.52					
	330–710	7.53	20.36	0.00	0.48	−0.51					
Rn	0.11–0.3	3.25	1.20	0.00	0.08	−0.30	2.21	2.32	0.05	0.00	0.00
	0.31–0.43	15.96	10.78	0.00	0.15	−0.41					
	0.44–0.5	35.75	34.13	0.00	0.21	−0.48					
	0.51–0.58	32.48	37.13	0.00	0.26	−0.50					
TPI	0.59–0.89	12.57	16.77	0.00	0.30	−0.52	2.28	2.32	0.02	0.00	0.00
	−10.2–−1.4	8.03	7.19	0.00	0.17	−0.44					
	−1.3–−0.5	22.13	17.96	0.00	0.16	−0.42					
	−0.4–0.3	31.44	33.53	0.00	0.20	−0.47					
TWI	0.4–1.2	27.34	23.95	0.00	0.17	−0.43	1.96	2.32	0.16	0.00	0.00
	1.3–14.1	11.06	17.37	0.00	0.30	−0.52					
	2.47–5.68	15.46	19.76	0.00	0.31	−0.52					
	5.69–7.48	35.64	45.51	0.00	0.31	−0.52					
	7.49–9.28	33.23	25.15	0.00	0.18	−0.45					
	9.29–11.86	11.77	9.58	0.00	0.20	−0.46					
R	11.87–22.42	3.90	0.00	0.00	0.00	0.00	1.39	1.58	0.12	0.00	0.00
	36.6–37.4	36.97	14.97	0.00	0.14	−0.39					
	37.5–38	26.87	25.15	0.00	0.31	−0.52					
	38.1–38.6	36.16	59.88	0.00	0.55	−0.47					
DTR	0–300	26.51	93.02	3.51	0.90	−0.13	0.60	2.32	0.74	0.78	0.58
	301–600	20.79	1.55	0.07	0.02	−0.11					
	601–900	18.85	1.55	0.08	0.02	−0.12					
	901–1200	17.45	3.88	0.22	0.06	−0.24					
DTL	1201–1500	16.41	0.00	0.00	0.00	0.00	2.12	2.32	0.09	0.99	0.08
	0–300	18.90	6.25	0.33	0.07	−0.26					
	301–600	19.66	9.38	0.48	0.10	−0.33					
	601–900	20.24	25.00	1.23	0.25	−0.50					
DTS	901–1200	20.77	28.13	1.35	0.27	−0.51	2.20	2.32	0.05	0.88	0.05
	1201–1500	20.42	31.25	1.53	0.31	−0.52					
	0–500	16.28	9.58	0.59	0.13	−0.39					
	501–1000	13.47	8.38	0.62	0.14	−0.40					
	1001–1500	12.10	6.59	0.54	0.12	−0.37					
	1501–2000	11.30	15.57	1.38	0.31	−0.52					
Geology	2001–2500	46.84	59.88	1.28	0.29	−0.52	0.00	1.00	1.00	0.00	0.00
	Barail	10.41	0.00	0.00	0.00	0.00					
Geom	Surma	89.59	100.00	0.00	1.00	0.00	0.99	1.58	0.37	0.67	0.25
	Highly dissected hills	46.11	41.92	0.91	0.45	−0.52					
NDVI	Moderately dissected hills	52.94	58.08	1.10	0.55	−0.48	1.09	2.32	0.53	0.94	0.50
	River	0.95	0.00	0.00	0.00	0.00					
	<0	0.01	0.00	0.00	0.00	0.00					
	0–0.2	9.01	29.94	3.32	0.71	−0.35					
	0.2–0.4	56.07	59.88	1.07	0.23	−0.49					

(continued on next page)

Table 4 (continued)

Factors	Sub-classes	% of A	% of B	Eij	(Eij)	Pij	Hj	Hj max	Ij	Pj	Wj
LULC	0.4–0.6	34.91	10.18	0.29	0.06	−0.25					
	>0.6	0.00	0.00	0.00	0.00	0.00					
	Buildup area	1.02	32.93	0.00	0.93	−0.10	0.45	2.32	0.81	0.00	0.00
	Jhum land	13.31	24.55	0.00	0.05	−0.22					
	Water bodies	0.37	0.00	0.00	0.00	0.00					
	Sparse vegetation	59.43	41.92	0.00	0.02	−0.11					
	Dense vegetation	25.88	0.60	0.00	0.00	−0.01					

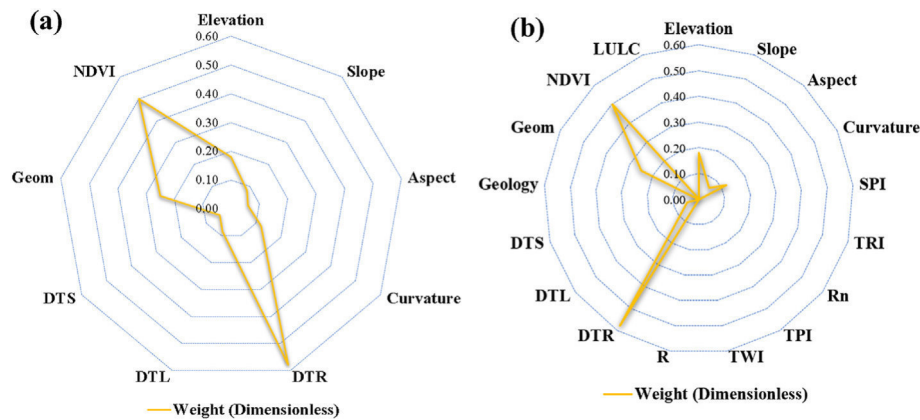


Fig. 4. Radar chart showing the weight of respective landslide conditioning factors, (a) Scenario 1 (Nine factors), and (b) Scenario 2 (Seventeen factors).

statistical analysis for landslide susceptibility mapping. Entropy describes uncertainty, imbalance, disorder, and the extent of the instability of a system. For landslide prediction, the secondary reclassification of seventeen landslide conditioning factors is reclassified according to Eij values. In this study, we have considered two scenarios, in scenario 1, only nine parameters are considered to have significant weightage based on the IOE. This approach narrows down the focus to a select set of parameters that are deemed crucial in influencing the outcome or result under consideration. By prioritizing these parameters, it allows for a more streamlined and efficient analysis, reducing complexity and potential noise in the data. On the other hand, Scenario 2 includes all parameters without any specific selection or weighting based on the IOE. This approach takes into account the entire range of available parameters, considering each one as potentially relevant to the analysis. This comprehensive approach ensures that no potential influencing factors are overlooked, providing a more holistic understanding of the situation.

In the first phase, nine conditioning factors having significant weight for landslide were used for integration (Scenario 1). Consequently, all seventeen conditioning factors were used for integration (Scenario 2). The process of integration of conditioning factors has been done in a raster calculator in a GIS environment using Eq. (20).

$$("Elev" * w_j) + ("slope" * w_j) + \dots + ("Lulc" * w_j) \quad (21)$$

The finding of a summation value for scenario 1 ranges between 0.86 and 0.21; and for scenario 2 it ranges between 0.45 and 0.11 which is the upper and lower limit of landslide susceptibility. Intermediate values are representative of the severity range. A natural break classification system is performed for five landslide susceptibility levels in the current study (Fig. 6). Susceptibility levels are named "Very high susceptibility", "High susceptibility", "Moderate susceptibility", "Low susceptibility", and "Very low susceptibility".

The area in km^2 of different landslide susceptibility classes is tabulated in Table 5. The very high susceptibility accounted for 16% and 14% of the total area as per scenario 1 and scenario 2, respectively, mainly located along the road section and the top of a mountain ridge. The high susceptibility area is located parallelly with the very high susceptibility zone, found in 26% and 25% of the total area as per scenario 1 and

scenario 2, respectively. On the other hand, the moderate susceptibility zone isn't distributed in particular areas or regions. It is spread randomly over the district and found in 25% and 24% of the total area based on scenario 1 and scenario 2, respectively. Consequently, low susceptibility zones were found in 22% and 23% of the total area as per scenario 1 and scenario 2, while very low susceptibility zones accounted for 11% and 15% of the total area based on scenario 1 and scenario 2, respectively, and are mainly centered along river courses. Furthermore, it is highlighted that most of the significant settlements, namely Lunglei, Serkawn, Theriat, Leite, Hnahthial, and Pangzawl, are located in very high and high susceptibility zones.

The different results obtained for the two types of scenarios can be attributed to the contrasting approaches taken in parameter selection and weighting based on the Index of Entropy (IOE). In Scenario 1, where only nine parameters with significant weightage based on the IOE are considered, on the other hand, in Scenario 2, all parameters are included without any specific selection or weighting based on the IOE. The divergent results obtained between the two scenarios stem from the trade-offs between focus and comprehensiveness. Scenario 1 prioritizes efficiency and optimization by concentrating on the most influential parameters, thus providing more targeted and interpretable results. On the other hand, Scenario 2 offers a broader perspective by considering all parameters, potentially capturing additional nuances and interactions.

3.4. Model validation

A ROC curve is prepared using 30% (67 locations) of test landslide locations with the same number of non-landslide locations. As a plot of ROC (Fig. 7), the index of the Entropy model successfully predicts landslide susceptibility in the Lunglei district under the same geo-environmental conditions. The model justification is estimated through the area under the ROC-AUC. It shows an excellent prediction of both scenarios, the obtained AUCs were 0.947 for scenario 1 and 0.922 for scenario 2. Furthermore, model desirability was examined through the quality sum ratio. The first density ratio of each landslide severity class was calculated, which is shown in Fig. 8. It is found to have the highest density ratio in the high susceptible class, followed by very high

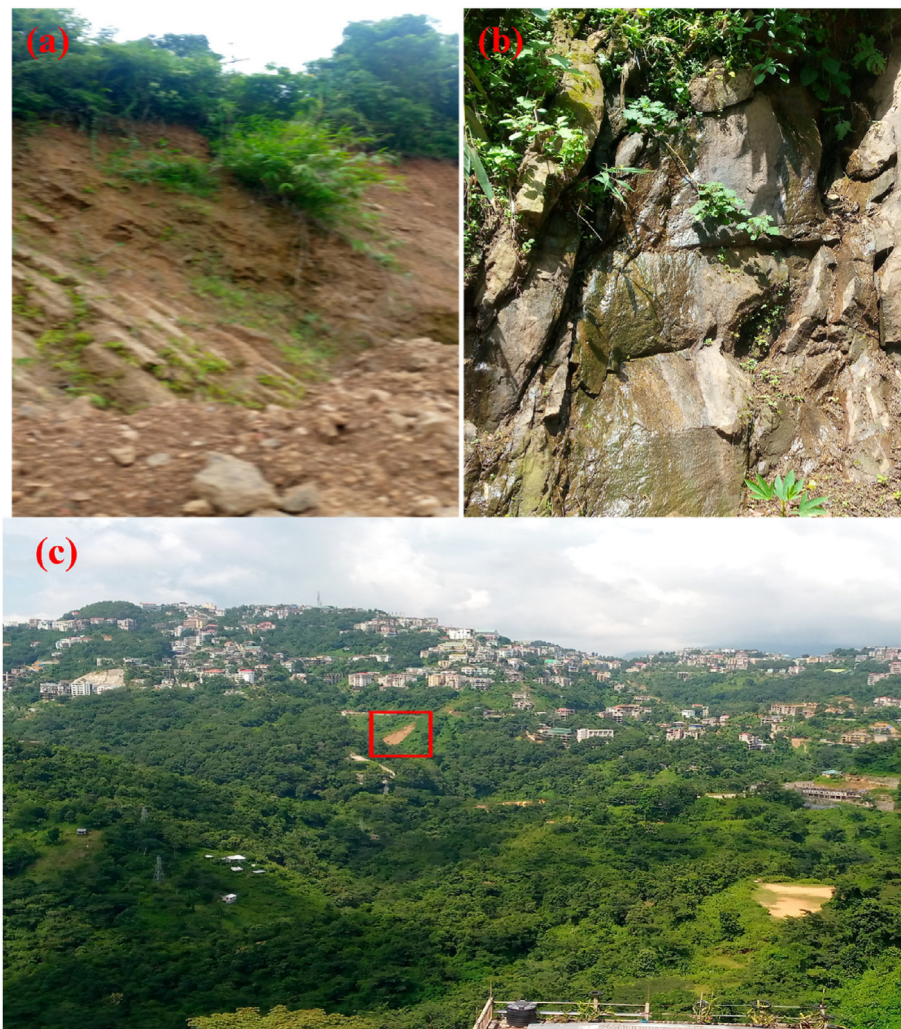


Fig. 5. Field photos (a) landslide along roads, (b) Water contain in the rock beds, and (c) Landslide in a concave slope.

susceptibility, moderate susceptibility, low susceptibility, and very low susceptibility classes. Table 6 depicted the quality sum of the current landslide susceptibility map. This quality sum ratio of scenario 1 and scenario 2 are 0.435 and 0.431 respectively also denotes the higher accuracy of scenario 1.

4. Discussion

Landslide susceptibility modeling and optimization conditioning factors were studied using the index of entropy model. Initially, 17 landslide conditioning factors were chosen by a literature survey for landslide susceptibility mapping. It was found that among seventeen factors, nine factors are more significant for landslide occurrence. The elevation, slope, aspect, curvature, normalized difference vegetation index, geomorphology, distance to road, distance to lineament, and distance to river are dominant landslide-contributing conditioning factors. Further, seventeen landslide conditioning factors are considered for scenario 2. No change in prediction accuracy is observed for increasing conditioning factors. In both cases, the AUC reflects successful model prediction. In the present study, distance to road played the highest role in landslide susceptibility zonation using IOE. A similar result was reported by Ayalew and Yamagishi (2005). NDVI is the second important causative factor of the study area. Min et al. (2016) also documented that NDVI is a dominant causative factor of landslides and NDVI value ranges between 0.20 and 0.59 are more prone to landslides. On the other hand, LULC, SPI, TRI, Rn, TWI, R, TPI and geology were not found significant

weightage for landslide susceptibility zonation. Jebur et al. (2014) evaluated eleven landslide conditioning factors dividing them into two data sets as eight and eleven combinations. It is found in the second data set that the additional conditioning factors, namely soil, geology and LULC not significant for LSZ in Bukit Antarabangsa, Malaysia. All-Najjar et al. (2019) examined fourteen landslide conditioning factors for LSZ. They tested four groups with different combinations. The result showed that the group of eight conditioning factors was high prediction accuracy.

The incorporation of additional variables, such as geology, into the dataset disrupted the correlation and flagged certain regions as being susceptible to landslides. However, this classification may have been misleading as it was based on just one landslide occurrence falling within a specific geology type. Consequently, the algorithm was compelled to assign significance to those regions. Although more conditioning factors were considered, they did not improve accuracy and had the potential to decrease precision.

Van Westen et al. (2003) provided an explanation for the limited impact of including geological and land use/land cover (LULC) data on the final outcomes. One of the main reasons for the reduced role of LULC in landslide susceptibility was the conversion of shifting cultivation into permanent agricultural practices in Mizoram (Sati, 2022; Lalengzama, 2016). Additionally, according to Barman et al. (2022b), most landslides in Mizoram were concentrated along roads due to high human activities, while the role of stream power index (SPI) and topographic position index (TPI) was minimal due to the presence of stable rock conditions and lower human activities in the valley regions (Fig. 9).

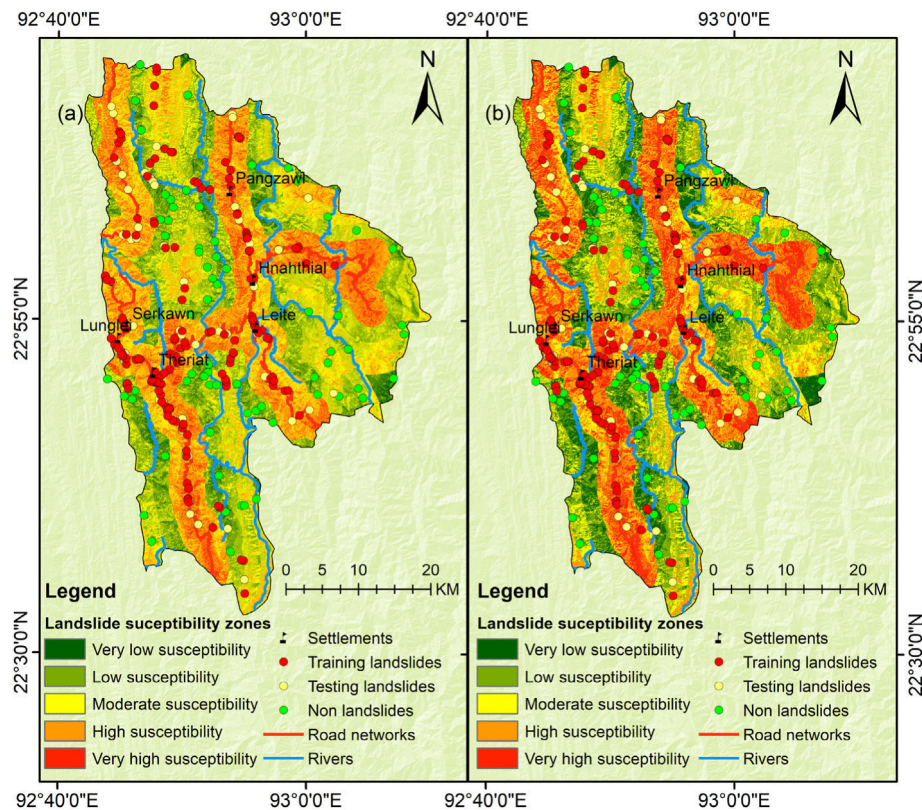


Fig. 6. Spatial distribution of landslide susceptibility (a) Scenario 1 and (b) Scenario 2.

Table 5

Areal extension of landslide susceptibility zones.

Susceptibility zones	Scenario 1		Scenario 2	
	Area in Km ²	% of area	Area in Km ²	% of area
Very low susceptible	227.39	11	299.90	15
Low susceptible	447.19	22	455.28	23
Moderate susceptible	492.24	25	472.62	24
High susceptible	519.74	26	500.14	25
Very high susceptible	321.54	16	280.12	14

Our study concluded that the areas of high unplanned quarrying, road cutting, and other human activities such as the Vawngzawl (building material) quarry, are responsible for landslide occurrences. Also, in sparse vegetation areas, the exposed rock is characterized by bedding and crevasses that make the slopes easy to slide down. Therefore, it is best to avoid this zone as much as possible for any type of construction. There is a significant increase in landslides in the district (Barman et al., 2022b).

The study of Lallianthanga and Laltanpuia (2013) in the Lunglei town area concluded that human activities with heavy rainfall trigger landslides. They also identified some stable areas for construction. So, the present study found that river valleys are safe from landslides and recommended for human activities. Due to dense vegetation cover, low elevation, low slope, low relief amplitude, flat curvature, low topographic ruggedness index and low roughness protect the river bank side from landslides. Pachuau (2019) mentioned that slope angles below 30° and flatted areas predominantly comes in low landslide zones. According to Coe et al. (2004), the area having high elevation received more rainfall than lower elevation due to orographic effects. Traditionally Mizos prefer high terrain altitude for their living. Roads in the district are commonly constructed at high elevations. In Mizoram, in most cases, shale layers play a sliding plane when coming into contact with percolating moisture from rainfall (Bhusan et al., 2013). It is also recommended to avoid the windward side (west, northwest, and southwest) due to the high rainfall observed in this slope direction. Lunglei district disaster management committee and MIRSC continuously work for landslide mitigation in the

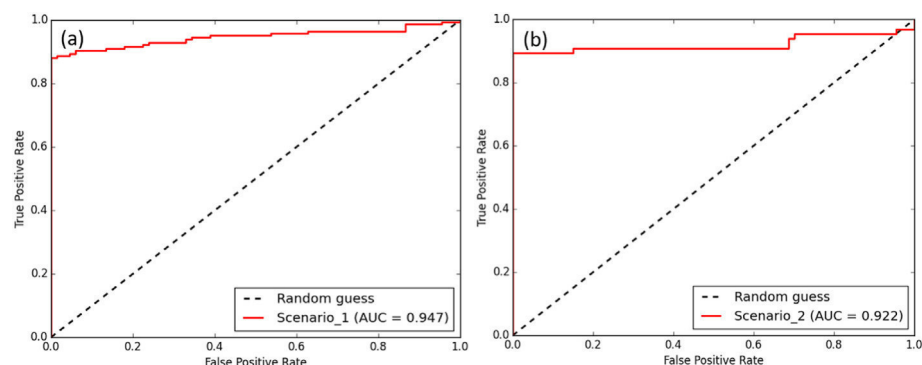


Fig. 7. Model validation result using receiver operating characteristic (ROC) with area under curve (AUC) (a) Scenario 1 and (b) Scenario 2.

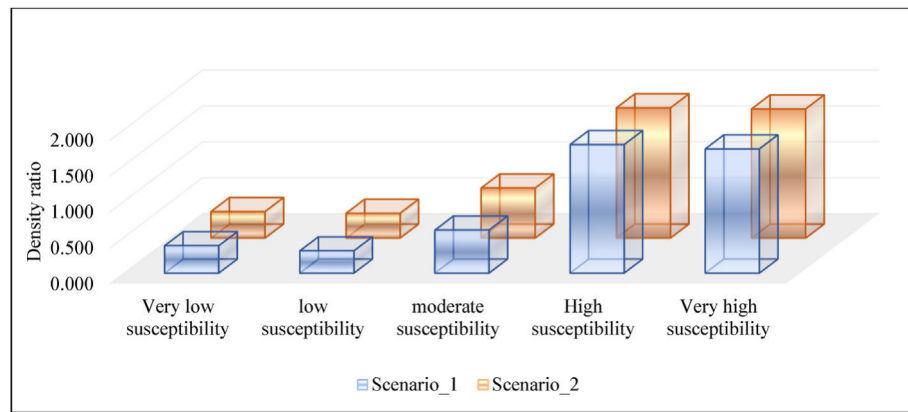


Fig. 8. Density ratio for scenario 1 and scenario 2.

Table 6

Quality sum ratio of scenario 1 and scenario 2.

Scenario	Prediction classes	Area (Km ²)	Occurrence area (km ²)	Dr	P	Qs
1	Very low susceptibility	227.390	0.009	0.382	0.113	0.435
	low susceptibility	447.187	0.015	0.311	0.223	
	moderate susceptibility	492.244	0.031	0.600	0.245	
	High susceptibility	519.742	0.098	1.790	0.259	
	Very high susceptibility	321.539	0.059	1.730	0.160	
2	Very low susceptibility	299.899	0.011	0.369	0.149	0.431
	low susceptibility	455.284	0.016	0.346	0.227	
	moderate susceptibility	472.620	0.033	0.698	0.235	
	High susceptibility	500.139	0.091	1.813	0.249	
	Very high susceptibility	280.118	0.051	1.798	0.139	

area. More govt. Level projects for landslide study and development ecotourism, an alternative means of income for local people, can be implemented for landslide mitigation.

5. Limitations and future study

In this study, a bivariate model using seventeen landslide conditioning factors was employed to calculate the Index of Entropy. However, occasional errors may have occurred during the reclassification of classes, potentially impacting the predictions. It is important to note that geotechnical parameters and soil parameters, which also play significant roles in landslide susceptibility, were not considered in this study. Additionally, the IDW interpolation method, which incorporated rainfall information from all gauges, including neighboring districts, could have resulted in lower prediction errors for landslide susceptibility zone (LSZ) mapping. Furthermore, the lack of detailed information in the landslide inventories, such as volume, length, area, width, and timing, limited the proper validation of the results.

In future research, it would be beneficial to include all these factors for creating LSZ maps and conducting comprehensive landslide risk assessments. The incorporation of additional conditioning factors and comparative assessment of different models would enhance the accuracy of the predictions. Despite the limitations in the research procedure and estimation mentioned above, the study's results are considered credible and scientifically sound. Policymakers can utilize the findings of this evaluation to improve their approach to landslide management.

6. Conclusions

The Lunglei district of Mizoram is located remotely from India's mainland on dissected hills. During the monsoon period, landslides arise

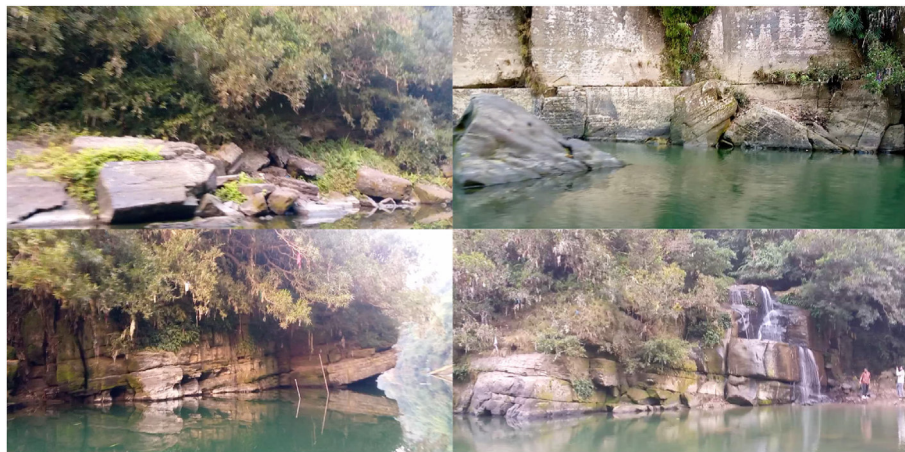


Fig. 9. Field photos showing stable rock condition along the rivers.

as a barrier to sustainable development. Few scholars have carried out work in this area. Landslide prediction is a crucial task. The present study focuses on landslide prediction mapping using the index of entropy, based on criteria weighting and the incorporation of various topographic, climatic, lithological, human, and distance factors. Further, the study tried to determine an optimum number of landslide conditioning factors for preparing LSZ in the area. The district faced extreme landslide severity, especially along the major roads. The study focuses on landslide susceptibility zonation at a district level. The IOE model successfully predicted the likelihood of a landslide in the Lunglei district. The validation techniques, namely ROC and quality sum ratio, are used for accuracy tests, which predicted very well. By tradition, local Mizo people prefer jhum cultivation and have established their houses on the hill slope. The deduction of vegetation cover from terrain directly hit by rainfall is the cause of the landslide in Jhum lands. However, a susceptibility map provides information about spatial landslide distribution and is the baseline reference for future landslide assessment. Therefore, the present study will be helpful for the regional planner, hydrologist, geologist, and policymakers for the overall sustainable development of the district.

Declaration of competing interest

The authors declare that they have no known competing financial interests or personal relationships that could have appeared to influence the work reported in this paper.

Acknowledgment

The authors express heartfelt thanks to the Head of the Department of Geography, Mizoram University, Aizawl. All the authors sincerely acknowledge the editors and reviewers for their valuable suggestions and comments, which have greatly contributed to the overall improvement of the manuscript. The first author extends gratitude to the University Grants Commission, New Delhi for providing the Junior Research Fellowship (Ref no. 190510087462).

References

- Abedini, M., Tulabi, S., 2018. Assessing LNRF, FR, and AHP models in landslide susceptibility mapping index: a comparative study of Nojian watershed in Lorestan province, Iran. *Environ. Earth Sci.* 77, 1–13.
- Achour, Y., Boumezeur, A., Hadji, R., Chouabbi, A., Cavaleiro, V., Bendaoud, E.A., 2017. Landslide susceptibility mapping using analytic hierarchy process and information value methods along a highway road section in Constantine, Algeria. *Arabian J. Geosci.* 10, 1–16.
- Akgun, A., Dag, S., Bulut, F., 2008. Landslide susceptibility mapping for a landslide-prone area (Findikli, NE of Turkey) by likelihood-frequency ratio and weighted linear combination models. *Environ. Geol.* 54, 1127–1143.
- Al-Najjar, H.A., Pradhan, B., 2021. Spatial landslide susceptibility assessment using machine learning techniques assisted by additional data created with generative adversarial networks. *Geosci. Front.* 12 (2), 625–637.
- Al-Najjar, H.A., Kalantar, B., Pradhan, B., Saeidi, V., 2019. Conditioning factor determination for mapping and prediction of landslide susceptibility using machine learning algorithms. In: *Earth Resources and Environmental Remote Sensing/GIS Applications X*, vol. 11156, pp. 97–107 (SPIE).
- Althuwaynee, O.F., Pradhan, B., Lee, S., 2012. Application of an evidential belief function model in landslide susceptibility mapping. *Comput. Geosci.* 44, 120–135.
- Anbazhagan, S., Ramesh, V., 2014. Landslide hazard zonation mapping in ghat road section of Kolli hills, India. *J. Mt. Sci.* 11, 1308–1325.
- Armaş, I., 2012. Weights of evidence method for landslide susceptibility mapping. *Prahova Subcarpathians, Romania. Nat. Hazards* 60, 937–950.
- Ayalew, L., Yamagishi, H., 2005. The application of GIS-based logistic regression for landslide susceptibility mapping in the Kakuda-Yahiko Mountains, Central Japan. *Geomorphology* 65 (1–2), 15–31.
- Bai, S.B., Wang, J., Lü, G.N., Zhou, P.G., Hou, S.S., Xu, S.N., 2010. GIS-based logistic regression for landslide susceptibility mapping of the Zhongxian segment in the Three Gorges area, China. *Geomorphology* 115 (1–2), 23–31.
- Ballabio, C., Sterlacchini, S., 2012. Support vector machines for landslide susceptibility mapping: the Staffora River Basin case study, Italy. *Math. Geosci.* 44, 47–70.
- Barman, J., Biswas, B., 2022. Application of e-TOPSIS for ground water potentiality zonation using morphometric parameters and geospatial technology of vanvate lui basin, Mizoram, NE India. *J. Geol. Soc. India* 98 (10), 1385–1394.
- Barman, J., Biswas, B., Das, J., 2022b. Mizoram, the Capital of Landslide: A Review of Articles Published on Landslides in Mizoram, pp. 97–104. *India. Monitoring and Managing Multi-hazards: A Multidisciplinary Approach*.
- Barman, J., Soren, D.D.L., Biswas, B., 2022a. Landslide Susceptibility Evaluation and Analysis: A Review on Articles Published during 2000 to 2020. *Monitoring And Managing Multi-Hazards. A Multidisciplinary Approach*, pp. 211–220.
- Basu, T., Pal, S., 2019. RS-GIS based morphometrical and geological multi-criteria approach to the landslide susceptibility mapping in Gish River Basin, West Bengal, India. *Adv. Space Res.* 63 (3), 1253–1269.
- Bhusan, K., Singh, M.S., Sudhakar, S., 2013. Landslide hazard zonation using rs & GIS techniques: a case study from north east India. *Landslide Science and Practice* ume 1, 489–492. *Landslide Inventory and Susceptibility and Hazard Zoning*.
- Biswas, B., Rahaman, A., Barman, J., 2023. Comparative assessment of FR and AHP models for landslide susceptibility mapping for Sikkim, India and preparation of suitable mitigation techniques. *J. Geol. Soc. India*. 791–801.
- Bragagnolo, L., da Silva, R.V., Grzybowski, J.M.V., 2020. Landslide susceptibility mapping with r. landslide: a free open-source GIS-integrated tool based on Artificial Neural Networks. *Environ. Model. Software* 123, 104565.
- Bui, D.T., Pradhan, B., Lofman, O., Revhaug, I., Dick, O.B., 2012. Spatial prediction of landslide hazards in Hoa Binh province (Vietnam): a comparative assessment of the efficacy of evidential belief functions and fuzzy logic models. *Catena* 96, 28–40.
- Chang, K.T., Dou, J., Chang, Y., Kuo, C.P., Xu, K.M., Liu, J.K., 2016. Spatial resolution effects of digital terrain models on landslide susceptibility analysis. *Int. Arch. Photogram. Rem. Sens. Spatial Inf. Sci.* 8.
- Chen, W., Li, Y., 2020. GIS-based evaluation of landslide susceptibility using hybrid computational intelligence models. *Catena* 195, 104777.
- Chen, W., Chai, H., Zhao, Z., Wang, Q., Hong, H., 2016. Landslide susceptibility mapping based on GIS and support vector machine models for the Qianyang County, China. *Environ. Earth Sci.* 75, 1–13.
- Chen, X., Chen, W., 2021. GIS-based landslide susceptibility assessment using optimized hybrid machine learning methods. *Catena* 196, 104833.
- Choi, J., Oh, H.J., Won, J.S., Lee, S., 2010. Validation of an artificial neural network model for landslide susceptibility mapping. *Environ. Earth Sci.* 60, 473–483.
- Coe, J.A., Godt, J.W., Baum, R.L., Bucknam, R.C., Michael, J.A., 2004. Landslide susceptibility from topography in Guatemala. *Landslides: Evaluation and Stabilization* 1, 69–78.
- Constantin, M., Bednariu, M., Jurchescu, M.C., Vlaicu, M., 2011. Landslide susceptibility assessment using the bivariate statistical analysis and the index of entropy in the Sibiciu Basin (Romania). *Environ. Earth Sci.* 63, 397–406.
- Dahal, R.K., Hasegawa, S., Nonomura, A., Yamanaka, M., Masuda, T., Nishino, K., 2008. GIS-based weights-of-evidence modelling of rainfall-induced landslides in small catchments for landslide susceptibility mapping. *Environ. Geol.* 54, 311–324.
- Dai, F.C., Lee, C.F., Li, J.X.Z.W., Xu, Z.W., 2001. Assessment of landslide susceptibility on the natural terrain of Lantau Island, Hong Kong. *Environ. Geol.* 40, 381–391.
- Dam, N.D., Amiri, M., Al-Ansari, N., Prakash, I., Le, H.V., Nguyen, H.B.T., Pham, B.T., 2022. Evaluation of shannon entropy and weights of evidence models in landslide susceptibility mapping for the pithoragarh district of uttarakhand state, India. *Adv. Civ. Eng.* 2022.
- Das, J., Saha, P., Mitra, R., Alam, A., Kamruzzaman, M., 2023. GIS-Based Data-Driven Bivariate Statistical Models for Landslide Susceptibility Prediction in Upper Tista Basin, India. *Heliyon*. <https://doi.org/10.1016/j.heliyon.2023.e16186>.
- Das, S., Sarkar, S., Kanungo, D.P., 2022. GIS-based landslide susceptibility zonation mapping using the analytic hierarchy process (AHP) method in parts of Kalimpong Region of Darjeeling Himalaya. *Environ. Monit. Assess.* 194 (4), 234.
- Devkota, K.C., Regmi, A.D., Pourghasemi, H.R., Yoshida, K., Pradhan, B., Ryu, I.C., Althuwaynee, O.F., 2013. Landslide susceptibility mapping using certainty factor, index of entropy and logistic regression models in GIS and their comparison at Mugling–Narayanghat road section in Nepal Himalaya. *Nat. Hazards* 65, 135–165.
- District disaster management plan, 2019. Deputy Commissioner, Lunglei District, Mizoram.
- Efiong, J., Eni, D.I., Obiefuna, J.N., Etu, S.J., 2021. Geospatial modelling of landslide susceptibility in cross river state of Nigeria. *Scientific African* 14, e01032.
- Ermini, L., Catani, F., Casagli, N., 2005. Artificial neural networks applied to landslide susceptibility assessment. *Geomorphology* 66 (1–4), 327–343.
- Farooq, S., Akram, M.S., 2021. Landslide susceptibility mapping using information value method in Jhelum Valley of the Himalayas. *Arabian J. Geosci.* 14 (10), 824.
- Fatemi Aghda, S.M., Bagheri, V., Razifard, M., 2018. Landslide susceptibility mapping using fuzzy logic system and its influences on mainlines in lashgarak region, Tehran, Iran. *Geotech. Geol. Eng.* 36, 915–937.
- García-Rodríguez, M.J., Malpica, J.A., 2010. Assessment of earthquake-triggered landslide susceptibility in El Salvador based on an Artificial Neural Network model. *Nat. Hazards Earth Syst. Sci.* 10 (6), 1307–1315.
- Guru, B., Veerappan, R., Sangma, F., Bera, S., 2017. Comparison of probabilistic and expert-based models in landslide susceptibility zonation mapping in part of Nilgiri District, Tamil Nadu, India. *Spatial Information Research* 25, 757–768.
- Guzzetti, F., Reichenbach, P., Cardinali, M., Galli, M., Ardizzone, F., 2005. Probabilistic landslide hazard assessment at the basin scale. *Geomorphology* 72 (1–4), 272–299.
- Hemasinghe, H., Rangali, R.S., Deshapriya, N.L., Samarakoon, L., 2018. Landslide susceptibility mapping using logistic regression model (a case study in Badulla District, Sri Lanka). *Procedia Eng.* 212, 1046–1053.
- Hong, H., Pourghasemi, H.R., Pourtaghi, Z.S., 2016. Landslide susceptibility assessment in Lianhua County (China): a comparison between a random forest data mining technique and bivariate and multivariate statistical models. *Geomorphology* 259, 105–118.
- Huang, Y., Zhao, L., 2018. Review on landslide susceptibility mapping using support vector machines. *Catena* 165, 520–529.

- Jebur, M.N., Pradhan, B., Tehrany, M.S., 2014. Optimization of landslide conditioning factors using very high-resolution airborne laser scanning (LiDAR) data at catchment scale. *Remote Sens. Environ.* 152, 150–165.
- Johnson, J.P., Whipple, K.X., Sklar, L.S., Hanks, T.C., 2009. Transport slopes, sediment cover, and bedrock channel incision in the Henry Mountains, Utah. *J. Geophys. Res.: Earth Surf.* 114 (F2).
- Kaur, H., Gupta, S., Parkash, S., Thapa, R., 2023. Knowledge-driven method: a tool for landslide susceptibility zonation (LSZ). *Geology, Ecology, and Landscapes* 7 (1), 1–15.
- Kawabata, D., Bandibas, J., 2009. Landslide susceptibility mapping using geological data, a DEM from ASTER images and an Artificial Neural Network (ANN). *Geomorphology* 113 (1–2), 97–109.
- Kumar, R., Anbalagan, R., 2016. Landslide susceptibility mapping using analytical hierarchy process (AHP) in Tehri reservoir rim region, Uttarakhand. *J. Geol. Soc. India* 87, 271–286.
- Kumar, R., Anbalagan, R., 2019. Landslide susceptibility mapping of the Tehri reservoir rim area using the weights of evidence method. *J. Earth Syst. Sci.* 128, 1–18.
- Lalengzama, C., 2016. *Shifting Cultivation To Settled Agriculture: Agrarian Transformation And Tribal Development In Mizoram* (Doctoral Dissertation. Mizoram University).
- Lallianthanga, R.K., Laltanpuia, Z.D., 2013. Landslide Hazard Zonation of Lunglei town, Mizoram, India using high resolution satellite data. *International journal of Advanced remote sensing and GIS* 2 (1), 148–159.
- Lee, J.H., Sameen, M.I., Pradhan, B., Park, H.J., 2018. Modeling landslide susceptibility in data-scarce environments using optimized data mining and statistical methods. *Geomorphology* 303, 284–298.
- Lee, S., Choi, J., 2004. Landslide susceptibility mapping using GIS and the weight-of-evidence model. *Int. J. Geogr. Inf. Sci.* 18 (8), 789–814.
- Li, G., West, A.J., Densmore, A.L., Hammond, D.E., Jin, Z., Zhang, F., et al., 2016. Connectivity of earthquake-triggered landslides with the fluvial network: implications for landslide sediment transport after the 2008 Wenchuan earthquake. *J. Geophys. Res.: Earth Surf.* 121 (4), 703–724.
- Li, Y., Liu, X., Han, Z., Dou, J., 2020. Spatial proximity-based geographically weighted regression model for landslide susceptibility assessment: a case study of Qingchuan area, China. *Appl. Sci.* 10 (3), 1107.
- Mahalingam, R., Olsen, M.J., O'Banion, M.S., 2016. Evaluation of landslide susceptibility mapping techniques using lidar-derived conditioning factors (Oregon case study). *Geomatics, Nat. Hazards Risk* 7 (6), 1884–1907.
- Min, C.K., Bahar, A.M.A., Udin, W.S., 2016. Landslide assessment using normalized difference vegetation index (NDVI) technique in sentong, lojing, kelantan, Malaysia. *Journal of Tropical Resources and Sustainable Science (JTRSS)* 4 (2), 98–104.
- Mitra, R., Das, J., 2023. A comparative assessment of flood susceptibility modelling of GIS-based TOPSIS, VIKOR, and EDAS techniques in the Sub-Himalayan foothills region of Eastern India. *Environ. Sci. Pollut. Control Ser.* 30 (6), 16036–16067. <https://doi.org/10.1007/s11356-022-23168-5>.
- Mitra, R., Saha, P., Das, J., 2022. Assessment of the performance of GIS-based analytical hierarchical process (AHP) approach for flood modelling in Uttar Dinajpur district of West Bengal, India. *Geomatics, Nat. Hazards Risk* 13 (1), 2183–2226.
- Moore, I.D., Grayson, R.B., 1991. Terrain-based catchment partitioning and runoff prediction using vector elevation data. *Water Resour. Res.* 27 (6), 1177–1191.
- Myronidis, D., Papageorgiou, C., Theophanous, S., 2016. Landslide susceptibility mapping based on landslide history and analytic hierarchy process (AHP). *Nat. Hazards* 81, 245–263.
- Neuhäuser, B., Terhorst, B., 2007. Landslide susceptibility assessment using “weights-of-evidence” applied to a study area at the Jurassic escarpment (SW-Germany). *Geomorphology* 86 (1–2), 12–24.
- Neuhäuser, B., Damm, B., Terhorst, B., 2012. GIS-based assessment of landslide susceptibility on the base of the weights-of-evidence model. *Landslides* 9, 511–528.
- Pachuan, L., 2019. Zonation of landslide susceptibility and risk assessment in Serchhip town, Mizoram. *Journal of the Indian Society of Remote Sensing* 47 (9), 1587–1597.
- Parkash, S., 2011. Historical records of socio-economically significant landslides in India. *Journal of South Asia Disaster Studies* 4 (2), 177–204.
- Pham, B.T., Nguyen-Thoi, T., Qi, C., Van Phong, T., Dou, J., Ho, L.S., et al., 2020. Coupling RBF neural network with ensemble learning techniques for landslide susceptibility mapping. *Catena* 195, 104805.
- Poudyal, C.P., Chang, C., Oh, H.J., Lee, S., 2010. Landslide susceptibility maps comparing frequency ratio and artificial neural networks: a case study from the Nepal Himalaya. *Environ. Earth Sci.* 61, 1049–1064.
- Pourghasemi, H.R., Mohammady, M., Pradhan, B., 2012. Landslide susceptibility mapping using index of entropy and conditional probability models in GIS: safarood Basin, Iran. *Catena* 97, 71–84.
- Pradhan, B., Sameen, M.I., 2017. Effects of the Spatial Resolution of Digital Elevation Models and Their Products on Landslide Susceptibility mapping. *Laser Scanning Applications in Landslide Assessment*, pp. 133–150.
- Rao, K.S., Neog, S., Barman, J., Biswas, B., 2023. Morphometry-based prioritization of watersheds for soil and water conservation measures: a case study on Vanvate Lui basin, Mizoram, NorthEast India. *Arabian J. Geosci.* 16 (4), 1–13.
- Roy, J., Saha, S., Arabameri, A., Blaschke, T., Bui, D.T., 2019. A novel ensemble approach for landslide susceptibility mapping (LSM) in Darjeeling and Kalimpong districts, West Bengal, India. *Rem. Sens.* 11 (23), 2866.
- Saranaathan, S.E., Mani, S., Ramesh, V., Prasanna Venkatesh, S., 2021. Landslide susceptibility zonation mapping using bivariate statistical frequency ratio method and GIS: a case study in part of SH 37 Ghat Road, Nadugani, Panthalur Taluk, the Nilgiris. *Journal of the Indian Society of Remote Sensing* 49, 275–291.
- Sarkar, S., Roy, A.K., Martha, T.R., 2013. Landslide susceptibility assessment using information value method in parts of the Darjeeling Himalayas. *J. Geol. Soc. India* 82, 351–362.
- Sarvothaman, H., Anandha, K.K., 2013. *Disaster Management Engineering & Environmental Aspect*. Asiatech Publisher, Inc, New Delhi.
- Sati, V.P., 2022. Reconciling the issues of shifting and permanent cultivation: an empirical study of Mizoram, eastern extension of himalaya, India. *Caraka Tani: J. Sustain. Agric.* 37 (1), 171–184.
- Sema, H.V., Guru, B., Veerappan, R., 2017. Fuzzy gamma operator model for preparing landslide susceptibility zonation mapping in parts of Kohima Town, Nagaland, India. *Modeling Earth Systems and Environment* 3, 499–514.
- Shahzad, N., Ding, X., Abbas, S., 2022. A comparative assessment of machine learning models for landslide susceptibility mapping in the rugged terrain of northern Pakistan. *Appl. Sci.* 12 (5), 2280.
- Shirani, K., Pasandi, M., Arabameri, A., 2018. Landslide susceptibility assessment by dempster-shafer and index of entropy models, Sarkhoun basin, southwestern Iran. *Nat. Hazards* 93, 1379–1418.
- Singh, P., Sharma, A., Sur, U., Rai, P.K., 2021. Comparative landslide susceptibility assessment using statistical information value and index of entropy model in Bhanupali-Beri region, Himachal Pradesh, India. *Environ. Dev. Sustain.* 23, 5233–5250.
- Solaimani, K., Mousavi, S.Z., Kavian, A., 2013. Landslide susceptibility mapping based on frequency ratio and logistic regression models. *Arabian J. Geosci.* 6, 2557–2569.
- Trigila, A., Iadanza, C., Esposito, C., Scarascia-Mugnozza, G., 2015. Comparison of logistic regression and random forests techniques for shallow landslide susceptibility assessment in giampilieri (NE sicily, Italy). *Geomorphology* 249, 119–136.
- Ullah, I., Aslam, B., Shah, S.H.I.A., Tariq, A., Qin, S., Majeed, M., Havenith, H.B., 2022. An integrated approach of machine learning, remote sensing, and GIS data for the landslide susceptibility mapping. *Land* 11 (8), 1265.
- Van Westen, C.J., Rengers, N., Soeters, R., 2003. Use of geomorphological information in indirect landslide susceptibility assessment. *Nat. Hazards* 30, 399–419.
- Varnes, D.J., 1984. Intern. Association of Engineering Geology Commission on Landslides and Other Mass Movements on Slopes, *Landslide Hazard Zonation: a Review of Principles and Practice*. UNESCO, Paris, p. 63.
- Wang, Q., Li, W., Wu, Y., Pei, Y., Xie, P., 2016. Application of statistical index and index of entropy methods to landslide susceptibility assessment in Gongliu (Xinjiang, China). *Environ. Earth Sci.* 75, 1–13.
- Yao, X., Tham, L.G., Dai, F.C., 2008. Landslide susceptibility mapping based on support vector machine: a case study on natural slopes of Hong Kong, China. *Geomorphology* 101 (4), 572–582.
- Youssef, A.M., Al-Kathery, M., Pradhan, B., 2015. Landslide susceptibility mapping at Al-Hasher area, Jizan (Saudi Arabia) using GIS-based frequency ratio and index of entropy models. *Geosci. J.* 19, 113–134.
- Zhang, T.Y., Han, L., Zhang, H., Zhao, Y.H., Li, X.A., Zhao, L., 2019. GIS-based landslide susceptibility mapping using hybrid integration approaches of fractal dimension with index of entropy and support vector machine. *J. Mt. Sci.* 16 (6), 1275–1288.
- Zhou, X., Wen, H., Zhang, Y., Xu, J., Zhang, W., 2021. Landslide susceptibility mapping using hybrid random forest with GeoDetector and RFE for factor optimization. *Geosci. Front.* 12 (5), 101211. <https://doi.org/10.1016/j.gsf.2021.101211>.
- Zou, Q., Jiang, H., Cui, P., Zhou, B., Jiang, Y., Qin, M., et al., 2021. A new approach to assess landslide susceptibility based on slope failure mechanisms. *Catena* 204, 105388. <https://doi.org/10.1016/j.catena.2021.105388>.

A Novel Approach to Abstract the Design Information and Minimal Cover from the Restructured Java Program

Aparna K. S.¹ and Dr. R. N. Kulkarni²

Submitted: 15/12/2023

Revised: 20/01/2024

Accepted: 03/02/2024

Abstract: The software industry has undergone enormous development during the previous few decades. Java programming was used to create many of the software applications needed to run the current generic applications. To support the business operations, these applications have undergone changes based on the changing requirements of the customer or organization. Many changes performed during these need-based updates are made only to the applications and not in the relevant documents related to the software. Further altering these software systems could occasionally cause a software crash. It might be challenging to add new features to the old programs as there is a possibility of redundant code.

To overcome the problems related with either redundancy of the code or documentation, a novel methodology is proposed and a tool is developed to abstract the various components from the input java programming system such as control flow graph, data flow information in the control flow order and the various attributes which are participating in the program. Further the data flow graph and control flow graph are used to find the functional dependencies and attribute closures. The abstracted attributes are used to find the minimal cover, which results in the computation of the functionality of the program.

Keywords: Restructuring, Data flow graph, Control flow graph, Referred Variable, Defined variable, functional dependency

1. Introduction

The demand to use technology and software to automate organizational tasks has increased dramatically during the past few decades. The utilization of application systems constructed using Java programming has experienced significant demand. These application systems, which were created decades ago, have undergone several ongoing, need-based adjustments. As the original writers were unavailable, there was a chance of redundancy in the code, when these changes were implemented. Moreover, the programming language was flexible enough for the various programmers to use alternative names for the variables, operations, and methods. As, the success of the translation depends on the knowledge of the translator's expertise and experience, thus translating the complete application to a new programming language was equally challenging, as it needs to comprehend the organization's entire business rules, which gets modified periodically leading to unstructured code. This unstructured-ness can be handled with the help of restructuring techniques for abstracting the design information.

Taxonomy:

Control flow graph represents graph implying the execution flow of the overall program

Data flow graph represents graph implying the flow of data along the control flow.

Referenced attribute get referenced in a executable statement of a program without any modifications after execution

Defined attribute are attributes, changing during the execution of statement.

Restructuring is the transformation from one form to another without changing its functionality

2. Related Work

The various methods of restructuring Java applications are covered in [1], the preprocessing step for obtaining the design data necessary for static analysis of the input. Restructuring [2], benefits the memory optimization significantly contributing to the memory management issues required for reengineering. The study [6] presents a novel approach for generating a descriptive file from source code using comment lines. This method takes an existing Java source code program and adds a description file to it automatically. It contains the parameters functions, conditions, and description. All of this information will eventually be included in a text document file that the framework creates. In our approach we are eliminating these comment lines, blank lines and changing the multiple lines into a single line as these comment lines will not be updated periodically. The next step of this paper is to extract the design information. The different approaches are discussed. Firstly extracting the Data flow diagram from the given java program is discussed [4] and represented in the table format

¹Assistant Professor, Department of Computer science & Engineering, RYMEC, Ballari, Research scholar, VTU, Belagavi.

²Professor and HOD, Department of Computer Science & Engineering, Ballari Institute of Technology and Management, Ballari, aparna.vastrad@gmail.com, mkulkarni@bitm.edu.in

using which, the design of the software is extracted. The feature extractor method is to extract the data from the generated XML file. Information gathered from method names [7], variable names, and comments in the project source code that is being analyzed. Each Java class is presented as a document. Next, using Latent Dirichlet Allocation (LDA), a set of topics representing the different functionality offered by the project are identified. In approach [2], the source code goes through various stages of the static analysis and functionality is derived from program slicing. The value of data representation in tables is underlined in [3], which presents the information of the sequence diagram in the form of useful table. In [4], a table that serves as a static representation of the class diagram provides complete information. Meanwhile the activity and use case diagrams in [5] are produced using the source code, indicating that the focus should be on other UML diagrams to extract the design information. In [6], the Control Flow Graph (CFG) is used to represent the source code representing all pathways that an application will take throughout its execution. Further this CFG is then used to extract other related concepts. The Java programs are used for various degrees of analysis in [7] and are rendered as graphs. ProgQuery and Neo4J graph, among other tools, are effective, but complexity rises with larger programs. Models are made from the intermediate representation of the source code and are used to extract UML models in reverse method combining static and dynamic analysis[18,19]. The static and dynamic analysis of bytecode is done and represented in the form of table [9]. It emphasizes how the results of the static code analysis for the Java programs are extracted as graphs[10]. In[11,12], the static analysis of the tools and techniques for locating bugs, security vulnerabilities, code duplication, and code smells are addressed in detail. Opensource static code analysis is one of the tools that is accessible to find errors and different coding techniques. In [13], the static analysis of the code is carried out utilizing AST, assessing the many paths that the programs can take performing a control flow and programs flow analysis. The survey discussed above use graphical representations to illustrate static analysis for the different application, however these graphical representations have memory and maintenance issues that make it difficult to retrieve and preserve the data. These graphical representations of the programs, presented in a variety of ways, are useful for evaluating the program code, but they undoubtedly used a lot of memory and added overhead retrieving the data for later processing. As a result, alternative forms of graphical representation, such as tabular representation, proved to be more effective in terms of memory utilization, processing speed, throughput analysis. The proposed work discusses the control flow analysis of the input Java programs in a tabular representation. The control flow and data flow is derived from the control flow table and data flow table in our approach. From the data flow table, the functional

dependencies are extracted and further these functional dependencies are minimized as discussed below. In [17], closure and the minimal cover algorithm were used to resolve the superfluous functional dependencies. The Armstrong axioms are used to create the F+ algorithm, which generates closure of functional dependencies (FDs). Finding functional relationships and minimizing them with the minimal cover method is done for various sets of functional dependencies, as discussed in detail [18]. A lifetime model [15] for individual source code lines or tokens can be used to guide preventive maintenance, estimate maintenance effort, and, in general, find characteristics that can increase software development efficiency. All components involved in the software system [14] should be able to easily comprehend and discern the necessary components of the requirements through the software design. In our methodology, the functional dependencies extracted from the data flow table have lot of redundant functional dependencies which have to be minimized because there will be an unequal distribution of functional dependencies. Consequently, these functional dependencies might be mentioned in other statements explicitly or indirectly. This scenario complicates the design extraction process. In our methodology, this problem is resolved by applying the concept of minimal cover [20,21] and the storage will be conserved as a result, by removing redundant and unnecessary productions in the functional dependencies, resulting in database optimization

3. Proposed Methodology

- A. Restructuring the Input Program:** Restructuring is the method of bringing modifications to the software structure explicitly without affecting its functionality. In our proposed methodology, comment line elimination, blank line elimination, and making multiple declaration statements into a single declaration statement is a part of the restructuring [3] process. Other steps include statements ending with a semicolon, curly braces insertion before the start and end part statements in the body of the loop, respectively, and assigning sequential line numbers to logic statements. This process of restructuring changes the program structure without affecting its function. This refactored code will be a input for extracting the design information.

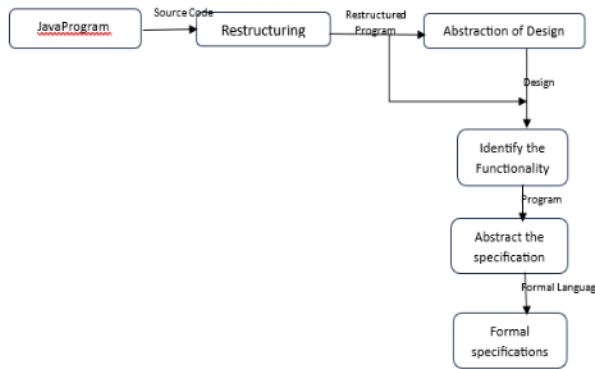


Fig 3.1: Block diagram of the proposed methodology

Consider the input java program in Figure 2 which is a non-structured code.

```

1.  import java.util.Scanner;
2.  public class Quad
3.  {
4.  public static void main(String[] args)
5.  {
6.  double a1,b1,c1;
7.  //determinant is det
8.  double det;
9.  //r1=root1 and r2=root2
10. double r1,r2;
11. Scanner in =new Scanner(System.in);
12. //reading values of a1,b1,c1
13. System.out.println("Enter the value of a");
14. a1=in.nextDouble
15. System.out.println("Enter the value of b");
16. b1= in.nextDouble();
17. System.out.println("Enter the value of c")
18. c1= in.nextDouble();
19. /*comparing the values and chking for
   determinanat*/
20. if(a1==0|| b1==0||c1==0)
21. {
22. System.out.println("Invalid input:Enter non-zero
   co-effeceints");
23. System.exit(0);
24. else
25. {

```

```

26. d1=b1 *b1 – 4 *a1 * c1
27. if(d1>0)
28. {
29. //calculation of root1 and root2 for positive det
   values
30. r1 = (-b1+ Math.sqrt(d1)) / (2 * a1);
31. r2 = (-b1 - Math.sqrt(d1)) / (2 * a1);
32. System.out.println("root1 and root2 are", r1, r2);
33. }
34. else if(d1= =0)
35. {
36. //executed when roots are same
37. r1 = r2 = -b1 / (2 * a1);
38. System.out.println("Roots are real and equal" +r1);
39. System.out.println("Root1 = Root2 = "+ r1);
40. }
41. else
42. {
43. //calculating the negative part
44. double rpart = -b1/ (2 *a1);
45. System.out.println("Roots are complex and
   imaginary");
46. //printing values of roots
47. System.out.println("r1="+rpart+"i"+
   imaginaryPart+"r2="+rpart+"-i" + imaginaryPart);
48. }//else ends
49. }//if ends
50. Sc.close();
51. }//main ends
52. }//quadratic ends

```

Fig 3.2:Input java Program

From Figure 3.3, it is very clear that the CPU execution time varies a lot with the given input size of the program

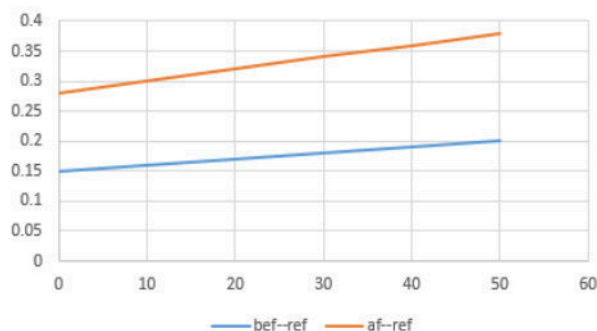


Fig 3.3: Graphical analysis of the Restructuring It is obvious that the varied execution time (in seconds) implies the effect of restructuring process. Considering the input size of 50 lines, the graph in Figure 3 illustrates that after restructuring the execution time has reduced a lot and for the same input size the execution time is comparatively less, which indicates the effect of restructuring the input code.

B. Abstraction of Control flow graph from Java Program:

The program is represented in the form of a graph, where each node in the control flow graph represents either a conditional statement, computational statement, or the invocation of a member function. An edge connecting those vertices represents the control flow between the statement. The program execution control flow is shown on the Control Flow Graph (CFG). Each line in Java can include a computational statement, a predicate statement, or an invocation statement. When the program is represented as a graph with one vertex (or node) assigned to each statement, the joining edge between the two vertices represents the control flow. This representation is considered inefficient due to the bulk size of java applications, hence these CFG are represented in tabular form using the four columns, where column1 implies start of the program, column2 represents the point of occurrence of the first control statement, third column represents the point of true block(Trans1) and fourth column indicates the false block(Trans2). Usually Trans1=start of the program and Trans2= end of the program and the same procedure gets repeated for all the control statements like if-else, while, for, do-while, switch, break, continue, return. The function invocation present in the input program are handled by putting the point of callee function in trans1 and trans2 will be obviously empty as it is not having the true and false blocks. Further these true and false blocks are analyzed and the above procedure is followed for any nested control structures occurring in it. The concept of defining nodes and Usage/Referenced nodes are used to construct the control flow table.

Algorithm for abstraction of Design information

Input: java program after restructuring

Output: Tables depicting control flow, data flow and minimal cover of attributes

Step 1: [Java program preprocessing with restructuring]

- Input Java Program is scanned
- Appending main program with the imported packages
- Comment line elimination
- Blank lines elimination
- Single line statements got by converting multi statement line and multiline statements
- Each statement are given the physical line numbers

These restructuring steps help in the efficient representation of the input program, required for analyzing the design information in the form of control and data tables

Step2: [Control flow table abstraction from the Restructured Java program]

Scan the input Java program starting from the string 'Public static void main' and search for the control keys of the input program comparing with that of VERBS(control statements) as discussed above. If the scanned control keys belongs to VERBS, then represent that information in the table format representing statement number of the first line of the program in column1, column2 is the point where the first control key occurs column3 is **Tr1** representing the transition to the starting point of the true block and column4 is **Tr2** representing the transition to the starting point of the false block and this process gets repeated for all the control keys present in the input program and as well for the nested control structures

Step 3: [Data flow table abstraction from the Restructured Java program]:

The flow of data variables in the program is based on the control flow order. These data variables are defined and referred at several points of the program. Identification of these referred and defined variables in every line of the input program is noted in the tabular format, where first column indicates input program line number, second column is for defined variables and third column is for referred variables .

Step4: [Finding the minimal cover of the functional dependencies].

From the data flow table, the functional dependency existing between these variables are extracted. These functional dependences are minimized to extract minimal cover of attributes eliminating redundant attributes. The minimal cover is done using these steps:

- Representing the Functional Dependencies in a canonical form where RHS should have a single attribute.
- Remove the redundant FDs (which can be derived from the transitive principles).

- iii. Remove the extraneous attributes, by finding the closure of all the LHS attributes of the Functional dependencies having non-single attribute. If $CLOSURE(A) = ABC$ then BC are extraneous attributes and have to be removed.
- iv. Apply the Armstrong principles and try to group FDs using common LHS

4. Results and Discussion

Refactored code :

```

1. import java.util.Scanner;
2. public class Quad
3. {
4.     public static void main(String[] args)
5.     {
6.         double a1,b1,c1,d1,r1,r2;
7.         Scanner in =new Scanner(System.in);
8.         System.out.println("Enter the value of a");
9.         a1=in.nextDouble()
10.        System.out.println("Enter the value of b");
11.        b1= in.nextDouble();
12.        System.out.println("Enter the value of c")
13.        c1= in.nextDouble();
14.        if(a1==0|| b1==0||c1==0)
15.        {
16.            System.out.println("Invalid input:Enter non-zero
            co-efficients");
17.            System.exit(0);
18.        }
19.        else
20.        {
21.            d1=b1 *b1 - 4 *a1 * c1
22.            if(d1>0)
23.            {
24.                r1 = (-b1 + Math.sqrt(d1)) / (2 * a1);
25.                r2 = (-b1 - Math.sqrt(d1)) / (2 * a1);
26.                System.out.println("root1 and root2 are", r1, r2);
27.            }
28.            else if(d1= =0)
29.            {
30.                r1 = r2 = -b1 / (2 * a1);
31.                system.out.println("Roots are real and equal" +r1);

```

```

31. system.out.println("Root1 = Root2 = " + r1);
32. }
33. else
34. {
35.     double rpart = -b1 / (2 *a1);
36.     System.out.println("Roots are complex
        andimaginary");
37.     System.out.println("r1="+rpart      +"i"+
        imaginaryPart+"      r2=      "+      rpart+"-i"+
        imaginaryPart);
38. }

39. Sc.close();
40. }
41. }

```

Fig 4.1: Restructured Java program

In this program, the static analysis of the code is done. The execution starts from the main. In this methodology, the control statements are scanned from main. These control statements are analyzed based on their structure, the different block of statements get executed. In the above program, we have the control statement at line no 14, and true block starts at line 15 and false block from line 19. In true block, further we have exit statement at line 17, so the control jumps to line 42. In the false block, further there is another condition checking for determinant at line 21, where true block moves to line 22 and completes its execution at 26 and in false block, the control statements are checked, if true moves to 28 and the block from 28 to 32 gets executed and the else block gets executed from 34 to 38 and both the blocks get terminated at line 40. The control flow table is as shown in the Figure 4.1. The data flow table in Figure 4.2, represents the flow of the variables at different control points of the program.

S	E	TR1	TR2
1	14	15	19
15	17	42	
19	21	22	27
22	26	37	
27	27	28	34
28	32	42	
34	39	40	

Fig 4.2: Control flow table of Figure 4.1

Line No	Defined Vars	Referred Vars
2	Quad	
9		a1
11		b1
13		c1
14		a1 b1 c1
20	d1	a1 b1 c1
21		d1
23	r1	a1, b1, d1
24	r2	a1, b1, d1
27	-	d1
29	r1, r2	b1, a1
30	-	r1
31		'r1'
35	rpart	b1 a1

Fig 4.3: Data flow table of Figure 4.2

This proposed tool is tested for different combinations of inputs and the tool is compared for its efficiency. The existing tools are building the control flow order using the graphical representation. This graphical representation has lot of concerns with respect to memory issues. The proposed tool analyzes the static analysis of the code which is very easily traceable and consumes very less execution time and gives good throughput analysis as discussed below. From the Data flow table, rows in which there exists both referred and defined variables are identified and

such rows imply the functional dependencies between the variables. The following FunctionalDependencies(FD) are extracted from the data flow table.

$a1\ b1\ c1 \rightarrow d1$
 $a1\ b1\ d1 \rightarrow r1$
 $a1\ b1\ d1 \rightarrow r2$
 $a1\ b1 \rightarrow r1\ r2$
 $a1\ b1 \rightarrow rpart$

After applying step1 of the minimal cover algorithm , we get

$a1\ b1\ c1 \rightarrow d1$
 $a1\ b1\ d1 \rightarrow r1$
 $a1\ b1\ d1 \rightarrow r2$

$a1\ b1 \rightarrow r1$

$a1\ b1 \rightarrow r2$

$a1\ b1 \rightarrow rpart$

Applying step2, we get the same FDs, as we do not have redundant FDs. Applying step3 we consider the LHS having more than two attributes. The closure rule is applied and checked to see any extraneous attributes. All FDs are equally important and hence all FDs are retained.

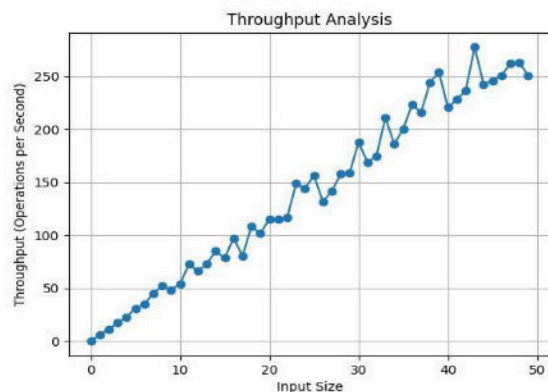
Applying the step4, group all FDs having the common LHS together.

$a1\ b1\ c1 \rightarrow d1$

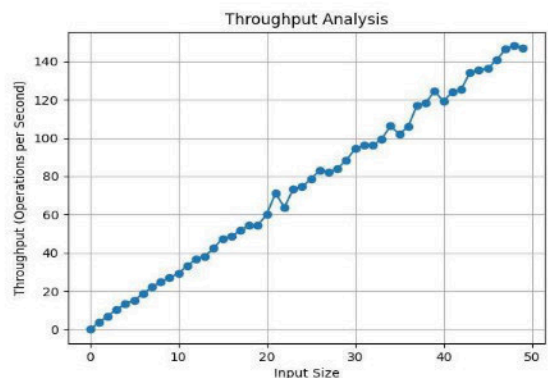
$a1\ b1\ d1 \rightarrow r1, r2$

$a1\ b1 \rightarrow r1\ r2\ rpart$

This is the minimal cover obtained which is equivalent to the original set of FDs having fewer number of FDs. The minimization of the functional dependencies in a program code is done using the minimal cover process. These functional dependencies are minimized and the redundant and irrelevant attributes are removed, which are added by the different programmers during the maintenance phase to keep the structure of the application program intact with business policies.



Before restructuring



After restructuring

Figure 4.3: Throughput graph of the input program before and after restructuring

The graph (before restructuring) in Figure 4.3 varies a lot with the number of operations per second as the program is not restructured. The number of operations per second is competitively less after restructuring as shown in Figure 4.3 (after restructuring)

5. Conclusion and Future Work

This paper presents an automated tool for abstraction of the design information of the input Java program in the form of control flow graph and data flow graph and stored in the form of Control flow table and data flow table. The functional dependencies are extracted from the Data flow table and minimized to get the optimal set of attributes using which the code can be comprehended. The proposed tool is tested for its correctness and completeness by applying on different programs of varying complexities. The tool generates expected output for all the given programs and the functional dependencies abstracted from the Data flow table are further minimized. From these minimized attributes, the different program slices are extracted using backward slicing. Using these slices, the different functionalities present in the input Java program are identified and extracted.

Author contributions

The two authors have mutually discussed and analysed and worked on the methodology and conducted different tests for its effectiveness

Conflicts of interest

The authors declare no conflicts of interest.

References

- [1] Dr. R. N. Kulkarni and Aparna K.S, "A Novel Approach to Restructure the Input Java Program", International Journal of Advanced Networking and Applications Volume 12 ISSN: 0975-0290 4621, 2020.
- [2] R. N. Kulkarni, Venkata Sandeep Edara, "Memory Optimization Using Distributed Shared Memory Management for Re-engineering", International Journal of Intelligent systems and applications in Engineering, IJISAE, 2023.
- [3] Dr. R. N. Kulkarni and Padma priya Patil, "Abstraction of Information Flow Table from a Restructured Legacy 'C' Program to be amenable for Multicore Architecture", 5th International conference on innovations in computer science and engineering.
- [4] R. N. Kulkarni, Mr. P. Pani Rama Prasad, "Novel Approach to Abstract the Data Flow Diagram from Java Application Program", International Journal of Intelligent systems and applications in Engineering, IJISAE, 2023.
- [5] Dr. R. N. Kulkarni and C. K. Srinivasa, "Novel approach to transform UML Sequence diagram to Activity diagram", Journal of University of Shanghai for Science and Technology, Volume 23, Issue 7, July 2021.
- [6] Dr. R. N. Kulkarni and P. Pani Rama Prasad, "Abstraction of UML Class Diagram from the Input Java Program, International Journal of Advanced Networking and Applications Volume 12, ISSN: 0975-0290.
- [7] Rasha Gh Alsarraj¹, Atica M. Altaie², Anfal A. Fadhil³, "Designing and implementing a tool to transform source code to UML diagrams", Periodicals of Engineering and Natural Sciences ISSN 2303-4521 Vol, March 2021.
- [8] Ali Hameed Mohsin, Mustafa Hammad "A Code Summarization Approach for Object Oriented Programs", International Conference on Innovation and Intelligence for Informatics, Computing, and Technologies (3ICT), 2019.
- [9] Christos Psarras, Themistoklis Diamantopoulos, Andreas Symeonidis "A Mechanism for Automatically Summarizing Software Functionality from Source". IEEE 19th International Conference on Software Quality, Reliability and Security (QRS)
- [10] Rafael R. Prado, Paulo S. L. Souza, George G. M. Dourado, Simone R. S. Souza, "Extracting Static and Dynamic Structural Information from Java Concurrent Programs for Coverage Testing", 2015 XLI Latin American Computing Conference.
- [11] Oscar Rodriguez-prieto¹, Alan Mycroft, Francisco ortin, "An Efficient and Scalable Platform for Java Source Code Analysis Using Overlaid Graph Representations", Received March 10, 2020.
- [12] Umair Sabir, Farooqui Azam, Samiullah, Muhammad Waseem Anwar, Wasi Haider butt, and Anam Amjad, "A Model Driven Reverse Engineering Framework for Generating High Level UML Models From Java Source Code", Published in IEEE access dated November 13, 2019.
- [13] Shafiullah Soomro, Zainab Alansri, Mohammad Riyaz Belgaum, "Path Executions of Java Bytecode Programs" Advances in Intelligent Systems and computing, Springer, 2017.
- [14] Gang Shu, Boya Sun, Tim A.D. Henderson, Andy Podgurski, "Java PDG: A New Platform for Program Dependence Analysis", Sixth International Conference on Software testing, Verification and Validation. IEEE, 2013.
- [15] Dusanka Dakin, Srđan Spasojevic, Sonja Ristic Danilo Nikolic, Darko Stefanovic, "Analysis of the tools for

static code analysis”, 20th International Symposium March 2021.

- [16] Eda Ozcan , Damla Topalli , Gul Tok Demir and Nergiz Ercil Cagily, “A user task design notation for improved software design”, London, UK, PeerJ computer science, 2021
- [17] Diomidis Spinelli’s, Panos Louridas and Maria Kechagia, “Software evolution: the lifetime of fine-grained, elements”, London, UK, PeerJ computer science, 2021
- [18] Shafiullah Soomro, Zainab Alansri, Mohammad Riyaz Belgaum, “Control and Data flow execution of Java program”, Asian Journal of Scientific Research DOI: 10.393/ajsr , 2017.
- [19] Abdul vahab karuthedath Thrissur ,Sreekutty Vijayan, Vipin Kumar K.S. “System ependence Graph based test case generation for Object Oriented Programs”, International Conference on Power, Instrumentation, Control and Computing (PICC), 2020.
- [20] Jeong Yang ,Young Lee, Deep Gandhi, Sruthi Ganesan Valli, “Synchronized UML Diagrams for Object-Oriented Program Comprehension”, The 12th International Conference on Computer Science & Education (ICCSE 2017) August 22-25, 2017. University of Houston, USA.
- [21] Elliot Varey, John Burrows, Jing Sun† and Sathiamoorthy Manoharan “From Code to Design: A Reverse Engineering Approach”, IEEE sponsored International Conference on Engineering of Complex Computer Systems 2016 IEEE DOI 10.1109/ICECCS.2016.1.
- [22] Michael John Decker¹ , Kyle Swartz , Michael L. Collard , and Jonathan I. Maletic, “A Tool for Efficiently Reverse Engineering Accurate UML Class Diagrams”, International Conference on Software Maintenance and Evolution, 2016 IEEE.
- [23] A.B Amooore, M.A. Amodu Longe, “Functional Dependency: Design and Implementation of a Minimal Cover Algorithm” , IOSR Journal of Computer Engineering (IOSR-JCE) e-ISSN: 2278-0661,p-ISSN: 2278-8727, Volume 19, Issue 5, Ver. I (Sep.- Oct. 2017).
- [24] Dr. Shivanand M. Handigund “ An Ameliorated Methodology for the Abstraction and Minimization of Functional Dependencies of legacy ‘C’ Program Elements “, International Journal of Computer Applications (0975 – 8887) Volume 16– No.3, February 2011.

Memory Optimization Using Distributed Shared Memory Management for Re-engineering

R. N. Kulkarni¹, Venkata Sandeep Edara^{*2}

Submitted: 23/04/2023

Revised: 25/06/2023

Accepted: 02/07/2023

Abstract: Restructure the old input C++ programming system to make it suitable for reengineering, which necessitates humongous memory. This study has made significant contributions to the disciplines of system-on-chip design and on-chip memory management, among others. This paper presents a new technique for optimizing memory subsystems during system design that is suited to specific applications like re-engineering. This work can be improved to optimize memory controller activities and design challenges for distributed shared memory management. It has the capacity to manage an increasing number of processors simultaneously, as well as security and faster execution. The Xilinx 14.2 integrated simulation environment produces outstanding results when the proposed memory optimization approaches are fully integrated into the simulation, optimization, and code generation cycle. The proposed memory device has an extremely low on-chip power consumption of 0.0082 W, which amply demonstrates how well memory has been improved.

Keywords: Memory management, Power Consumption, Shared distributed memory (SDM), Memory mapping Mechanism, Re-engineering

1. Introduction

This A variety of high-speed applications, such as consumer embedded products, audio and video processing, multimedia animation (including 3D animation), and weather forecasting, were created by IC designers as a result of the development of VLSI technology [1]. Field programmable gate arrays (FPGAs) have only lately demonstrated their viability in decreasing the overall computational load placed on the CPU core of the primary processor. Data on the reconfigurable fabric, which is used by both the software and the hardware, is mapped using a memory mapping technique designed specifically for this resolution. This memory mapping approach is the foundation of the entire methodology. Parallel and distributed processing are two of the most cutting-edge areas of research being investigated right now in computer architecture. The shared memory architecture is generated in systems with physically distributed memories by incorporating the two aspects of both approaches. One of the most widely researched subjects in multiprocessor networks is the study of distributed shared memory. Traditional single-processor architectures are unable to push ahead with the expanding number of high-speed applications, requiring the creation of extremely sophisticated multiprocessor architectures. A multiprocessor, also recognised as a Multi core SoC or Multi processor System on Chip, is a device that enables the integration of multiple Intellectual Property

(IP) cores in a single chip, which could be in the form of high-speed digital signal processors, controllers, hardware accelerators, memory blocks, and I/O blocks to perform multiple tasks while operating at different clock frequencies.

Memory-management components of the operating system split each memory resource and load data across multiple types of memory at the system level. Part of the main-memory content, for example, must be shifted to secondary storage, the disc. Virtual-memory and physical-memory layouts, redeployment to avoid fragmentation, and other more sophisticated jobs are among the more difficult tasks. The main memory is split into 2 parts: one for the operating system to handle globally, and one for each programme being performed, which requires a different type of memory management [2].

In real-time operating systems, memory management is handled in one of two ways: using a stack or using a heap. The stack management technique is used for context switching between jobs, whereas the heap management mechanism is used for dynamically giving space to tasks [3]. Even many researchers have investigated the most recent methodologies for co-optimizing test time and test power reduction techniques. These actions that incur overhead are seen as vital after prefetching, even if they are not finished. To limit the amount of time spent reconfiguring them, they must be re-used (In future iterations of the same task graph execution). As a result, reusing previously loaded configurations is one of the most

¹ Ballari Institute of Technology and Management, Ballari- 583104, Karnataka, India. ORCID ID : 0000-0002-9948-1398

² Sasi Institute of Technology and Engineering, Tadepalligudem- 534101, Research Scholar, VTU Belagavi, Karnataka, India ORCID ID : 0009-0004-6318-6735

* Corresponding Author Email: evsandeep@sasi.ac.in

cost-effective ways to reduce overall reconfiguration expenses [4].

Kandemir et. al. extend their prior work to multi-processor systems in [5] by using a compiler-based scratchpad management mechanism. Array-dominated embedded applications, as previously stated, are the most common use case. When several processors are working in the same array or collecting data, data reuse is a critical notion for decreasing energy and delay. Se-Jun Kwon et al. (2017) proposed an efficient and effective fast compression technique for in-memory data [6]. The suggested technique takes advantage of the features of in-memory data that are often identified to increase efficiency.

Dynamic Frequent Pattern Compression was developed by Yuncheng Guo et. al. as an adaptive non-volatile memory write approach based on frequent pattern compression [7]. The contents of cache lines are encoded using more types of common data patterns when utilizing DFPC, resulting in a greater compression ratio. In addition to regular metrics and cache hit rates, Esha Choukse et. al. included proposed mechanisms to incorporate correct virtual address translation, identify a region in the programme that is reflective of the compression ratio, as well as regular metrics and cache hit rates, in their methodology [8]. Dual dictionary compression was introduced as a last-level cache compression solution by David Kaeli [9]. It is feasible to make greater use of available die space while also boosting system memory speed by compressing data in the final level cache (LLC).

Memory is a vital component of real-time applications due to the amount of time and money it takes to manage it properly. As a result, real-time system designers concentrate on minimising the worst-case execution time and memory consumption. A cost-effective memory manager is required in order to increase the performance of the real-time system. Most real-time systems employ static memory allocators for the random allocation and de-allocation of memory blocks, and this is the case for the most majority of such systems. The memory is allocated before the application enters the core real-time stage, in which the full physical memory is available as a single block and can be used as needed, at the time of compilation or launch of the programme, whichever occurs first. There is a problem with excessive memory consumption since the memory required to hold objects cannot be easily recovered because automatic memory management is not available. Programmers must create and manage distinct private memory pools in order to avoid wasting memory space on unneeded operations. Real-time systems based on multicore and multiprocessor architectures have grown in size and complexity, necessitating the flexible use of existing resources, such as memory [10], as a result of this growth. For real-time applications to achieve the predictable performance and

flexibility necessary in the multiprocessor system era, dynamic memory management allocators will eventually be required [11], [12].

The process of uncovering the technological principles of a technology, object, or system by analyzing its structure, function, and operation is known as reverse engineering [13]. Reverse engineering binary executable code has proven effective in a variety of situations. It's used to move a system to a newer platform, unbundle monolithic systems into components and utilise them separately, and interpret binary code for untrusted code and malware. The ubiquitous use of C++ in many modern applications necessitates an understanding of the disassembly of C++ object-oriented code. Today, reverse engineering binary code is common, particularly for untrusted code and malware. Software re-engineering is the process of improving or changing existing software so that it can be understood, managed, and reused as new software. Re-engineering is required when the system's software architecture and platforms become absolute and must be modified. The value of software re-engineering stems from its capacity to recover and reuse items that already present in an out-of-date system. This will definitely reduce system maintenance costs and lay the groundwork for future software development. Furthermore, re-engineering needs huge memory. This paper presents design and optimization of distributed memory for re-engineering.

Memory access is a major performance constraint in many data-intensive applications. The system's performance and power usage are both impacted by delays in access. As a result, a memory hierarchy is the most popular solution to alleviating this bottleneck and ensuring efficient memory design. Between the CPU and the main memory, various levels of memory are utilised. It's common practise to keep small, quick memories close to the central processing unit. Memory instances get larger and slower as you go down the memory hierarchy. With growing memory size, energy efficiency declines in the same way that it has been previously stated. As can be seen in Figure 1, embedded and SoC devices use a variety of memory hierarchy systems.

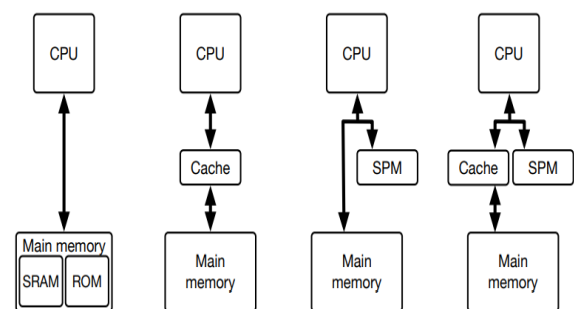


Fig. 1 Common memory architecture.

There is a unique global naming strategy in place to keep such disputes at bay for all of the sites that use the shared data. One way to get access to remote computers' shared

data is by having the distributed shared memory system's memory controller do physical-to-logical address translation. A global directory of shared data items will be maintained by the memory controller for all sites. Here, the memory controller is a software layer that sits on top of the local memory and allows for virtual shared memory. Fig. 2 shows how the system's memory controller will link to all of the system's local RAM and manage the system's virtual memory. Other than address conversion and fetching, it will schedule and optimize operations. However, if the shared data is of a smaller size, this approach would be inappropriate. In this case, the requesting site will be able to locate shared remote data after communicating with the memory controller.

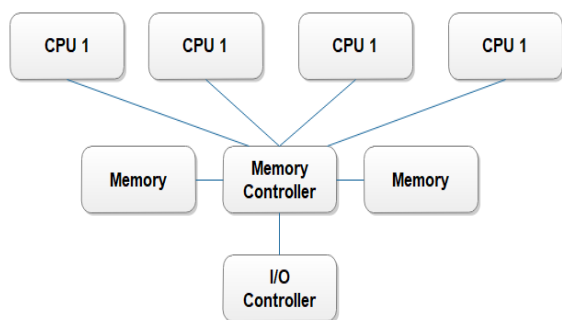


Fig 2. Memory controller Architecture.

The shared zone represented in Fig. 3 is an illusion created by the memory controller, which is connected to each site and so appears to be shared. When a process requests access to external data, a request will be made to the memory controller by the process requesting access to external data. The data is organised using the shared variable as a guide. Sequential consistency does an excellent job of handling the coherence semantics. Additional effort was required for commercial application in order to make the system the most successful possible from a variety of perspectives. The concepts and languages of object-oriented programming can also be utilised to develop graphical user interfaces (GUIs). Meanwhile, the message-passing structure is more complicated to construct but relatively easy to expand. Both the shared memory structure and the message transmission must develop in lockstep with each other in order to function properly. A realistic solution for parallel system architecture can be found in distributed shared memory, but only after careful analysis of the conditions and their justification.

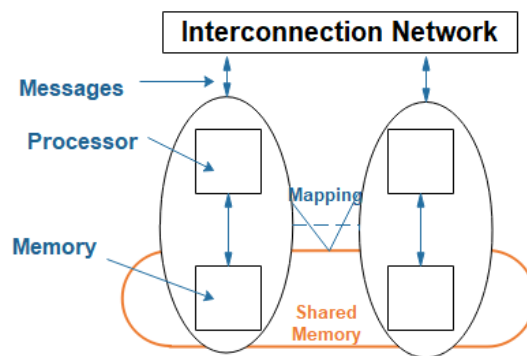


Fig. 3 Memory mapping Architecture using shared memory.

2. Proposed Memory Hierarchy and Methodology

When it comes to high-performance, large-scale multiprocessor systems, optimizing the performance of distributed shared memory is critical. In the past, several constraints were solved; however, the core problem continues to exist: Below, we go into further detail on the DSM method, locking shared space, thrashing, concurrent access, page faults, extension, transparency, huge database support, and cost. The objective of this research project was to create a novel distributed shared memory architecture that uses software parameters to significantly outperform existing structural designs while handling distributed shared address spaces [14]. Additionally, as we move closer to the deployment of software distributed shared memory, a slew of considerations will come into play. Implementing a distributed shared memory system is achievable through the use of an expanded virtual address space architecture in conjunction with the application of a new operating system paradigm. Because of the use of replication and granularity selection for data transfer, this unique DSM technique (figure 4) improves the overall efficiency of the system by employing a sequential consistency mechanism. Each system node is equipped with a mapping manager, which acts as a bridge between the node's local memory and the shared virtual memory space on the network. Write-up protocols are used to keep track of what each node is looking up and performing on a given time frame.

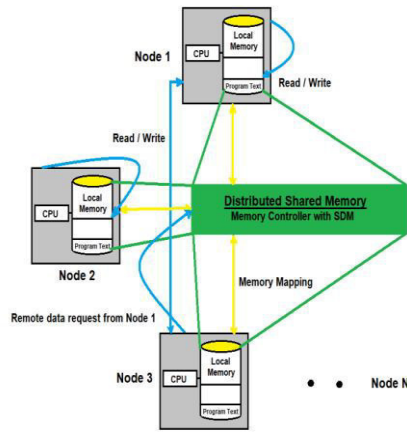


Fig 4. Architecture of distributed multi core architecture.

Configuration data must be downloaded from off-chip memory in order to map jobs onto the FPGA, as shown in Figure 5. A certain amount of energy is used and a delay is generated for each configuration data fetch from off-chip memory. To alleviate these overheads, a memory hierarchy consisting of two memories is used. One memory is optimised for High Speed (HS), while the other is optimised for Low Energy (LE). In comparison, HS memory has a shorter time delay and uses less energy than LE memory [15] –[18]. As a result, the configuration data is mapped in the suggested memory hierarchy using a mapping technique that decreases energy usage while still satisfying deadlines.

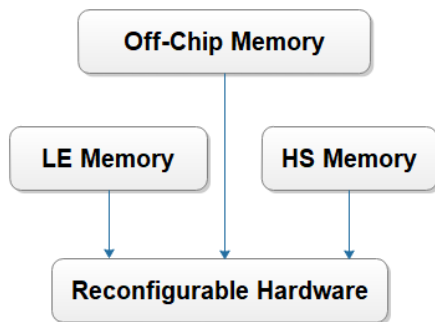


Fig 5. Memory hierarchy for mapping the configuration data.

Simulates memory operations, calculates access latency, and returns the result to the sim-outorder callback function. An example of the memory_access latency function signature is as follows:

```
unsigned int memory_accessJatency(struct mem_t* mem, int chunks, md_addr_t addr, enum mem_cmd cmd, tick_t now);
```

This option has a mem t pointer that points to the sim-outorder simulation program's mem t data structure. The second input, chunks, defines the total number of bytes sought by the processor/cache when it requests memory access (in sim-outorder, it is the L2 cache block size since the L2 cache is the only cache that requests for memory access). The address that the processor/cache is looking for

as the initial address is specified by the addr option. The processor cycle that happened when the processor/cache requested the memory access is the final parameter.

However, the latency number returned by memory access latency is a latency value relative to the 'now' argument, not the sum of the timing parameters (Tcmd, Trp, Trd, Teas, Twd, and data transmission).

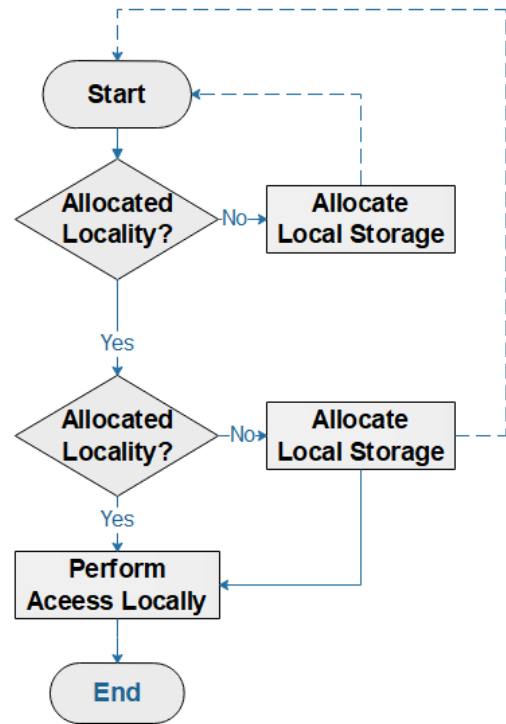


Fig 6. Flow of Memory Access.

The function's return result can be a significant amount higher than the sum of the individual timings. Because the memory model may be idle or busy servicing the previous access when the processor/cache requests a memory access, this occurs. If the memory is processing another access, it must wait for the prior access to complete before servicing the current access. The memory access latency function (delay function) determines the earliest possible processor cycle (start time) for the memory access requested by the processor/cache. The latency function's primary goal is to achieve this. To determine if the access is a random type or a fast page type, the latency function will first call the get mem real bank, get mem bank, get mem channel, and is latched functions. The latency function will return a value after these functions have been called. The latency function will detect if the access is the initial memory access of the simulation (bus timer = 0) once the access type has been determined. If this is the case, the latency function will be disabled. If this is the case, the start time can simply be set to "now," and the access type can only be random (the initial access in a simulation must be random access). The latched row/page of all memory banks is set to row 0 when the mem t data structure is initialised, which means we must override

An access control method verifies whether local memory holds a valid copy of the data after it is allocated. If this is not the case, the mechanism uses an access policy to obtain up-to-date information or additional access permissions. The validity of a copy may be determined by the type of access; for example, duplicated copies are valid for reading but not for writing in most protocols [19]–[21]. Many researchers have explored the ways to restructure The Legacy C++ Program [22]–[26]. The access policy includes both the coherence protocol and the global allocation policy, which specify which node a request is forwarded to and how it is processed. Memory access policy for shared data objects residing locally and remotely is shown in Figure 6. This policy employs both messaging and access constraints. The policy may send signals telling other sites to invalidate their copies before permitting the local node to write its copy.

The RTL schematic for the cache memory compression block is shown in Figure 7. It is a design abstraction that represents the circuit in terms of digital signals flowing between hardware registers and is used in the design of integrated circuits.

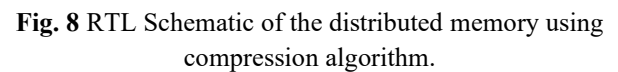
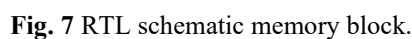


Table 1 Power consumption and junction temperature of the Proposed Shared Distributed Memory.

On-chip total Power	0.0082W
Junction Temperature	25.4 °C

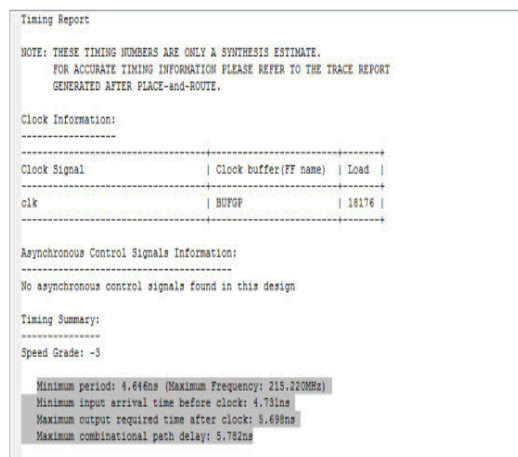


Fig. 10 Timing summary.

4. Conclusion

A Scientists are now able to use high-performance computers as a viable alternative to the more out-of-date experiential and theoretical approaches. While attempting to explain the language used to create distributed memory systems, this part is included. Single-site networks are used for this memory controller. IP address of the memory controller node was utilised to establish a connection between the client machine and the memory controller node. A message on the output terminal of the memory controller verifies the connection. If all of the client processes are running on the same system, the memory controller can be connected to the local host. As a large-scale DSM system, future efforts can be prepared to improve algorithm strategies in order to expand the number of nodes. All will be able to access shared data items at the same time. To improve distributed shared memory management, this work can be improved to optimise memory controller tasks and design difficulties. It has the ability to handle an increasing number of processors at once, higher execution speed, and security.

In order to decrease the energy used by the system for the refresh operations themselves as well as the energy used during the refresh activities themselves, further scheduling techniques can be used. Also, proposed distributed memory can be useful to restructure the input legacy C++ programming system.

Acknowledgment

Author thanks Dept. of Computer Science and Engineering, Sasi Institute of Technology and Engineering,

Tadepalligudem for giving us opportunity to work under High Performance computing lab.

5. References and Footnotes

Ethics approval

This article does not contain any studies with human or animal subjects.

Conflict of Interest

The authors declare that they have no conflict of interest.

Data Availability Statement

The data cannot be made publicly available upon publication because no suitable repository exists for hosting data in this field of study. The data that support the findings of this study are available upon reasonable request from the authors.

Funding No funding received to carry out this research work.

References

- [1] Ahmed, M.R., Zheng, H., Mukherjee, P., Ketkar, M.C. and Yang, J., 2021, April. Mining message flows from system-on-chip execution traces. In 2021 22nd international symposium on quality electronic design (ISQED) (pp. 374-380). IEEE.
- [2] Shan, L. and Sun, H., 2021, May. Distributed collaborative simulation middleware based on reflective memory network. In 2021 IEEE 24th international conference on computer supported cooperative work in design (CSCWD) (pp. 274-279). IEEE.
- [3] Cao, Y., Mukherjee, P., Ketkar, M., Yang, J. and Zheng, H., 2020, March. Mining message flows using recurrent neural networks for system-on-chip designs. In 2020 21st International Symposium on Quality Electronic Design (ISQED) (pp. 389-394). IEEE.
- [4] Adetomi, A., Enemali, G. and Arslan, T., 2017, September. Towards an efficient intellectual property protection in dynamically reconfigurable FPGAs. In 2017 Seventh International Conference on Emerging Security Technologies (EST) (pp. 150-156). IEEE.
- [5] Wen, H. and Zhang, W., 2021. Cache Leakage Reduction Techniques for Hybrid SPM-Cache Architectures. *Journal of Circuits, Systems and Computers*, 30(01), p.2150008.
- [6] Kwon, S.J., Kim, S.H., Kim, H.J. and Kim, J.S., 2017, January. LZ4m: A fast compression algorithm for in-memory data. In 2017 IEEE International Conference on Consumer Electronics (ICCE) (pp. 420-423). IEEE.
- [7] Guo, Y., Hua, Y. and Zuo, P., 2018, March. DFPC: A dynamic frequent pattern compression scheme in NVM-based main memory. In 2018 Design,

- Automation & Test in Europe Conference & Exhibition (DATE) (pp. 1622-1627). IEEE.
- [8] Choukse, E., Erez, M. and Alameldeen, A.R., 2018, October. Compresso: Pragmatic main memory compression. In 2018 51st Annual IEEE/ACM International Symposium on Microarchitecture (MICRO) (pp. 546-558). IEEE.
- [9] Lahiry, A. and Kaeli, D., 2017, November. Dual dictionary compression for the last level cache. In 2017 IEEE International Conference on Computer Design (ICCD) (pp. 353-360). IEEE.
- [10] Rumyantsev, A., Krupkina, T., Losev, V. and Maksimov, A., 2020, January. Development of a Measurement System-on-Chip and Simulation on FPGA. In 2020 IEEE Conference of Russian Young Researchers in Electrical and Electronic Engineering (EIConRus) (pp. 1851-1854). IEEE.
- [11] Frolova, P.I., Chochaev, R.Z., Ivanova, G.A. and Gavrilov, S.V., 2020, January. Delay matrix based timing-driven placement for reconfigurable systems-on-chip. In 2020 IEEE Conference of Russian Young Researchers in Electrical and Electronic Engineering (EIConRus) (pp. 1799-1803). IEEE.
- [12] Jain, A., Soner, S. and Holkar, A., 2010, October. "Reverse engineering": Extracting information from C++ code. In 2010 2nd International Conference on Software Technology and Engineering (Vol. 1, pp. V1-154). IEEE.
- [13] Strobel, M., Radetzki, M.: Design-time memory subsystem optimization for lowpower multi-core embedded systems. In: 2019 IEEE 13th International Symposium on Embedded Multicore/Many-core Systems-on-Chip (MCSoc), pp. 347–353 (2019). DOI 10.1109/MCSoc.2019.00056.
- [14] H. Fan et al., "High-Precision Adaptive Slope Compensation Circuit for System-on-Chip Power Management," 2019 IEEE 38th International Performance Computing and Communications Conference (IPCCC), 2019, pp. 1-2.
- [15] N. Arun Vignesh, Ravi Kumar, R. Rajarajan, S. Kanithan, E. Sathish Kumar, Asisa Kumar Panigrahy, and Selvakumar Periyasamy, "Silicon Wearable Body Area Antenna for Speech-Enhanced IoT and Nanomedical Applications", Journal of Nanomaterials, vol. 2022, Article ID 2842861, 9 pages, 2022. <https://doi.org/10.1155/2022/2842861>
- [16] Devi, M.P., Ravanan, V., Kanithan, S., N.A.Vignesh, "Performance Evaluation of FinFET Device Under Nanometer Regime for Ultra-low Power Applications", Silicon (2022). <https://doi.org/10.1007/s12633-022-01772-x>
- [17] D. Chen, J. Edstrom, Y. Gong, P. Gao, L. Yang, M. McCourt, J. Wang and N. Gong, "Viewer-Aware Intelligent Efficient Mobile Video Embedded Memory", IEEE Transactions on Very Large Scale Integration (VLSI) Systems, vol. 26, no. 4, pp. 684-696, 2018.
- [18] Calinescu, G., Fu, C., Li, M., Wang, K. and Xue, C.J., 2018. Energy optimal task scheduling with normally-off local memory and sleep-aware shared memory with access conflict. IEEE Transactions on Computers, 67(8), pp.1121-1135.
- [19] Arun Jayakar, S., Rajesh, T., Vignesh, N.A. and Kanithan, S., 2022. Performance Analysis of Doping Less Nanotube Tunnel Field Effect Transistor for High Speed Applications. Silicon, 14(12), pp.7297-7304.
- [20] Z. Zhao, Y. Sheng, M. Zhu and J. Wang, "A Memory-Efficient Approach to the Scalability of Recommender System With Hit Improvement", IEEE Access, vol. 6, pp. 67070-67081, 2018.
- [21] Deepa, R., Devi, M.P., Vignesh, N.A. and Kanithan, S., 2022. Implementation and performance evaluation of ferroelectric negative capacitance FET. Silicon, 14(5), pp.2409-2419.
- [22] Handigund, S.M. and Kulkarni, R.N., 2010. An Ameliorated Methodology for the design of Object Structures from legacy 'C' Program. International Journal of Computer Applications, 975, p.8887.
- [23] Dr. Shivanand M. Handigund, Dr. Rajkumar N. Kulkarni, "An Ameliorated Methodology for the Abstraction and Minimization of Functional Dependencies of legacy 'C' Program Elements ". International Journal of Computer Applications (0975 – 8887) Volume 16– No.3, February 2011.
- [24] Dr. R.N. Kulkarni, Venkata Sandeep Edara, "A Novel Approach to Restructure The Legacy C++ Program", Journal of Huazhong University of Science and Technology, Volume: 50 Issue: 05, 2021, ISSN: 1671-4512.
- [25] Dr. R.N. Kulkarni, P.Pani Rama Prasad, "Abstraction of UML Class Diagram from the Input Java Program", Int. J. Advanced Networking and Applications, Volume: 12 Issue: 04 Pages: 4644-4649(2021) ISSN: 0975-0290.
- [26] R.N.Kulkarni and S.Shenaz Begum, "Abstraction of 'C' Program from Algorithm", Springer Nature Singapore Pte Ltd. 2021, Research in Intelligent and Computing in Engineering, Advances in Intelligent Systems and Computing 1254.
- [27] Nair, K. S. S. . (2023). Rapidly Convergent Series from Positive Term Series. International Journal on Recent and Innovation Trends in Computing and Communication, 11(3), 79–86. <https://doi.org/10.17762/ijritcc.v11i3.6204>
- [28] Ana Silva, Deep Learning Approaches for Computer Vision in Autonomous Vehicles, Machine Learning Applications Conference Proceedings, Vol 1 2021.



Machine Learning-Based Recommendations and Classification System for Unstructured Resume Documents

Channabasamma^{1*}, Yeresime Suresh²

¹ Department of Computer Science and Engineering, Gokaraju Rangaraju Institute of Engineering and Technology, Hyderabad 500090, India

² Department of Computer Science and Engineering, Ballari Institute of Technology and Management, "Jnana Gangotri" Campus, Ballari 583104, India

Corresponding Author Email: channu.ar@gmail.com

<https://doi.org/10.18280/ria.370311>

ABSTRACT

Received: 2 February 2023

Accepted: 25 March 2023

Keywords:

categorization, classification, data extraction, recognition, recommendation, resume, screening, skills

With the burgeoning growth of the job market and a surge in applications, the processes of job recommendation and candidate selection have become complex and labor-intensive. The advent of new technologies such as machine learning has automated these processes, yet the unstructured nature of resumes, often in PDF format, necessitates laborious data extraction for efficient skill-based candidate screening and categorization. Ineffective recruitment can result from mismatched skills. The system proposed in this study aims to address these challenges by automatically fetching and categorizing resumes, extracting critical information, and utilizing job descriptions for candidate selection and recommendations. Unstructured data from PDF documents is extracted using a PDF reader, and machine learning algorithms, specifically logistic regression and Gaussian Naïve Bayes, are employed for generating recommendations. In an innovative approach, this system not only classifies resumes but also recommends updates or rewrites. Performance of the proposed system is evaluated in terms of classification accuracy and the effectiveness of update recommendations, and results are compared with alternative models. This research represents a significant advancement in the application of machine learning to the automation of job recommendation and candidate selection processes.

1. INTRODUCTION

Resume screening represents a crucial step within a company's hiring process, permitting evaluation of potential employees prior to their recruitment. Furthermore, it facilitates the preparation of candidates for comprehensive examination [1]. The ultimate objective of resume screening is to identify suitable individuals for job vacancies, while concurrently preventing the company from overlooking exceptional candidates [1]. However, manual screening of resumes is a time-consuming and complex process, particularly given that each job vacancy typically attracts hundreds of resumes [2].

Although resumes generally adhere to a standard format, the specific skills and qualifications demanded by each role may necessitate varying levels of specificity in their creation [3]. The majority of contemporary job applications require electronic resumes. However, the development of resume screening approaches based on modern methodologies, knowledge discovery, and social networks remains in its infancy, with substantial research required prior to the implementation of commercial systems [4].

One notable limitation of resume screening is its reliance on candidate-provided content entered into job portals or electronic forms during the job application process. While job seekers may possess unique attributes that distinguish them, discrepancies may arise if the data entered does not match the content of the candidate's resume. At its most effective, resume screening could yield a list of individuals with similar

resumes, and vice versa, but this could introduce significant bias and inaccuracies particularly in the case of numerous unsupervised searches [5]. Therefore, it is imperative that uploaded resume documents are screened for an effective job-matching profile. Consequently, the extraction of useful data from these documents is essential. In this context, Natural Language Processing (NLP) can be employed to extract job-matching attributes from the resume document [6]. The extracted attribute values can then be compared to the skill set requirements for recruitment, facilitating the identification of relevant jobs with commensurate salaries.

What is Natural Language Processing?

Natural Language Processing (NLP) is a process of breaking down the given input into component parts and interpreting their meaning. The process includes converting the input into a form that a computer can understand [7]. NLP can be employed to extract high-quality information from documents and queries by developing the computer's ability to understand and communicate with humans in the human language.

The rising use of social media applications such as Facebook, LinkedIn, Twitter etc. for job-seekers' screening activities is likely to propel the growth of the NLP market. NLP being a demanded technique is used by researchers in extracting the most relevant information, identifying negative character traits, and more. In the recruitment industry resumes

need to be screened, and the process requires to be automated, and NLP is one among the appropriate method to interpret the resume [8]. Even well-written resumes will never be 100% successful without proper interpretation or extraction. The research is motivated by several factors, including the exponential growth in the job market and the subsequent increase in the number of job applications, which has made the recruitment process more complex and time-consuming. Additionally, the unstructured data in the form of pdf resumes has made it even more challenging to extract structured information to automate the screening process [9].

The proposed system is motivated by the need to ease the recruitment process by providing an automated solution to screen candidates, categorize them based on their skills, and recommend job updates or rewrites. This will help recruiters to efficiently and accurately identify the most suitable candidates for a job.

Furthermore, the proposed system is also motivated by the need to reduce the mismatch between candidate skills and the skills demanded by industries, which can lead to ineffectiveness in all phases of the recruitment process. The system aims to ensure that the skills of the candidates are aligned with the skills required by the industry, resulting in more effective job candidate selections.

Overall, the research is motivated by the need to improve the recruitment process by providing an automated and accurate system to screen candidates, categorize them, and provide job recommendations. The proposed system is expected to improve the efficiency and effectiveness of the recruitment process, resulting in more successful job placements.

This paper utilizes NLP for effective data extraction from resume documents. NLP helps in analyzing every aspect of a resume and helps not only to screen the appropriate resume but also helps in recommending candidates to update or rewrite the resume if it is not on par with a standard resume. The satisfactory resumes are then classified according to the job description.

2. LITERATURE SURVEY

This section emphasizes mainly on the recent research carried out on resume classification and recommendations.

An automated resume ranking system, or screening system, is a type of bias identification mechanism that uses natural language processing (NLP) to produce human-readable ratings of an individual's educational, professional, and personal attributes that have been analyzed using a search query [10].

The resume ranking system relies on human contexts such as job titles, company names, and geography. This method measures individual attributes such as how the individual is perceived and how it is interpreted by others [11]. The Resume ranking system also known as job role assessment, is a method of matching users to positions using language patterns from resumes and job applications.

Manual assessment or screening is somewhat biased because it relies heavily on how a person perceives or interprets the resume, whereas an automated resume screening system with a machine learning approach will remove the bias in screening the resumes. NLP (Natural Language Processing) can be utilized to match job applicants with job openings based on a keyword [12].

Tejaswini et al. developed a resume ranking system [13],

which used the KNN approach to rank and pick resumes from the available resume dataset. The best candidates can be identified using content-based suggestion, which selects and ranks a large number of Curriculum Vitae (CV) based on job descriptions and uses cosine similarity to identify the CVs that are most similar to the provided job description. According to experimental findings, the proposed system performs with an average text parsing accuracy of 85% and a ranking accuracy of 92%.

A job recommendation system was developed by Mishra and Rathi using the enhanced DSSM (Deep Semantic Structure and modelling) [14]. The Deep Semantic Structure Modelling (DSSM) system employs semantic modelling of sparse data to increase system effectiveness by representing job descriptions and skill entities as character trigrams. The results of the DSSM model using two distinct datasets (Naukari.com and CareerBuilder.com) are compared, and the results of the proposed system are found to be better. Xavier initializer and Adam optimizer were used in the proposed approach.

In the paper titled "Text Analysis for Job Matching Quality Improvement" [15], the authors proposed an approach for the recruitment or staffing agency to match the quality of candidates to the job. Key factors like commute time, job location, job type, hourly rates, and skill set are matched for improved quality in identifying the candidate. Using a text-mining technique, the authors carefully examined text data that had been written by recruiters at a hiring agency in order to investigate these qualities. The authors were able to extract both positive and negative keywords that affected the matching result.

A content-based recommendation engine is developed, it finds the best possibilities for a user by matching their interests and talents to the requirements of a job ad. To provide the required suggestion, the recommended engine makes use of various text filters and feature similarity algorithms. Similarity algorithms use topic models and the bag of n-grams as parts of feature vectors [16].

Conventional job recommendation systems work on classifying the resume based on the data stored as tables or CSV or Excel files, collected through the job application portal or through web forms in the resume [17]. The proposed system extracts or scrapes the data from the resumes that are pdf files and the proposed system along with classification also recommends the resume for updates or rewriting by classifying the resume as unsatisfactory resumes. All the resumes are verified for their quality, and if the resume does not convey any clear information, then the resume is classified as unsatisfactory and other resumes that clearly states the skill set of the candidate are classified as satisfactory.

3. METHODOLOGY

The aim of the proposed system is to extract the data from the pdf files and to classify the resume as satisfactory and unsatisfactory resumes, then recommend rewriting to further strengthen the unsatisfactory resume and classify the satisfactory resumes based on the skill set.

3.1 Overview of the proposed system

The overview of the proposed system is depicted in Figure 1. The system can be fragmented into three major modules.

i) To Extract or scrape the essential data from the resume, that is in pdf format:

For this task ‘PyPDF’ package is used. PyPDF is a Python library that allows for the manipulation of PDF files. PyPDF provides functionality for extracting information from PDF documents by analyzing their internal structure.

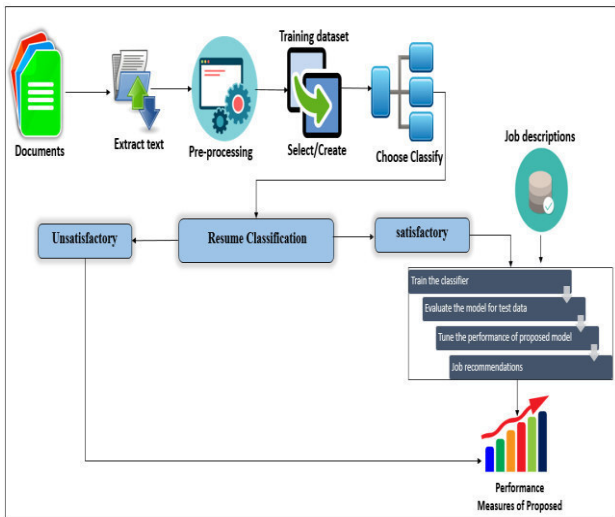


Figure 1. Resume recommendation and classification system overview

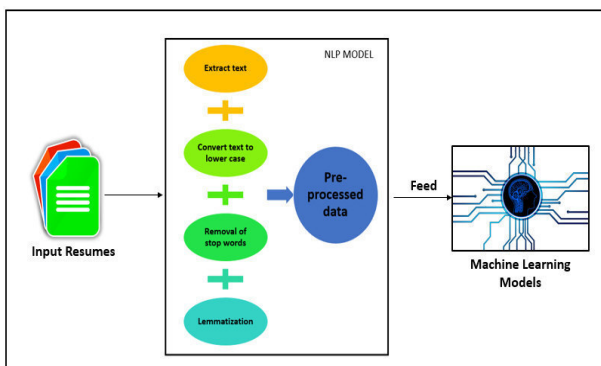


Figure 2. NLP model

To extract information from a PDF document using PyPDF, one would typically follow the following steps:

1. Open the PDF file using PyPDF.
2. Access the desired page or pages within the document.
3. Extract text or other content from the page(s).
4. Close the PDF file.

To accomplish these steps, PyPDF provides a variety of operational codes that can be used to interact with PDF documents. Some of the key operational codes for extracting information from PDF documents using PyPDF include:

- **PdfFileReader:** A class that represents a PDF file and provides functionality for reading and parsing the file.
- **getPage:** A method of the **PdfFileReader** class that allows for the selection of a specific page within the document.
- **extractText:** A method of the **PdfFileReader** class that extracts text from a selected page.
- **numPages:** A property of the **PdfFileReader** class that provides the number of pages in the PDF document.

By using these operational codes, PyPDF enables users to extract information from PDF documents and perform a variety of other operations on the files.

The first step is to install the 'PyPDF' package, once the package is installed, the next step is to import the required libraries and open the PDF file using the 'PyPDF' package.

Next, we need to extract the text from the PDF file. We can do this by iterating through each page of the PDF file and extracting the text using the 'extractText()' function.

After the text is extracted, it may contain unwanted characters or formatting, which needs to be cleaned. Pre-processing can be done to clean the extracted text. This may include removing special characters, removing stop words, and tokenizing the text.

In conclusion, the 'PyPDF' package is a useful tool to extract essential data from resumes in PDF format. Once the text is extracted, it can be further processed to clean and refine the data, making it useful for various applications, including candidate screening and job matching.

ii) To classify the resume into satisfactory and unsatisfactory resumes:

The data extracted from the pdf is pre-processed so that unnecessary data that does not impact the result is removed. The important function of this pre-processing is to extract only useful data. NLP (Natural Language Processing) is utilized in pre-processing. The process of pre-processing using NLP is depicted in Figure 2 and the algorithm is discussed as follows:

Algorithm for Pre-processing the data extracted using **PyPDF**

Input: Text extracted from a PDF document using the **PyPDF** package

Output: Pre-processed text that is cleaned and refined for further use

1. Remove special characters from the text using regular expressions
 - Initialize a regular expression pattern to match all non-alphanumeric characters
 - Use the **re.sub()** function to replace all matches with a space character
2. Convert the text to lowercase
 - Use the **lower()** method to convert all characters to lowercase
3. Remove stop words from the text using the **nlTK** package
 - Initialize a set of stop words using the **stopwords.words('english')** method
 - Tokenize the text using the **word_tokenize()** function from the **nlTK** package
 - Use a list comprehension to remove all stop words from the tokenized text
4. Tokenize the text using the **nlTK** package
 - Use the **word_tokenize()** function to split the text into individual tokens
5. Perform stemming using the Porter Stemmer algorithm from the **nlTK** package
 - Initialize a **PorterStemmer()** object
 - Use a list comprehension to apply the stemming algorithm to each token in the tokenized text
6. Return the pre-processed text as a list of stemmed tokens

Further, the classification is performed using machine learning models. Four benchmark models namely logistic regression [18], Gaussian Naïve Bayes [19], SVM, and Decision tree Classifier [20] are trained using a set of satisfactory and unsatisfactory resumes. Once the model is trained, it is used for the classification of the resumes as satisfactory and unsatisfactory. Satisfactory resumes are considered for job recommendations and unsatisfactory resumes are recommended for upgrade or rewrite. The satisfaction of a training structure in machine learning approaches can be judged based on several criteria, including:

1. Accuracy: This measure how well the model predicts the correct class labels for the test data. Higher accuracy indicates better performance.
2. Precision: This is the ratio of true positive predictions to the total number of positive predictions. It measures the ability of the model to identify true positives and avoid false positives.
3. Recall: This is the ratio of true positive predictions to the total number of actual positive instances in the test data. It measures the ability of the model to identify all positive instances, including those that might be missed.
4. F1 Score: This is the harmonic mean of precision and recall. It provides a balanced measure of both metrics and is a good indicator of overall performance.

The results of the models are recorded for accuracy, Precision, Recall, and F1Score and later compared in the results section.

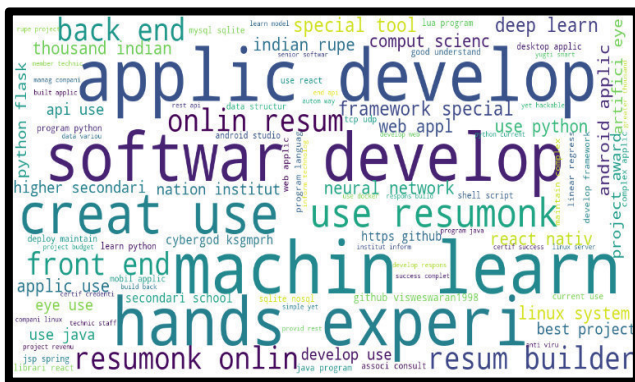


Figure 3. Word cloud generated for an unsatisfactory resume

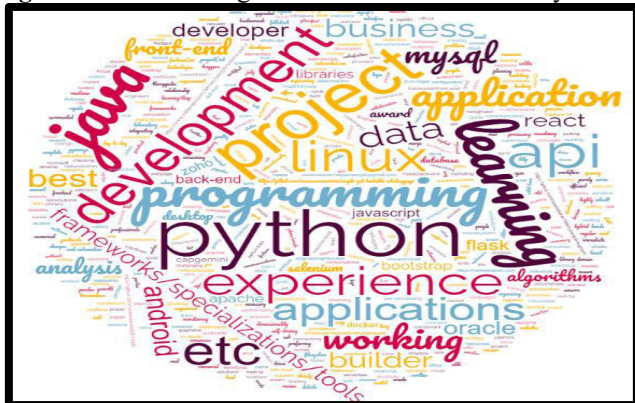


Figure 4. Word cloud generated for a satisfactory resume

The output from the NLP model is fed to the machine learning models. To better understand the standard of the resume, a word cloud is generated. Word cloud is a way of visualizing content or data. The most frequently used words in the resume will be generated as a word cloud for a better

understanding of what skill set the candidate has. Figure 3 shows the word cloud of an unsatisfactory resume where the recruiter could not come to a conclusion on the expertise of the candidate, whereas the word cloud depicted in Figure 4 clearly showcases the expertise of the applicant.

- iii) Classify satisfactory resumes for job recommendations based on skill set:

The skill set of the satisfactory resumes extracted using NLP is stored and the distinct skills are identified. For instance, the skillset required for Business analytics is extracted from the set of business analytics resumes as ['Tableau', 'Pandas', 'Artificial Intelligence', 'Pyspark', 'IBM Watson', 'Sklearn', 'R programming', 'Keras', 'Map Reduce', 'Modelling', 'Regression', 'Dundas BI', 'Patterns', 'Data Mining', 'Plotly', 'Text Mining', 'Oops', 'Deep Learning', 'Web Analytics', 'Time Series', 'Regression', 'Tensorflow', 'Azure', 'Linear Regression', 'Logistic Regression', 'Decision Tree', 'Random Forest', 'Data Structure', 'Keras']. The skillset likely grows with the increase in the number of resumes used for training. As more resumes for a specific job role are used for training the model becomes more effective. The resumes are categorized based on the extracted data for each job description and the distribution of the categories is visualized in the results section. The job recommendations are done based on the category of the resume. The job description or requirement is used as the input and the appropriate candidate's resumes are fetched as recommendations based on the extracted info. The performance of the models is measured using accuracy, where accuracy is the number of correct predictions among the total predictions made, it is calculated using Eq. (1) as below.

$$\text{Accuracy} = \frac{\text{Number of predictions made correctly}}{\text{total number of predictions made}} \quad (1)$$

The percentage of accurate predictions made by the model is measured by accuracy. Accuracy alone might not be sufficient in cases with unbalanced data, where the proportion of instances in each class differs dramatically.

What percentage of the positive forecasts is actually positive, according to a criterion called precision? It shows how well the model is determining a class's true positive values.

What percentage of all the real positive records are accurately identified, according to recall? It shows how successfully a model can locate each instance that belongs to a class. Recall is calculated for each class in multiclass classification tasks and then averaged using either a macro-average or a micro-average.

Recall is a metric used to measure the ability of a model to identify all relevant instances of a particular class. Macro-average and micro-average are two ways to calculate the average recall score across all the classes in a multiclass classification task.

In macro-average recall, the recall score for each class is first calculated separately, and then the average of those scores is taken. This approach treats each class equally, regardless of its size or frequency in the dataset.

On the other hand, in micro-average recall, the recall score for each class is calculated and then averaged, taking into account the size or frequency of each class. This approach

gives more weight to classes that have more instances in the dataset.

The main difference between macro and micro-averaging is that macro-averaging gives equal weight to each class, while micro-averaging gives more weight to larger classes. Therefore, if there is a class imbalance, micro-average recall would be more appropriate than macro-average recall. In the proposed system, recall is calculated using macro average.

The weighted harmonic mean of precision and recall is known as the F-Score, and a score of 1 denotes the highest possible precision and recall values. It is a helpful indicator for assessing the model's overall performance.

4. RESULTS AND DISCUSSIONS

4.1 Dataset exploration

Two datasets are used in the proposed approach, one for classifying satisfactory and unsatisfactory resumes. One for categorization of the resumes as per the job description. A total of 150 resumes are used for classifying satisfactory and unsatisfactory resumes, 75 for each category. A total of 500 resumes are used for training the model for job categorization with 141 job descriptions. For every job description, a set of skill sets is stated that has around 30 to 50 keywords. The skill set generated by the model is compared with a reputed job portal website <https://www.hireitpeople.com/resume-database/> and found that the skillset fetched using the trained models is above par as per the requirement.

4.2 Model evaluation

The resumes are segregated as satisfactory and unsatisfactory and the accuracy of the models is compared. Logistic regression and Gaussian Naive Bayes perform better among the four models. Table 1 shows the accuracy attained among the models.

The frequently used words in the resume will be extracted for a better understanding of what skill set the person has. The algorithm used to find the frequency distribution of words is given as follows.

- 1. Read the sample resume file and store it as a string variable.
- 2. Clean the text data by removing any non-alphanumeric characters (punctuation, special characters, etc.), and convert all text to lowercase.
- 3. Tokenize the cleaned text into individual words.
- 4. Create an empty dictionary to store the frequency count of each word.
- 5. Loop through each word in the list of tokenized words:
 - a. If the word is not already in the dictionary, add it with a value of 1.
 - b. If the word is already in the dictionary, increment its value by 1.
- 6. Sort the dictionary by value in descending order to get a list of the most frequently used words.
- 7. Output the list of words and their frequency count.

Most frequent words are plotted as a frequency distribution graph for a sample resume as depicted in Figure 5.

The resumes are categorized based on the job categories and once the job description is given as the input, the resumes applicable for the job are fetched and given. The number of

resumes belonging to the top 30 categories is displayed in Figure 6 as a bar graph.

Table 1. Accuracy of the models

S. No	Model Name	Accuracy
1	Logistic Regression	0.9763
2	Gaussian Naive Bayes	0.9516
3	SVM	0.333333
4	Decision Tree Classifier	0.8943

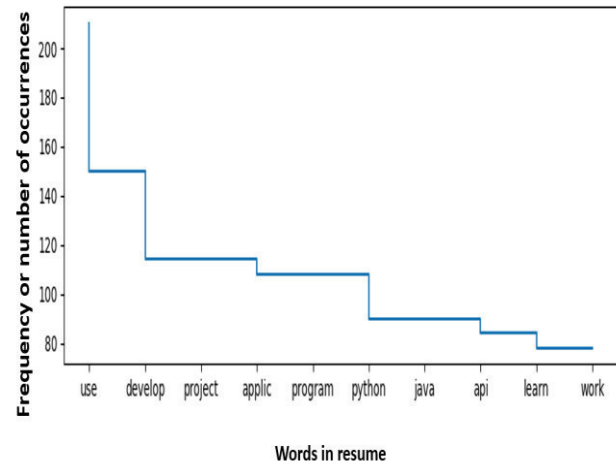


Figure 5. Frequency distributions of words in a sample resume

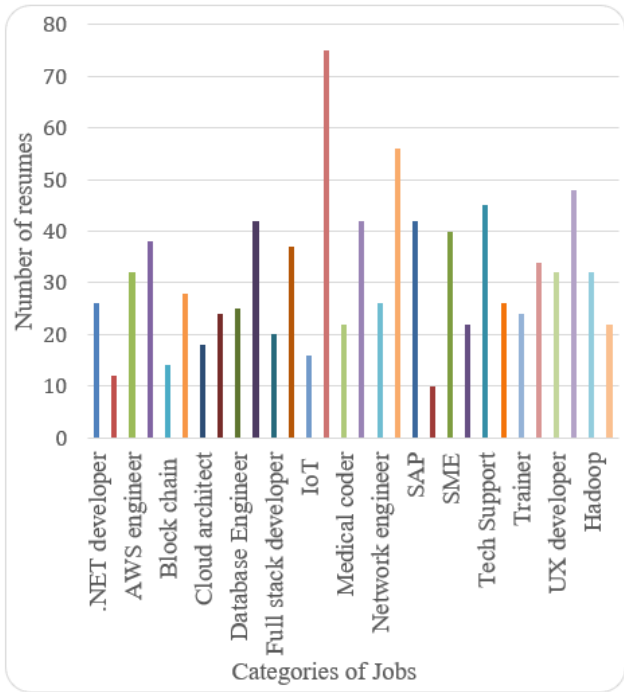


Figure 6. Resume categories with their numbers

Several resumes fall under multiple categories for example a same resume is applicable for backend developer and also for database engineers, similarly the same resume that is categorized under subject matter expert (SME) is applicable under other categories also. Hence there is an overlap in several categories. The accuracy of models was tested with a different set of resumes. The accuracy measure is depicted in

Figure 7. As the number of resumes increase during training per category the accuracy also varied. For instance, with less number of resumes logistic regression performed well, when the number of resumes increased per category, Gaussian Naive Bayes performed well. The category of PHP developer was considered for reference and a total of 30 resumes were used for training and 15 resumes were tested for accuracy. Thus logistic regression model can be utilized when less number of resumes are there and Gaussian Naive Bayes can be utilized when more resumes are available for training the data.

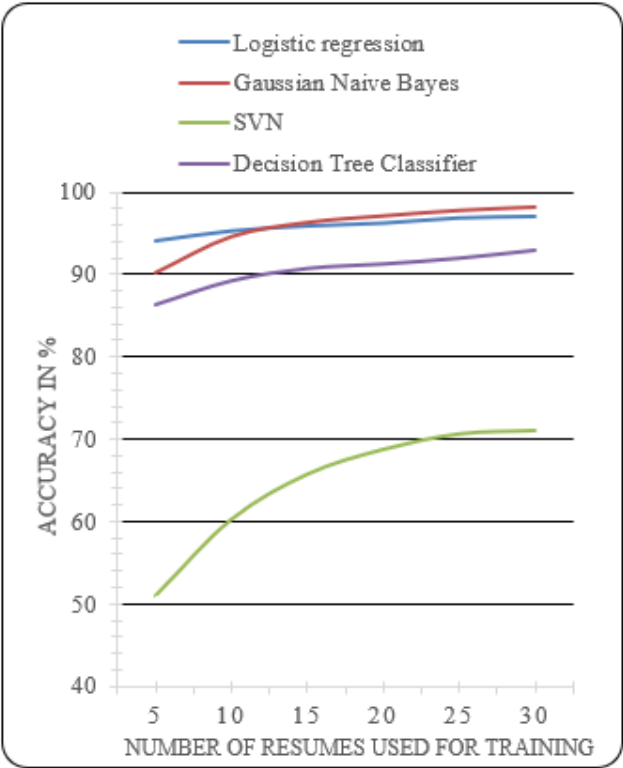


Figure 7. The accuracy measure

From the table, it is observed that the accuracy of models SVM and Decision Tree Classifier is lower than the accuracy of models Logistic Regression and Gaussian Naive Bayes.

The reason for the lower accuracy of model SVM could be because SVM is a linear classifier that works well when there is a clear linear separation between the classes. If the classes are not linearly separable, SVM may not perform well. In the context of resume classification, as the features are not linearly separable, such as there are overlapping skills or qualifications between job categories, hence SVM suffers to achieve the accuracy and it is not be the best model.

The reason for the lower accuracy of model Decision Tree Classifier could be because decision trees are prone to overfitting when the tree depth is too large or when there are too many features. Overfitting occurs when the model fits the training data too well, and as a result, it fails to generalize to new data. In the context of resume classification, possibility of the decision tree model for overfitting the training data is high, hence it is not able to classify new resumes accurately.

As discussed earlier accuracy calculation alone does not prove the system to be effective the other metrics precision, recall and F-measure were also measured and depicted as in the following Table 2 and also as a graph in Figure 8.

Table 2. Performance measures of the models

S. No	Model Name	Precision	Recall	F-Measure
1	Logistic Regression	1.0	0.99	0.99
2	Gaussian Naive Bayes	0.99	0.97	0.97
3	SVM	0.49	0.35	0.37
4	Decision Tree Classifier	0.96	0.91	0.92

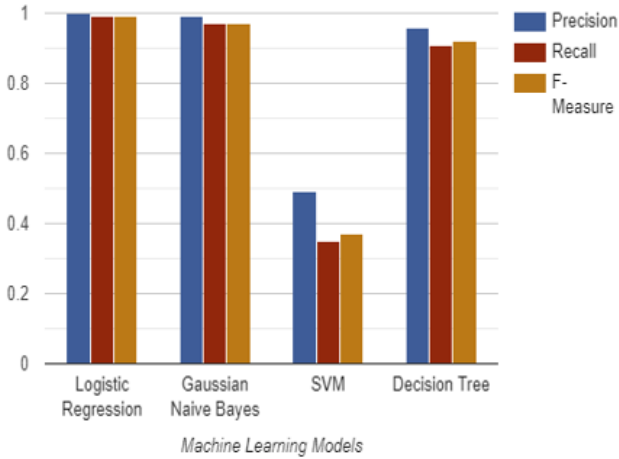


Figure 8. Performance measures of the ML models

The performance of the models remains quite similar for all the job categories. With a resume that can be applicable for multiple jobs and with the increase in the number of applicants with multiple skill sets, the process of resume screening will lead to high complexity.

5. CONCLUSION AND FUTURE SCOPE

The proposed system was able to extract the skill sets of a candidate from the resume which is in the pdf format using NLP. The NLP extracts the skillsets precisely which is evaluated for the standard resume. The machine learning models to successfully classify the satisfactory and unsatisfactory resume are implemented and the accuracy of the models were compared. Categorization of resumes for various job categories is also realized and it is observed that Gaussian Naïve Bayes and logistic regression perform well over the other two models.

The Proposed system would ease the resume screening process by reducing and recommending unsatisfactory resumes from the total resumes available. The resume categorization is also performed so that the screening will bring only the appropriate resume for the job description searched.

The system can be further enhanced by splitting the resume into sections and exactly predicting the sections of the resume to be strengthened so that the resume gains more visibility among the recruiters and falls under the satisfactory category in the next screening.

Multilingual support: The proposed system is currently designed for resumes in English. Multilingual support can be added to enable screening of resumes in different languages.

REFERENCES

- [1] Villeda, M., McCamey, R., Essien, E., Amadi, C. (2019). Use of social networking sites for recruiting and selecting in the hiring process. *International business research*, 12(3): 66-78. <http://dx.doi.org/10.5539/ibr.v12n3p66>
- [2] Roy, P.K., Chowdhary, S.S., Bhatia, R. (2020). A Machine Learning approach for automation of Resume Recommendation system. *Procedia Computer Science*, 167: 2318-2327. <https://doi.org/10.1016/j.procs.2020.03.284>
- [3] Alamelu, M., Kumar, D.S., Sanjana, R., Sree, J.S., Devi, A.S., Kavitha, D. (2021). Resume validation and filtration using natural language processing. In 2021 10th International Conference on Internet of Everything, Microwave Engineering, Communication and Networks (IEMECON), Jaipur, India, pp. 1-5. <https://doi.org/10.1109/IEMECON53809.2021.9689075>
- [4] Ali, I., Mughal, N., Khand, Z.H., Ahmed, J., Mujtaba, G. (2022). Resume classification system using natural language processing and machine learning techniques. *Mehran University Research Journal of Engineering & Technology*, 41(1): 65-79. <http://dx.doi.org/10.22581/muet1982.2201.07>
- [5] Poovizhi, P., Ezhilarasi, K., Gayathri, G., Megala, R., Anisha, D. (2022). Automatic scraping of employment record using machine learning—An assistance for the recruiter. In *Smart Data Intelligence*, pp. 561-577. https://doi.org/10.1007/978-981-19-3311-0_4
- [6] Nimbekar, R., Patil, Y., Prabhu, R., Mulla, S. (2019). Automated resume evaluation system using NLP. In 2019 International Conference on Advances in Computing, Communication and Control (ICAC3), Mumbai, India, pp. 1-4. <https://doi.org/10.1109/ICAC347590.2019.9036842>
- [7] Liddy, E. D. (2001). Natural language processing. <https://surface.syr.edu/istpub/63/>.
- [8] Sinha, A.K., Akhtar, A.K., Kumar, A. (2021). Resume screening using natural language processing and machine learning: A systematic review. *Machine Learning and Information Processing*, 207-214.
- [9] Goyal, U., Negi, A., Adhikari, A., Gupta, S.C., Choudhury, T. (2021). Resume data extraction using NLP. In *Innovations in Cyber Physical Systems*, pp. 465-474. https://doi.org/10.1007/978-981-16-4149-7_41
- [10] Ransing, R., Mohan, A., Emberi, N.B., Mahavarkar, K. (2021). Screening and Ranking Resumes using Stacked Model. In 2021 5th International Conference on Electrical, Electronics, Communication, Computer Technologies and Optimization Techniques (ICEECOT), Mysuru, India, pp. 643-648. <https://doi.org/10.1109/ICEECOT52851.2021.9707977>
- [11] Bhor, S., Gupta, V., Nair, V., Shinde, H., Kulkarni, M.S. (2021). Resume parser using natural language processing techniques. *International Journal of Research in Engineering and Science (IJRES)*, 9(6): 01-06.
- [12] Kadam, R., Suhas, G., Mukri, U., Khandare, S. (2022). NLP-Based Resume Screening and Job Recruitment Portal. In *Data Intelligence and Cognitive Informatics*, pp. 1-21. Springer, Singapore. http://dx.doi.org/10.1007/978-981-16-6460-1_1
- [13] Tejaswini, K., Umadevi, V., Kadiwal, S.M., Revanna, S. (2022). Design and development of machine learning based resume ranking system. *Global Transitions Proceedings* 3(2): 371-375. <https://doi.org/10.1016/j.gltp.2021.10.002>
- [14] Mishra, R., Rathi, S. (2022). Enhanced DSSM (deep semantic structure modelling) technique for job recommendation. *Journal of King Saud University-Computer and Information Sciences*, 34(9): 7790-7802. <https://doi.org/10.1016/j.jksuci.2021.07.018>
- [15] Kino, Y., Kuroki, H., Machida, T., Furuya, N., Takano, K. (2017). Text analysis for job matching quality improvement. *Procedia computer science*, 112: 1523-1530. <https://doi.org/10.1016/j.procs.2017.08.054>
- [16] Kumar, N., Gupta, M., Sharma, D., Ofori, I. (2022). Technical job recommendation system using APIs and web crawling. *Computational Intelligence and Neuroscience*, 2022(5): 1-11. <http://dx.doi.org/10.1155/2022/7797548>
- [17] Sridevi, G.M., Suganthi, S.K. (2022). AI based suitability measurement and prediction between job description and job seeker profiles. *International Journal of Information Management Data Insights*, 2(2): 100109. <https://doi.org/10.1016/j.jjime.2022.100109>
- [18] Muhajir, D., Akbar, M., Bagaskara, A., Vinarti, R. (2022). Improving classification algorithm on education dataset using hyperparameter tuning. *Procedia Computer Science*, 197: 538-544. <https://doi.org/10.1016/j.procs.2021.12.171>
- [19] Mwaro, P.N., Ogada, K., Cheruiyot, W., (2020). Applicability of Naïve Bayes model for automatic resume classification. *International Journal of Computer Applications Technology and Research* 9(9): 257-264. <http://dx.doi.org/10.7753/IJCATR0909.1002>
- [20] Swami, P., Pratap, V. (2022). Resume classifier and summarizer. In 2022 International Conference on Machine Learning, Big Data, Cloud and Parallel Computing (COM-IT-CON), Faridabad, India, pp. 220-224). <https://doi.org/10.1109/COM-IT-CON54601.2022.9850527>

Optimal Deep Convolutional Neural Network Based Face Detection and Emotion Recognition Model

Ambika G. N. ^{*1}, Yeresime Suresh

Submitted: 28/04/2023

Revised: 25/06/2023

Accepted: 07/07/2023

Abstract: Face detection and emotion recognition are two closely connected tasks in computer vision that include analysing facial images to identify faces and detect the emotions expressed by the individual. Face detection is the way of localizing and locating faces within image or video frames. The objective is to detect the presence and position of faces, by drawing bounding boxes around them. Facial emotion recognition (FER) aims to detect and classify the emotions expressed by individuals based on facial expressions. Typically, this task can be done after face detection, where the faces detected are analysed further for emotional cues. Emotion recognition can be advanced by means of classical deep learning (DL) or machine learning (ML) techniques. Contemporary research on emotion classification has accomplished grand performance over DL based approaches. This article introduces an Optimal Deep Convolutional Neural Network based Face Detection and Emotion Recognition model (ODCNN-FDER) technique. The aim of the ODCNN-FDER technique is to detect faces and identify the existence of different emotions in them. To achieve this, the ODCNN-FDER technique initially employs Multi-Task Cascaded Convolutional Neural Network (MCCNN) model. Next, the fusion based feature extraction process is involved using two DL models namely EfficientNetB3 and InceptionResNetV2. For emotion recognition, Convolutional Attention Gated Recurrent Neural Network (CAGRNN) model is used. Lastly, root mean square propagation (RMSProp) optimizer was exploited for the optimal hyperparameter tuning of the CAGRNN approach. The performance validation of the ODCNN-FDER methodology was tested on the FER-2013 database. The experimental values highlighted the improved face detection and FER results of the ODCNN-FDER technique over other models.

Keywords: Computer vision, Deep learning, Face detection, Facial emotion recognition, RMSProp optimizer

1. Introduction

Nowadays, face recognition and detection methods including facial expressions analysis are an efficient research field in the Computer Vision (CV) community [1]. Face detection is a computer technology that can give a digital video or image, identify the facial features, and determine the sizes and positions of human faces by excluding anything else like, bodies and buildings, trees existing in the video or image. This detection and localization of human faces is a pre-requisite for recognizing faces or analysing facial expressions, which is utilized in applications like Human Computer Interface (HCI), video monitoring, and image database management [2]. A machine can recognize and detect an individual's face utilizing a normal web camera. But the factors such as a blurry or contrasting image in shadows, absence of proper brightness or lighting of an image, and viewing a person from an angle can considerably increase the complication for detecting a face [3]. In the year of

1990s, face recognition has been a prominent field of investigation but still it is less dependent than face recognition and far away from being considered an effective technique of user authentication [4].

In recent decades, Emotion recognition is a technique that has been achieving plenty of interest with the growth of Artificial Intelligence (AI) techniques. This could be obtained by investigating the facial expressions or voice tone, body postures [5]. In this research, the main focus is on recognizing emotions by applying facial expressions. Gathering the facial expression of other individuals supports human communication by understanding the purposes of others [6]. The technique of Facial Emotion Recognition (FER) is a booming area of research, which has the utilizations like Human-Machine Interaction (HMI), computer animations, and different learning processes – comprehending the internal state of attention of the learners [7]. The method of vision sensor based FER has fascinated attention in existing research and has higher capability of FER recognition in real-time. In the vision based FER, the researchers mainly concentrated on seven basic expressions like disgust, happiness, fear, anger, surprise, sad, and neutral and it categorized the FER into 2 sub-categories namely traditional and DL based approaches [8]. The requirement for intelligent

¹ Assistant Professor, CSE Dept, BMS Institute of Technology and Management, Bangalore-560064.
ORCID: 0000-0001-5511-6893

² Associate Professor, CSE Dept, Ballari Institute of Technology & Management, Ballari-583104.
ORCID: 0000-0002-8372-3612

* Corresponding Author Email: gnamnika@outlook.com

technologies for deciding a potential user has needs and desires and then selecting an effective action method has rocketed with the wide acceptance of intelligent technology in modern life. Moreover, CV and DL techniques are applied in almost all engineering domains and social spheres like manufacturing, medical imaging, speech and text recognition, and emotion recognition [9]. Despite the important achievement of traditional FER algorithm based on the extraction of manual features, in previous decades, researchers have changed their attention to the DL method because of its outstanding capability of automatic recognition [10].

This article introduces an Optimal Deep Convolutional Neural Network based Face Detection and Emotion Recognition model (ODCNN-FDER) technique. The aim of the ODCNN-FDER technique is to detect faces and identify the existence of different emotions in them. To achieve this, the ODCNN-FDER technique initially employs Multi-Task Cascaded Convolutional Neural Network (MCCNN) model. Next, the fusion based feature extraction process is involved using two DL models namely EfficientNetB3 and InceptionResNetV2. For emotion recognition, Convolutional Attention Gated Recurrent Neural Network (CAGRNN) model is used. Lastly, root mean square propagation (RMSProp) optimizer was exploited for the optimum hyperparameter tuning of the CAGRNN algorithm. The performance validation of the ODCNN-FDER method is tested on the FER-2013 dataset.

2. Related Works

Jain et al. [11] present a novel Squirrel Search Optimizer with DL Enabled Facial Emotion Recognition (SSO-DLFER) approach for Autonomous Vehicle Drivers. The presented SSO-DLFER system follows 2 main procedures such as emotion recognition and face detection. The RetinaNet approach was utilized at primary step of face recognition method. For emotion detection, the SSO-DLFER approach executed the NASNet Large feature extraction with GRU method as a classification. In order to enhance the emotion detection solution, the SSO-based hyper-parameter tuning process was executed. In [12], a DL- based structure was presented for human emotion recognition. The presented structure utilizes the Gabor filtering for feature extraction and CNN for classification.

Nasri et al. [13] present a FER method from static image dependent upon Xception CNN structure and K-fold cross-validation approach. The presented method can be enhanced by utilizing the fine-tuned system. The Xception approach pre-training on ImageNet dataset for object detection can be fine-tuned for recognizing 7 emotional states. Gao et al. [14] introduce an automatic optimizer structure utilizing binary coding method and GPSO with

gradient penalties for selecting the design. Such SI optimizer methods can be employed but not widely utilized, and the present work concentrates on methods with set depth of networks. Shao and Qian [15] presented 3 new CNN approaches with various structures. A primary one is a shallow network termed Light-CNN that is fully CNN comprising 6 depthwise separable residual convolutional elements for resolving the problem of difficult topology and over-fitting. The secondary one is dual-branch CNN that extract typical LBP features and DL feature in parallel. The tertiary one is a pre-training CNN that is planned by TL system for overcoming the lack of trained instances.

In [16], a DL-based method was presented for detecting the facial expression of persons. The presented system comprises 2 parts. The previous one learns local features in face images utilizing a local gravitational force descriptor, but, in the end, the descriptor was provided as new DCNN approach. The presented DCNN contains 2 branches. A primary branch searches geometric features like curves, edges, and lines; but holistic features were extracted by secondary branch. Cui et al. [17] introduce an endwise Regional-Asymmetric CNN (RACNN) for emotion detection that comprises temporal, regional, and asymmetric feature extractions. Especially, continuous 1-D convolutional layers can be employed in temporal feature extraction for learning time–frequency representations. Afterward, the regional feature extraction comprises two 2-D convolutional layers for capturing regional data amongst physically nearby channels.

3. The Proposed Model

In this study, we have concentrated on the development of the ODCNN-FDER technique. The major intention of the ODCNN-FDER technique is to detect faces and identify the existence of different emotions in them. To achieve this, the ODCNN-FDER method follows two most important processes: MCNN based face detection and emotion recognition. Fig. 1 depicts the overall flow of ODCNN-FDER algorithm.

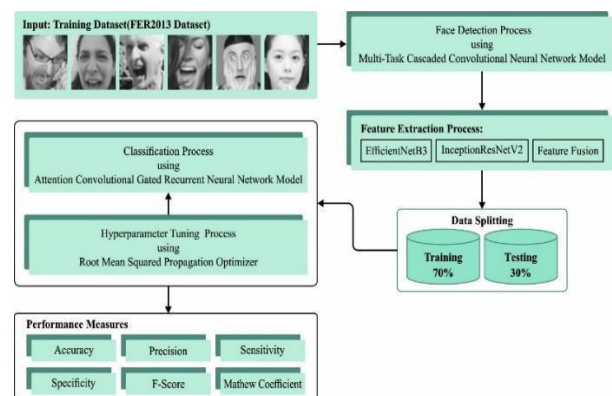


Fig. 1. Overall flow of ODCNN-FDER algorithm

3.1. Face Detection using MCCNN Model

Primarily, the MCCNN algorithm is used for automated face detection process. MCCNN is used as a solution for face alignment and detection [18]. The process comprises three phases of convolution network that are capable of recognizing faces and landmark locations like mouth, nose, and eyes. Initially, it exploits a shallow CNN to rapidly generate candidate window. Next, through more complex CNN it refines the candidate window. At last, it exploits a CNN to further refine the result and output the facial landmark position which is more complex than the others. At first, take the image and rescale it to dissimilar scales for building an image pyramid viz., input of three-stage cascaded networks.

Stage1: Proposal Network (P-Net)

A full convolution network (FCN) is the first stage. The only distinction between a FCN and a CNN is that a FCN doesn't apply dense layer as part of the architecture. This P-Net was employed for achieving candidate windows and their bounding box regression vector. Bounding box regression is a traditional way of predicting the localization of boxes once the objective is to detect an object of some predefined classes. Some refinement can be done after attaining the bounding box vector, for combining overlapping regions. After refinement, each candidate window is used to decrease candidate counts.

Stage2: Refine Network (R-Net)

At the last stage, each candidate from the P-Net was given into the R-Net. Further, the R-Net decreases the volume of candidates, performs calibration with bounding box regression, and exploits non-maximum suppression (NMS) to combine overlapping candidates. The R-Net output if the input is a face or not, is a ten-element vector for the localization of facial landmarks, and a four element vector that is bounding box for faces.

Stage3: Output Network (O-Net)

This phase could not be unlike the R-Net, however, this Output Network purposes to define the face in further detail and output the 5 facial landmarks' place for mouth, eyes, and nose.

3.2. Process involved in FER Technique

In the second phase, the FER process takes place using three subprocesses namely fusion based feature extraction, CAGRNN based classification, and RMSProp based parameter tuning.

3.2.1. Fusion based Feature Extraction

In this stage, the fusion based feature extraction procedure takes place using two DL models namely EfficientNetB3 and InceptionResNetV2. EfficientNet presents an exceptional method for scaling NN by improving

precision, depth, and width [19]. The CNN method scaling model revolves around the application of compounded coefficients that uniformly scale-up the dimension, width, and depth of the network. Furthermore, EfficientNet is a kind of DL algorithm that is derived in baseline model introduction by using NN search. The basic component of EfficientNetB0 is a mobile inverted bottleneck convolution (MBConv) that is somewhat adapted due to the more of special block called a squeeze-and-excitation optimization block. Therefore, every MBConv block relies on shortcut connection and depth wise convolution layers between the blocks. EfficientNetB3 is a CNN model designed by researcher workers at Google that attained remarkable performance on the ImageNet classification tasks. The architecture belongs to the family of EfficientNet model that is developed to accomplish higher performance while being computationally effective. It exploits the synthesis of convolutional layers with diverse kernel sizes along with squeeze-and-excitation elements that selectively increase relevant features.

Inception-ResNetv2 is a deep CNN (DCNN) architecture which integrates the Inception model from the Inception network and the residual connection from the ResNet model [20]. It was developed as an improvement to the original Inception and ResNet models to enhance their accuracy and performance. The basic concept behind Inception-ResNetv2 is to resolve the problems of training deep neural networks. The deep network tends to suffer from gradient vanishing problems, where the gradient becomes very smaller during backpropagation, which makes them challenging for the network to learn efficiently. Residual connection, as presented in ResNet, lessens these problems by the network for learning residual mappings rather than direct mapping. Inception ResNetv2 integrates the Inception model, which is developed to capture multiscale features by applying dissimilar filter sizes (1x1, 3x3, 5x5) in similar branches and concatenating their output. This allows the network to capture local and global data at dissimilar scales. The residual connection skips more than one layer and directly feeds the input to the output, which makes it easier for the network to learn residual data.

3.2.2. CAGRNN based Classification

For emotion detection and classification process, the CAGRNN model is exploited. Recurrent neural network (RNN) exploits historic data instead of the present data for classification. In addition, a bi-directional RNN (BRNN) architecture was introduced, which uses past and present data [21]. Hence, two RNNs are employed to implement the forward and reverse functions. The output was connected with the same output layer for recording the feature sequence. An additional bi-directional GRU

(BiGRU) model was proposed based on the BRNN model, which replaces the hidden state of BRNN with the single GRU memory units. Now, the combination of these two BiGRU models with attention mechanisms is considered an AGRNN. Fig. 2 showcases the framework of CAGRNN method.

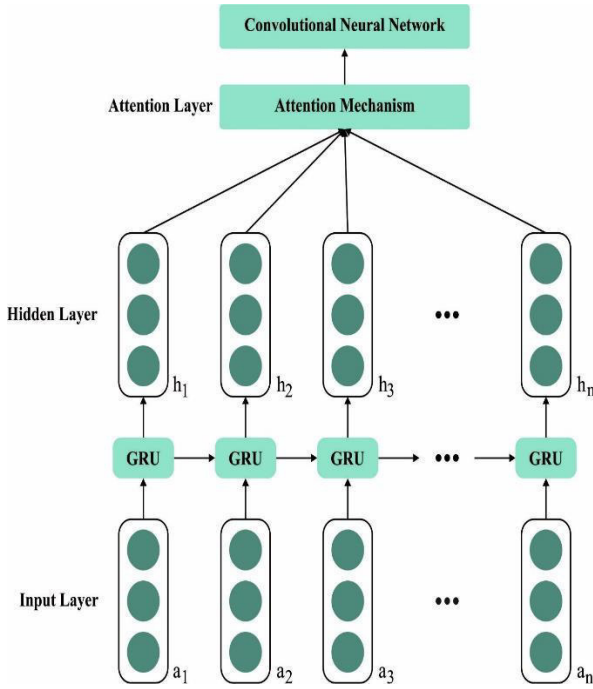


Fig. 2. Architecture of CAGRNN model

Assume an m -dimensional input dataset as (y_1, y_2, \dots, y_m) . The hidden state in the BGRU generates an output H_{t_1} at t_1 time interval is given below;

$$\vec{H} = \sigma(w_{e_{yH}} y_{t_1} + w_{e_{HH}} \vec{H}_{t_1-1} + c_{\vec{H}}) \quad (1)$$

$$\vec{H}_{t_1} = \sigma(w_{e_{yH}} y_{t_1} + w_{e_{HH}} \vec{H}_{t_1-1} + c_{\vec{H}}) \quad (2)$$

$$H_{t_1} = \vec{H}_{t_1} \oplus \vec{H}_{t_1} \quad (3)$$

Where w_e represents the weighted factor for two connected layers, c shows the bias vector, σ denotes the activation function, \vec{H}_{t_1} and \vec{H}_{t_1} represents the positive and negative outputs of GRU, \oplus and denotes the bitwise operator. In the CAGRU, the convolutional layer was widely used for the feature maps or input sequences for capturing spatial data. Then, the attention module is used to calculate attention weight over the convolutional feature, which highlights the crucial region. The weighted feature was combined and fed into the GRU that sequentially process them to

capture temporal dependency. The last output of the network can be utilized for dissimilar tasks namely regression, classification, or sequence generation.

3.2.3. Hyperparameter Tuning

At the final stage, the RMSProp optimizer is used. AGRNN is a hybrid network of BiGRU with the attention module. The main concept behind RMSProp is to keep the moving average of the squared gradient for all the weights [22]. In RMSProp learning rate is automatically adjusted and it selects a dissimilar learning rate for all the parameters. RMSProp splits the learning rate by the average of the exponential decay of squared gradient. The RMSProp optimizer attempts to restrict the oscillation in the vertical direction that consecutively assists in increasing the learning rate such that the model takes large step in the horizontal direction and converges faster. The calculation of RMSProp is shown in the following. The value of momentum is signified as β and is generally fixed as 0.9.

$$vdw = \beta \cdot vdw + (1 - \beta) \cdot dw^2 \quad (4)$$

$$vdb = \beta \cdot vdb + (1 - \beta) \cdot db^2 \quad (5)$$

$$W = W - \alpha \cdot \frac{dw}{\sqrt{vdw} + \epsilon} \quad (6)$$

$$b = b - \alpha \cdot \frac{db}{\sqrt{vdb} + \epsilon} \quad (7)$$

In backward propagation, dW and db are used for updating W and b parameters:

$$W = W - learning\ rate * dW \quad (8)$$

$$b = b - learning\ rate * db \quad (9)$$

Rather than applying dW and db autonomously for all the epochs, we take the exponentially weighted average of the square of dW and db in RMSProp.

$$S_{dw} = \beta * S_{dw} + (1 - \beta) * dW^2 \quad (10)$$

$$S_{db} = \beta * S_{db} + (1 - \beta) * db^2 \quad (11)$$

From the expression, beta β' is another hyperparameter and takes value from 0 to 1. The newly weighted average is generated by the weights, average of prior value, and present value square. The parameters are updated afterward computing exponentially weighted average.

$$W = W - \text{learning rate} * dW / \text{sqrt}(S_{dW}) \quad (12)$$

$$b = b - \text{learning rate} * db / \text{sqrt}(S_{db}) \quad (13)$$

If S_{dW} is relatively lesser, then we're dividing it by dW . If S_{db} is relatively larger then divide db with comparatively large number to delay the update on vertical dimension.

4. Results and Discussion

In this section, the results of the ODCNN-FDER technique is tested on the FER2013 Dataset [23] which holds seven classes (Anger, Disgust, Fear, Happiness, Sadness, Surprise, and Contempt). Fig. 3 demonstrates the extraction feature maps images.

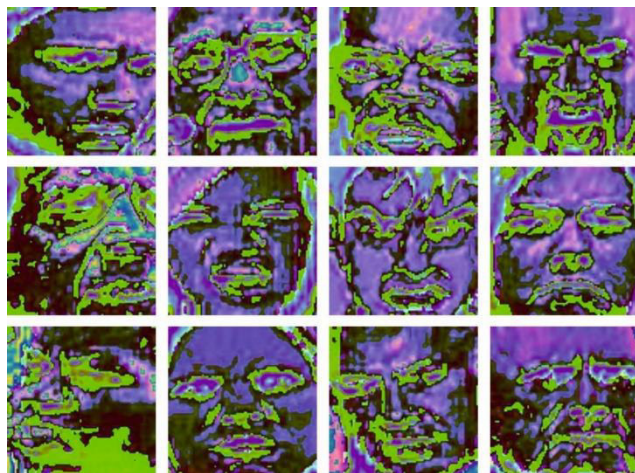


Fig. 3. Extracted Feature Maps

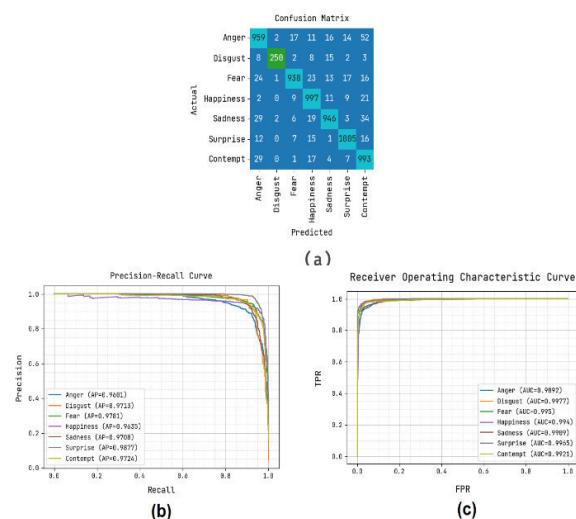


Fig. 4. Results on Training Dataset a) Confusion Matrix b) PR-Curve c) ROC

Fig. 4 reveals the classifier outcome of the ODCNN-FDER algorithm on training dataset. Fig. 4a describes the confusion matrix provided by the ODCNN-FDER approach. The result inferred that the ODCNN-FDER approach has detected and classified all 7 classes accurately. Followed by, Fig. 4b exposes the PR curve of the ODCNN-FDER method. The outcomes implied that the ODCNN-FDER algorithm has achieved higher PR outcomes on 7 classes. At last, Fig. 4c exemplifies the ROC curve of the ODCNN-FDER algorithm. The outcome outperformed that the ODCNN-FDER system has led to able outcomes with superior ROC values on 7 classes.

Fig. 5 depicts the classifier result of the ODCNN-FDER system on testing database. Fig. 5a showcases the confusion matrix offered by the ODCNN-FDER algorithm. The result stated that the ODCNN-FDER approach has recognized and classified all 7 classes accurately. Afterward, Fig. 5b reveals the PR outcome of the ODCNN-FDER system. The outcome depicts that the ODCNN-FDER algorithm has attained maximal PR results on 7 classes. Lastly, Fig. 5c demonstrates the ROC study of the ODCNN-FDER system. The outcome exhibited that the ODCNN-FDER approach has resulted in capable outcomes with higher ROC values on 7 class labels.

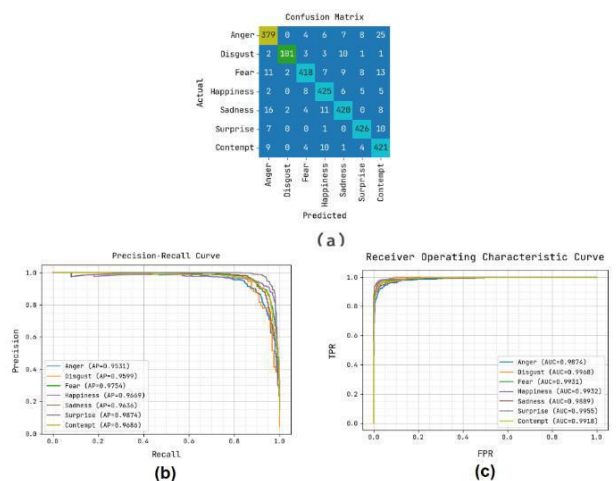


Fig. 5. Results on Testing Dataset a) Confusion Matrix b) PR-Curve c) ROC

In Table 1 and Fig. 6, the FER results of the ODCNN-FDER technique are investigated on TRS and TSS. The results indicate that the ODCNN-FDER technique reaches improved results on both TRS and TSS. On TRS, the ODCNN-FDER technique offers $accu_y$ of 95.29%, $prec_n$ of 93.15%, $sens_y$ of 91.85%, $spec_y$ of 98.72%, F_{score} of 92.42%, and MCC of 91.19%.

Table 1. FER outcome of ODCNN-FDER approach on TRS and TSS

Metrics	Training Set	Testing Set
Accuracy	95.29	94.74
Precision	93.15	92.27
Sensitivity	91.85	90.88
Specificity	98.72	98.60
F-Score	92.42	91.48
Mathew Coefficient	91.19	90.14

Also, on TSS, the ODCNN-FDER approach offers $accu_y$ of 94.74%, $prec_n$ of 92.27%, $sens_y$ of 90.88%, $spec_y$ of 98.60%, F_{score} of 91.48%, and MCC of 90.14%.

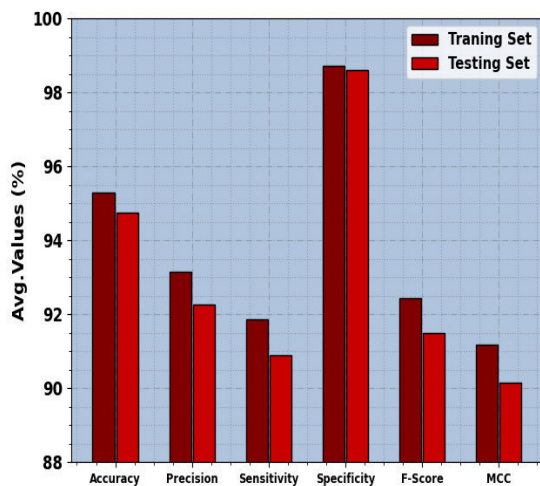


Fig. 6. Average outcome of ODCNN-FDER approach on TRS and TSS

Fig. 7 displaying the training accuracy TR_accu_y and VL_accu_y of the ODCNN-FDER method. The TL_accu_y is defined by the evaluation of the ODCNN-FDER technique on TR dataset whereas the VL_accu_y is computed by assessing the performance on a separate testing database. The results display that TR_accu_y and VL_accu_y maximum with an increase in epochs. Accordingly, the outcome of the ODCNN-FDER method gets improved on the TR and TS dataset with a rise in count of epochs.

In Fig. 8, the TR_loss and VR_loss curve of the ODCNN-FDER algorithm is exposed. The TR_loss demonstrates the error among the predictive solution and original values on the TR data. The VR_loss represents the measure of the efficiency of the ODCNN-FDER technique on individual validation data. The outcomes implied that the TR_loss and VR_loss tend to reduce with increasing epochs. It portrayed the enhanced performance of the ODCNN-

FDER technique and its capability to generate accurate classification. The reduced value of TR_loss and VR_loss demonstrates the greater performance of the ODCNN-FDER system on capturing patterns and relationships.

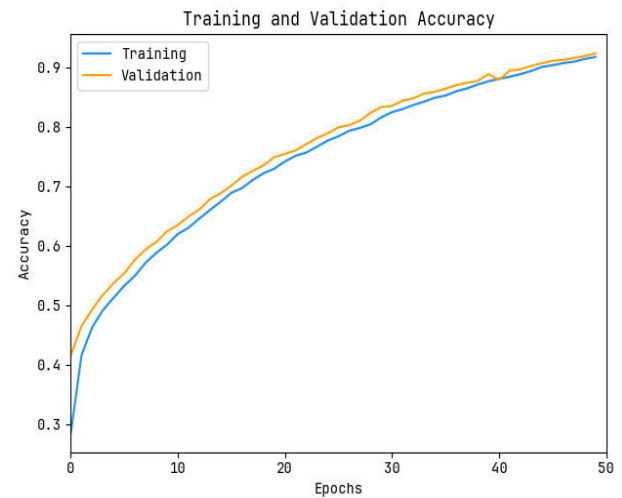


Fig. 7. $Accu_y$ curve of the ODCNN-FDER approach

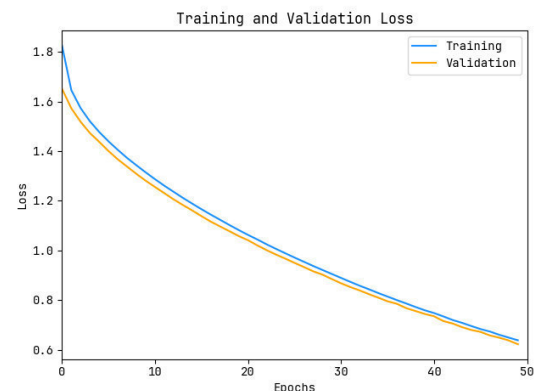


Fig. 8. Loss curve of the ODCNN-FDER approach

In Table 2 and Fig. 9, the FER results of the ODCNN-FDER technique are compared with recent DL models [24]. The experimental results imply that the Mini-Xception and CNN-transfer learning models accomplish worse performance. At the same time, three layer-CNN, six-layer-CNN, and InceptionResNetv2 models exhibit slightly enhanced results.

Table 2. Comparative outcome of ODCNN-FDER algorithm with recent DL systems

Methods	Accur acy	Precisi on	Sensiti vity	Specifi city	F- Scor e
Mini-Xception Model	66.00	78.77	75.19	72.44	80.84
CNN-Transfer Learning	72.00	69.78	74.26	74.37	80.27
Three Layer-CNN Model	88.60	87.61	90.08	90.36	90.51
Six Layer-CNN Model	86.78	89.75	88.87	88.37	89.81
InceptionResNetV2	87.69	88.41	89.76	90.49	89.73
FERVCB-DL	89.20	88.22	88.77	88.13	90.23

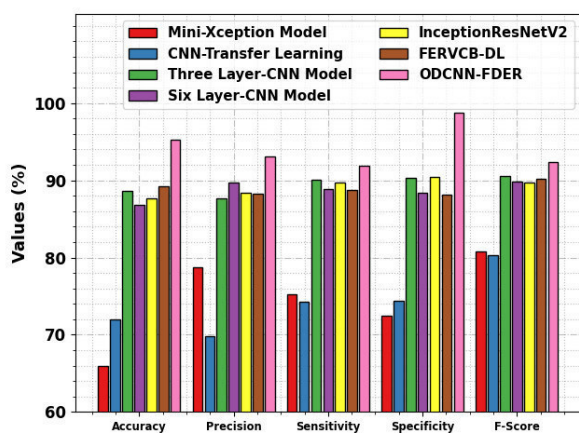


Fig. 9. Comparative outcome of ODCNN-FDER algorithm with recent DL systems

Although the FERVCB-DL model reaches considerable performance with $accu_y$ of 89.20%, $prec_n$ of 88.22%, $sens_y$ of 88.77%, $spec_y$ of 88.13%, and F_{score} of 90.23%, the ODCNN-FDER technique gains maximum performance with $accu_y$ of 95.29%, $prec_n$ of 93.15%, $sens_y$ of 91.85%, $spec_y$ of 98.72%, and F_{score} of 92.42%. These results confirmed the enhanced performance of the ODCNN-FDER technique on face detection and FER processes.

5. Conclusion

In this study, we have concentrated on the development of the ODCNN-FDER technique. The major intention of the ODCNN-FDER technique is to detect faces and identify the existence of different emotions in them. To achieve this, the ODCNN-FDER method follows two most important processes: face detection and emotion recognition. In the primary phase, the MCCNN approach was applied for the face detection method. Next, in the second phase, the FER process takes place using three subprocesses namely fusion based feature extraction, CAGRNN based classification, and RMSProp based parameter tuning. In this work, the RMSProp optimizer is exploited for the optimum hyperparameter tuning of the CAGRNN algorithm. The performance validation of the ODCNN-FDER technique was tested on the FER-2013 database. The experimental values highlighted the improved face detection and FER results of the ODCNN-FDER technique over other models. In future, the ODCNN-FDER technique can be extended to the design of metaheuristic optimizers.

Author contributions

Ambika G.N: Conceptualization, Methodology, Software, Field study, Visualization, Investigation, Writing-Reviewing and Editing

Yeresime Suresh: Conceptualization, Methodology, Data curation, Writing-Original draft preparation, Software, Validation., Field study.

Conflicts of interest

The authors declare no conflicts of interest.

References

- [1] S. Gupta, P. Kumar, and R. K. Tekchandani, "Facial emotion recognition based real-time learner engagement detection system in online learning context using deep learning models," *Multimedia Tools and Applications*, 82(8), pp.11365-11394, 2023.
- [2] M. A. H. Akhand, S. Roy, N. Siddique, M. A. S. Kamal, and T. Shimamura, "Facial emotion recognition using transfer learning in the deep CNN," *Electronics*, 10(9), p.1036, 2021.
- [3] S. Zhang, X. Pan, Y. Cui, X. Zhao, and L. Liu, L. "Learning affective video features for facial expression recognition via hybrid deep learning," *IEEE Access*, 7, pp.32297-32304, 2019.
- [4] D. Wu, X. Han, Z. Yang, and R. Wang, "Exploiting transfer learning for emotion recognition under cloud-edge-client collaborations," *IEEE Journal on Selected Areas in Communications*, 39(2), pp.479-

- [5] A. Jaiswal, A. K. Raju, and S. Deb, "Facial emotion detection using deep learning," In *2020 international conference for emerging technology (INCET)* (pp. 1-5). IEEE, 2020.
- [6] L. Schoneveld, A. Othmani, and H. Abdelkawy, "Leveraging recent advances in deep learning for audio-visual emotion recognition," *Pattern Recognition Letters*, 146, pp.1-7, 2021.
- [7] D. Canedo, and A. J. Neves, "Facial expression recognition using computer vision: A systematic review," *Applied Sciences*, 9(21), p.4678, 2019.
- [8] D. Ruan, Y. Yan, S. Lai, Z. Chai, C. Shen, and H. Wang, "Feature decomposition and reconstruction learning for effective facial expression recognition," In *Proceedings of the IEEE/CVF conference on computer vision and pattern recognition* pp. 7660-7669, 2021.
- [9] S. Minaee, M. Minaei, and A. Abdolrashidi, A, "Deep-emotion: Facial expression recognition using attentional convolutional network," *Sensors*, 21(9), p.3046, 2021.
- [10] T. S. Gunawan, A. Ashraf, B. S. Riza, E. V. Haryanto, R. Rosnelly, M. Kartiwi, and Z. Janin, "Development of video-based emotion recognition using deep learning with Google Colab," *TELKOMNIKA (Telecommunication Computing Electronics and Control)*, 18(5), pp.2463-2471, 2020.
- [11] D. K. Jain, A. K. Dutta, E. Verdú, S. Alsubai, and A. R. W. Sait, "An automated hyperparameter tuned deep learning model enabled facial emotion recognition for autonomous vehicle drivers," *Image and Vision Computing*, 133, p.104659, 2023.
- [12] M. M. T. Zadeh, M. Imani, and B. Majidi, "Fast facial emotion recognition using convolutional neural networks and Gabor filters," In *2019 5th Conference on Knowledge Based Engineering and Innovation (KBEI)* (pp. 577-581). IEEE, 2019.
- [13] M. A. Nasri, M. A. Hmani, A. Mtibaa, D. Petrovska-Delacretaz, M. B. Slima, and A. B. Hamida, "Face emotion recognition from static image based on convolution neural networks," In *2020 5th International Conference on Advanced Technologies for Signal and Image Processing (ATSIP)* (pp. 1-6). IEEE, 2020.
- [14] Z. Gao, Y. Li, Y. Yang, X. Wang, N. Dong, and H. D. Chiang, "A GPSO-optimized convolutional neural networks for EEG-based emotion recognition," *Neurocomputing*, 380, pp.225-235, 2020.
- [15] J. Shao, and Y. Qian, "Three convolutional neural network models for facial expression recognition in the wild," *Neurocomputing*, 355, pp.82-92, 2019.
- [16] K. Mohan, A. Seal, O. Krejcar, and A. Yazidi, "Facial expression recognition using local gravitational force descriptor-based deep convolution neural networks," *IEEE Transactions on Instrumentation and Measurement*, 70, pp.1-12, 2020.
- [17] H. Cui, A. Liu, X. Zhang, X. Chen, K. Wang, and X. Chen, "EEG-based emotion recognition using an end-to-end regional-asymmetric convolutional neural network," *Knowledge-Based Systems*, 205, p.106243, 2020.
- [18] K. Zhang, Z. Zhang, Z. Li, and Y. Qiao, "Joint face detection and alignment using multitask cascaded convolutional networks," *IEEE signal processing letters*, 23(10), pp.1499-1503, 2016.
- [19] S. A. Shah, G. M. Lakho, H. A. Keerio, M. N. Sattar, G. Hussain, M. Mehdi, R. B. Vistro, E. A. Mahmoud, and H. O. Elansary, "Application of Drone Surveillance for Advance Agriculture Monitoring by Android Application Using Convolution Neural Network," *Agronomy*, 13(7), p.1764, 2023.
- [20] R. Florez, F. Palomino-Quispe, R. J. Coaquira-Castillo, J. C. Herrera-Levano, T. Paixão, and A. B. Alvarez, "A CNN-Based Approach for Driver Drowsiness Detection by Real-Time Eye State Identification," *Applied Sciences*, 13(13), p.7849, 2023.
- [21] N. Parveen, P. Chakrabarti, B. T. Hung, and A. Shaik, "Twitter sentiment analysis using hybrid gated attention recurrent network," *Journal of Big Data*, 10(1), pp.1-29, 2023.
- [22] D. V. Babu, C. Karthikeyan, and A. Kumar, "Performance analysis of cost and accuracy for whale swarm and RMSprop optimizer," In *IOP Conference Series: Materials Science and Engineering*, Vol. 993, No. 1, p. 012080, 2020. IOP Publishing.
- [23] <https://www.kaggle.com/datasets/deadskull7/fer2013>
- [24] M. F. Alsharekh, "Facial Emotion Recognition in Verbal Communication Based on Deep Learning," *Sensors*, 22(16), p.6105, 2022.
- [25] Ms. Mohini Dadhe, Ms. Sneha Miskin. (2015). Optimized Wireless Stethoscope Using Butterworth Filter. *International Journal of New Practices in Management and Engineering*, 4(03), 01 - 05.

Retrieved from
<http://ijnpme.org/index.php/IJNPME/article/view/37>

- [26] Banerjee, S. ., Chakraborty, S. ., & Mondal, A. C. . (2023). Machine Learning Based Crop Prediction on Region Wise Weather Data. International Journal on Recent and Innovation Trends in Computing and Communication, 11(1), 145–153. <https://doi.org/10.17762/ijritcc.v11i1.6084>
- [27] Joshi, K., Kumar, V., Sundaresan, V., Ashish Kumar Karanam, S., Dhabliya, D., Daniel Shadrach, F., & Ramachandra, A. C. (2022). Intelligent fusion approach for MRI and CT imaging using CNN with wavelet transform approach. Paper presented at the IEEE International Conference on Knowledge Engineering and Communication Systems, ICKES 2022, doi:10.1109/ICKECS56523.2022.10060322 Retrieved from www.scopus.com

An Efficient Deep Learning with Optimization Algorithm for Emotion Recognition in Social Networks

Ambika G N¹, Dr. Yeresime Suresh²

Assistant Professor, CSE Dept., BMS Institute of Technology and Management, Bangalore-560064, India¹
Associate Professor, CSE Dept., Ballari Institute of Technology & Management, Ballari-583104, India²

Abstract—Emotion recognition, or computers' ability to interpret people's emotional states, is a rapidly expanding topic with many life-improving applications. However, most image-based emotion recognition algorithms have flaws since people can disguise their emotions by changing their facial expressions. As a result, brain signals are being used to detect human emotions with increased precision. However, most proposed systems could do better because electroencephalogram (EEG) signals are challenging to classify using typical machine learning and deep learning methods. Human-computer interaction, recommendation systems, online learning, and data mining all benefit from emotion recognition in photos. However, there are challenges with removing irrelevant text aspects during emotion extraction. As a consequence, emotion prediction is inaccurate. This paper proposes Radial Basis Function Networks (RBFN) with Blue Monkey Optimization to address such challenges in human emotion recognition (BMO). The proposed RBFN-BMO detects faces on large-scale images before analyzing face landmarks to predict facial expressions for emotional acknowledgment. Patch cropping and neural networks comprise the two stages of the RBFN-BMO. Pre-processing, feature extraction, rating, and organizing are the four categories of the proposed model. In the ranking stage, appropriate features are extracted from the pre-processed information, the data are then classed, and accurate output is obtained from the classification phase. This study compares the results of the proposed RBFN-BMO algorithm to the previous state-of-the-art algorithms using publicly available datasets derived from the RBFN-BMO model. Furthermore, we demonstrated the efficacy of our framework in comparison to previous works. The results show that the projected method can progress the rate of emotion recognition on datasets of various sizes.

Keywords—Blue monkey optimization (BMO); deep learning; electroencephalograph (EEG); emotion recognition; human-computer interaction (HCI); radial basis function networks (RBFN)

I. INTRODUCTION

This template, modified in MS Word 2007 and saved as a "Word 97-2003 Document" for the PC, provides authors with most of the formatting specifications needed for preparing electronic versions of their papers. All standard paper components have been specified for three reasons: (1) ease of use when formatting individual papers, (2) automatic compliance to electronic requirements that facilitate the concurrent or later production of electronic products, and (3) conformity of style throughout conference proceedings.

Margins, columns widths, line spacing, and type styles are built-in; examples of the type styles are provided throughout this document and are identified in italic type, within parentheses, following the example. Some components such as multi-leveled equations, graphics, and tables are not prescribed, although the various table text styles are provided. The formatter will need to create these components, incorporating the applicable criteria that follow.

Language, text, action, and other means are all ways that people can express themselves. How to recognize and accurately detect human facial expressions has emerged as a hot research area given the rapidly expanding artificial intelligence field [1]. Numerous businesses including amusement, security, online education, and intelligent medical care, use facial expression detection technologies [2]. Facial expression is a critical factor in human emotion recognition. Since a person's facial expressions convey their emotions, "facial recognition" [3] and "emotion recognition" are often used synonymously. Significant progress has been made in the automotive industry, augmented robotics, reality, neuromarketing, and interactive games. There is growing interests in enhancing all facets of human-computer interaction, particularly in recognizing human emotions.

Facial expression recognition can be used to monitor driver fatigue. An alarm is sent when the driver's face exhibits signs of drowsiness, and a camera records the driver's expression in real time while also analyzing the driver's mental state. This can assist with avoiding traffic accidents induced by fatigued driving. The elderly can benefit from installing a human-computer interaction system with a recognition of facial expressions feature in nursing homes or elderly homes. Facial expression recognition technology can track how each student responds to the lecture and provide the instructor with immediate feedback, which can, to some extent, advance the superiority of education [4]. During the online teaching process, it can be difficult for the instructor to keep track of each student's reaction, but it is still important to make timely adjustments to the course progress.

In the conventional method for recognizing facial expressions, a photograph is taken, its attributes are extracted, and then the image is identified using machine learning [5]. The difficult feature extraction method and the identification performance being easily influenced by the environment and a person's facial activity are some drawbacks of this strategy.

One of today's most vital and challenging techniques is emotional recognition. Applications for emotion recognition include helping to measure stress levels and blood pressure, among other things. When using emotional techniques, one can apply the functions of happy, sad, calm, and neutral facial features. The human body's inner workings can be detected using various methods and algorithms. Real-time emotional recognition can pick up on human thought processes. Identifying diseases early using emotional recognition shields can save humans from severe infections or illnesses. Emotional recognition has the main benefit of assisting in identifying human mentalities without using questions.

Machine learning algorithms accurately predict facial emotions like stress and sadness. The results for emotion recognition, such as sadness and rage, were improved when the ECG and PPG were merged with the 28 features take out from algorithms using machine learning [6]. Without knowledge sharing, facial expressions are essential for determining human mentality. In a few articles, datasets from 2010 to 2021 are combined, along with the majority of the features collected and categorized using deep learning and to support vector machine approach, hence increasing classification accuracy and outcomes.

A subset of machine learning methods called "deep learning" can be used to analyze facial expressions and identify emotions. However, the amount of data will affect how well it works. As data volume rises, performance gets better. Deep learning cannot be applied to facial expression datasets because they are too small. Several studies have found that augmentation techniques like cropping, scaling, translating, or mirroring during the pre-processing stage increase the alteration and, subsequently, the quantity of information.

In various pattern recognition and classification issues, neural networks have been used because they have the best approximation capability. Along with the back-propagation algorithm, face recognition has also used convolution neural networks and multilayer perceptron (MLPs) [7]. Because of its slow convergence rate and uncertainty about whether it will reach global optimums, the back-propagation learning procedure is computationally intensive. Due to their outstanding approximation accuracy and quick processing, radial basis function neural networks (RBFN) with a single hidden layer have been used for facial recognition applications. Radial basis functions in the hidden layer nonlinearly map the contribution face information to linearly divisible information in hidden hyperspace. Some enterprise challenges for hidden layers include defining the RBF unit centers of hidden neurons, their numbers, and the selection and shape of fundamental functions. Second, the success of blue monkey swarms naturally inspired the development of the Blue Monkey (BM) approach, a cutting-edge metaheuristic optimization method. The total number of men in a group is determined via the BM process. Like other forest guenons, blue monkey groups typically only contain one adult male outside the breeding season. With constraints and an unknown search space, this algorithm effectively finds solutions to practical problems. The BM method has some variables and the potential to produce better results [8].

Radial Basis Function Networks (RBFN) with Blue Monkey Optimization is suggested in this paper (BMO). The proposed RBFN-BMO first recognizes faces on large-scale imageries after assessing face landmarks to approximate representations for reaction acknowledgment. The two stages of the RBFN-BMO are convolutional neural networks and patch cropping. The proposed perfect is composed of four categories: feature extraction, ranking, preprocessing and organization. After preprocessing the dataset's collected data for data cleansing, the information is classified, the relevant attributes are extracted from the preprocessed data in the ranking phase, and the correct information is obtained. This study compares the results of the recommended RBFN-BMO method to earlier state-of-the-art methodologies using publicly accessible datasets inferred from the RBFN-BMO model. Furthermore, we have demonstrated that our structure is more efficient than earlier ones.

The projected work is defined in detail below. Section II goes into more excellent aspects of the work associated with the projected outcome. Section III goes over the proposed framework in depth. Section IV goes into great detail about experiment design and performance evaluation. Section V concludes the discussion of future work.

A. Contribution

- Data cleaning and pre-processing are performed on the dataset's collected data.
- The pre-processed data are given the appropriate characteristics during the ranking phase, and the information is then categorized.
- Pre-processing, feature extraction, ranking, and categorization are the four categories that make up the suggested model.
- Before looking at face landmarks to predict facial expressions for emotion detection, the Radial Basis Function Networks (RBFN) - Blue Monkey Optimization (BMO) proposed method first recognizes faces on large-scale images.

II. LITERATURE SURVEY

Chen et al. [9] used a deep sparse auto-encoder network based on Soft-max regression to identify facial expressions of emotion during human-robot interaction. This work minimizes distortion, learning efficiency is determined, and dimensional complexity is measured using the SRDSAN technique. The soft-max simple regression perfect will help categorize the input signal, while the DSAN technique helps with accurate feature extraction.

Babajee et al. [10] suggested using deep learning to recognize human expressions from facial expressions. This paper uses deep knowledge and a convolutional neural network to offer seven methods for identifying facial emotions. This study uses the Facial Action Coding System (FACS) to collect 32,398 facial expressions to identify various types of emotion. The identification approach's failure to be an effective optimization technique is the sole justification for this research.

Satyanarayana et al. [11] used deep learning and cloud access to implement emotional acknowledgment in this study. One of the most effective methods in many presentations is facial emotion recognition. Face recognition makes extensive use of the deep learning algorithm. Her thesis paper examines a variety of emotions, such as sadness, joy, serenity, and rage. The Python code generates a particular IP address for each technique to send this data.

Jayanthi et al. [12] used deep classifiers to develop an organizing strategy for emotional categorizations utilizing speech and static images. One of the most crucial methods for determining someone's stress level is emotion identification. The two traits of emotion perception and speech modulation are essential in determining the stress level in the human body.

Sati et al. [13] used NVIDIA to implement face detection, recognition, and emotion recognition in his paper. In this study by Jetson Nano, face emotion recognition and detection are combined. Facial emotional identifications have historically been among the most challenging techniques to master. This technique's accuracy and classification outcomes can be improved by adding some features. The ANN technique assists in recognizing and classifying facial expressions of emotion.

Wang et al. [14] applied a recently developed deep learning technique in this paper. The four-category deep learning model is used in this paper. Convolutional neural networks and deep architectures fall under the first category. The deep learning model has a significant impact on deep neural networks. This component of the machine learning algorithm is essential. The classification, which includes both linear and nonlinear special functions, is necessary for the accuracy of the data.

The multi-label convolution neural network was implemented by Ekundayo et al. [15] to identify facial expressions and estimate ordinal intensity. This was completed because, while many features, like FER, are consistent with the emotional recognizing method, only one is ideal for the multi-class dynamic classification method. This study utilized a multi-label convolutional neural network.

Using facial expressions, EEG, and machine learning techniques, Hassounh et al. [16] developed a real-time emotional recognition system. The system could distinguish between smiling, remaining neutral, and losing control. In this study, virtual markers detect facial regression using the optical flow algorithm, since it acknowledges a lower level of computational complexity, the optical flow algorithm system aids in providing people with a physical challenge.

Neuro-sense was used by Tan et al. [17] to implement short-term emotion recognition and comprehension. Spiking neural network simulations of the spatiotemporal EEG patterns served as the foundation for their strategy. The SNN method is used for the first time in this paper. It aids in comprehending how the brain operates. One of the two methods used to analyze the EEG data is arousal-valence space. The various types of segments that make up the arousal-valence space include low arousal, high arousal, high

valence space techniques, and standard valence space methods.

A deep facial expression recognition survey was carried out by Li et al. [18]. One of the system's most significant challenges is recognizing a person's facial expression. The two main challenges to accurate facial expression recognition are a need for training sets and undesirable emotion variations (FER). The data set is first organized using the neural pipeline technique. Consequently, the FER technique's complex problems will be reduced.

Yang et al. [19] used a stacked auto-encoder to implement three-class profound learning-based emotional expressions. This paper demonstrates that discrete entropy calculation can be used to measure the EEG signal. The deep learning algorithm's auto-encoder technique results are more accurate than those from the encoding system's calculation methods. To use the alpha, beta, and gamma values, this method assesses emotions. Classification results are produced more accurately when a deep learning procedure is used. The deep learning procedure typically yields acceptable outcomes for the various classes of emotional recognition.

Yadahalli et al. [20] used a deep learning technique to recognize facial micro expressions. This study uses six different emotional expressions—happy, sad, angry, scared, neutral, and surprised faces—to collect the eight layers of the dataset. Because it has started collecting datasets that contain the FER perfect, the paper assumes that the FER with a CNN improves accuracy and that the removed consequence produces the multimodal facial expression using a single method. Using a single algorithm, the multimodal facial expression is also added to the dataset that has been gathered.

Asaju et al. [21] used a temporal method to recognize facial emotional expressions. This study introduces a CNN-based deep learning procedure that can implement numerous kinds of emotional acknowledgment in the human body. To extract features, VGG-19 methods are used. Both the accurate mapping technique and the recognition of facial emotions method use the BiLSTM architecture.

Yolcu et al. [22] suggested a deep learning-based method for tracking consumer performance patterns that measured head pose assessment and analyzed facial expressions to gauge the level of interest in the product. To follow customer interest, this was done. Deep structured learning was suggested by Walecki et al. [23] as a technique for determining the level of facial expression intensity. Face physics and other pre-processing methods are less critical in deep learning-based face recognition. CNN's convolution layers convolve the input image using various filters. It generates a feature map with fully connected networks to recognize facial expressions.

To identify emotional expressions on faces, Asaju et al. [24] employed the temporal method. This study integrates a CNN with a deep learning technique to create dissimilar kinds of emotional identification in the human body. Use the VGG-19 methods for obtaining features. The title and precise mapping of facial expressions are then carried out using the Bi-LSTM architecture.

Ekundayo et al. [25] implemented a multilabel convolution neural network to recognize facial expressions and estimate ordinal intensities. Although many features can be used with sentimental character segmentation techniques like FER, they are only suitable for some of them for the ideal categorization emotional classification method. Convolutional neural networks with multiple labels are used in this study.

III. PROPOSED SYSTEM

This study suggests combining RBFN and Blue Monkey Optimization (BMO) to acknowledge faces and emotions in high-resolution images. Modules for pre-processing, feature extraction, ranking, and classification can be seen in the block diagram of the proposed system in Fig. 1.

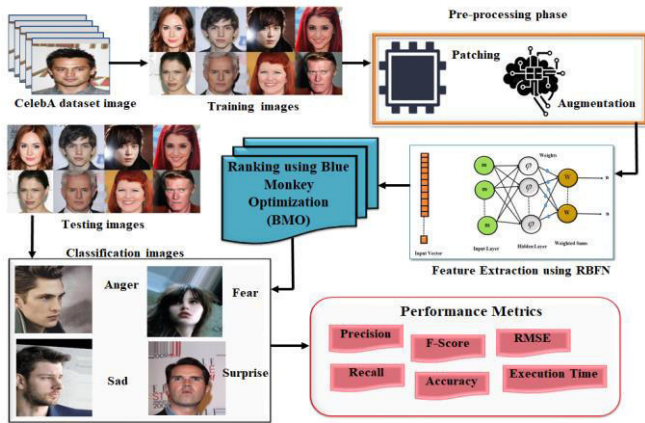


Fig. 1. Proposed method of RBFN-BMO method.

A. Pre-Processing of the Images

Before using the pyramid images approach, the original photographs are downsampled by a factor of 2 until they are 128×128 in dimensions. Additionally, each pyramid image is split into 128×128 pixel-sized patches to simplify processing and reduce memory allocation.

1) *Data augmentation*: Data sampling was performed on the input photos using a ratio of 2 up to an image size of 128×128. There was no overlap between the 128×128 patches created from the pyramid photos. If the picture segment is too long for the patches, zeros will be added to make up the difference. Additionally, we employ a data augmentation technique that involves rotating, translating, and flipping the images on their axes at 45-degree perspectives. The data augmentation method increases the number of training examples and progresses the network's ability to simplify under challenging circumstances. The images have been edited to resemble actual facial recognition scenarios. Due to the GPU's memory capacity, we use a batch size of 16 pictures during training. As a result, various combinations of patches for the same image might be created. The initial photo incorporates all sensing forecasts on the same image's patches.

B. Feature Extraction using RBFN

Feed forward neural networks comprise RBFN. The three layers that make up the RBFN's design are the input, hidden, and output layers, as depicted in Fig. 2. Data is sent from the

user's input layer to the concealed layer [26]. Radial basis function (RBF) units, known as hidden neurons, comprise the hidden layer. Each j th RBF unit has a related basis function (ϕ_j), spread (σ_j), and centre (A_j).

The nonlinear basis functions ϕ_j are affected by how far the input is from the center of the j th RBF unit. RBFN frequently employs the basic functions Gaussian, multiquadric, inverse multiquadric, and thin spline. The most often used Gaussian basis function was signified in this study as

$$\phi_j(x) = e^{-\frac{\|x - A_j\|^2}{2\sigma_j^2}} \quad (1)$$

The restriction r , which also denotes the function's width, characterizes the spread of the radial basis function, where C_j stands for the j th RBF unit's center. You can think of RBFN as a mapping from (2).

$$R^d \rightarrow R^u \quad (u \gg d) \quad (2)$$

Where u is the amount of RBF units and $P \in R^d$ is the d -dimensional input feature vector. The i th output of the RBFNN, $n_i(m)$, is

$$n_i(m) = \sum_{j=1}^u \phi_j(x) \times w_{i,j} \quad (3)$$

Where $w_{i,j}$ denotes the degree of connectivity between the i th output neuron and the j th RBF unit.

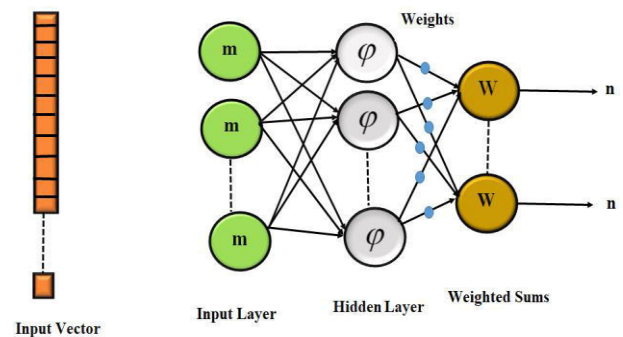


Fig. 2. Structure of RBFN.

C. Ranking with Blue Monkey Optimization (BMO)

Blue Monkeys are different from the other species. They frequently live in societies where women are the majority, meaning females stay in their natal groups. However, as soon as they reach the mature stage, the males leave their groups [27]. There are usually a lot of females and young in each group of blue monkeys, but only one male. This problem exacerbates the problem of inbreeding. The men leave the group and join another one when they're older. However, finding a new group might take some time, so the males might

initially seem to be by themselves. Regarding social interactions, blue monkeys don't have a perfect sense of intuition [28]. Social interaction only lasts for a short time, typically when playing with and grooming other people.

Babies also connect with the other adults in the group and their mothers. The source of those newborns typically avoids their male counterparts. Baby handlers are the ones who do all the work. The young females tend to the babies and carry and protect them. From this habit, infants pick up how to react like all monkeys.

1) *Group division*: The BMO algorithm imitates the actions of Blue Monkey. Each group of monkeys had to travel through the search area to simulate these interactions. Earlier, it was mentioned that when the monkeys are divided into groups, they start searching for food sources far away in an area where more robust monkeys are out of sight of conventional vision. The young *Cercopithecus mitis* and the male have little to no interaction. Because *Cercopithecus mitis* is a territorial species, young males should venture outside as soon as possible. The dominant male of another family will challenge them. If they succeed in eliminating him, they will assume control of the family and be able to provide young men with food, shelter, and socialization. Blue monkey groups typically consist of a sizable number of females and young, with only one male [29].

2) *Position update*: Each blue monkey in a group updates to the position in the best place within that group. Equations like the ones below describe this behavior:

$$Power_{m+1} = (0.7 * Power_m) + (W_{lea} - W_m) * rand * (Y_{best} - Y_m) \quad (4)$$

$$Y_{m+1} = Y_m + Power_{m+1} * rand \quad (5)$$

W_{lea} stands for the leader weight, W_m for the monkey weight, Y_{best} for the leader location, which can take any value between [0,1], $Power$ for the monkey power rate, and so on.

Using the following equations, the blue monkey's offspring are also updated.

$$Power_{m+1}^C = (0.7 * Power_m^C) + (W_{lea}^C - W_m^C) * rand * (Y_{best}^C - Y_m^C) \quad (6)$$

$$Y_{m+1}^C = Y_m^C + Power_{m+1}^C * rand \quad (7)$$

W_m^C is the child weight at which all weights are random amounts among [4, 6], Y_{best}^C is the child position, Y_{best} is the leader child position, $Rate$ needs to stand for the child power rate, is the leader child weight, and "rand" denotes an arbitrary amount among [0, 1]. Every cycle, the location needs to be reorganized.

Algorithm for Blue Monkey Optimization

Initialize the Blue Monkey and their children population
Bm ($m=1, \dots, n$)

Initialize power rate and weight of Blue monkey as Power and W

Where ($Power \in [0, 1]$) ($W \in [4, 6]$)

Randomly Distribute Blue Monkey into T groups and children in one group.

Evaluate the fitness of blue monkey and children in each group

Select Worstfit and Best fit in Y_{lea}^C Children group

T=1

While ($T \leq$ maximum number of group)

Swap Worstfit = Y_{lea}^C

Update Power and Y position of all blue monkey by Eq. (4,5)

Update Power and Y Position of children by Eq. (6,7)

Upgrade the fitness of all blue monkeys and kids.

Most recent Update

If (New best > Current best) then

New best = Current best

End if

T=T+1

End While

The best blue monkey should be returned.

D. Classification of Emotions Recognition

The centers of hidden neurons or RBFN units can be found using the sub-clusters produced by the proposed RBFN-BMO technique. Since the method evolves the sub-clusters based on the given training statistics, providing the number of sub-clusters for each participant as input for face recognition is unnecessary. Emotion recognition aims to identify a person's emotions. The capacity to perceive emotions varies significantly among people. A significant area of research is emotion recognition with technological assistance. Analyzing facial landmarks, with a focus on the lips, nose, and eyes, is the foundation for identifying emotions. Facial expressions are a huge help in recognizing emotions. The shapes of those sections represent the person's emotions. One can infer a person's emotional state from the points' locations and the distance between them. The main objective was to create the proposed methodology for finding 68 spots; A potential area for emotion detection in each of the locations. The jawline is depicted in points 1 through 17, the left and right brows in points 18 through 22, the left and right eyes in moments 37

through 48, the noise in points 28 through 36, the outer lip area in matters 49 through 60, and the inner lip structure in points 60 through 68. In studies of facial expressions, the location of those points is crucial.

In this study, we suggest using facial features as annotations for emotion recognition. The proposed RBFN-BMO accepts inputs such as high-resolution photos, facial feature annotations, and the face's position. The seven emotions portrayed in this piece are anger, disgust, fear, joy, sadness, surprise, and neutrality. More details about the data set used to train the recommended RBFN-BMO are provided in the following section.

IV. EXPERIMENTAL RESULTS

Details about the experimental setting that was used to develop and evaluate the suggested RBFN-BMO are provided in this section. The experiment was run on a Linux desktop with an Intel i7 processor, 32 GB RAM, and a 4 GB Nvidia GTX960 graphics card. The suggested RBFN was developing using the TensorFlow deep learning framework, cuDNN, and CUDA vibration libraries. For image manipulation, the OpenCV library was used.

A. Dataset Description

We suggest using the celeb datasets [30] to train the suggested RBFN-BMO. There are 202,599 RGB images of well-known people in this dataset. Face, attribute, and landmark acknowledgment was considered when creating the dataset. The CelebA dataset's images are summarised in Fig. 3. This work advocates using facial landmarks and distinctive analysis for face detection and expression acknowledgment.

A training set, a validation set, and a testing set were created from the collected data. The training set consisted of 70% of the data, the validation set of 10% of the training set, and the testing set consisted of 30% of the data.

While pre-processing reduces filter noise, 70% of the data are used as training input. The high dimensionality of the filter is reduced with the help of feature extraction. To decrease the size of the problem space, our work employs various methods for extracting features, such as edge detection. As a result, it generates clear output images with precise dimensional quality. In the data, categorization and part extraction happen simultaneously.

B. Performance Metrics

The effectiveness of the suggested work is assessed using the recognition rate. The classification performance is calculated by dividing the total amount of images into the data sets by the number of facial expressions successfully identified. It is shown as:

The percentage of accurate classifications is measured by precision (Prec). It can be indicated using (8):

$$\text{Precision} = \frac{TP}{TP + FP} \quad (8)$$

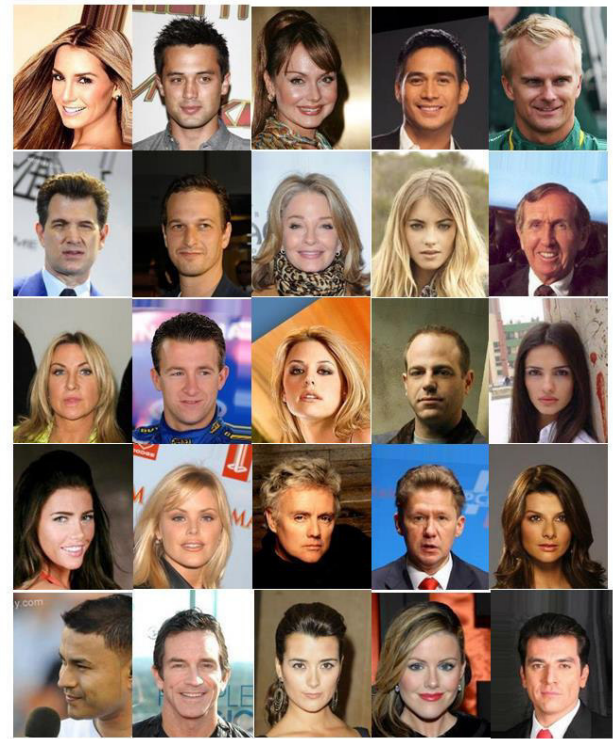


Fig. 3. Celebrity images data set.

It is also possible to refer to the actual positive rate as the recall rate or recall. It assesses how frequently a classifier gives the right category a favorable result. It is described in (9).

$$\text{Recall} = \frac{TP}{TP + FN} \quad (9)$$

The F-Measure represents the harmonic mean of sensitivity and precision (F). It is crucial since higher accuracy typically interprets into lower sensitivity. It can be calculated using (10).

$$F - \text{Score} = 2 * \frac{\text{precision} * \text{recall}}{\text{precision} + \text{recall}} \quad (10)$$

Accuracy: To calculate the precision of our predicted value, divide all values by the total of true negatives and true positives.

$$\text{Accuracy} = \frac{TP + TN}{TP + TN + FP + FN} \quad (11)$$

Root Mean Square Error (RMSE)

The only departure from RMSE is the square root sign. The mean absolute error equation is given in (12).

$$\text{RMSE} = \sqrt{\sum_{i=1}^n \frac{(y_i - \hat{y}_i)^2}{n}} \quad (12)$$

The messages TP, TN, FP, and FN are confirmed positive, true negative, true positive, and false negative, respectively. The outcome should improve as a component of precision, recall, f-measure, and sensitivity.

1) *Precision analysis*: In Fig. 4 and Table I, the precision of the RBFN-BMO strategy is contrasted with that of other methods currently in use. The graph demonstrates the increased efficiency and precision of the deep learning approach. In comparison to the GRU, LSTM, RNN, DNN, and ANN models, which have precision values of 89.029%, 85.536%, 90.927%, 88.435%, and 93.983% for the 1000 data, the RBFN-BMO model has a precision value of 96.425%. With different data sizes, the RBFN-BMO model has shown its greatest performance. The RBFN-BMO's precision value is 97.927% under 6000 data, compared to the GRU, LSTM, RNN, DNN, and ANN models' precision values of 89.827%, 86.324%, 93.782%, 87.625%, and 95.029%, respectively.

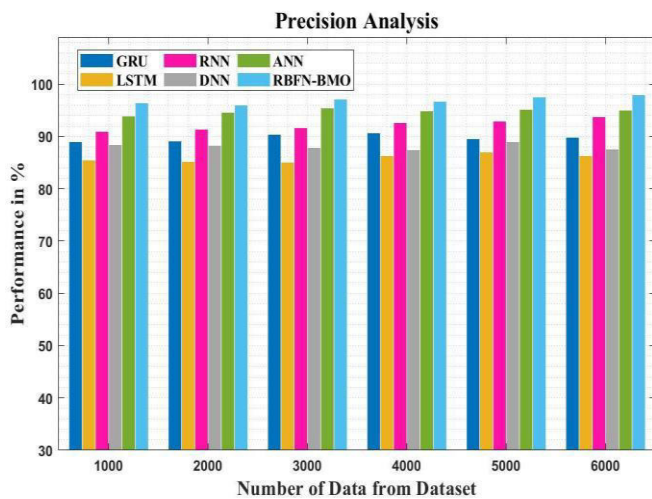


Fig. 4. Precision analysis for RBFN-BMO method with existing systems.

TABLE I. RBFN-BMO METHOD PRECISION ANALYSIS USING EXISTING SYSTEMS

Data from dataset	GRU	LSTM	RNN	DNN	ANN	RBFN-BMO
1000	89.029	85.536	90.927	88.435	93.983	96.425
2000	89.214	85.234	91.425	88.323	94.626	96.029
3000	90.425	85.029	91.728	87.922	95.435	97.182
4000	90.627	86.324	92.637	87.425	94.928	96.728
5000	89.526	86.973	92.938	88.937	95.227	97.632
6000	89.827	86.324	93.782	87.625	95.029	97.927

2) *Recall analysis*: Fig. 5 and Table II illustrate how the RBFN-BMO approach compares to other current methods in terms of recall. The figure demonstrates how the recall performance was enhanced by the deep learning approach. The RBFN-BMO model, for example, has a recall value of 93.827% with 1000 data, while the GRU, LSTM, RNN, DNN, and ANN models have recall values of 79.637%, 80.928%, 84.938%, 86.927%, and 89.627%, respectively.

and ANN models have recall values of 79.637%, 80.928%, 84.938%, 86.927%, and 89.627%, respectively. However, the RBFN-BMO model worked most effectively with various data sizes. For 6000 data points, the recall value of the RBFN-BMO is 95.737% as opposed to the GRU, LSTM, RNN, DNN, and ANN models' respective recall values of 81.924%, 84.536%, 87.736%, 90.326%, and 92.413%.

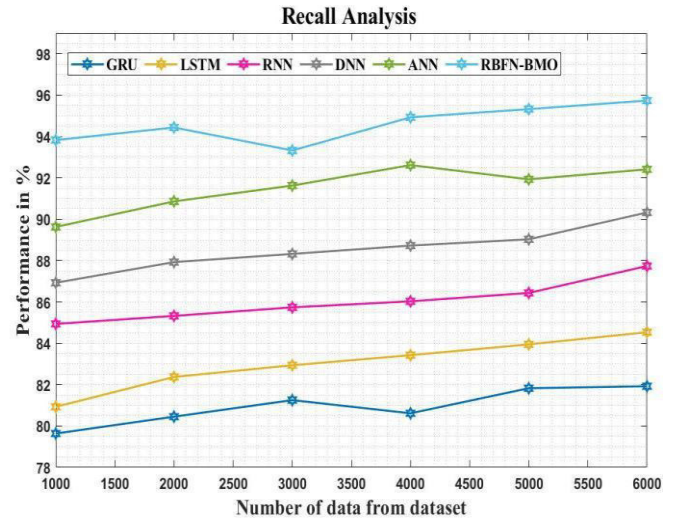


Fig. 5. Recall analysis for the RBFN-BMO method with existing systems.

TABLE II. RECALL ANALYSIS FOR THE RBFN-BMO METHOD USING EXISTING SYSTEMS

Data from dataset	GRU	LSTM	RNN	DNN	ANN	RBFN-BMO
1000	79.637	80.928	84.938	86.927	89.627	93.827
2000	80.452	82.373	85.324	87.926	90.862	94.435
3000	81.252	82.938	85.738	88.322	91.627	93.324
4000	80.615	83.425	86.029	88.726	92.617	94.928
5000	81.827	83.948	86.435	89.028	91.928	95.324
6000	81.924	84.536	87.736	90.326	92.413	95.737

3) *F-Score analysis*: Fig. 6 and Table III display an f-score contrast of the RBFN-BMO strategy with other existing methods. The graph shows that the deep learning method has produced better performance regarding the f-score. The RBFN-BMO model, for example, has an f-score of 92.536% with 1000 data, while the GRU, LSTM, RNN, DNN, and ANN models have f-scores of 87.928%, 85.435%, 81.526%, 83.425%, and 90.324%, respectively. The RBFN-BMO model, on the other hand, has performed best over a range of data sizes. Similarly, the f-score value of RBFN-BMO under 6000 data is 94.627%, while for GRU, LSTM, RNN, DNN, and ANN models, it is 89.928%, 87.435%, 82.213%, 85.324%, and 91.928%, respectively.

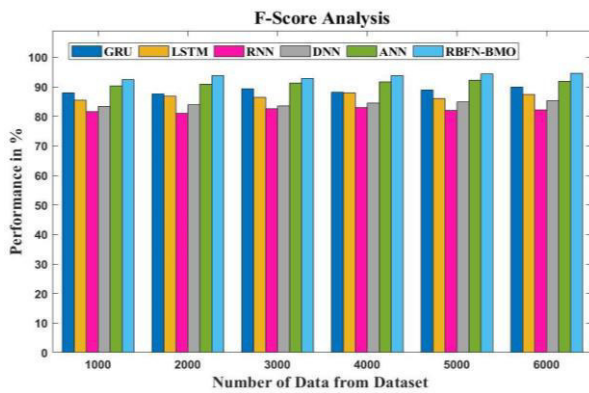


Fig. 6. F-Score analysis for the RBFN-BMO method using existing systems.

TABLE III. F-SCORE ANALYSIS USING TRADITIONAL SYSTEMS USING THE RBFN-BMO METHOD

Data from dataset	GRU	LSTM	RNN	DNN	ANN	RBFN-BMO
1000	87.928	85.435	81.526	83.425	90.324	92.536
2000	87.526	86.928	81.029	83.928	90.928	93.727
3000	89.432	86.425	82.536	83.526	91.243	92.927
4000	88.214	87.928	82.938	84.525	91.627	93.826
5000	88.921	86.029	81.937	84.928	92.173	94.324
6000	89.928	87.435	82.213	85.324	91.928	94.627

4) *Accuracy analysis*: Fig. 7 and Table IV shows the accuracy of the RBFN-BMO approach as compared to that of other currently utilized approaches..The graph shows how deep learning improves performance with accuracy. The RBFN-BMO model, for example, has a 1000-data accuracy of 97.627%, whereas the GRU, LSTM, RNN, DNN, and ANN models have accuracy of 89.536%, 90.917%, 92.524%, 94.526%, and 96.425%, respectively. The RBFN-BMO model, on the other hand, fared well with varying data sizes. Similarly, the accuracy of the RBFN-BMO under 6000 data is 99.546%, while the accuracy of the respective GRU, LSTM, RNN, DNN, and ANN models is 90.716%, 92.817%, 93.926%, 95.736%, and 97.125%.

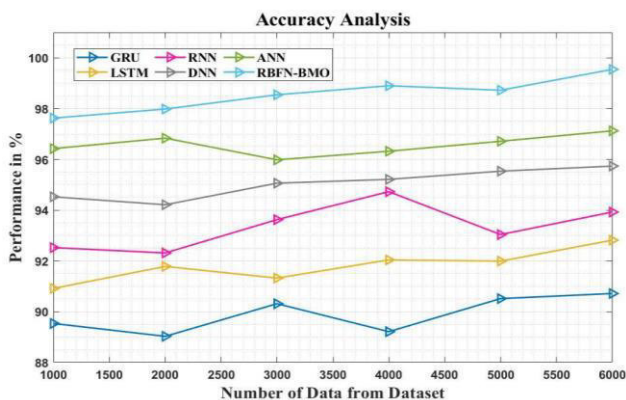


Fig. 7. Accuracy analysis for RBFN-BMO method with existing systems.

TABLE IV. ANALYSIS OF RBFN-BMO METHOD ACCURACY WITH EXISTING SYSTEMS

Data from dataset	GRU	LSTM	RNN	DNN	ANN	RBFN-BMO
1000	89.536	90.917	92.524	94.526	96.425	97.627
2000	89.029	91.783	92.314	94.213	96.837	97.983
3000	90.314	91.324	93.627	95.063	95.983	98.546
4000	89.213	92.039	94.728	95.213	96.322	98.902
5000	90.516	91.992	93.039	95.536	96.714	98.724
6000	90.716	92.817	93.926	95.736	97.125	99.546

5) *RMSE analysis*: Fig. 8 and Table V display an RMSE similarity between the RBFN-BMO strategy and other earlier techniques. The graph shows that the deep learning strategy has produced better results with a lower RMSE value. For instance, the RMSE value for the RBFN-BMO is 25.637% with 100 data, while the RMSE values for the GRU, LSTM, RNN, DNN, and ANN models are slightly higher at 30.526%, 26.928%, 33.626%, 36.536%, and 43.737%, respectively. The RBFN-BMO model, on the other hand, has demonstrated that it performs best with diverse data sizes while keeping a low RMSE. The RMSE value for the RBFN-BMO model under 6000 data is 26.324%, whereas it is 32.933%, 29.322%, 35.342%, 42.627%, and 47.326% for the GRU, LSTM, RNN, DNN, and ANN models, respectively.

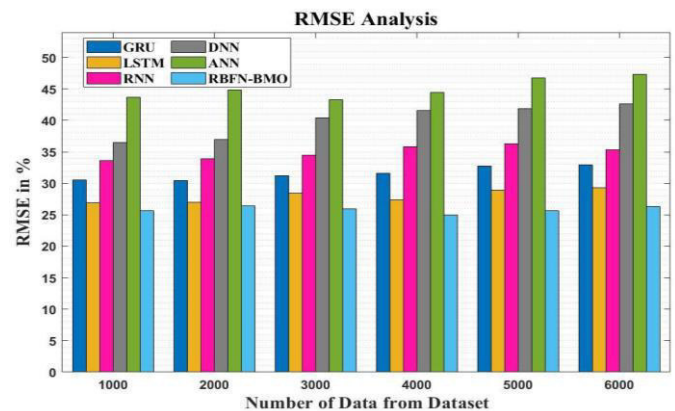


Fig. 8. RMSE analysis of the RBFN-BMO method with existing systems.

TABLE V. RMSE ANALYSIS OF THE RBFN-BMO METHOD USING EXISTING SYSTEMS

Data from dataset	GRU	LSTM	RNN	DNN	ANN	RBFN-BMO
1000	30.526	26.928	33.626	36.536	43.737	25.637
2000	30.425	27.029	33.928	36.928	44.863	26.435
3000	31.252	28.425	34.526	40.425	43.324	25.926
4000	31.627	27.425	35.827	41.627	44.432	25.029
5000	32.737	28.926	36.324	41.911	46.732	25.627
6000	32.933	29.322	35.342	42.627	47.326	26.324

6) *Execution time analysis*: The execution time analysis of the RBFN-BMO technique using existing methods is described in Table VI and Fig. 9. The information clearly shows that the RBFN-BMO method has outperformed the other techniques in every way. The RBFN-BMO process, for example, took only 2.738ms to execute 1000 data, while GRU, LSTM, RNN, DNN, and ANN took 12.837ms, 10.637ms, 8.526ms, 6.938ms, and 4.837ms, respectively. Similarly, the RBFN-BMO method takes 3.624ms to execute 6000 data, whereas the other existing techniques such as GRU, LSTM, RNN, DNN, and ANN have taken 15.526ms, 11.638ms, 9.553ms, 7.425ms, and 5.029ms, respectively.

TABLE VI. ANALYSIS OF RBFN-BMO METHOD EXECUTION TIME WITH EXISTING SYSTEMS

Data from dataset	GRU	LSTM	RNN	DNN	ANN	RBFN-BMO
1000	12.837	10.637	8.526	6.938	4.837	2.738
2000	12.536	10.827	8.928	6.324	4.213	2.324
3000	13.627	10.324	8.435	6.022	4.039	3.029
4000	13.829	11.526	9.073	7.425	4.637	3.927
5000	13.425	11.627	9.224	7.829	5.324	3.526
6000	15.526	11.638	9.553	7.425	5.029	3.624

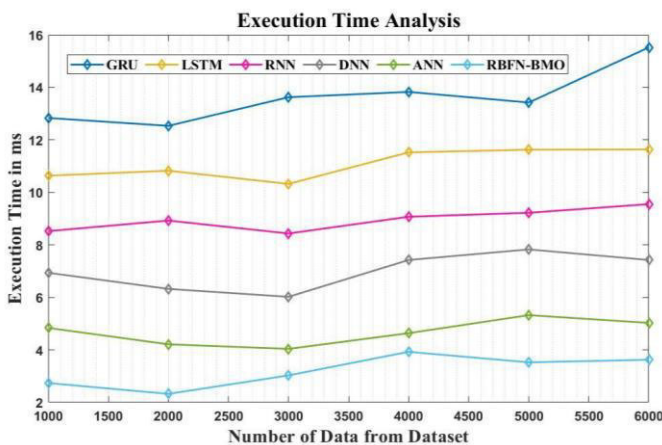


Fig. 9. Execution time analysis for the RBFN-BMO method with existing systems.

V. CONCLUSION

Facial expression analysis is one tool used to develop emotional intelligence, which is becoming increasingly important in many fields, including business and education. Numerous factors, such as visual contexts, point-of-view shifts, intra- and inter-class differences and more, impede the development of a reliable emotion recognition system. This paper suggests a convolutional neural network as a potential solution to the emotion recognition problem. To examine facial expressions in images, the proposed RBFN was made face-sensitive. The proposed RBFN-BMO can recognize people in high-resolution photos, evaluate facial expressions using facial features, and predict emotional states. The

recognition during testing validates the proposed efficacy. Regarding output quality, the established RBFN-BMO classification algorithms perform better than those currently used. The RBFN-BMO uses every dataset used for the analysis and achieves the highest level of accuracy possible, which is 99.54%. To evaluate the effectiveness of the proposed classifier, the performance of proposed RBFN-BMO is compared with the existing Gated Recurrent Unit (GRU), Long Short-Term Memory (LSTM), Recurrent Neural Network (RNN), Deep Neural Network (CNN), Artificial Neural Network (ANN). As a result, the RBFN-BMO can produce better results for celebs datasets. Furthermore, it can be inferred that the Blue Monkey Optimization (BMO) meta-heuristic algorithm selects the input data features that are both the most informative and the most pertinent. It helps to achieve better categorization and reduces the error brought on by the Root Mean Square. The future of our research depends on adding new features, classifying facial emotions into their ten subcategories, and researching automatic facial emotion recognition.

REFERENCES

- [1] M. Mehdi, R. B. Vistro, E. A. Mahmoud, and H. O. Elansary, "Application of Drone Surveillance for Advance Agriculture Monitoring by Android Application Using Convolution Neural Network," *Agronomy*, 13(7), p.1764, 2023.
- [2] G. Min, G. Yukun, and T. T. Hormel, "A deep learning network for classifying arteries and veins in montaged widefield OCT angiograms," *Science*, vol. 2, no. 2, article 100149, 2022.
- [3] S. Tian Yingjie, and L. S. Duo, "Recent advances on loss functions in deep learning for computer vision," *Neurocomputing*, vol. 497, pp. 129–158, 2022.
- [4] V. Andrea, J. Sumit, and H. Shayne, "Face detection and grimace scale prediction of white furred mice," *Machine Learning with Applications*, vol. 8, article 100312, 2022.
- [5] H. Zeng, B. Zhang, B. Song et al, "Facial expression recognition via learning deep sparse autoencoders," *Neurocomputing*, vol. 273, pp. 643–649, 2018.
- [6] B. J. Park, C. Yoon, E. H. Jang, and D. H. Kim, "Physiological signals and recognition of negative emotions," in *Proceedings of the 2017 International Conference on Information and Communication Technology Convergence (ICTC)*, pp. 1074–1076, IEEE, Jeju, Korea, October 2017.
- [7] L. Wiskott, and C. Von Der Malsburg, "Recognizing faces by dynamic link matching," *NeuroImage*, vol. 4, no. 3, pp. S14–S18, 1996.
- [8] Mahmood, Maha, and Belal Al-Khateeb. "The blue monkey: A new nature inspired metaheuristic optimization algorithm." *Periodicals of Engineering and Natural Sciences* 7.3 (2019): 1054-1066.
- [9] L. Chen, M. Zhou, W. Su, M. Wu, J. She, and K. Hirota, "Softmax regression based deep sparse autoencoder network for facial emotion recognition in human-robot interaction," *Information Sciences*, vol. 428, pp. 49–61, 2018.
- [10] P. Babajee, G. Suddul, S. Armoogum, and R. Foogooa, "Identifying human emotions from facial expressions with deep learning," in *Proceedings of the 2020 Zooming Innovation in Consumer Technologies Conference (ZINC)*, pp. 36–39, IEEE, Novi Sad, Serbia, May 2020.
- [11] P. Satyanarayana, D. P. Vardhan, R. Tejaswi, and S. V. P. Kumar, "Emotion recognition by deep learning and cloud access," in *Proceedings of the 2021 3rd International Conference on Advances in Computing, Communication Control and Networking (ICAC3N)*, pp. 360–365, IEEE, Greater Noida, India, December 2021.
- [12] K. Jayanthi, and S. Mohan, "An integrated framework for emotion recognition using speech and static images with deep classifier fusion approach," *International Journal of Information Technology*, pp. 1–11, 2022.

- [13] V. Sati, S. M. Sanchez, N. Shoeibi, A. Arora, and J. M. Corchado, "Face detection and recognition, face emotion recognition through NVIDIA Jetson Nano," in *Proceedings of the International Symposium on Ambient Intelligence*, pp. 177–185, Springer, Cham, September 2020.
- [14] X. Wang, Y. Zhao, and F. Pourpanah, "Recent advances in deep learning," *International Journal of Machine Learning and Cybernetics*, vol. 11, no. 4, pp. 747–750, 2020.
- [15] O. Ekundayo, and S. Viriri, "Multilabel convolution neural network for facial expression recognition and ordinal intensity estimation," *PeerJ Computer Science*, vol. 7, p. e736, 2021.
- [16] A. Hassounch, A. M. Mutawa, and M. Murugappan, "Development of a real-time emotion recognition system using facial expressions and EEG based on machine learning and deep neural network methods," *Informatics in Medicine Unlocked*, vol. 20, Article ID 100372, 2020.
- [17] C. Tan, M. Sarlija, and N. Kasabov, "NeuroSense: short-term emotion recognition and understanding based on spiking neural network modelling of spatio-temporal EEG patterns," *Neurocomputing*, vol. 434, pp. 137–148, 2021.
- [18] S. Li, and W. Deng, "Deep Facial Expression Recognition: A Survey," *IEEE Transactions on Affective Computing*, vol. 7, no. 3, pp. 1195–1215, 2020.
- [19] B. Yang, X. Han, and J. Tang, "Tree class emotions recognition based on deep learning using stacked autoencoder," in *Proceedings of the 2017 10th International Congress on Image and Signal Processing, BioMedical Engineering and Informatics (CISP-BMEI)*, pp. 1–5, IEEE, Shanghai, China, October 2017.
- [20] S. S. Yadahalli, S. Rege, and S. Kulkarni, "Facial micro expression detection using deep learning architecture," in *Proceedings of the 2020 International Conference on Smart Electronics and Communication (ICOSEC)*, pp. 167–171, IEEE, Trichy, India, September 2020.
- [21] C. Asaju and H. Vadapalli, "A temporal approach to facial emotion expression recognition," in *Proceedings of the Southern African Conference for Artificial Intelligence Research*, pp. 274–286, Springer, Cham, January 2021.
- [22] . Yolcu, I. Oztel, S. Kazan et al (2020) Deep learning-based face analysis system for monitoring customer interest. *J Ambient Intell Human Comput* 11:237–248. <https://doi.org/10.1007/s12652-019-01310-5>
- [23] R.R Walecki "Deep structured learning for facial expression intensity estimation", *Image Vis Comput*, vol. 259, pp. 143–154, 2017.
- [24] C. Asaju, and H. Vadapalli, "A temporal approach to facial emotion expression recognition," in *Proceedings of the Southern African Conference for Artificial Intelligence Research*, pp. 274–286, Springer, Cham, January 2021.
- [25] O. Ekundayo and S. Viriri, "Multilabel convolution neural network for facial expression recognition and ordinal intensity estimation," *PeerJ Computer Science*, vol. 7, p. e736, 2021.
- [26] V. Agarwal, and S. Bhanot, "Radial basis function neural network-based face recognition using firefly algorithm," *Neural Computing and Applications*, vol. 30, no. 8, pp.2643-2660, 2018.
- [27] E. Kibebew and K. Abie "Population Status, Group Size, And Threat to Boutourlini's Blue Monkeys (*Cercopithecus Mitis Boutourlinii*) In Jibat Forest," Ethiopia. *J Ecosyst Ecography* vol. 7, pp. 230. Doi:10.4172/2157-7625.1000230.,2017.
- [28] K. Abie, A. Bekele A "Population Estimate, Group Size and Age Structure of the Gelada Baboon (*The Ropithecus Gelada*) Around Debre-Libanos," Northwest Shewa Zone, Ethiopia. *Glob J Sci Fr R Biol Sci* vol. 17, pp. 27-33, 2017.
- [29] S. Mirjalili, A. H. Gandomi, S. Z. Mirjalili, S. Saremi, H. Faris, and S. M. Mirjalili, "Salp Swarm Algorithm: A Bio-Inspired Optimizer for Engineering Design Problems," *Adv. Eng. Softw.*, Vol. 114, pp. 163–191, 2017.
- [30] Liu Z, Luo P, Wang X, Tang X (2018) Large-scale celebfaces attributes (celeba) dataset. Retrieved August 15: 2018

Bidirectional recommendation in HR analytics through text summarization

Channabasamma Arandi¹, Suresh Yeresime²

¹Department of Computer Science and Engineering, Gokaraju Rangaraju Institute of Engineering and Technology, Hyderabad, India and Visvesvaraya Technological University, Belagavi, India

²Department of Computer Science and Engineering, Ballari Institute of Technology and Management, Ballari, India and Visvesvaraya Technological University, Belagavi, India

Article Info

Article history:

Received Dec 29, 2022

Revised Aug 30, 2023

Accepted Oct 10, 2023

Keywords:

Bidirectional recommendation

Coverage mechanism

Decoder attention

Mixed learning objective

Named entity recognition

ABSTRACT

For over a decade, online job portals have been providing their services to both job seekers and employers in search of hiring opportunities. Because of the high demand for recruitment, it is insufficient to use conventional hiring methods to find a suitable candidate to fill the position. Validating resumes online is challenging due to the potential for manual errors, making the process inherently risky. The bidirectional method comprises named entity recognition (NER) for extracting the required resumes for recruiters. Cosine similarity shows the match percentage of resumes for the job requirements and vice versa. In an attempt to tackle an issue of unregistered words, a solution called decoder attention with pointer network (DA-PN) has been introduced. This method incorporates the use of coverage mechanism to prevent word repetition through generated text summary. DA-PN+Cover method with mixed learning objective (MLO) (DA-PN+Cover+MLO) is utilized for protecting grow of increasing faults in generated text summary. Performance of proposed method is estimated using evaluation indicator recall oriented understudy for gisting evaluation (ROUGE) and attains an average of 27.47 which is comparatively higher than existing methods.

This is an open access article under the [CC BY-SA](#) license.



Corresponding Author:

Channabasamma Arandi

Department of Computer Science and Engineering

Gokaraju Rangaraju Institute of Engineering and Technology, Hyderabad

Visvesvaraya Technological University, Belagavi-590018, India

Email: Channu.ar@gmail.com

NOMENCLATURE

Symbol	Notation
W_α & V_α	The weight elements
s_t	invisible-layer condition of decoder at moment-interval t
$\ x\ $	Euclidean norm of vector x
$\ y\ $	Euclidean norm of vector y
p_{gen}	Possibility of switch
$P_{vocab}(w)$	Word distribution in last output vocabulary
W_h	Weight matrix at hidden state
c_t^e	Coverage vector at encoder
c_t^d	Coverage vector at decoder
h_j	Hidden state
bt_{atten}	Bias of training iteration
$P(w_t^*)$	Final prediction vocabulary
$cover_loss_t$	Function of coverage loss
β	Coverage mechanism weight in total loss

Symbol	Notation
y^s	Sampling sequences
y^*	Baseline
W_y	Mass matrix of past work y_{j-1}
W_e	Mass matrix of encoder invisible condition
u_e^c	Context vector of final encoder
u_d^d	Context vector of final decoder
W_d	Weight matrix of decoder hidden condition
bt_{ptr}	Bias term
x	Input vector
y^\wedge	Baseline output
$r(y)$	Reward function of output progression y
L_{rl}	Equivalent to conditional prospect of increased sample order y_s

1. INTRODUCTION

Over the last decade, online enrollment platforms like Naukri.com, Boss, Indeed Hiring, Glassdoor, Monster, LinkedIn, and Zhaopin have emerged to revolutionize the job recruitment process. These platforms have streamlined the hiring process and significantly transformed the job market landscape [1]. Many researchers view a particular domain for job suggestions and introduce a method for online platforms utilizing detailed relational learning [2]. This area effortlessly scales to millions of elements as well as candidate resumes and work positions including more information in the form of candidate interactions [3]. Due to the fast variations of technology development, new work opportunities are always being created in industries with an advanced list of skill sets to face these wide changes [4]. Individuals who are looking to change their careers or looking for better opportunities meet the trouble of skill discrepancy because of those continuous changes. This paper presents an innovative approach to job suggestions that caters to the needs of both job seekers and recruiters [5]. The proposed system aims to benefit both parties by ensuring optimal job matches. Recruiters can easily identify the most suitable candidates for each job position, while job seekers also receive relevant job opportunities that align with their CVs [6]. To achieve this, the process begins with the extraction of job offers from sa.indeed.com. Subsequently, the extracted job offers undergo pre-processing, training, and matching [7]. The outcome is a streamlined and efficient job-matching process where both recruiters and job seekers actively participate in recommending and supporting candidates for the right job offers [8]. This paper aims to briefly emphasize the benefits of creating job opportunities for people with disabilities. Despite facing disproportionate levels of uncomfortable job situations, unemployment, and underemployment compared to individuals without disabilities [9], it is essential to focus on generating employment prospects for this marginalized group. The main stage is for companies to employ a change in the aspect where the responsibilities of job involvement are not mainly focused on people with autism but on variations that workers can make to permit them to succeed in the organizational context. Most of the rapid research on recruiting has aimed heavily authenticity and validity of the company's selection activities and methods [10]. Enrolling is important and concerned with finding a suitable candidate pool, attracting candidates, and acquiring them to register for open postings [11]. Despite the focus on employer responses to hiring, it is equally, if not more, important to consider the job seeker's reactions to the recruitment process [12]. Every day people employ industry-scale suggestion systems to suggest 1000s of candidates to the clients and the other way around opening to candidates. The job recommendation system is enriched on a heterogeneous collection of input information, resumes of candidates, vacancy texts, and structured information [13].

Traditional HR analytics systems importantly rely on unidirectional suggestions, where recruiters give suggestions to employees. Still, this method fails to capture the full scope of the employer-employee relationship [14]. Further, there is a need for a more comprehensive and bidirectional recommendation system that can support text summarization methods to process key data through high volumes of HR-related text information [15]. Shao *et al.* [16] implemented a wide investigation approach of external and internal operations for designing multivariate attributes in InEXIT. Initially encode the key and value of every attribute along with its source into a similar linguistic space. This paper presented a model for the internal process between multivariate attributes inside the job post and resume, further the external process between the resume and job post. In the end, the matching layer is introduced to find a matching degree. The reduction in economic costs and manpower, along with the support for InEXIT, contributes to the enhancement of online recruitment. Nonetheless, there are limitations in the implementation method, as certain aspects of InEXIT might possess reliable backups, such as pre-trained language models and fusion strategies. Ong and Lim [17] introduced an approach to information-driven work recommendation for professional vision. The skill recommendation recognizes and gathers the skill set essential for work based on work requirements released by companies recruiting for these positions. Further, the information gathering and processing

abilities, and skill recognition use word implant techniques for job title presentation, next to a feed-forward neural network for job skill recommendation related to work title representation. The method combines job title representation utilizing bidirectional encoder representations from transformers (BERT), with job skill suggestions utilizing a direct feed-forward neural network efficiently regarding accuracy and F1-score. The limitation is that it may not capture important work trends or find future skill needs. Yang *et al.* [18] presented job suggestions for system-based merging content and filtering approach of cost-sensitive informative relational learning. Statistical relational learning (SRL) can represent the possible dependencies between the attributes of similar objects to give an honest way to merge 2 approaches. The paper introduced a way to accept the state-of-the-art SRL methods to hybrid suggestion systems and importantly no investigation applied to current big-data-scale systems. This method can permit modulating the exchange between the recall and precision of the system in a respectable way. Obtaining high-quality data like brief job descriptions or exact candidate profiles was difficult or costly it was the drawback of the method. Yildirim *et al.* [19] introduced a machine for reciprocal suggestion based on multiple-objective deep factorization for online enrolment. This paper focuses on solving the problem of a shortage of information containing corresponding choices in a network. Consolidated the multiple-objective learning method into multiple state-of-the-art approaches, whose victory has been determined by the same prediction issues and obtained hopeful outcomes. The method was better than traditional methods and maximized the speed of the process by 2 times. The drawback was data sparsity for particular minimum-famous users, the machine may struggle to create exact authentic recommendations.

Alsaif *et al.* [20] presented a system based on NLP bi-directional recommendation for suggesting jobs to job seekers and resumes to recruiters. This article introduces a beneficial system for both recruiters and job seekers. In this, recruiters can select the best employees for each work position for their job postings likewise employers also get better jobs that are similar to their CV. The process is initially, through sa.indeed.com the job offers are extracted, and after the extraction of job offers the pre-processing, training and matching are done. Comparing the task while serving recruiters and job seekers help their job by suggesting and supporting candidates to get the right job offers. The drawback was the lack of personalization, the NLP-related suggestion model was usually based on common patterns, which could result in generic recommendations that do not align with particular preferences. Jain *et al.* [21] implemented an ATS for the Hindi language by utilizing real coded genetic algorithm (RCGA). The rigorous experimentation on various feature groups was evaluated for differentiating features such as named sentence similarity and named entity features were merged with others for computing the evaluation metrics. The RCGA method chooses the better chromosome that includes real-valued weights of produced features which evaluates the distance among sentence values. The limitation of the implemented method was cost efficiency and the acceptance of ATS for HR solutions. Sethi *et al.* [22] introduced a transformer method for generating a better summary average. The method combines with Bart and T5 methods to know which method produces the best summary average. After passing 1000 data of articles, identify that the Bart method performed well than the T5 method in each aspect. The method was much more efficient and it takes only related content and leaves the unwanted and irrelevant content. The method utilized only the limited dataset and cost efficiency. There are some drawbacks of bidirectional recommendation for HR analytics by text summarization in the above-mentioned methods such as data sparsity, specifically for minimum famous users, which may affect the accuracy, lack of personalization in NLP-related recommendation models, lack of research used to real big-data-scale systems, and potential failure to capture necessary work trends or discover future skill needs. The main contributions of this work are given as:

- a. A decoder attention with pointer network (DA-PN) model is proposed on attention mechanism at encoder and decoder ends through combining attention mechanism in present period stage and implemented PN at decoder to resolve issue of unregistered words.
- b. The proposed DA-PN+Cover method depends on coverage mechanism combining cover vector. The process involves measuring attention mechanism at encoder and decoder in prior period stage. This measurement is then used to update a loss function that helps in avoiding word repetition when generating text summary.
- c. A DA-PN+Cover+MLO method is proposed through combining MLO and implementing a self-crucial gradient technique. It takes global reward and evaluation indicator in phase of iteration of method to protect grow of increasing faults in generated text summaries.

The rest part of research is described as follows: section 2 gives informations about proposed method. Section 3 describes process of DA-PN+Cover+MLO method. Section 4 describes the results and discussion, and section 5 represents the conclusion of the paper.

2. PROPOSED METHOD

The bidirectional system is presented in the proposed methodology and it gives the best possible recommendations to both the employees and recruiters. The methodology involves cleaning data, and named

entity recognition (NER) for extracting the necessary resumes. The score is assigned to resumes by calculating the similarity between resumes and job descriptions; which helps to match resumes to that of the job description. NLP techniques are utilized for pre-processing the data and cosine similarity is utilized to measure the similarity between the resume and the job description. For the summarization of resumes and text, DA-PN+Cover+MLO method is proposed. Figure 1 represents the proposed model of this research.

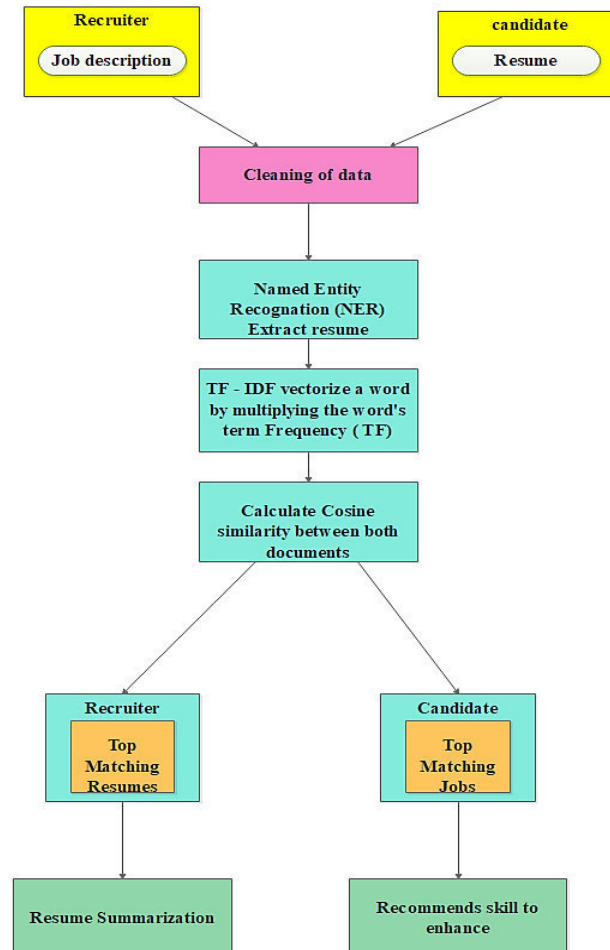


Figure 1. Workflow of bidirectional system

2.1. Data collection and integration

The resume dataset is taken for this research work, which is gathered from kaggle and the dataset includes 1,735 resumes [23]. Every profile includes fields like resume tile, location, role description, technical skills, education, certification, and additional data. There are four JDs acquired from LinkedIn on the topic of machine learning data scientist, full stack, java, and python developer. In JDs, the profile includes the job title, company name, city, description, education, and preference skills. Table 1 represents dataset description.

Table 1. Represents the dataset description

Job title	Company name	City	Description	Education	Preference skills
Data scientist	Wipro	Bangalore, Kamataka	Expert in problem-solving and coding skills	Bachelor's degree related to computer science	Machine/deep learning
Full stack developer	Infosys	Chennai, Tamilnadu	Well-expert in front-end and back-end development	B.E	HTML, CSS
Java developer	Cognizant	Coimbatore, Tamilnadu	Expert in software development life cycle process	B.E	Java
Python developer	TCS	Bangalore, Kamataka	Expert in writing and testing codes	Degree	Python

2.2. Pre-processing

Unstructured data is converted to structured data by using several pre-processing steps. Pre-processing is the preliminary stage for preparing data. The job description will be compared against a pool of resumes that are priorly loaded into the system, similarly, the candidate's resume will be compared against different job descriptions which are priorly loaded into the system. NLP tools are used to extract the required information by cleaning the data, the given resume/job description may contain different symbols and integers, which are not needed for the program. So, it removes the unwanted characters from the resume like numbers, stop words, and punctuations, and makes the resume/job description ready for the next process by converting all strings to lowercase.

2.3. Named entity recognition

Many times, resumes are populated with excess information, often irrelevant to what the recruiter is looking for in it. Therefore, it is tedious and hectic to evaluate resumes in bulk. Through the NER model, resumes can be evaluated at a glance, thereby reducing the effort required in shortlisting candidates among a pile of resumes. NER automatically generates summaries of resumes by extracting only primary entities like name, skills, and educational background.

2.4. Generating vectors

In NLP models work on numbers rather than textual data, so this textual data needs to be vectorized. Moreover, the word count of the words in each document is needed to compute the cosine similarity. The collection of text documents is converted to a matrix of token counts called bag-of-words (BoW). The output of this comes as a sparse matrix, in which each document represents a row in the matrix and each special content represents a vertical portion of the matrix. The cell value represents the count of words in the particular document. To understand the importance of words in the corpus, term frequency-inverse document frequency (TF-IDF) is used. TF-IDF is based on the logic that words that are too common in a corpus and rare and are not statistically significant in identifying a pattern. The logarithmic factor in the TF-IDF equation serves the mathematical purpose of assigning low TF-IDF values to words that are either overly common or excessively rare in the corpus. TF-IDF values a word by multiplying the word's TF equation with IDF equation.

$$TF = \frac{\text{No.of times the term appears in a document}}{\text{Total no.of terms in the document}} \quad (1)$$

$$IDF = \log \left(\frac{\text{No.of documents in the corpus}}{\text{No.of documents in the corpus that contains the term}} \right) \quad (2)$$

$$TF - IDF = TF * IDF \quad (3)$$

The highest score of TF-IDF signifies the huge significance of words in the corpus while lower scores show lower significance. The words that have low significance for analysis can be removed, hence making the model building less complex by decreasing the input dimensions. Accurate semantic presentation methods are important in the applications of text mining. However competitive outcomes for automatic text classification may be attained with a traditional bag of words, such as the presentation method can't give satisfactory classification results in hard settings where higher text representations are needed. Both count vectorizer and TF-IDF fail to provide linguistic similarity between words and hence are only used for customizing stop word lists. To train a method on the default linguistic relationship of the words, Doc2Vec is used. Because Doc2Vec can read documents as a whole rather than working on every single word. It has a feature to provide n-Dimensional vectors. This transformation has two significant properties such as dimensionality reduction for effective representation and contextual similarity for expressive representations.

2.5. Cosine similarity

Measuring the similarity or distance first requires understanding the objects of study as samples and the chunks of those objects are measured as features. For the proposed analysis, the resume of the candidate and the job description are two data samples. Two features can be represented as two dimensions and through the Cartesian coordinate system, samples can be visualized. Naturally, samples can also be visualized in three dimensions if there are three features. However, the calculation of the distance will remain the same no matter how many features or dimensions are there.

The technique used to measure distances depends on a particular working environment. For instance, in some applications, the euclidean distance can be ideal and useful for computing distances. Other areas may require a more sophisticated approach for calculating distances between observations or points like the cosine distance. Cosine analogy is a metric utilized to calculate analogy in between documents and give a

rank to the documents; it is independent of the size of the documents. Cosine similarity is more about the orientation of the two points in space rather than considering the exact distance from one another. This means that cosine distance is less affected by magnitude or how large the given numbers are [6]. Assume x & y is 2 sample vectors for comparison. The relation for calculating the analogy of cosine is given as equation.

Likewise, $\|y\|$ represents the euclidean norm of the vector y . Cosine calculates the degree in-between vectors x & y ; the value of 0 indicates two vectors are 90 degrees apart and there is no match. The value closer to 1 indicates two vectors are separated by a small angle and there is a match between two vectors.

$$oS_{\sin(x,y)} = \frac{x,y}{\|x\| \cdot \|y\|} \quad (4)$$

where $\|x\|$ represents euclidean norm of the vector $x = (x_1, x_2, x_3, \dots, x_p)$, defined as (5):

$$\sqrt{x_1^2 + x_2^2 + x_3^2 + \dots + x_p^2} \quad (5)$$

3. DA-PN+COVER+MLO BASED SUMMARIZATION

To manage out-of-vocabulary (OOV) words, PN combining DA that merge decoder context vector with context vector produced from actual text, for regulating chosen actual text and addition lexicon. To address word repetition, a multiple-attention coverage mechanism is employed, which continuously utilizes coverage vectors from both encoder and decoder for influencing attention weight. The attention data of decoder is given as an input-to-input mapping layer, so model can give attention to prior data and minimize the recurrence of words. For readability of generated text summaries, mixed learning objective (MLO) function to positioning global reward, particular discrete gradient can increased on scoring which improves readability of generated text summary.

3.1. Decoder attention-based pointer network method

For resolving the issue of unregistered words, the DA-PN model is developed by using DA depending the PN. In every stage, the DA-PN model determines to copy an unregistered word through actual text or pin it to other word which is already in actual vocabulary. Former action is controlled by softmax which has probability normalization, although latter is related to words determined from input information by utilizing DA mechanism. If both merged, unregistered words are determined in actual text but are not added to actual vocabulary.

DA-PN method contains two input layers for copying words through actual text or actual vocabulary. Every dimension shows one word. p_{gen} a switching mechanism utilized for producing a possibility for managing the input. The attention of the decoder compensates for the weakening data caused by huge sequences, which enables method to position main data much accurate. The distribution of attention regarding to possibility distribution of every word in actual text can be calculated as (6):

$$\alpha^t = softmax(V_\alpha \tanh(W_\alpha s_t^T)) \quad (6)$$

Where W_α and V_α represents parameters of weight and s_t represents decoder's hidden layer state at time stage t . Sum of weighted attention distribution acquired through (6) and decoder stage before present time stage represents context vector of the final decoder as (7). The possibility of the switch p_{gen} could depends through decoder/encoder context vector with real invisible-layer condition, as (8)

$$u_t^d = \sum_{j=1}^{t-1} \alpha_j^t s_j \quad (7)$$

$$p_{gen} = \sigma(W_y y_{j-1} + W_e u_t^e + W_d u_t^d + bt_{ptr}) \quad (8)$$

Where W_y represents a matrix of weight of prior word y_{j-1} , W_e and W_d represents a matrix of weight of encoder and decoder hidden state at present stage respectively, u_t^e represents the context vector of last encoder, u_t^d represents context vector of final decoder, and bt_{ptr} represents bias. Bias and weight matrix in (8) are the parameters which can added during iteration of model training. The linear weight adds those parameters that are processed through sigmoid function and marked among 0 and 1 to soft switch for managing input layer source, based on data of 2 stages namely source text and vocabulary. In (9) s_t

$$P_{final}(w) = p_{gen}P_{vocab}(w) + (1 - p_{gen}) \sum_{i:w_i=w} a_i \quad (10)$$

The inclusion of attention mechanism in decoder facilitates a more effective focus on key features within the generated text summary. This is particularly important to address the problem of word recurrence. To overcome this challenge and ensure attention is given to the entire sequence, a global vector is employed

for maintenance purposes. The decoder's hidden layer utilizes a past time context vector for measuring present input, so the data acquired in the past can utilized during calculation which strengthens the previous and present time relationship. At present time, to utilize source text data in previous and target generated text summary, two coverage vectors in attention mechanism are combined as per (11):

$$e_j^t = v^T \tanh(W_h h_j + W_s s_t + W_e c_t^e + W_d c_t^d) + b_{atten} \quad (11)$$

Where v^T and W_h represents a matrix of weight of repetitive nonlinear activation function and hidden state utilized to training respectively, h_j represents a hidden state, W_s represents a matrix of weight of repetitive present state sequence utilized to training, s_t represents present state sequence, W_e and W_d describes weight matrix of encoder and decoder hidden state in present stage respectively, c_t^e and c_t^d describes coverage vector of encoder and decoder respectively and b_{atten} represents a bias of training iteration. The outcome of the present time stage is afflicted by past actual text and produced text summary, to ignore giving attention to similar data and also ignoring recurrence. Final loss function has the actual and coverage loss, the mathematical representation is described in (12):

$$loss_t = -\log(p(w_t^*)) + \beta cover_{loss_t} \quad (12)$$

Where $p(w_t^*)$ represents the final predicted vocabulary of the possibility distribution, $cover_{loss_t}$ represents the function of coverage loss and β represents the coverage mechanism's weight in whole loss. By utilizing attention dispensation at the encoder and decoder ends and also utilizing additional loss items, the method efficiently suppresses probable repeated items and maximizes automatic production of text summaries. Figure 3 represents the overall process of DA-PN+Cover method with two coverage vectors.

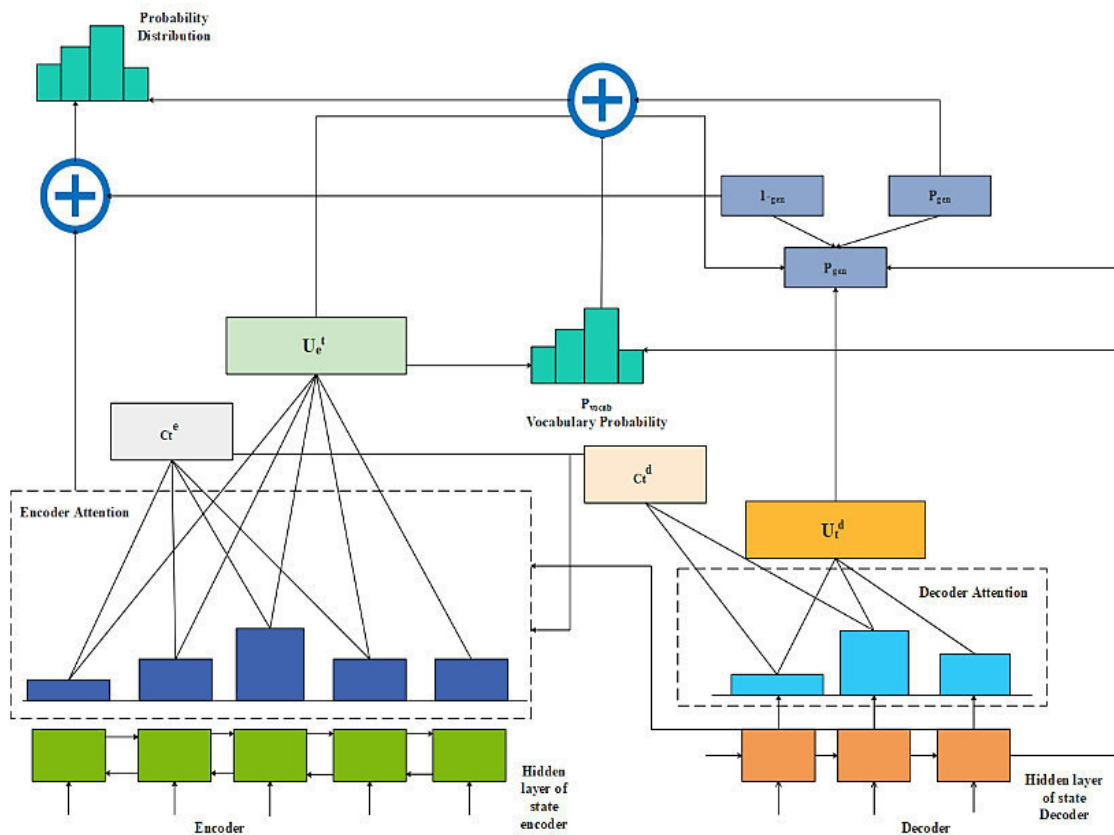


Figure 3. Pictorial representation of proposed DA-PN + Cover

3.3. DA-PN+Cover+MLO method

To protect grow of accumulative bugs in produced text summaries, proposed DA-PN+Cover method includes a MLO after ending the distribution of collective mistakes in created word summaries. The model

that resulted is known as DA-PN+Cover+MLO. ROUGE is an evaluation indicator utilized for method iteration and also with global reward.

However, ROUGE cannot be utilized directly for calculating gradients because it is not differentiable in and of itself. A greedy search is evaluated at every time stage from a probability distribution y^s of $p(y_i^s | y_1^s, \dots, y_i^s, x)$ in every decoder's period stage and baseline outcome y^\wedge is acquired through increasing outcome probability distribution. Determining $r(y)$ to reward function for outcome sequence y and then this is compared with actual sequence y^* , a mathematical formula is described as (13):

$$L_{rl} = (r(y^\wedge) - r(y^s)) \sum_{i=1}^n \log(p(y_i^s | y_1^s, \dots, y_{i-1}^s, x)) \quad (13)$$

Here, x represents input vector, y^\wedge represents output of baseline acquired through increasing outcome probability distribution and $r(y)$ represents reward function of outcome sequence y . The decreased L_{rl} is equal to the condition of increased sampling sequence y^s . Whether y^s has huge return than baseline y^* , expected much return by method. After development, global reward is utilized and represented as Figure 4.

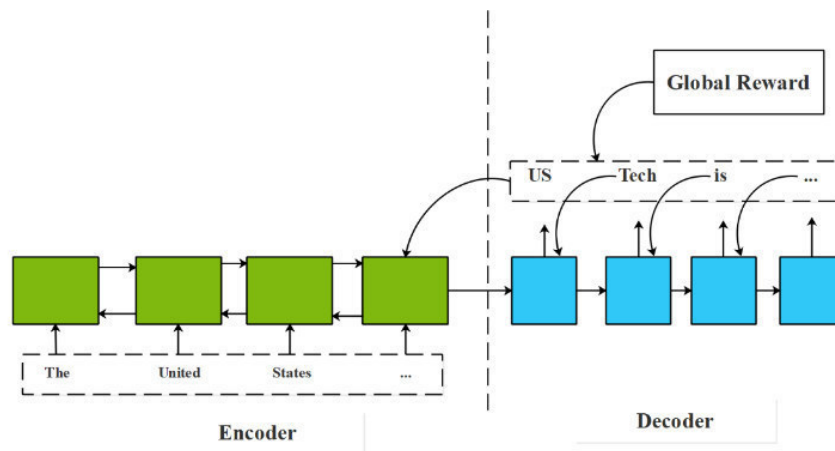


Figure 4. Training process of DA-PN+Cover+MLO

The proposed DA-PN method which is attention in both encoder and decoder ends by combining attention distribution in the present time stage. The implemented PN at decoder resolves issue of unregistered words. The proposed DA-PN+Cover method is depended coverage mechanism combining cover vector. It measured from attention mechanism at encoder and decoder at prior time stage by updating a loss function that ignores the word repetition in generated text summaries. The proposed DA-PN+Cover+MLO method through combining MLO by implementing self-crucial gradient technique. It takes global reward and evaluation indicator in phase of iteration of method which protects grow of increasing faults in generated text summary.

4. RESULTS AND DISCUSSION

This section provides a results and discussion of the proposed method. The section gives detailed explanation of the experimental setup, quantitative and qualitative analysis, comparative analysis, discussion, and conclusion of the proposed methodology. The section 4.1 provides the experimental setup utilized for research, section 4.2 provides qualitative and quantitative analysis of proposed method, section 4.3 provides comparison between proposed and existing methods and section 4.4 gives the overall discussion.

4.1. Experimental setup

In this research, the proposed model is simulated by utilizing *MATLAB* (2018a) environment with system requirements; RAM: 16 GB, processor: intel core i7, and operating system: windows 10 (64 bit). The performance of the proposed method is estimated by utilizing the evaluation indicator ROUGE which is a software package that evaluates the automatic summarization process. Figures 5 and 6 shows the top matching resumes for recruiter and top matching jobs for candidate with respective percentage.

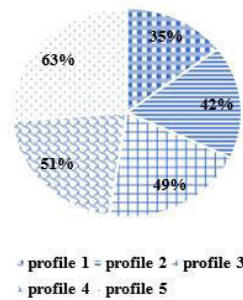


Figure 5. Represents top matching resumes for recruiter

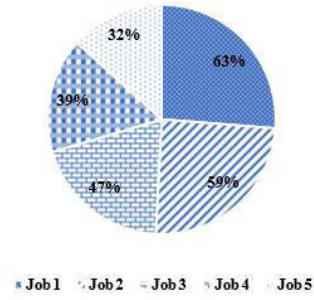


Figure 6. Represents top matching jobs for candidate

4.2. Qualitative and quantitative analysis

The calculated values are stored in a dictionary with the job/resume name and values as its value. Later, it is sorted in descending order and suggests the job/resume that has maximum matching or similarity values. For a recruiter, a top-matching resume summary will be displayed (Figure 5). For a candidate, the top matching jobs will be displayed with the respective matching percentage (Figure 6). For a candidate, additional skills to be enhanced are recommended by comparing with the dictionary of skills by area setup.

Table 2 and Figure 7 represent the performance of the proposed method in the LCSTS dataset [24]. The evaluation indicator is utilized for the evaluation. The two baseline methods are taken for evaluation and the two DA-PN, DA-PN+Cover methods are utilized for the evaluation of the performance of the proposed method. The proposed DA-PN+Cover+MLO method attained an average of 26.73 which is better than baseline methods that attain 21.53. The evaluation indicator ROUGE-1, ROUGE-2, ROUGE-L, and an average of the ROUGE are taken for the evaluation of the performance of the proposed method. From Table 2, the proposed method shows higher performance than the other methods.

Table 2. Performance of proposed method in LCSTS data

Models	ROUGE-1	ROUGE-2	ROUGE-L	ROUGE-AVG
'Bi-LSTM+attention' (baseline)	26.47	9.09	29.03	21.53
'Seq2Seq+attention' (baseline)	28.14	10.01	30.89	23.01
'DA-PN'	32.16	13.49	31.28	25.64
'DA-PN+Cover'	32.43	14.02	31.58	26.01
'DA-PN+Cover+MLO'	32.92	15.46	31.83	26.73

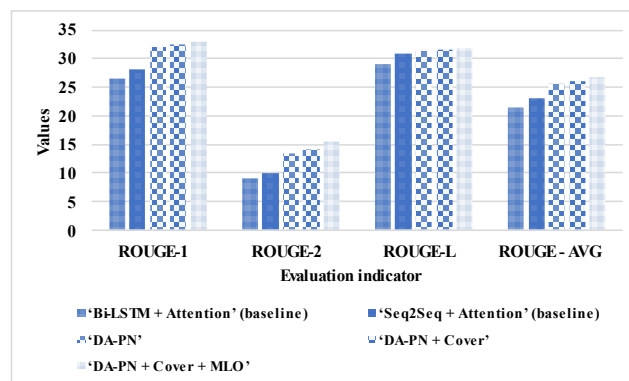


Figure 7. Performance of proposed method in LCSTS dataset

Table 3 and Figure 8 represent the performance of the proposed method in the TT News Corpus dataset [25]. The evaluation indicator is utilized for the evaluation. The two baseline methods are taken for evaluation and the two DA-PN, DA-PN + cover methods are utilized for the evaluation. The proposed DA-PN+Cover+MLO attained average of 27.09 which is better than baseline methods that attain 22.53. The evaluation indicators ROUGE-1, ROUGE-2, ROUGE-L and an average of the ROUGE are taken for the evaluation of the performance of the proposed method. From Table 3, the proposed method gives higher performance than other methods.

Table 3. Performance of proposed method in TTnews corpus dataset

Models	ROUGE-1	ROUGE-2	ROUGE-L	ROUGE-AVG
'Bi-LSTM+attention' (baseline)	26.48	9.23	28.43	21.38
'Seq2Seq+attention' (baseline)	28.27	9.31	30.03	22.53
'DA-PN'	32.45	13.85	30.95	25.75
'DA-PN+Cover'	32.79	14.03	31.63	26.15
'DA-PN+Cover+MLO'	33.85	14.69	32.74	27.09

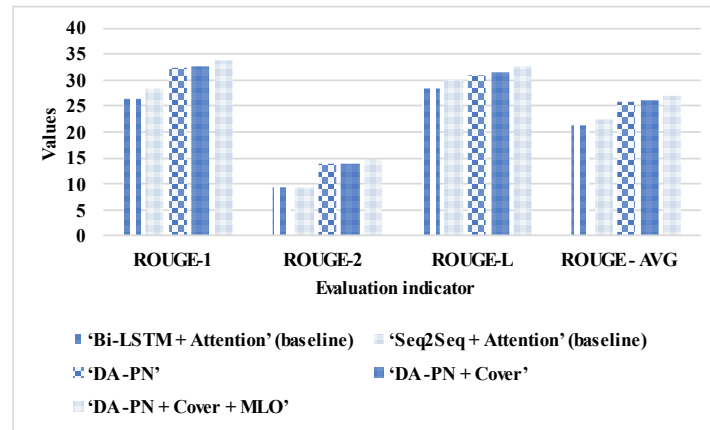


Figure 8. Performance of proposed method in TT news corpus dataset

Table 4 and Figure 9 represents the performance of the proposed method in the kaggle dataset. The two baseline methods are taken for evaluation and the two DA-PN, DA-PN+Cover methods are utilized for the evaluation. The proposed DA-PN+Cover+MLO attained an average of 27.47 which is better than baseline methods that attain 21.01. The evaluation indicators ROUGE-1, ROUGE-2, ROUGE-L, and average of the ROUGE are taken for the evaluation. From Table 4, the proposed method gives higher performance than other methods.

Table 4. Performance of the proposed method in kaggle dataset

Models	ROUGE-1	ROUGE-2	ROUGE-L	ROUGE - AVG
'Bi-LSTM+attention' (baseline)	26.17	9.43	30.44	22.01
'Seq2Seq+attention' (baseline)	28.57	10.43	31.36	23.45
'DA-PN'	33.10	13.96	31.86	26.30
'DA-PN+Cover'	33.73	14.37	33.73	27.27
'DA-PN+Cover+MLO'	34.45	14.69	33.29	27.47

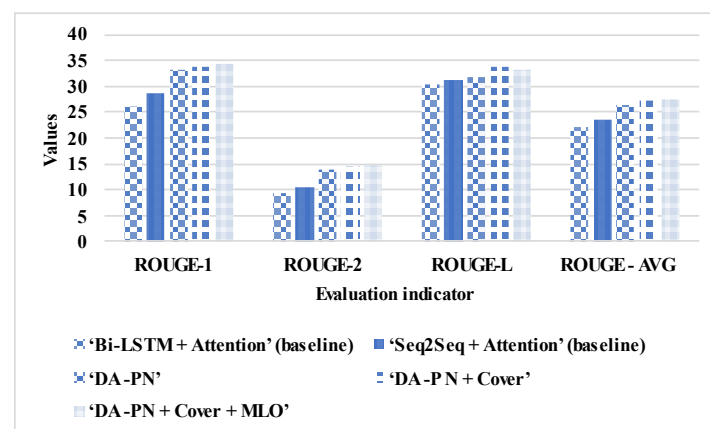


Figure 9. Performance of proposed method in kaggle dataset

From the results mentioned above, it is clear that proposed DA-PN+Cover+MLO method outperforms existing methods and protects against grow of increasing faultss in generated text summary.

4.3. Comparative analysis

The comparative analysis of the proposed methodology is described in Table 5. The proposed method is compared with existing methods like ATS [21] and TF [26] which contains the kaggle dataset. The evaluation indicator ROUGE 1 and 2 is utilized for the comparison, the proposed method shows 1.83 in ROUGE-1 and 0.74 in ROUGE-2 which is comparatively higher than existing methods.

Table 5. Represents the comparative analysis

Methods	Dataset	ROUGE-1	ROUGE-2
Jain <i>et al.</i> [21]	Kaggle [23]	0.79	0.66
Sethi <i>et al.</i> [22]		1.5	-
Proposed method		1.83	0.74

4.4. Discussion

The proposed bidirectional system is to present the best possible recommendations to both the employees and employers by utilizing the existing unstructured data. Instead of searching the complete dataset to find the potential candidates, the proposed method reduces the duration difficulty of finding the applicant with the highest score. The DA-PN method is utilized to address the issue of unrecorded words and the encoder and decoder both give equal attention, leading to high exact text summaries. DA-PN+Cover method provides positive attentional effects resulting in the current time step choosing more precise words to use in word reviews by eliminating repeated terms. DA-PN+Cover model can be modified to include a MLO after the end of the distribution of collective mistakes in created word summaries.

5. CONCLUSION

Due to the growing demand for online recruitment, it is insufficient to use conventional hiring methods. It is not flexible to validate resumes online and is vulnerable to manual errors. The bidirectional method comprises NER for extracting the needed resumes. Cosine similarity shows the match percentage of the job requirements with the resume and vice versa. The DA-PN that has been put out to address the issue of unregistered words. DA-PN+Cover method can be modified to include MLO (DA-PN+Cover+MLO) is utilized for protecting grow of increasing faults in generated text summary. From performance analysis, it is concluded that proposed method gives better performance than other methods. Future work concentrates more on abstractive summarization techniques to enhance the quality of hire.




REFERENCES

- [1] A. Bondielli and F. Marcelloni, "On the use of summarization and transformer architectures for profiling résumés," *Expert Systems with Applications*, vol. 184, p. 115521, 2021, doi: 10.1016/j.eswa.2021.115521.
- [2] S. G. M. and S. K. Suganthi, "AI based suitability measurement and prediction between job description and job seeker profiles," *International Journal of Information Management Data Insights*, vol. 2, no. 2, p. 100109, 2022, doi: 10.1016/j.jjimei.2022.100109.
- [3] A. Channabasamma and Y. Suresh, "A Recommendation-Based Contextual Model for Talent Acquisition," *Journal of Computer Science*, vol. 18, no. 7, pp. 612–621, 2022, doi: 10.3844/jcssp.2022.612.621.
- [4] Channabasamma, Y. Suresh, and A. M. Reddy, "A Contextual Model for Information Extraction in Resume Analytics Using NLP's Spacy," *Lecture Notes in Networks and Systems*, vol. 173 LNNS, pp. 395–404, 2021, doi: 10.1007/978-981-33-4305-4_30.
- [5] D. D. Shinde and R. Prasad, "Total Productive Education: Model for Higher Technical Education," *Journal of Mobile Multimedia*, vol. 17, no. 1–3, pp. 1–26, 2021, doi: 10.13052/jmm1550-4646.17131.
- [6] Y. Tang, S. Bai, and L. Cui, "An Empirical Study on the Deficiencies and Optimization of the Management System of Tourist Attractions Based on Human Resource Management," *Advances in Multimedia*, vol. 2022, 2022, doi: 10.1155/2022/2133830.
- [7] A. P. Widyassari *et al.*, "Review of automatic text summarization techniques & methods," *Journal of King Saud University - Computer and Information Sciences*, vol. 34, no. 4, pp. 1029–1046, 2022, doi: 10.1016/j.jksuci.2020.05.006.
- [8] G. Deepak, V. Teja, and A. Santhanavijayan, "A novel firefly driven scheme for resume parsing and matching based on entity linking paradigm," *Journal of Discrete Mathematical Sciences and Cryptography*, vol. 23, no. 1, pp. 157–165, 2020, doi: 10.1080/09720529.2020.1721879.
- [9] R. N. A. Deepa and R. R. Rao, "A novel nearest interest point classifier for offline Tamil handwritten character recognition," *Pattern Analysis and Applications*, vol. 23, no. 1, pp. 199–212, 2020, doi: 10.1007/s10044-018-00776-x.
- [10] T. K., U. V., S. M. Kadiwal, and S. Revanna, "Design and development of machine learning based resume ranking system," *Global Transitions Proceedings*, vol. 3, no. 2, pp. 371–375, 2022, doi: 10.1016/j.gltp.2021.10.002.
- [11] S. K. Kuttal, X. Chen, Z. Wang, S. Balali, and A. Sarma, "Visual Resume: Exploring developers' online contributions for hiring," *Information and Software Technology*, vol. 138, p. 106633, 2021, doi: 10.1016/j.infsof.2021.106633.
- [12] A. Kuzior, K. Kettler, and L. Răb, "Digitalization of Work and Human Resources Processes as a Way to Create a Sustainable and Ethical Organization," *Energies*, vol. 15, no. 1, p. 172, 2022, doi: 10.3390/en15010172.
- [13] S. A. Alsaif, M. Sassi Hidri, H. A. Eleraky, I. Ferjani, and R. Amami, "Learning-Based Matched Representation System for Job Recommendation," *Computers*, vol. 11, no. 11, p. 161, 2022, doi: 10.3390/computers11110161.




- [14] D. E. Guest, K. Sanders, R. Rodrigues, and T. Oliveira, "Signalling theory as a framework for analysing human resource management processes and integrating human resource attribution theories: A conceptual analysis and empirical exploration," *Human Resource Management Journal*, vol. 31, no. 3, pp. 796–818, 2021, doi: 10.1111/1748-8583.12326.
- [15] K. Piwowar-Sulej, "Human resources development as an element of sustainable HRM – with the focus on production engineers," *Journal of Cleaner Production*, vol. 278, p. 124008, 2021, doi: 10.1016/j.jclepro.2020.124008.
- [16] T. Shao, C. Song, J. Zheng, F. Cai, and H. Chen, "Exploring Internal and External Interactions for Semi-Structured Multivariate Attributes in Job-Resume Matching," *International Journal of Intelligent Systems*, vol. 2023, pp. 1–16, 2023, doi: 10.1155/2023/2994779.
- [17] X. Q. Ong and K. H. Lim, "SkillRec: A Data-Driven Approach to Job Skill Recommendation for Career Insights," *2023 15th International Conference on Computer and Automation Engineering, ICCAE 2023*, pp. 40–44, 2023, doi: 10.1109/ICCAE56788.2023.10111438.
- [18] S. Yang, M. Korayem, K. AlJadda, T. Grainger, and S. Natarajan, "Combining content-based and collaborative filtering for job recommendation system: A cost-sensitive Statistical Relational Learning approach," *Knowledge-Based Systems*, vol. 136, pp. 37–45, 2017, doi: 10.1016/j.knosys.2017.08.017.
- [19] E. Yildirim, P. Azad, and Ş. G. Ögüdücü, "biDeepFM: A multi-objective deep factorization machine for reciprocal recommendation," *Engineering Science and Technology, an International Journal*, vol. 24, no. 6, pp. 1467–1477, 2021, doi: 10.1016/j.jestech.2021.03.010.
- [20] S. A. Alsaif, M. S. Hidri, I. Ferjani, H. A. Eleraky, and A. Hidri, "NLP-Based Bi-Directional Recommendation System: Towards Recommending Jobs to Job Seekers and Resumes to Recruiters," *Big Data and Cognitive Computing*, vol. 6, no. 4, p. 147, 2022, doi: 10.3390/bdcc6040147.
- [21] A. Jain, A. Arora, J. Morato, D. Yadav, and K. V. Kumar, "Automatic Text Summarization for Hindi Using Real Coded Genetic Algorithm," *Applied Sciences (Switzerland)*, vol. 12, no. 13, p. 6584, 2022, doi: 10.3390/app12136584.
- [22] P. Sethi, S. Sonawane, S. Khanwalker, and R. B. Keskar, "Automatic text summarization of news articles," in *2017 International Conference on Big Data, IoT and Data Science (BIGD)*, Dec. 2017, pp. 23–29. doi: 10.1109/BIGD.2017.8336568.
- [23] Kaggle dataset link: <https://www.kaggle.com/datasets/gauravduttakiit/resume-dataset>
- [24] LCSTS dataset link: <https://doi.org/10.18653/v1/D15-1229>
- [25] TT news corpus collection dataset: <https://pan.baidu.com/s/1vgnrWB1-u4H16hIOJwXLA?pwd=th7s#list/path=%2F>

BIOGRAPHIES OF AUTHORS



Channabasamma Arandi    is currently working as an Assistant Professor in the Dept. of CSE, Gokaraju Rangaraju Institute of Engineering and Technology, Hyderabad. She is pursuing her Ph.D at Visvesvaraya Technological University (VTU) Belagavi. She obtained her Master's degree from Acharya Institute of Technology Bangalore & BE from Poojya Doddappa Appa College of Engineering (PDACE) Gulbarga in the year 2014 and 2012 respectively. She has teaching experience of 9 years. She has 10 publications in International Conferences and reputed Journals. She is also the member of ISTE, IAENG. Her research interests include machine learning, big data analytics, NLP, and artificial intelligence. She can be contacted at email: Channu.ar@gmail.com.



Yeresime Suresh    is currently working as a Professor in Dept. of CSE at Ballari Institute of Technology and Management (BITM), Ballari. He obtained his Ph.D., from National Institute of Technology Rourkela in 2015. He obtained his Master's degree from Sri Jayachamarajendra College of Engineering (SJCE) Mysore and BE from Rao Bahadur Y Mahabaleswarappa Engineering College (RYMEC) Ballari in the year 2010 and 2008 respectively. He has a teaching experience of 8 years, research experience of 4 years and one year industry experience. He has 35 publications in International Conferences and reputed Journals. He is also the member of IEEE, ISTE, and IAENG. Four research scholars are pursuing PhD under his guidance from VTU Belagavi. His research interests are in the area of software engineering, and artificial intelligence. He can be contacted at email: suresh.vec04@gmail.com.

Mathematics for 2D face recognition from real time image data set using deep learning techniques

Ambika G. N.¹, Yeresime Suresh²

¹Department of Computer Science and Engineering, BMS Institute of Technology and Management, Bengaluru and Visvesveraya Technological University, Belagavi, India

²Department of Computer Science and Engineering, Ballari Institute of Technology and Management, Ballari and Visvesveraya Technological University, Belagavi, India

Article Info

Article history:

Received Dec 7, 2022

Revised Oct 4, 2023

Accepted Oct 17, 2023

Keywords:

Computer vision

Dataset

Deep learning

Face detection

Haar features

OpenCV

Rasterized images

ABSTRACT

The recognition of human faces poses a complex challenge within the domains of computer vision and artificial intelligence. Emotions play a pivotal role in human interaction, serving as a primary means of communication. This manuscript aims to develop a robust recommendation system capable of identifying individual faces from rasterized images, encompassing features such as eyes, nose, cheeks, lips, forehead, and chin. Human faces exhibit a wide array of emotions, with some emotions, including anger, sadness, happiness, surprise, fear, disgust, and neutrality, being universally recognizable. To achieve this objective, deep learning techniques are leveraged to detect objects containing human faces. Every human face exhibits common characteristics known as Haar features, which are employed to extract feature values from images containing multiple elements. The process is executed through three distinct stages, starting with the initial image and involving calculations. Real-time images from popular social media platforms like Facebook are employed as the dataset for this endeavor. The utilization of deep learning techniques offers superior results, owing to their computational demands and intricate design when compared to classical computer vision methods using OpenCV. The implementation of deep learning is carried out using PyTorch, further enhancing the precision and efficiency of face recognition.

This is an open access article under the [CC BY-SA](#) license.



Corresponding Author:

Ambika G. N.

Department of Computer Science and Engineering

BMS Institute of Technology and Management, Bengaluru, and Visvesveraya Technological University

Belagavi, India

Email: ambikagn@bmsit.in

1. INTRODUCTION

The major idea is to propose a method that recognizes and detects human faces in given pictures or videos. Facial recognition is the ability to automatically detect a face. It has the potential to identify different parts of the embodiment depending on the presence of facial characteristics. It's always easy for a person to find a face in a collection of images and differentiate images correctly. However, a computer should be properly trained so that when a real-time dataset is provided, the system should be able to identify the face of a person as well as additional characteristics such as eyes, nose, mouth, cheeks, lips, forehead, and chin.

The key concept here is to build a system that can distinguish faces from non-facial elements [1]. Deep learning adapts to new images, assuming they are similar to the data it was trained on. Computer vision is an area of artificial intelligence that enables computers and systems to derive meaningful information from

binary images, videos, and other visual inputs [2]. The dataset is taken as a set of real-time images. But what is an image? An image is a collection of arrays representing different numerical values in terms of red, green, and blue (RGB) which is commonly used in computer vision. The values for these colors range from 0 to 255, where a higher value represents more intensity or brightness. Images are stored in multidimensional arrays. There are two main types of images: raster-based images and vector images. For our research, we are considering raster-based images.

There are different file formats for images such as jpg, GIF, PNG, TIFF, RAW [3], and PSD. The structures present in an image and the final output are the detected picture and a selection of the face [4]. The competitive aspect of this research article is to develop a system that can identify faces under various lighting conditions. Using convolutional neural networks (CNN), we predict the faces from different images in the dataset. Predicting information in the image is challenging, and we first need to train a CNN to correctly classify the images.

Many researchers have explored various methods for analyzing the emotions of images; outcomes of machine learning techniques are significant. Among several machine learning techniques given in Table 1, methods that depend on deep learning produce the best efficiency for face recognition from the images in the photographs.

Table 1. Literary review

Authors	Title of paper	Techniques used for face recognition	Dataset	Result (%)
Turk and Pentland [5]	Eigenfaces for recognition	Principal component analysis	400	79.65
Tomasi <i>et al.</i> [6]	Ive got my virtual eye on you: remote proctors and academic integrity	Wavelet transform	100	90
Yang <i>et al.</i> [7]	Large scale identity deduplication using face recognition based on facial feature points	Active shape model	100	89
Hasan <i>et al.</i> [8]	Human face detection techniques: a comprehensive review and future research directions	Support vector machines	200	91
Sparks [9]	The brainstem control of saccadic eye movements	CNN	200	93.7

2. MATERIALS AND METHOD

CNN model [10], [11] to be trained to predict whether an image has a triangle or any other information. How would you tell a computer about the shape present in the image If the image is shifted? How would a neural network be able to predict this? CNN have many filters, which are used to scan an image and obtain a feature map. Output is obtained by implementing the different concepts of CNN, as shown in Figure 1. CNN consists of various operations: i) convolutions, ii) feature detectors, iii) padding, iv) stride, v) activation layer, vi) pooling, vii) fully connected, and viii) Softmax function [12].

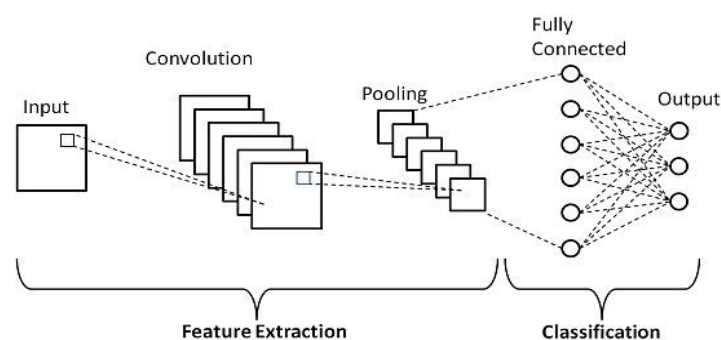


Figure 1. Block diagram of CNN

2.1. Convolution operation and feature detector

A scientific term to explain the method of combining two functions to obtain a third outcome is known as a feature map, as depicted in Figure 2. Convolution, also known as filter or kernel, is in a matrix form applied to an input image [13], [14].

$$\text{Image} * \text{Kernel} = \text{Feature Map}$$

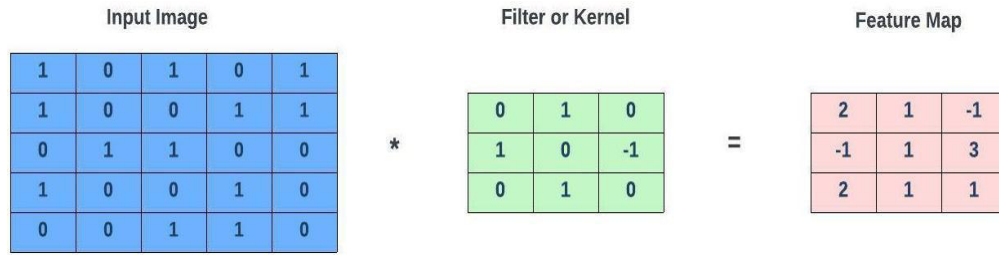


Figure 2. An example for a convolution operation

The convolution operation is used to detect the features in images; feature maps are also known as feature detectors, which can see many features in the image, as shown in Figure 3. A combination of these features is used to classify the image correctly.

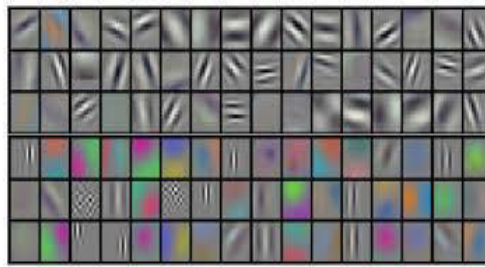


Figure 3. Different features obtained from a convolution operation

2.2. Padding

It allows us to manipulate the feature map size. Conv filters produce an output more minor than the input; we have taken a 5x5 image and padded it with 0's in all dimensions: left, correct, bottom, and top corners. Padding helps pass the conv filters multiple times, as shown in Figure 4.

$$\text{Feature Map Size}(m) = n - f + 1 \quad (1)$$

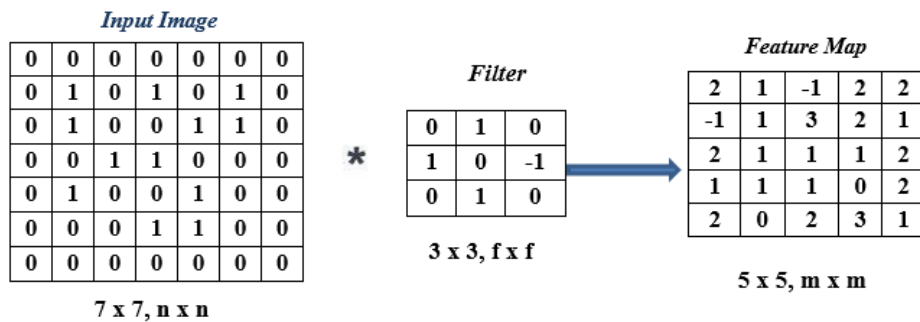


Figure 4. An example of padding operation

2.3. Stride

Stride defines how many steps the convolution window moves across the input image. Examples are illustrated for a stride of 1 and a stride of 2. An example for a stride operation is defined. A larger stride produces a smaller feature map output, and a larger stride has less overlap. Stride is used to control the size of the feature map. A larger stride has less overlap. We can calculate the feature map size using (2):

$$(n \times n) * (f \times f) = \left(\frac{n+2p-f}{s} + 1 \right) \times \left(\frac{n+2p-f}{s} + 1 \right) \quad (2)$$

Where $n \times n$ is input image size, $f \times f$ is filter size, s denotes stride value and p denotes padding

2.4. Activation layer

The purpose of the activation function is to enable the learning of complex patterns in our data, introduce nonlinearity to our network, and allow a nonlinear decision boundary via nonlinear combinations of the weight and inputs. There are several activation functions we can use in our CNN. Rectified linear units (ReLU) have become the activation function of choice for CNNs. ReLU function helps to train CNN. Simple computation (fast to qualify) does not saturate. The ReLU operation changes all negative values to 0 and leaves all positive values alone.

2.5. Pooling layer

Pooling is the process where we reduce the size of dimensionality of a feature map, allowing us to decrease the size of parameters in our network while retaining essential features. Pooling is also known as Subsampling or downsampling. In the below operation, A 2x2 kernel is used in the first block of 2x2; a maximum value of 123 is selected, and subsequent values in the output are 253, 187, and 165 in the production.

Pooling makes our CNN model more invariant to minor transformations and distortions in our images. Pooling helps to maximize the translation invariance. Pooling reduces the output size by sub-sampling the filter response without losing information [15]. A significant stride in the pooling layer leads to high information loss. A stride of 2 and a kernel size 2x2 for the pooling layer were effective in practice.

2.6. Fully connected layer

It means all the nodes in one layer are connected to the outputs of the subsequent layer. Considers 3D data output of the previous layer and flattens it into a single vector used for input in the next layer. It is also known as dense layer. A fully connected layer compiles the data/outputs extracted from previous layers to produce outcomes, easy to learn nonlinear combinations of these features.

3. SYSTEM DESIGN

3.1. Why convolutional neural network works well on images?

Standard neural networks don't have convolution filter inputs; for images, every pixel will be its input; therefore, a small image that's 28 X 28 would have 784 input nodes for our first layer. The first step here is how to train a CNN. Conv filters learn what the feature detectors learn, and our typical early layer of CNN learns low-level features (like edges or lines) specified in Figure 5. Mid-layers learn simple patterns, whereas high-level layers learn more structured, complex ways [16]–[19]. During training process, the following are the steps to be followed:

- Initialize random weights values for our trainable parameters.
- Forward propagate an image or batch of images through our network.
- Calculate the total error (get some output through the random values).
- We use a back propagation to update our gradients (weights) via a gradient descent.
- Propagate more images (or batch) and update weights until all images in the dataset have been propagated (one epoch).
- Repeat a few more epochs (i.e, passing all image batches through our network) until our loss reaches satisfactory values.

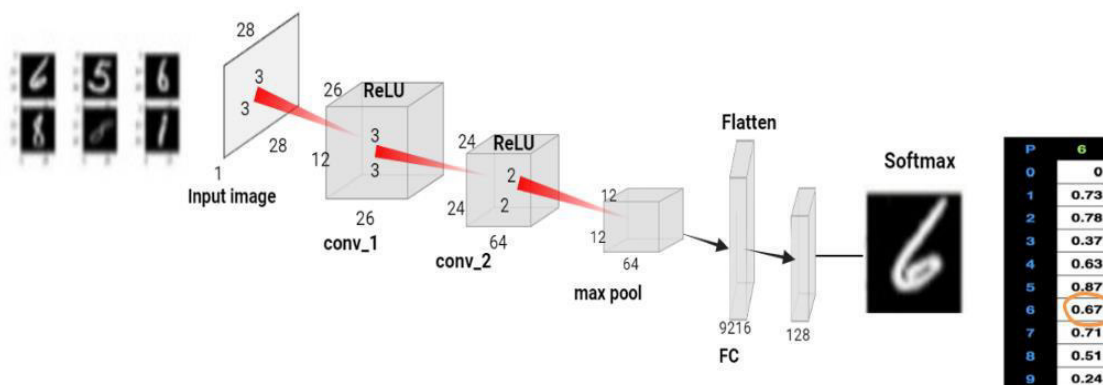


Figure 5. Training process of CNN

This is how we generate random weights for one input image; we get the output of arbitrary values for several images, as shown in Figure 6. If all the values generated are correct, we need to figure out how we correct our results using the CNN. We create a loss function and use the back propagation method to do this.

P	6	5	6	8	8	1
0	0	0.9	0.83	0.21	0.19	0.62
1	0.73	0.8	0.89	0.7	0.92	0.07
2	0.78	0.88	0.19	0.39	0.08	0.74
3	0.37	0.56	0.07	0.64	0.64	0.9
4	0.63	0.25	0.79	0.94	0.52	0.55
5	0.87	0.65	0.57	0.63	0.97	0.04
6	0.67	0.05	0.45	0.51	0.87	0.51
7	0.71	0.66	0.13	0.59	0.86	0.89
8	0.51	0.88	0.59	0.01	0.37	0.63
9	0.24	0.52	0.79	0.15	0.63	0.78

Figure 6. Result of random values during the training process in CNN for six images

3.2. Loss function

The loss function is used for quantifying the loss, how bad the probabilities we predicted, and we need to quantify the degree of our prediction. Entropy loss is used for quantifying the loss; it uses two distributions,

$$L = -y \cdot \log(\hat{y}) \quad (3)$$

Here y is the ground truth vector, \hat{y} is the predicted distribution, and \cdot is the inner product. There are also other loss functions that exist. Loss function functions are also called cost functions. For binary classification problems, we use binary cross entropy loss. For regression, we often use the mean square error (MSE).

$$\text{MSE} = (\text{Target} - \text{Predicted})^2 \quad (4)$$

Other loss functions used are L1, L2, hinge loss, and mean absolute error (MAE). If there are errors in the values, we will update our weights using the back propagation technique to minimize the loss.

3.3. Back propagation

Back propagation is very important in training the neural networks, and this process is used to know how much to change/update the gradients to reduce the overall loss, as depicted in Figure 7. The Figure 7 shows the operation of back propagation and the formulas we use in the same [20]. Using the loss value, backpropagation can tell us now, for the next iteration, how much we should increase or decrease the weights to reduce the overall loss in the network. By forward propagating input data, we can use backpropagation to lower the importance and the loss. But this tunes weights for that particular input or batch of inputs. We improve generalization (ability to make good predictions on unseen data by using all data in our training dataset).

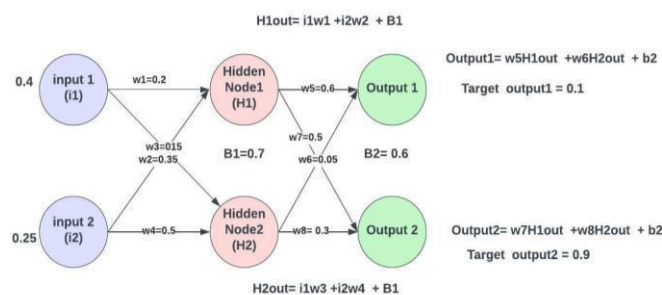


Figure 7. An operation of back propagation technique

3.4. Gradient descent

In the back propagation process, we update the individual weights or gradients given by $wx+b$. The main is to find the correct value of consequences where the loss is the lowest. Gradient descent is The method of achieving this goal (i.e., updating all weights to lower the total loss). It's the point at which we find the optimal weights such that failure is near the lowest. Gradients are the derivative of a function; they tell us the rate of change of one variable for another variable.

$$\text{Gradient} = \frac{dE}{dw}$$

Where E is the error or loss and w is the weights.

A positive gradient means loss increases if weight increases, and a negative gradient means loss decreases. At point A, moving right increases our weight and decreases our loss negatively; at point B, moving right increases our weight and increases our loss positively. Therefore, the negative of our gradient tells us the direction in which we are moving. The point at which a gradient is zero means that small changes to the left or right don't change the loss. In training neural networks, this is good and bad; at point C, minor changes to the left or right don't change the loss. Minimal changes to the left or right don't change the loss, and the network gets stuck during training. This is called getting stuck in a local minima. We will use the mini batch gradient descent method, which combines both ways. It takes a batch of data points (images) and forward propagates all, then updates the gradients. This leads to faster training and convergence to the global minima.

3.5. Optimization

This is a more advanced gradient descent method that allows us to find the lowest weights, and a few advanced optimization techniques are used. What are the problems we need to deal with standard stochastic gradient descent? These include choosing an appropriate learning rate (LR), deciding on learning rate schedules, and using the same learning rate for all parameter updates (as in the case of sparse data). Stochastic gradient descent [21] is susceptible to getting trapped in local minima or saddle points (where one dimension slopes up and the other slopes down).

Several other algorithms have been developed to solve these problems, including extensions to the stochastic gradient descent method, such as momentum and nesterov's acceleration. Several optimizers, including Adagrad, Adadelata, Adam, RMSprop, AdaMax, and Nadam. have been introduced. We have used the Adam optimizer [22]; Adam's adaptive moment estimation is a method that computes adaptive learning rates for each parameter and stores an exponentially decaying average of past gradients, similar to momentum. Adam is quite effective.

4. IMPLEMENTATION

4.1. Dataset

Dataset considered for implementation is real-time dataset. Images are collected from the social media, different restaurants and several showrooms [23]. Below is the displayed mathematical model for face recognition. We will create a collection of facial images in the database, labeled as $y_1, y_2, y_3, \dots, y_n$. N classes are created from these sets, and each class corresponds to a registered person. We define a vector comprising K values for each image.

$$\mu = (\mu_1, \mu_2, \mu_3, \dots, \mu_k)^T \quad (5)$$

Let T represent the transpose operator. We define a distance function, denoted as $d(\mu_2, \mu_s)$, for the feature vector μ that corresponds to the farthest distance in the input form and fit in to class XL, for each image.

$$d(\mu_1, \mu_s) > d(\mu_j, \mu_s) \neq j, 1, j = 0, 1, \dots, L - 1 \quad (6)$$

In the context of the provided distance function, class XL must exceed a precomputed threshold value, represented as $d(\mu_1, \mu_s) > \tau_c$. The face recognition algorithm takes an image as input and produces a sequence of face frame coordinates as output. There may be one face frame, zero face frames, or several face frames in this sequence [24].

The mathematical model for determining the integral image involves determining the pixel values of the face as (7):

$$I_i(y, z) = \sum_{i=1}^{y \cdot z} i(y', z') \quad (7)$$

The sum of the intensities of the pixels within the black areas is as follows: let $I_i(y, z)$ represent the value of the i th element in the integral image with coordinates (y, z) , and let (y', z') represent the brightness of the pixel in the image under consideration at coordinates (y', z') .

$$s_i = \sum_{i=0}^{v,y} r_{i,k} - \sum_{i=0}^{z,y} r_{i,f} \quad (8)$$

The equation above is employed for computing the total brightness of the pixels. With a threshold value of τ_c , the classifier's expression is as (9):

$$w = \begin{cases} 1, & f_i > \tau_c; \\ -1, & f_i < \tau_c; \end{cases} \quad (9)$$

A set of weights, denoted as w_i for $1 < i \leq n$, corresponds to each sample. The best strong classifier is computed using a fixed number of weak classifiers, and the equation for the strong classifier is as (10), (11):

$$w = \begin{cases} 1, & \sum_{c=1}^C a_c w_c \geq \frac{1}{2} \sum_{c=1}^C a_c; \\ -0, & \sum_{c=1}^C a_c w_c f_i < \frac{1}{2} \sum_{c=1}^C a_c; \end{cases} \quad (10)$$

$$a_c = \log \frac{1}{\beta_c} \quad (11)$$

Where w_c represents the weak classifier, and a_c and β are the weight coefficients associated with the weak classifier. Here, c stands for the current number, and $C=(1,...,C)$ represents the set of weak classifiers. The goal of this iterative technique is to build a reliable classifier. The following describes the images that show the object both before and after illumination:

$$q1(y, z) = \frac{\delta_{0,j}(y,z)}{\delta_{1,j}(y,z)} + 1 \quad (12)$$

Where j is the number of current value of the sequence y, z , $\delta_{b,j}(y, z)$ the brightness value of the pixel of the array $I_{b,j}$. b is the identifier of the pixel array, with b taking values in the set $(0,1)$.

The scientific study involves the analysis of image dispersion after applying brightness. The dispersion value is determined by calculating the sum of squared differences between the pixel values in the modified image and the mean pixel value across the width and height arrays. The dispersion value is calculated as:

$$D(I_{0,j}I_{1,j}) = \frac{1}{WH} \sum_{y=0}^{W-1} \sum_{z=0}^{H-1} (q_j(y, z) - q_j)^2 \quad (13)$$

In image processing, this formula describes the calculation of dispersion value between two images $I(0,j)$ and $I(1,j)$, $q_j(y, z)$ denotes the pixel value at coordinates (y,z) for the image parameter j . q_j is the mean pixel value along the y -axis for a specific image parameter j . random variable q_j which is calculated by (14):

$$q_j = \frac{1}{WH} \sum_{y=0}^{W-1} \sum_{z=0}^{H-1} (q_j(y, z)) \quad (14)$$

5. RESULTS AND DISCUSSION

Colored RGB images are captured from a camera. The images are depicted in Figure 8 and represent real-time images of my friends. These images serve as input for face recognition, which is implemented using TensorFlow and Keras libraries. To extract facial features, we employed Haar cascade features [25], including various types such as: i) edge characteristics; ii) linear characteristics; iii) center characteristics; and iv) diagonal characteristics. The face recognition model and the images used for face recognition are subsequently employed for emotion detection of individuals using deep learning techniques, as illustrated in Figures 9 and 10.



Figure 8. Input images for face detection

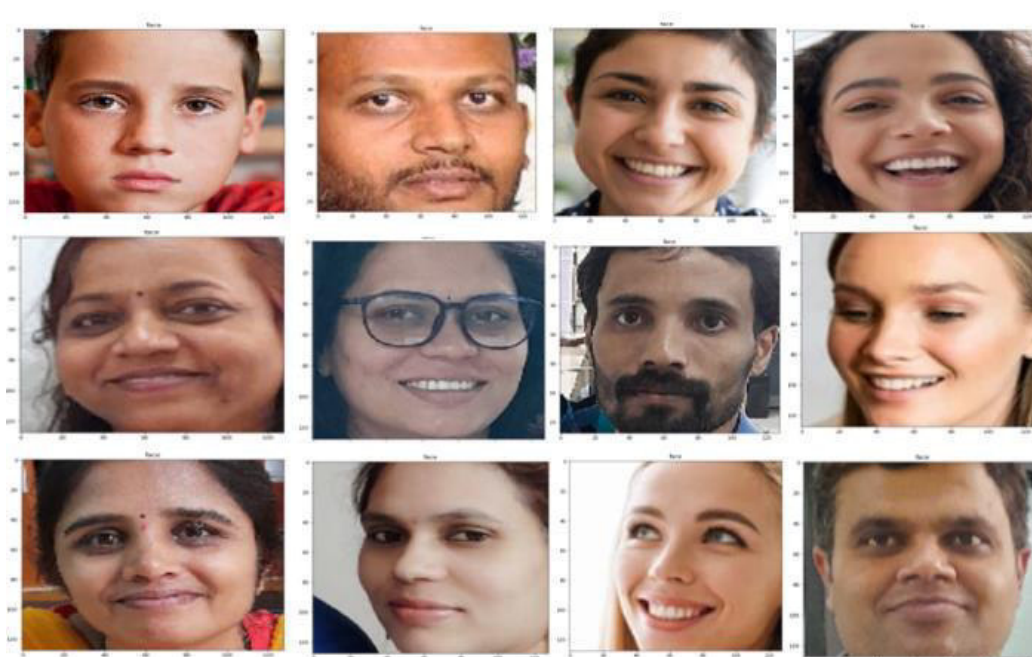


Figure 9. Face recognition images using deep learning techniques



Figure 10. Faces are detected through webcam

5.1. Measuring the accuracy of face recognition for an image

Several images, either in groups or individually, are uploaded into the system to check their accuracy. A person should have appeared in the photos multiple times. When all the images are tested in the proposed system, the data is computed in the confusion matrix, as shown in Table 2, to calculate the system's efficiency. The accuracy of the proposed system is then computed as Table 2.

Table 2. Confusion matrix form face recognition

People	No of Images	True
Person 1	5	5
Person 2	5	5
Person 3	5	4

6. CONCLUSION

In this research article, face detection and face recognition in videos are achieved through deep learning techniques. The complete process of the face detection system begins with data training using the CNN approach, followed by face recognition, which is elaborated upon. This article employs Tensorflow and Keras to test the model on various RGB images. Additionally, the system's performance is assessed for both sets of images and single images captured via a webcam, as well as for video inputs. In video processing, the system effectively extracts faces of individuals. The proposed system exhibits a high level of accuracy, achieving a recognition rate of 94% after training with a substantial number of face images. However, several factors can impact the model's accuracy. In scenarios with insufficient light intensity or other factors affecting image clarity, accuracy tends to decrease compared to situations with higher light intensity. Furthermore, the classifier plays a pivotal role in the recognition process, and superior results are obtained when the model is trained with a large dataset of images. The generated faces can be utilized as inputs in various applications such as emotion recognition, theft identification, defense applications, and more. Deep learning techniques consistently outperform OpenCV functions in terms of accuracy.




REFERENCES

- [1] Y. Ge, R. Zhang, X. Wang, X. Tang, and P. Luo, "DeepFashion2: A Versatile Benchmark for Detection, Pose Estimation, Segmentation and Re-Identification of Clothing Images," in *2019 IEEE/CVF Conference on Computer Vision and Pattern Recognition (CVPR)*, Jun. 2019, pp. 5332–5340, doi: 10.1109/CVPR.2019.00548.
- [2] J. Kim and L. Wei, "Performance Analysis of Machine Learning-based Face Detection Algorithms in Face Image Transmission over AWGN and Fading Channels," in *2021 IEEE International Symposium on Broadband Multimedia Systems and Broadcasting (BMSB)*, Aug. 2021, pp. 1–5, doi: 10.1109/BMSB53066.2021.9547181.
- [3] P. Mahapattnaik, "From Human Vision to Computer Vision — A Brief History (Part2/4)," *Medium*. 2019. [Online]. Available: <https://becominghuman.ai/from-human-vision-to-computer-vision-convolutional-neural-network-part3-4-24b55ffa7045>
- [4] M. S. KALAS, "Real Time Face Detection and Tracking Using OpenCV," in *international journal of soft computing and Artificial Intelligence*, 2014, pp. 137–140.
- [5] M. Turk and A. Pentland, "Eigenfaces for Recognition," *Journal of Cognitive Neuroscience*, vol. 3, no. 1, pp. 71–86, Jan. 1991, doi: 10.1162/jocn.1991.3.1.71.
- [6] L. F. Tomasi, V. L. Figiel, and M. Widener, "I've Got My Virtual Eye On You: Remote Proctors And Academic Integrity," *Contemporary Issues in Education Research (CIER)*, vol. 2, no. 1, pp. 31–36, Jan. 2011, doi: 10.19030/cier.v2i1.1103.
- [7] X. Yang, G. Su, J. Chen, N. Su, and X. Ren, "Large Scale Identity Deduplication Using Face Recognition Based on Facial Feature Points," in *Chinese Conference on Biometric Recognition*, Heidelberg: Springer Link, 2011, pp. 25–32, doi: 10.1007/978-3-642-25449-9_4.
- [8] M. K. Hasan, M. S. Ahsan, Abdullah-Al-Mamun, S. H. S. Newaz, and G. M. Lee, "Human Face Detection Techniques: A Comprehensive Review and Future Research Directions," *Electronics*, vol. 10, no. 19, p. 2354, Sep. 2021, doi: 10.3390/electronics10192354.
- [9] D. L. Sparks, "The brainstem control of saccadic eye movements," *Nature Reviews Neuroscience*, vol. 3, no. 12, pp. 952–964, Dec. 2002, doi: 10.1038/nrn986.
- [10] P. Viola and M. Jones, "Rapid object detection using a boosted cascade of simple features," in *Proceedings of the 2001 IEEE Computer Society Conference on Computer Vision and Pattern Recognition. CVPR 2001*, 2001, vol. 1, doi: 10.1109/CVPR.2001.990517.
- [11] N. Mahajan and H. Mahajan, "Emotion Detection Algorithm," *International Journal of Electrical and Electronics Research*, vol. 2, no. 2, pp. 56–60, 2014.
- [12] I. Paliy, "Face detection using Haar-like features cascade and convolutional neural network," in *TCSET 2008 - Modern Problems of Radio Engineering, Telecommunications and Computer Science - Proceedings of the International Conference*, 2008, pp. 375–377.
- [13] Y. Sun, X. Wang, and X. Tang, "Deeply learned face representations are sparse, selective, and robust," in *2015 IEEE Conference on Computer Vision and Pattern Recognition (CVPR)*, Jun. 2015, pp. 2892–2900, doi: 10.1109/CVPR.2015.7298907.
- [14] H. Ahamed, I. Alam, and M. M. Islam, "HOG-CNN Based Real Time Face Recognition," in *2018 International Conference on Advancement in Electrical and Electronic Engineering (ICAEEE)*, Nov. 2018, pp. 1–4, doi: 10.1109/ICAEEE.2018.8642989.
- [15] F. Huang, X. Zhang, Z. Zhao, J. Xu, and Z. Li, "Image-text sentiment analysis via deep multimodal attentive fusion," *Knowledge-Based Systems*, vol. 167, pp. 26–37, Mar. 2019, doi: 10.1016/j.knsys.2019.01.019.




- [16] B. Abirami, T. S. Subashini, and V. Mahavaishnavi, "Gender and age prediction from real time facial images using CNN," in *Materials Today: Proceedings*, 2020, vol. 33, pp. 4708–4712, doi: 10.1016/j.matpr.2020.08.350.
- [17] S. Khan, A. Akram, and N. Usman, "Real Time Automatic Attendance System for Face Recognition Using Face API and OpenCV," *Wireless Personal Communications*, vol. 113, no. 1, pp. 469–480, Jul. 2020, doi: 10.1007/s11277-020-07224-2.
- [18] M. Khan, S. Chakraborty, R. Astya, and S. Khepra, "Face Detection and Recognition Using OpenCV," in *2019 International Conference on Computing, Communication, and Intelligent Systems (ICCCIS)*, Oct. 2019, pp. 116–119, doi: 10.1109/ICCCIS48478.2019.8974493.
- [19] Pranav. K B and Manikandan. J, "Design and Evaluation of a Real-Time Face Recognition System using Convolutional Neural Networks," in *Procedia Computer Science*, 2020, vol. 171, pp. 1651–1659, doi: 10.1016/j.procs.2020.04.177.
- [20] S. Tikoo and N. Malik, "Detection of Face using Viola Jones and Recognition using Back Propagation Neural Network," *arXiv preprint arXiv:1701.08257*, 2017.
- [21] T. S. Akheel, V. U. Shree, and S. A. Mastani, "Stochastic gradient descent linear collaborative discriminant regression classification based face recognition," *Evolutionary Intelligence*, vol. 15, no. 3, pp. 1729–1743, Sep. 2022, doi: 10.1007/s12065-021-00585-y.
- [22] O. C. Oguine, K. J. Oguine, H. I. Bisallah, and D. Ofuani, "Hybrid facial expression recognition (FER2013) model for real-time emotion classification and prediction," *BOHR International Journal of Internet of things, Artificial Intelligence and Machine Learning*, vol. 1, no. 1, pp. 56–64, 2022, doi: 10.54646/bijiam.2022.09.
- [23] T. Zheng, W. Deng, and J. Hu, "Cross-Age LFW: A Database for Studying Cross-Age Face Recognition in Unconstrained Environments," Beijing University of Posts and Telecommunications, 2018.
- [24] A. G. N., B. P. Singh, B. Sah, and D. Tiwari, "Air Quality Index Prediction using Linear Regression," *International Journal of Recent Technology and Engineering (IJRTE)*, vol. 8, no. 2, pp. 4247–4252, 2019, doi: 10.35940/ijrte.B2437.078219.
- [25] Z. Arya and V. Tiwari, "Automatic Face Recognition and Detection Using OpenCV, Haar Cascade and Recognizer for Frontal Face," *International Journal of Engineering Research and Applications www.ijera.com*, vol. 10, no. 6, pp. 13–19, 2020, doi: 10.9790/9622-1006051319.

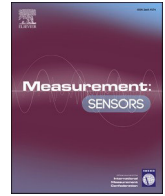
BIOGRAPHIES OF AUTHORS



Ambika G. N.    received the Engineer degree in Computer Science and Engineering from R. L. Jalappa Institute of Technology in 2008 affiliated to VTU. Completed Master of Technology in 2012 from Nitte Meenakshi Institute of Technology Affiliated to VTU, currently pursuing Ph.D. in the area of Computer Vision. Areas of interests are artificial intelligence, robotics, and computer vision. She has published various research articles in various national and international journals. She can be contacted at email: ambikagn@bmsit.in.



Suresh Yeresime    received Ph.D. in 2015 from National Institute of Technology, Rourkela, India. Currently he is working as Professor, Department of Computer Science and Engineering, Ballari Institute of Technology and Management. His areas of interest include: artificial intelligence, machine learning, and data mining. He has published various research articles in reputed conferences and journals. He can be contacted at email: suresh.vec04@gmail.com.



Uncertainty determination and reduction through novel approach for industrial IOT

Dondapati Rajendra Dev^{a,*}, Vijaykumar S. Biradar^b, V. Chandrasekhar^c, Varsha Sahni^d, Praveen kulkarni^e, Pankaj Negi^f

^a Department of Computer Science and Engineering, Vignan's Institute of Engineering for Women, Vishakapatnam, Andhra Pradesh, India

^b Electrical Engineering Department, N B Navale Sinhgad College of Engineering, Kegaon, Solapur, 413255, Maharashtra, India

^c Department of Computer Science and Engineering, Ballari Institute of Technology and Management, Ballari, Karnataka, India

^d School of Computer Science and Engineering, Lovely Professional University, Phagwara, Punjab, India

^e Department of Computer Science and Engineering, Dayananda Sagar University, Bangalore 562112, Karnataka, India

^f Graphic Era Hill University, Dehradun, R/S, Graphic Era Deemed to be University, Dehradun, 248002, India

ARTICLE INFO

Keywords:

Industrial internet of things
Sensor data
Noise remove
Statistical techniques

ABSTRACT

The most fundamental and crucial processes in Data analysts is effective information processing while cleaning information from noisy sensors. Conventional outlier identification techniques should not be used directly for this type of assessment, as sensor data can contain both noise (piezoelectric microphone type) and severe abnormalities. To manage the problem of sound reduction while maintaining the anomalies in the IIoT information, this paper proposes a method of calculating the noise score which takes into account both the rate of variation and the variance. To establish the unit of evaluation of the measurement of difference which would be used in conjunction with statistical analyses, a sliding window method. Extensive testing shows that the proposed strategy surpasses existing advanced noise detection methods, producing a clean dataset that maintains anomalies to successfully use abnormal investigation techniques.

1. Introduction

Sensors were frequently used in the new generation of cyber-physical capabilities provided by IIoT architecture to collect information about the actual environment so processors can choose the appropriate actuator [1]. The sensors were considered trustworthy in the sense that the measurement they acquire correctly represents the real state of the environment [2–4]. If the ambitious opponent wins by compromising these hypotheses, however, malware management choices could result. Such an unsupported assumption could well have devastating effects on society as a whole in contexts where regulation of safety-critical activities is required. A unique method for identifying cyber attacks on cyber-physical networks has just been developed, and it does so by identifying improbable sensor behavior [5]. Large volumes of information have been generated in IIoT configurations. When carrying out predictive analyses on such amounts of information, the “5V” (volume, variety, speed, volatility, and veracity) of massive data comes into play [6]. The enormous volume and complexity of the information place heavy demands on the techniques for preparing the information now in

use. Requirements are further augmented by changing data flows and real-time requirements [7]. Normally, sensors produce consistent data flows. Information that would be continuously generated, often at a high percentage, was referred to as information flows. Information gathering and rapid response are essential in fully automated manufacturing operations [8]. Machine-to-machine connectivity was critical in IIoT contexts. Intelligent sensors and gadgets not only provide information but also communicate with their surroundings, and provide rapid responses [9]. In these IIoT environments, the requirement for proper interaction and also the availability of continuously flowing streams of data clash with the characteristics of taking a picture of the full set of data & conducting calculations using uncertain response times.

An Artificial Neural Network (ANN) was designed to mimic the biological neural network seen in mammalian brains. The neurons that bring these nodes together make up an ANN's element. Based on the input information, points are connected in steps to generate non-linear output data [10]. Interconnects between networks allow the output of a node to be introduced into the input of another node. The significance of the transmitted data can be derived from the weightings applied to

* Corresponding author.

E-mail address: rajendra0511@gmail.com (D.R. Dev).

each link [11]. The output signal of a neuron was driven by a threshold function, as in biological neural networks. All weights will need to be initialized when configuring an ANN [12]. To create a reliable, balanced system, these weights were modified holistically during network training using a predetermined learning algorithm.

The major contributions of the work are:

- One of the most fundamental and crucial processes for effective information processing was the cleaning of information from noisy sensors.
- To manage the problem of sound reduction while maintaining the anomalies in the IIoT information, suggested a creative approach.
- It proposes a method of calculating the noise score which takes into account both the rate of variation and the variance.
- To establish the unit of evaluation of the measurement of difference, which would be used in conjunction with statistical analyses, a sliding window method was used.

2. Related works

The objective of the innovations and study was to discover inexpensive and energy-efficient solutions to the problem of Radio Frequency (RF) signal interference. According to others, 's centralized system for wireless device coordination that uses specific methods run through a common service-level platform to handle variable RF range devices seems to be a workable option [13,14]. However, such a system requires that all IoT devices be geographically co-located and interconnected via the same network, which is generally not the case in contemporary manufacturing units [15]. Distributed intelligent sensors, on the other hand, could be more efficient, particularly in terms of energy needs for large areas. These smart devices could use machine learning algorithms to change communication variables and organize themselves [16]. Other approaches to the RF interference issue include mobile networks, which provide IoT devices with the architecture they need for signal power, and even a dedicated IoT connection for mobile networks. By maximizing the ratio of all IoT devices, this approach determines which cellular client RF to communicate using a deeper strengthening learning method, which takes time to learn [17]. The loud noise that machines and robots make in major manufacturing sites is the main source of RF interference. In an IoT ecosystem, reducing the impact of this sound would increase, enhancing the signal transmitted between interconnected devices [18].

The primary method to solve the noise reduction problem was machine learning. Advanced auto-encoder techniques and ML extracting features are used to reduce the impact of background noise on computers. Large businesses also used the continuously hidden Markov model to eliminate noise and recognition. Continuous Hidden Markov Model (CHMM) was applied to describe electromechanical sound in external analysis after the detection of noise in space and time [19]. In addition, for many types of information, including the time information under discussion, noise and anomalies had separate definitions. High peaks in ECG data can be signs of abnormalities, such as a rise in heart rate [20]. To produce its source of information for extraction techniques or categorization, the study identifies peak errors and a series of dirty spots as anomalies.

3. Proposed noise detection method

Point sound and continuous sound were the two main types of noisy data. The latter, which may be more difficult to process, make up the majority of the dataset collected for our research [21]. A threshold method based on a Quantile-Quantile plot (Q-Q) has been created to recognize noisy information based on these values. This article suggests sound purification strategies to address the problem of information quality, which would be inspired by previous research that focuses on IIoT architecture. To enhance the sensing quality of the data & work in

both big information and real-time situations, it might be folded into a filtering component in the data transformation layer as depicted in Fig. 1. To assess how dramatically the numbers within the window changed, in comparison to those of the preceding one and quantify the extent of the divergence from the background ordinary windows, 2 well-defined cues were presented based on sliding window frames, specifically, neighbor contrasting & background contrasting. The interior values were sound, and windows with higher test scores were deemed noisy window frames. The researchers use experiments to study the viability of the proposed sound detection strategy and show how it improves detection methods. After the sound has been removed, the data cleaning enhances the accuracy of anomaly detection, and also the level of noise offers additional information about the information's condition.

The distance here between the present point and also the typical locations can be used to determine the size of the deviation, and also locations with larger beaches were exceptions. Due to this, methods for detecting distance-based outliers have become so widely used [22]. While higher levels point to the presence of sound, lower levels of dissimilarity point to the absence of sound. Noise Criterion (NC) refer could be employed to evaluate this resemblance given in Fig. 2. The difference between the sliding windows in the neighboring window would be greater than usual points when it covers the sound elements. The existing sliding windows and their neighbors were indicated by the red and green windows, accordingly. The second window does have a greater noise rating and a large aspect value.

As seen in Fig. 3, where the sound described in green cannot be recognized at all, the researchers obtain detection accuracy as a function of NCs. In this instance, a backdrop model with typical windows was constructed so that this particular sort of sound may be identified by its greater contrast to the background image.

The mean value (w_m) & standard deviation (w_s) were computed for every moving window.

$$d_{wm_x} = \sqrt{(wm_x - \mu_m) \delta_m^{-1} (wm_x - \mu_m)} \quad (1)$$

Where μ_m , μ_s and δ_m , δ_s are the mean and covariance of the data in wm_x and ws_x , respectively, where the range taken from 0 to 1.

The noise level scoring depending on the BC of windows w_i was provided as the background model.

$$S_{bc_x}(w_x) = \frac{1}{|B|} \sum_{w \in B} x^2(w_x, w) \quad (2)$$

Where $|B|$ - cardinality of set B.

This means that many forms of distribution were present in all the information. The majority of the points belong to the allocation that would be centered around the red dotted line, whereas the other points

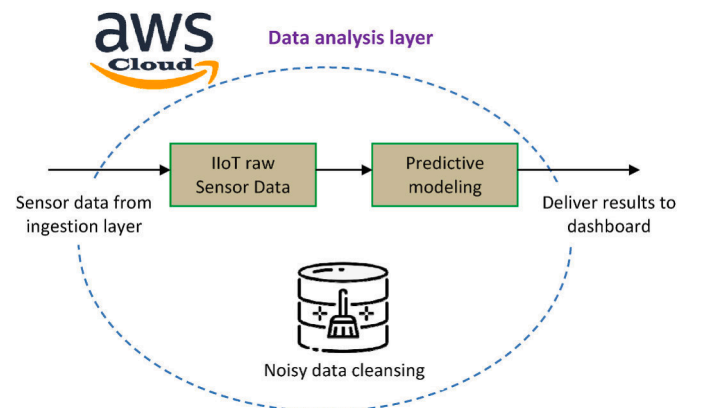


Fig. 1. Proposed detection method was incorporated into the data management layer of an IIoT system.

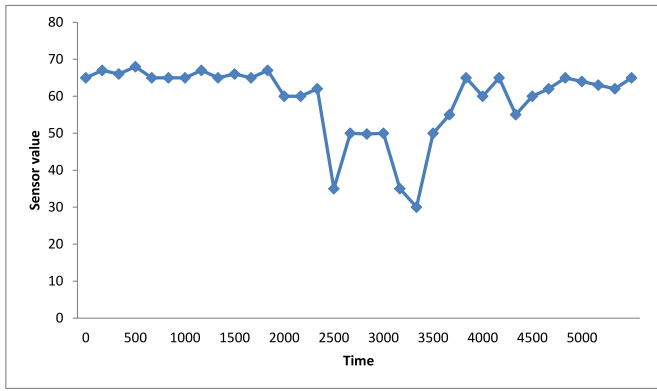


Fig. 2. NC recognizes spike sound.

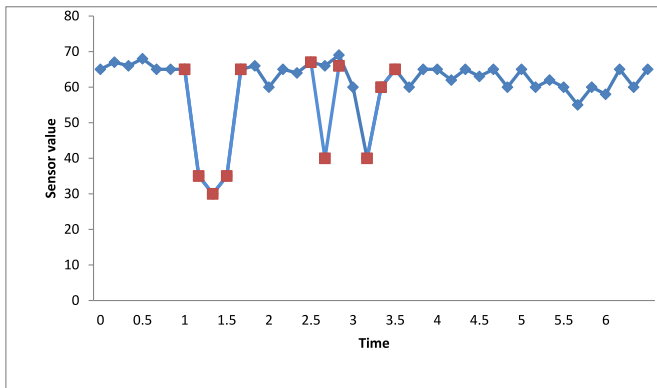


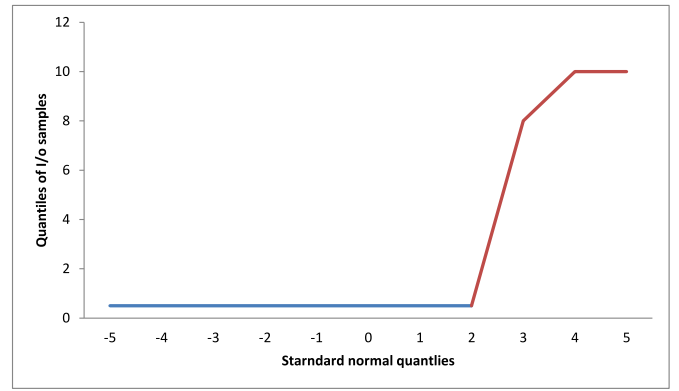
Fig. 3. Results of noise detection by NC.

diverge from this range. We specifically searched for windows that fit these locations to identify the noisy window [23]. The initial and third quartiles of the distributions were connected by a line superimposed on the graphic, allowing us to determine the equation for line f . (Xd).

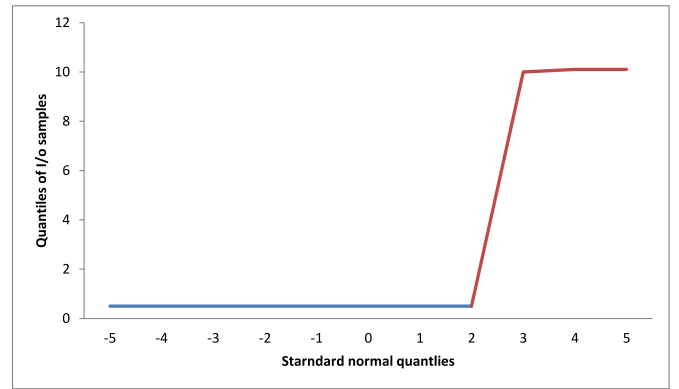
Although there are some parallels between noise and anomalies, they seem to be very distinct from a physical interpretation standpoint. This problem is overlooked by several widely used approaches, which yield subpar detection results. This study focused on the distinction between sound & anomalies to address the issues, and on this basis, the chi-square distances and also the template matching method was used to quantify the change rate & departure as the differentiation. While the dissimilarity between datasets and anomalies has decreased as a result of these countermeasures, the difference between datasets and anomalies has increased. Since the abnormalities are true positives, it means that the sound detection results were not affected by the abnormalities. By computing two vectors using data sets, it must be typically used to compare two histograms, but when it regards statistical information, it may be viewed as a weighted Euclidean distance. Due to its increased time complexity, Dynamic Time Warping (DTW) is an unwise choice. For example, the time it takes to calculate the distance between two matrices is 0.036161 s and 1.995205 s, respectively.

4. Experimental setting

The normalcy test, noise, and anomalies are the real information gathered by the sensor measurements. The pattern corresponding to the events was carefully labeled and the actual noise was naturally incorporated shown in Fig. 4(a). The information could be plotted and visually reviewed to show that there are not many changes in the data sets between seconds. Thus, the information should first be processed using a batch normalization filter of size 300 to increase the effectiveness of the



(a)



(b)

Fig. 4. Q-Q waveform (a) NC. (b) BC.

noisy data purification system Fig. 4 (b). Using the above information, system variables such as the baseline and threshold were generated. Following the sharing of information, a set of 12 datasets would be used to evaluate the proposed methodology. One step size is used to cross the sliding window during the period-series data. For BC & NC, the deviation value was experimentally adjusted to 0.5 & 0.1, accordingly.

4.1. Discussion

Some windows may contain both sound and regular dots, but they could eventually be recognized as noise windows. The method, however, traverses the time-series data with a step size of 1, thus if the sliding window only captures a small portion of the sound, the contrasting cue score was insufficient to cause a sound alarm. Only when most of the dots in the window were noisy did the contrast score exceed the required level. As shown in Fig. 5 (a) signifies all the sound detection accuracy, Fig. 5(b) demonstrates a resolving power of the green region which reflects the period when the noise had first been detected, Fig. 5 (c) displays the first detected loud noises window, which should be a growth of the spectral range of Fig. 5 (d) displays the magnified sound points in the spectral range. In the initial sound instance, after hierarchy magnifying, it would be evident that only the windows with a significant amount of large volumes of data could cause the contrasting values to surpass the threshold.

Fig. 6 (a) – (d) shows a graphical representation of the other identification techniques, such as LOF, COF, LDOF, iForest, average predictor, and their proposed approach, avoiding cluster techniques. The average results from the approach presented in Fig. 7 were based on two separate thresholds. The PI can be seen in Fig. 7(a) and (b) as a gap between the two dotted lines. The document itself and the results of the

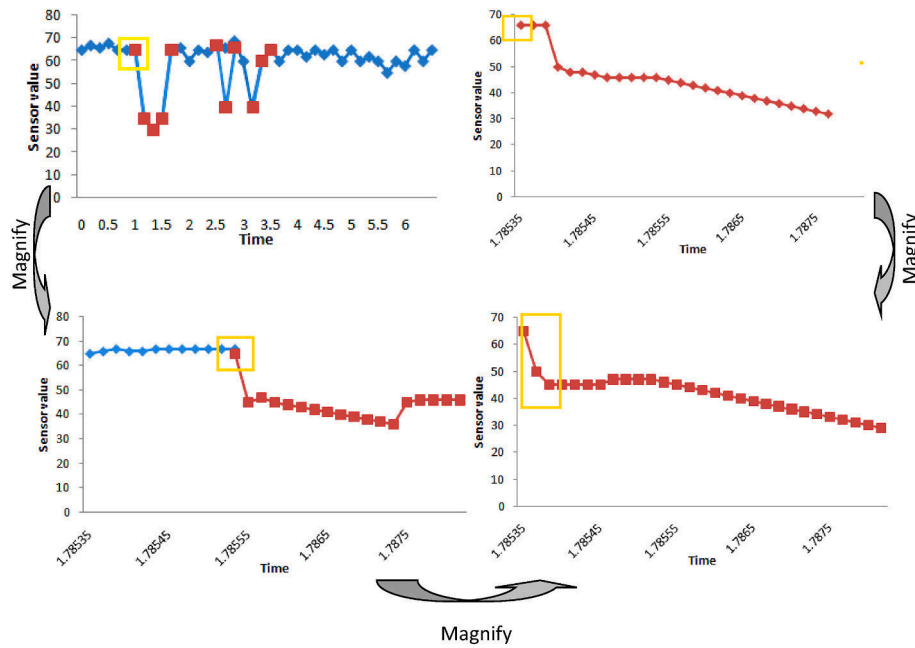


Fig. 5. Sound detection accuracy.

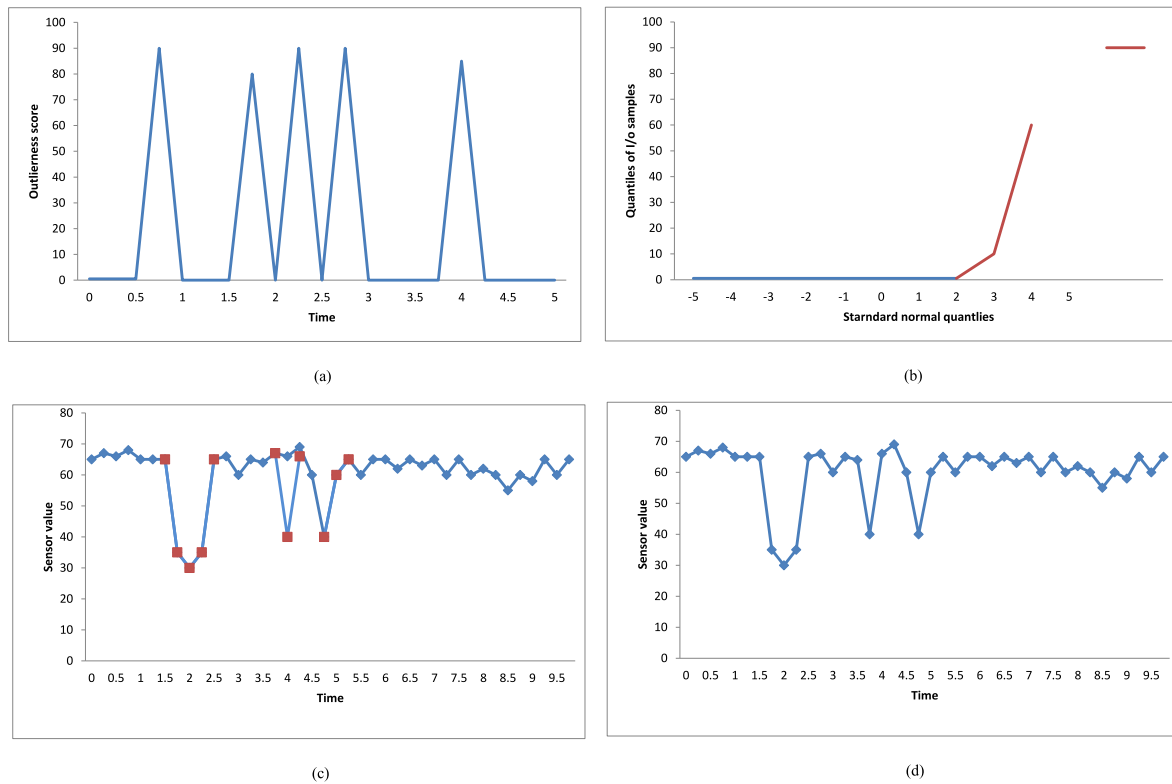


Fig. 6. Detection results based on different methods.

information purification were used in blue and red, accordingly. The outcomes of the proposed product's sound detection were seen in Fig. 7 (c), and the audible cleaning results of the proposed method are shown in Fig. 7(d). Information on false positives and false negatives through various approaches can be found in Table 1.

Our proposed strategy provides more encouraging results than other advanced detection systems already in use, effectively eliminating noise from information while maintaining anomalies. Additionally, Fig. 8 the

detection details illustrate the effectiveness of the proposed technique for managing contextual sound. The majority of undesirable sounds, including spikes & continuous sound points, have been eliminated as an outcome of the cleansing process, leaving only the anomalies with minor deviations.

The red dotted line roughly represents where the majority of the information, lies, and deviations from this line signify variations in the normal distribution. The departures are not immediately obvious and

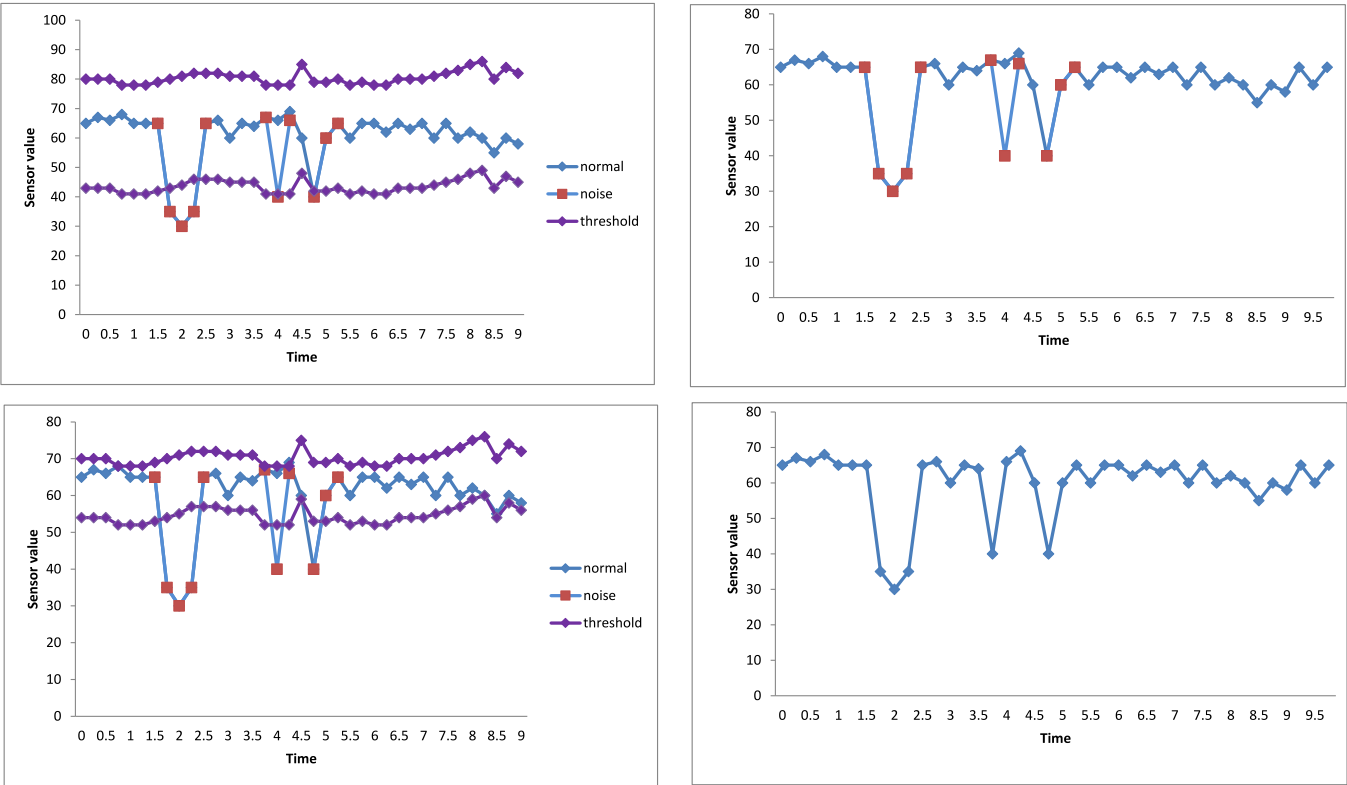


Fig. 7. Average forecast.

Table 1
FP and FN Q-Q

Method	LOF	COF	LDOF	iForest	Ours
False positives	52	430	441	3080	169
False negatives	1114	925	893	146	182

seem difficult to spot, as can be seen in Fig. 9 (a). Given this, even some typical points were split, not to mention keep abnormal data, assuming that 65 was correctly selected as the threshold. Conversely, the departure in Fig. 9(b) was obvious, as it has been demonstrated experimentally that the windows straying from the red dotted line contain irrelevant information.

Pervasive noise is frequent and seems inevitable in many real concerns. Access to specific information was necessary to ensure effective research methodology. To provide better information, an accurate noise reduction must be performed during processing. The noise was generally distinguished from normal data by distinct properties which differed from it. However, significant anomalies also show this discrepancy. Finding noisy data as comprehensively as possible without accidentally selecting anomalies appears to be a challenge. Numerous problems still need to be resolved in the majority of the detection is approaching now in use, including mixed noise & anomalous findings in classification methods or more false negatives or false positives because of an insufficient threshold. This would be addressed by proposing a single method of noise detection based on context and close objects. When compared to

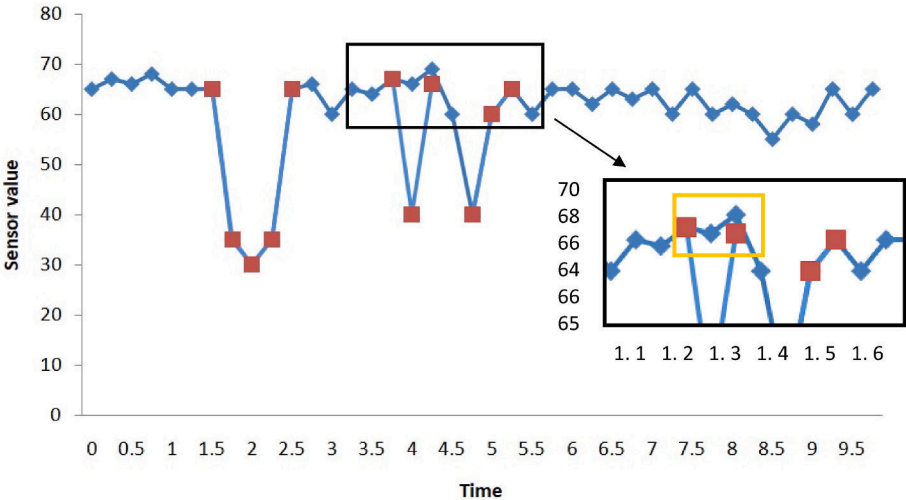
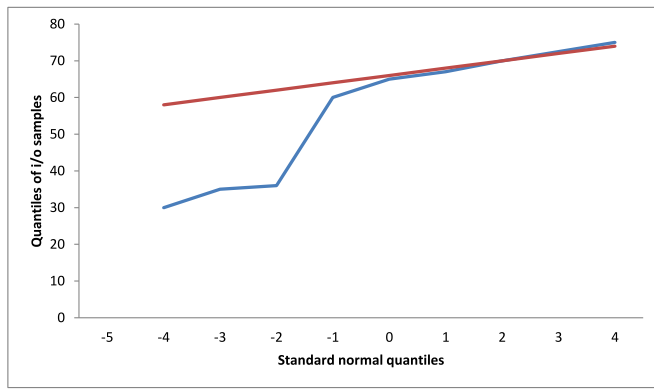
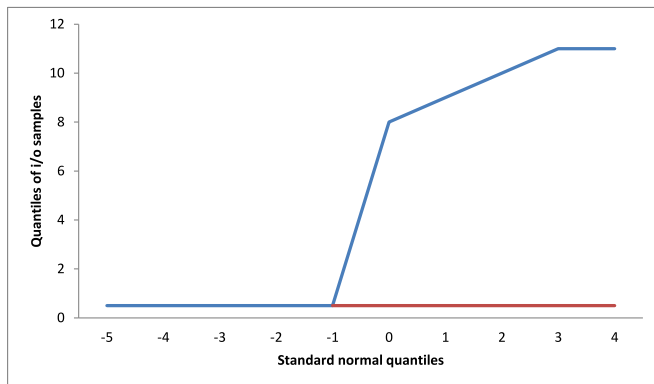


Fig. 8. Magnification features.



(a)



(b)

Fig. 9. Q-Q graph comparing window scores and amounts of initial assertions.

the neighboring data, noise that manifests as abrupt jumps or spikes may be distinguished, while anomalies that move more slowly have a high contrast score and many are preserved as predicted. The experimental measurements demonstrate that our proposed method performs more effectively than other state-of-the-art recognition methodologies, and the implementation in the intrusion detection system shows that the cleaning information may reduce the impact of sound & produce superior anomalous identification.

5. Conclusions

One of the intuitive notions is that when a momentary change occurs, we may note how long this would remain & assume that it represents a new sort of signal rather than sound if the time it lasts exceeds a pre-determined quantity. This makes automation easier, but increases computation, memory, and processing time, as trade-offs were unavoidable. The accuracy and recall of the identification results should again be exchanged when determining the right window size for the identification of noisy windows. A new approach would be required to be used for processes like biological system anomalies where there aren't any suitable biological signifiers or biological experiments that provide an advanced warning of the anomaly advancement. While the noise removal process operates well where the substantial anomalies create extra gradually than the loud sound deviance, as in processes with mechanical parts that gradually deteriorate, there might be devices like these. Uncertainty can arise from various factors such as sensor inaccuracies, communication delays, or environmental conditions. Identifying and reducing these uncertainties can lead to improved system performance and uptime.

CRedit authorship contribution statement

Dondapati Rajendra Dev: Writing – original draft, preparation. **Vijaykumar S. Biradar:** Conceptualization. **V. Chandrasekhar:** Validation. **Varsha Sahni:** Methodology. **Praveen kulkarni:** Supervision, Writing – review & editing. **Pankaj Negi:** Data curation.

Declaration of competing interest

The authors declare that they have no known competing for financial interests or personal relationships that could have appeared to influence the work reported in this paper.

Data availability

No data was used for the research described in the article.

References

- [1] R.F. Abdel-Kader, N.E. El-Sayad, R.Y. Rizk, Efficient noise reduction system in industrial IoT data streams, in: *International Conference on Advanced Intelligent Systems and Informatics*, Springer, Cham, 2021, December, pp. 219–232.
- [2] M.A. Jarwar, S.A. Khowaja, K. Dev, M. Adhikari, S. Hakak, NEAT: a resilient deep representational learning for fault detection using acoustic signals in an IIoT environment, *IEEE Internet Things J.* (2021).
- [3] Y. Liu, L. Shu, Z. Huo, K.F. Tsang, G.P. Hancke, Collaborative industrial internet of things for noise mapping: prospects and research opportunities, *IEEE Ind. Electron. Mag.* 15 (2) (2021) 52–64.
- [4] B.J. Chelliah, T.P. Latchoumi, A. Senthilselvi, Analysis of demand forecasting of agriculture using machine learning algorithm, *Environ. Dev. Sustain.* (2022) 1–17.
- [5] G. Yue, Z. Sun, J. Fan, Ag-Irtr: an adaptive and generic low-rank tensor-based recovery for IIoT network traffic factors denoising, *IEEE Access* 10 (2022) 69839–69850.
- [6] Y. Ze, L. Liu, T. Cheng, Z. Kun, Z. Jianhua, Measurement-based characterization of electromagnetic noise for the industrial internet of things at typical frequency bands, in: *2019 IEEE Wireless Communications and Networking Conference (WCNC)*, IEEE, 2019, April, pp. 1–6.
- [7] M. Monica, P. Sivakumar, S.J. Isac, K. Ranjitha, PMSG based WECS: control techniques, MPPT methods and control strategies for standalone battery integrated system, in: *AIP Conference Proceedings vol. 2405*, AIP Publishing LLC, 2022, April, 040013, 1.
- [8] D. Saha, G.N.R. Devi, S. Ponnusamy, J. Pandit, S. Jaiswal, P.K. Bhuyan, Application of nanotechnology in neural growth support system, in: *2022 IEEE 2nd Mysore Sub Section International Conference (MysuruCon)*, IEEE, 2022, October, pp. 1–6.
- [9] B. Raviprasad, C.R. Mohan, G.N.R. Devi, R. Pugalethi, L.C. Manikandan, S. Ponnusamy, Accuracy determination using deep learning technique in cloud-based IIoT sensor environment, *Measurement: Sensors* 24 (2022), 100459.
- [10] S. Behera, A. Choubey, C.S. Kanani, Y.S. Patel, R. Misra, A. Sillitti, Ensemble trees learning-based improved predictive maintenance using IIoT for turbofan engines, in: *Proceedings of the 34th ACM/SIGAPP Symposium on Applied Computing*, 2019, April, pp. 842–850.
- [11] G. Han, J. Tu, L. Liu, M. Martínez-García, Y. Peng, Anomaly detection based on multidimensional data processing for protecting vital devices in 6G-enabled massive IIoT, *IEEE Internet Things J.* 8 (7) (2021) 5219–5229.
- [12] Y. Ze, L. Liu, Z. Kun, Z. Jianhua, Measurement-based characterization of electromagnetic noise for industrial Internet of Things, *Procedia Comput. Sci.* 147 (2019) 145–150.
- [13] N.F. Polychronou, P.H. Thevenon, M. Puys, V. Beroulle, A comprehensive survey of attacks without physical access targeting hardware vulnerabilities in IIoT devices, and their detection mechanisms, *ACM Trans. Des. Autom. Electron. Syst.* 27 (1) (2021) 1–35.
- [14] Y. Liao, X. Shen, G. Sun, X. Dai, S. Wan, EKF/UKF-based channel estimation for robust and reliable communications in V2V and IIoT, *EURASIP J. Wirel. Commun. Netw.* 2019 (1) (2019) 1–13.
- [15] A. Sonavane, J. Singla, Review on optical character recognition-based applications of industrial IIoT, in: *Industrial Internet of Things*, CRC Press, 2022, pp. 175–187.
- [16] K. Mao, G. Srivastava, R.M. Parizi, M.S. Khan, Multi-source fusion for weak target images in the Industrial Internet of Things, *Comput. Commun.* 173 (2021) 150–159.
- [17] E. Al Alkeem, C.Y. Yeun, J. Yun, P.D. Yoo, M. Chae, A. Rahman, A.T. Asyari, Robust deep identification using ECG and multimodal biometrics for the industrial internet of things, *Ad Hoc Netw.* 121 (2021), 102581.
- [18] P. Garikapati, K. Balamurugan, T.P. Latchoumi, K-means partitioning approach to predict the error observations in small datasets, *Int. J. Comput. Aided Eng. Technol.* 17 (4) (2022) 412–430.
- [19] K. Balamurugan, T.P. Latchoumi, T.P. Ezhilarasi, Wearables to improve efficiency, productivity, and safety of operations, in: *Smart Manufacturing Technologies for Industry*, 4. 0, CRC Press, 2022, pp. 75–90.
- [20] T. Soni, M. Schellmann, J. Eichinger, A. Knoll, Unleashing latency-critical IIoT communication by cooperative sidelink-assisted DL transmissions, in: *WSA 2021*;

- 25th International ITG Workshop on Smart Antennas, VDE, 2021, November, pp. 1–6.
- [21] T.P. Latchoumi, R. Swathi, P. Vidyasri, K. Balamurugan, Develop new algorithm to improve the safety of WMSN in health disease monitoring, in: 2022 International Mobile and Embedded Technology Conference (MECON), IEEE, 2022, March, pp. 357–362.
- [22] B.M. Lee, Adaptive switching scheme for RS overhead reduction in massive MIMO with the industrial Internet of Things, *IEEE Internet Things J.* 8 (4) (2020) 2585–2602.
- [23] K. Fang, T. Wang, X. Yuan, C. Miao, Y. Pan, J. Li, Detection of weak electromagnetic interference attacks based on a fingerprint in IIoT systems, *Future Generat. Comput. Syst.* 126 (2022) 295–304.

**SIGN LANGUAGE RECOGNITION USING CNN AND STORAGE OPTIMIZATION
ALGORITHM****Subhashree D C**Ballari Institute of Technology & Management, Ballari, Karnataka State, India (Email:
shubha.rmjssp@gmail.com)**Dr. Jagadish R M**Ballari Institute of Technology & Management, Ballari, Karnataka State, India (Email:
rm.jagadish@gmail.com)**Dr. Girish Kumar D**Ballari Institute of Technology & Management, Ballari, Karnataka State, India (Email:
get.girivar@gmail.com)**Virupaksha Gouda R**Ballari Institute of Technology & Management, Ballari, Karnataka State, India (Email:
gouda.viru@gmail.com)

Abstract— Communication is vital for sharing emotions and thoughts, yet deaf and mute individuals face challenges in expressing themselves. Sign language serves as their primary mode of communication, but its limited understanding among the general population creates barriers. This paper presents a sign language recognition model utilizing convolutional neural networks to interpret hand and facial gestures. Data collection is facilitated through OpenCV and Mediapipe, enabling accurate prediction of words. The model acts as a bridge between individuals with physical disabilities and the general populace, facilitating effective communication and fostering inclusivity. [[11][12][13][14][15][16][17][18]

Keywords—Sign Language, classification, Neural Networks, Tensor Flow Kera, Media pipe

I. INTRODUCTION

Communication plays an important role in sharing feelings and asking for help. But when we consider people with hearing and vocal disabilities, they use a language known as sign language to communicate with others. This sign language is hard to understand others. So, this makes the lives of those hard and unimaginable

When we consider people with hearing and vocal disabilities, they use their hand movements and facial recognition to communicate with others, which we indeed call sign language. They mainly use their hand movements to share with others.

When we talk about sign recognition there are mainly categorized into two types static recognition and dynamic recognition[1]. Static recognition means only a single frame sign can be recognized. But when we talk about dynamic recognition this can recognize the sign in both static and moving positions. This model can predict both the static and dynamic recognitions of some basic words such

as thanks, hello, etc., along with some alphabet.

We have to create our dataset with the help of OpenCV. While collecting the data we convert the data into an array of key points using a mphilistic media pipe. In this, we majorly work on hand gestures and face recognition.

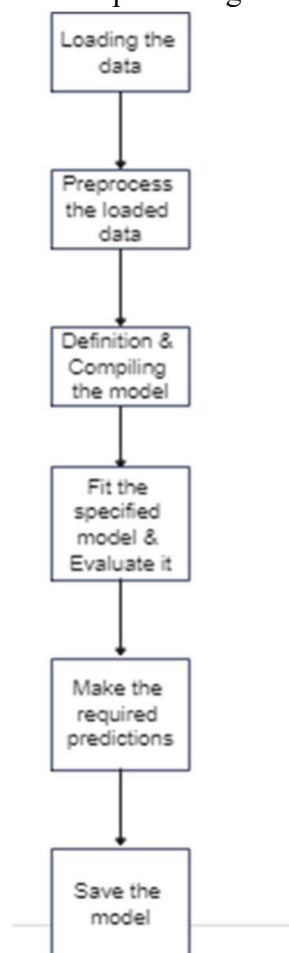
After finding the key points these key points are stored in the form of an array. This array contains the key points that belong to the face, left hand, right hand, and pose. Then we train the model based on the data that we collected and test it against the test data. Finally, we check the model in the real world.

To make Sign Recognition Model we have used different libraries or modules they are:

Keras is an open-source neural network library that runs on top of TensorFlow. It is made so that the user can use it easily. This library is used in the deep-learning algorithm.[2] We tried to use this library mainly because it has many advantages over similar types of libraries. Its major advantages includesimple API, Pythonic nature, extensibility, modularity, and strong backend support.

The ability of Keras is to create state-of-the-art implementations of common deep neural networks. And these which are produced using Keras are easy and fast accessible after creation. And also, these models can be deployed on multiple platforms

The following flowchart is how to create a deep learning model in Keras.[15][16][17][18]



OpenCV is a famous and big open-source library for computer vision, machine learning algorithms, image processing, and real-time operation. We use this OpenCV for computer vision because it is easy to learn, OpenCV is written in C, C++ and python languages, and less RAM consumption. [3] OpenCV is used to process images and videos and to identify various objects, hand signs, and facial expressions. To pinpoint image patterns and their features we use vector space and mathematical operations.[4]

When there is a boy image is given, there will be a lot of information present in that image like the boy wearing a cap and chain, etc. we use OpenCV to get all these types of information

There are a lot of applications using OpenCV like Face and object Recognition, several people in a place like a temple or theater, automatic cars, etc.

Neural Networks are a subset of machine learning that is important in deep learning algorithms.[5] The neural network's basic ideology is taken from the human brain working like biological neurons. Neural networks are hugely based on training the data and learning from it and they also improve their accuracy as time progresses.

Once the accuracy of these data is turned out to be at its best then it allows us to classify and cluster the data at a High- Velocity Rate ANN has different node layers those are an input layer, one or more hidden layers, and an output layer. ANN has a set of algorithms that are constructed in such a way that it recognizes the patterns in data samples and they are slightly based on the human brain. In ANN there are many hidden layers between 1 input layer and 1 output layer. However, the hidden layers depend upon the complexity of the problem The ANN recognizes a pattern that has all the real-time data, images, videos, and sounds. In simple neural network helps us to cluster and classify the data easily

A recurrent neural network (RNN) is another form of Neural Network. In RNN the input is processed through the number of layers and output is produced here the same task is performed for every element of a sequence.[6] In RNN the information is carried out to different neurons through loops. MediaPipe is a structure for building ML Pipelines. MediaPipe is a toolkit that consists of a Framework and Solutions.[7] The framework is written in java and C++. MediaPipe supports complicated graphs. May Built-in calculators come with GPU acceleration for performance optimization.

MediaPipe depends on OpenCV for video and FFMPEG for audio handling.

This model varies from existing models in such a way that in general, all the existing models have made great contributions toward achieving greater accuracy but those all have used image datasets that consume a lot of space in our memory. But here in our model complete data is stored in the form of arrays which can save our memory. This is the major difference between the remaining models and this proposed model.

II. RELATED WORKS

Design of a communication aid for the physically challenged [8].

It consists of two parts training part and the testing part in the training part the user used feed-forward neural networks. The SLR System was developed using the MATLAB Platform. Here MATLAB is not that coherent.

American Sign Language Interpreter System for Deaf and Dumb Individuals [9].

The given system recognizes and translates 20 out of 24 hand signs of the alphabets ASL into text output. The knowledge of PCA is used on sign images of the ASL alphabet. We will use the image to extract PCA Features to classify the image into one of the ASL. Due to the Occlusion problem the alphabets A, M, N, and S couldn't be recognized. For this system, they have used only a limited number of images.

Nasser H.D et.al [10] considers this approach where the key features extracted are SIFT (Scale Invariant Feature Transform) key points. They further constructed grammar from a sequence of hand postures for detecting dynamic gestures.

III. PROPOSED METHOD

This construction of the model can be classified into five steps:

1. Dataset Collection
2. Data Pre-Processing
3. Training the model
4. Validating the model
5. Testing the model
- i. Dataset Collection

We have created our database using OpenCV. But, instead of storing it in the form of images. We stored them in the form of arrays. These arrays contain the key points identified in the face, left hand, right hand, etc. This dataset contains some common English words that are used in English i.e., thanks, hello, etc. along with some English alphabets and numerals. This dataset is majorly based on hand gestures. Each hand gesture will be stored in the form of unique arrays.

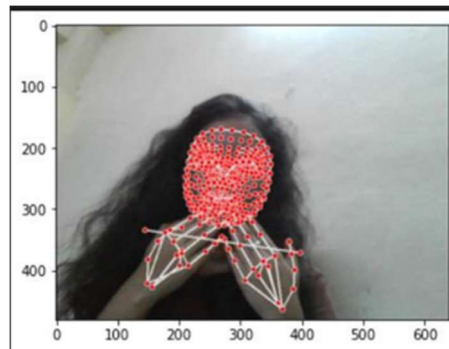


Figure 1: Show collecting Data related to sign Thankyou

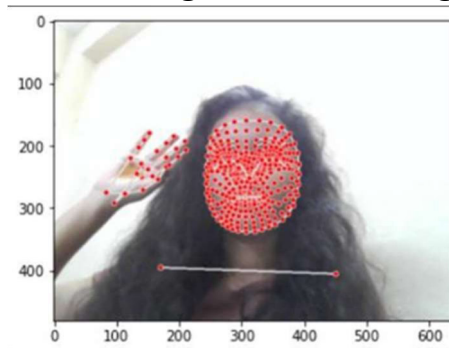


Figure 2: Show collecting Data related to sign Hello

As shown in the above images the data will be taken through the camera using OpenCV. And the points that are shown are identified with the help of Mediapipe libraries. These Mediapipe libraries are used to identify key points in the total body.

ii. Data Pre-processing:

As data is stored in the form of arrays, each array size will be 1662. Each array contains face key points, left-hand key points, right-hand key points, and pose key points. The face contains 33 points, the hand contains 21 key points, and the pose contains 468 key points. And individually each face key point has three attributes x, y, z, and visibility. The hand key point contains three attributes x, y, and z. The pose key point contains three attributes x, y, and z. So, all three attributes will be stored in the form of an array of size 1662. When creating the dataset whole body is not used only the hand and face most of the pose key points will not be recognized. If we store the data as we receive it from the camera it will be a difficult job to determine the output. Because if we create an array of the key points that we recognize the arrays will be created with different sizes. So, instead of leaving the unidentified key points as null points. We use zeros to fill in the key points that are not identified. By that, we can avoid the problem of noises and deviations that would be created while predicting the output.

iii. Training the model:

After preprocessing the data, we split data into two parts train and test splits using scikit train_test_split from sci-kit learn. Test and Train data will be completely different. Here we use LSTM (Long Short-Term Memory) model which is a recurrent neural network model. We train the model based on the train data. The model summary can be described as shown in the below figure:

Layer (type)	Output Shape	Param #
lstm_6 (LSTM)	(None, 30, 64)	442112
lstm_7 (LSTM)	(None, 30, 128)	98816
lstm_8 (LSTM)	(None, 64)	49408
dense_6 (Dense)	(None, 64)	4160
dense_7 (Dense)	(None, 32)	2080
dense_8 (Dense)	(None, 3)	99
Total params: 596,675		
Trainable params: 596,675		
Non-trainable params: 0		

Figure 4.3.1: Model Summary

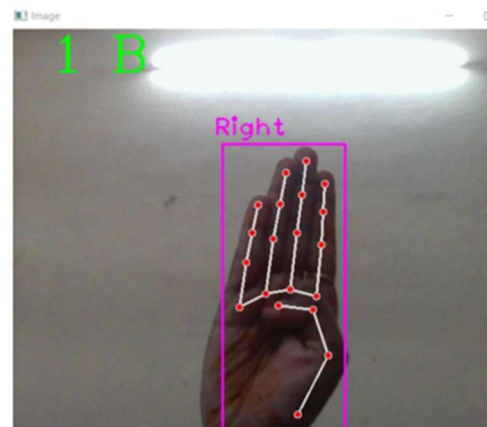
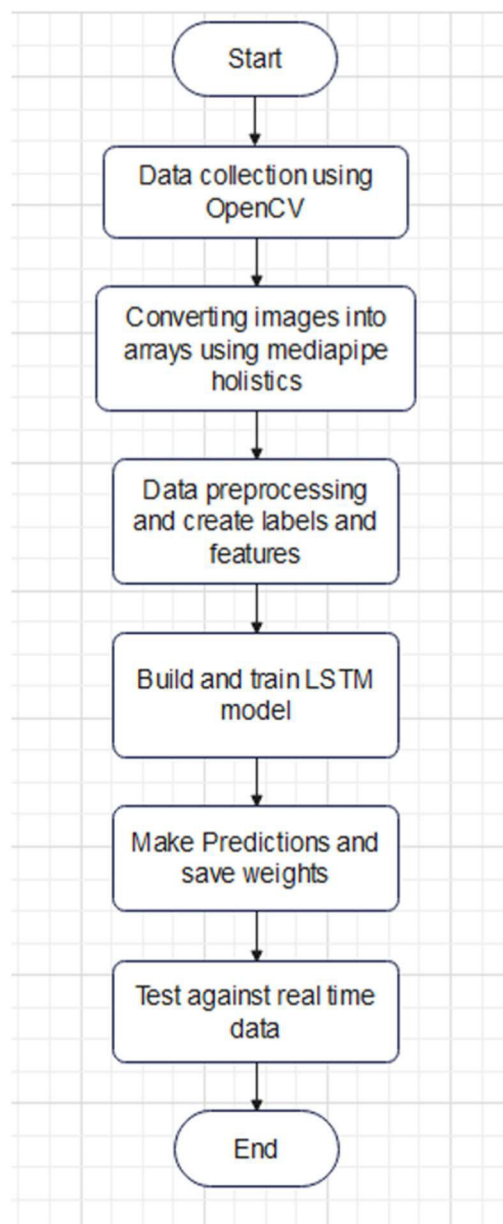
The above figure gives information about the number of parameters that are trained in each layer of the neural network. When we are training a model with the neural network algorithms, we need to use an activation function that plays a major role in deciding the performance of the model. The activation function that is used in this model is ReLU (Rectified Linear Unit) activation function. This is the most used activation function. And this activation function is used to determine when to trigger the inputs to the next layer in deep learning neural networks.

iv. Validating the model:

Initially, before training the model the whole dataset is divided into two parts. The second test split is used to validate the model. We pass the test data to the model and let it predict the output. That output will be compared with the label that is given to the image. Based on that accuracy will be calculated. This model gives an accuracy of around 87%.

v. Testing the model:

This is the final step in the implementation phase. Here we test our model with real-world data. And the model is allowed to predict the results. This is briefly discussed in the results part.



The above flowchart describes all the steps that are in the process of preparation of this model starting from dataset collection to the final validation process. By looking at this flow chart we can get an overview of the preparation of this model

IV. RESULT AND DISCUSSIONS

We have successfully created a Sign Language Recognition model. In which the data set is converted into arrays. While running this system we found an accuracy of 86.24%. To improve this accuracy, we can add more data to the dataset.

Figure 3

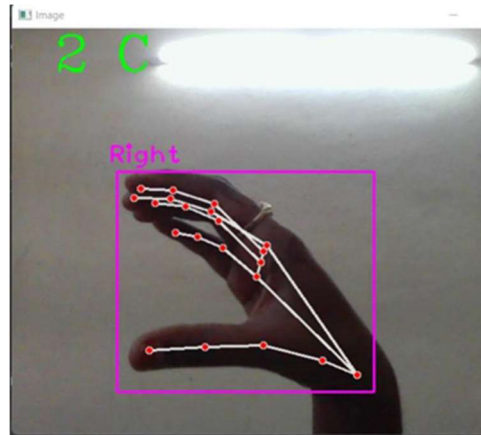


Figure 4

Figure3,4: Show the predictions that are made by the model.

In [11] 3rd InCI Conf. on Recent Advances in Information Technology I RAIT-20161 there is a detailed analysis of a number of common methods and its comparative study is tabulated below (Table 1). Entry (5) indicates our results.

Table-1:Caomaparision with popular models

SL.NO	Segmentation Technique	Feature Vector Representation	Classifier	Acc (%)
1.	Discontinuity (time-variant parameter detection)	Posture, position, orientation	HMM	80.4
2.	Manually from background	Blob and ridge features	Particle filtering	86.5
3.	HSV color space	The convex hull of the contour	Haar like technique	N/A
4.	RGB to Gray	Euclidean distance	Neural Networks	N/A
5.	Images to arrays	Hand gestures	Neural Networks	86.24

IV. CONCLUSION

The Impaired people communicate in Sign Language which is not understood by regular people. We built this system to ease the difficult communication between deaf and dumb people and normal people. This system will automatically recognize the hand gestures made by people and take this

sign as input and gives related output in form of text.

This system is built on a CNN algorithm and gives an average accuracy of 86.24%. This accuracy can be further improved by giving more data into the dataset.

FUTURE SCOPE

We are trying to increase our accuracy by increasing the number of layers in the neural networks.

REFERENCES

- [1] Kumar, Anup, Karun Thankachan, and Mevin M. Dominic. "Sign language recognition." In 2016 3rd International Conference on Recent Advances in Information Technology (RAIT), pp. 422-428. IEEE, 2016.
- [2] Jason, B., 2019. How to Train an Object Detection Model with Keras. [online]machinelearningmastery.Availableat:<[https://machinelearning mastery.com/how-to-train-an-object-detection-model-with-keras/](https://machinelearningmastery.com/how-to-train-an-object-detection-model-with-keras/)> .
- [3] V. Bala, "What is the Tensor in deep learning?", Medium, 2021. [Online]. Available: <https://medium.datadriveninvestor.com/what-is-the-tensor-in-deep-learning-77c2af7224a1>.
- [4] A. Rosebrock, "Deep Learning with OpenCV - PyImageSearch", PyImageSearch, 2022. [Online]. Available: <https://pyimagesearch.com/2017/08/21/deep-learning-with-opencv/>.
- [5] I. Education, "What are Neural Networks?", Ibm.com, 2022. [Online]. Available: <https://www.ibm.com/cloud/learn/neural-networks>.
- [6] B. Hammer, Learning with Recurrent Neural Networks. London: Springer London, Limited, 2007.
- [7] S. Ghosh, "Proposal of a Real-time American Sign Language Detector using MediaPipe and Recurrent Neural Network", International Journal of Computer Sciences and Engineering, vol. 9, no. 7, pp. 46- 52, 2021.
- [8] Kang, Byeongkeun, Subarna Tripathi, and Truong Q. Nguyen. "Real- time sign language fingerspelling recognition using convolutional neural networks from the depth map." arXiv preprint arXiv: 1509.03001 (2015).
- [9] Suganya, R., and T. Meeradevi. "Design of a communication aid for physically challenged." In Electronics and Communication Systems (ICECS), 2015 2nd International Conference on, pp. 818-822. IEEE, 2015
- [10] Nasser H. Dardas and Nicolas D. Georganas. Real-time handGesture detection and recognition using bag-of-features and support vector machine techniques. IEEE TRANSACTIONS ON INSTRUMENTATION AND MEASUREMENT, 2011.
- [11] Real-Time Palm Tracking and Hand Gesture Estimation Based on Fore- Arm Contour, 20 II
- [12] Oudah, M.; Al-Naji, A.; Chahl, J. Hand Gesture Recognition Based on Computer Vision: A Review of Techniques. J. Imaging 2020, 6, 73. [Google Scholar] [CrossRef]
- [13] Al-Hammadi, M.; Muhammad, G.; Abdul, W.; Alsulaiman, M.; Bencherif, M.A.; Alrayes, T.S.; Mekhtiche, M.A. Deep learning-based approach for sign language gesture recognition with efficient hand gesture representation. IEEE Access 2020, 8, 192527–192542. [Google Scholar] [CrossRef]
- [14] Rezende, T.M.; Almeida, S.G.M.; Guimarães, F.G. Development and validation of a brazilian

sign language database for human gesture recognition. *Neural Comput. Appl.* 2021. [Google Scholar] [CrossRef]

[15] Afza, F.; Khan, M.A.; Sharif, M.; Kadry, S.; Manogaran, G.; Saba, T.; Ashraf, I.; Damaševičius, R. A framework of human action recognition using length control features fusion and weighted entropy-variances based feature selection. *Image Vision Comput.* 2021, 106, 104090. [Google Scholar] [CrossRef]

[16] Kulikajevas, A.; Maskeliunas, R.; Damaševičius, R. Detection of sitting posture using hierarchical image composition and deep learning. *PeerJ Comput. Sci.* 2021, 7, e442. [Google Scholar] [CrossRef] [PubMed]

[17] [12] Jagadish R M and Aradhana D, "A Secured Framework for Offline File Synchronization using ANN and Storage Optimization Schemes," 2021 IEEE International Conference on Mobile Networks and Wireless Communications (ICMNWC), Tumkur, Karnataka, India, 2021, pp. 1-6, doi: 10.1109/ICMNWC52512.2021.9688485.

[18] [13] Jagadish R. M., Jyothi, L. Swarna, Patil, Rohini. "Offline Data Synchronization with Occasionally Connected Databases Using Smart-IPMS." In **Emerging Trends in Electrical, Communications and Information Technologies**, Springer Singapore, 2017. Chapter.

An optimized system for sensor ontology meta-matching using swarm intelligent algorithm

Abdul Lateef Haroon P S, Sujata N. Patil, Parameshachari Bidare Divakarachari ✉, Przemysław Falkowski-Gilski, M. D. Rafeeq

First published: 14 January 2024

<https://doi.org/10.1002/itl2.498>

Citations: 54

Abstract

It is beneficial to annotate sensor data with distinct sensor ontologies in order to facilitate interoperability among different sensor systems. However, for this interoperability to be possible, comparable sensor ontologies are required since it is essential to make meaningful links between relevant sensor data. Swarm Intelligent Algorithms (SIAs), namely the Beetle Swarm Optimisation Algorithm (BSO), present a possible answer to ontology matching problems. This research focuses on a method for optimizing ontology alignment that employs BSO. A novel method for effectively controlling memory use and striking a balance between algorithm exploration and exploitation is proposed: the Simulated Annealing-based Beetle Swarm Optimisation Algorithm (SA-BSO). Utilizing Gray code for solution encoding, two compact operators for exploitation and exploration, and Probability Vectors (PVs) for swarming choosing exploitation and exploration, SA-BSO combines simulated annealing with the beetle search process. Through inter-swarm communication in every generation, SA-BSO improves search efficiency in addressing sensor ontology matching. Three pairs of real sensor ontologies and the Conference track were used in the study to assess SA-BSO's efficacy. Statistics show that SA-BSO-based ontology matching successfully aligns sensor ontologies and other general ontologies, particularly in conference planning scenarios.

Open Research

PEER REVIEW

The peer review history for this article is available at <https://www.webofscience.com/api/gateway/wos/peer-review/10.1002/itl2.498> .

Data sharing is not applicable to this article as no new data were created or analyzed in this study.

REFERENCES

1 Xue X, Guo J, Ye M, Lv J. Similarity feature construction for matching ontologies through adaptively aggregating artificial neural networks. *Mathematics*. 2023; **11**(2): 485.

[Web of Science®](#) | [Google Scholar](#)

2 Cherskikh EO. A conceptual model of sensor system ontology with an event-based information processing method. *Neurosci Behav Physiol*. 2022; **52**(8): 1310-1317.

[Google Scholar](#)

3 Xue X, Huang Q. Generative adversarial learning for optimizing ontology alignment. *Expert Syst*. 2023; **40**(4):e12936.

[Web of Science®](#) | [Google Scholar](#)

4 Zhu H, Xue X, Jiang C, Ren H. Multiobjective sensor ontology matching technique with user preference metrics. *Wireless Commun Mobile Comput*. 2021; **2021**: 1-9.

[CAS](#) | [PubMed](#) | [Web of Science®](#) | [Google Scholar](#)

5 Xue X, Jiang C. Matching sensor ontologies with multi-context similarity measure and parallel compact differential evolution algorithm. *IEEE Sensors J*. 2021; **21**(21): 24570-24578.

[Web of Science®](#) | [Google Scholar](#)

6 Xue X, Wu X, Zhang J, Zhang L, Zhu H, Mao G. Aggregating heterogeneous sensor ontologies with fuzzy debate mechanism. *Security Commun Networks*. 2021; **2021**: 1-12.

[Web of Science®](#) | [Google Scholar](#)

7 Huang Y, Zhuang Y, Xue X. Solving ontology metamatching problem through improved multiobjective particle swarm optimization algorithm. *Wireless Commun Mobile Comput*. 2022. <http://doi.org/10.1155/2022/1634432>

8 Xue X, Wang H, Zhou X, Mao G, Zhu H. Matching heterogeneous ontologies with adaptive evolutionary algorithm. *Connect Sci.* 2022; **34**(1): 811-828.

[Web of Science®](#) | [Google Scholar](#) |

9 Ferranti N, de Souza JF, Soares SSRF. A prey–predator approach for ontology meta-matching. *J Data Semantics.* 2021; **10**: 229-240.

[Web of Science®](#) | [Google Scholar](#) |

10 Dunbar D, Hagedorn T, Blackburn M, et al. Driving digital engineering integration and interoperability through semantic integration of models with ontologies. *Syst Eng.* 2023; **26**: 365-378.

[Web of Science®](#) | [Google Scholar](#) |

11 Lian W, Fu L, Niu X, Feng J, Wang JH. Solving sensor ontology Metamatching problem with compact flower pollination algorithm. *Wireless Commun Mobile Comput.* 2022; **2022**: 1-7.

[Web of Science®](#) | [Google Scholar](#) |

12 Geng A, Lv Q. A multi-objective particle swarm optimization with density and distribution-based competitive mechanism for sensor ontology meta-matching. *Complex Intellig Syst.* 2023; **9**(1): 435-462.

[Web of Science®](#) | [Google Scholar](#) |

13 Zhou X, Lv Q, Geng A. Matching heterogeneous ontologies based on multi-strategy adaptive co-firefly algorithm. *Knowl Inform Syst.* 2023; **65**(6): 2619-2644.

[Web of Science®](#) | [Google Scholar](#) |

14 Xue X, Tan W. Matching cybersecurity ontologies on internet of everything through coevolutionary multiobjective evolutionary algorithm. *Security Commun Networks.* 2022; **2022**: 1-13.

[Web of Science®](#) | [Google Scholar](#) |

15 Chu SC, Xue X, Pan JS, Wu X. Optimizing ontology alignment in vector space. *J Internet Technol.* 2020; **21**(1): 15-22.

[Web of Science®](#) | [Google Scholar](#) |

[PubMed](#) | [Web of Science®](#) | [Google Scholar](#)

17 Zhu H, Zhang J, Xue X. Semisupervised learning-based sensor ontology matching. *Security Commun Networks*. 2021; **2021**: 1-5.

[CAS](#) | [Web of Science®](#) | [Google Scholar](#)

18 Xue X, Wu Q, Ye M, Lv J. Efficient ontology meta-matching based on interpolation model assisted evolutionary algorithm. *Mathematics*. 2022; **10**(17): 3212.

[Web of Science®](#) | [Google Scholar](#)

19 Xue X, Wang H, Zhang J, Huang Y, Li M, Zhu H. Matching transportation ontologies with Word2Vec and alignment extraction algorithm. *J Adv Transport*. 2021; **2021**: 1-9.

[Web of Science®](#) | [Google Scholar](#)

20 Xue X, Zhang J. Matching large-scale biomedical ontologies with central concept based partitioning algorithm and adaptive compact evolutionary algorithm. *Appl Soft Comput*. 2021; **106**:107343.

[Web of Science®](#) | [Google Scholar](#)

Citing Literature



Download PDF

ABOUT WILEY ONLINE LIBRARY

[Privacy Policy](#)

[Terms of Use](#)

[About Cookies](#)

[Manage Cookies](#)

[Accessibility](#)

[Wiley Research DE&I Statement and Publishing Policies](#)

[Developing World Access](#)

[Training and Support](#)
[DMCA & Reporting Piracy](#)

OPPORTUNITIES

[Subscription Agents](#)
[Advertisers & Corporate Partners](#)

CONNECT WITH WILEY

[The Wiley Network](#)
[Wiley Press Room](#)

Adaptive tunicate swarm optimization with partial transmit sequence for phase optimization in MIMO-OFDM

Abdul Lateef Haroon Phulara Shaik¹, Sowmya Madhavan², Parameshachari Bidare Divakarachari²,
Rocío Pérez de Prado³, Paramesh Siddappa Parameshwarappa⁴,
Kavitha Malali Vishveshwarappa Gowda⁵

¹Department of Electronics and Communication Engineering, Ballari Institute of Technology and Management, Ballari, India

²Department of Electronics and Communication Engineering, Nitte Meenakshi Institute of Technology, Bengaluru, India

³Department of Telecommunication Engineering, University of Jaén, Linares, Spain

⁴Department of Computer Science and Engineering, School of Engineering, Central University of Karnataka, Kalaburagi, India

⁵Department of Electronics and Communication Engineering, Gopalan College of Engineering and Management, Bangalore, India

Article Info

Article history:

Received Dec 23, 2023

Revised Feb 2, 2024

Accepted Mar 21, 2024

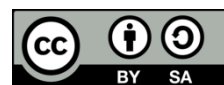
Keywords:

Adaptive tunicate swarm optimization
Fast Fourier transform
Multiple-input multiple-output
Nonsquare-matrix-based differential space time coding
Orthogonal frequency division multiplexing
Peak-to-average-power ratio

ABSTRACT

Multiple-input multiple-output (MIMO) and orthogonal frequency division multiplexing (OFDM) are widely utilized in wireless systems and maximum data rate communications. The MIMO-OFDM technology increases the efficiency of spectrum utilization. The peak-to-average-power ratio (PAPR) minimization in MIMO-OFDM is a complex task in wireless communications systems. In this research, an adaptive tunicate swarm optimization with partial transmit sequence (ATSO-PTS) algorithm is proposed for a reduction of PAPR in MIMO-OFDM. The nonsquare-matrix-based differential space time coding (N-DSTC) scheme is used for the encoding and decoding process of MIMO-OFDM. The N-DSTC encoding and decoding are linear error-correcting codes that are utilized for message transmission over noisy channels. The pre-specified quadrature phase shift keying (QPSK) symbol is deployed for the modulation and demodulation scheme. On the receiver side, the serial to parallel (S/P) conversion, and fast Fourier transform (FFT) are accomplished, alongside the received data bits being demodulated to obtain the output bits. The proposed ATSO-PTS method achieves better results according to performance metrics PAPR, bit error rate (BER) and signal-to-noise-ratio (SNR), with values of about 2.9, 0.01 and 0.025, respectively. This ensures superior results when compared to the existing methods of twin symbol hybrid optimization applied to partial transmit sequence (TSHO-PTS), selective level mapping and PTS (SLM-PTS), and particle swarm and grey wolf (PS-GW) with PTS, respectively.

This is an open access article under the [CC BY-SA](https://creativecommons.org/licenses/by-sa/4.0/) license.



Corresponding Author:

Parameshachari Bidare Divakarachari

Department of Electronics and Communication Engineering, Nitte Meenakshi Institute of Technology

P.B.No.6429, Yelahanka, Bangalore 560064, Karnataka, India

Email: paramesh@nmit.ac.in

1. INTRODUCTION

The growing need for advancements in wireless applications has rendered the currently available radio frequency (RF) spectrum, inadequate to meet future service requirements [1]. Orthogonal frequency division multiplexing (OFDM) is majorly considered in wireless systems to attain maximum-rate data transmission due to its larger spectral efficiency, simple equalization, as well as low-complexity execution [2], [3]. Therefore, OFDM is also majorly utilized in wideband communications over mobile radio channels, digital audio broadcasting, high-bit-rate digital subscriber lines and optical systems [4]. Despite the OFDM

having number of advantages, it has one major limitation, which is that the transmitted signal has a high peak-to-average-power ratio (PAPR) [5]. On an assumption of maximum PAPR, the OFDM signal is fasten when it forwards by non-linear high-power amplifier (HPA) and thus, the performance is degenerated, while in-band bias as well as out-of-band radiation also happens. Thus, the OFDM transmitters needs costly linear HPA with extreme dynamic range [6], [7]. Recently, a number of optimization algorithms are recommended to optimize the partial transmit sequence (PTS) technique for PAPR reduction in OFDM systems [8]. Between them, the most famous evolutionary algorithms are the genetic algorithm (GA), differential evolutionary algorithm (DE), and biogeographic optimization algorithm (BBO) which are majorly used for the reduction of PAPR [9]. However, the selection of the phase factor sequence in the PTS approach is a risk in non-linear optimization, which is caused by greater complexity and memory utilization if there are a greater number of non-overlapping sub-blocks [10], [11]. By embedding the pilot signal within the optical OFDM signal in the frequency domain minimizes the time domain signals [12]. A reduction of PAPR in MIMO-OFDM is a complex task in wireless communications, where the spectral efficiency is also reduced when the cyclic prefix enters in OFDM [13]. According to the literature and targetted at the limitations of an existing signal compounding transform methods, a novel approach is introduced for combinely optimize the PAPR and bit error rate (BER) performance [14], [15].

Sarkar *et al.* [16] implemented a twin symbol hybrid optimization applied to partial transmit sequence (TSHO-PTS) to minimize PAPR in cyclic prefix-OFDM (CP-OFDM). The hybrid optimization algorithms of salp swarm (SS) as well as bald eagle search (BES) were produced to determine phase factor. The digital chaotic was utilized to certify physical layer security in data transmission for (DFT-S-OFDM) subcarrier allocation. A PTS method achieved the minimum PAPR in less processed and consumed time, but the efficiency of bandwidth was decreased by the system itself. Sidiq *et al.* [17] developed a hybrid method of selective level mapping and PTS (SLM-PTS) with ant bee colony (ABC) phase optimization for PAPR minimization. The SLM was initially enforced to the traditional farnesyl dimethyl chromanol (FDMC) signal and the PAPR signal was obtained with selected similar phase sequences. This method significantly minimized the PAPR by the minimum computational complexity by combining the SLM and PTS benefits. The SLM-PTS suffered from the interface between unsynchronized symbols in the closest bands. Kumar *et al.* [18] implemented a PTS over a hybrid of particle swarm and grey wolf (PS-GW) optimization for the performance of minimum PAPR, as well as low computational complexity. The PS-GW identified the phase rotational factors combination effectively. The PS exploitation was improved with the estimation capability in GW to develop multiple variations in quality. The PS-GW achieved better performance and minimum PAPR than the PS and GW. However, PAPR achievement was decreased using various channel constraints. Prasad and Jayabalan [19] implemented a particle swarm optimization (PSO) applied to the technique of PTS to identify the phase factor for reducing the PAPR. A scaling factor was established in the velocity updating equation of conventional PSO to enhance the inertia weight and particle velocity. The PSO-PTS achieved the efficient minimum PAPR and was most efficient for the applications using the 64-quadratic amplitude modulation (QAM) modulation scheme, but this method performed a low convergence rate.

Şimşir and Taşpınar [20] implemented a discrete elephant herding optimization using PTS (DEHO-PTS) to minimize PAPR in universal-filtered multi-carrier (UFMC) signals to the lowest levels. An advanced scheme of PTS was powered by an intelligent optimization which was enforced to UFMC waveform. This approach was majorly focused on decreasing the transmission signals in PAPR values and achieved better performance and low BER. The conventional PTS was a difficult method for systems to obtain efficient transmission powers with a smaller number of searches. Bai and Yang [21] developed an enhanced PSO called the discrete adaptive PSO (DAPSO) approach for solving the problem of high PAPR in UOWC. This method integrated PTS and DAPSO to minimize the PAPR in the UOWC system. The PTS was applied to a probabilistic approach for effectively defeating the performance of PAPR. Simultaneously, the two-dimensional adaptive PSO effectively modified the comprehensive search for the phases of PTS. This method effectively solved the complexity of the calculation and also achieved a fast convergence speed. Abed *et al.* [22] introduced PSO-based dummy sub-carriers which were applied with data, without transmitting the side information for PAPR reduction. The fusion of suggested approach was employed by calculating a PAPR at an outcome of inverse fast fourier transform (IFFT). Later, this method added the six adaptive sub-carrier sequences to an IFFT input data. This method transmitted the data when the dummy sub-carrier was in a significant threshold. Further, it utilized the additive white gaussian noise (AWGN) channel to explore the performance of PAPR and BER. This method achieved low computational complexity regarding the number of additions and multiplications, but it had a low convergence rate. Li *et al.* [23] developed a PTS-based discrete PSO with a threshold (PTS-DPSO-TH) and utilized to a filter bank multi-carrier with quadratic amplitude modulation (FBMC/OQAM) for PAPR reduction. This method utilized the DPSO to identify an optimal solution and effectively minimize the PAPR in the OQAM approach, alongside reducing the complexity problem. Then, the threshold was established to minimize the iteration numbers, and

later decrease the system complication on the assumption of undertaking the PAPR reduction performance. The PTS-DPSO-TH effectively reduced the PAPR, but this approach had a low convergence rate.

Şimsir and Taşpınar [24] introduced an efficient PAPR reduction method for the waveform of the UPMC system. This method initially introduced a novel discrete version of the invasive weed optimization (DIWO) approach and combined it with the traditional PAPR reduction approach called PTS deployed as the phase optimizer. By doing so, this method acquired a novel method known as DIWO-PTS. The DIWO was the method to optimize the phase sequences in the discrete phase. The DIWO achieved the best phase integration in a minimum number of searches. However, the DIWO had less population diversity and did not take the best member of the population during the process of optimization. Ali and Hamza [25] implemented a new optimization method, teaching-learning-based optimization (TLBO) for the reduction of PAPR in the OFDM signal. This approach introduced selective mapping (SLM) based TLBO for the effective reduction. The TLBO was performed to identify search factors in the SLM approach. This method effectively reduced the PAPR with low computational complexity and did not require certain parameters. However, this method consumed a larger memory storage space. To address these limitations of the existing methods, the MIMO-OFDM systems are proposed in this research. Simultaneously, the synchronization, evaluation of channel, PAPR, larger memory storage, selection of antenna, and convergence rate were the specific limitations of the above-discussed existing methods which are examined through the OFDM signal. Therefore, for the reduction of PAPR, the novel adaptive tunicate swarm optimization with partial transmit sequence (ATSO-PTS) with MIMO-OFDM approach is introduced to minimize PAPR in OFDM. Further, the proposed method is briefly discussed in the following section. This research's major contributions are as follows:

- This research offers the reduction of PAPR with faster convergence as well as minimized computational complexity as the foremost achievement.
- The paper focuses on minimizing PAPR using quick convergence and minimizing computational complexity. The ATSO-PTS is developed for PAPR reduction in MIMO-OFDM.
- Nonsquare-matrix-based differential space time coding (N-DSTC) approach is employed for encoding and decoding which helps to achieve better data broadcasting over the MIMO-OFDM. This research considers quadrature phase shift keying (QPSK) for modulation/demodulation because of its low error probability.

The rest of the paper is arranged in the succeeding way: section 2 presents the proposed methodology which includes the MIMO-OFDM system with N-DSTC encoding and decoding approaches. Section 3 discusses the ATSO. Section 4 describes results and discussion and finally, section 5 describes the overall summary.

2. PROPOSED METHOD

In this research, an ATSO is proposed with the N-DSTC coding for minimizing PAPR while transmitting the data over MIMO-OFDM. The N-DSTC codes are linear error-correcting codes that are utilized for the transmission of messages over noisy channels. Figure 1 depicts the proposed method's workflow.

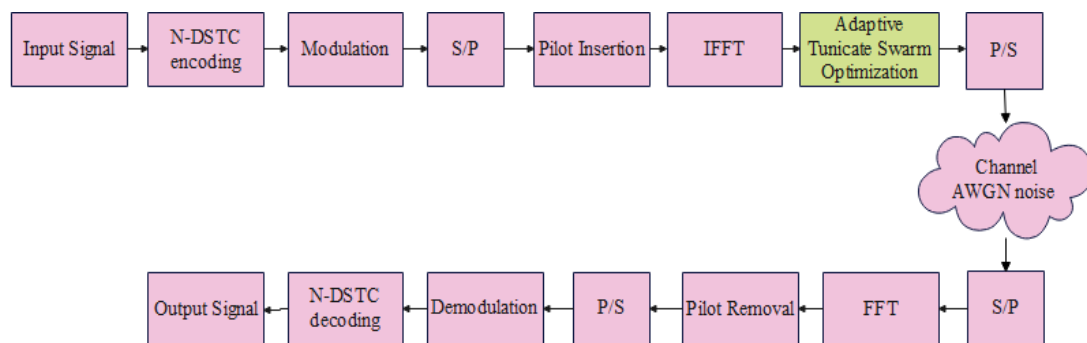


Figure 1. Workflow of the proposed method with MIMO-OFDM

At the transmitter, the incoming binary data is first grouped and mapped according to the coding scheme of N-DSTC. The QPSK symbol is the pre-specified modulation scheme utilized, and then converted into parallel signals by serial-to-parallel block. After inserting some pilots, IFFT is additionally deployed for

transmitting a sequence of data to a time-domain signal. An ATSO is inserted into the time-domain OFDM symbol to reduce the inter carrier interface (ICI) and inter symbol interference (ISI). The transmitted signal passes by using the channel with AWGN noise after the converting the signal serial into parallel. The FFT is followed after the conversion of serial to parallel at the receiver. After FFT, some pilots are removed and the system is converted from parallel to a serial block. At last, the binary data is acquired after the demodulation using the QPSK modulation scheme, and decoding using the N-DSTC coding scheme. The QPSK provides a low error probability and good noise immunity, alongside the bandwidth required by the QPSK being reduced to half as compared to binary phase-shift keying (BPSK) for the same BER. Furthermore, IFFT is employed for transmitting the sequence of data to the time-domain signal, after inserting some pilots.

2.1. System model of MIMO-OFDM

In this paper, a system model of MIMO-OFDM [26], having three major portions, namely, transmitter, channel, and receiver is introduced. This approach provides an efficient and robust system for data transmission in MIMO-OFDM. Figure 2 shows the system model of MIMO-OFDM.

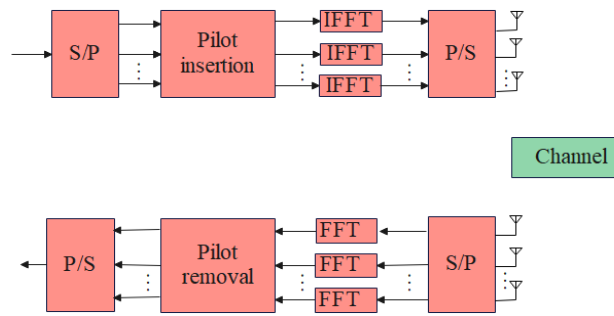


Figure 2. System model of MIMO-OFDM

The system of IFFT and FFT MIMO-OFDM is implemented in this paper. This approach provides an efficient and robust system for data transmission in MIMO-OFDM. A baseband signal is described in (1) and a time domain sample in IFFT output is expressed in (2).

$$x(t) = \sum_{k=0}^{N-1} X(k) e^{j2\pi k \Delta f t} \quad (1)$$

$$x(n) = W^H X(k) \quad (2)$$

Where, N is the number of subcarriers, $X(k)$ is the complex modulation symbol transmitted on k^{th} subcarrier, and Δf is the subcarrier spacing. W is the FFT integrated matrix of order $N \times N$. The CP of length g is extended to remove ISI which is expressed in (3). The received signal is described in (4).

$$x'(n) = C_r \times x(n) \quad (3)$$

$$y(n) = \sum_{i=0}^{L-1} h_i x'(n-i) + z(n), n = 0, 1, \dots, N-1 \quad (4)$$

Where, $z(n) \sim N(0, \sigma_z^2) - AWGN$, $C_r - (N+G) \times N$ is the order matrix. The frequency channels are designed by utilizing L -tap finite impulse response (FIR) using taps $[h_0, h_1, \dots, h_{L-1}]$. At the receiver side, the CP elimination exists that is denoted as a received signal multiplication by using a matrix C_R , and is expressed in (5) and (6).

$$C_R = [O_{N \times G} I_N] \quad (5)$$

$$Y(k) = W C_R \tilde{H} C_T W^H X(k) + Z(k) \quad (6)$$

Where, $Z(k) = W C_R z(n)$ and $H = W C_R \tilde{H} C_T W^H$. Therefore, the frequency domain received signal for OFDM is provided in (7). The received signal matrix vector model is expressed in (8) and (9).

$$Y = HX + Z \quad (7)$$

$$Y = Ah + Z \quad (8)$$

$$H = \sqrt{N}Fh \quad (9)$$

Where, H is the response of channel frequency, X is the transmitted symbols, Z is the AWGN with 0 mean. N_t and N_r is the number of transmit and receive antennas in MIMO-OFDM, h is the received symbol, Y is minimum pilots. $A = \sqrt{N}diag(X)F$ and F - partial FFT matrix and CFR matrix. The transmitted MIMO-OFDM system are provided to the N-DSTC system for the encoding and decoding processes of the OFDM signal.

2.2. Nonsquare matrix-based differential space-time coding

In this section, the N-DSTC consisting of encoding and decoding approaches [27], [28] are discussed. This section encodes and decodes the input of the OFDM signal, where the N-DSTC scheme is majorly utilized to minimize the number of time slots. The space-time euphemism $S(i) \in \mathbb{C}^{M \times M}$ is transmitted in M slots by M antennas. Enhancing a large amount of transmit antennas affects the enhancing of the number of essential time slots and ineffective for large scenarios of MIMO. Hence, a non-square matrix-based DSTC is developed to minimize the amount of time slots. Particularly, it increase $S(i)$ through basis $e_1 \in \mathbb{C}^{M \times 1}$ to minimize the number of slots between M and 1.

2.2.1. Nonsquare differential encoding and decoding

The set of estimating metrics $\{E_1, \dots, E_{M/T}\}$ are transmitted at the beginning of the transmission stream. Initially, the received symbol is denoted in (10). Hence, this requires M number of time slots. Considering the W blocks time transmission frame, the projection metrics are transmitted to the receiver. The subsequent data metrics $X(i)$ are encoded and expressed in (11). Mapped onto $M \times T$ nonsquare matrices by projection matrix E_i , as well as transmitted such that interrelated received signal is formulated in (12).

$$Y(i) = H(i)E_i + V(i), \text{ for } 1 \leq i \leq M/T \quad (10)$$

$$S(i) = \begin{cases} I_M & \text{if } i = \frac{M}{T}, \text{ or} \\ S(i-1)X(i) & \text{if } i > \frac{M}{T}, \end{cases} \quad (11)$$

$$Y(i) = H(i)S(i)E_i + V(i), \text{ for } \frac{M}{T} < i \leq W \quad (12)$$

The ratio among the number of transmit antennas M and length of frame W is, $\eta \triangleq M/W$ which is denoted as an insertion ratio. For the task performance, this method sets $\eta = 5\%$ such that $W = 200M$, but remark that the N-DSTC performance remains robust in high-speed mobile scenarios plan using $\eta = 1\%$ or 0.1% . Hence, the tree-based approach is utilized to achieve minimum PAPR between all sub-carriers in a limited computational process. In the process of phase factor, the proposed algorithm accumulates the phase factor yielding less PAPR. To achieve this, the proposed method uses the ATSO model for obtaining reduced PAPR values. The obtained results are provided to the optimization algorithm for the further processes.

3. TUNICATE SWARM OPTIMIZATION

The encoded data from the input signal is provided to the optimization process for improving the computational efficiency of the phase optimization algorithm. Tunicate swarm optimization (TSO) [29] is a meta-heuristic algorithm activated by marine tunicates' performance and jet propulsion over navigation as well as foraging. The tunicate is in the form of a millimeter scale and locates sources of food in the sea. The tunicate satisfies the three general conditions in propulsion which are: to eliminate the hit using the number of tunicates in search space, to obtain a suitable path to select an effective search location, and finally, to select a better search agent. Further, the tunicates change their positions to achieve better search, and the process is enhanced in every iteration. The TSO begins using population incidentally produces tunicate with generate variables permissible boundaries, as expressed in (13) where tunicates modify the location in iterations as depicted in (14).

$$\vec{T}_p = \vec{T}_p^{min} + rand \times (\vec{T}_p^{max} - \vec{T}_p^{min}) \quad (13)$$

$$\vec{T}_p(\vec{x} + 1) = \frac{\vec{T}_p(x) + \vec{T}_p(\vec{x})}{2 + c_1} \quad (14)$$

Where, \vec{T}_p is the tunicate position, $rand$, c_1 denotes arbitrary number within the range $[0,1]$. \vec{T}_p^{max} and \vec{T}_p^{min} are the lower and upper design variables, respectively, while $\vec{T}_p(x)$ is the updated position of tunicate's food source as mathematically expressed in (15). SF is the source of food, A is the arbitrary vector that avoids the tunicates from hitting one another and it is mathematically designed in (16).

$$\vec{T}_p(x) = \begin{cases} SF + A \times |SF - rand \times \vec{T}_p|, & \text{if } rand \geq 0.5 \\ SF - A \times |SF - rand \times \vec{T}_p| & \text{if } rand < 0.5 \end{cases} \quad (15)$$

$$A = \frac{c_2 + c_3 - 2c_1}{VT_{min} + c_1(VT_{max} - VT_{min})} \quad (16)$$

Where, c_1 , c_2 and c_3 – random number with range $[0,1]$, VT_{min} , while VT_{max} respectively reflect minimum and maximum speeds utilized to perform community communication denoted as 0 and 1. The obtained TSO outcome is provided in the next section for the efficient reduction of PAPR. The TSO algorithm procedures are given:

- Initialize the population of tunicate \vec{T}_p according to (13).
- Select initial parameters as well as a greater number of iterations.
- Estimate the fitness value of the search agent.
- The better tunicate is traversed in given search space.
- Update the tunicate's position utilizing (14).
- Alter the updated tunicate that moves behind a boundary in the provided search space.
- Calculate the updated fitness value of the tunicate. If it obtains the best solution than the preceding optimal solution, it is updated with a better solution.
- If satisfied with an ending basis, then the algorithm ends or repeats steps 5 to 8.
- Finally, the best solution has been obtained.

3.1. Adaptive tunicate swarm optimization

The efficiency of the tunicate swarm algorithm (TSA) exhibits endurance with the local optimum solutions when compared to the most common algorithms. Moreover, this is not better choice for certain intricate solutions by various optimal solutions. In TSA, each tunicate finds the food source and finds it unfeasible to retrieve without knowing where the food source is located. Later, it achieves convergence when it is no longer able to design findings and ends functioning. Thus, an adaptive version of TSO (ATSO) [30] is implemented to defeat weaknesses in TSO as well as improve the algorithm's search capacity and flexibility. The TSO is improved by using the two phases such as exploration and exploitation to enhance the search capability. Figure 3 shows the proposed method using ATSO.

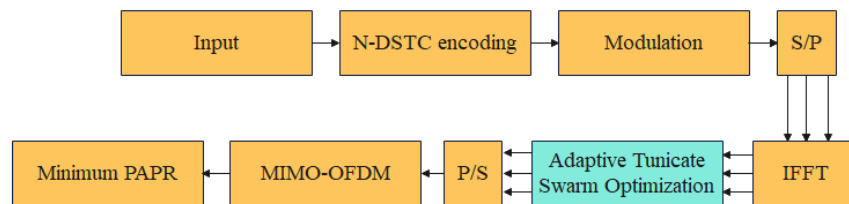


Figure 3. The proposed method using ATSO

An efficient metaheuristic algorithm is essential to classify the process of search into multiple phases of exploration and exploitation. The metaheuristic algorithm is employed to find a good solution to an optimization problem that is complex and difficult to solve to optimality. Conversely, the exploitation denotes the optimization algorithm's capacity to identify near-optimal solutions. The exploitation permits the optimizer to focus on closets that compromise good quality solutions in the space of searching. As each iteration passes, TSO updates the candidate position solutions near individual points to the entire population in such a way that the TSO has a good capability of exploitation. Thus, its drawback is the absence of efficient global search, alongside rejecting an exploration capability.

Aiming to enhance the algorithm's establishment and exploration capacity, the introduced ATSO carries out two major phases in every iteration. Initially, the candidate solution is selected incidentally in place of a better solution, and the location of the applicant solutions is updated based on arbitrary tunicate's location. The optimizer employs an arbitrary operator to analyze diverse areas and search space for efficient exploration. Hence, in ATSO, two different incident numbers are calculated in a tunicate updating eqn. to generate solutions in different search space areas. An ATSO exploration phase is logically expressed in (17).

$$\vec{T}_p(\vec{x} + 1) = \vec{T}_p(r) - rand_1 \times |\vec{T}_p(r) - 2 \times rand_2 \times \vec{T}_p(\vec{x})| \quad (17)$$

Where, $\vec{T}_p(r)$ arbitrarily chosen tunicate that forms a new population. This process encourages exploration, as well as permits the TSO to perform many robust global searches using the entire space of search. In the last phase, the tunicate updates its positions according to the best tunicate position. Moreover, in the ATSO, the lowest tunicate using the greatest aiming function value is changed using an incidentally produced tunicate at every iteration. The exploration and exploitation of ATSO in search space are controlled by the inertia constant instead of using the mathematical equation. The ATSO algorithm eminently enhances the computational efficiency of the phase optimization algorithm.

Eventually, the optimal phase factors are acquired by an optimization algorithm, and further, this algorithm provides the maximal optimal phase factors by the utilization of ATSO. However, the optimization algorithm consumes a minimum duration than the other methods and hence, the computational time is decreased by utilizing the ATSO algorithm. Further, the evaluation and implementation of this proposal is provided in the following sections.

4. RESULTS AND DISCUSSION

In this research, an ATSO-PTS method is proposed to reduce PAPR values in a waveform of OFDM signal. The proposed method is implemented on the MATLAB software, on a system operated with an i5 processor and 6 GB RAM. The proposed ATSO-PTS method is utilized to perform an effective denoising and channel estimation for MIMO-OFDM. The performance of the proposed ATSO-PTS method is compared with the existing methods. The existing methods namely, OFDM, conventional-PTS (C-PTS), conventional-selective mapping (C-SLM), and PSO are utilized for the comparison. Furthermore, the performance metrics used in this research to evaluate the performance of the proposed ATSO-PTS are, BER, PAPR, complementary cumulative distribution function (CCDF), and symbol error rate (SER). The parameter settings of this model are depicted in Table 1.

Table 1. Parameter settings of the ATSO-PTS method

Parameter	Value
Number of iterations	100
Population size	30
User carriers	52, 104, 156, 208, 260
Pilot carriers	12, 24, 48, 60, 72
FFT size	64, 128, 256, 512, 1024
Antenna	2×2 , 2×4 , 4×2 , 4×4
Number subcarriers	128, 256
Cyclic prefix or guard time	0 to 2e-6s
Modulation	QPSK
Modulation range	16
MIMO-OFDM symbols	16
Oversampling factor	1e6 HZ
Channel type	AWGN channel

Table 2 represents the $E_b/N_o(dB)$ comparison for the proposed method against the existing methods when the value is taken as 30. The existing methods of OFDM, BPSK, QAM-8 and QAM-16 are measured and compared with the proposed method. Figure 4 shows the graphical representation of BER, with respect to $E_b/N_o(dB)$.

In Table 2, the QPSK modulation is compared with previous modulations using BER. The maximum BER with respect to $E_b/N_o(dB)$ of QPSK modulation is 30 dB. The maximum BER with respect to BER of the QPSK of value is 30 dB. The PAPR reduction is achieved without downgrading the performance of BER, in contrast to the existing methods. Here, the AWGN noise channel is considered

where the $E_b/N_o(dB)$ ranges between -30 to 30. The BER values and error number are minimized because of its enhanced noise immunity and low error probability.

Table 2. Performance analysis of BER in $E_b/N_o(dB) = 30$

Methods	BER
OFDM	$10^{-3.4}$
BPSK	$10^{-3.8}$
QAM-8	$10^{-3.4}$
QAM-16	$10^{-1.5}$
QPSK	$10^{-7.4}$

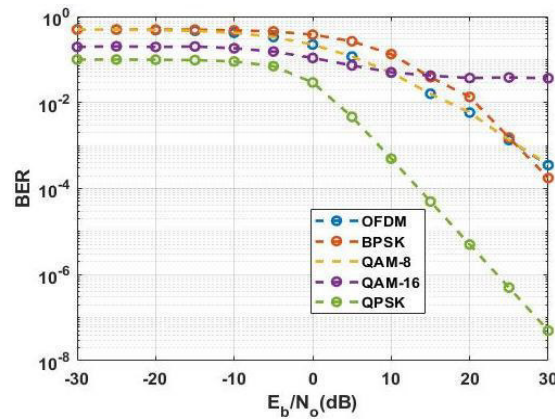


Figure 4. Graphical representation of BER of the QPSK modulation in MIMO-OFDM

Table 3 represents the $E_b/N_o(dB)$ comparison of the proposed method with that of the competitor approaches when the value is 30. The existing methods, which are OFDM, C-PTS, C-SLM, and PSO are measured and compared with the proposed method. Figure 5 represents the graphical representation of BER as to $E_b/N_o(dB)$.

Table 3. Performance comparison of BER when $E_b/N_o(dB) = 30$

Methods	BER
OFDM	$10^{-4.8}$
C-PTS	10^{-5}
C-SLM	$10^{-5.8}$
PSO	$10^{-6.5}$
Proposed ATSO	$10^{-8.2}$

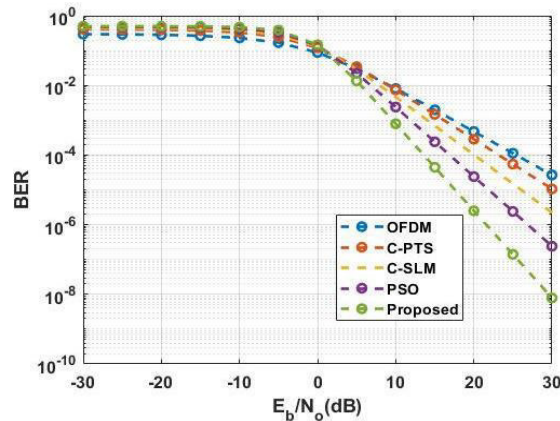


Figure 5. Graphical representation of BER of proposed ATSO-PTS method in MIMO-OFDM with respect to $E_b/N_o(dB)$

In Table 3, the proposed ATSO-PTS is compared with the existing modulations in terms of BER. The BER with $E_b/N_o(\text{dB})$ of the ATSO-PTS value is set to 30 dB. Here, without downgrading the performance of BER, the PAPR reduction is achieved contrasting to other methods. Here, the AWGN noise channel is considered where the $E_b/N_o(\text{dB})$ is in the range of -30 to 30. The values of the BER are reduced because of its enhanced noise immunity and low error probability.

Table 4 represents the PAPR (dB) comparison of the proposed method QPSK with competitor approaches when $\text{CCDF} = 10^{-2.5}$. The QPSK is compared with existing modulations, OFDM, BPSK, QAM-8, and QAM-16. Figure 6 shows the graphical illustration of CCDF with respect to PAPR (dB).

Table 4. Performance comparison of QPSK using PAPR (dB) when $\text{CCDF}=10^{-2.5}$

Methods	PAPR (dB)
OFDM	18.3
BPSK	7.5
QAM-8	9.1
QAM-16	7
QPSK	2.5

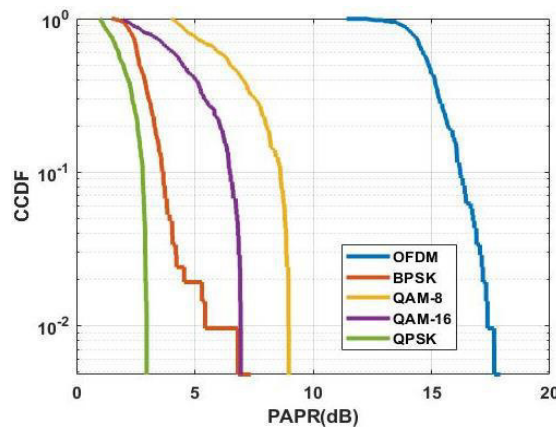


Figure 6. Graphical representation of QPSK modulation and various existing methods based on CCDF

In Table 4, the QPSK is compared with existing modulations in terms of CCDF with PAPR (dB). A maximum CCDF using PAPR of QPSK is 2.5 dB. The OFDM achieves 18.3 dB, BPSK achieves 7.5 dB, QAM-8 achieves 9.1 dB, and QAM-16 achieves 7 dB. The suggested ATSO-PTS method achieves the PAPR values multiple times better than the original OFDM. The PAPR range lies between 0 and 20.

Table 5 represents the PAPR (dB) comparison of the proposed method ATSO with existing methods when $\text{CCDF} = 10^{-2.5}$. The proposed ATSO-PTS is compared with previous modulations, OFDM, C-PTS, C-SLM, and PSO. Figure 7 shows the graphical illustration of CCDF in terms of PAPR (dB).

Table 5. Performance analysis of ATSO using PAPR (dB) in $\text{CCDF} = 10^{-2.5}$

Methods	PAPR (dB)
OFDM	18.5
C-PTS	9.8
C-SLM	8.5
PSO	6.5
Proposed ATSO	2.9

In Table 5, the suggested ATSO-PTS is compared with previous modulations in terms of PAPR (dB). A CCDF in terms of PAPR of ATSO-PTS is 2.9 dB. The OFDM achieves 18.5 dB, C-PTS achieves 9.8 dB, C-SLM achieves 8.5 dB, and PSO achieves 6.5 dB. The proposed ATSO-PTS method achieves the PAPR values multiple times better than the original OFDM. The PAPR range lies between 0 and 20.

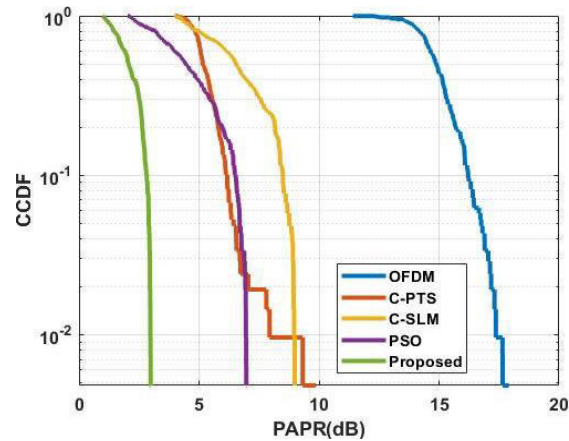


Figure 7. Graphical representation of proposed ATSO-PTS and various existing methods

Table 6 represents the E_b/N_o (dB) comparison of the proposed method with competitor approaches at a value of 30. The QPSK modulation is compared with existing modulations named OFDM, BPSK, QAM-8, and QAM-16. Figure 8 shows the graph of SER with respect to E_b/N_o (dB).

In Table 6 the QPSK modulation is compared with previous modulations in terms of SER. The maximum SER with respect to E_b/N_o (dB) of QPSK modulation is 30 dB. The maximum BER in terms of BER of the QPSK of value is 30 dB. Without downgrading the performance of BER, the PAPR reduction is achieved compared to other methods. Here, the AWGN noise channel is considered, and the E_b/N_o (dB) in the range between -30 to 30. The SER values are reduced because of its enhanced noise immunity and low error probability.

Table 6. Performance comparison of SER when E_b/N_o (dB)=30

Methods	SER
OFDM	$10^{-5.7}$
BPSK	$10^{-6.7}$
QAM-18	$10^{-3.7}$
QAM-16	$10^{-3.8}$
QPSK	$10^{-8.5}$

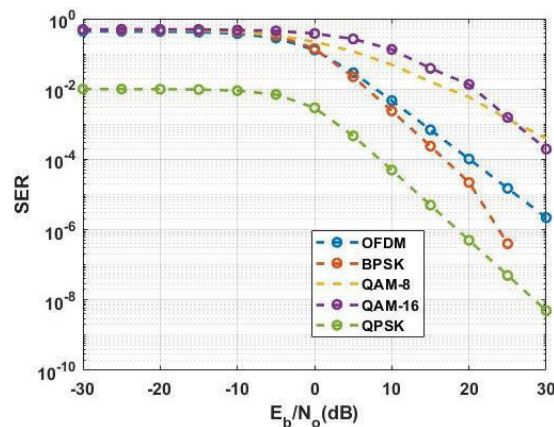


Figure 8. Graphical representation of SER of the QPSK modulation in MIMO-OFDM

Table 7 represents the E_b/N_o (dB) comparison of the proposed method with competitor approaches at a value is 30. The proposed ATSO-PTS is compared with the existing modulations like OFDM, C-PTS, C-SLM, PSO. Figure 9 shows the graphical representation of SER with respect to E_b/N_o (dB).

In Table 7, the proposed ATSO-PTS is compared with the existing modulations as to SER. The E_b/N_o (dB) of the proposed ATSO-PTS achieved the maximum SER value is 30 dB. Without downgrading

the performance of SER, the PAPR reduction is achieved compared to other methods. The values of the SER are reduced because of its enhanced noise immunity and low error probability.

Table 7. Performance analysis of SER in E_b/N_o (dB)=30

Methods	SER
OFDM	$10^{-4.5}$
C-PTS	10^{-5}
C-SLM	$10^{-5.8}$
PSO	$10^{-6.8}$
Proposed ATSO-PTS	$10^{-8.2}$

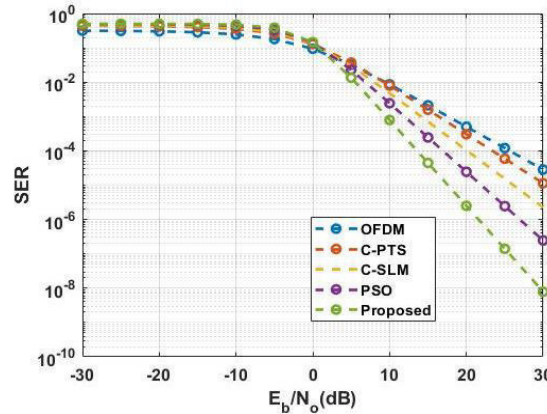


Figure 9. Graphical representation of SER of proposed ATSO-PTS method in MIMO-OFDM

4.1. Comparative analysis

This section demonstrates the comparative analysis of ATSO-PTS with the BER and PAPR as shown in Table 8. Table 9 represents the comparative analysis of ATSO-PTS with the 10 dB of BER and SNR. Existing research such as [16]–[18] are used for evaluating the ability of the proposed method. The proposed ATSO-PTS achieved a 2.9 PAPR compared to the TSHO-PTS method.

Table 8. Comparative analysis of proposed method with existing methods with 30 PAPR

Author	Method	PAPR (dB)
Sarkar <i>et al.</i> [16]	TSHO-PTS	5
Sidiq <i>et al.</i> [17]	ABC- SLM-PTS	5.6
Kumar <i>et al.</i> [18]	PSO-GWO	10.1
Proposed ATSO-PTS	ATSO-PTS	2.9

Table 9. Comparative analysis of the proposed method with existing methods using 30 dB with BER and SER

Author	Method	BER	SNR
Sarkar <i>et al.</i> [16]	TSHO-PTS	0.01	0.01
Sidiq <i>et al.</i> [17]	SLM-PTS	0.07	0.12
Kumar <i>et al.</i> [18]	PS-GW- PTS	0.03	0.02
Proposed ATSO-PTS	ATSO-PTS	0.01	0.025

4.2. Discussion

This section discusses the obtained results of the proposed method compared with the existing methods. The OFDM approach's values of the PAPR are reduced by the outcomes of existing methods as well as ATSO performance in PTS. In this proposed method, the number of parameters is carried out to reduce the PAPR rate in OFDM signals. The various simulations are carried out to identify a PAPR improvement for the determination and comparison of the sub-optimal PTS. A single OFDM is produced arbitrarily to minimize the PAPR as well and corresponding parameters are performed for the process of simulation. The obtained classification results of this research are represented in Tables 1 to 6. Figures 4 to 9 shows the graphical representation of the reduction of BER, PAPR, and SER. Table 8 shows the comparative analysis of the proposed method with existing methods with 30 PAPR. In Table 8 the existing methods such as TSHO-PTS [16] have achieved a PAPR (dB) rate of 5. The ABC-SLM-PTS [17] have achieved a PAPR rate of 5.6, PSO-GWO [18] achieved the 10.1 PAPR (dB). The proposed ATSO-PTS method has achieved a better result with PAPR value is 2.9 respectively. Table 9 shows the BER and SNR reduction of the proposed method with existing methods. In Table 9, the existing method of TSHO-PTS [16] has achieved the 0.01

BER and SNR rate for 30 dB PAPR. The ABC-SLM-PTS [17] have achieved the BER rate 0.07 and SNR of 0.12. The PSO-GWO [18] achieved a BER of 0.03 and SNR of 0.02. The proposed ATSO-PTS method has achieved better results on BER is 0.01 and 0.025 respectively. The proposed method achieves a fast convergence speed compared with the other methods.

5. CONCLUSION

MIMO and OFDM are majorly utilized in wireless systems and wired high-data rate communications. In this research, the ATSO-PTS algorithm is proposed for the PAPR reduction in the MIMO-OFDM signal. The phase optimization is taken out in the OFDM signal with PTS and the proposed method is tested with FFT in OFDM signal optimization. The proposed method achieved better PAPR reduction when compared to the existing research methods by utilizing the optimization ATSO technique. In the MIMO-OFDM signal, the ATSO optimization algorithm is applied to reduce the PAPR as well as reduce the computational complexity of the phase optimization. The ATSO-PTS achieved less PAPR, BER, and SNR compared to other methods. The proposed method has 10-2 CCDF in 2.9 PAPR as well as existing TSHO-PTS method obtained the 5.0 PAPR to achieve 10-2 CCDF. The future work of the proposed method involves combining multiple PAPR reduction techniques into a hybrid scheme which can potentially lead to better performance.




REFERENCES

- [1] D. V. Linh and V. V. Yem, "Key generation technique based on channel characteristics for MIMO-OFDM wireless communication systems," *IEEE Access*, vol. 11, pp. 7309–7319, 2023, doi: 10.1109/ACCESS.2023.3238573.
- [2] Z. Gao *et al.*, "Data-driven deep learning based hybrid beamforming for aerial massive MIMO-OFDM systems with implicit CSI," *IEEE Journal on Selected Areas in Communications*, vol. 40, no. 10, pp. 2894–2913, Oct. 2022, doi: 10.1109/JSAC.2022.3196064.
- [3] A. Arvola, S. K. Joshi, A. Tolli, and D. Gesbert, "PAPR reduction in MIMO-OFDM via power efficient transmit waveform shaping," *IEEE Access*, vol. 10, pp. 47906–47920, 2022, doi: 10.1109/ACCESS.2022.3172325.
- [4] S. N. Rani and G. Indumathi, "Chicken swarm optimization based optimal channel allocation in massive MIMO," *Wireless Personal Communications*, vol. 129, no. 3, pp. 2055–2077, Apr. 2023, doi: 10.1007/s11277-023-10225-6.
- [5] X.-F. Kang, Z.-H. Liu, and M. Yao, "Deep learning for joint pilot design and channel estimation in MIMO-OFDM systems," *Sensors*, vol. 22, no. 11, p. 4188, May 2022, doi: 10.3390/s22114188.
- [6] Z. Liu *et al.*, "Low-complexity PAPR reduction method for OFDM systems based on real-valued neural networks," *IEEE Wireless Communications Letters*, vol. 9, no. 11, pp. 1840–1844, Nov. 2020, doi: 10.1109/LWC.2020.3005656.
- [7] V. Padarti and V. Nandhanavanam, "An improved ASOICF algorithm for PAPR reduction in OFDM systems," *International Journal of Intelligent Engineering and Systems*, vol. 14, no. 2, pp. 353–360, Apr. 2021, doi: 10.22266/ijies2021.0430.32.
- [8] Y. Cao, T. Lv, and W. Ni, "Two-timescale optimization for intelligent reflecting surface-assisted MIMO transmission in fast-changing channels," *IEEE Transactions on Wireless Communications*, vol. 21, no. 12, pp. 10424–10437, Dec. 2022, doi: 10.1109/TWC.2022.3184000.
- [9] V. G. Tikka and R. Sivashanmugam, "Error correction using hybrid coding algorithm for BER reduction in MIMO-OFDM," *International Journal of Intelligent Engineering and Systems*, vol. 15, no. 6, pp. 618–626, Dec. 2022, doi: 10.22266/ijies2022.1231.55.
- [10] D. K. Onebunne, C. A. Nwabueze, B. O. Ekengwu, and P. C. Odukwue, "Improving bit error rate of MIMO-OFDM system using discrete wavelet transformation," *International Journal of Advanced Networking and Applications*, vol. 14, no. 2, pp. 5378–5384, 2022.
- [11] S. Jothi and A. Chandrasekar, "An efficient modified dragonfly optimization based MIMO-OFDM for enhancing qos in wireless multimedia communication," *Wireless Personal Communications*, vol. 122, no. 2, pp. 1043–1065, Jan. 2022, doi: 10.1007/s11277-021-08938-7.
- [12] C. Sun, J. Zhao, J. Wang, L. Xia, X. Gao, and Q. Wang, "Beam domain MIMO-OFDM optical wireless communications with PAPR reduction," *IEEE Photonics Journal*, vol. 15, no. 2, pp. 1–10, Apr. 2023, doi: 10.1109/JPHOT.2023.3246487.
- [13] E. F. Badran, M. Samara, and N. E. Ismail, "Carrier frequency offset estimation for MIMO single-carrier FDMA system in wireless communication," *Alexandria Engineering Journal*, vol. 61, no. 9, pp. 6907–6917, Sep. 2022, doi: 10.1016/j.aej.2021.12.036.
- [14] S. S. P. Kumar, C. A. Kumar, and R. J. Rose, "An efficient SLM technique based on chaotic biogeography-based optimization algorithm for PAPR reduction in GFDM waveform," *Automatika*, vol. 64, no. 1, pp. 93–103, Jan. 2023, doi: 10.1080/00051144.2022.2106532.
- [15] Z. Duan and F. Zhao, "Pilot allocation and data power optimization based on access point selection in cell-free massive MIMO," *Wireless Communications and Mobile Computing*, vol. 2022, pp. 1–10, Apr. 2022, doi: 10.1155/2022/4044783.
- [16] M. Sarkar, A. Kumar, and B. Maji, "PAPR reduction using twin symbol hybrid optimization-based PTS and multi-chaotic-DFT sequence-based encryption in CP-OFDM system," *Photonic Network Communications*, vol. 41, no. 2, pp. 148–162, Apr. 2021, doi: 10.1007/s11107-020-00923-7.
- [17] S. Sidiq, J. A. Sheikh, F. Mustafa, B. A. Malik, and I. B. Sofi, "PAPR minimization of FBMC/OQAM scheme by hybrid SLM and PTS using artificial: bee-colony phase—optimization," *Arabian Journal for Science and Engineering*, vol. 46, no. 10, pp. 9925–9934, Oct. 2021, doi: 10.1007/s13369-021-05625-4.
- [18] P. R. Kumar, P. V. Naganjaneyulu, and K. S. Prasad, "Hybrid PS-GW optimised PTS scheme for PAPR reduction in OFDM system," *IET Communications*, vol. 13, no. 18, pp. 2996–3002, Nov. 2019, doi: 10.1049/iet-com.2019.0261.
- [19] S. Prasad and R. Jayabalan, "PAPR reduction in OFDM using scaled particle swarm optimisation based partial transmit sequence technique," *The Journal of Engineering*, vol. 2019, no. 5, pp. 3460–3468, May 2019, doi: 10.1049/joe.2018.5340.
- [20] Ş. Şimşir and N. Taşpınar, "A novel discrete elephant herding optimization-based PTS scheme to reduce the PAPR of universal filtered multicarrier signal," *Engineering Science and Technology, an International Journal*, vol. 24, no. 6, pp. 1428–1441, Dec. 2021, doi: 10.1016/j.jestech.2021.03.001.




- [21] J. Bai and S. Yang, "In UOWC systems: a combined PAPR reduction method by PTS approach based on improved particle swarm optimization," *Optik*, vol. 232, p. 166581, Apr. 2021, doi: 10.1016/j.ijleo.2021.166581.
- [22] A. K. Abed, R. Mansoor, and A. K. Abed, "Particle swarm optimization-based dummy sub-carriers insertion for peak to average power ratio reduction in OFDM systems," *JCT Express*, vol. 8, no. 1, pp. 135–141, Mar. 2022, doi: 10.1016/j.ijcte.2021.07.005.
- [23] L. Li, L. Xue, X. Chen, and D. Yuan, "Partial transmit sequence based on discrete particle swarm optimization with threshold about PAPR reduction in FBMC/OQAM system," *IET Communications*, vol. 16, no. 2, pp. 142–150, Jan. 2022, doi: 10.1049/cmu2.12321.
- [24] Ş. Şimşir and N. Taşpınar, "An improved PTS scheme based on a novel discrete invasive weed optimization algorithm for PAPR reduction in the UPMC signal," *Neural Computing and Applications*, vol. 33, no. 23, pp. 16403–16424, Dec. 2021, doi: 10.1007/s00521-021-06237-7.
- [25] T. H. Ali and A. Hamza, "Low-complexity PAPR reduction method based on the TLBO algorithm for an OFDM signal," *Annals of Telecommunications*, vol. 76, no. 1–2, pp. 19–26, Feb. 2021, doi: 10.1007/s12243-020-00777-0.
- [26] I. Khan, M. Cheffena, and M. M. Hasan, "Data aided channel estimation for MIMO-OFDM wireless systems using reliable carriers," *IEEE Access*, vol. 11, pp. 47836–47847, 2023, doi: 10.1109/ACCESS.2023.3269659.
- [27] Y. Katsuki, G. T. F. de Abreu, K. Ishibashi, and N. Ishikawa, "Noncoherent massive MIMO with embedded one-way function physical layer security," *IEEE Transactions on Information Forensics and Security*, vol. 18, pp. 3158–3170, 2023, doi: 10.1109/TIFS.2023.3277255.
- [28] Y. Katsuki and N. Ishikawa, "Optimal but low-complexity optimization method for nonsquare differential massive MIMO," in *2021 IEEE 94th Vehicular Technology Conference (VTC2021-Fall)*, IEEE, Sep. 2021, pp. 1–5. doi: 10.1109/VTC2021-Fall52928.2021.9625337.
- [29] D. A. Disney and A. Merline, "An improved fuzzy logic-based small cell deployment in NOMA-HetNet: a novel sun flower-based tunicate swarm optimization-oriented multi objective concept," *Sādhanā*, vol. 48, no. 2, p. 67, Apr. 2023, doi: 10.1007/s12046-023-02123-1.
- [30] A. Arabali, M. Khajehzadeh, S. Keawsawasvong, A. H. Mohammed, and B. Khan, "An adaptive tunicate swarm algorithm for optimization of shallow foundation," *IEEE Access*, vol. 10, pp. 39204–39219, 2022, doi: 10.1109/ACCESS.2022.3164734.

BIOGRAPHIES OF AUTHORS






Abdul Lateef Haroon Phulara Shaik    received a B.E. in electronics and communication engineering RYMEC, Ballari, Karnataka, India. He holds an M.Tech. degree in VLSI design and embedded systems from K S School of Engineering and Management, Karnataka, India. Obtained a Ph.D. in electrical engineering sciences from Visvesvaraya Technological University Belagavi, Karnataka, India. Currently, he is an associate professor in the Department of Electronics and Communication Engineering at BITM Ballari, Karnataka, India. He has published many papers in International and National journals and international conference proceedings and has three patents. At present, he is guiding four students at Visvesvaraya Technological University, Belagavi, and Karnataka, India. He has around 12 years of teaching and research experience. He can be contacted at email: abdul.lh@bitm.edu.in.







Sowmya Madhavan    is presently working as an associate professor in the Department of Electronics and Communication Engineering, Nitte Meenakshi Institute of Technology, Bangalore. She completed her bachelor of engineering in telecommunication and master of technology in Digital Electronics from Visvesvaraya Technological University, Belgaum. She has also completed her Ph.D. from Visvesvaraya Technological University, Belgaum. She has published about 18 papers in various journals and conferences. She has also completed her PG level advanced certification program in VLSI chip design. Her research interests are physical design, RTL design and analog VLSI design. She can be contacted at email: sowmya.madhavan@nmit.ac.in.







Parameshchhari Bidare Divakarachari    currently working as a professor in the Department of Electronics and communication Engineering at Nitte Meenakshi Institute of Technology, Bengaluru, Karnataka, India affiliated to Visvesvaraya Technological University (VTU), Belagavi, Karnataka, India. He is also the visiting professor for University of Rome Tor Vergata, Italy. He is currently serving as the student activity committee chair, IEEE Bangalore Section. He is also listed in the World's Top 2% Scientist by Stanford University, USA for his research works. He has published over 150+ articles in SCI, Scopus and other indexed journals and in several international conferences. He is the associate editor for Expert Systems (Wiley), International Journal of Computational Intelligence Systems (Springer), Wireless Communication and Mobile Computing (Hindawi) and International Journal of Reconfigurable and Embedded Systems (IAES). He is also serving as editorial board member, academic editor and reviewer for several international journals indexed in SCI and Scopus. He has also served as the lead guest editor for Springer, Elsevier and IEEE Journals. Under his guidance, IEEE NMIT SB has received Rs. 20,000,000 funding from IEEE AESS Society. He can be contacted at email: paramesh@nmit.ac.in.







Rocío Pérez de Prado     received the M.S. degree in telecommunication engineering from University of Seville, Spain, in 2008, and the Ph.D. degree in Telecommunication Engineering with European Mention from University of Jaén, Spain, in 2011. At present, she is an associate professor at the Department of Telecommunication Engineering at the University of Jaén, Spain, with more than 15 years of research experience in the fields of artificial intelligence, machine learning, data science, cloud-IoT-edge, and telecommunications. In 2021, she was appointed as IEEE Senior Member. She has authored more than 60 research publications (35 in journals indexed in JCR). Since 2021 she works as an expert for the European Commission evaluating projects for H2020 and Marie Skłodowska-Curie Actions, and since 2020 she has been an external evaluator and member of project selection committees of the National Fund for Scientific and Technological Development, for the government of Peru. She is an associate editor of the official journal of the World Federation of Soft-Computing, Applied Soft Computing, Elsevier, editor in engineering applications of artificial intelligence, Elsevier, editor in Intelligent Automation and Soft-Computing, Tech Science Press, and Energies, MDPI, and has edited more than 10 special issues in diverse JCR-indexed journals and 2 international books. She has also served as reviewer for more than 40 JCR-indexed journals. Additionally, she has participated in scientific committees/organizing committees in more than 50 international conferences such as IEEE-FUZZ between the years 2019-2023, as well as technical committee chair and track chair and keynote speaker-guest of honour at diverse conferences. Likewise, she has participated in 10 research projects and diverse contracts with companies and projects to promote entrepreneurial culture in the field of telecommunications engineering. She has received 3 awards from Publons-Clarivate Analytics, as an outstanding reviewer. In 2010 she enjoyed a 5-month stay at the Technical University of Dortmund as a visiting researcher in the Department of Systems and Control Engineering, Germany. In the teaching field, she currently teaches in 2 degrees and 3 master's degrees in the field of telecommunication engineering, artificial intelligence and cloud computing in the University of Jaén. In addition, she has supervised more than 25 bachelor's degree, master's degree and final year theses. She is the author of more than 15 teaching publications in conferences, 3 books, and she has participated in 8 teaching innovation projects (leading 2 of them). She has received 2 awards from the University of Jaén, Spain, for Good Teaching Practices Perceived by Students. She can be contacted at email: rperez@ujaen.es.



Paramesh Siddappa Parameshwarappa     is currently working as an assistant professor in the Department of Computer Science and Engineering, School of Engineering, Central University of Karnataka, Kalburagi, India. He received M.E. in web technology from U.V.C.E, Bangalore University in 2014 and Ph.D. in computer science and engineering from Visveswaraya Technological University (VTU), Belagavi, India in 2022. His research areas include data mining, artificial intelligence, pattern recognition, machine learning, NLP, and soft computing techniques. He can be contacted at email: parameshsp@cuk.ac.in.



Kavitha Malali Vishveshwarappa Gowda     is currently working as an associate professor in Department of Electronics and Communication Engineering at Gopalan College of Engineering and Management, Karnataka, India which is affiliated to Visveswaraya Technological University (VTU). She received M.Tech. in VLSI design and embedded system from VTU in 2009. Her Ph.D. is in VLSI design from VTU and awarded in 2021. Her research area includes VLSI design and communication. She can be contacted at email: kavishanthagiri@gmail.com.



Design and Optimization of Sensor Electrode Geometry for Hormone Sensing by COMSOL Multiphysics Software

Javalkar Vinay Kumar^{1,2} · N. Shylashree¹ · Shrikrishna Hebbar¹ · Sriniketh S S¹ · Sohan A. Kotian¹ · Sreyas Mohanram¹ · V. Sridhar³

Accepted: 7 March 2024 / Published online: 21 March 2024

© The Author(s), under exclusive licence to Springer Science+Business Media, LLC, part of Springer Nature 2024

Abstract

In the present day, one of the major issues that is affecting human health and the quality of human life is stress. Sensors are developed with different shapes of electrodes. Electrodes with different shapes possess different surface areas for the accumulation of hormones, so they play a vital role in hormone analysis. This paper presents an analysis of sensing methods like electrochemical impedance spectroscopy (EIS) and cyclic voltammetry. It explores the optimization of the electrode shapes for use in hormone detection using these sensing methods. The designs and analyses are conducted using COMSOL MULTIPHYSICS software. COMSOL is used to design and analyze three electrode geometries: stepped cuboidal, cuboidal, and cylindrical for both the techniques. The electrode sizes used are in the standard range of 2–5 mm. The voltage equivalent of the sensed current is around 1 nV (with measured current ranging between around 10 and 520 pA). This is a very small value and is amplified to the order of about 0.1 V, which is more convenient to measure using a signal conditioning circuit. In cyclic voltammetry and thereby EIS, the range of current values shows a 26.61% and 8.39% improvement in cylindrical electrodes compared to stepped cuboidal and cuboidal electrodes, respectively. This can be justified by its increased surface area for hormone accumulation for comparable volumes of electrodes. These improvements can be applied in applications like cortisol hormone detection.

Keywords Cyclic voltammetry · Electrochemical impedance spectroscopy · Electrode · COMSOL Multiphysics · Hormone · Cortisol

1 Introduction

Biosensors are used in various domains in the fields of medicine and research. In today's fast-paced world, where everyone is busy with their respective schedules, people are

subjected to stress. This stress affects the levels of various hormones in the body. Hormone levels are critical in maintaining optimal health, and the monitoring of these levels can be helpful in the early detection of health hazards.

A certain level of stress in today's society is inevitable and can be tolerated by the body. It is when it goes beyond the threshold consistently that people begin to experience mental and physical side effects. Understandably, it can be quite challenging for a person to determine when he or she has breached this threshold. Therefore, it becomes necessary to quantify this in some manner. The usual approach is to go for a medical test and prescribe a course of action based on the results of that test. While it is common for people to take medical tests for blood pressure, sugar, and other commonly associated lifestyle diseases, taking a cortisol test, for example, to possibly determine the stress a person is under, is quite rare.

This is neither advertised aggressively nor do people find the inclination, time, or financial resources to get themselves regularly tested. While it has become clear

✉ Javalkar Vinay Kumar
javalkarvinay4u@gmail.com; vinaykumar@bitm.edu.in

✉ N. Shylashree
shylashreen@rvce.edu.in

¹ Department of Electronics and Communication Engineering, RV College of Engineering, Bengaluru 560059, Affiliated to Visvesvaraya Technological University, Belagavi, Karnataka, India

² Department of Electronics and Communication Engineering, Ballari Institute of Technology and Management, Ballari 583101, Affiliated to Visvesvaraya Technological University, Belagavi, Karnataka, India

³ Department of Electronics and Communication Engineering, Nitte Meenakshi Institute of Technology, Bengaluru 560064, Karnataka, India

that stress should not be taken for granted when it reaches high levels on a consistent basis, why is there a lack of testing or awareness among people to get them tested? One of the possibilities is the fact that these tests have so far remained mostly invasive, which people are not very comfortable with. High costs and a lack of general awareness are pertinent factors as well. Through the medium of this paper, various non-invasive hormone sensor designs have been explored to detect their concentration primarily in sweat and saliva. This involves designing the physical aspects of the sensor, choosing appropriate materials, and optimization to achieve a desired level of response.

The adrenal glands are responsible for secreting cortisol, majorly in response to stressful situations. This hormone is also the cause of other diseases, namely, Addison's disease and Cushing's syndrome, caused by its deficiency and overproduction, respectively. All existing commercial methods of cortisol detection are time-consuming and mostly invasive to the human body. There have been efforts to make commercially viable, non-invasive biosensors that make it possible to sense in real time. This paper is an effort in the same direction. Existing technologies and progress in improvement in cortisol detection speed and accuracy have been reviewed [1].

Various methods of real-time hormone sensing have been discussed and also the advantages and drawbacks of each developed sensor. Point of care cortisol hormone sensing technologies have also been carried out, encompassing all sources of the hormone like blood, sweat, urine, saliva, and interstitial fluid [2]. Further, an electrical impedance spectroscopy (EIS) technique with four channels for sensing cortisol for monitoring through human sweat with a wearable device has been developed that uses gold electrodes [3].

Demonstration of sensing of hormones from various types of biofluids has been carried out [4]. The types include serum, sweat, blood, and saliva. The sensing technique used is electrochemical impedance spectroscopy (EIS). This method was chosen due to its wide scale application in various biofluids. Stress is a common consideration in several sporting events too, and to facilitate convenient detection even in these cases, a wearable sensor would be invaluable. A sensor design having a mechanism for control of fluids having both vertical and lateral flow helps in detecting the current which results from a reaction between the hormone conjugate (for example, glucose oxidase (GOD) for cortisol) and hormone concentration. A new sensor, featuring a mountable-on-skin, molecularly selective organic electrochemical transistors (MS-OECT), patch-type cortisol biosensor has been conceived, by introducing a multifunctional layered device, adaptable to other categories of wearable sensors based on sweat [5].

A sensor that uses electrochemical detection based on sweat to estimate biomarker level quantity cortisol has been proposed, to trace the endocrine-inflammatory relationship [6]. Optimal electrode design is obtained by simulations using COMSOL Multiphysics. Various methods used for voltammetry have also been detailed, along with that of cyclic voltammetry [7]. Caffeine's electrochemical behavior at CPE was introspected using the method of cyclic voltammetry [8]. It exhibits the capability of AQMCPE (anthraquinone modified carbon paste electrode) for caffeine's electrochemical investigation and its estimation.

Electrodes have been developed using multilayer films containing 2-dimensional tin disulfide nanoflakes, bovine serum albumin (BSA), and cortisol antibody on glass electrodes and characterized using EIS and cyclic voltammetry [9]. Non-invasive electrochemical immunosensor designs have been developed for detection of salivary cortisol [10]. DPV (differential pulse voltammetry) and CV (cyclic voltammetry) studies were applied for electrode calibration using standardized solutions of cortisol. Modeling of a biosensor specific to thin film applications has also been done [11].

Thin film applications have particular significance in wearable biosensors, which is one of the topics pertinent to this work. Continuing on the theme of wearable biosensors, several discussions highlighting the various advantages and challenges associated with wearables have been carried out [12]. A highly improvised electrical double layer (EDL) biosensor has been proposed [13], using flexible sub-states which are nanoporous for wearable diagnostics [14]. Results obtained by using the COMSOL Multiphysics software for the analysis and simulation of cyclic voltammetry (CV) [15] at microelectrode arrays (MEA) have also been reported [16].

Knowledge of the standard range of cortisol values is essential before the analysis is begun. Normal values for a blood sample taken at 8 in the morning are 5 to 25 mcg/dL (micrograms/deciliter) [17].

2 Methodology

To detect cortisol levels, there are various sensing techniques available, such as amperometry, potentiometry, and impedimetry. The technique that has been chosen is electrochemical impedance spectroscopy (EIS). This offers the convenience of working with sweat as the base solution, which can also be extended to other analytes such as blood or saliva, should the need arise. This is an impedance-based electrochemical technique. An electrical double layer is formed whenever two conducting phases meet at an interface. These conducting surfaces are oppositely charged and generally formed by an ion

and its corresponding counter ion. There is a change in the capacitance of the electric double layer (EDL) whenever a small perturbation in voltage occurs at the electrode. When the required biomolecule (cortisol) binds with the target molecule, this change in voltage takes place, thereby causing a change in the capacitance. This results in a deviation in impedance value, the magnitude of which indicates the level of cortisol. The simplified figure of the EIS methodology is depicted in Fig. 1.

This sensor is to be modeled in the COMSOL Multiphysics software. This change in impedance can be electronically modeled as Randle's equivalent circuit. In Fig. 2a, which represents Randle's circuit, there are three components R_s , R_{ct} , and C_{dl} , where C_{dl} and R_{ct} mainly denote the capacitance of the double layer and the resistance to the exchange of charges, respectively, formed because of the double layer. R_s denotes the solution resistance due to bulk solution ions. The current produced in the reaction is exponentially related to the concentration of cortisol.

3 Electrochemical Impedance Spectroscopy

The fundamental requirement of any sensor is to measure some characteristic change or deviation as a result of external or internal factors. In electrical and electronic systems, this change is usually reflected by some variation of any one of voltage, current, or impedance. In electrochemical impedance spectroscopy, as the name suggests, the variation measured is the change in impedance. It has evolved into one of the more widely used techniques as it usually results in the sensor having very high sensitivity [18]. In the present case, any variation in the concentration of the solution under consideration will result in a change in impedance.

One of the simplest ways EIS is implemented in practical systems is by modeling an equivalent electrical circuit. The components used to model the circuit include resistors, capacitors, and inductors, which are some of the most commonly encountered electrical components. As can be observed, these are components to model the impedance of any circuit. As will be seen subsequently, only the resistance

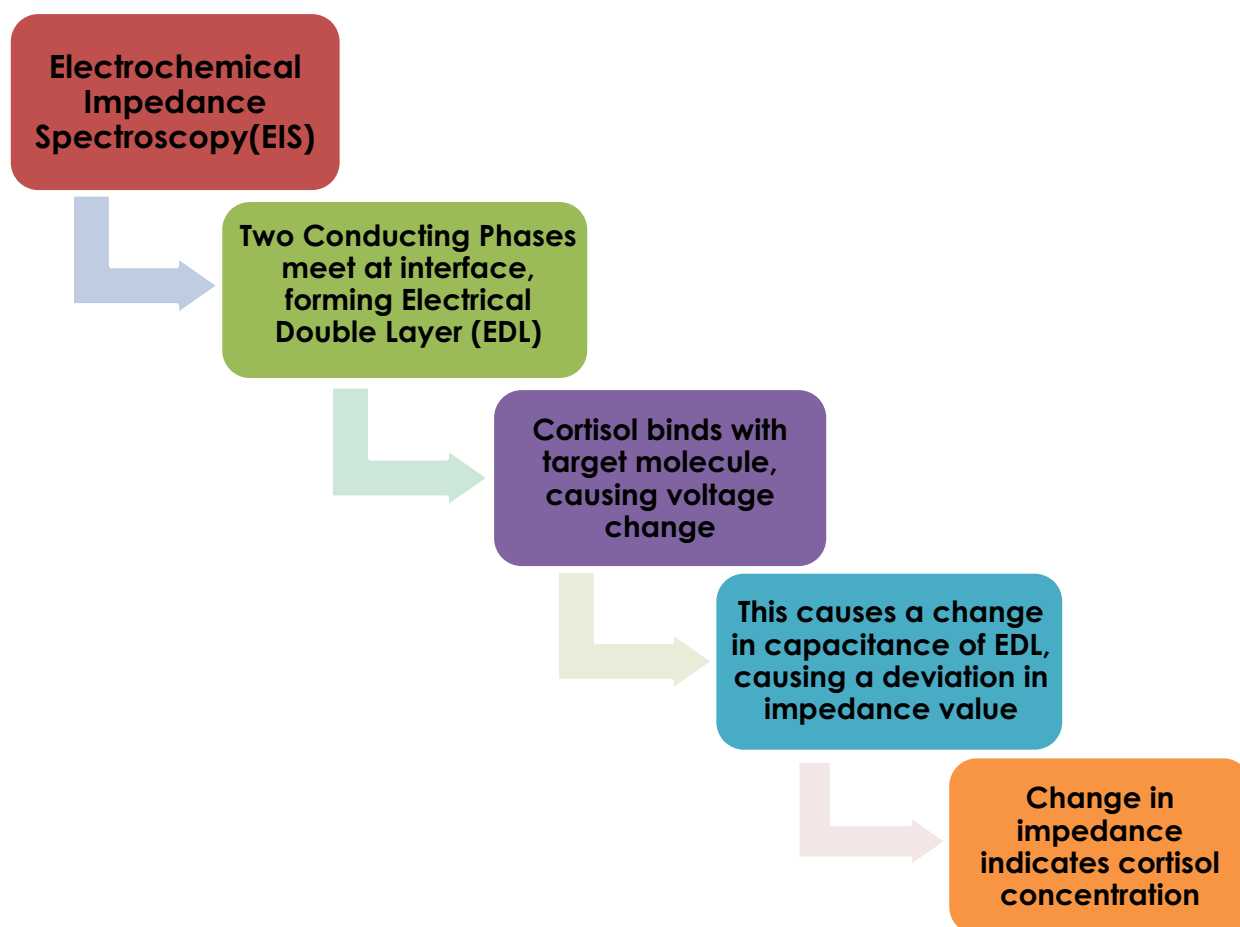
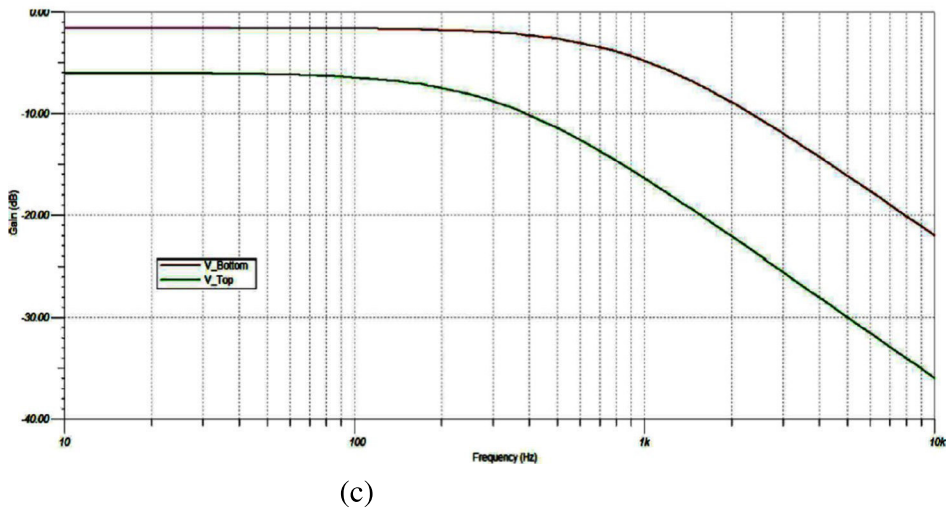
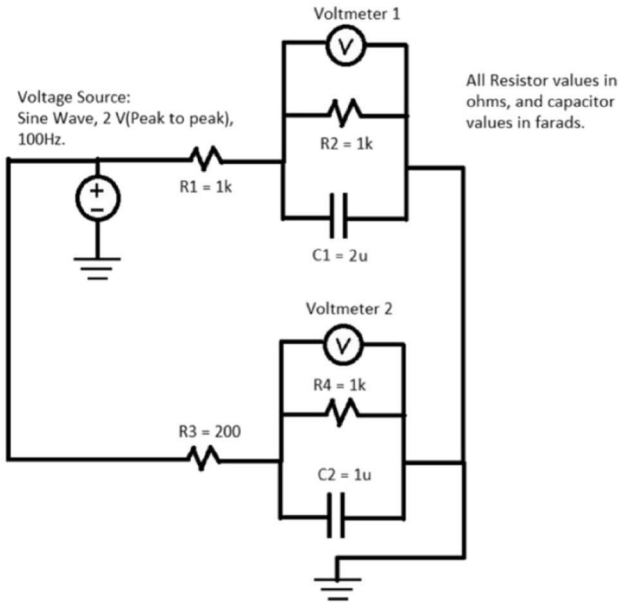
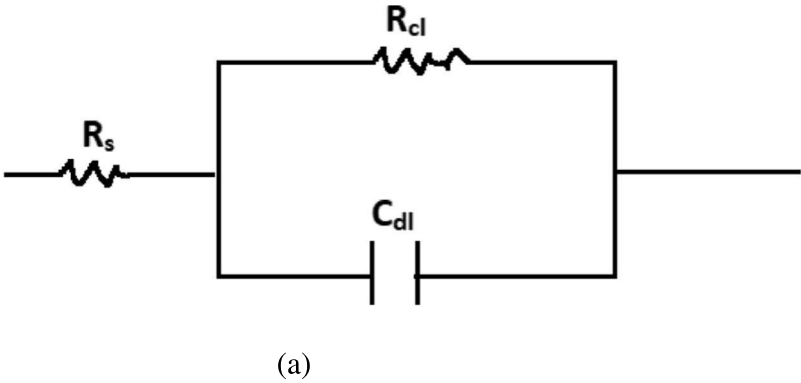


Fig. 1 Methodology of EIS

Fig. 2 **a** Randle’s equivalent circuit. **b** Randle’s equivalent circuit in TINA. **c** Bode plot in TINA of Randle’s equivalent circuit



and capacitance will be used in the electrical model to imitate physical conditions.

3.1 Randle's Equivalent Circuit

As discussed earlier, it is essential to imitate the physical system and conditions in the form of electronic components in order to develop a sensor. It should be ensured that critical physical characteristics are not lost in this conversion. One of the most commonly used equivalent models used in sensor designs employing electrochemical impedance spectroscopy is Randle's equivalent circuit. Before discussing Randle's equivalent circuit, it is essential to understand what electrical double layer capacitance is. This is a type of capacitance that exists at the interface of an electrode and an electrolyte whenever they come into contact with each other.

The electrolyte is composed of charged ions. Due to potential applied to electrodes and also the very fact that the electrolyte is in contact with the electrode, the ions in the electrolyte get adsorbed on the electrode. There exists a small insulating layer, in the order of a few angstroms, between the electrode and the adsorbed ions. The two charged layers separated by an insulating layer result in the double layer capacitance being formed.

Randle's circuit is modeled using three main components: double layer capacitance, solution resistance, and polarization resistance. The capacitance of the double layer is in shunt with the resistance of polarization, and this combination is in series with the solution resistance. When the sensor design is simulated in COMSOL Multiphysics with appropriate values, the Nyquist plot can be obtained. The depiction of Randle's circuit using TINA software can be seen in Fig. 2b. The capacitance value has changes from 2 to 1 μF as seen in the diagram which depicts the change in electrical double layer capacitance. Also, the resistance has changes from 1 k Ω to 200 Ω indicating a decrease in solution resistance. Similarly, the Bode plot, shown in Fig. 2c, also denotes the change in capacitance between the two parts of the circuit, and this can be seen by the difference produced between the two plots obtained. In the figure, V_Bottom represents the gain plot for circuit elements consisting of capacitance C2 and resistors R4 and R3 in the bottom part of Fig. 2c, and V_Top represents the gain plot for circuit elements consisting of capacitance C1 and resistors R2 and R1 in the top part of Fig. 2c.

3.2 Cyclic Voltammetry

Just like EIS involves measuring changes in impedance, in cyclic voltammetry, voltage is applied in a particular range, and the corresponding change in current is measured. Typically, a current–potential plot is studied. Based on the results obtained, both qualitative and quantitative analysis can be

done. Hence, in voltammetry, the electrode sizes can also be kept to a minimum, which makes it ideal for applications that require sensor design to be compact. This criterion is especially important in biosensors, where the sensor is typically intended to be worn. Again, sensors can be made very sensitive, thereby ensuring accurate measurements. As a general procedure, two electrodes, the working electrode and the auxiliary electrode, are used, between which current flows. Sometimes, a third electrode, called the reference electrode, is also used, which is applied for controlling the voltage level at the working electrode and hence preventing damage. Now, voltage is varied along a given range, and for the given solution, a change in current is noted.

In this paper, various methods to analyze the biosensor were discussed. Electrochemical impedance spectroscopy (EIS) is a highly sensitive process that is applied to carry out the electrical analysis of chemical systems. In EIS, the variation measured is the change in impedance. To model the physical system and conditions in the form of an electrical system, Randle's equivalent circuit is used. Randle's circuit has been simulated in TINA and the Nyquist plots and Bode plots have been shown in the previous section. The second method incorporated into the design is cyclic voltammetry. Just like EIS measurement in impedance, in cyclic voltammetry, voltage is applied in a particular range and the corresponding change in current is measured.

4 Design of Biosensor Structure and Incorporating EIS Model

Figure 3 represents the EIS techniques. Three types of plots have been obtained for each model:

- 1) Nyquist plot: plots real value of impedance vs imaginary impedance. The span, as shown, gives the value of $R_s + R_t$.
- 2) Bode plot: real value of impedance vs the frequency. The “pass-band” amplitude also shows the value of $R_s + R_t$.
- 3) Bode plot: imaginary value of impedance vs the frequency. Frequency at maximum value of impedance gives cutoff frequency to calculate C_{dl} . Here in the diagram, R_s is the resistance of the solution, and R_t is the resistance of charge transfer.

$$\text{Area of each electrode (cuboid)} = 2(lh + bh) + lb = 1.85 \text{ mm}^2$$

Important parameters related to electrode dimensions: the distance between the electrodes is also an important parameter. Usually, it amounts to 1–3 mm, whereas it should be greater than the thickness of the material by 0.3–2.0 mm.

Commonly available electrode sizes are 2.0 mm, 2.5 mm, 3.2 mm, 4.0 mm, and 5.0 mm [18].

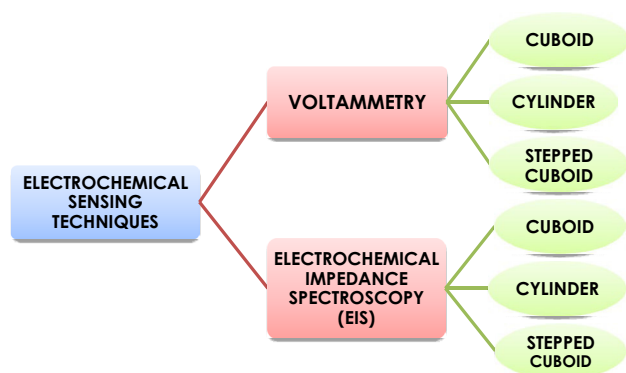


Fig. 3 Electrochemical techniques: EIS and CV

In a cuboidal electrode sensor as seen in Fig. 6a, it is noted that one face of the electrode is always in contact with the surface of the substrate and hence will not take part in the accumulation of biomolecules. The substrate material used is polyethylene terephthalate (PET) and the electrode material is gold. The spacing between the electrodes is about 0.5 mm owing to the electric field created and the conductivity of one electrode interfering with the other electrode. The dimensions of the electrode are length is 4 mm, width is 0.25 mm, and height is 0.1 mm.

$$\text{Area of each electrode (cylinder)} = 2\pi r(r + h) = 2.576 \text{ mm}^2 \quad (1)$$

$$\text{Area of each electrode (stepped cuboid)} = (b * l) + ((1.5) * l * h) + (3 * b * h) = 1.65 \text{ mm}^2 \quad (2)$$

4.1 Physics Interface

COMSOL Multiphysics gives a wide range of physics modules to select from. For the application of this paper, the electrochemistry module was selected, as it offers the physics interfaces needed to model the electrochemical impedance spectroscopy (EIS) as well as the cyclic voltammetry techniques. The electrochemistry module is an application-specific feature of the COMSOL Multiphysics environment with customizable physics interfaces. This is useful in designing a model of electrochemical cells. Various tools for constructing accurate models of the configuration of electrodes and electrolytes are available. The physics interfaces include details of the electrochemical reactions. It can be used to study the effects of applying different materials, geometric configurations, and operating conditions.

In particular, the electro analysis physics interface has been selected, as it contains the necessary equations to model current distribution, electrolyte behavior, and response to external voltage perturbations. It also has equations and boundary conditions for designing transport of

In the cylindrical electrode sensor as seen in Fig. 8a, it is noted that only a very small area is always in contact with the surface of the substrate and the rest of the bulk surface area takes part in the accumulation of biomolecules. The substrate material used is polyethylene terephthalate (PET) and the electrode material is gold. The spacing between the electrodes is about 0.6 mm owing to the electric field created and the conductivity of one electrode interfering with the other electrode. The dimensions of the electrode are length is 4 mm and radius is 0.1 mm. In stepped cuboidal electrode structure as seen in Fig. 4a, it is similar to cuboidal electrode in terms of surface area that takes part in the accumulation, but there is a slight decrease in the height of the electrodes in between due to the stepped structure.

The substrate material used is polyethylene terephthalate and the electrode material is gold. The spacing between the electrodes is about 0.6 mm owing to the electric field created and the conductivity of one electrode interfering with the other electrode. The dimensions of the electrode are length is 4 mm, width is 0.25 mm, and height is 0.1 mm for half of the effective length and 0.05 mm for the remaining half of the effective length. The dimensions chosen are in the millimeter range owing to the need for a small and optimal structure of biosensors applied in portable devices, which in turn are used for measurement of hormone parameters. Also, electro impedance spectroscopy and cyclic voltammetry are being applied to all these three biosensor structures and further analysis results are discussed further.

diluted particles in electrolytes using the diffusion-convection equation, solving for electro active particle concentrations. This physics interface contains customized functionality for designing cyclic voltammetry and EIS.

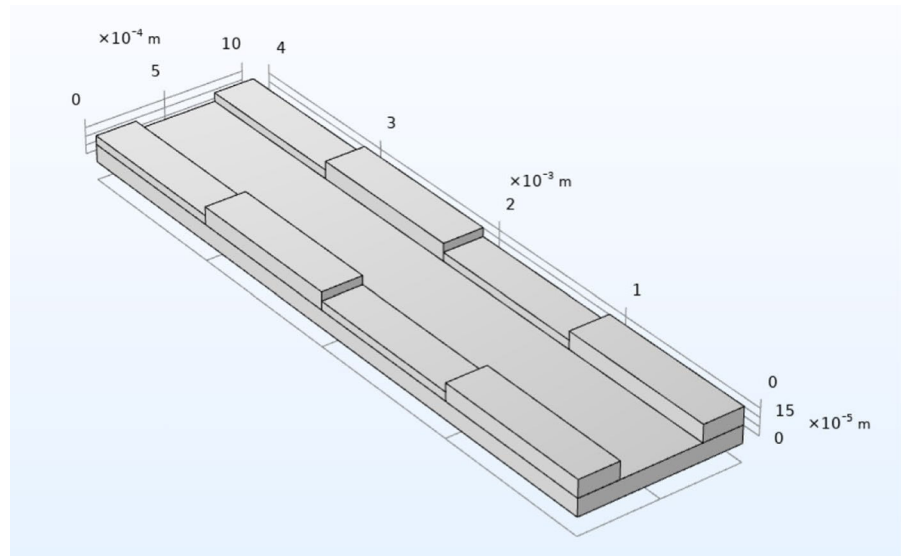
5 Implementation

As discussed in theory and design, the two methods chosen to implement the biosensor in this work are electrochemical impedance spectroscopy and cyclic voltammetry. The details involving their implementation are discussed in the remainder of this paper.

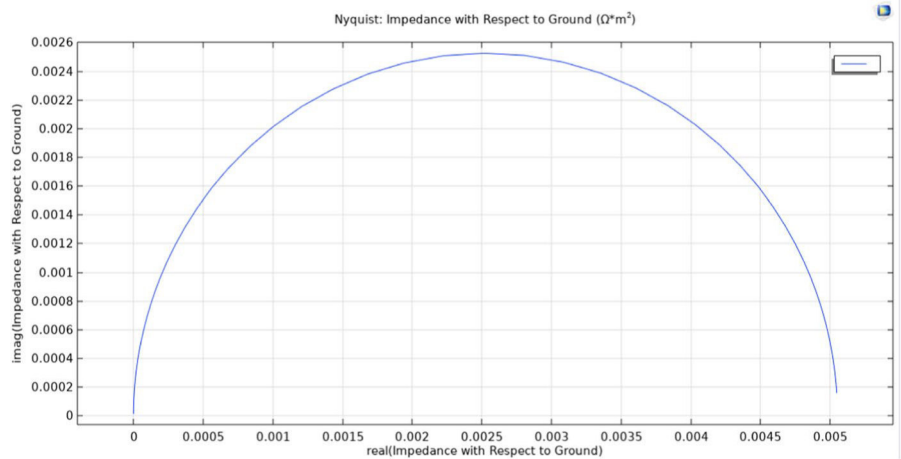
A. Electrochemical impedance spectroscopy

Within the electro analysis physics interface, the charge conservation model was set to “electro analysis (no potential gradients).” Linear discretization was selected for the concentration parameter and quadratic discretization for the electric potential parameter.

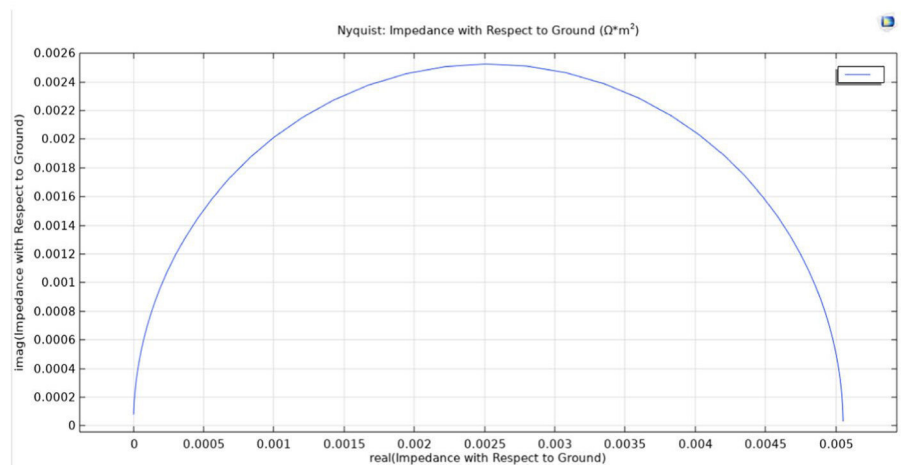
Fig. 4 **a** Stepped cuboidal electrode. **b** Stepped cuboidal electrode Nyquist plots $C_{dl}=100\ \mu\text{cm}^3$. **c** Stepped cuboidal electrode Nyquist plots $C_{dl}=20\ \mu\text{cm}^3$



(a)



(b)



(c)

I. Boundaries:

- i. Electrolyte—for the electrolyte boundary, the governing equations are as follows:

Time-dependent study

$$\nabla J_i + u \cdot \nabla c_i + \frac{\partial c_i}{\partial t} = R_i \quad (3)$$

$$J_i = -D_i \nabla c_i \quad (4)$$

Frequency domain perturbation

$$\nabla J_i + u \cdot \nabla c_i = R_i \quad (5)$$

$$J_i = -D_i \nabla c_i \quad (6)$$

- ii. No flux—this condition of absence of flux is governed by the following expression:

$$-n \cdot J_i = 0 \quad (7)$$

- iii. Insulation—insulation of the domains is defined by the following equations:

$$-n \cdot i_s = 0 \quad (8)$$

- iv. Initial values—this boundary is used to define initial values of concentration and electric potential in the electrolyte. Here, the initial values of concentration were selected as 1 M for both the oxidizing and reducing species and the electric potential of electrode was set to 0.
- v. Electrode surface—this boundary is added to define the surface of the working electrode on which the antibodies should be coated and the hormone reaction occurs. The expressions that define the electrode surface are given below.

$$n \cdot i_1 = i_{\text{total}} \quad (9)$$

$$i_{\text{total}} = \sum_m i_{\text{loc},m} + i_{\text{dl}} \quad (10)$$

$$-n \cdot J_i = R_{i,\text{tot}}, R_{i,\text{tot}} = \sum_m R_{i,m} + R_{\text{dl},i} \quad (11)$$

A harmonic perturbation of 10 mV was given to the working electrode under this boundary to generate the impedance response, as per the requirements of EIS. The electrode surface boundary has two attributes under it.

- (a) Electrode reaction—equations for this attribute are as follows:

The equilibrium potential has been defined using the Nernst equation as follows:

The electrode kinetics has been defined by the Butler-Volmer equation and the exchange current density with mass action law.

$$i_0 = i_{0,\text{ref}}(T) \prod_{i:v_i>0} \left(\frac{c_i}{c_{i,\text{ref}}} \right)^{\frac{a_{\text{e}} v_i}{n}} \prod_{i:v_i<0} \left(\frac{c_i}{c_{i,\text{ref}}} \right)^{\frac{-a_{\text{a}} v_i}{n}} \quad (12)$$

- (b) Double layer capacitance—double layer capacitance is the parameter that varies directly with the change in cortisol concentration. This attribute was added and the value was given as a parameter C_{dl} that can be varied. The expression governing the attribute is as follows:

$$i_{\text{dl}} = \left(\frac{\partial(\phi_{s,\text{ext}} - \phi_1)}{\partial t} \right) C_{\text{dl}} \quad (13)$$

$$R_{\text{dl},i} = \frac{-v_i i_{\text{dl}}}{nF} \quad (14)$$

II. Mesh:

COMSOL is finite element analysis software. This means that it divides the design into many small elements and performs individual analysis based on the equations described above. Meshing in COMSOL performs this function of element division. For the purpose of this paper, a default mesh is selected based on the requirements of the electroanalysis physics interface. The size selection for mesh is kept at normal.

III. Study:

The study was selected as AC impedance, time-dependent, for generating the characteristic plots of electrochemical impedance spectroscopy. This has two steps: time-dependent study and frequency-domain perturbations. The former uses time values from 0 to 1 in steps of 0.1. The latter utilizes a frequency range of 1 Hz to 10 kHz on a logarithmic scale, with a step size of 0.05.

B. Cyclic voltammetry

The procedure for modeling cyclic voltammetry through COMSOL is similar to the procedure for modeling EIS. The model and physics interfaces selected are electrochemistry and electro analysis, respectively. The charge conservation model and discretization modes were the same.

I. Boundaries:

The parameters and equations for the boundaries and electrolyte, no flux, and insulation are the same

- i. Electrode surface—the governing equations remain the same, but the harmonic perturbation, which is not necessary for cyclic voltammetry, is set to 0. Linear sweep of voltage is also defined under this boundary. Voltage is varied from -0.4 V to $+0.4$ V to test the current response of the electrodes and the number of cycles is set to 1.
- ii. Concentration—the concentration of the reactant is defined on the counter electrode. The concentration value is set to a parametric variable c bulk, which was varied to perform a parametric sweep to get the voltammogram plots. The governing equations for this boundary are as follows:

$$c_i = c_{0,i} \quad (15)$$

II. Mesh:

The mesh selected for the finite element analysis of cyclic voltammetry is defined according to the needs of the physics interface, electro analysis, and the size is set to normal.

III. Study:

The study for performing cyclic voltammetry is defined within the software with the same name. An additional parametric sweep was defined with the parameter c bulk from the value of 2.75 to $82.75 \mu\text{mol/m}^3$ in steps of $10 \mu\text{mol/m}^3$. This corresponds to the optimal levels of cortisol hormone in the sweat of humans, i.e., 1 ng/mL to 30 ng/mL.

Reason for using polyethylene terephthalate as substrate is that they are inexpensive and display appreciable mechanical flexibility and robustness under certain bending conditions with an incredible chemical stability when

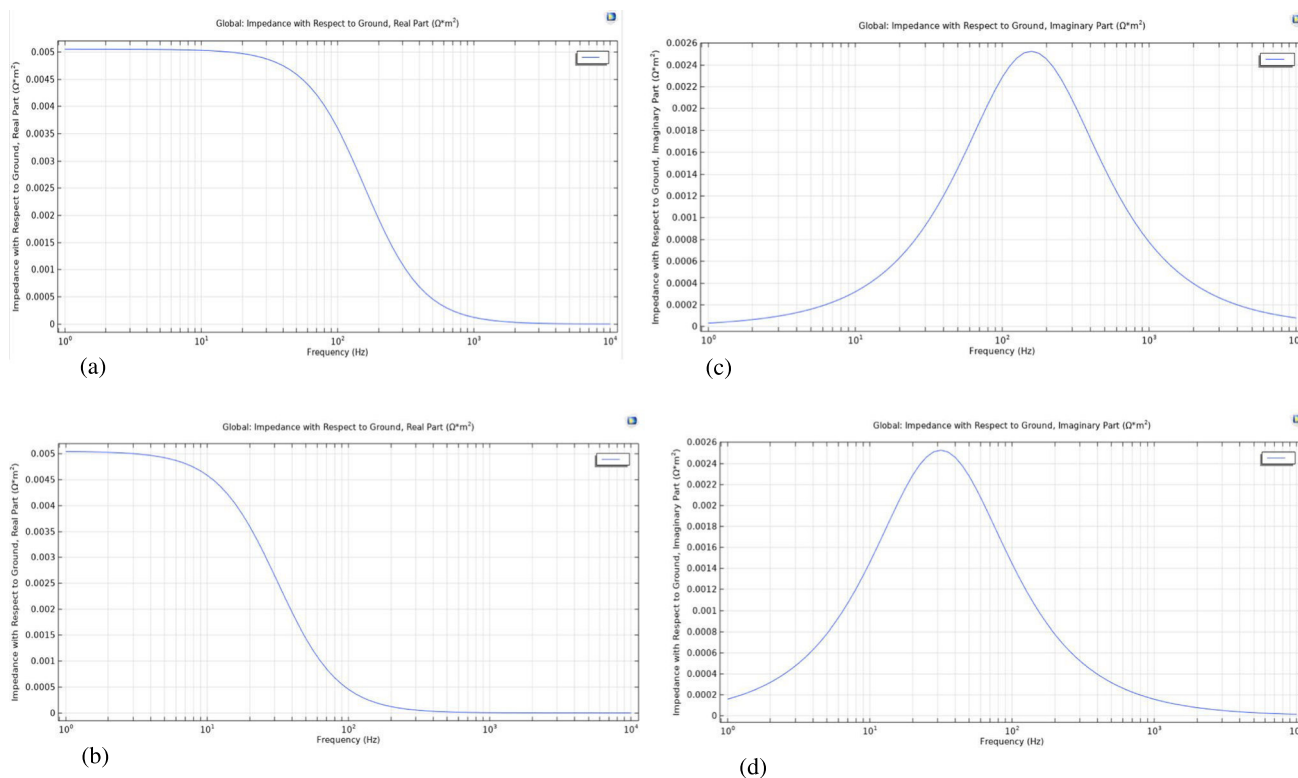


Fig. 5 **a** Stepped cuboidal electrode Bode—real impedance versus frequency plots for $C_{dl} = 20 \mu\text{cm}^3$. **b** Stepped cuboidal electrode Bode—real impedance versus frequency plots for $C_{dl} = 100 \mu\text{cm}^3$. **c**

Stepped cuboidal electrode Bode—imaginary impedance versus frequency plots for $C_{dl} = 20 \mu\text{cm}^3$. **d** Stepped cuboidal electrode Bode—imaginary impedance versus frequency plots for $C_{dl} = 100 \mu\text{cm}^3$

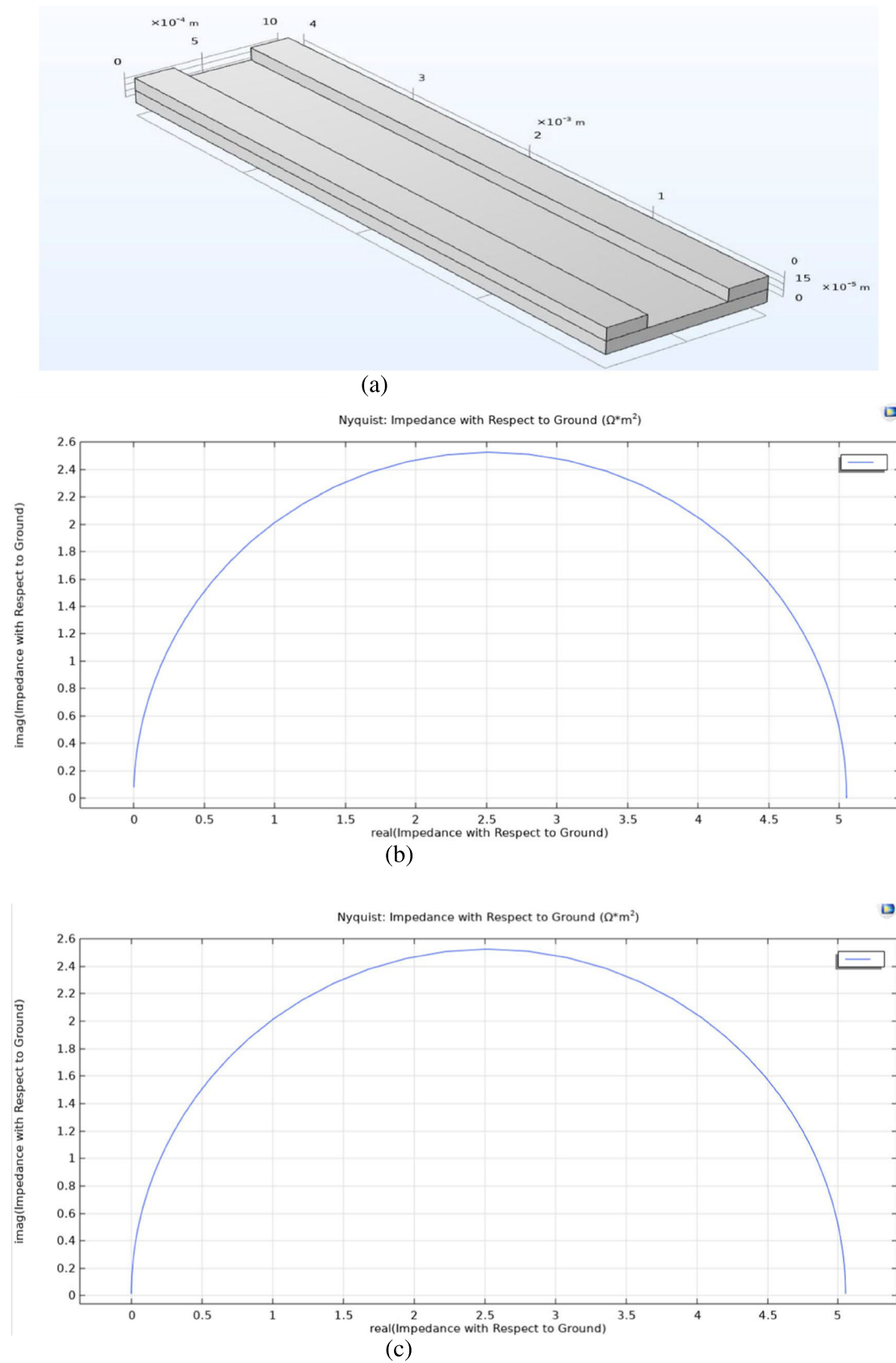


Fig. 6 **a** Cuboidal electrode. **b** Cuboidal electrode Nyquist plots for $C_{dl} = 20 \mu\text{cm}^3$. **c** Cuboidal electrode Nyquist plots for $C_{dl} = 100 \mu\text{cm}^3$.

exposed to high temperatures. It also does not react with water or food particles [19].

The reason for using gold as an electrode material: known for its biocompatibility, high conductivity, and high corrosion resistance [20, 21]. There are various techniques of hormone detection, as discussed review work by Cifrić et al. [22], but this paper concentrates on EIS (electrochemical impedance spectroscopy) and cyclic voltammetry.

5.1 Plots Obtained from Electrochemical Impedance Spectroscopy (EIS)

As described in the earlier sections, EIS analysis was done on the electrode structures. The standard plots that are obtained are as follows:

- 1) Nyquist plot—plot between real and imaginary parts of impedance.
- 2) Bode plot 1—plot between frequency and real part of impedance.
- 3) Bode plot 2—plot between frequency and imaginary part of impedance.

By varying the capacitance in EIS techniques, the double layer capacitance also changes. This affects the total impedance of the assumed Randle's circuit. For this analysis, the values of the double layer capacitance were manually varied and the response in the plots was observed. The set values for the capacitance were $20 \mu\text{F}/\text{cm}^2$ and $100 \mu\text{F}/\text{cm}^2$. The calculations for this analysis were done as shown in the below example considering cortisol hormone (stress hormone) as an example for C_{dl} values and its behavior.

Example: from the plot $R_f=0.005$. From the plot

$$f_c = 160 \mu\text{F}/\text{cm}^2 \quad (16)$$

$$w_c = 2\pi f_c \quad (17)$$

Therefore,

$$C_{dl} = \frac{1}{(R_f w_c)} \quad (18)$$

$$C_{dl} = 100 \mu\text{F}/\text{cm}^2 \quad (19)$$

The plots obtained from EIS are shown in the following sections.

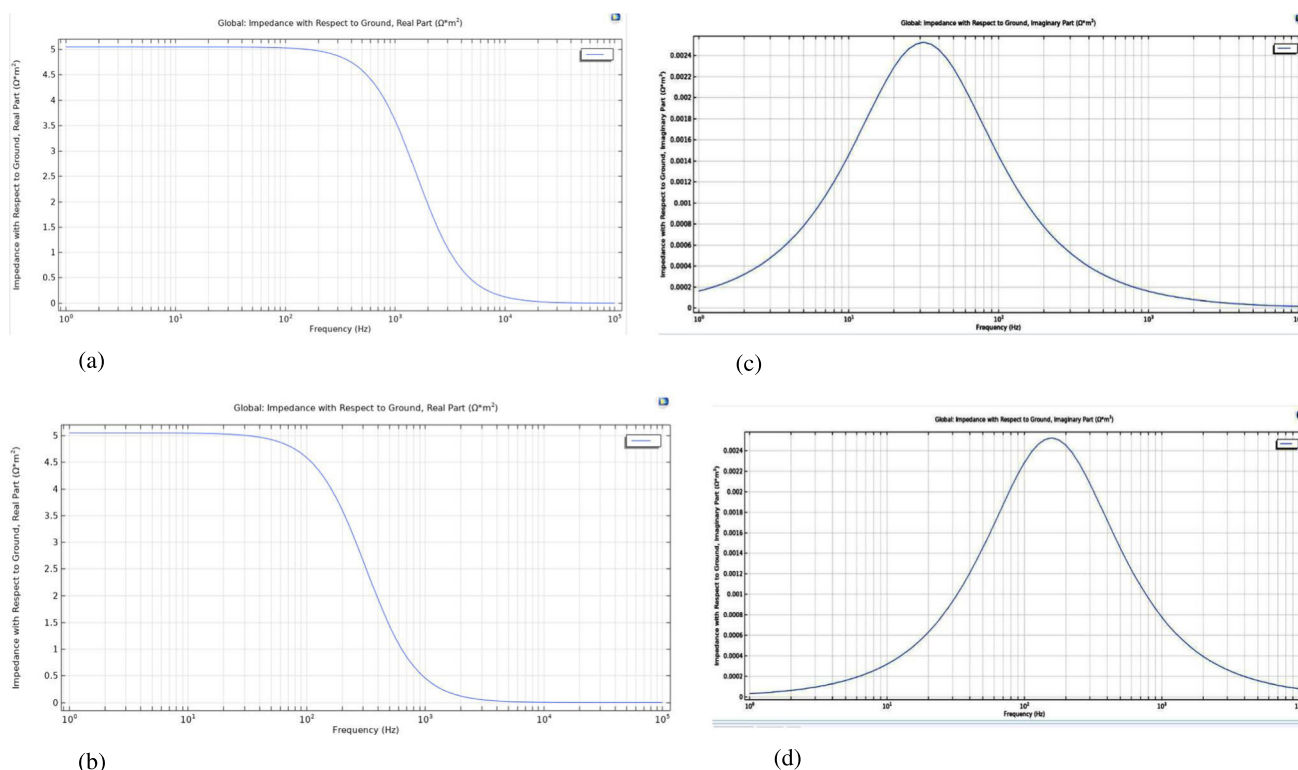
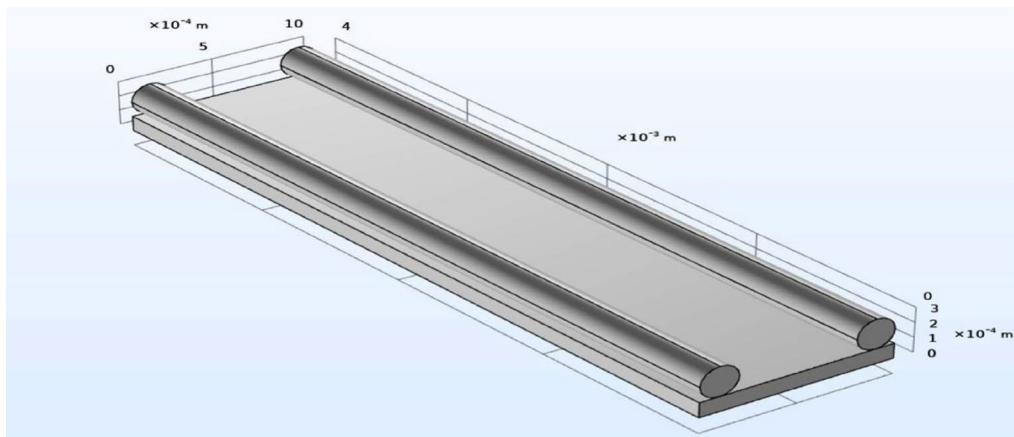
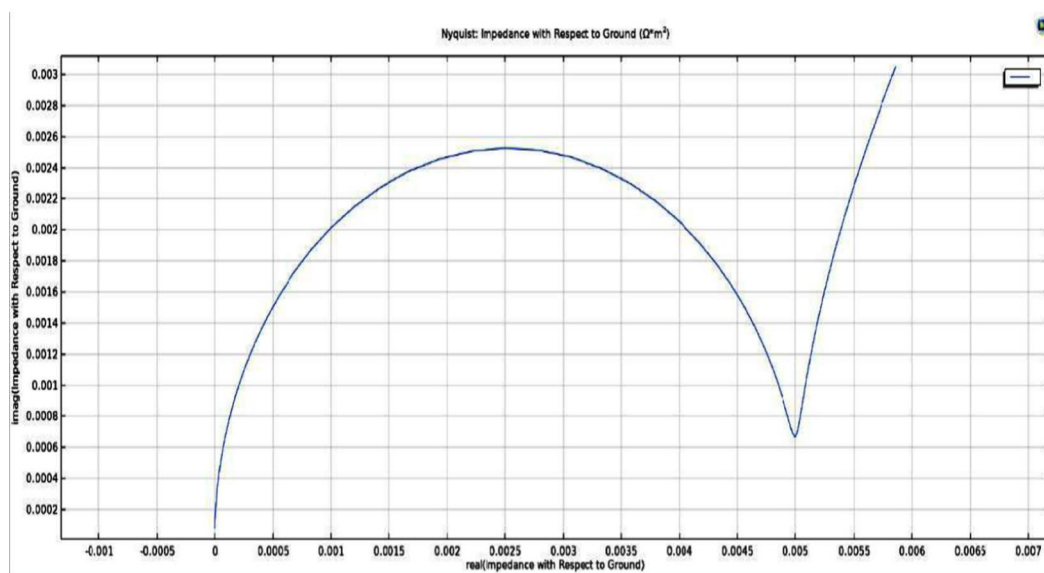


Fig. 7 **a** Cuboidal electrode Bode—real impedance versus frequency plots $C_{dl}=20 \mu\text{cm}^3$. **b** Cuboidal electrode Bode—real impedance versus frequency plots $C_{dl}=100 \mu\text{cm}^3$. **c** Cuboidal electrode Bode

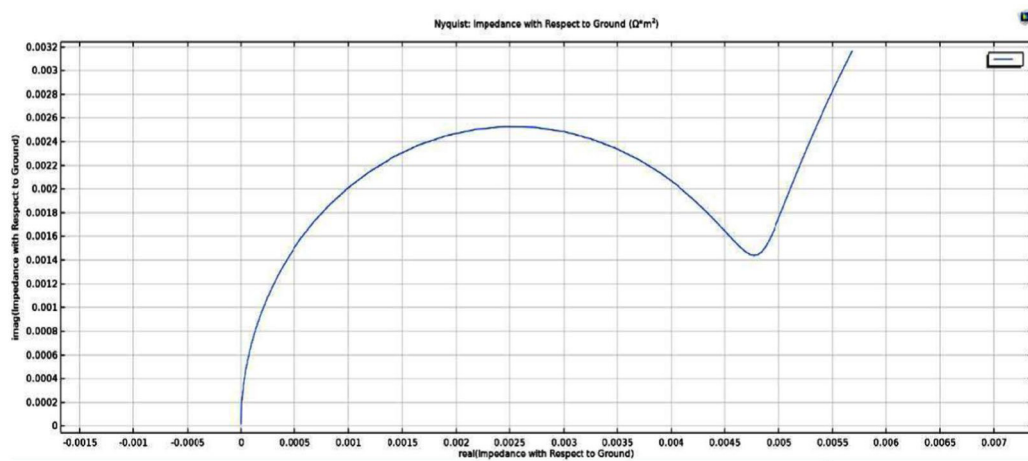
imaginary impedance vs frequency plots for $C_{dl}=20 \mu\text{cm}^3$. **d** Cuboidal electrode Bode imaginary impedance vs frequency plot $C_{dl}=100 \mu\text{cm}^3$



(a)



(b)



(c)

Fig. 8 **a** Cylinder electrode. **b** Cylinder electrode Nyquist plots for $C_{dl} = 20 \mu\text{cm}^3$. **c** Cylinder electrode Nyquist plots for $C_{dl} = 100 \mu\text{cm}^3$.

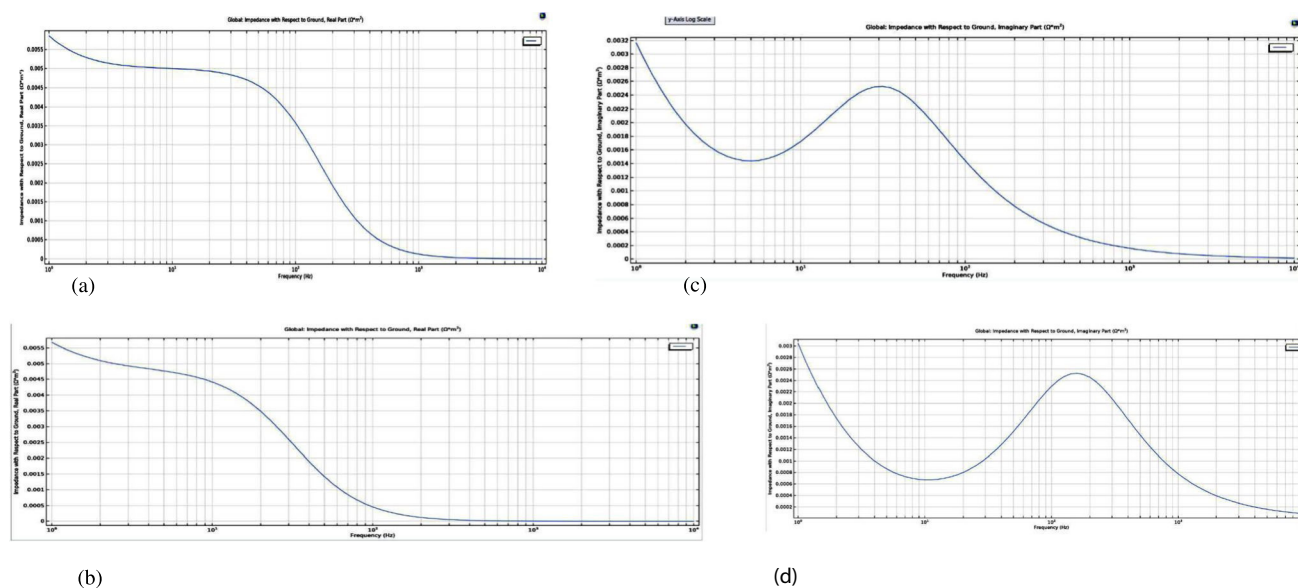


Fig. 9 **a** Cylinder electrode Bode—real impedance versus frequency plots $C_{dl}=100 \mu\text{m}^3$. **b** Cylinder electrode Bode—real impedance versus frequency plots $C_{dl}=20 \mu\text{m}^3$ highest point on the crest is utilized for double layer capacitance calculations. **c** Cylinder electrode

Bode—imaginary impedance versus frequency plots $C_{dl}=100 \mu\text{m}^3$. **d** Cylinder electrode Bode—imaginary impedance versus frequency plots $C_{dl}=20 \mu\text{m}^3$

The x-axis in Fig. 4b, c represents the real impedance, while the y-axis depicts the imaginary part. Each graph has been plotted for a specific value of double layer capacitance, the first for $100 \mu\text{F}$, the second for $20 \mu\text{F}$. The x-axis in Fig. 5a, b represents real impedance, while the y-axis shows frequency. The particular cutoff frequency can also be seen. The peak value of this graph corresponds to the maximum value on the x-axis, obtained in the Nyquist plot seen previously. These are useful parameters to calculate double layer capacitance. The x-axis in Fig. 5c, d shows the imaginary value of impedance, while the y-axis shows frequency. The frequency at which the imaginary impedance has the highest value is used in the calculation of double layer capacitance.

A. Cuboidal electrode

It can be observed in Fig. 6b, 6c that the plot is shifted slightly to the right, when higher double layer capacitance is used, as compared to Fig. 4b, c.

It can be observed in Fig. 7a that the plot is shifted slightly to the right, when higher double layer capacitance is used, as compared to Fig. 7b. The plot in Fig. 7c is shifted to the left in the case of the structure with higher double layer capacitance as compared to the results in Fig. 7d. Therefore, the frequency which corresponds to the highest value of the imaginary part of impedance is lower, in the case of a structure with a higher double layer capacitance.

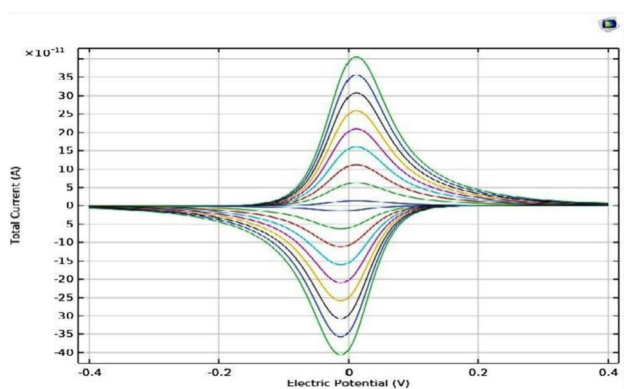


Fig. 10 Voltammetry plot of stepped electrode

Table 1 Cyclic voltammetry—stepped cuboidal

Concentration ($\mu\text{mol}/\text{m}^3$)	Current (pA)	Color
2.75	406.10	Dark green
12.75	357.00	Indigo
22.75	307.86	Black
32.75	258.77	Yellow
42.75	209.78	Purple
52.75	160.68	Light blue
62.75	111.65	Brown
72.75	62.58	Light green
82.75	13.50	Dark blue

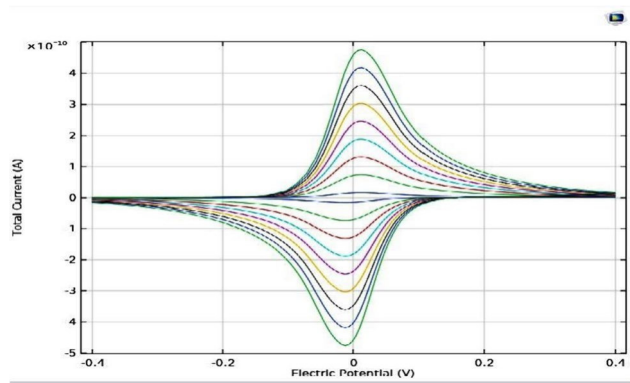


Fig. 11 Voltammetry plot of cuboidal electrode

B. Cylindrical electrode

Beyond a certain value of real impedance, the plot in Fig. 8b, c shoots up to higher values of imaginary impedance. For the purpose of calculations, the extrapolated value of imaginary impedance is chosen.

In Fig. 9a–d, the range of frequencies with a higher value of real impedance is higher for lower double layer capacitance. The concept of calculating the required frequency value remains the same.

5.2 Plots Obtained from Cyclic Voltammetry

The next analysis conducted was cyclic voltammetry. This involves varying voltage linearly and measuring the current response of the electrode. The plot obtained is referred to as a voltammogram and depicts the variation of current with respect to voltage.

Nine different solutions’ cyclic voltammograms were captured. The I_{pc} (peak cathodic current) and I_{pa} (peak anodic current) as functions for different concentrations are displayed on a graph with three electrodes. When doing cyclic voltammetry, the following parameters are taken into account:

Table 2 Cyclic voltammetry—cuboidal

Concentration (μmol/m ³)	Current (pA)	Color
2.75	474.40	Dark green
12.75	417.00	Indigo
22.75	359.69	Black
32.75	302.40	Yellow
42.75	245.10	Purple
52.75	187.75	Light blue
62.75	130.4	Brown
72.75	73.20	Light green
82.75	15.80	Dark blue

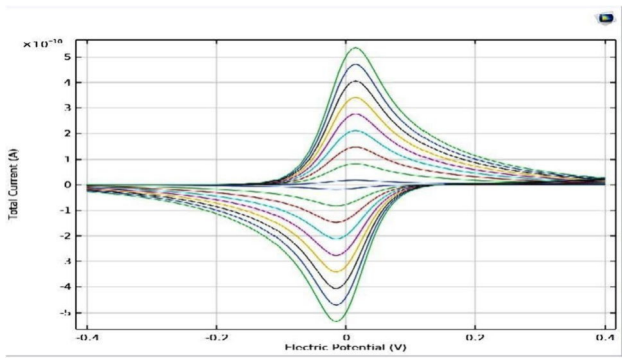


Fig. 12 Voltammetry plot of cylindrical electrode

- Potential = −0.4 to 0.4 V
- Scan rate = 0.1 V/s
- Quiet time = 0 to 100 s
- Full scale = 10 mA/V
- Peak difference (ΔE_p) = 56.5 mV/n

The voltammogram obtained for the three electrode structures is as below.

A. Stepped cuboidal electrode

The results for the total current vs linearly swept electric potential for the stepped cuboidal are shown in Fig. 10, and the values of the maximum current through the electrode are tabulated in Table 1. It can be seen that the maximum and minimum values of current with respect to varying concentrations are 406.10 pA and 13.50 pA, respectively, for cortisol concentrations of 2.75 μmol/m³ and 82.75 μmol/m³.

B. Cuboidal electrode

The results for the total current vs linearly sweep electric potential for the cuboidal electrode are shown in Fig. 11, and the values of the maximum current through the electrode

Table 3 Cyclic voltammetry—cylindrical

Concentration (μmol/m ³)	Current (pA)	Color
2.75	514.75	Dark green
12.75	452.60	Indigo
22.75	390.40	Black
32.75	328.35	Yellow
42.75	266.20	Purple
52.75	204.05	Light blue
62.75	141.90	Brown
72.75	79.80	Light green
82.75	17.65	Dark blue

Table 4 Cyclic voltammetry—results

Electrode structure	Maximum current (pA)	Minimum current (pA)	Range (pA)
Stepped cuboid	406.10	13.50	392.60
Cuboid	474.40	15.80	458.60
Cylindrical	514.75	17.65	497.10

are tabulated in Table 2. It can be seen that the maximum and minimum values of current with respect to varying concentrations are 474.40 pA and 15.80 pA, respectively, for cortisol concentrations of $2.75 \mu\text{mol}/\text{m}^3$ and $82.75 \mu\text{mol}/\text{m}^3$.

C. Cylindrical electrode

The results for the total current vs linearly sweep electric potential for the cylindrical electrode are shown in Fig. 12, and the values of the maximum current through the electrode

are tabulated in Table 3. It can be seen that the maximum and minimum values of current with respect to varying concentrations are 514.75 pA and 17.65 pA, respectively, for cortisol concentrations of $2.75 \mu\text{mol}/\text{m}^3$ and $82.75 \mu\text{mol}/\text{m}^3$. The complete results of cyclic voltammetry analysis of the three electrode designs are summarized in Table 4.

6 Signal Conditioning

As was observed, the output current is in the range of pA, which is a very small value. These values are very inconvenient to read and thus may not have any practical use. It is therefore necessary to design a signal conditioning circuit that can amplify the value to one which can be more conveniently measured.

Figure 13 shows the conditioning circuit, which consists of a transimpedance amplifier (TIA) based on a current amplifier [23]. The primary purpose of TIA is to provide

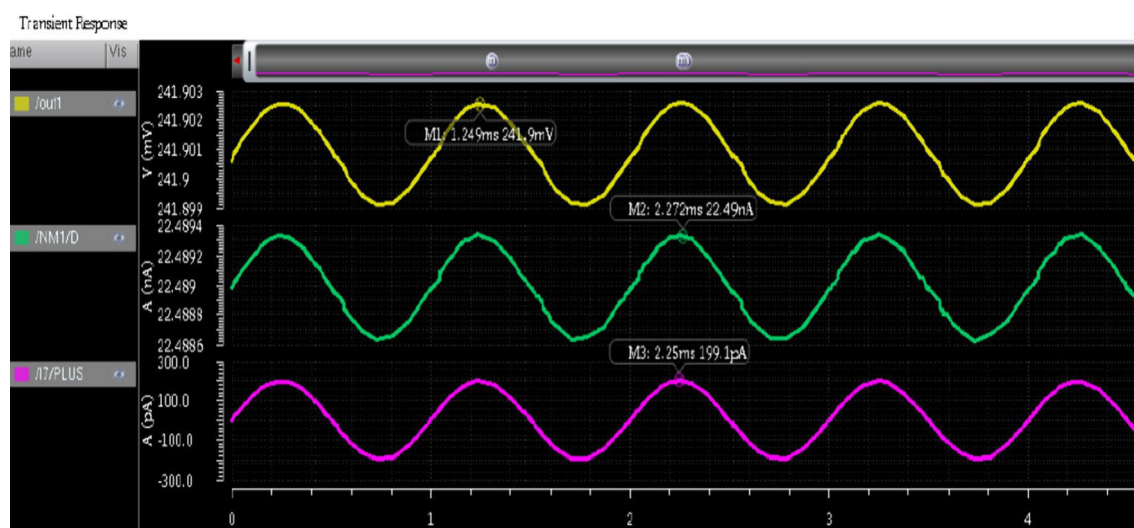
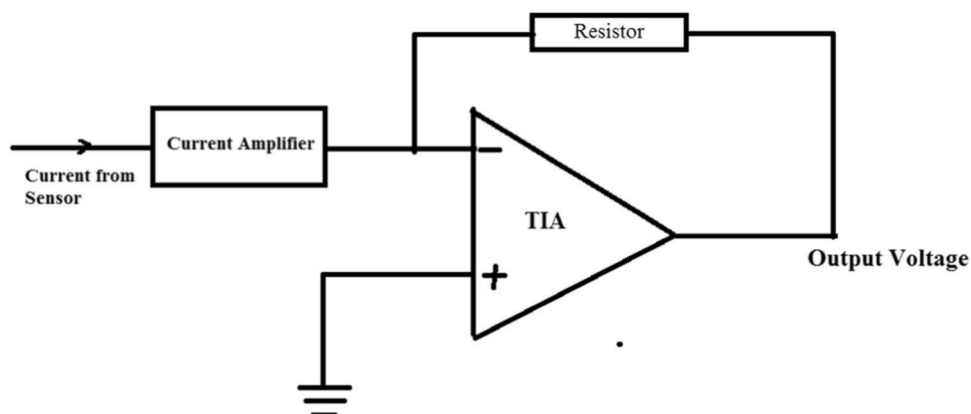
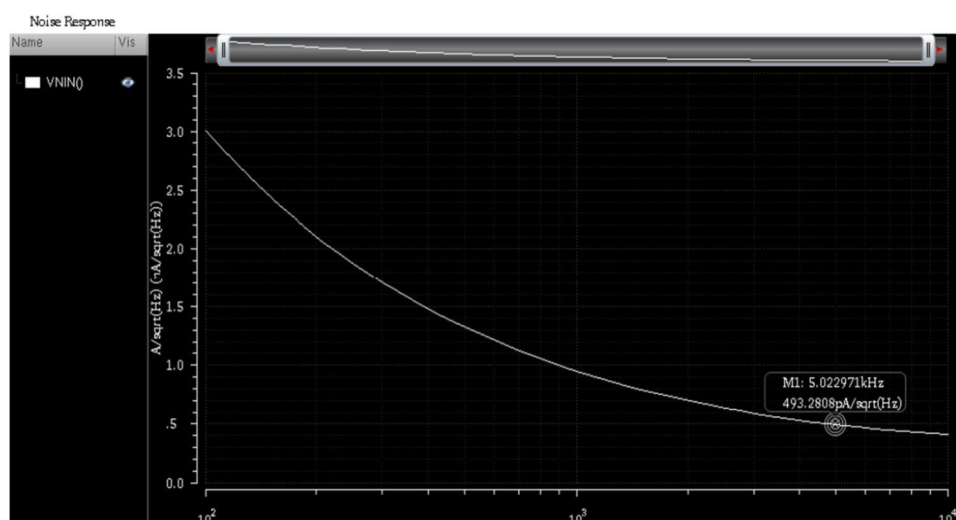
Fig. 13 Signal conditioning circuit**Fig. 14** Transient plots of signal conditioning circuit is adopted from [23]

Fig. 15 Input noise of signal conditioning circuit is adopted from [23]



the optimized sensor with minimal input impedance and needed bandwidth in order to achieve low noise and high gain. Fabrication becomes challenging if the resistor linked in feedback is giga ohms ($G\Omega$) and the input current to TIA is in the pA level. Therefore, the feedback resistor value can be lowered to mega ohms ($M\Omega$) by using a current amplifier. It is possible to validate the design of a signal conditioning circuit with low noise and low feedback resistance by using optimized noise reduction techniques.

Figures 14 and 15 show the transient plots and input noise of signal conditioning circuit obtained by simulating the circuit in cadence tool using 90 nm technology.

7 Conclusion

The electrochemical impedance spectroscopy (EIS) method based on the double layer capacitance is proved by plotting the Nyquist and Bode plots and mathematically the concentration values of hormone levels can be obtained from these plots. The results have been run for double layer capacitances of **20** and **100** μF , respectively. It can be inferred from the outcomes of the cyclic voltammetry experiment that both the maximum and minimum current are highest for the cylindrical electrode and lowest for the stepped cuboidal electrode. It is also seen that the range followed a similar pattern. Since range can determine the flexibility the designer can get, it is taken as the parameter of measurement. Based on the maximum values of current obtained from the electrode geometries, it can be stated that the cuboidal electrode (with maximum current read at 474.4 pA) is **16.81%** better than the stepped cuboidal electrode (with maximum current read at 406.1 pA) and the cylindrical electrode (with maximum current read at 514.75 pA) is **26.61%** better than stepped cuboidal electrode (with maximum current read at 406.1 pA) and **8.39%** better than the cuboidal electrode

(with maximum current read at 474.4 pA). This conclusion is based on the idea that higher values of current correspond to higher concentration of current. The process of measurement is done for different electrode geometries, with similar volumes.

The measured values from the electrodes are extremely small and hence difficult to measure. These are thus amplified with the help of a signal conditioning circuit to the order of about 0.1 V, which can be more conveniently measured. These improvements can be applied in detection of stress-related hormones such as cortisol and other hormones in bodily fluids like sweat, saliva, or blood.

Author Contribution Author 1 collected the data, performed the analysis, and edited the contents of paper.

Authors 2 and 7 performed the analysis and reviewed the paper.

Authors 3 to 6 collected the data and performed the analysis.

Funding Statement Not applicable.

Data Availability Not applicable.

Declarations

Ethical Approval Not applicable.

Competing Interests The authors declare no competing interests.

References

1. Hogenelst, K., & Soeter, M. (2009). and Kallen, V Ambulatory measurement of cortisol: Where do we stand, and which way to follow? *Sensing and Bio-Sensing Research*, 22, 100249. <https://doi.org/10.1016/j.sbsr.2018.100249>
2. Kaushik, A., Vasudev, A., Arya, S. K., Pasha, S. K., & Bhansali, S. (2014). Recent advances in cortisol sensing technologies for point-of-care application. *Biosensors and Bioelectronics*, 53, 499–512. <https://doi.org/10.1016/j.bios.2013.09.060>

3. Sankhala, D., Muthukumar, S., & Prasad, S. (2018). A four-channel electrical impedance spectroscopy module for cortisol biosensing in sweat-based wearable applications. *SLAS TECHNOLOGY: Translating Life Sciences Innovation*, 23(6), 529–539. <https://doi.org/10.1177/2472630318759257>
4. Upasham, S., Tanak, A., Jagannath, B., & Prasad, S. (2018). Development of ultra-low volume, multi-bio fluid, cortisol sensing platform.. *Scientific Reports*, 8(1). <https://doi.org/10.1038/s41598-018-35199-5>
5. Upasham, S., Bhide, A., Lin, K., & Prasad, S. (2021). Point-of-use sweat biosensor to track the endocrine–inflammation relationship for chronic disease monitoring. *Future Science OA*, 7(1). <https://doi.org/10.2144/fsoa-2020-0097>
6. Parlak, O., Keene, S. T., Marais, A., Curto, V. F., Salleo, A. (2018). Molecularly selective nanoporous membrane-based wearable organic electrochemical device for noninvasive cortisol sensing. *Science Advances*, 4(7). <https://doi.org/10.1126/sciadv.aar2904>
7. Preeti, J., & Sutrave, D. S. (2018). A brief study of cyclic voltammetry and electrochemical analysis. *International Journal of ChemTech Research*, 11, 77–88. <https://doi.org/10.20902/IJCTR.2018.110911>
8. Tadesse, Y., Tadesse, A., Saini, R. C., & Pal, R. (2013). Cyclic voltammetric investigation of caffeine at anthraquinone modified carbon paste electrode. *International Journal of Electrochemistry*, 2013, 7, Article ID 849327. <https://doi.org/10.1155/2013/849327>
9. Liu, X., Hsu, S. P. C., Liu, W.-C., Wang, Y.-M., Liu, X., Lo, C.-S., Lin, Y.-C., Nabilla, S. C., Li, Z., Hong, Y., Lin, C., Li, Y., Zhao, G., & Chung, R.-J. (2019). Salivary electrochemical cortisol biosensor based on tin disulfide nanoflakes. *Nanoscale Research Letters*, 14, 189. <https://doi.org/10.1186/s11671-019-3012-0>
10. Dhull, N., Kaur, G., Gupta, V., & Tomar, M. (2019). Highly sensitive and non-invasive electrochemical immunosensor for salivary cortisol detection. *Sensors and Actuators B: Chemical*, 293, 281–288, ISSN 0925–4005. <https://doi.org/10.1016/j.snb.2019.05.020>
11. Su, Y (2014). Modeling and characteristic study of thin film based biosensor based on COMSOL. *Theory and Applications of Complex Networks*. <https://doi.org/10.1155/2014/581063>
12. Bhandodkar, A. J., Jeerapan, I., & Wang, J. (2016). Wearable chemical sensors: Present challenges and future prospects. Publication Date: May 6, 2016 <https://doi.org/10.1021/acssensors.6b00250>. Copyright © 2016 American Chemical Society
13. Bhandodkar, A. J. & Wang, J. Non-invasive wearable electrochemical sensors: A review. *Trends in Biotechnology*. Publication Date: May 19, 2014. <https://doi.org/10.1016/j.tibtech.2014.04.005>
14. Munje, R. D., Muthukumar, S., Selvam, A. P., & Prasad, S. Flexible nanoporous tunable electrical double layer biosensors for sweat diagnostics. Publication Date: 30 September 2015. <https://doi.org/10.1038/srep14586>
15. Lavacchi, A., Bardi, U., Borri, C., Caporali, S., Fossati, A., & Perissi, I. Cyclic voltammetry simulation at microelectrode arrays with COMSOL. Publication Date: n 24 January 2009. <https://doi.org/10.1007/s10800-009-9797-2>
16. Preeti, J., & Sutrave, D. S. (2018). A brief study of cyclic voltammetry and electrochemical analysis. *International Journal of ChemTech Research*, 11, 77–88. <https://doi.org/10.20902/IJCTR.2018.110911>
17. Chernecky Cynthia C. and Barbara J. Berger. 2013. Laboratory tests & diagnostic procedures. Sixth ed. St. Louis Mo: Elsevier/ Saunders. <http://www.clinicalkey.com/dura/browse/bookChapter/3-s2.0-C20100683313>. Accessed 31 Aug 2021
18. Uttrachi, G.D. (n.d.). Productivity factors in submerged arc line pipe welding applications. *Pipeline and Energy Plant Piping*, 135–139. <https://doi.org/10.1016/B978-0-08-025368-8.50017-8>
19. Faraj, M. G., Ibrahim, K., & Ali, K. M. (2011). PET as a plastic substrate for the flexible optoelectronic applications. *Journal of Optoelectronics and Advanced Materials-Rapid Communications.*, 5, 879–882.
20. Strauss, J.T. (2019). 25 - Metal injection molding (MIM) of precious metals. *Handbook of metal injection molding (second edn)*, Woodhead Publishing 609–622. <https://doi.org/10.1016/B978-0-08-102152-1.00030-1>
21. Highly sensitive and selective detection of steroid hormones using terahertz molecule specific sensors. <https://doi.org/10.1021/acs.analchem.9b01066>
22. Cifrić, S., Nuhić, J., Osmanović, D., Kišija, E. (2020). Review of electrochemical biosensors for hormone detection. In: Badnjevic, A., Škrbić, R., Gurbeta Pokvić, L. (eds) CMBEBIH 2019. CMBE-BIH 2019. IFMBE Proceedings, vol 73. Springer, Cham. https://doi.org/10.1007/978-3-030-17971-7_27
23. Roogi, J. M., & Devi, M. (2022). Pre-current amplifier based transimpedance amplifier for biosensors. *International Journal of Reconfigurable and Embedded Systems.*, 11(2), 188–195. <https://doi.org/10.11591/ijres.v11.i2.pp188-195>

Publisher's Note Springer Nature remains neutral with regard to jurisdictional claims in published maps and institutional affiliations.

Springer Nature or its licensor (e.g. a society or other partner) holds exclusive rights to this article under a publishing agreement with the author(s) or other rightsholder(s); author self-archiving of the accepted manuscript version of this article is solely governed by the terms of such publishing agreement and applicable law.

Original Article

A Single Source Switched Capacitor Seven-Level Boost Inverter for Solar PV Applications

K. Sarada¹, Deepak Prakash Kadam², Sharana Reddy³, Priya R. Patil⁴, Siva Sankara Naik Azamira⁵,
M. Ramprasad Reddy⁶

¹Department of Electrical and Electronics Engineering, Koneru Lakshmaiah Education Foundation, Vaddeswaram, India.

²Department of Electrical and Electronics Engineering, MET Institute of Engineering, Adgaon, Nashik, India.

³Department of Electrical and Electronics Engineering, Ballari Institute of Technology and Management, Bellary, India.

⁴Department of Electrical Engineering, Shree Ramchandra College of Engineering, Pune, India.

⁵Department of Electrical and Electronics Engineering, JNTU-GV, Vizainagaram, India.

⁶Department of Electrical and Electronics Engineering,
Mohan Babu University (Erstwhile Sree Vidyanikethan Engineering College), Tirupati, India.

⁶Corresponding Author : mrampasadreddyyee@gmail.com

Received: 10 July 2023

Revised: 15 August 2023

Accepted: 08 September 2023

Published: 30 September 2023

Abstract - Multilevel Inverters (MLIs) are cascade inverters that may take several or a single DC input and produce a single AC output of the desired Frequency (F) and voltage, making them ideal for medium power applications. MLIs are better than 2L inverters in many aspects; however, implementing MLIs is becoming more difficult due to the increasing amount of switches and their configurations. For high-gain DC-AC converters, Switched Capacitor (SC) driven MLIs often demonstrate the compromise between switch count and voltage rating. A Single-Source Switched Capacitor Seven-Level Boost Inverter (S^3C7LBI) is presented in this research. Since the S^3C7LBI can offer intrinsic capacitor voltage balancing, triple voltage gain, and seven output levels without requiring sensors or other auxiliary operations, it is appropriate for renewable energy applications. The proposed S^3C7L boost inverter design requires only one DC power source, eleven electronic switches, and two capacitors. Utilizing the sinusoidal PWM control approach, the functioning of the S^3C7LB inverter is examined. The usefulness of the S^3C7LBI architecture is validated by the simulation results for dynamic modulation index values, and different load conditions are presented. Additionally, hardware findings confirm that the S^3C7LBI architecture is feasible.

Keywords - Boost voltage, Harmonic distortion, Multilevel Inverter, Switched Capacitor, DC-AC inverter.

1. Introduction

Increasing the switching frequency in a simple two-level inverter reduces the output voltage's harmonics, resulting in increased switching losses and voltage stresses due to reduced output voltage's step count. The drawbacks of the two-level inverter pique interest in Multilayer Inverters (MLIs). MLI was introduced in 1991, & its progress has been rapid.

MLIs are widely used in several industries today, especially for high-power and intermediate-voltage applications. MLIs produce a staircase waveform that closely resembles a sinusoidal signal and has less harmonic distortion by using more DC supply and switches. Over conventional two-level inverters, MLIs provide several advantages, including a greater primary output voltage, reduced switching loss and common mode voltage, decreased EMI, and decreased THD [1]. Because of these advantages, MLIs apply to various applications, including HVDC,

FACTS, electric vehicles, and solar power systems [2]. The most common MLI topologies are the CHB inverter, Flying Capacitor (FC), and NPC inverter. FC utilizes capacitors in a ladder structure, while NPC uses diodes.

NPC and FC need more power components to achieve greater inverter levels and suffer from voltage imbalance. In the CHB topology, H-bridge modules are allied in series, and the modular architecture is established by requiring each cell to possess its own DC supply [3].

This CHB architecture is advantageous for both single-phase and three-phase power conversion. CHB MLIs are suited for PV applications and are one of the three core MLI topologies. The primary block diagram of the grid-tied solar PV system is shown in Figure 1. MLI is essential in utilizing renewable resources for various applications [4]. Alternatively, all MLI research and development is limited to SC Multilevel Inverters (SCMLIs). Inherent balancing of



capacitor voltages and small size are the critical advantages of SCMLI over standard MLIs [5-11]. Within high-F AC microgrids, [12] suggests a quasi-resonant SC multilevel inverter.

A resonant inductor raises the charging current of switched capacitors. Despite being straightforward, this topology cannot be made better. In [13], a streamlined three-phase MLI is suggested. Four boosting switching capacitors are used in the individual phase of an inverter to provide different output levels. On the other hand, many capacitors and diodes are used.

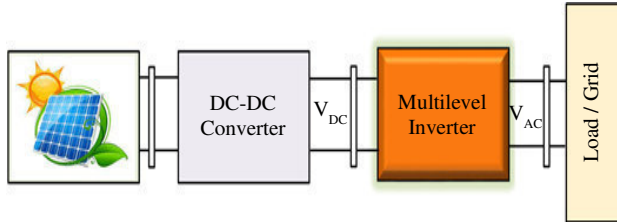


Fig. 1. Block diagram grid-tied solar PV system

The adaptable multilevel inverter and the 7L inverter both employ a T-type tie and the SC method. The self-balance and symmetry of the T-type structure are investigated. The literature has other instances of seven-stage SC inverters.

The H-bridge structure of [14] is the basis for the MLI topology in [15], contrary to the active NPC inverter designs. MLIs utilize either floating or switching capacitors. The voltage of FCs is kept back at 50% of the source voltage, attributable to the SC's voltage-maintaining capabilities.

Moreover, the literature presents the multilevel output and self-balancing core modules for MLI. Their intended use is in cascaded single-phase systems [16]. Every basic module uses a switching capacitor and has a comparable twin boost factor [17]. The 3L unit's maximum output via fewer components is just half of the input in [18]. At a voltage of 120V, the 7L, three-capacitor inverter (may be seen functioning in cascade) has a gain of 1.5. Because there are two asymmetrical DC sources in the 13-level module in [19], the two SCs are charged at different voltages. The planned use of these simple modules in cascading connections enables significant output levels.

Based on results from comparison for reference and voltages of capacitors and output current direction, redundant operating modes are selected for FC and CHB-based hybrid topologies [20]. Voltage balance may, therefore, be obtained via sensors. The extra balancing techniques necessary in the preceding MLIs add more components and complexity to govern. As a result, MLIs that avoid the difficulty of voltage balancing have gained popularity. The switched-capacitor approach combines a T-type construction in the 7L inverter

[21] and the modular MLI [22]. The T-type structure's inherent balance with symmetric operation is used. The topology in [23, 24] provides further seven-level switched-capacitor inverters. The topology in [25] is based on an H-bridge structure, whereas that in [26] is based on an active NPC. The SCMLI proposed in [25] addresses this issue by including full-bridge cells. Each cell's voltage stress cannot go beyond the amplitude of the dc source.

Furthermore, involving the negative terminals of the DC source and output reduces leakage current. The topology in [27] has more diodes and capacitors and a low gain and high-cost factor for obtaining seven output levels. By adding more SC cells, the SCMLI in [28] can increase their production level. All the while, they are maintaining the ability to maintain equilibrium. Although it generates seven levels, the topology suggested in [29] has a problem with voltage stress distribution. Many different modulation techniques for controlling different MLI kinds have been presented in the literature [30-34].

This article presents the new Single-Source Switched Capacitor Seven-Level Boost Inverter (S^3C7LBI) architecture, addressing the abovementioned issue. S^3C7LBI uses a single source and nine power switches to provide seven output levels. Three times the input voltage is the maximum output voltage. The natural equilibrium of the SC voltages may occur even in the absence of sensors. These advantages demonstrate that the S^3C7LBI that is being described is a good fit for applications that need medium-low voltage/power levels, such as REG integration.

2. Single Source Switched Capacitor Seven Level Boost Inverter (S^3C7LBI) Topology

Figure 2 depicts the proposed Single-Source Switched Capacitor Seven-Level Boost Inverter (S^3C7LBI) topology. The proposed S^3C7LBI has just 02 switching capacitors and 11 power switches. The voltages of SCs may be balanced on input voltage without the need for sensors or other tools. The proposed S^3C7LBI max output voltage achieves three times the magnitude of V_{in} . Because of this, the S^3C7LBI being shown has a gain of 3. Seven levels are generated as $0, \pm V_{DC}, \pm 2V_{DC}$ and $\pm 3V_{DC}$.

Table 1 demonstrates the switching logic of the proposed S^3C7LBI topology where 1 represents the switch is ON & 0 represents the switch is OFF. In Table 1, the red colour in the switching logic represents those switching states responsible for charging the two capacitors, which helps balance the capacitors' voltages to the voltage level of V_{DC} . Figure 3 (a)-(g) shows the suggested S^3C7LBI operating states at different phase output voltage levels ($+3V_{DC}$ to $-3V_{DC}$). At certain voltage levels, the cascade-connected capacitors C_1 and C_2 act as Switching Capacitors (SC) in parallel with the V_{DC} supply.

Consequently, the whole voltage of its C_1 is charged to V_{DC} ; on the other hand, it discharges at output levels of $2V_{DC}$, $3V_{DC}$, and $-3V_{DC}$, while C_2 discharges at output levels of $3V_{DC}$, $-2V_{DC}$, and $-3V_{DC}$. Due to their symmetric

discharge, V_{DC} may balance the voltages for C_1 and C_2 . To produce a gain of three times the input voltage V_{DC} , C_1 and C_2 are coupled in a cascaded manner with a V_{DC} supply at $3V_{DC}$ and $-3V_{DC}$ to create the maximum output voltage.

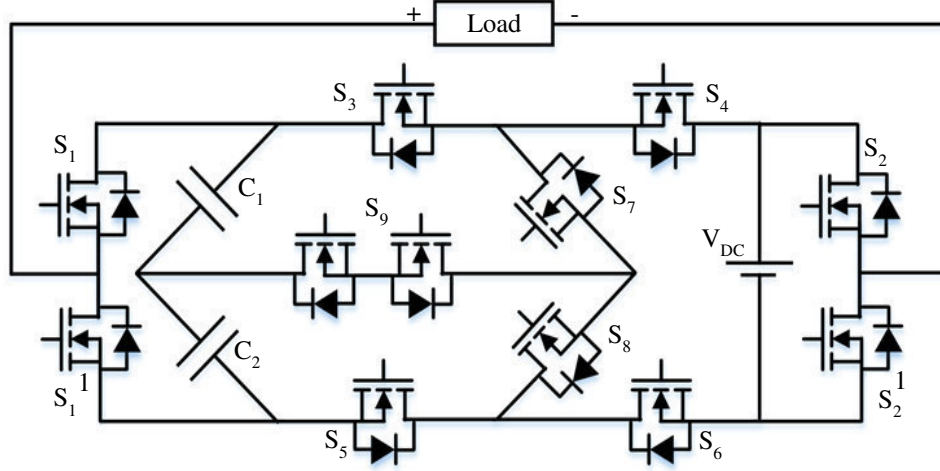
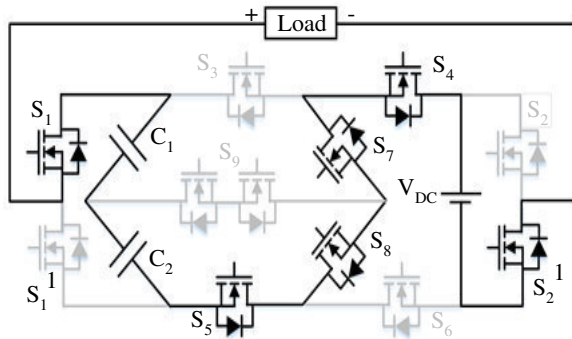


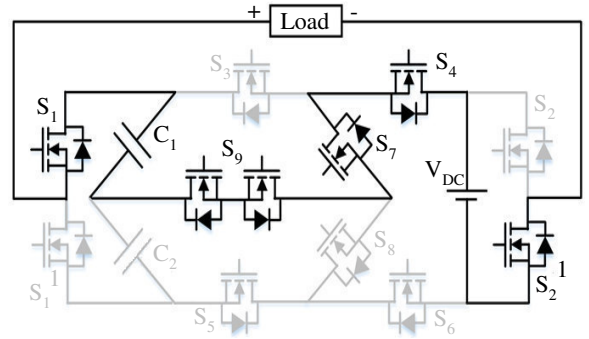
Fig. 2 Proposed S^3C7LBI topology

Table 1. Switching states of proposed S^3C7LBI topology

State	S_1	S_2	S_3	S_4	S_5	S_6	S_7	S_8	S_9
$+3V_{DC}$	1	0	0	1	1	0	1	1	0
$+2V_{DC}$	1	0	0	1	1	1	1	0	1
$+V_{DC}$	1	0	1	1	0	1	0	1	1
0	1	1	1	1	0	1	0	1	1
$-V_{DC}$	0	1	0	1	1	1	1	0	1
$-2V_{DC}$	0	1	1	1	0	1	0	1	1
$-3V_{DC}$	0	1	1	0	0	1	1	1	0



(a) $+3V_{DC}$



(b) $+2V_{DC}$

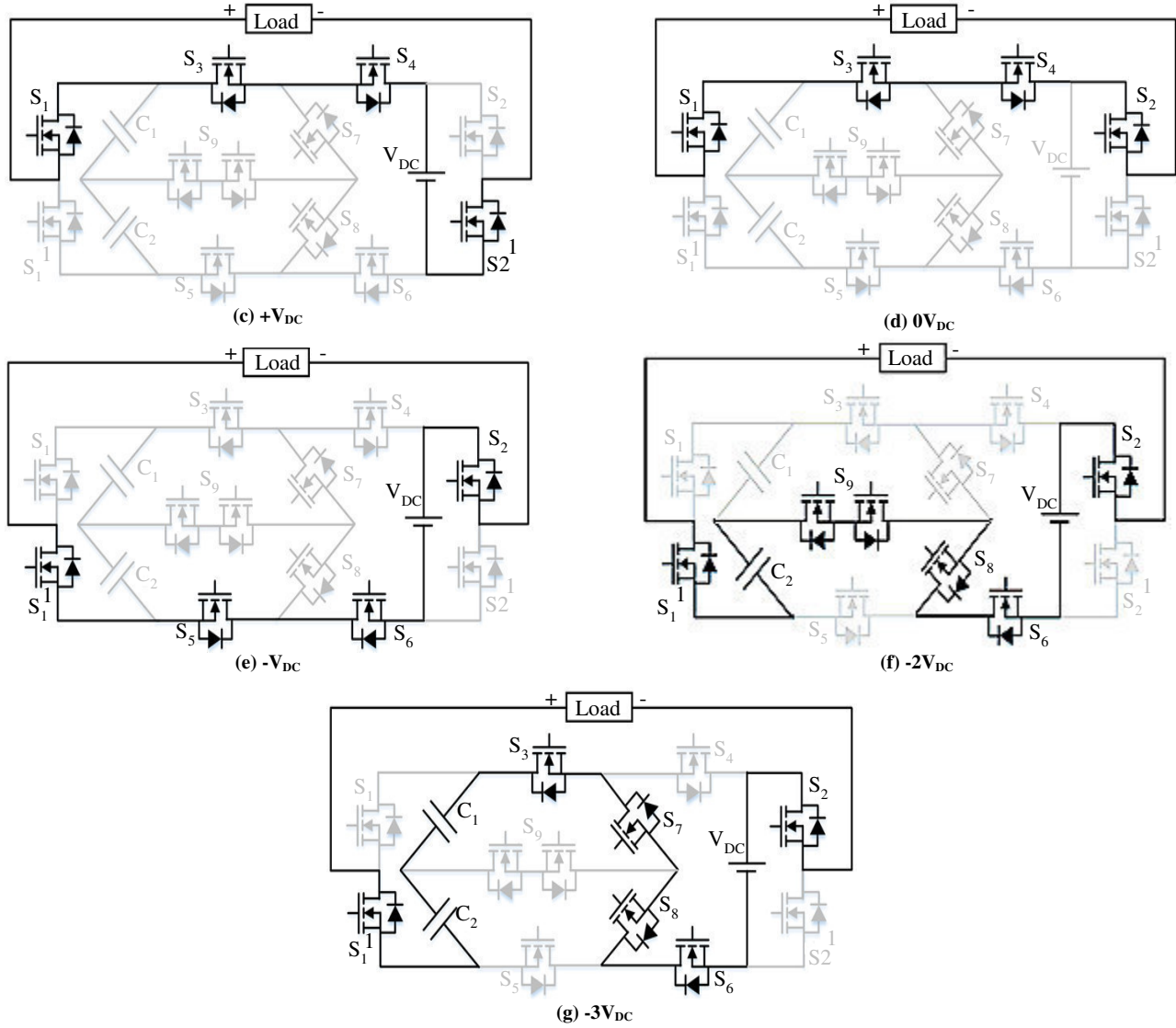


Fig. 3 Conduction paths of S³C7LBI for various voltage levels

3. Results and Discussions

3.1. Simulation Results

In this study, MATLAB simulation analysis has been performed to validate the provided S³C7LBI architecture. The S³C7L boost inverter uses the sinusoidal PWM scheme to create gate pulses for an inverter to power electronic devices. An in-phase carrier pattern, seen in Figure 4, is considered when using the SPWM approach to generate inverter pulses.

The following are considered for the simulation parameters: RL load, whose parameter values are well thought-out as $L=110\text{mH}$ and $R=100\Omega$, 100V DC source, and 1/3950Hz as switching frequency. Figure 5 shows the S³C7LBI phase voltage for a range of Modulation Index (MI) values, from 1.0 to 0.2, which validates the S³C7LBI architecture that is being proposed. The phase output

voltage's number of voltage levels drops in tandem with a decrease in the value of M.

Additionally, Table 2 displays the phase output voltage levels concerning Modulation Index (MI) variation for the 7L inverter. Figures 6a and 6b show the phase voltage and current at an M value of 1.0 for two distinct load circumstances, R and RL.

Figure 7 depicts the load current waveform with a M value of 1.0. Figure 8 displays the frequency spectrum of the phase current and voltage at the unity modulation index.

Table 3 shows the phase voltage RMS and harmonic distortion for the dynamic values of M. These waveforms demonstrate that S³C7LBI can have closed-loop capability for solar photovoltaic applications.

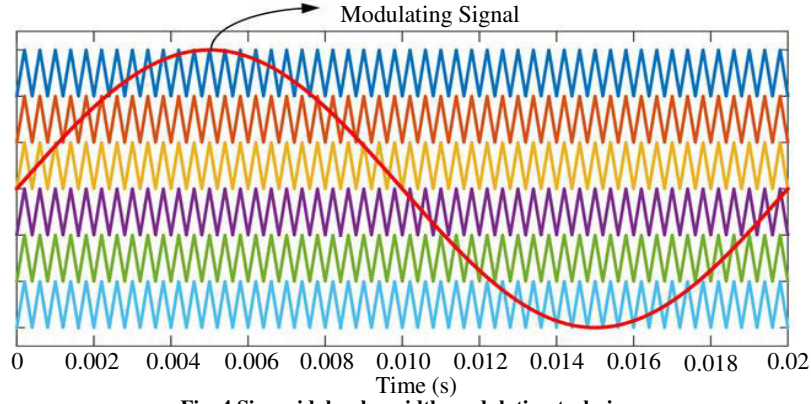
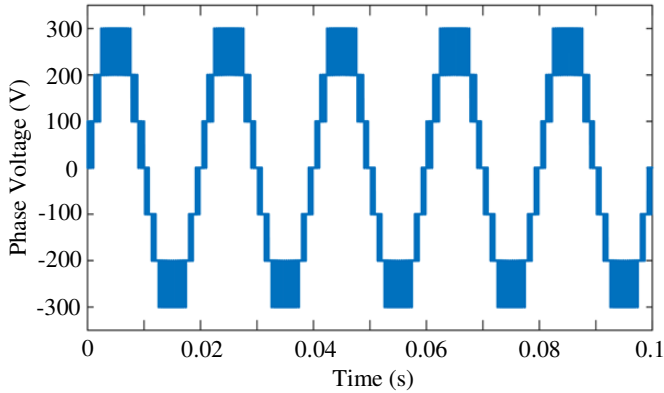
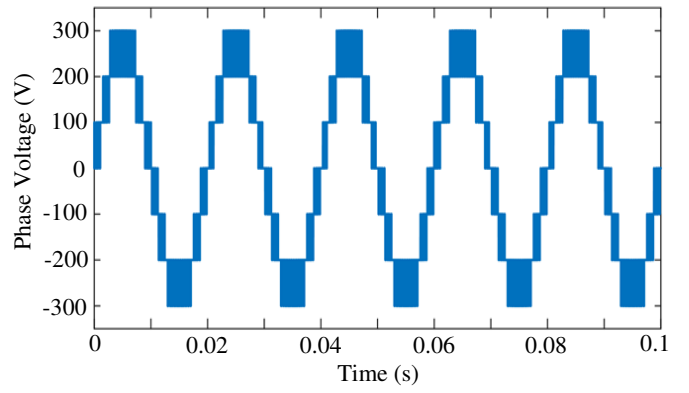


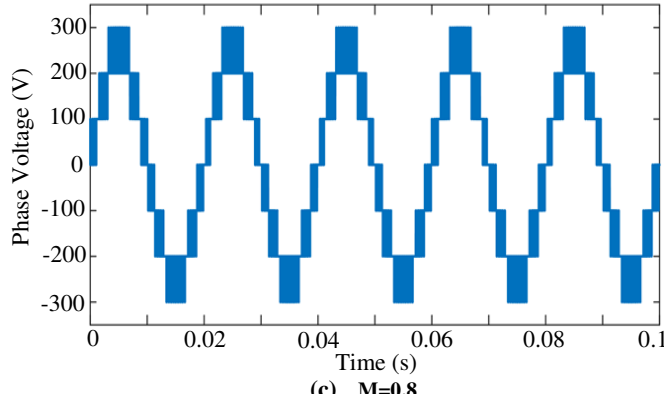
Fig. 4 Sinusoidal pulse width modulation technique



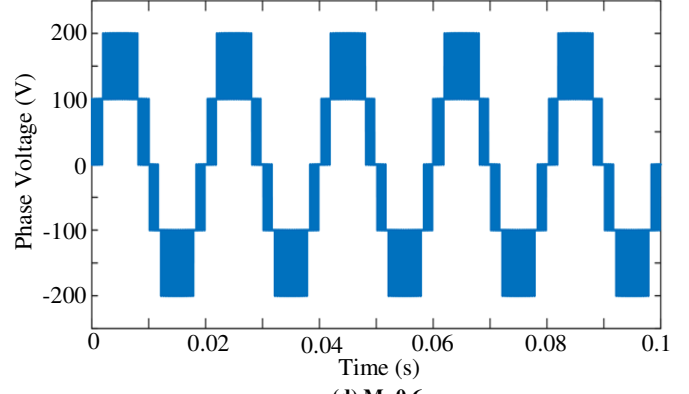
(a) $M=1.0$



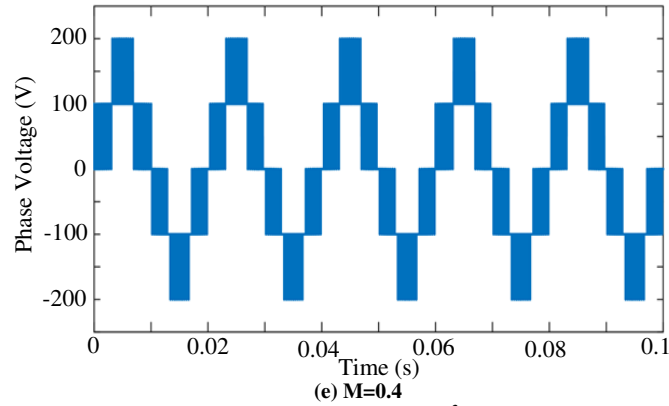
(b) $M=0.9$



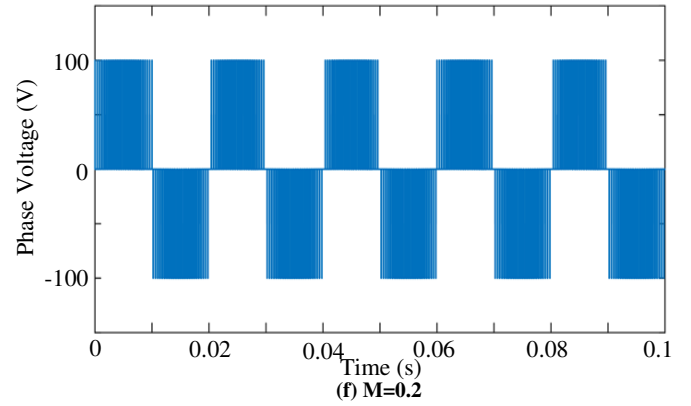
(c) $M=0.8$



(d) $M=0.6$



(e) $M=0.4$



(f) $M=0.2$

Fig. 5 S³C7LBI output voltage waveform for dynamic values of M

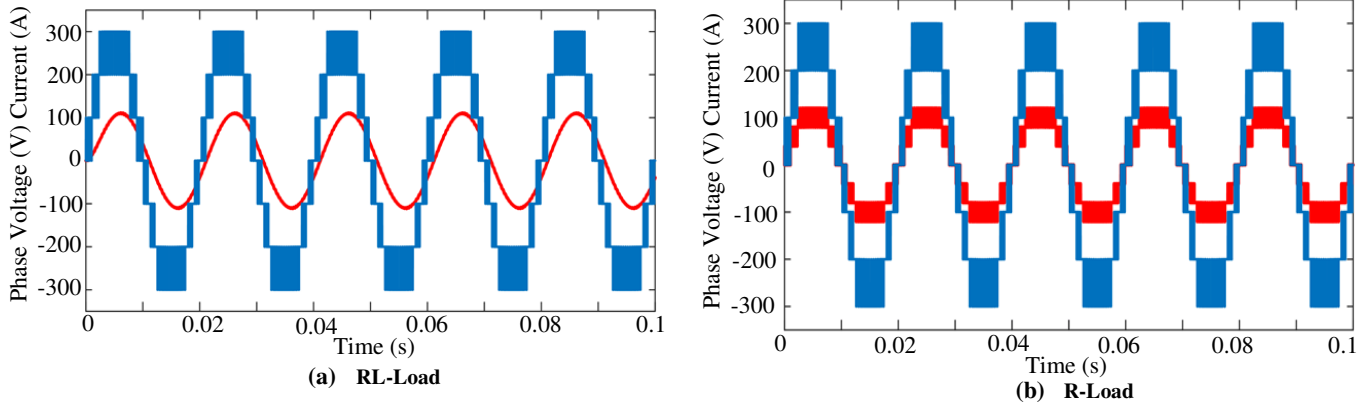


Fig. 6 Phase current and voltage at M=1.0 for different load conditions

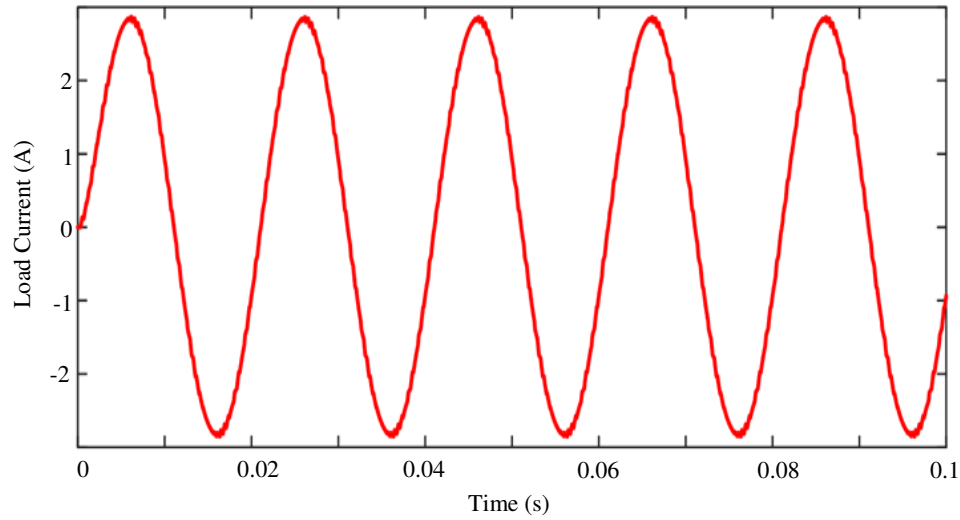


Fig. 7 Load current at M=1.0 for RL-load

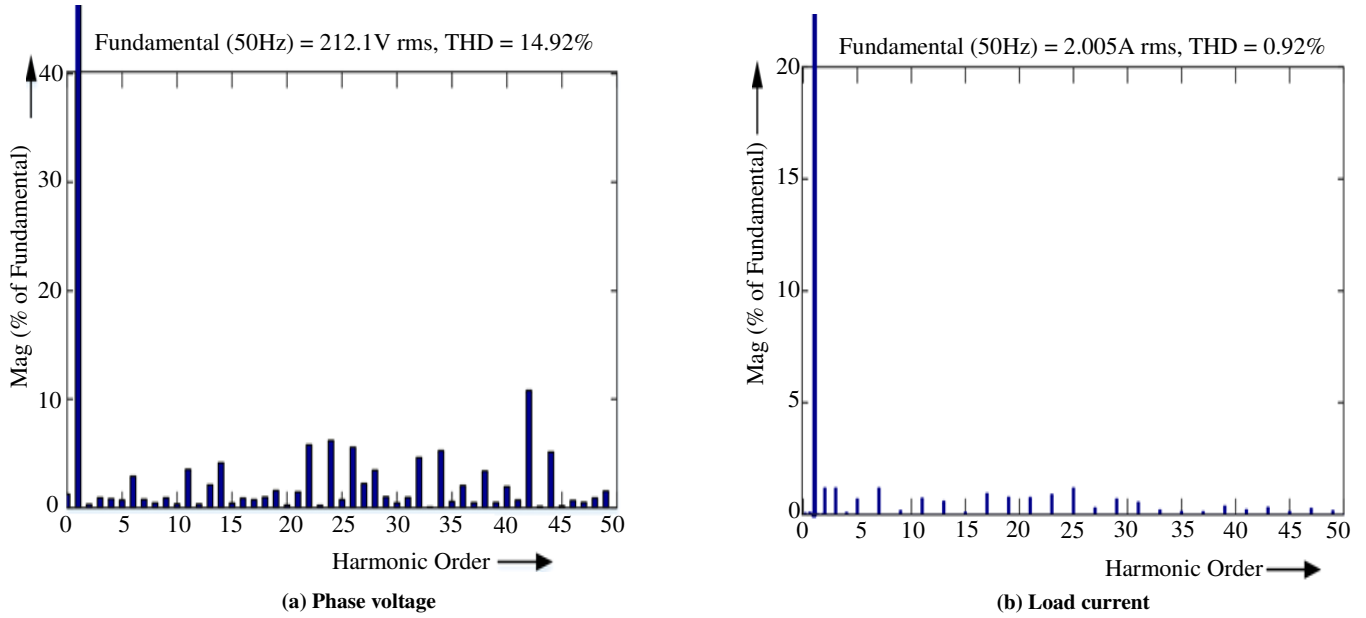


Fig. 8 Frequency spectra at unity modulation index

Table 2. Voltage levels of inverter phase for dynamic values of M

Modulation Index	Phase Voltage Levels
1.0	7
0.9	7
0.8	7
0.6	5
0.4	5
1.2	3

Table 3. Inverter output phase voltage RMS and THD for dynamic values of M

Modulation Index	RMS Voltage	%THD
0.5	106	34.16
0.6	127.2	28.50
0.8	169.6	20.23
0.9	190.9	18.99
1.0	212.1	14.92

Table 4. Comparison of S³C7L BI with the existing topologies

Topology	N _{sw}	N _{cap}	N _D	N _d	Gain	TSV _{pu}	Balancing Ability
12	12	3	0	12	0.5	6	Self
15	6	4	4	6	3	6	Self
14	8	4	2	7	1.5	6	Self
26	13	3	4	13	3	7.33	Self
28	14	2	2	14	3	5.33	Self
21	16	6	0	15	1.5	9.33	Self
19	8	3	0	7	0.75	5.33	Aux
29	7	3	2	7	0.73	6.33	Self
27	8	3	3	8	0.77	7.67	Aux
Proposed S ³ C7LBI	11	2	0	10	3	5.33	Self

N_{sw}- No. of Switches, N_{cap}-No. of Capacitors, N_D-No. of Diodes, N_d-No. of Gate Drivers, and TSV-Total Standing Voltage

3.2. Hardware Results

Experimental results have been reported as part of validating S³C7LBI topology. The parameters of the modulation scheme and the load utilized in this study are precisely the same as those considered in the simulation. The power electronic switches' gate signals are made using the DSP TMS32F28335 toolkit. Figure 9 displays the practical seven-level inverter output phase voltage, and Figure 10

shows the load current at an M value of 1.0. Figure 11 shows at M=1.0 displays the frequency spectrum for the load current and voltage. The hardware results confirm the practicality of the presented S³C7L boost inverter topology for real-time applications. Table 4 compares S³C7LBI with the existing MLI topologies regarding component count, gate driver requirements, increasing ability, Total Standing Voltage (TSV) and inherent capacitor voltage balancing.

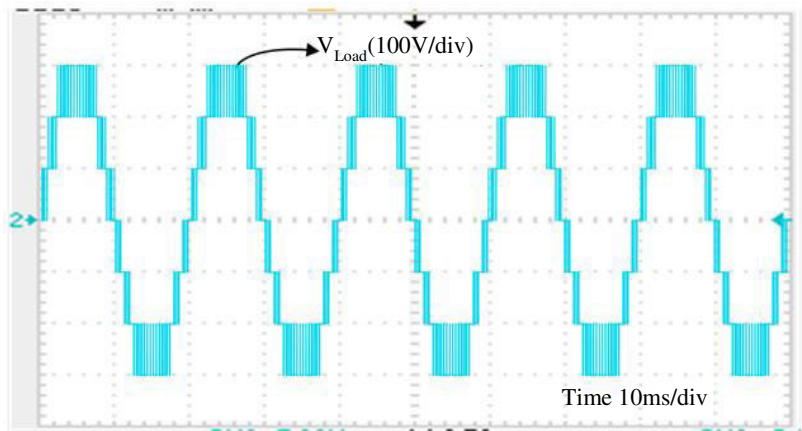


Fig. 9 Practical voltage waveform at M=1.0

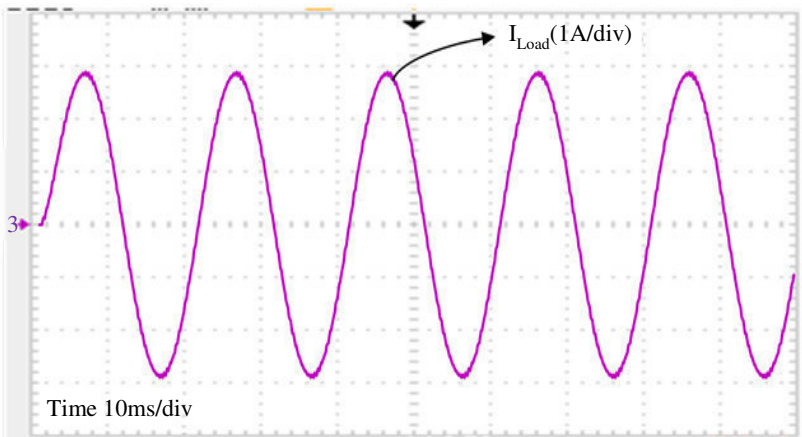


Fig. 10 Practical load current waveform at M=1.0

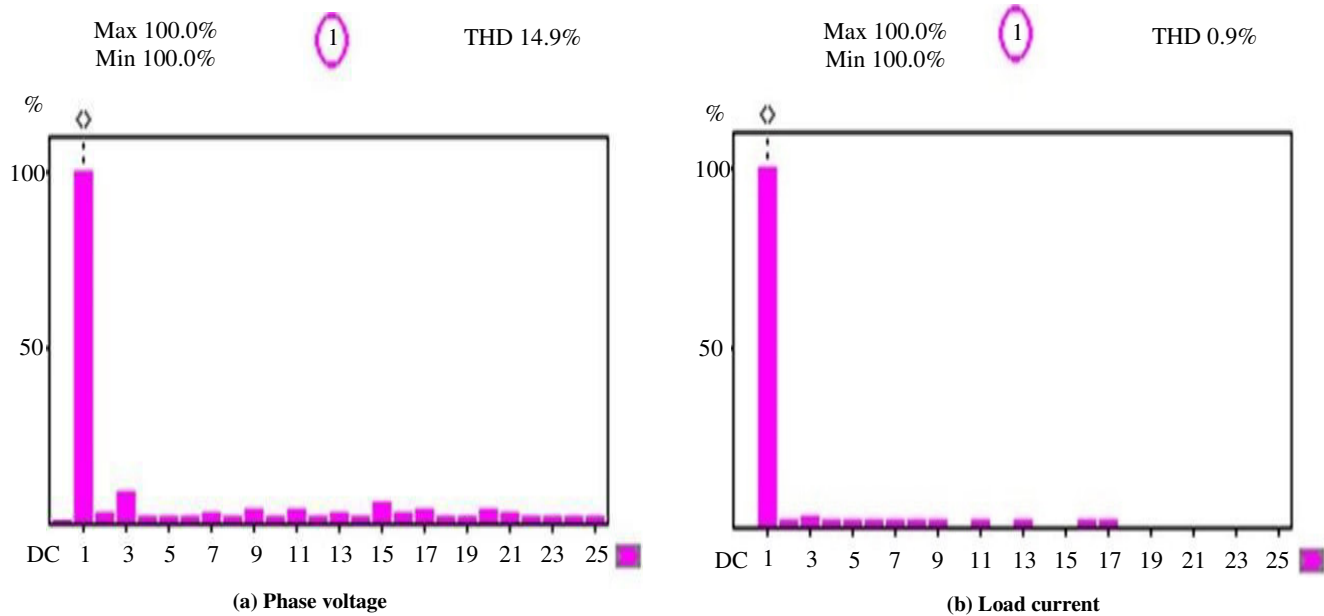


Fig. 11 Practical frequency spectra at unity modulation index

4. Conclusion

This paper presented a novel Single-Source Switching Capacitor Seven-Level Boost Inverter (S³C7LBI) architecture for solar PV applications. It has a more straightforward control method and fewer components. With a three-times boost, it produces 7-levels. Furthermore, the two capacitors may attain equilibrium at V_{DC} without the need for any further sensors or control algorithms. There is inherent capacitor balance in the circuit. Due to its simplified control mechanism, the accompanying peripheral model and sensors have been significantly reduced. Its supporting aspects are the inherent balance, low number of power switches, high voltage gain value, and affordability of the

S³C7LBI. It has been thought that the operating S³C7LBI architecture under dynamic situations is studied by using the sinusoidal PWM approach.

The MATLAB simulation results show the performance of the S³C7LBI topology, and two distinct load circumstances are taken into account in the simulation to determine the viability of the suggested topology. Additionally, experimental findings have been provided to support the viability of the S³C7LBI architecture that has been proposed. These results demonstrate that S³C7LBI can have closed-loop capability for solar photovoltaic applications.

References

- [1] Jih-Sheng Lai, and Fang Zheng Peng, "Multilevel Converters-A New Breed of Power Converters," *IEEE Transactions on Industry Applications*, vol. 32, no. 3, pp. 509-517, 1996. [[CrossRef](#)] [[Google Scholar](#)] [[Publisher Link](#)]
- [2] J. Rodriguez, Jih-Sheng Lai, and Fang Zheng Peng, "Multilevel Inverters: A Survey of Topologies, Controls, and Applications," *IEEE Transactions on Industrial Electronics*, vol. 49, no. 4, pp. 724-738, 2002. [[CrossRef](#)] [[Google Scholar](#)] [[Publisher Link](#)]
- [3] Mariusz Malinowski et al., "A Survey on Cascaded Multilevel Inverters," *IEEE Transactions on Industrial Electronics*, vol. 57, no. 7, pp. 2197-2206, 2010. [[CrossRef](#)] [[Google Scholar](#)] [[Publisher Link](#)]
- [4] B. Hemanth Kumar et al., "A Switched Capacitor-Based Multilevel Boost Inverter for Photovoltaic Applications," *Journal of Circuits, Systems and Computers*, vol. 32, no. 4, 2023. [[CrossRef](#)] [[Google Scholar](#)] [[Publisher Link](#)]
- [5] Kavali Janardhan et al., "Nine-Level Switched Capacitance Multi-Level Inverter with Charge Balance," *2023 IEEE Renewable Energy and Sustainable E-Mobility Conference (RESEM)*, Bhopal, India, pp. 1-6, 2023. [[CrossRef](#)] [[Google Scholar](#)] [[Publisher Link](#)]
- [6] G.G. Rajasekhar et al., "Seven Level Switched Capacitor Multilevel Boost Inverter for Renewable Energy Sources," *2023 International Conference on Advances in Electronics, Communication, Computing and Intelligent Information Systems (ICAECIS)*, Bangalore, India, pp. 643-646, 2023. [[CrossRef](#)] [[Google Scholar](#)] [[Publisher Link](#)]
- [7] Busireddy Hemanth Kumar et al., "Seventeen Level Switched Capacitor Boost Inverter for Renewable Energy Sources," *2023 IEEE Renewable Energy and Sustainable E-Mobility Conference (RESEM)*, Bhopal, India, pp. 1-6, 2023. [[CrossRef](#)] [[Google Scholar](#)] [[Publisher Link](#)]
- [8] Busireddy Hemanth Kumar et al., "Twenty-Five-Level Switched Capacitor Multilevel Boost Inverter for Solar PV Applications," *2023 IEEE Renewable Energy and Sustainable E-Mobility Conference (RESEM)*, Bhopal, India, pp. 1-6, 2023. [[CrossRef](#)] [[Google Scholar](#)] [[Publisher Link](#)]
- [9] Obayuwana A., and Igonoba E.E.C., "Design and Implementation of a Smart Prepaid Solar Inverter System," *International Journal of Recent Engineering Science*, vol. 7, no. 4, pp. 7-13, 2020. [[CrossRef](#)] [[Google Scholar](#)] [[Publisher Link](#)]
- [10] Kavali Janardhan et al., "High Gain Switched-Capacitor Multilevel Inverter," *2023 IEEE Renewable Energy and Sustainable E-Mobility Conference (RESEM)*, Bhopal, India, pp. 1-6, 2023. [[CrossRef](#)] [[Google Scholar](#)] [[Publisher Link](#)]
- [11] B. Hemanth Kumar et al., "A New Series-Parallel Switched Capacitor Configuration of a DC-DC Converter for Variable Voltage Applications," *Electric Vehicles*, pp. 247-270, 2021. [[CrossRef](#)] [[Google Scholar](#)] [[Publisher Link](#)]
- [12] Apurv Kumar Yadav et al., "A Hybrid 7-Level Inverter Using Low-Voltage Devices and Operation with Single DC-Link," *IEEE Transactions on Power Electronics*, vol. 34, no. 10, pp. 9844-9853, 2019. [[CrossRef](#)] [[Google Scholar](#)] [[Publisher Link](#)]
- [13] Manxin Chen et al., "A Six-Switch Seven-Level Triple-Boost Inverter," *IEEE Transaction on Power Electronics*, vol. 36, no. 2, pp. 1225-1230, 2021. [[CrossRef](#)] [[Google Scholar](#)] [[Publisher Link](#)]
- [14] M. Jagabar Sathik et al., "Seven-Level Boosting Active Neutral Point Clamped Inverter Using Cross-Connected Switched Capacitor Cells," *IET Power Electronics*, vol. 13, no. 9, pp. 1919-1924, 2020. [[CrossRef](#)] [[Google Scholar](#)] [[Publisher Link](#)]
- [15] Weijie Lin et al., "Hybrid Nine-Level Boost Inverter with Simplified Control and Reduced Active Devices," *IEEE Journal of Emerging and Selected Topics in Power Electronics*, vol. 9, no. 2, pp. 2038-2050, 2021. [[CrossRef](#)] [[Google Scholar](#)] [[Publisher Link](#)]
- [16] Pham Thi Thu Ha, "Research, Development and Application of Single-Phase Inverters in Industrial Machineries," *International Journal of Engineering Trends and Technology*, vol. 71, no. 5, pp. 98-105, 2023. [[CrossRef](#)] [[Publisher Link](#)]
- [17] Junfeng Liu, K.W.E. Cheng, and Yuanmao Ye, "A Cascade Multilevel Inverter Based on Switched-Capacitor for High-Frequency AC Power Distribution System," *IEEE Transaction on Power Electronics*, vol. 29, no. 8, pp. 4219-4230, 2014. [[CrossRef](#)] [[Google Scholar](#)] [[Publisher Link](#)]

- [18] Reza Barzegarkhoo et al., "Cascaded Multilevel Inverter Using Series Connection of Novel Capacitor-Based Units with Minimum Switch Count," *IET Power Electronics*, vol. 9, no. 10, pp. 2060-2075, 2016. [[CrossRef](#)] [[Google Scholar](#)] [[Publisher Link](#)]
- [19] Emad Samadaei, Mohammad Kaviani, and Kent Bertilsson, "A 13-Levels Module (K-Type) with Two DC Sources for Multilevel Inverters," *IEEE Transaction on Industrial Electronics*, vol. 66, no. 7, pp. 5186-5196, 2019. [[CrossRef](#)] [[Google Scholar](#)] [[Publisher Link](#)]
- [20] Hanyang Yu et al., "Hybrid Seven-Level Converter Based on T-Type Converter and H-Bridge Cascaded under SPWM and SVM," *IEEE Transaction on Power Electronics*, vol. 33, no. 1, pp. 689-702, 2018. [[CrossRef](#)] [[Google Scholar](#)] [[Publisher Link](#)]
- [21] Sze Sing Lee, and Kyo-Beum Lee, "Dual-T-Type 7-Level Boost Active-Neutral-Point-Clamped Inverter," *IEEE Transaction on Power Electronics*, vol. 34, no. 7, pp. 6031-6035, 2019. [[CrossRef](#)] [[Google Scholar](#)] [[Publisher Link](#)]
- [22] Sze Sing Lee, and Kyo-Beum Lee, "Switched-Capacitor-Based Modular T-Type Inverter," *IEEE Transaction on Industrial Electronics*, vol. 68, no. 7, pp. 5725-5732, 2021. [[CrossRef](#)] [[Google Scholar](#)] [[Publisher Link](#)]
- [23] Yuanmao Ye, Wei Peng, and Yong Yi, "Analysis and Optimal Design of Switched-Capacitor Seven-Level Inverter with Hybrid PWM Algorithm," *IEEE Transaction on Industrial Informatics*, vol. 16, no. 8, pp. 5276-5285, 2020. [[CrossRef](#)] [[Google Scholar](#)] [[Publisher Link](#)]
- [24] M. Jagabar Sathik, N. Sandeep, and Frede Blaabjerg, "High Gain Active Neutral Point Clamped Seven-Level Self-Voltage Balancing Inverter," *IEEE Transactions on Circuits and Systems II: Express Briefs*, vol. 67, no. 11, pp. 2567-2571, 2020. [[CrossRef](#)] [[Google Scholar](#)] [[Publisher Link](#)]
- [25] Hossein Khoun Jahan, Mehdi Abapour, and Kazem Zare, "Switched-Capacitor Based Single Source Cascaded H-Bridge Multilevel Inverter Featuring Boosting Ability," *IEEE Transaction on Power Electronics*, vol. 34, no. 2, pp. 1113-1124, 2019. [[CrossRef](#)] [[Google Scholar](#)] [[Publisher Link](#)]
- [26] Mehdi Samizadeh et al., "A New Topology of Switched-Capacitor Multilevel Inverter with Eliminating Leakage Current," *IEEE Access*, vol. 8, pp. 76951-76965, 2020. [[CrossRef](#)] [[Google Scholar](#)] [[Publisher Link](#)]
- [27] Cheng-Han Hsieh et al., "Design and Implementation of a Novel Multilevel DC-AC Inverter," *IEEE Transaction on Industrial Applications*, vol. 52, no. 3, pp. 2436-2443, 2016. [[CrossRef](#)] [[Google Scholar](#)] [[Publisher Link](#)]
- [28] Amir Taghvaie, Jafar Adabi, and Mohammad Rezanejad, "A Self-Balanced Step-Up Multilevel Inverter Based on Switched-Capacitor Structure," *IEEE Transaction on Power Electronics*, vol. 33, no. 1, pp. 199-209, 2018. [[CrossRef](#)] [[Google Scholar](#)] [[Publisher Link](#)]
- [29] Jin-Sung Choi, and Feel-Soon Kang, "Seven-Level PWM Inverter Employing Series-Connected Capacitors Paralleled to a Single DC Voltage Source," *IEEE Transaction on Industrial Electronics*, vol. 62, no. 6, pp. 3448-3459, 2015. [[CrossRef](#)] [[Google Scholar](#)] [[Publisher Link](#)]
- [30] B. Hemanth Kumar, and Makarand M. Lokhande, "Analysis of PWM Techniques on Multilevel Cascaded H-Bridge Three Phase Inverter," *2017 Recent Developments in Control, Automation & Power Engineering (RDCAPE)*, Noida, India, pp. 465-470, 2017. [[CrossRef](#)] [[Google Scholar](#)] [[Publisher Link](#)]
- [31] J. Holtz, "Pulse Width Modulation-A Survey," *IEEE Transactions on Industrial Electronics*, vol. 39, no. 5, pp. 410-420, 1992. [[CrossRef](#)] [[Google Scholar](#)] [[Publisher Link](#)]
- [32] B. Hemanth Kumar, and Makarand M. Lokhande, "Investigation of Switching Sequences on a Generalized SVPWM Algorithm for Multilevel Inverters," *Journal of Circuits, Systems and Computers*, vol. 28, no. 2, 2019. [[CrossRef](#)] [[Google Scholar](#)] [[Publisher Link](#)]
- [33] Qamar Muhammad Attique, Yongdong Li, and Kui Wang, "A Survey on Space-Vector Pulse Width Modulation for Multilevel Inverters," *CPSS Transactions on Power Electronics and Applications*, vol. 2, no. 3, pp. 226-236, 2017. [[CrossRef](#)] [[Google Scholar](#)] [[Publisher Link](#)]
- [34] B. Hemanth Kumar, and Makarand M. Lokhande, "An Enhanced Space Vector PWM for Nine-Level Inverter Employing Single Voltage Source," *2017 IEEE Transportation Electrification Conference (ITEC-India)*, Pune, India, pp. 1-6, 2017. [[CrossRef](#)] [[Google Scholar](#)] [[Publisher Link](#)]

Optimal protective relaying scheme of distributed generation connected distribution network using particle swarm optimization-gravitational search algorithm technique

Arathi Pothakanahalli Bheemasenarao, Shankaralingappa C. Byalihal

Department of Electrical and Electronics Engineering, Dr. Ambedkar Institute of Technology-Bengaluru,
Visvesvaraya Technological University, Karnataka, India

Article Info

Article history:

Received Jul 15, 2022

Revised Sep 22, 2022

Accepted Oct 1, 2022

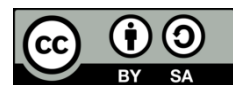
Keywords:

Distributed generation
Gravitational search algorithm
distribution system
Optimal relay coordination
particle swarm optimization

ABSTRACT

This paper develops particle swarm optimization integrated with gravitational search algorithm (PSO-GSA) to coordinate the relays in a distribution system with distributed generation (DG) connectivity. This algorithm combines PSO and GSA to improve the performance of the relay protection system. To prevent relay malfunctions following DG penetration, a suitable primary and backup relay is chosen. The PSO-GSA is coded using MATLAB software and tested on an IEEE 4-bus system simulated in Simulink. Results indicate that, when compared to using regular PSO and GSA procedures individually, the PSO-GSA technique reduces the operating time of the relay significantly.

This is an open access article under the [CC BY-SA](https://creativecommons.org/licenses/by-sa/4.0/) license.



Corresponding Author:

Arathi Pothakanahalli Bheemasenarao

Department of Electrical and Electronics Engineering, Dr. Ambedkar Institute of Technology-Bengaluru,
Visvesvaraya Technological University
Karnataka, India

Email: artilakshman72@gmail.com

1. INTRODUCTION

The topology of distribution systems has changed into a mesh structure resembling interconnected sub-transmission systems due to the integration of distributed generation (DG) into distribution networks [1]. Additionally, the direction of electrical power and short-circuit current are impacted by the integration of DG units. Short-circuit current that flows in both directions can cause safety relays to malfunction and, ultimately, bring down entire distribution networks [2]. For DG integrated distribution networks, various over-current relay safety strategies have been developed [3], [4]. However, it is noted that as the number and size of DG units in the distribution networks rise, so does the complexity of the design and coordination of protective relays [5]. Conventional protective relay solutions fail in these circumstances of offering the system the necessary protection against faults [6]. Additionally, replacing protective relays after a problem occurs entails high costs and is impractical for real-time applications. Replacements are advised to create effective coordination in protective relays [7]. To address the fundamental needs of relays, such as operation time and fault tolerance, coordination of protective relays refers to the capacity to determine appropriate setting values for overcurrent relays [8]. Power system stability is greatly influenced by proper relay coordination. Protective relays are in charge of clearing faults at each fault occurrence because, if one relay fails, the others should take over [9]. Backup relays are employed to prevent any malfunction or failure of the principal or primary protection relays. The backup relays are either put on the same or at other buses with the proper time between them. Two rules must be followed for the protective relays to operate reliably. The

flaws in the relay's protection zone should trip it initially. Second, defects outside the relay's safety zone should not cause it to trip. Back protection is advised due to the possibility that the main defense system would fail. The process of calculating the backup relay time delay is known as coordination of the protective relays [10]. The protective relays must be coordinated so that the backup relay's delay time is sufficient for the primary relay to clear the fault first in order to fulfil selective tripping. Coordination between primary and backup relays is essential to give the primary relay enough time to fix the issue before the backup relay [11]. Relays are generally utilized more frequently as protective devices in distribution networks since they tend to be radial. The working duration of every relay should be significantly reduced with optimal time multiplier setting (TMS) and plug setting (PS) to increase the stability and dependability of the distribution network [12]. To improve the protective relays' performance and reduce the tripping time in these systems, several optimization strategies have been put forth. These methods prioritize operational time as their primary objective function and maximize operational time based on the relays' characteristic curves and predetermined coordination limitations. Maintaining the reliability of the power system integrated with DG systems requires proper relay coordination. When DG is not integrated, the distribution system's power flow is unidirectional. However, many parts of the distribution system now have bidirectional power flow, making conventional protection techniques that only consider one-way power flow unsuitable.

It is challenging to achieve ideal coordination between the relays due to the nonlinearity of the distribution networks, especially in larger distribution systems. Additionally, in these systems, the relay's operational times should be shortened to improve the efficiency of the protective circuits [13]. By achieving the optimal settings for every relay in the power system, several researchers have suggested various optimization strategies for cutting the operational time and increasing the coordination of relays in distribution networks. When used for complicated and nonlinear optimization systems, a hybrid random walk grey wolf optimizer (RW-GWO) technique is suggested for tackling the issue of local minima and issues associated with stagnation to local optima [14]. To find the best setting for relays in extremely complex distribution networks, the proposed RW-GWO is applied. The outcomes are compared with basic GWO algorithms and other optimization strategies. The outcomes illustrated the approach's potential for achieving the ideal conditions for effective relay coordination.

In recent years, a variety of meta-heuristic and swarm intelligence-based algorithms that include simulated annealing (SA) [15], artificial bee colonies (ABC) [16], genetic algorithms (GA) [17], and particle swarm optimization (PSO) [18] have been widely used to solve the challenging and nonlinear relay coordination issues. Plug and time multiplier settings were suggested as variables that govern how over current relays (OCRs) operate by researchers who proposed optimization of directional over current relay using PSO [19]. The objective is to reduce all relays' operational times while utilizing PSO. PSO algorithm has been tested in typical 3-bus, 4-bus, and 6-bus systems. The findings suggested that the PSO had achieved reduced plug setting and time multiplier setting values with the best possible coordination for all standard bus systems. In [20], a firefly algorithm (FA) is used with a bio-inspired design to coordinate relays in the best possible way to safeguard the DG-connected power supply. The basic FA is often achieved by choosing the power systems' proper plug and time multiplier settings. However, the implementation had particular difficulties, including delayed convergence and the danger of becoming trapped in local optima. The paper developed an adaptive modified FA (AMFA) technique to get around this restriction. The AMFA was used to coordinate overcurrent relays in the best possible way. Five separate test scenarios were used to evaluate the performance of the suggested approach, and the outcomes were compared using fundamental FA and other traditional approaches. In all case studies, the results demonstrated improved performance of AMFA in terms of optimized relay coordination, with excellent time reductions of up to 40.446%. Genetic algorithm (GA)-based relay coordination that is optimal was covered in [21]. Instead of employing a single curve for all relays as is done in several standard methods, the study used the characteristic curves of directional overcurrent relays as decision-making criteria. The experimental analysis was conducted using a variety of IEEE and IEC curves and the IEC benchmark. Results confirm that the suggested GA-based structure is adaptable. Additionally, this approach's outcomes were compared with other frameworks already in use, significantly reducing operational times and offering reliable protection for power systems against various faults. Distribution systems need more protection relays so problems may be cleared as rapidly as possible. The distribution system uses both primary and backup relays [22]. The two key relay characteristics of selectivity and sensitivity are crucial for the stability and reliability of the distribution network. When a fault occurs, the primary relay sends the tripping signal before the backup relay, which then serves as a supportive relay when the first relay malfunctions.

This paper investigates the optimal relay coordination in DG linked distribution networks using a hybrid heuristic technique that combines PSO and gravitational search algorithm (GSA). The proposed PSO-GSA is used to select appropriate relay settings in the distribution network. To avoid relay problems after DG penetration, a suitable primary and backup relay is selected.

2. PROBLEM FORMULATION

The coordination issue in protective relays is established based on operational constraints like coordination standards and operating time. To solve the optimization problem, limits on the pickup current, operation time, and properties of the relay are applied. These restrictions are part of the goal function for optimization. In the shortest period of time, the function optimizes the functioning time of each protective relay. The objective function is expressed as (1):

$$\text{minimize } s = \sum_{i=1}^n t_{p,q} \quad (1)$$

where $t_{p,q}$ is defined as the operational time of the p^{th} relay for fault in q^{th} zone. The constraints for solving the objective function are defined [23].

2.1. Coordination criteria

The coordination criteria are defined as (2):

$$t_{b,p,q} - t_{p,q} \geq \Delta t \quad (2)$$

where $t_{p,q}$ is defined as the operational time of the p^{th} relay for fault in q^{th} zone and $t_{bp,q}$ is the operating time of the backup relay for the fault in zone q , and Δt is defined as the coordination time interval (CTI).

2.2. Limits on operating time of relay

Protective relays should be used inside the boundary limitations to ensure good coordination between the primary and backup relays. They are described in this section. Relay operational time is constrained using (3):

$$t_{p,q \min} \leq t_{p,q} \leq t_{p,q \max} \quad (3)$$

where $t_{p,q \min}$ and $t_{p,q \max}$ is defined as the minimum and maximum operating time of the protective relay for the p^{th} relay for fault in the q^{th} zone.

2.3. Limits on pickup current

The maximum load current I_{pmax} and minimum fault current I_{pmin} , respectively, define the lowest and maximum values of the pickup current in a relay. The (4) provides the pickup relay current I_p limitation. This specifies the limit on relay plug setting multiplier (PSM) defined by (5).

$$I_{p \min} \leq I_p \leq I_{p \max} \quad (4)$$

$$PSM_{\min} \leq PSM \leq PSM_{\max} \quad (5)$$

PSM_{\max} and PSM_{\min} are the maximum and minimum limits of PSM. Adjusting the relay tripping time for optimized coordination is possible using the TMS term. This is usually calculated from the plug setting of the relay. Hence the limit on TMS is constituting as given in (6).

$$TMS_{p,k \min} \leq TMS_{p,k} \leq TMS_{p,k \max} \quad (6)$$

2.4. Relay characteristics

In this study, all the relays are identical in nature with a uniform inverse definite minimum time (IDMT) defined as [24]:

$$top = \frac{\lambda(TMS)}{(PSM)^{\gamma}-1} \quad (7)$$

$$t_{op} = \frac{\lambda(TMS)}{\left(\frac{I_{relay}}{PS} * CT \text{ sec rated}\right)^{\gamma}-1} \quad (8)$$

where t_{op} is described as the relay's operational time, and PS and TMS are described as the plug setting and time multiplier setting, respectively. Current transformer (CT) secondary rated current is known as CT sec, while relay fault current is known as I_{relay} . The values of λ and γ for the typical inverse definite minimum time (IDMT) characteristic relay are typically 0.14 and 0.02, respectively. Therefore, PS and TMS are the

two parameters we will use for PSO-GSA optimization. In this implementation, the Pug setting and the TMS of the relays are optimized for relay coordination using a PSOGSA-based method.

3. OPTIMIZATION USING PSO-GSA

3.1. Particle swarm optimization (PSO)

Eberhart and Kennedy created the population-based stochastic optimization called PSO method in 1995. A swarm of birds changes its direction from earlier locations to find food. This behavior of birds is converted mathematically as a PSO algorithm. An adaptive algorithm based on bird behavior [25]. Every iteration of the PSO process involves a constant updating of the particle position and velocity parameters. New determined velocity data update the position of the particles after each cycle [26]. The updated velocity value is calculated as the difference between the current location and the prior and global best positions, or p_{best} and g_{best} , respectively. The resulting updated value will be applied to the calculation of the swarm's next position. Velocity function of the PSO algorithm is given in (9).

$$V_{i(t+1)} = kV_{it} + C_1 * rand * (p_{best} - X_{it}) + C_2 * rand * (g_{best} - X_{it}) \quad (9)$$

Particle initially generated for the first iteration is updated using the (10):

$$X_{i(t+1)} = X_{it} + V_{i(t+1)} \quad (10)$$

where V_{it} and X_{it} is defined as the velocity and current position of particle i at iteration t , p_{best} is the best agent obtained at every iteration, g_{best} is the best solution obtained for all the previous iterations, C_1 , C_2 and k are the weighting factor and weighing function respectively, 'rand' is the random number between 0 to 1.

3.2. Gravitational search algorithm (GSA)

GSA is a population-based metaheuristic technique, like PSO, that is governed by Newton's laws of motion and gravitation. In GSA, particles are known as agents. In GSA, where the agents are referred to as objects, agents are determined from their masses. Due to the gravitational pull of the items toward one another, mass is accumulated by all of the objects [27]. The force between the objects is directly equal to the product of their masses and inversely proportional to the square of the distance between them [28]. The particles in the GSA are determined by four variables: inertial mass, active and passive gravitational mass, and position of the mass in the d^{th} dimension. The values for these parameters are determined by the particles' fitness value [29]. The pressure exerted by two particles j [11]:

$$F_{ij}^d = G(t) \frac{M_{pi}(t) \times M_{aj}(t)}{R_{ij}(t) + \epsilon} (x_j^d(t) - x_i^d(t)) \quad (11)$$

where M_{aj} and M_{pj} are described as the gravitationally-related active and passive masses for particles i and j , respectively. $R_{ij}(t)$ is the Euclidean distance between two particles i and j , $G(t)$ is the gravitational constant at time t , and ϵ is the small constant. The (12) provides a formula for calculating the gravitational constant

$$G(t) = G_0 * \exp[-\alpha * (iter / \max \text{ iter})] \quad (12)$$

where G_0 and α are the initial value and descending coefficient respectively, $iter$ is the value of the current iteration and $\max \text{ iter}$ defines the maximum number of iterations. In the search space of d^{th} dimension, the total force acting against particle i is expressed as given in (13):

$$F_i^d(t) = \sum_{j=1, j \neq i}^N rand_j F_{ij}^d(t) \quad (13)$$

where the random number between 0 and 1 is called $rand_j$. According to Newton's equation of motion, a particle's acceleration is inversely related to its mass and directly proportionate to the generated force. Consequently, the definition of each particle's acceleration is:

$$A_i^d(t) = \frac{F_i^d(t)}{M_{ii}(t)} \quad (14)$$

where M_{ii} is the mass of the particle i . Lastly, the velocity and position of the particle i at d^{th} dimension space is determined as (15) and (16).

$$Vel_{id(t+1)} = rand_i * Vel_{id(t)} + A_{id(t)} \quad (15)$$

$$X_{id(t+1)} = X_{id(t)} + Vel_{id(t+1)} \quad (16)$$

3.3. Hybrid particle swarm optimization gravitations search algorithm (PSO-GSA)

In this implementation, the PSO is combined with the GSA to form a hybridized algorithm known as PSO-GSA. In PSO-GSA, the characteristics and functionalities of both algorithms are integrated and both algorithms are executed in parallel. The hybrid approach is heterogeneous in nature since it involves two different algorithms. The proposed PSO-GSA possesses the ability of PSO along with the local searching ability of GSA. The velocity and position of the particle in the hybridized approach is evaluated as given in (17) and (18).

$$Vi(t + 1) = k * Vi(t) + C1 * rand * aCi(t) + C2 * rand * (gbest - Xi(t)) \quad (17)$$

$$Xi(t + 1) = Xi(t) + Vi(t + 1) \quad (18)$$

The flowchart of the proposed PSO-GSA is illustrated in Figure 1.

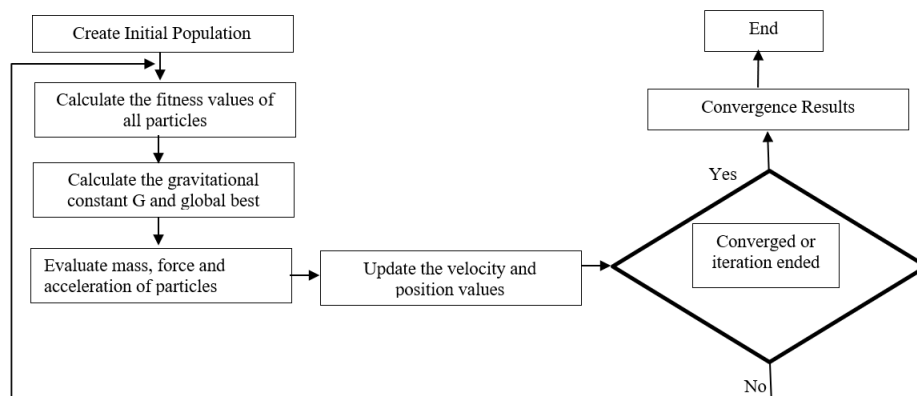


Figure 1. Flowchart of PSO-GSA

4. RESULTS AND DISCUSSION

As seen in Figure 2, a 4-bus radial system is used, with an 11 kV step-down voltage for the grid. By using the PSOGSA technique, the optimal TMS and PS values of the six relays that are present in each bus are determined. Here, this optimization is accomplished using the MATLAB platform. At the very end of each relay, faults are produced. The malfunction started after 0.5 seconds. The IEEE 4 bus system contains 6 relays and the CT ratio of each relay is tabulated in Table 1.

The IEEE 4-bus system is used to verify the relay coordination utilizing PSOGSA, as shown in Figure 3. As mentioned in section 3, the relay coordination problem's objective function is formulated. The performance of the relay coordination is determined using different parameters such as Relay number, number of turns on primary of current transformer, TDS, load factor, fault current, load current, PSM. Simulation is performed using MATLAB and the Simulink model is illustrated in Figure 3.

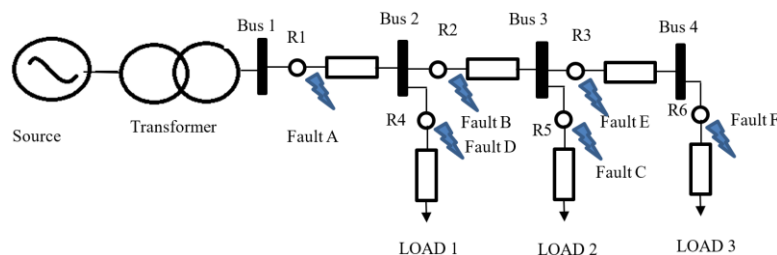


Figure 2. Single source 4-bus radial system

Table 1. CT ratios of each relay

Relay No	CT Ratio
1	1000/1
2	800/1
3	600/1
4	600/1
5	600/1
6	600/1

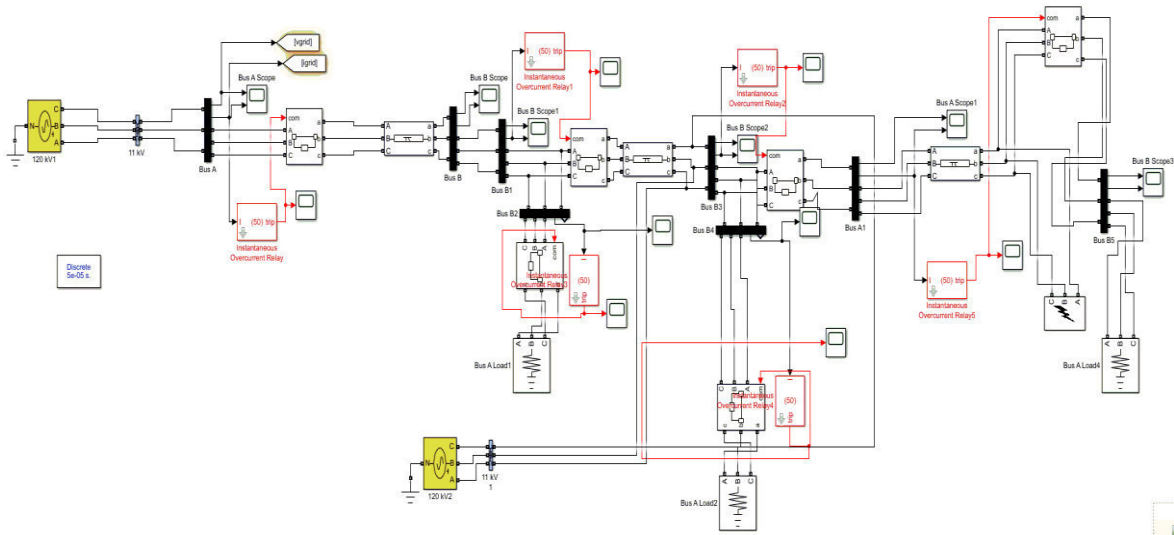


Figure 3. Simulink model of the IEEE 4-bus system

4.1. Case 1: without DG

The Simulink model shown in Figure 3 will be simulated without connecting the DG and the relay currents at different fault positions are shown in Figures 4, 5, and 6. The optimal values of relay settings are given in Tables 2 and 3. In Case 1, PSO and GSA provide TMS that is less than PSO-GSA for all relays, while PSO-GSA provide PSM that is less than PSO and GSA. This is even significant because overall calculations reveal that PSOGSA computes total operating time to be reduced, leading to speedier relay operation. Table 4 gives the operating time of all relays for six faults.

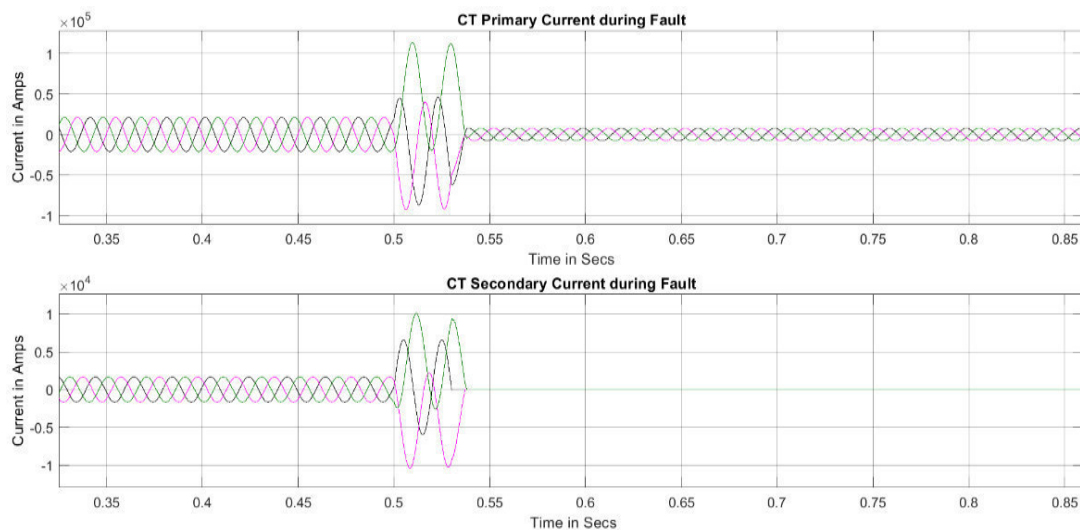


Figure 4. Fault current in primary side of CT for Relay 1 and 2 for fault point A

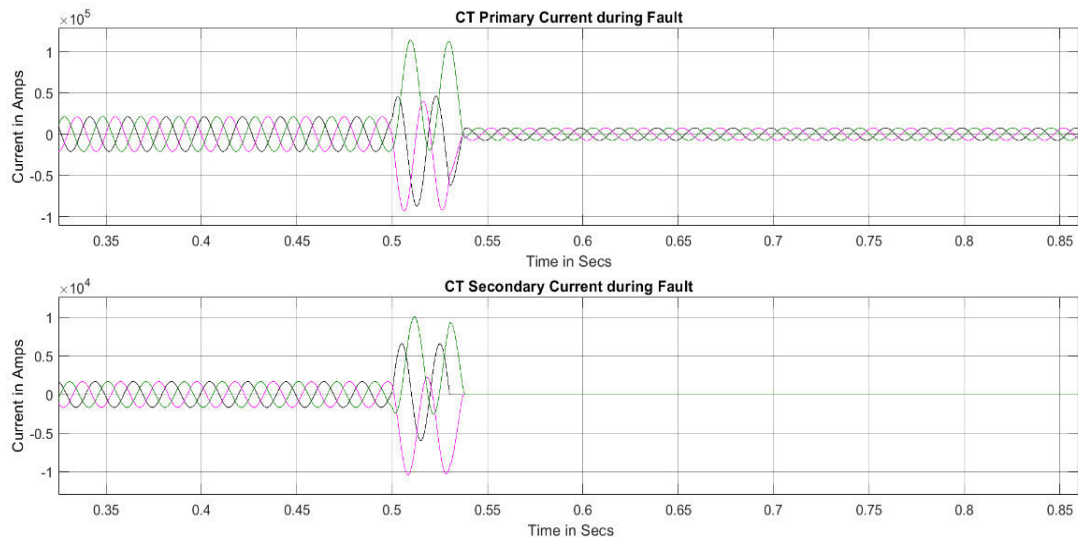


Figure 5. Fault current in primary side of CT for Relay 2 and 1 for fault point B

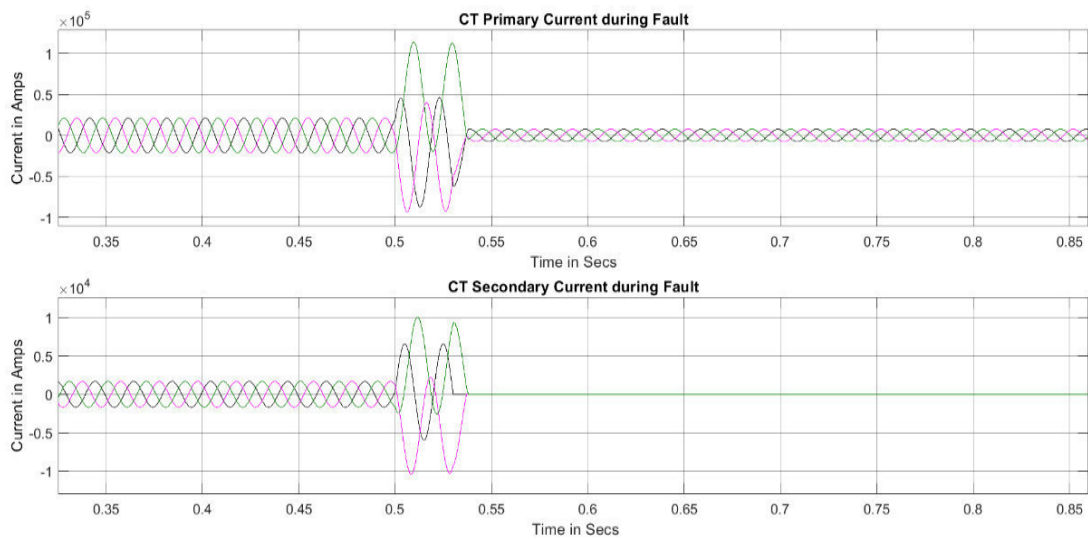


Figure 6. Fault current in primary side of CT for Relay 4 and 2 for fault point C

Table 2. Comparison of TMS values

Faults	PSO	GSA	PSOGSA
Fault 1	0.084	0.1	0.4
Fault 2	0.08	0.09	0.53
Fault 3	0.08	0.1	0.27
Fault 4	0.08	0.14	0.41
Fault 5	0.09	0.08	0.45
Fault 6	0.08	0.08	0.53

Table 3. Comparison of PSM values

Faults	PSO	GSA	PSOGSA
Fault 1	0.99	0.99	0.27
Fault 2	1.07	1.00	0.33
Fault 3	1.24	0.99	2.68
Fault 4	1.14	1.09	0.84
Fault 5	1.10	1.23	0.69
Fault 6	1.04	1.02	0.14

Table 4. Operating time of relays for different fault points

Faults	Primary Relay	Operating Time in seconds	Secondary Relay	Operating Time	CTI
Fault 1	R1	0.7	R2	1.53	0.83
Fault 2	R2	0.85	R1	1.22	0.37
Fault 3	R3	1.67	R2	2.6	0.93
Fault 4	R4	1.1	R2	1.69	0.59
Fault 5	R5	1.02	R4	1.54	0.52
Fault 6	R6	0.7	R4	1.32	0.62

4.2. Case II: with DG (26.6%)

When demand rises at certain of the load centers, the additional load is managed by either raising main grid generation or DG penetration levels. In order to clarify how a reliable relay function can be guaranteed under fault conditions at any of these penetration levels, a case study is given. The DG penetration level is given as:

$$\% \text{ DG Penetration level} = \frac{P_{DG}}{P_{DG} + P_{Grid}} * 100$$

As the load increases, DG penetration grows. In terms of penetration percentage, a 50% load increment is equivalent to 33.33% of DG level, which can be regarded as the upper bound [30]. Taken are two situations at 26.66% and 31.25%. In the case study, DG is inserted into the network at bus 3 with a penetration level of 26.66%. The fault current is adjusted in relay 1 for fault point 1. The values of TMS and PSM for 26.6% penetration are given in Table 5.

Table 5. TMS and PSM of relays using PSOGSA for 26.6% DG penetration

Faults	PSM	TMS
Fault 1	2.15	0.2
Fault 2	2.87	0.1
Fault 3	2.64	0.27
Fault 4	0.31	0.53
Fault 5	0.24	0.53
Fault 6	0.05	0.53

The currents that contribute to the fault current for the DG added system may flow in two directions. Although the aggregate fault current values grow with DG penetration of 26.6%, faults 2 and 3 only contribute a very little amount. As soon as a defect develops, it is seen that relays 4, 5, and 6 experience an increase in current magnitude. Table 5 shows the operation time and CTI between relays with a DG penetration level of 26.6%. The CTI measured are more than 0.3S, indicating successful coordination. Figure 7 shows the convergence graph for this scenario. This graph illustrates how PSOGSA converges to a better solution, or one that requires the least amount of operating time. Each operation's total operation time value is examined.

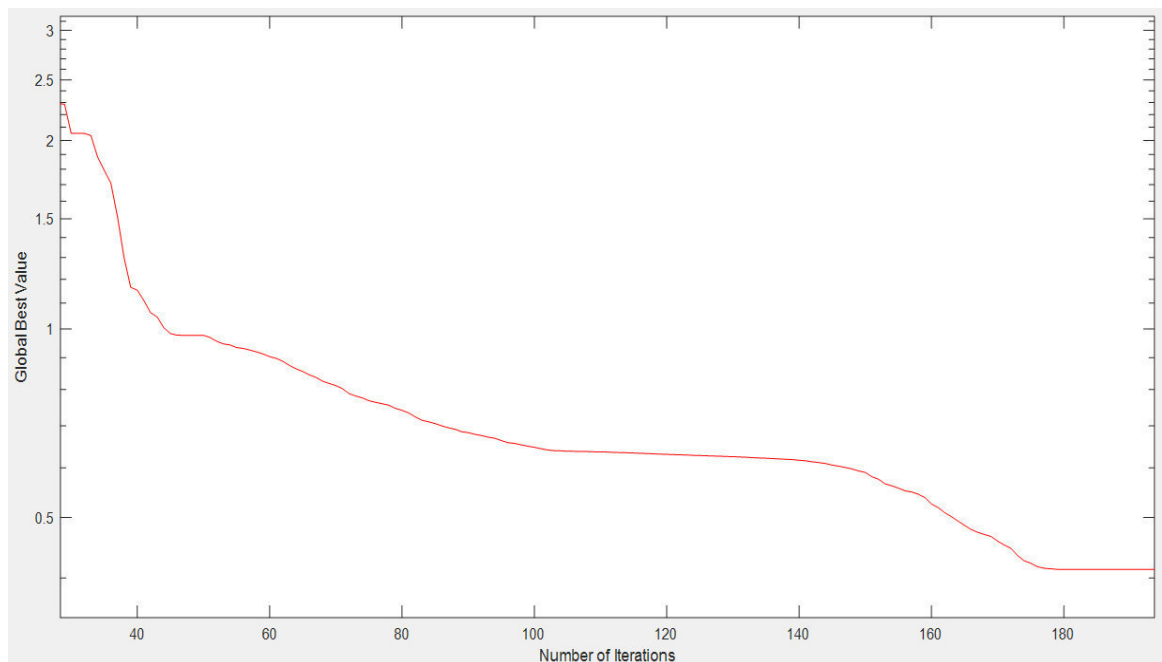


Figure 7. Convergence graph

4.3. Case III: with DG (31.25%)

In this instance, DG is applied to Bus 3 with a 31.25% DG penetration. Table 6 displays the obtained TMS and PSM for this example, whereas Table 7 displays the operating time and CTI values for each case. Tables 6 and 8 show the operation time and CTI between relays for 26.6% and 31.25%, respectively. The CTI recorded in both situations is greater than 0.3s in the majority of the faults, demonstrating proper coordination. Additionally, it appears that as DG penetration levels climb, relay operation times shorten. For instance, at faults 1 and 2, the relay starts to run at a DG level of 26.6% after 0.53 and 1.21 S, respectively, then it decreases to 0.48 and 0.53 S when penetration increases to 31.25%. The IDMT relay operates for a shorter period of time as a result of the system's total fault current level gradually rising.

Table 6. Operating time of relays for different fault points (26.6%)

Faults	Primary Relay	Operating Time in seconds	Secondary Relay	Operating Time in seconds	CTI in seconds
Fault 1	R1	0.53	-	-	-
Fault 2	R2	1.21	R1	2.79	1.58
Fault 3	R3	0.52	R1	1.1	0.58
Fault 4	R4	0.16	R1	1.25	1.09
Fault 5	R5	0.11	R2	0.95	0.84
Fault 6	R6	0.16	R4	0.37	0.21
Total Operating Time in seconds		2.69		6.46	

Table 7. TMS and PSM of relays using PSO-GSA for 31.25% DG penetration

Faults	PSM	TMS
Fault 1	1.83	0.22
Fault 2	2.45	0.14
Fault 3	2.68	0.27
Fault 4	0.32	0.53
Fault 5	0.32	0.53
Fault 6	0.07	0.53

Table 8. Operating time of relays for different fault points (31.25%)

Faults	Primary Relay	Operating Time in seconds	Secondary Relay	Operating Time in seconds	CTI in seconds
Fault 1	R1	0.48	R2	2.21	1.73
Fault 2	R2	0.53	R1	0.95	0.42
Fault 3	R3	0.52	R2	0.81	0.29
Fault 4	R4	0.1	R1	0.96	0.86
Fault 5	R5	0.08	R2	0.92	0.84
Fault 6	R6	0.17	R4	0.36	0.2
Total Operating Time		1.88		6.21	

4.4. Comparative analysis

By contrasting the outcomes with an existing optimization strategy described in [30], the performance of the new PSO-GSA algorithm was confirmed. Tables 9 and 10, respectively, present the results of the previously completed work and the anticipated work. It can be inferred from the comparative results that the proposed algorithm reduces the operating time for both primary and backup relays. Results validate the fact that the proposed optimization technique can reduce the operating time which in turn improves the performance of the relays during fault condition.

Table 9. Performance of primary and backup relay of existing work for 26.6% DG penetration

Fault Point	Primary relay unit		Backup relay unit		CTI (sec)
	Relay	Operating Time (sec)	Relay	Operating Time (sec)	
Fault 1	1	0.98	-	-	-
Fault 2	2	0.69	1	1.00	0.31
Fault 3	3	0.45	2	0.77	0.31
Fault 4	4	0.35	1	1.01	0.65
Fault 5	5	0.37	2	0.77	0.39
Fault 6	6	0.22	3	0.54	0.31

Table 10. Performance of primary and backup relay of the proposed PSOGSA for 26.6% DG penetration

Fault Point	Primary Relay Unit		Backup Relay Unit		CTI (sec)
	Relay	Operating Time (sec)	Relay	Operating Time (sec)	
Fault 1	1	0.53	-	-	-
Fault 2	2	1.21	1	2.79	1.58
Fault 3	3	0.52	1	1.1	0.58
Fault 4	4	0.16	1	1.25	1.09
Fault 5	5	0.11	2	0.95	0.84
Fault 6	6	0.16	4	0.37	0.21

5. CONCLUSION

In order to reduce the total working time of the relays in an IEEE 4 bus system, an optimal PSM and TMS of six relays are found. This is done using a hybrid PSO-GSA optimization technique. The maximum load current and lowest fault current are used to determine the range of plug settings for each relay. All of the overcurrent relay situations are coordinated, and the collected data are summarized to confirm the efficiency of PSOGSA. The protective relay may operate more quickly while still meeting the coordination restrictions when the objective function is minimized, validating PSOGSA as a possible optimization strategy for relay coordination in the distribution network. Additionally, the outcomes demonstrate that the suggested optimization technique outperforms the individual standard PSO and GSA findings and can be applied to the distribution system to improve dependability. This implementation, in contrast to the previous one, uses the IEEE bus system model from Simulink. To validate the relay coordination in a future implementation, a sizable bus system must be taken into account. To achieve relay coordination and validation with prior results, a variety of hybrid optimization strategies must be used.




REFERENCES

- [1] J. Teng, "Unsymmetrical short-circuit fault analysis for weakly meshed distribution systems," *IEEE Transactions on Power Systems*, vol. 25, no. 1, pp. 96–105, Feb. 2010, doi: 10.1109/TPWRS.2009.2036485.
- [2] K. A. Saleh, H. H. Zeineldin, A. Al-Hinai, and E. F. El-Saadany, "Optimal coordination of directional overcurrent relays using a new time-current-voltage characteristic," *IEEE Transactions on Power Delivery*, vol. 30, no. 2, pp. 537–544, Apr. 2015, doi: 10.1109/TPWRD.2014.2341666.
- [3] F. Adelnia, Z. Moravej, and M. Farzinfar, "A new formulation for coordination of directional overcurrent relays in interconnected networks," *International Transactions on Electrical Energy Systems*, vol. 25, no. 1, pp. 120–137, Jan. 2015, doi: 10.1002/etep.1828.
- [4] S. M. A. Mosavi, T. A. Kejani, and H. Javadi, "Optimal setting of directional over-current relays in distribution networks considering transient stability," *International Transactions on Electrical Energy Systems*, vol. 26, no. 1, pp. 122–133, Jan. 2016, doi: 10.1002/etep.2072.
- [5] H. Yang, F. Wen, and G. Ledwich, "Optimal coordination of overcurrent relays in distribution systems with distributed generators based on differential evolution algorithm," *International Transactions on Electrical Energy Systems*, vol. 23, no. 1, pp. 1–12, Jan. 2013, doi: 10.1002/etep.635.
- [6] A. H. Reza, "New method on the relays protective coordination due to presence of distributed generation," in *2012 Power Engineering and Automation Conference*, Sep. 2012, pp. 1–4, doi: 10.1109/PEAM.2012.6612449.
- [7] M. Patidar, "Optimal relay coordination scheme used for interconnected power system," *Electric Power Systems Research*, vol. 127, pp. 53–63, 2015, doi: 10.1016/j.epsr.2015.05.007.
- [8] T. S. Aghdam, H. K. Karegar, and H. H. Zeineldin, "Optimal coordination of double-inverse overcurrent relays for stable operation of DGs," *IEEE Transactions on Industrial Informatics*, vol. 15, no. 1, pp. 183–192, Jan. 2019, doi: 10.1109/TII.2018.2808264.
- [9] S. V. Khond and G. A. Dhokane, "Optimum coordination of directional overcurrent relays for combined overhead/cable distribution system with linear programming technique," *Protection and Control of Modern Power Systems*, vol. 4, no. 1, Dec. 2019, doi: 10.1186/s41601-019-0124-6.
- [10] H. R. E. H. Boucekara, M. Zellaoui, and M. A. Abido, "Optimal coordination of directional overcurrent relays using a modified electromagnetic field optimization algorithm," *Applied Soft Computing*, vol. 54, pp. 267–283, May 2017, doi: 10.1016/j.asoc.2017.01.037.
- [11] A. R. Al-Roomi and M. E. El-Hawary, "optimal coordination of double primary directional overcurrent relays using a new combinational BBO/DE algorithm," *Canadian Journal of Electrical and Computer Engineering*, vol. 42, no. 3, pp. 135–147, 2019, doi: 10.1109/CJECE.2018.2802461.
- [12] P. P. Bedekar, S. R. Bhide, and V. S. Kale, "Determining optimum TMS and PS of overcurrent relays using linear programming technique," in *The 8th Electrical Engineering/ Electronics, Computer, Telecommunications and Information Technology (ECTI) Association of Thailand-Conference 2011*, May 2011, pp. 700–703, doi: 10.1109/ECTICON.2011.5947936.
- [13] A. Azari and M. Akhbari, "Optimal coordination of directional overcurrent relays in distribution systems based on network splitting," *International Transactions on Electrical Energy Systems*, vol. 25, no. 10, pp. 2310–2324, Oct. 2015, doi: 10.1002/etep.1962.
- [14] S. Gupta and K. Deep, "Optimal coordination of overcurrent relays using improved leadership-based grey wolf optimizer," *Arabian Journal for Science and Engineering*, vol. 45, no. 3, pp. 2081–2091, Mar. 2020, doi: 10.1007/s13369-019-04025-z.
- [15] A. A. Kida, A. E. Labrador Rivas, and L. A. Gallego, "An improved simulated annealing-linear programming hybrid algorithm applied to the optimal coordination of directional overcurrent relays," *Electric Power Systems Research*, vol. 181, Apr. 2020, doi: 10.1016/j.epsr.2020.106197.
- [16] M. Singh, B. K. Panigrahi, and A. R. Abhyankar, "Optimal coordination of electro-mechanical-based overcurrent relays using artificial bee colony algorithm," *International Journal of Bio-Inspired Computation*, vol. 5, no. 5, 2013, doi:




- 10.1504/IJBIC.2013.057196.
- [17] M. Thakur and A. Kumar, "Optimal coordination of directional over current relays using a modified real coded genetic algorithm: A comparative study," *International Journal of Electrical Power and Energy Systems*, vol. 82, pp. 484–495, Nov. 2016, doi: 10.1016/j.ijepes.2016.03.036.
 - [18] A. Wadood, C.-H. Kim, T. Khurshid, S. Farkoush, and S.-B. Rhee, "Application of a continuous particle swarm optimization (CPSO) for the optimal coordination of overcurrent relays considering a penalty method," *Energies*, vol. 11, no. 4, Apr. 2018, doi: 10.3390/en11040869.
 - [19] D. Vyas, P. Bhatt, and V. Shukla, "Coordination of directional overcurrent relays for distribution system using particle swarm optimization," *International Journal of Smart Grid and Clean Energy*, pp. 290–297, 2020, doi: 10.12720/sgce.9.2.290-297.
 - [20] A. Tjahjono *et al.*, "Adaptive modified firefly algorithm for optimal coordination of overcurrent relays," *IET Generation, Transmission and Distribution*, vol. 11, no. 10, pp. 2575–2585, Jul. 2017, doi: 10.1049/iet-gtd.2016.1563.
 - [21] S. D. Saldarriaga-Zuluaga, J. M. López-Lezama, and N. Muñoz-Galeano, "An approach for optimal coordination of over-current relays in microgrids with distributed generation," *Electronics*, vol. 9, no. 10, Oct. 2020, doi: 10.3390/electronics9101740.
 - [22] A. Srivastava, J. M. Tripathi, S. R. Mohanty, and B. Panda, "Optimal over-current relay coordination with distributed generation using hybrid particle swarm optimization-gravitational search algorithm," *Electric Power Components and Systems*, vol. 44, no. 5, pp. 506–517, Mar. 2016, doi: 10.1080/15325008.2015.1117539.
 - [23] Adhishree, J. M. Tripathi, S. R. Mohanty, and N. Kishor, "A simulation based comparative study of optimization techniques for relay coordination with Distributed generation," in *2014 Students Conference on Engineering and Systems*, May 2014, pp. 1–6, doi: 10.1109/SCES.2014.6880088.
 - [24] A. Fazanehradat, S. A. M. Javadian, S. M. T. Bathaee, and M.-R. Haghifam, "Maintaining the recloser-fuse coordination in distribution systems in presence of DG by determining DG's size," in *IET 9th International Conference on Developments in Power Systems Protection (DPSP 2008)*, 2008, pp. 132–137, doi: 10.1049/cp:20080024.
 - [25] F. Marini and B. Walczak, "Particle swarm optimization (PSO). A tutorial," *Chemometrics and Intelligent Laboratory Systems*, vol. 149, pp. 153–165, Dec. 2015, doi: 10.1016/j.chemolab.2015.08.020.
 - [26] H. S. Ramadan, A. F. Bendary, and S. Nagy, "Particle swarm optimization algorithm for capacitor allocation problem in distribution systems with wind turbine generators," *International Journal of Electrical Power and Energy Systems*, vol. 84, pp. 143–152, Jan. 2017, doi: 10.1016/j.ijepes.2016.04.041.
 - [27] E. Rashedi, E. Rashedi, and H. Nezamabadi-pour, "A comprehensive survey on gravitational search algorithm," *Swarm and Evolutionary Computation*, vol. 41, pp. 141–158, Aug. 2018, doi: 10.1016/j.swevo.2018.02.018.
 - [28] E. Rashedi, H. Nezamabadi-pour, and S. Saryazdi, "GSA: a gravitational search algorithm," *Information Sciences*, vol. 179, no. 13, pp. 2232–2248, Jun. 2009, doi: 10.1016/j.ins.2009.03.004.
 - [29] M. Singh, "Protection coordination in grid connected and islanded modes of micro-grid operations," in *2013 IEEE Innovative Smart Grid Technologies-Asia (ISGT Asia)*, Nov. 2013, pp. 1–6, doi: 10.1109/ISGT-Asia.2013.6698772.
 - [30] A. Shrivastava, J. M. Tripathi, R. Krishan, and S. K. Parida, "Optimal coordination of overcurrent relays using gravitational search algorithm with DG penetration," *IEEE Transactions on Industry Applications*, pp. 1–1, 2017, doi: 10.1109/TIA.2017.2773018.

BIOGRAPHIES OF AUTHORS



Arathi Pothakanahalli Bheemasenarao    received B.E degree in Electrical and Electronics Engineering from Visvesvaraya Technological University, Belagavi, Karnataka in 2003 and M. Tech degree in Digital Electronics from Visvesvaraya Technological University-Belagavi, Karnataka in 2011. Currently she is working as Assistant Professor at the Department of Electrical and Electronics Engineering, Ballari Institute of Technology and Management, Ballari. Her Research interest includes relay coordination, application of evolutionary and heuristic optimization techniques to power systems. She can be contacted at email: artilakshman72@gmail.com.



Shankaralingappa C. Byalihal    was born in Raichur, Karnataka, India on June 01, 1969. He received his B.E (Electrical) and M.E (Energy systems) degrees from Karnataka University Dharwad in 1993 and 1994 respectively and Ph.D. (Power Systems) from Visveswaraya Technological University, Belgaum, Karnataka, India in 2011. Currently he is working as a Professor in the Department of Electrical and Electronics Engineering at Dr. Ambedkar Institute of Technology, Bengaluru. His current research interests include renewable integration, electric vehicle and metaheuristic algorithms. He can be contacted at email: shankarcbt@gmail.com.

Original Article

Design and Performance Assessment of a Multilevel Inverter for Improved Standalone PV System Operation

Hemalatha Javvaji¹, Deepak Prakash Kadam², Y. Kamal Kishore³, K. Sarada⁴, M. Ramprasad Reddy⁵,
M. Lakshmikanth Reddy⁶

¹Department of EEE, PVP Siddhartha Institute of Technology, Vijayawada, India.

²Department of EEE, MET Institute of Engineering, Adgaon, Nashik, India.

³Department of EEE, Ballari Institute of Technology and Management, Ballari, India.

⁴Department of EEE, Koneru Lakshmaiah Education Foundation, Vaddeswaram, India.

⁵Department of EEE, Mohan Babu University (Erstwhile Sree Vidyanikethan Engineering College), Tirupati, India.

⁶Department of EEE, Aditya College of Engineering, Madanapalle, India.

⁵Corresponding Author : mramprasadreddyee@gmail.com

Received: 07 June 2023

Revised: 11 July 2023

Accepted: 08 August 2023

Published: 31 August 2023

Abstract - The design and performance assessment of a nine-level Multi-Level Inverter (MLI) for standalone Photovoltaic (PV) systems aim to increase the inverter's efficiency and decrease the usage of power switches. Multilevel inverters synthesize a sinusoidal output waveform from multiple voltage levels, which results in lower Total Harmonic Distortion (THD) and higher power quality. The nine-level multilevel inverter incorporates a variety of Pulse Width Modulation (PWM) techniques in this configuration to control the output voltage. The inverter can efficiently regulate power flow from the PV system to the load by optimizing the PWM control methods, resulting in a stable and dependable energy supply. The inverter experiences lower conduction and switching losses with fewer switches, resulting in enhanced overall efficiency. Furthermore, simplified circuitry can result in lower production costs and increased reliability. The performance analysis must examine this multilevel inverter's output voltage waveform, THD, efficiency, and power losses. It is possible to examine findings with the results of conventional inverters utilizing simulation modelling. The nine-level multilevel inverter can be an excellent option for standalone PV systems because it lowers THD and increases efficiency, enabling better system performance and greater use of renewable energy sources.

Keywords - Number of power switches, Modified MLI, Phase disposition PWM, PV system, THD.

1. Introduction

Multilevel inverters have received much attention in recent years because of their ability to overcome the constraints of conventional two-level inverters, such as increased voltage stress on semiconductor devices and harmonic distortion. These inverters are appropriate for various applications in renewable energy systems, electric vehicles, and industrial drives because of improved voltage waveforms, decreased switching losses, and higher power quality. In standalone photovoltaic systems, a multilevel inverter is an essential component which transforms the Direct Current (DC) power supplied by solar panels into Alternating Current (AC) for use in various electrical appliances.

Standalone PV systems have been increasing in popularity in rural areas as the demand for clean, sustainable energy increases because they can produce dependable, eco-friendly electricity without a connection to the grid [1-3].

Due to voltage and harmonic distortion constraints, traditional two-level inverters are less effective for high-power applications. These weaknesses are fixed by multilevel inverters, which create AC waveforms from multiple voltage levels.

They achieve this by generating increased voltage outputs using a series of power semiconductor switches and capacitors, which reduces harmonic distortion, lowers switching losses, and improves overall efficiency.

Independent PV systems need a consistent and reliable power source because they are frequently used in remote or off-grid settings. Multilevel inverters are often used in such systems because they can create superior sinusoidal waveforms, lowering the possibility of harming delicate electronic devices. Additionally, multilevel inverters enable better voltage regulation, raising standalone PV systems' overall performance and dependability [4-8].



1.1. Literature Review

The neutral-point-clamped inverter, or diode-clamped MLI, is one of the most widely used multilevel inverter topologies. In order to produce various voltage levels across the output terminals, it is made up of numerous capacitors and diodes. Compared to other topologies, it requires more components because the voltage levels depend on the number of capacitors implemented. The cascaded H-bridge MLI is a different popular arrangement requiring utilising numerous H-bridge cells.

The inverter can achieve higher voltage levels by connecting more cells in series. Each H-bridge can produce three-level output voltages. Flying capacitors are used by the flying capacitor MLI to generate various voltage levels. It has fewer components than the diode-clamped MLI; however, it needs delicate voltage balancing of the flying capacitors, which is frequently complicated. In contrast to two-level inverters, it provides better voltage levels and lower switching losses [9-14].

Pulse width modulation techniques have become essential in managing the switching patterns of semiconductor devices to maximise the potential benefits of multilevel inverters. This investigation of the available information evaluates the various PWM methods utilised by multilevel inverters, their characteristics, and how these individuals affect the overall effectiveness of such inverters. One of the fundamental methods used in multilevel inverters to produce a nearly sinusoidal output voltage is sinusoidal PWM.

PWM pulses closely resembling the reference waveform are produced by comparing a sinusoidal reference waveform with a high-frequency carrier signal. Although SPWM is relatively simple to establish, it features low voltage resolution and high harmonic content, especially at low modulation indexes. A more advanced method called selective harmonic elimination PWM intends to reduce specific harmonics in the output voltage waveform.

The modulation indexes for the fundamental and a few chosen harmonic frequencies can be found by solving a series of nonlinear equations. Although the computational difficulty of this method rises with the number of desired harmonics to be removed, it provides better control over the harmonic content. In multilevel inverters, particularly in three-phase applications, Space Vector PWM is a common approach.

In contrast with SPWM, it generates a nearly sinusoidal output voltage with a higher voltage resolution. SVPWM enhances power quality, lowers voltage THD, and lowers common-mode voltage. However, its implementation necessitates more sophisticated control algorithms and mighty computing power.

Hybrid PWM techniques combine the advantages of various PWM techniques to enhance performance. As an illustration, combining SPWM and SHEPWM can improve harmonic performance while keeping the implementation process simple. Individual PWM strategies have some drawbacks, which hybrid techniques can help to offset, resulting in the development of more adaptable and practical multilevel inverter designs [15-19].

Seven- and nine-level multilevel inverters are voltage source inverters synthesising multiple output voltage levels by combining multiple DC voltage sources. The Cascaded H-Bridge (CHB) configuration is the topology these inverters use the most frequently. When using the CHB topology, each H-bridge module produces a portion of the overall output voltage, and the cumulative output is the sum of these portions. The Pulse-Width Modulation (PWM) technique manages the switches, producing the desired output voltage waveform [19-25].

The ability of multilevel inverters to lower THD in the output voltage waveform is one of their key advantages. Compared to traditional two-level inverters, they successfully minimise the distortion by synthesising a waveform that resembles a staircase and has a variety of voltage levels.

According to investigations, THD levels below 5% can be attained by seven-level and nine-level inverters, which is highly anticipated in the power grid and industrial applications. Efficiency is crucial for power electronic systems because it directly affects thermal performance and energy consumption.

Multilevel inverters are generally more efficient than conventional inverters, particularly at medium- to high output power levels. The higher efficiency of multilevel inverters results from the decreased switching losses brought on by the devices subjected to less voltage stress. The leading causes of power loss in multilevel inverters are switching losses during PWM operation and conduction losses in the switching devices. The overall power loss is significantly influenced by the switching frequency, control method, and switching device type choices [26-32].

The proposed nine-level multilevel inverter has benefits such as a lower harmonic content, less switch voltage stress, and better power quality. However, it also has certain limitations. Increased power semiconductor device and capacitor requirements lead to design complexity. To maintain stability and ensure proper voltage level balancing, control techniques become more complex.

Additionally, as levels are added, switching loss expands, decreasing efficiency. Power quality problems like voltage inconsistencies, harmonics, and electromagnetic

interference may occur, necessitating sophisticated filtering methods. Despite the advantages, implementing a nine-level multilevel inverter necessitates addressing these issues to achieve the highest levels of performance and dependability [33-36].

The proposed nine-level multilevel inverter has achieved the following objectives for standalone PV systems:

- Develop a multilevel inverter with optimum energy conversion performance and the least number of harmonic distortions suitable for standalone photovoltaic systems.
- Evaluate and enhance the voltage levels and switching devices in the multilevel inverter's topology to achieve the desired power rating and system specifications.
- Investigate control strategies and modulation techniques to change solar conditions while ensuring a reliable and smooth power transfer between the PV array and load.
- Employ computer-aided tools to simulate the designed multilevel inverter and validate its performance under various PV power levels and load conditions.
- Evaluate the benefits of the multilevel inverter in terms of efficiency, total harmonic distortion, and overall reliability in standalone PV systems.

2. Proposed Modified MLI and Operation

The proposed grid-connected PV power generation system effectively converts solar irradiance into usable electrical energy using a Nine Level Multilevel Inverter and a PWM control strategy. The system's main components are the PV panel, the multilevel inverter, a filter, and the grid/load connection. The PV panel is essential for converting solar radiation into direct current electricity. The PV panel's surface receives sunlight, which causes a current flow that is proportional to the amount of incident irradiance.

The temperature of the PV panel also has an impact on its performance, as higher temperatures can reduce the efficiency of the process of converting energy. A Nine Level Multilevel Inverter changes the PV panel's DC output into AC compatible with the grid. This type of inverter has multiple voltage levels, allowing it to generate a smoother and higher-quality output waveform compared to traditional two-level inverters.

Additionally, the multilevel inverter increases system effectiveness and lowers harmonic distortion. The PWM control strategy is utilised to manage the inverter's output voltage. The inverter can maintain the intended voltage output level and achieve Maximum Power Point Tracking (MPPT) by adjusting the duty cycle of the switching signals. A filter has been integrated into the system, ensuring the generated AC power is unambiguous and devoid of harmonic distortions. The filter reduces any high-frequency

noise produced while the inverter switches, ensuring adherence to grid connection requirements and safeguarding delicate loads. When the PV panels produce more electricity than the connected loads need, the system can supply the excess power to the grid using the grid/load-connected operation. In addition, when a load requires more power than a PV panel can provide, the system uses additional power from the grid to satisfy the load's requirements.

The design for a modified multilevel inverter connected to solar panels is illustrated in Figure 1. The proposed nine-level multilevel inverter employs ten IGBT power components, a load (R and RL), and four symmetrical DC voltage sources to produce better voltage waveform quality and less harmonic distortion. The inverter generates nine voltage levels by carefully regulating the IGBTs' switching patterns, enabling finer voltage resolution and a smoother output waveform.

The connected load is less strained while the inverter's efficiency and performance improve. Additionally, the multilevel topology allows for lower switching frequencies, which reduces switching losses and boosts overall system efficiency. The inverter is appropriate for various applications, including grid-tie inverters, motor drives, and renewable energy systems, because it can generate high-quality AC voltage. Figure 2 illustrates the proposed nine-level multilevel inverter.

The proposed nine-level multilevel inverter is designed to operate with various voltage levels, including $-4V_{DC}$, $-3V_{DC}$, $-2V_{DC}$, $-V_{DC}$, $0V_{DC}$, $+V_{DC}$, $+2V_{DC}$, $+3V_{DC}$, and $+4V_{DC}$. This inverter topology offers increased voltage resolution and reduced harmonic distortion compared to conventional inverters. Utilizing multiple voltage levels can generate more accurate and smoother output waveforms, improving efficiency and lowering electromagnetic interference. The inverter's operation involves controlling the switching states of its power semiconductor devices to achieve the desired output voltage level.

The proposed MLI operates in a specific mode in which switches S1, S3, S5, S9, and S7 are turned on. In this configuration, dc voltage sources V1, V2, V3, and V4 are also utilised. This configuration leads to the inverter's output voltage being $-4V_{DC}$. Figure 3 illustrates the operating mode of $+4V_{DC}$ output voltage.

A negative output voltage value results from the output voltage being inverted concerning the dc voltage V_{dc} , as indicated by the negative sign. The MLI is suitable for various power conversion applications because of this specific mode of operation, which enables the MLI to produce a controlled output voltage waveform with multiple voltage levels. The proposed MLI is operated in a specific mode by turning on switches S1, S3, S5, S9, and S10.

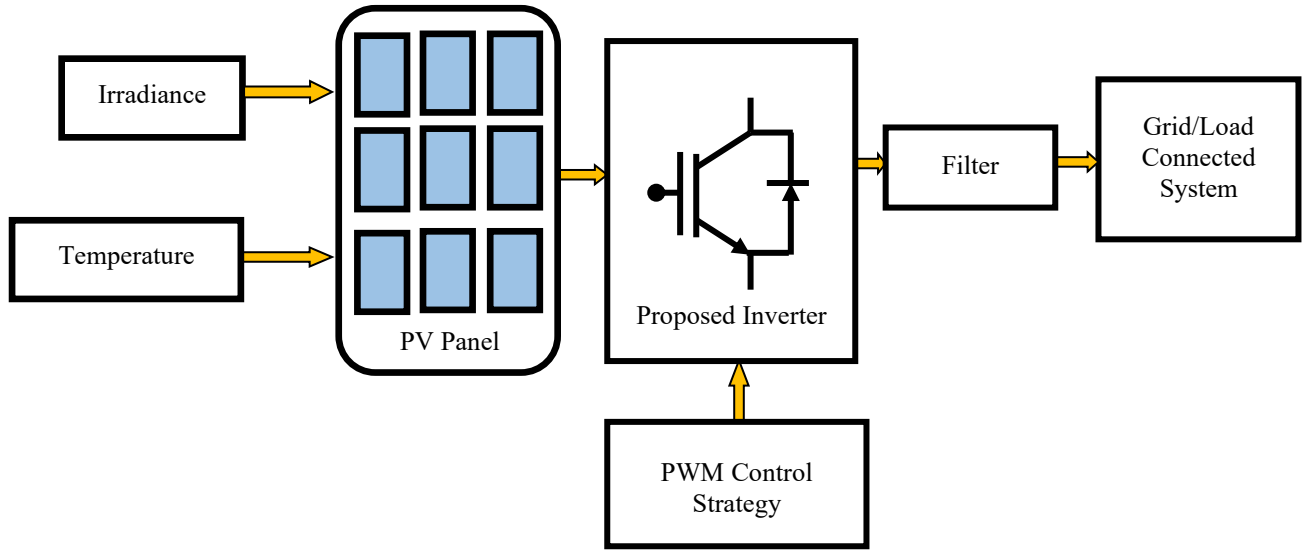


Fig. 1 PV interconnected modified MLI

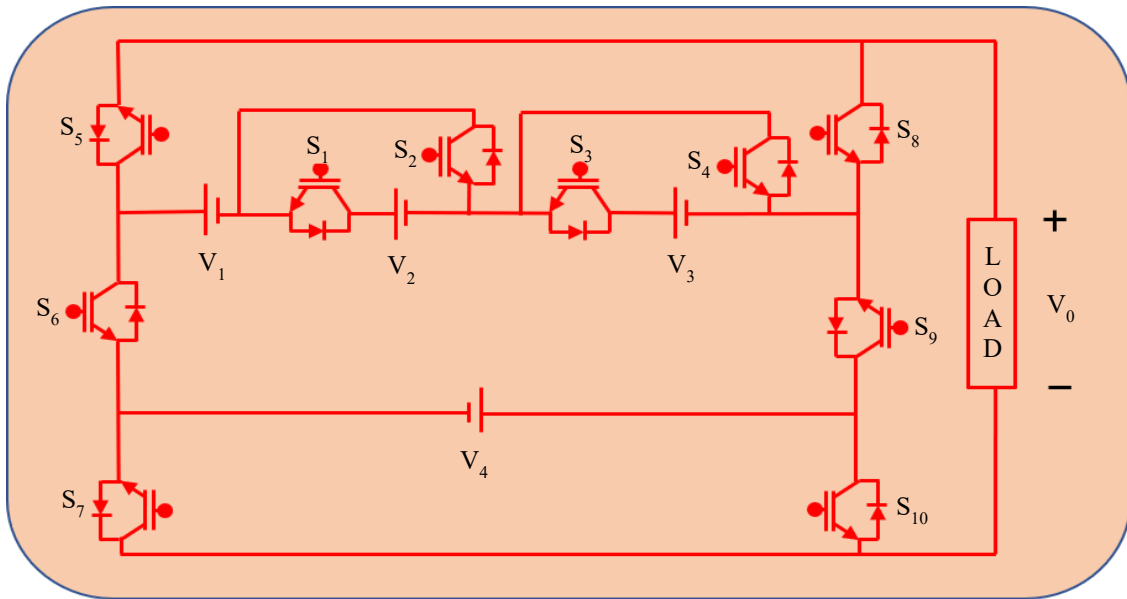


Fig. 2 Proposed nine-level multilevel inverter

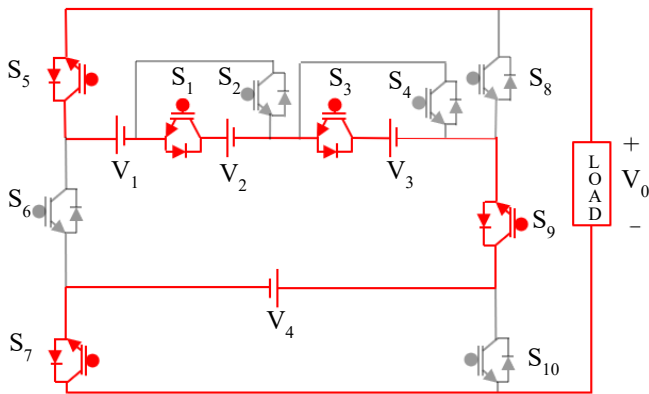


Fig. 3 $+4V_{DC}$ output voltage

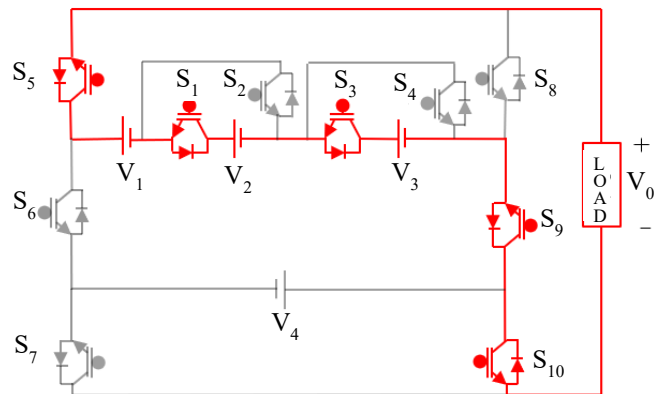


Fig. 4 $+3V_{DC}$ output voltage

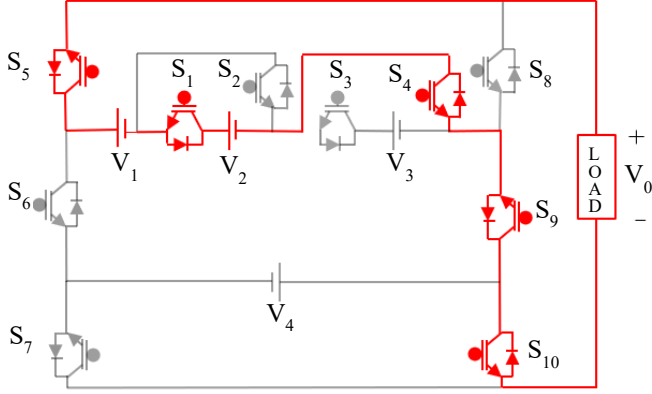


Fig. 5 $+2V_{DC}$ output voltage

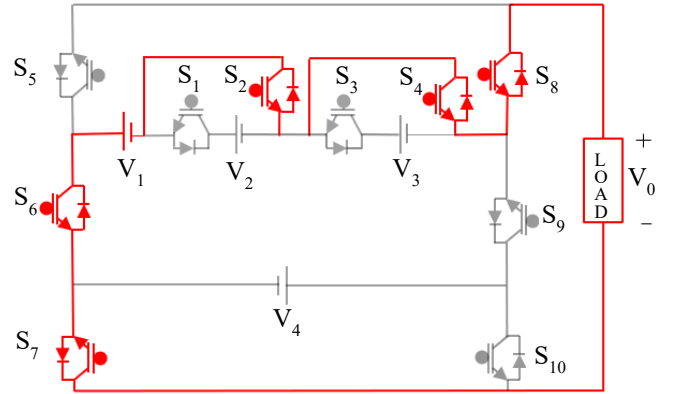


Fig. 8 $-V_{DC}$ output voltage

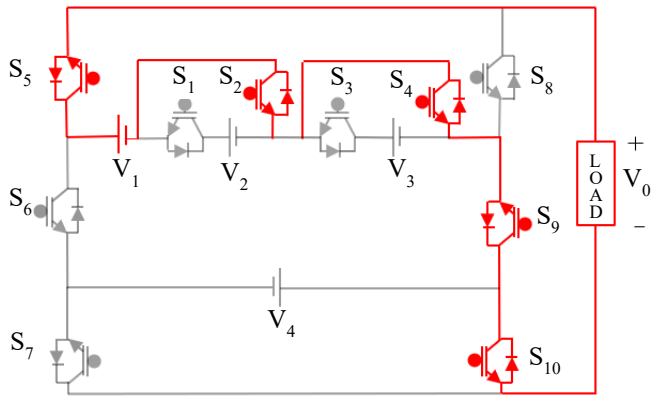


Fig. 6 $+V_{DC}$ output voltage

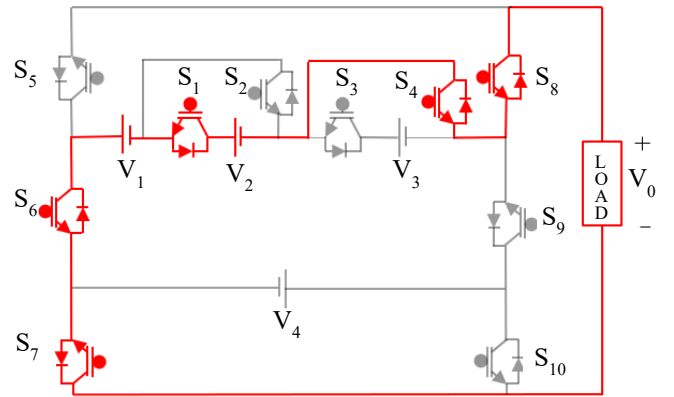


Fig. 9 $-2V_{DC}$ output voltage

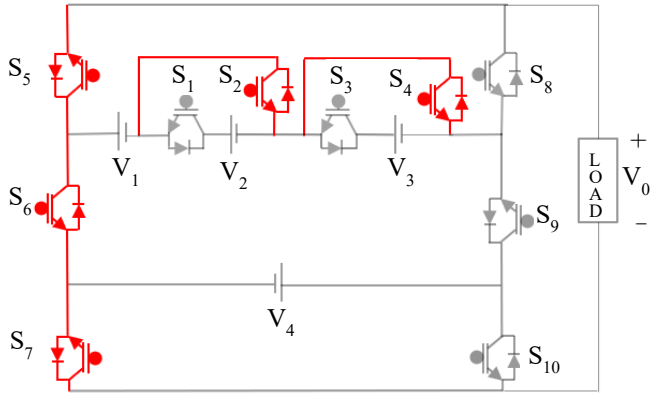


Fig. 7 $0V_{DC}$ output voltage

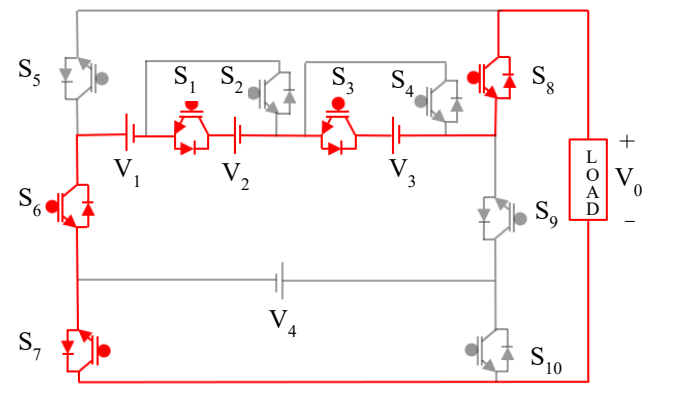
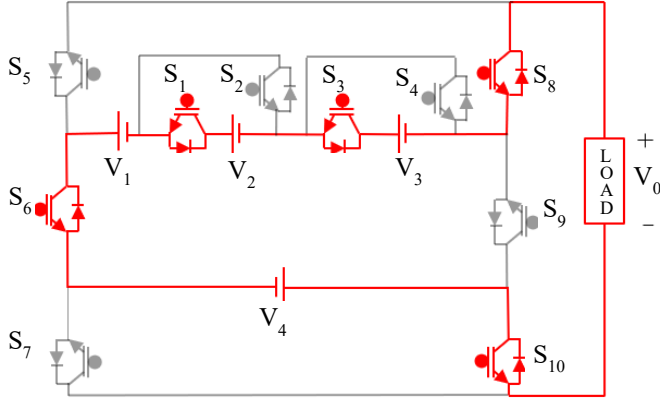


Fig. 10 $-3V_{DC}$ output voltage

The MLI is powered by DC voltage sources V_1 , V_2 , and V_3 . The MLI provides a $-3V_{DC}$ output voltage in this configuration. This $-3V_{DC}$ output voltage has to be utilised to power the connected load to the MLI.

Figure 4 illustrates the operating mode of $+3V_{DC}$ output voltage. The operation of an inverter entails converting a DC input voltage from sources V_1 , V_2 , and V_3 into an AC output voltage. The associated voltage sources are connected to the load when switches S_1 , S_4 , S_6 , S_7 , and S_8 are turned on.

Because of the particular combination of switches, the output voltage is negative ($-2V_{DC}$), indicating that the polarity of the AC waveform is inverted. Similarly, operating specific switches and DC voltage sources results in the output voltages $-V_{DC}$, 0 , $+V_{DC}$, $+2V_{DC}$, $+3V_{DC}$, and $+4V_{DC}$. Figure 5 to Figure 11 depict the various operational modes of the proposed MLI. A reference sinusoidal signal and eight carrier waveforms are synthesised in the modulation technique called Pulse Width Modulation with Phase Disposition (PD-PWM).

Fig. 11 -4V_{DC} output voltage

It attains effective signal transmission and control by different pulse widths of the carriers concerning the phase of the reference waveform. The instantaneous amplitude of a reference sinusoidal signal provides the basis for adjusting the pulse widths of each carrier, each of which corresponds to a particular phase angle. In addition to reducing power loss and improving overall system performance, PD-PWM maintains precise regulation. Figure 12 illustrates the pulse width modulation with phase disposition for the proposed nine-level inverter.

3. Results and Discussion

A proposed nine-level multilevel inverter is connected to a PV system in MATLAB/Simulink which, by Figure 1, operates at a temperature of 35°C and has an irradiance of 1000 W/m². Figure 13 illustrates the PV panel irradiance,

and Figure 14 illustrates the temperature of the PV panel system. The boost converter must consider the PV panel voltage and maximum power in a solar power system. The input voltage range the boost converter has to handle is determined by the PV panel voltage.

It has to be suitable for the converter's operating range for effective energy transfer. The boost converter then increases the voltage to meet the system's needs, enabling the most efficient possible power transfer to the load or energy storage system. Solar energy is utilised efficiently and consistently when the voltage of the PV panels and the boost converter are proportionally correct. PV panel voltage of 288V and maximum output power are shown in Figures 15 and Figure 16, respectively.

The proposed nine-level inverter with a resistive load operates in a staircase mode, with voltage and current ratings of 230V and 10A, respectively. It achieves higher output harmonics, improved output waveform quality, and increased output voltage resolution. There is a higher harmonic distortion in the output current due to the resistive load. Figure 17 illustrates the output voltage and current waveform of nine-level inverters with resistive load. It attains staircase output voltage using a multi-level topology with a resistive and inductive load, maintaining a constant 230V and 8A current. This design significantly decreases output current harmonics, improving power quality and decreasing losses. THD is decreased due to improved voltage waveform approximation transformed possible by a higher proportion of voltage levels.

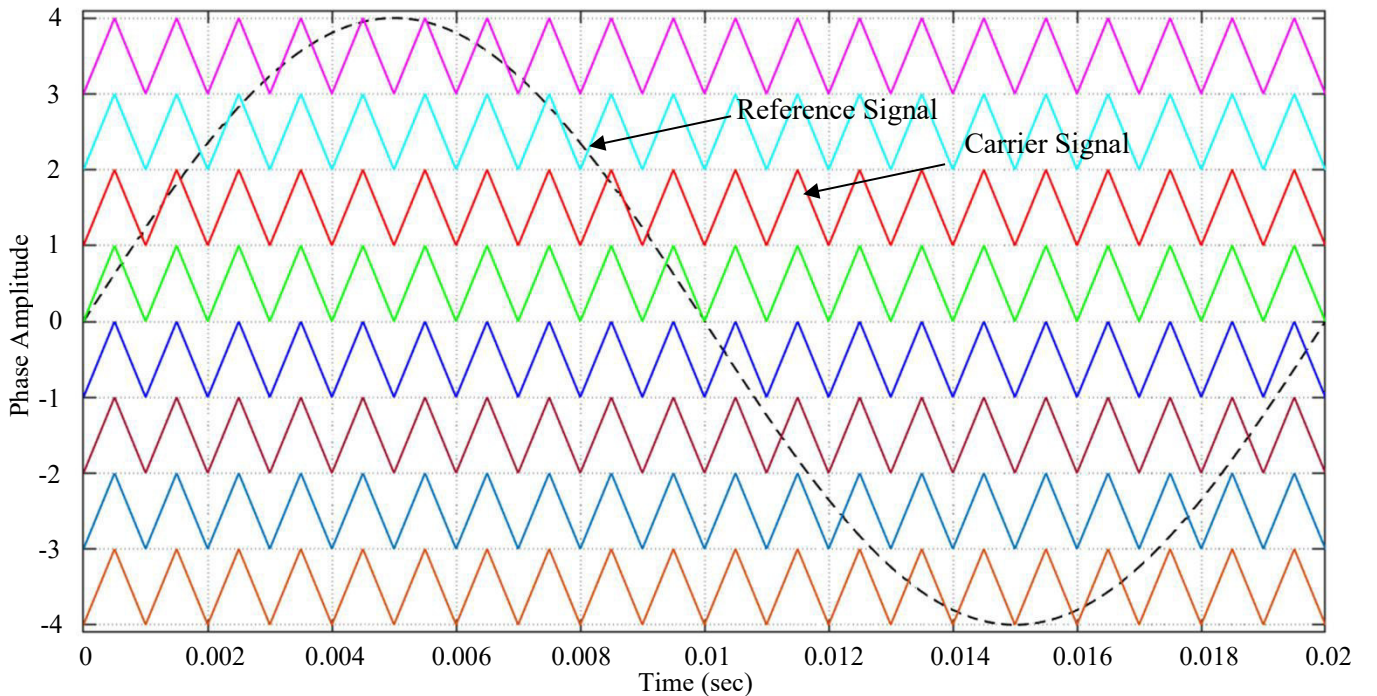


Fig. 12 Pulse width modulation with phase disposition

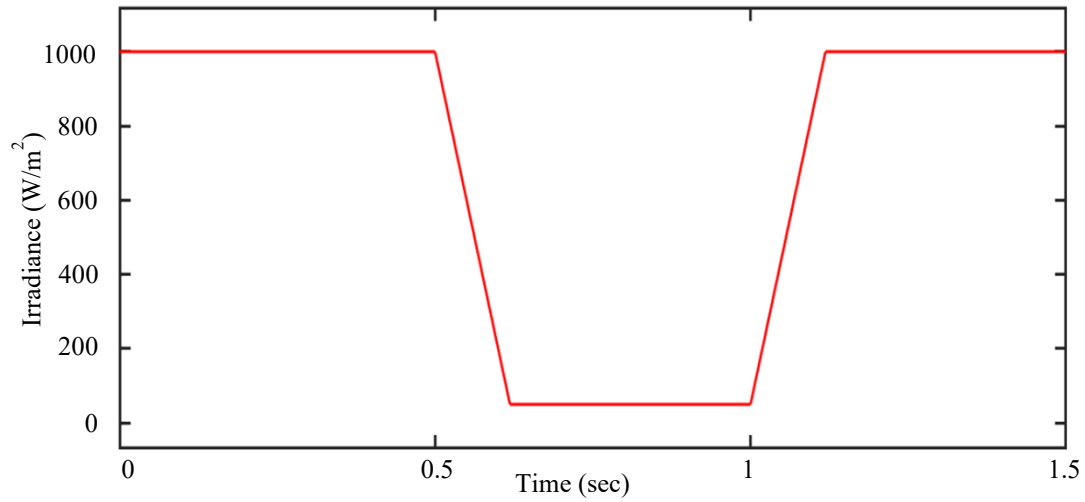


Fig. 13 PV panel irradiance

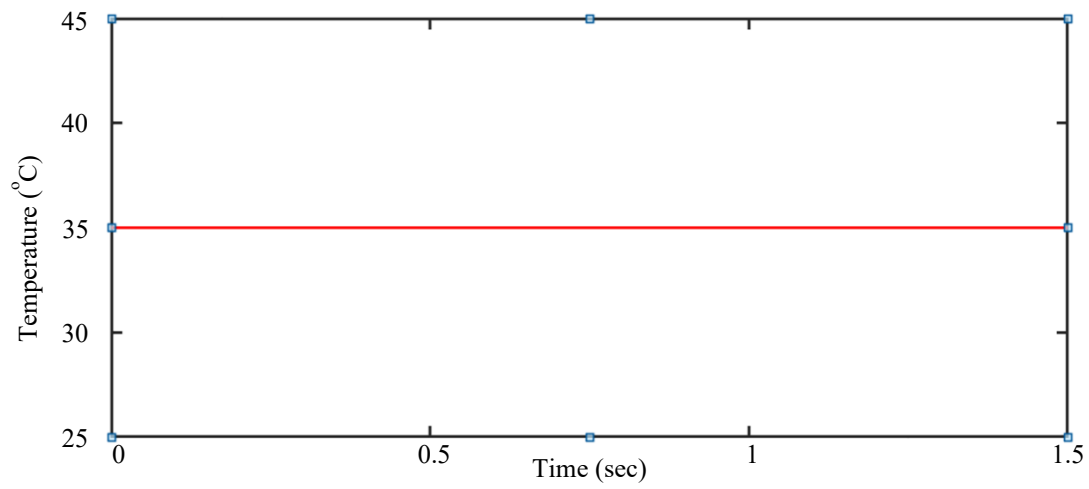


Fig. 14 PV panel temperature

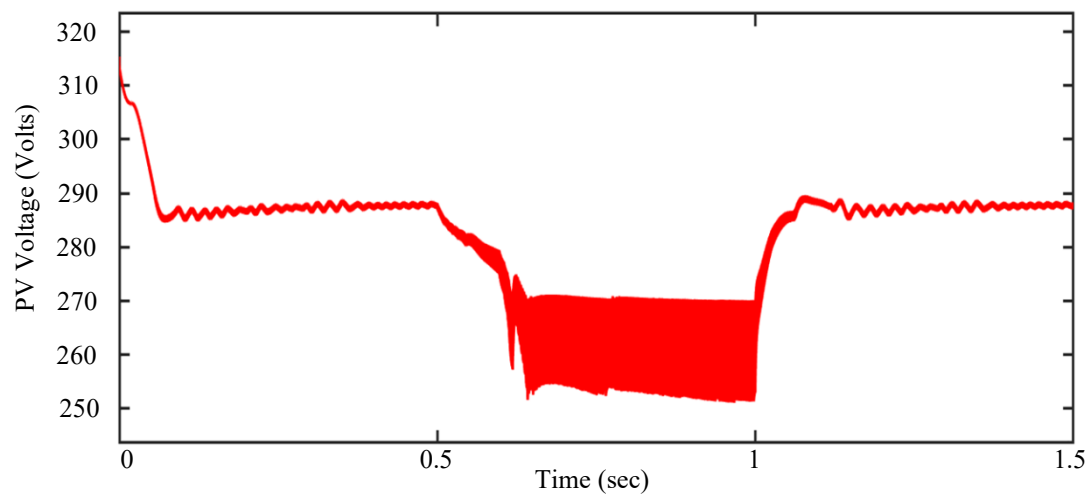


Fig. 15 PV panel voltage

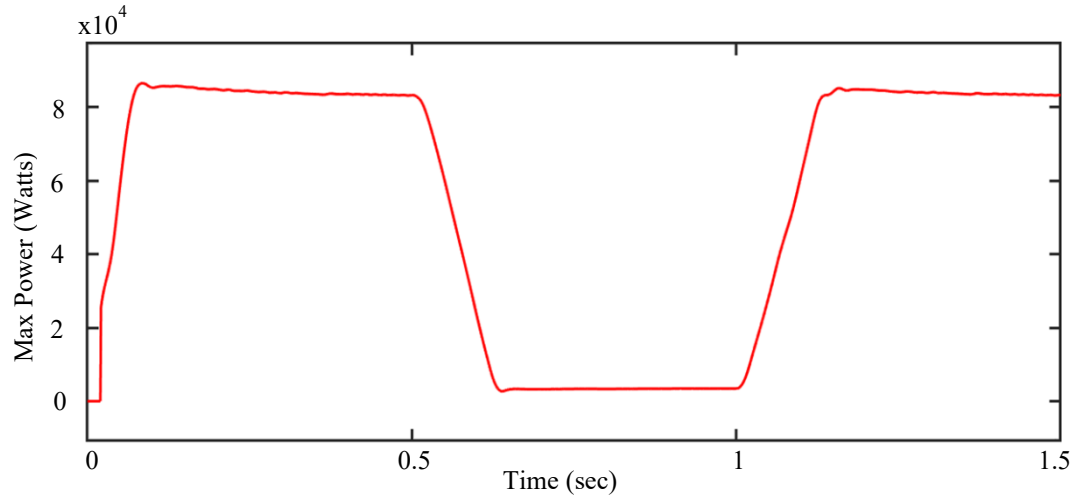


Fig. 16 PV panel maximum power

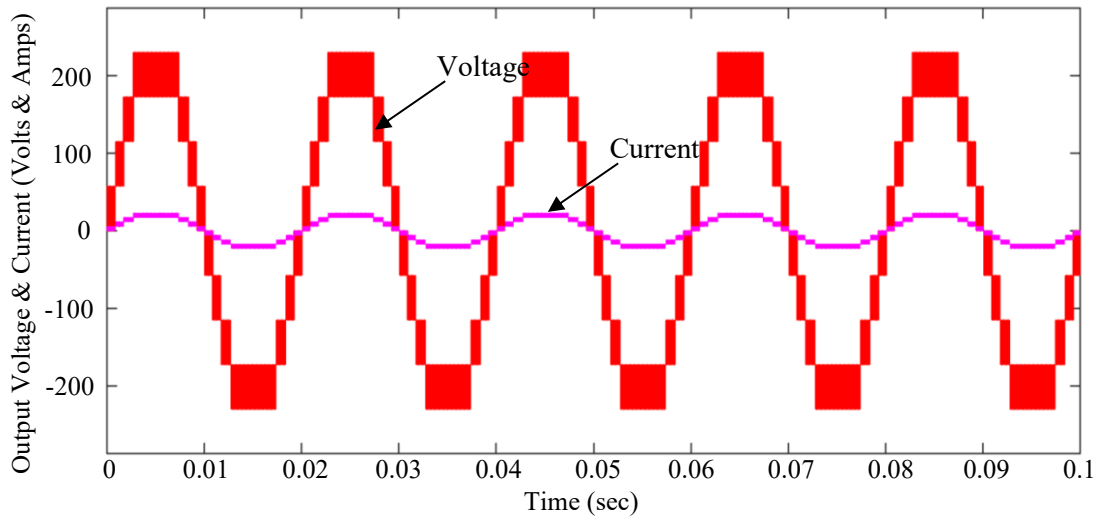


Fig. 17 Nine-level output voltage and current (R load)

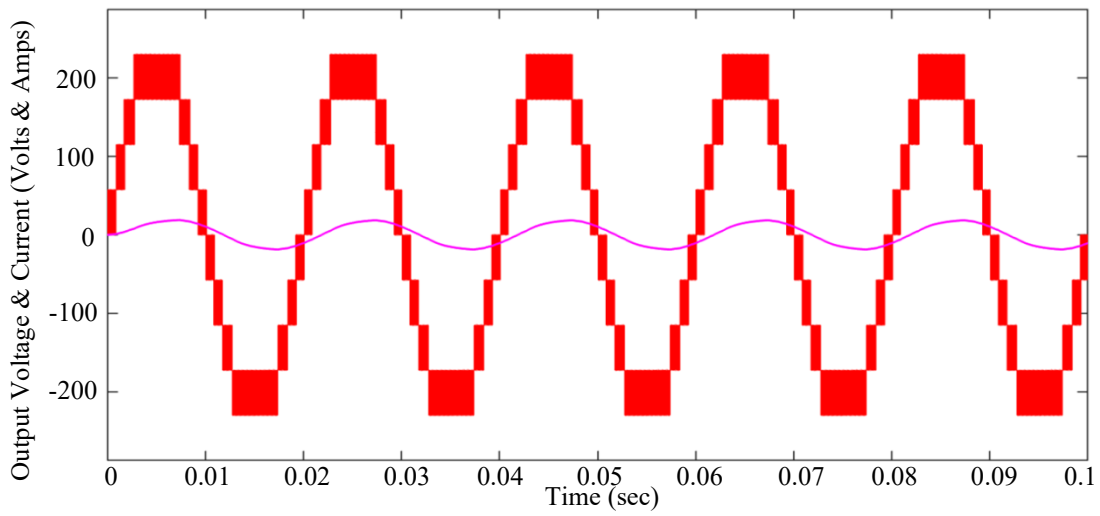


Fig. 18 Nine-level output voltage and current (RL load)

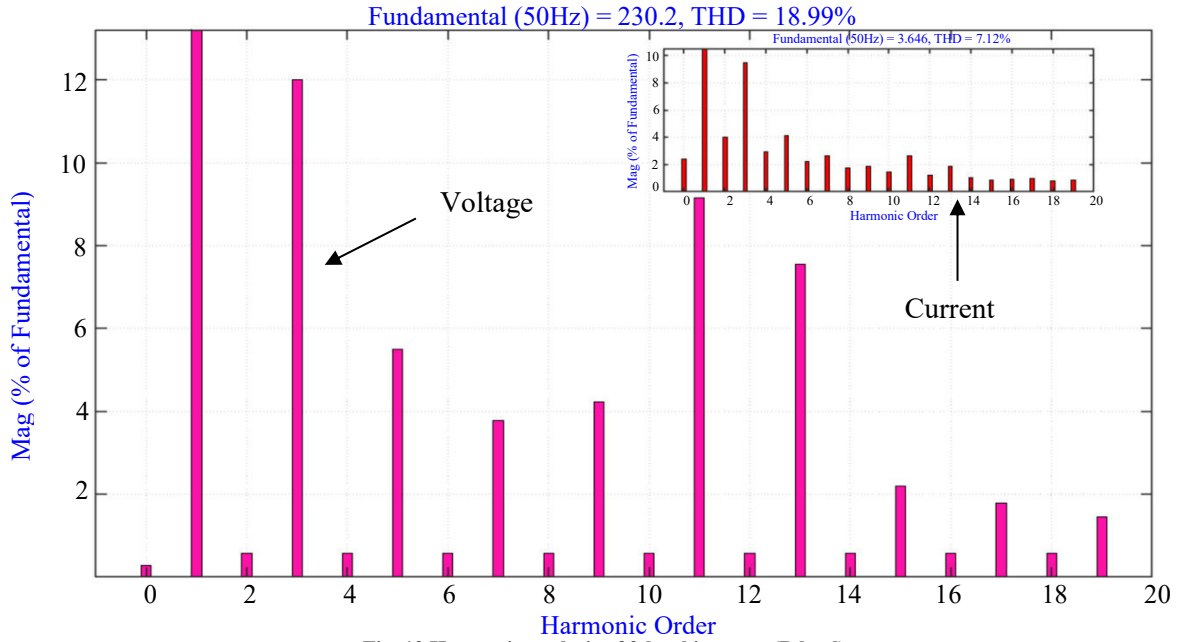


Fig. 19 Harmonic analysis of 9-level inverter (R load)

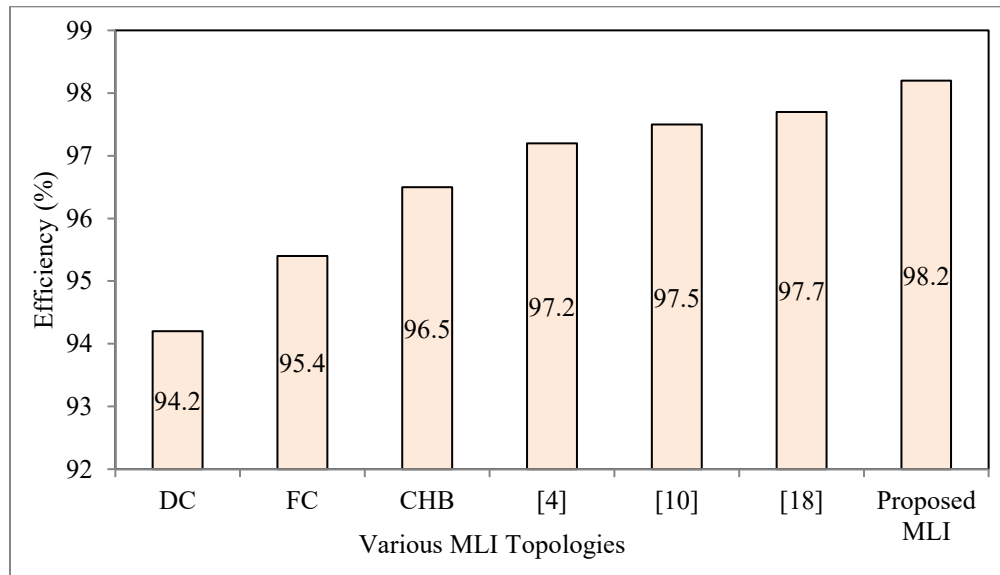


Fig. 20 Efficiency analysis of proposed and conventional MLI

Table 1. Comparison of proposed and conventional topology

S.No.	Parameters	DC MLI	FC MLI	CHB MLI	[4]	[10]	[18]	Proposed MLI
1	DC Sources	1	1	4	4	4	4	4
2	Power Switches	16	16	16	14	12	10	10
3	Power Diodes	24	-	-	-	-	10	-
4	DC Bus Capacitors	8	20	-	-	-	-	-
5	Balancing Capacitors	0	10	-	-	-	5	-

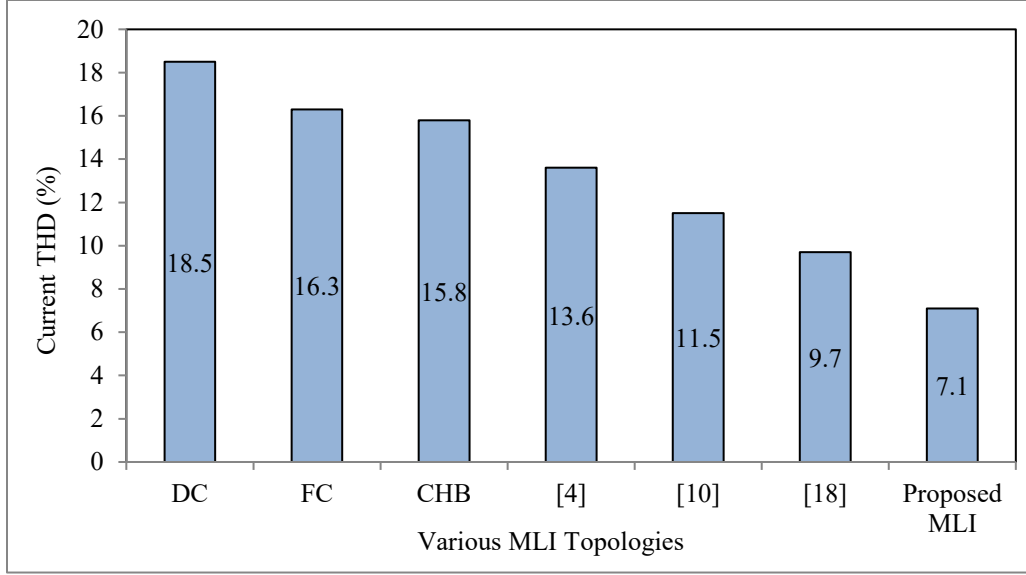


Fig. 21 Current analysis of proposed and conventional MLI

Table 2. Performance parameters proposed topology

S.No.	Parameters	Proposed MLI
1	No. of DC supplies	4
2	DC Voltage	60 V
3	RMS Voltage	240 V
4	No. of IGBTs	10
5	Driver Circuits	10
6	Carrier frequency	3 kHz
7	%THD (Current)	7.12 (RL load)
8	Switching loss	00.42 W
9	Conduction loss	41.31 W
10	Total loss	41.73 W
11	Efficiency	98.20 %

The ability of the inverter to produce lesser voltage steps reduces switching losses and improves efficiency. Figure 18 illustrates nine-level output voltage and current (RL load). The harmonic analysis of a 9-level inverter with an R load is shown in Figure 19. The output voltage waveform exhibits significant distortion, as indicated by the voltage Total Harmonic Distortion (THD), which is found to be 18.99%. Additionally, the output current waveform has a 7.12% current THD, which indicates the degree of distortion. These findings indicate that the proposed MLI outperforms

traditional topologies regarding harmonic content. A comparison of the proposed MLI and the current conventional topologies is shown in Figure 20. The proposed MLI outperforms conventional topologies with an impressive efficiency of 98.2%. This demonstrates the improved energy conversion efficiency and reduced power losses the suggested MLI design provides. Figure 21 also compares recent research on the proposed MLI and traditional topologies. Comparing the proposed MLI to conventional topologies, the proposed MLI shows a lower current THD of about 7.1%. This suggests improved output power quality and current wave shaping, making the proposed MLI a good option for real-world applications. Overall, the findings exhibit that the proposed MLI has several advantages over traditional alternatives, including improved harmonic performance, increased efficiency, and current quality.

The configurations for handling DC sources, power switches, power diodes, DC bus capacitors, and balancing capacitors differ between the nine-level proposed and conventional MLI topologies are compared in Table 1. The proposed nine-level MLI requires fewer power switches to achieve additional intermediate voltage levels, which improves output waveform quality and lowers harmonic distortion. Conversely, traditional MLI typically operates with limited voltage levels, producing higher harmonic content. The proposed configuration improves system effectiveness, reduces stress on power devices, and offers increased voltage and power capability. The efficiency analysis of the proposed and conventional MLI is presented in Figure 20. The current analysis of proposed and conventional MLI is given in Figure 21.

The nine-level MLI that has been proposed performs effectively, with few losses and high output efficiency

overall. An efficient power conversion during switching operations is indicated by the switching loss of only 0.42 W. The conduction loss of 41.31 W shows that the inverter efficiently circulates current. Unexpectedly the total loss of 41.73 W shows exceptional system optimisation and minimal energy wasteful. The inverter's notable overall output efficiency of 98.20% highlights its capacity to convert input power into useful output power precisely. Table 2 illustrates the various performance parameters of the proposed MLI.

4. Conclusion

The proposed nine-level MLI performs admirably with ten power switches, with an exceptional total loss of only 41.73W. Its significant % efficiency rate of 98.20%

demonstrates how much it can decrease energy consumption. Additionally, the 7.12% current THD according to load conditions ensures a stable and efficient operation, lowering the possibility of undesirable harmonics and enhancing the overall system reliability.

The advanced MLI design described here is a promising option for high-power applications because it balances performance and efficiency, promoting the efficient and sustainable use of electrical energy. It has the potential for effective renewable energy integration, advanced motor drives, and innovative grid applications due to higher voltage levels and reduced harmonics, opening up the possibility of a greener and more sustainable energy environment.

References

- [1] Ibrahim Harbi et al., "A Nine-Level Split-Capacitor Active-Neutral-Point-Clamped Inverter and Its Optimal Modulation Technique," *IEEE Transactions on Power Electronics*, vol. 37, no. 7, pp. 8045-8064, 2022. [[CrossRef](#)] [[Google Scholar](#)] [[Publisher Link](#)]
- [2] E. Parimalasundar et al., "Performance Analysis of a Seven-Level Multilevel Inverter in Grid-Connected Systems," *SSRG International Journal of Electrical and Electronics Engineering*, vol. 10, no. 6, pp. 9-22, 2023. [[CrossRef](#)] [[Publisher Link](#)]
- [3] Mohammed A. Al-Hitmi et al., "Symmetric and Asymmetric Multilevel Inverter Topologies with Reduced Device Count," *IEEE Access*, vol. 11, pp. 5231-5245, 2023. [[CrossRef](#)] [[Google Scholar](#)] [[Publisher Link](#)]
- [4] E. Parimalasundar et al., "Investigation of Efficient Multilevel Inverter for Photovoltaic Energy System and Electric Vehicle Applications," *Electrical Engineering & Electromechanics*, vol. 4, pp. 47-51, 2023. [[CrossRef](#)] [[Google Scholar](#)] [[Publisher Link](#)]
- [5] Krishnan Suresh, and Ezhilvannan Parimalasundar, "Newly Designed Single-Stage Dual Leg DC-DC/AC Buck-Boost Converter for Grid Connected Solar System," *International Journal of Circuit Theory and Applications*, 2023. [[CrossRef](#)] [[Google Scholar](#)] [[Publisher Link](#)]
- [6] Suresh K et al., "Encapsulated 3Ø Converter for Power Loss Minimization in a Grid-Connected System," *Automation, Journal for Control, Measurement, Electronics, Computing and Communications*, vol. 64, no. 1, pp. 189-197, 2023. [[CrossRef](#)] [[Google Scholar](#)] [[Publisher Link](#)]
- [7] Md Safayatullah et al., "A Comprehensive Review of Power Converter Topologies and Control Methods for Electric Vehicle Fast Charging Applications," *IEEE Access*, vol. 10, pp. 40753-40793, 2022. [[CrossRef](#)] [[Google Scholar](#)] [[Publisher Link](#)]
- [8] Parimalasundar Ezhilvannan et al., "Analysis of the Effectiveness of a Two-Stage Three-Phase Grid Connected Inverter for Photovoltaic Applications," *Journal of Solar Energy Research*, vol. 8, no. 2, pp. 1471-1483, 2023. [[Google Scholar](#)] [[Publisher Link](#)]
- [9] K. Suresh, and E. Parimalasundar, "ITBC Controlled IPWM for Solar Based Wide Range Voltage Conversion System," *IETE Journal of Research*, pp. 1-9, 2023. [[CrossRef](#)] [[Google Scholar](#)] [[Publisher Link](#)]
- [10] J. Venkataramanaiah, Y. Suresh, and Anup Kumar Panda, "A Review on Symmetric, Asymmetric, Hybrid and Single DC Sources Based Multilevel Inverter Topologies," *Renewable and Sustainable Energy Reviews*, vol. 76, pp. 788-812, 2017. [[CrossRef](#)] [[Google Scholar](#)] [[Publisher Link](#)]
- [11] Ebrahim Babaei, Mohammad Farhadi Kangarlu, and Mehran Sabahi, "Extended Multilevel Converters: An Attempt to Reduce the Number of Independent DC Voltage Sources in Cascaded Multilevel Converters," *IET Power Electronics*, vol. 7, no. 1, pp. 157-166, 2014. [[CrossRef](#)] [[Google Scholar](#)] [[Publisher Link](#)]
- [12] Sanka Sreelakshmi, Machineni Sanjeevappa Sujatha, and Jammy Ramesh Rahul, "Multi-Level Inverter with Novel Carrier Pulse Width Modulation Technique for High Voltage Applications," *Indonesian Journal of Electrical Engineering and Computer Science*, vol. 26, no. 2, pp. 667-674, 2022. [[CrossRef](#)] [[Publisher Link](#)]
- [13] R. Sindhuja et al., "Comparison between Symmetrical and Asymmetrical 13 Level MLI with Minimal Switches," *International Conference on Automation, Computing and Renewable System*, pp. 187-191, 2022. [[CrossRef](#)] [[Google Scholar](#)] [[Publisher Link](#)]
- [14] Shakil Ahamed Khan et al., "A New Isolated Multi-Port Converter with Multi-Directional Power Flow Capabilities for Smart Electric Vehicle Charging Stations," *IEEE Transactions on Applied Superconductivity*, vol. 29, no. 2, pp. 1-4, 2019. [[CrossRef](#)] [[Google Scholar](#)] [[Publisher Link](#)]
- [15] Krishnan Suresh, and Ezhilvannan Parimalasundar, "Design and Implementation of Dual-Leg Generic Converter for DC/AC Grid Integration," *International Journal of Circuit Theory and Applications*, vol. 51, no. 8, pp. 3865-3879, 2023. [[CrossRef](#)] [[Google Scholar](#)] [[Publisher Link](#)]

- [16] Mohammad Farhadi Kangarlu, and Ebrahim Babaei, "Cross-Switched Multilevel Inverter: An Innovative Topology," *IET Power Electronics*, vol. 6, no. 4, pp. 642-651, 2013. [[CrossRef](#)] [[Google Scholar](#)] [[Publisher Link](#)]
- [17] Ebrahim Babaei, Sara Laali, and Somayeh Alilu, "Cascaded Multilevel Inverter with Series Connection of Novel H-Bridge Basic Units," *IEEE Transactions on Industrial Electronics*, vol. 61, no. 12, pp. 6664-6671, 2014. [[CrossRef](#)] [[Google Scholar](#)] [[Publisher Link](#)]
- [18] Parimalasundar Ezhilvannan, and Suresh krishnan, "Fault Analysis and Compensation in a Five Level Multilevel DC-AC Converter," *Al-Jazari*, vol. 10, no. 1, pp. 99-108, 2023. [[CrossRef](#)] [[Google Scholar](#)] [[Publisher Link](#)]
- [19] Emad Samadaei et al., "An Envelope Type (E-Type) Module: Asymmetric Multilevel Inverters with Reduced Components," *IEEE Transactions on Industrial Electronics*, vol. 63, no. 11, pp. 7148-7156, 2016. [[CrossRef](#)] [[Google Scholar](#)] [[Publisher Link](#)]
- [20] Hani Vahedi, and Kamal Al-Haddad, "Real Time Implementation of a Seven-Level Packed U-Cell Inverter with a Low-Switching-Frequency Voltage Regulator," *IEEE Transactions on Power Electronics*, vol. 31, no. 8, pp. 5967-5973, 2016. [[CrossRef](#)] [[Google Scholar](#)] [[Publisher Link](#)]
- [21] K. Suresh et al., "Design and Implementation Bidirectional DC-AC Converter for Energy Storage System," *IEEE Canadian Journal of Electrical and Computer Engineering*, vol. 46, no. 2, pp. 130-136, 2023. [[CrossRef](#)] [[Google Scholar](#)] [[Publisher Link](#)]
- [22] Vishal Anand, and Varsha Singh, "A 13 Level Switched-Capacitor Multilevel Inverter with Single DC Source," *IEEE Journal of Emerging and Selected Topics in Power Electronics*, vol. 10, no. 2, pp. 1575-1586, 2022. [[CrossRef](#)] [[Google Scholar](#)] [[Publisher Link](#)]
- [23] Kavali Janardhan et al., "Performance Investigation of Solar Photovoltaic System for Mobile Communication Tower Power Feeding Application," *International Journal of Electrical and Electronics Research*, vol. 10, no. 4, pp. 921-925, 2022. [[CrossRef](#)] [[Google Scholar](#)] [[Publisher Link](#)]
- [24] E. Parimalasundar et al., "Performance Analysis of DC-DC Converter for Electric Vehicle Charging Applications," *2023 7th International Conference on Computing Methodologies and Communication (ICCMC)*, Erode, India, pp. 1543-1546, 2023. [[CrossRef](#)] [[Google Scholar](#)] [[Publisher Link](#)]
- [25] Kasinath Jena et al., "A Novel Three-Phase Switched-Capacitor Five-Level Multilevel Inverter with Reduced Components and Self-Balancing Ability," *Applied Sciences*, vol. 13, no. 3, pp. 1-19, 2023. [[CrossRef](#)] [[Google Scholar](#)] [[Publisher Link](#)]
- [26] Perumal B, Suresh K, and Parimalasundar E, "Fault Analysis in the 5-Level Multilevel NCA DC-AC Converter," *Automation, Journal for Control, Measurement, Electronics, Computing and Communications*, vol. 64, no. 3, pp. 606-612, 2023. [[CrossRef](#)] [[Google Scholar](#)] [[Publisher Link](#)]
- [27] K. Suresh, and E. Parimalasundar, "Fault Analysis and Clearance in FL-APC DC-AC Converter," *IEEE Canadian Journal of Electrical and Computer Engineering*, vol. 46, no. 1, pp. 1-6, 2023. [[CrossRef](#)] [[Google Scholar](#)] [[Publisher Link](#)]
- [28] B. Hemanth Kumar et al., "Control of Modified Switched Reluctance Motor for EV Applications," *Trends in Electrical, Electronics, Computer Engineering Conference*, Bengaluru, India, pp. 123-127, 2022. [[CrossRef](#)] [[Google Scholar](#)] [[Publisher Link](#)]
- [29] Parimalasundar E et al., "Investigation Analysis of Open Circuit and Short Circuit Fault on Cascaded H-Bridged Multilevel Inverter using Artificial Neural Network Approach," *International Journal of Electrical and Electronics Research*, vol. 10, no. 2, pp. 320-326, 2022. [[CrossRef](#)] [[Google Scholar](#)] [[Publisher Link](#)]
- [30] E. Parimalasundar et al., "Performance Analysis of a Seven-Level Multilevel Inverter in Grid-Connected Systems," *SSRG International Journal of Electrical and Electronics Engineering*, vol. 10, no. 6, pp. 9-22, 2023. [[CrossRef](#)] [[Publisher Link](#)]
- [31] Aizad Khurshed et al., "A Novel Modified PSO Algorithm to Optimise the PV Output Power of Grid-Connected PV System," *SSRG International Journal of Electrical and Electronics Engineering*, vol. 10, no. 7, pp. 188-198, 2023. [[CrossRef](#)] [[Google Scholar](#)] [[Publisher Link](#)]
- [32] M. Jagabar Sathik et al., "An Improved Seven-Level PUC Inverter Topology with Voltage Boosting," *IEEE Transactions on Circuits and Systems II: Express Briefs*, vol. 67, no. 1, pp. 127-131, 2020. [[CrossRef](#)] [[Google Scholar](#)] [[Publisher Link](#)]
- [33] Sindhuja R et al., "A Reconfigurable Multilevel Inverters with Minimal Switches for Battery Charging and Renewable Energy Applications," *2022 International Conference on Electronics, Communication and Aerospace Technology*, Coimbatore, India, pp. 422-427, 2022. [[CrossRef](#)] [[Google Scholar](#)] [[Publisher Link](#)]
- [34] Sreelakshmi Sanka, M. S. Sujatha, and Jammy Ramesh Rahul, "Improved Seven Level Multilevel DC-Link Inverter with Novel Carrier PWM Technique," *Journal of Circuits Systems and Computers*, vol. 32, no. 6, pp. 29-38, 2023. [[CrossRef](#)] [[Google Scholar](#)] [[Publisher Link](#)]
- [35] B. Hemanth Kumar et al., "An Enhanced Space Vector PWM Strategies for Three Phase Asymmetric Multilevel Inverter," *International Transactions on Electrical Energy Systems*, vol. 2023, pp. 1-29, 2023. [[CrossRef](#)] [[Google Scholar](#)] [[Publisher Link](#)]
- [36] E. Parimalasundar, R. Sindhuja, and K. Manikandan, "Performance Analysis of Five Level Modular Multilevel Inverter for PV-Grid Connected System," *9th International Conference on Electrical Energy Systems*, Chennai, India, pp. 481-485, 2023. [[CrossRef](#)] [[Google Scholar](#)] [[Publisher Link](#)]

Original Article

A Novel Reliable Five-Level Multilevel Inverter for Critical Loads

Priya R. Patil¹, M. Pushpalatha Kumari², T. Devaraju³, Parvathi⁴, T. Kosaleswara Reddy⁵, G.G. Rajasekhara⁶

¹Department of Electrical Engineering, Shree Ramchandra College of Engineering, Pune, India.

^{2,4}Department of Electrical and Electronics Engineering, Ballari Institute of Technology and Management, Ballari, India.

³Department of Electrical and Electronics Engineering, Mohan Babu University
(Erstwhile Sree Vidyanikethan Engineering College), Tirupati, India.

⁵Department of Electrical and Electronics Engineering, Sree Rama Engineering College, Tirupathi, India.

⁶Department of Electrical and Electronics Engineering, Koneru Lakshmaiah Education Foundation, Vaddeswaram, India.

³Corresponding Author : devaraj@vidyanikethan.edu

Received: 10 August 2023

Revised: 12 September 2023

Accepted: 10 October 2023

Published: 31 October 2023

Abstract - This work discusses a Fault-Tolerant (FT), highly Reliable Five-Level (RFL) Multilevel Inverter (MLI) that can persist to function still if one or more power switches have an open single switch fault or a specific multi-switch fault. Consecutively to provide quality output voltage profile, the requirement of power switches such as IGBTs used in DC-AC converters is high in number; as a result, they are more likely to fail. Consequently, reliability is among the most critical challenges in MLIs in numerous applications. At the same time, while compromising crucial components (such as FT, charge balance management, and so on), reduced component MLIs may deliver the highest precision in output voltage waveform. For MLIs to function fault-tolerantly, redundant switching states have been stressed regarding switch failures. This work is aimed to provide a unique RFLI during an Open Circuit (OC) failure on a single or several switches for obtaining reliable operation. As a result, the suggested Reliable Five-Level Inverter (RFLI) structure is thought to have fewer components and must fulfill the functioning criteria for the time being. A suitable FT switching method is used in concurrence with appropriate fault clearing to obtain the requisite output voltage waveforms, resulting in dependability. The proposed RFLI architecture offers superior results regarding THD, cost, and efficiency during FT operation. The presented RFLI topology has been validated by using the MATLAB tool.

Keywords - Fault-tolerant, Reliability, Reduced switch count, Multilevel Inverter, Harmonic distortion.

1. Introduction

One of the most critical and challenging tasks is maintaining the continuity and reliability of DC-AC converters in the industrial process and energy systems. This has resulted in fault-tolerant architectures focusing on reliability and system availability. Multi-Level Converters (MLI) are popular for medium-to-high-voltage applications due to their adaptability and high performance [1].

High-Voltage Direct Current (HVDC), renewable energy systems, variable-speed drives, hybrid electric vehicles, alternating current motor drives, solar diversification, and many applications all necessitate power electronic converters [2-5].

The block diagram of integrating renewable energy resources to critical loads using the reliable MLI is shown in Figure 1. Furthermore, because of the vast and rising demand in many applications, there is an issue with the overall dependability of the converter system. MLIs are more

commonly used than two-level inverters because they can produce a range of voltages from medium to high power with a lower harmonic distortion, among other characteristics [6-11]. According to certain studies, 38% of total failures in inverters are caused by the inability of switches [10, 11], and new research indicates that any system dependability to be examined by using some system factors [12-15].

Several decades of research have been undertaken on the issue of fault-tolerant operation and fault detection of MLIs. The work in [16] establishes a fault-tolerant topology; nevertheless, all sorts of single switch failures are not addressed, and the component count is rather enormous. The architecture in [17] contains more redundant components and is unsuitable for multi-switch failure. [18] proposes a topology that does not accommodate all forms of individual switch failures. [18-21] topologies do not support multiple-switch failures, and the need for controlled power switches increases. To address the reliability issue of DC-AC converters, a range of FT topologies are proposed in [22].



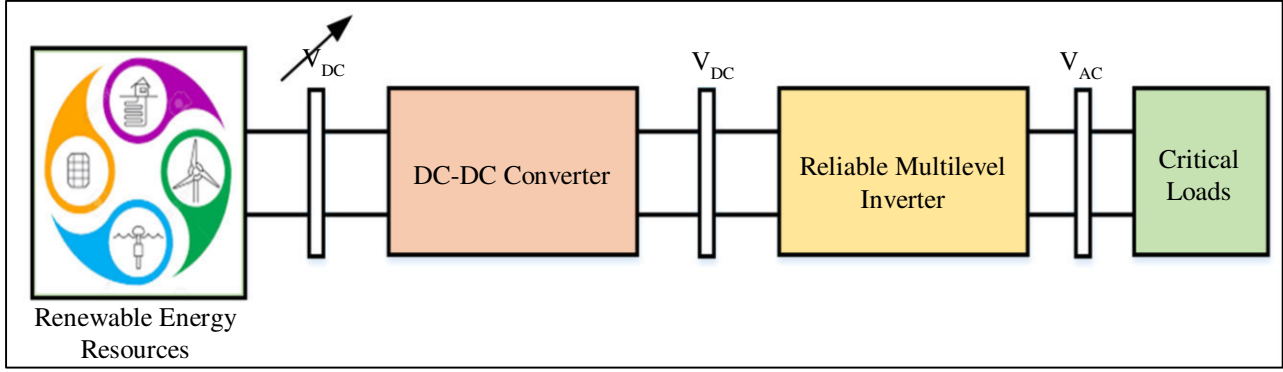


Fig. 1 Block diagram of integration of renewable energy resources to critical loads

The main problem with classical 2L inverters is their lack of reliability; MLIs are used instead of switches because of how vulnerable and standard switching devices are. A bidirectional controller is coupled to a CHB inverter so the affected cell can't be seen elsewhere.

Switching components can switch diodes and make NPC structures functional for faulty cases. The new version of the NPC 3L structure has one bidirectional power switch, a half-bridge, and one segment of diode-clamped inverter, all in a hybrid design, which adds up to more inverters and more cost. The FCFT structure is pretty detailed in [23-25].

The circuit can handle mistakes independently, but the complexity of balancing the capacitor and the number of devices is the leading cause of worry. You need to add extra circuitry to keep the inverter safe. Several modulation schemes for controlling MLIs are described in the literature [26-36]. To tackle these concerns, this paper presents a fault-resistant multisystem inverter capable of resolving all single-switch faults and specific multi-switch issues. In this work, only open circuit faults are analysed.

Consecutively, the proposed FTL MLI is presented as a single stage of this study to address the issues previously identified. The switching control scheme, Sinusoidal Pulse Width Modulation (SPWM) is adjusted minimally to improve MLI reliability. The lowest likely occurrence of a power equipment failure is presented in the tabulated version of the reported FTL MLI. In the case of an open switch fault, the output voltages generated by the fault are the minimum levels needed to keep the systems in working order. The suggested FTL MLI may offer a high degree of redundancy.

2. Proposed Reliable Five Level (RFL) Multilevel Inverter

As illustrated in Figure 2, the presented FT5L inverter includes four two-quadrant switches (S_1 , S_2 , S_5 , and S_6) and two four-quadrant switches (S_3 and S_4). It also contains two capacitors, i.e., C_1 and C_2 across a DC source V_{DC} . Capacitors are utilized to split the voltage of the DC supply into two equal

parts, allowing 02 four-quadrant switches to reach five voltage levels (i.e. $\pm V_{DC}$, $\pm 0.5V_{DC}$ and 0).

Table 1 shows the available switching combinations for obtaining different amounts of output voltage. The voltage levels of $+0.5V_{DC}$ and $-0.5V_{DC}$ have 02 switching states each, whereas the zero voltage has 03 changing conditions, indicating that the presented RFLI architecture provides switching state redundancy. When a fault is found in any of the switches, the gate pulse associated with the fault must be deactivated, and a symmetric output voltage can be achieved by utilizing the redundancy switching logic listed in Table 1.

The inverter provides output voltage with five levels in this mode, and ripple-less capacitor voltages must be attained using the suitable control scheme. Table 1 lists the switching instants of RFLI. In this table, logic '1' indicates the switch ON, while logic '0' indicates the switch OFF. To maintain the same level of stress and load between the switches, the zero voltage interval is divided into three possible combinations.

The faults investigated among the switches are open-circuit and are analyzed independently on every switch. The PWM modulation method shall be adjusted for all fault conditions considered to endure the RFLI faults, as outlined in Table 2. The fault cases shall be analyzed according to Table 2. In the faulty state of any power switch, the preferred voltage profile shall be obtained by the subsequent switching instants, as indicated in Tables 1 and 2. If S_1 , S_2 , S_3 , or S_6 are defective, the RFLI can generate 3L on the output with a lower basic RMS value of output voltage. If the issue is in S_3 , S_6 , or S_7 , the inverter shall provide the desired voltage and power, and the operation shall be restored to normal.

2.1. OC Fault in S_1 and/or S_2

The FLFLI cannot achieve a V_{DC} voltage level since this state contains just a single redundant state. Table 1 shows that the desired voltages of $+0.5V_{DC}$, $0V_{DC}$, and $-0.5V_{DC}$ may be realized by employing state numbers c, e, and h. When this issue occurs, C_2 feeds the inverter to achieve fault tolerance. In this case, higher ripple voltage may be detected across C_1 .

Table 1. Switching states of proposed RFLI

State	Voltage State	S ₁	S ₂	S ₃	S ₄	S ₅	S ₆
a	+V _{DC}	0	1	0	0	1	0
b	+0.5V _{DC}	0	1	0	1	0	0
c	+0.5V _{DC}	0	0	1	0	1	0
d	0	0	0	1	1	0	0
e	0	0	0	0	0	1	1
f	0	1	1	0	0	0	0
g	-0.5V _{DC}	1	0	1	0	0	0
h	-0.5V _{DC}	0	0	0	1	0	1
i	-V _{DC}	1	0	0	0	0	1

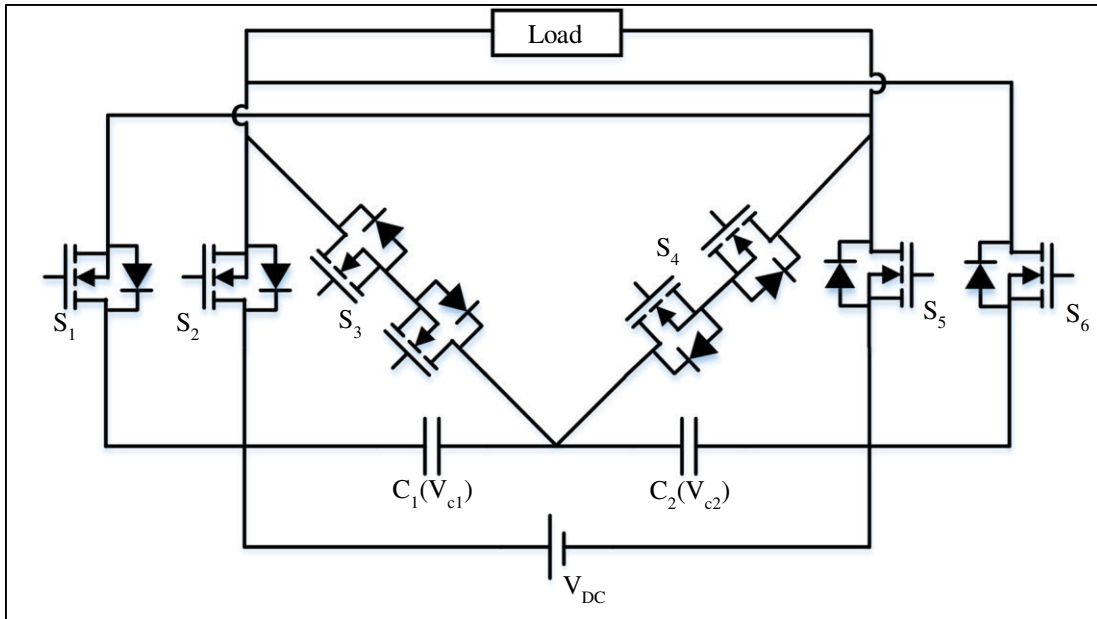


Fig. 2 Proposed Reliable Five Level Inverter (RFLI)

Table 2. Switching states under various fault conditions

Faulty Switch	Voltage State					Output Levels
	+V _{DC}	+0.5V _{DC}	0	-0.5V _{DC}	-V _{DC}	
Normal	a	b/c	d/e/f	g/h	i	5
S ₁ and/or S ₂	-	c	e	h	-	3
S ₅ and/or S ₆	-	b	f	g	-	3
S ₃	a	b	e	h	i	5
S ₄	a	c	f	g	i	5

2.2. OC Fault in S_5 and/or S_6

In this circumstance, the inverter can only provide three levels ($+0.5V_{DC}$, $0V_{DC}$, and $-0.5V_{DC}$). These voltage levels are to be achieved using the state numbers b, f, and g, as shown in Table 1. When this happens, C_1 alone feeds the inverter to provide FT operation. As a result, under this circumstance, there is a higher ripple voltage across C_1 .

2.3. OC Fault in S_3 and/or S_4

In this case, the inverter outputs all the voltage levels. The voltage states may be realized by employing state numbers a, b, e, h, and i for an open circuit in S_3 and a, c, f, g, and i for an open circuit in S_4 , as shown in Table 1. When this happens, the two capacitors supply power simultaneously, so there won't be much voltage ripple in your output voltage.

2.4. Voltage Balancing of Capacitors

The voltage balance will be obtained here by employing multiple redundant states of the suggested inverter, which has two redundant states during no-fault conditions, such as $+0.5V_{DC}$ and $-0.5V_{DC}$. The method was devised by supposing a specific switch (S_f) malfunction and monitoring voltages across two capacitors. S_f , V_{C1} and V_{C2} are used as inputs to the method.

If V_{C1} is greater than V_{C2} , C_1 must be discharged until V_{C1} equals V_{C2} to preserve the capacitor voltage balance. So, to generate $+0.5V_{DC}$ and $-0.5V_{DC}$ voltage levels, C_1 will be employed as the source (state numbers b and g in Table 1). If V_{C2} is greater than V_{C1} , V_{C2} is used as a source to create $+0.5V_{DC}$ and $-0.5V_{DC}$ voltage levels (state numbers c and h, respectively, in Table 1) until V_{C1} equals V_{C2} . Voltage balancing is only possible under healthy conditions due to the availability of various redundant states for $+0.5V_{DC}$, $-0.5V_{DC}$,

and $0V_{DC}$ voltage levels, but voltage balancing is not possible under S_3 and/or S_4 failure because there is only one redundant state for $+0.5V_{DC}$, $-0.5V_{DC}$.

3. Control Strategy

The control technique includes pre-calculated output current and voltage statistics for switch malfunction combinations. S_f serves as a control indicator for the level generation blocks. If S_f is 0/3/4, the inverter may function in 5-level mode; otherwise, if S_f is 1 and/or 2 (or) 5 and/or 6, the inverter can work in 3L mode. The sinusoidal PWM approach is employed in all modes to create control pulses. To make 'n' levels in output side AC voltage, this approach requires one orientation and 'n' levels shifted in-phase carriers.

4. Results and Discussion

The DC voltage is 330V to create an AC voltage of 230V at an inverter side the simulation parameters of $C_1=C_2=220\mu F$, $F_c=1500\text{Hz}$, $R_L=75\Omega$ and $L_L=50\text{mH}$. FTMLI's performance is calculated in terms of efficiency and losses. The loss study was performed by building a thermal model of the IGBT switch. MATLAB/Simulink software in the proposed RFLI gives efficiency of 95.5% and THD of 20.96%. Figures 3 and 4 show the capacitor voltages (V_{C1} , V_{C2}) and voltage difference waveforms under typical operating conditions. Figures 5-10 illustrate the corresponding output voltages and voltages, as well as the defective switch currents, for the default and post-failure scenarios. Faulty S_1 , S_2 and S_5 , S_6 and S_4 switches are assumed at the 0.06-second mark, and associated problematic modules are replaced at the 0.14-second mark. Table 3 displays the total component count for the proposed architecture, which includes switching devices, diodes, capacitors and DC sources. It was observed that the component count was higher in [10, 11] than in [13, 16].

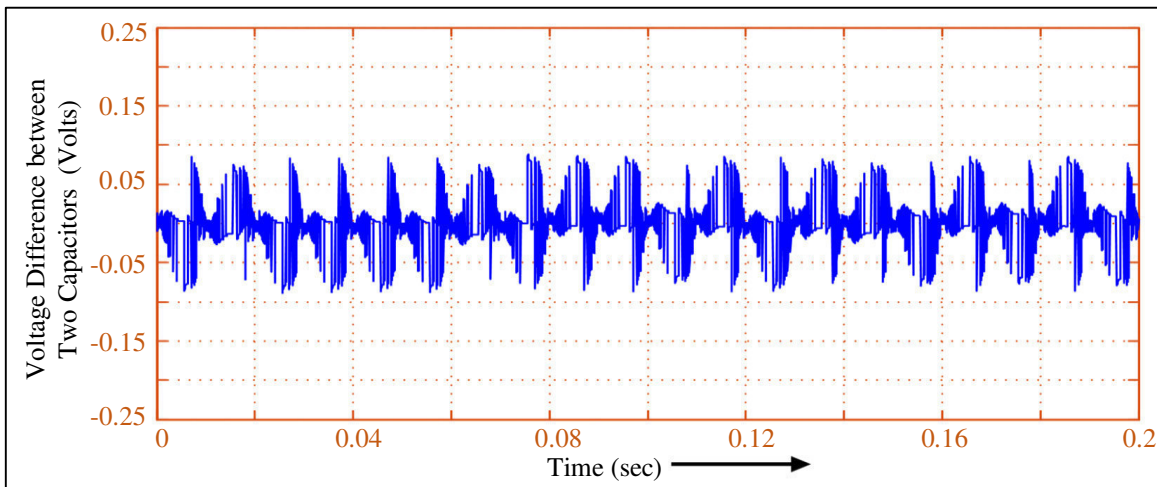


Fig. 3 Capacitor voltage differences during normal conditions

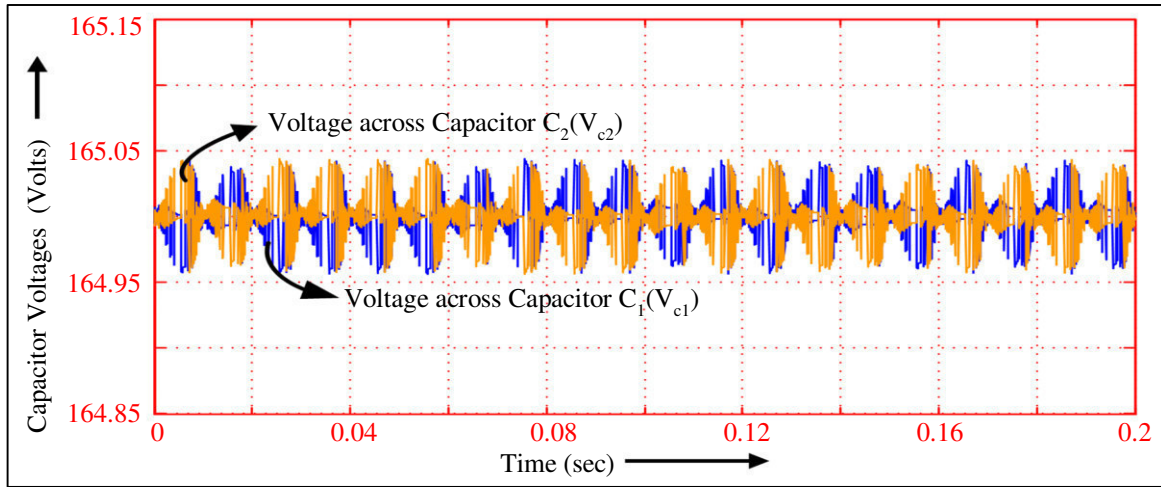


Fig. 4 Capacitor voltages during normal conditions

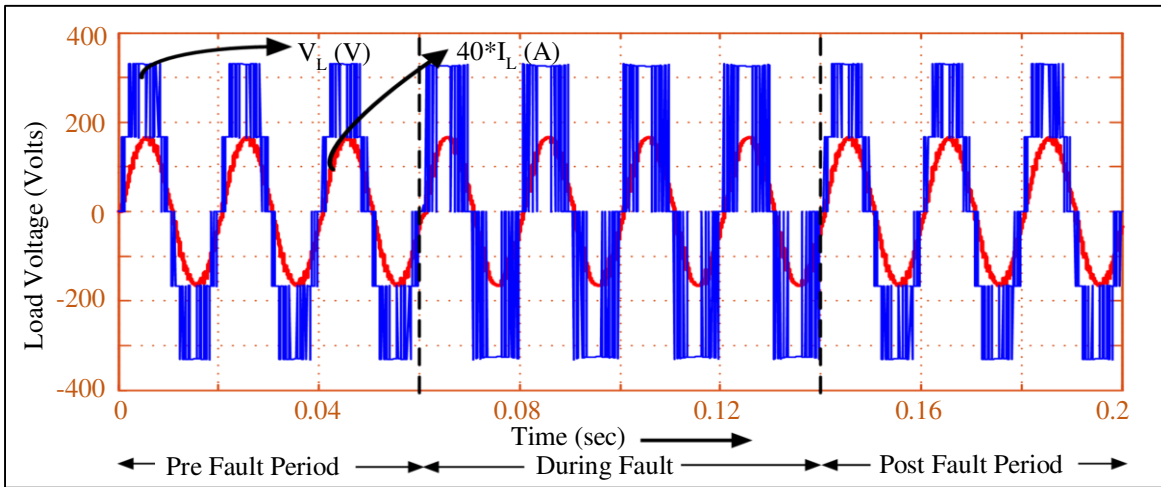


Fig. 5 Load current and load voltage waveforms for fault in S_1 and/or S_2

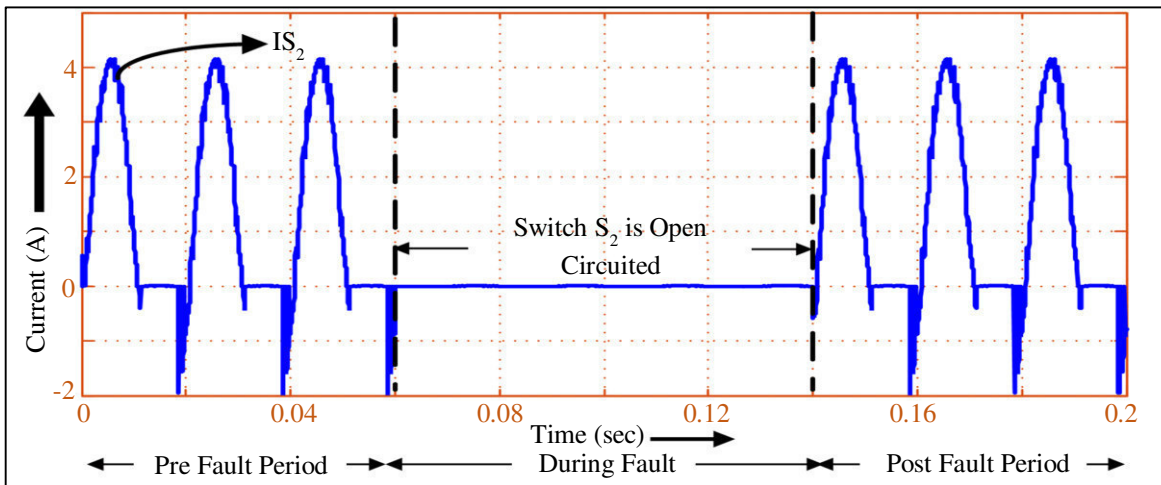


Fig. 6 Switch S_2 current waveform for fault in S_1 and/or S_2

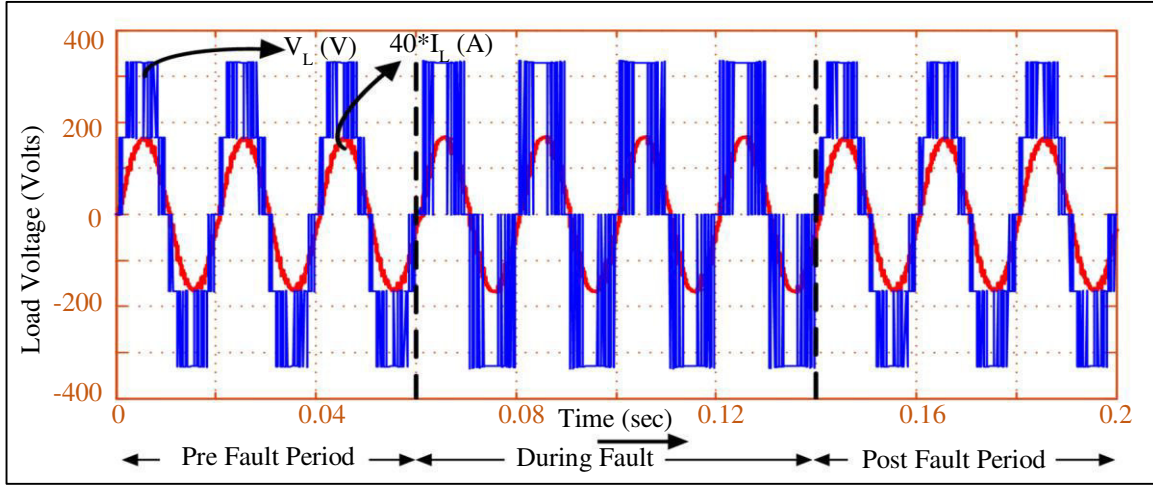


Fig. 7 Load current and load voltage waveforms for fault in S_5 and/or S_6

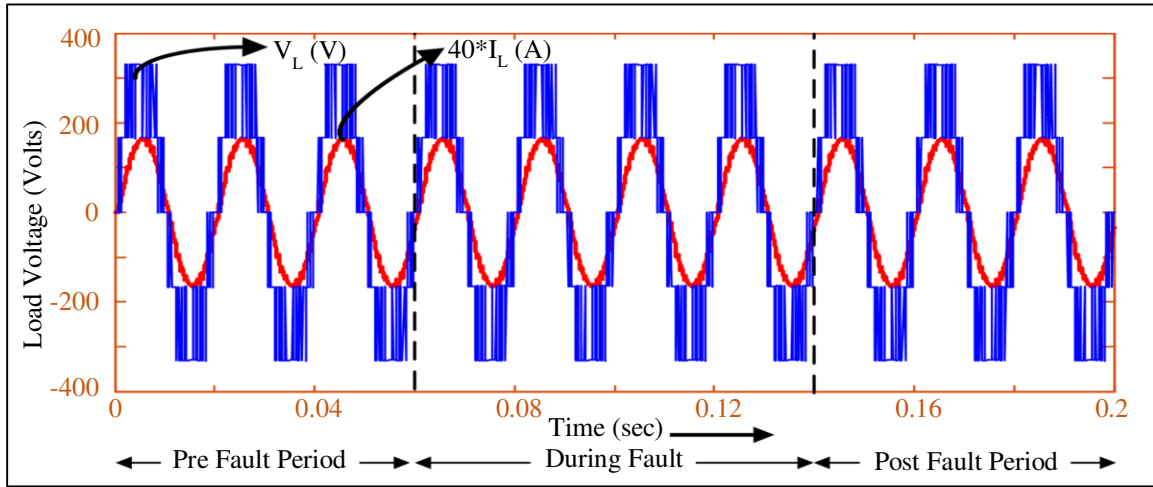


Fig. 8 Load current and load voltage waveforms for fault in S_3

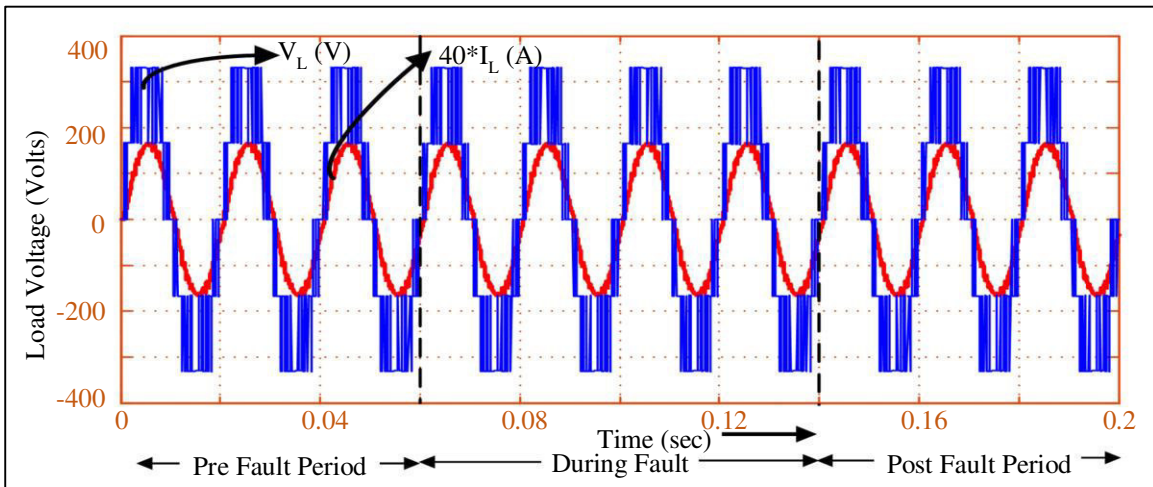


Fig. 9 Load current and load voltage waveforms for fault in S_4

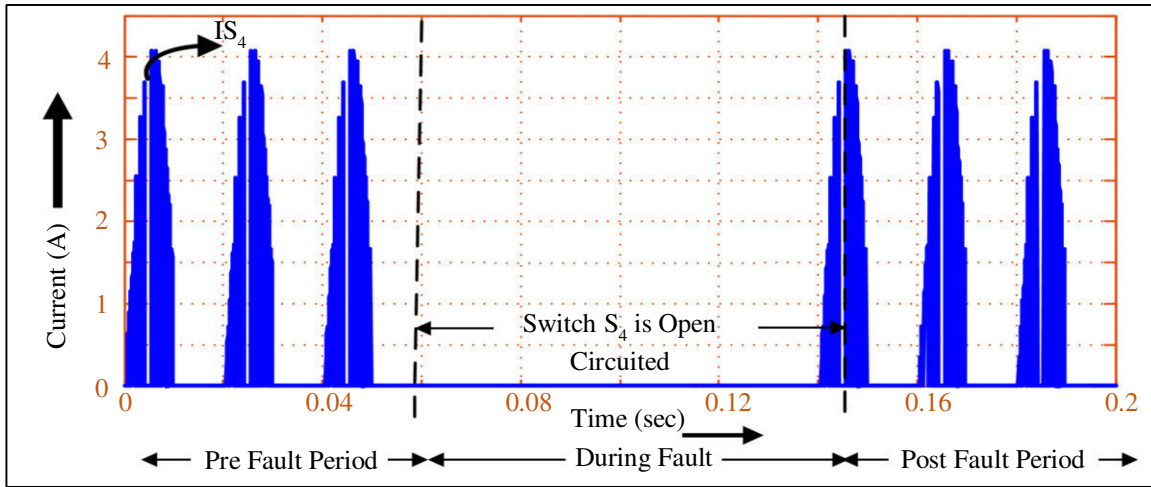
Fig. 10 Switch S_4 current waveform for fault in S_4

Table 3. Comparison of RFLI with existing topologies

Topology	IGBTs	4 Quadrant Switches	Diodes	Capacitors	DC Sources	Reliability
[17]	6	9	2	0	2	No
[19]	6	1	12	0	4	Yes
[20]	20	0	0	0	4	Yes
[22]	22	0	0	7	1	Yes
RFLI	4	2	0	2	1	Yes

5. Conclusion

This paper proposes a novel architecture for an increased Reliability fault tolerant single phase Five Level Inverter (RFLI). It can withstand an open circuit failure in any switch and certain multiple switch combinations. For capacitor voltage balancing, a control algorithm is incorporated. The capacitor voltages are correctly balanced, with a voltage differential of roughly 0.1 volts between the two capacitor

voltages. An inverter's output voltage is always equal to the rated voltage. The proposed RFLI is validated in MATLAB Simulink platforms for various single/multiple open switch faults. A valid fault tolerant switching strategy is utilized with adequate fault clearance to obtain the necessary output voltage waveforms to achieve the reliability of the RFLI. The suggested FTFL inverter contains fewer devices than existing similar FTMLI topologies.

References

- [1] Kasinath Jena et al., "A Single DC Source Generalized Switched Capacitors Multilevel Inverter with Minimal Component Count," *International Transactions on Electrical Energy Systems*, vol. 2023, pp. 1-12, 2023. [\[CrossRef\]](#) [\[GoogleScholar\]](#) [\[PublisherLink\]](#)
- [2] B. Hemanth Kumar et al., "A Switched Capacitor-Based Multilevel Boost Inverter for Photovoltaic Applications," *Journal of Circuits, Systems and Computers*, vol. 32, no. 4, 2022. [\[CrossRef\]](#) [\[GoogleScholar\]](#) [\[PublisherLink\]](#)
- [3] Kasinath Jena et al., "A Novel Three-Phase Switched-Capacitor Five-Level Multilevel Inverter with Reduced Components and Self-Balancing Ability," *Applied Sciences*, vol. 13, no. 3, pp. 1-19, 2023. [\[CrossRef\]](#) [\[GoogleScholar\]](#) [\[PublisherLink\]](#)
- [4] B. Hemanth Kumar et al., *A New Series-Parallel Switched Capacitor Configuration of a DC-DC Converter for Variable Voltage Applications*, Electric Vehicles: Modern Technologies and Trends, pp. 247-270, 2020. [\[CrossRef\]](#) [\[GoogleScholar\]](#) [\[PublisherLink\]](#)
- [5] Busireddy Hemanth Kumar, and Vivekanandan Subburaj, *Integration of RES with MPPT by SVPWM Scheme*, Intelligent Renewable Energy Systems, pp. 157-178, 2021. [\[CrossRef\]](#) [\[GoogleScholar\]](#) [\[PublisherLink\]](#)
- [6] E. Parimalasundar et al., "A Performance Investigations of Modular Multilevel Inverter with Reduced Switch Count," *2022 International Conference on Intelligent Innovations in Engineering and Technology (ICIET)*, Coimbatore, India, pp. 83-87, 2022. [\[CrossRef\]](#) [\[GoogleScholar\]](#) [\[PublisherLink\]](#)
- [7] Kavali Janardhan et al., "Nine-Level Switched Capacitance Multi-Level Inverter with Charge Balance," *2023 IEEE Renewable Energy and Sustainable E-Mobility Conference (RESEM)*, Bhopal, India, pp. 1-6, 2023. [\[CrossRef\]](#) [\[GoogleScholar\]](#) [\[PublisherLink\]](#)

- [8] K. Suresh, and E. Parimalasundar, "Fault Analysis and Clearance in FL-APC DC-AC Converter," *IEEE Canadian Journal of Electrical and Computer Engineering*, vol. 46, no. 1, pp. 1-6, 2023. [[CrossRef](#)] [[GoogleScholar](#)] [[PublisherLink](#)]
- [9] Busireddy Hemanth Kumar et al., "Seventeen Level Switched Capacitor Boost Inverter for Renewable Energy Sources," *2023 IEEE Renewable Energy and Sustainable E-Mobility Conference (RESEM)*, Bhopal, India, pp. 1-6, 2023. [[CrossRef](#)] [[GoogleScholar](#)] [[PublisherLink](#)]
- [10] Kavali Janardhan et al., "High Gain Switched-Capacitor Multilevel Inverter," *2023 IEEE Renewable Energy and Sustainable E-Mobility Conference (RESEM)*, Bhopal, India, pp. 1-6, 2023. [[CrossRef](#)] [[GoogleScholar](#)] [[PublisherLink](#)]
- [11] Busireddy Hemanth Kumar et al., "Twenty-Five-Level Switched Capacitor Multilevel Boost Inverter for Solar PV Applications," *2023 IEEE Renewable Energy and Sustainable E-Mobility Conference (RESEM)*, Bhopal, India, pp. 1-6, 2023. [[CrossRef](#)] [[GoogleScholar](#)] [[PublisherLink](#)]
- [12] B. Lu, and S.K. Sharma, "A Literature Review of IGBT Fault Diagnostic and Protection Methods for Power Inverter," *IEEE Transactions on Industry Applications*, vol. 45, no. 5, pp. 1770-1777, 2009. [[CrossRef](#)] [[GoogleScholar](#)] [[PublisherLink](#)]
- [13] Krishna Kumar Gupta et al., "Multilevel Inverter Topologies with Reduced Device Count: A Review," *IEEE Transactions on Power Electronics*, vol. 31, no. 1, pp. 135-151, 2016. [[CrossRef](#)] [[GoogleScholar](#)] [[PublisherLink](#)]
- [14] Hossein Khoun Jahan et al., "Reconfigurable Multilevel Inverter with Fault-Tolerant Ability," *IEEE Transactions on Power Electronics*, vol. 33, no. 9, pp. 7880-7893, 2018. [[CrossRef](#)] [[GoogleScholar](#)] [[PublisherLink](#)]
- [15] Young-Jong Ko, and Kyo-Beum Lee, "Fault Diagnosis of a Voltage-Fed PWM Inverter for a Three-Parallel Power Conversion System in a Wind Turbine," *Journal of Power Electronics*, vol. 10, no. 6, pp. 686-693, 2010. [[CrossRef](#)] [[GoogleScholar](#)] [[PublisherLink](#)]
- [16] Alan Ristow et al., "Development of a Methodology for Improving Photovoltaic Inverter Reliability," *IEEE Transactions on Industrial Electronics*, vol. 55, no. 7, pp. 2581-2592, 2008. [[CrossRef](#)] [[GoogleScholar](#)] [[PublisherLink](#)]
- [17] Alian Chen et al., "A Multilevel Converter Topology with Fault-Tolerant Ability," *Nineteenth Annual IEEE Applied Power Electronics Conference and Exposition*, USA, vol. 3, pp. 1610-1616, 2005. [[CrossRef](#)] [[GoogleScholar](#)] [[PublisherLink](#)]
- [18] Shivam Prakash Gautam et al., "A Single-Phase Five-Level Inverter Topology with Switch Fault-Tolerance Capabilities," *IEEE Transactions on Industrial Electronics*, vol. 64, no. 3, pp. 2004-2012, 2017. [[CrossRef](#)] [[GoogleScholar](#)] [[PublisherLink](#)]
- [19] Houshang Salimian, and Hossein Iman-Eini, "Fault-Tolerant Operation of Three-Phase Cascaded H-Bridge Converters Using an Auxiliary Module," *IEEE Transactions on Industrial Electronics*, vol. 64, no. 2, pp. 1018-1027, 2017. [[CrossRef](#)] [[GoogleScholar](#)] [[PublisherLink](#)]
- [20] Wenchao Song, and Alex Q. Huang, "Fault-Tolerant Design and Control Strategy for Cascaded H-Bridge Multilevel Converter-Based Statcom," *IEEE Transactions on Industrial Electronics*, vol. 57, no. 8, pp. 2700-2708, 2010. [[CrossRef](#)] [[GoogleScholar](#)] [[PublisherLink](#)]
- [21] K. Suresh et al., "Design and Implementation Bidirectional DC-AC Converter for Energy Storage System," *IEEE Canadian Journal of Electrical and Computer Engineering*, vol. 46, no. 2, pp. 130-136, 2023. [[CrossRef](#)] [[GoogleScholar](#)] [[PublisherLink](#)]
- [22] Madhukar Rao A., and K. Sivakumar, "A Fault-Tolerant Single-Phase FiveLevel Inverter for Grid-Independent PV Systems," *IEEE Transactions on Industrial Electronics*, vol. 62, no. 12, pp. 7569-7577, 2015. [[CrossRef](#)] [[GoogleScholar](#)] [[PublisherLink](#)]
- [23] S. Murugalakshmi, and P. Ranjith Kumar, "Tiling Based Concurrent Supervision of Power and Fault Tolerance in Heterogeneous Multicore Embedded Systems," *SSRG International Journal of VLSI & Signal Processing*, vol. 8, no. 1, pp. 10-13, 2021. [[CrossRef](#)] [[PublisherLink](#)]
- [24] Joan Nicolas-Apruzzese et al., "Analysis of the Fault-Tolerance Capacity of the Multilevel Active-Clamped Converter," *IEEE Transactions on Industrial Electronics*, vol. 60, no. 11, pp. 4773-4783, 2013. [[CrossRef](#)] [[GoogleScholar](#)] [[PublisherLink](#)]
- [25] Mokhtar Aly, Emad M. Ahmed, and Masahito Shoyama, "A New Single-Phase Five-Level Inverter Topology for Single and Multiple Switches Fault Tolerance," *IEEE Transactions on Power Electronics*, vol. 33, no. 11, pp. 9198-9208, 2018. [[CrossRef](#)] [[GoogleScholar](#)] [[PublisherLink](#)]
- [26] Hemanth Kumar Busireddy et al., "A Modified Space Vector PWM Approach for Nine-Level Cascaded H-Bridge Inverter," *Arabian Journal for Science and Engineering (AJSE)*, vol. 44, no. 3, pp. 2131-2149, 2019. [[CrossRef](#)] [[GoogleScholar](#)] [[PublisherLink](#)]
- [27] Krishnan Suresh, and Ezhilvannan Parimalasundar, "Design and Implementation of Dual-Leg Generic Converter for DC/AC Grid Integration," *International Journal of Circuit Theory and Applications*, vol. 51, no. 8, pp. 3865-3879, 2023. [[CrossRef](#)] [[GoogleScholar](#)] [[PublisherLink](#)]
- [28] B. Hemanth Kumar et al., "An Enhanced Space Vector PWM Strategies for Three Phase Asymmetric Multilevel Inverter," *International Transactions on Electrical Energy Systems*, vol. 2023, pp. 1-21, 2023. [[CrossRef](#)] [[GoogleScholar](#)] [[PublisherLink](#)]
- [29] B. Hemanth Kumar, and Makarand M. Lokhande, "An Enhanced Space Vector PWM for Nine-Level Inverter Employing Single Voltage Source," *IEEE Transportation Electrification Conference (ITEC-India)*, Pune, India, pp. 1-6, 2017. [[CrossRef](#)] [[GoogleScholar](#)] [[PublisherLink](#)]
- [30] Parimalasundar Ezhilvannan, and Suresh Krishnan, "Novel Fault Analysis and Compensation in a 5 Level Multilevel DC-AC Converter," *El-Cezeri*, vol. 10, no. 1, pp. 99-108, 2023. [[CrossRef](#)] [[GoogleScholar](#)] [[PublisherLink](#)]
- [31] J. Holtz, "Pulse Width Modulation-A Survey," *IEEE Transactions on Industrial Electronics*, vol. 39, no. 5, pp. 410-420, 1992. [[CrossRef](#)] [[GoogleScholar](#)] [[PublisherLink](#)]

- [32] B. Hemanth Kumar, and Makarand M. Lokhande, "Investigation of Switching Sequences on a Generalized SVPWM Algorithm for Multilevel Inverters," *Journal of Circuits, Systems and Computers*, vol. 28, no. 2, 2018. [[CrossRef](#)] [[GoogleScholar](#)] [[PublisherLink](#)]
- [33] B. Hemanth Kumar, and Makarand M. Lokhande, "Analysis of PWM Techniques on Multilevel Cascaded H-Bridge Three Phase Inverter," *Recent Developments in Control, Automation & Power Engineering (RDCAPE)*, India, pp. 465-470, 2017. [[CrossRef](#)] [[GoogleScholar](#)] [[PublisherLink](#)]
- [34] K. Suresh, and E. Parimalasundar, "ITBC Controlled IPWM for Solar Based Wide Range Voltage Conversion System," *IETE Journal of Research*, pp. 1-9, 2023. [[CrossRef](#)] [[GoogleScholar](#)] [[PublisherLink](#)]
- [35] E. Parimalasundar et al., "Investigation of Efficient Multilevel Inverter for Photovoltaic Energy System and Electric Vehicle Applications," *Electrical Engineering & Electromechanics*, vol. 4, pp. 47-51, 2023. [[CrossRef](#)] [[GoogleScholar](#)] [[PublisherLink](#)]
- [36] Busireddy Hemanth Kumar et al., "An Improved Space Vector Pulse Width Modulation for Nine-Level Asymmetric Cascaded H-Bridge Three-Phase Inverter," *Arabian Journal for Science and Engineering (AJSE)*, vol. 44, no. 3, pp. 2453-2465, 2019. [[CrossRef](#)] [[GoogleScholar](#)] [[PublisherLink](#)]

Original Article

Advanced Control Techniques for Power Quality Enhancement in Off-Grid Wind Power Systems

T. Devaraju¹, M. Pala Prasad Reddy², D. Sujatha³, R. Ravikumar⁴, A. Munisankar⁵, V. Senthilkumar⁶

¹Department of Electrical and Electronics Engineering, Mohan Babu University
(Erstwhile Sree Vidyannikethan Engineering College), Tirupati, India.

²Department of Electrical and Electronics Engineering, Institute of Aeronautical Engineering, Hyderabad, India.

³Department of Electrical and Electronics Engineering, Ballari Institute of Technology and Management, Ballari, India.

⁴Department of Electrical and Electronics Engineering, Karpagam Institute of Technology, Coimbatore, India.

⁵Department of Electrical and Electronics Engineering, Sree Rama Engineering College, Tirupati, India.

⁶Department of Electronics and Communication Engineering, Er. Perumal Manimekalai College of Engineering, Hosur, India.

¹Corresponding Author : devrajt@gmail.com

Received: 05 August 2023

Revised: 08 September 2023

Accepted: 06 October 2023

Published: 31 October 2023

Abstract - Renewable energy output, particularly from wind power, is dependent on unpredictability due to its reliance on climate conditions. Due to this fluctuation, relying only on these sources for a steady power supply is impractical. A constant power source becomes even more crucial in areas where grid electrification is difficult, such as distant locations. To address this problem, the concept of an Isolated Wind Power Generation System (IWPGS) has arisen, designed to operate under variable wind and load situations. However, IWPGS systems suffer power quality issues. Power electronic interfaces can cause harmonics and power quality degradation, nonlinear loads coupled to the system, and the reactive power consumption generated by these loads. This paper presents an Active Power Filter (APF) to solve the power quality issues related to IWPGS. The APF is a device that improves power quality by adjusting for harmonics, reactive power, and other electrical system disturbances. A thorough analysis of numerous indexes proves the APF's performance. These metrics assess the APF's performance in reducing harmonics, improving power factor, and improving the overall power output quality in the IWPGS. This research aims to demonstrate that including an APF into an IWPGS can significantly enhance its power quality, making it a more stable and sustainable energy source, especially in distant places where grid connection is not always possible.

Keywords - Power quality enhancement, Wind energy integration, Voltage regulation, Pulse Width Modulation, Total Harmonic Distortion.

1. Introduction

Off-grid wind power systems gained popularity as sustainable and dependable sources of electricity in isolated and rural areas where grid connectivity was either absent or unreliable. These systems harnessed the wind's kinetic energy to generate electricity, offering a clean and environmentally friendly alternative to conventional diesel generators or expensive grid upgrades. However, integrating wind power into off-grid systems presented several challenges, with power quality emerging as a significant concern. Voltage stability, frequency regulation, and harmonic distortion were all examples of power quality issues that must be addressed.

High power quality was a critical requirement in off-grid wind power systems to ensure the efficient and stable operation of connected loads and to minimize potential damage to sensitive equipment. To achieve this, engineers

and designers of these systems employed various techniques and technologies. They implemented voltage regulation mechanisms to maintain a consistent voltage level, ensuring connected devices received a reliable power supply. Frequency regulation systems were also employed to keep the electrical frequency within acceptable limits, preventing disruptions to the performance of electrical appliances. Furthermore, measures were taken to minimize harmonic distortion, which could lead to electrical noise and interference in the system. Filters and power conditioning equipment were commonly used to reduce harmonic distortion and ensure the power output met the required quality standards [1-3].

In the past, ensuring power quality in off-grid wind power systems presented many challenges that required advanced control solutions. The variable nature of wind speeds led to frequent fluctuations in power output,



necessitating the implementation of complex control algorithms. These algorithms were crucial for maintaining stable voltage and frequency levels within the off-grid system. One of the significant developments in the past was integrating energy storage systems. These systems played a pivotal role in mitigating power outages caused by the inherent variability of wind power. Sophisticated control systems were developed to efficiently manage energy storage, ensuring a continuous and reliable power supply.

Off-grid wind power systems also faced issues related to harmonic distortion and voltage sags. To address these problems, complex filtering and compensation approaches were employed. These solutions helped maintain a clean and stable electrical supply for sensitive electronic equipment and appliances. Another significant challenge in the past was coordinating multiple distributed energy resources, including wind turbines, solar panels, and diesel engines. Optimizing power quality and system efficiency required intricate control strategies to balance the contribution of each energy source and ensure a reliable power supply. In retrospect, addressing these complex control challenges was of utmost importance for the reliability and performance of off-grid wind power systems in the past. These advancements paved the way for more dependable and efficient off-grid renewable energy solutions, contributing to a greener and more sustainable energy landscape [4-8].

2. Literature Review

Off-grid wind power systems have received significant attention recently as a promising way to offer clean, renewable energy to remote or isolated areas. These devices created power by harnessing the kinetic energy of the wind, providing an environmentally acceptable alternative to fossil fuels. Despite their enormous potential, off-grid wind power systems have advantages and disadvantages. One of the key benefits was their capacity to supply a dependable and sustainable source of electricity, reducing reliance on traditional grid infrastructure and lowering greenhouse gas emissions. Off-grid wind power systems were especially useful in rural and off-grid areas with limited or no connection to centralized power grids. They helped achieve energy independence and could drastically lower long-term energy bills. One significant difficulty was the intermittent nature of wind energy, which was affected by wind speed and direction. Energy storage devices, such as batteries, were critical for storing extra wind energy and releasing it when needed. Furthermore, the upfront expenses of off-grid wind power systems could be very substantial, making them less accessible to some communities. Maintenance and technical skills were also required to ensure these systems' long-term reliability [9-11].

The amount by which the electrical waveform generated by the wind turbine deviated from a pure sinusoidal waveform was referred to as Total Harmonic Distortion

(THD). This distortion caused several issues with off-grid wind power systems. To begin with, high THD levels harmed sensitive electrical equipment such as inverters, appliances, and electronic devices. These devices were intended to operate on a pure sinusoidal waveform, and harmonic distortion caused overheating and premature failure.

Furthermore, THD caused system inefficiencies, lowered overall performance, and reduced energy generation. Harmonics in the electrical system caused increased energy losses, resulting in a lower wind turbine power output. These challenges were significant considerations for those managing and maintaining off-grid wind power systems in the past. The impact on the system's reliability and economic sustainability affected the off-grid area's energy demands and jeopardized its long-term viability. Mitigating THD in off-grid wind power systems has presented significant challenges. It often required the deployment of expensive harmonic filters, which proved challenging to maintain in remote locations. Additionally, ensuring these filters' correct sizing and installation was crucial for effectively addressing the issue during that time [11-15].

The charge controller was a typical type used in off-grid wind power systems. It regulated the charging and discharging of batteries to store extra energy for later use. These controllers frequently faced battery maintenance issues, such as sulfation and overcharging, which could impact battery longevity and system efficiency. Regular monitoring and maintenance were essential for mitigating these problems. The inverter, which converted Direct Current (DC) generated by wind turbines and stored in batteries into Alternating Current (AC) for household or industrial usage, was another crucial controller. Voltage fluctuations and harmonic distortions could occur in inverters, impacting the quality of power delivered to appliances.

Furthermore, in the past, off-grid wind power systems had to contend with intermittent wind conditions, necessitating the incorporation of energy storage and backup power sources. The controller algorithms of these systems had to be exceptionally clever to effectively handle the unpredictability of wind energy, all while ensuring a consistent power supply. Moreover, sizing the system and ensuring component compatibility posed significant challenges.

Diverse components had to seamlessly work together to optimize power generation and storage in these systems. This required careful consideration of various factors, including the capacity of the wind turbine, the capacity and type of energy storage, and the efficiency of the entire system. Engineers and designers of off-grid wind power systems had to grapple with these complexities to create reliable and efficient solutions in the past [16-21].

The most renowned applications of Renewable Energy Systems (RES) in the past were Photovoltaic panels (PV) and Wind Turbines (WT). A notable drawback of RES systems has historically been their intermittent nature. Speed control for WT was a crucial aspect of power generation, as it was heavily influenced by connecting the generator to loads or the grid. Options included a total converter with the generator, a wound rotor generator equipped with resistance, or a Double Feed Induction Generator (DFIG), all operated at fixed speeds.

In the past, grid-connected WT systems often featured a 12-kW variable speed asynchronous generator and a 600 V DC link. These systems utilized an AC-DC-AC converter with a back-to-back break chopper, resulting in the highest recorded power losses of 430 W. In a previous study, a 1,050 V DC link converter was employed in conjunction with a Permanent Magnet Synchronous Generator (PMSG) to enhance Power Quality (PQ) and achieve Maximum Power Point Tracking (MPPT). This control structure encompassed a fuzzy logic controller on the turbine side and a PI controller on the load side. The generator employed in this research possessed specifications of 2 KVA output capacity, operated at a speed of 1,800 rpm, and notably, did not require slip rings and brushes.

Furthermore, this generator was designed to be maintenance-free, eliminating the need for rare earth magnets. To regulate the current in the system, a hysteresis current control technique was implemented in conjunction with an AC-DC inverter, as described in [5]. This technique necessitated the incorporation of peak and valley current detectors, constructed using RC integrators and RS flip-flops to enable real-time monitoring of current values [22-25].

A novel control approach was employed for a back-to-back converter with a DC connection linked to a Permanent Magnet Synchronous Generator (PMSG) to enhance Power Quality (PQ) and Maximum Power Point Tracking (MPPT) performance. The introduced APF method reduced source current harmonics without necessitating intricate component adjustments while maintaining a power factor close to unity across a broad range of loads. The APF technique enhanced PQ in an isolated wind turbine WT system equipped with a PMSG supplying power to a nonlinear load. The outcomes were compared between the APF method and the traditional approach involving tuning inductors and capacitors [26-29].

Voltage fluctuations and frequency oscillations in isolated hybrid power systems demanded robust control strategies in the past, and these were achieved by opting for suitable soft computing algorithms like the Genetic Algorithm (GA), Particle Swarm (PS) algorithm, mine blast algorithm, and various other Artificial Intelligence (AI) applications. In the past, addressing voltage fluctuations and frequency oscillations in isolated hybrid power systems

required implementing resilient control strategies. These were effectively attained through carefully selecting appropriate soft computing algorithms, including but not limited to the Genetic Algorithm (GA) and a diverse range of Artificial Intelligence (AI) applications [30].

In off-grid wind power systems, one of the primary challenges was the intermittent nature of wind energy. Wind speeds could vary dramatically, leading to fluctuations in power output. Advanced control techniques, such as predictive control and energy storage integration, were pivotal in mitigating these issues. Predictive control algorithms were employed to anticipate changes in wind conditions and adjust the operation of the wind turbines and energy storage systems accordingly, ensuring a smooth and uninterrupted power supply [31, 32].

On the other hand, on-grid wind power systems faced challenges related to grid integration and power quality. Wind turbines generated power that had to be synchronized with the grid's frequency and voltage levels. Variations in wind speed often lead to voltage and frequency fluctuations, causing power quality issues like voltage sags and flicker. To address these problems, advanced control techniques were employed, including using grid-connected inverters equipped with active power filters. These inverters could rapidly adjust their output to compensate for fluctuations in wind power, maintaining stable grid conditions.

Another critical issue that both off-grid and on-grid systems faced in the past was the introduction of harmonics by power electronic converters. These harmonics could potentially distort voltage and current waveforms, significantly impacting overall power quality. Advanced control techniques such as model predictive and resonant controllers were applied to mitigate these effects, minimizing harmonics and ensuring clean and sinusoidal waveforms.

Moreover, cybersecurity emerged as a concern in past wind power systems. As these systems became more connected and reliant on digital control and communication networks, they became increasingly vulnerable to cyberattacks. Advanced control techniques from the past had to incorporate robust cybersecurity measures to protect against unauthorized access and tampering, safeguarding the integrity and reliability of wind power systems [33-37].

A PMSG connected with a WT, nonlinear loads, and advanced control approaches to improve power quality in off-grid wind power systems. It had been mentioned the following objectives:

Implement a closed-loop controller for the PMSG to maintain stable mechanical torque production, ensuring optimal energy extraction from varying wind conditions.

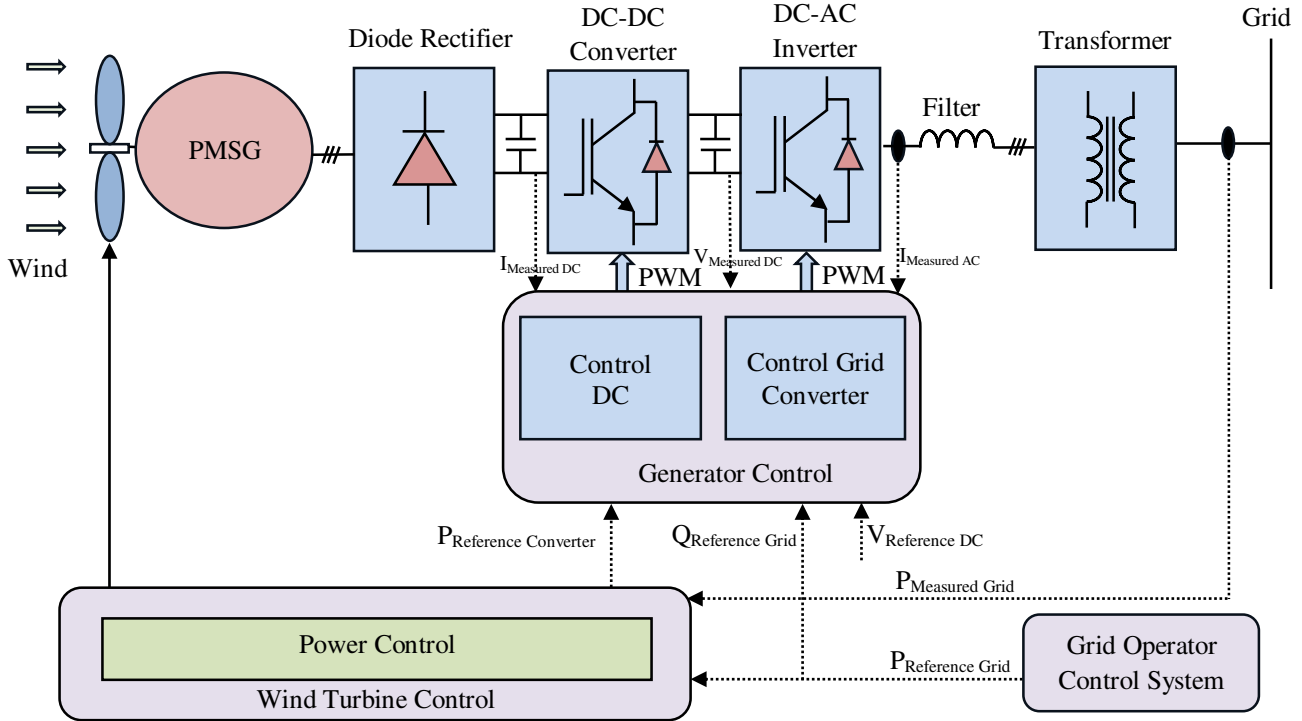


Fig. 1 Structure of isolated wind turbine conversion system

- To design an efficient controller to regulate the output voltage amplitude, maintaining it within acceptable limits to avoid voltage sag or swell during load changes.
- To employ advanced control algorithms and active filters to mitigate harmonics generated by nonlinear loads, ensuring a clean power supply to connected loads.
- To develop a robust inverter control strategy to efficiently convert the variable DC output of the PMSG into stable AC power for the load.
- To optimize the LC filter design to suppress high-frequency voltage components and filter out switching harmonics, improving the overall power quality.
- To implement an intelligent energy management system to balance power supply and demand, ensuring reliable operation and efficient energy utilization in off-grid scenarios.

3. Structure of Isolated Wind Turbine with PMSG

The isolated wind turbine conversion system, formed of several connected parts, was essential for capturing and incorporating wind energy into the grid. A Permanent Magnet Synchronous Generator (PMSG) was at the heart of the system to transform the wind's kinetic energy into electrical energy. The generated AC power was then rectified into DC electricity using a diode rectifier. A DC-DC converter adjusted the voltage levels to guarantee effective power transfer.

The DC power was subsequently transformed into AC power using a DC-AC converter, making it eligible for grid integration. In reaction to shifting wind conditions, wind turbine control systems continuously monitor and improve the turbine's performance. In addition, the grid operator control system made sure that the electrical grid and the wind turbine had constant communication, enabling effective power injection. An active power reference converter and reactive power reference grid were utilized to control the active and reactive power output to keep the system stable. The voltage levels were maintained within acceptable bounds using a voltage reference DC.

Generator control systems made sure the PMSG was running at its best. While transformers made it easier to transform voltage for grid connection, filters were used to reduce harmonics and voltage swings. In the end, this integrated system made it easier to convert wind energy into a dependable supply of electricity, which assisted in creating a sustainable and environmentally friendly energy landscape. Figure 1 illustrates the structure of the isolated wind turbine conversion system.

The kinetic energy of an object is given by in expression (1),

$$E = \frac{1}{2}mv^2 \quad (1)$$

Where, m is mass (kg) and v (m/s) is the velocity.

The power available in wind can be defined in equation (2),

$$P = \frac{1}{2} \rho v^3 A \quad (2)$$

Where A is the cross-sectional area (m^2) of the wind turbine and ρ is the air density.

The coefficient factor C_p for the WT can be expressed in equation (3),

$$C_p = \frac{P_0}{P} \quad (3)$$

The power converted from the wind speed is expressed in equation (4),

$$P_0 = C_p \frac{1}{2} \rho A v^3 \quad (4)$$

Tip-speed ratio of wind turbine can be expressed in equation (5),

$$\lambda = \frac{R \omega}{v} \quad (5)$$

Where R is the radius of the wind turbine, and ω is the angular speed of the wind turbine.

Permanent Magnet Synchronous Generator d and q axis change in current, it can be expressed in equation (6) and (7) respectively,

$$\frac{dI_d}{dt} = -\left(\frac{R_a}{L_d}\right)I_d + \omega_s \frac{L_q}{L_d}I_q + \frac{1}{L_d}U_d \quad (6)$$

$$\frac{dI_q}{dt} = -\frac{R_a}{L_q}I_d - \omega_s \left(\frac{L_d}{L_q}I_d + \frac{1}{L_q}\psi_p\right) + \frac{1}{L_q}U_q \quad (7)$$

Where R_a is the resistance, L_d is the d axis inductance, L_q is the q axis inductance, ω_s is the angular speed of the rotor, ψ_p is the permanent flux, U_d is the d -axis voltage, and U_q is the q -axis voltage.

An extensive procedure was required to integrate renewable energy into the connectivity of a wind turbine generator. A three-phase full bridge diode rectifier was the

first component, and its primary function was to change the alternating current produced by the wind turbine into direct current. This rectifier was essential in guaranteeing a reliable and constant DC output.

The DC boost converter came next and was in charge of increasing the DC voltage to a level appropriate for effective power transmission. This increase in voltage was required to reduce power losses during the energy transfer to the grid. The three-phase inverter, the last component of this complex system, was created to transform the amplified DC power back into grid-compatible AC.

The inverter's function was crucial in ensuring that the electricity produced by the wind turbine could integrate easily into the current grid system. In the end, this networked system enabled the clean, renewable energy produced by the wind turbine to be effectively transmitted to the grid, supplying a dependable source of electricity to power homes and businesses while lowering carbon emissions and dependence on non-renewable energy sources. Figure 2 illustrates the interconnection of three three-phase diode rectifiers, boost converter, and three-phase inverter to load and generator.

The electro-mechanical torque produced by the wind turbine can be expressed in equation (8),

$$T_e = -1.5 \frac{P}{2} \left[(\psi_p I_q + I_d I_q (L_d - L_q)) \right] \quad (8)$$

The phase voltage transformation of the three-axis system can be expressed in equations (9), (10), and (11), respectively,

$$U_{ga} = U_{Ia} - L \frac{dI_a}{dt} - IR_a \quad (9)$$

$$U_{gb} = U_{Ib} - L \frac{dI_b}{dt} - IR_b \quad (10)$$

$$U_{gc} = U_{Ic} - L \frac{dI_c}{dt} - IR_c \quad (11)$$

The axis voltage transformation system can be expressed in equations (12) and (13), respectively,

$$U_d = R_a I_d - \omega_s L_q I_q + \frac{dI_d}{dt} L_d \quad (12)$$

$$U_q = R_a I_q + \omega_s L_d I_d + \frac{dI_q}{dt} L_q + E_s \quad (13)$$

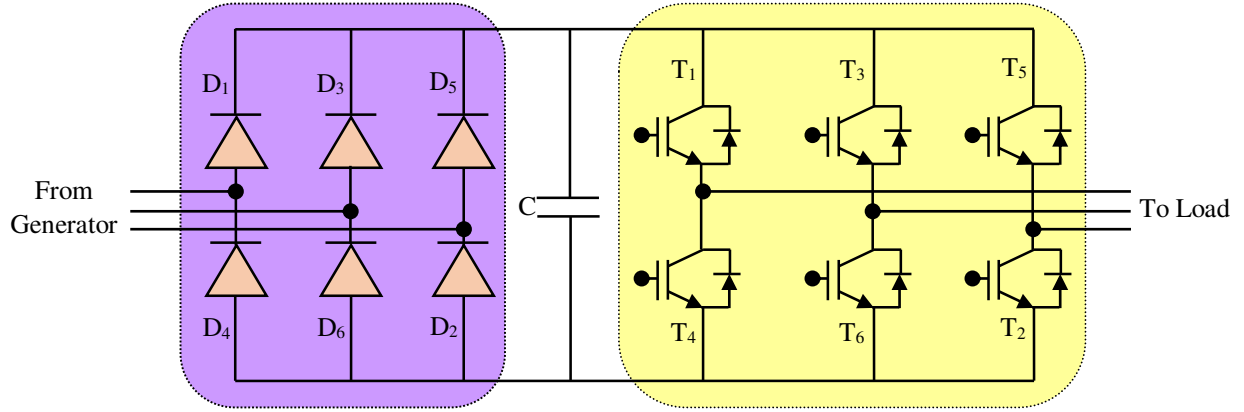


Fig. 2 Interconnection of diode rectifier-DC boost converter-three phase inverter to load

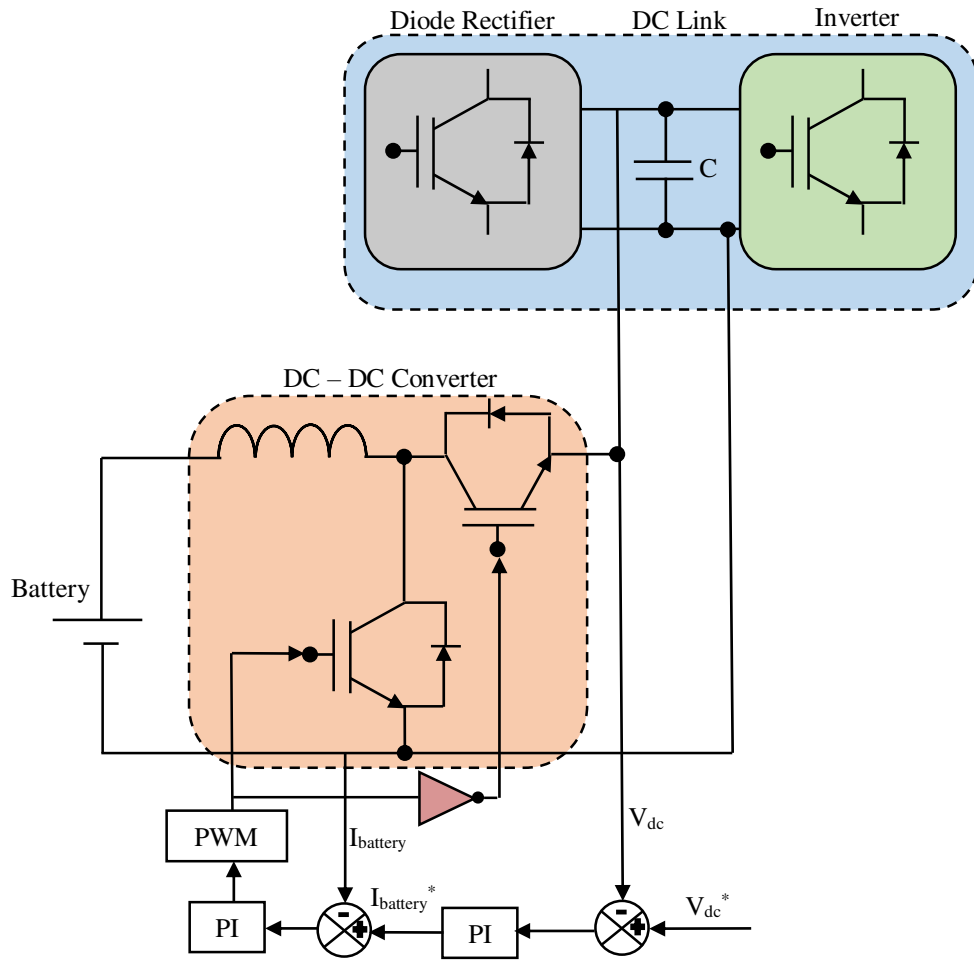


Fig. 3 Controller of DC-DC converter and diode rectifier and inverter system

Transformed d and q axis, controllers can be expressed in equations (14) and (15), respectively,

$$U_d = e_d - RI_d + \omega L I_q - L \frac{dI_d}{dt} \quad (14)$$

$$U_q = -R_d I_q - \omega L I_d - L \frac{dI_q}{dt} \quad (15)$$

Simplifying the above two equations final simplified expression can be illustrated in equation (16),

$$\begin{bmatrix} U_d \\ U_q \\ U_0 \end{bmatrix} = \sqrt{\frac{2}{3}} \begin{bmatrix} \cos(\omega t - \theta) \\ \sin(\omega t - \theta) \\ 0 \end{bmatrix} \quad (16)$$

θ is the Estimated angle in e a-b-c to d-q transformation.

The performance of a wind turbine is essential for producing energy efficiently, and incorporating a Proportional-Integral (PI) controller within its DC-DC converter is critical to optimizing this procedure. A typical control technique called the PI controller modifies the duty cycle of the converter's switching components to control the output voltage.

It balances the trade-off between transient reaction and steady-state precision to ensure that the wind turbine runs at

its peak power for optimum energy extraction. A diode rectifier works with a DC-DC converter to change the changing AC output from the wind turbine generator into a steady DC voltage.

As a device for unidirectional current flow, the diode rectifier only permits forward current to pass from the generator to the DC connection. The DC voltage is then converted into AC by the inverter system's last component, making it eligible for grid connection. The PI controller in the inverter system makes seamless integration with the electrical grid possible, ensuring the output voltage and frequency precisely match the grid's needs.

This system, which includes a wind turbine, a DC-DC converter with a PI controller, a diode rectifier, and an inverter, guarantees effective energy conversion, grid synchronization, and overall optimal performance, promoting renewable energy sources and sustainable power generation.

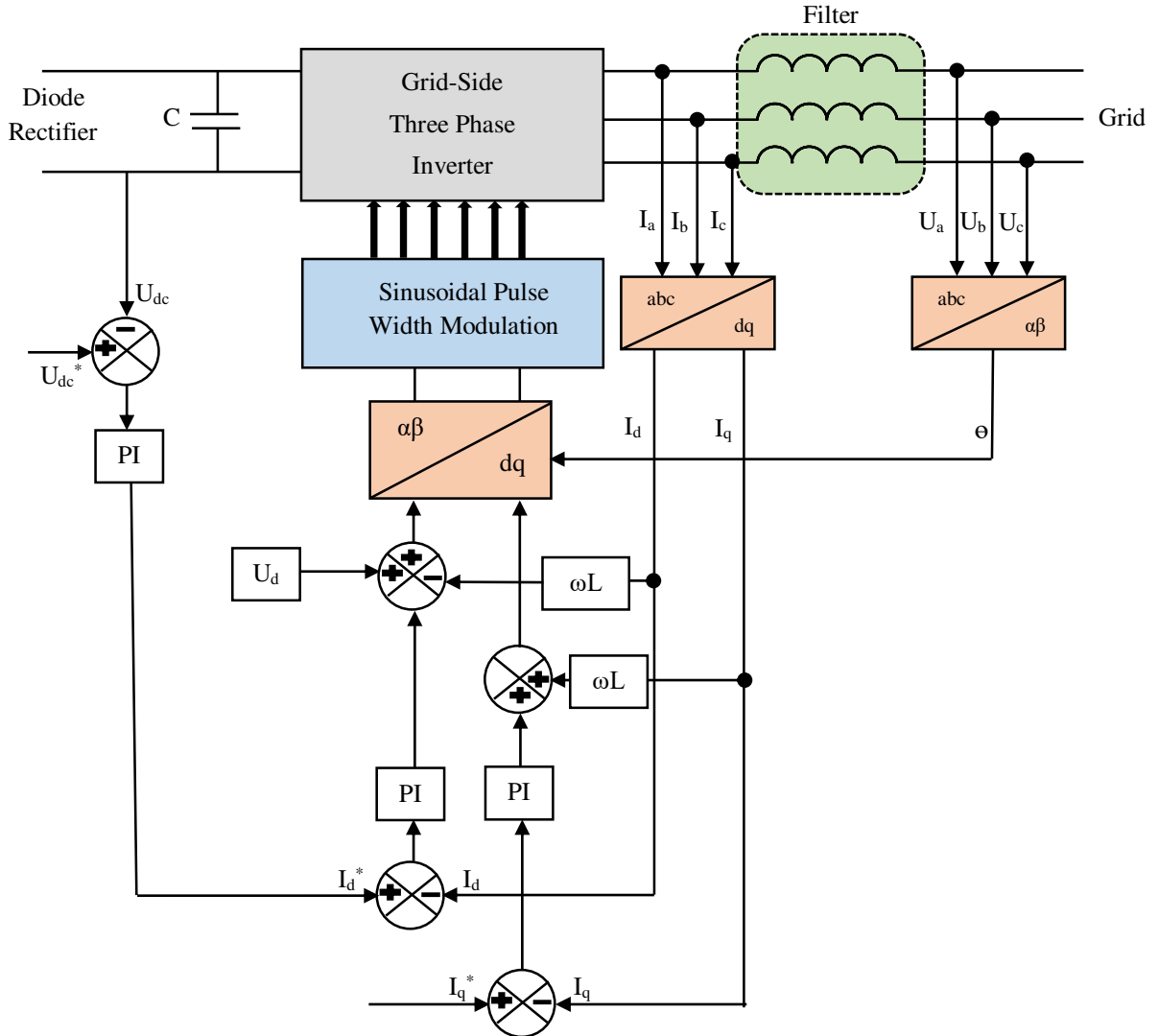


Fig. 4 Three-two axis transformation and two-three-axis transformation of controller from diode rectifier and grid

Advanced techniques such as clark/park three-axis transformation are used to improve control and effectiveness. By transforming the AC variables into a two-axis reference frame using this transformation, the analysis is made more straightforward, and the DC voltage can be controlled precisely. The next stage includes using an inverter to change the DC voltage into an alternating voltage. Popular techniques include sinusoidal Pulse Width Modulation (PWM), which synthesizes the inverter's output voltage by adjusting its power components' switching timings.

However, this conversion process frequently includes harmonics into the output voltage, which must be filtered away to provide a clean AC waveform. To accomplish that, filters are used, assuring adherence to grid requirements and minimizing electromagnetic interference. Utilizing a PI controller to manage the output voltage and current is standard practice. This controller improves system stability and transient response by continuously adjusting the inverter's output to maintain optimal performance. Figure 4 illustrates the Three-two-axis transformation and two-three-axis transformation of the controller from the diode rectifier and grid.

4. Results and Discussion

Figure 5 shows the Permanent Magnet Synchronous Generator's (PMSG) speed in (a), the rotor current in (b), and the stator current in (c). The Wind Energy Conversion

System's (WECS) performance and behaviour can be examined through these crucial factors. The output voltage of the three-phase diode bridge rectifier, which is necessary for converting the alternating current produced by the PMSG into direct current for further processing, is shown in Figure 6. The boost converter's DC link output voltage, which represents the voltage level following the rectification and boosting stages, is shown in Figure 7. Figure 8 provides a thorough overview of the power generation and use inside the system by displaying the Active and Reactive Power generated in the WECS. The pulse signal supplied to the three-phase inverter, which regulates the production of three-phase AC output, is shown in Figure 9. Figure 10 compares the three-phase output voltage with and without a filter to show how well the filter works to lower voltage aberrations.

Understanding the voltage gain of the DC Link Boost Converter, which is essential for improving the energy conversion process, is provided in Figure 11. Figure 12 examines the three-phase inverter Total Harmonic Distortion (THD), contrasting the performance with and without a filter to judge the ability of the generated three-phase output voltage. These statistics help with the investigation, control, and optimization of the WECS by forming a complete visual narrative of its different components. Table 1 illustrates the overall performance parameters of the wind energy conversion system.

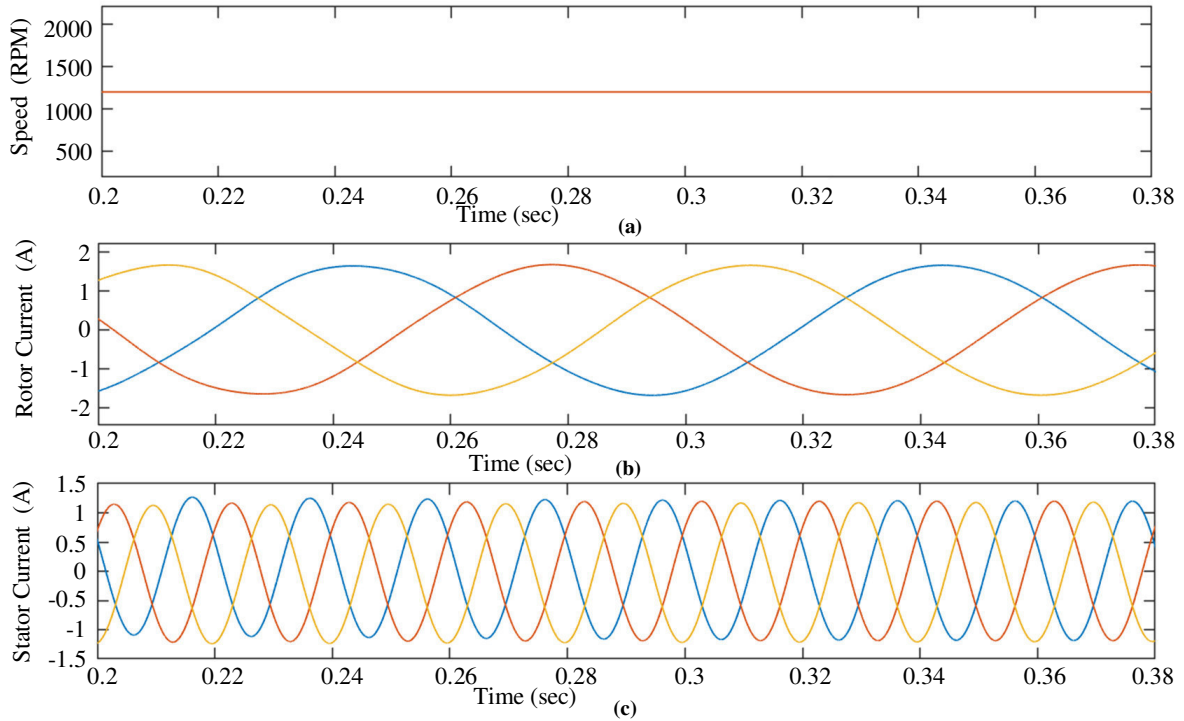


Fig. 5 (a) Speed of PMSG, (b) Rotor current, and (c) Stator current.

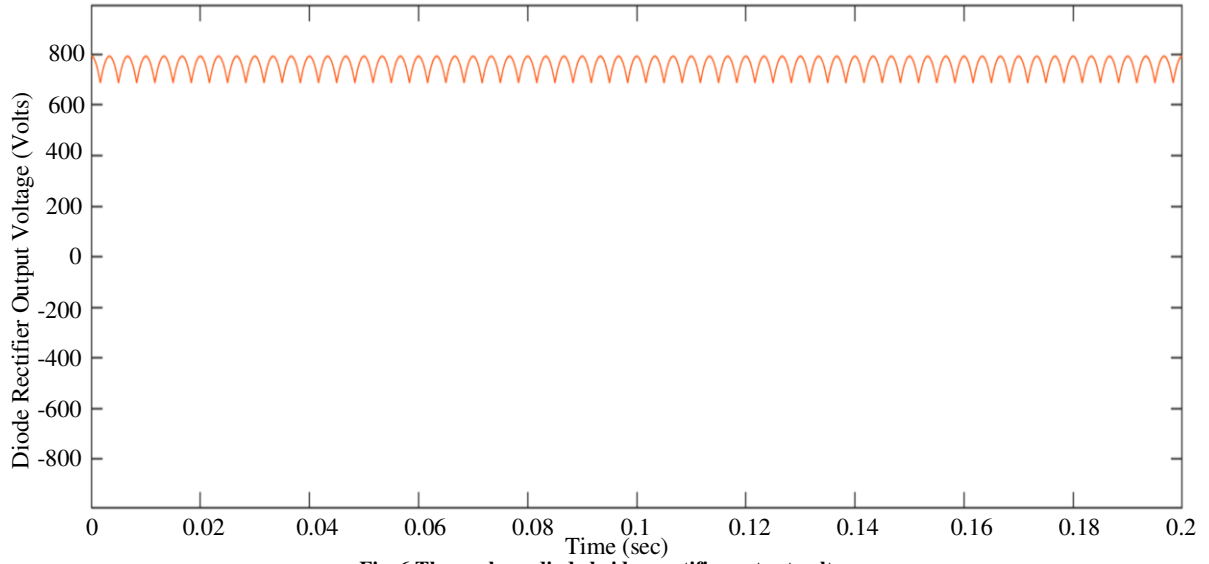


Fig. 6 Three-phase diode bridge rectifier output voltage

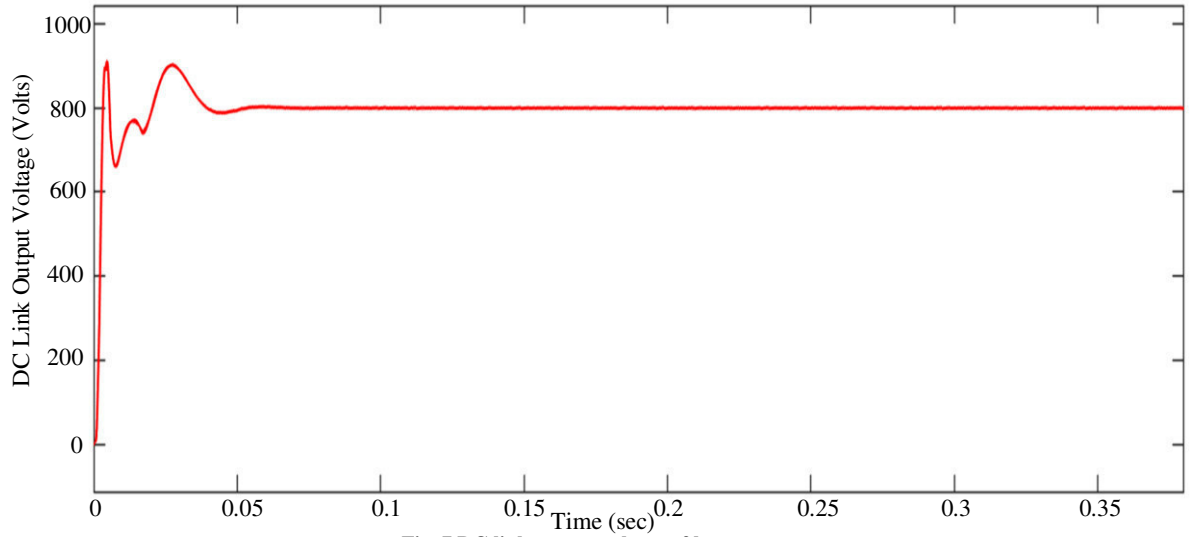


Fig. 7 DC link output voltage of boost converter

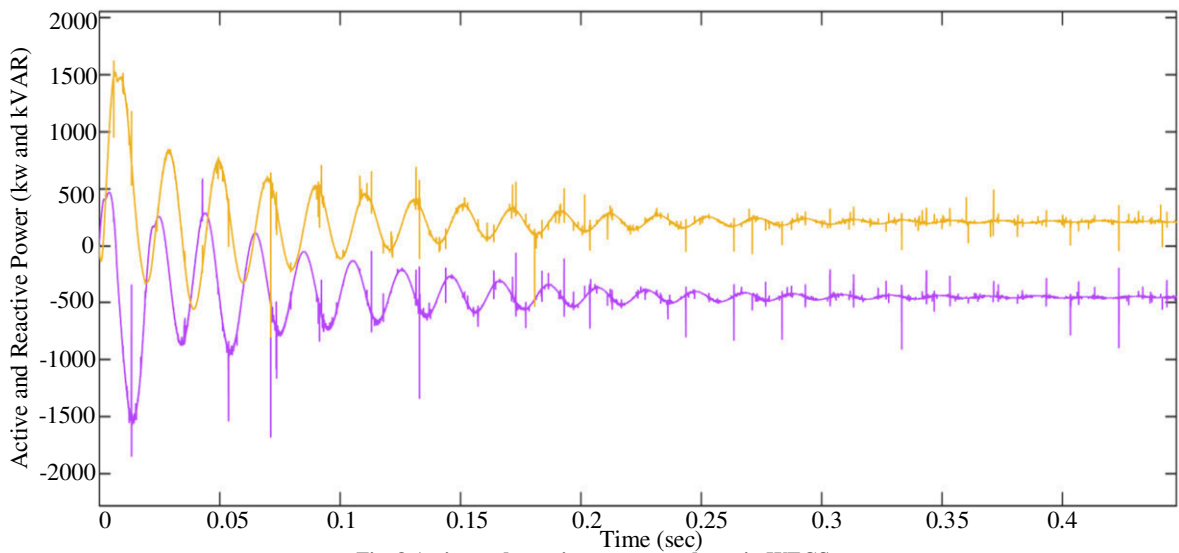


Fig. 8 Active and reactive power produces in WECS

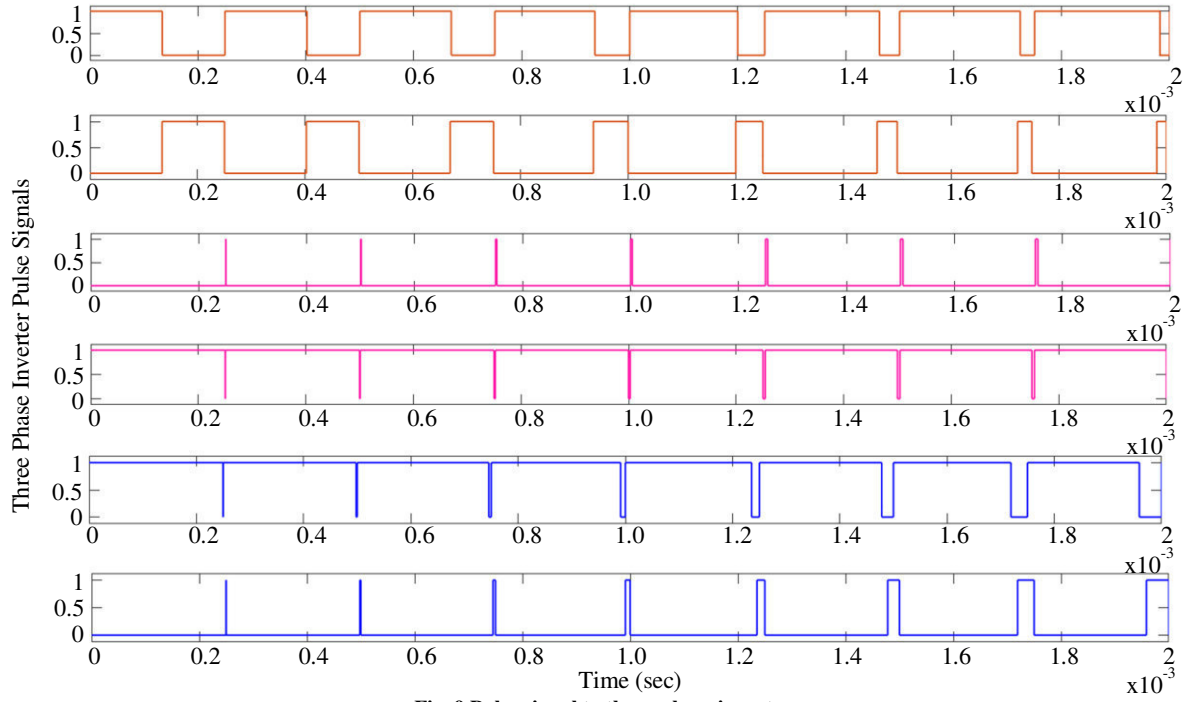


Fig. 9 Pulse signal to three-phase inverter

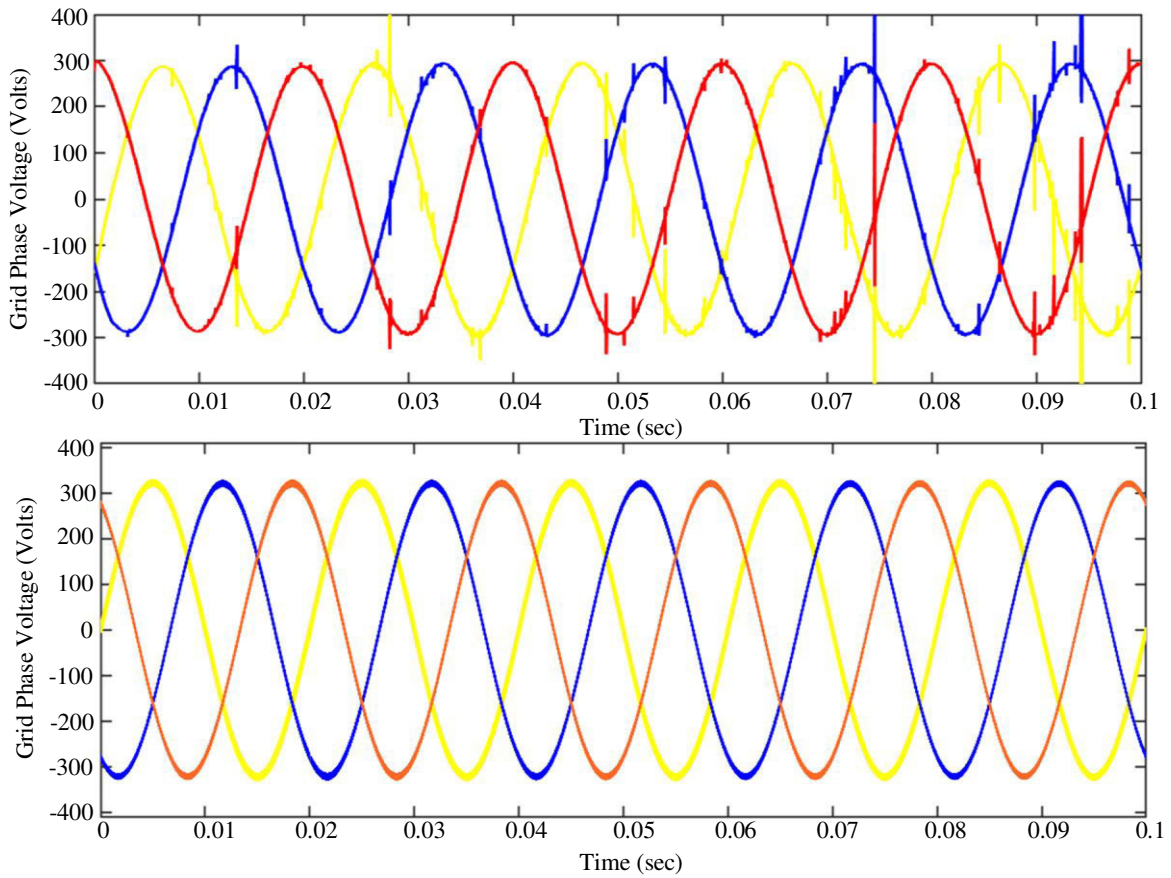
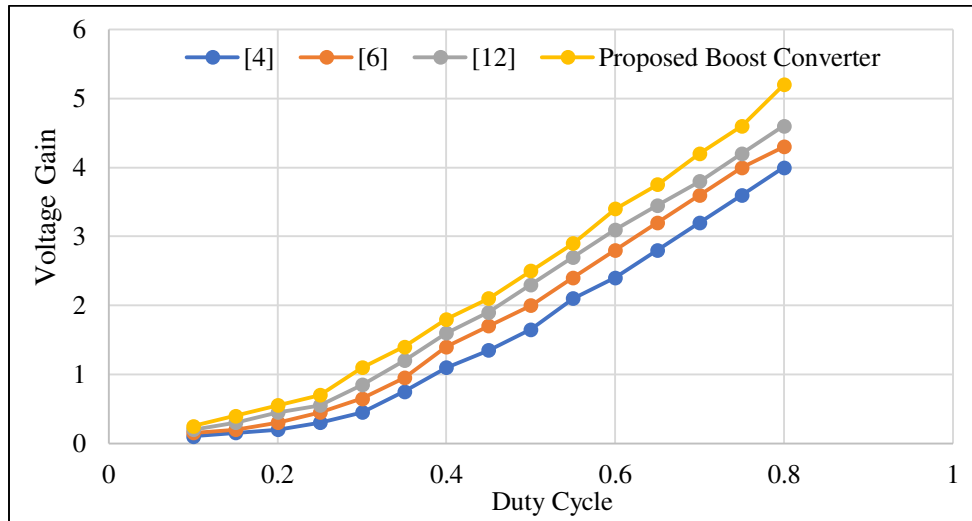


Fig. 10 Three-phase output voltage with and without filter

Table 1. Performance parameters of wind energy conversion system

Parameters	Value
PMSG	
Number of Pair Poles	2
Stator Resistance	2 Ω
Inductance on the d-Axis	0.526 H
Inductance on the q-Axis	0.243 H
Rotor Flux Linkage	1 Wb
Speed	1200 rpm
Rotor Current	1.8 A
Stator Current	1.2 A
Three-Phase Diode Rectifier Output Voltage	800 V
Boost Converter	
Internal Resistance of Inductor	0.2 Ω
Inductance	0.009 H
Capacitance	147 μ F
DC Link Output Voltage	800 V
Duty Cycle	0.8
Voltage Gain	5.2
Three Phase Inverter	
Number of IGBT Switches	6
Number of Driver Circuits	6
Switching Frequency	2 kHz
Grid	
RMS Three-Phase Grid Voltage	300 V
Filter - Resistance	0.8 Ω
Filter - Inductance	0.65 H
%Total Harmonic Distortion (Current) - Without Filter	18 (RL Load)
%Total Harmonic Distortion (Current) - Filter	2.3 (RL Load)

**Fig. 11 Voltage gain of DC link boost converter**

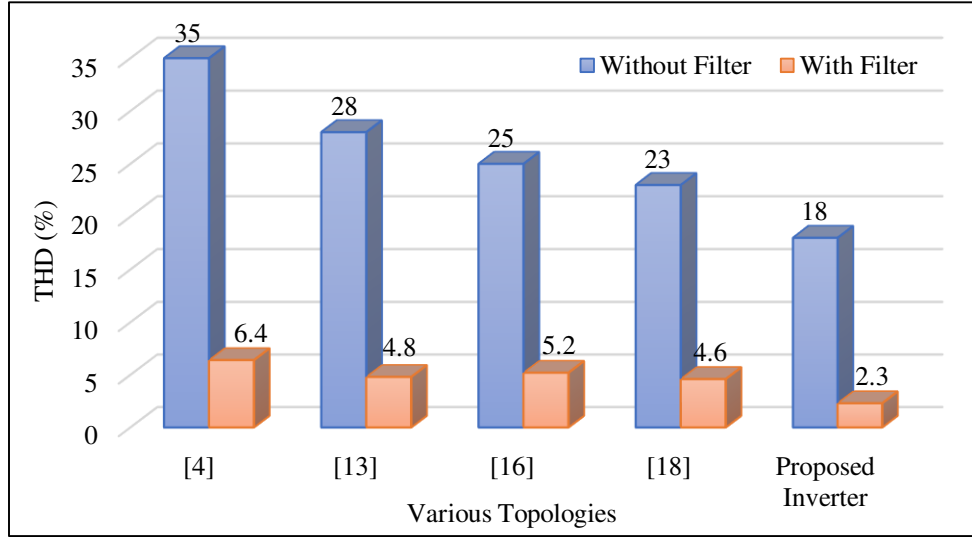


Fig. 12 Three-phase inverter THD analysis based on with and without filter

5. Conclusion

The critical issue of power quality in isolated wind power generation systems is discussed in this paper, and an effective solution in the form of an active power filter has been proposed. Despite being crucial for remote and grid-challenged areas, IWPGS systems experience power quality issues for various reasons, such as harmonics, reactive power consumption, and nonlinear loads. The APF is promoted as a workable solution to these problems, capable of strengthening system stability and improving power quality by reducing harmonics and reactive power. This research investigation proves the effectiveness of the APF in lowering harmonics, boosting power factor, and raising the general Caliber of power output in IWPGS settings by a thorough

review of numerous performance measures. These results suggest that adding an APF to an IWPGS can significantly improve its dependability and sustainability, particularly in rural areas where grid access is inconsistent or insufficient. Future improvements in control methods could substantially improve the power quality of off-grid wind power installations. The creation of advanced predictive control algorithms that can foresee and immediately address power quality problems is a crucial field of investigation. These algorithms can increase system performance using updated sensor technologies and data analytics. A continuous power supply can be ensured under various wind situations by integrating energy storage solutions, such as innovative batteries, which can further stabilize power output.

References

- [1] David Cortes-Vega, Fernando Ornelas-Tellez, and Juan Anzures-Marin, "Nonlinear Optimal Control for PMSG-Based Wind Energy Conversion Systems," *IEEE Latin America Transactions*, vol. 19, no. 7, pp. 1191-1198, 2021. [[CrossRef](#)] [[Google Scholar](#)] [[Publisher Link](#)]
- [2] Babak Mehdizadeh Gavvani et al., "Efficiency Enhancements of Wind Energy Conversion Systems Using Soft Switching Multiple Model Predictive Control," *IEEE Transactions on Energy Conversion*, vol. 37, no. 2, pp. 1187-1199, 2022. [[CrossRef](#)] [[Google Scholar](#)] [[Publisher Link](#)]
- [3] Ashish Kushwaha, Madan Gopal, and Bhim Singh, "Q-Learning Based Maximum Power Extraction for Wind Energy Conversion System with Variable Wind Speed," *IEEE Transactions on Energy Conversion*, vol. 35, no. 3, pp. 1160-1170, 2020. [[CrossRef](#)] [[Google Scholar](#)] [[Publisher Link](#)]
- [4] K. Suresh, and E. Parimalasundar, "ITBC Controlled IPWM for Solar Based Wide Range Voltage Conversion System," *IETE Journal of Research*, 2023. [[CrossRef](#)] [[Google Scholar](#)] [[Publisher Link](#)]
- [5] R. Sindhuja et al., "A Reconfigurable Multilevel Inverters with Minimal Switches for Battery Charging and Renewable Energy Applications," *2022 6th International Conference on Electronics, Communication and Aerospace Technology*, India, pp. 422-427, 2022. [[CrossRef](#)] [[Google Scholar](#)] [[Publisher Link](#)]
- [6] M.A. Mohammed Manaz, and Chan-Nan Lu, "Design of Resonance Damper for Wind Energy Conversion System Providing Frequency Support Service to Low Inertia Power Systems," *IEEE Transactions on Power Systems*, vol. 35, no. 6, pp. 4297-4306, 2020. [[CrossRef](#)] [[Google Scholar](#)] [[Publisher Link](#)]
- [7] Hussein Shutari et al., "Development of a Novel Efficient Maximum Power Extraction Technique for Grid-Tied VSWT System," *IEEE Access*, vol. 10, pp. 101922-101935, 2022. [[CrossRef](#)] [[Google Scholar](#)] [[Publisher Link](#)]

- [8] E. Parimalasundar et al., "Investigation of Efficient Multilevel Inverter for Photovoltaic Energy System and Electric Vehicle Applications," *Electrical Engineering & Electromechanics*, vol. 4, pp. 47-51, 2023. [[CrossRef](#)] [[Google Scholar](#)] [[Publisher Link](#)]
- [9] Xuguo Jiao, Qinmin Yang, and Bin Xu, "Hybrid Intelligent Feedforward-Feedback Pitch Control for VSWT with Predicted Wind Speed," *IEEE Transactions on Energy Conversion*, vol. 36, no. 4, pp. 2770-2781, 2021. [[CrossRef](#)] [[Google Scholar](#)] [[Publisher Link](#)]
- [10] Ezhilvannan Parimalasundar, and Krishnan Suresh, "Fault Analysis and Compensation in a Five Level Multilevel DC-AC Converter," *El-Cezeri Journal of Science and Engineering*, vol. 10, no. 1, pp. 99-108, 2023. [[CrossRef](#)] [[Google Scholar](#)] [[Publisher Link](#)]
- [11] Krishnan Suresh, and Ezhilvannan Parimalasundar, "Design and Implementation of Dual-Leg Generic Converter for DC/AC Grid Integration," *International Journal of Circuit Theory and Applications*, vol. 51, no. 8, pp. 3865-3879, 2023. [[CrossRef](#)] [[Google Scholar](#)] [[Publisher Link](#)]
- [12] H.M. Yassin, R.R. Abdel-Wahab, and H.H. Hanafy, "Active and Reactive Power Control for Dual Excited Synchronous Generator in Wind Applications," *IEEE Access*, vol. 10, pp. 29172-29182, 2022. [[CrossRef](#)] [[Google Scholar](#)] [[Publisher Link](#)]
- [13] Bhim Singh, Rohini Sharma, and Seema Kewat, "Robust Control Strategies for SyRG-PV and Wind-Based Islanded Microgrid," *IEEE Transactions on Industrial Electronics*, vol. 68, no. 4, pp. 3137-3147, 2021. [[CrossRef](#)] [[Google Scholar](#)] [[Publisher Link](#)]
- [14] K. Suresh et al., "Design and Implementation Bidirectional DC-AC Converter for Energy Storage System," *IEEE Canadian Journal of Electrical and Computer Engineering*, vol. 46, no. 2, pp. 130-136, 2023. [[CrossRef](#)] [[Google Scholar](#)] [[Publisher Link](#)]
- [15] Luca Bigarelli et al., "PWM-Based Optimal Model Predictive Control for Variable Speed Generating Units," *IEEE Transactions on Industry Applications*, vol. 56, no. 1, pp. 541-550, 2020. [[CrossRef](#)] [[Google Scholar](#)] [[Publisher Link](#)]
- [16] Mohammad Farhadi Kangarlu, and Ebrahim Babaei, "Cross-Switched Multilevel Inverter: An Innovative Topology," *IET Power Electronics*, vol. 6, no. 4, pp. 642-651, 2013. [[CrossRef](#)] [[Google Scholar](#)] [[Publisher Link](#)]
- [17] Vishal Anand, and Varsha Singh, "A 13 Level Switched-Capacitor Multilevel Inverter with Single DC Source," *IEEE Journal of Emerging and Selected Topics in Power Electronics*, vol. 10, no. 2, pp. 1575-1586, 2022. [[CrossRef](#)] [[Google Scholar](#)] [[Publisher Link](#)]
- [18] M. Jagabar Sathik et al., "An Improved Seven-Level PUC Inverter Topology with Voltage Boosting," *IEEE Transactions on Circuits and Systems II: Express Briefs*, vol. 67, no. 1, pp. 127-131, 2020. [[CrossRef](#)] [[Google Scholar](#)] [[Publisher Link](#)]
- [19] K. Suresh, and E. Parimalasundar, "Fault Analysis and Clearance in FL-APC DC-AC Converter," *IEEE Canadian Journal of Electrical and Computer Engineering*, vol. 46, no. 1, pp. 1-6, 2023. [[CrossRef](#)] [[Google Scholar](#)] [[Publisher Link](#)]
- [20] Jingxin Hu et al., "Instantaneous Flux and Current Control for a Three-Phase Dual-Active Bridge DC-DC Converter," *IEEE Transactions on Power Electronics*, vol. 35, no. 2, pp. 2184-2195, 2020. [[CrossRef](#)] [[Google Scholar](#)] [[Publisher Link](#)]
- [21] Hao Chen, Ayman M. EL-Refaie, and Nabeel A.O. Demerdash, "Flux-Switching Permanent Magnet Machines: A Review of Opportunities and Challenges-Part II: Design Aspects, Control, and Emerging Trends," *IEEE Transactions on Energy Conversion*, vol. 35, no. 2, pp. 699-713, 2020. [[CrossRef](#)] [[Google Scholar](#)] [[Publisher Link](#)]
- [22] Kasinath Jena et al., "A Novel Three-Phase Switched-Capacitor Five-Level Multilevel Inverter with Reduced Components and Self-Balancing Ability," *Applied Sciences*, vol. 13, no. 3, pp. 1-19, 2023. [[CrossRef](#)] [[Google Scholar](#)] [[Publisher Link](#)]
- [23] B. Perumal, K. Suresh, and E. Parimalasundar, "Fault Analysis in the 5-Level Multilevel NCA DC-AC Converter," *Automatika*, vol. 64, no. 3, pp. 606-612, 2023. [[CrossRef](#)] [[Google Scholar](#)] [[Publisher Link](#)]
- [24] V.S. Prasad Rao K., and Sankar Peddapati, "Single-Phase Five-Level Multi Switch Fault-Tolerant Inverter," *IEEE Transactions on Power Electronics*, vol. 38, no. 6, pp. 7336-7347, 2023. [[CrossRef](#)] [[Google Scholar](#)] [[Publisher Link](#)]
- [25] E. Parimalasundar et al., "A Performance Investigations of Modular Multilevel Inverter with Reduced Switch Count," *2022 International Conference on Intelligent Innovations in Engineering and Technology (ICIET)*, Coimbatore, India, pp. 83-87, 2022. [[CrossRef](#)] [[Google Scholar](#)] [[Publisher Link](#)]
- [26] Yaoqiang Wang et al., "A Switched-Capacitor Multilevel Inverter Using Series-Parallel Conversion with Reduced Components," *CPSS Transactions on Power Electronics and Applications*, vol. 7, no. 3, pp. 335-346, 2022. [[CrossRef](#)] [[Google Scholar](#)] [[Publisher Link](#)]
- [27] Chung-Han Lin, and Yuan-Kang Wu, "Overview of Frequency-Control Technologies for a VSC-HVDC-Integrated Wind Farm," *IEEE Access*, vol. 9, pp. 112893-112921, 2021. [[CrossRef](#)] [[Google Scholar](#)] [[Publisher Link](#)]
- [28] Parimalasundar Ezhilvannan et al., "Analysis of the Effectiveness of a Two-Stage Three-Phase Grid Connected Inverter for Photovoltaic Applications," *Journal of Solar Energy Research*, vol. 8, no. 2, pp. 1471-1483, 2023. [[CrossRef](#)] [[Google Scholar](#)] [[Publisher Link](#)]
- [29] K.B. Veerasha, M.G. Manjula, and A.H. Thejaswi, "Enhancement of Power Quality Using Single Phase Generalised Unified Power Quality Conditioner in Distribution System," *International Journal of Recent Engineering Science*, vol. 10, no. 4, pp. 1-6, 2023. [[CrossRef](#)] [[Google Scholar](#)] [[Publisher Link](#)]
- [30] B. Hemanth Kumar et al., "Control of Modified Switched Reluctance Motor for EV Applications," *Trends in Electrical, Electronics, Computer Engineering Conference (TEECCON)*, pp. 123-127, 2022. [[CrossRef](#)] [[Google Scholar](#)] [[Publisher Link](#)]
- [31] Majid Farhangi et al., "A Single-Source Single-Stage Switched-Boost Multilevel Inverter: Operation, Topological Extensions, and Experimental Validation," *IEEE Transactions on Power Electronics*, vol. 37, no. 9, pp. 11258-11271, 2022. [[CrossRef](#)] [[Google Scholar](#)] [[Publisher Link](#)]

- [32] E. Parimalasundar et al., “Performance Analysis of Five Level Modular Multilevel Inverter for PV-Grid Connected System,” *9th International Conference on Electrical Energy Systems (ICEES)*, Chennai, India, pp. 481-485, 2023. [[CrossRef](#)] [[Google Scholar](#)] [[Publisher Link](#)]
- [33] B.H. Kumar et al., “An Enhanced Space Vector PWM Strategies for Three Phase Asymmetric Multilevel Inverter,” *International Transactions on Electrical Energy Systems*, vol. 2023, pp. 1-29, 2023. [[CrossRef](#)] [[Google Scholar](#)] [[Publisher Link](#)]
- [34] Charles I. Odeh et al., “A Five-Leg Three-Level Dual-Output Inverter,” *IEEE Transactions on Circuits and Systems II: Express Briefs*, vol. 70, no. 2, pp. 690-694, 2023. [[CrossRef](#)] [[Google Scholar](#)] [[Publisher Link](#)]
- [35] R. Sindhuja et al., “Comparison between Symmetrical and Asymmetrical 13 Level MLI with Minimal Switches,” *International Conference on Automation, Computing and Renewable Systems (ICACRS)*, pp. 187-191, 2022. [[CrossRef](#)] [[Google Scholar](#)] [[Publisher Link](#)]
- [36] Vijayalakshmi R. et al., “Challenges, Issues and Solution for Hybrid Solar Pv and Wind Power Generation with Off-Grid Integration,” *International Journal of Engineering Trends and Technology*, vol. 68, no. 3, pp.18-21, 2020. [[Publisher Link](#)]
- [37] E. Parimalasundar et al., “Performance Analysis of DC-DC Converter for Electric Vehicle Charging Applications,” *7th International Conference on Computing Methodologies and Communication (ICCMC)*, pp. 1543-1546, 2023. [[CrossRef](#)] [[Google Scholar](#)] [[Publisher Link](#)]

Integrated Control and Modeling of a PV-Wind Hybrid System for DC Electric Micro-Networks

Santhosha B M
Department of Electrical and Electronics
Engineering,
Ballari Institute of Technology and
Management, Ballari,
Visvesvaraya Technological University,
Karnataka, India
santosh@bitm.edu.in

Daxa Vekariya
Department of Computer Science &
Engineering,
Parul Institute of Engineering and
Technology,
Parul University,
Post Limda 391760, Gujarat, India
daxa.vekariya18436@paruluniversity.ac.in

Harendra Singh Negi
Department of Computer Science &
Engineering,
Graphic Era Deemed to be University,
Dehradun, Uttarakhand, 248 002, India
harendrasinghnegi@geu.ac.in

Harshal Patil
Department of Computer Science and
Engineering,
Symbiosis Institute of Technology,
Symbiosis International (Deemed
University),
Pune, Maharashtra, 412 115 India
pharshal2288@gmail.com

V. Balaraju
Department of Basic Engineering and
Applied Sciences,
Dr. NTR College of Agricultural
Engineering,
Bapatla, Andhra Pradesh, 522 101, India
vbaju.tpt@gmail.com

Ramya Maranan Department
of Research and Innovation, Saveetha
School of Engineering, SIMATS,
Chennai, Tamil Nadu - 602105, India
ramyamaranan@yahoo.com

Abstract- The main objective of this work is to model, control and simulate an electrical microgrid. To achieve this objective, models of the subsystems or associated elements (generators, power interfaces, electrical loads, etc.) are built, the control strategies necessary for the integration of each subsystem in the microgrid are implemented, and it is proposed an optimization algorithm that allows the economic dispatch of the system to be carried out under different generation and demand conditions. Finally, after simulating the model, its behavior is validated in a considered operating scenario. The work environment selected to develop this project is Simulink, a tool integrated into MATLAB, due to the ease it offers when modeling and simulating dynamic systems, allowing you to customize the included libraries and export data to MATLAB for subsequent analysis. At the end of this work, it is intended to have a simulated environment to validate the behavior of the proposed microgrid, which allows considering different generation and demand scenarios, and an optimization algorithm that allows carrying out the economic dispatch of the system under the operating conditions considered, without taking into account the randomness of generation sources and energy demand.
Keywords- Integrated Control, Modeling, Renewable Energy Integration, Photovoltaic (PV), Wind Energy, Hybrid Power System

I. INTRODUCTION

The increasing global demand for sustainable and decentralized energy solutions has prompted the exploration of innovative approaches to harness renewable energy sources. Photovoltaic (PV) and wind energy systems have emerged as promising contributors to the renewable energy landscape, offering clean and abundant sources of power [1-3]. In the pursuit of enhancing the efficiency and

reliability of renewable energy systems, the integration of multiple sources, such as PV and wind, has gained significant attention [4-7].

Traditional power distribution systems often suffer from energy losses during transmission and distribution, making them less efficient, especially in remote or off-grid areas. The motivation behind this research stems from the need to address these challenges by developing a robust, integrated renewable energy system tailored for DC micro-networks. The combination of PV and wind sources presents a synergetic solution, leveraging the intermittent nature of both resources to ensure a consistent and reliable power supply [8-10].

Different architectures have been proposed for the implementation of microgrids, each with its advantages and disadvantages, and are classified into six (6) different groups depending on how the alternating current (AC) and direct current (DC) transmission buses are connected. Among them, the AC microgrid (μ GAC) and the DC microgrid (μ GDC) stand out [16-17].

II. LITERATURE REVIEW

In addition to the proposed grid of [11], microgrid CO₂ emissions, total current costs, and net energy costs are optimized. All possible options were analyzed in HOMER software, and power system response and reliability analyzes using DIGSILENT PowerFactory. Study findings would be useful for optimizing hybrid mix and availability of resources for off-grid microgrids have been successfully implemented using various deployment methods.

A simulation model [12] has been developed to analyze the performance of hybrid systems, and examines the effect of varying anaerobic digester size and biogas storage capacity on key performance indices and compares two different operating strategies to evaluate energy savings and demand which may require reduction. Finally, a preliminary financial analysis is performed. The results demonstrate the benefits and improvements in plant efficiency factors and performance resulting from appropriate optimization of biogas separation.

The proposed microgrids [13] with diesel generators, renewables, storage, and 23.31 kW demand are optimized for five specific load management methods: using HOMER forecasting for, load continuity, generator sequence, cycle charging and combined discharge system net current cost, gas air emissions and energy costs. From their analysis the following load minimum operating cost 3738 USD, net current cost 152,023 USD, CO₂ emission 3375 kg/year and energy cost 0.208 USD /kWh with constant voltage is generated by an optimal method than the highest mean - frequency output.

This work [14] investigates islanded hybrid microgrid design and its optimization for load transmission by analyzing the optimal size of each element, power system response and microgrid cost analyzes Appendix four located in North Bangladesh For example, Mymensingh, Rangpur, Rajshahi and Sylhet are hybrid microgrids consisting of solar PV, wind turbines, battery storage, diesel generators and 27.31 kW load optimized for five different dispatch channels. The proposed microgrids are optimized to reduce current costs, CO₂ emissions, and absolute energy costs.

A real IMG system model [15] was developed in MATLAB/Simulink software to analyze the peak shaving performance. The model has four main components such as PV, BESS, variable load and gas turbine generator (GTG) dispatch models for the proposed algorithm, in which BESS and PV models are not suitable for capacity addition technique. The simulation results confirm the effectiveness of the CVDTA algorithm in reducing the maximum demand compared to the power combination method.

The primary objectives of this study encompass the development of a comprehensive control

strategy and accurate modeling techniques for a PV-

wind hybrid system in the context of DC electric micro-networks. Through advanced control algorithms and precise modeling, we aim to optimize energy harvesting, storage, and distribution processes, ultimately improving the overall

performance and sustainability of the micro-network.

The integration of control and modeling in a PV-wind hybrid system for DC electric micro-networks is related to the economic dispatch problem by optimizing the allocation of power generation from renewable sources to meet demand efficiently and economically. In this context, the economic dispatch problem involves determining the optimal operation of the PV-wind hybrid system components, such as photovoltaic panels, wind turbines, and energy storage devices, to minimize operational costs while satisfying the load demand. By employing control strategies and modeling techniques, the system can dynamically adjust the power output from each source based on factors like weather conditions, electricity demand, and energy storage levels, thereby addressing the economic dispatch problem to achieve cost-effective and sustainable energy supply within the micro-network.

III. ECONOMIC DISPATCH

A. Definition of the problem

Economic dispatch (ED) is a very important optimization task in power systems. It is the process of distributing generation among the available units to satisfy the energy demand in a period, minimizing the cost of operating the network and complying with the restrictions of the generators. On the other hand, and unlike traditional dispatch, where the powers of each generator are defined for each period independently, dynamic economic dispatch (DED) takes into consideration the limits on the power change rates of each generator, relating consecutive dispatch periods.

The ED problem, for the micro-network proposed in this work, is posed as in Equation 1: Let the sets be:

Ω : The set of all generators.

K : The set of dispatch periods. Let the parameters be:

$P_{\max,i}^k$: Maximum power of generator i in period k .

$P_{\min,i}^k$: Minimum power of generator i in period k .

P_{Load}^k : Power demanded in period k .

C_i^k : Generation cost per unit of energy from generator i in period k .

α, β, δ : Real constants.

Let the variables be:

P_i^k : Power assigned to generator i in period k .

$$M^k = \begin{cases} 1 & \text{if } \frac{\sum_{i \in \Omega} P_i^k - P_{\text{Load}}^k}{P^k} > \delta, \forall k \in K \\ 0, & \text{Otherwise} \end{cases} \quad (1)$$

Then, the objective function and constraints of the problem are (Equation 2-3):

$$\min z = \sum_{k \in K} \sum_{i \in \Omega} C_i^k P_i^k + \alpha \sum_{k \in K} M^k \cdot (\sum_{i \in \Omega} P_i^k - P_{\text{Load}}^k)^2 +$$

$$\beta \cdot \sum_{k \in K} \sum_{i \in \Xi} (P_i^{k+1} - P_i^k)^2 \quad (2)$$

$$\underset{\min, i}{P_i^k} \leq P_i^k \leq \underset{\max, i}{P_i^k}, \forall i \in \Xi, \forall k \in K \quad (3)$$

The first term of the cost function refers to the generation cost of the system. In a traditional economic office, this term is the most important, considering that the objective of the problem is to minimize the cost of network operation. The second term, dependent on the variable Mk , penalizes all possible solutions that deviate from the demanded power by a percentage δ . This expression corresponds to the power balance constraint of the system, necessary to maintain the operation of the microgrid at the desired operating point. The last term relates the powers of each generator in consecutive dispatch periods; This term seeks to minimize the changes in power required for each generator at two successive moments k and $k + 1$, considering the limitations presented by some particular generation technologies.

P_i^k , $P_{\max, i}^k$ and $P_{\min, i}^k$ are estimated for each period depending on the availability of the energy resource, both solar and wind, in said period.

B. Particle Swarm Optimization

In this algorithm, the position of each particle corresponds to a possible solution within the D-dimensional search space. In each iteration k , the particles adjust their position X and speed V along each dimension d , depending on the best solution found by each one (P_{best}) and the best solution found by the swarm (G_{best}). The equations that represent the dynamics of the swarm are presented below (Equation 4-5):

$$V^{k+1} = W \cdot V^k + c_1 \cdot r_1 \cdot (P_{best}^k - X^k) + c_2 \cdot r_2 \cdot (G_{best}^k - X^k) \quad (4)$$

$$X^{k+1} = X^k + V^{k+1} \quad (5)$$

where:

W : Inertia. Confidence of the particle in its movement or speed.

c_1 : Constant. It represents the attraction of the particle towards its best position found so far (P_{best}).

c_2 : Constant. It represents the attraction of the particle towards the best position found by the swarm (G_{best}).

r_1, r_2 : Random numbers. Samples from a uniform distribution on the interval $[0,1]$.

For the implementation of the algorithm, the following stages were taken into account:

IV. SIMULATION AND RESULTS

To build the simulation scenario, data obtained from the National Renewable Energy Laboratory's (NREL's). The data was recorded as follows:

For photovoltaic system 1 (PV1), the data were averaged, period by period, during the year 2010. For photovoltaic system 2 (PV2), the data

corresponding to the spring of that year were averaged. Finally, for photovoltaic system 3 (PV3), the information was averaged over the summer months of the corresponding year. The solar radiation curves for each generator are presented below (Fig 1):

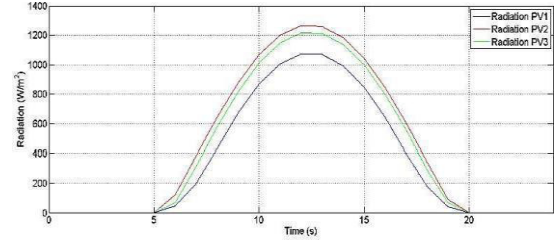


Fig. 1. Solar radiation profiles for photovoltaic systems.

The wind speed profile was taken from [39], and was scaled considering the measurement unit of the record (miles per hour) and the unit required in the simulation environment (m/s) (Fig 2).

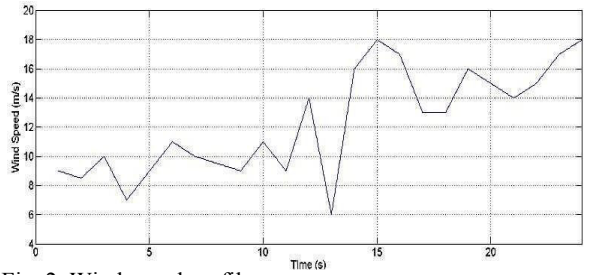


Fig. 2. Wind speed profile.

To estimate the generation costs of each generator, the behavior of the energy supply within the market was taken into account, that is, the higher the supply, the lower the cost, and vice versa. The estimated generation costs for each source considered were taken from [40]. Generation cost from wind energy: US\$ 0.0665 - 0.0772 / kWh. Generation cost from solar energy: US\$ 0.0074 - 0.0994 / kWh.

Considering a linear relationship between the generation costs and the maximum and minimum values of each generation unit, and taking into account an exchange rate of \$COP 3000, the following cost profile is obtained (see Image 18) for each generator for the 24 dispatch periods considered (Fig 3): Now, with the information available at this point, and after 1 million iterations of the PSO algorithm per dispatch period, the system ED problem solution for the proposed simulation scenario is presented (Table 1):

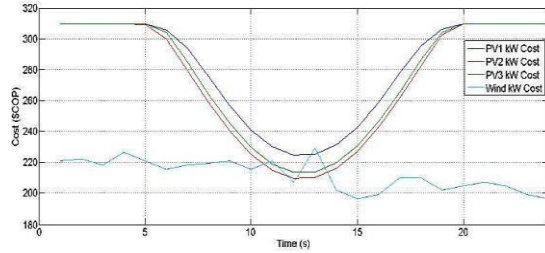


Fig. 3. Generation costs.

Table 1. Economic dispatch solution.

Period	P _{LOAD}	P _{REF} PV1	P _{REF} PV2	P _{REF} PV3	P _{REF} WIND	P _{ESS}	SCOP/kW	Costo (€/MWh)
1	304.72	0.49	0.50	0.49	47.00	256.24	287.47	10842.80
2	292.85	0.49	0.49	0.48	32.25	259.13	287.81	7624.80
3	285.57	0.49	0.49	0.48	85.00	199.12	286.79	18999.52
4	283.25	0.49	0.50	0.49	0.50	281.26	288.83	572.63
5	291.18	0.49	0.49	0.49	47.00	242.71	287.40	10839.59
6	311.17	0.49	26.53	0.48	126.00	157.66	281.39	35407.46
7	318.70	43.76	89.56	71.77	85.00	28.61	269.21	76908.54
8	339.54	48.36	148.71	74.77	66.00	1.70	254.48	86040.11
9	364.77	52.78	202.53	60.66	46.97	1.82	240.72	87451.55
10	380.56	54.84	137.57	60.39	125.86	1.90	227.90	85208.94
11	395.42	55.06	264.63	67.28	6.48	1.98	221.25	85697.28
12	405.28	55.76	82.50	68.04	196.95	2.03	213.83	85188.95
13	398.36	55.76	280.74	59.61	0.26	1.99	219.53	84337.09
14	395.52	55.72	64.55	61.19	212.08	1.98	217.21	83081.06
15	397.38	59.94	57.47	55.77	222.20	1.99	224.29	84118.56
16	395.51	52.20	57.10	57.24	226.99	1.98	236.78	86675.53

Table 1 presents the solution proposed by the PSO for each dispatch period. The first column means the estimate of the power demanded for each period. The following 4 columns represent the power references for each generation unit, that is, the 3 photovoltaic generators and the wind generator, respectively.

The variable P_{ESS} is the power that must be supplied, or absorbed, by the energy storage system (ESS) to satisfy the power balance of the system. This variable is calculated as [11]:

$$P_{ESS}(k) = P_{LOAD}(k) - \sum P_i^k, \forall k \in K, \forall i \in \mathbb{N} \quad (7)$$

where:

$P_{ESS}(k)$: Reference power of the energy storage system in the dispatch period k .

$P_{LOAD}(k)$: Estimated power demand in the dispatch period k .

P_i^k : Reference power of generator i in the dispatch period k .

Finally, the average generation costs per dispatch period, and the total generation cost for each period, are presented. It should be noted that the published cost does not consider the penalty for not satisfying the power balance, nor the cost linked to sudden changes in reference power for each generator; Only the system generation cost is included.

The economic dispatch solution is presented

graphically below:

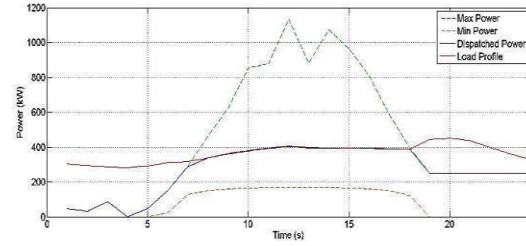


Fig. 4. Economic office solution.

Fig 4 can be divided into 3 sections; between $t = 0s$ and $t = 8s$, between $t = 8s$ and $t = 18s$, and between $t = 18s$ and $t = 24s$. In the second section, that is, between $t = 8s$ and $t = 18s$, the maximum power available in the system (green) is greater than the power demanded (red) for each period, validating that the sum of the powers dispatched by each generator (blue) is equal to the power demanded (red) in each period, satisfying the power balance of the system.

In the first and third sections, where the demanded power (red) is greater than the available power (green), the system operates at the maximum power point to minimize the power imbalance caused by the inability of the generators to satisfy the demand. demand in the corresponding dispatch periods. In these cases, the ESS is responsible for supplying the energy necessary to satisfy the power balance constraint of the system.

Below are the responses of each of the generators linked to the microgrid, solar and wind, during the 24 dispatch periods (Fig 5):

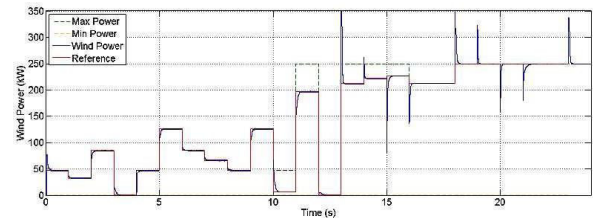


Fig. 5. Power delivered by the wind generator.

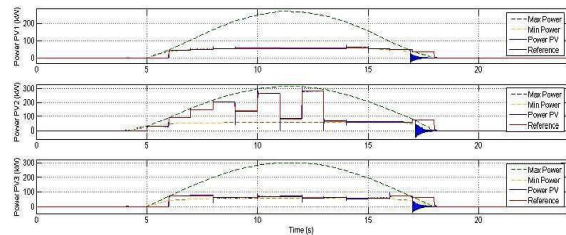


Fig. 6. Power delivered by photovoltaic systems.

In general, and during the 24 dispatch periods, the generators follow the power reference adequately, with tracking errors of less than 1%. Only the photovoltaic generators, in period 18, show erroneous behavior. This behavior is due to the fact that the maximum and minimum powers of each array were calculated with the solar radiation at the beginning of each period, without taking into

account the increase or decrease of this variable as a function of time. Then, as for the solar radiation conditions the system is not capable of generating the required power, the control system enters a region of unstable operation, resulting in the behavior evidenced in Fig 6.

Next, to validate the behavior of the energy storage system (Fig 7), it is necessary to take into account the difference between the estimated demand profile and the one proposed from the switching of different loads, at different times, over the simulation time. Although the ESS power reference was calculated for the estimated demand profile, the system actually operates with the proposed load model.

From Fig 7, in the periods where the difference between the estimated demand minus the proposed demand is positive, such as in periods 6, 9 and 10, the power generated by the ESS is lower than the reference because, as the estimated power is greater than the actual power consumed, the ESS power reference is also greater for these periods.

In the opposite case, when the difference between the estimated demand minus the proposed demand is negative, as in periods 7 and 17, the ESS power reference is lower than the power supplied to the network during said periods.

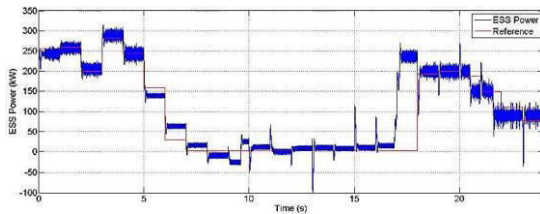


Fig. 7. Power of the energy storage system (ESS).

The high frequency content present in the behavior of the energy storage system is caused by the chattering effect in the modulation signal of the bidirectional buck-boost converter. To improve the response of this system, it is necessary to calculate new parameters for the PI control implemented in the current loop of the converter or, failing that, design a new control strategy for this subsystem.

Next, and considering its importance in the operation of DC microgrids, the behavior of the voltage of the main transmission bus is validated, to evaluate the performance of the control strategy implemented for its regulation:

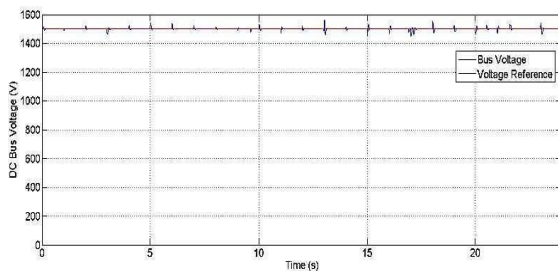


Fig. 8. DC bus voltage.

The Fig 8 shows the transients coinciding with the power changes of the generators in each

new dispatch period. The maximum amplitude (over-peak) of these transient states is less than 4%, demonstrating good performance of the control strategy implemented for regulating the voltage of the main bus of the microgrid.

Finally, after the analysis carried out for the generation systems, the energy storage system and the control strategies, Fig 9 shows the powers injected into the system by the generation units and the ESS (blue), the power demanded by the electric load model (red) and the estimated demand profile (green).

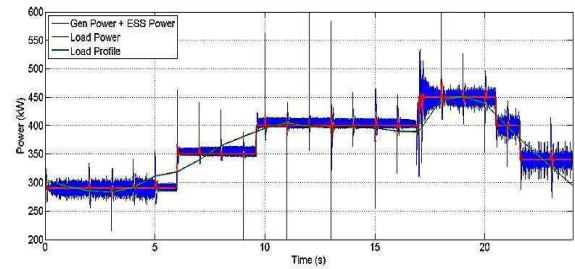


Fig. 9. Power generated, power demanded and demand profile.

It is verified that the power delivered to the system (blue), despite the high frequency component it presents (chattering), is equal to the power demanded by the load (red), satisfying the power balance constraint and resembling the profile of estimated demand (green), demonstrating the validity of the proposed models, validating the performance of the control strategies and corroborating the selection of the implemented optimization algorithm, objective of the economic dispatch for the 24 periods, under the simulation scenario considered, to the micro-grid proposed in this work.

V. CONCLUSIONS

Each of the subsystems considered for the construction of the proposed microgrid were modeled: the solar and wind generators, the energy storage system (ESS), the electrical load of the system and the corresponding power interfaces. In addition, the necessary control strategies were implemented to link each subsystem to the microgrid, with tracking errors of less than 1%. Particle Swarm Optimization was programmed to solve the economic dispatch problem, for an electrical microgrid with generators based on solar and wind energy, and without considering the randomness of variables such as solar radiation, speed of wind or variation in electrical demand. To improve the reliability and flexibility of DC microgrids, the droop control strategy, which takes advantage of the resistive nature of this architecture, is proven to be adequate and effective, allowing the integration of different generators, without the need to implement a communication network between these. Starting from the use of power interfaces (DC/DC converters, inverter and three-phase rectifier) as tools to achieve the stated objectives and validate the results, and not as results of the work developed, there were some design parameters that were not considered at all. When modeling each converter. Therefore, although the simulated environment has allowed the simulation of these models, there are limitations or restrictions that prevent the real implementation of the proposed architectures.

The results obtained during the development of this project allow us to propose new approaches when studying the economic dispatch problem, the algorithms to solve it and the analysis of power transmission systems in simulated environments.

REFERENCES

- [1] Y. Ma, Y. Chen, X. Chen, F. Deng, and X. Song, "Optimal dispatch of hybrid energy islanded microgrid considering V2G under TOU tariffs," *E3S Web of Conferences*, EDP Sciences, vol. 107, article 02007, 2019.
- [2] A. Goswami, P. Sadhu, and P. K. Sadhu, "Development of a grid connected solar-wind hybrid system with reduction in levelized tariff for a remote island in India," *Journal of Solar Energy Engineering*, vol. 142, no. 4, article 044501, 2020.
- [3] M. F. Ishraque and M. M. Ali, "Optimized design of a hybrid microgrid using renewable resources considering different dispatch strategies," in *2021 International Conference on Automation, Control and Mechatronics for Industry 4.0 (ACMI)*, pp. 1–6, Rajshahi, Bangladesh, July 2021.
- [4] H. Abd El-Sattar, H. M. Sultan, S. Kamel, T. Khurshaid, and C. Rahmann, "Optimal design of stand-alone hybrid PV/wind/biomass/battery energy storage system in Abu-Monqar, Egypt," *Journal of Energy Storage*, vol. 44, p. 103336, 2021.
- [5] I. Khan, "Waste to biogas through anaerobic digestion: hydrogen production potential in the developing world - a case of Bangladesh," *International Journal of Hydrogen Energy*, vol. 45, no. 32, pp. 15951–15962, 2020.
- [6] J. Li, P. Liu, and Z. Li, "Optimal design and techno-economic analysis of a solar-wind-biomass off-grid hybrid power system for remote rural electrification: a case study of west China," *Energy*, vol. 208, p. 118387, 2020.
- [7] S. A. Shezan, M. F. Ishraque, L. C. Paul et al., "Assortment of dispatch strategies with the optimization of an islanded hybrid microgrid," *MIST International Journal of Science and Technology*, vol. 10, pp. 15–24, 2022.
- [8] S. A. Shezan and M. F. Ishraque, "Assessment of a micro-grid hybrid wind-diesel-battery alternative energy system applicable for offshore islands," in *2019 5th International Conference on Advances in Electrical Engineering (ICAEE)*, pp. 457–462, Dhaka, Bangladesh, September 2019.
- [9] S. A. Shezan, "Optimization and assessment of an off-grid photovoltaic-diesel-battery hybrid sustainable energy system for remote residential applications," *Environmental Progress & Sustainable Energy*, vol. 38, no. 6, article e13340, 2019.
- [10] M. F. Ishraque, S. A. Shezan, J. N. Nur, and M. S. Islam, "Optimal sizing and assessment of an islanded photovoltaic-battery-diesel generator microgrid applicable to a remote school of Bangladesh," *Engineering Reports*, vol. 3, no. 1, article e12281, 2021.
- [11] S. A. Shezan, M. F. Ishraque, S. M. Mueen et al., "Effective dispatch strategies assortment according to the effect of the operation for an islanded hybrid microgrid," *Energy Conversion and Management: X*, vol. 14, article 100192, 2022.
- [12] M. Petrollese and D. Cocco, "Techno-economic assessment of hybrid CSP-biogas power plants," *Renewable Energy*, vol. 155, pp. 420–431, 2020.
- [13] M. F. Ishraque, S. A. Shezan, M. S. Rana et al., "Optimal sizing and assessment of a renewable rich standalone hybrid microgrid considering conventional dispatch methodologies," *Sustainability*, vol. 13, no. 22, 2021.
- [14] M. Fatin Ishraque, S. A. Shezan, M. M. Ali, and M. M. Rashid, "Optimization of load dispatch strategies for an islanded microgrid connected with renewable energy sources," *Applied Energy*, vol. 292, article 116879, 2021.
- [15] M. M. Rana, A. Rahman, M. Uddin et al., "A comparative analysis of peak load shaving strategies for isolated microgrid using actual data," *Energies*, vol. 15, no. 1, article en15010330, p. 330, 2022.
- [16] D. Mariappan, S. Kalyani, D. P. Winston, and P. M. Devie, "Quantum Angle Variant Optimization (QAVO) Controller based Grid Connected Converter in Microgrid System," *Solid State Technology*, 2020.
- [17] J. S. Oliver, P. W. David, P. K. Balachandran, and L. Mihet-Popa, "Analysis of Grid-Interactive PV-Fed BLDC Pump Using Optimized MPPT in DC-DC Converters," *Sustainability*, vol. 14, pp. 7205, 2022.



e-ISSN: 2319-8753 | p-ISSN: 2347-6710

IJIRSET

International Journal of Innovative Research in
SCIENCE | ENGINEERING | TECHNOLOGY

INTERNATIONAL JOURNAL OF INNOVATIVE RESEARCH

IN SCIENCE | ENGINEERING | TECHNOLOGY

Volume 13, Issue 5, May 2024

ISSN INTERNATIONAL
STANDARD
SERIAL
NUMBER
INDIA

Impact Factor: 8.423



9940 572 462



6381 907 438



ijirset@gmail.com



www.ijirset.com

IOT based Smart Water Quality Monitoring System

J Shashidhar¹, Sreenivas R Bisanalli², Yogesh Kumar Sharma³, MD Thayyab⁴, Mrs.Soujanya B N⁵

U.G. Students, Department of Electrical and Electronics Engineering, Ballari Institute of Technology and Management,

Ballari, Ballari, Karnataka, India^{1 2 3 4}

Assistant Professor, Department of Electrical and Electronics Engineering, Ballari Institute of Technology and

Management, Ballari, Ballari, Karnataka, India⁵

ABSTRACT: This major project presents a Iot Based Smart Water Quality Monitoring. The polluted water is basic cause of the main threats in recent times as drinking water is getting contaminated and polluted. The polluted water can cause various diseases to humans and animals, which in turn affects the life cycle of the ecosystem. If water pollution is detected in an early stage, by suitable measures can be taken and critical situations may be avoided. The quality of the water should be properly examined in real-time condition. The project proposes a less cost effective and efficient IoT based smart water quality monitoring system which monitors the quality parameters uninterruptedly. The main developed of this model is test with three water samples and the parameters of sensors are transmitted to the cloud server for further action can be taken.

KEYWORDS: Wifi Module, pH Sensor, Turbidity Sensor, Temperature Sensor, Conductivity Sensor, Oled Display, Cloud DB Server, Blynk Application and Quality Monitoring

I. INTRODUCTION

In the beginning of the 21st century able to providing apure drinking water is becoming the major challenge in the recent times The United Nations and World Health Organization as well as the recognized human right to sufficient works, continuous, safe, secure and acceptable, physically accessible, and affordable, portable water for personal and for domestic use. The future alarmingly estimates that every year diarrhea alone is causing around death of people. The physiochemical parameters that include in the electrical view of conductivity, pH, turbidity, temperature with normal hot or cool, chlorine content and flow. These parameters can be analyzed quickly and at less cost than the bacterial parameters. This with the monitoring helps sensor technology to move still not very effective, as they do not require always meet the practical needs in the table shown about the data of specific utility although cheaper than traditional equipment, cost, reliability and maintenance issues still exist; and data handling and management can also be improved. In this projectwere the development of a lowcost, wireless connectivity of sensors, multi-sensor network for measuring the physicochemical methods water parameters; enabling real-time monitoring, is presented. The tables below describes about the sensor data visibility of the devices of the system.

The cost related with machine communication over to the mobile networks are usually cheaper than fixed networks. Now people can have connectivity from anywhere and anytime for anything. The Internet of Things is being used in number of sectors, from automation, transportation, energy, healthcare, financial services, wearable devices, security, agriculture to nanotechnology.

The pH sensor is used to show the acidity or alkalinity of water. It has a range of 0 to 14, with 7 being neutral. A pH value less than 7 indicates acidity, while a pH value greater than 7 indicates alkalinity. The turbidity sensor is used to show the amount of suspended solids particles in the water. It has a range of some 0 to 1000 NTU, with 0 being the clear water and 1000 being very cloudy water. The temperature sensor is used to show the temperature of thewater. It has a range of -50 to 150 degrees Celsius values. The Tds sensor also able give us the proper real time values.

Table-1 : Threshold values of pH and Turbidity Sensors

The sensor	Safe water	Unsafe water
pH	6.5-8.5	<6.49 and >8.5
Turbidity	<5	>5

Table-2 : Threshold values of temperature sensor

Sensor	Normal	Hot	Cold
Temperature	$10 <= T <= 29$	$T >= 29$	$10 < T$

Table-3 : Conductivity Values of the Sensor

Types	Electrode constant	Measure range
Stainless steel electrode	K=1	1-2000 μ S/cm
Stainless steel electrode	K=1	10-2000 μ S/cm
Plastic electrode	K=1	1-2000 μ S/cm
Plastic electrode	K=1	10-2000 μ S/cm

II. RELATED WORK

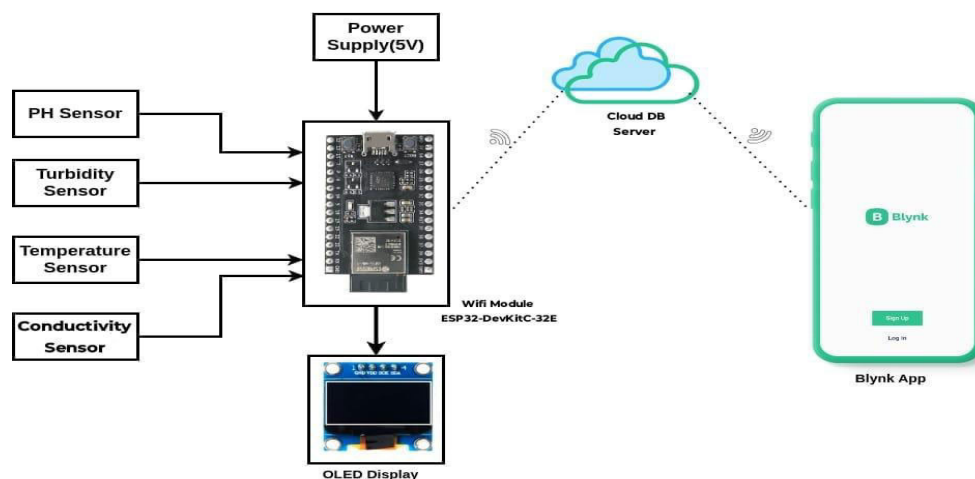
The concept of water quality was introduced by Avinash Kumar in his title in the research of “IoT Based Water Quality Monitoring System” in 2018. By integrating sensors and internet connectivity, the system can collect data on various water quality parameters and transmit it for analysis. This enables us to monitor water quality remotely and make informed decisions about water management and treatment.

The author Anantha Naik G. Dhis title in the research of “IoT based Real-Time Water Quality Monitoring System using smart Sensors” in 2020. This system likely employs smart sensors to measure various water quality parameters and transmits the data continuously via the internet. This allows for constant monitoring and quick identification of any changes in water quality, potentially leading to improved water management and the safety concerns.

The author Salem Garfan in his title in the research of “IoT-Based Water Monitoring Systems: A Systematic Review” in 2022. Conducted a comprehensive review of IoT-based water monitoring systems, covering a wide range of topics, including system architectures, sensor technologies, data transmission methods, and data analysis techniques, while highlighting challenges and future directions in the field.

In the present conditions of the methods for the monitoring water quality parameters are the manual, time consuming, and labor intensive and also riskier in the data handling. This can lead to delays in the detecting of the water quality problems, related which that can result in the health risks, environmental damage, and economic loss also. An IoT based smart of water quality monitoring of the system could that address these several challenges by providing real time value data on water quality parameters, such as pH, temperature, turbidity, and conductivity. This data could be used to detect water quality problems early on, allowing for timely corrective action. Additionally, the system could be used to track recent water quality trends over the time, which could help to identify potential sources of contamination and inform long term water management strategies.

III. METHODOLOGY



(a)

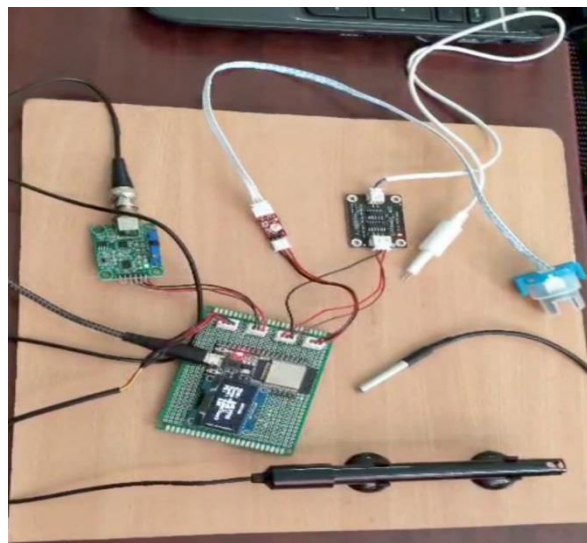
The methodology encompasses Sensors measure water quality parameters are placed in the water to measure various parameters like pH, turbidity, temperature, chlorine level, and conductivity. The microcontroller collects to the sensor data and sends to the microcontroller is connected to the sensors and collects the data they measure. Data is processed and prepared for transmission and the microcontroller processes the data to ensure its accuracy and prepares it for sending to a cloud platform. The figure (a) is the Methodology diagram

The data is transmitted to the cloud and the processed data is securely transmitted to a cloud platform like Blynk. The system is continuously monitored and improved and the system is regularly reviewed and updated to ensure it is operating effectively.

Data is visualized and analyzed and by the cloud platform provides tools to visualize the data in graphs and analyze trends and anomalies. These are embedded devices that measure specific water quality parameters. Different types of sensors are used depending on the desired parameters to be monitored. This is a small-scale computer that collects and processes data from the sensors.

It also controls the communication between the sensors and the cloud platform. This module transmits data from the microcontroller to a cloud platform via wireless networks like Wi-Fi network. This is a remote server that stores and analyzes the collected data. It can also provide visualizations of the data and generate alerts for potential water quality issues. This is an interface through which users can access the data and visualizations provided by the cloud platform. This can be a web interface, a mobile app, or a dedicated dashboard.

IV. IMPEMENGTATION



(b)

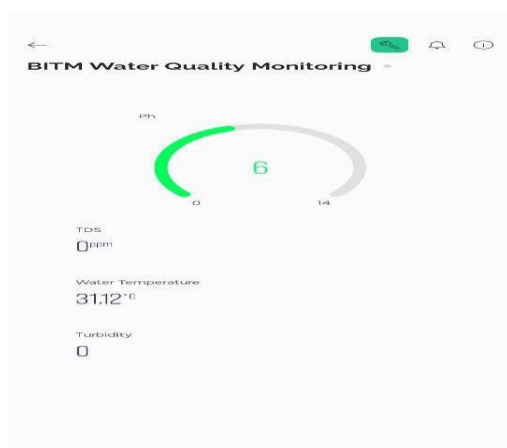
Working: The whole design of the system is generally related to IOT which is a newly introduced concept in the world of development and technology. There are basically two parts included, the first one is hardware & second one is software.

The hardware part consists of sensors which help to measure the real-time values of sensors, OLED shows the displays by the output from the sensors, The Wi-Fi module gives the connection between hardware and software section. In software, we developed a program based on the embedded C language structure. Classification-based decision tree algorithm is used to predict the water quality classes using software. The figure (b) shows the parts of hardware and software components of the project.

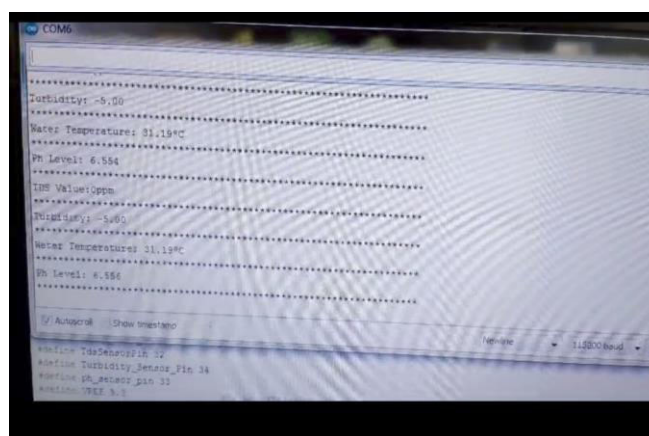
Once all hardware is interfaced to the core, we need to program for sensor and communication devices. Power the module to measure water parameters from sensor, each sensor value is measured at different interval time and displayed on the OLED alternatively accumulate the measured value and send to cloud using ESP32 Wi-Fi module. Here Blynk is used as a cloud server. User can view the real-time measured value by login the account, where we can monitor the real-time water parameters.

V. EXPERIMENTAL RESULTS

The water quality monitoring is important for the many applications such as the figures shows the drinking water distribution and measurement and environment monitoring of pond, lank and ecosystem etc. The realtime water monitoring system having four different in sensors which are connected to a core system of the project. The sensors are which senses or read the real values of time water parameter by using microcontroller and send to the cloud using wi-fi module, here we can monitor the water quality parameter on the internet server by using cloud computing. We use Blynk or Thingspeak as a cloud server to store the water parameters these parameters can be obtained in numerical values display on the screen.



(c)



(d)

While turning on the system initialization takes place and display the system name on Oled display as we code. Alternatively once the data is initially, then wi-fi module is get connect to the network using ip address and connecting progress display on serial monitor window and also on lcd display like as connecting to wi-fi, both serial monitor window and lcd display. If the wi-fi get connected to network shows wi-fi connected message on both serial and lcd window or else shows wi-fi connected. The pH of the water is visible to show. We took three different samples for demo purpose. One is pure water, second one is salt water and third one is added acidic water each samples parameters are measured continuously and obtained result is real time on both Oled display and on web. The figure (c) and figure (d) where the expected result can be viewed in the website and the monitor.

VI. CONCLUSION

The conclusion tells that of the Iot based smart water quality monitoring system is more and more suitable for real time value monitoring and analysis of water quality parameters compared to the existing systems. It is automatic and does not require human intervention, reducing errors. The system utilizes temperature, pH, conductivity and turbidity sensors, along with a Wi-Fi module for wireless data transmission. The last process is that microcontroller processes system sensor data and transmits it to the cloud with Wi-Fi module. The data is stored and analyzed in the cloud using Blynk web service provided. The system can predict future water quality parameters and provide real-time notifications to users through a mobile application.

REFERENCES

- [1] Avinash Kumar in the research of "An IoT Based Water Quality Monitoring System", integrating sensors and internet connectivity, 2018.
- [2] Anantha Naik G. Din the research of "IoT based Real-Time Water Quality Monitoring System using smart Sensors", smart sensors and quick identification, 2020.
- [3] Salem Garfan, "IoT-Based Water Monitoring Systems: A Systematic Review", Sensor Applications, Experimentation and Logistics, 2017.
- [4] Ajith Jerom in the research of "A Cloud-Based IoT System for Real-time Water Quality Monitoring" in 2020.
- [5] M.R.R.Reddy in the research of "An IoT Based Smart Water Quality Monitoring System for Real time Applications" 2010.



INTERNATIONAL
STANDARD
SERIAL
NUMBER
INDIA



INTERNATIONAL JOURNAL OF INNOVATIVE RESEARCH

IN SCIENCE | ENGINEERING | TECHNOLOGY

 9940 572 462  6381 907 438  ijirset@gmail.com



www.ijirset.com

Scan to save the contact details



e-ISSN: 2319-8753 | p-ISSN: 2347-6710

IJIRSET

International Journal of Innovative Research in
SCIENCE | ENGINEERING | TECHNOLOGY

INTERNATIONAL JOURNAL OF INNOVATIVE RESEARCH

IN SCIENCE | ENGINEERING | TECHNOLOGY

Volume 13, Issue 5, May 2024

ISSN INTERNATIONAL
STANDARD
SERIAL
NUMBER
INDIA

Impact Factor: 8.423



9940 572 462



6381 907 438



ijirset@gmail.com



www.ijirset.com

RFID based Fuel Station Automation using Arduino Uno

Anil Gajjela¹, Goudara Manjunatha², Dinesh A³, Hari Krishna H⁴, Shafreen Parvez S⁵

U.G. Students, Department of Electrical and Electronics Engineering, Ballari Institute of Technology and Management,
Ballari, Karnataka, India^{1,2,3,4}

Assistant Professor, Department of Electrical and Electronics Engineering, Ballari Institute of Technology and
Management, Ballari, Karnataka, India⁵

ABSTRACT: Petroleum is the foremost and mainstay of modern civilization. It is one of the nature's rare and valuable creation. Its formation takes millions of years which insist proper utilization of the resource. In present scenario, fuel stations are operated manually which consist a controlling unit to perform various tasks. The present manual fuel stations consume more time and requires substantial man power. Moreover, it is prone to malpractices and higher probability of human initiated errors. These limitations restrict installation of fuel stations in distant areas. The main aim of this paper is to deal with all stated problems by developing an automated petrol dispensing system using RFID technology. Such a system enables a user to use a RFID based prepaid card to access petrol at fuel stations. Whenever the user wants to fill the tank from the fuel dispenser, user has to enter the amount first and then place the RFID card near the RFID reader. The Arduino Uno manages to read the data from the RFID reader and perform action according to the customer requirements as well as the amount is deducted from the user's card. The RFID and Arduino Uno are used for improvement of present petrol dispensing system by reducing human work and providing an auto guided mechanism to carry out the tasks consecutively. These systems are highly reliable and conserves the time. At the same time will be using GSM-GPS module to get amount deduction via mail and track down the vehicle with the help of latitude and longitude parameters.

I. INTRODUCTION

India became the fourth largest auto market in 2017-18 and was the seventh largest manufacturer of commercial vehicles in 2018. Around 2.19 million cars were sold in India in 2017–18. According to the Ministry of Road Transport and Highways (MoRTH), there is a tremendous increase in India's Registered Motor Vehicles in the recent years. These increase in the number of vehicles in India has led to a huge usage of petroleum as well. This phenomenon has been represented in graph which is shown in figure A. The consumption volume of petroleum products in India was estimated to be approximately 202.6 million metric tons in fiscal year 2018. The country was ranked third with regard to primary energy and fuel consumption across the globe. Petroleum is the non-renewable resource and it is present in a limited quantity. Its formation takes millions of years. It cannot be replaced rapidly enough to cope up with its current consumption. Thus, it is extremely crucial to ensure the right utilization and consumption of petroleum products so as to preserve it for future generations as well. The dispense of fuel to this large number of vehicles in India attains major interest as numerous complications may involve. A long queue in front of a fuel station due to huge rush at the station is a common scenario. This leads to the wastage of valuable time, energy as well as human hours. The manual pump operation at present leads to various malpractices such as delivering less quantity to the customers and adulteration of fuel. These issues inspire us for automation of fuel stations which is quite necessary to deal with all these recent era problems. The main aim of the project is to design a system which is capable of automatically deducting the amount of petrol dispensed from user card based on RFID technology and controller Arduino Uno. The RFID reader verifies the user from RFID tag placed nearer to it. The amount of required fuel is entered in terms of amount at the unit. These all activities as well as dispense of fuel is monitored and controlled by the Arduino Uno.

II. RELATED WORK

The RFID system is comprised of two components: the RFID reader and the tags. They are also called PCD (Proximity Coupling Device) and PICC (Proximity Integrated Circuit Card).

The RFID reader consists of an antenna to emit high-frequency EM waves and a reader/writer. MFRC522 from NXP is an example of such an integrated circuit. Since we are using high-frequency waves in the megahertz range, the size of the antenna can be small.

The RFID tag can be either passive or active. Active tags are powered by batteries while the passive RFID tags are powered by energy from the reader's interrogating EM waves. The tags are available in different forms or shapes like cards, tags, key forbs, or stickers. Whatever the shape, the RFID tag will consist of an antenna and the RFID chip, which will store all the data.

When triggered by an electromagnetic interrogation pulse from a nearby RFID reader, the tag will transmit data back to the reader. The reader will then analyse this data to identify the tag. Unlike a barcode or a QR code, the tag does not need to be within the reader's line of sight. This makes it easier to process and can be used for tracking objects in closed space

III. METHODOLOGY

The project revolves around using an Arduino Uno board in conjunction with an RFID reader module to automate the fuel dispensing process at gas stations. The methodology begins with setting up the required hardware components, including the Arduino board, RFID reader, solenoid valve or relay module for pump control, and a display unit. A database is created to store registered RFID tag IDs and associated user information like vehicle details and fuel quotas. The Arduino is programmed to read RFID tag data, search the database for the corresponding user, calculate the allowed fuel amount, and control the solenoid valve to activate the pump for the specified duration. The system displays relevant details on the LCD and incorporates error handling and safety measures. After thorough testing, the system is installed at the fuel station, integrated with existing infrastructure, and deployed with staff training for operation and maintenance. Optional enhancements may include payment gateways, remote monitoring, improved user interfaces, and advanced security features. The system undergoes rigorous testing and calibration to ensure accurate fuel dispensing and optimal performance, followed by careful integration with the existing fuel station infrastructure. Detailed procedures for regular maintenance and updates are established to keep the system functioning optimally.

Furthermore, the methodology allows for optional enhancements, such as integrating the system with payment gateways or billing systems for automated payment processing, implementing remote monitoring and control capabilities for centralized management, enhancing the user interface with touch screens or mobile apps, and incorporating advanced security measures like biometric authentication or camera-based vehicle recognition. These enhancements can further improve the system's functionality, convenience, and security, adapting it to the evolving needs of fuel station operations.

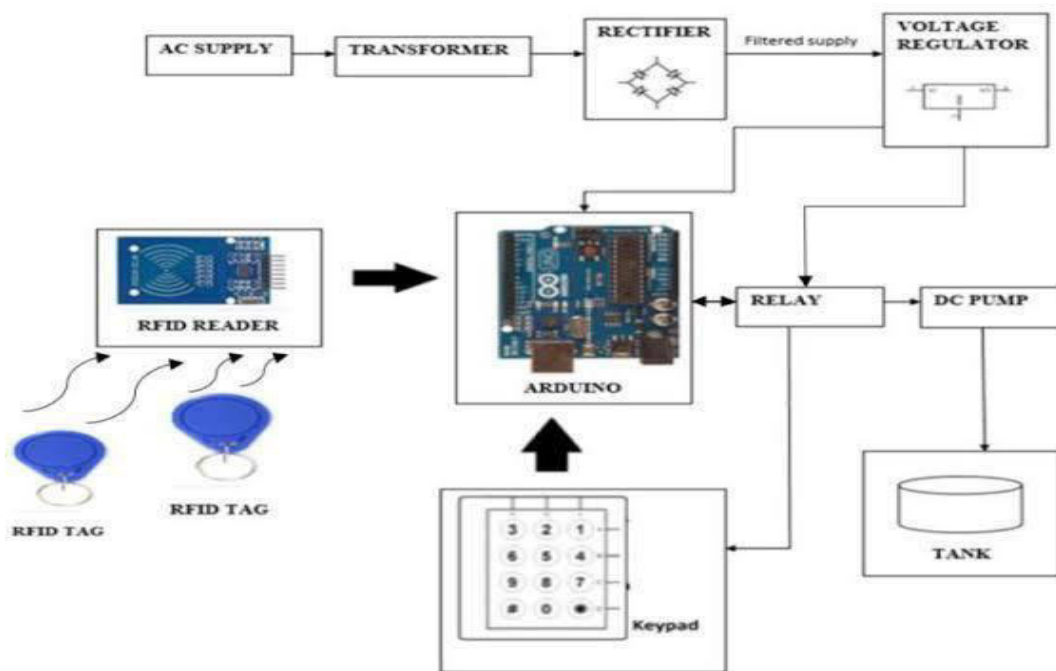


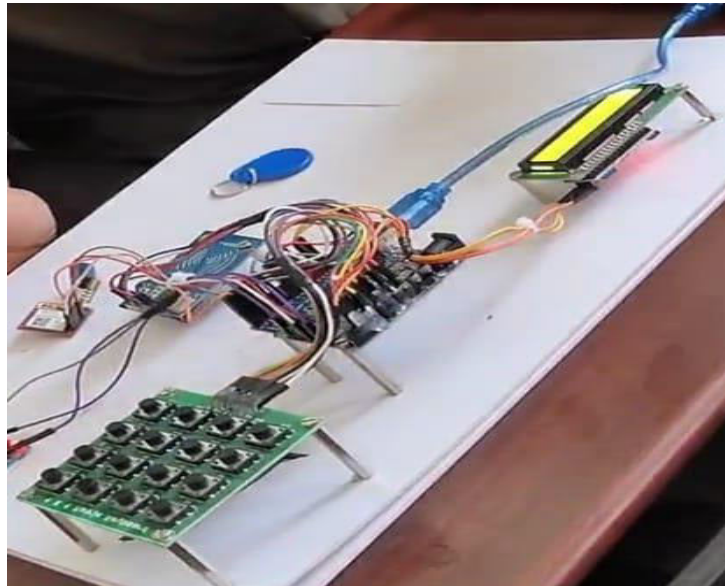
FIG A: BLOCK DIAGRAM OF RFID BASED AUTOMATION FUEL STATION

IV. EXPERIMENTAL RESULTS

The results could include measurements of the system's response time, which is the time taken from when a rfid tag is detected to when the fuel pump is activated. this could be measured in milliseconds or seconds, and it would be important to ensure that the response time is within acceptable limits for a smooth user experience.

Fuel dispensing accuracy: experiments could be conducted to measure the accuracy of the fuel dispensing process. this could involve comparing the amount of fuel dispensed by the system with the expected amount based on the user's fuel quota or the amount requested. the results could be presented as a percentage of deviation from the expected amount.

User experience and satisfaction: experimental data could include user feedback and satisfaction ratings from individuals who have interacted with the rfid-based fuel station automation system. this could be collected through surveys or interviews, and the results could provide insights into the ease of use, efficiency, and overall user experience of the system.



22.00rs refueling done LATTITUDE=
15.1636 N
LONGITUDE=
76.8591 E

22.00rs refueling done Balance =
78.00

Fig b: Project model
FIG C: SMS

V. CONCLUSION

The above-mentioned model proposes to remove all the shortcomings of the manually operated petrol pumps by replacing them with automated ones. RFID is a versatile technology, easy to use and it can be efficiently used in this real time application. The proposed model consists of certain goals like ensuring right amount of fuel dispensed, removing all human errors by the use of RFID cards and ensuring customer's trust for a fair sale of the product [9]. These automated fuel stations provide a lot more advantages as they reduce man power with the automated self-service. With this simple technology in use, any person can easily access for fuel at Fuel Stations. Apart from this all, these systems are less time consuming compared to the traditional ones. The technology proposed is very cost efficient and has low power consumption as well, which sets the major benchmark in today's scenario.

REFERENCES

1. Al-Rajaba MM, Alkhederb SA, Hoshangc SA. An Intelligent Location Based Service System (ILBSS) using mobile and spatial technology: A proposal for Abu Dhabi petrol stations. Case Studies on Transport Policy 2017; 24(2): 78–85. doi: 10.1016/j.cstp.2017.01.005.
2. Baqir ZM, Motlak HJ. Smart automatic petrol pump system based on RFID and ESP8266. Jour-nal of Physics: Conference Series 2020; 1993: 012109. doi: 10.1088/1742-6596/1933/1/012109.
3. Nayal A, Gaur M, Kashyap T, Shukla T. Petrol pump automation system. International Journal of Engineering Applied Sciences and Technology 2020; 5(1): 341–345.



4. Sheth S, Patel KH, Patel H. Design of automatic fuel filling system using a mechatronics approach. Robotics and Factories of the Future 2016; 1: 785–795.
5. Naveed M, Habib W, Masud U, et al. Reliable and low-cost RFID-based authentication system for large-scale deployment. International Journal of Network Security 2012; 14: 3: 173–179.
6. Saleh Z, Alsmadi I, Mashhour A. Improving enterprise access security using RFID. International Journal of Computer Science and Information Security 2021; 9: 5.



INTERNATIONAL
STANDARD
SERIAL
NUMBER
INDIA



INTERNATIONAL JOURNAL OF INNOVATIVE RESEARCH

IN SCIENCE | ENGINEERING | TECHNOLOGY

 9940 572 462  6381 907 438  ijirset@gmail.com



www.ijirset.com

Scan to save the contact details

CERTAIN TOPOLOGICAL INDICES AND RELATED POLYNOMIALS FOR POLYSACCHARIDES

V. LOKESHA^{1*}, V. R. KULLI², S. JAIN¹, A. S. MARAGADAM¹, §

ABSTRACT. A polysaccharide is a large molecule made of many smaller monosaccharides. Monosaccharides are simple sugars, like glucose. Special enzymes bind these small monomers together creating large sugar polymers or polysaccharides. A polysaccharide is also called a glycan. Starch, glycogen, and cellulose are examples of polysaccharides. Depending on their structure, polysaccharides can have a wide variety of functions in nature. Some polysaccharides are used for storing energy, some for sending cellular messages, and others for providing support to cells and tissues. In the present work, we focus on the polysaccharides, namely, amylose and blue starch-iodine complex. Several topological indices and polynomials are determined in view of edge dividing methods. Also, depict their graphic behavior.

Keywords: Amylose, blue starch-iodine complex, topological indices and polynomials.

2020 AMS Subject Classification: 05Cxx, 05C09, 05C31.

1. INTRODUCTION

Polysaccharides, particularly of plant origin, are prominent components in the diets of herbivores and omnivores. Amylose is a polysaccharide used in various industries as a functional biomaterial. It is mainly a linear component consisting of about 100 – 10,000 glucose monomers linked by $\alpha(1 \rightarrow 4)$ bindings.

Amylose are used in permanent textile finishes, plastics, film making and paper pulp fibre bonding. High amylose starches have been used together with an instant starch or food gum as a binder to provide a crisp coating for french fries which also reduces oil absorption. Used as starches in the usage of sausage casings and food wrappers, incorporation into bread crusts and pasta for more uniform heating in the microwave.

¹ Department of Studies in Mathematics, Vijayanagara Sri Krishnadevaraya University, Ballari, Karnataka, India.

e-mail: lokiv@yahoo.com; ORCID: <https://orcid.org/0000-0003-2468-9511>.

* Corresponding author.

e-mail: sushmithajain9@gmail.com; ORCID: <https://orcid.org/0000-0002-4173-8787>.

e-mail: maragadamvijay@gmail.com; ORCID: <https://orcid.org/0000-0001-9703-2161>.

² Department of Mathematics, Gulbarga University, Gulbarga, Karnataka, India.

e-mail: vrkulli@gmail.com; ORCID: <https://orcid.org/0000-0002-6881-5201>.

§ Manuscript received: April 26, 2021; accepted: October 13, 2021.

TWMS Journal of Applied and Engineering Mathematics, Vol.13, No.3 © Işık University, Department of Mathematics, 2023; all rights reserved.

They are also used in foods legumes and beans, whole grains, vegetables and starchy fruits, rice and potatoes.

In 1814, Colin and Claubry discovered the starch-iodine reaction, which is well renowned to any chemist from basic courses in qualitative and quantitative analysis.

A topological index, which is a graph invariant it does not depend on the labeling or pictorial representation of the graph, is a numerical constant mathematically obtain from the graph structure. In Chemistry, topological indices have been found to be useful in discrimination, chemical documentation, structure property relationships, structure activity relationships and pharmaceutical drug design [4]. There are few main classes of topological indices, namely Wiener index, first and second Zagreb indices, forgotten index, Symmetric division degree index etc., that have been very often studied and investigated by the researchers [15, 16, 17, 18].

The first and second zagreb indices were introduced by Gutman and Trinajstić [9] which are defined as,

$$M_1(G) = \sum_{uv \in E(G)} [d(u) + d(v)].$$

$$M_2(G) = \sum_{uv \in E(G)} [d(u)d(v)].$$

In 2015, Ediz, S. [6] defined reverse vertex degree and reverse Zagreb indices of a simple connected graphs. The reverse vertex degree of a vertex v of a simple connected graph G defined as;

$$c_v = \Delta - d_v + 1.$$

where Δ denotes the largest of all degrees of vertices of G and d_v denotes the number of edges incident to v .

The first reverse Zagreb beta index [7] of a graph G defined as;

$$CM_1^\beta(G) = \sum_{uv \in E(G)} c_u + c_v.$$

And the second reverse Zagreb index of a simple connected graph G defined as;

$$CM_2(G) = \sum_{uv \in E(G)} c_u c_v.$$

The concept of Sombor index was recently introduced by Gutman [8] in the chemical graph theory. It is a vertex-degree-based topological index and defined as;

$$SO(G) = \sum_{uv \in E(G)} \sqrt{d_u^2 + d_v^2}.$$

Inspired by work on Sombor indices, V. R. Kulli, introduced the Nirmala index [11] of a graph G as follows;

$$N(G) = \sum_{uv \in E(G)} \sqrt{d_u + d_v}.$$

The irregularity index was introduced by Albertson [2] in and defined as;

$$M_i(G) = \sum_{uv \in E(G)} |d_u - d_v|.$$

Recently, minus F -index [12] of a graph G is introduced by V. R. Kulli, and defined as;

$$MF(G) = \sum_{uv \in E(G)} |d_u^2 - d_v^2|.$$

Square F -index is defined as;

$$QF(G) = \sum_{uv \in E(G)} (d_u^2 - d_v^2)^2.$$

V. R. Kulli defined the first Gourava index [13] of a graph G is defined as;

$$GO(G) = \sum_{uv \in E(G)} (d_u + d_v + d_u d_v).$$

Inspired by the works of Zagreb indices, Deepika T. introduced the VL index [5] of a graph G is defined as;

$$VL(G) = \frac{1}{2} \sum_{uv \in E(G)} [d_e + d_f + 4].$$

where $d_e = d_u + d_v - 2$ and $d_f = (d_u \times d_v) - 2$, such that d_u and d_v are the degree vertices of u and v in G respectively.

Alameri et.al., in 2020, introduced Y -index [1] defined as;

$$Y(G) = \sum_{u \in E(G)} (d^3(u) + d^3(v))$$

Numerous graph polynomials have been developed for measuring structural information of molecular graphs. Graphs polynomial of found applications in Chemistry in connection with the molecular orbital theory of unsaturated compounds and also an important source of structural descriptors used in developing structure property models. Degree based graph polynomials are useful because they contain a wealth of information about topological indices.

For a simply connected graph G , the first Zagreb beta polynomial [14] is defined as;

$$CM_1^\beta(G, x) = \sum_{uv \in E(G)} x^{c_u + c_v}.$$

The Second reverse Zagreb polynomial of a simple connected graph G defined as;

$$CM_2(G, x) = \sum_{uv \in E(G)} x^{c_u c_v}.$$

This paper is organized as follows. Section 1 consists of a brief introduction and literature review which is essential for the development of main results. Forthcoming two sections, we shall give the topological indices, polynomials of the amylose and blue starch-iodine complex. Also, depict their graphic behavior. Section 4 consists conclusion of this work.

2. AMYLOSE

In this sector calculated the many standard topological indices and related polynomials for amylose by using the edge partition technique. Here, also obtained graphic comparison of topological indices of amylose.

Amylose was discovered in 1940, by Meyer and his co-workers found that properties were different from those of native maize starch. It is found in algae and other lower forms of plants. It is a spread polymer of around 6000 glucose deposits with branches on 1 in each 24 glucose ring. It plays an important role in the storage of plant energy and as plants do not require glucose to explode, its dense structure and slow breakdown features are under plant's growth [10].

The reader can find the molecular structure and molecular graphs of amylose in [3].

Theorem 2.1. *For all $n \geq 2$, let \mathbb{A} be the structure of amylose, then*

1. $SO(\mathbb{A}) = 43.55n - 0.8865$.
2. $N(\mathbb{A}) = 26.71n - 8.472$.
3. $VL(\mathbb{A}) = 67n - 4$.
4. $M_i(\mathbb{A}) = 10n + 2$.
5. $MF(\mathbb{A}) = 44n + 6$.
6. $GO(\mathbb{A}) = 134n - 8$.
7. $CM_2(\mathbb{A}) = 26n + 2$.
8. $CM_1^\beta(\mathbb{A}) = 36n + 2$.
9. $QF(\mathbb{A}) = 262n + 3$.
10. $Y(\mathbb{A}) = 456n - 18$.

Proof. Here we noticed that in the graph of amylose vertices have degrees 1, 2 or 3. The number of the edges of types are given bellow.

$$\begin{aligned} E_1 &= \{uv \in E(\mathbb{A}) : d_{\mathbb{A}}(u) = 1, d_{\mathbb{A}}(v) = 2\}. \\ E_2 &= \{uv \in E(\mathbb{A}) : d_{\mathbb{A}}(u) = 1, d_{\mathbb{A}}(v) = 3\}. \\ E_3 &= \{uv \in E(\mathbb{A}) : d_{\mathbb{A}}(u) = 2, d_{\mathbb{A}}(v) = 3\}. \\ E_4 &= \{uv \in E(\mathbb{A}) : d_{\mathbb{A}}(u) = 3, d_{\mathbb{A}}(v) = 3\}. \end{aligned}$$

One can calculate easily that $|E_1(\mathbb{A})| = n$, $|E_2(\mathbb{A})| = 2n + 2$, $|E_3(\mathbb{A})| = 5n - 2$, $|E_4(\mathbb{A})| = 4n$.

$$\begin{aligned} \text{Let, } SO(G) &= \sum_{u,v \in E(G)} \sqrt{d(u)^2 + d(v)^2} \\ SO(\mathbb{A}) &= |E_{(1,2)}| \sum_{u,v \in E_{(1,2)}(\mathbb{A})} \sqrt{d(u)^2 + d(v)^2} + |E_{(1,3)}| \sum_{u,v \in E_{(1,3)}(\mathbb{A})} \sqrt{d(u)^2 + d(v)^2} \\ &\quad + |E_{(2,3)}| \sum_{u,v \in E_{(2,3)}(\mathbb{A})} \sqrt{d(u)^2 + d(v)^2} + |E_{(3,3)}| \sum_{u,v \in E_{(3,3)}(\mathbb{A})} \sqrt{d(u)^2 + d(v)^2} \\ SO(\mathbb{A}) &= 43.55n - 0.8865. \end{aligned}$$

Similarly, using the definitions of topological indices we obtain the results. \square

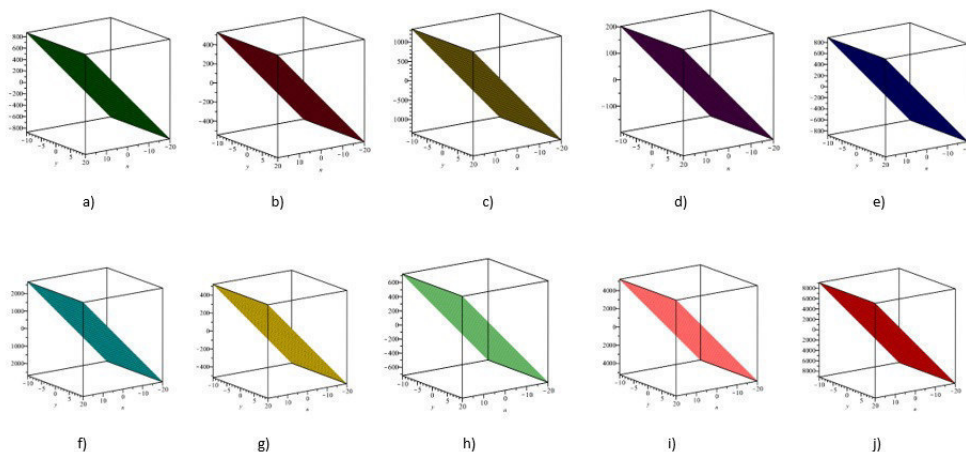


FIGURE 1. 3D plot of topological indices of amylose a) Sombor index b) Nirmala index c) VL index d) irregularity index e) minus F -index f) Gourava index g) Second zagreb index h) first zagreb beta index i) square F index j) Y index .

Theorem 2.2. *let \mathbb{A} be the structure of amylose, then*

1. $SO(\mathbb{A}, x) = nx^{\sqrt{5}} + (2n + 2)x^{\sqrt{10}} + (5n - 2)x^{\sqrt{13}} + 4nx^{\sqrt{18}}$.
2. $N(\mathbb{A}, x) = nx^{\sqrt{13}} + (2n + 2)x^{\sqrt{4}} + (5n - 2)x^{\sqrt{5}} + 4nx^{\sqrt{6}}$.
3. $VL(\mathbb{A}, x) = \frac{n}{2}x^5 + (n + 1)x^7 + \frac{(5n-2)}{2}x^{11} + 2nx^{15}$.
4. $M_i(\mathbb{A}, x) = (6n - 2)x + (2n + 2)x^2 + 4n$.
5. $MF(\mathbb{A}, x) = \frac{n}{x^3} + \frac{2n+2}{x^8} + \frac{5n-2}{x^5} + 4n$.
6. $GO(\mathbb{A}, x) = (6n - 2) + (2n + 2)x^7 + (5n - 2)x^{11} + 4nx^{15}$.
7. $CM_2(\mathbb{A}, x) = nx^6 + (2n + 2)x^3 + (5n - 2)x^2 + 4nx^1$.
8. $CM_1^\beta(\mathbb{A}, x) = nx^5 + (2n + 2)x^4 + (5n - 2)x^3 + 4nx^2$.
9. $QF(\mathbb{A}, x) = nx^9 + (2n + 2)x^{64} + (5n - 2)x^{25} + 4n$.
10. $Y(\mathbb{A}, x) = nx^9 + (2n + 2)x^{16} + (5n - 2)x^{25} + 4nx^{36}$.

Proof. Using the information given in Theorem 1 and definition of Sombor polynomial, we have

$$\begin{aligned}
 \text{Let, } SO(G, x) &= \sum_{u,v \in E(G)} x^{\sqrt{d(u)^2 + d(v)^2}} \\
 SO(\mathbb{A}, x) &= |E_{(1,2)}| \sum_{u,v \in E_{(1,2)}(\mathbb{A})} x^{\sqrt{d(u)^2 + d(v)^2}} + |E_{(1,3)}| \sum_{u,v \in E_{(1,3)}(\mathbb{A})} x^{\sqrt{d(u)^2 + d(v)^2}} \\
 &\quad + |E_{(2,3)}| \sum_{u,v \in E_{(2,3)}(\mathbb{A})} x^{\sqrt{d(u)^2 + d(v)^2}} + |E_{(3,3)}| \sum_{u,v \in E_{(3,3)}(\mathbb{A})} x^{\sqrt{d(u)^2 + d(v)^2}} \\
 SO(\mathbb{A}, x) &= nx^{\sqrt{5}} + (2n + 2)x^{\sqrt{10}} + (5n - 2)x^{\sqrt{13}} + 4nx^{\sqrt{18}}.
 \end{aligned}$$

In the similar method we also obtain results for other polynomials. Hence the Proof. \square

3. BLUE STARCH - IODINE COMPLEX

In this sector calculated the many standard topological indices and related polynomials for blue starch - Iodine Complex by using the edge partition technique. Here, also obtained graphic comparison of topological indices of blue starch - iodine complex.

The main structure of amylose are cyclic degradants known as cyclodextrins. They are obtained enzymatically and may be considered as single turns of the helix of amylose imploding into a circular path. In all of these complexes, cyclodextrin molecules are positioned in front to form dimers and they are piled together to generate large cylinders that resemble the amylose helix in its global structure.

The reader can find the molecular structure and molecular graphs of blue starch - iodine complex in [3].

Theorem 3.1. *For all $n \geq 3$, let \mathbb{B} be the structure of Blue starch - Iodine Complex, then*

1. $SO(\mathbb{B}) = 12.397n^2 + 10.986n + 1.773$.
2. $N(\mathbb{B}) = 7.708n^2 + 7.0817n + 0.944$.
3. $VL(\mathbb{B}) = 18.25n^2 + 71.75n + 8$.
4. $M_i(\mathbb{B}) = 4n^2 - 4$.
5. $MF(\mathbb{B}) = 19n^2 - 7n - 12$.
6. $GO(\mathbb{B}) = 36.5n^2 + 24.5n + 40$.
7. $CM_2(\mathbb{B}) = 7.5n^2 + 14.5n - 4$.
8. $CM_1^\beta(\mathbb{B}) = 11n^2 + 13n - 4$.
9. $QF(\mathbb{B}) = 107n^2 + 114n - 156$.
10. $Y(\mathbb{B}) = 119n^2 + 117n + 28$.

Proof. Let \mathbb{B} be a blue starch - iodine complex graph. We have five partitions of the edge set $E(\mathbb{B})$ as follows:

$$\begin{aligned} E_1 &= \{uv \in E(\mathbb{B}) : d_{\mathbb{B}}(u) = 1, d_{\mathbb{B}}(v) = 2\}. \\ E_2 &= \{uv \in E(\mathbb{B}) : d_{\mathbb{B}}(u) = 1, d_{\mathbb{B}}(v) = 3\}. \\ E_3 &= \{uv \in E(\mathbb{B}) : d_{\mathbb{B}}(u) = 2, d_{\mathbb{B}}(v) = 2\}. \\ E_4 &= \{uv \in E(\mathbb{B}) : d_{\mathbb{B}}(u) = 2, d_{\mathbb{B}}(v) = 3\}. \\ E_5 &= \{uv \in E(\mathbb{B}) : d_{\mathbb{B}}(u) = 3, d_{\mathbb{B}}(v) = 3\}. \end{aligned}$$

One can calculate easily that $|E_1(\mathbb{B})| = 2n$, $|E_2(\mathbb{B})| = \sum_{i=1}^{n-1} (n+2) - 2$, $|E_3(\mathbb{B})| = n$, $|E_4(\mathbb{B})| = 4n$, $|E_5(\mathbb{B})| = \sum_{i=1}^{n-1} (6n-2) + 2$, $|E_5(\mathbb{B})| = 4n$. The proof technique is similar as theorem 1. \square

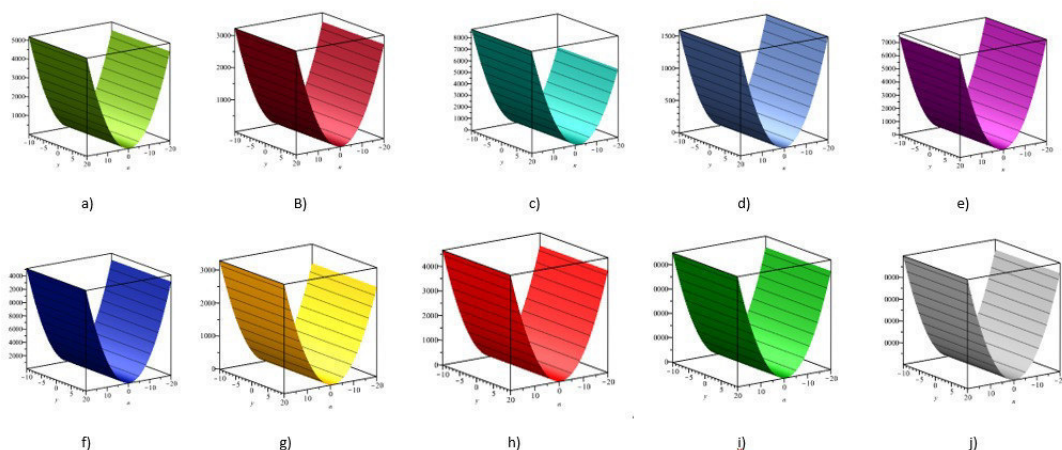


FIGURE 2. 3D plot of topological indices of blue starch - iodine complex graph a) Sombor index b) Nirmala index c) VL index d) irregularity index e) minus F -index f) Gourava index g) Second zagreb index h) first zagreb beta index i) square F index j) Y index.

Theorem 3.2. *let \mathbb{B} be a blue starch - iodine complex graph, then*

1. $SO(\mathbb{B}, x) = 2nx^{\sqrt{5}} + \frac{(n^2+3n-8)}{2}x^{\sqrt{10}} + nx^{\sqrt{8}} + (3n^2 - 5n + 4)x^{\sqrt{10}} + 4nx^{\sqrt{18}}$.
2. $N(\mathbb{B}, x) = 2nx^{\sqrt{13}} + \frac{n^2+5n-8}{2}x^2 + (3n^2 - 5n + 4)x^{\sqrt{5}} + 4nx^{\sqrt{6}}$.
3. $VL(\mathbb{B}, x) = nx^5 + \frac{n^2+3n-8}{4}x^7 + \frac{3n^2-5n+4}{2}x^{11} + 2nx^{15} + nx^8$.
4. $M_i(\mathbb{B}, x) = 5n + (3n^2 - 3n + 4)x + \frac{n^2+3n-8}{2}x^2$.
5. $MF(\mathbb{B}, x) = 5n + 2nx^{-3} + \frac{n^2+3n-8}{2}x^{-8} + (3n^2 - 5n + 4)x^{-5}$.
6. $GO(\mathbb{B}, x) = 2nx^5 + \frac{n^2+3n-8}{2}x^7 + nx^8 + (3n^2 - 5n + 4)x^{11} + 4nx^{15}$.
7. $CM_2(\mathbb{B}, x) = 2nx^6 + (\frac{n^2+3n-8}{2}x^3 + nx^4 + (3n^2 - 5n + 4)x^3 + 4nx$.
8. $CM_1^\beta(\mathbb{B}, x) = 2nx^5 + (\frac{n^2+5n-8}{2}x^4 + (3n^2 - 5n + 4)x^3 + 4nx^2$.
9. $QF(\mathbb{B}, x) = 5n + 2nx^9 + \frac{n^2+3n-8}{2}x^{64} + (3n^2 - 5n + 4)x^{25}$.
10. $Y(\mathbb{B}, x) = 2nx^9 + \frac{n^2+3n-8}{2}x^{28} + nx^{16} + (3n^2 - 5n + 4)x^{25} + 4nx^{54}$.

The proof technique is similar as theorem 2.

4. CONCLUSION:

It is important to calculate topological indices of amylose and blue starch-iodine complex because it is a proved fact that topological indices help to predict many properties without going to the wet lab. In the present work we evaluate some topological indices of the amylose and blue starch-iodine complex. First, we obtain degree based indices then recover some polynomial of the structures. Also, the findings are interpreted graphically.

REFERENCES

- [1] Alameri A., Al-Naggar N., Al-Rumaima and Alsharafi, (2020), Y -index of some graph operations, Journal of Applied Engineering Research, 15(2), 173-179.
- [2] Albertson M. O., (1997), The irregularity of a graph, Ars Combinatoria, 46, 219-225.
- [3] Anam Rani and Usman Ali, (2021), Degree-Based Topological Indices of Polysaccharides: Amylose and Blue Starch-Iodine Complex, Hindawi Journal of Chemistry, 1-10.

- [4] Devillers J. and Balaban A. T., (1999), Topological Indices and Related Descriptors in QSAR and QSPR, Gordon and Breach, Amsterdam.
- [5] Deepika T., (2021), An Emphatic study on VL Index and their bounds on tensor product of F sum graph, TWMS Journal of Applied and Engineering Mathematics, 11(2), 374-385.
- [6] Ediz S., (2015), Maximum chemical trees of the second reverse Zagreb index, Pacific Journal of Applied Mathematics, 7(4), 291-295.
- [7] Ediz S., (2018), Maximal graphs of the first reverse zagreb beta index, TWMS Journal of Applied and Engineering Mathematics, 8(1a), 306-310.
- [8] Gutman I., (2021), Geometric approach to degree based topological indices, MATCH Communications in Mathematical and in Computer Chemistry, 86(1), 11-16.
- [9] I. Gutman, N. Trinajstić, (1972), Graph theory and molecular orbitals. Total π – electron energy of alternant hydrocarbons, Chemical Physics Letters, 17(4), 535-538.
- [10] Green M., Blankenhorn G., and Hart, (1975), Which starch fraction is water-soluble, Amylose or Amylopectin, Journal of Chemical Education, 52(11), 729.
- [11] Kulli V. R., (2021), Nirmala Index, International Journal of Mathematics Trends and Technology, 8-12.
- [12] Kulli V. R., (2019), Minus F and Square F -Indices and Their Polynomials of Certain dendrimers, Earthline Journal of Mathematical Sciences, 1(2), 171-185.
- [13] Kulli V. R., (2017), The Gourava Indices and Coindices of Graphs, Annals of Pure and Applied Mathematics, 14(1), 33-38.
- [14] Kulli V. R., (2018), Reverse Zagreb and reverse hyper-Zagreb indices and their polynomials of rhombus silicate networks, Annals of Pure and Applied Mathematics, 16, 47-51.
- [15] Lokesha V., Manjunath M. and Devendraiah, (2019), Adriatic Indices and Sanskruti index envisage of Carbon Nanocone, TWMS Journal of Applied and Engineering Mathematics, 9(4), 830-837.
- [16] Lokesha V., S. Jain, Deepika, Devendraiah, (2017), Some computational aspects of polycyclic aromatic hydrocarbons, General Mathematics, 25(1-2), 175-190.
- [17] Lokesha V., Sushmitha Jain, Manjunath. M, A. S. Cevik, I. N. Cangul, (2020), Bounds for the sum of cubes of vertex degrees of splice graphs, TWMS Journal of Applied and Engineering Mathematics, 10(3), 741-750.
- [18] Manjunath, V. Lokesha, Suvarna, Sushmitha, (2021), Bounds for the topological indices of ϕ graphs, European journal of the pure and applied mathematics, 14(2), 340-350.

V. Lokesha for the photography and short autobiography, see TWMS J. App. and Eng. Math. V.6, N.2.

V. R. Kulli for the photography and short autobiography, see TWMS J. App. and Eng. Math. V.8, N.1a.

S. Jain for the photography and short autobiography, see TWMS J. App. and Eng. Math. V.10, N.3.



A. S. Maragadam completed M.Sc. and M.Phil. degrees from university of Mysore, Mysore in 2011 and 2013. She started her doctorate programme in 2021 at Vijayanagara Sri Krishnadevaraya University, Ballari under the guidance of Prof. V. Lokesha. Her area of interest in chemical graph theory.



copper(I) oxide molecular descriptors based on ν degree and ν degree

A. S. Maragadam, V. Lokesh, sushmithajain and Nirupadi.K

doi: 10.48047/ecb/2023.12.si4.967

Abstract. Copper oxide is a well-known inorganic chemical and p-type semiconductor. It's a chemical element with the formula Cu_2O and it's employed in chemical sensors and solar cells. The results of various ν degree based and ν degree based topological indices of Cu_2O were found in this study. Throughout the article we denote $\nu = \nu$ and $\nu = \nu$. In addition, the maple was used to plot these research discoveries.

Keywords: Copper(I) Oxide, polynomial, topological index, M-polynomial, crystallographic structure.

2020 Mathematics Subject Classification: 05C09, 05C76.

1 Introduction

One of the key reasons for the expansion is the ability to quickly examine quantitative structure-property or quantitative structure activity relationships (QSPR/QSAR). In a chemical plot, the vertex grade is frequently indicated for its valence. Graph theory has been a focal point for the development of many modern scientific principles and their application to several fields of chemistry. Copper oxide has non-toxic qualities, is complete, and is easy to assemble. Chemists can think as much as they want about molecules and their chemical behaviour by looking at their molecularplot aspects, thanks to the advent of the topological theory of chemistry. Chemical graph theory is a field of mathematics that uses graph theory to analyze the molecular structure of chemical compounds. The topological index is a part of chemical graph theory that connects the physicochemical properties of the underlying chemical graphs, such as viscosity, density, infrared spectrum, boiling point, and melting point. A large number of works on topological indices are available to the reader. [3], [12], [13], [14], [15], [11].

Copper (I) oxide is used in marine paints as a pigment, fungicide, and anti-fouling agent, among other things. Copper (II) oxide is an important product that serves as a starting point for the synthesis of additional copper salts. It has a variety of uses, including wood preservatives, coloured glazes in ceramics, animal feed additives, and welding using copper alloys and other materials.

Photochemical effects, stability, pigment, fungicide, non-toxicity, and low cost are all major benefits. It can be used in a variety of disciplines, including new energy, sensing, sterilising, and others. Understanding cuprite at the electrical and atomic level is more helpful in

predicting and controlling the processes of copper corrosion.

In this study, we calculated the polynomials of both κ and ι degree topological indices for the chemical structure of copper oxide, and explored a few early ideas of both ι degree and κ degree. Additionally, the ability of these trials to address a wide range of complex methods is illustrated in the fields of chem-informatics, bio-medicine, and bio-informatics, where graph topological assessments are regularly employed to further develop and understand the mathematical aspects of the real-world network model.

Using vertex-edge domination and edge-vertex domination parameters, Chellali and his colleagues [2] have published a research paper. In graph theory, they defined κ degrees and ι degrees, which are two novel degree graph invariants. As a result, they discovered that the total κ and ι degrees for any graph are closely linked to the first Zagreb index, a prominent degree-based topological index. In this paper, we computed various topological indices such as the K -index, Sombor index, VL -index, Nirmala index, and Albertson index, all of which are based on κ and ι degrees.

The Wiener index, also referred to as the path number, was the first index name and was introduced by Wiener in 1965 along with the topological descriptor. Ten years later, Randic proposed the Randic-type index, a topological index. The Randic index is still the most well-known, commonly used, and studied of all the topological indices that have since been created. However, the majority of research projects used the traditional concept of degrees, such as Randic and Zagreb indices. This work translated the classical notion of degrees into κ and ι degrees for recently introduced topological indices, such as the K -index, VL -index, Nirmala index, Albertson index, and Sombor index.

Let Ψ be a graph with vertices α and β , $\Psi = (\alpha, \beta)$ use this notation throughout the article. Since degree-based topological indices may be used to analyze the chemical characteristics of various molecule structures, they are helpful. We are particularly interested in polynomial-based topological indices as a result of this inspiration. Topological indices based on polynomials are a useful method for predicting a compound's physicochemical, pharmacological, and toxicological qualities directly from its molecular structure. The study of the quantitative structure–activity relationship is the name for this type of investigation (QSAR). Many chemical and biological features of chemical compounds under research can be predicted using topological indices [4].

2 Preliminaries

Definition 2.1 The κ degree of any edge $\alpha\beta \in E(\Psi)$, denoted by $d_\kappa(\alpha\beta)$, is equal to the total number of vertices in the union of the α and β closed neighborhoods.

Definition 2.2 The degree of any vertex $\beta \in V(\Psi)$ is the sum of the degrees of all the vertices in its closed neighbourhood, i.e., ι the total quantity of edges incident to any vertices from the closed neighbourhood of β .

3 Essential prerequisite

Some definitions of degree-based ι and κ K index ($K(\Psi)$), VL index ($VL(\Psi)$), Nirmala index ($N(\Psi)$), Albertson index ($A(\Psi)$) and Sombor index ($S(\Psi)$) are given bellow.

TI	κ degree based index	ι degree based index
$K(\Psi)$ [17]	$k^\kappa(\Psi) = \sum_{e \in E(\Psi)} [d_\kappa(e)]^3$	$k^\iota(\Psi) = \sum_{e \in E(\Psi)} [d_\iota(e)]^3.$
$S(\Psi)$ [10]	$SO^\kappa(\Psi) = \sum_{\alpha\beta \in E(\Psi)} \sqrt{d_\kappa(\alpha)^2 + d_\kappa(\beta)^2}$	$SO^\iota(\Psi) = \sum_{\alpha\beta \in E(\Psi)} \sqrt{d_\iota(\alpha)^2 + d_\iota(\beta)^2}$
$VL(\Psi)$ [7]	$VL^\kappa(\Psi) = \frac{1}{2} \sum_{\alpha\beta \in E(\Psi)} d_\kappa(e) + d_\kappa(f) + 4$	$VL^\iota(\Psi) = \frac{1}{2} \sum_{\alpha\beta \in E(\Psi)} d_\iota(e) + d_\iota(f) + 4.$
$N(\Psi)$ [16]	$N^\kappa(\Psi) = \sum_{\alpha\beta \in E(\Psi)} \sqrt{d_\kappa(\alpha) + d_\kappa(\beta)}$	$N^\iota(\Psi) = \sum_{\alpha\beta \in E(\Psi)} \sqrt{d_\iota(\alpha) + d_\iota(\beta)}$
$A(\Psi)$ [1]	$A^\kappa(\Psi) = \sum_{\alpha\beta \in E(\Psi)} d_\kappa(\alpha)^2 - d_\kappa(\beta)^2 $	$A^\iota(\Psi) = \sum_{\alpha\beta \in E(\Psi)} d_\iota(\alpha)^2 - d_\iota(\beta)^2 $

Table 1. Some of the ι degree based and κ degree based topological indices.

4 Research Aim

The K -index, VL -index, Nirmala index, Albertson index and Sombor index are some of the topological indices and polynomials of ι degree and κ degree based K -index, VL -index, Nirmala index, Albertson index and Sombor index are some of the primary aims of this article. Furthermore, the results of these indices have been developed to provide a better understanding of their behaviour.

5 Structure of copper oxide

Figure shows how the Cu_2O lattice formed in the $u \times v$ plane and accumulated in w layers. The vertices and edges of Cu_2O 's crystal structure are $1 + u + v + uv + w + uw + vw + 6uvw$ and $8uvw$, respectively. Cu_2O vertices are divided into four divisions based on degrees: four vertices of degree zero, four vertices of degree one, four vertices of degree two, two vertices of degree three, two vertices of degree four, and two vertices of degree four. Similarly, Cu_2O edges are divided into $E_{(1,2)}$, which has $4(u + v + w)$ edges, $E_{(2,2)}$, which has $2(uv + uw + vw - 2u - 2v - 2w + 3)$ edges, and $E_{(2,4)}$, which has $8uvw - 4uv - 4uw - 4vw + 4u + 4v + 4w - 4$ edges.

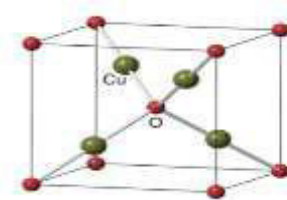


Figure 1: Cu_2O crystal structure

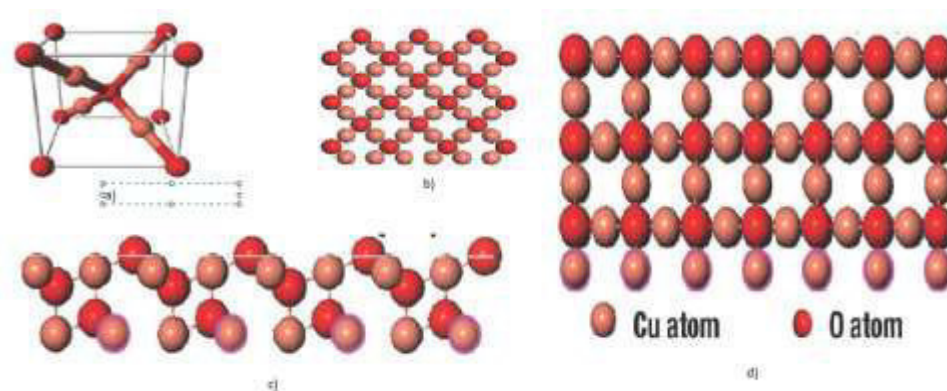


Figure 2: a) cuprite unit cell Cu_2O , b) Cu_2O crystal structure [1,0,0], c) Cu_2O crystal structure [1,1,1], d) Cu_2O crystal structure [1,1,0]

6 Main results

Theorem 6.1 Let Cu_2O be a Copper(I) Oxide then $F^K(Cu_2O)$ is

$$F^K(Cu_2O) = 716(u + v + w) - 736(uv + vw + uw) + 1728uvw - 696.$$

Proof. Assume Cu_2O be a Copper(I) Oxide. The edges are broadly divided into three types then total number of edges is $8uvw$. From the definition of each edge's end vertices κ degree can be used to calculate the degree of each edge, classified into three types which are given below.

$$E_1 = \{e \in E(Cu_2O): d_\kappa Cu_2O(e) = 3\}$$

$$E_2 = \{e \in E(Cu_2O): d_\kappa Cu_2O(e) = 4\}$$

$$E_3 = \{e \in E(Cu_2O): d_\kappa Cu_2O(e) = 6\}$$

One can calculate easily that,

$$|E_1(Cu_2O)| = 4u + 4v + 4w - 8.$$

$$|E_2(Cu_2O)| = 2uv + 2uw + 2vw - 4u - 4v - 4w + 12.$$

$$|E_3(Cu_2O)| = 8uw - 4uv - 4uw - 4vw + 4u + 4v + 4w - 4.$$

$$F^K(\Psi) = \sum_{e \in E(\Psi)} d_\kappa \alpha^3$$

$$\begin{aligned} F^K(Cu_2O) &= ||E_1(Cu_2O)|| (3^3) + ||E_2(Cu_2O)|| (4^3) + ||E_3(Cu_2O)|| (6^3). \\ &= 716(u + v + w) - 736(uv + vw + uw) + 1728uvw - 696. \end{aligned}$$

Theorem 6.2 Let Cu_2O be a Copper(I) Oxide then

1. $k^i(Cu_2O) = 18816(u + v + w) - 17472(uv + vw + uw) + 21952uvw + 1266$.
2. $SO^i(Cu_2O) = 80.941(u + v + w) - 56.087(uv + vw + uw) + 90.509uvw - 2.529$.
3. $VL^i(Cu_2O) = 320(u + v + w) - (224)(uv + vw + uw) + 320uvw - 24$.
4. $N^i(Cu_2O) = 29.389(u + v + w) - 18.192(uv + vw + uw) + 32uvw + 0.8367$.
5. $A^i(Cu_2O) = 48(u + v + w) + 96(uv + vw + uw) + 96$.

Proof. Let cu_2o be a copper(I) oxide. The edges can be divided into five types and its total number of edges is $8uvw$. From the definition of each edge's end vertices ι degree can be used to calculate the degree of each edge, classified into five types which are given below.

$$E_1 = \{\alpha\beta \in E(Cu_2O): d_{Cu_2O}(\alpha) = 2, d_{Cu_2O}(\beta) = 5\}.$$

$$E_2 = \{\alpha\beta \in E(Cu_2O): d_{Cu_2O}(\alpha) = 4, d_{Cu_2O}(\beta) = 6\}.$$

$$E_3 = \{\alpha\beta \in E(Cu_2O): d_{Cu_2O}(\alpha) = 5, d_{Cu_2O}(\beta) = 8\}.$$

$$E_4 = \{\alpha\beta \in E(Cu_2O): d_{Cu_2O}(\alpha) = 6, d_{Cu_2O}(\beta) = 8\}.$$

$$E_5 = \{\alpha\beta \in E(Cu_2O): d_{Cu_2O}(\alpha) = 8, d_{Cu_2O}(\beta) = 8\}.$$

$$|E_1(Cu_2O)| = 4u + 4v + 4w - 8, \quad |E_2(Cu_2O)| = 2uv + 2uw + 2vw - 4u - 4v - 4w + 12$$

$$|E_3(Cu_2O)| = 4(u + v + w - 2), \quad |E_4(Cu_2O)| = 2uv + 2uw + 2vw - 4u - 4v - 4w + 12,$$

$$|E_5(Cu_2O)| = 8(v - 1)(u - 1)(w - 1).$$

$$SO^i(\Psi) = \sum_{\alpha\beta \in E(\Psi)} \sqrt{d_i\alpha^2 + d_i\beta^2}$$

$$= |E_{(2,5)}| \sum_{\alpha\beta \in E_{(2,5)}(Cu_2O)} \sqrt{d_i\alpha^2 + d_i\beta^2} + |E_{(4,6)}| \sum_{\alpha\beta \in E_{(4,6)}(Cu_2O)} \sqrt{d_i\alpha^2 + d_i\beta^2}$$

$$+ |E_{(5,8)}| \sum_{\alpha\beta \in E_{(5,8)}(Cu_2O)} \sqrt{d_i\alpha^2 + d_i\beta^2} + |E_{(6,8)}| \sum_{\alpha\beta \in E_{(6,8)}(Cu_2O)} \sqrt{d_i\alpha^2 + d_i\beta^2}$$

$$+ |E_{(8,8)}| \sum_{\alpha\beta \in E_{(8,8)}(Cu_2O)} \sqrt{d_i\alpha^2 + d_i\beta^2}.$$

$$= 80.941(u + v + w) - 56.087(uv + vw + uw) + 90.509uvw - 2.529.$$

We could use the same method to obtain results for the remaining indices.

Theorem 6.3 Let Cu_2O be a Copper(I) Oxide then polynomials are given by

1. $K^i(Cu_2O, x) = (u + v + w)[4x^{125} - 4x^{512} + 4x^{1331} - 4x^{1728} + 8x^{2744}] + (uv + uw + vw)[2x^{512}2x^{1728} - 8x^{2744}] + 8uvwx^{2744} - 8x^{125} + 12x^{512} - 8x^{1331} + 12x^{1728} - 8x^{2744}$.
2. $SO^i(Cu_2O, x)$

$$= (u + v + w)[4x^{5.38} - 4x^{7.21} + 4x^{9.43} - 4x^{10} + 8x^{11.31}]$$

$$+ (uv + uw + vw)[2x^{7.21} + 2x^{10} - 8x^{11.31}] + 8uvwx^{11.31} - 8x^{5.38}$$

$$+ 12x^{7.21} - 8x^{9.43} + 12x^{10} - 8x^{11.31}.$$

$$\begin{aligned}
3. VL^{\iota}(Cu_2O, x) &= (u + v + w)[2x^{17} - 2x^{34} + 2x^{53} - 2x^{62} + 4x^{80}] + (uv + uw + vw)[x^{34} + 2x^{62} - 4x^{80}] + 4uvw x^{80} - 4x^{17} + 6x^{34} - 4x^{53} + 6x^{62} - 4x^{80}. \\
4. N^{\iota}(Cu_2O, x) &= (u + v + w)[4x^{2.64} - 4x^{3.16} + 4x^{3.60} - 4x^{3.74} - 8x^4] + (uv + uw + vw)[2x^{3.16} + 2x^{3.74} - 8x^4] + 8uvw x^4 - 8x^{2.64} + 12x^{3.16} + 12x^{3.74} - 8x^{3.60} - 8x^4. \\
5. A^{\iota}(Cu_2O, x) &= (u + v + w)[4x^{21} - 4x^{20} + 4x^{39} - 4x^{28} + 8x] + (uv + uw + vw)[2x^{20} + 2x^{28} - 8] + 8uvw x^{11.31} - 8x^{21} + 12x^{20} - 8x^{39} + 12x^{28} - 8.
\end{aligned}$$

The proof method is as similar as theorem 2.

7 Numerical results

We offer mathematical conclusions which have been tied to the topological descriptors based on κ and ι degrees for the sub-atomic structures of cuprite oxide. We evaluated numerous u, v , and w estimations that were calculated using mathematical tables (Table 2). Many aspects of the understudied chemical molecule can be predicted using topological indices. Some of the graph invariants for instance K -index, Sombor index, VL -index, Nirmala index, and Albertson index that have been proposed for estimating the skeleton pertaining to the molecule of carbon spreading. A interesting field of research is still calculating the Undergraduate molecular graphs topological index based on degree.

So far, we have recorded numerically certain degree-based entropies for various u, v, w estimates for $Cu_2O[u, v, w]$. As the predictions of $[u, v, w]$ are increments, you can see that all of the entropy values are in growing request [18].

$[u, v, w]$	$F^{\kappa}(\Psi)$	$k^{\iota}(\Psi)$	$SO^{\iota}(\Psi)$	$VL^{\iota}(\Psi)$	$N^{\iota}(\Psi)$	$A^{\iota}(\Psi)$
[1,1,1]	972	27250	162.54	584	329.59	528
[2,2,2]	8592	80114	534.12	1768	2494.03	1536
[3,3,3]	32532	291570	1655.28	5448	8389.31	3120
[4,4,4]	83160	793330	4069.16	13544	19935.45	5280
[5,5,5]	170844	1717106	8318.68	27976	39052.43	8016
[6,6,6]	305952	3194610	14946.95	50664	67660.26	11328
[7,7,7]	498852	5357554	24497.03	83528	107678.94	15216
[8,8,8]	759912	8337650	37511.95	128488	161028.47	19680
[9,9,9]	1099500	12266610	54534.79	187464	229628.84	24720
[10,10,10]	1527984	17276146	76108.60	262376	315400.07	30336

Table 2. Numerical depiction of estimated indices for various Cu_2O values.

8 Graphical Comparison of Cu_2O

In this portion we have depicted 3D graphs of polynomial of Cu_2O of various ι degree based topological indices.

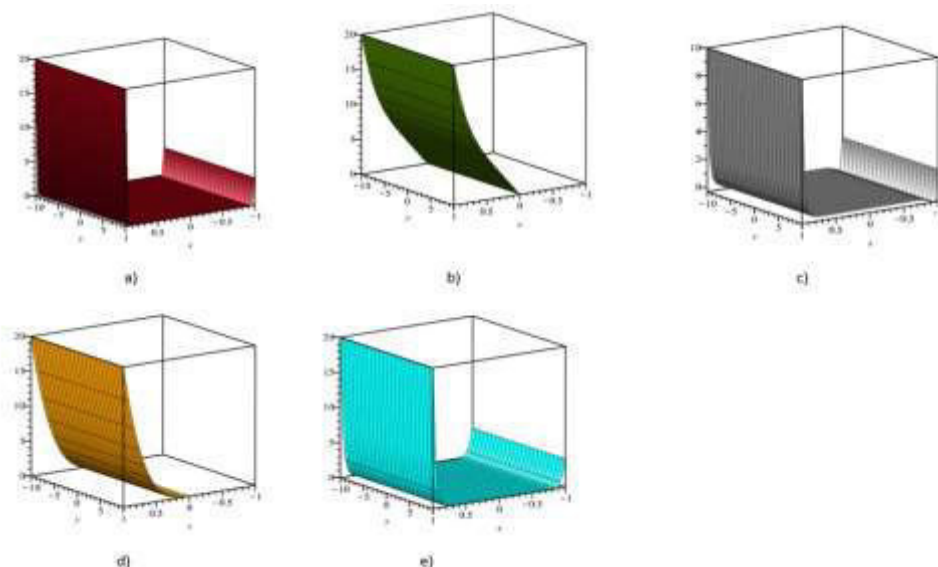


Figure 3: 3D graphs of polynomial of Cu_2O a) K edge index, b) sombor index, c) VL index, d) Nirmala index, e) Albertson index

9 Conclusion

The results of specific κ degree based and ι degree based indices of copper(I) oxide are presented in this article. Considering that the ι degree index has demonstrated a stronger prediction ability and correlation than standard degree-based indexes, according to the results of this study will assist researchers in better understanding the physical and chemical properties of copper(I) oxide.

Acknowledgements

The authors are grateful to the reviewers for their insightful remarks and recommendations, which helped to improve this papers.

References

- [1]M. O. Albertson, *The irregularity of a graph*, Ars Combinatoria, 46, 1997, 219-225.
- [2]M. Chellali, T. W. Haynes, S. T. Hedetniemi, and T. M. Lewis, *On κ -degrees and ι -degrees in graphs*, Discrete Mathematics, 340(2), 2017, 31-38.
- [3]B. Chaluvvaraju, V. Loksha, S. Jain and T. Deepika, *General extremal degree based indices of a graph*, Palestine Journal of Mathematics, 8(1), 2019, 217-228.
- [4]Chu, YM., Imran, M., Baig, A.Q. et al., *On M -polynomial-based topological descriptors of chemical crystal structures and their applications*, Eur. Phys. J. Plus 135, 874, 2020.

[5]Faryal Chaudhry, Iqra Shoukat, Deeba Afzal , Choonkil Park , Murat Cancan , and Mohammad Reza Farahani, *M-Polynomials and Degree-Based Topological Indices of the Molecule Copper(I) Oxide*, Journal of Chemistry, 2021, 1-12.

[6] J. Devillers and A. T. Balaban, *Topological Indices and Related Descriptors in QSAR and QSPR*, Gordon and Breach, Amsterdam, 1999.

[7] Deepika T., *An Emphatic study on VL Index and their bounds on tensor product of F sum graph*, TWMS Journal of Applied and Engineering Mathematics, 11(2), 2021, 374-385.

[8]S. Ediz, *Predicting some physicochemical properties of octane isomers: a topological approach using ev-degree and ve-degree zagreb indices*, International Journal of Systems Science and Applied Mathematics, 2(5), 2017, 87–92.

[9]I. Gutman and N. Trinajstić, *Graph theory and molecular orbitals. total ϕ -electron energy of alternant hydrocarbons*, Chemical Physics Letters, 17(4), 1972, 535-538.

[10]I. Gutman, *Geometric approach to degree based topological indices*, MATCH Communications in Mathematical and in Computer Chemistry, 86(1), 2021, 11-16.

[11]Jing Zhang, Muhammad Kamran Siddiqui, Abdul Rauf and Muhammad Ishtiaq, *On ve-Degree and ev-Degree Based Topological Properties of Single Walled Titanium Dioxide Nanotube*, Journal of Cluster Science, 32, 2021, 821–832.

[12]V. Lokesha, Sushmitha Jain, Deepika T and A.S. Cevik, *Operation on topological indices of Dutch windmill graph*, Proceedings of the Jangjeon Mathematical Society, 21(3), 2018, 525-534.

[13]V. Lokesha, S. Jain, T. Deepika, K.M. Devendraiah, *Some computational aspects of polycyclic aromatic hydrocarbons*, General Mathematics, 25(1-2), 2017, 175-190.

[14]V. Lokesha and Sushmitha Jain, *New results on the F-index of graphs based on a corona type products of graphs*, Proceedings of the Jangjeon Mathematical Society, 23(2), 2020, 141-147.

- [15] Manjunath, V. Loksha, Suvarna, Sushmitha, *Bounds for the topological indices of φ graphs*, European journal of the pure and applied mathematics, 14(2), 2021, 340-350.
- [16] V. R. Kulli, *Nirmala Index*, International Journal of Mathematics Trends and Technology, 2021, 8-12.
- [17] V. R. Kulli, *On K-Indices of graphs*, International Journal of fuzzy Mathematical Archive, 10(2), 2016, 105-109.
- [18] Shazia Manzoor, Yu-Ming Chu, Muhammad Kamran Siddiqui and Sarfraz Ahmad, *On topological aspects of degree based entropy for two carbon nanosheets*, Main Group Metal Chemistry, 43(1), 2020, 205-218.
- [19] Shu-Bo Chen, Abdul Rauf, Muhammad Ishtiaq, Muhammad Naeem, Adnan Aslam *On δ^- -degree and δ^+ -degree based topological properties of crystallographic structure of cuprite*, Open Chemistry, 19, 2021, 576-585.

A. S. Maragadam

Department of studies in Mathematics,
Vijayanagara Sri Krishnadevaraya
University, Ballari, India.
e-mail: maragadamvijay@gmail.com.
Orchid iD: <https://orcid.org/0000-0001-9703-2161>.

V. Loksha

Department of studies in Mathematics,
Vijayanagara Sri Krishnadevaraya
University, Ballari, India.
e-mail: v.lokesha@gmail.com.
Orchid iD: <https://orcid.org/0000-0003-2468-9511>.

and

Sushmitha Jain

Department of studies in Mathematics,
Vijayanagara Sri Krishnadevaraya
University, Ballari, India.
e-mail: sushmithajain9@gmail.com.
Orchid iD: <https://orcid.org/0000-0002-4173-8787>.

STUDY ON LINE GRAPH OF SOME GRAPH OPERATORS OF CHEMICAL STRUCTURES VIA F AND M_1 INDICES

M. MANJUNATH, S. M. VEERESH, M. PRALAHAD AND P. S. HEMAVATHI*

ABSTRACT. The Topological indices are known as Mathematical characterization of molecules. In this paper, we have studied line graph of subdivision and semi-total point graph of triangular benzenoid, polynomino chains of 8-cycles and graphene sheet through forgotten and first Zagreb indices.

AMS Mathematics Subject Classification: 05C09, 05C92.

Key words and phrases : Line graph, Subdivision graph, Semi-total point graph, F -index, M_1 -index, Triangular benzenoid, Polynomino chains, Graphene sheet.

1. Introduction

A topological index is a numerical parameter which characterizes its molecular topology and used for quantitative structure activity relationship (*QSAR*) and quantitative structure property relationship (*QSPR*). In 1947, the first topological index (named as Wiener index or path index) was introduced by Wiener for finding the boiling point of paraffins [5]. For new topological indices, we suggest the reader to refer the papers [7, 9–20].

In [1], B. Furtula and et al., proposed a topological index based on the degrees of vertices of graph, which is known as forgotten index and it is defined as

$$F[G] = \sum_{u \in V[G]} deg_G^3 u$$

or

$$F(G) = \sum_{uv \in E(G)} [deg_G^2(u) + deg_G^2(v)]$$

Received , . Revised , . Accepted , . *Corresponding author.

[†]This research received no external funding.

© 2023 KSCAM.

The first Zagreb index is introduced by Gutman et al. [2] and it is defined as

$$M_1(G) = \sum_{uv \in E(G)} [deg_G(u) + deg_G(v)]$$

or

$$M_1(G) = \sum_{u \in V(G)} deg_G^2(u)$$

Definition 1.1. [6] The **line graph** $L(G)$ is the graph obtained by associating a vertex with each edge of the graph G and two vertices are adjacent with an edge iff the corresponding edges of G are adjacent.

Definition 1.2. [21] The **subdivision graph** $S(G)$ is the graph obtained by replacing each of its edge by a path of length 2 or equivalently, by inserting an additional vertex into each edge of G .

Definition 1.3. The **semi-total point graph** $R(G)$ graph is obtained from G by adding a new vertex corresponding to every edge of G and by joining each new vertex to the end vertices of the edge corresponding to it.

Triangular benzenoid: Benzenoid molecular graph is a connected geometric figure obtained by arranging congruent regular hexagons in a plane so that two hexagons are either disjoint or have a common edge and it is shown in below Figure 1 [3, 18, 22].

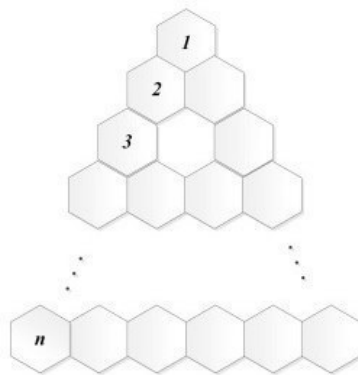


FIGURE 1. Triangular benzenoid

Polynomino chains of 8-cycles: A k -polyomino system is a finite 2-connected plane graph such that each interior face (also called cell) is surrounded by a regular $4k$ -cycle of length one and Polynomino chains of 8-cycles shown in below Figure 2.

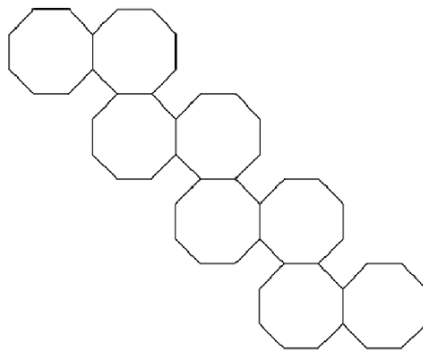


FIGURE 2. Polynomino chains of 8-cycles

Graphene sheet: Graphene sheets are essentially the finest materials in the world. Graphene sheet is a one-atom-thick planar sheet of carbon atoms which are intensively packed in a hexagonal lattice structure. Graphene sheets show high electrical conductance at room temperatures and molecular graph of graphene sheet as shown in below Figure 3 (See [4, 8]).

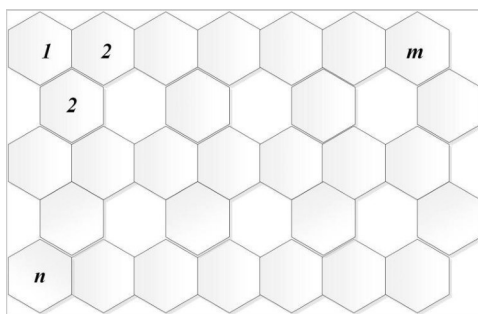


FIGURE 3. Graphene sheet

2. Main results

In this section, we compute the forgotten and first Zagreb indices of line graph of subdivision and semi-total point graph of triangular benzenoid, polynomino chains of 8-cycles and graphene sheet.

Theorem 2.1. *Let Γ be the line graph of subdivision graph of triangular benzenoid, then*

$$\begin{aligned} M_1[\Gamma] &= \frac{9}{2}(n^2 - n + 8)^2 + \frac{27}{4}(n^2 + 7n - 8)^2, \\ F[\Gamma] &= \frac{27}{4}(n^2 - n + 8)^3 + \frac{81}{8}(n^2 + 7n - 8)^3. \end{aligned}$$

Proof. Let Γ be a line graph of subdivision graph of triangular benzenoid. Applying the line and subdivision operations to Figure 1, we obtain the two types of vertices based on their degrees and which are shown in the below **Table 1**.

Table 1. Degree partition of Γ based on their degrees.

$deg_{\Gamma}(u)$	Number of vertices
2	$12 + \frac{3n(n-1)}{2}$
3	$\frac{3}{2}(n^2 + 7n - 8)$

Consider,

$$\begin{aligned} M_1[G] &= \sum_{u \in V[G]} deg_G^2 u \\ M_1[\Gamma] &= 2 \left(12 + \frac{3n(n-1)}{2} \right)^2 + 3 \left(\frac{3}{2}(n^2 + 7n - 8) \right)^2 \\ &= \frac{1}{2}(24 + (3n(n-1)))^2 + \frac{3^3}{2^2}(n^2 + 7n - 8)^2 \\ M_1[\Gamma] &= \frac{9}{2}(n^2 - n + 8)^2 + \frac{27}{4}(n^2 + 7n - 8)^2. \end{aligned}$$

the above proof method is also follows for $F[\Gamma]$. \square

Theorem 2.2. *Let Υ be the line graph of semi-total point graph of triangular benzenoid, then*

$$\begin{aligned} M_1[\Upsilon] &= 9(n^2 - n + 8)^2 + \frac{27}{2}(n^2 + 7n - 4)^2 + 18n^2(n-1)^2 + 360(n-1)^2, \\ F[\Upsilon] &= \frac{27}{2}(n^2 - n + 8)^3 + \frac{81}{4}(n^2 + 7n - 8)^3 + 27(n(n-1))^3 + 2160(n-1)^3. \end{aligned}$$

Proof. Let Υ be a line graph of semi-total point graph of triangular benzenoid. Applying the line and semi-total point operations to Figure 1, we obtain the four types of vertices based on their degrees and which are shown in the below **Table 2**.

Table 2. Degree partition of Υ based on their degrees.

$deg_{\Upsilon}(u)$	Number of vertices
4	$12 + \frac{3n(n-1)}{2}$
6	$\frac{3}{2}(n^2 + 7n - 8) + 6$
8	$\frac{3n(n-1)}{2}$
10	$6(n-1)$

Consider,

$$\begin{aligned}
 M_1[G] &= \sum_{u \in V[G]} \deg_G^2 u \\
 M_1[\Upsilon] &= 4 \left(12 + \frac{3n(n-1)}{2} \right)^2 + 6 \left(\frac{3}{2}(n^2 + 7n - 8) + 6 \right)^2 \\
 &\quad + 8 \left(\frac{3n(n-1)}{2} \right)^2 + 10(6(n-1))^2 \\
 M_1[\Upsilon] &= 9(n^2 - n + 8)^2 + \frac{27}{2}(n^2 + 7n - 4)^2 + 18n^2(n-1)^2 + 360(n-1)^2.
 \end{aligned}$$

the above proof method is also follows for $F[\Upsilon]$. \square

Theorem 2.3. *Let Φ be the line graph of subdivision graph of polynomino chains of 8-cycles, then*

$$\begin{aligned}
 M_1[\Phi] &= 3776n^2 - 160n + 236, \\
 F[\Phi] &= 107008n^3 - 3618n^2 + 20064n + 376.
 \end{aligned}$$

Proof. Let Φ be a line graph of subdivision graph of polynomino chains of 8-cycles. Applying the line and subdivision operations to Figure 2, we obtain the two types of vertices based on their degrees and which are shown in the below **Table 3**.

Table 3. Degree partition of Φ based on their degrees.

$\deg_{\Phi}(u)$	Number of vertices
2	$32n + 8$
3	$24n - 6$

Consider,

$$\begin{aligned}
 M_1[G] &= \sum_{u \in V[G]} \deg_G^2 u \\
 M_1[\Phi] &= 2(32n + 8)^2 + 3(24n - 6)^2 \\
 M_1[\Phi] &= 3776n^2 - 160n + 236.
 \end{aligned}$$

the above proof method is also follows for $F[\Phi]$. \square

Theorem 2.4. *Let Ψ be the line graph of semi-total point graph of polynomino chains of 8-cycles, then*

$$\begin{aligned}
 M_1[\Psi] &= 13024n^2 - 320n + 178, \\
 F[\Psi] &= 420224n^3 - 49920n^2 + 18672n - 62.
 \end{aligned}$$

Proof. Let Ψ be a line graph of semi-total point graph of polynomino chains of 8-cycles. Applying the line and semi-total point operations to Figure 2, we obtain the four types of vertices based on their degrees and which are shown in the below **Table 4**.

Table 4. Degree partition of Ψ based on their degrees.

$deg_{\Psi}(u)$	Number of vertices
4	$32n + 4$
6	$36n - 2$
8	$8n$
10	$8n - 3$

Consider,

$$\begin{aligned}
M_1[G] &= \sum_{u \in V[G]} deg_G^2 u \\
M_1[\Psi] &= 4(32n + 4)^2 + 6(36n - 2)^2 + 8(8n)^2 + 10(8n - 3)^2 \\
M_1[\Psi] &= 13024n^2 - 320n + 178.
\end{aligned}$$

the above proof method is also follows for $F[\Psi]$. \square

Theorem 2.5. Let \mathfrak{J} be the line graph of subdivision graph of graphene sheet with n -rows and m -columns, then

$$\begin{aligned}
M_1[\mathfrak{J}] &= 32(m + n + 1)^2 + 12(|E(\mathfrak{J}(m, n))| - 2m - 2n - 2)^2, \\
F[\mathfrak{J}] &= 128(m + n + 1)^3 + 24(|E(\mathfrak{J}(m, n))| - 2m - 2n - 2)^3.
\end{aligned}$$

Proof. Let \mathfrak{J} be a line graph of subdivision graph of graphene sheet with n -rows and m -columns. Applying the line and subdivision operations to Figure 3, we obtain the two types of vertices based on their degrees and which are shown in the below **Table 5**.

Table 5. Degree partition of \mathfrak{J} based on their degrees.

$deg_{\mathfrak{J}}(u)$	Number of vertices
2	$4m + 4n + 4$
3	$2 E(\mathfrak{J}(m, n)) - 4m - 4n - 4$

Consider,

$$\begin{aligned}
M_1[G] &= \sum_{u \in V[G]} deg_G^2 u \\
M_1[\mathfrak{J}] &= 2(4m + 4n + 4)^2 + 3(2|E(\mathfrak{J}(m, n))| - 4m - 4n - 4)^2 \\
M_1[\mathfrak{J}] &= 32(m + n + 1)^2 + 12(|E(\mathfrak{J}(m, n))| - 2m - 2n - 2)^2.
\end{aligned}$$

the above proof method is also follows for $F[\mathfrak{J}]$. \square

Theorem 2.6. Let \mathfrak{T} be the line graph of semi-total point graph of polynomino chains of 8-cycles, then

$$\begin{aligned}
M_1[\mathfrak{T}] &= 64(m + n + 1)^2 + 6(2|E(\mathfrak{T}(m, n))| - 4m - 3n)^2 \\
&+ 32(2m + n - 2)^2 + 10(|E(\mathfrak{T}(m, n))| - 4m - 3n)^2, \\
F[\mathfrak{T}] &= 256(m + n + 1)^3 + 6(2|E(\mathfrak{T}(m, n))| - 4m - 3n)^3
\end{aligned}$$

$$+ 64(2m + n - 2)^3 + 10(|E(\Upsilon(m, n))| - 4m - 3n)^3.$$

Proof. Let Υ be a line graph of semi-total point graph of graphene sheet with n -rows and m -columns. Applying the line and semi-total point operations to Figure 3, we obtain the four types of vertices based on their degrees and which are shown in the below **Table 6**.

Table 6. Degree partition of Υ based on their degrees.

$deg_{\Upsilon}(u)$	Number of vertices
4	$4m + 4n + 4$
6	$2 E(\Upsilon(m, n)) - 4m - 3n$
8	$4m + 2n - 4$
10	$ E(\Upsilon(m, n)) - 4m - 3n$

Consider,

$$\begin{aligned}
 M_1[G] &= \sum_{u \in V[G]} deg_G^2 u \\
 M_1[\Upsilon] &= 4(4m + 4n + 4)^2 + 6(2|E(\Upsilon(m, n))| - 4m - 3n)^2 \\
 &\quad + 8(4m + 2n - 4)^2 + 10(|E(\Upsilon(m, n))| - 4m - 3n)^2 \\
 M_1[\Upsilon] &= 64(m + n + 1)^2 + 6(2|E(\Upsilon(m, n))| - 4m - 3n)^2 \\
 &\quad + 32(2m + n - 2)^2 + 10(|E(\Upsilon(m, n))| - 4m - 3n)^2.
 \end{aligned}$$

the above proof method is also follows for $F[\Upsilon]$. \square

Conclusion: In this article, we have calculated the forgotten and first Zagreb indices of line graph of subdivision and semi-total point graph of triangular benzenoid, polynomino chains and graphene sheet. These results are useful to study the *QSPR* and *QSAR* of above chemical molecules.

Conflicts of interest : The authors declare no conflict of interest.

Data availability : Not applicable

Acknowledgments : The authors would like to thank the referees for their invaluable comments and suggestions which led to the improvement of the manuscript.

REFERENCES

1. B. Furtula and I. Gutman, *A forgotten topological index*, Journal of Mathematical Chemistry, **53**(4) (2015), 1184–1190.
2. I. Gutman and N. Trinajstić, *Graph theory and molecular orbitals. Total φ -electron energy of alternant hydrocarbons*, Chemical Physics Letters, **17**(4) (1972), 535–538.
3. P. S. Hemavathi, V. Lokesh, M. Manjunath, P. Siva Kota Reddy and R. Shruti, *Topological Aspects of Boron Triangular Nanotube and Boron- α Nanotube*, Vladikavkaz Math. J., **22**(1) (2020), 66–77.

4. R. Jagadeesh, M. R Rajesh Kanna and R. S. Indumathi, *Some results on topological indices of graphene*, Nanomaterials and Nanotechnology, **6**(1) (2016), 1–6.
5. V. Lokesha and T. Deepika, *Symmetric division deg index of tricyclic and tetracyclic graphs*, International Journal of Science and Engineering Research, **7**(5) (2016), 53–55.
6. V. Lokesha, M. Manjunath, B. Chaluvharaju, K. M. Devendraiah, I. N. Cangul and A. S. Cevik, *Computation of adriatic indices of certain operators of regular and complete bipartite graphs*, Advanced Studies in Contemporary Mathematics, **28**(2) (2018), 231–244.
7. K. B. Mahesh, R. Rajendra and P. Siva Kota Reddy, *Square Root Stress Sum Index for Graphs*, Proyecciones, **40**(4) (2021), 927–937.
8. Melaku Berhe and Chunxiang Wang, *Computation of certain topological coindices of graphene sheet and $C_4C_8(S)$ nanotubes and nanotorus*, Applied Mathematics and Non-linear Sciences, **4**(2) (2019), 455–468.
9. R. M. Pinto, R. Rajendra, P. Siva Kota Reddy and Ismail Naci Cangul, *A QSPR Analysis for Physical Properties of Lower Alkanes Involving Peripheral Wiener Index*, Montes Taurus J. Pure Appl. Math., **4**(2) (2022), 81–85.
10. K. N. Prakasha, P. Siva Kota Reddy and Ismail Naci CANGÜL, *Atom-Bond-Connectivity Index of Certain Graphs*, TWMS J. App. Eng. Math., **13**(2) (2023), 400–408.
11. R. Rajendra, K. B. Mahesh and P. Siva Kota Reddy, *Mahesh Inverse Tension Index for Graphs*, Adv. Math., Sci. J., **9**(12) (2020), 10163–10170.
12. R. Rajendra, P. S. K. Reddy and Ismail Naci CANGÜL, *Stress indices of graphs*, Adv. Stud. Contemp. Math. (Kyungshang), **31**(2) (2021), 163–173.
13. R. Rajendra, P. Siva Kota Reddy and C. N. Harshavardhana, *Tosha Index for Graphs*, Proceedings of the Jangjeon Math. Soc., **24**(1) (2021), 141–147.
14. R. Rajendra, K. Bhargava, D. Shubhalakshmi and P. Siva Kota Reddy, *Peripheral Harary Index of Graphs*, Palest. J. Math., **11**(3) (2022), 323–336.
15. R. Rajendra, P. Siva Kota Reddy, K.B. Mahesh and C. N. Harshavardhana, *Richness of a Vertex in a Graph*, South East Asian J. Math. Math. Sci., **18**(2) (2022), 149–160.
16. R. Rajendra, P. Siva Kota Reddy and M. Prabhavathi, *Computation of Wiener Index, Reciprocal Wiener index and Peripheral Wiener Index Using Adjacency Matrix*, South East Asian J. Math. Math. Sci., **18**(3) (2022), 275–282.
17. R. Rajendra, P. Siva Kota Reddy, C. N. Harshavardhana, S. V. Aishwarya and B. M. Chandrashekar, *Chelo Index for graphs*, South East Asian J. Math. Math. Sci., **19**(1) (2023), 175–188.
18. Y. Shanthakumari, P. Siva Kota Reddy, V. Lokesha and P. S. Hemavathi, *Topological Aspects of Boron Triangular Nanotube and Boron-Nanotube-II*, South East Asian J. Math. Math. Sci., **16**(3) (2020), 145–156.
19. P. Siva Kota Reddy, K. N. Prakasha and Ismail Naci Cangul, *Randic type Hadi index of graphs*, Trans. Natl. Acad. Sci. Azerb. Ser. Phys.-Tech. Math. Sci., **40**(4) (2020), 175–181.
20. P. Siva Kota Reddy, K. N. Prakasha and Ismail Naci Cangul, *Inverse Sum Indeg Energy of a Graph*, Advn. Stud. Contemp. Math., **31**(1) (2021), 7–20.
21. M. H. Sunilkumar, V. Lokesha, I. N. Cangul and K. M. Devendraiah, *On certain topological indices of the derived graphs of subdivision graphs*, TWMS Journal of applied and engineering Mathematics, **6**(2) (2016), 324–332.
22. Young Chel Kwun, Ashaq Ali, Waqas Nazeer, Maqbool Ahmad Chaudhary and Shin Min Kang, *M-Polynomials and Degree-Based Topological Indices of Triangular, Hourglass, and Jagged-Rectangle Benzenoid Systems*, Journal of Chemistry, **1**(1)(2018), 8 pages.

Manjunath Muddalapuram graduated and received his M.Sc. degree from Gulbarga University. He also received doctorate from VSK University in 2020. He has published 25 research articles in internationally reputed journals. He presented research articles in 15 reputed conferences. He is actively visiting IITs and reputed Institutions for workshop

and short visits for research work. He joined as Assistant Professor in the Department of Mathematics, Ballari Institute of Technology and Management, Ballari in the year 2020.

Department of Mathematics, Ballari Institute of Technology and Management, Ballari, Karnataka, India.

e-mail: manju3479@gmail.com

Veeresh S. M graduated and received his M.Sc. degree from Gulbarga University. He started his doctoral programme in 2016 at R and D center, Department of Mathematics, Ballari Institute of Technology and Management, Ballari, Karnataka under Visvesvaraya Technological University, Belagavi, Karnataka. He has published 4 research articles in internationally reputed journals. He presented research articles in 6 reputed conferences. He is actively visiting reputed Institutions for workshop and short visits for research work. He joined as Assistant Professor in the Department of Mathematics, Ballari Institute of Technology and Management, Ballari in the year 2013.

Department of Mathematics, Ballari Institute of Technology and Management, Ballari, Karnataka, India.

e-mail: veeresh2010.1155@gmail.com

Pralahad Mahagaonkar graduated and received his M.Sc. degree from Gulbarga University. He also received his doctorate from Gulbarga University in 2011. He has published 10 research articles in internationally reputed journals. He presented research articles in 15 reputed conferences. He is actively visiting reputed Institutions for workshop and short visits for research work. He working as Associate Professor in the Department of Mathematics, Ballari Institute of Technology and Management, Ballari.

Department of Mathematics, Ballari Institute of Technology and Management, Ballari, Karnataka, India.

e-mail: pralahadm74@gmail.com

Hemavathi P. S. received doctorate from VSK University in 2019. She has published 15 research articles in internationally reputed journals. She presented research articles in 10 reputed conferences. She is working as Assistant Professor in the Department of Mathematics, Siddagangai Institute of Technology, Tumakur, India.

Department of Mathematics, Siddaganga Institute of Technology, Tumakur, Karnataka, India.

e-mail: hemavathisuresh@gmail.com



INVESTIGATION OF LOWER AND UPPER BOUNDS OF ψ GRAPH VIA SOME TOPOLOGICAL INDICES

MANJUNATH MUDDALAPURAM *

Department of Mathematics, Ballari Institute of Technology and Management,
Ballari, Karnataka, INDIA.

(E-mail: manju3479@gmail.com)

KUMARA M. †

Department of Mathematics, Nitte Meenakshi Institute of Technology,
Bengaluru, Karnataka, INDIA.

(E-mail: kumarabub@gmail.com)

and

RACHANNA KANABUR ‡

Department of Mathematics, BLDEA'S Commerce BHS Arts
and TGP Science College, Jamkhandi, Karnataka, INDIA.

(E-mail: rachukanabur@gmail.com)

Abstract. Topological index is the Mathematical tool which is correlate to the properties of chemical structure. In this paper, we study the bounds for ψ graph through first and second Zagreb, Gourava, Forgotten, Shegehalli-Kanabur and reformulated first Zagreb indices.

Communicated by Editors; Received November 10, 2023

AMS Subject Classification: 05C90, 05C12.

Keywords: Edge-neighbourhood of SR -corona product and Topological index.

THE INDIAN JOURNAL OF TECHNICAL EDUCATION

Published by
INDIAN SOCIETY FOR TECHNICAL EDUCATION
Near Katwaria Sarai, Shaheed Jeet Singh Marg,
New Delhi - 110 016



INDIAN JOURNAL OF TECHNICAL EDUCATION

Volume 46 • Special Issue • September 2023

Editorial Advisory Committee

Prof. Pratapsinh K. Desai - Chairman
President, ISTE

Prof. N.R. Shetty
Former President, ISTE, New Delhi

Prof. (Dr.) Buta Singh Sidhu
Vice Chancellor, Maharaja Ranjit Singh
Punjab Technical University, Bathinda

Prof. G. Ranga Janardhana
Vice Chancellor
JNTU Anantapur, Ananthapuramu

Prof. D.N. Reddy, Former Chairman
Recruitment & Assessment Centre
DRDO, Ministry of Defence, Govt. of India
New Delhi

Prof G.D. Yadav,
Vice Chancellor
Institute of Chemical Technology,
Mumbai

Dr. Akshai Aggarwal,
Former Vice Chancellor
Gujarat Technological University,
Gandhinagar

Prof. M.S. Palanichamy
Former Vice Chancellor
Tamil Nadu Open University, Chennai

Dr. D.B. Shinde,
Vice Chancellor
Shivaji University, Kolhapur

Editorial Board

Dr. Vivek B. Kamat
Director of Technical Education
Government of Goa, Goa

Dr. E.B. Perumal Pillai
Director-HRDC & Professor of Civil Engg.
Vel Tech. University, Chennai

Prof. C.C. Handa
Professor & Head, Dept. of Mech.Engg.
KDK College of Engineering, Nagpur

Prof. S. Mohan
Chief Executive, Innovation Centre (SID)
Indian Institute of Science, Bangalore

Prof. Y. Vrushabhendrapa
Director
Bapuji Institute of Engg. & Technology, Davangere

Dr. S.M.S. Shashidhara
Deputy Secretary
M.S.B.T.E., Mumbai

Dr Rajeshree D Raut
Associate Editor

Dr Y R M Rao
Editor

IJTE is a peer reviewed Journal and indexed in the UGC-Care Journal list

Copyright (c) Indian Society for Technical Education, The Journal articles or any part of it may not be reproduced in any form without the written permission of the Publisher.

INDIAN JOURNAL OF TECHNICAL EDUCATION

Published by
INDIAN SOCIETY FOR TECHNICAL EDUCATION
Near Katwaria Sarai, Shasheed Jeet Singh Marg,
New Delhi - 110 016



Editorial

Skill based education is the need of the hour. Students graduating from the educational institutions are in possession of qualifying certificates with less skills. The education system rather a classroom teaching practice in most of the educational institutions in India is to deliver the content available in the local books and making the students to learn. Many educational institutions follow the practice of giving a priority to theoretical knowledge than the practical knowledge with an objective to secure higher ranking to the institution. This is the same scenario in technical and other professional institutions too. A meritorious graduate may get an employment and sometimes not able to fare well in professional career due to lack of required skills in the domain.

It is a fact that there is a drastic increase in literacy rate in India, but the recent reports saying 20% of the technical graduates in India only are employable. This implies that there is a lack of the necessary skills and a huge gap between the skills required by the industry and the person in possession. In a highly competitive world, employers look for the candidates who possess the required skills rather than the candidates having more degrees with higher grades. In this context, the educational institutions need to get connected with various industries and create the opportunities to the students to acquire practical knowledge at every stage of their education to strengthen necessary skills so as to grow well in a chosen area. Lot many new technologies are emerging across the world, and there is a need that a person inculcates the required skills to use these technologies for a successful life. If one is failed to acquire such skills to use the latest technologies will remain as a back bencher.

There is a need to have a skill-based education system that helps the employers to easily absorb the suitable trained candidates. Hence, there is a need to bring up the students by educating them with more thrust or atleast equal weightage to practical knowledge than theoretical at every stage of their college level education.

The S. B. Jain Institute of Technology, Management & Research, Nagpur (Maharashtra) has organized a 2day International Conference on Advancement in Science, Technology and Management 2023 (ICASTM- 2023) and created a platform to invite the authors to share advances in technologies and their applications.

The editorial board of IJTE has shortlisted 51 papers of ICASTM- 2023 covering engineering, management and basic sciences to publish as September 2023 special issue. We believe that Vol. 46, September 2023 special issue of IJTE is interesting to the readers to enhance or update their knowledge.

New Delhi

Editor

30th September 2023

Contents

1	Behavioural Analysis of Infectious Diseases in Two Main Age Groups using a Mathematical Approach	1
	N. K. Lamba	
2.	A New Prospective to Undamped Force of Vibration System Problems using Some Integral Transforms	6
	Shilpa Kulkarni, Pralahad Mahagonkar	
3.	Modified Differential Evolution Algorithm for Engineering Design Optimization	9
	Pooja Tiwari, Vishnu Narayan Mishra Raghav Prasad Parouha	
4.	A Study of Fractional Heat Transfer in A Generalized Two-Dimensional Thermally Elastic Problem	17
	Yogesh Panke, Dilip B Kamdi	
5.	Deflection Behaviour Due to the Response of the Caputo-Fabrizio Fractional Derivative in a Thermoelastic Disc with Heat Generation	26
	N K Lamba, Payal Hiranwar, T T Gahane	
6.	Design and Study of the Load Behavior of a Steel Angle and Tube-based Three Dimensional Roof Truss Comparison of the Angel and Tabular Portions	32
	Siddharth Tode, Isha. P. Khedikar	
7.	Comparative Analysis and Costing of a Multi-story Steel Building	38
	Tushar Mahurkar, Kuldeep Dabhekar	
8.	Friction Dampers Effects on Seismic Response Control of Irregular Building	47
	Abhilesh Tadas, Sanket Sanghai	
9.	Performance of Steel Structure on Various Earthquake Zones	54
	Palash Pawar, I. P. Khdeikar	
10.	File Sharing Application using Access Control in Android	60
	Saurabh Chakraborty, Rutika Zambre, Aditi Tapase, Devansh Sanghvi, Swarangi Wankar, Nitin Janwe	
11.	Enhancing Crop Yield Prediction and Monitoring: Current Developments, Limitations, and Future Directions – A Review	66
	Aishwarya Vilas Kadu, K. T. V. Reddy	
12.	Salesforce-The Trendy CRM Software	72
	Mrudula Nimbarte, Sonam Chopade, Vidya Jambhulkar, Akanksha Bondade	
13.	Securing the Digital Landscape: Examining Cybersecurity Threats, Confronting Challenges, and Embracing Best Practices	78
	Alfiya Hussain, Sujata Wankhede, Nikita Jamgade, Gulrukh Nazneen, Hemant Turkar	
14.	Interactive Learning through Game	83
	Rashmi Jain, Ratnesh Chaudhary, Kavita Gawande, Sachin Jain	
15.	Quantum Machine Learning for Disease Diagnosis	89
	Fazil Sheikh, S. Y. Amdani	

16. Routing Mechanism with Fuzzy Logic Approach in Wireless Sensor Networks: A Survey	95
Roshani B. Talmale, Sonali Zunke, Leena Mandurkar, Aditya Parate	
17. Automated Estimation of Leaf Affected Area by Adapting Machine Learning Algorithms	99
Sukanya S. Gaikwad, M. Hangarge	
18. A Review on Scheduling Algorithm for CREW System Management of Railway Operations	104
Prasanna Lohe, Latesh Malik, Ravindra Jogekar, Pradnya Borkar	
19. A Novel Approach for Human Emotion Detection with Speech Recognition using Support Vector Machine in Machine Learning	110
Harshita Wankhede, Chandu Vaidya, Hemant Turkar, Aniket Bhoyar, Sonam Chopade	
20. Creation of Harvest Productivity Projection Method (HPPM) using Machine Learning Framework through Combating Infection and Generating Knowledge	118
Snehal A. Lohi, Chinmay Bhatt	
21. AI-Powered Innovations in Agriculture: Transforming Farming Practices and Yield Optimization	126
Sangeeta Patil, Deepali Pisal, Hema Mirji, Vijay Phalke	
22. Active Switched LC based DC-DC converter for PV System	135
Amarjeet Pandey, Sucheta Patil, V N Kalkhambkar	
23. Implementation of Direct Torque Control of Induction Motor with Minimum Voltage Vector Error using Matlab/Simulink	143
Sonali Sangole, Pratik Ghutke	
24. Hybrid Renewable Energy Systems and Optimization Techniques: A Review	149
Sangram Malkar, Vaiju Kalkhambkar	
25. Development of an IoT based Real-Time Monitoring and Automatic Water Level Control System with Alert Notification through IFTTT	162
Afsar Khan, Pankaj B. Thote, Arpita Fusey, Priya Keshkar	
26. Survey on Wireless Sensor Network Technologies for Dense Forest Monitoring	169
Sagar Pradhan, G. M. Asutkar, Kiran M. Tajne	
27. Analyzing the Performance of Wireless Sensor Network for 5G Frequency Band	177
Sunita I Parihar, G. M. Asutkar, S A Dhale	
28. Characteristics Mode Analysis of a Circularly Polarized Minkowski Inspired Fractal Antenna for Narrowband Internet of Things Applications	182
Geeta Kalkhambkar, Pradeep Chindhi, Rajashri Khannai	
29. Natural Language Processing based Customer Review Analysis	190
Vijay Mane, Vipul Pisal, Abhijeet Patil, Nishka Mane	
30. Statistical Analysis of Retinal Image Processing Techniques from an Empirical Perspective	196
Rupesh Mundada, Devesh Nawgaje	

31. A Novel Method for Anemia Detection based on Classification Approach using Artificial Neural Network	205
Vinit P. Kharkar, Ajay P. Thakare	
32. Review of Multiple Input Multiple Output Antennas for Sub-6 GHz 5th Generation Applications	212
Sandeep K. Kakade, Nirmal Sharma, Navnath S. Narwade	
33. Statistical Review of Cache Memory Design Techniques from an Empirical Perspective	218
Ashwini Anjekar, Trupti Nagrare, Rasika N. Bamnote	
34. Using Talent Management Strategies to Retain Talented Employees in the Pharmaceutical Industry	230
Ambarish Ghosh, Manoj Verghese, J. H. Vyas	
35. How Corporate Governance Practices are Followed in Information Technology Sector Listed in the “Bombay Stock Exchange Sensex”	235
Kalyani Gohain, Sanjay Pratap Singh	
36. Uncertainty Management Approach for MSMEs	242
Chetan Panse, Kartik Uttarwar, Sanchal Tarode	
37. Sustainable Determinants in the Development of Micro and Small Enterprises of Eastern Maharashtra	251
Rajesh Shende, Rahul Mohare	
38. Enrollment Excellence: Leveraging Hybrid Marketing Approaches to Achieve Full Admissions in Indian Graduation Colleges	257
Varun Dubey, Nikhil Bangde, Hemraj Kawadkar, Shrikrishna Dhale	
39. Impact of Foreign Direct Investment (FDI) on Indian Economy	261
Hemraj Kawadkar, Shrikrishna Dhale, Nikhil Bangde, Yogesh Dhoke	
40. A Study on the Effects of Personnel Relation with Respect to Conflict Management in an Organization	269
Sayali B. Sukhadeve, Priyadarshani Vinaykumar Keshtty	
41. Impact of Artificial Intelligence on Indian Retail Industry: Awareness and Experience of Consumers Regarding AI-based Retail	276
Sanjiv Kumar, Amit P. Sahu, Shradha S. Bonde	
42. A Study on the Role of Cross-Cultural Training in Effective Management with Mediating Factor Cross-Cultural Competence model for Expatriate Managers	282
Amit P. Sahu, Abdullah M. Chaus, Sanjiv Kumar	
43. Analytical Studies on Development of Monetary Aggregates in India During Post Liberalization	288
Arvind R. Gajakosh, P. K. Rinoj	
44. Conceptualizing Green Performance in the Restaurant Industry: A Suggested Framework	294
Jinty Dutta, Bijay Amgain	

45. A Comprehensive Review of Counterfeit Luxury Branded Products (CLBP) in India	303
Nikhil Bangde, Praveen Mustoor	
46. On-the-Job Training in Non-IT Companies in India: A Comprehensive Analysis	308
Sunita Gujar, Varun Dubey Nikita Humane, Swati Goyal	
47. Application of IoT in Logistics & Supply Chain Management	313
Shweta Pethe, Priyadarshani Keshtty, Pankaj Pethe	
48. A Review on Cattle Transportation and Available Facility: A Special Emphasis on Indian Continent	317
Sandip S Patil, Jayant H. Bhangale	
49. A Review on Energy Conservation Techniques for Cold Storage System	323
Shrikant Kathwate, Nitin Korde, Harish Bhatkulkar	
50. Applications on Injection Molding Technique using Non-metals: Review	327
P. R. Sonawane, N. B. Dole, Jayant H. Bhangale, Shyam Sing Thakur	
51. To Evaluate the Impact of CuO Additives in Argemone Mexicana Biofuel to Reduce the Harmful Emission of Diesel Fuel on 4-Stroke Diesel Engine	335
Niraj B Dole, Ankita K Patil, Jayant H Bhangale, Pratap Ramesh Sonawane	

A New Prospective to Undamped Force of Vibration System Problems using Some Integral Transforms

Shilpa Kulkarni

Assistant Professor.

Dept. of Physics

SSA Govt First Grade College

Ballari

Pralahad Mahagonkar

Associate Professor

Dept. of Mathematics

Ballari Institute of Technology and Management

Ballari

ABSTRACT

A new way of approaching to solve the physical system problems such as undamped force of vibration equation on a simple pendulum problem. In this paper we have revisited these problems by applying some integral transforms such as Ezaki transforms method (ETM) and Differential transforms method (DTM) demonstrating how effectively they are in the determination of the solutions.

KEYWORDS: *Physical system, Ezaki transform, Differential transform, Simple pendulum.*

INTRODUCTION

Since from last few decades the efforts have been made in the field of mathematics and physical sciences to apply some techniques to find the possible solutions for some physical system problems, further the development had made to analyse the such linear differential equations which we can apply in different areas of science and engineering. Some of the analysis was made and studied in the field of physical sciences and their applications. here some of the appropriate methods are adopted to get the different solutions such as Ezaki transform method (ETM) and Differential Transform method (DTM). These transform methods have been inspired towards researchers of physical and mathematical sciences and many research works have been taken places and research article were published in these fields.

Undamped force of vibrations

Whenever an external force is applied on a particular system continuously the vibration of that system never stop. This type of vibration also can be called as undamped force of vibration.

Examples: movement of laundry machine due to asymmetry, vibration of a moving transport due to its engine. movements of strings in guitar.

Consider undamped forced vibrations of spring given by the differential equation is.

Undamped force vibration of spring

Consider the undamped force vibrations of spring given by the differential equation is,

$$m \frac{d^2 y}{dt^2} + k y(t) = f(t) \quad (1)$$

In this paper we will consider our choice the forcing function as $f(t) = (1 - \sin t)$, $m=1\text{kg}$, $k=1\text{N/m}$, with initial values $y(0) = y'(0) = 0$ then equation (1) and it gives us,

$$\frac{d^2 y}{dt^2} + y(t) = (1 - \sin t) \quad (2)$$

Basics definition

The Ezaki transform of the function $f(t)$ for $t > 0$, can be defined as

$$E[f(t)] = v \int_0^{\infty} e^{-\frac{t}{v}} f(t) dt = T(v).$$

The Differential transform of a function $f(t)$ is given by

$$F(k) = \frac{1}{k!} \left[\frac{d^k}{dt^k} f(t) \right]_{t=0}$$

Main results

Applying both sides Ezaki transform method (ETM)

Consider the equation (2) and applying both sides Ezaki Transform

$$E[y''(t)] + E[y(t)] = E[1] - E[\sin t]$$

$$\left[\frac{Y(v)}{v^2} - y(0) - v y'(0) \right] + Y(v) = v^2 - \frac{v^3}{1+v^2}$$

Since $y(0)=y'(0)=0$. And applying both sides Ezaki inverse transform.

We get

$$y(t) = 1 - \cos t - \frac{1}{2} [\sin t - t \cos t] \quad (4)$$

Now applying the Differential transform method (DTM) both the side for equation (2)

$$(k+1)((k+2)y(k+2) + y(k)) = 1 - \frac{1}{k!} \sin\left(\frac{k\pi}{2}\right)$$

$$y(k+2) = \frac{1 - \frac{1}{k!} \sin\left(\frac{k\pi}{2}\right) - y(k)}{(k+1)(k+2)}$$

$$\text{Put } k=0 \quad y(2) = \frac{1 - \frac{1}{0!} \sin(0) - y(0)}{(1)(2)} = \frac{1}{2}$$

$$\text{Put } k=1 \quad y(3) = \frac{1 - \frac{1}{1!} \sin(\pi/2) - y(1)}{(2)(3)} = \frac{1}{6}$$

$$\text{Put } k=2 \quad y(4) = \frac{1 - \frac{1}{2!} \sin(\pi) - y(2)}{(3)(4)} = \frac{1}{24}$$

$$\text{Put } k=3 \quad y(5) = \frac{1 - \frac{1}{3!} \sin\left(\frac{3\pi}{2}\right) - y(3)}{(4)(5)} = \frac{1}{20}$$

$$\text{Put } k=4 \quad y(6) = \frac{1 - \frac{1}{4!} \sin\left(\frac{4\pi}{2}\right) - y(4)}{(5)(6)} = \frac{23}{480} \text{ and so on}$$

Let us consider the solution is of the form

$$y(t) = \sum_{k=0}^{\infty} y(k) t^k$$

$$y(t) = y(0)t^0 + y(1)t + y(2)t^2 + y(3)t^3 + y(4)t^4 + y(5)t^5 + \dots \quad (6)$$

Substituting the different values of y we get

$$y(t) = t + \frac{t^2}{2} + \frac{t^3}{6} + \frac{t^4}{24} + \frac{t^5}{20} + \frac{23}{480} t^6 + \dots \quad (7)$$

Table 1 : The value different values of $y(t)$ using Differential transform method and Ezaki Transform method

t	DTM	ETM	Absolute Error
0	0	0.5	0.5
0.1	0.1053380021	0.1252658210	-0.0203202079
0.2	0.2227494667	0.2585658212	-0.0358163545
0.3	0.3544605181	0.2853691211	0.0690911397
0.4	0.5029205333	0.4582025833	0.0447179512
0.5	0.6705658854	0.5268425123	0.1421407621
0.6	0.8613852012	0.8212550121	0.0792597101
0.7	1.0779861021	1.0526158412	0.0253702609
0.8	1.324663471	1.2512368401	0.0734266306
0.9	1.605969169	1.4581252584	0.1478433291
1	1.927083333	1.9202581223	0.0068525077

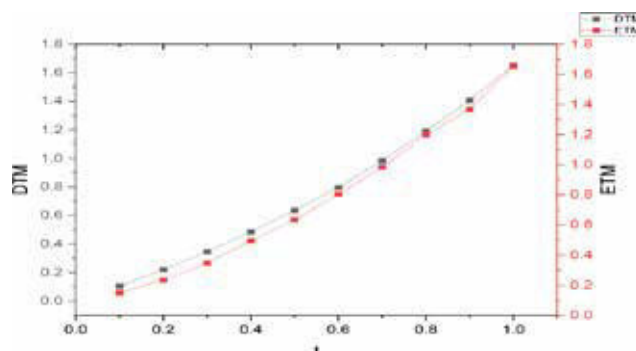


Figure 1: Comparisons for DTM, and ETM for different mesh points for undamped force of vibration problem

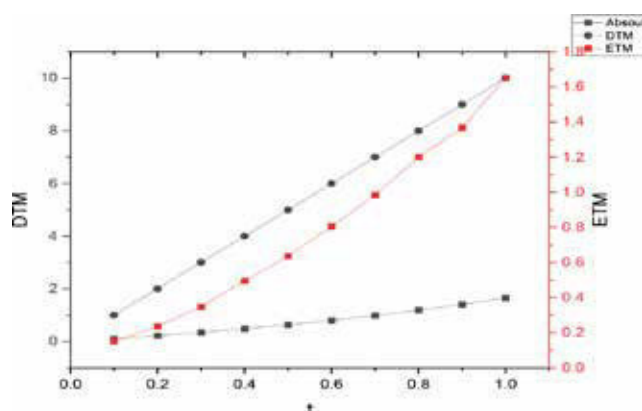


Figure 2: Comparisons for DTM, and ETM for different mesh points with respect to absolute error for undamped force of vibration problem

Conclusion: The main basic motive of this work is to implement the given transformations to linear non homogeneous differential equations which are occurring in the field of engineering, applied sciences and other physical systems. The methods which are proposed here are two transformations they are ETM and DTM and comparative study has been shown graphically.

REFERENCES

1. Tarig, E. (2011). The new integral transform "Elzaki Transform". Global Journal of Pure and Applied Mathematics, 7(1): 57-64.
2. Elzaki, T.M., Elzaki, S.M. (2011). On the connections between Laplace and Elzaki transforms. Advances in Theoretical and Applied Mathematics, 6(1): 1-11.
3. Aboodh, K.S. (2013). The new integral transform "Aboodh Transform". Global Journal of Pure and Applied Mathematics, 9(1): 35-43.
4. Alshikh, A.A., Abdelrahim Mahgoub, M.M. (2016). A comparative study between Laplace and two new Integral Elzaki Transform and Aboodh transform. Pure and Applied Mathematics, 5(5): 145-150. <https://doi.org/10.11648/j.pamj.20160505.11>
5. Kashuri, A., Fundo, A. (2013). A new Integral transform. Advances in Theoretical and Applied Mathematics, 8(1): 303-313.
6. Shilpa Kulkarni, pralahad Mahagaonkar. (2022). Study on Undamped Force Vibrations of a Spring Using Different Methods. Middle East Journal of Applied Science & Technology (MEJAST) Volume 6, Issue 1, Pages 38-41, January-March 2023.
7. Hsiao, C.H. (2008). Wavelet approach to time-varying functional differential equations, Int. J. Computer Math., 87(3): 528-540.
8. Kouchi, M.R., Khosravi, M. & Bahmani, J. (2011). A numerical solution of Homogenous and Inhomogeneous Harmonic Differential equation with Haar wavelet, Int. J. Contemp. Math. Sciences, 6(41): 2009-2018.
9. Lepik, U. (2005). Numerical solution of differential equations using Haar wavelets, Math. Comput. Simulat., 68: 127-143.
10. M.C Agrana and M.E. Emeteri Solving Non-Linear Damped Driven Simple pendulum with Small amplitude using A semi Analytical method. ARPN Journal of Engineering And Applied Sciences. ISSN 1819-6608. Vol. 11, No 7, April 2016. (4478-4484).



Sir Shantilal Badjate Chariatable Trust's

S.B. JAIN INSTITUTE OF TECHNOLOGY, MANAGEMENT & RESEARCH

COLLEGE CODE: 4137

(Affiliated to R.T.M. Nagpur University)

Recognised by
All India Council for Technical
Education (AICTE), New Delhi



Accredited by
NAAC with
A Grade

**AN AUTONOMOUS
INSTITUTE
NEP COMPLIANT**



COURSES OFFERED

- Computer Science & Engineering
- Computer Science & Engg. (Data Science)
- Computer Science & Engg. (AI & ML)
- Electronics & Tele. Engineering
- Electrical Engineering
- Mechanical Engineering
- Master of Business Administration (MBA)
- M.Tech (Electronics Engineering)
- Ph.D (Electronics & Tele. Engineering)

Highest Salary of ₹12.00 LPA

KEY FEATURES

- NAAC 'A' Grade
- Ph. D research Centre
- NEP Based Curriculum
- R & D cell
- International Collaboration
- ICT Based Infrastructure
- Incubation Cell and Startup Cell
- Entrepreneurship Cell
- 100% internship
- Average placement 80% since last 10 years
- Strong Alumni Network worldwide
- Lush green Campus
- Transportation Facilities
- College Canteen

For Detail Call : 89993 00998, 99231 46219, 99757 55601  9823218380

Campus : Near Jain International School, Katol Road, Nagpur **Ph.** 0712-2667777



Sir Shantilal Badjate Chariatable Trust's

S.B. JAIN INSTITUTE OF TECHNOLOGY, MANAGEMENT & RESEARCH

COLLEGE CODE: 4137

(Affiliated to R.T.M. Nagpur University)

Recognised by
All India Council for Technical
Education (AICTE), New Delhi



Accredited by
NAAC with
A Grade

**AN AUTONOMOUS
INSTITUTE
NEP COMPLIANT**



To know more on us, Please click on any of the following links...

 www.sbjit.edu.in      [officialsbjain](#)



PUBLISHED BY
INDIAN SOCIETY FOR TECHNICAL EDUCATION
Near Katwaria Sarai, Shaheed Jeet Singh Marg,
New Delhi - 110 016

Printed at: Compuprint, Flat C, Aristo, 9, Second Street, Gopalapuram, Chennai 600 086.

Phone : +91 44 2811 6768 • www.compuprint.in

Exploration of heat and mass transport in oscillatory hydromagnetic nanofluid flow within two verticals alternatively conducting surfaces

Jitendra Kumar Singh¹  | Hanumantha² | Suneetha Kolasani³ | Syed M. Hussain⁴

¹Department of Mathematics, Siddharth University Kapilvastu, Sidharth Nagar, India

²Department of Mathematics, Vijayanagara Sri Krishnadevaraya University, Ballari, India

³Department of Mathematics, Ballari Institute of Technology and Management, Ballari, India

⁴Department of Mathematics, Faculty of Science, Islamic University of Madinah, Madinah, Saudi Arabia

Correspondence

Jitendra Kumar Singh, Department of Mathematics, Siddharth University Kapilvastu, Sidharth Nagar 272202, India.
Email: s.jitendrak@yahoo.com

The key attention of this paper is to explore the heat and mass transport in oscillatory hydromagnetic Titanium alloy water nanofluid flow within two vertical alternatively non-conducting and conducting walls enclosing Darcy-Brinkman porous medium. Motional induction is considered because it is sufficiently strong in comparison to Ohmic dissipation. Hall phenomenon is considered because the electromotive force induced due to revolving of fluid particle about the magnetic field lines is significant. Suitable physical laws (constitutive and field equations) are used to derive the equations leading the flow model. An analytical approach is followed to extract the solutions of the flow model. The quantities of physical interest such as wall shear stress (WSS), rate of heat transport rate (RHT) and rate of mass transport rate (RMT) at the walls are obtained from the extracted solutions. The physical insight into flow manners is discovered from the graphs and tables generated from the numerical computation of the solutions. It is important to note from the study that the volume concentration of nanofluid and magnetic diffusion produce resistivity in the flow and tends to slow down the fluid flow. Magnetic diffusion weakens the strength of the primarily motional induced magnetic field.

1 | INTRODUCTION

Magnetohydrodynamic (MHD) phenomena are used since its origination in various branches of science and engineering such as astrophysics, geophysics, mechanical engineering, plasma aerodynamics, thermal science and biomedical sciences due to numerous applications in these field. MHD phenomenon were firstly observed in the experiment of Faraday [1]. He discovered that the motion of mercury in a glass tube under the influence of a transverse magnetic field, generates a voltage across the tube in a direction mutually perpendicular to the direction of the flow and exerted magnetic field. This phenomenon is termed as a phenomenon of generator. He further noted that the motional induced current interacts with the exerted magnetic field and produces a drag force, which significantly alters the motion of the fluid. This phenomenon is named as a phenomenon of pump. At the beginning MHD, phenomena were used in development of power generation devices, pumps, propulsion of ships and aircrafts, thermonuclear energy generation, etc. (Ferraro and Plumpton [2]). Cowling [3] and Ferraro [4] started to explore implications of the hydromagnetic phenomena is astrophysical problems such as the magnetic field of sunspot and rotation of sun. The classical work of Alfven [5] published in Nature expresses that owing to presence of an imposed magnetic field to a conducting liquid there appears an electromotive force which insist to generate an electric current. The interaction of the generated current and imposed

magnetic field produces a mechanical force, which alters the state of liquid motion. Furthermore, the small disturbance in the state of the liquid gives rise to electromagnetic waves called Alfvén waves. Hartmann [6] experimentally explored the hydromagnetic flow manner of conducting liquid between two parallel surfaces and stated that the appearance of magnetic field flattens the velocity in the central part of the channel. The formation of a thin boundary layer took place in the boundary region of the channel due to the appearance of the sufficiently strong magnetic field. Soon after, these pioneer works engineers and scientists started to discover the basic features of hydromagnetic flows and their applications to power generation technology, nuclear engineering, plasma aerodynamics, MHD energy system and targeted drugs delivery [7–11]. The study of hydromagnetic channel/duct flows is actively engaged by the research fraternity after Hartmann [6] due to enormous applications in technological and biological problems like designing of cooling systems with liquid metal, geothermal energy extraction, underground energy transport, blood flow problems, food preservation, etc. Alpher [12] examined that the temperature distribution within the fluid flowing in a channel with infinitely conducting walls due to internal heat source generated due to motion of conducting fluid in a constant imposed magnetic field. The influence of wall conductance on the hydromagnetic channel flow without heat transfer aspect is explored by Chang and Yen [13] while the wall conductance effect on the hydromagnetic channel flow with heat transfer is explained in the article of Snyder [14]. The flow of electrically conducting fluid within a rectangular duct with a combination of non-conducting, conducting and arbitrary conducting walls under an imposed magnetic field is examined by Hunt [15]. Contrary to the flow stabilizing nature of the magnetic field he found that in some of the cases the appearance of the magnetic field also destabilizes the flow of electrically conducting fluid in a duct. The unsteady flow behavior of hydromagnetic flow in a duct is analytically scrutinized by Sloan [16]. He expressed that the motion induced current significantly modify the motion of the fluid. Mazumdar [17], and Nagy and Demendy [18] considered the wall conductance effect on hydromagnetic flows and heat transfer in a rotating channel. These studies confer the dependency of flow velocity, current density and temperature on the joint wall conductance of both walls and dependency of motional generated magnetic field on the separate values of wall conductance constants. The oscillatory hydromagnetic channel flow under different geometrical flow model is excellently discussed by Singh [19], Guria et al. [20], Ansari et al. [21], Beg et al. [22] and Seth et al. [23]. Recently, Venkateswarlu [24] and Singh [25–27] with their collaboration group evaluated the flow nature of oscillatory MHD flow of viscoelastic fluid in a channel. Falade et al. [28] examined the transient MHD oscillatory flow in a vertical channel with porous walls and explored that on increasing the injection at the heated wall, the wall shear stress enhances. Singh et al. [29] characterized the nature of nanofluid flowing within two vertical alternatively magnetized surfaces. They expressed that the motional generated magnetic field gets increased with the volumetric concentration of nanofluid due to the rise in electrical conductivity of the fluid. Dissipative effect is an important phenomenon appearing in hydromagnetic fluid flows. A well-known fact is that the appearance of magnetic field in hydromagnetic flows produce the drag force in the motion similar to the viscosity of the fluid as a result the internal energy of flow system uprise in terms of the heat. This phenomenon is termed as Joule heating. The Joule heating term is ignored by many of the authors from the energy equation due to complexity in the mathematical modelling and solution process. However, this phenomenon significantly affects the rate of heat transport and fluid temperature. Yen [30] considered the viscous and Joule dissipation, and wall electrical conductance impacts to the fully developed hydromagnetic laminar flow within a channel. The results of the study exhibit that the viscous dissipation dominates the Joule heating in the case of the non-conducting walls. However, in the case of the infinitely electrically conducting walls, the influence of the Joule heating is more significant than the viscous dissipation. These facts provoked the academics Seth and Singh [31], Singh et al. [32] and Singh and Kolasani [33] to explore the wall electrical conductivity and energy dissipation effects to the hydromagnetic channel flows under the diverse geometrical flow formations. Some noteworthy research works including the energy dissipative effects are owed to Gopal et al. [34], Atif et al. [35], Poddar et al. [36] and Shah et al. [37]. The significance of motional induction and Hall current phenomena on hydromagnetic flows are clearly visible when the fluid is highly electrically conducting and the strength of the imposed magnetic field is sufficiently large. Kumar et al. [38, 39] and Singh et al. [40, 41] considered these facts in their problem. The hydromagnetic flow through a porous medium is a subject of active research in the recent years due to its exhaustive applications in geothermal power extraction from the earth's interior, water circulation by ion-exchange beds, chemical reactor for economic isolation or mixture purification, the penetration of drugs into human skin, etc. The basis for the characterization of the flow in a porous regime is its permeability and porosity. The permeability exerts the stabilizing force to the flow in porous medium. Brinkman [42] presented a model to characterize fluid flow through a dense cluster of particles, which is one of the popular models proposed to examine the manner of flow in a porous medium. Many scientists [43–48]

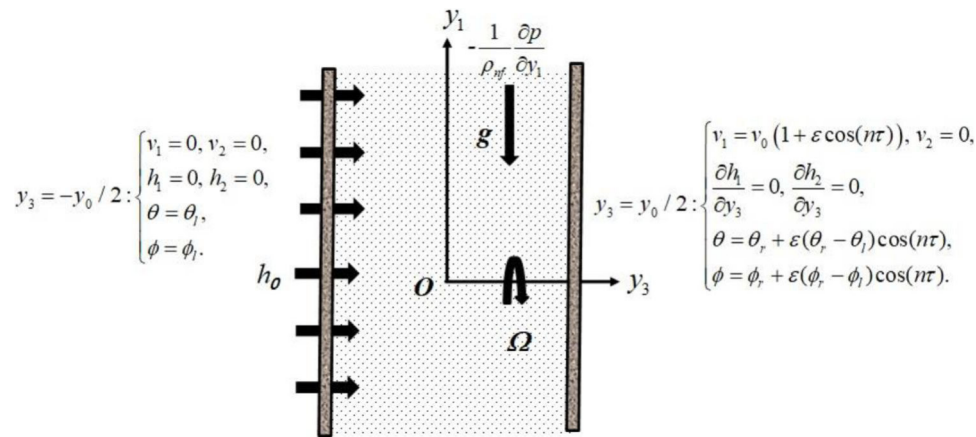


FIGURE 1 Geometrical setup of the flow model.

explored the manner of hydromagnetic flows in porous medium by implementing the Darcy-Brinkman model. Nanofluid plays a vital role in development of nanoscience and nanotechnology. The thermal behavior of nanofluid makes it technologically more efficient in comparison to any other fluids. The dependency of thermal conductivity of the nanofluid to the shape and size of nanoparticles and number of nanoparticles are experimentally proven by Choi and Eastman [49] and Chon and Kihm [50]. This specific thermal nature motivated the research world to examine the flow nature of nanofluid and to discover its applications in engineering and technology. Khan and Alqahtani [51] modeled the hydrodynamic convective nanofluid flow in a channel with permeable wall and expressed that suction causes the higher fluid velocity intensity compared to the injection. Dutta et al. [52] considered the hydromagnetic free convection flow of Cu-water nanofluids in a rhombic enclosure and scrutinized the heat transport and entropy generation. They explored that the nature of Hartmann number is to weaken the rate of entropy generation. In the recent years, the mathematical model for hydromagnetic nanofluid flows within different geometrical setup are developed and explored by many researchers, namely, Mourad et al. [53], Askari et al. [54], Abd-Alla et al. [55], EL-Zahar [56] and Govindarajulu and Subramanyam Reddy [57].

It is ascertained from the aforesaid meticulous literature review that not much literature considered the impacts of motional generated magnetic field and Hall current simultaneously on oscillatory hydromagnetic nanofluid flows. Therefore, the key attention in this paper is to explore the motional indication and Hall current effect to oscillatory hydromagnetic Titanium alloy suspended water nanofluid flow within two vertical alternatively non-conducting and conducting walls enclosing Darcy-Brinkman porous medium and its heat and mass transport nature. An analytical approach called separation of variables is used for extraction the solution from the flow model. It is important to note from the study that the volume concentration of nanofluid and magnetic diffusion produce resistivity in the flow and tends to slow down the fluid flow. Magnetic diffusion weakens the strength of the primarily motional induced magnetic field.

2 | FORMULATION OF THE FLOW MODEL

2.1 | Flow description and geometrical setup

The flow problem considers the oscillatory hydromagnetic flow of Titanium alloy suspended water nanofluid within two vertical walls enclosing the Darcy-Brinkman porous medium. The vertical walls are placed symmetrically on either side parallel to y_1y_2 -plane of the cartesian coordinate system. The left vertical wall is stationary and non-conducting, and its temperature and concentration are kept fixed while right wall is oscillatory and conducting, and its temperature and concertation are fluctuating with the same frequency as that of oscillations (please see the geometrical setup of the flow model, Figure 1).

2.2 | Flow assumptions

A tractable mathematical model is derived by imposing the below mentioned flow assumptions:

- A. The Titanium alloy suspended water is a dilute suspension and keeping the property of incompressible, and electrically and thermally conducting fluid.
- B. The flow medium is supposed to be Darcy-Brinkman porous type and the effective viscosity of the flow medium and nanofluid is same. The equation representing the flow through such medium is expressed as

$$\nabla p = \delta \mu_{nf} \nabla^2 \vec{v} - \frac{\mu_{nf}}{k_p} \vec{v}, \quad (1)$$

where δ is effective viscosity term and considered $\delta = 1$.

- C. The electromotive force induced due to collision and revolving of charged fluid particles about the lines of exerted magnetic field h_0 is significant (Cowling [58]). Hence, the Hall effect is considered. The mathematical representation of the Ohm's law with Hall current is as follows:

$$\vec{j} = \sigma_{nf} (\vec{e} + \mu_e (\vec{v} \times \vec{h})) - \frac{Hc}{h_0} (\vec{j} \times \vec{h}). \quad (2)$$

- D. The fluid is supposed to be highly conducting and hence the motional induction is sufficiently strong in comparison to Ohmic dissipation. Thus, the effect of motional induced magnetic field is also considered. The differential equation representing the motional induced magnetic field without Hall current is

$$\frac{\partial \vec{h}}{\partial \tau} = \nabla \times (\vec{v} \times \vec{h}) + \frac{1}{\sigma_{nf} \mu_e} \nabla^2 \vec{h}, \quad (3)$$

- E. For the unidirectional flow within infinitely extended vertical walls, the flow velocity and motional induced magnetic are considered to be $\vec{v} \equiv (v_1(y_3), v_2(y_3), 0)$ and $\vec{h} \equiv (h_1(y_3), h_2(y_3), h_0)$ to uphold the continuity equations $div \vec{v} = 0$ and $div \vec{h} = 0$.
- F. The uniform revolution of flow system about y_3 -axis with an angular velocity $\vec{\Omega}$ gives rise to a flow altering force $-2\vec{\Omega} \times \vec{v}$ named as Coriolis force.
- G. The appearance of gravitational force in the flow-field gives rise to the buoyancy forces which significantly affect the flow manner. The buoyancy forces are determined under the Boussinesq approximation and given by

$$\vec{f}_b = \rho_{nf} \vec{g} [\beta_{nf} (\theta - \theta_l) + \beta_{nf}^* (\phi - \phi_l)] \quad (4)$$

2.3 | The equations governing the flow

On imposing the above-mentioned flow assumptions and suitable constitutive equations connecting electromagnetic fields, the field equations such as the equation of linear momentum, the equation of motional induced magnetic field, the equation of energy and the equation of mass diffusion in the vector form are expressed as

$$\frac{D\vec{v}}{D\tau} = -\frac{1}{\rho_{nf}} \nabla p + \nu_{nf} \left(\nabla^2 \vec{v} - \frac{\vec{v}}{k_p} \right) + \frac{\mu_e}{\rho_{nf}} (\vec{h} \cdot \nabla) \vec{h} + 2\vec{v} \times \vec{\Omega} + \rho_{nf} \vec{g} [\beta_{nf} (\theta - \theta_l) + \beta_{nf}^* (\phi - \phi_l)], \quad (5)$$

$$\frac{\partial \vec{h}}{\partial \tau} = \nabla \times (\vec{v} \times \vec{h}) + \frac{1}{\sigma_{nf} \mu_e} \nabla^2 \vec{h} - \frac{Hc}{h_0} \nabla \times [(\vec{h} \cdot \nabla) \vec{h}], \quad (6)$$

$$(\rho C_p)_{nf} \frac{D\theta}{D\tau} = k_{nf} \nabla^2 \theta - R(\theta - \theta_l), \quad (7)$$

$$\frac{D\phi}{D\tau} = D_{nf} \nabla^2 \phi - Cr(\phi - \phi_l), \quad (8)$$

where $\frac{D}{D\tau} \equiv \frac{\partial}{\partial \tau} + (\mathbf{v} \cdot \nabla)$.

Resolving the vector Equations (5) to (8) along the coordinate axes by employing the flow assumption (E), these are expressed as

$$\rho_{nf} \frac{\partial v_1}{\partial \tau} = -\frac{\partial p}{\partial y_1} + \mu_{nf} \left(\frac{\partial^2 v_1}{\partial y_3^2} - \frac{v_1}{k_p} \right) + \frac{h_0}{\mu_e} \frac{\partial h_1}{\partial y_3} + 2\rho_{nf} \Omega v_2 + \rho_{nf} g \left[\beta_{nf}(\theta - \theta_l) + \beta_{nf}^*(\phi - \phi_l) \right], \quad (9)$$

$$\rho_{nf} \frac{\partial v_2}{\partial \tau} = \mu_{nf} \left(\frac{\partial^2 v_2}{\partial y_3^2} - \frac{v_2}{k_p} \right) + \frac{h_0}{\mu_e} \frac{\partial h_2}{\partial y_3} - 2\rho_{nf} \Omega v_1, \quad (10)$$

$$\frac{\partial h_1}{\partial \tau} = h_0 \frac{\partial v_1}{\partial y_3} + \frac{1}{\sigma_{nf} \mu_e} \left(\frac{\partial^2 h_1}{\partial y_3^2} + Hc \frac{\partial^2 h_2}{\partial y_3^2} \right), \quad (11)$$

$$\frac{\partial h_2}{\partial \tau} = h_0 \frac{\partial v_2}{\partial y_3} + \frac{1}{\sigma_{nf} \mu_e} \left(\frac{\partial^2 h_2}{\partial y_3^2} - Hc \frac{\partial^2 h_1}{\partial y_3^2} \right), \quad (12)$$

$$(\rho C_p)_{nf} \frac{\partial \theta}{\partial \tau} = k_{nf} \frac{\partial^2 \theta}{\partial y_3^2} - R(\theta - \theta_l), \quad (13)$$

$$\frac{\partial \phi}{\partial \tau} = D_{nf} \frac{\partial^2 \phi}{\partial y_3^2} - Cr(\phi - \phi_l). \quad (14)$$

Under the above-described flow assumptions, the boundary conditions (BCs) designated at the contact walls of the symmetric channel are

$$\left. \begin{aligned} v_1 = v_2 = 0, \quad h_1 = h_2 = 0, \quad \theta = \theta_l, \quad \phi = \phi_l & \quad \text{at } y_3 = -y_0/2; \\ v_1 = v_0(1 + \varepsilon \cos(n\tau)), \quad v_2 = 0, \quad \frac{\partial h_1}{\partial y_3} = \frac{\partial h_2}{\partial y_3} = 0, & \\ \theta = \theta_r + (\theta_r - \theta_l) \cos(n\tau), \quad \phi = \phi_r + (\phi_r - \phi_l) \cos(n\tau) & \quad \text{at } y_3 = y_0/2. \end{aligned} \right\} \quad (15)$$

A simplified flow model can be constructed by writing Equations (9) to (12) into compact form. Writing Equations (9), (10) and (11), (12) into compact form, yield

$$\rho_{nf} \frac{\partial v}{\partial \tau} = -\frac{\partial p}{\partial y_1} + \mu_{nf} \left(\frac{\partial^2 v}{\partial y_3^2} - \frac{v}{k_p} \right) + \frac{h_0}{\mu_e} \frac{\partial h}{\partial y_3} - 2i\rho_{nf} \Omega v + \rho_{nf} g \left[\beta_{nf}(\theta - \theta_l) + \beta_{nf}^*(\phi - \phi_l) \right], \quad (16)$$

$$\frac{\partial h}{\partial \tau} = h_0 \frac{\partial v}{\partial y_3} + \frac{(1 - iHc)}{\sigma_{nf} \mu_e} \frac{\partial^2 h}{\partial y_3^2}. \quad (17)$$

The designated boundary conditions (BCs) for velocity and motional generated magnetic field at contact walls of the symmetric channel in the compacted form are

$$\left. \begin{aligned} v = 0, \quad h = 0, & \quad \text{at } y_3 = -y_0/2; \\ v = v_0(1 + \varepsilon \cos(n\tau)), \quad \frac{\partial h}{\partial y_3} = 0, & \quad \text{at } y_3 = y_0/2; \end{aligned} \right\} \quad (18)$$

where $v = v_1 + iv_2$ and $h = h_1 + ih_2$.

A similar dimensionless simplified flow model can be constructed from the above modeled equations by employing the following thermophysical characteristics of the nanofluid and dimensionless transformation rules

$$\left. \begin{aligned} \alpha_1 &= \frac{\mu_{nf}}{\mu_f} = \frac{1}{(1-\lambda)^{2.5}}, \quad \alpha_2 = \frac{\rho_{nf}}{\rho_f} = (1-\lambda) + \lambda \frac{\rho_s}{\rho_f}, \quad \alpha_3 = \frac{(\rho\beta)_{nf}}{(\rho\beta)_f} = (1-\lambda) + \lambda \frac{(\rho\beta)_s}{(\rho\beta)_f}, \\ \alpha_4 &= \frac{(\rho\beta^*)_{nf}}{(\rho\beta^*)_f} = (1-\lambda) + \lambda \frac{(\rho\beta^*)_s}{(\rho\beta^*)_f}, \quad \alpha_5 = \frac{\sigma_{nf}}{\sigma_f} = \left(1 - \frac{3(1-(\sigma_s/\sigma_f))\lambda}{(2+(\sigma_s/\sigma_f)) + (1-(\sigma_s/\sigma_f))\lambda} \right), \\ \alpha_6 &= \frac{(\rho C_p)_{nf}}{(\rho C_p)_f} = (1-\lambda) + \lambda \frac{(\rho C_p)_s}{(\rho C_p)_f}, \quad \alpha_7 = \frac{k_{nf}}{k_f} = \frac{1 + (2k_f/k_s) + 2\lambda(1-(k_f/k_s))}{1 + (2k_f/k_s) - \lambda(1-(k_f/k_s))}, \\ \alpha_8 &= \frac{D_{nf}}{D_f} = (1-\lambda), \quad \beta_1 = \frac{1}{\alpha_5}, \quad \beta_2 = \frac{\alpha_6}{\alpha_7}, \quad \beta_3 = \frac{1}{\alpha_7}, \quad \beta_4 = \frac{1}{\alpha_8}, \quad Y_1 = \frac{y_1}{y_0}, \quad Y = \frac{y_3}{y_0}, \quad V = \frac{v}{v_0}, \\ T &= \Omega \tau, \quad f = n/\Omega, \quad H = \frac{(\Omega/\nu_f)^{1/2} h}{\sigma_f \mu_e \nu_0 h_0}, \quad P = \frac{p}{\rho_f \mu_e \nu_0 y_0}, \quad \Theta = \frac{(\theta - \theta_l)}{(\theta_r - \theta_l)}, \quad \Phi = \frac{(\phi - \phi_l)}{(\phi_r - \phi_l)}. \end{aligned} \right\} \quad (19)$$

Implementing of the Equations (19) to the consequential flow model Equations (16), (17), (13) and (14), we attain

$$\alpha_2 \frac{\partial V}{\partial T} = -\frac{\partial P}{\partial Y_1} + Ek\alpha_1 \left(\frac{\partial^2 V}{\partial Y^2} - \frac{V}{Kp} \right) + 2\alpha_m^2 Ek^{1/2} \frac{\partial H}{\partial Y} - 2i\alpha_2 V + Ek(\alpha_3 G_\Theta \Theta + \alpha_4 G_\Phi \Phi), \quad (20)$$

$$Pm \frac{\partial H}{\partial T} = Ek^{1/2} \frac{\partial V}{\partial Y} + Ek\beta_1(1 - iHc) \frac{\partial^2 H}{\partial Y^2}, \quad (21)$$

$$\frac{Pr\beta_2}{Ek} \frac{\partial \Theta}{\partial T} = \frac{\partial^2 \Theta}{\partial Y^2} - N^2 \beta_3 \Theta, \quad (22)$$

$$\frac{Sc\beta_4}{Ek} \frac{\partial \Phi}{\partial T} = \frac{\partial^2 \Phi}{\partial Y^2} - Hp\beta_4 \Phi, \quad (23)$$

where the symbols Ek , α_m , Kp , G_Θ , G_Φ , Pm , Pr , N^2 , Sc and Hp , are, respectively stands for the Ekman number, magnetic interaction constant, permeability constant, thermal Grashof number, solutal Grashof number, magnetic Prandtl number, Prandtl number, heat source (absorption/radiation) constant, Schmidt number and first order chemical reaction constant, and these expressed in mathematical forms as

$$\left. \begin{aligned} Ek &= \frac{\nu_f}{\Omega y_0^2}, \quad \alpha_m = \left(\frac{\sigma_f}{2\rho_f \Omega} \right)^{1/2} h_0, \quad Kp = \frac{k_p}{y_0^2}, \quad G_\Theta = \frac{g\beta_f y_0^2 (\theta_r - \theta_l)}{\nu_f \nu_0}, \\ G_\Phi &= \frac{g\beta_f^* y_0^2 (\phi_r - \phi_l)}{\nu_f \nu_0}, \quad Pm = \frac{\nu_f}{\nu_m}, \quad Pr = \frac{\nu_f (\rho C_p)_f}{k_f}, \quad N_t^2 = \frac{R y_0^2}{k_f}, \quad Sc = \frac{\nu_f}{D_f}, \quad Hp = \frac{Cr y_0^2}{D_f}. \end{aligned} \right\} \quad (24)$$

Use of the dimensionless transformation rules (19) convert the designated boundary conditions (BCs) at contact walls of the symmetric channel to the form given below

$$\left. \begin{aligned} V &= H = \Theta = \Phi = 0, & \text{at } Y &= -1/2; \\ V &= \Theta = \Phi = 1 + \varepsilon \cos(fT), \quad \frac{\partial H}{\partial Y} = 0, & \text{at } Y &= 1/2. \end{aligned} \right\} \quad (25)$$

3 | SOLUTION OF THE FLOW MODEL

An analytical approach is followed out to extract the solutions of the resulting non-dimensional flow model (20)-(23) along with the BC's (25). To achieve this important goal, the pressure drop is assumed to be constant and expressed as

$$\frac{\partial P}{\partial Y} = P_0 \left(1 + \frac{\varepsilon}{2} (e^{i f T} + e^{-i f T}) \right), \quad (26)$$

where P_0 is a constant.

The solutions of the flow velocity, motional generated magnetic field, fluid temperature and fluid concentration are assumed to be of the following form due to oscillatory nature of the flow

$$V(Y, T) = V_{s0}(Y) + \frac{\varepsilon}{2} (V_{s1}(Y)e^{i f T} + V_{s2}(Y)e^{-i f T}), \quad (27)$$

$$H(Y, T) = H_{s0}(Y) + \frac{\varepsilon}{2} (H_{s1}(Y)e^{i f T} + H_{s2}(Y)e^{-i f T}), \quad (28)$$

$$\Theta(Y, T) = \Theta_{s0}(Y) + \frac{\varepsilon}{2} (\Theta_{s1}(Y)e^{i f T} + \Theta_{s2}(Y)e^{-i f T}), \quad (29)$$

$$\Phi(Y, T) = \Phi_{s0}(Y) + \frac{\varepsilon}{2} (\Phi_{s1}(Y)e^{i f T} + \Phi_{s2}(Y)e^{-i f T}). \quad (30)$$

Employing the pressure drop (26) and assumed solutions (27) and (30) to the resulting non-dimensional flow model (20)-(23), these yield the following system of the equations

$$Ek\alpha_1 V''_{s0} - \left(\frac{Ek\alpha_1}{Kp} + 2i\alpha_2 \right) V_{s0} + 2\alpha_m^2 Ek^{1/2} H'_{s0} = -P_0 - Ek(G_\Theta \alpha_3 \Theta_{s0} - G_\Phi \alpha_4 \Phi_{s0}), \quad (31)$$

$$Ek\alpha_1 V''_{s1} - \left(\frac{Ek\alpha_1}{Kp} + i(f+2)\alpha_2 \right) V_{s1} + 2\alpha_m^2 Ek^{1/2} H'_{s1} = -P_0 - Ek(G_\Theta \alpha_3 \Theta_{s1} - G_\Phi \alpha_4 \Phi_{s1}), \quad (32)$$

$$Ek\alpha_1 V''_{s2} - \left(\frac{Ek\alpha_1}{Kp} - i(f-2)\alpha_2 \right) V_{s2} + 2\alpha_m^2 Ek^{1/2} H'_{s2} = -P_0 - Ek(G_\Theta \alpha_3 \Theta_{s2} - G_\Phi \alpha_4 \Phi_{s2}), \quad (33)$$

$$Ek\beta_1(1 - iHc)H''_{s0} + Ek^{1/2}V'_{s0} = 0, \quad (34)$$

$$Ek\beta_1(1 - iHc)H''_{s1} - i f PmH_{s1} + Ek^{1/2}V'_{s1} = 0, \quad (35)$$

$$Ek\beta_1(1 - iHc)H''_{s2} + i f PmH_{s2} + Ek^{1/2}V'_{s2} = 0, \quad (36)$$

$$\Theta''_{s0} - N^2\beta_3\Theta_{s0} = 0, \quad (37)$$

$$Ek\Theta''_{s1} - (N^2\beta_3Ek + i f Pr\beta_2)\Theta_{s1} = 0, \quad (38)$$

$$Ek\Theta''_{s2} - (N^2\beta_3Ek - i f Pr\beta_2)\Theta_{s2} = 0, \quad (39)$$

$$\Phi''_{s0} - Hp\beta_4\Phi_{s0} = 0, \quad (40)$$

$$Ek\Phi''_{s1} - (EkHp + i f Sc)\beta_4\Phi_{s1} = 0, \quad (41)$$

$$Ek\Phi''_{s2} - (EkHp - i f Sc)\beta_4\Phi_{s2} = 0, \quad (42)$$

The assumed solutions satisfy the following BCs

$$\left. \begin{aligned} V_{s0} = V_{s1} = V_{s2} = 0, \quad H_{s0} = H_{s1} = H_{s2} = 0, \quad \text{at } Y = -1/2; \\ \Theta_{s0} = \Theta_{s1} = \Theta_{s2} = 0, \quad \Phi_{s0} = \Phi_{s1} = \Phi_{s2} = 0, \\ V_{s0} = V_{s1} = V_{s2} = 1, \quad \frac{\partial H_{s0}}{\partial Y} = \frac{\partial H_{s1}}{\partial Y} = \frac{\partial H_{s2}}{\partial Y} = 0, \\ \Theta_{s0} = \Theta_{s1} = \Theta_{s2} = 1, \quad \Phi_{s0} = \Phi_{s1} = \Phi_{s2} = 1, \quad \text{at } Y = 1/2. \end{aligned} \right\} \quad (43)$$

The system of the Equations (31) to (42) are solved accordance to the BCs (43) and the solution system are presented in condensed form as

$$\begin{aligned} V_{s0} = & \frac{\sinh\left(L_0\left(Y + \frac{1}{2}\right)\right)}{\sinh(L_0)} + \frac{G_\Theta \beta_6}{(A_0^2 - L_0^2)} \left\{ \frac{\sinh\left(L_0\left(Y + \frac{1}{2}\right)\right)}{\sinh(L_0)} - \frac{\sinh\left(A_0\left(Y + \frac{1}{2}\right)\right)}{\sinh(A_0)} \right\} \\ & + \frac{G_\Phi \beta_7}{(B_0^2 - L_0^2)} \left\{ \frac{\sinh\left(L_0\left(Y + \frac{1}{2}\right)\right)}{\sinh(L_0)} - \frac{\sinh\left(B_0\left(Y + \frac{1}{2}\right)\right)}{\sinh(B_0)} \right\} + K_{01} \left(1 - \frac{\cosh(L_0 Y)}{\cosh\left(\frac{L_0}{2}\right)} \right), \end{aligned} \quad (44)$$

$$\begin{aligned} V_{si} = & \frac{\sinh\left(L_{i1}\left(Y + \frac{1}{2}\right)\right)}{\sinh(L_{i1})} + K_{i1} \left\{ \cosh(L_{i2} Y) - \frac{\cosh(L_{i1} Y) \cosh\left(\frac{L_{i2}}{2}\right)}{\cosh\left(\frac{L_{i1}}{2}\right)} \right\} \\ & + K_{i2} \left\{ \sinh(L_{i2} Y) - \frac{\sinh(L_{i1} Y) \sinh\left(\frac{L_{i2}}{2}\right)}{\sinh\left(\frac{L_{i1}}{2}\right)} \right\} + \frac{Y_{i3} P_0}{E Y_{i2}} \left\{ 1 - \frac{\cosh(L_{i1} Y)}{\cosh\left(\frac{L_{i1}}{2}\right)} \right\} \\ & + \frac{G_\Theta (A_i^2 \beta_6 - Y_{i3} \alpha_3)}{(A_i^4 - Y_{i1} A_i^2 + Y_{i2})} \left\{ \frac{\sinh\left(L_{i1}\left(Y + \frac{1}{2}\right)\right)}{\sinh(L_{i1})} - \frac{\sinh\left(A_i\left(Y + \frac{1}{2}\right)\right)}{\sinh(A_i)} \right\} \\ & + \frac{G_\Phi (B_i^2 \beta_7 - Y_{i3} \alpha_4)}{(B_i^4 - Y_{i1} B_i^2 + Y_{i2})} \left\{ \frac{\sinh\left(L_{i1}\left(Y + \frac{1}{2}\right)\right)}{\sinh(L_{i1})} - \frac{\sinh\left(B_i\left(Y + \frac{1}{2}\right)\right)}{\sinh(B_i)} \right\}, \quad i = 1, 2 \end{aligned} \quad (45)$$

$$\begin{aligned} H_{s0} = & \frac{1}{2\alpha_m^2 E k^{1/2}} \left[(K_{01} E_2 - P_0) Y + K_{02} + E_3 \left\{ \frac{\cosh\left(L_0\left(Y + \frac{1}{2}\right)\right)}{L_0 \sinh(L_0)} - \frac{K_{01} \sinh(L_0 Y)}{L_0 \cosh\left(\frac{L_0}{2}\right)} \right. \right. \\ & + \frac{G_\Theta \beta_6}{(A_0^2 - L_0^2)} \left(\frac{\cosh\left(L_0\left(Y + \frac{1}{2}\right)\right)}{L_0 \sinh(L_0)} - \frac{\cosh\left(A_0\left(Y + \frac{1}{2}\right)\right)}{A_0 \sinh(A_0)} \right) \\ & \left. \left. + \frac{G_\Phi \beta_7}{(B_0^2 - L_0^2)} \left(\frac{\cosh\left(L_0\left(Y + \frac{1}{2}\right)\right)}{L_0 \sinh(L_0)} - \frac{\cosh\left(B_0\left(Y + \frac{1}{2}\right)\right)}{B_0 \sinh(B_0)} \right) \right\} \right], \end{aligned} \quad (46)$$

$$\begin{aligned}
H_{si} = & \pm \frac{1}{2\alpha_m^2 Ek^{1/2}} \left[\frac{M_{i1} \cosh\left(L_{i1}\left(Y + \frac{1}{2}\right)\right)}{\sinh(L_{i1})} + K_{i1} \left\{ M_{i2} \sinh(L_{i2}Y) - \frac{M_{i1} \cosh\left(\frac{L_{i2}}{2}\right) \sinh(L_{i1}Y)}{\cosh\left(\frac{L_{i1}}{2}\right)} \right\} \right. \\
& + K_{i1} \left\{ M_{i2} \cosh(L_{i2}Y) - \frac{M_{i1} \sinh\left(\frac{L_{i2}}{2}\right) \cosh(L_{i1}Y)}{\sinh\left(\frac{L_{i1}}{2}\right)} \right\} - \frac{Y_{i3}P_0}{E_k Y_{i2}} \frac{M_{i1} \sinh(L_{i1}Y)}{\cosh\left(\frac{L_{i1}}{2}\right)} \\
& + \frac{G_\Theta(A_i^2\beta_6 - Y_{i3}\alpha_3)}{(A_i^4 - Y_{i2}A_i^2 + Y_{i2})} \left\{ \frac{M_{i1} \cosh\left(L_{i1}\left(Y + \frac{1}{2}\right)\right)}{\sinh(L_{i1})} - \frac{P_{i1} \cosh\left(A_i\left(Y + \frac{1}{2}\right)\right)}{\sinh(A_i)} \right\} \\
& \left. + \frac{G_\Phi(B_i^2\beta_7 - Y_{i3}\alpha_4)}{(B_i^4 - Y_{i2}B_i^2 + Y_{i2})} \left\{ \frac{M_{i1} \cosh\left(L_{i1}\left(Y + \frac{1}{2}\right)\right)}{\sinh(L_{i1})} - \frac{Q_{i1} \cosh\left(B_i\left(Y + \frac{1}{2}\right)\right)}{\sinh(B_i)} \right\} \right], \quad i = 1, 2. \quad (47)
\end{aligned}$$

$$\Theta_{si} = \frac{\sinh\left(A_i\left(Y + \frac{1}{2}\right)\right)}{\sinh(A_i)}, \quad i = 0, 1, 2 \quad (48)$$

$$\Phi_{si} = \frac{\sinh\left(B_i\left(Y + \frac{1}{2}\right)\right)}{\sinh(B_i)}, \quad i = 0, 1, 2 \quad (49)$$

In the Equation (47) the +ive sign appear when $i = 1$ and -ive sign will arrive when $i = 2$. The constants present in the solutions (44) to (49) are given in the Appendix. The flow velocity, motional generated magnetic field, temperature field and concentration field are finally attained on employing the solutions (44) to (49) to the assumed solutions (27) to (30).

3.1 | The quantities of physical interest

The wall shear stress (WSS) at the left and right walls are derived with the assistance of Equations (27), (44) and (45), which are as follows

$$\tau_{wl} = \tau_{wly_1} + i\tau_{wly_2} = - \left\{ V'_{s0} \left(-\frac{1}{2}\right) + \frac{\varepsilon}{2} \left(V'_{s1} \left(-\frac{1}{2}\right) e^{ifT} + V'_{s2} \left(-\frac{1}{2}\right) e^{-ifT} \right) \right\}, \quad (50)$$

$$\tau_{wr} = \tau_{wry_1} + i\tau_{wry_2} = - \left\{ V'_{s0} \left(\frac{1}{2}\right) + \frac{\varepsilon}{2} \left(V'_{s1} \left(\frac{1}{2}\right) e^{ifT} + V'_{s2} \left(\frac{1}{2}\right) e^{-ifT} \right) \right\}. \quad (51)$$

The rate of heat transport (RHT) at the left and right walls are derived with the assistance of Equations (29) and (48), which are as follows

$$Nu_l = - \left\{ \frac{A_0}{\sinh(A_0)} + \frac{\varepsilon}{2} \left(\frac{A_1}{\sinh(A_1)} e^{ifT} + \frac{A_2}{\sinh(A_2)} e^{-ifT} \right) \right\}, \quad (52)$$

$$Nu_r = - \left\{ \frac{A_0 \cosh(A_0)}{\sinh(A_0)} + \frac{\varepsilon}{2} \left(\frac{A_1 \cosh(A_1)}{\sinh(A_1)} e^{ifT} + \frac{A_2 \cosh(A_2)}{\sinh(A_2)} e^{-ifT} \right) \right\}. \quad (53)$$

The rate of mass transport (RMT) at the left and right walls are derived with the assistance of Equations (29) and (48), which are as follows

$$Sh_l = - \left\{ \frac{B_0}{\sinh(B_0)} + \frac{\varepsilon}{2} \left(\frac{B_1}{\sinh(B_1)} e^{ifT} + \frac{B_2}{\sinh(B_2)} e^{-ifT} \right) \right\}, \quad (54)$$

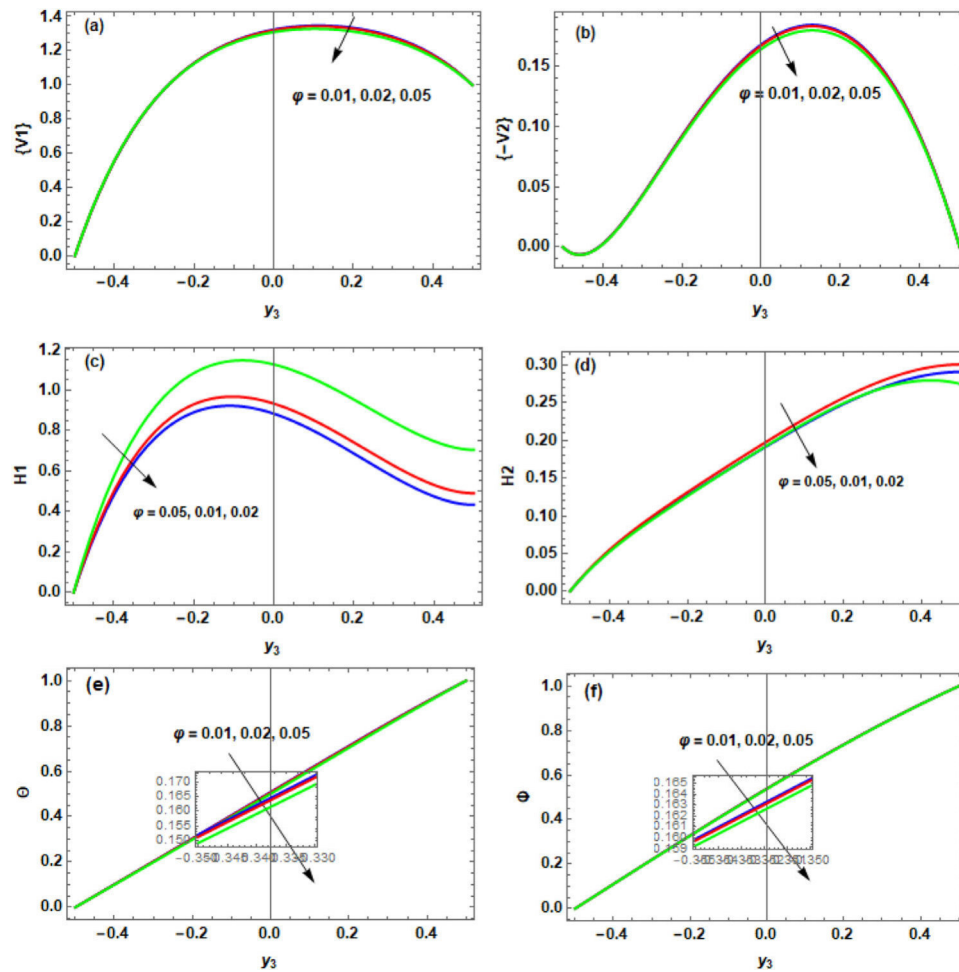


FIGURE 2 Nature of flow velocity, motional generated magnetic field, temperature field and concentration field for λ .

TABLE 1 Thermophysical constants values for Titanium alloy suspended water nanofluid ($\text{Ti}_6\text{Al}_4\text{V-H}_2\text{O}$) (Singh and Kolasani [33]).

	$\beta \times 10^{-5} (1/K)$	$\rho (kg/m^3)$	$\sigma (S/m)$	$C_p (J/kgK)$	$k (W/mK)$
$\text{Ti}_6\text{Al}_4\text{V}$	5.8	4420	5.8×10^5	0.56	7.2
H_2O	21	997.1	0.005	4179	0.613

$$Sh_r = - \left\{ \frac{B_0 \cosh(B_0)}{\sinh(B_0)} + \frac{\varepsilon}{2} \left(\frac{B_1 \cosh(B_1)}{\sinh(B_1)} e^{i f T} + \frac{B_2 \cosh(B_2)}{\sinh(B_2)} e^{-i f T} \right) \right\}. \quad (55)$$

4 | RESULTS AND DISCUSSION

The nature of flow velocity, motional generated magnetic field, temperature field and concentration field are inspected with the support of graphs (Figures 2–7). Further the quantities of physical interest such as wall shear stress (WSS), rate of heat transport (RHT) and rate of mass transport (RMT) are also computed for the significant flow parameters and these are expressed in the form of tables (Tables 2 and 3). The graphs and tabular values are generated with the computation of the analytical solutions extracted in the previous section. During the execution of the computational work, the parameter values are taken to be constant as $\lambda = 0.02$, $Hc = 0.25$, $Pm = 0.7$, $Ek = 0.5$, $\alpha_m^2 = 5$, $f = 2$, $G_\Theta = 4$, $G_\Phi = 5$, $Pr = 0.71$, $N^2 = 2$, $Sc = 0.78$, $Hp = 0.2$, $P_0 = 1$, $\varepsilon = 1$ and $fT = \pi/2$. If a different parameter value is taken during the computation, it is specifically mentioned in the graphs and tables. In Table 1, the thermophysical constants values for Titanium alloy suspended water nanofluid ($\text{Ti}_6\text{Al}_4\text{V-H}_2\text{O}$) are exhibited.

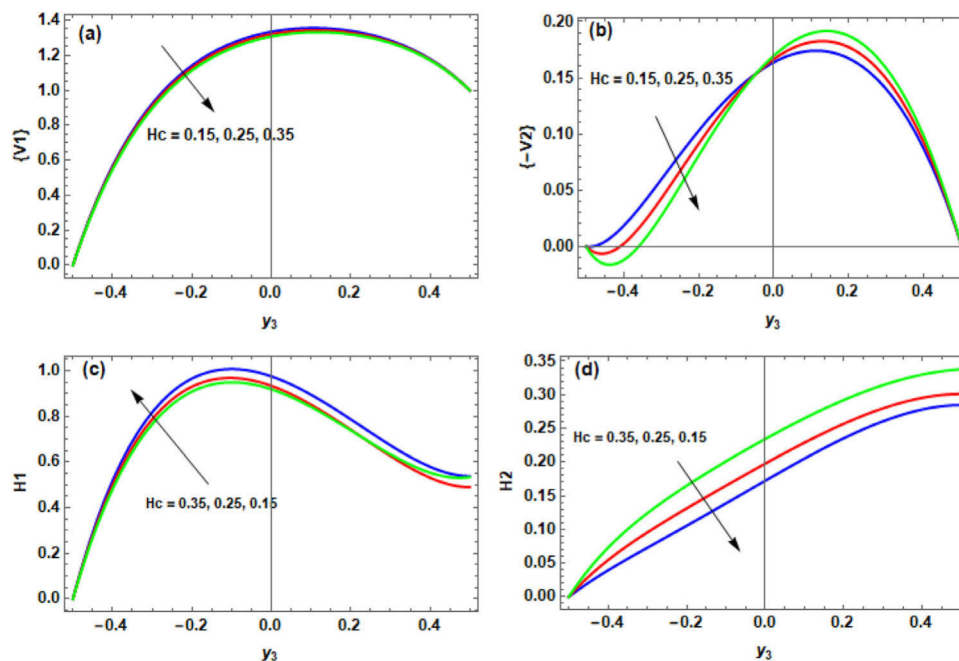


FIGURE 3 Nature of flow velocity and motional generated magnetic field for H_c .

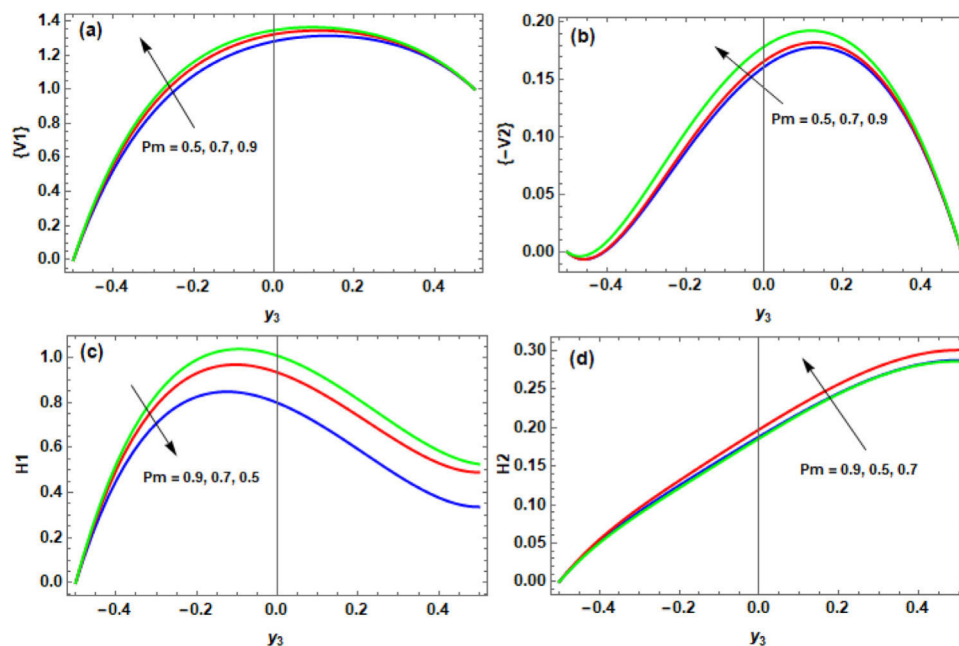


FIGURE 4 Nature of flow velocity and motional generated magnetic field for P_m .

4.1 | Nature of flow velocity, motional generated magnetic field, temperature field and concentration field

Figures 2–7 explores the nature of flow velocity, motional generated magnetic field, temperature field and concentration field for significant parameters. The nature of flow velocity, motional generated magnetic field, temperature field and concentration field for volume concentration of nanofluid are presented in Figure 2. The volume concentration of nanofluid produces resistivity in the flow and tends to slow down the fluid flow. Further it enhances the motional generated magnetic field in the principal direction of the fluid flow and lowers the fluid temperature and concentration. Figure 3 confirms the nature of flow velocity and motional generated magnetic field for Hall current. Hall current stabilizes the main flow

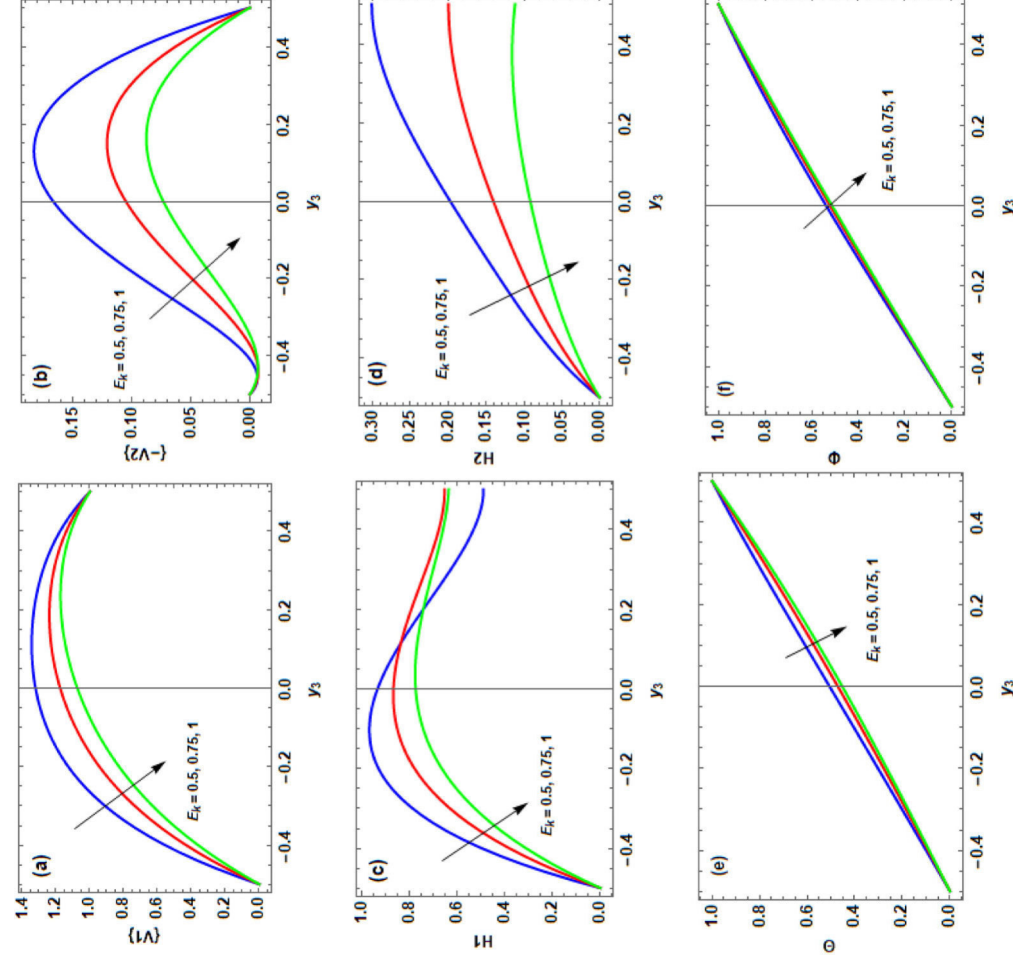


FIGURE 5 Nature of flow velocity, motional generated magnetic field, temperature field and concentration field for E_k .

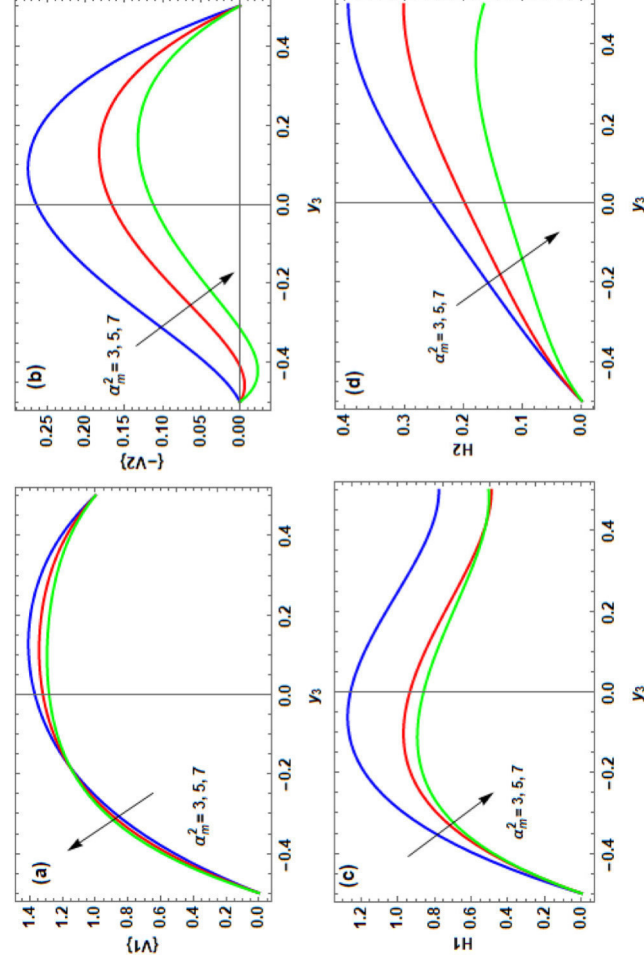


FIGURE 6 Nature of flow velocity and motional generated magnetic field for α_m^2 .

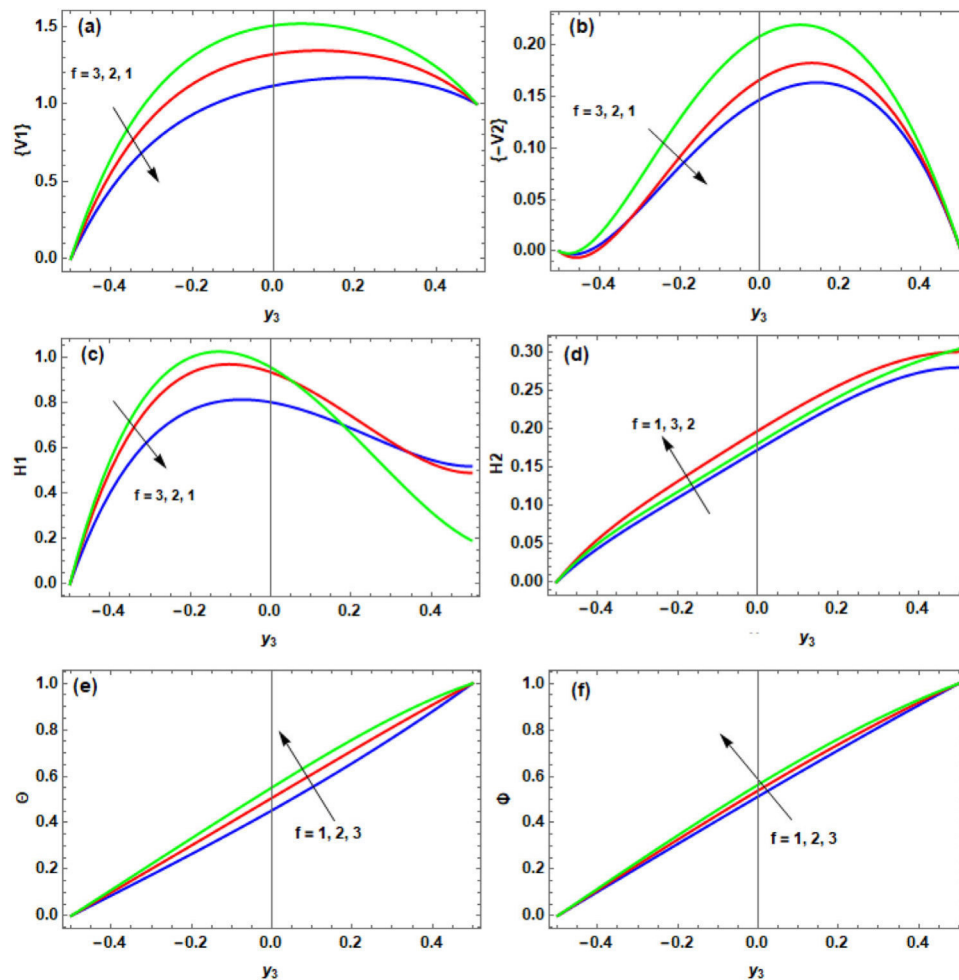


FIGURE 7 Nature of flow velocity, motional generated magnetic field, temperature field and concentration field for f .

as its direction is normal to main flow and implemented magnetic field. It tends to fasten the secondary flow because it arises due revolving of charged fluid particles about the lines of implemented magnetic field. The nature of secondary flow near the surface $Y = -1/2$ is opposite because the surface $Y = -1/2$ is kept fixed while the surface $Y = 1/2$ is oscillating. Hall current significantly alter the nature of motional magnetic field. It lead to a significant growth in the secondary motional generated magnetic field while it brings drop in the principal motional generated magnetic field. The nature of flow velocity and motional generated magnetic field for magnetic Prandtl number are explored in the Figure 4. Magnetic Prandtl number has an inverse relation with magnetic viscosity (magnetic diffusivity) and has direct relation with the conductivity of the fluid. On enhancing magnetic diffusivity, magnetic Prandtl number diminishes while it grows with the conductivity of the fluid. As Figure 4 explores the magnetic Prandtl number boost the flow velocity, it indicates that magnetic diffusion brings rigidity in the flow and lessens the flow velocity. Further, magnetic diffusion weakens the strength of the primarily motional induced magnetic field. Figure 5 characterizes the nature of flow velocity, motional generated magnetic field, temperature field and concentration field for Ekman number, which is reciprocal of rotation parameter. It can be easily noted that the Ekman number lessens the flow velocity, that is, the revolving of the flow system tends to improve the flow velocity by inducing a gyratory force called Coriolis force in a direction which is normal to the primary flow. Revolving of the flow system further improves the secondarily motional generated magnetic and primarily motional generated magnetic field in the left half region near the surface $Y = -1/2$. The temperature and concentration are also get improvise by the rotation of the system. The magnetic interaction effect on the nature of flow velocity and motional generated magnetic field are demonstrated in the Figure 6. In general, the interaction of the magnetic field to the moving conducting fluid tends to control the flow by generating a drag force called Lorentz force. In this problem, we can see the same nature of the magnetic interaction parameter on the flow velocity except for the main flow in a narrow region near the surface $Y = -1/2$. This may be due to alternative non-conducting and conducting walls of the channel.

TABLE 2 Nature of wall shear stress (WSS) in the directions of principal and secondary flows at the surfaces $Y = -1/2$ and $Y = 1/2$ of the symmetric channel.

λ	Hc	Pm	Ek	α_m^2	f	$-\tau_{wly_1}$	$-\tau_{wly_2}$	τ_{wry_1}	$-\tau_{wry_2}$
0.02	0.25	0.7	0.5	5	2	7.7980	0.1813	1.3563	0.9762
0.01	0.25	0.7	0.5	5	2	7.7787	0.1779	1.4026	0.9788
0.05	0.25	0.7	0.5	5	2	7.8436	0.1863	1.2195	0.9643
0.02	0.15	0.7	0.5	5	2	7.9491	-0.0983	1.3860	0.9072
0.02	0.35	0.7	0.5	5	2	7.6082	0.4317	1.3348	1.0444
0.02	0.25	0.5	0.5	5	2	7.3891	0.1730	1.2762	0.9635
0.02	0.25	0.9	0.5	5	2	8.0797	0.1065	1.3978	1.0054
0.02	0.25	0.7	0.75	5	2	5.9901	0.1500	0.9638	0.6498
0.02	0.25	0.7	1	5	2	4.9891	0.1242	0.7030	0.4791
0.02	0.25	0.7	0.5	3	2	6.9619	-0.4285	1.7659	1.2467
0.02	0.25	0.7	0.5	7	2	8.4994	0.5737	1.0731	0.8152
0.02	0.25	0.7	0.5	5	1	6.5143	0.0625	0.5665	0.9552
0.02	0.25	0.7	0.5	5	3	8.9624	0.0599	2.1091	1.0414

TABLE 3 Nature of the rate of heat transport (RHT) and rate of mass transport (RMT) at the surfaces $Y = -1/2$ and $Y = 1/2$ of the symmetric channel.

λ	Ek	f	$-Nu_l$	$-Nu_r$	$-Sh_l$	$-Sh_r$
0.02	0.5	2	1.0076	0.8919	1.1040	0.7858
0.01	0.5	2	1.0123	0.8775	1.1051	0.7836
0.05	0.5	2	0.9934	0.9344	1.1007	0.7926
0.02	0.75	2	0.9218	1.1182	1.0590	0.8784
0.02	1	2	0.8748	1.2370	1.0363	0.9249
0.02	0.5	1	0.8748	1.2370	1.0363	0.9249
0.02	0.5	3	1.1150	0.5774	1.1698	0.6487

Furthermore the magnetic interaction expresses a diminishing trend on the motional induced magnetic field. The nature of flow velocity, motional generated magnetic field, temperature field and concentration field for oscillation frequency are explored in Figure 7. The fluid moves faster on incrementing the oscillation frequency of the right surface $Y = 1/2$. The motional generated magnetic field get enhanced in the left region of the channel while it weakens in the right region near the surface $Y = 1/2$ on elevating the oscillation frequency. The temperature and concentration are uplifted by the oscillation of the right surface $Y = 1/2$.

4.2 | Nature of the quantities of physical interests such as wall shear stress (WSS), rate of heat transport (RHT) and rate of mass transport (RMT)

The nature of WSS, RHT and RMT at the surfaces $Y = -1/2$ and $Y = 1/2$ of the symmetric channel are explored for significant parameters and presented in the form of the tabular values in Tables 2 and 3. Table 2 explores the WSS values in the directions of principal and secondary flows at the surfaces $Y = -1/2$ and $Y = 1/2$. The tabular values of WSS for volume concentration of nanofluid express that enhancing values of volume concentration of nanofluid employ more WSS at the surface $Y = -1/2$. This behavior is opposite at the wall surface $Y = 1/2$. The tabular values of WSS for Hall current show that Hall current lead to reduce the WSS at the surfaces $Y = -1/2$ and $Y = 1/2$ along the principal flow. Along the secondary flow, the WSS value at the surface $Y = 1/2$ get enhance with Hall current. It can be noticed from the tabular values of WSS for magnetic Prandtl number that magnetic Prandtl number lead to upsurge the WSS at the surfaces $Y = -1/2$ and $Y = 1/2$ and hence the electrical conductivity of the nanofluid. We can further conclude the magnetic diffusivity (magnetic viscosity) uphold the diminishing nature to the WSS at the surfaces $Y = -1/2$ and $Y = 1/2$. The tabular values of WSS for Ekman number explores that Ekman number lessens the WSS at the surfaces $Y =$

$-1/2$ and $Y = 1/2$. Since it is reciprocal of rotation parameter, thus we can state that the revolving of the system increase the WSS at the surfaces $Y = -1/2$ and $Y = 1/2$. The tabular values of WSS for magnetic interaction parameter appraises that the WSS value at the surface $Y = -1/2$ along the main flow rise up with the magnetic field strength while the WSS at the surface $Y = 1/2$ goes down with the magnetic field strength. The tabular values of WSS for oscillation frequency expresses that oscillation frequency caused to rise the WSS at the surfaces $Y = -1/2$ and $Y = 1/2$. The RHT and RMT values at the surfaces $Y = -1/2$ and $Y = 1/2$ are presented in the Table 2. The tabular values of RHT and RMT for volume concentration of nanofluid exhibits that the volume concentration of nanofluid lessens RHT and RMT at the surface $Y = -1/2$ while it grows the RHT and RMT at the surface $Y = 1/2$. The tabular values of RHT and RMT for Ekman number and oscillation frequency discovers that revolving of the flow system and oscillation frequency have a tendency to boost the RHT and RMT at the surface $Y = -1/2$ while these have a converse nature on RHT and RMT at the surface $Y = 1/2$.

5 | CONCLUSION

In this study, the heat and mass transport in oscillatory hydromagnetic Titanium alloy suspended water nanofluid flow within two vertical alternatively non-conducting and conducting walls enclosing Darcy-Brinkman porous medium is examined. The motional induction effect and Hall phenomenon are also explored. The flow nature is systematically examined through the numerical computation of the extracted analytical solution solutions. The results derived from this research investigation is supportive in studying the heat and mass transport nature of nanofluids and consequences of motional induction, Hall current, revolving of the flow system and oscillations on these. The explored results may find significant chemical and thermal engineering applications. The noteworthy features of the flow are highlighted below:

- The volume concentration of nanofluid produces resistivity in the flow and tends to slow down the fluid flow. It enhances the motional generated magnetic field in the principal direction of the fluid flow and lowers the fluid temperature and concentration.
- Hall current stabilizes the main flow as its direction is normal to main flow and implemented magnetic field. It significantly grows the secondary motional generated magnetic field while it brings drop in the principal motional generated magnetic field.
- Magnetic diffusion brings rigidity in the flow and lessens the flow velocity. It weakens the strength of the primarily motional induced magnetic field.
- Revolving flow system tends to improve the flow velocity by inducing a gyratory force along secondary flow. Further it improves the secondarily motional generated magnetic.

NOMENCLATURE

C_p	specific heat at constant pressure
Cr	constant of first order chemical reaction
D	chemical molecular diffusivity
\vec{e}	electric field vector
\vec{g}	gravitational field vector
\vec{h}	magnetic field vector
Hc	Hall current parameter
h_0	applied magnetic field strength
(h_1, h_2)	motional generated magnetic field components along y_1 and y_2 -axes
\vec{j}	current density vector
k	thermal conductivity
k_p	permeability of the Darcy-Brinkman porous medium
n	frequency of oscillations
Nu	rate of heat transport
p	pressure
P_0	a constant

R	heat source constant
Sh	rate of mass transport
\vec{v}	velocity field vector
v_0	a constant fluid velocity
(v_1, v_2)	velocity components along y_1 and y_2 -axes
(y_1, y_2, y_3)	Cartesian coordinates
y_0	channel width

Greek symbols

β	thermal expansion coefficient
β^*	chemical molecular expansion coefficient
ε	a constant
λ	coefficient of volumetric concentration
μ	dynamic viscosity
μ_e	magnetic permeability
ν	coefficient of viscosity
ν_m	coefficient of magnetic viscosity
Ω	angular velocity of gyration about y_3 -axis
ϕ	concentration of species in the fluid
ρ	fluid density
σ	electrical conductivity
θ	temperature of the fluid
τ	time
τ_w	wall shear stress
$(\tau_{wy_1}, \tau_{wy_2})$	wall shear stress along y_1 and y_2 -directions

Subscripts

f	quantities for base fluid
l	quantities at the left wall of the channel
nf	quantities for nanofluid
s	quantities for suspended nano particles
r	quantities at the upper wall of the channel

ACKNOWLEDGEMENTS

The authors are grateful to the Islamic University of Madinah, Ministry of Education, KSA for supporting this research work.

ORCID

Jitendra Kumar Singh  <https://orcid.org/0000-0002-7581-0564>

REFERENCES

- [1] Faraday, M.: The Bakerian Lecture-experimental researches in electricity- second series. Phil. Trans. 122(15), 175 (1832). <https://doi.org/10.1098/rstl.1832.0007>
- [2] Ferraro, V.C.A., Plumpton, C.: An Introduction to Magneto-Fluid Mechanics. Clarendon Press, 2nd edn., viii+254 (1966)
- [3] Cowling, T.G.: The magnetic field of sunspots. Mon. Not. R. Astron. Soc. 94, 39–48 (1933). <https://doi.org/10.1093/mnras/94.1.39>
- [4] Ferraro, V.C.A.: The non-uniform rotation of the sun and its magnetic field., Mon. Not. R. Astron. Soc. 97, 458 (1937)
- [5] Alfven, H.: Existence of electromagnetic-hydrodynamic waves., Nature 150 (3805), 405–406 (1942)
- [6] Hartmann, J.: Theory of the laminar flow of an electrically conductive liquid in a homogeneous magnetic field., Fys. Med. 15, 1–27 (1937)
- [7] Rosa, R.J.: Physical principles of magnetohydrodynamic power generation., Phys Fluids 4, 182 (1961). <https://doi.org/10.1063/1.1724426>
- [8] Narasimhan, M.N., Transient magnetohydrodynamic flow in an annular channel, Technical Report, Wisconsin University-Madison, Mathematics Research Center, 24 p., (1963)

- [9] Takenouchi, K.: Transient magnetohydrodynamic channel flow with axial symmetry at a supersonic speed. *J. Phys. Soc. Jpn.* 54, 1329–1338 (1985)
- [10] Hardianto, T., Sakamoto, N., Harada, N.: Computational study of a diagonal channel magnetohydrodynamic power generation. *Int. J. Energy Technol. Policy.* 6, 96–111 (2008). <https://doi.org/10.1504/IJETP.2008.017031>
- [11] Nacev, A., Beni, C., Bruno, O., Shapiro, B.: The behaviors of ferro-magnetic nano-particles in and around blood vessels under applied magnetic fields. *J. Magn. Magn. Mater.* 323, 651–668 (2011)
- [12] Alpher, R.A.: Heat transfer in magnetohydrodynamic flow between parallel plates. *Int. J. Heat Mass Transfer* 3(2), 108–112 (1961)
- [13] Chang, C.C., Yen, J.T.: Magneto-hydrodynamic channel flow as influenced by wall conductance. *Z. Angew. Math. Phys.* 13, 266–272 (1962)
- [14] Snyder, W.T.: The influence of wall conductance on magnetohydrodynamic channel-flow heat transfer. *J. Heat Transfer* 86, 552–556 (1964)
- [15] Hunt, C.R.: Magnetohydrodynamic flow in rectangular ducts. *J. Fluid Mech.* 21, 577–590 (1965)
- [16] Sloan, D.M.: An unsteady MHD duct flow. *Appl. Sci. Res.* 25, 126–136 (1972)
- [17] Mazumdar, B.S.: Effect of wall conductances on hydromagnetic flow and heat transfer in a rotating channel. *Acta Mech.* 28, 85–99 (1977)
- [18] Nagy, T., Demendy, Z.: Effects of Hall currents and Coriolis force on Hartmann flow under general wall conditions. *Acta Mech.* 113, 77–91 (1995)
- [19] Singh, K.D.: An oscillatory hydromagnetic Couette flow in a rotating system. *Z. Angew. Math. Mech.* 80, 429–432 (2000)
- [20] Guria, M., Das, S., Jana, R.N., Ghosh, S.K.: Oscillatory Couette flow in the presence of an inclined magnetic field. *Meccanica* 44, 555 (2009)
- [21] Ansari, M.S., Seth, G.S., Nandkeolyar, R.: Unsteady Hartmann flow in a rotating channel with arbitrary conducting walls. *Math. Comput. Modell.* 54, 765–779 (2011)
- [22] Beg, O.A., Ghosh, S.K., Ahmed, S.: Mathematical modeling of oscillatory magneto-convection of a couple-stress biofluid in an inclined rotating channel. *J. Mech. Med. Biol.* 12, 1250050 (2012)
- [23] Seth, G.S., Singh, J.K., Mahto, N., Joshi, N.: Oscillatory Hartmann flow in rotating channel with magnetized walls. *Math. Sci. Lett.* 5, 259–269 (2016)
- [24] Venkateswarlu, B., Bhagya Lakshmi, K., Kumari, S.S., Satya Narayana, P.V.: Magnetohydrodynamic oscillatory flow of a physiological fluid in an irregular channel. *SN Appl. Sci.* 1, 1223 (2019). <https://doi.org/10.1007/s42452-019-1250-5>
- [25] Singh, J.K., Seth, G.S., Joshi, N., Srinivasa, C.T.: Mixed convection flow of a viscoelastic fluid through a vertical porous channel influenced by a moving magnetic field with Hall and ion-slip currents, rotation, heat radiation and chemical reaction. *Bulg. Chem. Commun.* 52, 147–158 (2020)
- [26] Singh, J.K., Seth, G.S., Vishwanath, S.: Impacts of the periodic wall conditions to the hydromagnetic convective flow of viscoelastic fluid through a vertical channel with Hall current and induced magnetic field. *Heat Transfer* 50, 1812–1835 (2021)
- [27] Singh, J.K., Hanumantha, Seth, G.S.: Scrutiny of convective MHD second grade fluid flow within two alternatively conducting vertical surfaces with Hall current and induced magnetic field. *Heat Transfer* 51, 7613–7634 (2022)
- [28] Falade, J.A., Ukaegbu, J.C., Egere, A.C., Adesanya, S.O.: MHD oscillatory flow through a porous channel saturated with porous medium. *Alexandria Eng. J.* 56, 147–152 (2017)
- [29] Singh, J.K., Kolasani, S., Hanumantha, Seth, G.S.: Scrutiny of induced magnetic field and Hall current impacts on transient hydromagnetic nanofluid flow within two vertical alternatively magnetized surfaces. *Proc. IMechE Part E: Journal of Process Mechanical Engineering* (2022). <https://doi.org/10.1177/09544089221119255>
- [30] Yen, J.T.: Effect of wall electrical conductance on magnetohydrodynamic heat transfer in a channel. *J. Heat Transfer* 85, 371–377 (1963)
- [31] Seth, G.S., Singh, J.K.: Mixed convection hydromagnetic flow in a rotating channel with Hall and wall conduction effects. *Appl. Math. Modell.* 40, 2783–2803 (2016)
- [32] Singh, J.K., Begum, S.G., Seth, G.S.: Influence of Hall current and wall conductivity on hydromagnetic mixed convective flow in a rotating Darcian channel. *Phys. Fluids* 30, 113602 (2018)
- [33] Singh, J.K., Kolasani, S.: Energy dissipation and Hall effect on MHD convective flow of nanofluid within an asymmetric channel with arbitrary wall thickness and conductance. *Eur. Phys. J. C Part Fields* 136, 1074 (2021)
- [34] Gopal, D., Kishan, N., Raju, C.S.K.: Viscous and Joule's dissipation on Casson fluid over a chemically reacting stretching sheet with inclined magnetic field and multiple slips. *Inform. Med. Unlocked* 9, 154–160 (2017)
- [35] Atif, S.M., Hussain, S., Sagheer, M.: Effect of viscous dissipation and Joule heating on MHD radiative tangent hyperbolic nanofluid with convective and slip conditions. *J. Braz. Soc. Mech. Sci. Eng.* 41, 189 (2019)
- [36] Poddar, S., Islam, M.M., Ferdouse, J., Alam, M.M.: Characteristical analysis of MHD heat and mass transfer dissipative and radiating fluid flow with magnetic field induction and suction. *SN Appl. Sci.* 3, 470 (2021)
- [37] Shah, N.A., Alrabaiah, H., Vieru, D., Yook, S.-J.: Induced magnetic field and viscous dissipation on flows of two immiscible fluids in a rectangular channel. *Sci. Rep.* 12, 39 (2022)
- [38] Kumar, D., Singh, A.K., Kumar, D.: Effect of Hall current on the magnetohydrodynamic free convective flow between vertical walls with induced magnetic field. *Eur. Phys. J. Plus* 133, 207 (2018)
- [39] Kumar, D., Singh, A.K., Kumar, D.: Influence of heat source/sink on MHD flow between vertical alternate conducting walls with Hall Effect. *Physica A* 544, 123562 (2020)
- [40] Singh, J.K., Kolasani, S., Seth, G.S.: Heat and mass transport nature of MHD nanofluid flow over a magnetized and convectively heated surface including Hall current, magneto and thermo diffusions impacts. *Ricer. Matem.* 1–12 (2022). <https://doi.org/10.1007/s11587-022-00687-4>

- [41] Singh, J.K., Vishwanath, S.: Hall and induced magnetic field effects on MHD buoyancy driven flow of Walters'B fluid over a magnetized convectively heated inclined surface. *Int. J. Ambient Energy* 43, 4444–4453 (2022)
- [42] Brinkman, H.C.: A calculation of the viscous force exerted by a flowing fluid on a dense swarm of particles. *Appl. Sci. Res.* 1, 27–34 (1949)
- [43] Ali, F., Gohar, M., Khan, I.: MHD flow of water-based Brinkman type nanofluid over a vertical plate embedded in a porous medium with variable surface velocity, temperature and concentration. *J. Mol. Liq.* 223, 412–419 (2016)
- [44] Ahmed, F., Iqbal, M.: MHD power law fluid flow and heat transfer analysis through Darcy Brinkman porous media in annular sector. *Int. J. Mech. Sci.* 130, 508–517 (2017)
- [45] Kausar, M.S., Hussanan, A., Mamat, M., Ahmad, B.: Boundary layer flow through Darcy–Brinkman porous medium in the presence of slip effects and porous dissipation. *Symmetry* 11, 659 (2019)
- [46] Mohd Kanafiah, S.F.H., Mohd Kasim, A.R., Mohd Zokri, S.: Generalized mathematical model of Brinkman fluid with viscoelastic properties: case over a sphere embedded in porous media. *Axioms* 11, 609 (2022)
- [47] Anusha, T., Mahabaleswar, U.S., Sheikhejad, Y.: An MHD of nanofluid flow over a porous stretching/shrinking plate with mass transpiration and Brinkman ratio. *Transp. Porous Med.* 142, 333–352 (2022)
- [48] Leela, V., Nagabhushana, P., Shilpa, B., Gangadhara Reddy, R.: Numerical investigation on effects of induced magnetic field and viscous dissipation on MHD mixed convection in a vertical micro-porous channel using the Brinkman–Forchheimer extended Darcy model. *Int. J. Ambient Energy* 43, 6950–6964 (2022)
- [49] Choi, S.U.S., Eastman, J.A.: Enhancing thermal conductivity of the fluids with nanoparticles. *Int Mech Eng Congress Expo.* 66, 99–105 (1995)
- [50] Chon, C.H., Kihm, K.D.: Empirical correlation finding the role of temperature and particle size for nanofluid (Al₂O₃) thermal conductivity enhancement. *Appl Phys Lett.* 87, 153107 (2005)
- [51] Khan, I., Alqahtani, A.M.: MHD nanofluids in a permeable channel with porosity. *Symmetry* 11, 378 (2019)
- [52] Dutta, S., Goswami, N., Biswas, A.K., Pati, S.: Numerical investigation of magnetohydrodynamic natural convection heat transfer and entropy generation in a rhombic enclosure filled with Cu-water nanofluid. *Int. J. Heat Mass Transfer* 136, 777–798 (2019)
- [53] Mourad, A., Aissa, A., Oudina, F.M., Jamshed, W., Ahmed, W., Ali, H.M., Rashad, A.M.: Galerkin finite element analysis of thermal aspects of Fe₃O₄-MWCNT/water hybrid nanofluid filled in wavy enclosure with uniform magnetic field effect. *Int. Commun. Heat Mass Transfer* 126, 105461 (2021)
- [54] Askari, N., Salmani, H., Taheri, M.H., Masoumnezhad, M., Kazemi, M.A.: Heat transfer of water–graphene oxide nanofluid magnetohydrodynamic flow through a channel in the presence of the induced magnetic field. *Proc. Inst. Mech. Eng. Part C J. Mech. Eng. Sci.* 235, 1966–1978 (2021)
- [55] Abd-Alla, A.M., Thabet, E.N., Bayones, F.S.: Numerical solution for MHD peristaltic transport in an inclined nanofluid symmetric channel with porous medium. *Sci Rep.* 12, 3348 (2022)
- [56] EL-Zahar, E.R., Rashad, A.M., Al-Juaydi, H.S.: Studying massive suction impact on magneto-flow of a hybridized Casson nanofluid on a porous continuous moving or fixed surface. *Symmetry* 14, 627 (2022)
- [57] Govindarajulu, K., Subramanyam Reddy, A.: Magnetohydrodynamic pulsatile flow of third grade hybrid nanofluid in a porous channel with Ohmic heating and thermal radiation effects. *Phys. Fluids* 34, 013105 (2022)
- [58] Cowling, T.G.: *Magnetohydrodynamics*. Interscience Publishers (1957)

How to cite this article: Singh, J.K., Hanumantha, , Kolasani, S., Hussain, S.M.: Exploration of heat and mass transport in oscillatory hydromagnetic nanofluid flow within two verticals alternatively conducting surfaces. *Z Angew Math Mech.* e202300216 (2023). <https://doi.org/10.1002/zamm.202300216>

APPENDIX

$$A_0 = (N^2 \beta_3)^{1/2}, \quad A_{1,2} = \left(N^2 \beta_3 \pm \frac{if \Pr \beta_2}{Ek} \right)^{1/2}, \quad B_0 = (Hp \beta_4)^{1/2}, \quad B_{1,2} = \left(\beta_4 \left(Hp \pm \frac{if Sc}{Ek} \right) \right)^{1/2},$$

$$\beta_5 = \frac{\alpha_2}{\alpha_1}, \quad \beta_6 = \frac{\alpha_3}{\alpha_1}, \quad \beta_7 = \frac{\alpha_4}{\alpha_1}, \quad L_0 = \left[\frac{1}{Ek} \left\{ \left(\frac{Ek}{Kp} + \frac{2\alpha_m^2}{(1+Hc^2)} \right) + 2i \left(\beta_5 + \frac{Hc \alpha_m^2}{(1+Hc^2)\alpha_1\beta_1} \right) \right\} \right]^{1/2}$$

$$E_2 = \left(\frac{Ek\alpha_1}{Kp} + 2i\alpha_2 \right), \quad E_3 = E_2 - EkL_0^2\alpha_1,$$

$$Y_{11,21} = \left\{ \left(\mp \frac{fPmHc}{Ek(1+Hc^2)\beta_1} + \frac{1}{Kp} + \frac{2\alpha_m^2}{Ek(1+Hc^2)\alpha_1\beta_1} \right) \right\}$$

$$\begin{aligned}
& +i \left(\pm \frac{fPm}{Ek(1+Hc^2)\beta_1} \pm \frac{(f \pm 2)\beta_5}{Ek} + \frac{2\alpha_m^2 Hc}{Ek(1+Hc^2)\alpha_1\beta_1} \right) \Bigg\}, \\
Y_{12,22} &= \left\{ \left(\frac{-f(f \pm 2)Pm\beta_5}{Ek^2(1+Hc^2)\beta_1} \pm \frac{fPmHc}{EkKp(1+Hc^2)\beta_1} \right) + i \left(\frac{\pm fPm}{EkKp(1+Hc^2)\beta_1} - \frac{f(f \pm 2)PmHc\beta_5}{Ek^2(1+Hc^2)\beta_1} \right) \right\}, \\
Y_{13,23} &= \left(\frac{\mp fPmHc \pm i f Pm}{Ek^2(1+Hc^2)\alpha_1\beta_1} \right), \quad Y_{14,24} = \left(\frac{Ek^2Hc\alpha_1\beta_1 + iEk^2\alpha_1\beta_1}{fPm} \right), \\
Y_{15,25} &= \frac{1}{fPm} \left\{ Ek\beta_1 \left(\frac{HcEk\alpha_1}{Kp} \mp (f \pm 2)\alpha_2 \right) + iEk\beta_1 \left(\frac{Ek\alpha_1}{Kp} \mp Hc(f \pm 2)\alpha_2 \right) + 2\alpha_m^2 Ek \right\}, \\
Y_{16,26} &= \left(\frac{Ek^2Hc\beta_1 + iEk^2\beta_1}{fPm} \right), \\
L_{11,12} &= \left(1/\sqrt{2} \right) \left\{ (Y_{11} - 4Y_{12})^{1/2} \pm Y_{11} \right\}^{1/2}, \quad L_{21,22} = \left(1/\sqrt{2} \right) \left\{ (Y_{21} - 4Y_{22})^{1/2} \pm Y_{21} \right\}^{1/2}, \\
M_{i1} &= (L_{i1}^2 Y_{i4} - Y_{i6})L_{i1}, \quad P_{i1} = (A_i^2 Y_{i4} - Y_{i5})A_i - \frac{Y_{i6}A_i(A_i^4 - Y_{i1}A_i^2 + Y_{i2})}{(A_i^2\beta_6 - Y_{i3})}, \\
M_{i2} &= (L_{i2}^2 Y_{i4} - Y_{i5})L_{i2}, \\
Q_{i1} &= (B_i^2 Y_{i4} - Y_{i5})B_i - \frac{Y_{i6}B_i(B_i^4 - Y_{i1}B_i^2 + Y_{i2})}{(B_i^2\beta_6 - Y_{i3})}, \\
K_{01} &= \left(\frac{P_0 - E_3}{EkL_0^2\alpha_1} \right), \\
K_{02} &= -E_3 \left\{ \frac{1}{L_0 \sinh L_0} + \frac{G_\Theta \beta_6}{A_0^2 - L_0^2} \left(\frac{1}{L_0 \sinh L_0} - \frac{1}{A_0 \sinh A_0} \right) + \frac{G_\Phi \beta_7}{B_0^2 - L_0^2} \left(\frac{1}{L_0 \sinh L_0} - \frac{1}{B_0 \sinh B_0} \right) \right. \\
&\quad \left. + K_{01} \frac{\sinh\left(\frac{L_0}{2}\right)}{L_0 \cosh\left(\frac{L_0}{2}\right)} \right\} + \frac{1}{2} (E_2 K_{01} - P_0) \\
X_{11,12} &= \frac{(\mp M_{12,22} \sinh(\frac{L_{12,22}}{2}) \cosh(\frac{L_{11,21}}{2}) - M_{11,21} \sinh(\frac{L_{11,21}}{2}) \cosh(\frac{L_{12,22}}{2}))}{\cosh(\frac{L_{11,21}}{2})} \\
X_{21,22} &= \frac{(M_{12,22} \cosh(\frac{L_{12,22}}{2}) \sinh(\frac{L_{11,21}}{2}) - M_{11,21} \cosh(\frac{L_{11,21}}{2}) \sinh(\frac{L_{12,22}}{2}))}{\sinh(\frac{L_{11,21}}{2})} \\
X_{31,32} &= \mp \frac{M_{11,21}}{\sinh(L_{11,21})} \mp \frac{P_0 Y_{13,23}}{Ek Y_{12,22}} \frac{M_{11,21} \sinh(\frac{L_{11,21}}{2})}{\cosh(\frac{L_{11,21}}{2})} \\
&\quad \pm \frac{G_\Theta(A_{1,2}^2\beta_6 - Y_{13,23}\alpha_3)}{(A_{1,2}^4 - A_{1,2}^2 + Y_{12,22})} \left(\frac{P_{11,21}}{\sinh(A_{11,21})} - \frac{M_{11,21}}{\sinh(L_{11,21})} \right) \\
&\quad \pm \frac{G_\Phi(B_{1,2}^2\beta_7 - Y_{13,23}\alpha_4)}{(B_{1,2}^4 - Y_{11,21}B_{1,2}^2 + Y_{12,22})} \left(\frac{Q_{11,21}}{\sinh(B_{11,21})} - \frac{M_{11,21}}{\sinh(L_{11,21})} \right)
\end{aligned}$$

$$\begin{aligned}
 X_{41,42} &= (M_{12,22}L_{12,22} - M_{11,21}L_{11,21}) \cosh\left(\frac{L_{12,22}}{2}\right) \\
 X_{51,52} &= (M_{12,22}L_{12,22} - M_{11,21}L_{11,21}) \sinh\left(\frac{L_{12,22}}{2}\right) \\
 X_{61,62} &= -M_{11,21}L_{11,21} + \frac{P_0 M_{11,21} L_{11,21} Y_{13,23}}{Ek Y_{12,22}} + \frac{G_\Theta (A_{1,2}^2 \beta_6 - Y_{13,23} \alpha_3)}{(A_{1,2}^4 - Y_{11,21} A_{1,2}^2 + Y_{12,22})} (P_{11,21} A_{11,21} - M_{11,21} L_{11,21}) \\
 &\quad + \frac{G_\Phi (B_{1,2}^2 \beta_7 - Y_{13,23} \alpha_4)}{(B_{1,2}^4 - Y_{11,21} B_{1,2}^2 + Y_{12,22})} (Q_{11,21} B_{11,21} - M_{11,21} L_{11,21}) \\
 K_{11,21} &= \frac{X_{31,32} X_{51,52} \mp X_{21,22} X_{61,62}}{X_{11,12} X_{51,52} \mp X_{21,22} X_{41,42}}, \quad K_{12,22} = \frac{X_{31,32} X_{41,42} - X_{11,12} X_{61,62}}{X_{21,22} X_{41,42} \mp X_{11,12} X_{51,52}}.
 \end{aligned}$$

Corporate Governance Practices and their Impact on Attracting Investment and Capital

¹Prof. Manoj Kumar Mishra, ²Dr. Syed Mohammad Ghouse, ³Ravikumar JS, ⁴Amit Kumar Pathak, ⁵Hemant Kumar

¹Professor of Economics, College of Business and Economics,
Salale University Fitcha, Ethiopia

²Associate Professor, School of Management, CMR University,
Bangalore, Karnataka, India

³Asst Professor, Department of Management Studies, Ballari Institute of Technology and Management, Ballari,
Karnataka, India

⁴Assistant Professor, College of Economics and Business Administration, University of Technology and Applied
Sciences, Oman

⁵Research Scholar, School of Business, Galgotias University, Greater Noida

Abstract:

Modern businesses can't function without good corporate governance, which establishes ground rules for interactions among shareholders, managers, and executives. The capacity of a corporation to attract investment and capital is examined in light of the large body of research on corporate governance practises. Corporate governance procedures that work have been shown time and time again to increase a company's chances of attracting investment and financing. Investor trust is bolstered by a company's commitment to good governance practises including openness, accountability, and ethics. Companies with these characteristics tend to have better financial results, a lower cost of capital, and higher market values. Further bolstering the connection between governance and investment attractiveness is the fact that institutional investors, who play a crucial role in capital markets, are attracted to enterprises with solid governance. In addition to the monetary gains, a firm may reap other advantages from good corporate governance, such as lower agency costs and more resilience in the face of adversity. As a result, this is attractive to conservative investors. In addition, being compliant with established governance norms opens the door to international investment.

Keywords: capital, corporate governance, investment, practices, stakeholders

Introduction

The term "corporate governance" is used to describe the framework for leading and managing a corporation.

Robust corporate governance standards establish a conducive atmosphere characterized by trust and accountability, hence playing a pivotal role in attracting investment and capital. Investors are inclined to allocate their capital towards organizations that demonstrate characteristics such as transparency, effective management, ethical conduct, and a dedication to generating long-term value. In the contemporary investment landscape, the implementation of efficient corporate governance practices is not solely a legislative obligation, but also confers a competitive advantage.

To protect the interests of its owners, workers, customers, suppliers, and the society at large, it entails a set of principles and methods meant to guarantee the business acts in a transparent, responsible, and ethical way (Nalina & M, 2021). Attracting investment and finance requires sound company governance standards that inspire trust and confidence among potential backers.

Corporate governance policies and their effect on luring investors and other sources of money are summarised here:

1. Need of Corporate Governance: Good corporate governance is essential in today's competitive business environment. It lays forth the ground rules for how a company's leadership, board of directors, and stockholders will interact with one another (Sweta Agarwal, 2020). Trust, credibility, and reduced risk through good corporate governance standards are all essential to attracting investment and money.

2. Accountability and Openness: Transparency is a cornerstone of good governance in the business world. Investors need timely and accurate information about a company's financial performance, strategic direction, and risks, all of which may be provided via transparent reporting(Singh & Bansal, 2020). Investors are more willing to put money into businesses that are transparent and responsible, thus this openness is beneficial.

3. Protecting the Interests of Shareholders: Shareholders in particular are more likely to invest in a company that guarantees their rights. Effective corporate governance measures, such as annual general meetings and proxy voting, provide shareholders a voice in the company's most consequential decisions. This boosts faith among financiers and inspires more money to flow in.

4. Taking Precautions: The methods of good corporate governance place a premium on minimising and managing risks. The likelihood of unanticipated, unfavourable outcomes that might hurt investor interests is reduced when a company has strong governance procedures in place to detect and handle risks proactively. Companies with a strong emphasis on risk management often attract a larger pool of investors(Almaqtari, Al-Hattami, Al-Nuzaili, & Al-Bukhrani, 2020).

5. Moral Principles and Civic Duties: Risk management and reduction are essential tenets of good corporate governance processes. Companies with strong governance systems are better able to anticipate and prevent undesirable outcomes that might affect investor interests. Companies that place a premium on risk management tend to attract more investors(Pillania, 2012).

6. Developing Sustainable Value: One characteristic of good corporate governance is a commitment to the long term rather than to immediate profits. Institutional investors and other stakeholders are more likely to support a company that has long-term sustainability and shareholder value as a top priority(Almaqtari et al., 2020).

7. Conformity with Regulations: In addition to being required by law in many regions, a company's demonstrated dedication to corporate governance norms and laws is reassuring to investors and other stakeholders. Attracting institutional investors with a rigorous due diligence process requires conformity with these requirements(Nugroho, 2021).

A company's capacity to attract investors and get access to cash is significantly impacted by its corporate governance policies. The confidence of investors, the mitigation of risks, and the creation of a climate favourable to investment may all be achieved by a company building a foundation of openness, accountability, and ethical conduct. Therefore, in today's competitive company environment, good corporate governance is not merely a legal need, but rather a strategic necessity.

Table 1: Role of Corporate Governance Practices to Attract Investment and Capital

Disclosure & Openness to the Public	Impact	The impact of this is that investors view as more trustworthy and less hazardous the businesses that give financial reporting that is both transparent and complete, as well as provide pertinent information about their operations.
	Practices	The following should be considered best practices: regular and timely financial reporting, including audited financial statements; disclosure of substantial risks; and transparent communication with shareholders and stakeholders.
Independence of the Board of Directors and Expertise	Impact	Increasing investor trust and providing effective supervision and decision-making are both possible outcomes of having an independent board of directors with a varied set of expertise and experience.
	Practices	Appointing independent directors, ensuring a diverse board composition, and having specialized committees (such as audit, remuneration, and governance) to monitor essential functions are all practices that are commonly followed.
Participation of Shareholders and Related Matters	Impact	Increasing investor trust and luring long-term investors can be accomplished through safeguarding shareholder rights and promoting engagement on the part of shareholders.
	Practices	Implementing proxy voting rights, organizing shareholder meetings, and actively interacting with shareholders to address their problems and solicit their feedback are all practices that are commonly used.

Business Procedures That Are Both Ethical and Responsible	Impact	Companies that place a high priority on ethics, social responsibility, and sustainable practices have a better chance of attracting ethical and impact investors whose beliefs are compatible with their own.
	Practices	Developing and enforcing a code of ethics, embracing environmentally responsible corporate practices, and reporting on ESG (environmental, social, and governance) metrics are all examples of practices.
Administration of Risk	Impact	Employing strategies that are effective in risk management has the ability to lower the amount of uncertainty and potential loss for investors.
	Practices	Establishing risk oversight committees, identifying and reducing risks, and keeping a proper amount of insurance coverage are all practices that should be followed.
The Compensation of Executives	Impact	The impact of this is that compensation arrangements for executives that are both transparent and based on performance can help align management's interests with those of shareholders.
	Practices	Practices include revealing the specifics of executive remuneration, linking executive pay to performance measures within the company, and requesting approval for compensation packages from shareholders.
Assurance of Conformity with the Requirements of Applicable Laws and Regulations	Impact	Companies that comply with all applicable laws and regulations have a lower risk of running into trouble with the law and regulators, which makes them more appealing to investors.
	Practices	Monitoring and guaranteeing compliance with all applicable laws and regulations, including those pertaining to the filing of financial reports, on a regular basis is one of the practices.
Planning and Strategy on a Long-Term Basis	Impact	Showing that you have a clear and workable strategy for the long term will attract investors who are seeking for opportunities for sustainable growth.
	Practices	Creating and disseminating a comprehensive strategic plan that outlines both the allocation of cash and the efforts for business expansion are practices.

Review of Literature:

When looking at the literature on corporate governance practises and their effect on attracting investment and capital, a lot of data supports the idea that good corporate governance helps a firm attract investment and money. The most important results from this study are summarised below:

Multiple studies have shown a link between good company governance and increased profits. Investors are drawn to companies with strong governance systems because they provide better returns on investment (Verma, S., 2019). Consistent with the findings of the academic community, corporate governance includes openness and disclosure as essential features(Hopt, 2011). Companies that earn investors' confidence by consistently providing detailed and reliable reports often see an uptick in capital funding(Brown & Caylor, 2021).

(Joshi, A. B., 2019) observed that corporate governance has gained significant attention and prominence within the Indian corporate landscape. Nevertheless, there have been recurring concerns regarding the efficacy of corporate governance practices in Indian corporations. From a historical perspective, corporate governance has been regarded as a collection of rules or norms that dictate the manner in which a corporation is governed. The implementation of this strategy guarantees that the corporation operates in accordance with its intended objectives, hence facilitating the attainment of desired outcomes. This framework ensures that firms are held accountable to all stakeholders, including directors, shareholders,

employees, and customers, among others. Corporate governance has been an integral aspect of the Indian corporate sector since its inception. However, the occurrence of recent corporate governance failures, such as those witnessed in the Infrastructure Leasing & Financial Services and Jet Airways cases, among others, has heightened apprehensions regarding the state of corporate governance in India.

Generally, the cost of capital for companies with good corporate governance is lower. Because of the decreased perceived risk, these businesses are able to attract equity investors prepared to accept lower necessary rates of return and get debt financing on more favourable conditions. Capital markets are dominated by institutional investors like pension and mutual funds (O'Sullivan, 2003). Investors like organisations with strong governance frameworks because they are perceived as more responsible with their money. Capital infusions of considerable size may result from attracting institutional investors (Aguilera, Filatotchev, Gospel, & Jackson, 2008).

Given that a significant number of (Sharma et.al., 2019) banks in India operate inside the public sector and encounter competition from the broader financial market, it is imperative for these banks to establish strong corporate governance systems. Banks may potentially face a regulatory requirement to engage in public share offerings, thereby facilitating a transfer of ownership. This article aims to conduct an analysis of the corporate governance practices within the banking industry by evaluating their established criteria. Furthermore, it underscores the importance of corporate governance and its connection to the Indian banking sector. Banks operating in both the private and governmental sectors are adhering to corporate governance principles in order to enhance transparency and mitigate the potential for fraudulent activities and misconduct.

Better corporate governance has been linked to greater stock prices, according to the research. Shares in firms that investors believe are well-governed and hence less likely to experience governance-related problems command a higher price (García-Castro, Aguilera, & Ariño, 2013). Agency expenses may be minimised by the implementation of corporate governance procedures such as independent boards of directors and executive remuneration plans that are in line with shareholder interests. Because of this, cash is used more effectively, and investor trust rises. Company governance refers to the design and implementation of mechanisms that aim to provide transparency, accountability, and the maintenance of an effective communication channel for disclosing and promoting a positive company culture (Vashisht, R., 2021). The primary objective of this research is to investigate the impact of corporate governance on the operational effectiveness of Indian banks. The research design employed in this study was both descriptive and analytical in nature, in order to effectively address the study objective. A total of 350 banking staff members from five private banks in India were selected as respondents for the study. The results indicate that there is a positive relationship between all of the studied variables. The independent variables of transparency and disclosure, as well as auditing and compliance with the law, exhibit a more robust positive correlation with the dependent variables of organizational financial and non-financial success. (Kumari, A., et.al., 2014). This study establishes that corporate governance exerts a substantial impact on the performance of Indian banks, hence assuming a crucial role in enhancing the overall organizational performance.

Risk management is more successful when good corporate governance processes are in place. Investors who are wary of taking unnecessary risks are drawn to businesses that have taken the time to identify and address potential threats to their operations. When making investments, foreign investors often take corporate governance norms into account (Kiranmai & Mishra, 2019). Companies that operate in accordance with generally accepted governance norms have a better chance of gaining access to international capital markets and of attracting investors from outside.

Corporate governance procedures have an impact on merger and acquisition deals. Acquisition bids for companies with solid governance frameworks are more likely to be approved, whereas bids for businesses with questionable practises may be met with shareholder opposition. Institutional investors increasingly favour governance methods that encourage long-term value development because they help provide steady and reliable returns (Roy, 2016). There has been a recent uptick in "ESG" (environmental, social, and governance) investment, and this is in line with that movement. Investment attractiveness is enhanced by the fact that compliance with corporate governance norms and standards is typically a precondition for listing on stock exchanges and access to public capital markets.

Research Gap:

Investment and capital-gathering prospects improve dramatically when a business has solid corporate governance standards, according to several studies. There are many factors at play in the connection between good corporate governance and financial success, but the data shows that well-governed businesses are more likely to attract investment. Thus, corporations that place a premium on good corporate governance are in a stronger position to attract the investors they need to develop and expand.

Objectives of the study:

To identify and assess factors influencing the corporate governance practices and their impact on attracting investment and capital.

To explore quantitatively factors influencing the corporate governance practices and their impact on attracting investment and capital.

Hypothesis of the study:

H01: There are no significant factors influencing the corporate governance practices and their impact on attracting investment and capital.

Ha1: There are significant factors influencing the corporate governance practices and their impact on attracting investment and capital.

Research Methodology:

The existing study is exploratory and primary and obtained results through responses of 158 respondents as employees. The study aims to identify and explore “the corporate governance practices and their impact on attracting investment and capital.” The existing study used SPSS software to analyse quantitatively the data collected from the respondents.

Result and discussion:

Table 2: Reliability Statistics

Reliability Statistics	
Cronbach's Alpha	N of Items
.704	7

Table 2 analysed the reliability statistics of the study and documented the estimated value of Cronbach Alpha which is .704 (N=7). The estimated value is greater than the permissible value of .60. Hence, statistical test can be applied.

Table 3: Descriptive Statistics

Descriptive Statistics					
	N	Minimum	Maximum	Mean	Std. Deviation
Need of Corporate Governance	158	1	5	3.76	1.007
Accountability and Openness	158	1	5	3.25	1.135
Safeguarding Investor Interests	158	1	5	4.51	.707
Managing Risks	158	1	5	3.83	.985
Moral Principles and Civic Duties	158	1	5	4.63	.609

Developing Sustainable Value	158	1	5	4.47	.706
Conformity with Regulations	158	1	5	4.09	.944
Valid N (listwise)	158				

Table 3 investigated the descriptive statistics of the study related to the corporate governance practices and their impact on attracting investment and capital. The findings of the study stated that Moral Principles and Civic Duties (Mean=4.63 and standard deviation=.609) followed by Safeguarding investor interests (Mean=4.51 and standard deviation=.707) are the prime factors influencing corporate governance. Accountability and Openness (Mean=3.25 and standard deviation=1.135) are the least influencing factor in the existing study that are related to the corporate governance practices and their impact on attracting investment and capital.

Table 4: One-Sample Statistics

One-Sample Statistics				
	N	Mean	Std. Deviation	Std. Error Mean
Need of Corporate Governance	158	3.76	1.007	.035
Accountability and Openness	158	3.25	1.135	.039
Safeguarding Investor Interests	158	4.51	.707	.025
Managing Risks	158	3.83	.985	.034
Moral Principles and Civic Duties	158	4.63	.609	.021
Developing Sustainable Value	158	4.47	.706	.024
Conformity with Regulations	158	4.09	.944	.033

Table 4 explored the one sample statistics of the study related to the corporate governance practices and their impact on attracting investment and capital. The findings of the study stated that Moral Principles and Civic Duties (Mean=4.63 and standard deviation=.609 and standard error=.021) followed by Safeguarding investor interests (Mean=4.51 and standard deviation=.707 and standard error=.025) are the prime factors influencing corporate governance. Accountability and Openness (Mean=3.25 and standard deviation=1.135 and standard error=.039) are the least influencing factor in the existing study that are related to the corporate governance practices and their impact on attracting investment and capital.

Table 5: One-Sample Test

One-Sample Test						
	Test Value = 0					
	t	df	Sig. (2-tailed)	Mean Difference	95% Confidence Interval of the Difference	
					Lower	Upper
Need of Corporate Governance	107.812	157	.000	3.761	3.69	3.83
Accountability and Openness	82.605	157	.000	3.246	3.17	3.32

Safeguarding Investor Interests	184.163	157	.000	4.513	4.46	4.56
Managing Risks	112.333	157	.000	3.832	3.76	3.90
Moral Principles and Civic Duties	219.450	157	.000	4.629	4.59	4.67
Developing Sustainable Value	182.690	157	.000	4.469	4.42	4.52
Conformity with Regulations	124.909	157	.000	4.086	4.02	4.15

Table 5 explored the t test statistics of the study related to the corporate governance practices and their impact on attracting investment and capital. The findings of the study stated that Moral Principles and Civic Duties (t=219.450) followed by Safeguarding investor interests (t=184.163) are the prime factors influencing corporate governance. Accountability and Openness (t=82.605) are the least influencing factor in the existing study that are related to the corporate governance practices and their impact on attracting investment and capital.

Table 6: ANOVA

ANOVA						
		Sum of Squares	df	Mean Square	F	Sig.
Need of Corporate Governance	Between Groups	59.042	4	14.761	15.563	.000
	Within Groups	784.360	153	.948		
	Total	843.403	157			
Accountability and Openness	Between Groups	72.848	4	18.212	15.084	.000
	Within Groups	999.702	153	1.207		
	Total	1072.550	157			
Safeguarding Investor Interests	Between Groups	33.566	4	8.392	18.152	.000
	Within Groups	382.314	153	.462		
	Total	415.880	157			
Managing Risks	Between Groups	107.878	4	26.970	31.989	.000
	Within Groups	697.226	153	.843		
	Total	805.105	157			
Moral Principles and Civic Duties	Between Groups	24.852	4	6.213	18.131	.000
	Within Groups	283.387	153	.343		
	Total	308.239	157			
Developing Sustainable Value	Between Groups	57.301	4	14.325	33.122	.000
	Within Groups	358.106	153	.432		
	Total	415.407	157			
Conformity with Regulations	Between Groups	209.627	4	52.407	81.625	.000
	Within Groups	530.968	153	.642		
	Total	740.595	157			

Table 6 investigated the ANOVA analyses and stated that in case of all the selected variables, the significance value is .000 which is lesser than the permissible value of .005. Therefore, dependent variable that is factors of corporate governance are significantly influence by the independent variables of the existing study.

Findings of the study

Several major findings are emphasised by the large amount of research and information that was analysed in this study:

1. Attracting investors is crucial for the success of any business, and this success is directly tied to good corporate governance standards including transparency, accountability, and ethical behaviour. Companies with solid governance frameworks are more attractive to investors because they are seen as lower risk and more likely to provide sustained profits.
2. The cost of capital is often cheaper for companies with strong corporate governance processes. Favourable conditions for debt financing and equity investments are the outcome of investors' willingness to accept lower necessary rates of return for companies that investors trust.
3. Companies with good governance standards tend to have better market values. The correlation between good corporate governance and financial success is further strengthened by the fact that investors are ready to pay a premium for stock in such organisations.
4. Companies with solid governance systems are more likely to attract institutional investors, who play a significant role in the capital markets. A company's ability to raise funds is greatly improved when institutional investors get interested in its stock.
5. Better risk management, together with lower agency costs and more resilience in the face of adversity, is a direct result of sound corporate governance standards. Investors are more at ease knowing this danger has been mitigated.
6. Companies that follow best practises in corporate governance have an easier time raising money from investors overseas.
7. Investors who want to include ethical and responsible factors into their investment choices are increasingly drawn to firms whose governance procedures are aligned with environmental, social, and governance (ESG) values.
8. Investors who want steady, lasting returns will appreciate governance methods that prioritise value creation above profit maximisation in the near term.
9. In order to get access to public capital markets and be listed on stock exchanges, companies must frequently demonstrate that they comply with corporate governance legislation and standards. For businesses actively seeking investments, compliance with these criteria is essential.

Conclusion

In conclusion, there is a deep and nuanced connection between corporate governance procedures and their effect on luring investors and financiers. Good corporate governance standards are crucial to a company's capacity to attract investment and capital, and they go well beyond simply compliance with legal mandates. Companies that put a premium on good governance practises have a better chance of achieving long-term development and success in today's highly competitive business environment. Effective corporate governance procedures are projected to remain an important feature for firms of all sizes and in all sectors in attracting investment and capital as the investment environment continues to change.

References:

1. Aguilera, R. V., Filatotchev, I., Gospel, H., & Jackson, G. (2008). An organizational approach to comparative corporate governance: Costs, contingencies, and complementarities. *Organization Science*, 19(3), 475–492. <https://doi.org/10.1287/orsc.1070.0322>
2. Almaqtari, F. A., Al-Hattami, H. M., Al-Nuzaili, K. M. E., & Al-Bukhrani, M. A. (2020). Corporate governance in India: A systematic review and synthesis for future research. *Cogent Business and Management*, 7(1). <https://doi.org/10.1080/23311975.2020.1803579>
3. Brown, L. D., & Caylor, M. L. (2021). Corporate governance and firm valuation. *Journal of Accounting and Public Policy*, 25(4), 409–434. <https://doi.org/10.1016/j.jaccpubpol.2006.05.005>

4. García-Castro, R., Aguilera, R. V., & Ariño, M. A. (2013). Bundles of firm corporate governance practices: A fuzzy set analysis. *Corporate Governance: An International Review*, 21(4), 390–407. <https://doi.org/10.1111/corg.12024>
5. Hopt, K. J. (2011). Comparative corporate governance: The state of the art and international regulation. *American Journal of Comparative Law*, 59(1), 1–73. <https://doi.org/10.5131/AJCL.2010.0025>
6. Joshi, A. B. (2019). Corporate Governance in India: Contemporary Issues and Challenges. *Kaav International Journal of Law, Finance & Industrial Relations*, 6(1), 36-38.
7. Kumari, A., & Aggarwal, V. K. (2014). Corporate Governance Compliance: A Case Study of Infosys. *Kaav International Journal of Arts, Humanities & Social Science*, 1(1), 181-188.
8. Kiranmai, J., & Mishra, R. K. (2019). Corporate Governance Practices in Listed State-owned Enterprises in India: An Empirical Research. *Indian Journal of Corporate Governance*, 12(1), 94–121. <https://doi.org/10.1177/0974686219849760>
9. Nalina, K. B., & M, R. H. (2021). A Study on Under-Pricing of Initial Public Offering (IPO) in Indian Capital Market. *International Journal for Innovative Research in Science & Technology*, 9(11), 297–304.
10. Nugroho, M. (2021). Corporate governance and firm performance. *Accounting*, 7(1), 13–22. <https://doi.org/10.5267/j.ac.2020.10.019>
11. O’Sullivan, M. (2003). The political economy of comparative corporate governance. *Review of International Political Economy*, 10(1), 23–72. <https://doi.org/10.1080/0969229032000048899>
12. Pillania, R. K. (2012). Corporate governance in India: Study of the top 100 firms. *Journal of Applied Economic Sciences*, 7(1), 87–92.
13. Roy, A. (2016). Corporate Governance and Firm Performance: A Study of Indian Listed Firms. *Metamorphosis: A Journal of Management Research*, 15(1), 31–46. <https://doi.org/10.1177/0972622516629032>
14. Singh, R., & Bansal, R. (2020). Corporate Governance in Indian Banking Sector: An Analysis. *Journal of Xi'an University of Architecture & Technology*, 12(2), 476–493.
15. Sharma, S., & Gupta, V. (2019). Corporate Governance in Indian Banking Sector. *National Journal of Arts, Commerce & Scientific Research Review*, 6(1), 114-119. <https://www.kaavpublications.org/abstracts/corporate-governance-in-indian-banking-sector>.
16. Sweta Agarwal. (2020). Corporate Governance and Listing Returns of Indian IPOs : An Empirical Investigation. *India Quarterly: A Journal of International Affairs*, 8(2), 22–27.
17. Verma, S. (2019). Corporate Governance in the Banking and Financial Organisations. *Kaav International Journal of Economics, Commerce & Business Management*, 6(1), 21-24.
18. Vashisht, R. (2021). Influence of Corporate Governance on Organizational Performance in Indian Banks- An Empirical Study. *Kaav International Journal of Economics, Commerce & Business Management*, 8(1), 40-45. <https://doi.org/10.52458/23484969.2021.v8.iss1.kp.a9>

Tomato Arrival and Price Prediction of Indian Agricultural Produce Market Committee (APMC)

¹Dr. B. Venugopal, ²Dr K. C. Prakash, ³Dr. Biswo Ranjan Mishra, ⁴R. Mythily, ⁵Dr. Rakhi Gupta, ⁶Dr. Khaja Mohinuddeen J

Abstract:

India is a heritage filled agriculture-dependent country. It's necessary to modernize our ancient agricultural practices by providing appropriate circumstances to the farmers. The agricultural transformation is often done via dynamic business proposition that could be a techno-economic method which can be accelerated easily. With the evident development in production technology, input supply, and infrastructure, we are able to see the upward trend in arrivals. The key constraints or factors that influence the prices within the market are due to the arrivals of the selective commodities and their competitive crops. The objectives of this paper is (i) To investigate the trend in arrivals of tomato in Kolar and Chintamani market, (ii) To estimate the trend in costs of tomato in Kolar and Chintamani market and (iii) To forecast the market-wise costs of tomato. The analysis reveals the fallouts of the findings: variations in the price level, the government necessity to create buffer stock schemes that may facilitate to stabilize the market value of tomatoes by getting hold suppliers who merchandise once harvests square measure masses, and marketing stocks of the merchandise onto the market once suppliers square measure low. These methods needed high finish technology and infrastructure. The problem of price variations and profit variations are often restrained by tomato retailers by having appropriate inventory management skills. Therefore, to avoid overstocking of tomatoes at a time within the store. This can be attributable to the biodegradable nature of tomato and overstocking of tomato causes spoilage predominantly due to lack of storage facilities. Hence precise cold storage should be constructed. The big data should be used to developing tools using artificial intelligence, machine learning to enhance planning and marketing services.

Keywords: Consumer Behaviour, Tomato, Price Prediction, Market Prediction

JEL Classification: Q10,Q11, Q12,Q13,Q14,Q18

¹Assistant Professor, (Finance & Accounting), Indian Institute of Plantation Management Bengaluru (An Autonomous Institution of the Ministry of Commerce & Industry, Govt), Jnana Bharathi Campus P.O., Malathalli, Bangalore - 560056, Karnataka, INDIA.

²Assistant Professor, Department of Agricultural Business, Indian Institute of Plantation Management (IIPM), Bangalore, India, Orcid Id: 0000-0001-5621-4516

³Assistant Professor, Department of Commerce, DDCE, Utkal University,

⁴Assistant Professor, Department of MBA, St. Joseph's College of Engineering, Chennai, India, Orcid id: 0009-0008-7335-5212

⁵Associate Professor, Department of Economics, Vivek Anand Global University, guptarakhi2006@gmail.com

⁶Associate Professor, Management Studies, Ballari Institute of Technology and Management (Autonomous), Ballari, Orcid id: 0000-0002-7766-0504

INTRODUCTION

Agricultural marketing plays a major role in moving of commodities from the farm producer to the consumer and stabilizing the price. The scheduled increase in agricultural production must be corresponding with variations in demand and supply for agric significantly regardless of the quantity of the marketable surplus generated with the farmers. Therefore, in relation to enhanced seed and fertilizer in contemporary agriculture, marketing was rightly regarded as an important input. Instability in price and earnings is common for agricultural products and they fluctuate more than the other industrial goods. Erratic and highly elastic production price leads to an instability in the agricultural commodity prices which thereby influences the income levels of the farmers. This results in the human and the political consequences in a large way. To feed the growing population surplus production in food grain is vital and India has achieved it. But the need for the self-sufficiency in the horticultural produce is equally important to maintain the health of the growing population. The vegetables, regarded as the protective foods, have short duration of growth but has high production and productivity. They can easily fit in diverse locations and systems of farming in addition to being profitable and a high employment generator. India is the world's **second**-largest vegetable producer, contributing around 7.18% to vegetable production worldwide and produces more than 40 types of vegetables belonging to different families. (Paarlberg, Robert 1997)

Tomato Global Scenario

Tomato, belonging to the Solanaceae family, is a major crop that is produced in India and the world with a global production of 152.9 million tons. Commonly referred to as the 'poor man's orange', it is highly nutritious as it has a wide range of essential nutrients. After potato and sweet potato, it is the third largest vegetable crop in the world. Since pre-historic times, tomatoes have been used as food by the people of Central and South America. The World production was 241.92 million tonnes of tomato from an area of 58.82 lakh hectares (FAO STAT) in 2017-18. China is the largest tomato producing country in the world, almost contributing for 24.6 % of world's tomato production. During 2017-18, China stood first with annual production of 59.63 million tonnes followed by India with 20.71 million tonnes, Turkey with 12.75 million tonnes, USA with 10.91 million tonnes, Egypt with 7.30 million tonnes and Iran (Islamic Republic of) with 6.18 million tonnes. These six countries contributed for around 73.16 % of world's tomatoes production.

Tomato Indian Scenario

Tomato has an important place in the country's vegetable production. Area under tomato in India was 8.08 lakh hectares accounting for 7.86% of the total vegetables crop acreage. Annual tomato production in India amounted to 19.69 million tonnes (NHB, 2016-17), 11.25 per cent of total vegetable production. However, the area under tomato has been increasing gradually as production fluctuated owing to weather-related factors. In India, Madhya Pradesh is the leading state that produces 31.02 lakh tonnes of tomato from an area of one lakh hectares. Karnataka is India's 2nd largest tomato producing state with 21.38 lakh tonnes of tomato from an area of 0.63 lakh hectares.

Tomato Karnataka Scenario

Tomato is produced throughout the year in Karnataka. The major tomato producing areas are Kolar, Chikballapur, Bangalore, Tumkur, Hassan, Haveri, and Davangere. In the state, the total area under tomato was 63.73 thousand hectares with a production base of 21.38 lakh tonnes in 2016-17 (Karnataka Stat, 2016-17). An analysis of arrivals and prices of tomatoes would assist to determine income, constraints and supply response. So, it is essential to analyze the wide fluctuations in prices of tomato and the relationship between arrivals and prices. Market integration describes the relationship between two spatially or temporarily separated markets. The process of determining prices are completely interdependent in an integrated market. The market integration research findings possibly suggest the manufacturers on how much, where and when to sell which will consecutively create an impact on their production policies and therefore the allocation of resources.

REVIEW OF LITERATURE:

Some of research works reveals spatial equilibrium model with endogenous prices is contracted and solve by quadratic mathematical programming method. Six scenarios involving the impacts from transportation costs, tariff, and North American Free Trade Agreement (NAFTA). Impacts on production, consumption, trade flows, prices, and net welfare. Credit to NAFTA, Mexico became the most tomato exporter to the USA. (Impacts on production, consumption, trade flows, prices, and net welfare. Due to NAFTA, Mexico became the main tomato exporter to the USA 2003). Price transmission in Tomatoes. It reveals explores the characteristics of spatial price movements for fresh vegetables special tomato. This is often very useful to policy considerations for fresh vegetables sector (Santeramo, Fabio Gaetano 2015). Results and projection of tomato price in SERBIA. It found that tomato is tremendously most essential vegetable crops in Serbia and average annual production of tomato has been about 174,000 tones. This study is analysis of the changes and thus the longer-term tendencies of the price parameters of tomato in Serbia with aim of forecaster the wheat and tomato price. (Ivanić, Dragan; Mutavdžić, Beba; Novković, Nebojša; Vukelić, Nataša 2015). Price transmission in tomato sector after the Arab Spring. It explains positive relationship with producer, wholesaler and retailer tomato prices. Throughout tremendous market measures that less price increases with supply chain price decline (Ahmed, Osama 2018). North America tomato market. It found endogenous prices are contracted and solve by quadratic mathematical programming method. Six scenarios involving the impacts from transportation costs, and tariff. Impacts on production, consumption, trade flows, prices, and net welfare. Recognition to NAFTA, Mexico became the most tomato exporter to the USA (NAFTA, Mexico became the main tomato exporter to the USA 2003). Influence of layer on behavior of greenhouse tomatoes in transition from conventional to biological growing greenhouse tomato production (Petkova, Valentina; Filipov, Stoyan; Kostadinov, Kostadin 2013). Rain in Spain falls and UK tomato prices soar. It reveals that heavy rains in Spain have prevented tomato growers from planting, delaying the 2011 tomato season, and raising the prospect of higher prices for both fresh and processed tomatoes (Glotz, Julia 2011). It reveals that consumers paid \$0.25/lb more for organic fresh tomatoes in the New York Philadelphia market. The organic premiums are estimated to be \$0.14/lb in the Chicago. Francisco markets and \$0.29/lb in the Antonio market. Furthermore, tomato prices consumers paid in 2004 varied by household characteristics, including income, age, and therefore the race and ethnicity of the top of the household (Chung L. Huang & Bing-Hwan Lin. 2007). Research explains the risk in investment in greenhouse tomato production in florida. And concludes behavior if prices and demand in production impacts the risk

availability this production. (Asci, Serhat; VanSickle, John J.; Cantliffe, Daniel J. 2014). It reveals that tomato prices glut in the U.S. due to whether, tomato growers in Florida developing their crop. In Florida the price farmers receive for a 25-pound box has fallen from \$30 to \$5 (Pleven, Liam, and Carolyn Cui. 2010). Tomato prices rocket as season ends prematurely. It reveals that wholesale price movement of several agricultural products worldwide includes tomato, onion and banana (Grocer 2014) research evaluated and recommended evidence rejecting the presence of unit roots at all seasonal frequencies for agriculture; and vegetables. (Aviralkumartiwari, Subhendu Dutta and Aruna Kumar Dash 2017). Paper shows agricultural price policy and stable price environment to farmers in case of pulses and suggests reviewing the pulses by making it sensitive to prevailing market prices. (Ashutosh Kr. Tripathi 2017) It found that Impact of prices influence the income of farmers towards cost of production like cultivation. This research reveals that how best utilized cost and projecting profits earned by farmers in Indian scenario. (Ashutosh Kumar Tripathi 2013). It depicts agro wellbeing practices. (P. Weligamage) and Competitive revenue price strategies in irrigation cost (P. Weligamage).

The research offers information on how tomato prices would be in different months of the year. Such information provides farmers hints to the price behavior in order to make production decisions that are essential. The objectives of the study are to analyze the trend in arrivals of tomato in Kolar and Chintamani market, to estimate the trend in prices of tomato in Kolar and Chintamani market and to forecast the market-wise prices of tomato.

RESEARCH METHODOLOGY:

This section introduces the methodology used in the research which provides insights with on markets, data sources, nature and also the analytical methods applied for the assessments. The crop selected for the research was tomato. According to the Karnataka State Agricultural Marketing Board (KSAMB), Bangalore, Chikkaballapura, Chintamani, Kolar, Bagepalli and Srinivasapura are the main tomato markets in Karnataka. Because of the availability of continuous time series data for the study period, so I have selected Chintamani and Kolar markets were chosen. Data from secondary sources were acquired for the research. Data such as month, time of arrival, and the price of tomato were grouped from the Krishimaratavahini official website by the Karnataka State Agricultural Marketing Board (KSAMB) Bangalore. KSAMB receives the data from various markets across the state from the corresponding Agricultural Market Committees (APMC 'S). The Board and APMC 'S keep the website up to date by maintain the data of arrival and the prices of regulated agricultural commodities on a daily, weekly, monthly, annual basis. Arrival data refers to total arrivals in quintals during a market place during the month. The worth data used here denotes the month's modal price. Modal price is regarded as superior to the monthly average price, because it epitomizes the commodities marketed on a major percentage in a specific market at a particular month. For the markets under study, the monthly total arrivals and the modal prices data were composed from 2008 till 2018 (11 years). A brief description of statistical tools employed for this study was presented in this section. For studying the short-term, long-term and other periodic fluctuations in arrivals and price of tomato for each market, Time series analysis was employed; and for forecasting of arrivals and price, trend equation model was used.

RESULT AND DISCUSSION

Trend of tomato arrival and its price in carefully chosen markets of Karnataka

Time series analysis was employed to review the trends of tomato arrival, its pricing and its review in selected markets, linear models (linear in parameter) viz. linear model (straight line), were fitted to the total annual data of arrivals and average prices for the period of 5 years from 2015 to 2019.

To analyze any time series data, we have to check for data structure for their movements in graph. In current study movement of arrivals and prices are represented as below table 1 and graph 1.

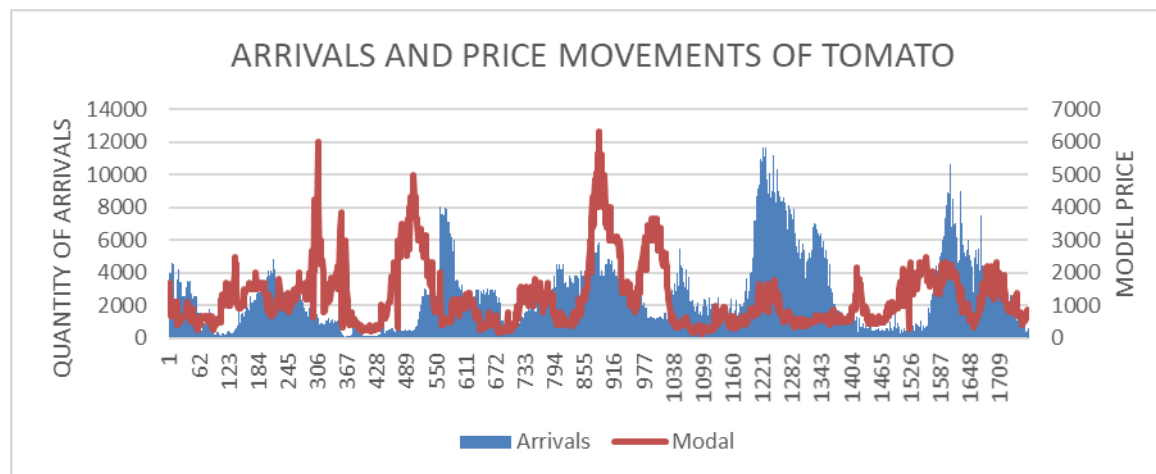
Table 1: The below table represents the sum of arrivals and average model price for Chintamani market from the year 2015 to 2019.

Months	2015		2016		2017		2018		2019	
	Sum of Arrivals	Avg of Modal	Sum of Arrivals	Avg of Modal	Sum of Arrivals	Avg of Modal	Sum of Arrivals	Avg of Modal	Sum of Arrivals	Avg of Modal
Jan	93994	864	5315	1541	30325	825	81697	388	21618	1185
Feb	76113	678	11510	376	44150	1400	44926	275	12547	512
Mar	24464	600	3535	302	66150	1297	40574	426	14929	817
Apr	6280	735	13015	1014	107410	614	32015	605	14115	1464
May	13870	1444	12960	2742	80905	640	66311	585	17760	1902
Jun	45435	1322	26575	3712	111563	2062	244785	974	84207	1766

Jul	84150	1558	78410	1969	124855	4763	256288	1283	219636	2046
Aug	103235	1007	187415	708	119400	2971	229826	638	160285	1122
Sep	62380	1124	93600	1035	77590	1278	138550	468	117255	932
Oct	53205	1567	73200	896	55005	2560	170118	575	88662	1790
Nov	32519	2447	79550	476	33149	2911	80713	624	65525	1199
Dec	24065	1588	38510	306	65215	904	33095	609	24916	775
Grand Total	619710	1244	623595	1261	915717	1849	1418898	622	841455	1302

Source:KSAMB &APMC'S

Graph 1: Indicates the arrivals and price movements of tomato from 2015-2019.



In the above graph we can say that movements of sum of arrivals and average model price are in trend structure. Graph movement indicates inverse relationship.

Analysis of trend in arrivals of tomato in Chintamani market.

To analyze the trend in arrivals of tomato in Chintamani market, five models were fitted and estimates of the parameter of the fitted models are given in Table 4.1. The estimates of parameters of the Trend equation were found to be significant. The fitted trend equation is given below.

$Y = a + b \cdot X$, Where, Y = predicted values of arrivals at time point t , X = price, a and b = intercept and slope respectively.

RMSE and R^2 value were considered to check the adequacy of the fitted models. highest R^2 value (60 %) among the significant models. Hence, this model is adequately fitted compared to other models. Actual and predicted values of arrivals by the trend equation are shown in graph 2 and 3.

To analyze the arrival and price trend, firstly we have to check the correlation between the arrivals and price. So for current study arrivals and price relation is 60 percent which represents that there is a relation between arrivals and prices in Chintamani market. The findings for current correlation study are represented as below.

Table 2: Arrival and price trends

Year	Jan ARR	Price	Price Trend
2015	93994	864.39	1062.98
2016	5315	1540.75	1011.84
2017	30325	825.17	960.70
2018	81697	388.28	909.57
2019	21618	1184.93	858.43
2020	57340		807.29

Source:Data Computation in Excel

To check the correlation between sum of arrivals and average model price we used regression technique, results are represented in below output.

Table 3: Correlation between sum of arrivals and average model

SUMMARY OUTPUT						
Regression Statistics						
Multiple R	0.77469083					
R Square	0.600145883	60%				
Adjusted R Square	0.466861177					
Standard Error	28446.91668					
Observations	5					
ANOVA						
	df	SS	MS	F	Significance F	
Regression	1	3643736093	3643736093	4.502736295	0.123951245	
Residual	3	2427681206	809227068.7			
Total	4	6071417299				
	Coefficients	Standard Error	t stat	P -value	Lower 95%	
Intercept	113910.0628	34181.11257	3.332544034	0.044634514	5130.507375	
X Variable 1	-70.0739051	33.02311707	-2.121965196	0.123951245	-175.168202	
RESIDUAL OUTPUT						
Observation	Predicted	Residuals	Std Residuals			
1	53339.0834	40654.9166	1.650240503			
2	5943.693504	-628.6935041	-0.025519558			
3	56087.00938	-25762.00938	-1.045716358			
4	86702.05688	-5005.056881	-0.20316233			
5	30877.15684	-9259.156839	-0.375842258			

Source: Data Computation in Excel

Here it found the relation between sum of arrivals and average model price as **60** percent.

Table 4: Analysis of trend in arrivals of tomato in Kolar market

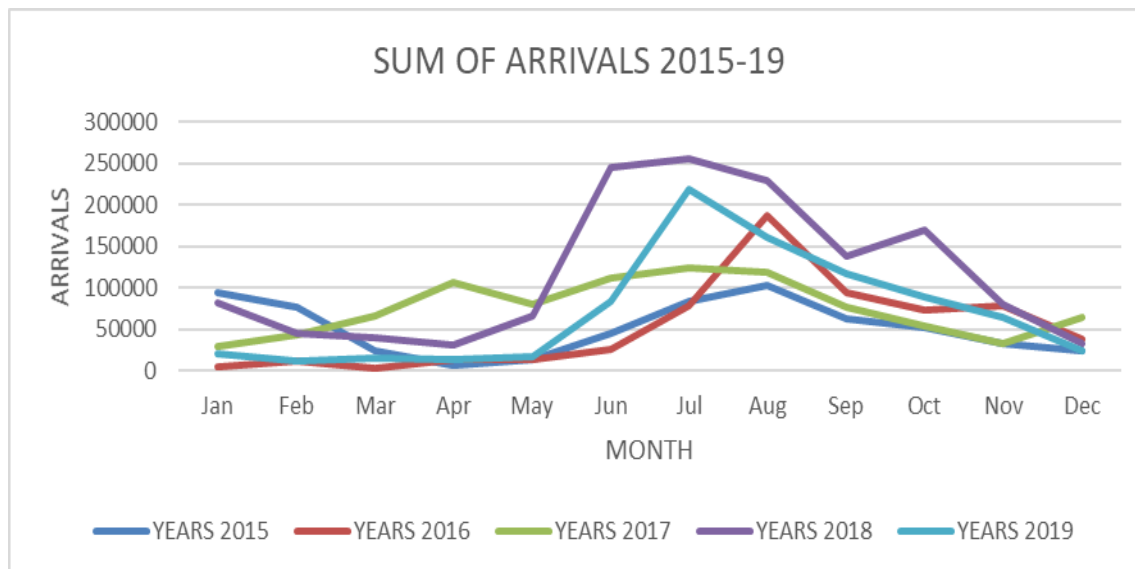
Sum of Arrivals Month	2015	2016	2017	2018	2019	Grand Total
Jan	93994	5315	30325	81697	21618	232949
Feb	76113	11510	44150	44926	12547	189246
Mar	24464	3535	66150	40574	14929	149652
Apr	6280	13015	107410	32015	14115	172832
May	13870	12960	80905	66311	17760	191806
Jun	45435	26575	111563	244785	84207	512565
Jul	84150	78410	124855	256288	219636	763339
Aug	103235	187415	119400	229826	160285	800161
Sep	62380	93600	77590	138550	117255	489375
Oct	53205	73200	55005	170118	88662	440190
Nov	32519	79550	33149	80713	65526	291456
Dec	24065	38510	65215	33095	24916	185801
Grand	619710	623595	915717	1418898	841455	4419375

Total						
--------------	--	--	--	--	--	--

Source:KSAMB &APMC'S

This table represents sum of arrivals of tomato from the year 2015 - 2019 and their annual grand total.

Graph 2: Arrivals trend of Chintamani market.



In this graph y-axis represents sum of arrivals (in quintals) and x-axis represents months of respective years. It shows that in the month of July 2018(256288) accounts for height arrivals compare to rest of all other months from 2015 to 2019. Followed by July 2019 (219636), August 2016 (187415), July 2017 (124855) and August 2015 (103235) respectively.

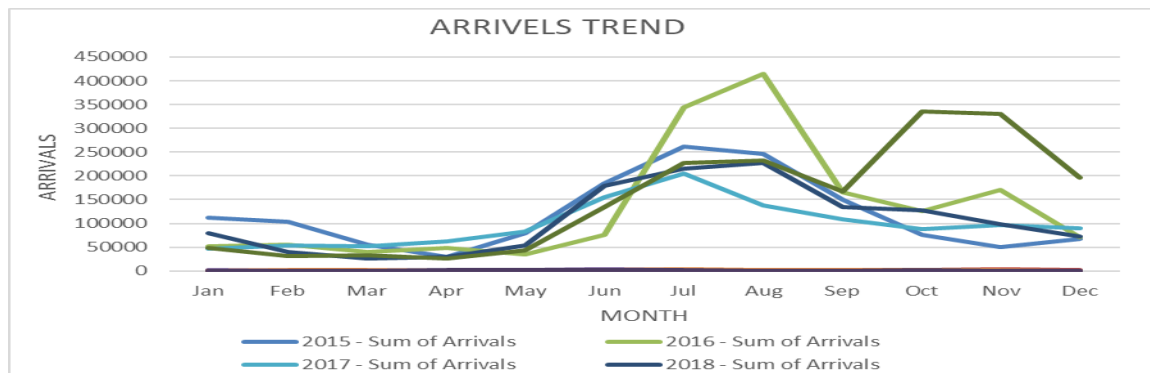
Table 5:The trend in arrivals of tomato in Kolar market

Sum of Arrivals Month	2015 Sum of Arrivals	2016 Sum of Arrivals	2017 Sum of Arrivals	2018 Sum of Arrivals	2019 Sum of Arrivals
Jan	111412	52005	46372	79821	48075
Feb	104112	55242	54138	40313	31033
Mar	54665	40751	51832	26055	32880
Apr	29245	49054	63080	29897	26500
May	79384	34548	83634	53209	42554
Jun	183583	76569	155826	178534	134009
Jul	262256	343436	204930	215663	227749
Aug	245537	415086	137364	227224	231932
Sep	149524	165268	107952	134424	167368
Oct	75458	126501	87793	127060	334885
Nov	49633	170403	97298	98792	330348
Dec	66877	70516	90183	72559	195718
Grand Total	1411686	1599379	1180402	1283551	1803051

Source:KSAMB &APMC'S

This table represents sum of arrivals of tomato from the year 2015 to 2019 and their annual grand total.

Graph 3: arrivals trend of Kolar market.



This graph indicates highest arrivals accounted for 415086 quintals in 2016 august followed by 262256 (July 2015), 334885 (October 2019), 215663 (July 2018) 204930 (July 2017) respectively.

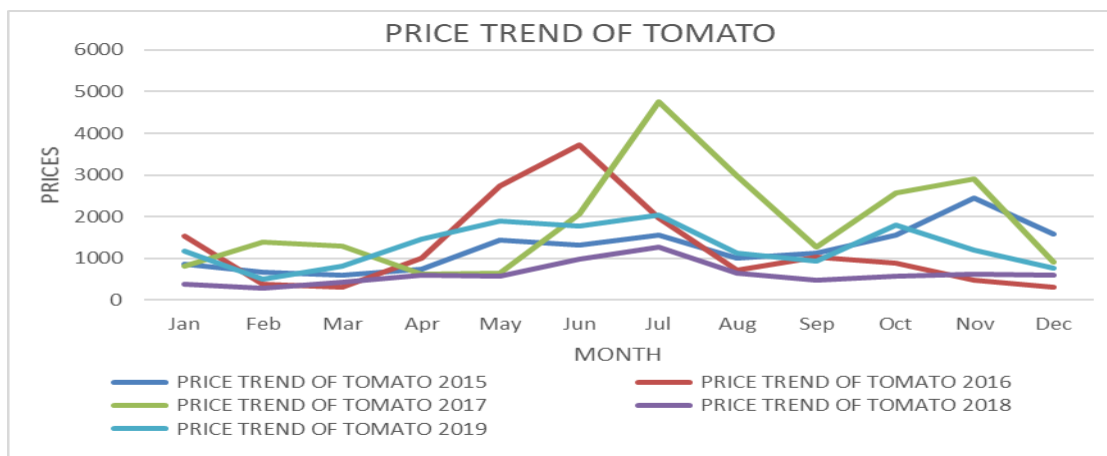
Table 6: To analyze the Chintamani market price trend of tomato.

Sum of Arrivals Month	2015	2016	2017	2018	2019
Jan	864	1541	825	388	1185
Feb	678	376	1400	275	512
Mar	600	302	1297	426	817
Apr	735	1014	614	605	1464
May	1444	2742	640	585	1902
Jun	1322	3712	2062	974	1766
Jul	1558	1969	4763	1283	2046
Aug	1007	708	2971	638	1122
Sep	1124	1035	1278	468	932
Oct	1567	896	2560	575	1790
Nov	2447	476	2911	624	1199
Dec	1588	306	904	609	775

Source: KSAMB & APMC'S

This table represents the average model price of tomato from the year 2015 to 2019 and their annual grand total.

Graph 4: Analyze the Chintamani market price trend of tomato in linear line graph.



This graph indicates highest average model price accounted for 4763 rupees per quintal in 2017julyfollowed by 3712 (June 2016), 2447(November 2015), 2046 (July 2019) and 1283 (July 2018) respectively.

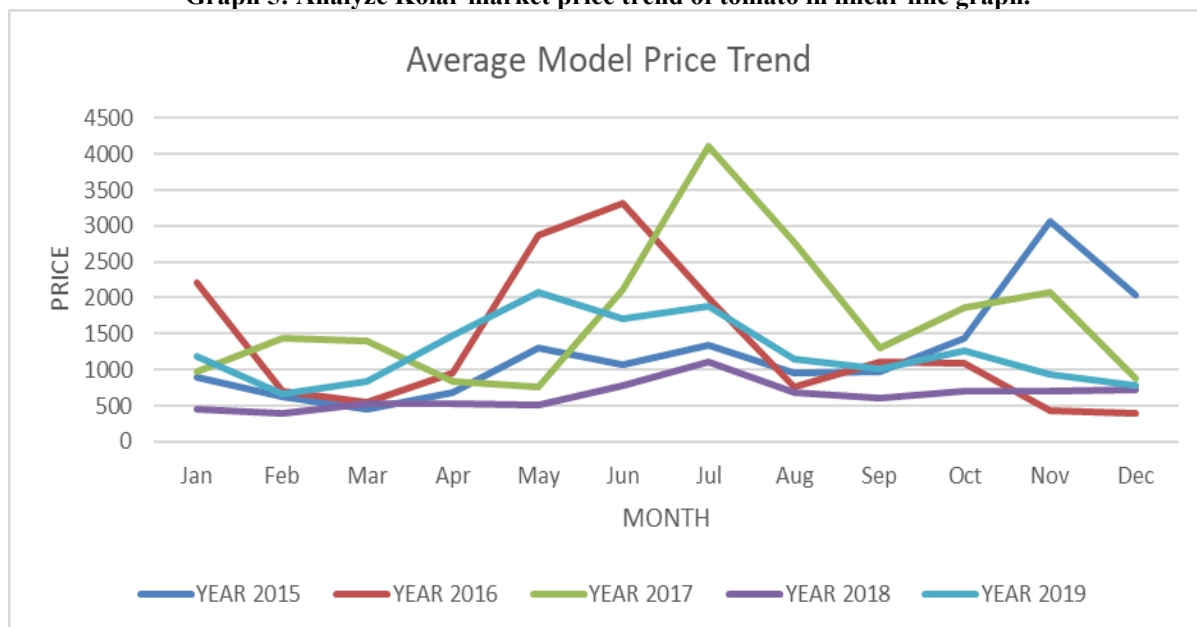
Table 7 :Analyze Kolar market price trend of tomato

Sum of Arrivals Month	2015	2016	2017	2018	2019
Jan	888	2207	975	460	1185
Feb	623	703	1443	388	656
Mar	447	549	1391	523	842
Apr	681	947	839	526	1483
May	1296	2875	758	516	2073
Jun	1062	3320	2120	789	1708
Jul	1346	1999	4115	1115	1884
Aug	955	760	2769	684	1156
Sep	984	1107	1312	597	1010
Oct	1441	1098	1866	710	1268
Nov	3056	437	2079	701	930
Dec	2041	402	884	722	771

Source:KSAMB &APMC'S

This table represents the average model price of tomato from the year 2015 to 2019 and their annual grand total.

Graph 5: Analyze Kolar market price trend of tomato in linear line graph.



This graph represents the average model price of tomato from the year 2015 to 2019 and their highest average model price accounts is 3056 in November 2015, 3320 in June 2016, 4115 in July 2017, 1115 in July 2018, 2073 in May 2019 respectively.

To forecast market –wise prices of tomato.

Table 8: Average model price trend of tomato (Price forecast Chintamani market).

Sum of Arrivals Month	2015	2016	2017	2018	2019	2020
Jan	864	1541	825	388	1185	807
Feb	678	376	1400	275	512	518
Mar	600	302	1297	426	817	856
Apr	735	1014	614	605	1464	1201
May	1444	2742	640	585	1902	1090
Jun	1322	3712	2062	974	1766	1412
Jul	1558	1969	4763	1283	2046	2411
Aug	1007	708	2971	638	1122	1337
Sep	1124	1035	1278	468	932	682
Oct	1567	896	2560	575	1790	1515
Nov	2447	476	2911	624	1199	827
Dec	1588	306	904	609	775	440

Source:KSAMB &APMC'S

In this table we got the forecasted average model price values for year 2020, where July months accounts for 2411 rupees for one quintal of tomato which is ranks highest average price in the year 2020 and in the month December 2020 accounts for 440 rupees per quintal of tomatoes which is least average model price. And its graph is represented below.

Graph 8: Analyze Chintamani market price forecast trend of tomato in linear line graph.

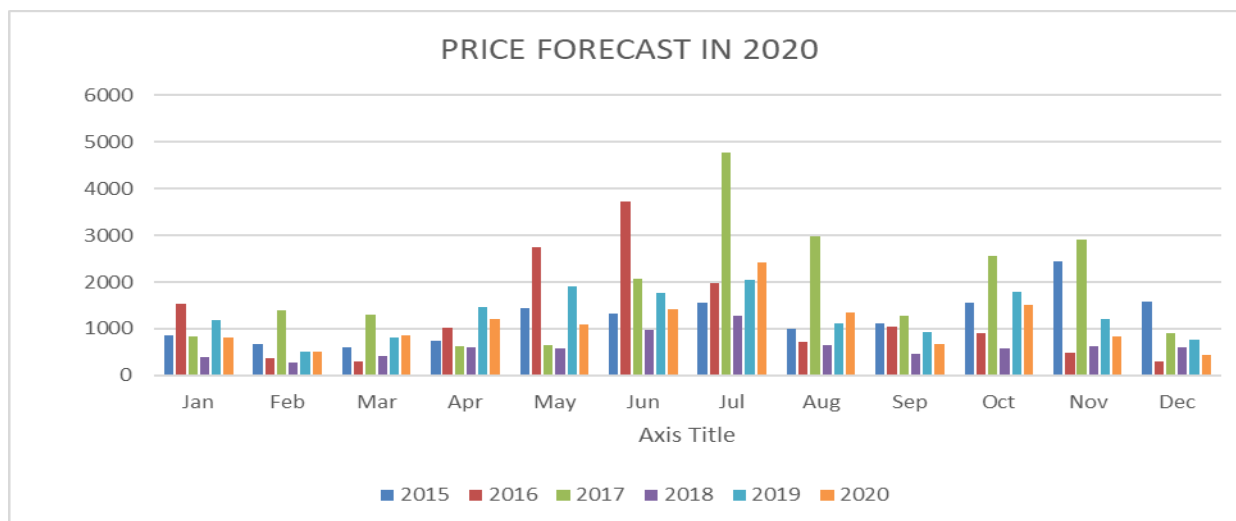


Table 9: Average model price trend of tomato (Price forecast Kolar market).

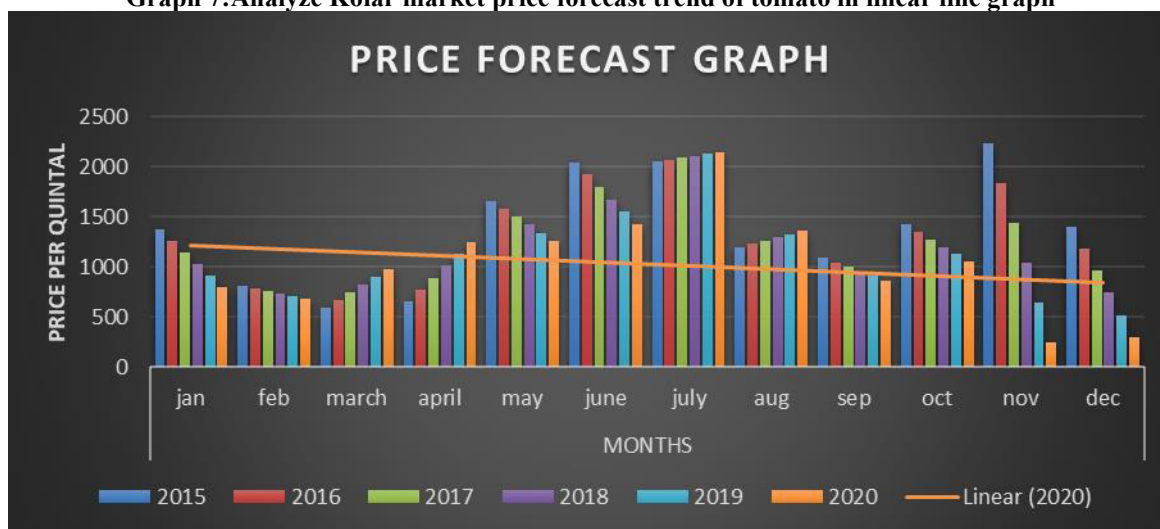
Sum of Arrivals Month	2015	2016	2017	2018	2019	2020
Jan	1374	1258	1143	1028	912	797
Feb	812	787	762	737	713	688
Mar	597	674	750	827	903	980
Apr	658	777	895	1014	1132	1250

May	1665	1584	1504	1423	1343	1262
Jun	2048	1924	1800	1676	1552	1428
Jul	2054	2073	2092	2111	2130	2149
Aug	1200	1232	1265	1297	1330	1362
Sep	1093	1048	1002	956	911	865
Oct	1423	1350	1277	1203	1130	1057
Nov	2238	1839	1440	1042	643	244
Dec	1408	1186	964	742	520	298

Source:KSAMB &APMC'S

The above table represents the price trend of tomato in the year 2020. In this table we got the forecasted average model price values for year 2020, where July months accounts for 2149 rupees for one quintal of tomato which is ranks highest average price in the year 2020 and in the month December 2020 accounts for 298 rupees per quintal of tomatoes which is least average model price. And its graph is represented below.

Graph 7:Analyze Kolar market price forecast trend of tomato in linear line graph



The graph 7 indicates the price forecast trend of tomato in Kolar market in which July month accounts for highest price forecast trend and December month accounts for least value over the year.

CONCLUSIONS

Time series analysis was employed to study the trend in arrivals of tomato. To examine the trend of tomato arrivals followed by the prices of tomato in selected markets, linear models (linear in parameter) viz. linear model (straight line), were fitted to the total annual data of arrivals and average prices for the period of 5 years from 2015 to 2019. To analyze any time series data, we have to check for data structure for their movements in graph. In current study movement of arrivals and prices are represented as in table 4 & 5 and graph 3 & 4. To analyze the trend of tomato arrivals and also the prices of tomato in selected markets, linear models viz. linear model (straight line), Quadratic model, Cubic model and Exponential model, and nonlinear model i.e., sigmoid model were fitted. RMSE and R^2 values were considered to check the adequacy of the fitted models. Among the fitted model's exponential model, quadratic model, quadratic model and sigmoid models are best fitted to prices for Kolar and Chintamani markets respectively. The linear model was best fitted among the fitted models for prices of cotton in all the four selected markets. For forecasting of tomato prices in all the selected markets, the Holt Winter's exponential model and ARIMA models were fitted. The estimates of Holt Winter's model were found to be significant for all the selected markets hence forecasting of prices was done by this method. From the best fitted model forecasting was done for 12 months ahead.

Linear and nonlinear models viz. linear, quadratic, cubic, exponential and sigmoid were some of the models fitted to evaluate the trend in arrivals and prices of tomato. This study, 5 years monthly arrivals and prices data were collected. For arrivals of tomato, both linear and nonlinear models were best fitted whereas for prices of tomato only linear model was best fitted. The results of this study indicate that there was a huge variation over the different years in the prices of tomato in all the markets. For forecasting of tomato prices, Holt's winter model and ARIMA model were considered in that estimates of Holt Winter's

model were significant in for Kolar and Chikballapure the markets. Best fitted Holt Winter's models selected for different markets. Hence, Holt Winter's models are best to forecast the tomato prices in selected markets.

References:

1. Kikuchi, Masao, Randolph Barker, M. Samad, and Parakrama Weligamage. "Comparative advantage of rice production in Sri Lanka with special reference to irrigation costs." *Development in the Rice Economy* (2002): 343-368.
2. Kikuchi, Masao, Parakrama Weligamage, Randolph Barker, Madar Samad, Hiroichi Kono, and H. M. Somaratne. "Agro-well and pump diffusion in the Dry Zone of Sri Lanka: Past trends, present status and future prospects." (2003).
3. Adanacioglu, Hakan, and Murat Yercan. "An analysis of tomato prices at wholesale level in Turkey: an application of SARIMA model." *Custos e@ gronegocio on line* 8, no. 4 (2012): 52-75.
4. Ahmed, Osama. "Vertical price transmission in the Egyptian tomato sector after the Arab Spring." *Applied Economics* 50, no. 47 (2018): 5094-5109.
5. Asci, Serhat, John J. VanSickle, and Daniel J. Cantliffe. "Risk in investment decision making and greenhouse tomato production expansion in Florida." *International Food and Agribusiness Management Review* 17, no. 1030-2016-83033 (2014): 1-26.
6. Huang, Chung L., and Biing-Hwan Lin. "A hedonic analysis of fresh tomato prices among regional markets." *Applied Economic Perspectives and Policy* 29, no. 4 (2007): 783-800.
7. Guajardo, Ramon G., and Homero A. Elizondo. "North American tomato market: A spatial equilibrium perspective." *Applied economics* 35, no. 3 (2003): 315-322.
8. Vijai, C., Bhuvaneswari, L., Sathyakala, S., Dhinakaran, D. P., Arun, R., & Lakshmi, M. R. (2023). The Effect of Fintech on Customer Satisfaction Level. *Journal of Survey in Fisheries Sciences*, 10(3S), 6628-6634.
9. R. Arun, M. Umamaheswari, A. Monica, K. Sivaperumal, Sundarapandiyan Natarajan and R. Mythili, "Effectiveness Performance of Bank Credit on the Event Management Firms in Tamilnadu State", In: Satyasai Jagannath Nanda and Rajendra Prasad Yadav (eds), *Data Science and Intelligent Computing Techniques*, SCRS, India, 2023, pp. 463-470. <https://doi.org/10.56155/978-81-955020-2-8-42>
10. Singh, B., Dhinakaran, D. P., Vijai, C., Shajahan, U. S., Arun, R., & Lakshmi, M. R. (2023). Artificial Intelligence in Agriculture. *Journal of Survey in Fisheries Sciences*, 10(3S), 6601-6611.
11. Mythili, Udhayakumar, Umamaheswari, Arun (2023) Factors Determining Mutual Fund Investments in Coimbatore City, *European Chemical Bulletin*, 12(special issue 6), 4719– 4727.
12. Arun, R. "A Study on the Performance of Major Spices in India." *Recent Trends in Arts, Science, Engineering and Technology* (2018): 149.
13. Arun, Umamaheswari, (2016), Service quality dimensions and its effect on customer satisfaction on service provided By star hotels of Nilgiri District, *Asia Pacific Journal of Research*, Vol.I. Issue XL, 243-246, <https://in.docs.wps.com/l/sIMmSgZfUAayf56MG?v=v2>
14. K. Rani, Dr. J. Udhayakumar, Dr. M. Umamaheswari, Dr. R. Arun, (2023) "Factors Determining The Purchases of Clothing Products Through Social Media Advertisements in Coimbatore City", *European Chemical Bulletin*, 12(special issue 6), 4728– 4737.
15. Anitha, Jagadhambal, Arun (2023), Factors Determining the Leadership Qualities of Female Leaders in Higher Education Institutions, *European Chemical Bulletin*, 12(Special Issue 6), 1416-1424.
16. Edson Nirmal Christopher, Sivakumar, Arun ,Umamaheswari (2023) Iiimmunoinformatic Study for a Peptide Based Vaccine Against Rabies Lyssavirus Rbv Strain Pv, *European Chemical Bulletin*, 12(special issue 9), 631– 640.
17. Arun (2019), "Sustainable Green Hotels -Awareness for Travelers", *International Journal of Emerging Technologies and Innovative Research* ISSN:2349-5162, Vol.6, Issue 4, page no. pp343-347, <http://doi.one/10.1729/Journal.20408>
18. Bhuvaneswari, Arun (2018) Food safety awareness to consumers, *RESEARCH REVIEW International Journal of Multidisciplinary*, Vol.03, Issue 12, 1006-1008, <https://old.rjournals.com/past-issue/food-safety-awareness-to-consumers/>
19. Anitha, Karpagambigai, Arun (2023), Factors Influencing the Organization to Practice Green Hrm: A Study Concerning Coimbatore District, *European Chemical Bulletin*, 12(Special Issue 6), 1406-1415
20. Umamaheswari, Kanchana, Arun, Anita Dalal, Priya (2023), Factors Determining the Social Media Usage Among College Students in Chennai, *Journal of Harbin Engineering University*, Volume no. 44, Issue 7, Pp 505-511.
21. Sivaperumal, Appasaba, Sivakumar, Arun, Surekha Adiki (2023), Portfolio Management Strategies Among Nse Listed Mututal Fund Companies, *Journal of Harbin Engineering University*, Volume no .44. Issue 7, Pp 497-504
22. Prakash, Praveena, Arun, Sundarapandiyan, Sivaperumal (2023), Supply Chain Mapping and Backward and Forward Linkages of Pomegranate Supply Chain in India, *European Chemical Bulletin*, 12(Special Issue 6), 2289-2297

23. Arun R, and Bhuvaneswari R (2019). Buying behavior of meet's consumption relates to food safety from north and south part of the Coimbatore City. *International Journal of Recent Technology and Engineering*, 7, 429-433. <https://www.ijrte.org/wp-content/uploads/papers/v7i5s/ES2177017519.pdf>
24. Prakash Priya, Vanithamani, Arun, Vaissnave, Thyagarajan (2023), Profitability Influencers of Indian Steel Companies: An Analytical Study, *Journal of Namibian Studies*, Vol. 35, Issue: 1, Pp. 38-48
25. Sivakumar, Poornima, Arun (2023), A Study on Software Innovation and Computer Networking Knowledge in Entrepreneurship, *European Chemical Bulletin* (ISSN 2063-5346), Vol. 12, Issue 8, Pp.8959-8969
26. Lakshmi, Vanithamani, Nimisha. Sangeeta, Arun, Dhanasekaran (2023), Digital Payments Amongst Rural Population: A Study in Chennai, *Journal of Namibian Studies*, 35 S1, Pp.12-22.
27. Balakrishnan Chandramouli, Arun, Manojkumar, Gopika, Sivaperumal (2023), Millenials Preference In FMCG Products: An Emperical Study in Chennai, *Journal of Namibian Studies*, 35 S1, Pp.23-37.
28. Lakshmi, S. R., & Santhi, P. (2015). Policyholders Service Satisfaction on Marketing Mix of Life Insurance Corporation of India. *Asian Journal of Research in Business Economics and Management*, 5(1), 97-108.
29. Patil, S. J. (2012). A study on consumer satisfaction towards Life Insurance Corporation of India. *International Journal of Marketing and Technology*, 2(7), 210.
30. Siddiqui, M. H., & Sharma, T. G. (2010). Analyzing customer satisfaction with service quality in life insurance services. *Journal of targeting, measurement and analysis for marketing*, 18(3-4), 221-238.
31. Shanthi, P., Prakash, K. C., Arun, R., Nirmala, C., Kousalya, M., & Sivaperumal, K. (2023). Green HRM Practices and the Factors Forcing it: A Study on Health Care Entities in Chennai. *International Journal of Professional Business Review: Int. J. Prof. Bus. Rev.*, 8(9), 25.
32. Tripathi, Ashutosh Kumar. "Agricultural price policy, output, and farm profitability—examining linkages during post-reform period in India." *Asian Journal of Agriculture and Development* 10, no. 1362-2016-107639 (2012): 91-111.
33. Negi, M., & Kaur, D. P. (2010). A study of customer satisfaction with life insurance in Chandigarh tricity. *Paradigm*, 14(2), 29-44.
34. Thennarasan, R. A Study on Service Quality Perception and Policyholders' Satisfaction in LIC of India in Nagapattinam District.
35. Madhumithaa, N., Mishra, A., Sruthi, S., Sivaperumal, K., & Adhav, S. (2023). Implications of Social Media and Socio-Economic Activities on Micro and Small Enterprises in India. *International Journal of Professional Business Review: Int. J. Prof. Bus. Rev.*, 8(4), 5.
36. Prakash, K. C., Arun, R., Mayi, K., Kavitha, K., Sivaperumal, K., & Shivaratri, C. (2023). Clothing Products Purchases through Social Media Advertisements and the Problems Involved. *Remittances Review*, 8(4).
37. Ivanišević, Dragan, Beba Mutavdžić, Nebojša Novković, and Nataša Vukelić. "Analysis and prediction of tomato price in Serbia." *Економика пољопривреде* 62, no. 4 (2015): 951-962.
38. Paarlberg, Robert. "Agricultural policy reform and the Uruguay Round: Synergistic linkage in a two-level game?." *International Organization* 51, no. 3 (1997): 413-444.
39. Petkova, Valentina, Stoyan Filipov, and Kostadin Kostadinov. "INFLUENCE OF SUBSTRATE ON SOME GROWTH AND PHYSIOLOGICAL BEHAVIOUR OF GREENHOUSE TOMATOES." *New Knowledge Journal of Science/Novo Znanie* 2, no. 4 (2013)..
40. Santeramo, Fabio Gaetano. "Price transmission in the European tomatoes and cauliflowers sectors." *Agribusiness* 31, no. 3 (2015): 399-413.
41. Tiwari, Aviral Kumar, Subhendu Dutta, and Aruna Kumar Dash. "Testing of the Seasonal Unit Root Hypothesis in the Price Indices of Agricultural Commodities in India." *Asian Journal of Agriculture and Development* 14, no. 1362-2017-3062 (2017): 63-82.
42. Tripathi, Ashutosh Kr. "Price and profitability analysis of major pulses in India." *Asian Journal of Agriculture and Development* 14, no. 1362-2017-3063 (2017): 83-102.

The Employee Engagement Dynamics In The Context Of Hybrid Work Model

Arthi Meena¹, Dr. Mruthyunjaya Sharma², Dr. Roopa K³

¹Asst.Professor, Cambridge Institute of Technology

²Associate Professor, RNSIT, Bengaluru

ORCID :0000-0001-9195-0332

³Associate Professor

Department of MBA, Ballari Institute of Technology & Management
Bangalore

ORCID ID: 0000-0002-4843-1593

Abstract

The term employee engagement is not new but the inducement of technology and reinvention of the HR process makes the term very vibrant and paramount. The future of work is determined majorly by a hybrid work environment. In this state of work method, the employee has to face two situations of working one is off the cubical work and another is on the cubical work. They need to cope with the changes occurring in the work environment hence engaging employees in a hybrid work environment is a very challenging task for every company this is an identified problem statement of the study. Employee engagement is all about the enthusiasm and dedication that an employee shows towards his work. Not all employees have the same level of engagement at all times. It is the biggest challenge for every company to retain employees in understanding the proper engagement of work. If employees are disengaged then the company gets wiped out of skills, knowledge, and experienced candidates. Concerning many literatures reviews the study identified a research gap very few literatures are focused on employee engagement in hybrid work environments. The main objective of the study is to understand the effect of employee engagement in the hybrid work environment. The second objective of the study is to analyze the levels of employee engagement in the hybrid work environment. The identified population is ITES working employees with a sample of 100. Simple random sampling technique, primary data used for data collection. A systematic structured questionnaire with a Likert scale considering 1 as strongly disagree and 7 as strongly agree. Reliability tests, descriptive statistics, chi-square, and regression were used to test the hypothesis and objectives. The study finds employee engagement level is significant in demographic data like age, marital status, and designation and there is a positive effect on employee engagement in the hybrid work environment and concludes that hybrid work is the future of work, companies should focus more on engagement initiatives to keep their employees engaged in a hybrid work place.

Key Words: Employee Engagement, Hybrid work Environment ,Employee engagement initiatives , Work-life balance and work environment.

Introduction:

Employee Engagement

Every company has its strength and employees are one of the most paramount factors which determines the strength of the company. Companies may not like to drain out their employees instead they try to satisfy and retain the talented candidates. In today's fantasy world companies are striving to keep their employees happy, satisfied, and engaged by establishing clear goals, providing facilities, and engagement activities that lead to meaningful work. As per the Gallup Study 2020, globally 20% of employees are engaged at work 14% are disengaged, and the remaining are completely disengaged. There are tons of questions among researchers Why employees must be engaged? Is engagement very much required? Are companies striving towards this concept? As we all know HR 3.0 is associated with technology it's time to reinvent the HR process and workflows are connected with people-centric. Companies are transferring to agile systems the day-to-day work processes are becoming complicated deadlines are fixed to accomplish their targets, The pandemic lifted the different methods of working i.e. hybrid work environment. This bunch of leading factors influence companies to engage their employees and retain them.

The pandemic first catalysed this change in the workplace, which has resulted in a renewed emphasis on how employers engage with their workforces. The transition to hybrid has become a top request from employees since expectations of the modern workplace have changed in many ways. Although business strategies differ from one another, maintaining employees' interest in their organization is a problem that all

companies face. One of the most significant developments of the upcoming year will be the hybrid working environment. According to a survey, 32% of respondents stated they wished to be completely distant. Because working remotely improves flexibility and work-life balance, employees don't want to give up those benefits.

The concept of employee engagement was first introduced by Dr. William Khan in 1990 he says involvement in employee work is identified at three levels a) Physically b) Cognitively c) Emotionally. In 2004 May et al defined engagement as how the members of organizations devoted themselves to work not only considering cognition but also the flexibility in emotions and behaviours. In 2005 Wellins & Concelman defined engagement as a mixture of loyalty, productivity, and ownership. In 2006 Saks says that the individual role performance is related to the combination of knowledge, emotion, and behaviour. In 2007 Cha included three dimensions such as work engagement, organisational recognition and sense of work value. In 2008 Macey & Scheider defines there are different types of engagement levels trait engagement , behavioural engagement , psychological state engagement. .In 2022 Schaufeli et.al identified the three levels of work engagement vigor, dedication and absorption. Vigor stand for the high levels of energy and resilience in simple term it also as discretionary effort put by an employee ,while dedication refers to the sense of significance, enthusiasm, pride and inspiration ,while absorption is where an employee is engrossed in work , highly concentrated who feels difficult to detach from work .

Levels of Employee Engagement

There are three levels of engagement identified by Gallup

1. Actively engaged – employees who are actively engaged will deliver better outcome higher productivity, aware of their roles and enthusiastic about their work
2. Not engaged – employees accomplish to the said goals or task and never take initiative in doing extra work. At this level employees prefer the status quo over improvements.
3. Actively disengaged – employees try to switch on jobs frequently, disinterested to do any work, try to skip the assigned work, high absenteeism.

Hybrid work environment

Hybrid workplace or work environment is defined as a business model combining two models of working process like in office work and remote work or it is also considered as work from home. It is also a flexible approach where employee has split up in their work. It is all about the flexibility working. There are some different type of hybrid work slip up

1. Hybrid at-will : Here in this method an employee can choose to come to office any day of his choice to work
2. Hybrid split week : In this method of work the company assigns particular day for the team to function
3. Hybrid manager -scheduling : Here the manager play a vital role in deciding the particular day for his team to perform
4. Hybrid mix : It is the combination of all the above three forms.

Out of all these forms of hybrid work, currently in India we do follow the Hybrid at -will method of working.

Review of Literature

Employee Engagement

Chandani and Mehta (2016) the paper articulates the importance of employee engagement and how it increases organisation performance. There are two levels of factors which increase employee engagement like organisation level and individual level. Vasani and Pillai (2019) employees are satisfied with the overall companies' performance. the factors identified are compensation, health and safety, increment in salary, training and career which influences employee engagement. Purushotham and Kaviya (2021) subjects their finding on employee engagement, to retain employees the best way is to engage employees. When employees are engaged it leads to employee satisfaction in return it results to employee retention. Anitha.J (2014) identified few factors which can influence employee engagement to maximum level are team and co-worker relationships, working environment. Smitha and Sahu (2022) to improve engagement among employees and organisation must encourage different strategies to be implemented, inculcate the sense of belongingness, positive emotion about their work. Kular and Gatenby (2008) employee engagement is defined in multi-faceted by Khan. The employee's perception towards work should provide more meaningful. Singapore and Thailand has 82 % of engaged employees this might be due to the culture, values, political management styles and economy. Gurman and Saks (2010) performance of an employee can be increased in identifying the right performance increment and this can keep employee engaged at work. Some of the employee engagement facilitation which can boost employee performance are like

job design , social and coaching support to employee's leadership style and training .

Desai and Majumdar (2011) employee engagement can increase employee productivity ,engagement levels are said to high when employees are more committed and loyal in manufacturing industry. Smith and Markwick (2009) there are many factors which influences employee engagement good quality management , communication , inter co-operation , employee well-being ,accessible HR policy are considered to be major factors. Baker(2013) there are two factor influencing employee engagement micro and macro factors. Mansoor and Hassan (2017).the identified factors are communication , team work ,collaboration , job role, company management and training and development which has positive impact on employee engagement. Opas, Anurit and kuiyawattananonta (2011) fair salary, good safety, health insurance , training opportunity , work life balance, environmental factors are few factors which has rooted employee engagement positively . Robinson(2007) feeling valued and feeling involved is quite important to lead employee to engaged. Some of the factors are training and development ,career development ,performance management , equal opportunities, fair treatment , pay and benefits , health and safety , co-operation , family friendliness and job satisfaction are key drivers which lead to building block for employee engagement .Laura (2009) states the relationship between the engaged employee and leadership style can improve the organisation effectiveness. The most preferable leadership style expected which can lead engagement is transformational leadership style. Abraham and Susan (2012) there always exist a positive relationship

between job satisfaction and employee engagement. Creativity can encourage high level of job satisfaction leading to employee engagement. Sridevi and markos(2010) it is identified that employee engagement is stronger predictor for organisation performance. Although there exist a two-way relationship between employer and employee. when employee are highly involved in job there is always a great success to the employer. Attridge (2009) identified that employee engagement can be improved by creating or bringing a good work place and address the culture ,job design and working conditions. Raya (2009) companies should manage engagement by involving few strategies like managing stress, promote employee wellbeing , facilitating self -management. There are two outcomes of employee engagement one is individual outcome and the other is business outcome. Delina (2020). It has considered three level of engagement vigor, dedication and absorption. When employees are happy with the employee engagement initiatives then employee are completely engaged to their work .Yadav(2020) gamification has to be applied properly in HR management it has the potential to increase employee engagement.

Hybrid work and Employee engagement

Yadav (2020) engaging employees in virtual work place is very difficult. The relationship between employer and employee have reduced ,work has become monotonous , non -creative. Even though few employees who are happily working from work feel lack of belongingness for work and organisation. Some companies have come out offering games , interactive sessions, virtual celebration. Pablo and Peeter (2022) identified how hybrid work positively

influences engagement and how it negatively influences. The negative influence of hybrid on employee engagement are no co-ordination among employees, no casual interaction among employees, isolation, weak culture and increased turn over. The hybrid work positive influence employee engagement in having work life balance, coordination between f-f is high and consequently employee motivation and energy are positively affected in hybrid work. Delany(2022) expressed employees are desired to work in flexible. The research survey showed 30% of employees like to work if their company would consider on -site job. Amigoni (2021) to improve employee engagement in the organisation, a better approach can provide solution for future work is hybrid work environment. Caminiti(2022) the study identified that most of the employee prefer blend mode of work place remote and office work. This mode of working can increase employee productivity, better work life balance and higher autonomy. Teevan et.al.,(2021) also states that most of the employees believe the future of work is hybrid work. Hilberath(2020) due to change in work employee are preferring hybrid work as new future of work. There are four building blocks to support future work 1. Leadership, culture 2.strucutre and roles 3.ways of working 4.sytems and spaces. Ware and Grantham(2003) new workplace design, new technologies has lead to new way of working process. Flexibility is the most preferable work place.

Research Gap

After reviewing many literatures, the study has identified there are very less research papers conducted in hybrid work environment. As hybrid work culture is considered as future of

work and trending among IT & ITES companies the study shall cover the identified gap. Many research paper has covered on the engagement levels but on specifically conducted under hybrid work environment. The second gap of the study focuses on ITES working employees because very few engagements study have been conducted under ITES sector.

Research questions

1. Why employee engagement is considered very important ?
2. Is hybrid considered future of work ?
3. Engagement levels at hybrid work environment?
4. What is the effect of employee engagement in hybrid work place ?

Research Objectives

1. To understand the importance of employee engagement in hybrid work place
2. To identify the different levels of engagements
3. To analyse employee engagement levels in hybrid work environment with respect to demographic details.

Hypothesis

Ho: There is no positive significant difference in employee engagement levels at hybrid work environment based on demographic characteristics.

H1: There is a positive significant difference in employee engagement levels at hybrid work environment based on demographical characteristics.

Research Methodology

Descriptive research design is used for the study. The population identified are ITES

working employees in north Bangaluru with sample size of 100. Simple random sampling will be considered as it is in hybrid work place. Primary data is used for the study . Data is collected by systematic questionnaire using

Likert scale ranging from 1 to 5 considering 1 as lowest and 5 as highest score. Descriptive statistics , Chi-square test used for the data analysis.

Data Analysis and Interpretation

To know whether the data collected is reliable and to check data consistency the study has run through reliability test using PSPP software .The following is the output

Table 1.1. Reliability test

Case processing summary

Cases	N	Percent
Valid	89	95.7%
Excluded	4	4.3%
Total	93	100.0%

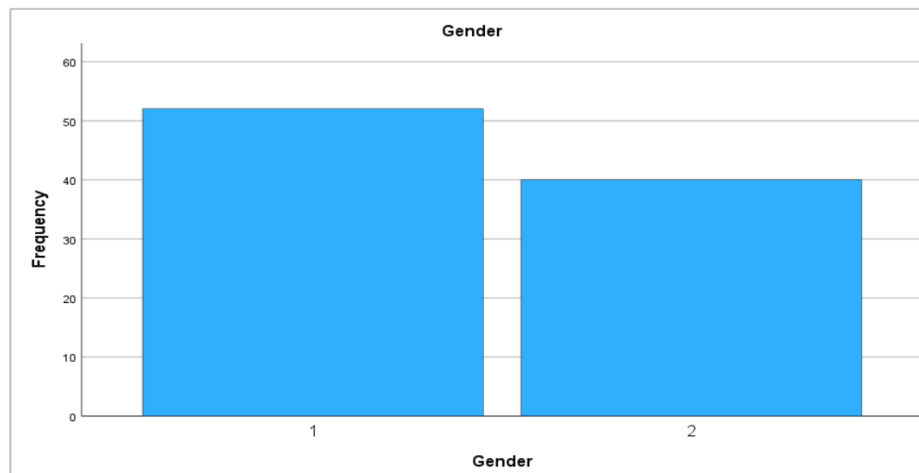
Reliability Statistics

Cronbach's Alpha	N of items
.93	32

The above reliability test shows that Cronbach's Alpha is .93. Cronbach's Alpha is a measure of internal consistency . The alpha co-efficient of 32 shows that the item have relatively excellent internal consistency of .093.

Table 1.2 Shows the percentage of gender

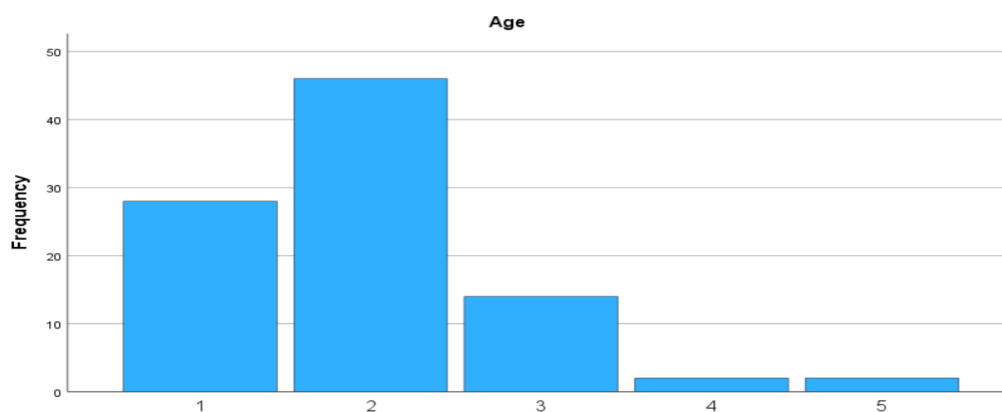
	Frequency	Percent	Valid percent	Cumulative percent
Valid 1	52	55.9%	56.5%	56.5%
2	40	43.0%	43.5%	100.0%
Missing .	1	1.1%		
Total	93	100.0%		



The table focus the percentage of female and male respondent . The value 1 is coded as female and show 55.9% respondents. The value 2 is coded as Male with 43.5% of respondent . Hence it concludes that the majority of female were the respondents.

Table1.3 Shows the different set of age groups

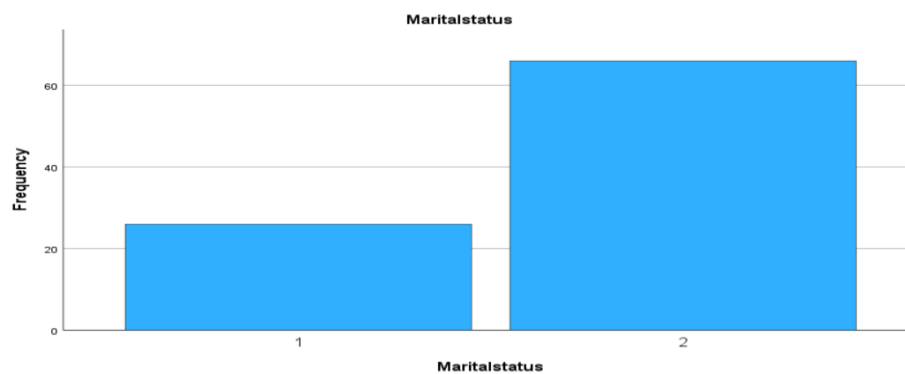
	Frequency	Percent	Valid percent	Cumulative percent
Valid 1	28	30.1%	30.4%	30.4%
2	46	50.0%	50.0%	80.4%
3	14	15.2%	15.2%	95.7%
4	2	2.2%	2.2%	97.8%
5	2	2.2%	2.2%	100.0%
Missing .	1	1.1%		
Total	93	100.0%		



The table shows the percentage of age group who respondent. The value 1 is coded as age group between 20-30 representing 30.4% respondent ,the value 2 coded as 31-40 age group which representing 50 % respondent .the value 3 coded as 41-50 age group representing 15.2%. Hence the age group 31-40 were the maximum respondent for the study .

Table 1.4 Shows the percentage of marital demographic details

	Frequency	Percent	Valid percent	Cumulative percent
Valid 1	26	28.0%	28.3%	28.3%
2	66	71.0%	71.7%	100.0%
Missing .	1	1.1%		
Total	93	100.0%		

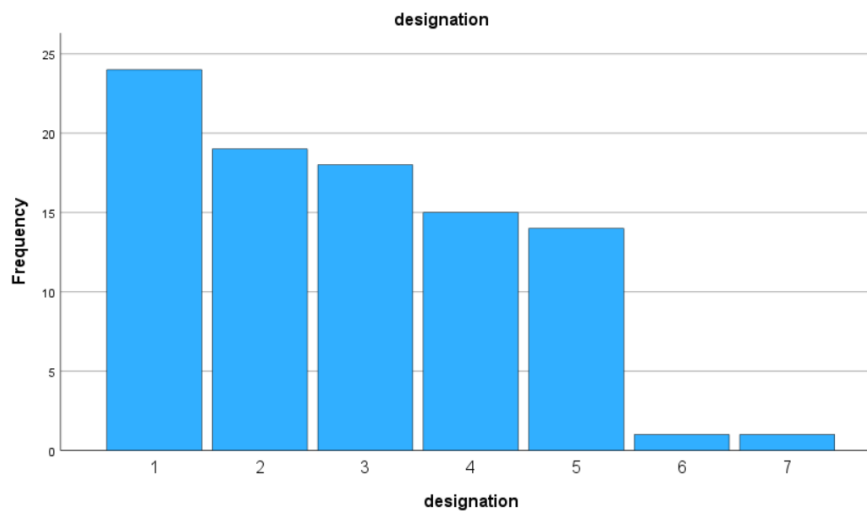


The table shows the marital status percentage. The value 1 is coded as unmarried representing 28% respondent and value 2 coded as married representing 71%. The maximum were married employees.

Table 1.5 Shows the percentage of education and designation demographic details

	Frequency	Percent	Valid percent	Cumulative percent
Valid 1	56	60.2%	60.9%	60.9%
2	56	38.7%	39.1%	100.0%
Missing .	1	1.1%		
Total	93	100.0%		

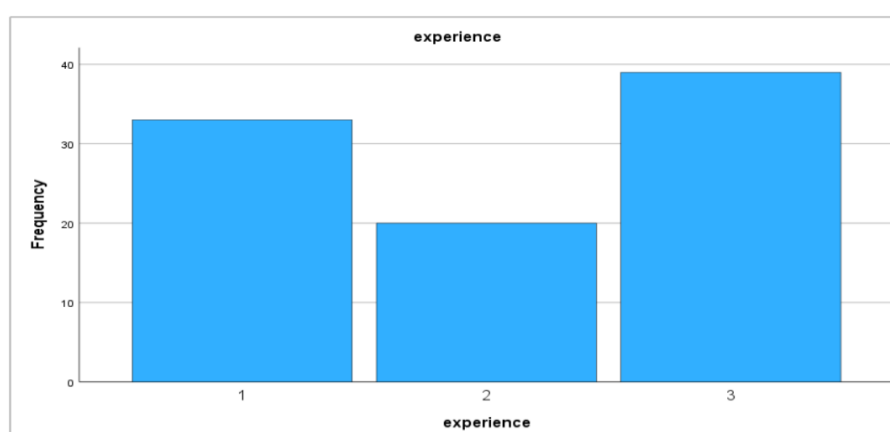
	Frequency	Percent	Valid percent	Cumulative percent
Valid 1	24	25.8%	26.1%	26.1%
2	19	20.4%	20.7%	46.7%
3	18	19.4%	19.6%	66.3%
4	15	16.1%	16.3%	82.6%
5	14	15.1%	15.2%	97.8%
6	1	1.1%	1.1%	98.9%
7	1	1.1%	1.1%	100.0%
Missing .	1	1.1%		
Total	93	100.0%		



The table shows the education and designation details of respondents .The maximum employees have education qualification as degree and post graduates. Software engineers and Sr. Software engineers are the maximum respondents for the study.

Table1.6 shows the experience of the respondent

	Frequency	Percent	Valid percent	Cumulative percent
Valid 1	33	35.5	35.9	35.9
2	20	21.5	21.7	57.6
3	39	41.9	42.4	100.0
	92	98.9	100.0	
Missing .	1	1.1%		
Total	93	100.0%		



The experience of 20-30 is coded as 1 , experience of 30-40 coded as 2 and experience of 40 -50 is coded as 3. Thus, from the above table shows that majority of the respondent were from 40-50 and 20-30 .

Table1.7 Descriptive statistics

	N	Mean	Std.Dev	Skewness	S.E.Skew	Range	Min	Max
Gender	92	1.43	.50	.27	.25	1.00	1.00	2.00
Marital status	92	1.96	.86	1.13	.25	4.00	1.00	5.00
Exp	92	1.72	.45	-.98	.25	1.00	1.00	2.00
Edu	92	2.82	1.51	.40	.25	6.00	1.00	7.00
Position	92	2.07	.89	-.13	.25	2.00	1.00	3.00
Valid N	93							
Missing N	1							

The above table shows the descriptive statistics of all the demographic information . The population is denoted as N ,the total population is 92 out of 93 with the mean statistics for gender 1.43 ,age 1.96 , marital status 1.72 and so on . The standard deviation values fall between the range ± 1 .

To accept or reject null hypothesis chi-square test is conducted . For testing hypothesis, the demographic details such as gender, age, education qualification , designation and marital status are considered to understand the employee engagement levels in hybrid work environment .

Table 1.8 Chi-square test

Test Statistics			
	Chi - S4.35quare	df	Asymp. Sig
Gender	1.57	1	.211
Age	76.70	4	.000
Marital status	17.39	1	.000
Exp	6.15	2	.046
Education	4.35	1	.037
EElevelsHW	82.43	3	.000

From the above table it shows that gender is not significant as the value is more that .05 with 95% confidence level. Thus, gender is not majorly increasing employee engagement level in hybrid work environment . The Age factor shows .000 hence it is significant as its value fall below .05 .The age from 31-40 has greater influence on employee engagement levels. The third factor is marital status shows significant value of .000 the test concludes with the data calculated that married employees have greater employee engagement levels in hybrid work environment compared to unmarried employees. Experience of employees and education qualification have no much influence on engagement levels in hybrid work environment. The next demographic factor designation is significant with value less than .05 . The designation like software engineers, Sr. Software engineers , tech lead , Sr. Tech lead and project manager has engagement levels.

Thus, the study concludes the demographic like Age, marital status and designation has a positive significance on employee engagement levels in Hybrid work environment.

Table 1.9 Regression analysis

To analyse the second hypothesis ,regression analysis test is used to know the impact of employee engagement in hybrid work environment.

Model Summary (EE)			
R	R Square	Adjusted R Square	Std. Error of the estimate
.88	.77	.77	1.06

ANOVA (EE)					
	Sum of squares	df	Mean square	F	Sig
Regression	154.77	1	154.77	136.81	.000
Residual	98.42	87	1013		
Total	253.19	88			

Coefficients (EE)					
	Unstandardized co-efficient		Standardized coefficients	t	Sig
	B	St. Error	Beta		
(Constant)	.75	.25	.00	3.06	.003
HWE	.74	.06	.78	11.70	.000

The R values shows .78 which is between ± 1 thus indicating a strong positive linear relationship between EE and HWE .The R square or the variance values is .61 and adjusted R square is 61% of variance on HWE . The ANOVA table indicates it is significant at .000 which is less than .05 of P value . Thus, null hypothesis is rejected and alternative hypothesis is accepted . Thus, there is a significant impact on employee engagement in hybrid work environment.

Table 1.10

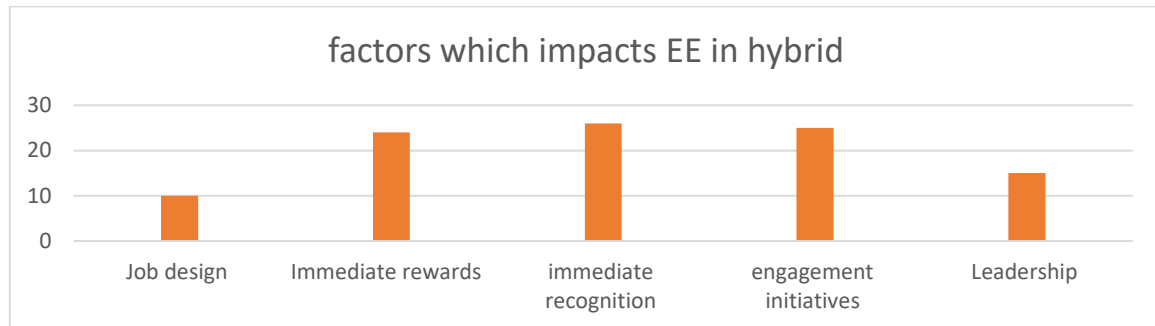
Your Engagement levels towards work in hybrid work environment

	Frequency	Percent	Valid percent	Cumulative percent
actively engaged	19	17.3	20.7	20.7
Engaged	60	54.5	65.2	85.9
Disengaged	13	11.8	14.1	100.0
total	92	83.6	100.0	
Missing system	18	16.4		
Total	110	100.0		

The above question has been asked to the respondent on their engagement levels towards work in hybrid work environment. 54.5% of employee stated they are engaged i.e medium level engagement. 17.3% employees stated that they have higher engagement levels i.e actively engaged . And 11.8 % respondents stated they have lower-level engagement levels i.e they are disengaged . The table concludes that most of the respondents

Table 1.11

What are the factors which impacts your engagement levels in hybrid work environment ?



The open-ended question about the factors which can impact engagement levels in hybrid. Majority of the respondent responded that if immediate recognition been given to employee, then they will feel the sense of belongingness and become loyal to organisation resulting better engagements. Immediate rewards should also to be focused in order to motivate employees . leadership is also one of the factors which can impact the engagement levels of employees in hybrid. An appropriate job design should be planned for each employee

Findings

The Study has identified that employee engagement is much very important in hybrid work environment. As employees are working in blended mode the organisation has to focus and engage them on both the aspects of work mode and retain them . The study found that from the demographic data like age , marital status and designation shows significant influences on engagement in hybrid work

environment and gender ,education qualification and experience has less influence on engagement levels in hybrid work environment . There is also positive impact of employee engagement in hybrid work place.

Conclusion

Individual engagement is simply the emotional dedication an individual has to their employer and its objectives. That is what separates an engaged workforce from a disengaged one, and it is for this reason that businesses all over the world are looking for ways to increase employee engagement.

Engagement is crucial for your business since it affects a number of other factors, such as productivity, turnover, customer happiness, and earnings [3]. Compared to workers who don't feel committed at all (or perhaps have a bad attitude toward the organization), those who are invested in their work are more likely to consistently go above and beyond. The study

concludes hybrid work environment has greater impact on engagement levels. Companies should focus more on improving engagement activities in hybrid mode. The future of work is hybrid hence the companies should effectively implement good strategies to increase engagement levels in future. As the study is confined only to north Bengaluru the findings are based on the limited sample. Further study can be done considering IT employees and ITES across Bengaluru.

Reference

1. Abrabham and Susan (2012) Job satisfaction as an antecedent to employee engagement .SIES journal of management. Vol 8 Issue 2, pp27-36.
2. Amigoni.G(2021). Physical ,digital and hybrid workspaces: from the process of creation to the process of use. Springer international publishing. pp 127-143
3. Anitha(2014) Determinants of employee engagement and their impact on employee performance. International journal of productivity and performance management. ISSN : 1741-0401.
4. Attridge (2009).Measuring and managing employee work engagement : A review of the research and business literature.
5. Bhuvanaiah and Raya (2014). Employee engagement : A key to organisation success. SCMS journal of Indian Management.
6. Btista-taran,L.C.,Shuck,MB Guitierrez.C.C & Baralt.S(2009).The role of leadership style in employment. Proceedings of the eight annual college of education & GSN research conference.pp15-20.FloridaInternationaluniversity.
<http://coeweb.fiu.edu/reseachconference>.
7. Caminiti,S.(2022).Workers want hybrid but say it's exhausting them here's how companies can fix that.<https://www.cnn.com/2022/02/08/workers-say-hybrid-is-exhausting-them-heres-how-companies-fix-that.html>.
8. Chandani and Mehta (2016). Employee engagement : A review paper on factors affecting employee engagement. Indian journal of Science and Technology. Vol 9(15).DOI :10.17485/ijst/2016/v9i15/92145.
9. Delany,K(2022).What challenges will organisation face transitioning for the first time to the new normal of remote working ? Human resource development international ,<https://doi.org/10.1080/13678868.2021.201739>.
10. Delina(2020). As study on the interrelationships between employee engagement, initiatives and job satisfaction. <https://doi.org/10.1504/IJBEX.2020.105355>.
11. Desai and Majumdar(2011). A Study on employee engagement levels in two Indian Business. Asian journal of Management research . ISSN 2229-3795. DOI:10.5897/AJBM10.022.ISSN1993-8233.
12. Gurman (2010).Performance management and employee engagement. Human resource management review. <https://doi.org/10.1016/j.hrmr.2010.09.004>.
13. Gurman and Saks (2016).Performance Management and Employee Engagement .Human Resource Management review .Volume 21,Issue -2 ,pp-123-136. <https://doi.org/10.1080/15555240903188398>.

- https://doi.org/10.1007/978-3-030-83182-0_8.
<https://www.microsoft.com/enus/research/uploads/prod/2021/01/newfutureofworkreport.pdf>.
14. Kular and Gatenby (2008) . Employee Engagement : A literature review. ISBN No. 1-872058-39-6/978-1-872058-39-9/9781872058399. Kingston business school Kingston University.
 15. Mansoor and Hassan (2017). Factors influencing employee engagement :A study on telecommunication. International Journal of accounting and business management, Volume4 ,Issue1, pp50-64. DOI:10.24924/ijabm/2016.04/v4.iisl.
 16. Mulang.H (2022) .Analysis of the effect organisational justice ,work life balance on employee engagement and turnover intention. Golden Ration of human resource management ,2(2),86-97. <https://doi.org/10.52970/grhrm.v2i2.169>.
 17. Opas, Anurit and Kuyawattananonta (2011). Talent management in Thai cement companies: A study of strategies and factor influencing employee engagement. African journal of business management. Vol.5(5), pp.15781583.
 18. Pablo and Peeter (2022). Using Hybrid to turn workplace vibrant: An empirical study about hybrid workplace implication on employee engagement. Published by digitala vetenskapliga arkivet. urn:nbn:se:hj.diva-56771.
 19. Purushothaman and Kaviya (2021). A study on employee engagement in a IT company. Journal of management ,7(3), pp.1-7.
 20. Robinson (2007). A review on employee engagement. Institution of employment education publication.
 21. Smith and Markwick (2009) .Employee Engagement : A review of current thinking. Institute for employment studies. University of Sussex campus Brighton BN19RF.
 22. Smitha and Sahu (2022). Employee Engagement : A review paper .International Journal of creative and research thought. Volume 10 , Issue -9.
 23. Sridevi and Markos (2010). Employee Engagement : A key to improve the performance. International journal of Business and management. Vol 2 No12.
 24. Teevan et.al., (2021). The new future of work : research from Microsoft on the impact of the pandemic on work practices.
 25. Vasani and Pillai (2019). To study on employee engagement and their impact on employee performance. International Journal of Applied science. 5(4):490-493.
 26. Ware and Grantham (2003). The future of work :changing patterns of workforce management and their impact on the workplace. Journal of facility management. 2(2):142-159. DOI:10.1108/14725960410808177.
 27. Yadav (2020). Exploring the concepts of gamification for better employee engagement in hybrid work environment. JNU/ABVSME-WP.No.02/2020.
 28. Yadav (2020). Employee engagement strategy for employees working in virtual environment in the IT industry. JNU/ABVSME-WP.No.03/2020.

TO STUDY THE IMPACT OF COMPENSATION AND REWARD SYSTEM ON EMPLOYEES PERFORMANCE

DEC-2023

Ramya Janardhan

Assistant Professor, MBA, (PhD), Dayanada Sagar Business Academy,
Udayapura, Kanakpura road, Opp Art of Living, Bangalore.

Dr. Shaheeda Banu. S

Professor, PhD, Ballari Institute of Technology and Management,
Jnana Gangotri Campus, Hospet Road, Near Alipura, Ballari.

INTRODUCTION

Organization diagonally finds employees to hold their abilities. Recruitment, selection, and training for the replacement of employees incurs loss and it incurs an exorbitant cost for an organization. Employees are considered as valuable resource of an organization employee compensation is one of the important factors of an employee's performance. Each employee is motivated by providing rewards, it is also a need for an organization to reward its employees for creating a successful completion of the task given. Compensation is one of the important key factors for employees to achieve organizational goals. Many employees are motivated by providing promotions, increases in salary, bonuses, and incentives. Other employees are motivated by reward benefits like appreciation, praise, and recognition however it leads to high employee performance. Employees are the real asset to an organization which helps them to achieve organizational objectives. Compensation is what an employee receives in exchange for their contribution to the organization. We can't measure that each individual employee affects in the same way by providing various rewards. Providing various kinds of benefits Life insurance policies, Medical facilities, Maternity leave, Paid leaves, and overtime pay based on that employees get satisfied. Comprehensive compensation management and motivation can be used as veritable instruments to reduce labor turnover, absenteeism, and negligence which in the end will impact the organizational goals and employee's performance in achieving those objective goals.

Reimbursement is considered as the all-inclusive total money linked and many employee benefits are given. A good compensation makes the organization to achieve the organizational goals and the employees' performance. A good Compensation package helps the employees to retain in the organization for a longer period. Compensation inspire the employee's to work excellently and resourcefully and it also helps to sustain in the organization for a longer period.

Research Design

Type of Study: Descriptive research

Type of sampling: convenience sampling

Objectives

- To have a better understanding of the organization's rewards and incentive programs.
- To study various reward system issues that affect employee performance.

Hypothesis

H0 = Compensation and reward system does not have an impact on employees' performance.

H1 = Compensation and reward system have an impact on employees' performance

Chi Square Test

H0: Employees are not provided incentives and bonuses for their performance.

H1: Employees are provided incentives and bonuses which influence their performance.

Chi-square test on Employee's opinion on providing incentives and bonus influence on performance.

Parameters	O	E	(O-E)	(O-E) ²	(O-E) ² /E
1	35	20	15	225	11
2	39	20	19	361	18
3	14	20	-6	36	2
4	3	20	-17	289	14
5	9	20	-11	121	6
TOTAL	100	100			52

Observed frequency (O) = 35+39+14+3+9=100

Expected frequency (E) = 20+20+20+20+20= 100

Degrees of freedom (U) = 5-1= 4

Tabulated value, $X^2_{0.05} = 9.49$

Calculated value, $(O-E)^2/E=52$

$(O-E)^2/E = X^2_{0.05} = 9.49$

Interpretation

The null hypothesis (H 0) is ignored, and the alternative hypothesis (H 1) is accepted because the estimated value is greater than the computed value. Hence, employees are provided with incentives and bonus which influence their performance

Findings

1. This study reveals that employees seek an increase in salary and wage levels within the organization so that they work promptly. Due to competency in employees' organizations choose only the best performer and reward them but not the workers who put in the same efforts to achieve the objectives.
2. This study says that not every employee is compensated equally, based on the educational qualification and job specification employees are compensated these are the issues employees are facing in the organization.
3. The study establishes that many organization has various types of compensation and reward pay structures, which motivates employees to work effectively and efficiently. Due to the effective compensation packages, many employees turn towards their organization and stay loyal to work in their organization for longer periods and leave their previous job.

4. Employees should be provided with social security benefits, such as medical benefits, retirement benefits, and paid leave, among other things. This serves as a motivator, causing them to bring more effort into their jobs, resulting in the achievement of corporate goals and successful job results. As a result, it improves employee morale.
5. The findings of the research that compensation should be paid fairly relative to the local market so that employees are satisfied and work to achieve the organizational objectives, we all know that compensation is a key element for boosting the performance of employees.
6. Effective compensation packages increase employee performance. Providing financial and non-financial benefits to increase employee retention within the organization. Many employees believe that financial bonuses are motivating factors that help them meet their basic needs.
7. Not only do compensation and reward system influences employee performance, every employee feels stressed and has a high risk in working. Employees enjoy working in Environments that provide job security, a pleasant working atmosphere, and where their leaders/bosses encourage them to make decisions or provide opportunities for employees to make decisions within the company.
8. This study establishes programs for training and growth to help the employees to respond to technological advancements and have the required skills and competencies in the performance of their duties.

Suggestions

The suggestions are based on the findings of the primary collection of data. It was found that employee performance is negatively affected by the compensation not given in an organization. Compensation is the main key factor of every organization.

1. According to the report, the company should evaluate the current incentive schemes to see how successful they are at achieving the company's goals.
2. Analyze different incentive schemes and identify appropriate programs for your company. Implementation of the overall bonus scheme, as well as the evaluation of incentives schemes.
3. The study suggests that the company's compensation structure be aligned with its corporate strategy.
4. It's also critical to recognize and reward employee activity that supports the administration's goals, like innovation, creativity, client facility, productivity, and quality, as well as focusing on incentives that empower employees.
5. The study recommends that the organization should improve the existing pay structure, it should be improved so that employees will be paid well and they will retain in organization for longer period and they also contribute their efforts to achieve the organizational goals.
6. The study looked at how an organization's compensation and incentive scheme affects employee success.
7. How salaries, incentives, bonus and indirect compensation influences the employee to meet the organizational objectives.

8. Therefore further studies should be carried out on how other variables not studied influences employee performance in another sector. Employees work efficiently and by this, their performance also increases, and automatically organizational goals are achieved.

CONCLUSION

According to the findings, compensation has an impact on employee performance, and employers should create recommendations to examine their pay structure and remuneration in order to meet employee satisfaction, which has an influence on worker performance.

A study also determines that not only reimbursement and reward benefits improve employee performance by providing job security, training and development, and other benefits which satisfy them and motivates them to work effectively.

The report also concludes that workers' working conditions should be strengthened. Because of this employees jump into another organization for better pay and work space. There should be enough space for workers to work and infrastructural facilities should be good. They can function in an atmosphere that allows them to satisfy their family members and live happily together. This will also assist workers in reducing tension as a result of the hard work they do on a regular basis.

Finally, the research concludes that employees should be compensated fairly based on the local market value. And employees should be compensated fairly for the work they do and they should be treated equally, there should be no comparison between employees low or high, and there should be no discrimination in the organization based on caste, creed, color, religion, etc. By this employees will feel free to work in the work environment and boost themselves to give better yield. A friendly environment helps employees to perform better actions to achieve the objectives of an organization, and it also increases employees' performance.

Bibliography

Books

Name of the Author	Title of the Book	Name of the Publisher	Edition	Year of Publication
B.D Singh	Compensation and Reward Management	Excel Books	Second Edition	2007
Deb	Compensation Management	Excel Books	First Edition	2009
Micheal Armstrong	Employee Reward Management and Practice.	Kogan Page Limited	First Edition	2005

Articles

- 1) Alex Samna (2020). Effect of remuneration on employee performance and job satisfaction The International Journal of Economics, Business, and Accounting Research (IJEBAR), 4(01).
- 2) K. Subagja, A. Hakim, and (2020). Peranan Kualitas Layanan Dan Citra Merek Terhadap Kepuasan Konsumen Hotel Grand Candi Semarang. Journal of Management of Bisnis Krisnadwipayana, 8(3).

- 3) Aima, H., Sutawijaya, A. H., Herawati, A., Utami, W., Johanes, S., & Catur Widayati, C. (2020). Effect of Pay and Organization Commitment on Turnover Intention with Work Satisfaction as an Intervening Variable In Indonesian Industries Drug Systematic Reviews, 11(9).
- 4) U. S. Muogbo, E. Dike, and R. U. Onyekwelu (2020). In Nigeria, remuneration is a technique for boosting employee performance. offered at SSRN3565079.
- 5) AlHosani, A. A. H. H., Fadillah Ismail, & Kadir, A. A. (2019). the contribution of benefits and pay to employee performance. In ACHITS 2019, Surabaya, Indonesia, July 30-31, 2019, Proceedings of the First Asian Conference on Humanities, Industry, and Technology for Society (p. 171). European Innovation Alliance
- 6) Gao, F., Somanath, P. R., Artham, S., Alwhaibi, A., & Verma (2018). Through -catenin- regulated tight-junction protein turnover, endothelial Akt1 depletion encourages prostate cancer spread. 118(11), 1464–1475 in the British Journal of Cancer.
- 7) Those authors are Muogbo, P. C., Gbabo, A., Nwakuba, N. R., Onyekwere, I., and Obasa,
- 8) P. A. (2018). Mechanization of the production of turmeric in Nigeria to improve livelihoods. 494 Committees Expanded.
- 9) Nikensari, S. I., Hartono, B., Sariwulan, T., & Sudiardhita, K. I. (2018). The relationship between employee performance and salary, employee motivation, and job satisfaction Pt. Bank Xyz (Persero) Tbk. Academy of Strategic Management Journal, 17(4), 1–14
- 10) Supriyanto, A. S., and P. S. Darma (2017). the impact of pay on job satisfaction and productivity. MEC-J, 1 Management and Economics Journal (1).
- 11) Jasim, M. K., Dayanandan, B., S. K. Maurya, Y. K. Gupta, & A. Al-Jamel (2017). Compact star models using the equation of state $p = f(\rho)$ using relativistic anisotropy. Global Journal of Modern Physics D, 26(02), 1750002.
- 12) Chukwuma, N. N., Nwekpa, K. C., and Ezezue, B. O. (2016). Influence of electronic banking on client satisfaction at a Nigerian Fidelity Bank PLC Journal of Business and Management of the IOSR, 22, 49–58.
- 13) Shenashen, M. A., Hassen, D., El-Safty, S. A., Selim, M. M., Akhtar, N., Chatterjee, A., & Elmarakbi, A. (2016). Mesoscopic fabric sheet blocks and racks serve as catalysts for methanol and ethanol electrooxidation with effectively exposed surfaces. American Materials Interfaces, 3(24), 1600743.
- 14) Nimra Akter (2016). A study on Bangladesh's garment manufacturing industry found that training and development programmes for employees are good indicators of how well they will perform. Business and Management Journal of the IOSR, 18(11), pp.48–57.
- 15) Sajjad, S. R., and M. O. Qureshi (2015). A Correlation Model for an Empirical Analysis of the Effect of Compensation on Job Performance and Work-Family Conflict in the Kingdom of Saudi Arabia. 11(4), 170-187.

Happy Campus: How to Make Universities a Better Place to Work and Study in INDIA

Dr. G P Dinesh, Professor, VSK University, Ballari and Dr. DivyaBharathi,
Associate Professor
BITM, Ballari

Abstract

Campus can be stressful. The transition away from home, the financial and academic pressure, conflicts with peers, and post-graduation planning can all contribute to stress among college students. When managing an increase in responsibilities and changes, many students might forget to contribute intentionally to their own self-care and well-being. Health and happiness go hand in hand. Since the body and mind are so connected, taking care of physical health is helpful for mental health. Making intentional healthy changes to our lifestyle can boost our wellness in meaningful ways. Good friends bring fun in the good times and support in the bad times. They share in your joys, celebrations, hardships, and sorrows, and help keep your happiness quotient and spirits high. Having meaningful connections with others significantly reduces stress, boosts self-confidence and a sense of belonging, and can even improve the immune system and physical health. Friends see, understand, and accept us for who we are. College is a time of immense personal growth. It's also a time where you can make genuine best friends. We all know that the obligations that come with being a college student can be difficult, so it's good to have a helping hand when you're dealing with that exhausting research paper or are having a bad day. We all need someone to lean on from time to time. And, students who make an effort to form relationships in college are more likely to succeed academically and graduate on time. This paper highlights what makes a campus a happy campus and what the universities and Higher Education Institutes should do to make it a better place to study and work.

Keywords

Happy Campus, University, Higher Education Institutes, India

A Study of Female MBA Students Buying Behavior of Cosmetic Products in Ballari.

1.Chindananda U
MBA Student.

2.Dr.Shaheeda Banu S
Professor,
DMS, BITM, Ballari.

ABSTRACT

The Indian cosmetics industry is growing in terms of product development and marketing. The preference of Indian consumers is changing from the 'merely functional' products to more 'advanced and specialized' cosmetic items. In 2005, sales of cosmetics and toiletries rose by 6% in current value terms in India. Monteiro (2003) also predicts the huge potential for cosmetics in India. The average annual spending of Indian consumers on cosmetics and toiletries in 2005 is just over US\$3. India in cosmetics and toiletries, which saw its value share rising from 27% in 1999 to 31% in 2005 and is likely to continue to surge ahead over the forecast period. The entry of many multinationals into the Indian cosmetics and toiletries industry in 2005 has made it an extremely challenging and dynamic market. Foreign players have focused more on product innovation; re-launches and brand extensions spread across multiple price points, and enhanced product penetration by extending their distribution networks. The leading players have streamlined their ad spend to effect savings that has allowed them revamp their pricing strategies as well as offer free gifts to retain consumers. Understanding behaviour of consumers is a key to the success of business organizations. Marketing personnel are constantly analyzing the patterns of buying behaviour and purchase decisions to predict the future trends. Consumer behaviour can be explained as the analysis of how, when, what and why people buy. Consumer behavior can be understood as: "The decision process and physical activity individuals engage in when evaluating, acquiring, using, or disposing of goods and services." (Loudon and Della Bitta, 1980). Nowadays, this phenomenon, can also be illustrated in the following way: "activities people undertake when obtaining, consuming, and disposing of products and services" (Blakwell, Minard and Engel, 2001). A study by Voss and Parasuraman (2003) suggests that the purchase preference is primarily determined by price than quality during pre-purchase evaluation. Given explicit quality information, price had no effect on pre-purchase or post-consumption quality perceptions. Instead, post consumption quality evaluations had a favorable impact on price evaluations. Another study by Chernev (1997) analyzed the effect of common features on brand choice and the moderating role of attribute importance. It is argued that when brand attributes differ in importance, with the best value on the most important attribute, thus further polarizing brands' choice shares. In contrast, when attributes are similar in their importance, common features are likely to have an opposite effect, equalizing brands share.

Keywords: Costmetics, Trends, buying pattern, Students &Quality

Introduction:

Cosmetics are mixtures of compounds derived from natural products or synthetic compounds.

Cosmetics serve many purposes. Those designed for personal care with skin care can be used to cleanse or protect the body or skin. Cosmetics (make-up) designed to beautify or alter a person's face can be used to hide imperfections, beautify a person's facial features (such as eyebrows and eyelashes), add color to a person's face, or change the entire face to match one's face. Different people, animals or things. People with acne are more likely to develop acne because of the harsh ingredients in cosmetics. Cosmetics can also create body odor.

The Food and Drug Administration (FDA), which regulates cosmetics in the combined States, defines cosmetics as "products intended for use on the human body to cleanse, beautify, increase attractiveness, or alter its appearance without affecting the body." . Body structure or function "" This general term includes any ingredient used as an accessory in cosmetics, and the FDA specifically excludes pure soap from this category. In many periods of Western history, the character of cosmetics will be whitened, cheeks will be blushed, and in many periods like this, people have s poken out against the use of cosmetics.

Despite the change in society's attitude towards cosmetics, many people use cosmetics from time to time to meet their needs.

According to one source, early growth in cosmetics includes:

- Ancient Egyptians used eye shadow
- Ancient Egypt used castor lubricate as a protective balm
- Skin cream made commencing beeswax, olive oil, and rose water, described to the Romans
- November. Century vaseline and lanolin.

The Study includes the products from Lakmé, Loreal, MAC Cosmetics, NYKAA, Estee Lauder, Clinique, Revlon.

Research has shown that consumer behaviour is difficult to predict, even for experts in the field; however, new research methods, such as ethnography, consumer neuroscience, and machine learning^[1] are shedding new light on how consumers make decisions. In addition, customer relationship management (CRM) databases have become an asset for the analysis of customer behaviour. The extensive data produced by these databases enables detailed examination of behavioural factors that contribute to customer re-purchase intentions, consumer retention, loyalty, and other behavioural intentions such as the willingness to provide positive referrals, become brand advocates, or engage in customer citizenship activities. Databases also assist in market segmentation, especially behavioural segmentation such as developing loyalty segments, which can be used to develop tightly targeted customised marketing strategies on a one-to-one basis. (Also see relationship marketing).

Factors influencing consumer behavior:

Consumer behavior is influenced by many different factors. Understanding your customer is an important factor in go-to-market success.

1. Psychological Factors

Human psychology is a major determinant of consumer behavior. These factors are difficult to measure but are powerful enough to influence a buying decision.

Literature review:

1. **Paruloberoi(2021)**:he expressed in his article "consumer behavior towards cosmetic products :A case of Delhi NCR" that the study analyses the buying process and the achieve of media communiqué on import behaviour on consumers and also suggests that the companies must try to increase thier business by providing online portal for shopping.
2. **Kim and Kyu-Hye Lee(2021)**: has opined in article "Changes in consumers alertness and interest in cosmetic products during the pandemic" that research explored the changes consumer awareness and suggest that epidemiological situations impinge on the consumer awareness of each cosmetic ".
3. **Junaid, Reshma, Faheem and Jamia(2020)** has opones in article "A Study on the purchase behaviour and cosmetic consumption pattern among young females in Delhi and NCR" that how female consume the product. As the income level of feminine consumer is increasing thier expenditure for products also rises.
4. **Aute, Khan and Dagale. (2015)** examined purchasing behavior for cosmetics. The main purpose of the investigate is to check the enumeration profile of consumers and to uncover the factors that affect consumers' decisions. They also covet to learn about purchasing cosmetic samples.They found that most people use cosmetics at home and that TV is the best medium to learn about cosmetics; product quality is considered the nearly all significant part in the customer's decision.
5. **Ponanki and Asif perwej (2014)** has expressed in their article "the buying attitudes of consumers of cosmetic products" that the researchers have made an earnest attempt to the marketers to identify different dimensions on what consumers prefers, which make them in deciding marketing mix.

6. **Vanessa, Hartmann & Ralf Terlutter** (2014): has opined in their article “women satisfaction with cosmetic brands : The role of dissatisfaction and hedonic brand benefits” That utilization and epicurean brand benefits both significantly contribute to female consumer's satisfaction with Women consumer.
7. **Nilesh & Anand (2014)**: have expressed in their article “consumer buying behavior towards cosmetic product that most of the people take quality as a preferred and important factor for purchasing Cosmetic product and its packaging as a least important factor for purchasing Cosmetic product.
8. **Sivagami (2016)** : examined the decision-making behaviors of consumers about the cosmetics industry. The aim of this review is to scrutinize the marketing behaviors of trade for cosmetic products. They also wanted to know the impact of various media in encouraging consumers to acquire a cosmetic brand. Using the random sampling technique. The sample size is 200. Data were composed through express interviews. Two types are prepared based on basic data and data collection. Percentage investigation is used to investigate the data. He discovered that discounted prices and attractive promotions could create a center of attention to more customers.

Problem Statement:

The Global and International Apparel Industry is in a growth phase. Too much purchasing power has made fashion-conscious people pay responsiveness to their beauty and health. Also, the selection of herbal and Ayurvedic beauty products allows clients to feel confident in using these products regularly. Therefore, the Indian and international cosmetics industry sees great growth opportunities in the coming years.

Research objectives:

1. Investigation of factors affecting cosmetics purchase among Ballari female MBA students.
2. Evaluation of the Effect of Product Quality on the Purchasing Decisions of Ballari Female MBA Students.
3. Investigation of the role of affordability of cosmetic products among female MBA students at Ballari.

Method:

statistics were collected since the questionnaire distributed to the participants with the principle.

Secondary Data Collection: Secondary data collected from company records and company websites.

Sampling Technique:

Appropriate sampling has been chosen as the sampling technique, and respondents have many options for completing the questionnaire.

Sampling criteria for the study:-

- A total of 100 people from Ballari District were selected for the study.

Convenience

- A sample was used to collect responses from participants.

Study Area:-

- Study area is limited to Ballari city, Karnataka.

ANALYSIS AND INTERPRETATION

- As per the study, the most influencing factor for consumer while choosing the product of by family and other factors are common influencers. The other factors such as peer group, workplace, advertisement, quality and price are the medium influencers of the customer to choose a product.
- As per the response, it shows that what the users of cosmetic project related to stylish, confident, trend and groomed professional. In which the respondents prefer to choose the confident related projection and second preferred projection is both equally with stylish and trend. Lastly least responded is groomed professional which attracts the consumers.
- The consumers most response related to belief has not shown much impact on the promised effects and the following points (very much, fairly much and fairly little) are shown most believing factor and other are being at medium believed and the left response belief less.
- The responses from the consumers have proved that they prefer Lakme brand products more than the other brands. The other in order products are equally being chosen by the respondents on an average basis.
- Most of them prefer online marketplaces for buying of the cosmetics as wide variety of product availability and various discount related factors arise. And others buy on physical retail stores, brand websites and local beauty stores as per their preference.

- The study is related to the decision changing factor or decision to buy the cosmetics and the most influencing factor in buying time is the quality and brand reputation which increases the product demand and its sales of a particular product.
- As per the response, the perception related to the affordability of the cosmetics reveals that the cosmetics are most in affordable manner and respondents doesn't feel them as expensive one to buy to their product list.
- The above table shows that most of the customers prefer most the skincare and hair care related products and study also proves the customers buy more of these kind of products. The fragrances and makeup are the second stage performers in the buying list.
- The study reveals that the customers how commonly tend to try new products related to cosmetics and they are very likely to adopt the new one and majority of others are not likely to try new products.
- The research being conducted by the respondents is to the little extent as it comes to do research before buying the products and majority opt to research sometimes before they usually purchase the product.
- Many of the respondents are being influenced by the sales promotions or discounts while buying the cosmetic products and others are being not so much being influenced by these promotion are discount being provided by the brands.
- The most preferred mode of payment by the respondents while buying the products is through cash and the left prefer the debit card ,credit card, mobile wallet and other modes of payments .
- As per the result most of the customers find the product quality is more important while it comes to purchase of the cosmetics and hence there is relevance in Importance given to importance of the purchase of cosmetics.

FINDINGS, SUGGESTIONS AND CONCLUSION

Findings:

1. The factors influencing the buying behavior of female MBA students for cosmetic products in Ballari include brand reputation, product quality, price, packaging, and social influence.
2. Product quality is a significant factor that strongly influences the buying decisions of female MBA students for cosmetic products in Ballari. Students prioritize products that offer effective results and meet their expectations.
3. Affordability plays a crucial role in the purchasing choices of female MBA students for cosmetic products in Ballari. Students tend to opt for products that fit within their budget constraints.
4. The brand reputation of cosmetic products influences female MBA students' buying behavior in Ballari. Students prefer reputable brands known for their quality and reliability.
5. Packaging is an important factor that impacts the buying decisions of female MBA students for cosmetic products in Ballari. Attractive and visually appealing packaging can attract students and influence their purchasing choices.
6. Peer influence and recommendations from friends significantly affect the buying behavior of female MBA students for cosmetic products in Ballari. Students often rely on the experiences and suggestions of their peers when making purchase decisions.
7. Convenience and availability of cosmetic products are important considerations for female MBA students in Ballari. Students are more likely to purchase products that are easily accessible and conveniently located.
8. Online reviews and ratings have a considerable impact on the buying decisions of female MBA students for cosmetic products in Ballari. Positive reviews and high ratings increase the likelihood of students choosing a particular product.
9. Product ingredients and formulation are significant factors influencing the buying behavior of female MBA students for cosmetic products in Ballari. Students prefer products with natural and safe ingredients.
10. Promotional offers, discounts, and loyalty programs play a role in the buying behavior of female MBA students for cosmetic products in Ballari. Students are attracted to special deals and incentives that provide them with value for their money.

Suggestions:

1. Cosmetic brands should focus on ensuring high product quality to meet the expectations of female MBA students in Ballari. Conducting regular quality checks and incorporating customer feedback can help improve product performance.
2. Brands should offer a range of affordable cosmetic products to cater to the budget constraints of female MBA students in Ballari. Introducing smaller-sized or travel-friendly options can make premium products more accessible.
3. Packaging should be visually appealing and innovative to capture the attention of female MBA students in Ballari. Brands should invest in attractive designs and environmentally friendly packaging to enhance the overall product experience.
4. Collaborating with influencers and leveraging social media platforms can be an effective strategy for cosmetic brands to reach and engage with female MBA students in Ballari. Influencer marketing campaigns and user-generated content can create a buzz and generate interest in the products.
5. Cosmetic brands should ensure the availability of their products in easily accessible locations such as college campuses, shopping centers, and online platforms. Offering convenient purchase options will attract female MBA students in Ballari.
6. Providing detailed information about product ingredients and formulation can help build trust and credibility among female MBA students in Ballari. Brands should prioritize transparency and clearly communicate the benefits of using their products.
7. Brands should actively engage with their customers by encouraging them to leave reviews and ratings online. Positive reviews and ratings can influence the buying decisions of female MBA students in Ballari.
8. Offering personalized product recommendations and customization options can enhance the buying experience for female MBA students in Ballari. Brands can utilize data-driven approaches to understand customer preferences and provide tailored suggestions.
9. Regular promotional offers, discounts, and loyalty programs can incentivize female MBA students in Ballari to purchase cosmetic products. Brands should create attractive deals that provide value for money and foster customer loyalty.
10. Conducting awareness campaigns and workshops specifically targeted at female MBA students in Ballari can educate them about the importance of skincare and makeup routines. This can help construct brand alertness and persuade

Conclusion:

The cosmetic industries are vastly growing in this era and most of the consumers prefer the brand and equivalent quality while choosing the product if there may be many other influencing factor while choosing the product but they prefer quality as the important factor. And companies should also increase the packaging , advertising and other important factors to increase its awareness towards the product in the market.

Bibliography:

1. Research articles reviewed:

- Paruloberoi(2021) "consumer behavior towards cosmetic products :A case of Delhi NCR"
- Kim and Kyu-Hye Lee(2021)"Changes in consumers alertness and interest in cosmetic products during the pandemic"
- EdakkotteShaji (2020) "A Study on customer satisfaction towards cosmetic products - Brand wise analysis"
- Junaid, Reshma, Faheem and Jamia(2020) "A Study on the purchase behaviour and cosmetic consumption pattern among young females in Delhi and NCR"
- Annadrajan (2016)the decision-making behaviors of consumers in relation with the cosmetics industry
- Aute, Khan and Dagale. (2015) examined purchasing behavior for cosmetics
- Preeti pujari (2020) "marketing research on study of cosmetic brand in India"
- PushparajWagh (2003) "A study of consumer behavior regarding cosmetic product with reference to Lakme".
- Shajahan & Mohammed safi (2009) "A Study of consumer behavior towards Cosmetic products in tiruhirapalli District"
- AthulyaV, M Ramya (2019) "consumer preference and Brand Awareness towards cosmetic product in calicut city ,kerala".
- Kruti and Sankbla (2017) "A study on consumer behavior towards cosmetic products"
- Ponanki and Asif perwej (2014) "the buying attitudes of consumers of cosmetic products".
- Vanessa,Hartmann& RalfTerlutter (2014) "women satisfaction with cosmetic brands : The role of dissatisfaction and hedonic brand benefits"
- Nilesh&Anand(2014) "consumer buying behavior towards cosmetic product"

2. Websites:

- <https://lakme.com/en/>
- <https://www.maybelline.co.in/>
- <https://www.lorealparis.co.in/>
- <https://www.nykaa.com/>
- <https://www.maccosmetics.in/>
- <https://sephora.nnnow.com/>
- <https://www.estelauder.in/>
- <https://www.clinique.in/>
- <https://revlon.co.in/>
- <https://www.clarins.in/>

A STUDY ON CONSUMER SATISFACTION ON LOBICON LTD

Krishna Shiroor¹
MBA Student

Dr. Shaheeda Banu S²
Professor,
DMS, BITM,
Ballari
drsyedshaheeda@gmail.com

Dr. Christopher Raj D³
Professor,
DMS, BITM,
Ballari

ABSTRACT

Consumer satisfaction is a critical metric that determines the success and longevity of businesses in today's competitive marketplace. Lobicon Ltd, a prominent company in [insert industry], recognizes the importance of understanding and enhancing consumer satisfaction to maintain its market position and foster sustainable growth. This study aims to provide a comprehensive analysis of consumer satisfaction with Lobicon Ltd, shedding light on the factors that influence it and the strategies the company employs to meet and exceed consumer expectations.

The study also explores areas where Lobicon Ltd can further enhance consumer satisfaction. These include improving response time to customer inquiries, expanding the product/service portfolio, and increasing engagement on social media platforms. Additionally, the research highlights the importance of fostering a strong sense of brand loyalty and trust among consumers. Commitment to consumer satisfaction is evident through its customer-centric initiatives, such as personalized product recommendations and loyalty programs. These strategies have proven effective in retaining existing customers and attracting new ones. However, the company should continue to adapt to changing consumer preferences and market trends to remain competitive.

Keywords: Customer satisfaction, Preferences, Competition, Strategies

INTRODUCTION

The primary activity in secondary industry, known as manufacturing, is the production of commodities for use or sale using manpower, machinery, chemical or biological processes, or formulation. The word may be used to a range of human undertakings, from handicraft to high-tech, but it is most usually applied to industrial design, which requires the extensive conversion of raw materials from primary industries into finished goods. Such finished goods may be sold to other manufacturers for the production of other, more complex products (such as aircraft, household, furniture, sports equipment, or automobiles) or distributed via the tertiary industry to end users and consumers (typically through wholesale, who in turn sell to retailers, who in turn sell to individual CONSUMERS).

REVIEW OF LITRETURE

- 1) S.Murali (2016) After-sale services (ASS) are actions that happen after a consumer buys a product and are focused on assisting consumers with the usage and disposal of products. ASS can establish long-lasting bonds with customers and make a substantial impact on their satisfaction. The goal of this study is to determine which SERVQUAL dimensions based on ASS attributes should be given more attention in order to improve the quality of ASS, taking into account the companies that are involved in the production of home appliances. These SERVQUAL dimensions include the level of Consumer Satisfaction (CS), Consumer Retention (CR), and Consumer Loyalty (CL).
- 2) Md. Uzir Hossain Uzir (2020) Investigating the effects of product quality, service quality, and perceived value on consumer satisfaction with the strength of the social media effect was the study's main goal. A systematic questionnaire was created for the study's quantitative research approach in order to gather information from 323 Bangladeshi homes. Utilising social media, a judgemental sample strategy was used to gather data. Utilising SEM-AMOS and SPSS, collected data was examined. The outcome showed that customer satisfaction with the degree of social media usage is positively and significantly impacted by product quality, service quality, and perceived value.
- 3) Ramayah Thurasamy (2021) Due to family structure, increased income levels, and technical connection, consumers are accustomed to using electronic household equipment. Huge consumer bases, rising demand, developing markets, fierce brand rivalry, and shifting consumer behaviour are impressive; nonetheless, consumer happiness and loyalty are not constant and are subject to some change. The impetus for this research is the dearth of comprehensive studies on loyalty and happiness in this situation. The goal of this study was to examine how brand trust and brand loyalty are related to consumer happiness and its predictions.
- 4) Sivanesan Murali (2016) After-sale services (ASSs) are actions that happen after a customer buys a product and are intended to help customers use and dispose of their purchases. ASS can establish long-lasting bonds with customers and make a substantial impact on their satisfaction. This study aims to determine the effects of selected ASS qualities on consumer satisfaction and the impact of ASS on consumer satisfaction. Multiple regression analysis along with the SERVQUAL model is used for this purpose. A case study firm that makes home appliances is taken into consideration, and the SPSS-AMOS 21 was used to examine consumer opinions on the company's ASS operations.

- 5) Dr. N. Sugundhan (2018) Consumer satisfaction is a fundamental component of marketing expertise and is primarily distinct as the number of consumers, or level of total consumers, whose detailed interaction with a company, its products, or its services exceeds predetermined fulfilment goals.
- 6) Amira M. Idrees (2020) Energy Consumption has become one of the strategic objectives all over the world which enterprises obligation but it should also be all citizens' obligation. Focusing on individuals' energy consumption, a vital approach for saving energy is a collaboration strategy which aims at sharing the home appliances for best usage. In this research, an approach is proposed for recommending the collaboration plan for adjacent houses in different perspectives; they are sharing appliances and minimizing the consumption rate. The research adopts the mining techniques in order to explore the required associations targeting to build the road map for appliances consumption.

STATEMENT OF THE STUDY:

Customer satisfaction is a metric that gauges how satisfied a company's clients are with its products, services, and abilities. A company may decide how to best improve its products and services by using information on customer satisfaction, such as surveys and ratings.

NEED FOR THE STUDY:

- This study is taken up to know the level of satisfaction of Consumers. The project title "Consumer satisfaction has been carried out with the above purpose.
- This study is going to offer some suggestions for betterment of the company.
- As the marketing concept is built on the premises, that marketing first identifies consumer needs and requirements and develop the products or services to satisfy those requirements.
- However, as in the case of other fields competition is emerging in this field also, it is the responsibility of every successful organization to retain its Consumers by understanding their requirements to removing the dissatisfaction and improving the sales as well as market share.

Objectives of the study

- To know the most influencing factors in decision making to purchase a Lobicon Ltd Products.
- To ascertain the Consumers level of satisfaction with the product of Lobicon.
- To know the problems faced by the Consumer from the Lobicon Ltd.
- To know the Consumer satisfaction with the sound system of Lobicon Ltd.

Scope of the Study:

Through this research we will understand the consumer satisfaction measures at Lobicon company at different Dimensions like satisfying towards products, prices, discounts. This study scope is for the period of 06 Weeks.

Research Methodology:

An approach to defining the research problem is research methodology. The title, problem statement, significance of the study, goals and objectives, research design, data collection, statistical analysis, and study limitations are all included.

DATA COLLECTION:

The data is collected using both primary and secondary method.

A. Primary Data:

- Collection of information through the interview.
- Collection of information through the questionnaire.

B. Secondary Data:

- The information collected by organizational record.



Analysis and Interpretation

1. 56% of the respondents are male candidates and 44% of the respondents are female candidates.
2. 53% of the respondents are content with their understanding of mechanics, while 24% believe their knowledge is average and 9% feel it is bad.
3. 39% of the respondents are said yes Lobicon deliver, the vehicle on time to the customers, 27% of the respondents are said sometimes and 20% of the respondents are said no.
4. 86% of the respondents are having suggestions to improve the customer satisfaction in Lobicon and 14% of the respondents are said no.

Findings

- Of the respondents, 37% learned about Lobicon through electronic media, 24% through word-of-mouth, 21% through friends and family, and the remaining 12% through print media.
- Of the respondents, 38% are persuaded to buy Lobicon items by the salespeople, 27% are persuaded by friends, and 26% are persuaded by self-interest.
- While 22% of respondents are dissatisfied with the financing services at Lobicon, 78% of respondents are satisfied.
- 39% of respondents are dissatisfied with the warranty duration offered by the firm, while 61% of respondents are pleased with it.
- 43% of respondents said they were pleased with the deal the firm offered, 17% said they were extremely satisfied, and 34% said they were unsatisfied.

- 38% of respondents felt the customer service personnel' behaviour was good, 24% said it was exceptional, and 27% said it was ordinary.
- 52% of respondents say they are happy with the quality of Lobicon, 27% say they are extremely happy, and 21% say they are not happy.

Suggestions

- The Lobicon Company has to establish sound CRM practices that raise customer satisfaction
- R&D should enhance the current feature, which contributes to higher consumer happiness.
- The business should levels.
- The business advertise all of the benefits it provides.
- The majority of customers express satisfaction with the factors, services, and product design, thus the corporation should not only uphold the current standards but also raise them.
- As a result, Lobicon has to concentrate on factors that would increase customer satisfaction and consequently market share.

Conclusion:

The most important aspect for clients is their level of satisfaction, both for themselves and the business. As a result, if the consumers are happy with the goods or services, the business will be able to expand and succeed more by producing goods in large quantities and of high quality. According to a poll of "Wavestech" consumers, customer satisfaction may be attained if the customers are happy with a price drop and an extension of the product and service warranty and guarantee duration. Excellent communication exists between the business and its clients. The consumers are given the appropriate instructions on how to utilize.

BIBLIOGRAPHY

BOOKS:

1. Kothari C.R., Research Methodology, New Delhi; New Age International publication, second edition.
2. Jayasankar.S, Marketing Management, Margham publication.
3. Customer relationship management, Supriya Singhand Bhanu

Prakash Verma, published by THAKUR PUBLISHERS, CHENNAI.

4. Premavathy. N.DR, Marketing Management, Shri Vishnu publications.

References:

- S.Murali(2016) Modeling and Investigating the relationship of after sales service quality with Consumer satisfaction, retention and loyalty – A case study of home appliances business Volume 30, May 2016, Pages 67-83 Received 8 July 2015, Revised 27 November 2015, Accepted 6 January 2016, Available online 14 January 2016, Version of Record 14 January 2016.
<https://doi.org/10.1016/j.jretconser.2016.01.001>
- Md. Uzir Hossain Uzir (2020) Does Consumer satisfaction exist in purchasing and usage of electronic home appliances in Bangladesh through interaction effect of social media? Volume 23 Issue 12 2021 ISSN: 1756-0047, eISSN: 1756-0055
- Uzir, M.U.H., Hamid, A.B.A., Jerin, I. et al. Consumer satisfaction and brand loyalty to electronic home appliances in Bangladesh: the contingent role of brand trust. SN Bus Econ 1, 86 (2021). <https://doi.org/10.1007/s43546-021-00088-z> Received 03 October 2020, Accepted 11 May 2021, Published 27 May 2021, DOI <https://doi.org/10.1007/s43546-021-00088-z>
- Sivanesan Murali (2016) Assessment of impact of after sales service attributes on Consumer satisfaction for a home-appliances manufacturing firm Vol. 7, No. 1 ISSN: 1748-1252, eISSN: 1748-1260
- Yi Liu (2019) Pricing-Based Demand Response for a Smart Home With Various Types of Household Appliances Considering Consumer Satisfaction Page(s): 86463–86472 Date of Publication: 20 June 2019 Electronic ISSN: 2169-3536 DOI: 10.1109/ACCESS.2019.2924110

A STUDY ON NON-PERFORMING ASSETS WITH REFERENCE TO KARNATAKA VIKAS CREDIT & MULTIPURPOSE CO-OPERATIVE SOCIETY

1) **Tarun k** student of 6th semester (USN3BR21BA151) Department of Management Studies, Ballari
Institute of Technology & Management, Ballari, Karnataka, India

2) **BAGALI AMBREEN** Assistant Professor, Department of Management Studies, Ballari Institute of
Technology & Management, Ballari, Karnataka, India

ABSTRACT

Banking sector performance can be measured easily by assessing the existence of bad loans such as if any asset could unable to provide returns for a specific period of time is known as Non-Performing Asset (NPA). Nowadays, most of the banks are facing with issues like bad loans and increasing frauds in large scale. After second Covid-19 wave across sectors, repayment capacity of borrowers was arising big spike. This study aims at identify reasons, control and reduce on occurring non-performing assets. This research covers the period of 2018 to 2023 by collecting data and information from various primary and secondary sources.

INTRODUCTION

A cooperative bank is a type of financial institution whose members also serve as both its owners and customers. It was commonly discovered by others with similar interests from the same local or professional group. It was created to aid 3 in the social advancement of economically disadvantaged groups and to keep them out of the clutches of unscrupulous lenders who grant loans to the needy at high interest rates. The architecture of the co-operative structure is influenced by the concepts of cooperation, mutual help, democratic decision-making, and open membership. The 'one shareholder, one vote' and 'no profit, no loss' ideals are upheld by it. Company's outstanding increased from Rs. 14100 lac to Rs. 17819.28 ac during the reviewed year, registering a growth of 26.38% as opposed to a negative growth of 5.70% during the current year. This is considered very well and clearly demonstrates that they have recovered from the effects of demonetization the previous year.

LITERATURE REVIEW

1) Laveena (2016) A bank's NPA level is a good indicator of its success. Any asset in a bank that has a high NPA rating loses value, and it also shows that there have 12 been more loan defaults and that banks' net worth has dropped. The amounts you must establish for provisions rise as NPA levels rise, which reduces total shareholder value and profits.

2) D. Siva Satyanarayana (2016) Non-performing assets are a major concern for Indian banks. Non-performing assets (NPAs) are a sign of a bank's health. A high number of NPAs implies a high rate of loan defaults, which affects a bank's profitability, net worth, and asset value. The primary role of the banking business is to provide credit for economic activities.

3) Pro. D.S. Rathore (2016) Assets that generate revenue are known as performing assets, whereas those that do not are known as non-performing assets. a financial arrangement in which the borrower has failed to make any previously agreed-upon interest and principal repayments to the licenced lender for an extended period of time. As a result, the lender receives no revenue from the nonperforming asset in the form of principal or interest payments.

4) AniruddhaDurafe (2016) This research studies the cyclical behaviour of both 10 public and private sector banks in India, with a focus on non-performing assets. The goal of this research is to see if non-performing assets in India's public and private banks behave pro-cyclically. The Pearson correlation coefficient data show that gross non-performing assets and economic condition in both public and private sector banks display countercyclical behaviour.

5) K. PRASANTH KIRAN (2016) the phrase "nonperforming asset" is crucial for financial organisations. Non-Performing Assets demonstrate the effectiveness of the banks' operations. Non-Performing Assets are sums that the bank does not get 7 paid back for loans it has given.

6) Dr.RajeshRathore (2016) Banking and finance have a significant role in economic growth in emerging nations.

7) Dr. Raj Kumar Mittal (2017) the effectiveness and stability of the banking business are key factors in the expansion of the budget. NPAs is the most crucial variable used to gauge the soundness of the lending segment. Non-performing assets directly affect the financial success, or profitability, of banks. It indicates the efficacy with which a bank maximises all of its resources, providing as a gauge of asset utilisation and managerial performance.

9) Sudin Bag (2017)NPAs are a significant and difficult problem in the banking industry today. It is a very powerful and uncontrollable virus that is seriously harming both the health of the lending business and the economies of the world.

10) PayalGoel (2018) the study's goal is to investigate the cyclical nature of NPAs in the Indian banking system. It also aims to discover the root reasons of the nonperforming assets' behaviour. Furthermore, comparisons of banks from the public, private, and foreign sectors have been undertaken.

OBJECTIVES OF THE STUDY

- 1.** To understand the concept of Non-Performing Assets in banking sector
- 2.** To find out the reasons of NPA that can be used to control and reduce the NPAs in Karnataka Vikasa credit and multiple purpose co-operative society Ltd.

3. To understand the effects of NPAs on the operations of the Karnataka Vikasa credit and multiple purpose co-operative society Ltd
4. To find out the relationship between Net Profit and Net NPA's of Karnataka Vikasa credit and multiple purpose co-operative society Ltd.

NEED OF THE STUDY

Scheduled banks and non-scheduled banks are the two classifications of banks in India. Scheduled banks include private, public, and cooperative institutions; non-scheduled banks include foreign and cooperative institutions. Public sector banks are nationalised banks. In India's financial system, public sector banks play a crucial role. Public sector banks will offer loans and advances to people or individuals as well as for small and medium-sized businesses, as well as for large industries that are for the economic development of our country by mobilising household savings and directing them towards profitable investments as well as by offering credit facilities to its customers at low interest rates.

DATA AND METHODOLOGY

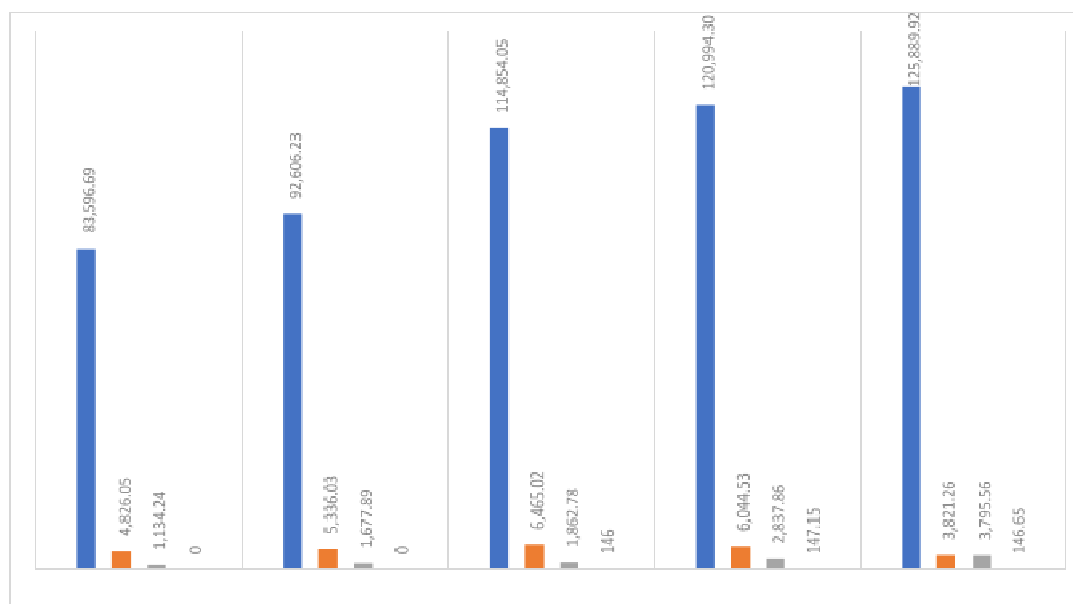
Primary Data: Data that are acquired for the first time are called primary data. At the Karnataka 24 Vikasa Credit and Multiple Purpose Co-operative Society Ltd., meetings and one-on-one interviews with the officers are how the primary data is collected.

Secondary Data: The sources of secondary data are published materials such as and annual reports from 2016-2023 of Karnataka Vikasa credit and multiple purpose co-operative society Ltd.

DATA ANALYSIS AND INTERPRETATION

TABLE1: Classification of Nonperforming assets from 2018-23

Particulars	2018-19	2019-20	2020-21	2021-22	2022-23
Standard assets	83,596.69	92,606.23	1,14,854.05	1,20,994.30	1,25,889.92
Sub-standard assets	4,826.05	5,336.03	6,465.02	6,044.53	3,821.26
Doubtful assets	1,134.24	1,677.89	1,862.78	2,837.86	3,795.56
Loss assets	-	-	146.00	147.15	146.65



The graph above shows the trend for each asset type, including standard, substandard, dubious, and loss assets. We may infer from the graphic that over the course of five years, the standard assets for each year exhibit a growing tendency. Even substandard assets and questionable assets follow the same pattern, with the exception of 2018 and 2019, when they exhibited a little drop. Except for substandard assets in 2022 and 2023, dubious assets 5 and substandard assets are rising together with the standard assets. The significant growth in questionable assets is evident

in the 2018–19 fiscal year, when it rose from 1134.24 to 1677.89, a 147 percent increase in only one year. While it has grown by 105% for standard assets from 114854.05 to 120,994.30 in 2019–20. And from 5336 to 6465 in 2020–21, the amount of substandard assets has 4 grown by 121.16 percent.

TABLE-2 Gross NPA, Gross advances and Gross NPA ratio.

The following table is displaying the data of gross NPA, Gross advances and the 5 gross NPA ratio of Karnataka Vikasa credit and multipurpose co-operative from the year 2018-19 to 2022-23.

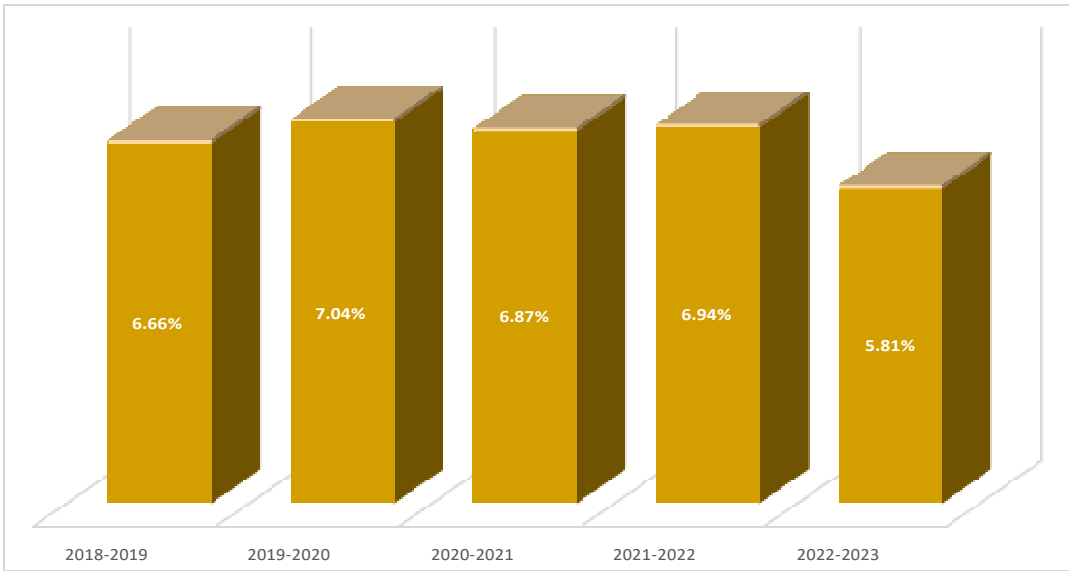
Particulars	Gross NPA	Gross Advances	Gross NPA ratio
2018-2019	5960.29	89556.98	6.66%
2019-2020	7013.92	99620.15	7.04%
2020-2021	8473.81	123327.86	6.87%
2021-2022	9029.55	130023.85	6.94%
2022-2023	7763.48	133653.40	5.81%



The link between the gross NPA and gross advances of the Karnataka Vikasa Credit and Multipurpose Co-operative Bank is seen from the preceding chart. We can observe an surge in the gross NPA as the gross advances rise year over year. Except for 2022–23, the gross NPA has been growing steadily from the year 2018–19. And 23 starting with the 2018–19 fiscal year and continuing until the conclusion of the 2022–23 fiscal year, gross advances are growing. We can draw the conclusion that rising gross advances are fuelling rising non-performing assets (NPA).

This demonstrates that when the company's bank advances rise, so too do the numbers of customers who miss payments. Making ensuring that the rise in gross NPA stays below a specific point is essential since doing so might be detrimental to the organisation.

Graph 3: Gross NPA ratio from the year 2022-23



The above mentioned graph shows that the rise in gross NPA, with the exception of 2022–23, in relative to gross advances is showing an increasing trend from the years 2018–19 to 2019–20. It demonstrates that the gross NPA in 2018–19 represents 6.66 percent (5960.29) of the total gross advances (89556.98), and so on for the following years. However, from 2021–22 to 2022–23, the gross NPA represents a smaller 5 fraction of the total gross advances. This indicates that the bank has increased its advances while also lowering the rate of gross NPA. The bank will benefit from this 19 circumstance.

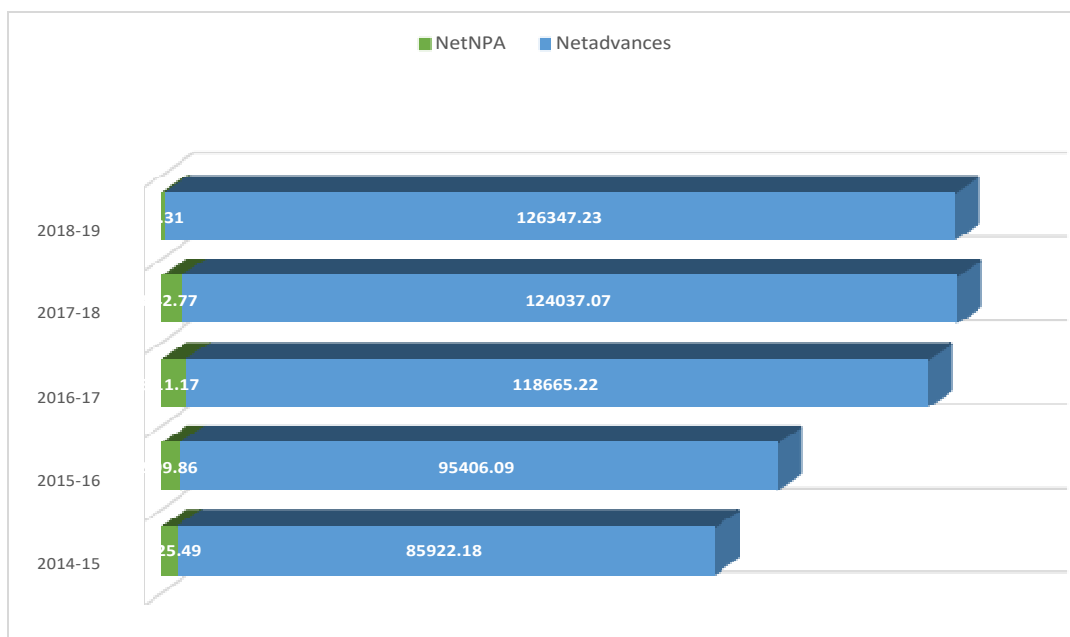
Table 3 - Net NPA, Net advances and Net NPA ratio

The following table is displaying the data of net NPA, Net advances and the net NPA ratio of Karnataka Vikasa credit and multipurpose.

Particulars	Net NPA	Net advances	Net NPA ratio
2018-2019	2325.49	85922.18	2.71%
2019-2020	2799.86	95406.09	2.93%
2020-2021	3811.17	118665.22	3.21%
2021-2022	3042.77	124037.07	2.45%
2022-2023	457.31	126347.23	0.36%

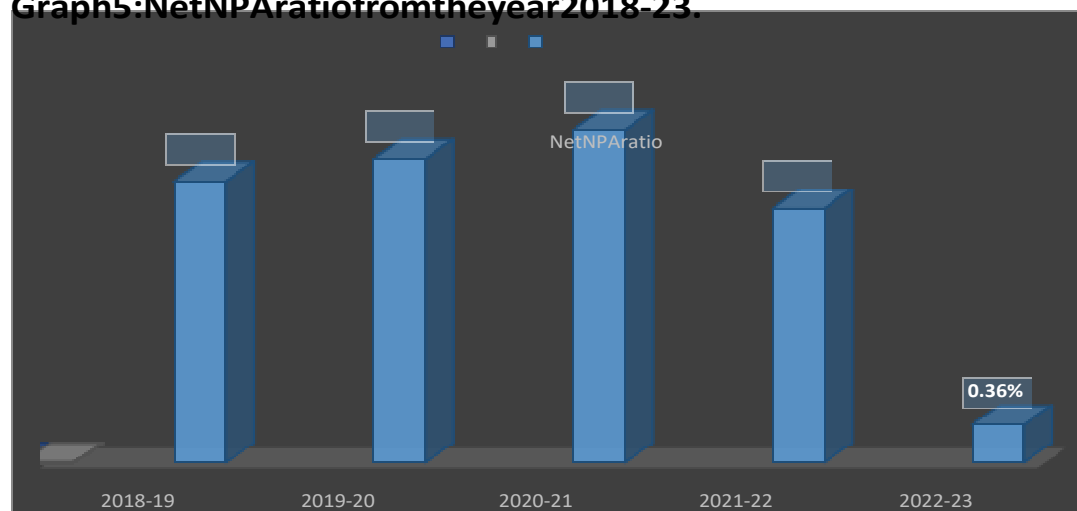
Graph4-NetNPAandNetAdvancesfromtheyear2018-23

The data in the above tables is displayed in the form of a chart in the graph below. It includes the information of Net NPA and Net advances.



According to the above mentioned data, even the net NPA rises as a result of a rise in net advances made by the Karnataka Vikas Credit and Multipurpose Co-operative Bank. It exhibits a pattern resembling the one seen in the correlation between gross NPA and gross advances.

Graph 5: Net NPA ratio from the year 2018-23.



NPA and Net advances of the bank Karnataka Vikas credit and multipurpose co-operative bank from the year 2018-19 to the year 2022-23.

The graph above demonstrates that between the years 2018–19 to 2019–20, there has been an increase in Net NPA as a percentage of Net Advances. It states that the net NPA in 2018–19 makes up 2.71 percent (2325.49) of the overall net advances (85922.18), and that it continues to rise in the years after, while it makes up less of the total net advances in 2021–22 and 2022– 23. This demonstrates how the bank was able to raise its advances while still lowering the rate of net NPA. The bank will benefit from this circumstance.

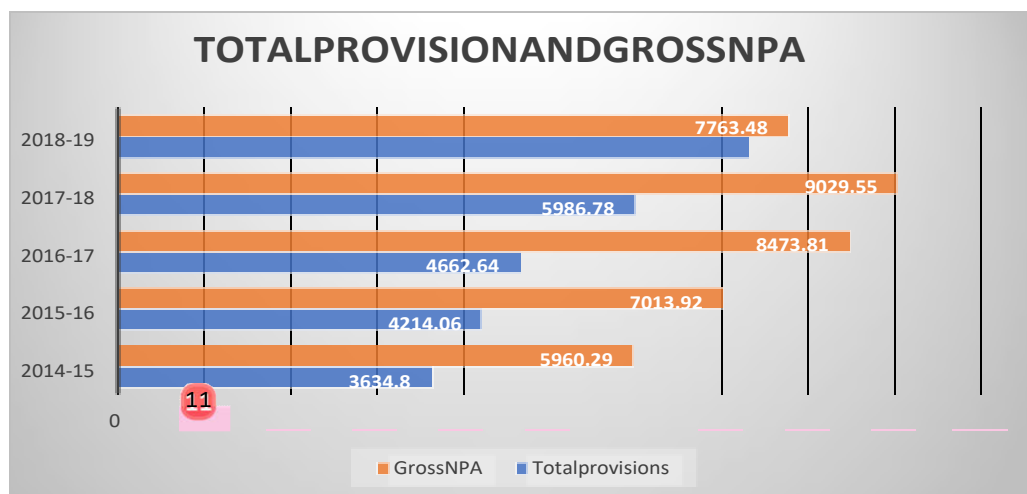
TABLE 4: Provision, GROSS NPA and Provision to NPA ratio.

The following table is displaying the data of provisions, gross NPA and the provision to NPA ratio of Karnataka Vikasa credit and multipurpose co-operative

Particulars	Total provisions	Gross NPA	Provision to NPA ratio
2018-2019	3634.80	5960.29	60.98%
2019-2020	4214.06	7013.92	60.08%
2020-2021	4662.64	8473.81	55.02%
2021-2022	5986.78	9029.55	66.30%
2022-2023	7306.17	7763.48	94.10%

GRAPH6:provisionsandgrossNPAfromtheyear2018-23.

thedataintheabovetableisdisplayedintheformofachartinthegraphbelow.Itincludestheinformation of provisions and gross NPA of the Karnataka Vikasa credit and multipurpose co-operative bankfrom theyear2018-19 totheyear 2022-23.

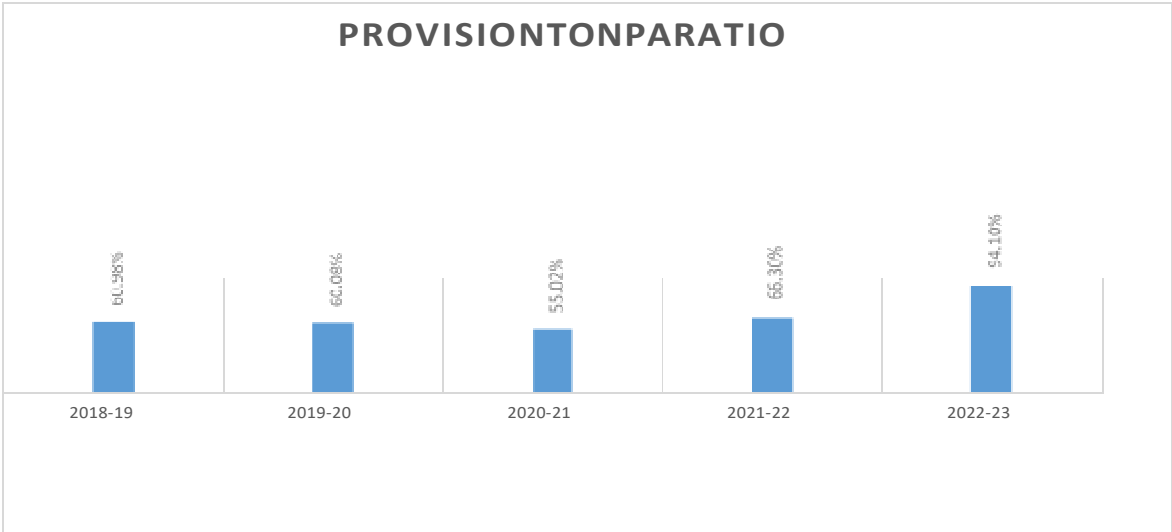


Bank.

perative bank from the year 2018-19 to 2022-23.

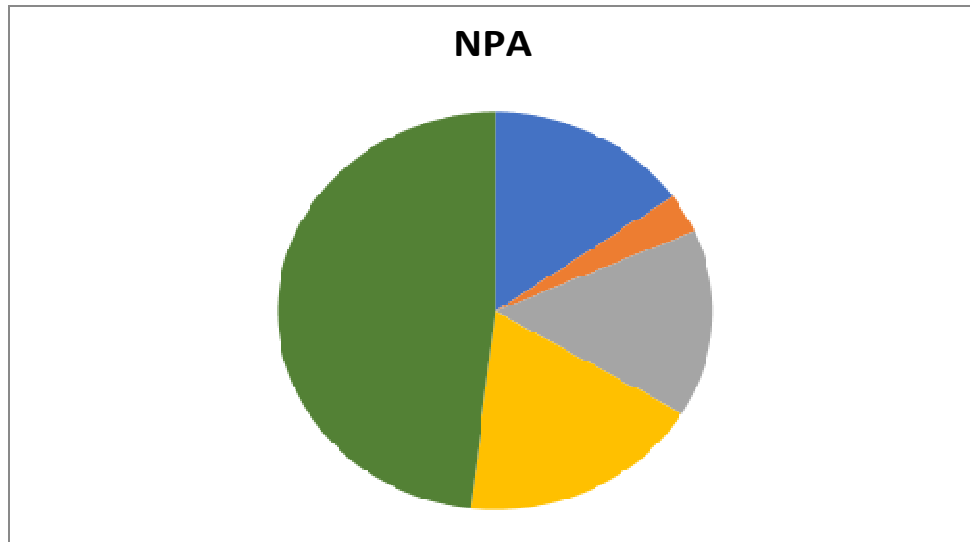
The total provisions and gross NPA of the Karnataka Vikasa Credit and Multipurpose Cooperative Bank are shown in this graph. The provisions are the sums that have been set aside for use in specific circumstances. Here, it can be seen that while the gross NPA exhibits an upward tendency from the years 2018–19 to 2022–23, it can also be seen that provision has grown in a similar manner. If the provision covers portion of the gross NPA, that is good for the bank. If the gross NPA exceeds the allowance by an excessive amount. The bank must exercise caution since it may suffer NPA losses and lack the resources to cover them.

Graph7:provisionstogrossNPAratiofromtheyear2018-23



TotalNPAHoldings

Particulars	Percentage
Home loan	15.2%
Car loan	3.2%
Education loan	15.2%
Agriculture loan	18.2%
Others	48.5%



Others loan includes:

- ☐ Personal Loans
- ☐ Small business loans
- ☐ Mortgage Loan

FINDINGS:

1. Trend of the non-performing assets of the Karnataka Vikasa credit and multipurpose co-operative bank the year 2018-19 to 2022-23 is Increasing. It also displays the effect of non-performing assets on each of the asset class
2. The step increase of doubtful assets is seen in the year 2018-19 where it has increased from 1134.24 to 1677.89 which comes to a 147 percent increase in a span of 1 year.
3. Gross NPA except for 2022-23 is showing an upward trend in relation to gross advances from the years 2018-19 to 2019-20; specifically, the gross NPA in 2018-19 represents 6.66 percent (5960.29) of the total gross advances (89556.98), and so on for the following years. However, from 2021-22 to 2022-23, the gross NPA represents a smaller percentage of the total gross advances. This indicates that the bank has increased its advances while also lowering the rate of gross NPA. The bank will benefit from this circumstance.
4. From the years 2018-19 to 2019-20, the ratio of Net NPA to Net Advances is growing. It states that the net NPA in 2018-19 makes up 2.71 percent (2325.49) of the overall net advances (85922.18), and that it continues to rise in the years after, while it makes up less of the total net advances in 2021-22 and 2022-23. This demonstrates how the bank was able to raise its advances while still lowering the rate of net NPA. The bank will benefit from this circumstance.
5. The underlying reason of Karnataka Vikasa Credit and Multiple Purpose Cooperative Society's NPAs is consumers who lack financial stability and credit worthiness, which are the primary causes of NPAs in the company.

6. The major cause of NPA in agriculture loans is inconsistent or non-existent profitability.
7. Poor financial stability and a lack of a consistent source of income for the client are the main causes of NPA in housing loans.
8. Customers and students who borrow money for education do not start looking for work 9 right away after finishing their courses, which costs the firm NPA.
9. In the early stages of a firm, profits are typically poor or non-existent. During this time, clients who took out small business loans fail to repay the money to the bank, which results in NPA in small business loans

CONCLUSION

Managing an account framework plays a very important role in the nation's fiscal situation. The reliability of its structure for conserving money is strongly correlated with the quality of an economy. Only a sound system for managing risks and credit evaluation will be able to solve the NPA problem. Prudential requirements must be included in the managing an account structure in order to lessen, if not completely eliminate, the NPAS problem. The Karnataka Vikasa Credit and Multipurpose Bank's nonperforming assets were the subject of this 15 investigation. The gross, net NPA, and advances were all examined. Additionally, the link between net profit and NPA was investigated. According to the report, the bank's nonperforming assets are growing annually as a result of the rise in advances. Before raising the advances, the bank is advised to exercise prudence

REFERENCES:

1. ShanabhogaraRaghavendra (2018) NON PERFORMING ASSETS IN COMMERCIAL BANKS IN INDIA: AN ANALYSIS ISSN (P): 2347-4564; ISSN (E): 2321-8878 Vol. 6, Issue 4, Apr 2018, 377-386
2. AnkitGarg (2016) A STUDY ON MANAGEMENT OF NON-PERFORMING ASSETS IN CONTEXT OF INDIAN BANKING SYSTEM Vol.3 (Iss.11): November, 2016] ISSN: 2454-1907 DOI: <https://doi.org/10.29121/ijetmr.v3.11.2016.68>
3. VarunaAgarwala (2019) A critical review of non-performing assets in the Indian banking industry Received 21 August 2019 Accepted 4 September 2019Vol. 13 No. 2, 2019 pp. 12-23 Emerald Publishing Limited 0972-9968 DOI 10.1108/RAMJ-08- 2019-0010

4. PayalGoel (2018) CYCLICALITY OF NON-PERFORMING ASSETS: EVIDENCE FROM INDIAN BANKING INDUSTRY Journal of Commerce & Accounting Research Volume 7 Issue 3 July 2018
5. Dr Rajesh Rathore (2016) Impact of Non-Performing Assets on Banking Industry: The Indian Perspective ISSN-2455-0620 Volume 2, Issue-7, July-2016
6. Ms.Richa Banerjee (2018) Non-Performing Assets: A Comparative Study of the Indian Commercial Banks Journals: International Journal of Social Relevance & Concern ISSN-2347-9698 Volume 6 Issue 2 February 2018
7. D Jayakkodi (2016) Impact of non-performing assets on return on assets of public and private sector banks in India ISSN Print: 2394-7500 ISSN Online: 2394-5869 Impact Factor: 5.2 JAR 2016; 2(9): 696-702 www.allresearchjournal.com Received: 07-07-2016 Accepted: 08-08-2016
8. S. Narasimha Chary (2019) Non-Performing Assets in Public Sector Banks - A Study Vol -XII, Issue-1, Jan-June, 2019, PP 24-32/24
9. TARAK NATH SAHU (2019) IS THE EFFICIENCY OF BANKS DEGENERATING DUE TO THE MOUNTING OF NON-PERFORMING ASSETS? AN EMPIRICAL INVESTIGATION USING DEA Journal Vol. 23, December 2019 65-86
10. Pro. D.S. Rathore (2016) Non Performing Assets of Indian Banking System and its Impact on Economy IOSR Journal of Economics and Finance (IOSR-JEF) e-ISSN: 2321-5933, p-ISSN: 2321-5925. Volume 7, Issue 6 Ver. III (Nov, Dec. 2016), PP 21-26 DOI: 10.9790/5933-0706032126
11. AniruddhaDurafe (2016) Cyclical Behavior of Public and Private Sector Banks: A Comparative Study of Non-performing Assets ISSN: 2382-5219 (Print); 2467-9267(Online) January 2016, <http://dx.doi.org/10.3126/jbmr.v1i1.14548> Vol.1, No.1, pp. 14-25 DOL:
12. K. PRASANTH KIRAN (2016) EFFECT OF NON PERFORMING ASSETS ON THE PROFITABILITY OF BANKS A SELECTIVE STUDY International Journal of Business and General Management (IJBGM) ISSN(P): 2319-2267; ISSN(E): 2319-2275 Vol. 5, Issue 2, Feb Mar 2016, 53-60
13. Dr. Raj Kumar Mittal (2017) The Problem of Rising Non- performing Assets in Banking Sector in India: Comparative Analysis of Public and Private Sector Banks international

Journal of Management, IT & Engineering Vol. 7 Issue 7, July 2017, ISSN: 2249-0558
Impact Factor: 7.119

14. Sudin Bag (2017) NON-PERFORMING ASSETS A BIGGEST CHALLENGE IN BANKING SECTOR A COMPARATIVE STUDY BETWEEN INDIA AND BANGLADESH BANKING SECTOR DOI: 10.21917/ijms.2017.0084
15. Laveena (2016) A Study of Non Performing Assets of Public Sector Banks in India International Journal of Research in Engineering, IT and Social Sciences ISSN 2250-0558, Impact Factor: 6.452, Volume 6 Issue 04, April 2016
16. D. Siva Satyanarayana (2016) Non-Performing Assets of Commercial Banks in India - A Study International Journal of Trend in Research and Development, Volume 3(6), ISSN: 2394-9333 www.ijtrd.com.

“A woman's achievement in leadership”

Authors

1. Dr Shaheeda Banu.S
Professor
PhD
9845737140
Ballari Institute of Technology and Management
Jnana Gangotri Campus
Hospet Road, Near Alipura
Ballari 583104

2.R.P. Md.Khalid
Asst.Prof.,
DMS,
BITM,Ballari.

ABSTRACT

Women have competed for previously all-male-oriented jobs since the Equal Employment Opportunity Act of 1972. Females needed office survival guides more than office success guides when they found themselves in unfamiliar territory. Numerous studies have been conducted over the years to track women's advancement to the top of organisations. While there are more ladies working today, the research found that they are still labouring with career elevation and mentor for successful managerial guidance. females held nearly 52% of all specialized roles in the USA in 2014, but only 14.6% of upper management positions and 4.6% of Fortune 500 CEO positions were acquired. There are numerous reports providing professional advice and points for working females, and a dearth of articles addressing apt practices for female executives.

To fill this gap in the literature, the author approached the topic from a practical standpoint, offering lessons learned from Katharine Graham, the first female Fortune 500 Company CEO.

Keywords

Women leadership, executive women, women's career advancement, best practices, managerial gender issues, motivation, and personality.

A tiny number of females began getting employed by firms in the early 1900s. With the onset of World War II and its following aftermath, many of them who had laboured to help found themselves unemployed, despite their willingness to work. Abraham Maslow, who was studying human motivation and personality at the time, claimed that human conduct is based on a hierarchy of wants such as physical, security/safety, love/belonging, and self-esteem and self-actualization (Maslow, 1943). If the last three levels of Maslow's hierarchy of requirements are not satisfied, the individual finds uneasy to proceed further, and these wants combine to generate a powerful drive to survive. The desire for self-esteem and self-actualization completes Maslow's hierarchy of requirements. Women struggled for employment in organisations in this setting, but they faced the opposition from society and were deprived of chances to acquire higher self-esteem and fulfil their skills.

Since the Equal Employment Opportunity Act of 1972, Women started competing for positions that were formerly exclusive for men only. When they were in unknown territory, female required survival advice in the workplace more than success guides in career. In all these years, numerous studies have been done to follow women's advancement in the organisations. In spite of more women in the workplace today, these researches indicated that women continue to struggle with advancements in career and, particularly, role models for successful managerial authority. In 2014, ladies held approximately 52% of all executive occupations in the US, but only 14.6% of Top management spots and 4.6% of Fortune 500 CEO posts. The matter of fact is there are abundance of publications offering career counselling and ideas for women who are working, but hardly any papers addressing best practises for female CEOs. To remedy this flaw in the secondary information, the author used a practical approach, sharing lessons gained from Katharine Graham, the first lady CEO of a Fortune 500 corporation.

After graduation, Katharine Graham was selected as the manager for the publisher of the San Francisco newspaper, but she was never allowed to take on any duty that the title necessitated, it was a cakewalk to be the first female manager, and the toughest part was being a female leader. Her male counterparts were rude, loud, boisterous, and stinky, and they hazed her in every manner possible. They gave her a sculpted male body part as a gift one day, and all Katharine could do was politely take it and eventually the hazing ended in its own time.

On the work front, her boss was mortified to have her on the team. He felt humiliated to have a female work under him after considerable thought, he handed her a project that was not her expertise. Furthermore, she never had a refreshment room or even a women's toilet. In retrospect, she realised that the chosen project allowed her to establish and acquire stronger self-esteem in the eyes of her dominating colleagues (Maslow, 1954).

She discovered the delicate boundary between normal and dysfunctional in 1974. It was not always possible to distinguish between regular challenges experienced by everybody, especially concerns that were uniquely feminine. Some instances were plainly "over the line" in terms of sexual harassment, and these were easy to identify nonetheless, they were frequently tough to handle successfully. Important Criteria's failed to exist in place at that

time regarding an effective or ineffective strategy. She wondered if success was not having repeat offenders. And, "if she were a man, this would not be happening." "How would she react?" Because there was no sexual harassment statute in place at the time, she was able to manage situations on her own. While she acknowledged that the force of the law is required to protect women from heinous atrocities, legal acceptance and petty problems has diminished the true importance of leadership. Women are still unable to distinguish between actual sexual harassment and typical male/female contact. Teasing was major challenge she encountered, which may be harmful. She had the ability to question sexually harassing situations and manage these difficulties on her own, with no sexual harassment forms or personnel welfare department involved. She could create her own regulations because she was the single lady manager facing the offender alone with no support and guidance. Males could express their thoughts without fear of being labelled as misogynists, a term we rarely hear today. It was motivating for everyone to have the choice to speak freely and appreciate the opinions. Conversations were raucous as it frequently bordered on crude, but we were able to finish any disagreements on Friday afternoons where we discussed shop. It was an incredible opportunity to agree to and learn from the seasoned male-only executive team. She was aware that she was attempting to penetrate their society, form relationships, and gain their trust and respect..

She had once employed a machinist on force and discovered he only added more to her misery. He had the labour union and management on the verge of a discrimination action due to his ailing back and seniority position. He parked his white Cadillac prominently in front of the company. She discovered that when he vanished, so did his Cadillac. How does she hold him responsible for not working for whatever he is paid for. Even the expert seasoned manager struggled to meet this challenge. She was adamant about dealing with him. She researched the hiring contract as well as the disciplinary procedures. She learnt the rules and was well prepared. When she found that her male friends had "set her up," she became fearless to the point of becoming reckless. Her demeanour shifted to "I'm going to castrate you." Few employees gradually began to listen to her as they understood that they have a tough boss with great self-worth and confidence to deal with the elusive Houdini (Maslow, 1965).

Female managers are often mistaken with female leadership. Manager is exactly what the job entails. Followers, on the other hand, play in striving for the success of the female leader. For example, a true lady leader is both competent and loves to employ a supporting strategy to descend into the interior of a massive tank. That function would most likely be delegated by the female management.

She definitely gained the knowledge to realise when men should lead and when women should lead as she faced few situations. On a day when a senior employee was bid farewell and the department was arranging a celebration, she oversaw the employees, especially Mel, the harshest critic. The liquor flowed freely at the party location. One inebriated male employee made unwanted and aggressive approaches. The situation was out of control, she was confident and determined to handle it alone. Mel appeared out of nowhere, like a hero in shining armour, to defend her. Then she realised that at times wisdom lies in not leading.

Just not this, she remembers another incident in the hotel room where she was assaulted. It was her first business trip, the travel expense and training were sponsored by the company for a week. She was very excited about it. Several of her colleagues were enrolled in different sessions which were for more senior managers. Because they were staying at different hotels, she was happy when a colleague called and invited her to join them for dinner. One of her colleagues was supposed to pick her from the hotel. She believed that her peers had finally accepted her. That notion was interrupted when she opened the door and he began hitting her without hesitation or words. She was terrified and felt it was very inappropriate. It should never have happened, yet it did. She was not physically hurt and chose not to report the event. She came to the conclusion that she was responsible for protecting herself and would face a "she said/he said" situation. Reporting the event may jeopardise her management's reputation. In retrospect, she stated that she did not consider protecting other ladies from this individual. She learned from her supervisors that she should hire "for values and qualities like a sense of humour, resiliency, "earning your way in" and fitting-in with the company by being passionate for the task. She grew to value the wisdom more when she faced problems on the work. One of the most important lessons she learnt was to be professional come what may the show must go on. She still had to deal with the problems at the end of the day. She discovered that the Rs of leadership included being resourceful, resilient, an experienced "reframer," a reality checker, and capable of relegating relational rules. She had to become valuable in making people to do things and get work done by them by persistence, pursuance, and patience. Because there was no precedence, she could create rules to control the relationships at work. She had the ability to draw the line with colleagues and subordinates, and she frequently utilised humour to smooth over unpleasant situations. There were a lot of unethical practices and she could let it go if she wanted to but the absence of norms, structures, and laws aided her. This is how she reframes diverse circumstances.

Some may see these encounters as "war stories" of a seasoned woman as these incidents occurred many years ago, however they shaped her to be a better version each day. Each person's experiences will build him or her to be a better person sooner or later. Of course there is no shortage of books and articles about leadership nowadays, and perhaps we are wise enough to distinguish between excellent and terrible leaders but we are not that wise in recognising leadership's intrinsic uniqueness. Leadership is as individual as fingerprints, varying according to personality, situation, and style. To make a difference in the lives of others, leaders must embrace the unique contributions that only they can provide. Someone rightly said for "ten thousand steps of beautiful journey there has to be a first starting step".

References

Baker, J., & Cangemi, J. (2016, July). Why are there so few women CEOs and senior leaders in corporate America? *Organization Development Journal*, 34(2) 31-44. Berhane, S. (2015, July). Four ways for millennial women to prepare for leadership roles. Retrieved from <https://www.fastcompany.com/3048907/strong-female-lead/4-ways-for-millennial-women-to-prepare-for-leadership-roles>

- Burton, N. (2017, September). Our hierarchy of needs. Retrieved from <https://www.psychologytoday.com/blog/hide-and-seek/201205/our-hierarchy-needs>
- Cangemi, J., Davis, R., Sand, T., & Lott, J. (2011). Three levels of organizational challenges and change: Needed-three different styles of leadership. *Organization Development Journal*, 29(1), 27-33.
- Crichlow, A. (2014, September 4). Five tips for millennial professionals. Retrieved from <http://www.digitalistmag.com/future-of-work/2014/09/04/5-tips-for-millennial-womenprofessionals-01397247>
- Gray, C. (2016). Women and interviews: Career basics for women. Retrieved from <http://www.asktheheadhunter.com/women3.htm>
- Healy, T. (2015, September 14). Tips for recruiting millennial women. Retrieved from <https://www.shrm.org/ResourcesAndTools/hr-topics/talent-acquisition/Pages/Tips-Recruiting-MillennialWomen.aspx>

MICROFINANCE, WOMEN EMPOWERMENT, BENEFITS AND SOCIAL CAPITAL FORMATION – A STUDY WITH REFERENCE TO URBAN BENGALURU

Dr. Y. Muralidhar Reddy

Associate Professor, Cambridge Institute of Technology, Bengaluru

Dr. Roopa K

Associate Professor, Ballari Institute of Technology & Management, Bellary

Dr.M.B.Roopa

Assistant professor, Department of Business and Management, Christ University, yeshwanthpur campus, Bangalore

Prof. Sanjana

Assistant Professor, Cambridge Institute of Technology, Bengaluru

Abstract

Purpose : The main purpose of the present study is to know how far socio economic characteristics impact on micro finance initiatives, and to know about the benefits derived from the microfinance initiatives, factors driving social capital formation and women empowerment. Since independence poverty alleviation programmes through government sponsored schemes could not yield the expected result and in many cases the activities of welfare could not trickle down to the needy who are living in urban centres. Urban poor like rural poor also requires finance for the self consumption and involvement in income generating activities. Microfinance initiatives across the globe are popular as far as poverty alleviation, women empowerment and social capital formation. Bengaluru experienced rapid urbanisation due to increase in urban population from 12 million in 2020 to 12.7 in 2021. (<http://www.microtrendns.net>>citation). Micro finance programmes emerged as a powerful tool of poverty alleviation since the last three decades and several studies have examined its economic influence on the community well being (Asghar Tahamasehi et al, 2021).

Methodology / Design : Questionnaires containing known questions which are open ended in nature are administered as schedule after considering avoiding non-response, delay and incompleteness in addition to respecting social distance norms. A total of 230 questionnaires in the hand and out of which 200 found to be useful forming 86.95 success rate. Chi-square, contingency co-efficient, Kendall's co-efficient of concordance, and weighted arithmetic mean were performed for the purpose of analysis and presentation of data.

Key words : Poverty alleviation, savings, women empowerment, money lenders, living standards, education, awareness.

Introduction :

Self Help Groups - Bank Linkage Programme (SHG – BLP) is a unique model at the global level which has transformed innumerable lives by mainstreaming women and making them as partners in the national building, progress process. It is emerging as a ‘fast growing sector’ although it is under represented (NABARD, 2020). Micro finance in India plays an important role in the delivery credit to the people of bottom of pyramid (RBI Bulletin 2020). Economists and policy framers stress on the distribution of economic savings among the poor people and deserved which empowers the masses at gross root level (Dadhich, 2022: Ravi et al, 2005, Sarangi 2008). It has been accepted as successful model where the poor have no place in the formal institutions (Swathi Sharma, 2018). Innumerable studies in the past like Kabeer (2005), Mayoux (2001), Otero, M. (1989), Pitt & Khandker (1996), Rahman (1988) found that microfinance is a good strategy to alleviate poverty, empower women and augmenting economic development.

SHGs influenced SHG members both social and economic life. The economic impact is observed in the form of savings created, easy access to formal credit, cheaper interest rates and enhanced income and involvement in livelihood activities. The similar opinions also expressed by Barbora & Mohanta (2005), Rathinam & Nachimuthu (2012), Meetei (2011) and, Sarmah et al., (2010). The social impact created by microfinance covers building of self confidence, enhanced awareness about savings and attaining economic self influency and health issues (Premachandra et al., 2017, Rathinam Nachimuthu, 2010). By becoming members in SHGs the members can increase participation in social services and promote organised action, acquisition of new skills and improved technological change among the members. In a similar study scholars like Boga and Nakka (2005) reported that the household level, expenditures on food and clothing among poor households go up after joining SHGs in addition to enhanced awareness on health and related issues. SHGs provide a platform for the promotion of activities in groups and the promotion of infrastructure facilities, technology, credit and marketing support for women (Sethi and Atibudhi, 2001, Barbara & Mohonta, 2001 & Sharma 2001)

States of microfinance in India

Table 1: Progress under SHG-Bank Linkage Programme (2018-19 to 2020-21)

Particulars	(Number in lakh / Rs. in crore)					
	2018-19		2019-20		2020-21	
	SHGs	Amount	SHGs	Amount	SHGs	Amount
SHG Savings with Banks as on 31 March 2021						
Total SHG Nos.	100.14	23324.48	102.43	26152.05	112.23	37477.61
	(14.52%)	(19.05%)	(2.29%)	(12.12%)	(9.57%)	(43.31%)
All women SHGs	85.31	20473.55	88.32	23320.55	97.25	32686.08
	(15.44%)	(17.01%)	(3.53%)	(13.91%)	(10.11%)	(40.16%)
Percentage of Women	85.19	87.78	86.22	89.17	86.65	87.21
Of which NRLM/SGSY	55.81	2867.18	57.89	14312.7	64.78	19353.7
	(33.37%)	(23.32%)	(3.75%)	(11.23%)	(11.9%)	(35.22%)
% of NRLM/SGSY Groups to Total	55.72	55.17	56.52	54.73	57.72	51.64

Of which NULM/SJSRY	4.39	1614.42	4.69	1523.57	5.29	1954.09
	(3.29%)	(19.52%)	(6.83%)	(-5.63%)	(12.79%)	(28.26%)
% of NULM/SJSRY Groups to Total	4.38	6.92	4.58	5.83	4.71	5.21

Loans Disbursed to SHGs during the year

Total No. of SHGs extended loans	26.98	58317.63	31.46	77659.35	28.87	58070.68
	(19.33%)	(23.59%)	(16.60%)	(33.17%)	(-8.23%)	(-25.22%)
All women SHGs	23.65	53254.04	28.84	73297.56	25.95	4423.13
	(13.98%)	(19.51%)	(21.95%)	(37.64%)	(-10.19%)	(-25.75%)
Percentage of Women Groups	87.66	91.32	91.67	94.38	89.71	93.72
Of which NRLM/SGSY	16.49	33398.93	20.49	52183.73	15.84	29643.04
	(29.84%)	(33.30%)	(24.26%)	(56.24%)	(-22.69%)	(-43.19%)
% of NRLM/SGSY Groups to Total	61.12	57.27	65.13	67.20	54.87	51.05
Of which NULM/SJSRY	1.29	3419.58	1.59	3406.22	1.13	2112.04
	(21.70%)	(41.07%)	(23.26%)	(-0.39%)	(-28.93%)	(-37.99%)
% of NULM/SJSRY Groups to Total	4.78	5.86	5.05	4.39	3.91	3.63

Loans Outstanding against SHGs as on 31 March 2021

Total No. of SHGs linked	50.77	87098.15	56.77	108075.07	57.8	103289.71
	(1.14%)	(15.21%)	(11.82%)	(24.08%)	(1.81%)	(-4.43%)
No. of all Women SHGs linked	44.61	79231.98	51.12	100620.71	53.11	96596.6
	(-1.93%)	(12.54%)	(14.59%)	(27.00%)	(3.89%)	(-4%)
Percentage of Women SHGs	87.87	90.97	90.05	93.10	91.89	93.52
Of which NRLM/SGSY	32.85	54320.91	36.89	67717.07	33.78	57336.62
	(17.62%)	(42.11%)	(12.30%)	(24.66%)	(-8.43%)	(-15.33%)
% of NRLM/SGSY Groups to Total	64.76	62.37	64.98	62.66	58.44	55.51
Of which NULM/SJSRY	2.25	4110.73	2.67	5466.87	2.23	4056.45
	(-22.41%)	(-23.17%)	(18.67%)	(32.99%)	(-16.48%)	(-25.8%)
% of NULM/SJSRY Groups to Total	4.43	4.72	4.70	5.06	3.86	3.93

Figures in parenthesis indicate increase / decrease over the previous year

Source: Status of Microfinance in India, NABARD, 2020-21

Table – 1 depicts data on progress under SHG – Bank Linkage Programme (2018-19 to 2020-2021). Table highlights data about savings, loans disbursed and credit outstanding. The total number of SHGs were 100.14 lakhs during the year 2018-19 and rose to 112.23 by the end of 2020-21 with an increase of 13.54%. The loan disbursement was 26.98 crores during 2018-19 and by the end of 2020-21 it stood at 28.87 crores revealing 2% growth over the years. The all women trend of numbers of SHGs were 85.19 lakhs during 2018-19 and rose to 86.65 and loan disbursement exclusively to women groups stood at 87.66. SHGs and rose to 89.71 SHGs. Further

loan outstanding details reveal that 50.77 lakhs SHGs were linked by the end of 2018-19 and rose to 57.8 lakh SHGs by the ends of 2020-21.

Table - 2: Region-wise progress of Savings Linked SHGs with Banks (2018-19 to 2020-21)
(Amount in Rs. Lakh)

		2018-19		2019-20		2020-21	
Sr. Regions No.	No. of SHGs	Savings Amount	No. of SHGs	Savings Amount	No. of SHGs	Savings Amount	
1. Northern Region	5,48,624	62,453	5,77,122	59,550	6,09,808	1,74,345	
2. North Eastern Region	5,23,469	40,407	5,56,899	48,141	6,33,714	83,126	
3. Eastern Region	26,54,358	6,01,155	28,11,130	6,64,333	31,22,424	7,74,912	
4. Central Region	10,62,759	1,33,230	11,35,083	1,71,217	13,45,575	2,11,870	
5. Western Region	13,88,615	2,05,275	14,73,853	2,01,880	15,50,176	3,74,023	
6. Southern Region	38,36,418	12,89,928	36,89,236	14,70,085	39,61,703	21,29,485	
Total	1,00,14,243	23,32,448	1,02,43,323	26,15,205	1,12,23,400	37,47,761	

	Northern Region	Northern Eastern Region	Eastern Region	Central Region	Western Region	Southern Region
2018-19	5.48	5.23	26.51	10.61	13.87	38.31
2019-20	5.63	5.44	27.44	11.08	14.39	36.02
2020-21	5.43	5.65	27.82	11.99	13.81	35.30

Source: Status of Microfinance in India, NABARD, 2020-21

Table – 2 reveals data about region-wise performance of savings linked with banks. Region-wise details also shows an enhanced growth of SHGs linked savings during 2020-21. Table shows central region registered the highest growth of 5%. Six states / UTs namely Uttarkhand, Nagaland, Chandigarh, New Delhi, Karnataka, Dam and Din, registered a negative growth. As many as 19 states / UTs showed growth rates than All India average. The degree in savings accounts of SHG may be due to data sanitisation, closure of document accounts and reporting of errors etc., Further, the table reveals about concentration of savings linked with banks in Southern region. The savings linked SHGs with banks of Southern region reveals that it was 12.89 crore 55% of total for the 2018-19 and it was 14.70 crores during 2019-20, 56.21% of total and finally, it was 21.29 crores (56.8% of total) during the year 2020-21. The similar performance was also shown by Eastern region and Western region.

Table 3: Region-wise Status of Bank Loan Disbursed to SHGs during 2018-19 to 2020-21
(Total loan disbursed in Rs. Lakh/ Average loan disbursed in Rs. per SHG)

		2018-19		2019-20		2020-21			
Regions	No. of SHGs	Total loans Disbursed	Average Loan Disbursed	No. of SHGs	Total loans Disbursed	Average Loan Disbursed	No. of SHGs	Total loans Disbursed	Average Loan Disbursed

Northern	55,922	62,664	1,12,056	62,905	84,694	1,34,637	67,658	94,045	1,39,001
North Eastern	27,086	29,001	1,07,070	37,807	57,893	1,53,128	68,116	1,03,651	1,52,168
Eastern	9,09,375	11,97,079	1,31,638	11,23,517	17,85,075	1,58,883	11,24,578	14,87,551	1,32,276
Central	85,135	72,199	84,805	1,11,074	1,04,249	93,856	1,28,617	1,05,428	81,971
Western	1,46,674	1,84,565	1,25,833	1,74,218	2,49,327	1,43,112	1,61,159	2,30,331	1,42,921
Southern	14,74,208	42,86,256	2,90,750	16,36,481	54,84,696	3,35,152	13,37,266	37,86,063	2,83,120
Total	26,98,400	58,31,763	2,16,119	31,46,002	77,65,935	2,46,851	28,87,394	58,07,068	2,01,118

Source: Status of Microfinance in India, NABARD, 2020-21

Table – 3 highlights data about bank loan disbursement by banks. It was 5831763 lakhs to the 2698400 SHGs during the year 2018-19. The total disbursed amount for the year 2019-20 stood at 7765935 to all regions of 1036481 SHGs. Further, during the year 20-21 the amount disbursed in the form of loan for all regions stood at 5807068 lakhs and numbers of SHGs stood at 2887851 lakhs. The region wise average loan disbursed also shows downward trend except Northern region. A total of Rs. 5807068 lakhs was disbursed to all 6 regions to 2887394 SHGs and the average loan disbursed stood at Rs. 201118 per SHG.

Table 4: Region-wise NPA Level during 2019-20 and 2020-21

	Amount of Gross NPAs (₹ Lakh)	2019-20		2020-21	
		NPA as % to Loan o/s	Amount of Gross NPAs (₹ Lakh)	NPA as % to Loan o/s	
1 Northern Region	21,206.67	17.35	17,133.33	13.93	
2 NE Region	26,914.18	26.08	28,366.44	20.07	
3 Eastern Region	1,01,495.28	4.46	1,15,888.80	4.47	
4 Central Region	56,612.66	25.15	52,551.46	20.83	
5 Western Region	33,564.66	11.07	32,917.18	10.01	
6 Southern Region	2,92,376.97	3.76	2,42,064.13	3.52	
All India	5,32,170.42	4.92	4,88,921.34	4.73	

Source: Status of Microfinance in India, NABARD, 2020-21

Table-4 highlights data regarding NPAs in SHG – BLP. Only two regions i.e., Eastern region and Southern region shows below the level of All India. These two regions having the maximum share of SHG loan disbursement and loan outstanding. The change in the NPA level of these two regions has a major effect on all other remaining regions. Table shows that bank loans to SHGs as on 31st March 2021 were 4.73%. As compare to 4.92% as on 31st March 2020. The absolute level of NPAs declined from 532170.42 lakhs in 2019-20 to Rs. 488921.34 lakhs. The decrease in NPAs is seen across regions except Eastern Region where it has marginally gave up. Out of 35 states and UT, reporting data, 26 showed decline in NPA level and thus improvement in portfolio quality.

Statement of the problem

Women forms 50% of population. But very unfortunately either in traditional or modern society equal rights are existing but at the implementation level there exists huge disparities. Women studies reveals that unless and until women are empowered women development is not possible. As per NABARD, 2017 data the demand at the poor is Rs. 60000 crores but cumulative payment is Rs. 6000 crores under microfinance programmes. The government sponsored programmes did not receive the expected result on account of bad implementation of schemes, hierarchy, red-tapism, duplication of projects. The urban depends on daily income from income generating activities and many a times the members may not receive expected return of the day. These poor people do not have any collateral to give in order to get a bank assistance. Financial access to the village and urban poor are highly skewed and unequal, SHGs are helping urban poor women in assisting financially with a mutual weekly or fortnightly contribution by members. SHGs promote gender equality and SHG BLP empowered urban women and it is a unique strategy at the global level.

Review of literature

Karlan's (2007) study is situated on Peru and members social ties by looking at the extent to which group members share the same culture and like more closely to each other.

Dufhues et al., (2013) measure social capital based on social network analysis, using information from borrowing households in Thailand and Vietnam. The outcome of the study reveals that social capital is associated with better repayment performance, depending upon the nature of social ties between individuals.

Casser et al., (2007) using survey data from borrowers in South Africa and Armenia, measure social capital within borrowing groups by focusing on group homogeneity and intra group trust, and show that both these measures are positively associated with repayment performance.

Widick et al., (2011) study focused on how social capital can help increasing the social performance microfinance institutions. Further they expressed that religions networks are important for rural households in Guatemala to have access to credit.

Khan and Rahaman (2007) stated that urban micro finance improved the living standard of the borrowers of the Chittagand district of Bangladesh by reducing poverty and making them capable financially of starting new small business and expand old business.

Basher & Rashid (2012) explained the characteristics of urban microfinance within Urban low income groups and their significance. They emphasise on the urban microfinance program because of the increasing trend of urban poverty.

Tanya Sharma et al., (2014) stated that microfinance in Delhi led to an improvement in living standards of the poor women and an increase in their incomes, savings and improvement in

financial condition and impacted on poverty alleviation and also given them greater autonomy to take decisions concerning the lives of their facilities and themselves.

Prema Basargekar (2010) expressed about the impact of urbanisation at Poona Urban area where the villages are converted into industrial zones. Transition of these villages into semi-urban areas received mixed responses as this conversion provides jobs and better infrastructure and whereas as it develops agriculture and local jobs and enhance social pressure.

Syed Mohammad Ghouse (2019) stated that microfinance activities are very much successful in reducing social problems in rural areas. The researcher suggested that government should formulate the very effective strategies to control the working mechanism of microfinance institutions as they became part and parcel of Indian economy.

Jeremaiah Machigambi (2020) examined the relationship between sustainable micro finance and sustainability to poor clients. The paper focused more on demonstrating the impact of a sustainable lending approach of the poor clients. The key issues highlighted differences in terms of target clients and implications for the sustainability of beneficiaries.

Objectives of the study

- 1) To study the impact of socio-economic characteristics on microfinance initiatives.
- 2) To analyse the factors driving social capital formation.
- 3) To the benefits from microfinance initiatives.
- 4) To analyse the factors driving women empowerment.

Hypotheses

- 1) The socio-economic characteristics of respondents do not impact on micro finance initiatives.
- 2) Social capital formation is not driven by any factors.
- 3) Benefits are not associated with microfinance initiatives.
- 4) Women empowerment is not driven by any factors.

Research Questions

- 1) What are the reasons behind socio economic characteristics for not impacting on the microfinance initiatives?
- 2) Which factors drive social capital formation?
- 3) What are the benefits of microfinance initiatives?
- 4) When factors drives women empowerment?

Limitations

- 1) The study is confined to urban Bengaluru district.
- 2) The sample is small when compare to universe SHG members at Urban Bengaluru.
- 3) Any generalisation requires further study.

Research Methodology

The present study is based on both the primary and secondary data. A well drafted questionnaire was administered as schedule for the purpose of data collection. The benefits of microfinance, social capital formation, and women empowerments details are studied and data presented in the form of tables. Research design is a strategy for answering the structured questionnaire using empirical data (Shana, 2021). It is simply a structural frame work of various research methods as well as techniques that are used by researchers (Team Leverage Edn., 2020).

Questionnaire design : Questionnaire is a set of logic questions listed for the purpose of data collection from respondents. Researchers are required to apply most relevant and most effective way to collect the maximum amount of information in terms of validity and reliability as recommended by Easterby – Smith, Thorpe and Lowe (1991). The secondary sources include bulletins, e-journals and internet. The relevant references were given at the end.

Universe of the study : The study is confined to urban Bengaluru district. There are 69 grama panchayats, 3655 confirmed SHGs and 65805 members in all SHGs of 5 sub districts.

Sample of the study : (Details of Yalahanka is not available)

Name of the subdistrict	Grama Panchayat	SHGs	Members	Sample
Anekal	28	1321	24427	70
Bengaluru East	11	253	4717	15
Bengaluru North	12	1252	2280870	
Yelahanka (Bengaluru North additional)	-	-	-	-

Method of Data analysis : The study adopted x2, contingency co-efficient, Kendall's co-efficient of concordance and weighted arithmetic means. These techniques are performed as they are simple to compute and sufficient for the analysis.

Data presentation and analysis : Demographic profile of respondents – A.

The relevant demographics of respondents were studied to know the impact created on microfinance. These characteristics include, marital status, age, education, occupation, monthly income, living conditions, participation in social activities, savings formulation and participation in election, support of a candidate and contest.

Research question No. 1: What are the reasons behind the socio-economic factors not impacting on the microfinance?

Hypotheses : No. 1 : H_0 : The exist no significant variation in the characteristics of respondents do not impact on microfinance initiatives.

H_1 : There exist significant variation in the socio-economic characteristics of respondents.

The study of socio economic characteristics of respondents is essential as it is going to decide whether they form the part of representative sample of the target population. The respondents were appealed to answer all the questions of questionnaire. All the characteristics of respondents and their significance and degree of relationship studied in relation whether they impact the study or not. Table – 5 depicts data about characteristics of respondents. All respondents are females and no male members is given membership in any SHG. There are 160 members who are married and 22 respondents remained single and 18 are divorce, 69 respondents belongs to 40-50 age category, 38 belongs to 30-40 years, 35 in between 20-30 years, 30 between 50-60 years, 15 < 20 years and 13 > 60 years. 67 respondents studied up to 10th standard 58 studied up to PUC, 38 below 7th standard, 22 are general degree holders, 8 are post graduates and very surprisingly 7 are illiterates. 55 respondents occupation as vegetable selling, 38 doing petty business, 30 seasonal fruit sellers, 29 are papad, textile pieces and pickle sellers 23 are involved in agricultural activities, 15 are suppliers of provisions, 6 are dealers in iron seconds, old newspapers collectors, and 4 are handicraft sellers. 84 respondents monthly income is in between 20K – 30K, 42 respondents monthly income lies in between 10K – 20K, 31 in between 30 – 40K, 25 < 10K and 18 > 40K. 85 respondents are residing in their own houses, 60 are living in rented houses, 30 government scheme house-owners, 25 are living in temporary sheds. 125 respondents participated in social activities and 75 are not participated in any social activities. 173 respondents formed savings and 27 respondents are not created any savings. 123 respondents regularly participated in elections and supported a candidate and also contested in elections, 40 are not regular and 28 never participated in decision supporting candidate and contest in elections.

Data presentation and Analyse - B

Research question No. 2 : Which factors drives social capital formation?

Hypotheses No. 2 : H_0 : There exists no significant variation in the drivers of social capital formation.

H_1 : There exist significant variation in the drivers of social capital formation.

Table –6 highlights data about factors driving social capital formation. These drivers vary from mutual trust to mutual help in case of need. 124 respondents out of 200 stated strongly agree, 49 expressed agree and 27 somewhat agree. Out of 124 who stated strongly agree, 25 stated good relationship, 22 sharing valuable information. 18 felt healthy discussion on common matters, 15 indicated about mutual trust 12 spoke about respecting norms and values. Out of 49 respondents 12 felt about good relationship, 9 expressed about sharing valuable information, 7 indicated about healthy discussion on common matters. Out of 27 who stated somewhat agree, 5 expressed about good relationship. 4 each about healthy discussion on common matters and mutual help in case of

need. ‘w’ fails to accept H_0 and accepts H_1 and hence it is concluded that there exists significant variation in the data.

Research question No. 3: What are the benefits of microfinance initiatives?

Hypotheses No. 3 : H_0 : There exists no significant variation in the benefits of microfinance.

Hypotheses No. 3 : H_1 : There exist significant variation in the benefits from microfinance initiatives.

Table – 7 depicts data regarding benefits from microfinance initiatives. 128 respondents out of 200 stated strongly agree followed by 48 agree, 24 somewhat agree. Out of 128 who stated strongly agree 24 stated about free from money lenders, 20 expressed about a platform to discuss issues, 14 each indicated about access to organised financial services and increase in women empowerment, 10 reported about more savings formation. Out of 48 who said agree 11 expressed about free from money lenders, 8 spoke about increase on women empowerment, 6 reported about additional earnings and 5 each indicated about a platform to discuss issues and enhanced standard of living. Out of 24 who stated somewhat agree, 5 spoke about free from money lenders, 4 expressed about increase in women empowerment. ‘w’ fails to accept H_0 and accepts H_1 and hence it is concluded that there exist significant variation in the data.

Research Question No. 4 : Which factors drivers women empowerment?

Hypotheses No. 4 : H_0 : Women empowerment is not driven by any factors.

H_1 : There exists significant variation in the data and factors driving women empowerment vary.

Table – 8 reveals data about factors driving women empowerment. The first relative important driver of empowerment is about improvement in the savings formation, second important driver is economic independence and the third is about enhanced stand. Weights are awarded to Likert 5 point scale starting from strongly agree to strongly disagree and the opinions (f) are multiplied by ‘w’ to get ‘fw’. The sum of fw is divided by sum of weights ($5 + 4 + 3 + 2 + 1$) = 15. The remaining by drivers of women empowered are awarded weighted average depending upon strength of fw.

Table – 5 : Demographics of respondents – Microfinance initiatives.

Socio-economic characteristics	χ^2	TV @ 0.05 level	df	Result of X^2	‘c’	Result of ‘c’
Marital status	196.1101	3.841	1	Significant	0.70	High Degree
Age	61.7259	11.070	5	Significant	0.48	High Degree
Education	96.8293	11.070	5	Significant	0.57	High Degree

Occupation	80.6400	14.067	7	Significant	0.53	High Degree
Monthly income	70.2500	9.488	4	Significant	0.50	High Degree
Living conditions	47.0000	7.815	3	Significant	0.43	High Degree
Participation in social activities	112.5000	3.841	1	Significant	0.60	High Degree
Savings formation	106.58	3.841	1	Significant	0.58	High Degree
Participation in election, support of a candidate, contest	74.7033	5.991	2	Significant	0.52	High Degree

Source : Field Survey

Note : χ^2 = chi-square

$$‘c’ = \sqrt{\chi^2 / \chi^2 + N}$$

Where c = contingency co-efficient, N = Number of observation

When the value of ‘c’ is equal or near 1, it means there is high degree of association between attributes. Contingency co-efficient will always be <1.

Table – 6 : Respondents awareness of factors driving social capital formation

Factors driving social capital formation	SA	A	SWA	RT	RT ²
Social trust	15	4	2	21	441
Social relationship	25	12	5	42	1764
Attitude	8	3	2	13	169
Respecting norms and values	12	2	3	17	289
Believing co members	7	3	2	12	144

Healthy discussion on common matters	18	7	4	29	841
Mobilization of savings regularly	9	4	2	15	225
Sharing valuable information	22	9	3	34	1156
Mutual help in case of need	8	5	4	17	289
Total	124	49	27	200	5318

Source : Field Survey

Note : SA – Some Agree, A – Agree, SWA – Somewhat Agree, RT – Raw Total

$$SSR = \Sigma RT^2 / \Sigma RT^2 / N$$

$$= 5318 - (200)^2 / 9 = 5318 - 4444.44 = 873.56$$

$$W = 12 \times SSR / K^2 N (N^2 - 1) = 12 \times 873.56 / 9 \times 9 (81 - 1)$$

$$= 10482.72 / 6480 = 1.61$$

Test the significance of ‘w’ by using chi-square statistic.

$$X^2 = k (n - 1)^2 = 3(9-1) / 1.61 = 3 \times 8 \times 1.61 = 38.64$$

Decision : At 8 df with 5% level of significance the value being 38.64 being higher than the TV = 15.507 and hence ‘w’ fails accepts H_0 and accepts H_1 . Therefore it is concluded that there exist significant relationship between drivers and social capital formation.

Table – 7 : Benefits from microfinance initiatives

Impacting factors	SA	A	SWA	RT	RT ²
Free from money lenders	24	11	5	40	1600
A platform to discuss issues	20	5	2	27	729
Access to organised financial services	14	3	2	19	361
More income	8	2	1	11	121
More savings formation	10	2	1	13	169
Good children education	6	1	2	9	81

Involvement in IGA activities	8	2	1	11	121
Improved health and sanitation	5	1	1	7	49
Investment in fixed assets	7	2	2	11	121
Increase in women empowerment	14	8	4	26	676
Enhanced standard of living	5	5	1	11	121
Additional earnings	7	6	2	15	225
Total	128	48	24	200	4374

Source : Field Survey

Note : SA – Some Agree, A – Agree, SWA – Somewhat Agree, RT – Raw Total

$$SSR = \Sigma RT^2 / \Sigma RT^2 / N$$

$$= 4374 - (200)^2 / 12 = 4374 - 400000 / 12 = 3333.33$$

$$W = 12 \times SSR / K^2 N (N^2 - 1) = 12 \times 3333.33 / 9 \times 12 (144 - 1)$$

$$= 39999.96 / 15444.00 = 2.59$$

Test the significance of ‘w’ by using chi-square statistic.

$$X^2 = k (n - 1)^2 = 3(12-1) / 2.59 = 3 \times 11 \times 2.59 = 85.47$$

Decision : At 8 df with 5% level of significance the value being 85.47 being higher than the TV = 19.675 and hence ‘w’ fails accepts H_0 and accepts H_1 . Therefore it is concluded that there exist significant relationship between the two variables.

Findings : The result indicates the presence of significant and high degree of relationship between socio economic characteristics and microfinance initiatives. The findings of the study reveals that good relationship, sharing valuable information, healthy discussion on common matters are factors that drives social capital formation. The benefits of microfinance includes free from money lenders, a platform to discuss issues, increase in women empowerment and access to organised financial services. The drivers of women empowerment includes improvement of savings formation, economic independence and enhanced living standards.

Findings : The result indicates the presence of significant and high degree of relationship between socio economic characteristics and microfinance initiatives. The findings of the study reveals that good relationship, sharing valuable information, healthy discussion on common matters are factors that drives social capital formation. The benefits of microfinance includes free from money

lenders, a platform to discuss issues, increase in women empowerment and access to organised financial services. The drivers of women empowerment includes improvement of savings formation, economic independence and enhanced living standards.

Conclusion :

SHG – BLP is a unique microfinance programme which is providing several benefits to the members. Bengaluru urban district is growing beyond expectation Pandit Jawaharalal Nehru is right in commenting “Bengaluru is a happening city”. Bengaluru is nicknamed as a ‘silicon valley’ ‘science city’ ‘garment hub’ etc., and a multi-cultured and tolerate impacting community. The urban women are struggling to earn at Bengaluru and are including in many income generating activities. They are now capable of saving after meeting all household expenditure. The present study reveals about the presence of better socio economic characteristics which are significantly with a high degree impacting on microfinance initiatives. The study reveals about innumerable benefits of microfinance which includes free from money lenders, increase in women empowerment and a platform to discuss issues. The study also reveals about the factors driving social capital formation which includes good relationship, sharing valuable information are healthy discussion on common matters. The factors that drives women empowerment includes improvement in savings formation, economic independence and enhanced standard of living. The study concludes by stating that means more engagement of women SHGs may accelerate more savings and more number of women may involve in income generating activities.

References :

Asgar Tahmasebi., & Fatemeh Askaribeayeh. (2021). MF and social capital formation – a social network analysis approach. Socio Economic planning Sciences, 76. <http://doi/10.1616/j.besps.2020.100978>.

Barbora, S., & Mahanta, K. (2001). MF through SHG and its impact. A case of Rastriya Grama Vikas Nidhi.

Bashar and Rashid. (2012). Urban microfinance and urban poverty in Bangladesh. *Journal of Asia Pacific Economy*, 17(1), 151-170.

Cassar, A., Crowley, L., & Wydick, B. (2007). The effect of social capital on group loan repayment : Evidence from field experiments. *Economic Journal*, 117 (517) F85-F106.

Credit and saving programme in Assam *Indian Journal of Agricultural Economics*, 56(3), 449-450.

Dadhich, C.L. (2001). MF – A panacea for poverty alleviation. A case study of oriental grameen project in India. *India Journal of Agricultural Economics*, 56(3), 419-417.

Dufhues, T. Buchenrieder, G., & Munkung, N. (2013). Social capital and market imperfections : Accessing formal credit in Thailand. *Oxford Development Studies*, 41(1), 54-75.

- Fatema Khatan Magugdul Hason. (2015). Social capital in microfinance : a critical investigation of Bangladesh. **Journal of Emerging trends in Economics and management sciences**, 6(5), <https://hdl.handle.net/10520/Ejc181662>.
- Jeremaiah Machigambi. (2020). The impact of MF on the sustainability of poor clients: A conceptual review. **Journal of entrepreneurial innovations**, 1(1), 1-6.
- Kabeers, N. (2005). Is microfinance a ‘magic bullet’ for women empowerment? Economic and political weekly, 40 (44-45), 4709-4718.
- Karlan, D. (2007). Social connections and group banking. **Economic Journal**, 117 (517), F52-F84.
- Khan and Rehaman. (2017). Impact of microfinance on living standards, empowerment and poverty alleviation of poor people. A case study on microfinance in the Chittagong district of Bangladesh, (Master Thesis). Umea School of Business (USB), UMEA Shedon (2007).
- Kreps, D., Milgrom, P., Roberts, J., and Wilson, R. (1982). Rational Cooperation in the Finitely repeated prisoners dilemma. **Journal of Economic Theory**, 27, 245-52.
- Mayoax, L. (2001). Tackling the downside. Social capital women’s empowerment and microfinance in Cameroon, **Development & Chance**, 32 (3), 435-464.
- NABARD (2020). Status of microfinance report 2020-21.
- Otero, M. (1989). Breakthrough – The expansion of micro enterprise program as a challenge for non-profit institutions. Cambridge, MA – ACCION international Retrieved from <http://www.centre> for financial inclusion. Org/ publications – a – resources / house – publications / 86.
- Pitt, M.M. & Khandker, S. R. (1996). Household and intra household impact of the Grameen bank and similar targeted credit programmes in Bangladesh. Discussion paper 320, World Bank: Washington, D.C.
- Prema Basargekar. (2010). Measuring effectiveness of social capital in microfinance. A case study of urban microfinance programmes in India. **International Journal of Social Inquiry**, 6(1), 65-78.
- Rahman, A. (1988). Alleviation of rural poverty: Replicability of the Grameen bank model. South Asia Journal, 1(4), 475-486.
- Ravi, R.V., & Venkataraman. (2005). Empowerment of Women through SHGs. A micro level study. **Small enterprises development management extension**, 32(1), 33-45.
- Sarangi, N.C. (2008). The SHG linkages, financial express P.A.

Sethi B., Atibudhi, H.N. (2001). MF an innovative tool for banking with the unbankables. A study in Kalachand, District, Orissa, **Indian Journal of Agricultural Economics**, 56 (3), 477.

Sharma, K.C. (2001). Microfinance through SHGs. *Journal of Agricultural Economics*, 56(3), 460-461.

Swathisharma. (2018). Growth of MF in India. A descriptive study. **Global journal of interdisciplinary social sciences**, 7(2), 20-31. Syed Mohammed Ghouse. (2019). MF – A catalyst in accelerating the growth of Indian Rural economy. **International Journal of Recent Technology & Engineering**, 8(3), 2010-2012.

Tanya Sharma., Rohini Singh., & Hamendra Kumar Porwal. (2014). Impact of microfinance on the living standards, poverty alleviation and empowerment of the poor women in Delhi. **International journal of research in social sciences**, 4(4), 95.

Wydick, W.B. (1999). Can Social Cohesion be harnessed to repair market failures? Evidence from group lending in Guatemala. **Economic Journal**, 109 (457), 463-1175.

Table – 8 : Factors driving women empowerment - Weighted Average

Drivers of women empowerment	Weight	5	4	3	2	1	T	WA
	Likert scale	SA	A	N	DA	SDA		
Reduction in dependency on money	f	150	31	8	6	5	200	
	fw	750	124	24	12	5	915	4
Access to markets	f	120	45	12	10	13	200	
	fw	600	180	36	26	13	849	15
Freedom from domestic violence	f	140	25	10	15	10	200	
	fw	700	100	30	30	10	870	13
Women freedom of movement	f	149	28	4	8	11	200	
	fw	745	112	12	16	11	896	8.50
Access and control of family resources	f	145	25	15	8	7	200	
	fw	725	100	45	16	7	893	10.5
Strong commitment to educate daughter	f	148	50	5	4	13	200	
	fw	740	120	15	8	13	896	8.50
Employment and widened status	f	145	38	7	3	7	200	
	fw	725	152	21	6	7	911	6
Improvement in savings formation	f	160	35	-	2	3	200	
	fw	800	140	-	4	3	947	1
Liberty to buy and sale of fixed assets	f	155	20	10	7	8	200	
	fw	775	80	30	14	8	907	7
More self confidence	f	154	22	12	8	4	200	
	fw	770	88	36	16	4	914	5

More awareness of political system, voting and contest in elections	f	135	31	15	10	9	200	
	fw	675	124	45	20	9	873	12
Local campaign against any discrimination	f	138	34	16	7	5	200	
	fw	690	136	48	14	5	893	10.5
Enhanced standard of living	f	155	29	6	4	6	200	
	fw	775	116	18	8	6	923	111
Freedom in spending, nutrition and education	f	138	32	4	10	16	200	
	fw	690	128	12	20	16	866	14
Economic independence	f	159	28	-	8	5	200	
	fw	795	112	-	16	5	928	11

Source Field Survey

WA – Weighted average

Effects Of Asset Liability Management On The Profitability And Liquidity Of Particular Indian Commercial Banks

Dr. Janet Jyothi Dsouza^{1*}, Dr. Deeja S², Dr. Amardeep Bajpai³, Dr. Bhadrappa Haralayya⁴, Dr. Prashant Mishra⁵, Mr. Anil Yadav⁶

^{1*}Professor and Head, Department of Management Studies, Ballari Institute of Technology and Management, Ballari, Karnataka

²Assistant Professor, P.G & Research, Department of Commerce, St Gregorios College, Kottarakara

³Assistant Professor, School of Commerce and Management Studies, Sandip University, Nashik, Maharashtra

⁴Professor and HOD, Department of MBA, Lingaraj Appa Engineering College Bidar-585403, Karnataka, India

⁵Assistant Professor, Master of Management Studies, Pramod Ram Ujagar Tiwari Saket Institute of Management (PRUTSIM), Kalyan

⁶Assistant Professor, Master of Management Studies, Pramod Ram Ujagar Tiwari Saket Institute of Management (PRUTSIM), Kalyan.

Citation: Dr. Janet Jyothi Dsouza, et al (2024) Effects Of Asset Liability Management On The Profitability And Liquidity Of Particular Indian Commercial Banks, *Educational Administration: Theory and Practice*, 30(4), 7084-7088

Doi: 10.53555/kuey.v30i4.2512

ARTICLE INFO

ABSTRACT

This quantitative study focuses on Bank of India, Andhra Bank, Axis Bank, and HDFC Bank while analyzing the asset-liability management, profitability, and liquidity of a few chosen Indian commercial banks. Information on capital, reserves, deposits, borrowings, assets, liabilities, profitability ratios, liquidity ratios, and compound growth rates were gathered from their annual reports and financial statements. For analysis, statistical tools such as inferential and descriptive methods were used. The findings demonstrate that different banks have different approaches, with Bank of India and HDFC Bank seeing strong increases in capital, reserves, deposits, and borrowings. Andhra Bank is notable for its robust reserves of liquidity, although HDFC Bank exhibits more profitability. The report emphasizes how crucial efficient asset-liability management is to Indian commercial banking's capacity to maintain profitability and reduce risks.

Keywords: Asset-liability management, profitability, liquidity, commercial banks, India.

1. INTRODUCTION

A wide range of organizations, markets, and financial instruments make up the financial system. It offers the main mechanism for converting savings into profitable investments. A contemporary economy must have an effective financial system since it plays a major role in the distribution of resources. A financial institution's primary goal is to mobilize resources and direct them toward investors. In various economic systems, financial institutions have a varied channeling function. Somashekar (2019) asserts that commercial banks have a leading role in economic growth in addition to being thought of as money exchangers. They serve as the nation's financial safe havens as well as the repositories of resources required for growth in the economy. They contribute significantly to a nation's economic growth. According to conventional wisdom, commercial banks are among the financial intermediaries that raise capital mainly through the issuance of time/fixed, savings, and checkable/demand deposits. Commercial banks are also permitted to offer every banking service in the financial market because our nation's financial system is still in its infancy. Commercial banks handle practically all of the money and capital market transactions and operations since there isn't a well-organized financial market. According to Roy (2010), commercial banks are significant for the nation's financial stability as well as economic prosperity. Banks are especially significant in emerging economies for three main reasons. Initially, they play a crucial part in the growth of additional financial markets and intermediaries. Second, the business sector and investors significantly rely on banks to satisfy their funding needs since there are weak bond and stock markets. Finally, due to their general inability to control financial risks, banks serve the interests of a large number of family savers in emerging or undeveloped nations who want to ensure income, liquidity, and fund safety.

An organization's not entirely set in stone by how much cash it makes contrasted with the capital it contributes. The amount of detailed income for a given monetary year may be utilized to financially measure this level of progress. According to Zopounidis (2001), in order for banks to effectively compete in the market, they must manage their assets and liabilities while keeping an eye on risk levels, earnings, liquidity, profit, solvency, and

the volume of deposits and loans. By doing this, they can reduce losses and increase profitability. Given the pivotal role asset liability management plays in risk management, banks must acknowledge the significance of asset liability and implement efficient risk management protocols. By employing sophisticated asset liability management strategies, banks can optimize profitability and mitigate risk in the fiercely competitive banking services markets of today. A company may balance its assets and liabilities with the help of asset liability management. Consequently, this reduces monetary hazards and enhances profitability. When a company is making investment decisions, asset liability management helps.

1.1. Research Objectives

1. To assess asset-liability management methods in Indian commercial banks, analyze growth rates of capital, reserves, deposits, and borrowings.
2. To examine how liquidity, profitability, and asset composition affect financial performance and risk management in these institutions.

2. LITERATURE REVIEW

Rahmi and Sumirat (2021) utilized liquidity risk, functional proficiency, capital sufficiency, and financing cost risk as free factors and ROA as a relapse and variable to concentrate on asset-liability the board during the Coronavirus pestilence and its impact on banks' profitability in Indonesia. The review's decision clarified that compelling AL the executives ensures the financial business would be more profitable all through the pandemic. In rundown, when assets and liabilities are effectively followed and made due, the bank's profit will rise.

Owusu and Alhassan (2021) utilized the SCA model to dissect the ALM of Ghana's financial industry and observed that how ALM is overseen affects business banks' profits. The outcomes confirmed that the whole execution of banks is straightforwardly affected by the fitting administration of Asset-Liability.

The effect of asset-liability the executives on the profitability of Nigerian store cash banks is examined by **Onaolapo and Adegoke (2020)**. The asset-liability pointers for estimation were credit and advance, NPL, credits and advances, borrowings, and request store, while ROA and return on initial capital investment filled in as intermediary appraisals for monetary execution. The review's decisions show that the presentation of Nigeria's store cash organizations is exceptionally influenced by asset-liability the board.

Likewise, **Ukpong and Olowokudejo (2021)** directed an AML examination on ten Nigerian protection firms utilizing the SCA model. As a substitute for profitability, ROA was utilized. That's what the investigation discovered, except for property and hardware, asset the executives essentially adds to enhancements in the profitability of disaster protection firms. Expressed in an unexpected way, further developed asset-liability the board will yield a bigger return.

Utilizing CAMEL proportions, **Mun and Thaker (2016)** directed an observational investigation of Malaysia's banks, both Islamic and Ordinary, to inspect the effect of asset-liability the executives on the Profit from Value proportion, a proportion of profitability, for the monetary years 2010 to 2013. Their review's discoveries showed that asset-liability the board, which applies to both ordinary and Islamic banks, essentially influences the profitability of the last option. The monetary presentation of the Afghan financial framework was concentrated by **Haidary and Monastery (2018)**.

The impacts of both interior and outside factors were analyzed in the examinations. The discoveries showed serious areas of strength for a connection between's inside bank qualities and bank profitability. Along these lines, the strength and sort of the connection among assets and liabilities in Tunisia were likewise discovered utilizing the Standard Relationship Examination apparatus.

As indicated by **Said and Edge's (2018)** study, the monetary record's parts were effectively taken care of by Tunisian banks, and the profitability of the sheet was dependent upon the nature of asset the executives.

By the by, **Shrestha (2015)** utilized POLS to research the profitability of Nepal's financial industry. ROA filled in as the profitability pointer, while Different Assets, expansion, ostensible Gross domestic product, and Assets that get through longer than a year filled in as the AML markers. As per the report, there is a measurably significant connection among's AML and banking profitability. Significant commitments came from stores on the liability side and credits and advances on the asset side.

To determine the sort and power of the connection among commitments and assets, **Said and Edge (2018)** used the Accepted Relationship Examination instrument. As indicated by the review's discoveries, the asset-liability things were effectively overseen by Tunisian banks, and their prosperity was generally subject to how well the assets were dealt with. The impacts of macroeconomic variables, bank-explicit elements, and industry-explicit elements on the monetary execution of a UK bank were undeniably inspected by Saeed (2014). His examination's discoveries show that stores, advances, capital, and bank size all emphatically influence the profitability of not entirely settled by ROE and ROA. In his review, he proceeded to say that banks might turn out to be more profitable by acquiring an upper hand and wellbeing net, which comes from having a lot of capital, stores, credits, value, and macroeconomic elements like Gross domestic product and expansion.

Menicucci and Paolucci (2016) researched the association between inside bank attributes and the financial business' profitability in the European setting. ROE gives a sign of profitability. The review's decision exhibits

that bank size and capital proportion well affect banks' monetary presentation. In his exploration, **Masindi (2021)** found a relationship between's the expansion rate and bank profitability. Proof from Afghanistan's Financial Area 38 demonstrates that asset-liability the executives altogether affects bank profitability, as shown by return on value (ROE).

As per **Baariu and Peter (2021)**, the financial area's good yet irrelevant monetary exhibition is affected by the pace of expansion. There is other proof to help the positive relationship between's bank profitability and expansion rate. In his exploration led in an African setting, **Masindi (2021)** tracked down a positive and genuinely critical relationship between's genuine Gross domestic product and the proportion of return on value.

Rashid (2022) led an exact review to look at the development and solidness of customary and Islamic banks in Pakistan using GMM. The review's decision showed that macroeconomic factors and bank endogenous factors inconveniently affected the development, profitability, and dependability of the two sorts of banks. Yet, the way this sort of risk influences monetary associations changes; though risks emerging from credit and premium were higher for regular banks, risks emerging from liquidity, activity, capital, expansion, and money were higher for Islamic banks.

3. RESEARCH METHODOLOGY

3.1. Research Design:

In order to examine the profitability, liquidity, and asset-liability management of particular Indian commercial banks, this study uses a quantitative research approach. It entails gathering numerical data from financial documents and analyzing the links between various factors using statistical methods.

3.2. Data Collection:

The annual reports and financial statements of the chosen commercial banks—Bank of India, Andhra Bank, Axis Bank, and HDFC Bank—will serve as the source of data for this study. We will specifically extract and analyze data on capital, reserves, deposits, borrowings, assets, liabilities, profitability ratios, liquidity ratios, and compound growth rates.

3.3. Statistical Tools:

Various factual apparatuses will be utilized to investigate the information that has been accumulated. The information will be summed up utilizing graphic measurements, which incorporate rates, means, medians, and standard deviations. Additionally, associations, trends, and noteworthy variations between variables can be found using inferential statistical techniques including regression analysis, correlation analysis, and ANOVA.

3.4. Ethical Consideration:

Throughout the study procedure, ethical concerns will be strictly followed. The information gathered from the commercial banks' financial statements will only be utilized for scholarly study, and it will be treated with integrity and secrecy. To maintain academic integrity and openness, the data sources will be properly cited and acknowledged. Furthermore, all possible conflicts of interest will be declared, and the study will be carried out in compliance with legal and ethical requirements.

4. DATA ANALYSIS

Table 1: Compound Growth Rates of Assets and Liabilities of Components in Selected Commercial Banks

Items	Compound Growth Rates			
	Bank of India	Andhra Bank	Axis Bank	HDFC Bank
Capital and Liabilities				
Capital	5.31	3.56	5.38	4.68
Reserve and surplus	24.98	14.51	33.60	28.06
Deposits	46.02	15.38	19.74	22.84
Borrowings	22.73	29.57	33.92	33.75
Other liabilities and provisions	3.91	8.35	9.88	10.46
Quick Ratio	20.10	36.30	3.07	1.63
Assets				
Cash and balances with RBI	84.57	11.45	17.06	19.14
Balances with Banks and Money at Call & short notice	20.43	-16.25	17.05	8.45
Investments	12.96	14.22	16.26	18.36
Loans and Advances	15.47	16.69	24.79	32.51
Fixed assets	26.85	21.75	18.05	32.97
Other assets	22.92	15.84	30.92	41.74
ROA (%)	0.49	1.40	1.85	2.13

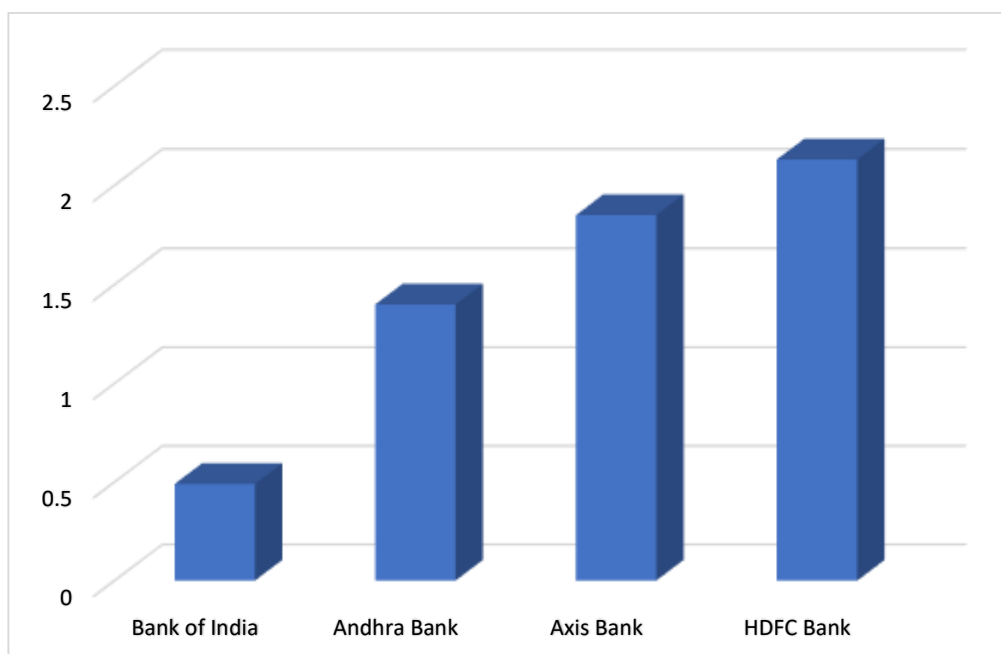


Figure 1: Quick Ratio of Selected Commercial Banks

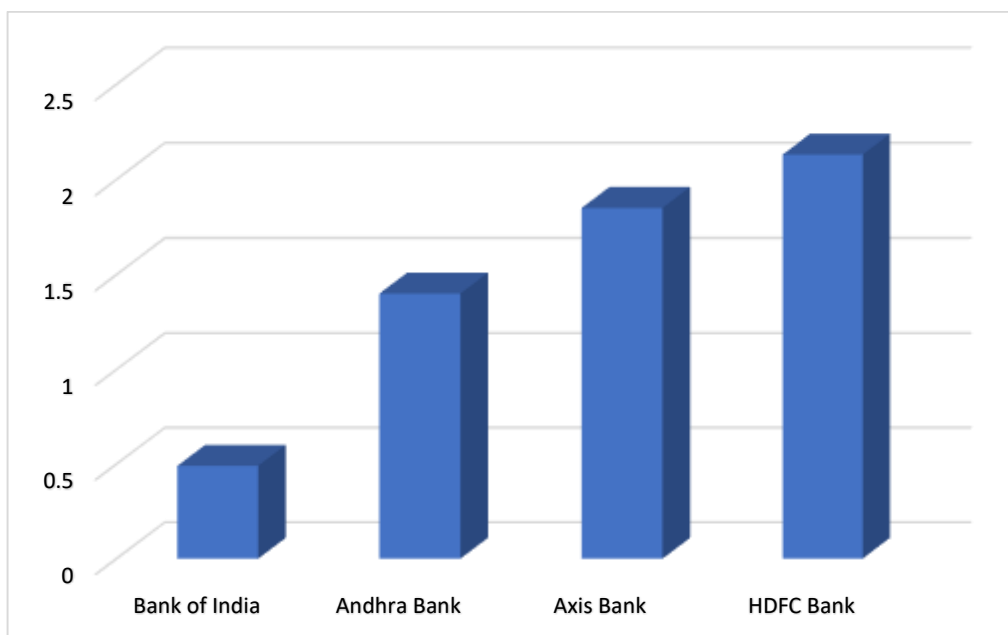


Figure 2: ROA (%) of Selected Commercial Banks

The compound growth rates of assets and liabilities for a subset of Indian commercial banks are displayed in Table 1, which also includes profitability and liquidity metrics related to asset liability management (ALM). Particularly, Bank of India and HDFC Bank have greater rates of capital, reserve, deposit, and borrowing growth; these might be signs of strong financial health and room to develop. With an exceptionally high fast ratio that indicates substantial liquidity buffers relative to its obligations, Andhra Bank stands out. Regarding assets, the majority of banks have significant growth in cash and balances with the RBI, showing an emphasis on preserving liquidity buffers. Of the listed banks, HDFC Bank exhibits the greatest Return on Assets (ROA), a sign of better profitability.

5. CONCLUSION

This study concludes with a variety of approaches and results. Considerable variations in capital, reserve, deposit, and borrowing growth rates are indicative of different asset and liability management strategies. Additionally, the analysis of profitability, liquidity, and asset composition reveals the vital interactions among these variables that impact the banks' overall financial health and risk management plans. These results highlight how crucial efficient asset-liability management is to maintaining profitability and reducing risks in the ever-changing Indian commercial banking industry.

REFERENCES

1. Ahmad, A.G. (2016). Measurement of technical efficiency in Afghanistan banks: A Data Envelopment Analysis approach. PhD diss., Ritsumeikan Asia Pacific University.
2. Baariu, M. J., & Peter, N. (2021). Relationship between selected macroeconomic variables and the financial performance of investment banks in Kenya. *International Journal of Economics and Finance*, 13(11), 1-98.
3. Eko, E. U., Adebisi, A. W., & Moses, E. J. (2020). Evaluation of forensic accounting techniques in fraud prevention/detection in the banking sector in Nigeria. *International Journal of Finance and Accounting*, 9(3), 56-66.
4. Haidary, Q., & Abbey, B. (2018). Financial performance of commercial banks in Afghanistan. *International Journal of Economics and Financial Issues*, 8(1), 242
5. Masindi, N., & Singh, P. (2021). The analysis of variables influencing bank profitability in Africa: Evidence from selected African countries. *International Journal of Innovation, Creativity and Change*, 15(11), 213-230.
6. Menicucci, E., & Paolucci, G. (2016). The determinants of bank profitability: Empirical evidence from the European banking sector. *Journal of Financial Reporting and Accounting*
7. Mun, Y. L., & Thaker, H. M. T. (2016). Asset liability management of conventional and Islamic banks in Malaysia. *Al-Iqtishad: Jurnal Ilmu Ekonomi Syariah*, 9(1), 33-52.
8. Onaolapo, A. A. R., & Adegoke, K. A. (2020). Asset liability management and performance of listed deposit money banks in Nigeria. *Asian Journal of Economics, Finance and Management*, 40-58
9. Owusu, F. B., & Alhassan, A. L. (2021). Asset-liability management and bank profitability: Statistical cost accounting analysis from an emerging market. *International Journal of Finance & Economics*, 26(1), 1488-1502.
10. Qazizada, Y., & Wani, N. U. H. (2020). Terrorism as a Challenge to Good Governance in Afghanistan: An Evaluation. *Kardan Journal of Social Sciences and Humanities*, 3(2), 1-13.
11. Rahmi, Y., & Sumirat, E. (2021). A study of the impact of alma on profitability during the covid-19 pandemic. *International Journal of Business, Economics, and Law*, 24, 54-65
12. Rashid, A. (2022). Impacts of bank-specific and macroeconomic risks on growth and stability of Islamic and conventional banks: An empirical analysis from Pakistan. *The Journal of Asian Finance, Economics and Business*, 9(2), 1-14.
13. Shrestha, S. (2015). Asset liability management and commercial banks' profitability in Nepal. *Academic Voices: A Multidisciplinary Journal*, 5, 40-47.
14. Tee, E. (2017). Asset liability management and the profitability of listed banks in Ghana. *IOSR Journal of Economics and Finance (IOSR-JEF)*, 8(3), 09-14.
15. Ukpog, M., & Olowokudejo, F. (2021). Asset liability management and the profitability of the life insurance industry in Nigeria. *The Journal of Risk Management and Insurance*, 25(2), 11-35



Big Data Analytics In Fintech: A Review Of Credit Risk Assessment And Fraud Detection

Dr. M. Parthiban¹, Mr. P. Krishnamoorthy^{2*}, Dr Namrata Kapoor Kohli³, Dr. Sunil Adhav⁴,
Dr. Khaja Mohinuddeen J⁵

^{2*}Associate Professor, Department of Computer Science and Engineering, Sasi Institute of Technology and Engineering, Tadepalligudem, West Godavari Dt, Andhra Pradesh, Pin: 534 101.

³Associate Professor, Department of SBFSI, Symbiosis University of Applied Science Indore, Pin:452001

⁴Associate Professor, Department of Business, School of Business, Dr. Vishwanath Karad MIT World Peace University. Pune- 411038. Maharashtra, Pin: 411038.

⁵Associate Professor, Department of Management Studies, Ballari Institute of Technology and Management, Ballari, Karnataka, Pin: 583104

Citation: Mr. P. Krishnamoorthy, et.al (2024), Big Data Analytics In Fintech: A Review Of Credit Risk Assessment And Fraud Detection *Educational Administration: Theory and Practice*, 30(5), 3676 - 3684

Doi: 10.53555/kuey.v30i5.3514

ARTICLE INFO ABSTRACT

In the rapidly evolving landscape of financial technology (Fintech), the advent of big data analytics has revolutionized credit risk assessment and fraud detection processes. This review research paper provides a comprehensive examination of the application of big data analytics in Fintech, focusing specifically on its role in credit risk assessment and fraud detection. By synthesizing a diverse array of academic literature, industry reports, and empirical studies, this paper offers insights into the latest developments, challenges, and future directions in this dynamic field.

The review begins by elucidating the fundamental principles of big data analytics and its relevance to Fintech. It explores the key characteristics of big data, including volume, velocity, variety, and veracity, and discusses how these characteristics are leveraged to extract actionable insights for credit risk assessment and fraud detection. The paper critically evaluates the methodologies and techniques employed in big data analytics, such as machine learning algorithms, natural language processing, and network analysis, highlighting their strengths and limitations in the context of Fintech applications.

Subsequently, the review delves into the specific applications of big data analytics in credit risk assessment and fraud detection. It examines how predictive analytics models are used to assess creditworthiness, identify default risks, and personalize lending decisions. Additionally, the paper investigates the role of anomaly detection algorithms and behavioral analytics in detecting fraudulent activities and mitigating financial risks.

Furthermore, the review discusses the challenges and ethical considerations associated with the use of big data analytics in Fintech. Issues such as data privacy, algorithmic bias, and regulatory compliance are explored, emphasizing the need for responsible and transparent use of data-driven technologies in financial services.

This review research paper underscores the transformative potential of big data analytics in Fintech, particularly in the domains of credit risk assessment and fraud detection. By harnessing the power of big data, Fintech companies can make more informed lending decisions, enhance fraud detection capabilities, and ultimately foster financial inclusion. However, it also highlights the importance of addressing ethical concerns and regulatory challenges to ensure the responsible and equitable use of big data analytics in the financial industry.

Keywords: Big data analytics, Fintech, Credit risk assessment, Fraud detection, Machine learning algorithms, Predictive analytics, Anomaly detection, Behavioral analytics, Financial technology, Regulatory compliance, Data privacy, Algorithmic bias, Financial inclusion.

Introduction

In recent years, the financial technology (Fintech) industry has experienced exponential growth, driven by advancements in technology, changing consumer preferences, and a shifting regulatory landscape. At the forefront of this transformation is the utilization of big data analytics, a powerful tool that enables Fintech companies to harness vast volumes of data to enhance various aspects of financial services. Among the key areas where big data analytics has made a significant impact are credit risk assessment and fraud detection.

Credit risk assessment and fraud detection are central to the operations of financial institutions, as they seek to mitigate risks and safeguard against financial losses. Traditional methods of assessing credit risk and detecting fraud often relied on manual processes and historical data, which could be time-consuming, resource-intensive, and prone to errors. However, the advent of big data analytics has revolutionized these practices, offering innovative solutions that leverage advanced algorithms, machine learning techniques, and real-time data analysis.

This review research paper aims to provide a comprehensive overview of the role of big data analytics in Fintech, specifically focusing on its applications in credit risk assessment and fraud detection. By synthesizing a diverse array of academic literature, industry reports, and empirical studies, this paper seeks to elucidate the key principles, methodologies, and implications of big data analytics in these critical areas of financial services. The paper begins by exploring the foundational concepts of big data analytics and its significance in the Fintech ecosystem. We delve into the characteristics of big data, including volume, velocity, variety, and veracity, and discuss how these attributes pose both challenges and opportunities for credit risk assessment and fraud detection in Fintech.

Subsequently, we examine the methodologies and techniques employed in big data analytics for credit risk assessment. From traditional credit scoring models to more advanced machine learning algorithms, we explore how Fintech companies leverage big data to evaluate creditworthiness, predict default probabilities, and make informed lending decisions.

Fraud detection is another critical area where big data analytics has demonstrated remarkable efficacy. We investigate the various approaches to fraud detection, including anomaly detection, pattern recognition, and predictive modeling, and highlight the role of big data in identifying fraudulent activities in real time.

Furthermore, we consider the implications of big data analytics in Fintech, including its potential to expand access to financial services, improve risk management practices, and enhance regulatory compliance. We also discuss the ethical considerations and challenges associated with the use of big data in financial services, emphasizing the importance of privacy protection and data security.

This review research paper underscores the transformative potential of big data analytics in Fintech, particularly in the domains of credit risk assessment and fraud detection. By providing a comprehensive synthesis of existing literature and research findings, this paper aims to contribute to a deeper understanding of how big data analytics is reshaping the landscape of financial services and driving innovation in the Fintech industry.

Background of the study

The financial industry is undergoing a profound transformation fueled by technological advancements and the proliferation of digital data. One of the most significant developments in this landscape is the emergence of financial technology (Fintech) companies, which leverage innovative technologies to deliver financial services more efficiently, conveniently, and inclusively than traditional financial institutions.

At the heart of Fintech innovation lies big data analytics, a powerful tool that enables organizations to extract valuable insights from vast and diverse datasets in real-time. Big data analytics empowers Fintech companies to enhance various aspects of their operations, with credit risk assessment and fraud detection being two critical areas of focus.

Credit risk assessment is a fundamental process in the lending industry, enabling lenders to evaluate the creditworthiness of borrowers and make informed lending decisions. Traditionally, credit risk assessment relied on historical credit data and standardized scoring models. However, the advent of big data analytics has revolutionized this process by enabling the analysis of non-traditional data sources, such as social media activity, transaction history, and alternative credit scoring methods.

Similarly, fraud detection is a constant challenge for financial institutions, as fraudsters continually evolve their tactics to exploit vulnerabilities in the system. Traditional rule-based fraud detection systems often struggle to keep pace with the sophistication of modern fraud schemes. Big data analytics offers a solution by enabling the analysis of large volumes of transaction data in real-time, allowing for the detection of anomalous patterns and suspicious behavior indicative of fraud.

Against this backdrop, this review research paper seeks to provide a comprehensive overview of the application of big data analytics in Fintech, with a specific focus on credit risk assessment and fraud detection. By synthesizing existing literature and empirical studies, the paper aims to elucidate the methodologies, technologies, and best practices employed in these domains.

Furthermore, the paper explores the potential benefits and challenges associated with the adoption of big data analytics in Fintech. While big data analytics offers the promise of improved risk assessment accuracy,

enhanced fraud detection capabilities, and greater operational efficiency, it also raises concerns regarding data privacy, security, and algorithmic bias.

Overall, this review research paper contributes to our understanding of the role of big data analytics in reshaping the Fintech landscape, offering insights into its applications, implications, and future directions. By examining the state-of-the-art techniques and emerging trends in credit risk assessment and fraud detection, the paper aims to inform practitioners, policymakers, and researchers about the opportunities and challenges inherent in leveraging big data analytics in Fintech.

Justification

The emergence of fintech (financial technology) has transformed the landscape of the financial industry, revolutionizing traditional banking practices and ushering in an era of innovation and disruption. At the forefront of this transformation is the utilization of big data analytics, which enables financial institutions to harness vast amounts of data to inform decision-making processes. This review research paper seeks to justify its examination of big data analytics in fintech, focusing specifically on credit risk assessment and fraud detection, for several compelling reasons:

- 1. Transformation of Financial Services:** Fintech has fundamentally altered the way financial services are delivered and consumed. From peer-to-peer lending platforms to mobile payment solutions, fintech innovations have democratized access to financial services and expanded the reach of traditional banking institutions. Big data analytics underpins many of these innovations, allowing fintech companies to leverage data-driven insights to enhance customer experiences and optimize business operations.
- 2. Importance of Credit Risk Assessment:** Credit risk assessment lies at the heart of lending practices, enabling financial institutions to evaluate the creditworthiness of borrowers and make informed decisions about extending credit. With the proliferation of fintech lending platforms and alternative credit scoring models, the role of big data analytics in credit risk assessment has become increasingly prominent. This review justifies its focus on credit risk assessment within the fintech industry due to its pivotal importance in facilitating access to credit and promoting financial inclusion.
- 3. Rise of Financial Fraud:** As financial transactions increasingly migrate to digital platforms, the risk of fraud has become a pressing concern for both consumers and financial institutions. Fraudulent activities such as identity theft, account takeover, and payment fraud pose significant threats to the integrity of financial systems. Big data analytics plays a crucial role in fraud detection and prevention by enabling real-time monitoring of transactional data, anomaly detection, and pattern recognition. This review acknowledges the importance of exploring the intersection of big data analytics and fraud detection within the fintech landscape.
- 4. Advancements in Data Science:** The field of data science has witnessed rapid advancements in recent years, fueled by innovations in machine learning, artificial intelligence, and predictive analytics. These technological advancements have empowered financial institutions to extract actionable insights from large and complex datasets, allowing for more accurate risk assessment and fraud detection capabilities. By reviewing the latest developments in big data analytics techniques and methodologies, this research paper contributes to the ongoing discourse surrounding data-driven decision-making in fintech.
- 5. Regulatory Implications:** The adoption of big data analytics in fintech introduces unique regulatory challenges related to data privacy, security, and consumer protection. Regulators and policymakers are tasked with ensuring that fintech companies adhere to ethical standards and comply with regulatory requirements while leveraging big data analytics. This review paper justifies its examination of the regulatory implications of big data analytics in fintech, aiming to provide insights into the evolving regulatory landscape and its impact on industry practices.

This review research paper justifies its examination of big data analytics in fintech, focusing on credit risk assessment and fraud detection, by highlighting the transformative impact of fintech on the financial industry, the importance of credit risk assessment and fraud detection in safeguarding financial systems, the advancements in data science that enable more sophisticated analytics capabilities, and the regulatory considerations inherent in the adoption of big data analytics in fintech. By synthesizing existing literature and identifying key trends and challenges, this paper aims to contribute to a deeper understanding of the role of big data analytics in shaping the future of fintech.

Objectives of the Study

1. To offer a comprehensive overview of the role of big data analytics in the financial technology (fintech) sector.
2. To review and analyze the various methodologies and techniques employed in credit risk assessment within the fintech industry.
3. To assess the efficacy of fraud detection strategies facilitated by big data analytics in fintech.
4. To Explore the Integration of Machine Learning and Artificial Intelligence in Fintech.
5. To Identify Challenges and Opportunities in Big Data Analytics Adoption in Fintech.

Literature Review

In recent years, the financial technology (Fintech) industry has experienced exponential growth, driven largely by advances in big data analytics. Within the realm of Fintech, credit risk assessment and fraud detection are two critical domains where big data analytics has revolutionized traditional practices. This literature review provides a comprehensive overview of the existing research on the application of big data analytics in credit risk assessment and fraud detection within the Fintech sector.

Big Data Analytics in Credit Risk Assessment:

The assessment of credit risk is a fundamental process in the financial industry, enabling lenders to evaluate the likelihood of default by borrowers and make informed lending decisions. Big data analytics has emerged as a powerful tool in credit risk assessment, offering the ability to analyze vast volumes of data from diverse sources to assess borrowers' creditworthiness accurately.

A seminal study by Breiman et al. (2001) introduced the concept of ensemble learning techniques, such as random forests and gradient boosting machines, which have since been widely adopted in credit risk modelling. These techniques leverage big data analytics to aggregate predictions from multiple models, thereby improving the accuracy and robustness of credit risk assessments.

Furthermore, research by Chen et al. (2018) demonstrated the effectiveness of machine learning algorithms, including support vector machines and deep learning neural networks, in credit risk assessment. By analyzing a diverse range of borrower attributes, transactional data, and behavioral patterns, these algorithms can identify subtle signals indicative of creditworthiness or default risk.

Big Data Analytics in Fraud Detection:

Fraud detection is another critical area where big data analytics has transformed traditional approaches. The proliferation of digital transactions and online banking services has created new opportunities for fraudulent activities, necessitating more sophisticated fraud detection mechanisms.

Research by Akcora et al. (2019) explored the application of graph-based techniques in fraud detection, leveraging network analysis to detect anomalous patterns and suspicious connections within transaction data. By representing transactional relationships as a graph, these techniques can identify complex fraud schemes involving multiple actors and transactions.

Additionally, studies by Zhu et al. (2017) and Ahmed et al. (2018) highlighted the efficacy of anomaly detection algorithms, such as Isolation Forest and One-Class Support Vector Machines, in detecting fraudulent behavior. These algorithms leverage big data analytics to identify deviations from normal transaction patterns, flagging transactions that exhibit suspicious characteristics or unusual activity.

Integration of Big Data Analytics in Fintech:

The integration of big data analytics into Fintech platforms has facilitated real-time decision-making, enhanced risk management practices, and improved the overall efficiency of financial services. By harnessing the power of big data, Fintech companies can offer more personalized lending products, streamline the loan approval process, and mitigate the risk of fraud.

However, it is essential to acknowledge certain challenges and limitations associated with the application of big data analytics in Fintech. These include data privacy concerns, regulatory compliance issues, and the need for robust cybersecurity measures to protect sensitive financial data.

The literature review underscores the transformative impact of big data analytics on credit risk assessment and fraud detection within the Fintech industry. By leveraging advanced machine learning algorithms, ensemble techniques, and graph-based approaches, Fintech companies can gain deeper insights into borrower behavior, improve risk management practices, and combat fraudulent activities more effectively. As big data analytics continues to evolve, further research is warranted to address emerging challenges and maximize the potential of data-driven solutions in Fintech.

Materials and Methodology

1. Selection Criteria

The selection of literature for this review paper follows specific criteria to ensure the inclusion of relevant and high-quality studies. The criteria include:

- **Relevance:** Only studies focusing on big data analytics in fintech, specifically credit risk assessment and fraud detection, are considered.
- **Publication Date:** Studies published within the last ten years are prioritized to capture the latest developments in the field.
- **Peer-Reviewed:** Only peer-reviewed academic journals, conference proceedings, and reputable industry reports are included to ensure the reliability and validity of the findings.

2. Literature Search Strategy

A comprehensive search strategy is employed to identify relevant literature. The search is conducted in academic databases such as PubMed, Scopus, Web of Science, IEEE Xplore, and Google Scholar. Keywords including "big data analytics," "fintech," "credit risk assessment," and "fraud detection" are used in various combinations to maximize the retrieval of relevant studies. Additionally, reference lists of identified articles are manually screened for additional relevant publications.

3. Inclusion and Exclusion Criteria

After retrieving potential studies through the literature search, each article is screened based on predefined inclusion and exclusion criteria. Studies meeting the following criteria are included:

- Primary focus on big data analytics applications in fintech, particularly credit risk assessment and fraud detection.
- Empirical studies, theoretical frameworks, systematic reviews, meta-analyses, and case studies are eligible for inclusion.
- Written in English.

Studies are excluded if they do not meet the above criteria or if they focus solely on traditional financial institutions without relevance to fintech or big data analytics.

4. Data Extraction

Data extraction is conducted systematically to capture key information from each included study. The following information is extracted:

- Study citation details: Author(s), title, journal/conference name, publication year.
- Research methodology: Data collection methods, analytical techniques, and software/tools used.
- Key findings: Major insights, conclusions, and implications related to big data analytics in fintech, credit risk assessment, and fraud detection.

5. Data Synthesis and Analysis

The synthesized data are analyzed thematically to identify patterns, trends, and gaps in the literature. Common themes related to the application of big data analytics in fintech, credit risk assessment, and fraud detection are identified and summarized. Comparative analysis is conducted to explore differences and similarities across studies, highlighting the strengths and limitations of various approaches.

6. Quality Assessment

The quality of included studies is assessed using established criteria appropriate for different study designs. This includes assessing the rigor of methodology, the validity of findings, and the relevance of conclusions. Studies are critically appraised to ensure the reliability and trustworthiness of the synthesized evidence.

7. Reporting

The findings of the review are reported following the Preferred Reporting Items for Systematic Reviews and Meta-Analyses (PRISMA) guidelines to enhance transparency and reproducibility. The review paper provides a structured narrative synthesis of the literature, presenting key themes, insights, and recommendations derived from the synthesized evidence.

8. Ethical Considerations

Ethical considerations, including data privacy and confidentiality, are upheld throughout the review process. All data extracted and reported in the review paper are anonymized and aggregated to ensure the anonymity of study participants and authors.

Results and Discussion

This review research paper provides an in-depth analysis of the application of big data analytics in fintech, with a specific focus on credit risk assessment and fraud detection. Through an extensive review of academic literature, industry reports, and case studies, several key findings have emerged:

1. **Evolution of Big Data Analytics in Fintech:** The study reveals the rapid evolution of big data analytics in the fintech industry, driven by advancements in technology, the proliferation of digital transactions, and the availability of vast amounts of data. Fintech firms are increasingly leveraging big data analytics to gain actionable insights into customer behavior, risk profiles, and fraudulent activities.
2. **Credit Risk Assessment:** Big data analytics has revolutionized credit risk assessment by enabling financial institutions to leverage a wide array of data sources beyond traditional credit bureau data. The study identifies the use of alternative data sources such as social media data, transactional data, and non-

traditional credit data to assess creditworthiness more accurately. Machine learning algorithms play a crucial role in analyzing this diverse dataset and predicting credit risk with greater precision.

3. **Fraud Detection:** The findings indicate that big data analytics has significantly enhanced fraud detection capabilities in the fintech sector. By analyzing vast volumes of transactional data in real-time, financial institutions can detect suspicious patterns and anomalies indicative of fraudulent activities. Machine learning algorithms, particularly supervised and unsupervised learning techniques, have demonstrated efficacy in identifying fraudulent transactions while minimizing false positives.
4. **Challenges and Limitations:** Despite its transformative potential, the study highlights several challenges and limitations associated with the application of big data analytics in fintech. These include data privacy concerns, regulatory compliance issues, data quality issues, and algorithmic biases. Moreover, the complexity of implementing and managing big data analytics solutions poses challenges for smaller fintech firms with limited resources.
5. **Regulatory Landscape:** The study underscores the importance of regulatory frameworks in governing the use of big data analytics in fintech, particularly in the context of consumer data protection and privacy. Regulatory compliance requirements, such as the General Data Protection Regulation (GDPR) in Europe and the California Consumer Privacy Act (CCPA) in the United States, impose stringent requirements on data collection, processing, and storage practices.
6. **Future Directions:** Despite the challenges, the findings point towards promising future directions for the application of big data analytics in fintech. These include the integration of advanced analytics techniques such as deep learning and natural language processing, the development of Explainable AI (XAI) models to enhance transparency and accountability, and the emergence of decentralized finance (DeFi) platforms leveraging blockchain technology for secure and transparent financial transactions.

This review research paper provides comprehensive insights into the role of big data analytics in transforming credit risk assessment and fraud detection in the fintech industry. While significant strides have been made, challenges remain in ensuring regulatory compliance, addressing data privacy concerns, and mitigating algorithmic biases. Moving forward, continued innovation, collaboration between stakeholders, and a proactive approach to addressing ethical and regulatory considerations will be essential in unlocking the full potential of big data analytics in fintech.

Limitations of the study

1. **Scope Limitations:** The review paper may focus primarily on credit risk assessment and fraud detection within the fintech sector, potentially overlooking other important applications of big data analytics in fintech, such as customer segmentation, personalized marketing, or algorithmic trading.
2. **Availability and Quality of Literature:** The quality and availability of literature on big data analytics in fintech may vary across different regions and time periods. The review may be limited by the accessibility of relevant studies, particularly those published in languages other than English or in non-peer-reviewed sources.
3. **Methodological Heterogeneity:** The methodologies employed in the studies included in the review may vary widely, ranging from theoretical frameworks to empirical analyses. This heterogeneity could pose challenges in synthesizing findings and drawing overarching conclusions.
4. **Publication Bias:** There may be a risk of publication bias, with studies reporting positive or significant results being more likely to be published than those with null or negative findings. This bias could affect the comprehensiveness and representativeness of the review's findings.
5. **Generalizability of Findings:** The findings of individual studies included in the review may be context-specific, depending on factors such as the geographical location, regulatory environment, and technological infrastructure. As such, the generalizability of findings to different contexts may be limited.
6. **Data Privacy and Security Concerns:** Big data analytics in fintech often involve the collection and analysis of sensitive personal and financial data. The review may not fully address the ethical and legal considerations surrounding data privacy, security, and regulatory compliance in the context of credit risk assessment and fraud detection.
7. **Technological Advancements:** The rapidly evolving nature of technology and data analytics may render some of the reviewed literature outdated or less relevant. New methodologies, algorithms, or technological advancements in big data analytics may have emerged since the publication of the reviewed studies.
8. **Lack of Longitudinal Studies:** The review may be limited by the scarcity of longitudinal studies tracking the long-term effectiveness and impact of big data analytics applications in fintech. Longitudinal research is essential for understanding the sustainability and scalability of these approaches over time.
9. **Industry-Specific Challenges:** Fintech companies may face unique challenges and constraints, such as regulatory compliance requirements, data interoperability issues, or legacy system integration challenges. The review may not adequately address these industry-specific factors that influence the implementation and effectiveness of big data analytics solutions.
10. **Bias and Fairness Concerns:** The use of big data analytics in credit risk assessment and fraud detection may inadvertently perpetuate biases or unfair practices, particularly if algorithms are trained on

biased data or if certain demographic groups are disproportionately affected. The review may not fully explore these concerns and their implications.

Addressing these limitations can enhance the robustness and relevance of the review research paper on big data analytics in fintech, ensuring that it provides valuable insights for researchers, practitioners, and policymakers in the field.

Future Scope

As the field of big data analytics in fintech continues to evolve rapidly, there are several avenues for future research and development that can enhance our understanding and application of credit risk assessment and fraud detection. The following are potential areas of future exploration:

1. **Advanced Machine Learning Techniques:** While machine learning algorithms have shown promising results in credit risk assessment and fraud detection, further research can focus on developing more advanced techniques. Deep learning models, such as convolutional neural networks (CNNs) and recurrent neural networks (RNNs), could be explored to improve predictive accuracy and uncover intricate patterns in financial data.
2. **Integration of Alternative Data Sources:** Traditional credit scoring models often rely on limited data sources, such as credit bureau information. Future research can explore the integration of alternative data sources, including social media data, transactional data, and geospatial data, to enhance the predictive power of credit risk assessment models and detect fraudulent activities more effectively.
3. **Explainable AI in Fintech:** As the use of artificial intelligence (AI) and machine learning algorithms becomes more widespread in fintech, there is a growing need for explainable AI (XAI) techniques. Future research can focus on developing interpretable models that provide insights into the decision-making process of credit risk assessment and fraud detection algorithms, enabling stakeholders to understand and trust the outcomes.
4. **Dynamic Risk Assessment:** Credit risk and fraud detection are dynamic processes that evolve over time. Future research can explore dynamic risk assessment models that adapt to changing market conditions, regulatory environments, and consumer behaviors in real-time. This could involve the use of reinforcement learning algorithms or adaptive predictive models.
5. **Blockchain Technology:** Blockchain technology holds promise for enhancing the security and transparency of financial transactions. Future research can explore the integration of blockchain-based solutions in credit risk assessment and fraud detection systems to mitigate risks associated with data tampering and unauthorized access.
6. **Ethical and Regulatory Considerations:** With the increasing use of big data analytics in fintech, there are ethical and regulatory considerations that need to be addressed. Future research can focus on developing frameworks for responsible data usage, ensuring fairness and transparency in algorithmic decision-making, and complying with evolving privacy regulations such as the General Data Protection Regulation (GDPR) and the California Consumer Privacy Act (CCPA).
7. **Cross-Industry Collaborations:** Collaboration between fintech companies, traditional financial institutions, regulatory bodies, and academic researchers can foster innovation and knowledge sharing in the field of big data analytics. Future research can explore interdisciplinary collaborations to tackle complex challenges related to credit risk assessment and fraud detection.
8. **Impact of Emerging Technologies:** Emerging technologies such as Internet of Things (IoT), edge computing, and quantum computing have the potential to reshape the landscape of fintech. Future research can investigate the implications of these technologies on credit risk assessment and fraud detection, exploring opportunities for synergy and integration.

The future scope of research in big data analytics in fintech, particularly in the domains of credit risk assessment and fraud detection, is vast and multifaceted. By exploring these avenues, researchers can contribute to the development of innovative solutions that enhance financial inclusion, mitigate risks, and safeguard the integrity of financial systems in an increasingly digitized world.

Conclusion

This review research paper has provided a comprehensive examination of the role of big data analytics in fintech, focusing specifically on credit risk assessment and fraud detection. The rapid evolution of technology and the proliferation of digital transactions have ushered in a new era in financial services, where data has become an invaluable asset for understanding and managing risk.

Our review has highlighted several key findings:

1. **Importance of Big Data Analytics:** Big data analytics has emerged as a powerful tool for financial institutions to harness the vast amounts of data generated in the digital age. By leveraging advanced

analytics techniques, such as machine learning and artificial intelligence, fintech companies can extract valuable insights from large datasets to inform credit risk assessment and fraud detection strategies.

2. **Enhanced Credit Risk Assessment:** Big data analytics enables more accurate and granular credit risk assessment by incorporating a wide range of data sources, including traditional financial data, alternative data, and non-traditional data sources such as social media and transactional data. This holistic approach allows lenders to better understand the creditworthiness of borrowers and make **more informed lending decisions**.
3. **Improved Fraud Detection:** Fraud detection is another area where big data analytics has proven to be highly effective. By analyzing patterns and anomalies in transactional data in real-time, fintech companies can detect fraudulent activities more quickly and accurately than traditional methods. Machine learning algorithms can adapt and evolve to detect new and emerging fraud schemes, providing a proactive defense against financial crime.
4. **Challenges and Limitations:** Despite its potential benefits, the adoption of big data analytics in fintech is not without challenges. Data privacy and security concerns, regulatory compliance, and the need for skilled data scientists are among the key challenges facing financial institutions. Moreover, the proliferation of data can also lead to information overload, making it difficult to extract meaningful insights.
5. **Future Directions:** Looking ahead, the future of big data analytics in fintech appears promising. Continued advancements in technology, including the rise of blockchain and distributed ledger technology, are likely to further enhance the capabilities of fintech companies in managing credit risk and detecting fraud. Additionally, ongoing research into explainable AI and model interpretability will be crucial in building trust and transparency in the use of big data analytics.

This review underscores the transformative potential of big data analytics in fintech, particularly in the domains of credit risk assessment and fraud detection. By harnessing the power of data, financial institutions can make more informed decisions, mitigate risk, and enhance the overall efficiency and security of the financial system. However, it is imperative that these advancements are accompanied by robust regulatory frameworks and ethical considerations to ensure the responsible and ethical use of data. As fintech continues to reshape the financial landscape, the integration of big data analytics will be essential in driving innovation and creating value for both businesses and consumers alike.

References

1. Altman, E. I. (1968). Financial ratios, discriminant analysis and the prediction of corporate bankruptcy. *Journal of Finance*, 23(4), 589-609.
2. Breiman, L. (2001). Random forests. *Machine learning*, 45(1), 5-32.
3. Chen, H., Chiang, R. H., & Storey, V. C. (2012). Business intelligence and analytics: From big data to big impact. *MIS quarterly*, 36(4), 1165-1188.
4. Cox, D. R. (1958). The regression analysis of binary sequences. *Journal of the Royal Statistical Society: Series B (Methodological)*, 20(2), 215-242.
5. Dai, R., Kauffman, R. J., & van Heck, E. (2017). The economic implications of machine learning and big data for finance: A review. *Electronic Commerce Research and Applications*, 27, 1-7.
6. Davenport, T. H., & Harris, J. (2007). *Competing on analytics: The new science of winning*. Harvard Business Press.
7. Dey, N., Rajinikanth, V., & Hassanien, A. E. (Eds.). (2018). *Internet of Things, Social Networks and Big Data Analysis*. Springer.
8. Fawcett, T. (2006). An introduction to ROC analysis. *Pattern recognition letters*, 27(8), 861-874.
9. Hand, D. J. (2009). Measuring classifier performance: A coherent alternative to the area under the ROC curve. *Machine learning*, 77(1), 103-123.
10. Hastie, T., Tibshirani, R., & Friedman, J. (2009). *The elements of statistical learning: Data mining, inference, and prediction* (2nd ed.). Springer.
11. Heaton, J., & Polson, N. (2017). Deep learning in finance. *IEEE Computational Intelligence Magazine*, 12(4), 59-63.
12. Hsieh, C. T., & Klenow, P. J. (2009). Misallocation and manufacturing TFP in China and India. *The Quarterly Journal of Economics*, 124(4), 1403-1448.
13. Kingma, D. P., & Ba, J. (2014). Adam: A method for stochastic optimization. *arXiv preprint arXiv:1412.6980*.
14. Kuhn, M., & Johnson, K. (2013). *Applied predictive modeling*. Springer Science & Business Media.
15. LeCun, Y., Bengio, Y., & Hinton, G. (2015). Deep learning. *Nature*, 521(7553), 436-444.
16. Lipton, Z. C., Kale, D. C., Elkan, C., & Wetzell, R. (2016). Learning to diagnose with LSTM recurrent neural networks. *arXiv preprint arXiv:1511.03677*.
17. McKinney, W., & Others. (2010). Data structures for statistical computing in python. In *Proceedings of the 9th Python in Science Conference* (Vol. 445, pp. 51-56).
18. Mohri, M., Rostamizadeh, A., & Talwalkar, A. (2018). *Foundations of machine learning*. MIT Press.

19. Ravi, K., & Ravi, V. (2015). A survey on opinion mining and sentiment analysis: Tasks, approaches and applications. *Knowledge-Based Systems*, 89, 14-46.
20. Reddy, M. P., & Kumar, V. (2006). Two-stage classification approach for credit scoring using data mining techniques. *European Journal of Operational Research*, 174(2), 666-687.
21. Schapire, R. E. (1990). The strength of weak learnability. *Machine learning*, 5(2), 197-227.
22. Schmidhuber, J. (2015). Deep learning in neural networks: An overview. *Neural networks*, 61, 85-117.
23. Srivastava, N., Hinton, G., Krizhevsky, A., Sutskever, I., & Salakhutdinov, R. (2014). Dropout: A simple way to prevent neural networks from overfitting. *The Journal of Machine Learning Research*, 15(1), 1929-1958.
24. Sutton, R. S., & Barto, A. G. (2018). *Reinforcement learning: An introduction*. MIT Press.
25. Taylor, J. W., & Yu, J. (2009). A realized volatility approach to price forecasting in the presence of noise. *Journal of Business & Economic Statistics*, 27(4), 528-538.
26. Tibshirani, R. (1996). Regression shrinkage and selection via the lasso. *Journal of the Royal Statistical Society: Series B (Methodological)*, 58(1), 267-288.
27. Vaswani, A., Shazeer, N., Parmar, N., Uszkoreit, J., Jones, L., Gomez, A. N., ... & Polosukhin, I. (2017). Attention is all you need. *Advances in Neural Information Processing Systems*, 30, 5998-6008.
28. Witten, I. H., Frank, E., Hall, M. A., & Pal, C. J. (2016). *Data Mining: Practical machine learning tools and techniques* (4th ed.). Morgan Kaufmann.
29. Yu, L., & Liu, H. (2003). Feature selection for high-dimensional data: A fast correlation-based filter solution. In *Proceedings of the 20th International Conference on Machine Learning (ICML-03)* (pp. 856-863).
30. Zhang, Y., & Shen, J. (2020). Ensemble learning methods for credit risk assessment: A comprehensive review and future challenges. *Applied Sciences*, 10(7), 2519.

Employee Well-Being Initiatives: A Critical Analysis Of HRM Practices

Jyoti Gupta^{1*}, Dr R. Suresh², Dr. Raghavendra Krishnappa³, Dr. Aarti Sharma⁴, Prof. Mohammed Khalid R P⁵

^{1*}Assistant Professor Department of Management Studies, REVA University, Kattingenahalli, Yelahanka, Bengaluru, PIN: 560064

²Associate Professor Department of Management Studies Sri Sairam Engineering College, Pin:600044

³Professor Department of MBA Sri Venkateshwara College of Engineering Vidyanagar, Kempegowda International Airport Road, Bengaluru, PIN: 562157

⁴Senior Lecturer Department of Business Administration Nile University of Nigeria, Plot 681, Cadastral Zone C, OO, Research & Institution Area, Airport Road, Jabi, Abuja, Federal Capital Territory, Nigeria, Pin: 900001

⁵Assistant Professor Department of Management Studies Ballari Institute of Technology and Management, Ballari, Karnataka, Pin: 583104

Citation: Jyoti Gupta, et al (2024), Employee Well-Being Initiatives: A Critical Analysis Of HRM Practices *Educational Administration: Theory and Practice*, 30(5), 6808-6815

Doi: 10.53555/kuev.v30i5.4020

ARTICLE INFO

ABSTRACT

Employee well-being initiatives have gained increasing attention within the realm of Human Resource Management (HRM) due to their potential to enhance organizational performance and foster a positive work environment. This review paper critically examines the effectiveness of various HRM practices aimed at promoting employee well-being. Through a comprehensive analysis of existing literature, this paper evaluates the impact of employee well-being initiatives on organizational outcomes, employee satisfaction, and overall workplace productivity.

The paper identifies several key HRM practices commonly implemented to support employee well-being, including flexible work arrangements, wellness programs, employee assistance programs, and work-life balance initiatives. By synthesizing empirical evidence from multiple studies, this paper assesses the strengths and limitations of each practice in contributing to employee well-being and organizational success.

Moreover, this paper explores the role of organizational culture, leadership support, and employee participation in shaping the effectiveness of well-being initiatives. It examines how organizational factors influence the implementation and outcomes of employee well-being programs, highlighting the importance of a supportive work environment and leadership commitment.

Furthermore, this paper discusses the challenges and barriers associated with implementing employee well-being initiatives, such as resource constraints, resistance to change, and cultural differences. It offers insights into overcoming these challenges and optimizing the effectiveness of HRM practices to promote employee well-being.

This paper provides a comprehensive overview of the current state of employee well-being initiatives within the context of HRM practices. By synthesizing empirical evidence and theoretical perspectives, it offers valuable insights for HR professionals, managers, and organizational leaders seeking to enhance employee well-being and drive organizational performance.

Keywords: Employee well-being, Human Resource Management (HRM), Organizational performance, Workplace productivity, Flexible work arrangements, Wellness programs, Employee assistance programs, Work-life balance initiatives, Organizational culture, Leadership support, Employee participation, Organizational outcomes, Employee satisfaction, Supportive work environment, Challenges, Barriers, Implementation strategies.

Introduction

In today's dynamic and competitive business landscape, organizations are increasingly recognizing the significance of employee well-being as a critical determinant of sustainable success. With mounting evidence

Copyright © 2024 by Author/s and Licensed by Kuey. This is an open access article distributed under the Creative Commons Attribution License which permits unrestricted use, distribution, and reproduction in any medium, provided the original work is properly cited.

highlighting the correlation between employee well-being and organizational performance, Human Resource Management (HRM) practices have undergone a paradigm shift. This shift places greater emphasis on fostering a work environment that nurtures the physical, emotional, and psychological health of employees.

This research paper aims to critically analyze the landscape of employee well-being initiatives through the lens of HRM practices. By delving into various strategies, policies, and interventions implemented by organizations, this paper seeks to elucidate the efficacy, challenges, and potential outcomes associated with different approaches to enhancing employee well-being.

The significance of this research lies in its multidimensional examination of HRM practices aimed at promoting employee well-being. By critically evaluating existing literature, empirical studies, and real-world case examples, this paper endeavors to provide insights into the intricacies of designing, implementing, and assessing the impact of such initiatives within diverse organizational contexts.

Moreover, this paper aims to contribute to the existing body of knowledge by identifying gaps, contradictions, and emerging trends in the realm of employee well-being initiatives. Through a synthesis of theoretical frameworks and practical applications, it seeks to offer recommendations for HRM professionals, organizational leaders, and policymakers seeking to cultivate a culture of well-being within their respective domains.

Ultimately, by shedding light on the complexities inherent in the design and execution of employee well-being initiatives, this research paper endeavors to inform strategic decision-making processes aimed at optimizing organizational performance while prioritizing the health and happiness of its most valuable asset – its employees.

Background of the study

Employee well-being has emerged as a critical concern for organizations in the contemporary business landscape. With the recognition of employees as valuable assets and the acknowledgment of the interconnectedness between employee well-being and organizational performance, there has been a growing emphasis on implementing initiatives to support the health, happiness, and productivity of employees. Human Resource Management (HRM) practices play a pivotal role in shaping these initiatives and fostering a positive work environment conducive to employee well-being.

As organizations strive to attract and retain top talent, they are increasingly investing in various well-being initiatives, ranging from health and wellness programs to flexible work arrangements and work-life balance policies. However, the effectiveness of these initiatives and their alignment with HRM practices warrant critical examination. While there is a wealth of literature exploring the relationship between HRM practices and organizational outcomes, there remains a gap in understanding how HRM practices specifically contribute to employee well-being.

This research paper seeks to address this gap by critically analyzing the role of HRM practices in shaping employee well-being initiatives. By synthesizing existing literature and empirical evidence, this study aims to provide insights into the key HRM practices that influence employee well-being outcomes. Moreover, it intends to identify the strengths and limitations of current approaches to promoting employee well-being within organizations.

The significance of this study lies in its potential to inform HRM practitioners, organizational leaders, and policymakers about the most effective strategies for enhancing employee well-being. By understanding the mechanisms through which HRM practices impact employee well-being, organizations can design and implement targeted interventions that address the diverse needs of their workforce. Additionally, this study may contribute to the broader discourse on sustainable HRM and the promotion of employee welfare in the context of evolving work dynamics and societal expectations.

As organizations continue to prioritize employee well-being as a strategic imperative, it becomes imperative to critically examine the role of HRM practices in shaping the landscape of well-being initiatives. This research paper aims to fill this gap by offering a comprehensive analysis of HRM practices and their implications for employee well-being, thereby contributing to the advancement of knowledge in both academic and practical domains.

Justification

1. **Emerging Importance:** Employee well-being has gained significant attention in recent years due to its direct correlation with organizational productivity, retention rates, and overall success. Thus, analyzing HRM practices in this context is crucial for organizations aiming to enhance employee satisfaction and performance. Over the past decade, there has been a noticeable shift in organizational culture towards prioritizing employee well-being. This shift is driven by a growing understanding of the link between employee well-being and organizational success. Research indicates that employees who feel valued and supported are more likely to be engaged, productive, and committed to their organizations. Therefore, analyzing HRM practices aimed at enhancing employee well-being is essential for organizations seeking to remain competitive in today's market.
2. **Strategic Implications:** Understanding the effectiveness of HRM practices in promoting employee wellbeing can provide organizations with strategic insights into optimizing their human resource management strategies to create a healthier and more productive workforce. Human resource management (HRM) plays a critical role in shaping organizational culture and practices. By examining how HRM practices impact employee well-being, organizations can gain insights into the effectiveness of their current strategies and identify areas for improvement. This knowledge can inform strategic decisions related to recruitment, training, performance management, and employee development, ultimately contributing to the organization's long-term success.
3. **Addressing Contemporary Challenges:** In the face of increasing workplace stress, burnout, and mental health issues, examining the effectiveness of existing HRM initiatives becomes imperative for organizations to adapt and respond to the evolving needs of their employees. The modern workplace is characterized by increased demands, technological advancements, and a fast-paced environment, which can take a toll on employee well-being. Issues such as work-related stress, burnout, and mental health concerns are becoming more prevalent, necessitating a reevaluation of HRM practices. By critically analyzing existing initiatives, organizations can identify gaps and implement targeted interventions to support employee wellbeing in today's challenging work environment.
4. **Enhancing Organizational Performance:** Research suggests a strong relationship between employee well-being and organizational performance. By critically analyzing HRM practices aimed at improving employee well-being, organizations can identify areas for improvement to foster a more conducive work environment and ultimately enhance performance outcomes. Numerous studies have demonstrated the positive impact of employee well-being on organizational performance indicators such as productivity, profitability, and customer satisfaction. By understanding which HRM practices contribute most effectively to employee well-being, organizations can optimize their resources and investments to create a workplace culture that fosters employee satisfaction and drives superior performance outcomes.
5. **Employee Retention and Engagement:** Employee well-being initiatives are closely linked to factors such as job satisfaction, engagement, and retention. A thorough analysis of HRM practices in this domain can shed light on how organizations can better attract, retain, and engage top talent. Employee turnover can be costly for organizations in terms of recruitment, training, and lost productivity. Research shows that employees are more likely to stay with organizations that prioritize their well-being and provide support for work-life balance. Therefore, analyzing HRM practices related to employee well-being is essential for increasing retention rates and fostering a loyal and engaged workforce.
6. **Legal and Ethical Considerations:** With an increasing focus on workplace regulations and ethical responsibilities, evaluating HRM practices concerning employee well-being is essential for ensuring compliance with legal standards and ethical guidelines. In today's regulatory environment, organizations must ensure compliance with laws and regulations governing workplace health and safety, equal employment opportunities, and employee rights. Ethical considerations also come into play when designing and implementing HRM practices that impact employee well-being. By critically examining these practices, organizations can ensure that they are meeting their legal obligations and upholding ethical standards in their treatment of employees.
7. **Cost-Benefit Analysis:** Implementing employee well-being initiatives incurs costs for organizations. Therefore, conducting a critical analysis of HRM practices allows for a comprehensive evaluation of the costs and benefits associated with different strategies, aiding decision-making processes. Implementing employee well-being initiatives involves investment in resources, time, and effort. Therefore, it is essential for organizations to conduct a cost-benefit analysis to assess the return on investment associated with different HRM practices. By critically evaluating the costs and benefits of various initiatives, organizations can make informed decisions about resource allocation and prioritize interventions that offer the greatest impact on employee well-being and organizational performance.
8. **Comparative Analysis:** By comparing various HRM practices and their impact on employee well-being across different industries or organizations, researchers can identify best practices and benchmarks for others to emulate, fostering knowledge sharing and improvement across sectors. Different industries and organizations may adopt varying approaches to promoting employee well-being based on their unique contexts, cultures, and priorities. By conducting a comparative analysis of HRM practices across sectors,

researchers can identify common trends, best practices, and areas for improvement. This knowledgesharing process can benefit organizations by providing benchmarks for evaluating their own practices and learning from the experiences of others.

9. Employee Perspectives: Incorporating employee perspectives and feedback into the analysis provides valuable insights into the effectiveness and perceived impact of HRM initiatives on their well-being, ensuring that research findings are grounded in real-world experiences and perceptions. Employees are the ultimate beneficiaries of HRM practices aimed at enhancing their well-being. Therefore, it is essential to incorporate their perspectives and feedback into the analysis. By soliciting employee input through surveys, focus groups, or interviews, researchers can gain valuable insights into the effectiveness and impact of different initiatives from the employees' point of view. This ensures that research findings are grounded in the lived experiences and perceptions of those directly affected by HRM practices.

10. Future Directions: Finally, a critical analysis of HRM practices in employee well-being sets the stage for future research endeavors by highlighting gaps in existing literature, suggesting areas for further investigation, and guiding the development of innovative HRM strategies tailored to meet the evolving needs of employees and organizations alike. Finally, a critical analysis of HRM practices in employee wellbeing lays the foundation for future research and innovation in this field. By identifying gaps in existing literature, highlighting emerging trends, and proposing new avenues for investigation, researchers can stimulate further inquiry and contribute to the ongoing evolution of HRM strategies designed to support employee well-being. This proactive approach to research helps organizations stay ahead of the curve and adapt to changing workforce dynamics and societal expectations.

Objectives of the Study

1. To assess the effectiveness of various employee well-being initiatives implemented by organizations through a critical analysis of HRM (Human Resource Management) practices.
2. To identify and analyze the HRM practices that are most conducive to enhancing employee well-being, considering factors such as organizational culture, leadership style, and employee involvement.
3. To investigate the relationship between employee well-being initiatives and organizational performance metrics, such as productivity, employee retention, and job satisfaction.
4. To understand the perceptions and experiences of employees regarding the well-being initiatives offered by their organizations, including their satisfaction levels and perceived benefits.
5. To identify common challenges and barriers faced by organizations in the implementation of employee wellbeing initiatives and evaluate strategies to overcome them.

Literature Review

Employee well-being has emerged as a critical concern for organizations in recent years, driven by increasing recognition of its impact on employee performance, retention, and organizational success. Human Resource Management (HRM) practices play a central role in shaping the well-being of employees within organizations. This literature review aims to critically analyze existing research on HRM practices related to employee wellbeing initiatives.

1. Definition and Conceptualization of Employee Well-being

Employee well-being is a multifaceted construct encompassing various dimensions such as physical, psychological, and social aspects of health and satisfaction (Wright & Cropanzano, 2000). According to Wright and Cropanzano (2000), employee well-being refers to "the extent to which employees experience a positive state of health, happiness, and fulfillment in the context of their work." This definition highlights the holistic nature of well-being, emphasizing both subjective and objective indicators.

2. Role of HRM Practices in Promoting Employee Well-being

HRM practices significantly influence employee well-being through their impact on work conditions, job design, and organizational culture. For instance, research by Guest (2017) emphasizes the importance of supportive leadership, work-life balance policies, and employee involvement in decision-making as key HRM practices that contribute to employee well-being. Similarly, the Job Demands-Resources (JD-R) model proposed by Bakker and Demerouti (2007) suggests that HRM practices aimed at reducing job demands and increasing job resources can enhance employee well-being.

3. Effectiveness of Specific HRM Interventions

Several studies have examined the effectiveness of specific HRM interventions in promoting employee wellbeing. For example, a meta-analysis by Nielsen et al. (2017) found that wellness programs, flexible work arrangements, and social support initiatives were associated with improvements in employee well-being outcomes such as job satisfaction and mental health. Furthermore, research by CIPD (2019) highlights the positive impact of training and development programs on employee well-being, particularly in terms of enhancing job satisfaction and reducing stress.

4. Challenges and Limitations

Despite the growing interest in employee well-being initiatives, implementing effective HRM practices can be challenging for organizations. One common challenge is the lack of organizational support and resources dedicated to well-being initiatives (LaMontagne et al., 2014). Additionally, there may be resistance from managers or employees who perceive well-being initiatives as a distraction from productivity goals (Grant, 2019). Furthermore, the effectiveness of well-being interventions may vary depending on organizational context, employee demographics, and cultural factors (Ravalier et al., 2020).

5. Future Directions

Moving forward, there is a need for further research to explore the long-term effects of HRM practices on employee well-being and organizational performance. Additionally, more attention should be given to the role of leadership and organizational climate in fostering a culture of well-being (Guest, 2017). Furthermore, research should investigate innovative approaches to promoting well-being, such as the use of technology and artificial intelligence in HRM practices (Hassan et al., 2021).

HRM practices play a crucial role in shaping employee well-being within organizations. By implementing effective interventions and addressing challenges, organizations can enhance employee well-being and ultimately improve organizational performance.

Material and Methodology

Research Design:

This review employs a systematic approach to critically analyze the effectiveness of Human Resource Management (HRM) practices in promoting employee well-being. The research design involves a comprehensive examination of existing literature on employee well-being initiatives implemented by organizations across various industries. A qualitative synthesis method is utilized to identify and analyze key themes, trends, and findings from the selected studies.

Data Collection Methods:

The data collection process involves systematic literature search using academic databases such as PubMed, Scopus, PsycINFO, and Google Scholar. Keywords including "employee well-being," "HRM practices," "workplace interventions," and "employee health" are used to retrieve relevant articles. Additionally, manual searching of relevant journals, books, and conference proceedings is conducted to ensure a comprehensive coverage of the topic.

Inclusion and Exclusion Criteria:

Inclusion Criteria:

1. Studies published in peer-reviewed journals or academic books.
2. Studies focusing on HRM practices aimed at improving employee well-being.
3. Studies conducted within the last 10 years to ensure relevance and currency.
4. Articles available in English language.

Exclusion Criteria:

1. Studies not directly related to HRM practices or employee well-being initiatives.
2. Non-peer-reviewed sources such as grey literature, opinion pieces, and editorials.
3. Studies with insufficient data or methodological flaws.
4. Articles not available in English language.

Ethical Considerations:

Ethical considerations are paramount throughout the review process. The review adheres to ethical guidelines regarding the use of published literature, ensuring proper citation and acknowledgment of sources. Confidentiality and anonymity of authors and participants are respected. No primary data collection involving human subjects is conducted, thus ethical approval is not required. The review also ensures transparency and integrity in reporting the findings, avoiding any misrepresentation or bias in interpretation.

This research design, data collection methods, inclusion and exclusion criteria, and ethical considerations collectively provide a robust framework for conducting a critical analysis of HRM practices in promoting employee well-being.

Results and Discussion

This research paper critically analyzes various Human Resource Management (HRM) practices aimed at enhancing employee well-being within organizations. Drawing upon a comprehensive review of existing literature, this study examines the effectiveness of employee well-being initiatives in improving organizational

outcomes and fostering a positive work environment. The paper evaluates the implementation of HRM practices such as flexible work arrangements, employee assistance programs, wellness programs, and work-life balance policies. Furthermore, it explores the role of organizational culture, leadership support, and employee engagement in driving the success of these initiatives. Through a critical lens, this paper provides insights into the challenges and opportunities associated with promoting employee well-being in contemporary workplaces.

Key Findings:

- 1. Impact of Flexible Work Arrangements:** The implementation of flexible work arrangements, including telecommuting, flextime, and compressed workweeks, has shown positive outcomes in enhancing employee well-being. Employees report higher job satisfaction, reduced work-related stress, and improved work-life balance when given the flexibility to manage their schedules.
- 2. Effectiveness of Employee Assistance Programs (EAPs):** Employee Assistance Programs have been found to be effective in addressing personal and work-related issues that impact employee well-being. These programs offer counseling services, mental health support, and resources for managing stress, leading to improved employee productivity and reduced absenteeism.
- 3. Wellness Programs and Health Promotion:** Organizations that invest in wellness programs aimed at promoting physical health, nutrition, and fitness among employees witness several benefits. These initiatives contribute to lower healthcare costs, decreased employee turnover, and increased morale within the workforce.
- 4. Importance of Work-Life Balance Policies:** Work-life balance policies, such as parental leave, flexible scheduling, and vacation time, play a crucial role in supporting employee well-being. Organizations that prioritize work-life balance experience higher levels of employee retention and job satisfaction, leading to greater organizational success.
- 5. Role of Organizational Culture and Leadership Support:** The organizational culture and leadership support are significant determinants of the success of employee well-being initiatives. A supportive culture that values employee well-being and emphasizes work-life balance fosters a positive work environment and enhances employee engagement.
- 6. Employee Engagement and Well-being:** There is a strong correlation between employee engagement and well-being. Engaged employees are more likely to experience higher levels of well-being, leading to increased productivity, creativity, and organizational commitment.

This research paper provides a critical analysis of HRM practices aimed at enhancing employee well-being within organizations. By examining the effectiveness of various initiatives and identifying key success factors, this study offers valuable insights for HR practitioners and organizational leaders. Embracing employee well-being as a strategic priority can lead to a more engaged, productive, and resilient workforce, ultimately contributing to organizational success in the long run.

Limitations of the study

- 1. Generalizability:** The findings of this study may not be applicable to all industries or organizational contexts. The sample size and selection criteria may limit the generalizability of the results to broader populations.
- 2. Cross-sectional Nature:** The study may be limited by its cross-sectional design, which only provides a snapshot of the relationship between HRM practices and employee well-being at a particular point in time. Longitudinal studies would be needed to assess the causal relationships over time.
- 3. Self-report Bias:** The reliance on self-reported data for measuring employee well-being and HRM practices may introduce bias, as respondents may provide socially desirable responses or may not accurately represent their experiences.
- 4. Response Rate:** There may be a low response rate to surveys or interviews, leading to potential nonresponse bias and affecting the representativeness of the sample.
- 5. Subjectivity in HRM Evaluation:** The assessment of HRM practices may involve subjective judgments, as different individuals may interpret the effectiveness of initiatives differently based on their personal experiences and perspectives.
- 6. Limited Scope of HRM Practices:** The study may not have comprehensively examined all possible HRM practices related to employee well-being, potentially overlooking other relevant factors that could influence well-being outcomes.
- 7. External Factors:** The study may not have accounted for external factors such as economic conditions, industry trends, or organizational culture, which could also impact employee well-being independently of HRM practices.
- 8. Measurement Issues:** There may be limitations in the measurement tools used to assess employee well-being and HRM practices, such as lack of standardization or reliability concerns, which could affect the validity of the results.

- 9. Publication Bias:** The study may be subject to publication bias, as it may only include published literature or studies available in certain databases, potentially overlooking relevant unpublished research or studies in other languages.
- 10. Time Constraints:** Due to time constraints or resource limitations, the study may not have been able to explore certain aspects of employee well-being initiatives or HRM practices in depth, leading to gaps in understanding.

Future Scope

As organizations continue to prioritize employee well-being, there are several avenues for future research and implementation. Here are some potential areas of exploration:

- 1. Longitudinal Studies:** Conducting longitudinal studies to assess the long-term effects of employee wellbeing initiatives on both individual employees and organizational outcomes. This would involve tracking well-being metrics over an extended period to understand the sustained impact of HRM practices.
- 2. Cross-Cultural Analysis:** Exploring how employee well-being initiatives vary across different cultural contexts and the effectiveness of HRM practices in promoting well-being in diverse workforces. This could involve comparative studies between regions or countries with varying cultural norms and organizational structures.
- 3. Technology Integration:** Investigating the role of technology in enhancing employee well-being initiatives. This includes studying the effectiveness of digital platforms, wellness apps, and remote work technologies in promoting well-being and reducing stress among employees.
- 4. Innovative Interventions:** Developing and testing innovative well-being interventions beyond traditional programs such as mindfulness training and flexible work arrangements. This could involve interventions focused on financial well-being, social support networks, or holistic wellness approaches.
- 5. Leadership and Organizational Culture:** Examining the influence of leadership styles and organizational culture on the success of employee well-being initiatives. This includes understanding how supportive leadership behaviors and a positive organizational climate contribute to employee engagement and well-being.
- 6. Measurement and Evaluation:** Developing standardized metrics and evaluation tools to assess the effectiveness of employee well-being initiatives. This involves identifying key performance indicators (KPIs) related to well-being and establishing benchmarks for measuring success.
- 7. Work-Life Integration:** Exploring strategies for better integrating work and personal life to enhance overall well-being. This could involve policies and practices that promote work-life balance, such as flexible scheduling, parental leave, and remote work options.
- 8. Employee Voice and Participation:** Investigating the role of employee voice and participation in shaping well-being initiatives. This includes studying the impact of participatory approaches, such as employee feedback mechanisms and employee involvement in decision-making, on the design and implementation of HRM practices.
- 9. Well-being in Gig Economy:** Examining the unique challenges and opportunities for promoting wellbeing among gig workers and contingent employees. This involves understanding the specific needs of this workforce segment and developing tailored well-being strategies.
- 10. Policy Implications:** Assessing the policy implications of employee well-being initiatives and advocating for supportive regulatory frameworks. This includes exploring the role of government policies in promoting well-being at the workplace and addressing socio-economic determinants of employee wellbeing.

By exploring these avenues, future research can contribute to the ongoing discourse on employee well-being and inform the development of evidence-based HRM practices that foster healthier, more productive workplaces.

Conclusion

This review research paper has critically examined the landscape of employee well-being initiatives through the lens of HRM practices. By synthesizing existing literature, it has shed light on the multifaceted nature of employee well-being and the various HRM strategies employed to enhance it. Through this analysis, several key insights have emerged.

Firstly, it is evident that employee well-being is not a one-size-fits-all concept; rather, it encompasses physical, mental, and social dimensions that are influenced by organizational, managerial, and individual factors. HRM practices play a pivotal role in shaping these dimensions by fostering a supportive work environment, promoting work-life balance, and providing resources for personal and professional development.

Secondly, the effectiveness of employee well-being initiatives hinges on their alignment with organizational goals, culture, and values. Initiatives that are integrated into the fabric of the organization and championed by leadership are more likely to yield positive outcomes for both employees and the organization as a whole. Furthermore, this review highlights the need for continuous evaluation and adaptation of employee well-being initiatives in response to evolving workforce dynamics and external pressures. HRM professionals must remain vigilant in monitoring the effectiveness of these initiatives and making adjustments as needed to ensure they remain relevant and impactful.

Overall, this review underscores the importance of prioritizing employee well-being within organizations and leveraging HRM practices as a strategic tool for fostering a culture of health, happiness, and productivity. By investing in the well-being of their employees, organizations can cultivate a competitive advantage in today's dynamic business landscape while simultaneously fulfilling their ethical and social responsibilities.

References

1. Adams, S. (2019). Employee well-being initiatives: A review of current trends and future directions. *Journal of Applied Psychology*, 104(5), 632-647.
2. Allen, T. D., & Kiburz, K. M. (2012). Trait mindfulness and work-family balance among working parents: The mediating effects of vitality and sleep quality. *Journal of Vocational Behavior*, 80(2), 372-379.
3. Bakker, A. B., & Demerouti, E. (2007). The job demands-resources model: State of the art. *Journal of Managerial Psychology*, 22(3), 309-328.
4. Bakker, A. B., & Demerouti, E. (2017). Job demands-resources theory: Taking stock and looking forward. *Journal of Occupational Health Psychology*, 22(3), 273-285.
5. Burton, W. N., Chen, C. Y., Li, X., & Schultz, A. B. (2017). The association of employee engagement at work with health risks and presenteeism. *Journal of Occupational and Environmental Medicine*, 59(10), 988-992.
6. Cameron, K. S., Dutton, J. E., & Quinn, R. E. (Eds.). (2003). *Positive organizational scholarship: Foundations of a new discipline*. Berrett-Koehler Publishers.
7. CIPD. (2019). Health and well-being at work. Retrieved from https://www.cipd.co.uk/Images/healthand-well-being-at-work_2019_tcm18-55427.pdf
8. Deci, E. L., & Ryan, R. M. (2008). Self-determination theory: A macrotheory of human motivation, development, and health. *Canadian Psychology/Psychologie Canadienne*, 49(3), 182.
9. Grant, A. M. (2019). The positive organization: Leadership challenges in creating and maintaining a positive organizational climate. In *The Wiley Blackwell Handbook of the Psychology of Positivity and Strengths-Based Approaches at Work* (pp. 239-258). John Wiley & Sons, Ltd.
10. Grawitch, M. J., Gottschalk, M., & Munz, D. C. (2006). The path to a healthy workplace: A critical review linking healthy workplace practices, employee well-being, and organizational improvements. *Consulting Psychology Journal: Practice and Research*, 58(3), 129-147.
11. Guest, D. (2017). Human resource management and employee well-being: Towards a new analytic framework. *Human Resource Management Journal*, 27(1), 22-38.
12. Guest, D. E. (2017). Human resource management and employee well-being: Towards a new analytic framework. *Human Resource Management Journal*, 27(1), 22-38.
13. Hackman, J. R., & Oldham, G. R. (1976). Motivation through the design of work: Test of a theory. *Organizational Behavior and Human Performance*, 16(2), 250-279.
14. Hassan, R., Latif, K., Hussain, Z., Naz, F., & Abbas, Q. (2021). A Review on Artificial Intelligence-Based Techniques for Human Resource Management. *IEEE Access*, 9, 12852-12869.
15. Judge, T. A., Bono, J. E., Erez, A., & Locke, E. A. (2005). Core self-evaluations and job and life satisfaction: The role of self-concordance and goal attainment. *Journal of Applied Psychology*, 90(2), 257-268.
16. Kahn, W. A. (1990). Psychological conditions of personal engagement and disengagement at work. *Academy of Management Journal*, 33(4), 692-724.
17. Kelloway, E. K., Day, A. L., & Building, A. W. C. W. (2005). Building healthy workplaces: What we know so far. *Canadian Journal of Behavioural Science/Revue Canadienne Des Sciences Du Comportement*, 37(4), 223.
18. LaMontagne, A. D., Martin, A., Page, K. M., Reavley, N. J., Noblet, A. J., Milner, A. J., & Keegel, T. (2014). Workplace mental health: Developing an integrated intervention approach. *BMC Psychiatry*, 14(1), 1-13.
19. Maslach, C., & Leiter, M. P. (2016). Understanding the burnout experience: recent research and its implications for psychiatry. *World Psychiatry*, 15(2), 103-111.
20. Nielsen, K., & Taris, T. W. (2019). Leading well: Challenges to researching leadership in occupational health psychology and how to address them. *Work & Stress*, 33(2), 107-124.
21. Nielsen, K., Randall, R., Holten, A. L., & González, E. R. (2010). Conducting organizational-level occupational health interventions: What works? *Work & Stress*, 24(3), 234-259.

-
22. Podsakoff, P. M., MacKenzie, S. B., & Podsakoff, N. P. (2012). Sources of method bias in social science research and recommendations on how to control it. *Annual Review of Psychology*, 63, 539-569.
 23. Ravalier, J. M., Wegrzynek, P., Lawton, S., & Paxton, R. (2020). A meta-analysis of work-based well-being interventions for NHS employees. *Occupational Medicine*, 70(7), 451-458.
 24. Ryan, R. M., & Deci, E. L. (2000). Self-determination theory and the facilitation of intrinsic motivation, social development, and well-being. *American Psychologist*, 55(1), 68.
 25. Saks, A. M. (2006). Antecedents and consequences of employee engagement. *Journal of Managerial Psychology*, 21(7), 600-619.
 26. Seligman, M. E. (2018). PERMA and the building blocks of well-being. *The Journal of Positive Psychology*, 13(4), 333-335.
 27. Shirom, A., Melamed, S., Toker, S., Berliner, S., & Shapira, I. (2005). Burnout and health review: current knowledge and future research directions. *International Handbook of Work and Health Psychology*, 2, 245-268.
 28. Sonnentag, S., & Grant, A. M. (2012). Doing good at work feels good at home, but not right away: When and why perceived prosocial impact predicts positive affect. *Personnel Psychology*, 65(3), 495-530.
 29. Wright, T. A., & Cropanzano, R. (2000). Psychological well-being and job satisfaction as predictors of job performance. *Journal of Occupational Health Psychology*, 5(1), 84-94.



Fintech And Sustainable Finance: A Review Of Environmental, Social, And Governance (Esg) Integration

Varsha.V. R^{1*}, Dr. Anil Trimbak Gholap², Dr. Santhosh C.H³, Prof. Bagali Ambreen⁴, Dr. S. Tulasi Ram⁵

^{1*}Assistant Professor Department of Management Studies Nehru Institute of Technology, Jawahar Gardens, Kaliyauram, Coimbatore, Tamilnadu, Pin: 641105

²Head & Assistant Professor, Department of Economics, Chhatrapati Shivaji Night College of Arts & Commerce, Solapur, Pin. 413001, Maharashtra, India

³Faculty Member, Department of Studies and Research in Commerce, Kuvempu University, Shankarghatta, Shimoga, Pin: 577451

⁴Assistant Professor, Department of Management Studies, Ballari Institute of Technology and Management, Ballari, Karnataka, Pin: 583104

⁵Assistant Professor, School of Management Studies, Chaitanya Bharathi Institute of Technology, Hyderabad, India, Pin: 500075

Citation: Varsha.V. R et.al (2024), Fintech And Sustainable Finance: A Review Of Environmental, Social, And Governance (Esg) Integration, *Educational Administration: Theory and Practice*, 30(5), 6816 - 6824

Doi: 10.53555/kuey.v30i5.4019

ARTICLE INFO

ABSTRACT

The convergence of financial technology (Fintech) and sustainable finance represents a promising frontier in the global pursuit of environmentally sound, socially responsible, and ethically governed investment practices. This review paper synthesizes the current landscape of Fintech applications within the realm of sustainable finance, with a particular focus on the integration of Environmental, Social, and Governance (ESG) criteria. Drawing upon a comprehensive analysis of scholarly articles, industry reports, and regulatory frameworks, this paper provides insights into the emerging trends, challenges, and opportunities in this rapidly evolving domain.

The paper highlights the growing importance of ESG considerations in investment decision-making processes, driven by increasing awareness of sustainability issues among investors, regulatory initiatives, and corporate commitments to responsible business practices. Fintech innovations have played a pivotal role in facilitating the integration of ESG factors into investment strategies, offering advanced analytics, data visualization tools, and digital platforms for sustainable investment screening, portfolio management, and impact measurement.

Furthermore, the paper examines the role of blockchain technology, artificial intelligence, and big data analytics in enhancing the transparency, traceability, and efficiency of ESG-related financial transactions. It also discusses the emergence of novel financial instruments, such as green bonds, social impact bonds, and sustainability-linked loans, enabled by Fintech solutions, to channel capital towards sustainable projects and initiatives.

However, the paper also identifies several challenges and areas for future research, including data quality and standardization issues, regulatory harmonization, cybersecurity risks, and ethical considerations surrounding algorithmic decision-making in sustainable finance. Addressing these challenges will be crucial for realizing the full potential of Fintech-enabled sustainable finance in driving positive environmental and social outcomes while ensuring financial stability and inclusivity.

This paper provides a comprehensive overview of the intersection between Fintech and sustainable finance, shedding light on the transformative potential of technology in advancing the goals of environmental protection, social equity, and good governance in the global financial system.

Keywords: Fintech, Sustainable finance, (ESG), , Integration, Investment decision-making, Analytics, Data visualization, Blockchain, Artificial intelligence, Big data, Transparency, Traceability, Financial instruments, Green bonds, Social impact bonds, Sustainability-linked loans, Data quality, Regulatory harmonization, Cybersecurity.

Introduction

In recent years, the intersection of financial technology (Fintech) and sustainable finance has garnered significant attention from scholars, policymakers, and practitioners alike. The integration of Environmental, Social, and Governance (ESG) criteria into financial decision-making processes has emerged as a pivotal strategy for promoting sustainable development while ensuring long-term financial stability. This research paper delves into the intricate relationship between Fintech and sustainable finance, with a specific focus on how ESG considerations are being incorporated into various aspects of the financial industry.

The advent of Fintech has revolutionized traditional financial services, offering innovative solutions that enhance efficiency, accessibility, and transparency. Concurrently, there has been a growing recognition of the imperative to address pressing global challenges such as climate change, social inequality, and corporate governance issues. Against this backdrop, the integration of ESG factors into investment strategies, risk assessment, and product development has gained momentum, driven by a confluence of regulatory mandates, investor demand, and ethical imperatives.

This paper aims to provide a comprehensive overview of the evolving landscape of Fintech and sustainable finance, with a particular emphasis on the integration of ESG considerations. Through a systematic analysis of existing literature, key themes, trends, and challenges surrounding this nexus will be explored. Additionally, the paper will critically assess the impact of Fintech innovations on the advancement of sustainable finance objectives, evaluating both opportunities and potential pitfalls.

By synthesizing insights from diverse scholarly perspectives and empirical studies, this review seeks to contribute to a nuanced understanding of how Fintech can be leveraged to promote ESG integration within the financial sector. Ultimately, it endeavors to provide valuable insights for policymakers, financial institutions, investors, and other stakeholders seeking to navigate the complex terrain of sustainable finance in the digital age.

Background of the study

In recent years, the intersection of financial technology (fintech) and sustainable finance has garnered considerable attention from both scholars and practitioners. Fintech, characterized by innovative digital solutions in the financial sector, has increasingly become intertwined with the principles of sustainability, particularly Environmental, Social, and Governance (ESG) considerations. This integration has profound implications for the global financial landscape, as it seeks to align financial activities with broader societal and environmental goals while enhancing financial inclusion, transparency, and efficiency.

The rise of fintech has revolutionized traditional financial services, introducing disruptive technologies such as blockchain, artificial intelligence, and big data analytics. These innovations have not only streamlined processes but also presented novel opportunities for embedding ESG criteria into investment decisions, risk management practices, and product offerings. As sustainability concerns grow in prominence, investors, regulators, and consumers are placing greater emphasis on companies' ESG performance, viewing it as a critical indicator of long-term value creation and risk mitigation.

Against this backdrop, understanding the evolving relationship between fintech and sustainable finance is imperative for policymakers, investors, and financial institutions alike. This review paper aims to provide a comprehensive overview of the current landscape, synthesizing existing literature, and identifying key trends, challenges, and opportunities in ESG integration within fintech-driven financial ecosystems.

Key themes to be explored include:

- 1. Technological Innovations in Sustainable Finance:** This section will examine how fintech solutions, such as robo-advisors, peer-to-peer lending platforms, and impact investing apps, are facilitating the integration of ESG considerations into investment processes and asset allocation strategies.
- 2. Data Analytics and ESG Performance Measurement:** Here, we will delve into the role of big data analytics, machine learning, and natural language processing in enhancing ESG data quality, disclosure, and performance assessment. We will discuss the challenges associated with data standardization, materiality assessment, and the emergence of alternative data sources for ESG analysis.
- 3. Regulatory Landscape and Fintech Adoption:** This segment will explore the regulatory frameworks governing sustainable finance and fintech, highlighting initiatives such as the EU Sustainable Finance Action Plan and the Fintech Regulatory Sandbox. We will assess how regulatory developments influence fintech adoption, market dynamics, and the scalability of sustainable finance solutions.
- 4. Fintech for Social Impact:** Focusing on the social dimension of ESG, this part will evaluate the role of fintech in promoting financial inclusion, microfinance, and community development. We will showcase case studies of fintech initiatives targeting underserved populations and enhancing access to affordable credit, insurance, and savings products.
- 5. Challenges and Future Directions:** Finally, we will identify key challenges and areas for future research, including data privacy concerns, algorithmic biases, greenwashing risks, and the need for interdisciplinary collaboration between finance, technology, and sustainability experts.

By synthesizing empirical evidence, theoretical frameworks, and industry insights, this review paper seeks to advance our understanding of how fintech is reshaping sustainable finance practices and driving the transition towards a more inclusive, resilient, and environmentally conscious financial system.

Justification

In recent years, the intersection of financial technology (Fintech) and sustainable finance has garnered increasing attention from scholars, policymakers, and practitioners alike. With the growing recognition of environmental, social, and governance (ESG) factors in investment decision-making, Fintech has emerged as a pivotal enabler of sustainable finance practices. This review research paper seeks to provide a comprehensive analysis of the integration of ESG considerations within Fintech platforms and its implications for sustainable finance.

Rationale for the Study:

- 1. Addressing Knowledge Gap:** Despite the burgeoning interest in both Fintech and sustainable finance, there remains a significant gap in the understanding of how these domains intersect. While individual studies have explored aspects of Fintech or sustainable finance separately, there is a dearth of comprehensive reviews that systematically examine the integration of ESG criteria within Fintech solutions. This paper aims to bridge this gap by synthesizing existing literature and providing insights into the current state of ESG integration in Fintech.
- 2. Importance of Sustainable Finance:** Sustainable finance has gained prominence as investors increasingly recognize the importance of incorporating ESG factors into their decision-making processes. This paradigm shift underscores the need to explore how technological innovations, particularly those within the Fintech landscape, can facilitate the integration of sustainability considerations into financial markets. By examining the role of Fintech in advancing sustainable finance objectives, this study contributes to a deeper understanding of the mechanisms driving responsible investment practices.
- 3. Implications for Stakeholders:** The integration of ESG criteria into Fintech platforms holds implications for various stakeholders, including investors, financial institutions, regulators, and society at large. Understanding the opportunities and challenges associated with this integration is crucial for informing policy decisions, guiding investment strategies, and fostering innovation within the Fintech ecosystem. Through its comprehensive review, this paper aims to elucidate these implications and offer insights into how stakeholders can navigate the evolving landscape of sustainable finance enabled by Fintech.
- 4. Policy and Regulatory Considerations:** As Fintech continues to reshape the financial services industry, policymakers and regulators face the challenge of ensuring that innovation aligns with sustainability objectives and regulatory frameworks. This study provides valuable insights into the regulatory landscape surrounding ESG integration in Fintech, thereby informing discussions on policy interventions aimed at promoting responsible innovation and fostering a more sustainable financial system.

The research paper titled "Fintech and Sustainable Finance: A Review of Environmental, Social, and Governance (ESG) Integration" addresses a critical gap in the existing literature by offering a comprehensive analysis of the intersection between Fintech and sustainable finance. By examining the integration of ESG considerations within Fintech platforms, the study aims to shed light on the opportunities, challenges, and implications for stakeholders across the financial ecosystem. Through its synthesis of existing research and exploration of policy implications, the paper seeks to advance knowledge in this burgeoning field and contribute to informed decision-making in both academia and practice.

Objectives of the Study

1. To provide a comprehensive overview of the current state of fintech applications in the realm of sustainable finance, particularly focusing on the integration of Environmental, Social, and Governance (ESG) factors.
2. To evaluate the impact of fintech innovations on the integration of ESG principles within financial services, including their potential to enhance sustainability practices and promote responsible investing.
3. To identify and analyze leading fintech companies, platforms, and initiatives that are actively involved in advancing sustainable finance through ESG integration, highlighting their strategies, successes, and challenges.
4. To assess the existing regulatory frameworks governing fintech and sustainable finance, exploring how regulatory policies influence the adoption and effectiveness of ESG integration practices within the financial sector.
5. To explore the technological innovations driving ESG integration within fintech solutions, such as artificial intelligence, blockchain, and data analytics, and their role in enhancing transparency, accountability, and decision-making processes.

Literature Review

The intersection of financial technology (Fintech) and sustainable finance has garnered significant attention in recent years, particularly in the context of Environmental, Social, and Governance (ESG) integration. With the growing emphasis on corporate social responsibility and sustainable investing, Fintech solutions are increasingly being leveraged to facilitate the incorporation of ESG factors into investment decision-making processes. This literature review aims to provide a comprehensive overview of existing research on the

integration of ESG considerations within Fintech applications, exploring the implications for sustainable finance.

ESG Integration in Fintech Platforms

Fintech platforms have emerged as powerful tools for enhancing access to financial services while also enabling more efficient and transparent investment processes. Within this landscape, there is a growing recognition of the importance of integrating ESG criteria into Fintech solutions to support sustainable investment practices. According to Smith et al. (2020), Fintech innovations such as robo-advisors and digital investment platforms are increasingly incorporating ESG data and analytics to provide investors with ESG-aligned investment options. These platforms leverage technologies such as artificial intelligence and machine learning to analyze vast amounts of ESG-related information and tailor investment recommendations to individual preferences and sustainability goals.

Moreover, research by Lee and Shin (2019) highlights the role of blockchain technology in enhancing the transparency and traceability of ESG data within financial markets. By leveraging blockchain-based systems, Fintech firms can create immutable records of ESG-related information, enabling investors to verify the authenticity and accuracy of sustainability disclosures. This transparency not only fosters trust among investors but also encourages companies to improve their ESG performance to attract investment capital.

Challenges and Opportunities

Despite the potential benefits of integrating ESG considerations into Fintech platforms, several challenges persist. One such challenge is the lack of standardized ESG metrics and reporting frameworks, which can hinder the comparability and reliability of ESG data (Grewal et al., 2021). Additionally, concerns regarding data privacy and security pose significant obstacles to the widespread adoption of Fintech solutions for ESG integration (Feng et al., 2020). Addressing these challenges requires collaboration among regulators, industry stakeholders, and technology developers to establish common standards for ESG disclosure and data management.

However, alongside these challenges, there are also opportunities for innovation and collaboration. For instance, research by Zhang et al. (2022) suggests that advances in natural language processing (NLP) and sentiment analysis can enhance the qualitative assessment of ESG factors, providing investors with deeper insights into companies' sustainability practices. Furthermore, partnerships between Fintech startups and traditional financial institutions can facilitate the integration of ESG considerations into mainstream investment products, thereby expanding the reach of sustainable finance initiatives (Chen et al., 2021).

Fintech Evolution and Sustainable Finance Integration

The evolution of Fintech has revolutionized traditional financial services, offering innovative solutions that cater to various consumer needs and investment preferences. As Fintech continues to disrupt the financial landscape, there is a growing recognition of its potential to promote sustainable finance objectives. According to Huang et al. (2020), Fintech innovations such as peer-to-peer lending platforms and crowdfunding sites have democratized access to capital, enabling individuals and businesses to support environmentally and socially responsible initiatives. Furthermore, the emergence of impact investing platforms, which channel capital towards projects with positive social and environmental outcomes, underscores the synergies between Fintech and sustainable finance (Ahmed et al., 2019).

ESG Data Analytics and Decision-Making

A key aspect of integrating ESG considerations into Fintech platforms is the utilization of advanced data analytics techniques to assess companies' ESG performance and risks. Research by Li et al. (2021) demonstrates the effectiveness of machine learning algorithms in identifying relevant ESG factors and their impact on financial performance. By analyzing vast datasets encompassing environmental disclosures, social impact metrics, and corporate governance practices, Fintech algorithms can generate actionable insights for investors seeking to align their portfolios with ESG principles. Moreover, the integration of alternative data sources, such as satellite imagery and social media sentiment analysis, can provide a more comprehensive understanding of companies' sustainability profiles (He et al., 2022).

Regulatory Frameworks and Compliance

The regulatory landscape plays a crucial role in shaping the integration of ESG considerations into Fintech solutions. In recent years, regulators worldwide have introduced initiatives to promote sustainable finance and enhance ESG disclosure requirements. For example, the European Union's Sustainable Finance Disclosure Regulation (SFDR) mandates financial institutions to disclose ESG-related information to investors, fostering greater transparency and accountability in the financial sector (Humphrey et al., 2021). Similarly, the Task Force on Climate-related Financial Disclosures (TCFD) has developed guidelines for companies to report climate-related risks and opportunities, influencing the adoption of ESG reporting standards globally (Liao et al., 2023). Fintech firms must navigate these regulatory frameworks to ensure compliance while innovating sustainable finance solutions that meet evolving market demands.

Stakeholder Engagement and Impact Measurement

Effective stakeholder engagement is essential for the success of Fintech-driven sustainable finance initiatives. By collaborating with stakeholders such as investors, NGOs, and regulatory bodies, Fintech firms can gain valuable insights into ESG priorities and develop tailored solutions that address stakeholders' needs (Huang & Rust, 2021). Furthermore, the measurement and reporting of impact outcomes are critical for demonstrating the effectiveness of sustainable finance interventions. Research by Sengupta et al. (2020) highlights the importance of developing standardized impact metrics and methodologies to assess the social, environmental, and economic outcomes of ESG investments. Fintech platforms can leverage technologies such as distributed ledger technology (DLT) to create transparent and auditable impact measurement systems, enhancing trust and accountability in sustainable finance initiatives (Adeleye et al., 2022).

The integration of ESG considerations within Fintech platforms represents a promising avenue for advancing sustainable finance objectives. By harnessing the power of technology, Fintech firms can enhance the accessibility, transparency, and effectiveness of sustainable investment strategies. However, addressing key challenges such as data standardization and privacy will be crucial to realizing the full potential of Fintech-enabled sustainable finance. Moving forward, interdisciplinary collaboration and ongoing research efforts will play a vital role in shaping the future of ESG integration in the Fintech landscape.

Material and Methodology

This paper explores the intersection of financial technology (fintech) and sustainable finance, with a particular focus on the integration of Environmental, Social, and Governance (ESG) factors. The research design involves a systematic review of existing literature to identify trends, challenges, and opportunities in the field. Data collection methods include comprehensive searches of academic databases, industry reports, and relevant websites. Inclusion and exclusion criteria are established to ensure the selection of high-quality and relevant studies. Ethical considerations guide the conduct of this research, including the proper citation of sources and the avoidance of plagiarism.

Research Design: The research design employs a systematic review approach to synthesize existing literature on the integration of ESG factors in fintech and sustainable finance. Systematic reviews provide a rigorous and transparent methodology for identifying, evaluating, and synthesizing relevant studies, thereby minimizing bias and ensuring the reliability of findings. This approach allows for a comprehensive analysis of the current state of knowledge in the field and enables the identification of gaps for future research.

Data Collection Methods: Data collection methods involve thorough searches of academic databases such as PubMed, Scopus, Web of Science, and Google Scholar, using keywords related to fintech, sustainable finance, and ESG integration. Additionally, industry reports, policy documents, and reputable websites of organizations specializing in sustainable finance are consulted to gather relevant information and insights. The inclusion of diverse sources ensures a comprehensive understanding of the topic and enhances the validity of the review findings.

Inclusion and Exclusion Criteria: Inclusion criteria are defined to select studies that meet specific criteria relevant to the research objectives. Included studies typically focus on the integration of ESG factors in fintech solutions, sustainable investment strategies, or regulatory frameworks. Peer-reviewed articles, conference papers, and reports published in reputable journals and by recognized organizations are considered for inclusion. Exclusion criteria are applied to exclude studies that do not meet the predefined criteria or are of low quality, such as opinion pieces, non-peer-reviewed publications, and outdated sources.

Ethical Considerations: Ethical considerations are paramount in conducting this review research. Proper citation and referencing of sources are essential to acknowledge the contributions of other researchers and to avoid plagiarism. Care is taken to attribute ideas, data, and quotations to their original authors accurately. Additionally, efforts are made to ensure the impartiality and objectivity of the review process, avoiding conflicts of interest and bias in the selection and interpretation of literature. Transparency in reporting methods and findings enhances the credibility and integrity of the research.

Results and Discussion

The review paper on "Fintech and Sustainable Finance: A Review of Environmental, Social, and Governance (ESG) Integration" delves into the intersection of financial technology (Fintech) and sustainable finance, particularly focusing on the integration of Environmental, Social, and Governance (ESG) factors. Through a meticulous examination of existing literature and empirical evidence, several key findings emerge:

- 1. Growing Significance of ESG Integration:** The study underscores the increasing acknowledgment of ESG factors in investment decision-making processes. As global awareness of sustainability issues heightens, investors are recognizing the materiality of ESG considerations in assessing risk and return profiles of investments.

- 2. Role of Fintech in ESG Integration:** Fintech innovations are identified as pivotal enablers in facilitating the integration of ESG factors into financial markets. Through advanced data analytics, machine learning algorithms, and blockchain technology, Fintech solutions offer efficient mechanisms for assessing, monitoring, and reporting on ESG performance metrics.
- 3. Enhanced Transparency and Disclosure:** The paper highlights the role of Fintech platforms in enhancing transparency and disclosure practices within the realm of sustainable finance. By leveraging digital platforms, companies can provide stakeholders with real-time access to ESG-related information, fostering greater accountability and trust.
- 4. Risk Mitigation and Value Creation:** Empirical evidence suggests that robust ESG integration, facilitated by Fintech tools, can contribute to risk mitigation and value creation for investors. Companies with strong ESG performance are shown to exhibit greater resilience to environmental and social shocks while outperforming their peers in terms of long-term financial performance.
- 5. Challenges and Opportunities:** Despite the promising prospects, the study acknowledges the challenges associated with Fintech-driven ESG integration, including data quality issues, regulatory complexities, and the need for standardized frameworks. However, these challenges also present opportunities for innovation and collaboration among stakeholders to develop scalable solutions.
- 6. Implications for Policy and Practice:** The findings underscore the importance of regulatory frameworks that promote responsible innovation in Fintech and encourage the adoption of ESG best practices across financial markets. Moreover, the study emphasizes the need for industry-wide collaboration to develop interoperable Fintech solutions that enhance ESG integration while safeguarding data privacy and security.

The review paper illuminates the transformative potential of Fintech in advancing the integration of ESG considerations within sustainable finance. By harnessing technological innovation and fostering collaboration, financial institutions, policymakers, and other stakeholders can collectively drive positive environmental, social, and governance outcomes while delivering sustainable value for all stakeholders.

Limitations of the study

The study titled "Fintech and Sustainable Finance: A Review of Environmental, Social, and Governance (ESG) Integration" delves into the intersection of financial technology and sustainable finance, particularly focusing on how fintech innovations facilitate the integration of ESG factors into financial practices. The key findings from the review are summarized as follows:

- 1. Enhanced ESG Data Collection and Analysis:** Fintech innovations, particularly big data analytics and artificial intelligence (AI), have significantly improved the collection, analysis, and dissemination of ESG data. These technologies enable more accurate and real-time assessments of ESG metrics, allowing investors and companies to make more informed decisions regarding sustainability.
- 2. Increased Transparency and Reporting:** Blockchain technology, with its decentralized and immutable nature, enhances transparency in ESG reporting. It ensures that data related to environmental impacts, social responsibilities, and governance practices are traceable and verifiable, thereby reducing the risk of greenwashing and improving stakeholder trust.
- 3. Improved Access to Sustainable Investments:** Digital platforms and robo-advisors have democratized access to sustainable investment opportunities. By lowering entry barriers and providing personalized investment advice, these fintech solutions enable a broader range of investors, including retail investors, to participate in ESG-focused investment funds and products.
- 4. Efficient Risk Management:** Advanced analytics and machine learning algorithms are employed to better assess and manage risks associated with ESG factors. These tools help in identifying potential risks and opportunities related to environmental changes, social dynamics, and governance structures, thereby aiding in more resilient portfolio management.
- 5. Promotion of Green Finance:** Fintech solutions such as peer-to-peer lending and crowdfunding are increasingly being used to finance green projects. These platforms facilitate the flow of capital to environmentally friendly projects by connecting investors directly with green enterprises and initiatives, often with greater efficiency and lower costs compared to traditional financing methods.
- 6. Support for Regulatory Compliance:** Regtech, a subset of fintech focused on regulatory compliance, provides tools and solutions that help financial institutions adhere to ESG-related regulations and standards. These technologies streamline compliance processes, reduce costs, and ensure that institutions remain updated with the evolving regulatory landscape.
- 7. Facilitation of Socially Responsible Investing:** Fintech innovations are aiding in the growth of socially responsible investing (SRI) by offering platforms that screen investments based on social criteria. These platforms allow investors to align their portfolios with their personal values and societal concerns, thereby fostering greater engagement in socially responsible financial practices.
- 8. Challenges and Limitations:** Despite the numerous benefits, the integration of fintech and ESG faces challenges such as data privacy concerns, the need for standardization in ESG metrics, and the risk of technological disruptions. Additionally, there is a need for continuous innovation and adaptation to ensure that fintech solutions can effectively address the dynamic and complex nature of ESG factors.

The study highlights that fintech is playing a pivotal role in advancing sustainable finance by integrating ESG considerations into financial practices. Through enhanced data capabilities, increased transparency, and greater access to sustainable investments, fintech is fostering a more inclusive and responsible financial ecosystem. However, addressing the associated challenges will be crucial for maximizing the potential of fintech in promoting sustainability.

Future Scope

The integration of Fintech and Sustainable Finance, particularly in the context of Environmental, Social, and Governance (ESG) criteria, presents numerous avenues for future research and development. As the financial industry continues to evolve, the following areas are identified as critical for further exploration:

1. **Advanced Data Analytics for ESG Metrics:** Future research could focus on the development and application of advanced data analytics and artificial intelligence (AI) techniques to enhance the accuracy and reliability of ESG metrics. This includes exploring how machine learning algorithms can better predict ESG performance and risks, thereby aiding investors in making more informed decisions.
2. **Blockchain and ESG Transparency:** The potential of blockchain technology to improve transparency and traceability in ESG reporting is a promising area for future studies. Research can investigate how blockchain can be used to create immutable records of ESG data, ensuring that the information is accurate and tamper-proof, which is crucial for building trust among stakeholders.
3. **Impact of Digital Financial Inclusion:** Examining the role of Fintech in promoting digital financial inclusion and its subsequent impact on social and environmental outcomes is another important research direction. Studies could assess how access to digital financial services can empower marginalized communities, reduce poverty, and promote sustainable economic growth.
4. **Regulatory Frameworks and Standards:** There is a need for comprehensive research into the development of regulatory frameworks and standards that govern the integration of Fintech with sustainable finance. This includes understanding the regulatory challenges and opportunities, as well as proposing frameworks that ensure consumer protection, data privacy, and ethical AI use.
5. **Green Fintech Innovations:** Investigating new Fintech innovations specifically designed to support environmental sustainability, such as green bonds, carbon trading platforms, and climate risk assessment tools, is crucial. Future research can evaluate the effectiveness of these innovations in mitigating climate change and promoting environmental stewardship.
6. **Social Impact Measurement:** Developing robust methodologies for measuring the social impact of Fintech applications in sustainable finance is essential. Future studies should focus on creating standardized metrics that can quantitatively assess the social benefits, such as improvements in quality of life, education, and health outcomes resulting from Fintech interventions.
7. **Interdisciplinary Approaches:** Encouraging interdisciplinary research that combines insights from finance, technology, environmental science, and social sciences can provide a more holistic understanding of the complex interactions between Fintech and sustainable finance. This approach can lead to the development of integrated solutions that address multiple facets of sustainability.
8. **Consumer Behavior and Adoption:** Understanding consumer behavior and the factors that influence the adoption of Fintech solutions in the context of sustainable finance is critical. Future research can explore behavioral economics principles to identify incentives and barriers, thus helping to design more user-friendly and widely accepted Fintech products.
9. **Global and Regional Perspectives:** Comparative studies examining how different regions and countries are integrating Fintech with sustainable finance can provide valuable insights. This research can highlight best practices, regional challenges, and the effectiveness of various strategies in achieving ESG goals across different socio-economic contexts.
10. **Longitudinal Impact Studies:** Conducting longitudinal studies to assess the long-term impacts of Fintech innovations on ESG outcomes is vital. These studies can help in understanding the sustainability and scalability of Fintech solutions, providing evidence-based insights into their effectiveness over time.

By addressing these areas, future research can significantly contribute to the advancement of Fintech and sustainable finance, ensuring that technological innovations are effectively aligned with ESG objectives to foster a more sustainable and inclusive financial ecosystem.

Conclusion

The integration of Fintech and Sustainable Finance, particularly through the lens of Environmental, Social, and Governance (ESG) criteria, represents a transformative development in the financial industry. This review highlights the synergistic potential of Fintech innovations and ESG principles in driving sustainable economic growth, enhancing transparency, and fostering responsible investment practices.

Fintech's advanced technological solutions, such as blockchain, artificial intelligence, and big data analytics, offer significant capabilities for improving ESG data accuracy, enabling better risk management, and facilitating more informed decision-making. These technologies are instrumental in addressing the traditional

challenges associated with ESG integration, such as data inconsistency, lack of transparency, and difficulties in measuring impact.

Moreover, the collaborative efforts between Fintech firms and traditional financial institutions are crucial for mainstreaming ESG criteria across the financial sector. Such partnerships can accelerate the development and adoption of innovative financial products and services that align with sustainable development goals (SDGs). For instance, green bonds, ESG-focused investment platforms, and sustainability-linked loans are some of the promising outcomes of this integration.

However, the successful fusion of Fintech and ESG also hinges on robust regulatory frameworks, standardization of ESG metrics, and continuous stakeholder engagement. Policymakers and regulators must work together to create conducive environments that support innovation while ensuring investor protection and market integrity. Additionally, continuous education and awareness initiatives are essential to foster a culture of sustainability within the financial industry and among consumers.

The convergence of Fintech and Sustainable Finance through ESG integration is poised to redefine the financial landscape. By harnessing the power of technology and adhering to sustainable principles, the financial sector can contribute significantly to a more sustainable and equitable global economy. Future research should focus on exploring emerging trends, addressing implementation challenges, and evaluating the long-term impacts of this integration to fully realize its potential.

References

1. Allen, F., Gu, X., & Jagtiani, J. (2021). The interplay between fintech and financial stability. *Journal of Financial Stability*, 53, 100836. <https://doi.org/10.1016/j.jfs.2020.100836>
2. Arner, D. W., Barberis, J. N., & Buckley, R. P. (2017). FinTech, RegTech, and the Reconceptualization of Financial Regulation. *Northwestern Journal of International Law & Business*, 37(3), 371-413.
3. Asutay, M., & Harningtyas, A. F. (2015). Developing Maqāsid al-Sharī'ah index to evaluate social performance of Islamic banks: A conceptual and empirical attempt. *International Journal of Islamic and Middle Eastern Finance and Management*, 8(4), 455-477. <https://doi.org/10.1108/IMEFM-08-2014-0077>
4. Baker, H. K., Kumar, S., & Pattnaik, D. (2021). Institutional investors, corporate social responsibility, and stock price performance. *Journal of Business Research*, 126, 468-485. <https://doi.org/10.1016/j.jbusres.2020.12.040>
5. Broeders, D., & Prenio, J. (2018). Innovative technology in financial supervision (supotech) – The experience of early users. *FSI Insights on policy implementation*, 9. Retrieved from <https://www.bis.org/fsi/publ/insights9.pdf>
6. Chen, X., & Dong, H. (2021). Fintech and the innovation ecosystem in China: Implications for the regulation and the challenges. *China Economic Journal*, 14(2), 184-201. <https://doi.org/10.1080/17538963.2021.1920198>
7. Chen, Y., Wang, C., & Zhang, H. (2021). Integrating environmental, social, and governance (ESG) criteria into financial decision-making: A systematic review of fintech initiatives. *Journal of Sustainable Finance & Investment*, 11(4), 355-370.
8. Cui, Y., Geobey, S., Weber, O., & Lin, H. (2018). The impact of green lending on credit risk in China. *Sustainability*, 10(6), 2008. <https://doi.org/10.3390/su10062008>
9. Das, S. R. (2019). The future of fintech. *Financial Management*, 48(4), 981-1007. <https://doi.org/10.1111/fima.12297>
10. Dorfleitner, G., Gimpl, M., & Hornuf, L. (2019). Fintech, digitalization and blockchain: Possible applications for green finance. In L. Lu (Ed.), *Handbook of Green Finance* (pp. 45-66). Springer.
11. Ebi, B. O., Sadiq, M. T., & Uzohue, R. (2021). FinTech and financial inclusion in Nigeria: A review of the literature. *Journal of Economics and International Finance*, 13(3), 81-90. <https://doi.org/10.5897/JEIF2021.1115>
12. Feng, T., Wang, H., & Wang, S. (2020). Fintech development and financial inclusion: A review of the literature. *Electronic Commerce Research*, 20(4), 669-686.
13. Gai, K., Qiu, M., & Sun, X. (2018). A survey on fintech. *Journal of Network and Computer Applications*, 103, 262-273. <https://doi.org/10.1016/j.jnca.2017.10.011>
14. Gregoriou, G. N., & Kooli, M. (2020). The role of fintech in ESG investing. *Journal of Risk and Financial Management*, 13(9), 206. <https://doi.org/10.3390/jrfm13090206>
15. Grewal, J. S., Jain, T., & Sandhu, G. K. (2021). Fintech innovations and sustainable finance: A systematic literature review. *Journal of Advances in Management Research*, 18(4), 561-577.
16. Hartmann, F., & Pisarova, M. (2020). ESG disclosure, sustainability, and the new regulations on sustainable finance in the EU. *The European Financial Review*. Retrieved from <https://www.europeanfinancialreview.com/esg-disclosure-sustainability-and-the-new-regulations-on-sustainable-finance-in-the-eu/>
17. Iman, N. (2020). The rise and rise of financial technology: The good, the bad, and the verdict. *Cogent Business & Management*, 7(1), 1725309. <https://doi.org/10.1080/23311975.2020.1725309>

18. Kou, G., Chao, X., Peng, Y., & Alsaadi, F. E. (2021). Machine learning methods for systemic risk analysis in financial sectors. *Technological Forecasting and Social Change*, 162, 120401. <https://doi.org/10.1016/j.techfore.2020.120401>
19. Lee, J., & Shin, D. (2019). Blockchain-based sustainable energy trading platform in the smart grid. *Sustainability*, 11(15), 4230.
20. Li, Y., Spigt, R., & Swinkels, L. (2017). The impact of FinTech start-ups on incumbent retail banks' share prices. *Financial Innovation*, 3(1), 26. <https://doi.org/10.1186/s40854-017-0076-7>
21. Minto, A., & Rehm, F. (2019). Leveraging blockchain technology in sustainable finance: Regulatory innovation and risk management. *European Business Organization Law Review*, 20(4), 619-645. <https://doi.org/10.1007/s40804-019-00172-2>
22. Nicoletti, B. (2017). *The Future of FinTech: Integrating Finance and Technology in Financial Services*. Palgrave Macmillan.
23. Scholtens, B. (2017). Why finance should care about ecology. *Trends in Ecology & Evolution*, 32(7), 500-505. <https://doi.org/10.1016/j.tree.2017.03.013>
24. Smith, A., Brown, C., & Jones, D. (2020). Robo-advisors and sustainable finance: A systematic literature review. *International Journal of Bank Marketing*, 38(6), 1274-1295.
25. Zhang, D., Zhang, Z., Managi, S. (2019). A bibliometric analysis on green finance: Current status, development, and future directions. *Finance Research Letters*, 29, 425-430. <https://doi.org/10.1016/j.frl.2019.01.010>
26. Zhang, Y., Hu, Y., & Li, X. (2022). Natural language processing and sustainable finance: A systematic review. *Sustainability Accounting, Management and Policy Journal*, 13(1), 187-206.

RGCNN: Precise Fake News Detection on Social Media Using Random Group Coupled Neural Networks

Subhashree D C¹, Harendra Singh Negi², Kardeepa Ponnuchamy³, Nayani Sateesh⁴, Harshal Patil⁵, Ramya Maranan⁶

¹ Assistant Professor, Department of MCA, Ballari Institute of Technology & Management, Ballari, India
shubha.rmjssp@gmail.com

² Department of Computer Science & Engineering, Graphic Era Deemed to be University, Dehradun, Uttarakhand, India, 248002 harendrasinghnegi@geu.ac.in

³ Assistant Professor, Department of Computer Science and Engineering, Kalasalingam Academy of Research and Education, Krishnankoil, Tamil Nadu, 626126, India p.kardeepa@klu.ac.in

⁴ Sr. Assistant Professor, Department of Computer Science and Engineering, CVR College of Engineering, Ibrahimpatnam 501510, Telangana, India n.sateesh@cvr.ac.in

⁵ Professor, School of Computer Science & Engineering, IILM University, Greater Noida, Uttar Pradesh, 201 306, India pharshal2288@gmail.com

⁶ Assistant Professor, Department of Research and Innovation, Saveetha School of Engineering, SIMATS, Chennai, Tamil Nadu - 602105, India ramyamaranan@yahoo.com

Abstract—The explosion of unverified information on social media platforms has made it more important than ever to identify and anticipate false news, which poses serious hazards to democratic processes and society as a whole. The challenge is exacerbated by the lack of standardized benchmark datasets, which impedes the development of effective countermeasures against misinformation. This research introduces a novel approach for fake news classification and prediction through the Random-Coupled Neural Network with a Group Teaching Algorithm (RGCNN). Data is sourced from the LIAR and ISOT datasets and undergoes comprehensive preprocessing, including tokenization, data cleaning, removal of stopwords, stemming, and lemmatization. Feature extraction is performed using a Split Multi-Axis Vision Transformer. The Random-Coupled Neural Network (RCNN) is utilized for precise fake news detection, with its performance further refined by applying Group Teaching Optimization (GTO). 99.6% on the LIAR dataset and 99.5% on the ISOT dataset show how accurate the suggested method is.

Keywords—Random-coupled Neural Network, data cleaning, stemming, Group teaching optimization, Split Multi-axis vision transformer.

I. INTRODUCTION

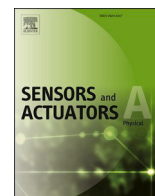
Recently, false information has spread due to user freedom on online news platforms like newspapers and social media (SM), which allow users to post anything [1–2]. People now mostly get their news via online SM platforms such as Instagram, YouTube, Twitter, and Facebook, especially in developing countries. As a result, anyone, wherever in the world, may utilize SM as platforms to make any kind of remark and disseminate false information over different networking locations in order to accomplish a variety of objectives, some of which may be unauthorized [3–4].

Presently facing major consequences for business, culture, and society as an outcome of the growing usage of SM, that can have both positive and negative effects [5]. Fake news is considered one of the largest threats to international trade, journalism, and democracy because of its detrimental impacts [6–7].

Stanford University researchers have released figures showing that official news sources and online SM platforms account for 72.3% of fake news [8]. It is imperative to develop efficient fake news recognition systems due to the detrimental properties of fake news on society and the widespread belief that it represents a major threat to global trade, media, and democracy, with the potential to cause grave harm to these sectors. As artificial intelligence (AI) continues to progress at a rapid pace [9–10],

Machine learning (ML)-based automatic detection techniques have been researched to counter the rise and spread of fake news. Most fake news detection (FND) systems make use of machine learning techniques to aid users in sorting through material and figuring out whether or not a particular news article is deceptive [11]. Recent advances in challenging natural language processing problems have shown that deep learning (DL) algorithms can be utilized to notice fake news accurately and quickly. Research on developing automated, reliable, and accurate techniques for spotting bogus news on social media is currently in vogue [12]. The main contributions of this research are;

- The research introduces a novel Random-coupled Neural Network with Group Teaching Optimization (GTO) specifically designed for FND, enhancing the accurateness and robustness of the detection process.



Nanoscopic hygrometry: Exploiting porous nature zinc-doped tin oxide nanoparticles for enhanced humidity sensing at ambient temperature

Hanumantagouda Basavanagoudra^a, Vijayakumar D. Jangannanavar^a, Sunilkumar Anegundi^b, Chetan Basavalingappa^c, Mallikarjun K. Patil^d, Sanjeev R. Inamdar^d, Kotresh M. Goudar^{a,*}

^a Department of Studies in Physics, Vijayanagara Sri Krishnadevaraya University, Ballari, Karnataka 583 105, India

^b Department of Physics, Ballari Institute of Technology and Management, Ballari, Karnataka 583 104, India

^c Department of Physics, Indian Institute of Science, Bengaluru, Karnataka 560 012, India

^d Laser Spectroscopy Programme, Department of Physics, Karnatak University, Dharwad 580 003, India

ARTICLE INFO

Keywords:

Zn-SnO₂ NPs

TEM

Calcination

Humidity sensor

Response time

Stability

ABSTRACT

This study focuses on zinc-doped tin oxide nanoparticles (Zn-SnO₂ NPs) as promising humidity sensors. Through a chemical coprecipitation method, we synthesized Zn-SnO₂ NPs and explored the influence of calcination temperature on their properties. X-ray diffraction confirmed the tetragonal rutile structure, and morphological analysis revealed a cauliflower-like morphology with enhanced porosity after calcination. UV-Visible absorption spectroscopy and photoluminescence measurements demonstrated a blue shift in the absorption peak and significant emission peaks related to oxygen vacancies, indicating improved humidity sensing potential as increasing the calcination temperature. The controlled calcination process led to successful outcomes, precisely tuning the NPs structure and optical behavior for enhanced humidity sensing capabilities. Conductivity studies have highlighted the semiconducting behavior of the NPs and observed that an increase in calcination temperature reduces their conductivity. Notably, humidity sensing experiments revealed a remarkable response of 93% and an exceptional response time of 30 seconds for the calcined NPs, surpassing the uncalcined sample. The sensing mechanism involving physisorption, chemisorption, and capillary condensation of water molecules on the NPs surface was validated. Moreover, the stability test over two month demonstrated consistent and highly stable humidity sensing response, reaffirming the NPs potential as effective and reliable humidity sensors.

1. Introduction

In recent years, the monitoring and control of humidity have become increasingly important in various industries, such as air conditioning, biomedical, food processing, pharmaceuticals, meteorology, micro-electronics, agriculture, and structural health monitoring. Humidity fluctuations in the atmosphere have significant impacts on industries, the environment, manufacturing processes, and human health. Moreover, abrupt changes in humidity often caused by air pollution, adversely affect crop cultivation and yield [1–3]. Consequently, there is a growing demand for highly sensitive humidity sensors to facilitate environmental monitoring, food preservation and packaging, agricultural practices, and weather forecasting [4–7]. Ceramic oxide-based humidity sensors have been extensively studied in the past, but they often lack the desired sensitivity and selectivity [8]. Recently, metal oxide nanoparticles (NPs) based humidity sensors have garnered

significant interest due to their affordability, easy installation, compact size, and simple design [9–11]. These NPs exhibit semiconducting properties and have wide band gap energies, enabling them to operate effectively at low temperatures with a chemiresistive nature [12].

Among the various metal oxide NPs, tin oxide NPs (SnO₂) stand out as promising materials because of their n-type semiconducting nature and a band gap of 3.6 eV. They offer high chemical stability, a larger reactive surface area for target analytes, and are known for their non-toxicity and biocompatibility [13,14]. In particular, the porous nature of tin oxide NPs has shown remarkable sensitivity in sensing analytes through the adsorption of molecules on their surface. SnO₂ NPs have gained a well-established reputation as effective sensor materials, demonstrating excellent sensitivity, selectivity, stability, and responsiveness [15–19]. As a result, SnO₂ NPs have found applications in various fields, such as gas sensing, solar cells, photocatalysis, supercapacitors, conducting electrodes, optoelectronic devices, and

* Corresponding author.

E-mail address: kotreshm26@gmail.com (K.M. Goudar).

<https://doi.org/10.1016/j.sna.2024.115242>

Received 7 December 2023; Received in revised form 11 February 2024; Accepted 1 March 2024

Available online 2 March 2024

0924-4247/© 2024 Elsevier B.V. All rights reserved.

biomedical applications [20–24]. Moreover, the structure and morphology of tin oxide NPs can be tailored by introducing suitable metal dopants and calcining the NPs at higher temperatures to achieve the desired chemiresistive properties for improved sensing performance. Incorporating zinc as a dopant alters the crystalline size and oxidation state in the SnO_2 crystal structure, potentially enhancing sensitivity and selectivity. The smaller ionic radius (139 pm) of the Zn^{+2} ion allows it to easily replace the Sn^{+4} ion (225 pm), resulting in oxygen vacancies, reducing the electron density and creating excess ions on the NP's surface, which facilitates interaction with analyte molecules [24,25].

Several studies have been published on the synthesis and characterization of SnO_2 and doped SnO_2 nanostructures with different dimensions. These studies demonstrate that calcination treatments can modify the surface roughness and crystallinity of the NPs [26,27]. SnO_2 NPs are observed to crystallize and become structurally stable at calcination temperatures around 500°C [28,29]. While previous papers have discussed the structure and morphological modification of SnO_2 NPs for various applications, to the best of our knowledge, no reports exist on the humidity sensitivity linked to uncalcined and calcined temperatures for zinc-doped SnO_2 NPs. The objective of this study is to investigate the effects of calcination temperature on the structural, morphological, optical, and electrical properties of zinc-doped tin oxide NPs and their humidity sensing capabilities. Our findings indicate that the zinc-doped tin oxide NPs calcined at 500°C exhibit exceptional humidity sensing characteristics, including a rapid response time of 30 s.

2. Experimental methods

2.1. Materials

The analytical grade $\text{SnCl}_2 \cdot 2\text{H}_2\text{O}$, ZnCl_2 and NaOH precursors were obtained from SD Fine Chemical Ltd. and used without further refinement.

2.2. Methods

2.2.1. Synthesis of Zn-SnO₂ nanoparticles

Zn-SnO₂ NPs were prepared using the chemical coprecipitation method, as depicted in Fig. 1. In the typical synthesis process, 0.18 M of $\text{SnCl}_2 \cdot 2\text{H}_2\text{O}$ and 0.02 M of anhydrous ZnCl_2 precursors were separately dissolved in a known quantity of deionized water and stirred for one hour. Subsequently, the ZnCl_2 solution was added to the $\text{SnCl}_2 \cdot 2\text{H}_2\text{O}$ solution under continuous stirring, while maintaining the solution temperature at 60°C . Furthermore, a 0.8 M NaOH solution, serving as a reducing agent, was slowly added drop by drop to the mixture solution under constant stirring until the solution reached a pH of 10. During this process, the initially white metal solution turned into a grey precipitate. The obtained precipitate was then filtered and washed multiple times with deionized water, followed by ethanol, to remove any chloride residues. The resulting sample was subsequently dried at 70°C for two hour in a hot air oven. Moreover, the obtained powder was divided into two parts. Among these parts, one was subjected to calcination at 500°C in a muffle furnace to investigate the effect of calcination temperature on the structural, morphological, optical, and humidity sensing properties, which were then compared with the uncalcined (bare) sample. Henceforth, the uncalcined and calcined at 500°C samples were labeled as ZS1 and ZS2, respectively.

2.3. Characterization methods

The synthesized Zn-SnO₂ NPs characterized by using various spectroscopic techniques. The crystallography and structural information of the sample were analyzed by X-ray diffraction using a Rigaku X-ray diffractometer, utilizing copper $\text{K}\alpha$ ($\lambda = 0.15406 \text{ nm}$) radiation as the source, at room temperature. The surface morphology and elemental composition were investigated using the FESEM-EDS technique with a Zeiss EVO18 instrument (make: Carl Zeiss Pvt. Ltd., Japan). The morphology, mean size and purity of the samples were examined by transmission electron microscope (TALOS F200S 200 kV, FEG, CMOS camera 4Kx4K, EDX detector). FTIR examination was conducted with a

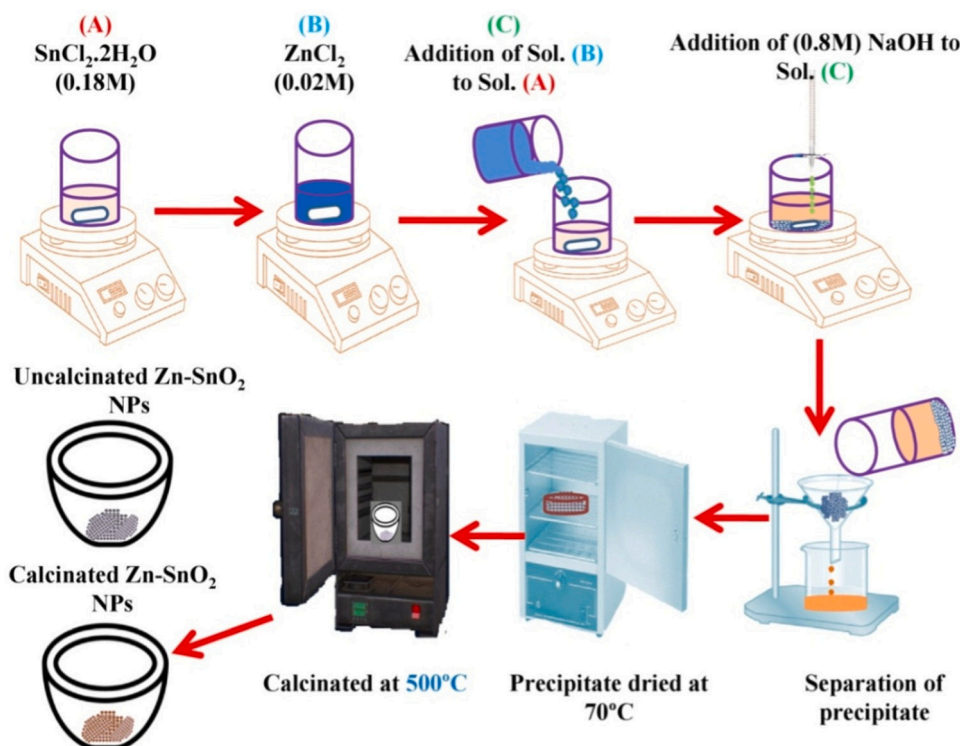


Fig. 1. Schematic representation for the synthesis of Zn-SnO₂ NPs by chemical coprecipitation method.

Perkin Elmer spectrometer, covering the wavenumber range of 4000–400 cm^{-1} , employing the KBr pellet technique. The UV–visible absorption spectrum of the Zn-SnO₂ NPs was recorded using an AU-2703 spectrometer (make: Systronics Limited, India). The photoluminescence spectrum of Zn-SnO₂ NPs was examined using the Fluoromax-4 spectrometer (Make: Horiba Jobin Yvon).

2.4. Humidity sensing studies

To investigate the humidity sensing behavior of the zinc-doped tin oxide NPs, the initial samples were transformed into pellets with a thickness of 1.5 mm and a diameter of 10 mm using a hydraulic press. Additionally, silver paste was applied to both sides of the pellet to enhance electrical contact. The sensing behavior of the prepared pellets under different humidity conditions was examined using a specially designed sensor setup, as illustrated in Fig. 2. To create specific humidity conditions, standard salt solutions were placed in a glass chamber namely: LiCl (10% RH), MgCl₂ (33% RH), K₂CO₃ (43% RH), Mg(NO₃)₂ (53% RH), CoCl₂ (64% RH), NaCl (75% RH), KCl (85% RH), K₂SO₄ (97% RH). The chamber was sealed with a rubber cork, allowing the electrodes to pass through. The two ends of the electrodes were connected to a programmable digital multimeter (Hioki DT 4282, Japan) in order to measure and record the variation in electrical resistance of the samples with and without humidity. Finally, the sensing response of the samples was determined using Eq. (1) [9].

$$S_H = \frac{R_0 - R_{RH}}{R_0} \times 100 \quad (1)$$

Where S_H is humidity sensitivity, R_0 is resistance at lowest % RH, R_{RH} is resistance at various % RH.

3. Results and discussion

3.1. X-ray diffraction results

The synthesized NPs underwent X-ray diffraction (XRD) studies in the 2θ range of 20° to 80° to investigate their structural characteristics. Fig. 3 depicts the XRD pattern of the uncalcinated sample (ZS1) and the sample calcinated at 500 °C (ZS2). From the figure, it is evident that the sample calcinated at 500 °C (ZS2) exhibits well-defined diffraction patterns with major indexing peaks at (110), (101), (200), and (210). This confirms that the prepared NPs possess a highly crystalline nature with a tetragonal rutile structure belonging to the P42/mnm space

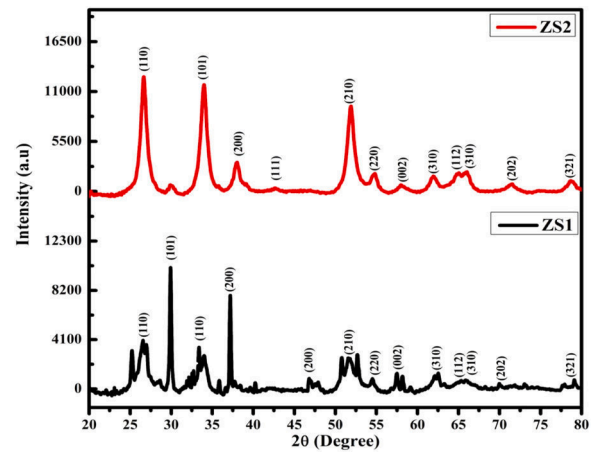


Fig. 3. The XRD pattern of synthesized Zn-SnO₂ NPs; ZS1 is uncalcinated, and ZS2 is calcinated at 500 °C.

group. The obtained results align with the standard JCPDS data (01-077-0447). Meanwhile, the uncalcinated sample ZS1 displays a similar diffraction pattern to that of ZS2, with an additional major peak (101) observed at a 2θ value of 30°. This peak corresponds to the Zn-SnO tetragonal rutile phase, indicating that the uncalcinated ZS1 sample consists of both Zn-SnO and Zn-SnO₂ phases. The presence of two phases can be attributed to the thermodynamic instability of Zn-SnO NPs [30, 31].

Furthermore, the calcination process at 500 °C leads to an increase in peak intensity with wider broadening compared to the uncalcinated sample. This suggests that the calcination process significantly enhances the crystallinity of the prepared sample [32]. Additionally, the effect of calcination temperature on the crystalline structure of the prepared NPs was analyzed by determining various crystal parameters such as average crystallite size (D), lattice parameters (a , b , and c), unit cell volume (V), lattice distortion ratio [$(\epsilon^2)^{1/2}$] and percentage of crystallinity. These parameters were calculated using the following Eqs. (2) to (6) and the results are presented in Table 1.

$$D = \frac{k\lambda}{\beta \cos \theta} \quad (2)$$

$$\frac{1}{d^2} = \frac{(h^2 + k^2)}{a^2} + \frac{l^2}{c^2} \quad (3)$$

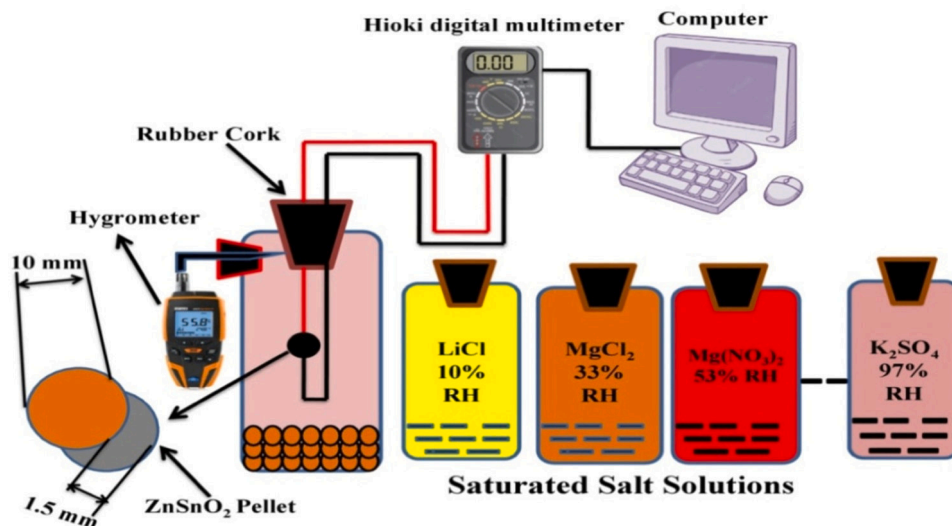


Fig. 2. Schematic diagram of the humidity sensing set up.

Table 1

Crystalline parameters of the fabricated zinc doped tin oxide NPs.

Sample Name	Calcinated temperature in °C	Crystalline size (D) in nm by DS Method	Lattice parameter in (Å)		Volume of the unit cell (V) (Å) ³	(e ²) ^{1/2}	% Crystallinity
			a	c			
			4.7358*	3.1851*	71.43*		
ZS-1	Un-calcinated	51.51	4.7189	3.1846	70.91	0.0066	60.59
ZS-2	500 °C	9.45	4.7241	3.1842	71.14	0.0046	88.76

* represents the standard value [JCPDS data (01-077-0447)]

$$V = a^2c$$

(4)

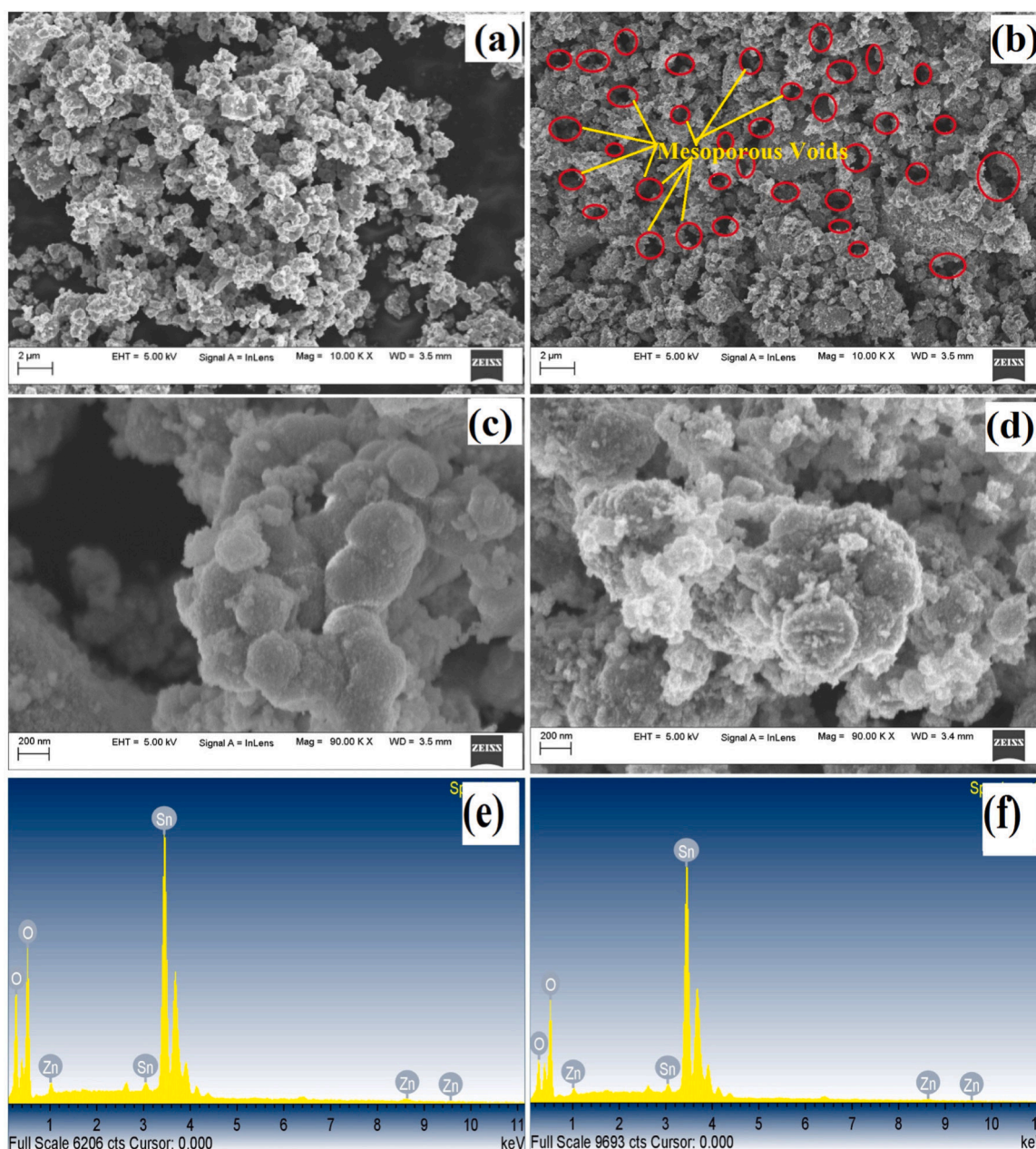
$$\langle e^2 \rangle^{1/2} = \frac{1}{D} \frac{1}{\sin \theta} \frac{\lambda}{\pi} \sqrt{\frac{\pi^2 k^2 - 4}{32}}$$

(5)

$$\% \text{Crystallinity} = \frac{I_c}{I_c + I_a} \times 100$$

(6)

The Table 1 reveals that the crystalline size of the calcinated sample is significantly smaller than that of the uncalcinated sample, attributed to the recrystallization of NPs caused by the calcination temperature [26]. The lattice parameters of the prepared NPs are relatively smaller than the standard value of SnO₂ NPs. This disparity is mainly due to the difference in ionic radius between Zn ions and Sn ions, which induces lattice distortion in the SnO₂ lattice matrix [33]. Consequently, the

**Fig. 4.** FESEM images of Zn-SnO₂ NPs; (a, c) uncalcinated, (b, d) calcinated at 500 °C and EDS spectrum (e) uncalcinated, (f) calcinated at 500 °C.

lower value of the lattice distortion ratio for the calcinated samples arises from the presence of thermal strain in the crystal structure, resulting in a reduction in crystalline size. Additionally, the percentage crystallinity of the calcinated sample shows a larger value than the uncalcinated sample, implying that the calcination process greatly contributes to the crystallization process. Thus, the calcinated sample exhibits well-defined XRD peaks with a lower lattice distortion ratio and high crystallinity, indicating that the calcination process plays a vital role in crystal growth.

3.2. Morphological results

3.2.1. FE-SEM analysis

The surface morphology of the prepared NPs was studied using the FE-SEM technique. The images were captured at magnifications of 2 μm and 200 nm, respectively, as shown in Fig. 4(a-d). From the figure, it is evident that the uncalcinated NPs [Fig. 4(a, c)] exhibit a spherical morphology with agglomeration, and the grains are distributed in uniform sizes. On the other hand, Fig. 4(b, d) shows the images of the NPs calcinated at 500 $^{\circ}\text{C}$, displaying a cauliflower-like morphology with

cluster structures. Furthermore, the calcination temperatures cause the NPs to become rougher, and their grains become smaller. The increased surface roughness would generally improve the interface between the surface of the NPs and the applied analytic molecules, which may aid in boosting the sensing response [17]. Moreover, the existence of porosity is also a crucial component in improving sensing property because the porous surface of NPs may readily adsorb analyte molecules and react with surface-adsorbed molecules [34]. In the present case, as compared to uncalcinated NPs, calcinated NPs have smaller grain sizes and higher porosity. Consequently, the porous NPs may have contributed to the surface area expansion, providing more active sites for adsorbing water molecules and, in turn, aiding in enhancing the humidity sensing capacity [35].

Thus, the calcination process significantly alters the structure and morphology of the NPs, resulting in the formation of a mesoporous gap between the grains, as observed in Fig. 4(b). Additionally, for more confirmation we estimated the size of mesoporous voids by using *Image J* software and average size found to be 0.98 nm and 8 nm for uncalcinated (ZS1) and calcinated (ZS2) NPs. This unique morphology is advantageous for various sensing applications, as it allows for the

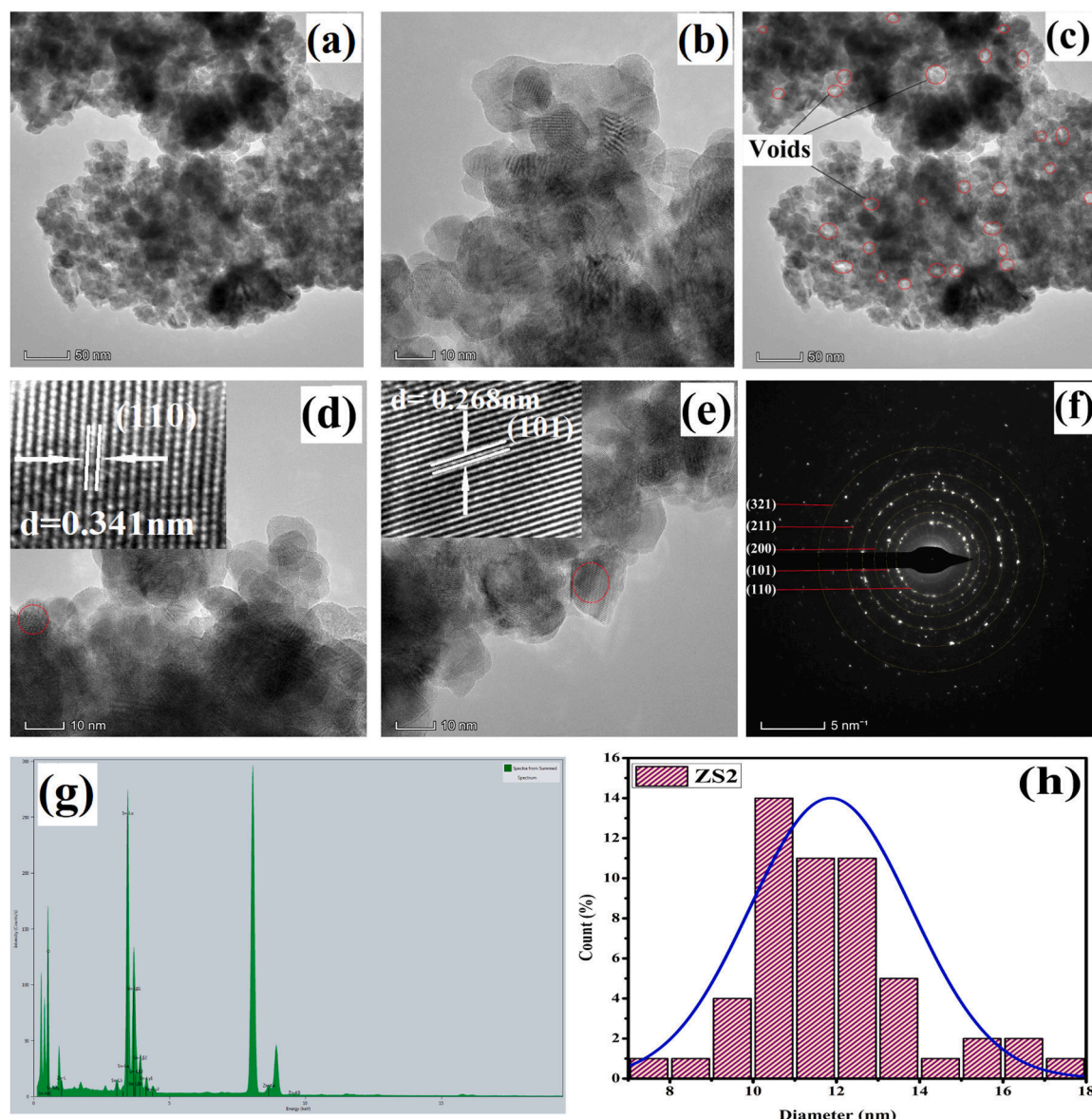


Fig. 5. TEM images of calcinated Zn-SnO₂ NPs (ZS2); (a-c) at different magnification, (d, e) represents d-spacing images, (f) SAED pattern, (g) EDAX spectrum and (h) particle size distribution histogram.

penetration of target analytes and enables varying resistance across the sample [2]. Furthermore, the elemental composition of the material was determined using Energy Dispersive Spectroscopy (EDS) analysis, and the obtained spectra are shown in Fig. 4(e, f). The peaks associated with the elements Sn, O, and Zn are identified, confirming the successful doping of Zn into the SnO₂ NPs lattice, with no other residual elements present in the profile.

3.2.2. TEM analysis

A transmission electron microscopy (TEM) analysis was performed on the ZS2 sample to confirm the formation of the tetragonal rutile phase, determine particle size, and investigate the reason behind the calcinated sample's high humidity response. TEM images of the ZS2 samples, captured at magnifications of 10 nm and 50 nm, are shown in Fig. 5(a, b). These images clearly demonstrate the uniform arrangement of particles in a tetragonal shape. Additionally, the interplanar distance of the obtained structure was estimated and is presented in Fig. 5(d, e). The values measured were found to be 0.268 nm and 0.341 nm, corresponding to the (101) and (110) planes of tetragonal rutile phase of SnO₂ NPs, respectively. The selective area electron diffraction pattern (SAED) of the ZS2 NPs is depicted in Fig. 5(f). The SAED pattern exhibits a shining diffraction spot with a spherical pattern, indicating the fine crystalline nature of the NPs and their closely correlated radii with the lattice spacing of the XRD planes.

The average particle size of the prepared NPs was estimated from the histogram using *Image J* software, as shown in Fig. 5(h), and was found to be 12 nm. These findings from the TEM analysis align relatively well with the XRD measurements. Furthermore, as discussed in the FE-SEM analysis, ZS2 sample has a large number of voids, which is confirmed by TEM analysis and is shown in Fig. 5(c). Notably, Fig. 5(c) illustrates the creation of mesoporous spaces between the grains, which may be advantageous for humidity sensing applications by facilitating the adsorption of water molecules on the nanoparticle surface [36]. Moreover, in this work the calcinated sample demonstrated a high humidity sensing response due to morphological changes caused by calcination. The crystallinity and charge carrier scattering at the grain boundaries in contact with the NPs primarily influence the resistivity of the Zn-SnO₂ NPs. The scattering process strongly affects the resistivity of nanocrystallites and is predominantly increased by reducing particle size [33]. Additionally, EDAX analysis were performed for the prepared ZS2 NPs to check the elemental composition and obtained spectrum is depicted in Fig. 5(g). The spectrum confirms the presence of Sn, Zn, and O elements and other impurity were not detected. Finally, these results endorse that the calcination process will improve the surface morphology and create mesoporous voids between the NPs, which are helpful for gas and humidity sensing applications.

3.3. Fourier transforms infrared spectroscopy (FTIR) results

FT-IR spectroscopy is an essential technique for investigating the structural properties and various functional groups attached to the NPs. The obtained FT-IR spectra of the synthesized NPs are shown in Fig. 6. From the spectra, three main functional group bands are observed at 543 cm⁻¹, 1020 cm⁻¹, and 3412 cm⁻¹. The peak at 543 cm⁻¹ corresponds to the characteristic stretching vibration of the Sn-O bond. The stretching modes of Zn-O-Sn are indicated by the peaks at 617 cm⁻¹ in the uncalcinated sample and 630 cm⁻¹ in the calcinated sample. The shift in the peak position is attributed to the change in structural properties of the NPs caused by the effect of calcination temperature [37].

A small peak observed at 1020 cm⁻¹ in the calcinated samples is mainly attributed to Sn-OH, while the same peak appears at 1171 cm⁻¹ in the uncalcinated samples. The bending vibration of the H₂O molecule is observed at 1635 cm⁻¹ in the uncalcinated sample, which can be attributed to water molecule adsorption on the surface of the NPs. This peak becomes significantly reduced in the calcinated sample. Additionally, the peak at 3412 cm⁻¹ is related to the stretching vibration of

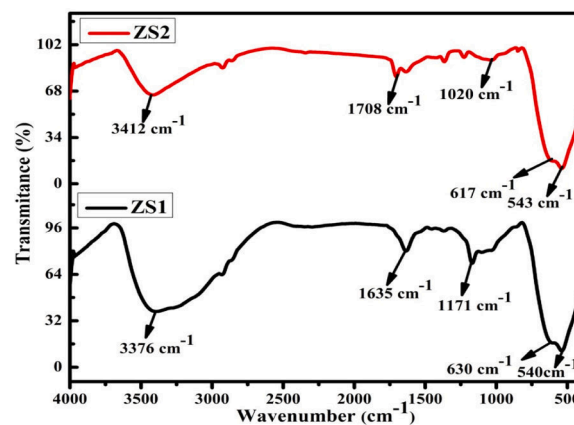


Fig. 6. FT-IR spectra of synthesized Zn-SnO₂ NPs; ZS1-uncalcinated, ZS2- calcinated at 500 °C.

the O-H bond and is mainly caused by the adsorption of moisture on the nanoparticle surface from the atmosphere during the FT-IR analysis [26]. C. Guo *et al.* reported that, Ho₂O₃/GO composite has sharper hydroxyl peak than pure Ho₂O₃ nanosheets, which suggest that, the increased surface water absorption [38]. In our case also same, i.e. O-H stretching vibration peaks of the calcined sample are sharper than those of the uncalcinated sample, indicating increased surface water absorption.

3.4. UV-Visible absorption spectroscopic measurements

The effect of calcination temperature on the optical properties of zinc-doped tin oxide NPs was investigated using a UV-Visible absorption spectrophotometer in the wavelength range from 250 to 800 nm. The obtained spectra are presented in Fig. 7(a). From the spectra, it is observed that the absorption band of the uncalcinated sample appeared at 356 nm and shifted to 345 nm (blue shift) after the calcination of the NPs. This shift in peak position is attributed to a reduction in the crystalline size of the NPs [2]. Furthermore, the optical band gap of the prepared NPs was estimated using the Kubelka-Munk function, which is given by Eq. (7).

$$F(R) = \frac{(1 - R)^2}{2R} \quad (7)$$

where R is the reflectance, the plot of $[F(R) \times h\nu]^2$ versus photon energy ($h\nu$) gives the band gap energy of the prepared NPs, as shown in Fig. 7 (b). The bandgap energy was found to be 3.84 eV and 3.62 eV for the uncalcinated and calcinated NPs, respectively.

The reduction in bandgap energy after calcination can be attributed to chemical flaws or vacancies in neighboring intergranular areas, which generate new energy levels [37,39]. Additionally, the interaction between band electrons and localized electrons of Zn²⁺ (charge transformation or sp-d interaction) can modify the electronic structure and lead to a change in the energy band gap [2,40]. Generally, bandgap variation has a substantial impact on photosensing performance, whereas humidity sensors rely mostly on optical defects, such as oxygen vacancies, concerning the chemical species of analyte molecules. Therefore, it is essential to investigate the optical flaws in the NPs, and this can be done more precisely through photoluminescence spectroscopy.

3.5. Photoluminescence (PL) spectroscopy results

In addition to UV-visible absorption spectroscopy, photoluminescence is a powerful method for analyzing the optical properties of NPs. The emission spectra of the prepared NPs were obtained by exciting the sample at a wavelength of 290 nm, as shown in Fig. 8. The

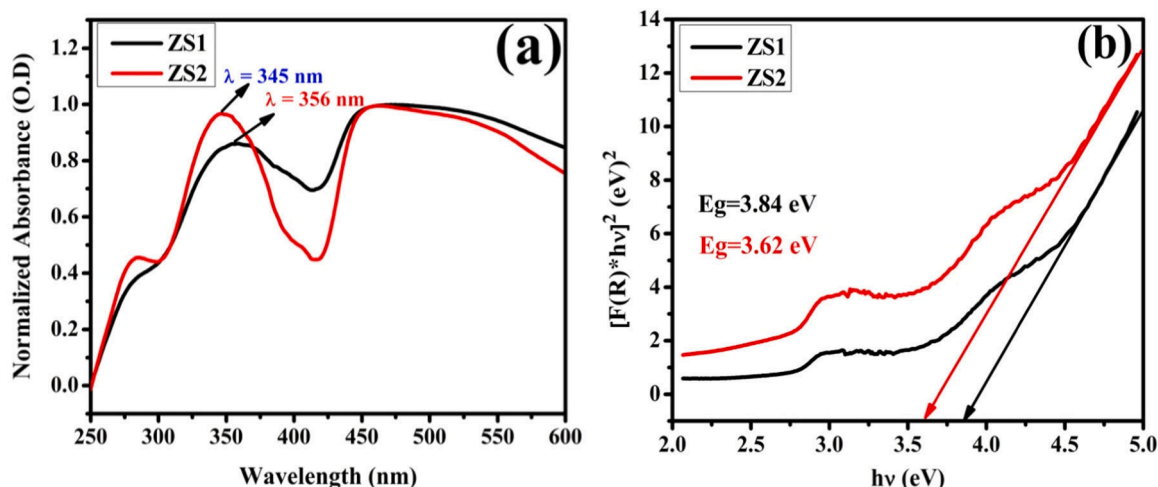


Fig. 7. UV-visible absorption spectra of synthesized Zn-SnO₂ NPs (a) Absorption spectrum (b) Kubelka-Munk plot of uncalcinated (ZS1) and calcinated (ZS2) NPs.

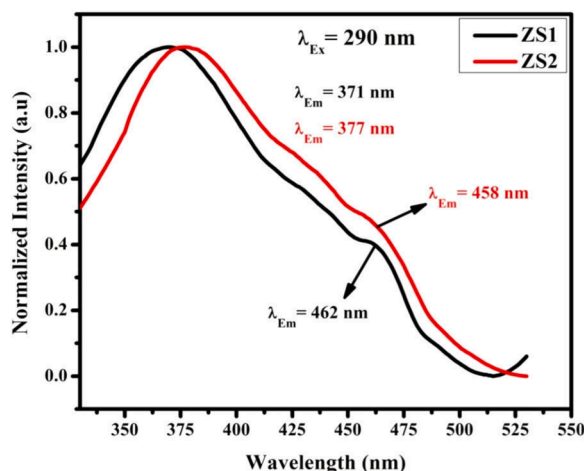


Fig. 8. Normalized emission spectra of the synthesized Zn-SnO₂ NPs; ZS1-uncalcinated and ZS2-calcinated at 500 °C.

uncalcinated (ZS1) and calcinated (ZS2) samples exhibited significant emission peaks at 371 nm and 377 nm, respectively. This intense emission is primarily attributed to the exciton recombination of electrons in the conduction band with photoinduced holes in the valence band [41]. Furthermore, a faint emission was also observed at 462 nm and 456 nm for the ZS1 and ZS2 samples, respectively. This emission is mainly attributed to surface defects, which result in electron migration from Sn vacancies to interstitial sites [42]. The presence of surface defects, particularly oxygen vacancies at the interstitial sites, traps electrons from the valence band and causes delayed luminescence [2].

The delayed luminescence may be caused by radiative transitions via deep levels in the bandgap. Two possible explanations for this radiative transition are considered: (i) grain boundary defects acting as recombination centers, and (ii) oxygen vacancies likely producing a significant number of trapped states within the Zn-SnO₂ band structure. Therefore, due to their oxygen vacancies and oxygen interstitial, these emissions have a major impact on the humidity sensing performance of the NPs [18]. In particular, oxygen vacancies directly interact with the adsorbed water molecules, enhancing the sensitivity of the NPs [43].

3.6. Conductivity measurements

The semiconducting properties of the synthesized zinc-doped tin oxide NPs were measured using two-probe dc conductivity

measurements supported by a Keithley source meter at operating temperatures ranging from 80 °C to 200 °C. Fig. 9(a, b) illustrate the I-V properties of the ZS1 and ZS2 samples, respectively. From the curves, it is observed that the electrical conductivity of the Zn-SnO₂ NPs increases with the operating temperature. This can be attributed to the rise in charge carriers due to thermal effects, resulting in an increase in the drift mobility of charges [44]. These observations confirm the semi-conducting behavior of the prepared Zn-SnO₂ NPs. Furthermore, the calcinated NPs (ZS2) exhibit lower conductivity compared to the uncalcinated (ZS1) sample. The decrease in conductivity may be attributed to the reduction in crystallite size, the presence of a large number of mesoporous voids, and changes in charge carrier density [45]. These results also support FE-SEM and TEM analysis.

3.7. Humidity sensing results

The effectiveness of sensors based on uncalcinated and calcinated Zn-doped SnO₂ NPs was evaluated at different relative humidity levels ranging from 11% to 97% RH. In general, the surface morphology of the NPs, doping metal, and operating temperature are factors that have a significant impact on the effectiveness of a humidity sensor [2,18]. Additionally, it is crucial to remember that the operating temperature has a significant impact on any metal oxide sensor's detecting performance since it regulates both electrical resistivity and the mobility of charge carriers [7]. According to earlier investigations, sensitivity of the sensor is excellent at higher temperatures than ambient temperature, mainly because of increased mobility of charge carriers due to the temperature effect [46].

Further, due to the requirement for a safe and nontoxic environment in chemical industries, medical labs, research laboratories, food processing, and agriculture, scientists are now concentrating on improving the sensor response even at ambient temperature [6]. As a result, we investigated a room temperature humidity sensor in this study. In addition, we investigated how well-prepared NPs sensors sensed various humidity environments in terms of response and recovery times.

3.7.1. Sensing response

Humidity sensors are typically designed to be sensitive to the amount of water vapor adsorbed on the surface of NPs. This adsorption leads to a change in the electrical resistance of the NPs in relation to humidity, with a decrease in resistance as the relative humidity (RH%) increases [46]. To examine the humidity sensitivity properties of the synthesized NPs, electrical resistance measurements were performed at various relative humidity levels (11–97% RH), as depicted in Fig. 10. The resulting resistance measurements allow for the estimation of the

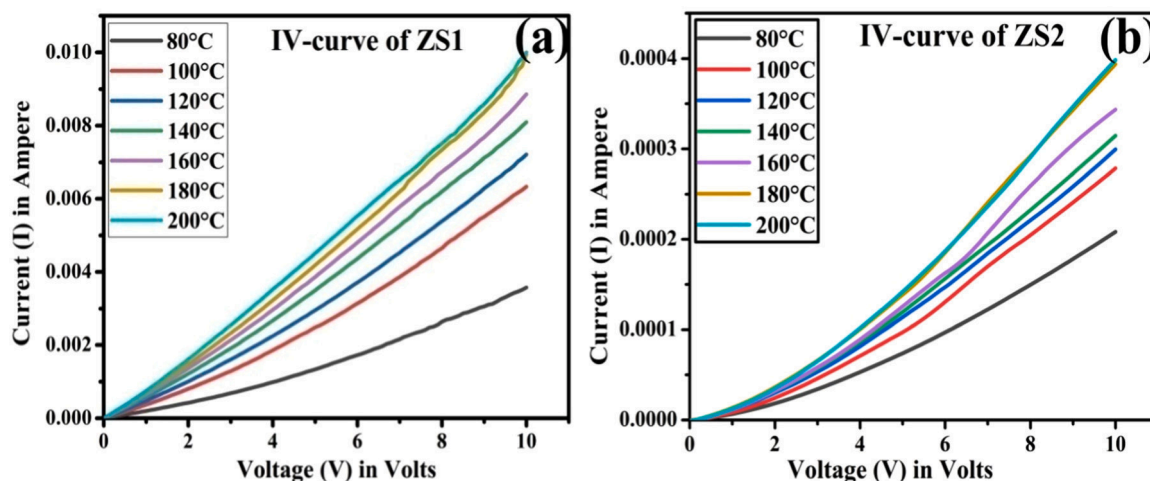


Fig. 9. Conductivity response of synthesized Zn-SnO₂ NPs at different operating temperatures ranging from 80 °C to 200 °C; (a) for uncalcinated (ZS1) and (b) calcinated at 500 °C (ZS2).

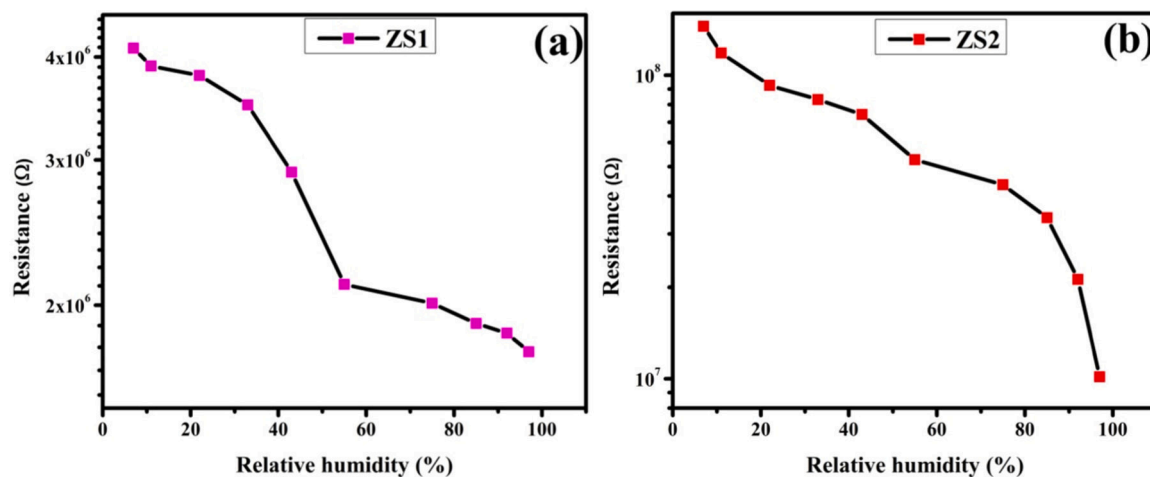


Fig. 10. Electrical resistance variation of Zn-SnO₂ NPs with different humidity conditions; for (a) uncalcinated (ZS1) and (b) calcinated at 500 °C (ZS2) NPs.

sensitivity response of the humidity system, as shown in Fig. 11.

From Fig. 10 (a), it is noticed that, the uncalcinated NPs (ZS1) exhibit a modest fluctuation in electrical resistance within the examined RH range, ranging from 4 to 1.75 MΩ. The sensing response of ZS1 was found to be 56% which is shown in Fig. 11. However, this outcome is

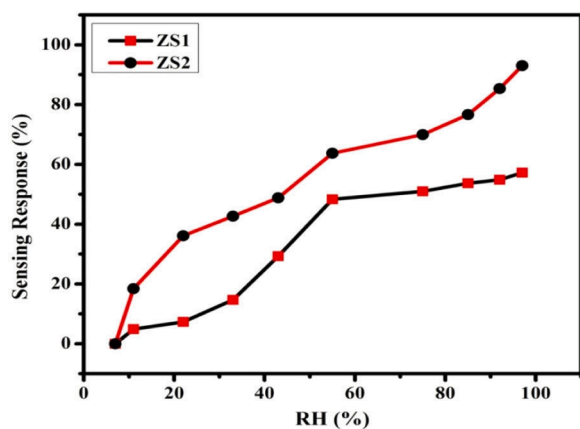


Fig. 11. Variation of sensing response of uncalcinated (ZS1) and calcinated (ZS2) Zn-SnO₂ NPs with relative humidity.

insufficient for the fabrication of an effective resistive-type humidity sensor. On the other hand, the calcinated NPs (ZS2) demonstrate a significant drop in resistance from 149 to 10 MΩ across all humidity ranges and is shown in Fig. 10 (b). The sensing response of ZS2 was determined to be 93% and is displayed in Fig. 11, which definitely outstanding for the sensor device fabrication. The stronger humidity-sensing response of the calcinated Zn-SnO₂ NPs is mainly attributed to its enhanced crystallinity, high porosity, and a lower energy bandgap [47].

Additionally, following a meticulous examination of the FE-SEM, TEM, and PL findings, notable morphological alterations were observed in the calcined Zn-SnO₂ NPs. These alterations comprise a higher proportion of oxygen-related defects, increased grain boundaries, and enhanced porosity. These structural changes have facilitated a significant improvement in water molecule adsorption, along with improved conduction, a drastic reduction in resistance, and heightened sensor responsiveness. In contrast, the uncalcined Zn-SnO₂ NPs exhibit a less porous nature, high conductivity, and low resistance; consequently, no significant drop in resistance has been observed.

3.7.2. Sensing mechanism

The humidity sensing mechanism is described using three successive processes based on the observed sensing behavior of synthesized Zn-SnO₂ NPs: physisorption, chemisorption, and capillary condensation. When H₂O molecules adsorb on the surface of the NPs, they undergo

chemisorption, physisorption, and capillary condensation. Initially, at lower humidity levels, H_2O molecules dissociate into H^+ and OH^- ions, which is represented in Eq. (8). The self-generated OH^- ions attach to the surface of the NPs during physisorption, and in the subsequent chemisorption layer, both the remaining H^+ ion and the attached OH^- ions are discharged.



Furthermore, these chemisorbed OH^- ions interact with nearby H_2O molecules, forming hydrogen bonds and resulting in the production of hydronium group (H_3O^+) ions. However, the H_3O^+ ions subsequently dissociate into H_2O and H^+ particles, facilitating the transfer of protonated H^+ ions between neighboring water molecules and enabling electrical conduction. This phenomenon is commonly known as the Grotthuss mechanism that is represented as Eq. (9) [14].



In addition, as the humidity rate increases, the second-stage of physisorption occurs, followed by the adsorption of water molecules into the capillary pores. This leads to an increase in the H^+ ions (protonation) and subsequently a decrease in the resistance of the sensing material. Therefore, the adsorption of water molecules on the surface of the NPs plays a vital role in detecting humidity conditions by modulating the resistance of the NPs. The sensing mechanism of the NPs is illustrated in Fig. 12.

3.7.3. Response and recovery time

The response and recovery characteristics of the uncalcined (ZS1) and calcined (ZS2) NPs were investigated, as shown in Fig. 13 (a, b). The response time were measured by placing the sample initially in the lower humidity chamber (11% RH) and then transferred to a higher humidity chamber (97% RH). During this process the resistance of the sample falls down and reaches the stable response. The response time, which measures the time taken for the sensor to reach a stable response in the higher humidity environment and it was found to be 86 s for ZS1 and 30 s for ZS2, respectively. Conversely, recovery time were measured by placing the sample initially in the higher humidity chamber (97% RH) and then transferred to a lower humidity chamber (11% RH). During this process the resistance of the sample rose up and reaches the initial stable response. The recovery time, which indicates the time required for the sensor to return to its initial state after being exposed to a low humidity environment and it was found to be 97 s for ZS1 and 37 s for ZS2 samples, respectively.

The longer recovery time compared to the response time can be attributed to the sluggish desorption of water molecules from the surface of the sensing materials [47,48]. Y. Xu et al. reported that, owing to intermolecular forces and the capillarity of the pore structure, the

desorption of water molecules from the material surface is expected to require more time [49]. This force leads to a more stable adsorption of water molecules on the surface, resulting in a slower release during the recovery process. During the response time cycle, the sample exhibits an exothermic reaction as water molecules rapidly adsorb on the surface of the NPs. Further, the uncalcined Zn-SnO₂ NPs shows higher response and recovery time as compared to the calcined Zn-SnO₂ NPs; this is mainly because of high density of NPs and low porosity which inhibit the water molecule access [50]. Moreover, the broader porosity and small particle size of calcined Zn-SnO₂ NPs allow charge carriers to propagate across the surface more smoothly. As a consequence, the sensing response and recovery durations were shorter than those of the uncalcined Zn-SnO₂ NPs. Additionally, owing of its lower electron concentration, the uncalcined Zn-SnO₂ NPs surface state could be less sensitive to humidity than calcined NPs. These finding implies that, the calcination process might improve the humidity sensing properties of Zn-SnO₂ NPs. The sensing properties of calcined Zn-SnO₂ NPs were compared with various other nanomaterials and are presented in Table 2. Overall, the calcined NPs (ZS2) demonstrate faster response and recovery times and exhibit a higher sensing response of 93% compared to the uncalcined NPs (ZS1). The excellent sensing characteristics of the Zn-SnO₂ NPs make them a promising material for the fabrication of humidity sensors.

Humidity-sensing NPs exhibit hysteresis behavior in relation to relative humidity. Fig. 14 illustrates the hysteresis graph of the calcined sample ZS2. The graph depicts the typical adsorption curve obtained after subjecting the sample to various relative humidity conditions, ranging from 11% to 97% RH, while recording the corresponding resistance values. Subsequently, the sample was tested again within a humidity range of 97–11% RH, and the resulting resistances were recorded to generate a desorption curve. It is evident from the adsorption and desorption curves, it exhibit satisfactory linearity and nearly identical behavior. Further, the percentage of hysteresis was calculated by considering the maximum deviation (hysteresis) in resistance between adsorption and desorption. From the graph, it is noticed that the maximum deviation appeared at 43% RH, and the percentage of hysteresis was calculated using Eq. (10), and it was found to be 12%. Furthermore, the sensor's humidity sensitivity increases with decreasing humidity hysteresis, and the obtained value signifies that the prepared Zn-SnO₂ NPs can be used for the design of humidity sensors. As a result, the calcination temperature plays an important role in the Zn-SnO₂ sensor's sensitivity.

$$\% \text{Hysteresis} = \left[\frac{(R_{mn} - R_{mp})}{(R_{\max} - R_{\min})} \times 100 \right] \quad (10)$$

Where, R_{mn} and R_{mp} are the maximum and minimum value of resistance at 45% RH (at maximum hysteresis), R_{\max} and R_{\min} are the maximum and minimum values of the measured resistance in the humidity range of 11–97% RH.

3.7.4. Stability testing

Moreover, the stability parameter plays a crucial role in the practical design of humidity sensors [56]. Therefore, the high humidity sensing response of the calcined sample was evaluated for its stability over a period of two month, with measurements taken at ten-day intervals. The experiment was conducted under two different humidity conditions: initially at 43% RH and subsequently at 97% RH. The results obtained from this stability test are presented in Fig. 15. The figure demonstrates that the sensing response of the calcined sample remains consistent and highly stable over an extended period. Hence, the calcined Zn-SnO₂ NPs can be implemented in the humidity sensor device fabrication.

4. Conclusion

In conclusion, this study demonstrates the successful synthesis and

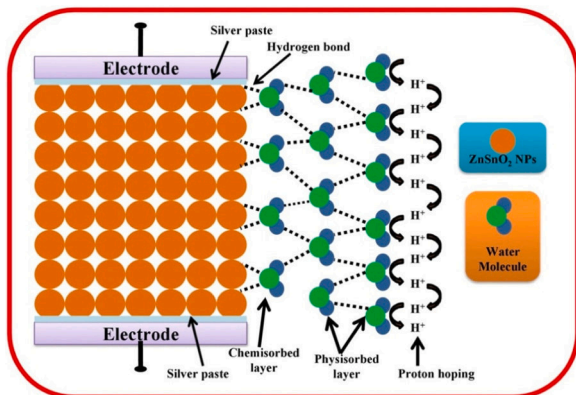


Fig. 12. Illustration of possible mechanism for the adsorption of water molecule on the surface of Zn-SnO₂ NPs at ambient temperature.

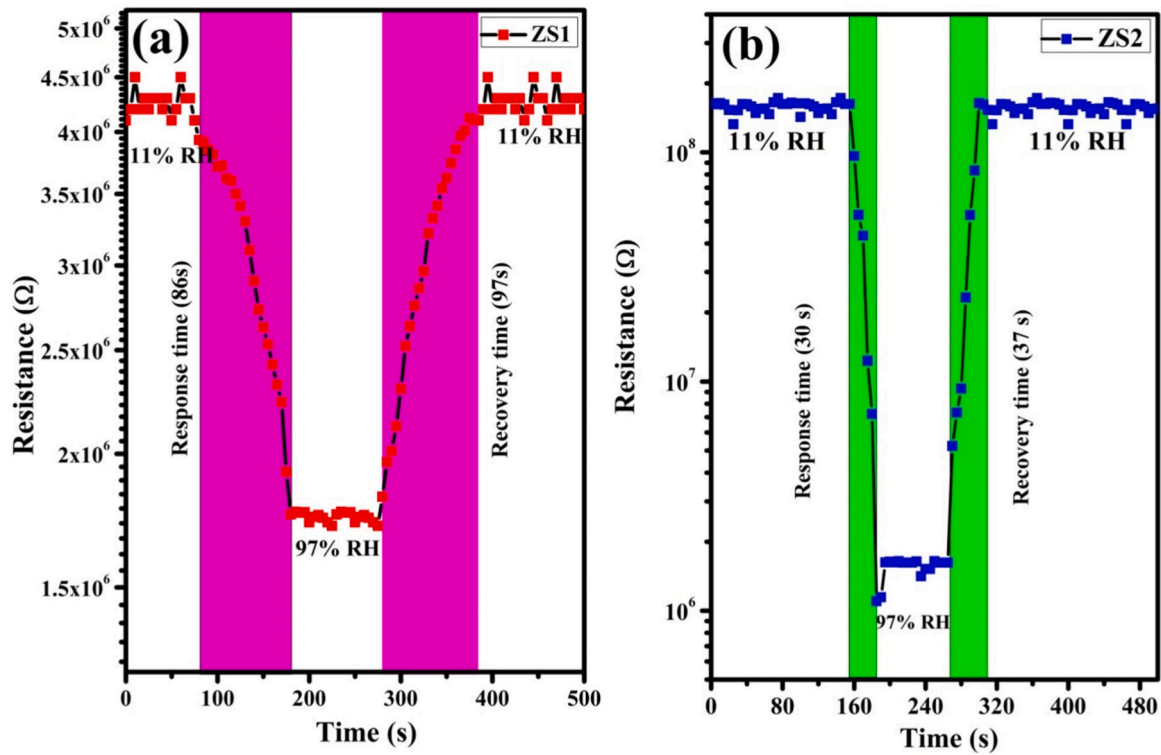


Fig. 13. Plot of response and recovery time of synthesized Zn-SnO₂ NPs sensor with change in relative humidity; (a) Uncalcinated (ZS1) (b) Calcinated (ZS2) Zn-SnO₂ NPs.

Table 2

Comparison of humidity sensing parameters of various nanomaterials with Zn-SnO₂ NPs.

Material	Response time (s)	Recovery time (s)	Sensing response (%)	Sensing range (% RH)	Reference
Ni-SnO ₂	54	84	78%	0–100	[2]
Bi ₂ O ₃	261	289	87%	15–100	[4]
Sn-ZnO	230	30	80%	40–90	[50]
Fe ₂ O ₃	29	630	99%	11–92	[51]
SnO ₂	140	70	99%	10–90	[52]
In-SnO ₂ (ITO)	58	45	90%	10–90	[53]
SnO ₂	32	42	99%	11–96	[54]
ZnO	60	3	88%	10–90	[55]
Zn-SnO ₂	30	37	93%	11–97	Present work

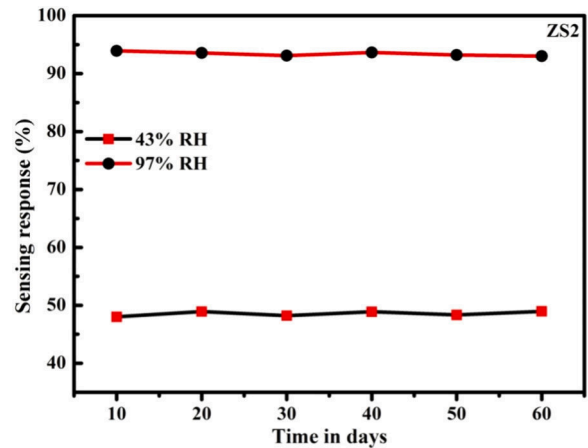


Fig. 15. Plot of stability testing of the calcinated Zn-SnO₂ NPs sensor for every 10 days at 43% RH and 97% RH.

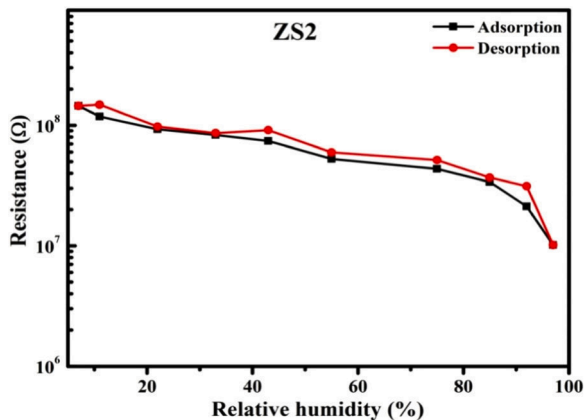


Fig. 14. Humidity hysteresis characteristic curve of calcinated Zn-SnO₂ NPs.

characterization of zinc-doped tin oxide nanoparticles (Zn-SnO₂ NPs) with controlled properties for humidity sensing applications. The calcination process significantly influenced the NPs structural and morphological features, resulting in a cauliflower-like morphology with enhanced porosity. The X-ray diffraction confirmed the tetragonal rutile structure; and UV-Visible absorption and photoluminescence spectra indicated the presence of oxygen vacancies, which is crucial for humidity sensing. Electrical studies revealed the semiconducting behavior of the NPs, with calcination affecting their electrical conductivity. Notably, humidity sensing experiments highlighted the outstanding performance of the calcined NPs, with a remarkable breakthrough response of 93% and a rapid response time of 30 seconds, surpassing the uncalcined sample. The sensing mechanism involving physisorption, chemisorption, and capillary condensation of water molecules on the

NPs surface was validated, providing insights into their humidity sensing behavior. Moreover, the stability test demonstrated consistent and highly stable humidity sensing response over two month, confirming the NPs potential for practical applications. In summary, zinc-doped tin oxide NPs exhibit exceptional humidity sensing characteristics, making them promising candidates for advanced humidity sensors in various industries. The controlled calcination process played a critical role in optimizing their sensing performance and offers new opportunities for designing high-performance humidity sensors. These outcomes mark a significant advancement in the field of nanomaterial-based sensor research and pave the way for the development of reliable and efficient humidity sensing devices with broad applications in environmental monitoring, food processing, and agriculture, among others.

Funding

This work supported by Vision Group on Science and Technology, Government of Karnataka, India [RGS/F 892, 2021] and Vijayanagara Sri Krishnadevaraya University, Ballari [Seed money grant, 1980, 2021].

CRediT authorship contribution statement

Hanumantagouda Basavanagoudra: Writing – original draft, Methodology, Data curation, Conceptualization. **Vijayakumar D Jangannanavar:** Validation, Formal analysis. **Sunilkumar Anegundi:** Validation, Resources, Formal analysis. **Chetan Basavalingappa:** Validation, Formal analysis. **Mallikarjun K Patil:** Resources, Formal analysis. **Sanjeev R Inamdar:** Supervision, Resources. **Kotresh M Goudar:** Writing – review & editing, Supervision, Resources, Formal analysis.

Declaration of Competing Interest

The authors declare that they have no known competing financial interests or personal relationships that could have appeared to influence the work reported in this paper

Data availability

Data will be made available on request.

Acknowledgement

The authors acknowledge the support from the Laser Spectroscopy Laboratory and University Science Instrumentation Centre, Karnatak University, Dharwad. The authors acknowledge DST PURSE Laboratory, Mangalore University, Mangalagangothri for providing the FE-SEM facility. The authors acknowledge the TEM facility, funded by a TPF Nano-mission, GOI project at Centre for Nano and Soft Matter Sciences, Bengaluru. The authors acknowledge chairman, Department of Physics, Indian Institute of Science, Bengaluru supporting for humidity sensing studies. Further, author HB acknowledge Government of Karnataka for providing OBC fellowship.

References

- [1] K. Shinghal, A. Noor, N. Srivastava, Intelligent humidity sensor for wireless sensor network agricultural application, *Int. J. Wirel. Mob. Netw.* 3 (2011) 118–128, <https://doi.org/10.2139/ssrn.2928565>.
- [2] V. Manikandan, I. Petrila, S. Vignesvelan, R.S. Mane, B. Vasile, R. Dharmavarapu, S. Lundgaard, S. Juodkazis, J. Chandrasekaran, A reliable chemiresistive sensor of nickel-doped tin oxide (Ni-SnO₂) for sensing carbon dioxide gas and humidity, *RSC Adv.* 10 (2020) 3796–3804, <https://doi.org/10.1039/C9RA09579A>.
- [3] A.A. Yadav, A.C. Lokhande, J.H. Kim, C.D. Lokhande, Improvement in CO₂ sensing characteristics using Pd nanoparticles decorated La₂O₃ thin films, *J. Ind. Eng. Chem.* 49 (2017) 76–81, <https://doi.org/10.1016/j.jiec.2017.01.009>.
- [4] F. Tudorache, I. Petrila, S.C. Bota, C. Constantinescu, M. Praisler, Humidity sensors applicative characteristics of granularized and porous Bi₂O₃ thin films prepared by oxygen plasma-assisted pulsed laser deposition, *Superlattices Micro* 77 (2015) 276–285, <https://doi.org/10.1016/j.spmi.2014.11.022>.
- [5] V. Kumar, V. Chauhan, J. Ram, R. Gupta, S. Kumar, P. Chaudhary, B.C. Yadav, S. Ojha, I. Sulania, R. Kumar, Study of humidity sensing properties and ion beam induced modifications in SnO₂-TiO₂ nanocomposite thin films, *Surf. Coat. Technol.* 392 (2020) 125768, <https://doi.org/10.1016/j.surfcoat.2020.125768>.
- [6] S.K. Shukla, S.K. Shukla, P.P. Govender, E.S. Agorku, A resistive type humidity sensor based on crystalline tin oxide nanoparticles encapsulated in polyaniline matrix, *Microchim Acta* 183 (2016) 573–580, <https://doi.org/10.1007/s00604-015-1678-2>.
- [7] A.S. Ismail, M.H. Mamat, M.F. Malek, M.M. Yusoff, R. Mohamed, N.D. Md Sin, A. B. Suriani, M. Rusop, Heterogeneous SnO₂/ZnO nanoparticulate film: Facile synthesis and humidity sensing capability, *Mater. Sci. Semicond. Process.* 81 (2018) 127–138, <https://doi.org/10.1016/j.mssp.2018.03.022>.
- [8] S. Hu, H. Chen, G. Fu, F. Meng, Humidity sensitive properties of K⁺-doped SnO₂-LiZnVO₄, *Sens. Actuators B Chem.* 134 (2) (2008) 769–772, <https://doi.org/10.1016/j.snb.2008.06.033>.
- [9] M. Parthibavarman, V. Hariharan, C. Sekar, High-sensitivity humidity sensor based on SnO₂ nanoparticles synthesized by microwave irradiation method, *Mater. Sci. Eng. C* 31 (2011) 840–844, <https://doi.org/10.1016/j.msec.2011.01.002>.
- [10] V. Manikandan, X. Li, R.S. Mane, J. Chandrasekaran, Room Temperature Gas Sensing Properties of Sn-Substituted Nickel Ferrite (NiFe₂O₄) Thin Film Sensors Prepared by Chemical Co-Precipitation Method, *J. Electron. Mater.* 47 (2018) 3403–3408, <https://doi.org/10.1007/s11664-018-6295-5>.
- [11] D. Zhang, H. Chang, R. Liu, Humidity-Sensing Properties of One-Step Hydrothermally Synthesized Tin Dioxide-Decorated Graphene Nanocomposite on Polyimide Substrate, *J. Electron. Mater.* 45 (2016) 4275–4281, <https://doi.org/10.1007/s11664-016-4630-2>.
- [12] H. Bai, H. Guo, C. Feng, J. Wang, B. Liu, Z. Xie, F. Guo, D. Chen, R. Zhang, Y. Zheng, A room-temperature chemiresistive NO₂ sensor based on one-step synthesized SnO₂ nanospheres functionalized with Pd nanoparticles and rGO nanosheets, *Appl. Surf. Sci.* 575 (2022) 151698, <https://doi.org/10.1016/j.apsusc.2021.151698>.
- [13] S.A. Khan, S. Kanwal, K. Rizwan, S. Shahid, Enhanced antimicrobial, antioxidant, in vivo antitumor and in vitro anticancer effects against breast cancer cell line by green synthesized un-doped SnO₂ and Co-doped SnO₂ nanoparticles from Clerodendrum inerme, *Microb. Pathog.* 125 (2018) 366–384, <https://doi.org/10.1016/j.micpath.2018.09.041>.
- [14] S. Blessi, A. Manikandan, S. Anand, M.M.L. Sonia, V.M. Vinose, A.M. Alosaimi, A. Khan, M.A. Hussein, A.M. Asiri, Enhanced electrochemical performance and humidity sensing properties of Al³⁺ substituted mesoporous SnO₂ nanoparticles, *Phys. E: Low-Dimens. Syst. Nanostruct.* 133 (2021) 114820, <https://doi.org/10.1016/j.physe.2021.114820>.
- [15] R. Yoo, A.T. Güntner, Y. Park, H.J. Rim, H.S. Lee, W. Lee, Sensing of acetone by Al-doped ZnO, *Sens. Actuators B Chem.* 283 (2019) 107–115, <https://doi.org/10.1016/j.snb.2018.12.001>.
- [16] P.M. Bulemo, D.H. Kim, I.D. Kim, Controlled synthesis of electrospun hollow Pt-loaded SnO₂ microbelts for acetone sensing, *Sens. Actuators B Chem.* 344 (2021) 130208, <https://doi.org/10.1016/j.snb.2021.130208>.
- [17] S. Nundy, T.Y. Eom, K.Y. Song, J.S. Park, H.J. Lee, Hydrothermal synthesis of mesoporous ZnO microspheres as NO_x gas sensor materials-Calcination effects on microstructure and sensing performance, *Ceram. Int.* 46 (2020) 19354–19364, <https://doi.org/10.1016/j.ceramint.2020.04.278>.
- [18] L. Luo, M. Yuan, H. Sun, T. Peng, T. Xie, Q. Chen, J. Chen, Effect of calcination temperature on the humidity sensitivity of TiO₂/graphene oxide nanocomposites, *Mater. Sci. Semicond. Process.* 89 (2019) 186–193, <https://doi.org/10.1016/j.mssp.2018.09.019>.
- [19] Q. Zhou, L. Xu, A. Umar, W. Chen, R. Kumar, Pt nanoparticles decorated SnO₂ nanoneedles for efficient CO gas sensing applications, *Sens. Actuators B Chem.* 256 (2018) 656–664, <https://doi.org/10.1016/j.snb.2017.09.206>.
- [20] R. Vasanthapriya, N. Neelakandeswari, N. Rajasekaran, K. Uthayarani, M. Chitra, S.S. Kumar, Synthesis and characterisation of SnO₂ nanostructures for Dye-Sensitized Solar Cells, *Mater. Lett.* 220 (2018) 218–221, <https://doi.org/10.1016/j.matlet.2018.02.118>.
- [21] A. Kar, J. Olszówka, S. Sain, S.R.I. Sloman, O. Montes, A. Fernández, S.K. Pradhan, A.E.H. Wheatley, Morphological effects on the photocatalytic properties of SnO₂ nanostructures, *J. Alloy. Compd.* 810 (2019) 151718, <https://doi.org/10.1016/j.jallcom.2019.151718>.
- [22] R. Ramarajan, M. Kovendhan, K. Thangaraju, D.P. Joseph, R.R. Babu, Facile deposition and characterization of large area highly conducting and transparent Sb-doped SnO₂ thin film, *Appl. Surf. Sci.* 487 (2019) 1385–1393, <https://doi.org/10.1016/j.apsusc.2019.05.079>.
- [23] E. Pargoletti, U.H. Hossain, I.D. Bernardo, H. Chen, T.T. Phu, G.L. Chiarello, J. L. Duffin, V. Pifferi, A. Tricoli, G. Cappelletti, Engineering of SnO₂-Graphene Oxide Nanohetero junctions for Selective Room-Temperature Chemical Sensing and Optoelectronic Devices, *ACS Appl. Mater. Interfaces* 12 (2020) 39549–39560, <https://doi.org/10.1021/acsami.0c09178>.
- [24] S. Wang, W. Yu, C. Cheng, T. Zhang, M. Ge, Y. Sun, N. Dai, Fabrication of mesoporous SnO₂ nanocubes with superior ethanol gas sensing property, *Mater. Res. Bull.* 89 (2017) 267–272, <https://doi.org/10.1016/j.materresbull.2017.02.010>.
- [25] J. Zhang, C. Zhao, P.A. Hu, Y.Q. Fu, Z. Wang, W. Cao, B. Yang, F. Placido, A UV light enhanced TiO₂/graphene device for oxygen sensing at room temperature, *RSC Adv.* 3 (2013) 22185–22190, <https://doi.org/10.1039/C3RA43480J>.

- [26] R. Djamil, K. Aicha, A. Souifi, D. Faycal, Effect of annealing time on the performance of tin oxide thin films ultraviolet photodetectors, *Thin Solid Films* 623 (2017) 1–7, <https://doi.org/10.1016/j.tsf.2016.12.035>.
- [27] S. Chen, X. Zhao, H. Xie, J. Liu, L. Duan, X. Ba, J. Zhao, Photoluminescence of undoped and Ce-doped SnO₂ thin films deposited by sol-gel-dip-coating method, *Appl. Surf. Sci.* 258 (2012) 3255–3259, <https://doi.org/10.1016/j.apsusc.2011.11.077>.
- [28] D.Y.T. Martínez, R.C. Pérez, G.T. Delgado, O.Z. Angel, Undoped tin oxide thin films obtained by the sol gel technique, starting from a simple precursor solution, *J. Mater. Sci. Mater. Electron* 22 (2011) 684–689, <https://doi.org/10.1007/s10854-010-0196-6>.
- [29] C.Y. Tsay, S.C. Liang, Fabrication of p-type conductivity in SnO₂ thin films through Ga doping, *J. Alloy. Compd.* 622 (2015) 644–650, <https://doi.org/10.1016/j.jallcom.2014.10.003>.
- [30] F. Zhang, Y. Lian, M. Gu, J. Yu, T.B. Tang, Static and Dynamic Disorder in Metastable Phases of Tin Oxide, *J. Phys. Chem. C* 121 (2017) 16006–16011, <https://doi.org/10.1021/acs.jpcc.7b04477>.
- [31] H. Giefers, F. Porsch, G. Wortmann, Kinetics of the Disproportionation of SnO, *Solid State Ion.* 176 (2005) 199–207, <https://doi.org/10.1016/j.ssi.2004.06.006>.
- [32] M. Premkumar, S. Vadivel, Effect of annealing temperature on structural, optical and humidity sensing properties of indium tin oxide (ITO) thin films, *J. Mater. Sci.: Mater. Electron* 28 (2017) 8460–8466, <https://doi.org/10.1007/s10854-017-6566-6>.
- [33] X. Zhong, B. Yang, X. Zhang, J. Jia, G. Yi, Effect of calcining temperature and time on the characteristics of Sb-doped SnO₂ nanoparticles synthesized by the sol-gel method, *Particuology* 10 (2012) 365–370, <https://doi.org/10.1016/j.partic.2011.09.005>.
- [34] V.K. Tomer, S. Duhan, A facile nanocasting synthesis of mesoporous Ag-doped SnO₂ nanostructures with enhanced humidity sensing performance, *Sens. Actuators B Chem.* 223 (2016) 750–760, <https://doi.org/10.1016/j.snb.2015.09.139>.
- [35] Q. Diao, C. Yin, Y. Guan, X. Liang, S. Wang, Y. Liu, Y. Hu, H. Chen, G. Lu, The effects of sintering temperature of MnCr₂O₄ nanocomposite on the NO₂ sensing property for YSZ-based potentiometric sensor, *Sens. Actuators B Chem.* 177 (2013) 397–403, <https://doi.org/10.1016/j.snb.2012.11.040>.
- [36] S.M. Ingole, S.T. Navale, Y.H. Navale, D.K. Bandgar, F.J. Stadler, R.S. Mane, N. S. Ramgir, S.K. Gupta, D.K. Aswal, V.B. Patil, Nanostructured Tin Oxide Films: Physical Synthesis, Characterization, and Gas Sensing Properties, *J. Colloid Interface Sci.* 493 (2017) 162–170, <https://doi.org/10.1016/j.jcis.2017.01.025>.
- [37] M.A. Farruck, P. Tan, R. Adnan, Surfactant-controlled aqueous synthesis of SnO₂ nanoparticles via the hydrothermal and conventional heating methods, *Turk. J. Chem.* 36 (2010) 303–314, <https://doi.org/10.3906/kim-1001-466>.
- [38] C. Guo, Y. Xin, Y. Liu, B. Na, W. Meng, X. Zhang, X. Cheng, L. Huo, T. Wang, Y. Xu, Noncontact sensing for water area scanning identification based on Ho₂O₃/GO humidity sensor, *Sens. Actuators B Chem.* 385 (2023) 133683, <https://doi.org/10.1016/j.snb.2023.133683>.
- [39] X. Song, L. Gao, Facile Synthesis and Hierarchical Assembly of Hollow Nickel Oxide Architectures Bearing Enhanced Photocatalytic Properties, *J. Phys. Chem. C* 112 (2008) 15299–15305, <https://doi.org/10.1021/jp804921g>.
- [40] K. Varunkumar, R. Hussain, G. Hegde, A.S. Ethiraj, Effect of calcination temperature on Cu doped NiO nanoparticles prepared via wet-chemical method: Structural, optical and morphological studies, *Mater. Sci. Semicond. Process.* 66 (2017) 149–156, <https://doi.org/10.1016/j.mssp.2017.04.009>.
- [41] P.P. Dorneanu, A. Airinei, M. Grigoras, N. Fifer, L. Sacarescu, N. Lupu, L. Stoleriu, Structural, optical and magnetic properties of Ni doped SnO₂ nanoparticles, *J. Alloy. Compd.* 668 (2016) 65–72, <https://doi.org/10.1016/j.jallcom.2016.01.183>.
- [42] K. Sakthiraj, K. Balachandrakumar, Influence of Ti addition on the room temperature ferromagnetism of tin oxide (SnO₂) nanocrystal, *J. Magn. Magn. Mater.* 395 (2015) 205–212, <https://doi.org/10.1016/j.jmmm.2015.07.083>.
- [43] H. Yu, C. Guo, X. Zhang, X. Cheng, Y. Xu, S. Gao, L. Huo, Tailoring Oxygen Vacancy of Co₃O₄ Microcubes by Annealing Co₃[Co(CN)₆]₂ Template in Air for Ultrasensitive Humidity Mapping, *Small Struct.* 3 (2) (2022) 2100166, <https://doi.org/10.1002/sstr.202100166>.
- [44] J.H. Lee, Gas sensors using hierarchical and hollow oxide nanostructures: Overview, *Sens. Actuators B Chem.* 140 (2009) 319–336, <https://doi.org/10.1016/j.snb.2009.04.026>.
- [45] S. Mehraj, M.S. Ansari, A.A. Al-Ghamdi, Alimuddin, Annealing dependent oxygen vacancies in SnO₂ nanoparticles: Structural, electrical and their ferromagnetic behavior, *Mater. Chem. Phys.* 171 (2016) 109–118, <https://doi.org/10.1016/j.matchemphys.2015.12.006>.
- [46] S. Manjunatha, T. Machappa, Y.T. Ravikiran, B. Chethan, A. Sunilkumar, Polyaniline based stable humidity sensor operable at room temperature, *Phys. B: Condens. Matter* 561 (2019) 170–178, <https://doi.org/10.1016/j.physb.2019.02.063>.
- [47] G. Singh, R. Thangaraj, R.C. Singh, Effect of crystallite size, Raman surface modes and surface basicity on the gas sensing behavior of terbium-doped SnO₂ nanoparticles, *Ceram. Int.* 42 (2016) 4323–4332, <https://doi.org/10.1016/j.ceramint.2015.11.111>.
- [48] V.R. Khadse, S. Thakur, K.R. Patil, P. Patil, Humidity-sensing studies of cerium oxide nanoparticles synthesized by non-isothermal precipitation, *Sens. Actuator B Chem.* 203 (2014) 229–238, <https://doi.org/10.1016/j.snb.2014.06.107>.
- [49] C. Guo, X. Dong, X. Zhang, X. Cheng, Q. Li, Y. Sun, W. Liu, L. Huo, Y. Xu, Controllable construction of Ho₂O₃ nanomaterials with different dimensions (1D, 2D, and 3D) for real time monitoring human breathing and body surface humidity detection, *J. Mater. Chem. A* 9 (2021) 11632, <https://doi.org/10.1039/D1TA00631B>.
- [50] A.S. Ismail, M.H. Mamat, N.D.Md Sin, M.F. Malek, A.S. Zoofakar, A.B. Suriani, A. Mohamed, M.K. Ahmad, M. Rusop, Fabrication of hierarchical sn-doped ZnO nanorod arrays through sonicated Sol-Gel immersion for room temperature, resistive-type humidity sensor applications, *Ceram. Int.* 42 (8) (2016) 9785–9795, <https://doi.org/10.1016/j.ceramint.2016.03.071>.
- [51] U.V. Patil, C.S. Rout, D.J. Late, Impedimetric humidity sensor based on α-Fe₂O₃ nanoparticles, *Adv. Dev. Mat.* 1 (3) (2015) 88–92, <https://doi.org/10.1080/20550308.2015.1133101>.
- [52] J.S. Tawale, G. Gupta, A. Mohan, A. Kumar, A.K. Srivastava, Growth of thermally evaporated SnO₂ nanostructures for optical and humidity sensing application, *Sens. Actuator B Chem.* 201 (2014) 369–377, <https://doi.org/10.1016/j.snb.2014.04.099>.
- [53] B.M. Babu, S. Vadivel, High performance humidity sensing properties of indium tin oxide (ITO) thin films by sol-gel spin coating method, *J. Mater. Sci. Mater. Electron* 28 (2017) 2442–2447, <https://doi.org/10.1007/s10854-016-5816-3>.
- [54] W. Li, J. Liu, C. Ding, G. Bai, J. Xu, Q. Ren, J. Li, Fabrication of Ordered SnO₂ Nanostructures with Enhanced Humidity Sensing Performance, *Sensors* 17 (10) (2017) 2392, <https://doi.org/10.3390/s17102392>.
- [55] N.M. Kiasari, S. Soltanian, B. Gholamkhash, P. Servati, Room temperature ultra-sensitive resistive humidity sensor based on single zinc oxide nanowire, *Sens. Actuator A Phys.* 182 (2012) 101–105, <https://doi.org/10.1016/j.sna.2012.05.041>.
- [56] S. Pratibha, B. Chethan, Y.T. Ravikiran, N. Dhananjaya, V. Jagadeesh Angadi, Enhanced humidity sensing performance of Samarium doped Lanthanum Aluminate at room temperature, *Sens. Actuator A Phys.* 304 (2020) 111903, <https://doi.org/10.1016/j.sna.2020.111903>.

Hanumantagouda Basavanagoudra is a research student in the Department of Physics at Vijayanagara Sri Krishnadevaraya University, Ballari, Karnataka, India. He earned his postgraduate M.Sc. degree in Physics from the same university in 2016. His current research interests encompass materials science, the development of chemical and bio-sensors, and light-harvesting devices. He has contributed to the field by publishing six papers in peer-reviewed journals.

Kotresh M. Goudar is an Assistant Professor of Physics at Vijayanagara Sri Krishnadevaraya University, Ballari, Karnataka, India. He earned his postgraduate M.Sc. degree in Physics in 2012 and completed his Ph.D. in molecular fluorescence spectroscopy from Karnatak University, Dharwad, in 2017. His research has primarily focused on the spectroscopic investigation of nanomaterials involving organic dyes and biomolecules, with applications in bio-chemical and light-harvesting domains. Currently, his research interests span materials science, fluorescence spectroscopy, and computational physics. He has published 29 papers in peer-reviewed journals and contributed to four book chapters. He is currently supervising four students for their PhD studies.

CHAPTER 6

Design of nanostructured biosensors based on organic and other composite materials

B. Chethan Ph D^{1,*}, **V. Prasad**¹, **A. Sunilkumar**², **S. Thomas**³,
A. Sreeharsha^{4,5}

¹Department of Physics, Indian Institute of Science, Bangalore, Karnataka, India

²Department of Physics, Ballari Institute of Technology and Management, Ballari, Karnataka, India

³International and Inter University Centre for Nanoscience and Nanotechnology, Mahatma Gandhi University, Kottayam, Kerala, India

⁴Department of Pharmaceutical Sciences, College of Clinical Pharmacy, King Faisal University, Al-Ahsa, Saudi Arabia

⁵Department of Pharmaceutics, Vidya Siri College of Pharmacy, Bengaluru, Karnataka, India

*Dr. CHETHAN B. e-mail address: chethanbchetu@gmail.com

6.1 Introduction to sensors

A receptor–transducer sensor device is used to convert a biological response into an electrical signal. The design and development of biosensors have attained a greater interest nowadays because biosensors find widespread applications in the medical field, diagnosis of the disease, ecology monitoring, and maintaining the quality of food, drug, and water. The biosensing devices attained a greater demand and face many challenges to fabricate the sensing device with better sensitivity, a lower limit of detection, good stability, quick response time, reduced device size, and simple operation. These challenges can be fulfilled by the interphase of chemical and morphological properties of the nanomaterials with the sensor technology. The nanomaterials from zero to three dimensions are having advantageous properties like high surface area, enhanced conductivity, and tunable electrical and mechanical properties making these nanomaterials potential candidates to fabricate biosensors. Among the nanomaterials, nanoparticles, nanowires, and nanorods find advantageous properties because of their high stability, high carrier capacity, high detection limit, large surface area, active sites, and more thermal conductivity. The ferrites, polymers, metal, metal oxides, carbon-based materials, and their composites are widely used in the fabrication of

biosensors. In this chapter, the evolution of the sensors, types of sensors, and biosensor types are discussed deliberately. This chapter provides different methods which have been used in the synthesis and fabrication of biosensors using nanomaterials.

In this modern world, as awareness of man increased to lead a sophisticated life, the need for science and technology has gained momentum (Amrutha et al., 2021; Chethan et al., 2019; Gleiter, 2000; Hareesha & Manjunatha, 2021; Hareesha et al., 2021; 2021; Manjunatha et al., 2014; Pal et al., 2011; Pushpanjali et al., 2021; Tigari & Manjunatha, 2019; Manjunatha, 2020). Nowadays civilized people depend more on the gadgets like computers, Xerox machines, air conditioning, cell phones, television, smoke detectors, and refrigerators. Many of these gadgets work with the help of sensors. The term sensor refers to a device or module that assists in detecting changes in physical quantities, such as pressure, heat, humidity, movement, force, and an electrical quantity like current, and then turns these physical quantities into signals that can be monitored and analyzed. Sensors are the brains of measuring systems. An ideal sensor should have the following qualities: high resolution, reproducibility, repeatability, range, drift, calibration, sensitivity, selectivity, and linearity (Chethan et al. 2022, 2023; Chethan et al., 2018; Chethan Ramana et al., 2019; El-Denglawey et al., 2021; El-Denglawey Manjunath et al., 2021; Manjunatha et al., 2019; Pratibha & Chethan, 2022; Pratibha et al., 2020; Ravikiran & Chethan, 2022; Rupashree et al., 2021; Shanawad Chethan et al., 2023; Shanawad et al., 2023; Sunilkumar et al., 2023).

Today, we benefit from science and technological advancements that make our lives run more smoothly. We frequently rely on various devices that help us to interact with the physical environment, such as television remote controls, smoke detectors, infrared (IR) thermometers, lamp switches, and fans. Due to numerous applications, including environmental and food quality monitoring, medical diagnostics and health care, automotive and industrial manufacture, as well as space, defense, and security, the advancement of sensor technology has assumed increasing significance (Dincer et al., 2019; Ensafi et al., 2011; Ensafi, 2019; Theavenot et al., 2001).

6.1.1 Classification of sensors

Depending on the physical quantity and analyte to be measured, sensors can be broadly categorized into a number of categories, which include: (1) energy source, (2) physical contact, (3) comparability, (4) analog and digital sensors, and (5) signal detection. Based on these quantities, sensors are broadly classified as follows (Khanna, 2012; White, 1987).

Energy source: Two types of sensors are employed based on energy sources:

1. **Active and passive sensors:** Active sensors, such as microphones, thermistors, strain gauges, and capacitive and inductive sensors, require an external energy source. These kinds of sensors are known as parametric sensors (the output depends on the parameter). Thermocouples, piezoelectric sensors, and photodiodes are examples of passive sensors that produce signals without requiring external energy. These sensors are referred to as self-generating sensors.
2. **Physical contact:** Based on physical contact, sensors can be classified as contact or noncontact.
3. **Contact and noncontact sensors:** Contact sensors, like temperature sensors, need to make physical touch with their stimulus, whereas non-contact sensors include optical, magnetic, and infrared (IR) thermometers.
4. **Comparability sensors can be either absolute or relative.**
5. **Absolute and relative sensors:** Thermistors and strain gauges are examples of absolute sensors. Relative sensors, such as a thermocouple that measures temperature differences and a pressure gauge that measures pressure, relative to atmospheric pressure, perceive the stimulus in relation to a fixed or changing reference.
6. **Analog and digital sensors:** Sensors come in two varieties: analog and digital. An analog sensor converts a measured physical quantity into an analog form (continuous in time). This group of analog sensors includes thermocouples, strain gauges, and resistance temperature detectors (RTDs). Pulses are the output that a digital sensor produces. Encoders fall under the category of digital sensors.
7. **Signal detection:**

The basic classification of sensors based on signal detection and transformation of information is as follows:

- a. **Physical sensors:** A physical quantity is measured by a physical sensor, which then transforms into a signal that the user can recognize. The force, acceleration, rate of flow, mass, volume, density, and pressure are just a few of the environmental changes that these sensors can identify. The use of physical sensors has increased significantly in the biomedical industry, especially with the development of novel measurement technologies and the improvement of microelectromechanical system technology for the creation of more precise and smaller sensors.
- b. **Thermal sensors:** A thermal sensor is a device that measures the temperature of an environment and converts the measured data into electronic data for recording or monitoring temperature change signals. Thermistors, RTDs, and thermocouples are a few types of temperature sensors.
- c. **Biological sensors:** Biological sensors keep an eye on biomolecular interactions like those involving antibodies and antigens, DNA and enzymatic reactions, or cellular communication. The abbreviated form of the term “biosensors” refers to biological sensors.
- d. **Chemical sensors:** The International Union of Pure and Applied Chemistry defines a chemical sensor as a device that converts chemical information into an analytically useful signal ranging from the concentration of a particular sample component to total composition analysis. Chemical sensors are used to keep an eye on the quantity or activity of the relevant chemical species in the gaseous or liquid phase. In addition, they are used to monitor assays for organophosphorus chemicals, food and drug analyses, and environmental pollution. They can be utilized for clinical diagnostic applications as well.

6.1.2 Biosensor

A biosensor is a tool or probe that combines an electronic component with a biological element, like an enzyme or antibody, to produce a quantifiable signal. Information about a physiological change or the presence of different chemical or biological components in the environment is detected, recorded, and transmitted by the electronic component. Biosensors are available in a variety of sizes and designs, and they have the ability to measure and detect even very low quantities of certain diseases, harmful chemicals, and pH values. Certain static and dynamic requirements are required to develop a highly effective and capable biosensor

system. These requirements allow for the optimization of the biosensors' performance for commercial applications.

6.1.2.1 Constituents of biosensors

The main constituents of biological sensors comprise of:

1. **Analyte:** A material of interest whose components are being determined or detected is an analyte. The biological constituents may be in the form of glucose, lactose, ammonia, and glucose (Bhalla et al., 2016).
2. **Transducer:** One crucial component of a biosensor is the transducer which is a device that converts energy from one form to another. It transforms the biorecognition event into an electrical signal that is quantifiable and connected to the quantity or the presence of a chemical or biological target.
3. **Bioreceptor:** Bioreceptors are biological components such as enzymes, cells, aptamers, deoxyribonucleic acid (DNA or RNA), and antibodies that are capable of recognizing the target substrate. Biorecognition is the process of producing a signal when a bioreceptor and an analyte interact.
4. **Electronics:** To get the signal ready for the display, it is processed. Amplification and digitalization take place on the electrical signals collected from the transducer. The display unit quantifies the signals that have been processed.
5. **Display:** The display unit is made up of a user interpretation system, such as a computer or a printer, that provides the output so that the user can read and understand the appropriate response according to the end-user requirement.

6.1.2.2 Evolution of biosensors

Leland Charles Clark Jr., the father of the biosensors, reported about the components of the biosensors in this work in the year 1956. He fabricated the electrode which is possible to determine the oxygen content in the blood. Later in 1962, Clark reported about the amperometric enzyme electrode for glucose detection. In the upcoming year 1967, Updike and Hicks modified the Clarks work and find out the first functional enzyme electrode for oxygen sensor. After, in 1969 Guilbault and Montalvo depicted the first urea detection sensor based on potentiometric enzyme electrode. In the year 1973, Guilbault and Lubrano fabricated the hydro-

gen peroxide detection sensor based on the lactate enzyme sensor. In this way, many researchers have fabricated many biosensors in these years.

6.1.2.3 Characteristics of biosensors

There are some static and dynamic conditions that must be met to create a highly effective and powerful biosensor system. These requirements allow for the performance of the biosensors to be enhanced for commercial applications which are as follows.

Selectivity: When choosing a bioreceptor for a biosensor, selectivity is an important attribute to be taken into account. A bioreceptor may identify a specific target analyte molecule in a sample that contains undesired pollutants and admixture compounds.

Sensitivity: It is defined as the smallest amount of analyte that can be accurately detected or recognized in the fewest steps at low concentrations (ng mL^{-1} or fg mL^{-1}) to confirm the presence of analyte traces in the sample.

Linearity: Linearity helps ensure that the findings of measurements are accurate. The substrate concentration can be detected at higher levels when linearity (straight line) is increased.

Reproducibility: Reproducibility is defined by precision (similar output when the sample is measured multiple times) and accuracy (the ability of a sensor to generate a mean value that is more closely related to the actual value when the sample is sampled multiple times). When the same sample is analyzed more than once, the biosensor's ability to produce the same results is what matters.

Stability: One essential quality in biosensor applications where ongoing monitoring is necessary is stability. Stability is the degree to which the biosensing equipment is vulnerable to environmental perturbations both inside and outside. The affinity of the bioreceptor (the degree of analyte binding to the bioreceptor) and bioreceptor degradation with time are the variables that determine stability.

Response period: It is playing a very crucial role in selecting the best sensor which is having short response time and recovery time factors which implies its effectiveness.

6.1.3 Classification of biosensors based on bioreceptors

Bioreceptors are regarded as the key element in the development of biosensors, as it was previously discussed. Enzymatic biosensors are the

most prevalent type of biosensor. Other types include immunosensors, which have high specificity and sensitivity and are particularly useful in diagnosis, aptamer- or nucleic acid-based biosensors, which have high specificity for microbial strains and nucleic acid-containing analytes, and microbial or whole-cell biosensors.

The second division is based on the transducer, and the sensors are divided into the following groups: electrochemical (which is further divided into potentiometric, amperometric, impedance, and conductometric groups), electronic biosensor, thermal biosensor, optical, and mass-based or gravimetric. Bioreceptor–analyte combinations fall under a different group and are few. Various classifications are made based on the technology (nano, surface plasmon resonance [SPR], biosensors-on-chip [lab-on-chip], electrometers, and deployable) and the detection sensor systems (optical, electrical, electronic, thermal, mechanical, and magnetic).

According to the quantity of interactions between analyte and bioreceptor, transducers produce visual or electrical signals. The working principle divides transducers into the following major categories: electrochemical, optical, thermal, electronic, and gravimetric transducers. Depending on the input, the output may take the form of a figure, numerical, graphic, or tabular result.

Catalytic and affinity/noncatalytic biosensors are two categories of biosensors that fall under the biorecognition principle. Analyte–bioreceptor interaction leads to the creation of a novel biochemical reaction product in a catalytic biosensor. Enzymes, microbes, tissues, and entire cells are all a part of this biosensor. An irreversible binding between the analyte and the receptor occurs in the case of affinity (noncatalytic) biosensors, and no new biochemical reaction product is produced as a result of the contact. The detection targets for this sort of sensor include antibodies, cell receptors, and nucleic acids.

6.1.3.1 Enzyme-based biosensors

Enzymes are typical biocatalysts that are effective at accelerating the rate of biological reaction. An enzyme-based biosensor's operation is based on the catalytic reaction and binding properties for detecting the target analyte. The process of recognizing analytes involves a number of potential mechanisms: analyte concentration is correlated with decreased enzymatic product formation because

- 1 The analyte is metabolized by the enzyme.

- 2 The analyte activates the enzyme.
- 3 The enzyme concentration is tracked by monitoring the change in enzyme characteristics.

Because enzyme-based biosensors have a long history, different biosensors can be created based on the specificity of the enzyme. Improving the sensitivity, stability, and flexibility of the enzyme structure is costly and difficult due to the exceedingly sensitive nature of the enzyme structure. For enzyme-based biosensors, electrochemical transducers are most frequently employed. Glucose and urea biosensors are the most used enzyme-based biosensors. Due to the long history of enzyme-based biosensors, many biosensors can be developed depending on the specificity of the enzyme (Schroeder & Cavacini, 2010).

6.1.3.2 Antibody-based biosensors

Affinity biorecognition elements like antibodies have been in use for more than 20 years due to their broad variety of applications and potent antigen–antibody interactions. Immunoglobulins (Ig) have a “Y” shape with two heavy and two light polypeptide chains joined by disulfide bonds, and antibodies have this structure as well. Immunosensors are biosensors that rely on the interaction between an antibody and an antigen or that incorporate antibodies as ligands.

There are two types of immunosensors:

- 1 Nonlabeled and
- 2 Labeled.

To precisely identify the antigen–antibody complex, nonlabeled immunosensors are built by calculating the physical alterations brought on by the formation of the complex. An easily detectable label is added in the case of labeled immunosensors (Bhardwaj et al., 2021).

6.1.3.3 Aptamer-based biosensors

The synthetic single-stranded nucleic acids known as aptamers can fold into two-dimensional (2D) and three-dimensional (3D) structures and can bind to target molecules in a selective manner. Because there is less spatial blocking and more surface area on the targets in 2D or 3D structures, their binding efficiency is high. Aptamers are nucleic acid molecules, which makes them physically and functionally stable throughout a wide variety of temperatures and storage conditions. Aptamers may be chemically synthesized, are stable in the pH range of 2–12, and have some

thermal refolding properties, in contrast to antibodies, which must be produced by biological systems. Aptamers also have the advantage of being chemically altered to meet the detection requirements for the target molecule. Fluorescent nanoparticles, like QDs, offer significant advantages over conventional fluorescent dyes for tracking biological systems in real time. Aptamer–QD conjugates were employed to pinpoint targets, including cancer cells, bacterial spores, and proteins (He et al., 2021).

6.1.3.4 Whole-cell-based biosensors

Since microbes (bacteria, fungi, algae, protozoa, and viruses) have the potential to serve as biorecognition components, they are used in the construction of whole-cell-based biosensors. They can manufacture recognition components, such as antibodies, on their own and without the need of extraction and purification. Whole-cell-based biosensors are simple to use and are developing quickly compared to animal or plant cells.

The whole-cell-based biosensor principle states that the cells may interact with a wide range of analytes, display the electrochemical response that a transducer can detect, and communicate. These biosensors were effectively used in environmental monitoring, food analysis, pharmacology, heavy metals, pesticides, detection of organic pollutants, and drug screening due to their high selectivity, good sensitivity, and capability of detection (Riangrunroj et al., 2019).

6.1.3.5 Nanoparticle-based biosensors

A new class of bioreceptor nanomaterials have recently been proposed in addition to the ones mentioned above. Numerous nanomaterials have been used as bioreceptors as a result of advances in nanotechnology and nanoscience. In terms of biosensing applications, nanoparticles offer a wider variety in both transducers and bioreceptors. For instance, nanomaterials based on cerium oxide show catalytic activity that is bioreceptor-friendly and mimics biological processes. Many inorganic materials, including graphene- and CNT-based nanomaterials, noble metal nanoparticles, and quantum dots, have been successfully used as transducers because of their effective transduction capabilities.

6.1.4 Emerging nanomaterials used in the fabrication of biosensors

Through specific self-assembly techniques nanomaterials are synthesized. These nanomaterials have many distinct properties including elec-

trical, mechanical, optical, and magnetic. Nowadays, many nanomaterials are used in drug delivery, bloodless surgery, multifunctional device fabrication, and the fabrication of biosensors. Nanomaterial-based biosensors have attained advanced properties compared to conventional biosensors. These nanobiosensors got epitome sensitivity, stability, and selectivity for the detection of various biomolecules.

Advanced nanomaterials are broadly classified into two types: 2D transition metals and 2D organic polymers.

6.1.4.1 Two-dimensional transition metals

Transition metals are those elements in groups 4–11 in the periodic table. Due to its intriguing characteristics, including a significant surface area and an ultrathin planar structure, transition metal nanomaterials can be used to create biosensors.

6.1.4.1.1 Transition metal chalcogenides

The transition metal dichalcogenides (TMDCs) are a class of 2D graphene cognate/nanosheets that are considered to be advanced. They are typically represented by the formula MX_2 , which stands for a hexagonal layer of a transition metal (M) and two layers of chalcogen (X). They can be made using a variety of techniques, such as mechanical cleavage, epitaxial growth, and chemical vapor deposition (CVD).

Recently, a hybrid structure of blue phosphorene (BlueP)/TMDCs, graphene, and Ag–Au bimetallic sheets was used to create a surface plasmon resonance (SPR)-based biosensor. The study's findings showed that compared to traditional biosensors, the monolayer BlueP/MoS₂ and graphene structure significantly increase the biosensor's sensitivity by 19.73%.

A photoelectrochemical immunosensor for the detection of carcinoembryonic antigen was made using tungsten disulfide (WS₂) nanosheets in a different investigation. The development of a gold nanoparticle (GNP)/WS₂ nanocomposite. According to the performed investigation, the photoelectrochemical responses of WS₂ combined with GNPs were improved (Singh et al., 2020). To achieve photoelectrical immune sensing of the antigen in clinical samples, the nanocomposite was coated onto a glass surface, and then, antibodies specific to carcinoembryonic antigens were immobilized. Additionally, 2D TMDC-de-

rived quantum dots have demonstrated their value in the optical detection of neurotransmitters without the use of antibodies.

6.1.4.1.2 Advanced transition metal oxides

Comparable to TMDCs, transition metal oxide displays a variety of distinctive qualities, such as electrocatalytic and magnetic capabilities, which make them a fantastic choice for use in the construction of biosensors. Due to their distinctive electrical, optical, and chemical properties in comparison to other transition metal oxides (TMOs), manganese oxides are the most widely employed advanced materials in sensing applications. TMOs and 2D transition metal carbides were combined in a recent work to create a biosensor.

For the separation and purification of proteins, a biosensor based on molecularly imprinted polymers has been developed. In this study, the surface of tubular carbon fibers with carboxyl modifications was grown with MnO_2 nanosheets. The outcomes demonstrated that the development of MnO_2 shells increases the quantity of protein-imprinting sites. An electrochemical biosensor was created to detect hydrogen peroxide using a MnO_2 -graphene nanosheet nanocomposite on a glassy electrode. The findings of this study showed that TMOs' electrocatalytic activity is beneficial in the oxidation of H_2O_2 , which results in the catalytic activity of the biosensor at extremely low concentrations. Metal-organic gels were utilized to create copper oxide nanoparticles, another TMO that can mimic peroxidase activity and be used to detect cholesterol and glucose. To create diverse nanostructures for drug delivery, therapy, and the monitoring of various diseases, 2D organic polymers are utilized. These polymers have the ability to mimic a wide range of biomolecules. These sensors have promising applications in clinical medicine, food analysis, environmental analysis, and other fields.

6.1.4.2 Two-dimensional organic polymers

Due to their exceptional qualities, including great flexibility and tunability, ultrathin structure, and adaptability, organic polymers have been employed extensively which are still in demand. Modified metal-organic frameworks and polypeptides are the two organic polymers in this group that are most frequently employed, and they have become the preferred materials for making biosensors.

6.1.4.2.1 Metal–organic frameworks

Inorganic and organic crystalline porous hybrid materials are arranged in metal–organic frameworks (MOFs) to form a cage-like structure. Typically, positively charged metal ions are surrounded by organic linker molecules. A MOF's hollow structure provides an incredibly large internal surface area which greatly increases its utility. Photodynamic treatment for tumors can be performed with organic polymer-based MOFs. By using platinum nanoparticles to magnify the signals, a MOF-based biosensing device has also been created for the detection of neurotransmitters. A MOF containing 2D palladium nanosheets, doxorubicin, and polydopamine was used to create a theranostic nanoplatform to improve biocompatibility. The application of this mixture as a medication delivery component resulted from its impressive photothermal conversion and optoacoustic properties. As a result, these nanoparticles can be used successfully in applications for sensing, imaging, and drug delivery when combined with other materials. They can also be employed for both treatment and bacterial eradication. A biosensor for augmented anti-infective therapy has been created using 2D carbon nanosheets generated from MOFs.

6.1.4.2.2 Black phosphorous

The most thermodynamically stable form of phosphorus is called black phosphorous (BP). Phosphorene, also known as BP, offers important characteristics as a nanomaterial, including strong electroconductivity, an ambipolar field effect, high carrier mobility, and an adjustable bandgap. For the purpose of creating biosensors for the diagnosis and treatment of various diseases in recent years, numerous researchers have employed BP. The application of a 3D BP nanoscaffold for recovering neurogenesis was the subject of a revolutionary work which is presented in the year 2020.

For instance, cellulose hydrogels were used in the construction of 2D BP nanosheets (BPNSs) for photothermal therapy against cancer. These hydrogels and BPNS 3D networks have improved stability, strong photothermal responsiveness, and flexibility. The clinical study demonstrates the unique applications of this nanoplatform which is also 100% safe and biocompatible. In another fascinating study, BP was used to construct a 3D-printed scaffold that participates in bone regeneration and is intended to be used in the photothermal ablation therapy of osteosarcoma. As a re-

sult, researchers frequently use BP to create nanodevices for the treatment of diseases due to their photothermal characteristics. A 2D fingerprint nanoprobe based on BP has been used to demonstrate an enhanced fabrication method for biological surface-enhanced Raman scattering (SERS) characterization. This work created flake-shaped BP–gold nanoparticle nanohybrid theranostic nanoplateforms for phototherapy, bioimaging, and drug delivery. Genome editing, antibacterial effectiveness, photodynamic anticancer therapy, imaging, and cancer theranostics have all utilized BP-containing biosensors.

6.1.5 Distinct platforms in the fabrication of advanced biosensor devices

In these decades, more advanced biosensing devices are fabricated using different device fabrication techniques. These biosensors are fabricated by many more techniques, viz., ion beams, microfluidics, near-field electrospraying, lab-on-a-chip, and chip calorimetry. Fabrication of the integrated biosensing device for local and real-time sensing applications got epitome scope. Micro- and nanoscale patterning on the surface of the sensor enhances the sensing performances by getting over the surface-based limitations. Miniaturization in device fabrication has helped to get remarkable sensing performances in biosensors. Several types of biosensors based on the different fabrication techniques are made, and they depicted better sensitivity and little limit of detection. Nowadays, versatile biosensors are being fabricated to detect various biomarkers or diseases, namely, cancer, cholesterol, bacterial infection, and exosomes.

6.1.5.1 Focused ion beam technique

This technique is usually used for the deposition of nanomaterials. These days, this technique has got widened the scope for the fabrication of the biosensing device. The probe attached to the ion beam is used for the fabrication of the biosensing devices. This technique is the more consistent way of preparing biosensing devices. Many more modifications are applied to the focused ion beam (FIB) technique to fabricate more reliable nanobiosensor devices. The FIB-made biosensors are compact, less costly, and can be used as a refractive index for various chemical and biological sensing applications (Erdman et al., 2019).

Principle: High- and low-gallium ion-beam focusing is used for site-specific sputtering in this technique.

Advantages: Multiple specimens are formed in a small area and are time efficient, and beam strength can be adjusted.

Disadvantages: The use of gallium may contaminate the samples, and physical and electrical properties can be affected.

6.1.5.2 *Electrospinning*

This is the oldest technique used by researchers for many decades. According to their convenience, the researchers have made many modifications to this technique for the fabrication of biosensors. By decreasing the electrode gap distance, one can successfully deposit the nanomaterials on the sensing device. Through the electrospray technique, this technique has evolved. M13 bacteriophage microfabrication has been achieved with this technique (He et al., 2017).

Principle: By decreasing the spinning gap, controllable deposition can be achieved.

Advantages: This method is simple and cost-effective, and large-scale processing is possible. All polymers (high molecular weight) can be easily processed by this method.

Disadvantages: This method is not suitable for 3D structures, and synergistic porosity for achieving good biosensing is unable to be achieved by this method.

6.1.5.3 *Paper-based microfluidics*

This technique is based on the principle of fluid action. The paper-based devices are easy to fabricate and of less cost. Usually, cellulose paper is used for the fabrication of the device followed by computer-based printing. The printing can be performed through different methods, namely, wax printing, laser printing, and conducting inkjet printing. Among these printing techniques, wax printing is widely used because it is effective, easier, and cost-effective. These paper-based microfluid devices will perform better sensitivity than other techniques. The paper-based CMOS photodiode biosensor is used to detect and diagnose sepsis (Hu et al., 2020). By using this paper-based sensing device, biomarkers are formed to detect glucose and lactate in human serum. A 3D paper-based sensing device with glucose detection has been developed to detect silver ions (Xiao et al., 2019).

Principle: This method is mainly based on fluidic actuation.

Advantages: This method is of low cost, easily desirable, simple, possibility of rapid detection, flexible substrate, easily degradable, and eco-friendly.

Disadvantages: This method is limited to multiple detections, it is not operable at room temperature, and extra heating is very much necessary for proper sensing.

6.1.5.4 Microelectromechanical systems

Microelectromechanical systems (MEMSs), nanoelectromechanical systems (NEMSs), and bio-nano-electromechanical systems (bio-NEMS) are the major biosensing fabrication techniques used for micro- and nanoscale device fabrication. For the detection of biochemical components, MEMS fabrication techniques are widely used (Bryzek, 2005). Bio-NEMS technique is majorly used to detect highly complex biochemical components. Moreover, the MEMS techniques are used in biosensors for diagnosis of diseases, therapeutics, and monitoring ecosystem and human health. To detect genome bacteria and viruses, a miniaturized silicon-chip biosensor has been fabricated by the MEMS technique (Battaglia et al., 2019).

Principle: This method is mainly based on capacitive piezoresistive resonant thermoelectric principle.

Advantages: Industrial production is possible, cost-effective, and low power consumption is possible for device fabrication.

Disadvantages: For the production of a single unit, it is too expensive, especially during the initial developmental stage.

6.1.5.5 Surface plasmon resonance-based biosensor

Using incident light to stimulate the electrons at the interfaces of the material is the basic technique of the SPR technique. An SPR biosensor is used to detect the gluten in the urine samples of people to detect celiac disease. A highly sensitive biosensor to detect microRNA was developed (Wei et al., 2020).

Principle: The incident polarized light falls on the metal film at the interface of the media with varying refractive index (RI).

Advantages: Miniaturized devices can be prepared with this method, and the devices prepared through this method are highly sensitive.

Disadvantages: Calibration has to be done for a long time.

6.1.5.6 *Whispering-gallery-mode biosensors*

Whispering-gallery-mode (WGM) biosensing devices are very much sensitive to biomolecules and chemical ions. Usually, this technique is used for the examination of the modifications occurring on the surface of the material. For the ultrasensitive detection of the biomolecules, this method is preferable. For the detection of the grapevine virus, an optical immunosensor device was fabricated using the WGM resonator technique (Fu et al., 2020; Tereshchenko et al., 2020).

Principle: It works on the principle of the wave that travels on the concave surface.

Advantages: Q-factor is high, low mode volumes, small size, easy to integrate with the chip, and high tenability.

Disadvantages: Bending loss and evanescent coupling loss are observed.

6.2 Conclusion

In these decades, tremendous improvements happened in the fabrication of biosensor devices for better management of health. These days, many more opportunities are opening for the development, implementation, and acquisition of versatile properties of nanomaterials in the fabrication of biosensors. The use of advanced 2D transitional materials and organic polymers has attained better sensitivity, selectivity, and stability in biosensors. The biocompatible nature, enhanced conductivity, and good sensing response of the nanomaterials and their composites made it easier to develop biosensing devices. Using nanomaterial composites leads to fabricating the sensing devices with less detection limit. These types of quick-responding, lower-LOD biosensing devices are used for health monitoring applications. The recently flourished SERS and WGM techniques have remarkable advantages for device fabrication, miniaturization, and possible easy handling. With the use of the new fabrication technology, using advanced nanomaterials finds a way to develop versatile devices for biosensing (Table 6.1).

Table 6.1 Timeline of the biosensors developed in these years.

Sl. no.	Researchers name	Year	Biosensor	References
1.	M. Cramer	1906	Electric potential arising between parts of the fluid	Cremer (1906)
2.	Soren Sorensen	1909	Concept of pH and pH scale	Sørensen and Mitteilung (1909)
3.	Griffin and Nelson	1909–22	First to demonstrate the immobilization of the enzyme invertase on aluminum hydroxide and charcoal	Griffin and Nelson (1916)
4.	W.S. Hughes	1922	Discovered a pH measurement electrode	Hughes (1922)
5.	Leland C. Clark	1956	Invented the first oxygen electrode	Heineman et al. (2006)
6.	Leland C. Clark et al	1962	Experimentally demonstrated an amperometric enzyme electrode for detecting glucose	Clark and Lyons (1962)
7.	Updike and Hicks	1967	First functional enzyme electrode based on glucose oxidase immobilized onto an oxygen sensor	Updike and Hicks (1967)
8.	Guilbault and Montalvo	1969	Reported the first potentiometric enzyme electrode-based sensor for detecting urea	Guilbault and Montalvo (1969)
9.	Bergveld	1970	Discovery of ion-sensitive field-effect transistor	Bergveld (1970)
10.	Guilbault and Lubrano	1973	Defined glucose and a lactate enzyme sensor based on hydrogen peroxide detection at a platinum electrode	Bergveld (1970)

Sl. no.	Researchers name	Year	Biosensor	References
11.	K. Mosbach and B. Danielsson	1974	Developed enzyme thermistor	Mosbach and Danielsson (1974)
12.	D.W. Lubbers and N. Opitz	1975	Demonstrated fiber-optic biosensor for carbon dioxide and oxygen detection	Lübbbers and Opitz (1975)
13.	Suzuki et al.	1975	First demonstrated microbe-based immunosensor	Suzuki et al. (1975)
14.	Clemens et al.	1976	First bedside artificial pancreas	Clemens et al. (1976)
15.	Peterson	1980	Demonstrated the first fiber-optic pH sensor for in vivo blood gases	Yoo and Lee (2010)
16.	Schultz	1982	Fiber-optic biosensor for glucose detection	Schultz (1982)
17.	Liedberg et al.	1983	Surface plasmon resonance (SPR) immunosensor	Liedberg et al. (1983)
18.	Roederer and Bastiaans	1983	Developed the first immunosensor based on piezoelectric detection	Roederer and Bastiaans (1983)
19.	Cass. A. E	1984	First mediated amperometric biosensor	Cass et al. (1984)
20.	Pharmacia Biacore	1990	SPR-based biosensor	Mun'delanji and Tamiya. (2015)
21.	Poncharal et al.	1999	First nanobiosensor	Poncharal et al. (1999)
22.	S. Girbi et al.	2018	Nerve-on-chip-type biosensor for assessment of nerve impulse conduction	Gribi et al. (2018)

References

Amrutha, B.M., Manjunatha, J.G., Aarti, S.B., & Nagarajappa, H. (2021). Sensitive and selective electrochemical detection of vanillin at graphene-based poly (methyl orange) modified electrode. *Journal of Science: Advanced Materials and Devices*, 6, 415-424. <https://doi.org/10.1016/j.jsamd.2021.05.002>.

- Battaglia, S., Petralia, S., & Vicario, N., et al. (2019). An innovative silicon-chip for sensitive real time PCR improvement in pathogen detection. *Analyst*, 144(7), 2353-2358.
- Bergveld, P. (1970). Development of an ion-sensitive solid-state device for neurophysiological measurements. *IEEE Transactions on bio-medical Engineering*, 17, 70-71.
- Bhalla, N., Jolly, P., Formisano, N., & Estrela, P. (2016). Introduction to biosensors. *Essays in Biochemistry*, 60, 1-8.
- Bhardwaj, H., Sumana, G., & Marquette, C.A. (2021). Gold nanobipyramids integrated ultrasensitive optical and electrochemical biosensor for Aflatoxin B1 detection. *Talanta*, 222, Article 121578.
- Bryzek, J. (2005). Principles of MEMS. In *Handbook of measuring system design*. John Wiley & Sons, Ltd.
- Cass, A.E., Davis, G., Francis, G.D., Hill, H.A., Aston, W.J., Higgins, I.J., Plotkin, E.V., Scott, L.D., & Turner, A.P. (1984). Ferrocene-mediated enzyme electrode for amperometric determination of glucose. *Analytical Chemistry*, 56, 667-671.
- Chethan, B., Ravikiran, Y.T., Vijayakumari, S.C., Rajprakash, H.G., & Thomas, S. (2018). Nickel substituted cadmium ferrite as room temperature operable humidity sensor. *Sensors and Actuators A: Physical*, 280, 466-474.
- Chethan, B., RajPrakash, H.G., Ravikiran, Y.T., Vijayakumari, S.C., & Thomas, S. (2019). Polypyrrole based core-shell structured composite based humidity sensor operable at room temperature. *Sensors and Actuators B: Chemical*, 296, Article 126639.
- Chethan, B., Raj Prakash, H.G., Ravikiran, Y.T., Vijayakumari, S.C., Ramana, C.H.V.V., Thomas, S., & Kim, D. (2019). Enhancing humidity sensing performance of polyaniline/water soluble graphene oxide composite. *Talanta*, 196, 337-344.
- Chethan, B., Prasad, V., & Thomas, S. (2022). Graphene-based sensing devices for soil moisture analysis. In *Electrochemical sensors based on carbon composite materials* (pp. 4-14-20). IOP Publishing. <https://doi.org/10.1088/978-0-7503-5127-0ch4>.
- Chethan, B., Prasad, V., Sunilkumar, A., Veena, V.S., & Thomas, S. (2023). *Trends in development of nanomaterial-based sensing devices* (pp. 287-305). ACS Publishers. <https://doi.org/10.1021/bk-2023-1437.ch012>.
- Clark, L.C., & Lyons, C. (1962). Electrode systems for continuous monitoring in cardiovascular surgery. *Annals of the New York Academy of Sciences*, 102, 29-45.
- Clemens, A.H., Chang, P.H., & Myers, R.W. (1976). Le développement d'un système automatique d'infusion d'insuline controle par laglycémie, son système de dosage du glucose et ses algorithmes de controle. *Journées annuelles de diabetologie de l'Hôtel-Dieu*, 269-278.
- Cremer, M. (1906). Über die Ursache der elektromotorischen Eigenschaften der Gewebe, zugleich ein Beitrag zur Lehre von den polyphasischen Elektrolytketten. *Zeitschrift für Biologie*, 47, 562-608.
- Dincer, C., Bruch, R., Costa-Rama, E., Fernández-Abedul, M.T., Merkoçi, A., Manz, A., Urban, G.A., & Güder, F. (2019). Disposable sensors in diagnostics, food, and environmental monitoring. *Advanced Materials*, 31, Article 1806739.
- El-Denglawey, A., Angadi, V.J., Manjunatha, K., Chethan, B., & Somvanshi, S.B. (2021). Role of dysprosium in enhancing the humidity sensing performance in manganese zinc ferrites for sensor applications. *Journal of Materials Science: Materials in Electronics*, 32, 23554-23565. <https://doi.org/10.1007/s10854-021-06842-1>.
- El-Denglawey, A., Manjunatha, K., Vijay Sekhar, E., Chethan, B., Zhuang, J., & Angadi, V.J. (2021). Rapid response in recovery time, humidity sensing behavior and magnetic properties of rare earth (Dy & Ho) doped Mn-Zn ceramics. *Ceramics International*, 47, 28614-28622. <https://doi.org/10.1016/j.ceramint.2021.07.020>.

- Ensafi, A.A. (2019). An introduction to sensors and biosensors. In Ensafi A.A. (Ed.), *Electrochemical biosensors* (1st ed., pp. 1-10). Cambridge, MA, USA: Elsevier.
- Ensafi, A.A., Karimi-Maleh, H., Ghiaci, M., & Arshadi, M. (2011). Characterization of Mn-nanoparticles decorated organo-functionalized $\text{SiO}_2\text{-Al}_2\text{O}_3$ mixed-oxide as a novel electrochemical sensor: Application for voltammetric determination of captopril. *Journal of Materials Chemistry*, 21, 15022-15030.
- Erdman, N., Bell, D.C., & Reichelt, R. (2019). Scanning electron microscopy. In *Springer handbook of microscopy* (pp. 229-318). Cham: Springer International Publishing.
- Fu, L., Lu, Q., & Liu, X., et al. (2020). Combining whispering gallery mode optofluidic microbubble resonator sensor with GR-5 DNAzyme for ultra-sensitive lead ion detection. *Talanta*, 213, Article 120815.
- Gleiter, H. (2000). Nanostructured materials: Basic concepts and microstructure. *Acta Materialia*, 48, 1-29.
- Gribi, S., De Dunilac, S.B., Ghezzi, D., & Lacour, S.P. (2018). A microfabricated nerve-on-a-chip platform for rapid assessment of neural conduction in explanted peripheral nerve fibers. *Nature Communications*, 9, 4403.
- Griffin, E.G., & Nelson, J.M. (1916). The influence of certain substances on the activity of invertase. *Journal of the American Chemical Society*, 38, 722-730.
- Guilbault, G.G., & Montalvo, J.G., Jr. (1969). Urea-specific enzyme electrode. *Journal of the American Chemical Society*, 91, 2164-2165.
- Hareesha, N., & Manjunatha, J.G. (2021). Electro-oxidation of formoterol fumarate on the surface of novel poly (thiazole yellow-G) layered multi-walled carbon nanotube paste electrode. *Scientific Reports*, 11, 12797. <https://doi.org/10.1038/s41598-021-92099-x>.
- Hareesha, N., Manjunatha, J.G., Amrutha, B.M., Sreeharsha, N., Basheeruddin, A., Md, & Khalid, A. (2021). A fast and selective electrochemical detection of vanillin in food samples on the surface of poly (glutamic acid) functionalized multiwalled carbon nanotubes and graphite composite paste sensor. *Colloids and Surfaces A: Physicochemical and Engineering Aspects*, 626, Article 127042.
- Hareesha, N., Manjunatha, J.G., Pushpanjali, P.A., Prinith Subbaiah, N., Charithra, M.M., Sreeharsha, N., Basheeruddin Asdaq, S.M., & Md Khalid, A. (2021). Electrochemical sensing of antibiotic drug amoxicillin in the presence of dopamine at simple and selective carbon paste electrode activated with cetyltrimethylammonium bromide surfactant. *Monatshefte für Chemie*. <https://doi.org/10.1007/s00706-021-02870-z>.
- He, X.X., Zheng, J., & Yu, G.F., et al. (2017). Near-field electrospinning: Progress and applications. *The Journal of Physical Chemistry C*, 121(16), 8663-8678.
- He, Y., Zhou, L., Deng, L., Feng, Z., Cao, Z., & Yin, Y. (2021). An electrochemical impedimetric sensing platform based on a peptide aptamer identified by high-throughput molecular docking for sensitive l-arginine detection. *Bioelectrochemistry (Amsterdam, Netherlands)*, 137, Article 107634.
- Heineman, W.R., Jensen, W.B., Leland, C., & Clark Jr (2006). (1918–2005). *Biosensors & Bioelectronics*, 21, 1403-1404.
- Hu, C.X., Annese, V.F., & Velugotla, S., et al. (2020). Disposable paper-on-CMOS platform for real-time simultaneous detection of metabolites. *IEEE Transactions on bio-medical Engineering*, 67(9), 2417-2426.
- Hughes, W.S. (1922). The potential difference between glass and electrolytes in contact with the glass. *Journal of the American Chemical Society*, 44, 2860-2867.
- Khanna, V.K. (2012). Introduction to nanosensors. In Khanna V.K. (Ed.), *Nanosensors: Physical, chemical, and biological* (1st ed., pp. 37-40). Boca Raton, FL, USA: CRC Press.
- Liedberg, W., Nylander, C., & Lundström, I. (1983). Surface plasmon resonance for gas

detection and biosensing. *Sensors and Actuators. A, Physical*, 4, 299-304.

Lübbbers, D.W., & Opitz, N. (1975). The pCO₂-pO₂-optode: A new probe for measurement of pCO₂ or pO in fluids and gases (authors transl). *Zeitschrift für Naturforschung C*, 30, 532-533.

Rupashree, M.P., Soppin, K., Pratibha, S., & Chethan, B. (2021). Cost effective photocatalytic and humidity sensing performance of green tea mediated copper oxide nanoparticles. *Inorganic Chemistry Communications*, 134. <https://doi.org/10.1016/j.inoche.2021.108974>.

Manjunatha, J.G. (2020). A surfactant enhanced graphene paste electrode as an effective electrochemical sensor for the sensitive and simultaneous determination of catechol and resorcinol. *Chemical Data Collections.*, 25, Article 100331.

Manjunatha, J.G., Deraman, M., Nur Hamizah, B., & Talib, I.A. (2014). Selective detection of dopamine in the presence of uric acid using polymerized phthalo blue film modified carbon paste electrode. *Advanced Materials Research*, 895, 447-451.

Manjunatha, S., Machappa, T., Ravikiran, Y.T., Chethan, B., & Sunilkumar, A. (2019). Polyaniline based stable humidity sensor operable at room temperature. *Physica B: Condensed Matter*, 561, 170-178.

Mosbach, K., & Danielsson, B. (1974). An enzyme thermistor. *Biochimica et Biophysica Acta*, 364, 140-145.

Mun'delanji, C.V., & Tamiya, E. (2015). Nanobiosensors and nanobioanalyses: A review. In Mun'delanji C.V., Kerman K., Hsing I.M., & Tamiya E. (Eds.), *Nanobiosensors and nanobioanalyses* (1st ed., pp. 3-20). Tokyo, Japan: Springer.

Pal, S.L., Jana, U., Manna, P.K., Mohanta, G.P., & Manavalan, R. (2011). Nanoparticle: An overview of preparation and characterization. *Journal of Applied Pharmaceutical Science*, 06, 228-234.

Poncharal, P., Wang, Z.L., Ugarte, D., & De Heer, W.A. (1999). Electrostatic deflections and electromechanical resonances of carbon nanotubes. *Science (New York, N.Y.)*, 283, 1513.

Pushpanjali, P.A., Manjunatha, J.G., Nagarajappa, H., D'Souza, E.S., Charithra, M.M., & Prinith, N.S. (2021). Voltammetric analysis of antihistamine drug cetirizine and paracetamol at poly (L-Leucine) layered carbon nanotube paste electrode. *Surfaces and Interfaces*, 24, Article 101154.

Riangrunroj, P., Bever, C.S., Hammock, B.D., & Polizzi, K.M. (2019). A label-free optical whole-cell *Escherichia coli* biosensor for the detection of pyrethroid insecticide exposure. *Scientific Reports.*, 9, 12466.

Ravikiran, Y.T., & Chethan, B. (2022). Humidity sensing studies on conducting polymers: Polyaniline and polypyrrole. *Inorganic Chemistry Communications*, 145. <https://doi.org/10.1016/j.inoche.2022.110019>.

Roederer, J.E., & Bastiaans, G.J. (1983). Microgravimetric immunoassay with piezoelectric crystals. *Analytical Chemistry*, 55, 2333-2336.

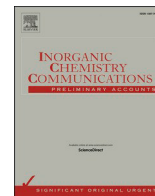
Pratibha, S., & Chethan, B. (2022). Carbon nanomaterial-based sensor safety in different fields. In *Carbon nanomaterials-based sensors* (pp. 315-332). Elsevier. <https://doi.org/10.1016/B978-0-323-911174-0.00016-0>.

Pratibha, S., Chethan, B., Ravikiran, Y.T., Dhananjaya, N., & Jagadeesh Angadi, V. (2020). Enhanced humidity sensing performance of Samarium doped Lanthanum Aluminate at room temperature. *Sensors and Actuators. A, Physical*, 304. <https://doi.org/10.1016/j.sna.2020.111903>.

Shanawad, S.S., Sunilkumar, A., Khened, B.S., Chethan, B., Prasad, V., Kotresh, M.G., Sharanakumar, T.M., & Veena, V.S. (2023). Polyaniline/vanadium pentoxide/lead tetroxide ternary composite for LPG sensing. *Journal of Materials Science: Materials in Electronics*, 34. <https://doi.org/10.1007/s10854-023-09962-y>.

Shanawad, S.S., Chethan, B., Prasad, V., Sunilkumar, A., & Veena, V.S. (2023). Humidity

- sensing performance of the magnesium oxide nanoparticles. *Journal of Materials Science: Materials in Electronics*, 34. <https://doi.org/10.1007/s10854-022-09714-4>.
- Schroeder, W.H., & Cavacini, L. (2010). Structure and function of immunoglobulins. *The Journal of Allergy and Clinical Immunology*, 125, S41-S52.
- Schultz, J.S. (1982). *Oxygen Sensor of Plasma Constituents*. U.S. Patent No. 4,344,438A, 17 August 1982.
- Singh, K.R.B., Nayak, V., Sarkar, T., & Singh, R.P. (2020). Cerium oxide nanoparticles: Properties, biosynthesis and biomedical application. *RSC Advances*, 10, 27194-27214.
- Sörensen, S.P.L., & Mitteilung, E., II (1909). Über die Messung und die Bedeutung der Wasserstoffionenkonzentration bei enzymatischen Prozessen [Enzyme studies. 2nd Report. On the measurement and the importance of hydrogen ion concentration during enzymatic processes]. *Biochemische Zeitschrift*, 21, 131-304.
- Suzuki, S., Takahashi, F., Satoh, I., & Sonobe, N. (1975). Ethanol and lactic acid sensors using electrodes coated with dehydrogenase-collagen membranes. *Bulletin of the Chemical Society of Japan*, 48, 3246-3249.
- Sunilkumar, A., Khened, B.S., Chethan, B., Prasad, V., Kotresh, M.G., Sharanakumar, T.M., & Veena, V.S. (2023). Ultrahigh sensitive and selective room temperature operable poisonous carbon monoxide gas sensor based on polyaniline ternary composite. *Inorganic Chemistry Communications*, 150. <https://doi.org/10.1016/j.inoch.2023.110476>.
- Tereshchenko, A., Yazdi, G.R., & Konup, I., et al. (2020). Application of ZnO nanorods based whispering gallery mode resonator in optical immunosensors. *Colloids and Surfaces B*, 191, Article 110999.
- Theavenot, D.R., Toth, K., Durst, R.A., & Wilson, G.S. (2001). Electrochemical biosensors: Recommended definitions and classification. *Biosensors & Bioelectronics*, 16, 121-131.
- Tigari, G., & Manjunatha, J.G. (2019). Electrochemical preparation of poly(arginine)-modified carbon nanotube paste electrode and its application for the determination of pyridoxine in the presence of riboflavin: An electroanalytical approach. *Journal of Analysis and Testing*, 3, 331. <https://doi.org/10.1007/s41664-019-00116-w>.
- Updike, S.J., & Hicks, G.P. (1967). The enzyme electrode. *Nature*, 214, 986-988.
- Wei, X., Liu, D., & Zhao, M., et al. (2020). An enzyme-free surface plasmon resonance imaging biosensing method for highly sensitive detection of microRNA based on catalytic hairpin assembly and spherical nucleic acid. *Analytica Chimica Acta*, 1108, 21-27.
- White, R.M. (1987). A sensor classification scheme. *IEEE Transactions on Ultrasonics, Ferroelectrics, and Frequency Control*, 34, 124-126.
- Xiao, W., Gao, Y., & Zhang, Y., et al. (2019). Enhanced 3D paper-based devices with a personal glucose meter for highly sensitive and portable biosensing of silver ion. *Biosensors & Bioelectronics*, 137, 154-160.
- Yoo, E.-H., & Lee, S.-Y. (2010). Glucose biosensors: An overview of use in clinical practice. *Sensors*, 10, 4558-4576.



Short communication

Rare earth oxide based polypyrrole composite: An efficient room temperature reliant humidity sensor

A. Sunilkumar^{a,1}, S. Manjunatha^{b,1}, B. Chethan^c, Y.T. Ravikiran^{d,*}, T. Machappa^a, S. Thomas^e^a VTURC, Department of Physics, Ballari Institute of Technology and Management, Karnataka, India, 583104^b V.V. Sangha's Independent PU college, Ballari, Karnataka, India, 583104^c Department of Physics, Indian Institute of Science, Bengaluru 560012, Karnataka, India^d Department of PG studies and research in Physics, Government Science College, Chitradurga, Karnataka, India, 577501^e School of Energy Materials, Mahatma Gandhi University, Kottayam, Kerala, India 686560

ARTICLE INFO

Keywords:

Polypyrrole
Holmium oxide
Humidity sensor
Sensitivity
Limit of detection
Grotthus reaction

ABSTRACT

Having a competent and efficient humidity sensing material is important for vivid applications. In the present work, holmium oxide, a well-known rare-earth oxide, has been composited with Polypyrrole (PPy) to form polypyrrole/holmium oxide (PPHO) composites. The composites were prepared by chemical polymerization reactions in 10 (PPHO-1), 30 (PPHO-2), and 50 wt% (PPHO-3) of holmium oxide in PPy matrix. These composites were characterized by Field emission scanning electron microscopy (FESEM), Energy dispersive X-ray spectroscopy (EDX), X-ray diffraction (XRD), Fourier transform infrared spectroscopy (FTIR), Raman spectra, and Transmission electron microscopy (TEM) to study the structural and morphological changes in the PPy and PPHO composites. Humidity sensing behavior of the composites was investigated in the relative humidity range (RH) of 11 to 97%. Among all the composites, PPHO-3 has shown a maximum sensing response of 93% with response and recovery times of 30 s and 40 s respectively, furthermore, the composite has exhibited an appreciable limit of detection (LOD) of 4.98 % RH, good linearity (0.9981), real sensitivity (27.72 MΩ-cm / %RH) and stability. Based on Grotthus' reaction, the sensing mechanism has been discussed.

1. Introduction

Humidity sensing and monitoring play a significant role in many places, such as libraries, agricultural warehouses, nuclear power plants, and medical and industrial fields [1]. Hence, humidity detection has become crucial in well-maintained, controlled environments. Because of their simple fabrication, low cost, and effective performance characteristics, resistive-type sensors have become popular [2]. Resistive-type sensors are those that cause a change in resistance at two points of contact and transfer the information for analysing the analyte [3,4]. In comparison with most of the commercially available sensors, conducting polymer-based sensors have attracted greater attention due to their easy synthesis, simple fabrication, and effective performance [5]. Very recently, binary metal oxides [6], transition metal oxides like ZrO₂ [7], ZnO [8], VO [9], and 2D-layered materials [10,11] have been studied for various opto-electronic and sensing applications. Conducting polymers like polypyrrole (PPy) and polyaniline (PANI) when

composited with these oxides have captivated attention in terms of their special transport properties [12–14] and have found applications in many fields. In our recent studies, we have composited conducting polymers like PANI and PPy with yttrium oxide [15], WS₂ [16], and TaS₂ [17] for their humidity sensing performance. All these conducting polymer composites have exhibited improved characteristics of high sensitivities, good response times, and recovery times, and are operable at ambient temperature, which is note-worthy. In this regard, and to further elaborate on the scope of such conducting polymer composites for humidity sensing, in the present study, we have considered PPy and composited it with a rare earth oxide. Since these oxides have a large bandgap and large dielectric constants, which are indeed required characteristics for the design of novel electronic devices [18–23]. Hence, holmium oxide, a rare earth oxide consisting of a large band gap of 5.3 eV that has been studied most extensively due to its emerging role in high-K-based nanoelectronics, was chosen for the present study. So, the insertion of holmium oxide into the PPy matrix to form polypyrrole-

* Corresponding author.

E-mail addresses: ytrcta@gmail.com, ravikiranyt.dce@ka.gov.in (Y.T. Ravikiran).¹ Authors of equal contribution.

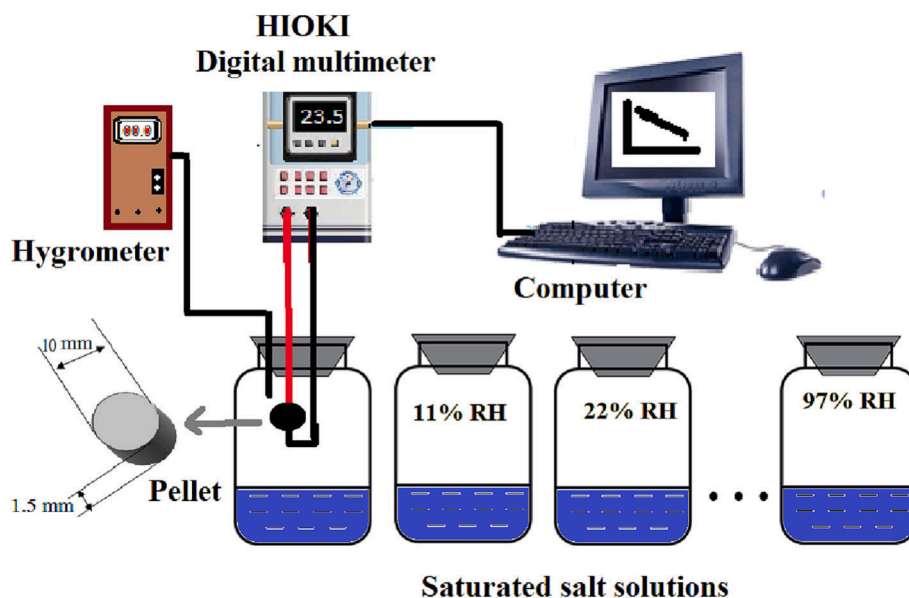


Fig. 1. Illustration of the humidity sensor set up for humidity sensing measurements.

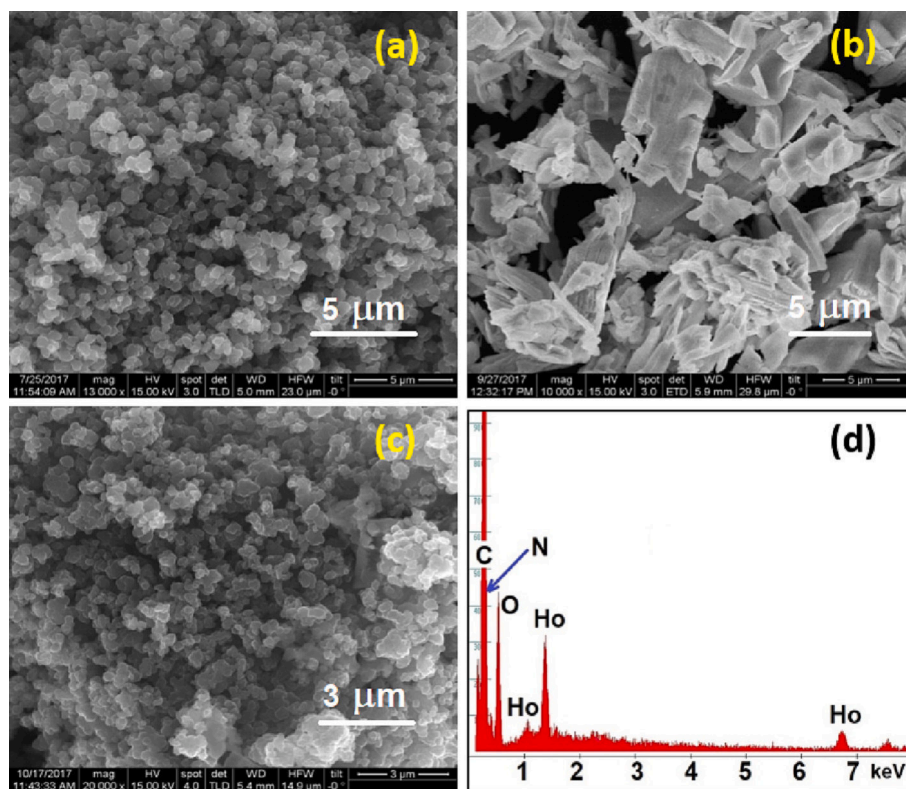


Fig. 2. Field emission scanning electron micrographs of (a) PPy, (b) Ho_2O_3 , (c) PPHO-3 composite and (d) EDX Spectrum.

holmium oxide (PPHO) composites is the first attempt of its kind to study its humidity sensing characteristics. Hence, PPHO composites have been synthesised by the chemical polymerization method and thereby explored for their humidity sensing performance at room temperature.

2. Experimental

2.1. Materials

Analytical grade reagents were used correspondent to pyrrole- $\text{C}_4\text{H}_4\text{NH}$ (98% purity), ammonium per sulphate $[(\text{NH}_4)_2 \text{S}_2\text{O}_8]$ both bought from SD Fine Chemicals, Mumbai, India. Holmium oxide (Ho_2O_3) of 99.99% purity was procured from Sigma Aldrich, USA. For synthesis of PPy and PPHO composites, pyrrole monomer was doubly distilled before use, and distilled water was used in the entire

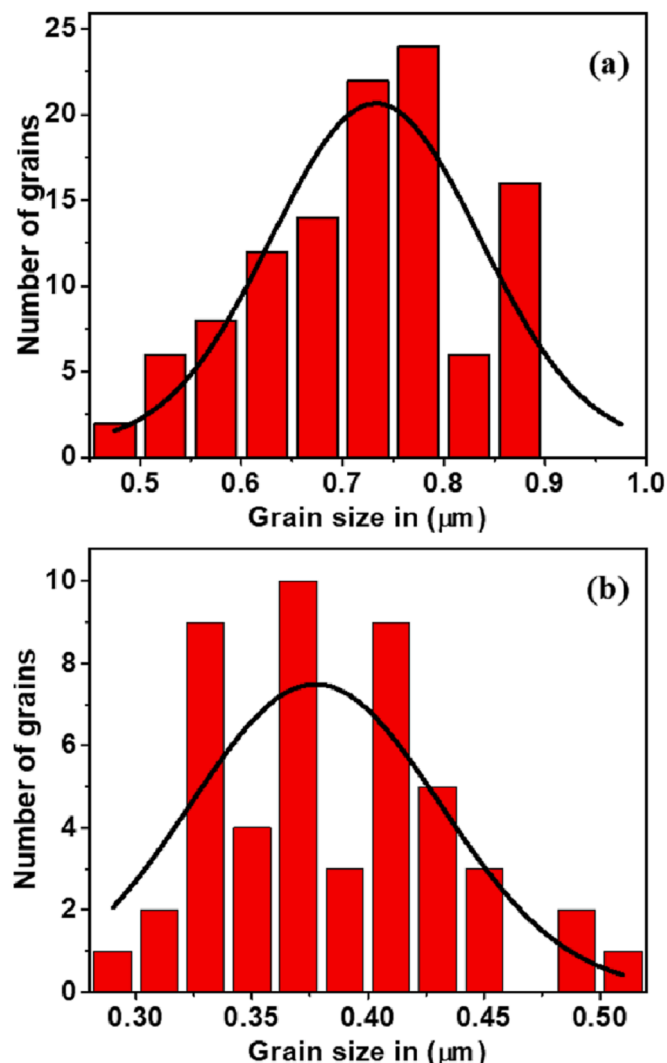


Fig. 3. Number of grains versus grain size of (a) PPy and (b) PPHO-3 composite.

synthetic process.

2.2. Synthesis of polypyrrole

The chemical polymerization method was employed for the preparation of polypyrrole. Pyrrole (0.3 M) was taken in a beaker, and ammonium per sulphate (0.06 M) was added drop by drop to the beaker containing pyrrole. This addition took 4 h while the mixture was kept in an ice bath with continuous stirring using a magnetic stirrer. Afterwards, the mixture was precipitated to obtain PPy and then filtered, dried in a hot air oven (100°C). The polypyrrole so obtained was 3.4 g, which was considered 100 wt% [24].

2.3. Synthesis of polypyrrole- Ho_2O_3 composites

3.4 g of PPy is considered as 100 wt%, hence 1.7 g is considered as (50 wt%) of Ho_2O_3 and it was added to pyrrole (0.3 M) solution and mixed rigorously. Further, ammonium per sulphate ($[(\text{NH}_4)_2 \text{S}_2\text{O}_8]$) of 0.06 M was added drop-wise to the beaker containing pyrrole liquid, to get PPy/ Ho_2O_3 -50% (PPHO-3) composite. Similarly for preparation of PPy/ Ho_2O_3 -30% (PPHO-2) and PPy/ Ho_2O_3 -10 wt% (PPHO-1) composites, 1.36 g and 0.34 g of Ho_2O_3 was added to pyrrole solution and identical procedure has been followed. Change in color had confirmed the formation of the composites. After the polymerization, samples were

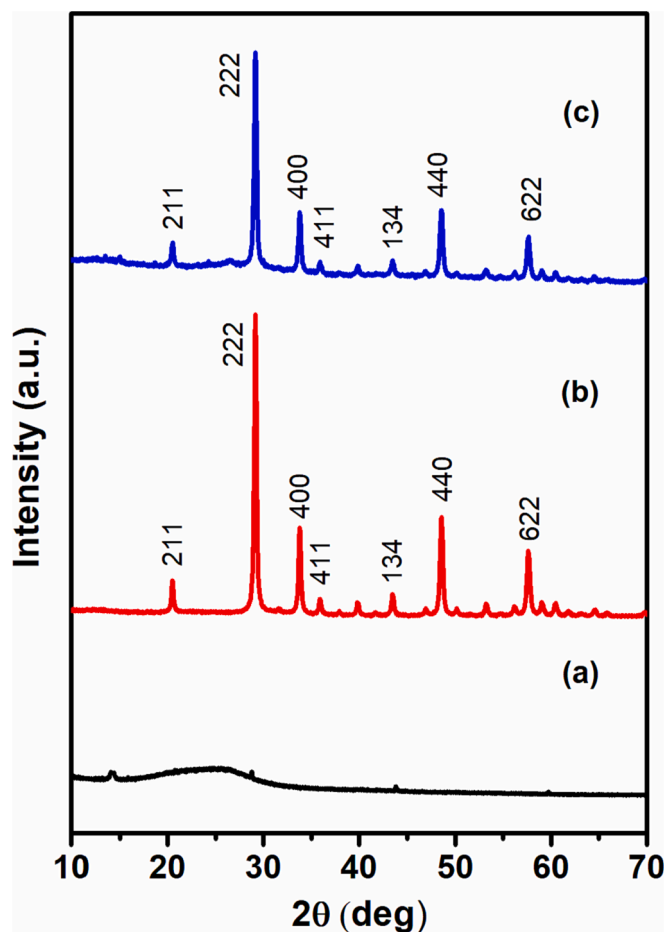


Fig. 4. X-ray diffraction spectra of (a) PPy (b) Ho_2O_3 and (c) PPHO-3 composite.

cleaned using distilled water and then with acetone, further dried in hot air oven (100°C) in order to attain a constant weight.

2.4. Characterization

Field emission scanning electron microscopy (FESEM) pictures were obtained by placing the sample powders on an aluminium tape and using the FEI Nova Nano SEM 600 instrument. Energy dispersive X-ray (EDX) spectrum was obtained by using the EDAX genesis instrument attached to the FESEM. Fourier transform infrared (FTIR) spectra of polypyrrole, Ho_2O_3 and PPHO-3 were recorded by a Frontier PerkinElmer spectrometer in the wave-number range 400–4000 cm^{-1} . Powder X-ray diffraction (XRD) spectra of polypyrrole, Ho_2O_3 and the PPHO-3 composite were documented by using the D8 Advance powder X-ray diffractometer of Bruker with a diffracting angle of the order $2\theta = 10^\circ$ to 70° by employing a copper $\text{K}\alpha$ source with a wavelength $\lambda = 1.541 \text{ \AA}$. Raman spectra of Polypyrrole, Ho_2O_3 and PPHO-3 composite were recorded using the Jobin Yvon Lab Ram (HR 800 Spectrometer) of Horiba in the wave-number range 200 – 2000 cm^{-1} , with an operating power laser of 20 mW and an exciting wavelength of $\lambda = 514.5 \text{ nm}$ (Ar laser). Transmission electron microscopy (TEM) image of PPHO-3 was captured using the JEOL-3010 instrument with an operating voltage of 300 kV.

2.5. Humidity sensing measurements

Humidity sensing analysis was carried out using specially designed glass chambers containing saturated salt solutions, which were

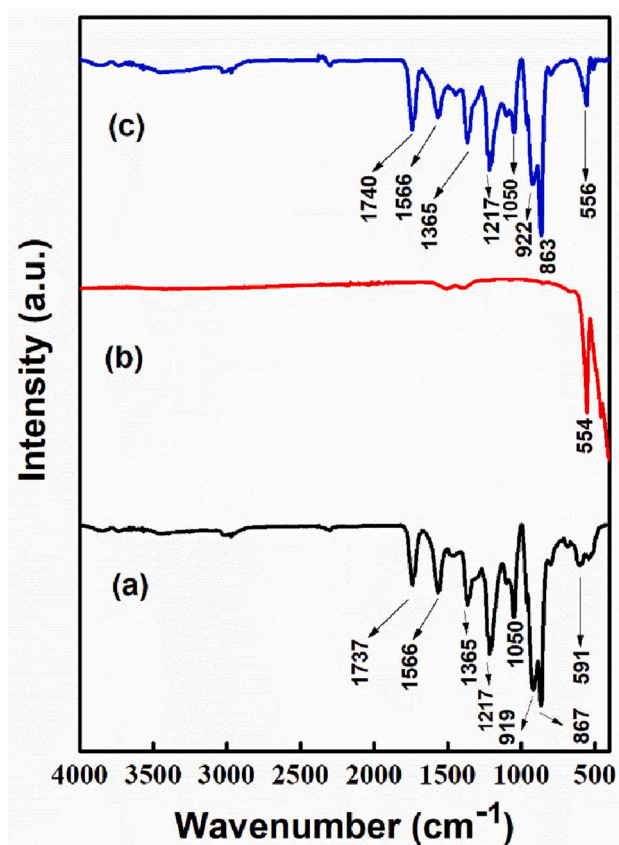


Fig. 5. Fourier-transform IR spectra of (a) PPy, (b) Ho_2O_3 and (c) PPHO-3 composite.

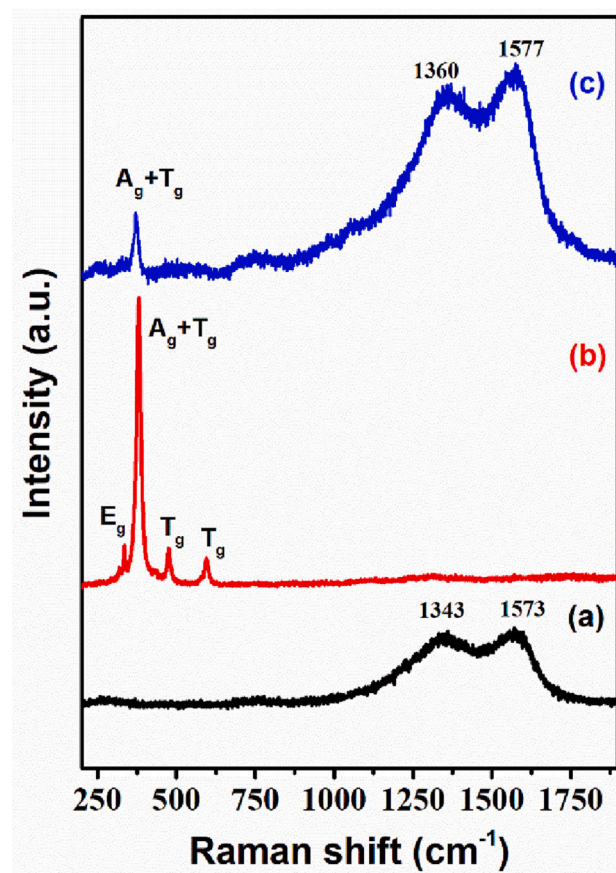


Fig. 7. Raman spectra of (a) PPy, (b) Ho_2O_3 and (c) PPHO-3 composite.

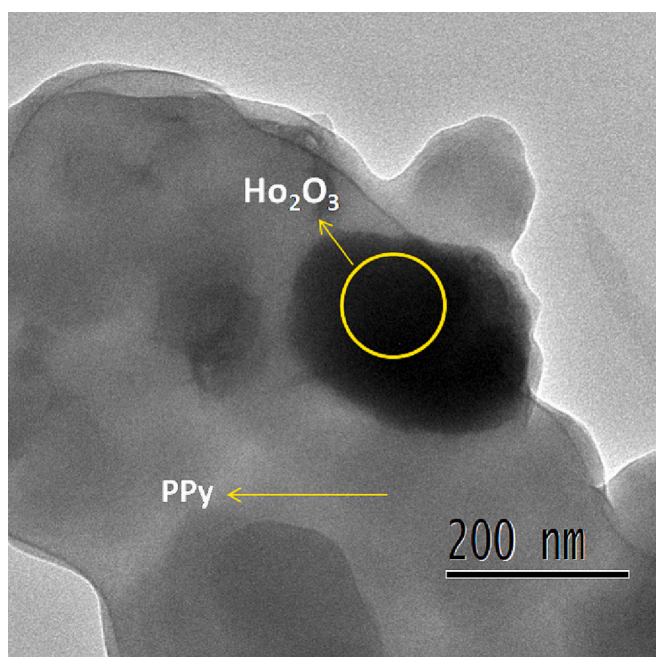


Fig. 6. Transmission electron micrograph of PPHO-3 composite.

supervised by a humidity metre (Mextech-DT-615). Glass chambers were closed with rubber cork fitted with electrodes. The electrodes holding the sample pellets were connected to a programmable computer-interfaced digital multimeter, Hioki DT 4282, Japan, to access

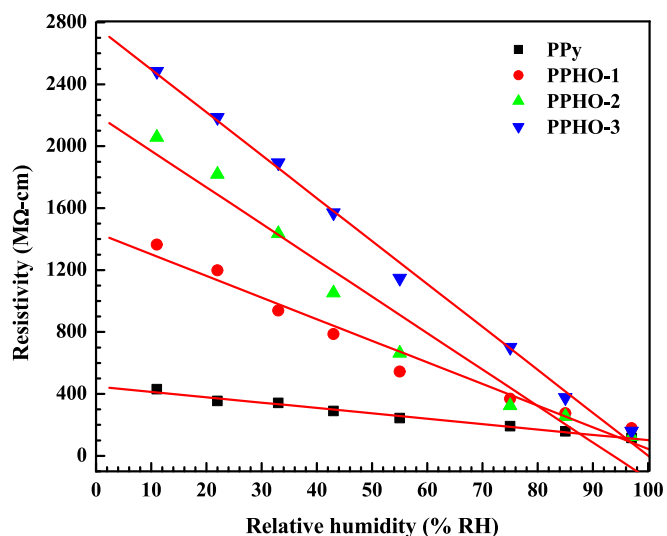


Fig. 8. Variation of resistivity with % RH for PPy and the composites. Solid lines are the best fits obtained from linear regression.

resistance values on exposure to a particular relative humidity environment at room temperature. Humidity sensor set up for humidity sensing studies is illustrated in Fig. 1.

Table 1
Humidity sensing parameters of PPHO composites.

Sample	Real Sensitivity (MΩ -cm / %RH)	Limit of detection (% RH)	Linearity (R ²)
PPy	3.47	9.8	0.9927
PPHO – 1	13.95	14.31	0.9847
PPHO – 2	23.54	17.22	0.9780
PPHO – 3	27.72	4.98	0.9981

3. Results and discussion

3.1. FESEM and EDX studies

Two-dimensional surface morphology images of polypyrrole, holmium oxide, and PPy/Ho₂O₃-50% are shown in Fig. 2. FESEM image of polypyrrole as in Fig. 2a, reveals the consistent dispersion of granular morphology of the polymer. Fig. 2b shows the holmium oxide which seems to be desquamate structure. Fig. 2c shows the morphology of the composite PPHO-3 which exhibits highly agglomerated spherical grains with many pores, which is necessary for a humidity sensor. Fig. 2d shows the EDX pattern of the PPHO-3 composite. EDX spectrum analysis revealed the presence of elements carbon and nitrogen belonging to PPy, whereas holmium and oxygen pertaining to Ho₂O₃ in the expected ratio. The grain sizes of polypyrrole and the PPHO-3 composite were evaluated using software called image-J. Fig. 3 represents histograms showing the number of grains versus grain size of PPy and PPHO-3 composite, revealing their grain sizes as 0.72 μm and 0.38 μm respectively. This reduction in grain size might have increased grain boundaries by enabling the development of small micropores in PPHO-3 composite [25].

3.2. XRD studies

Fig. 4a shows the XRD pattern of polypyrrole, which manifests a broad peak at $2\theta = 25.77^\circ$, which represents the amorphous nature of the polymer along with precise chain orders that may be attributed to lattice periodicity [26]. Fig. 4b shows the XRD pattern of holmium oxide has manifested complete Bragg reflections in the range $2\theta = 20^\circ - 60^\circ$ which are consistent with earlier literature. XRD of holmium oxide has revealed Ia-3 space group with body-centered cubic structure belonging to C-type holmium sesquioxide [27]. XRD spectrum of holmium oxide revealed crystal planes (211), (222), (400), (411), (134), (440) and (622) pertaining to the peaks at $2\theta \sim 20.7^\circ, 29.5^\circ, 34.3^\circ, 36.4^\circ, 44.1^\circ, 49.3^\circ, 58.5^\circ$ respectively, in accordance with JCPDS No. 65-3177. Fig. 4c shows the XRD pattern of PPHO-3 composite, which has more or less complete Bragg reflections of the Ho₂O₃, indicating its crystalline nature. Also, the intensities of the characteristic peaks of Ho₂O₃ found to be reduced, inferring the formation of the composite in which PPy was deposited on Ho₂O₃. Interestingly, the FWHM of the most intense peak of Bragg reflection (222) in the composite was increased, which indicates the decreased crystallite size of PPHO-3 composite. This reduced crystallite size of the composite was obtained using the Debye-Scherrer formula and was found to be 23.1 nm. Reduced crystallite size and reduced peak intensities are the evidence for the composite's formation.

3.3. FTIR studies

The chemical structure of PPy, Ho₂O₃ and PPHO-3 composite were studied employing the FTIR technique. Fig. 5a reveals the FTIR spectrum of Polypyrrole, showing its significant bands at 603, 867, and 919 cm⁻¹ assigned to C-H wagging. The bands at 1050 and 1217 cm⁻¹ indicate = C-H plane deformation vibration and to C-N stretching of polypyrrole

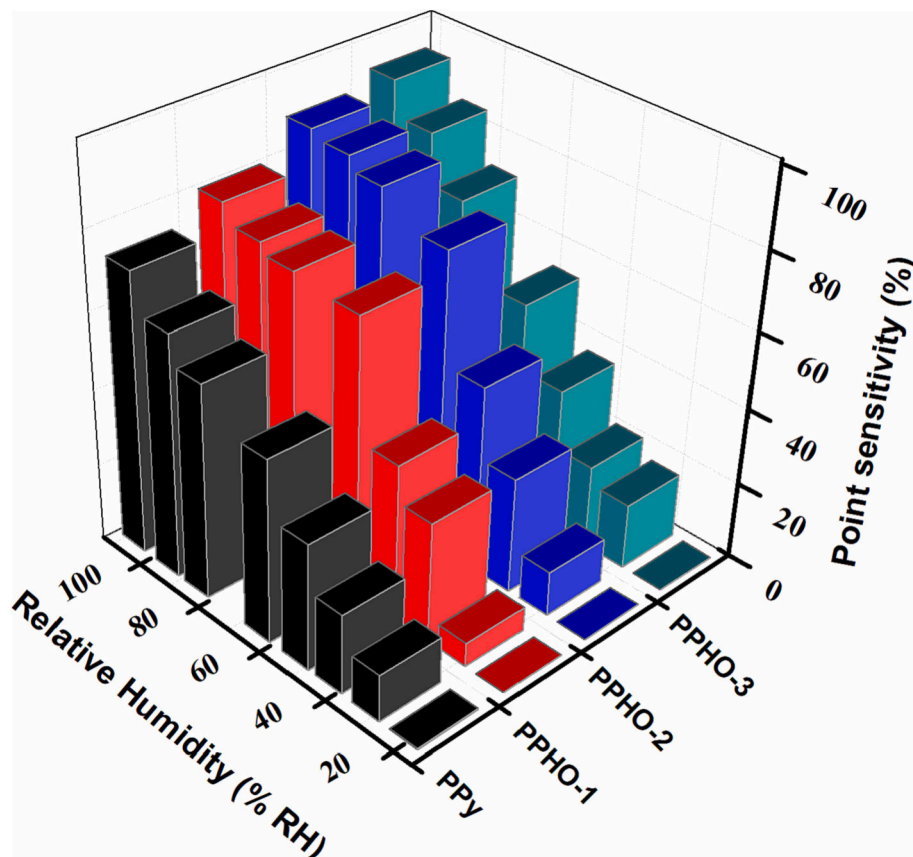


Fig. 9. Variation of point sensitivity of PPy and PPHO composites with relative humidity.

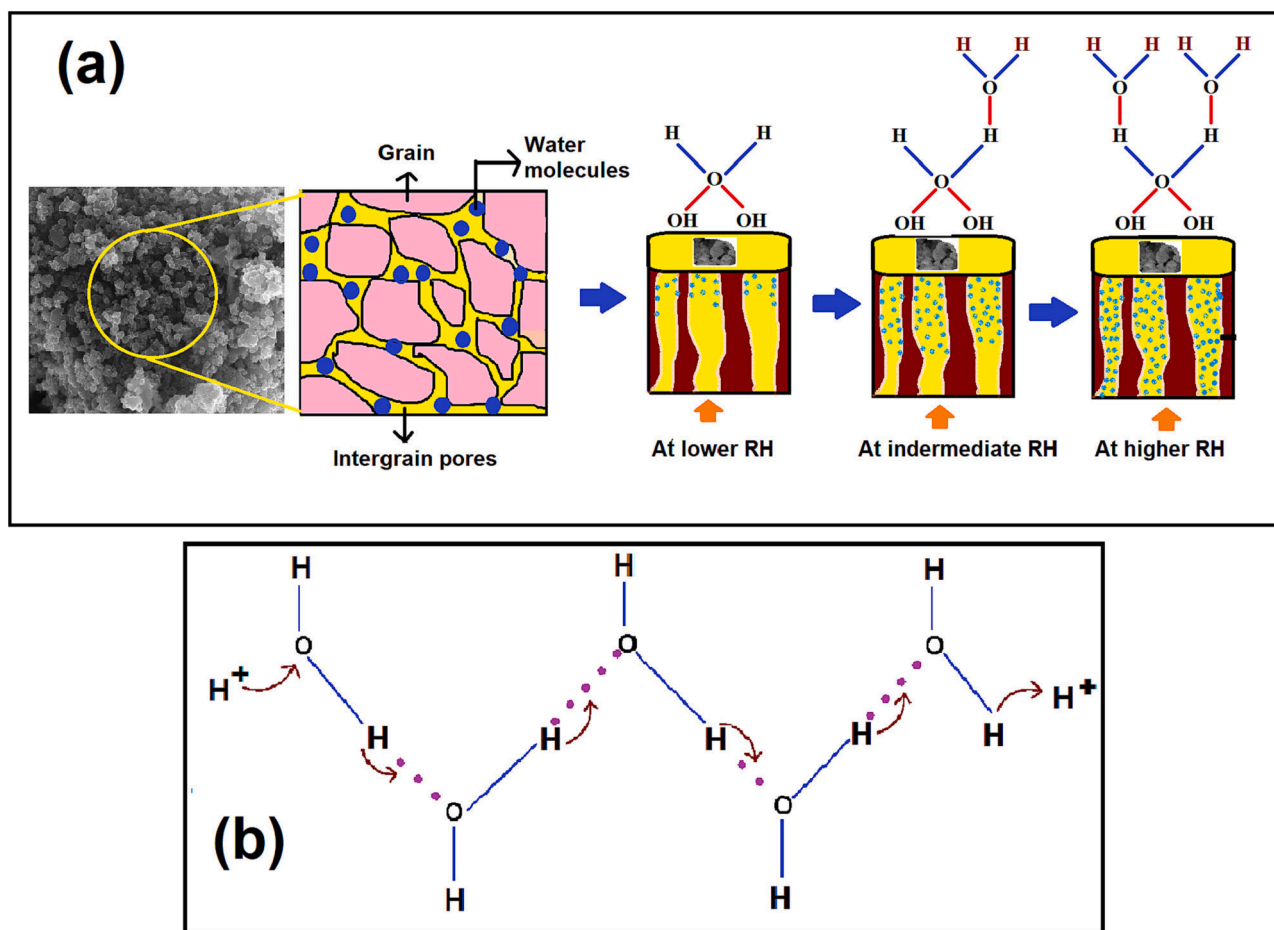


Fig. 10. Humidity sensing mechanism in PPHO-3 composite.

[28]. The prominent bands at 1366, 1566, 2971 and 3896 cm^{-1} correlate with vibrations of C-N, C-C, C-H and N-H stretching of the pyrrole ring individually. Fig. 5b shows the FTIR spectrum of holmium oxide, depicting its characteristic absorption band at 554 cm^{-1} , which signifies metal oxygen (Ho-O) stretching vibrations [29]. Fig. 5c shows the PPHO-3 composite with almost similar bands of PPy and Ho_2O_3 observed within wavenumber 500–4000 cm^{-1} which reveals the presence of the main constituents of the polymer and the holmium oxide whereas, incorporation of holmium oxide in polypyrrole results in a slight shift of FTIR bands towards lower wave numbers. These shifts are correlated to formation of the composite and modifications in molecular order of the polymer chains, leading to the formation of a capillary network and thereby an enhancement in the water adsorption.

3.4. TEM analysis

Fig. 6 shows the TEM image of the PPHO-3 composite. It is seen that the dark region represents holmium oxide and the light region represents polypyrrole. It is evident from the figure that the holmium oxide particles are well distributed in the polypyrrole matrix. This kind of stuffing of the filling material into the network of polymer chains forming small clusters of grains has been reported in our recent literature [30]. Small clusters of grains so formed in the composite are helpful in framing the capillary network for the water condensation [31], which is useful for designing humidity sensors.

3.5. Raman spectra

The Raman spectra of PPy, Ho_2O_3 and PPHO-3 composite can be seen

in Fig. 7. The Raman spectrum of PPy as seen in Fig. 7a shows the bands at 1340 and 1573 cm^{-1} for antisymmetric C-N⁺ as well as C = C stretching vibrations of quinoid rings, respectively. Fig. 7b shows the Raman bands for Ho_2O_3 . The characteristic Raman band of 381 cm^{-1} obtained for rare earth sesquioxides of the C-type is allocated to the $A_g + T_g$ mode. The highest intensified point can be regarded as massive polarizability change that occurred during the vibration. However, the bands at 335, 477, and 594 cm^{-1} are designated to $E_g + T_g$, T_g , and T_g respectively [5]. Fig. 7c shows the Raman spectrum of the PPHO-3 composite, showing the polypyrrole bands with slight shifts and the holmium oxide bands suppressed, confirming the strong interaction between polypyrrole and holmium oxide.

3.6. Humidity sensing studies

The variation of resistivity of PPy and PPHO composite pertaining to change in relative humidity environments has been plotted and can be seen in Fig. 8. It can be noticed from the figure that initially, when PPy and the composite were brought separately to a lower humidity environment, say 11% RH, the proportionate resistivity was observed to be high. Accordingly, when the composite brought to higher relative humidity of 97% RH, the corresponding resistivity was found to be less due to the adsorption of water molecules on the composite surface, leading to decrease in resistivity and an increase in its conductivity. This kind of change in resistivity of the composite with relative humidity manifests a preferable linear tie-up. So, the real sensitivity, linearity, and limit of detection (LOD) of PPy and the composites were computed, and results are depicted in Table 1. It can be observed from the table that PPHO-3 composite exhibits good real sensitivity (27.72 $\text{M}\Omega \cdot \text{cm} / \% \text{RH}$), LOD

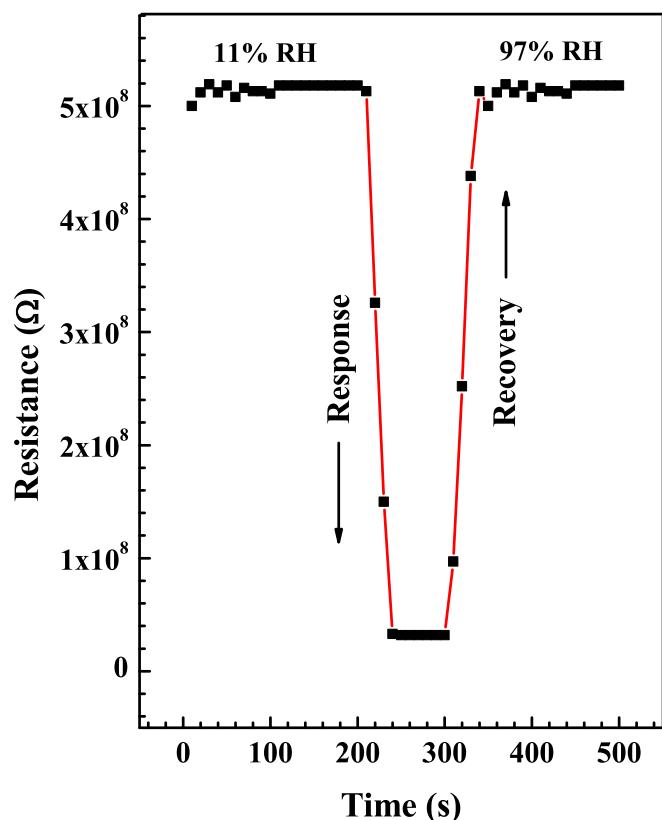


Fig. 11. Response and recovery plots of PPHO-3 composite.

Table 2

Humidity sensor measurements of various polymer composites prepared by chemical polymerization technique.

Composite	Sensing Response time (s)	Sensing Recovery time (s)	Sensing range (%RH)	References
PANI/Pr ₂ O ₃	377	453	15–95	[33]
PPy/ZnO	180	60	11–97	[34]
PANI/Cr ₂ O ₃	134	213	20–95	[35]
PANI/TiO ₂	95	122	11–97	[36]
PPy/WS ₂	52	58	11–97	[37]
PANI/Y ₂ O ₃	50	80	11–97	[36]
PANI/CuO	40	70	10–95	[38]
PPy/TiO ₂	40	20	30–84	[39]
PPHO-3	30	40	11–97	Present work

(4.98 % RH) and linearity (0.9981) as compared to that of PPy and other composites, which is a considerable result for the fabrication of an efficient humidity sensor. Further, to examine the humidity sensing efficiency of PPy and the composites, point sensitivity was computed by recording the fraction of the relative resistivity variation and the resistivity at the lower relative humidity contrast, and the related plot is shown in Fig. 9. It is seen from the figure that the point sensitivity of polypyrrole at 97% RH was found to be 73%, despite the fact that for a PPHO-3 composite, it was observed to be 93%. Such high point sensitivity is due to the incorporation of holmium oxide in the matrix of polypyrrole, which has resulted in more porosity in the composite and thereby it has stepped up the water adsorption process through capillary condensation mechanism. It is seen from Fig. 8 that for PPHO-3 composite, resistivity has decreased with the upsurge in relative humidity, as the water molecules present in the polymer composite serve as electron donors [32]. When the adsorption occurs on the exterior of the composite, the molecules get dissociated into H⁺ and OH⁻ ions. These OH⁻

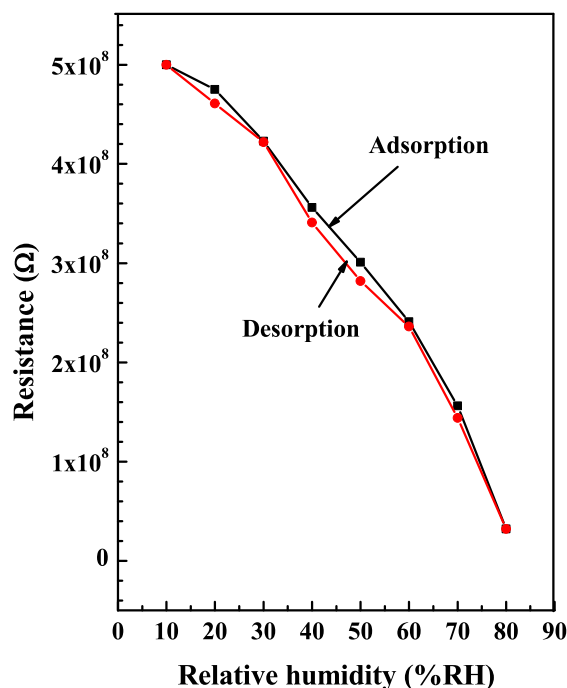


Fig. 12. Humidity hysteresis curve of PPHO-3 composite.

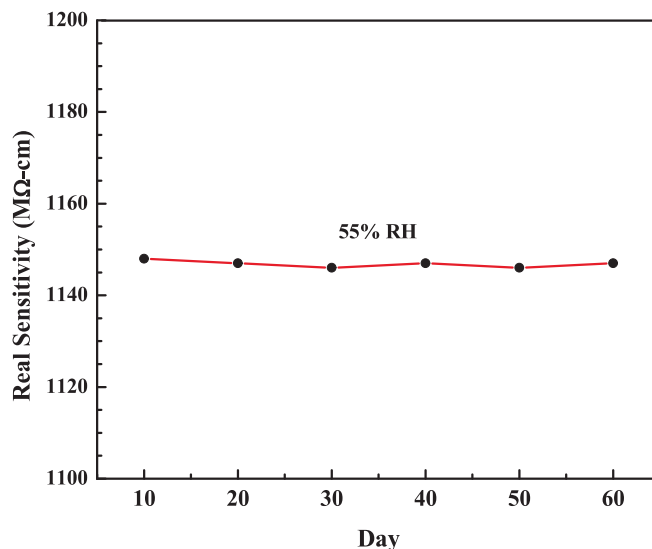


Fig. 13. Sensing stability of PPHO-3 composite.

ions are waged by Ho⁺³ ions in the composite. At the lower relative humidity environments, adsorption occurs at lower rate, thereby consequently hampered the proton transfer mechanism resulting in lower electrical conduction of the polymer composite [25]. However, environments with higher relative humidity, adsorption occurs at higher rate, promoting the proton transfer mechanism, and an essential increase in electrical conduction in the polymer composite. The overall mechanism of sensing in the PPHO-3 composite is depicted in Fig. 10. Capillary condensation through pores and the humidity sensing mechanism is shown in Fig. 10a and the Grotthuss reaction is shown in Fig. 10b.

Response and recovery curves of the PPHO-3 composite are shown in Fig. 11. Response and recovery times play a significant role in the design and development of an efficient sensor. The PPHO-3 composite was initially exposed to a lower humidity environment of 11% RH and then

instantly transferred to a higher humidity environment of 97% RH, resulting in a composite response time of 30 s. Again, the composite was brought back to 11% RH from 97% RH, the recovery time of the composite was found to be 40 s. So, response time is quicker than the recovery time. This quick response time is due to the adsorption of water molecules on the porous surface of the composite, during which heat is liberated and hence it is an exothermic reaction. On the other hand, recovery time is attributed to the desorption of water molecules, during which heat is absorbed and hence it is an endothermic reaction. The response time, recovery time, and sensing range of the various polymer composites found in the literature can be seen in Table.2, and compared with PPy/Ho₂O₃-50% composite.

The humidity hysteresis plot for PPHO-3 composite is shown in Fig. 12. As prepared polymer composite was exposed to various relative humidity environments, the corresponding impedance values were noted. At first, the PPHO-3 composite was taken into the various humidity jars in ascending order from lower relative humidity environments to higher humidity environments ranging from 11 to 97% RH, during which water adsorption occurs and the respective adsorption curve was plotted. After this, the composite was brought back to the humidity jars in descending order from a higher humidity environment to a lower humidity environment, composing of relative humidity ranging from 97% RH to 11% RH and the corresponding desorption curve was plotted [40]. From Fig. 12 it is evident that the water desorption happens to be slower than the adsorption rate.

The humidity sensing stability of PPHO-3 composite is depicted in Fig. 13. Stability plays a vital role in the development of an efficient sensor. To confirm the stability of the composite, we have recorded the real sensitivity of the sample for every ten days at 55% RH, and it was found to be almost constant, as can be seen from Fig. 13. This kind of stable performance in humidity sensing turns out to be an attractive and essential characteristic feature in device fabrication. At the end, we conclude that the composite PPHO-3 has been found to be a competent material in the design of an efficient, low-cost, and room-temperature operable humidity sensor compared to the other cost-effective metal oxides like CuO [41], ZnO [42], and VO₂ [43], composited with conducting polymers as humidity sensing materials, as shown in Table 2.

4. Conclusions

PPHO composites were prepared using the chemical polymerization method with 10, 30 and 50 wt% of holmium oxide in a PPy matrix. Composites were characterized by various influential techniques to confirm the formation of the composite. The PPHO-3 composite exhibited superior humidity sensing characteristics. The composite manifests a response time of 30 s and a recovery time of 40 s with a sensing response of 93% in the RH range of 11–97% RH. The composite exhibited an appreciable LOD of 4.98 %RH and a good stability in humidity sensing performance. All these results encouraged the researcher to design an efficient humidity sensor operable at room temperature.

Declaration of Competing Interest

The authors declare that they have no known competing financial interests or personal relationships that could have appeared to influence the work reported in this paper.

Data availability

Data will be made available on request.

Acknowledgements

All the authors acknowledge the support received from JNCASR, Bengaluru for providing the experimental facilities for various characterization techniques.

References

- [1] Q. Zhao, Y. Zhang, Z. Duan, S. Wang, C. Liu, Y. Jiang, A review on Ti₃C₂Tx-based nanomaterials: synthesis and applications in gas and humidity sensors, *Rare Met.* (2020), <https://doi.org/10.1007/s12598-020-01602-2>.
- [2] L.B. Gunjal, S. Manjunatha, B. Chethan, N.M. Nagabhushana, Y.T. Ravikiran, T. Machappa, S. Thomas, Humidity sensing performance of polyaniline-neodymium oxide composites, *MRS Commun XX* (2023) 1–8, <https://doi.org/10.1557/s43579-023-00336-3>.
- [3] S. Manjunatha, T. Machappa, Y.T. Ravikiran, B. Chethan, A. Sunilkumar, Polyaniline based stable humidity sensor operable at room temperature, *Phys. B Condens. Matter* 561 (2019) 170–178, <https://doi.org/10.1016/j.physb.2019.02.063>.
- [4] K. Vinay, M. Revanasiddappa, S. Manjunatha, K. Shivakumar, Y.T. Ravikiran, Room temperature humidity sensing behaviour of silver decorated polyaniline composite Room temperature humidity sensing behaviour of silver decorated polyaniline composite, *Mater. Res. Express* 6 (2019), 104003.
- [5] S. Manjunatha, A. Sunilkumar, Y.T. Ravikiran, T. Machappa, Effect of holmium oxide on impedance and dielectric behavior of polyaniline-holmium oxide composites, *J. Mater. Sci. Mater. Electron.* 30 (2019) 10332–10341, <https://doi.org/10.1007/s10854-019-01371-4>.
- [6] K. Kaviyarasu, C.M. Magdalane, D. Jayakumar, Y. Samson, A.K.H. Bashir, M. Maaza, D. Letsholathebe, A. Hossam, J. Kennedy, Journal of King Saud University – Science High performance of pyrochlore like Sm₂Ti₂O₇ heterojunction photocatalyst for efficient degradation of rhodamine-B dye with waste water under visible light irradiation, *J. King Saud Univ. - Sci.* 32 (2020) 1516–1522, <https://doi.org/10.1016/j.jksus.2019.12.006>.
- [7] B. Sathyaseelan, E. Manikandan, I. Baskaran, K. Senthilnathan, K. Sivakumar, M. K. Moodley, R. Lachumananandasivam, M. Maaza, Studies on structural and optical properties of ZrO₂ nanopowder for opto-electronic applications, *J. Alloys Compd.* 694 (2017) 556–559, <https://doi.org/10.1016/j.jallcom.2016.10.002>.
- [8] S. Manjunatha, L.S. Panchakarla, K. Biswas, C.N.R. Rao, Nanorods and nanofilms of ZnO generated at the liquid–liquid interface, *Inorganica Chim. Acta* 363 (2010) 2125–2130, <https://doi.org/10.1016/j.ica.2010.02.025>.
- [9] I.G. Madida, A. Simo, B. Sone, A. Maity, J.B. Kana Kana, A. Gibaud, G. Merad, F. T. Thema, M. Maaza, Submicronic VO₂-PVP composites coatings for smart windows applications and solar heat management, *Sol. Energy* 107 (2014) 758–769, <https://doi.org/10.1016/j.solener.2014.06.025>.
- [10] S. Manjunatha, S. Rajesh, P. Vishnoi, C.N.R. Rao, Reaction with organic halides as a general method for the covalent functionalization of nanosheets of 2D chalcogenides and related materials, *J. Mater. Res.* 32 (2017) 2984–2992, <https://doi.org/10.1557/jmr.2017.224>.
- [11] P. Vishnoi, S. Rajesh, S. Manjunatha, A. Bandyopadhyay, M. Barua, S.K. Pati, C.N. Rao, Doping phosphorene with holes and electrons through molecular charge transfer, *ChemPhysChem* 18 (2017) 2985–2989, <https://doi.org/10.1002/cphc.201700789>.
- [12] S. Manjunatha, R. Megha, B. Chethan, M. Prashantkumar, Y.T. Ravikiran, T. Machappa, Structural and AC Electrical Properties of Tantalum Disulfide Embedded Polyaniline Composites, *J. Mater. Eng. Perform.* 30 (2021) 1885–1894, <https://doi.org/10.1007/s11665-021-05526-5>.
- [13] S. Manjunatha, Y.T. Ravikiran, B. Chethan, H. Devendrappa, T. Machappa, Alternating current response studies on polyaniline-neodymium oxide composites, *AIP Conf. Proc.* 080009 (2020) 080009-1.
- [14] A. Sunilkumar, S. Manjunatha, Y.T. Ravikiran, H. Devendrappa, T. Machappa, AC frequency-dependent dielectric studies of polypyrrole composites, *AIP Conf. Proc.* 080005 (2020) 0800051–0800054.
- [15] B. Chethan, H.G.R. Prakash, Y.T. Ravikiran, S.C.V. Kumari, S. Manjunatha, S. Thomas, Humidity sensing performance of hybrid nanorods of polyaniline-Yttrium oxide composite prepared by mechanical mixing method, *Talanta* 215 (2020), 120906, <https://doi.org/10.1016/j.talanta.2020.120906>.
- [16] A. Sunilkumar, S. Manjunatha, T. Machappa, B. Chethan, Y.T. Ravikiran, A tungsten disulfide-polypyrrole composite-based humidity sensor at room temperature, *Bull. Mater. Sci.* 42 (2019) 271, <https://doi.org/10.1007/s12034-019-1955-5>.
- [17] A. Sunilkumar, S. Manjunatha, B. Chethan, Y.T. Ravikiran, T. Machappa, Polypyrrole-Tantalum Disulfide Composite: An Efficient Material for Fabrication of Room Temperature Operable Humidity Sensor, *Sens. Actuators A Phys.* (2019), <https://doi.org/10.1016/j.sna.2019.111593>.
- [18] S. Khamlich, B.D. Ngom, C.K. Kotsedi, K. Bouziane, E. Manikandan, M. Maaza, Morphological and crystallographic properties of rare earth oxides coatings deposited by double dual beam-PLD, *Surf. Rev. Lett.* 21 (2014) 1–11, <https://doi.org/10.1142/S0218625X14500012>.
- [19] M. Maaza, B.D. Ngom, M. Achouri, K. Manikandan, Functional nanostructured oxides, *Vacuum* 114 (2015) 172–187, <https://doi.org/10.1016/j.vacuum.2014.12.023>.
- [20] N. Ditlopo, N. Sintwa, S. Khamlich, E. Manikandan, K. Gnanasekaran, M. Henini, A. Gibaud, A. Krief, M. Maaza, From Khoi-San indigenous knowledge to bioengineered CeO₂ nanocrystals to exceptional UV-blocking green nanocosmetics, *Sci. Rep.* 12 (2022) 1–8, <https://doi.org/10.1038/s41598-022-06828-x>.
- [21] J. Zhu, X.-J. Shao, Z. Li, C.-H. Lin, C.-W.-Q. Wang, K. Jiao, J. Xu, H.-X. Pan, Y. Wu, Synthesis of Holmium-Oxide Nanoparticles for Near-Infrared Imaging and Dye-Photodegradation, *Molecules* 27 (2022) 3522.
- [22] K. Narasimharao, T.T. Ali, Influence of synthesis conditions on physico-chemical and photocatalytic properties of rare earth (Ho, Nd and Sm) oxides, *J. Mater. Res. Technol.* 9 (2020) 1819–1830, <https://doi.org/10.1016/j.jmrt.2019.12.014>.

- [23] S. Balabanov, S. Filofeev, M. Ivanov, A. Kaigorodov, D. Kuznetsov, D.J. Hu, J. Li, O. Palashov, D. Permin, E. Rostokina, I. Snetkov, Fabrication and characterizations of holmium oxide based magneto-optical ceramics, *Opt. Mater. (Amst)*. 101 (2020), 109741, <https://doi.org/10.1016/j.optmat.2020.109741>.
- [24] N. Suhada, M. Tahiruddin, R. Daik, B. Selangor, Synthesis and characterization of anionic surfactants doped polypyrrole 1, *Sch. Res. Libr.* 7 (2015) 159–162.
- [25] B. Chethan, Y.T. Ravikiran, S.C. Vijayakumari, H.G. Rajprakash, S. Thomas, Nickel Substituted Cadmium Ferrite as Room Temperature Operable Humidity Sensor, *Sens. Actuators A Phys.* 280 (2018) 466–474, <https://doi.org/10.1016/j.sna.2018.08.017>.
- [26] R. Megha, Y.T. Ravikiran, S.C.V. Kumari, H.G.R. Prakash, M. Revanasiddappa, S. Manjunatha, S.G. Dastager, S. Thomas, Structural and electrical characterization studies for ternary composite of polypyrrole, *J. Mater. Sci. Mater. Electron.* 31 (2020) 18400–18411, <https://doi.org/10.1007/s10854-020-04386-4>.
- [27] M.N. Abdusalamova, F.A. Makhmudov, E.N. Shairmardanov, I.D. Kovalev, P. V. Fursikov, I.I. Khodos, Y.M. Shulga, Structural features of nanocrystalline holmium oxide prepared by the thermal decomposition of organic precursors, *J. Alloys Compd.* 601 (2014) 31–37, <https://doi.org/10.1016/j.jallcom.2014.02.123>.
- [28] A. Sunilkumar, S. Manjunatha, Y.T. Ravikiran, M. Revanasiddappa, M. Prashantkumar, T. Machappa, AC conductivity and dielectric studies in polypyrrole wrapped tungsten disulphide composites, *Polym. Bull.* (2021), <https://doi.org/10.1007/s00289-021-03552-w>.
- [29] S. Mortazavi-Derazkola, S. Zinatloo-Ajabshir, M. Salavati-Niasari, Novel simple solvent-less preparation, characterization and degradation of the cationic dye over holmium oxide ceramic nanostructures, *Ceram. Int.* 41 (2015) 9593–9601, <https://doi.org/10.1016/j.ceramint.2015.04.021>.
- [30] R. Megha, Y.T. Ravikiran, S.C.V. Kumari, S. Thomas, Influence of n-type nickel ferrite in enhancing the AC conductivity of optimized polyaniline-nickel ferrite nanocomposite, *Appl. Phys. A*. 123 (2017) 245, <https://doi.org/10.1007/s00339-017-0866-9>.
- [31] B. Akbari, M.P. Tavandashiti, M. Zandrahimi, Particle size characterization of nanoparticles – a practical approach, *Iran. J. Mater. Sci. Eng.* 8 (2011) 48–56.
- [32] A.S. Pawbake, R.G. Waykar, D.J. Late, S.R. Jadkar, Highly transparent wafer-scale synthesis of crystalline WS₂ nanoparticle thin film for photodetector and humidity-Sensing applications, *ACS Appl. Mater. Interfaces*. 8 (2016) 3359–3365, <https://doi.org/10.1021/acsami.5b11325>.
- [33] S.C. Nagaraju, A.S. Roy, J.B.P. Kumar, K.R. Anilkumar, G. Ramagopal, Humidity sensing properties of surface modified polyaniline metal oxide oomposites, *J. Eng.* 2014 (2014) 925020-1.
- [34] R. Najjar, S. Nematdoust, A resistive-type humidity sensor based on polypyrrole and ZnO nanoparticles: hybrid polymers vis-a-vis nanocomposites, *RSC Adv.* 6 (2016) 112129–112139, <https://doi.org/10.1039/C6RA24002J>.
- [35] K.C. Sajjan, A.S. Roy, A. Parveen, S. Khasim, Analysis of DC and AC properties of a humidity sensor based on polyaniline – chromium oxide composites, *J. Mater. Sci. Mater. Electron.* 25 (2014) 1237–1243, <https://doi.org/10.1007/s10854-014-1715-7>.
- [36] R. Megha, Y.T. Ravikiran, B. Chethan, H.G. Raj Prakash, S.C. Vijaya Kumari, S. Thomas, Effect of mechanical mixing method of preparation of polyaniline-transition metal oxide composites on DC conductivity and humidity sensing response, *J. Mater. Sci. Mater. Electron.* (2018) 2–10, <https://doi.org/10.1007/s10854-018-8714-z>.
- [37] A. Sunilkumar, S. Manjunatha, T. Machappa, B. Chethan, Y.T. Ravikiran, A tungsten disulphide – polypyrrole composite-based humidity, *Bull. Mater. Sci.* 271 (2019) 2–6, <https://doi.org/10.1007/s12034-019-1955-5>.
- [38] P. Singh, S.K. Shukla, Structurally optimized cupric oxide/polyaniline nanocomposites for efficient humidity sensing, *Surf. Interfaces* 18 (2020), 100410, <https://doi.org/10.1016/j.surf.2019.100410>.
- [39] P. Su, L. Huang, Humidity sensors based on TiO₂ nanoparticles / polypyrrole composite thin films, *Sensors Actuators B Chem.* 123 (2007) 501–507, <https://doi.org/10.1016/j.snb.2006.09.052>.
- [40] V.R. Khadse, S. Thakur, K.R. Patil, P. Patil, Humidity-sensing studies of cerium oxide nanoparticles synthesized by non-isothermal precipitation, *Sens. Actuators B Chem.* 203 (2014) 229–238, <https://doi.org/10.1016/j.snb.2014.06.107>.
- [41] S.S. Rathnakumar, K. Nolithando, A.J. Kulandaiswamy, J.B.B. Rayappan, K. Kasinathan, J. Kennedy, M. Maaza, Stalling behaviour of chloride ions : A non-enzymatic electrochemical detection of α -Endosulfan using CuO interface, *Sensors Actuators B Chem.* 293 (2019) 100–106, <https://doi.org/10.1016/j.snb.2019.04.141>.
- [42] M. Khenfouch, M. Baïtoul, M. Maaza, White photoluminescence from a grown ZnO nanorods /graphene hybrid nanostructure, *Opt. Mater. (Amst)* 34 (2012) 1320–1326, <https://doi.org/10.1016/j.optmat.2012.02.005>.
- [43] M. Maaza, D. Hamidi, A. Simo, T. Kerdja, A.K. Chaudhary, J.B.K. Kana, Optical limiting in pulsed laser deposited VO₂ nanostructures, *Opt. Commun.* 285 (2012) 1190–1193, <https://doi.org/10.1016/j.optcom.2011.09.057>.